THE PHYSICAL REVIEW

VOLUME 89 Second Series NUMBER 1

JANUARY 1, 1953

Published for the

AMERICAN PHYSICAL SOCIETY

by the

AMERICAN INSTITUTE OF PHYSICS

Incorporated

LANCASTER, PA., AND NEW YORK, N. Y.

Information for Contributors

Manuscripts

Send manuscripts to [illegible], Brookhaven National Laboratory, [illegible], Long Island, New York.

Each article submitted will in general consist of (a) textual material, i.e., all material which is to be set in type, and (b) [illegible] photographs from which zinc etchings or copper halftones will be made. Textual material will consist of an abstract, the body of the paper, tabular material, references, and figure captions. All of this material must be in [illegible] typewritten (except mathematical expressions) double spaced with wide margins (for editorial notations to the printer) on a durable, white paper, preferably letter size. The original copy, not the carbon, should be submitted.

For general style, spelling, punctuation, and form, recent issues of this journal should be consulted.

The prime requisite is that the copy shall be clear to the typesetter, who is neither a physicist nor a mathematician.

Abstracts

An abstract must accompany each article. It should be adequate as an [illegible] or a summary. As an index, it should [illegible] all subjects, major and minor, concerning which [illegible] information is presented. As a summary, it should give the conclusions of the article [illegible] essential results of general interest.

Mathematical Expressions

All but the simplest mathematical expressions should be carefully printed in [illegible]. Be sure to distinguish between capital [illegible] letters. Indicate clearly superscripts [illegible] subscripts by inverted carets and carets, [illegible]. Avoid complicated superscripts and [illegible]. Avoid repetition of a complicated [illegible] by representing it by some convenient [illegible] the margin Greek letters and [illegible] symbols. Use fractional exponents [illegible] radical signs. Use the solidus (/) for fractions [illegible] wherever its use will save vertical space.

References

References should appear [illegible] numbered consecutively, and arranged [illegible]

[1] A. B. Smith, *Phys. Rev.* 43, [illegible].

[2] H. Lamb, *Hydrodynamics* (Cambridge University Press, Cambridge, England, 1940), [illegible] pp. 573, 643.

Tables

All but the simplest tabular material should be organized in tabular form rather than as a part of the running text. Tables may be typewritten on sheets separate from the manuscript with indications in the margin of the manuscript where the table is to be inserted. Each table must have a caption which will make the data in the table intelligible without reference to the text. Avoid complicated column headings; if necessary, use symbols which are explained in the table caption.

Figures

Wherever possible figures should be planned for the width of a column of the *Physical Review* (3 inches). A convenient reduction ratio is about 2:1 or 3:1. The original drawings or photographs should therefore be in general about 6 to 9 inches wide and the lettering and symbols should be large enough on the original that when reduced they shall not be less than about $\frac{1}{16}$ in. (~2 mm). If the reduction is 3:1, the original lettering should be not less than $\frac{1}{8}$ in. high.

The process of making zinc etchings or copper halftones is a black and white photographic one. Therefore line drawings must be in [illegible] ink on white paper or tracing cloth. Coordinate paper is not desirable but if used must be blue lined and the coordinate lines which are to show must be inked over.

Photographs should have maximum black and white contrast.

Plan figures to use space efficiently. Avoid wasting space, particularly at the top or bottom.

Identify on the black or other suitable place each original drawing or photograph with the author's name and the figure number. Figures should be numbered consecutively and their approximate position indicated in the margin of the running text. Figure captions should be typed and included with the manuscript (not as part of the figure).

Avoid round and oval photographs.

Alterations

Take great care that each manuscript is typographically accurate. A limited number of alterations in proof are unavoidable, but the cost of making extensive alterations after the article has been set in type will be charged to the author.

Proof and all correspondence concerning proof in the process of publication should be addressed to the Publication Manager, American Institute of Physics, 57 East 55 Street, New York 22, New York.

THE PHYSICAL REVIEW

A journal of experimental and theoretical physics established by E. L. Nichols in 1893

VOLUME 89

Second Series

JANUARY 1–MARCH 15, 1953

Published for the

AMERICAN PHYSICAL SOCIETY

by the

AMERICAN INSTITUTE OF PHYSICS
Incorporated

THE PHYSICAL REVIEW

A journal of experimental and theoretical physics established by E. L. Nichols in 1893

Published by the American Institute of Physics for the

AMERICAN PHYSICAL SOCIETY

Officers

President

J. H. VAN VLECK
Harvard University
Cambridge, Massachusetts

Vice-President

ENRICO FERMI
Institute for Nuclear Studies
University of Chicago
Chicago 37, Illinois

Secretary

K. K. DARROW
Bell Telephone Laboratories
Office:
Columbia University
New York 27, New York

Treasurer

G. B. PEGRAM
Columbia University
New York 27, New York

Local Secretary for the Pacific Coast

J. KAPLAN
University of California at Los Angeles
Los Angeles, California

Managing Editor

S. A. GOUDSMIT
Brookhaven National Laboratory
Upton, Long Island
New York

BOARD OF EDITORS

Editor

S. A. GOUDSMIT

Assistant Editor

S. PASTERNACK

Associate Editors

HARVEY BROOKS
R. F. CHRISTY
C. L. CRITCHFIELD
M. DEUTSCH
T. H. JOHNSON
BRUNO ROSSI
M. GOLDHABER
R. HOFSTADTER
A. W. LAWSON
A. PAIS
R. SERBER
C. H. TOWNES
W. P. ALLIS
F. G. BRICKWEDDE
W. B. FRETTER
CONYERS HERRING
H. W. LEVERENZ
ARNOLD NORDSIECK

Manuscripts for publication should be submitted to S. A. GOUDSMIT, Brookhaven National Laboratory, Upton, Long Island, New York. The authors' institutions are requested to pay a publication charge of $15 per page which, if honored, entitles them to 100 free reprints. Instructions will be sent with galley proofs.

Proof and all correspondence concerning papers in the process of publication should be addressed to the Publication Manager, American Institute of Physics, 57 East 55 Street, New York 22, New York.

Subscription Price

United States and Canada $30.00
Elsewhere $32.00

Back Numbers [1]

Yearly back number rate when complete year is available:
Prior to 1949: **$25.00**
Thereafter: **$33.00**
Single copies: **$3.00** each, prior to July, 1929;
$1.50 each, July, 1929–December, 1941;
$3.00 each, January, 1942–December, 1946;
$1.50 each, thereafter.
General index, 1893–1920: **$4.00**.

Subscriptions, renewals, and orders for back numbers should be addressed to the American Institute of Physics, 57 East 55 Street, New York 22, New York.

Changes of address in the case of members of the American Physical Society should be addressed to the Treasurer; in the case of other subscribers to the American Institute of Physics.

[1] For Series I inquire of Physics Department, Cornell University, Ithaca, New York.

The Physical Review is published semi-monthly at Prince and Lemon Streets, Lancaster, Pennsylvania.

Entered as second-class matter March 6, 1947, at the Post Office at Lancaster, Pennsylvania, under the Act of March 3, 1879.

Acceptance for mailing at special rate of postage provided for in paragraph (d-2), section 34.40, P. L. & R. of 1948, authorized January 27, 1933.

THE
PHYSICAL REVIEW

A journal of experimental and theoretical physics established by E. L. Nichols in 1893

SECOND SERIES, VOL. 89, NO. 1 JANUARY 1, 1953

Physical Analysis of Be and C Disintegration Induced by 330-Mev Protons

WALTER H. BARKAS, *Radiation Laboratory, University of California, Berkeley, California*

AND

HELGE TYREN, *Radiation Laboratory, University of California, Berkeley, California and Gustaf Werner Institute for Nuclear Chemistry, University of Uppsala, Uppsala, Sweden*

(Received September 24, 1952)

The disintegration products of carbon and beryllium emerging from thin targets bombarded by an internal cyclotron beam of 330-Mev protons have been studied. The magnetic field of the cyclotron is employed for momentum analysis and nuclear track plates for detection and range analysis. On plotting radius of curvature *versus* range, various nuclear species are found to fall on identifiable loci. The relative abundances of the products and their momentum spectra are obtained. Hydrogen, helium, lithium, and boron products have been found and their abundances tabulated. Alpha-particles prove to be the most important charged particle product. Beryllium yields significantly more tritium than carbon. Some of the heavy products are found with very high momenta.

INTRODUCTION

SUBSTANTIAL progress has been made in understanding high energy nuclear disintegrations by analyzing the radioactive products remaining in the target after bombardment. Nevertheless, many questions remain unanswered if one is limited to this method for the study of such processes. We have undertaken to develop another method of analysis which provides wholly new information regarding the identifications, populations, momentum distributions, and angular distributions of disintegration products, including those which are not radioactive. Early results[1] obtained on the disintegration products of carbon bombarded by protons were encouraging. The present paper reports a more comprehensive experiment which confirms the previous study and extends it to other momentum intervals and to a comparison element. While a study of these light element reactions appeared to be the most tractable problem at the beginning of the program, we have found that the methods are generally useful, and work is now in progress on a number of other target elements with proton, deuteron, and alpha-particle beams of various energies. Angular distributions of disintegration products, and, in some cases, absolute cross sections are also obtained and will be reported in subsequent publications.

[1] W. H. Barkas and J. K. Bowker, Phys. Rev. **87**, 205 (1952).

EXPERIMENTAL ARRANGEMENT

The magnetic field of the 184-inch cyclotron provides a means for analyzing the momentum of nuclear disintegration products emitted from an internal target. Nuclear track emulsion is employed to detect the products and at the same time enables one to measure their ranges. Measurements of the position and direction of a track also suffice for calculation of the radius of curvature of the particle orbit. As supplementary information, the ionization of the track is estimated in a manner to be explained later.

In the present experiment, ribbon targets of Be (8.7 mg/cm^2) and polystyrene (2.9 mg/cm^2) about 2 mm in width were exposed to the circulating beam of protons at a radius of 79 inches. The ribbon extended parallel to the magnetic field, and its smallest dimension was traversed by the protons. The hydrogen in the polystyrene plays no part in the present experiment, and the targets are sufficiently thin that the measured momentum spectrum of no important product is much affected by the target thickness.

The disintegration products, spiraling slightly downward from the forward direction, are collected on plates placed emulsion upward in a plane parallel to the median plane of the cyclotron and 5½ inches below it. The beam is clipped radially by a carbon block on the opposite side of the proton orbit at a radius two inches

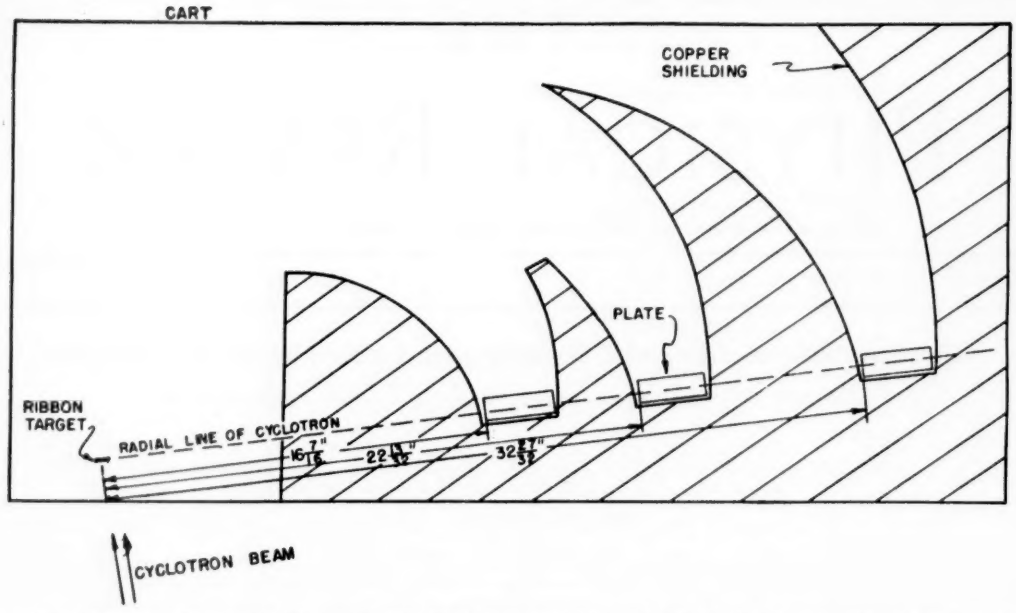

FIG. 1. Plan view of apparatus. The cart loaded with the copper shielding and with the plates in the positions shown enters the cyclotron vacuum tank through an air lock. The cart is low enough to be entirely under the circulating beam; only the ribbon target intercepts the beam. The disintegration products spiral down slightly and enter the plates through the surface of the emulsion. Blocks of wolfram are placed as roofs over the plates to reduce stray light and background particle tracks.

greater than the target radius. Vertical oscillations are also clipped so that the beam is largely confined to the height of $\frac{3}{4}$ inch as determined by radio-autographs of the target. Shielding is placed to protect the plates against stray particles of the main beam and against neutrons from the target. Channels are built in the shielding so as to permit fragments leaving the target with an azimuth angle of $0\pm10°$ to the beam to reach the plates, which are placed on the line extending from the center of the cyclotron to the target. Three 1-in.×3-in. plates are placed at nominal distances of 18 in., 24 in., and $34\frac{1}{2}$ in. from the target so that protons reaching them from the target will have energies of approximately 5, 10, and 20 Mev. Ilford C-2 emulsion of moderate sensitivity is used so as to obtain some ionization discrimination while yet being able to see the higher energy protons in the emulsion. The whole apparatus is mounted on a cart which enters the cyclotron tank through an air-lock, the dimensions of which limits the momentum interval studied. The nuclear fragments enter the emulsion through the surface at a small angle. Figure 1 is a schematic diagram showing the relationship of the target, detecting plates, and shielding.

METHOD OF ANALYSIS

The position, range, and azimuth angle of each track on a measured area of the plate are recorded. In addition the number of gaps, where developed grains are missing, is counted in each track. Only tracks entering the emulsion through the surface with an azimuth angle of $180°\pm10°$ are accepted. The calculated radius of curvature is then insensitive to small errors in the azimuth angle, which could be measured to $\pm1°$. A "radius of curvature" of each orbit is calculated allowing for the pitch of the spiral. The geometrical quantity calculated is equal to $pc/Z'eB$, where p is the total momentum, Z' the number of units of charge carried by the fragment when it is bent in the magnetic field, B is the effective magnetic induction in gauss, and e/c the electronic charge in emu. Using these data, the radius of curvature is plotted against the range, one track determining a point. In such a diagram the points of each nuclear type fall on a characteristic locus. The identification of each locus is made using curves which we have constructed relating radius of curvature and range for the various disintegration products. To do this, we first verified the existing[2] range-energy relations for hydrogen and helium isotopes using readily identified tracks in our plates. From light element targets, we also find numerous "hammer" tracks which are recognized as tracks of Li^8 and B^8. From these, range energy curves for all Li and B isotopes were constructed. The extension of the range arising from electron pick-up by slow ions is evaluated empirically,[3] and good estimates of the range energy relations for other light elements may then be obtained by interpolation and extrapolation. It was observed, as anticipated, that both Li^8 and B^8 splinters

[2] J. J. Wilkins, Atomic Energy Research Establishment Report AERE *G/R* 664 (Harwell, 1951) (unpublished).
[3] W. H. Barkas (to be published).

of low velocity fell on more than one locus, each locus corresponding to the charge carried by the ion when it was bent in the magnetic field. Appropriate[4] correction for the non-uniformity of the magnetic field was made in obtaining the range energy curves. Some loci, notably those of He^3 and H^2, overlap. Identification of such tracks are then made by the gap counts. If G is the number of gaps in a residual range R, and M the ionic atomic weight, then $G/M=f(R/M)$, where $f(R/M)$ is the same function of R/M for all isotopes of an element. Curves of $f(R/M)$, prepared from tracks of other isotopes which had been identified, provided the means for separating completely the He^3 from the H^2.

Background tracks, which arise chiefly from neutron collisions, have not been a serious problem. Selection of tracks which enter the surface of the emulsion in the proper direction serves almost completely to eliminate extraneous tracks, which in any case do not fall on definite loci. This statement must be qualified for some short tracks which we have as yet been unable to analyze. They are supposed to be fragments carrying reduced charges as well as heavy nuclei. In this region the background contamination is unknown.

Reduction of the data from plates at different distances from the target requires some analysis. The conversion of the observed number of tracks of a given species per unit area per unit interval of azimuth angle to the number per unit solid angle per unit radius of curvature interval leaving the target is accomplished in multiplying by the Jacobian of the transformation. The special case of 180° bending here employed is particularly simple and the Jacobian reduces to $2h[1+(\pi r/h)^2]$, where h is the distance of the plate from the median plane, and r is the radius of the orbit projected on the median plane. This transformation has been carried out so that the data from the different plates may be compared. The radius of curvature, as here employed, is $pc/Z'eB$. The momentum corresponding to a given radius of curvature therefore depends on Z'.

RESULTS

The data obtained are presented in Table I. It is normalized so that the same total number of fragments per unit solid angle are considered for carbon as for beryllium. The data from Be and C were plotted on a single diagram in finding the loci. Populations are tabulated only for recognizable loci, and the rest of the tracks are lumped as unclassified nuclei and background. We could not separate Li^6 and Be^7.

[4] W. H. Barkas, Phys. Rev. **78**, 90 (1950).

TABLE I. Normalized number of tracks per unit solid angle per unit radius of curvature interval in percent. The actual numbers of tracks counted are listed below the percentages in each case. Where the number is uncertain because of poor resolution, the number is bracketed. The magnetic field intensity was 14.3 kilogauss.

Radius of curvature interval	Beryllium products			Carbon products		
	22–24 cm	29.5–31.5 cm	43–45 cm	22–24 cm	29.5–31.5 cm	43–45 cm
H^1	11.6 121	10.0 90	5.9 84	13.1 106	8.8 72	6.7 52
H^2	4.3 45	3.7 34	3.7 52	2.5 20	2.9 24	3.5 27
H^3	4.5 47	4.0 37	3.3 48	1.7 (14)	1.6 13	1.8 15
He^3	4.6 48	4.5 42	1.6 23	3.5 28	3.4 28	2.2 17
He^4	14.0 146	15.4 143	4.1 58	17.1 137	16.9 143	6.2 49
Li^6, Be^7	0.8 (8)	1.2 11	0.2 3	0.9 (7)	0.9 8	0.1 1
Li^7	0.3 (3)	0.3 3	0.3 4	0.8 (6)	0.1 1	0.8 6
Li^8					0.1 1	
B^8						0.1 1
Unclassified products and background	0.7 7	0.7 6	0.6 9	2.1 17	1.2 10	1.1 9

The data reveal the following features: (a) A high percentage of the splinters are alpha-particles, suggesting a high degree of correlation between particles making up alpha-particle groups within these nuclei. The effect seems somewhat more pronounced in C than in Be. (b) From beryllium a significant excess of tritium is found which may be ascribed to an effect of the "extra" neutron in Be^9. (c) The momentum spectra of large nuclear fragments extend out to remarkably high values. Lithium products are found with more than $\frac{3}{8}$ of the momentum carried by the bombarding proton and the B^8 track listed carries the full momentum of the proton. (The identification of the B^8 is certain because it forms a hammer, and its range is as calculated.) (d) No new nuclear species were identified.

We wish to acknowledge the invaluable assistance of Miss Esther Jacobson in connection with the microscope measurements, and of Mr. Robert Deutsch and Mr. Wallace Conover in the construction of the apparatus.

PHYSICAL REVIEW VOLUME 89, NUMBER 1 JANUARY 1, 1953

Classical and Quantum Field Theories in the Lagrangian Formalism*

PETER G. BERGMANN AND RALPH SCHILLER†
Department of Physics, Syracuse University, Syracuse, New York
(Received August 12, 1952)

In this paper, we have first examined the relationship between the transformation properties of a (nonquantum) covariant field theory and its constraints, generating functionals, conservation laws, and "superpotentials" purely within the Lagrangian formalism and indicated the relevance of these quantities for the problem of motion of particles (singularities) in the field. This discussion includes a presentation of actual methods of computation of these important quantities suitable for a very wide class of theories. In the second part of the paper, we have discussed the probable structure of a quantum covariant field theory, both in the Hamiltonian and in the Lagrangian formalism. In the Hamiltonian formalism, it is suggested that those field variables canonically conjugate to constraints are not observables in the physical sense nor operators in Hilbert space, and that the states of a system which alone can be regarded as Hilbert vectors are those consistent with all the constraints inherent in the theory and its transformation properties. This approach permits the characterization of legitimate observables even if the isolation of the "constraint variables" is not feasible, as in the general theory of relativity; observables must commute with all the constraints. They are, thus, invariants under the group of invariant transformations. It is asserted that this selection of observables, which is mathematically self-consistent, does not lead to the discard of quantities of physical interest. On the other hand, all the so-called paradoxes between constraints (subsidiary conditions) and commutation relations are thereby avoided. In the development of the Lagrangian quantization, we are proposing a new set of field equations which are different from the usual ones but which can be shown to permit the transition to the canonical formulation if desired. Our proposal is to assert the stationary character of the Feynman-Schwinger action operator not with respect to all, but only with respect to those variations that correspond to invariant transformations. As a result, the number of operator equations at each point of space-time is finite, though it is different from the number of equations in the nonquantum theory. These equations, though considerably weaker than what would be obtained if the action integral were to be made stationary with respect to all conceivable variations, are sufficient to yield all the usual conservation laws and also to permit the transition to the Hamiltonian form of the theory if desired. Commutation relations can be obtained for the field variables and their time derivations on the same hypersurface, simply by requiring that the field variables and their derivatives be algebraically independent of each other. The procedure employed breaks down if applied to a variable that is canonically conjugate to a constraint, an indication that in the Lagrangian formulation, too, the set of observables must be selected if paradoxes are to be avoided. Altogether it appears that the Lagrangian and the Hamiltonian quantizations, if set up properly, are largely equivalent; but this does not preclude the possibility that one may be more useful heuristically than the other.

1. INTRODUCTION

IN a number of preceding papers[1–4] we have ascertained the properties of field theories that are covariant with respect to groups of transformations depending on arbitrary functions. The examination of such theories is suggested by the physical importance of such transformation groups in the general theory of relativity (i.e., the theory of gravitation) and in the theory of the electromagnetic field. We found that very generally invariance of a Hamiltonian principle from which the field equations can be derived results in the existence of certain differential identities between the field equations and of "strong conservation laws."[1]

If theories of this type are brought into the canonical scheme, we found that the canonical field variables satisfy a certain number of constraints (also known as subsidiary conditions in quantum electrodynamics) and that the Hamiltonian functional of such a theory is determined only up to a linear combination of the so-called primary constraints, the coefficients of this linear combination being arbitrary functions.[2] This degree of arbitrariness is equivalent to Dirac's proposal to leave a certain number of velocities remain in the Hamiltonian density.[5] Recently we found that all the constraints play a role in the so-called functional of the transformation group, which generates the infinitesimal canonical transformations with respect to which the theory is covariant.[4] In fact, the circumstance that this functional is a constant of the motion and that the commutator of two such canonical transformations must again be a member of the group leads to a powerful and convenient method of determining the structure of the whole function group encompassing the constraints and the Hamiltonian.

It had been recognized for some time that the constraints of the Hamiltonian formalism were related to the conservation laws of the Lagrangian formalism. The first purpose of the present paper is to trace out this relationship in specific detail. The existence of the strong conservation laws—the vanishing of a certain divergence—implies the existence of "superpotentials," i.e., a set of quantities of which the components of the energy-momentum-stress "tensor" form the curl. We have succeeded in obtaining these superpotentials directly from the Lagrangian and its transformation properties (Sec. 2). On the other hand, the transfor-

* This work was supported by the ONR. This article contains, *inter alia*, the results of a doctoral dissertation submitted by one of us (R.S.) to the Graduate School of Syracuse University.
† Now at Universidade de Sao Paulo, Brasil.
[1] P. G. Bergmann, Phys. Rev. **75**, 680 (1949).
[2] P. G. Bergmann and J. H. M. Brunings, Revs. Modern Phys. **21**, 480 (1949).
[3] Bergmann, Penfield, Schiller, and Zatzkis, Phys. Rev. **80**, 81 (1950).
[4] J. L. Anderson and P. G. Bergmann, Phys. Rev. **83**, 1018 (1951).
[5] P. A. M. Dirac, Can. J. Math. **2**, 129 (1950).

mation law of the Lagrangian may also be formulated in terms of the generating functional, and Sec. 3 deals with the relationship between the generating potential in the Hamiltonian theory and the transformation law of the Lagrangian in the Lagrangian theory. The generating functional, and with it the constraints, will be constructed from within the Lagrangian formalism; this derivation leads to a considerable simplification of the expressions given earlier.[4]

In Sec. 4, we have endeavored to construct a quantum field theory that is covariant with respect to the same transformation group as the corresponding classical field theory. In the Hamiltonian theory, it appears fairly obvious what the general scheme must be, because the pertinent quantum theoretical formations, in particular commutators, which characterize the structure of the invariant transformation group, all have their classical analogs, e.g., Poisson brackets. However, we have attempted to show that from among all the classical canonical field variables only those may be considered as Hilbert operators in the quantum field theory (and therefore as physically meaningful observables) which commute with all the constraints and which, therefore, are invariant with respect to the invariant transformation group.

We have also dealt with the Lagrangian theory, largely on the basis of the results obtained in the analysis of the classical Lagrangian theory and the possibility of introducing canonical transformations and generators into the Lagrangian formalism. While we follow to some extent the Feynman-Schwinger developments,[6,7] to relate the unitary mapping operator $U(t_2, t_1)$ to the action integral, we have found it impossible to adopt field equations exactly analogous to the classical Euler-Lagrange equations, as Schwinger does. Instead, we are putting forward, as a conjecture for the time being, a new set of "field equations" whose number does not depend on the number of field variables (as in the classical theory), but on the structure of the invariant transformation group. Our conjectured "field equations" lead to the usual conservation laws. While they may not go over into the usual Euler-Lagrange equations in the classical limit for all conceivable covariant field theories, they will do so for the general theory of relativity with electromagnetic field. Our field equations are obtained by the requirement that the action integral be stationary with respect to variations that correspond to members of the invariant transformation group, but not necessarily to all other conceivable variations. This requirement, we have found, leads to relatively simple covariant differential equations for the observables without special assumptions concerning the commutation properties of the infinitesimal variations. Our theory is sufficiently definite to lead to the Schrödinger equation (or its equivalent in the Heisenberg representation). Thus it appears to lead to a "Lagrangian" theory that is equivalent to a Hamiltonian quantum field theory.

[6] R. P. Feynman, Revs. Modern Phys. **20**, 367 (1948).
[7] J. Schwinger, Phys. Rev. **82**, 914 (1951).

2. THE SUPERPOTENTIALS

Instead of introducing the components of the metric tensor as our fundamental field variables, as is done in the general theory of relativity, we shall characterize our field variables by the symbol y_A $(A=1, \cdots, N)$, where N is the number of algebraically independent components. These are equal to ten in the general theory of relativity and four in electromagnetic theory. We shall further assume that the field equations are derivable from a variational principle of the form

$$\delta S=\delta \int L(y_A, y_{A,\sigma})d^4x, \tag{2.1}$$

where L is a function of the field variables y_A and their first partial derivatives with respect to the space-time coordinates.

The transformation properties of L are of some importance, and we shall specify them more fully than has been done in the past.[1]

If we desire to have covariant field equations (the field equations to transform as densities of weight one and contragrediently to the field variables), then we need only choose an invariant as our action integral. In fact, if we were to construct a new covariant theory, it is hard to envisage how one could find the correct field equations without using such an invariant action integral, for the covariance of our field equations and their compatibility is always assured if they are derivable from such a variational principle. However, the only known invariant density in the prototype of any new theory that we might propose, the general theory of relativity, contains second derivatives of the field variables. These higher-order derivatives appear in the Lagrangian in terms that have the form of a pure divergence. If we desire to go over from the Lagrangian to the usual Hamiltonian theory, it is desirable to subtract this divergence from the invariant density. The field equations will not be altered by this change in the Lagrangian, as the addition of a pure divergence to the Lagrangian density does not contribute to the variation of the action integral as long as the variations of the field variables are confined to the interior of the four-dimensional domain of integration. Thus, our Lagrangian density will differ from an invariant density by a pure divergence, and we shall always assume that the precise form of this divergence is known. In the general theory of relativity, this divergence has important transformation properties which we shall describe below [Eq. (2.17)].

We shall assume that our field variables transform in the following manner:

$$\bar{\delta} y_A=c_{Ai}{}^{\sigma}\xi^i{}_{,\sigma}+c_{Ai}\xi^i-y_{A,\rho}\delta x^{\rho}. \tag{2.2}$$

The $c_{Ai}{}^{\sigma}$ and the c_{Ai} are functions of the y_A, and their exact form depends upon the specific transformation properties of the field variables. The index σ, as well as all other Greek indices, refers to the space-time coordinates. The index i identifies the arbitrary functions ξ^i (descriptors) that appear in the transformation law.[8] For coordinate-covariant theories, i becomes the Greek index ι. The infinitesimal variations of the space-time coordinates depend on some or all of the arbitrary ξ^i,

$$\delta x^{\nu}=a_i{}^{\nu}\xi^i, \tag{2.3}$$

where the $a_i{}^{\nu}$ are constants, 0 and 1.

The complicated character of the infinitesimal transformation law (2.2), (2.3) (more general than the coordinate transformation law for tensors) arises only because we want to encompass within our formalism a wider class of transformations than mere coordinate transformations. It is necessary to have the variations of the space-time coordinates depend on the set of constants $a_i{}^{\nu}$ since in some cases we are going to vary the dependent variables y_A and the independent variables x^{ρ} independently of one another. We have introduced the variation $\bar{\delta}y_A$ because this transformation law obeys the group property. This requirement is met if the commutator of two successive infinitesimal $\bar{\delta}$-transformations is a transformation of the same type. If this commutator is calculated for a given field variable, the arbitrary constants that appear in $c_{Ai}{}^{\sigma}$ and c_{Ai} will satisfy certain identities.[9] $\bar{\delta}y_A$ is the infinitesimal difference $y_A'(\mathbf{x})-y_A(\mathbf{x})$, i.e., y_A' is compared with y_A at a point that has the same coordinate values, rather than with y_A at the same point in space-time.

We have assumed that our Lagrangian density differs from an invariant density by a known divergence. The transformation law of the invariant density is

$$\bar{\delta}K+(K\xi^{\rho})_{,\rho}=0, \quad K=L+S^{\rho}{}_{,\rho}, \tag{2.4}$$

where K, the invariant density, has been separated into the Lagrangian density, L, and a divergence, $S^{\rho}{}_{,\rho}$. The transformation law of the Lagrangian density is then

$$\bar{\delta}L=Q^{\rho}{}_{,\rho}, \tag{2.5}$$

where

$$Q^{\rho}=-(L\xi^{\rho}+S^{\sigma}{}_{,\sigma}\xi^{\rho}+\bar{\delta}S^{\rho}). \tag{2.6}$$

If we now actually carry out the variation indicated on the left-hand side of Eq. (2.5) and utilize Eq. (2.6), then it is possible to show that the right-hand side of Eq. (2.5) will hold only if the following identities are satisfied:

$$\begin{aligned}&(L^A c_{Ai}{}^{\rho})_{,\rho}+a_i{}^{\nu}L^A y_{A,\nu}\\&\quad+[c_{Ai}(\partial^{A\rho}L+\partial^A S^{\rho})+c_{Ai,\sigma}\partial^{A\sigma}S^{\rho}]_{,\rho}\equiv 0.\end{aligned} \tag{2.7}$$

[8] We shall use the Latin indices i, k, $\cdots$ to number the descriptors of the invariant transformation group. Coordinate indices running from 1 to 3 where needed will be identified by letters r, s, $\cdots$.

[9] Reference 1, Eq. (2.4).

In the general theory of relativity, a coordinate-covariant theory, they are known as the contracted Bianchi identities. We shall call them Bianchi identities even in the more general theory proposed in this paper, since our generalization is clearly based on the example of the gravitational field.

As a consequence of the existence of the Bianchi identities, it is possible to show that the divergence of the stress "tensor," $T_i{}^{\mu}$, vanishes identically,

$$\begin{aligned}&T_i{}^{\mu}{}_{,\mu}\equiv 0,\\&T_i{}^{\mu}=a_i{}^{\nu}(\partial^{A\mu}Ly_{A,\nu}-\delta_{\nu}{}^{\mu}L)\\&\qquad-c_{Ai}{}^{\mu}L^A-[c_{Ai}(\partial^{A\mu}L+\partial^A S^{\mu})+c_{Ai,\sigma}\partial^{A\sigma}S^{\mu}],\end{aligned} \tag{2.8}$$

even when the field equations are not satisfied. Equations (2.8) are known as the *strong conservation laws* of our theory. The stress "tensor" is not a geometric object; for the invariant class of transformations in which we are interested many of its components do not transform in any simple manner. One can only say that the identities hold in every coordinate, gauge, or "bein" (n-uple) system, and for all other frames of reference for which the field variables have a corresponding invariant significance. Closer inspection of these strong laws shows that the first few terms are similar in form to the conservation laws of energy and momentum that appear in Lorentz covariant field theories, where the conservation laws hold only if the field equations are satisfied ("weak" conservation laws). For our general theory these laws are

$$\begin{aligned}&t_i{}^{\mu}{}_{,\mu}=0,\\&t_i{}^{\mu}=a_i{}^{\nu}(y_{A,\nu}\partial^{A\mu}L-\delta_{\nu}{}^{\mu}L)\\&\qquad-[c_{Ai}(\partial^{A\mu}L+\partial^A S^{\mu})+c_{Ai,\sigma}\partial^{A\sigma}S^{\mu}].\end{aligned} \tag{2.9}$$

The essential mathematical distinction between weak and strong laws is that the former arise because of covariance with respect to a finite set of arbitrary *constants*, while the strong laws are related to covariance with respect to a finite set of arbitrary *functions*. One can look at the question of strong *versus* weak laws from another viewpoint. It is possible to formulate strong laws in weak theories, but they will be integral laws. On the other hand, generally covariant theories will always yield differential strong laws, i.e., they are satisfied at each space-time point.

Because of Eq. (2.8), it must be possible to write the strong stress "tensor" in the form

$$T_i{}^{\mu}\equiv U_i{}^{[\mu\sigma]}{}_{,\sigma}, \tag{2.10}$$

where the $U_i{}^{[\mu\sigma]}$ are antisymmetric in the indices μ and σ. Henceforth, we shall call the $U_i{}^{[\mu\sigma]}$ the superpotentials of our theory. For any applications of the theory they must be explicitly calculated. In the general theory of relativity this was done by Freud,[10] but by a method that is only applicable in this case. We shall

[10] Ph. von Freud, Ann. Math. **40**, 417 (1939).

now show that it is possible to find an explicit solution for the super-potentials.

If we carry out the operations indicated by Eqs. (2.5), (2.6), the terms will group themselves as the coefficients of the various differential orders of the descriptors, ξ^i,

$$M_i^{\mu\rho\sigma}\xi^i_{,\mu\rho\sigma}+L_i^{\mu\rho}\xi^i_{,\mu\rho}-(T_i^{\mu}+V_i^{\mu\sigma}{}_{,\sigma})\xi^i_{,\mu} -T_i^{\mu}{}_{,\mu}\xi^i\equiv 0, \quad (2.11)$$

where

$$\begin{aligned} M_i^{\mu\rho\sigma}&=c_{A_i}{}^{\mu}\partial^{A\rho}S^{\sigma},\\ L_i^{\rho\sigma}&=c_{A_i}{}^{\rho}\partial^{A\sigma}L+a_i{}^{\iota}(\delta_{\iota}{}^{\sigma}S^{\rho}-\delta_{\iota}{}^{\rho}S^{\sigma})\\ &\quad+c_{A_i}{}^{\sigma}{}_{,\iota}\partial^{A\iota}S^{\rho}+c_{A_i}{}^{\sigma}\partial^{A}S^{\rho}+c_{A_i}\partial^{A\sigma}S^{\rho}\\ &\quad-a_i{}^{\iota}y_{A,\iota}\partial^{A\sigma}S^{\rho}+(c_{A_i}{}^{\rho}\partial^{A\sigma}S^{\iota})_{,\iota},\\ V_i^{\rho\sigma}&=L_i^{\rho\sigma}-(c_{A_i}{}^{\rho}\partial^{A\sigma}S^{\iota})_{,\iota}. \end{aligned} \quad (2.12)$$

Since the descriptors and their derivatives at any one space-time point are arbitrary, their coefficients must vanish separately.[11] For the third-order terms in the descriptors the coefficients must vanish when they are completely symmetrized in the indices μ, ρ, and σ,

$$[c_{A_i}{}^{\mu}\partial^{A\rho}S^{\sigma}]_{(\mu\rho\sigma)}=0. \quad (2.13)$$

The parentheses indicate that the expression inside the brackets is to be summed over six terms that are completely symmetric with respect to the indices inside the parentheses, $(\mu\rho\sigma)$.

For the second-order term, we have likewise

$$L_i^{\rho\sigma}+L_i^{\sigma\rho}=0, \quad (2.14)$$

while the first and zeroth-order terms tell us that although the divergence of T_i^{μ} vanished, T_i^{μ} is apparently not equal to the divergence of an antisymmetric form: comparison of $V_i^{\rho\sigma}$ with $L_i^{\rho\sigma}$ shows that $V_i^{\mu\sigma}$ is antisymmetric except for the divergence of the coefficient of the third-order term. However, by making use of the symmetry properties of this term, we can antisymmetrize $V_i^{\rho\sigma}$ completely by adding to it the divergence of another skew-symmetric density,

$$W_i^{\mu[\rho\sigma]}=\tfrac{1}{3}(c_{A_i}{}^{\sigma}\partial^{A\mu}S^{\rho}-c_{A_i}{}^{\rho}\partial^{A\mu}S^{\sigma}). \quad (2.15)$$

The final form of the super-potentials is then

$$U_i^{[\mu\sigma]}=V_i^{\mu\sigma}+W_i^{\mu[\sigma\rho]}{}_{,\rho}. \quad (2.16)$$

The expressions for the super-potentials, (2.16), can be simplified even further if we restrict ourselves to the general theory of relativity. In that case the c_{A_i} vanish, and explicit calculation shows that

$$a_i{}^{\rho}S^{\sigma}-a_i{}^{\sigma}S^{\rho}=c_{A_i}{}^{\sigma}\partial^{A}S^{\rho}+c_{A_i}{}^{\sigma}{}_{,\iota}\partial^{A\iota}S^{\rho} -a_i{}^{\iota}y_{A,\iota}\partial^{A\sigma}S^{\rho}. \quad (2.17)$$

It is not clear whether the conditions (2.17) are to be required for all generally covariant theories. The existence of these relations certainly simplifies the general theory of relativity as compared with the very general theory dealt with in this paper, especially if we make the transition to the Hamiltonian formalism. However, the transition can be made even if (2.17) is not satisfied, only the general formalism then becomes quite involved.

[11] J. Heller, Phys. Rev. **81**, 946 (1951).

3. LAGRANGIAN FORMALISM AND GENERATING FUNCTIONAL

In what follows, we shall consider infinitesimal transformations of the (Lagrangian) field variables in the sense that at any one point in space-time the field variables y_A may be replaced by new field variables which are algebraic functions of the y_A and their first space-time derivations $y_{A,\rho}$. While eventually we shall focus our attention on transformations in which the Lagrangian does not change its form, this assumption will not be made at first. Given some function F of the field variables and their derivatives, we shall make a distinction between two infinitesimal expressions. We shall designate by the symbol $\bar{\delta}F$ the change in the value of F at the space-time point with the same coordinates x^{ρ}, on the assumption that we are describing in terms of our new variables the same original physical situation. We shall designate by the symbol $\delta'F$ the change in F as a function of its arguments y_A, $y_{A,\rho}$. The relationship between these two infinitesimal transformations is:

$$\begin{aligned} \delta'F&=\bar{\delta}F-\partial^{A\rho}F\bar{\delta}y_A-\partial^{A\rho}F\bar{\delta}y_{A,\rho},\\ \bar{\delta}y_{A,\rho}&=(\bar{\delta}y_A)_{,\rho}=\bar{\delta}(y_{A,\rho}). \end{aligned} \quad (3.1)$$

This notation is the same as that used in earlier papers.[1,4]

Let us now consider what happens to the Lagrangian density L as a result of the infinitesimal transformation

$$\bar{\delta}y_A=f_A(y_B, y_{B,\rho}). \quad (3.2)$$

If the Lagrangian density were not to change its value at all, we should have $\bar{\delta}L=0$. It is, however, possible to add to the Lagrangian density a complete divergence, $Q^{\rho}{}_{,\rho}$ without affecting the Euler-Lagrange equations. We set, therefore,

$$\begin{aligned} \delta'L&=Q^{\rho}{}_{,\rho}-f_A\partial^{A}L-f_{A,\rho}\partial^{A\rho}L,\\ f_{A,\rho}&=y_{B,\rho}\partial^{B}f_A+y_{B,\rho\sigma}\partial^{B\sigma}f_A,\\ Q^{\rho}&=Q^{\rho}(y_A, y_{A,\rho}), \end{aligned} \quad (3.3)$$

and hence,

$$\delta'L=y_{A,\rho}\partial_A Q^{\rho}-f_A\partial^{A}L-y_{B,\rho}\partial^{B}f_A\partial^{A\rho}L +(\partial^{B\sigma}Q^{\rho}-\partial^{B\sigma}f_A\partial^{A\rho}L)y_{B,\rho\sigma}. \quad (3.4)$$

This change in the functional dependence of the Lagrangian density on its arguments implies that even though our Lagrangian density originally depends only on the field variables and their first derivatives, the transformed L will depend on higher derivatives as well unless we can choose Q^{ρ} and f_A so that the last term in Eq. (3.4) cancels, i.e.,

$$(\partial^{A\rho}Q^{\sigma}+\partial^{A\sigma}Q^{\rho})-(\partial^{A\rho}f_B\partial^{B\sigma}L+\partial^{A\sigma}f_B\partial^{B\rho}L)=0. \quad (3.5)$$

We shall now consider more particularly that class of

transformations which will not produce second time derivatives. In that case, Eq. (3.5) must be satisfied merely with both ρ and σ equal to 4, and we have as a restriction on both the f_A and Q^A the following:

$$\partial^A \cdot Q^A - \partial^A \cdot f_B \cdot \pi^B = 0, \qquad \pi^B \equiv \partial^B \cdot L, \quad \partial^A \cdot \equiv \partial/\partial y_{A,A} \equiv \partial/\partial \dot{y}_A, \tag{3.6}$$

which may also be put in the form

$$f_B \partial^A \cdot \partial^B \cdot L = \partial^A \cdot (\pi^B f_B - Q^A). \tag{3.7}$$

This restriction may be put into a convenient form if we introduce instead of the $\dot{y}_A$ the π^A as new variables. If the matrix,

$$\Lambda^{AB} \equiv \partial^A \cdot \partial^B \cdot L, \tag{3.8}$$

is nonsingular, all that need to be done is to multiply Eq. (3.7) by the factor $(\partial \dot{y}_A/\partial \pi^C)$ to get

$$f_C = \partial_C (\pi^B f_B - Q^A), \quad \partial_C \equiv \partial/\partial \pi^C; \tag{3.9}$$

and we come to the conclusion that the class of transformations we have introduced are the *canonical* transformations, with the expression $\int (\pi^B f_B - Q^A) d^3x$ being the generating functional. In covariant field theories, however, the matrix (3.8) is always singular, and hence, Eq. (3.9) cannot be obtained that easily.

A theory is *covariant* (not Lorentz-covariant) if there exists a group of transformations, depending on one or several arbitrary *functions* of the four coordinates, which do not change the form of the Euler-Lagrange equations. The form of the Lagrangian may also be considered to remain unchanged under any transformation belonging to the group. In such a covariant theory, we can always produce a formally new solution out of an existing one by carrying out one of the *invariant* transformations. While this is also true of Lorentz-covariant theories, the peculiar feature of covariant theories is that the transformation may leave the solution unchanged for all values of $t = x^4 \leqslant t_0$, but change the solution *formally* for $t > t_0$. That means that the equations cannot determine the solution uniquely from a set of properly chosen initial conditions; it must be impossible to solve the equations with respect to the highest (i.e., second) time derivatives of all the field variables.

The coefficients of the highest time derivatives are just the Λ^{AB} of Eq. (3.8). We conclude that this matrix must have (at least) as many null-vectors as the transformation group of the theory possesses arbitrary functions. We conclude that there exists n algebraically independent quantities u_{iA}, $i = 1, \cdots, n$,

$$u_{iA} \Lambda^{AB} = 0. \tag{3.10}$$

Moreover, if we consider the π^A as functions of the velocities $\dot{y}_A$, then, because

$$\delta \pi^A = \Lambda^{AB} \delta \dot{y}_B, \tag{3.11}$$

the momentum densities will not change their values if the velocities are changed by amounts that are arbitrary linear combinations of the u_{iA},

$$\delta \pi^A = 0, \quad \delta \dot{y}_A = s^i u_{iA}. \tag{3.12}$$

We have, therefore, n algebraically independent "primary constraints," i.e., relationships between field variables, their spatial derivatives, and momentum densities that do not involve velocities,

$$g_i(y_A, y_{A,s}, \pi^A) = 0. \tag{3.13}$$

Because of Eq. (3.12), the u_{iA} are nothing but the partial derivatives of the expressions (3.13) with respect to the momentum densities:

$$u_{iA} = \partial_A g_i. \tag{3.14}$$

It is clear that the velocities cannot be uniquely determined functions of the canonical field variables, but even if (at one space-time point) values are adopted for the canonical variables in accordance with the primary constraints, then in addition to a particular solution for the velocities, say k_A, we have solutions depending on a set of arbitrary functions w^i,

$$\dot{y}_A = k_A(y_B, y_{B,s}, \pi^B) + w^i u_{iA}. \tag{3.15}$$

Values of the momentum densities are ruled out when not in accord with Eqs. (3.13). It makes no difference if we add to the functions k_A arbitrary linear combinations of the u_{iA} and also of the constraint expressions (3.13), because the latter additions vanish for all pertinent values of the canonical field variables. We shall utilize this freedom of choice later to make a desirable normalization.

In Eq. (3.15), we may consider the $\dot{y}_A$ as functions of the canonical field variables plus the functions w^i. In this sense, we may introduce partial derivatives of the velocities with respect to the momentum densities and with respect to these new arguments w^i. We may and shall require that

$$\Lambda^{AC} \partial_C \dot{y}_B + v^{iA} u_{iB} = \delta_B{}^A, \quad v^{iA} = \partial^A \cdot w^i. \tag{3.16}$$

In this set of conditions, the changes in the momentum densities by which the newly defined partial derivatives are multiplied are automatically consistent with the constraints (3.13). Hence, Eqs. (3.16) hold irrespective of the normalization of the functions k_A mentioned above. From them it follows that

$$u_{iA} v^{kA} = \delta_i{}^k. \tag{3.17}$$

Through normalization it is possible to accomplish further that

$$v^{iA} \partial_B \dot{y}_A = 0, \quad v^{iA} \partial_A \dot{y}_B = 0, \quad \partial_A \dot{y}_B - \partial_B \dot{y}_A = 0. \tag{3.18}$$

If these conditions are adopted, the chain rule of differentiation will hold for any functions that depend on the velocities, and also for any variables that depend on the momentum densities and the w^i in such a manner that

$$v^{iA} \partial_A F = 0. \tag{3.19}$$

Equation (3.19) represents no real restriction on the functional dependence of F, because it may always be satisfied by the addition of an appropriate combination of the constraints. That is, if some function F^* does not satisfy Eq. (3.19) initially, we may construct F,

$$F=F^*-g_s v^{iA}\partial_A F^*, \tag{3.20}$$

which will have the same value as F^* and will satisfy condition (3.19).

We shall now return to Eq. (3.6). Even though the matrix Λ^{AB} is singular, we shall obtain the relationship (3.9). We assume that we have defined the derivatives of the velocities with respect to the momentum densities in accordance with Eqs. (3.16) and (3.18) and also that the functions Q^4 and f_A all have been made to satisfy the condition (3.19) with the help of the procedure indicated in Eq. (3.20). Now we may multiply Eq. (3.6) by $\partial_C \dot{y}_A$, with the result,

$$\partial_C Q^4-\pi^B\partial_C f_B=0. \tag{3.21}$$

Integrating by parts yields

$$\begin{gathered} f_A=\partial_A C, \\ C=\pi^B f_B-Q^4, \quad v^{iA}\partial_A Q^4=0, \quad v^{iA}\partial_A f_B=0. \end{gathered} \tag{3.22}$$

If we multiply Eq. (3.6) by u_{iA}, we obtain the further relationship,

$$\partial C/\partial w^i=0. \tag{3.23}$$

It is interesting to note that the generating functional is not simply proportional to the integral of Q^4, as one might have suspected. It is possible to have canonical transformations that do not change the value of the action integral, i.e., transformations in which Q^4 is zero. This type of transformation is, of course, what is commonly called a point transformation (in configuration space), a transformation in which the transformed field variables are independent of the time derivatives of the original field variables. In that case, the generating functional is linear in the canonical momentum densities, a well-known fact; this special case is also consistent with Eq. (3.22).

The change in the action integral may be calculated either as the change if the physical situation remains unchanged and the values of the field variables are changed in accordance with Eq. (3.2); the four-dimensional action integral then changes by the amount,

$$\begin{gathered} \bar{\delta}S=\oint Q^\rho d\sum_\rho, \\ d\sum_\rho=\delta_{\rho\alpha_1\alpha_2\alpha_3}\prod_{s=1}^{3}\frac{\partial x^{\alpha_s}}{\partial u^s}du^s. \end{gathered} \tag{3.24}$$

Or, we may determine the change in S if under the transformation (3.2) we consider a new physical situation in which the transformed field variables have the same values as the untransformed field variables in the original situation. This calculation leads, of course, to the determination of $\delta' S$, the change in S as a function of its arguments. According to Eq. (3.3), this change is

$$\begin{gathered} \delta' S=\oint (Q^\rho-f_A\partial^{A\rho}L)d\sum_\rho-\int f_A L^A d^4x, \\ L^A\equiv\partial^A L-(\partial^{A\rho}L)_{,\rho}, \end{gathered} \tag{3.25}$$

where L^A is short for the left-hand side of the field equations. If we favor the x^4-directions by choosing a domain of integration which spatially extends to infinity and which extends between two $x^4=$ constant surfaces, then Eq. (3.25) becomes

$$\begin{aligned} \delta' S=&\left[\int_{x^4=t_1}\int_{x^s=-\infty}^{\infty}(Q^4-\pi^A f_A)d^3x\right] \\ &-\int_{x^4=t_1}^{t_2}\int_{x^s} f_A L^A d^4x. \end{aligned} \tag{3.26}$$

If the field equations are satisfied, the second term vanishes, of course, and the change in action equals the difference between the generating functionals at the two time surfaces.

It remains to determine the change in the Hamiltonian functional as a function of *its* arguments. Just as we denote by δ' the change in a quantity when the values of y_A and $\dot{y}_A$ are held fixed, we shall introduce another symbol, δ'', to denote changes of quantities in which y_A and π^A are held fixed. We have, then

$$\delta'' L=\delta' L+\pi^A\delta''\dot{y}_A, \quad \delta''\pi^A\equiv 0, \tag{3.27}$$

and as a result

$$\begin{aligned} \delta'' H&=-\delta'' L+\pi^A\delta''\dot{y}_A=-\delta' L \\ &=-\dot{C}+f_A L^A. \end{aligned} \tag{3.28}$$

To summarize these results, Eq. (3.25) indicates the role of a four-"vector" as the generator of a canonical transformation in the Lagrangian formalism if all four coordinates are treated on the same footing; while Eqs. (3.27) and (3.28) show the relationship to the single generating functional of the canonical formalism.

Among all the canonical transformations, there is a set of transformations that leave the form of the Lagrangian invariant. These transformations are those in which $\delta' L$ vanishes (or equals a divergence, this latter possibility being of no consequence). According to Eq. (3.3) we have

$$0\equiv\delta' L=(Q^\rho-f_A\partial^{A\rho}L)_{,\rho}-f_A L^A. \tag{3.29}$$

For a transformation that does not change the form of the field equations we have, therefore

$$f_A L^A=(Q^\rho-f_A\partial^{A\rho}L)_{,\rho}=-C^\rho{}_{,\rho}. \tag{3.30}$$

Among all the transformations satisfying Eq. (3.30), there are some that correspond to a general invariance

property of the theory and which by themselves form a significant subgroup. The term "invariant transformations" ordinarily applies to the members of that subgroup. In the case of invarient transformations, we call generating functionals more particularly the (three-dimensional) integrals over C^4, defined by Eq. (3.30). In the future we shall write this functional as

$$\bar{C} \equiv \int C^4 d^3x. \tag{3.31}$$

It remains to indicate the relationship between variations of the "path" (i.e., the field), which involve changes in the actual field, and transformations, which involve changes in representation. In a variation, the frame of reference remains fixed, and the values of the field variables are changed as functions of the four coordinates. But actually, no frame of reference can be identified without its contents, and thus the two operations are physically and mathematically equivalent. There is, however, a distinction between the trivial statement that the action integral S under a transformation changes only by a surface integral (that is how we arrange its transformation properties), and the requirement that the integral be stationary under an arbitrary variation. The difference is that in the first instance we change L by $\bar{\delta}L$, which leads to the result (3.24) and does not involve restrictions either on the original field or on the functions f_A. In the second instance, we ask for the change in S while we consider L a fixed function of its arguments y_A, $y_{A,\rho}$. This change is obtained if we subtract from the expression (3.24) the contribution that is due to the change of L as a function of its arguments, $\delta' L$, i.e., the expression (3.25). The requirement that the difference should also be a divergence, regardless of the choice of the variations f_A,

$$\bar{\delta}S - \delta' S \equiv \oint f_A \partial^{A\rho} L d\sum_\rho + \int f_A L^A d^4x = \oint N^\rho d\sum_\rho, \tag{3.32}$$

leads to the field equations $L^A = 0$.

We now proceed to examine the group of invariant variations described by (2.2) and (2.5). Under these transformations the C^ρ of (3.30) take the form

$$C^\rho = \partial^{A\rho} L(c_{Ai}{}^\sigma \xi^i{}_{,\sigma} + c_{Ai}\xi^i - y_{A,\sigma} a_i{}^\sigma \xi^i) + a_i{}^\rho (L + S^\mu{}_{,\mu})\xi^i + \bar{\delta}S^\rho, \tag{3.33}$$

or, more simply,

$$C^\rho = -U_i{}^{[\rho\sigma]}\xi^i{}_{,\sigma} - t_i{}^\rho \xi^i, \tag{3.34}$$

where $t_i{}^\rho$ and $U_i{}^{[\rho\sigma]}$ are defined by (2.9) and (2.16).

It is easily seen from (3.34), or more directly from (3.30) that when the field equations are satisfied, the divergence of C^ρ vanishes,

$$C^\rho{}_{,\rho} = 0. \tag{3.35}$$

The time derivative of $\bar{C}$ (the generator of the invariant infinitesimal transformation) then vanishes if we assume that there are no variations of the field variables on two-dimensional spatial surfaces at infinity; for if we integrate the divergence of C^ρ over all of space and discard two-dimensional surface integrals, we get

$$\int C^\rho{}_{,\rho} d^3x = \int \dot{C}^4 d^3x \equiv d\bar{C}/dt. \tag{3.36}$$

However, the generating functional contains arbitrary functions (the descriptors) and their time derivatives. Thus, the coefficients of the various orders of the time derivatives of the descriptors, ξ^i, in $\bar{C}$ and $d\bar{C}/dt$ vanish. In the Lagrangian form of the theory these coefficients will vanish identically or as a result of the field equations. In the Hamiltonian theory those coefficients that were formerly field equations do not appear as any of the Hamiltonian equations of motion, but as secondary constraints. The appearance of these missing equations in the generating functional, where they mush vanish, insures the complete equivalence of both formalisms.

The terms that vanished identically now become the primary constraints of the Hamiltonian theory. There are also those expressions of the field variables and the momentum densities that vanish and continue to do so in the course of the motion only if the missing field equations are satisfied. In the Hamiltonian theory these field equations are called the secondary constraints. Furthermore, if particles are present as singularities of the field, the primary constraints will continue to be satisfied in the course of time only if restrictions are placed on the motion of these bodies. The number of such restrictions per particle (they appear in the form of two-dimensional surface integrals that vanish when the field equations are satisfied on the surface of integration) is equal to the number of arbitrary functions that appear in the transformation law for the field variables. In electromagnetic theory, a gauge invariant theory, there is but one restriction, the conservation of charge. In a coordinate covariant theory there are four restrictions, the conservation laws of energy and linear momentum for particles. We shall now examine the generating functional in detail to see how these restrictions arise.

We write $\bar{C}$ in the form

$$\bar{C} = \int [-U_i{}^{[44]}\dot{\xi}^i + (U_i{}^{[4\sigma]}{}_{,\sigma} - t_i{}^4)\xi^i] d^3x, \tag{3.37}$$

and its time derivative

$$\frac{d\bar{C}}{dt} = \int [-U_i{}^{[44]}\ddot{\xi}^i + (U_i{}^{[4\sigma]}{}_{,\sigma} - t_i{}^4 - \dot{U}_i{}^{[44]})\dot{\xi}^i + \frac{\partial}{\partial t}(U_i{}^{[4\sigma]}{}_{,\sigma} - t_i{}^4)\xi^i] d^3x, \tag{3.38}$$

where $\dot{\xi}^i$ stands for the time derivative of ξ^i. We know from our previous considerations that the various terms in (3.37) and (3.38) vanish separately. The first equation tells us that

$$U_i^{[44]}=0 \tag{3.39}$$

and

$$U_i^{[4\sigma]}{}_{,\sigma}-t_i^4=0. \tag{3.40}$$

(3.39) are the primary constraints of our theory. (3.40) are the missing field equations, the secondary constraints.

From (3.38) we deduce that

$$\dot{U}_i^{[44]}=U_i^{[4\sigma]}{}_{,\sigma}-t_i^4 \tag{3.41}$$

and

$$\frac{\partial}{\partial t}(U_i^{[4\sigma]}{}_{,\sigma}-t_i^4)=0. \tag{3.42}$$

The first of these equations states that the primary constraints will continue to be satisfied in the course of time only if the secondary constraints vanish. Equation (3.42) will vanish identically if the field equations are satisfied everywhere. However, if we integrate (3.42) over space and convert the expression into a three-dimensional divergence by means of the weak conservation laws, (2.9), we get from Gauss' law:

$$\frac{d}{dt}\oint U_i^{[4\sigma]}n_\sigma dS+\oint t_i^\sigma n_\sigma dS=0. \tag{3.43}$$

If the field equations are satisfied on the surface of integration, but not everywhere inside (at the position of particles), then Eq. (3.43) (which will still hold) represents restrictions on the motion of these particles. We define the conserved particle qualities by the surface integrals,

$$T_i=\oint U_i^{[4\sigma]}n_\sigma dS. \tag{3.44}$$

The restrictions (3.43) are in the form of conservation laws which state that the rate of change of the particle characteristic T_i depends upon the amount of field flux t_i^σ that passes through the surface. Thus, in the most general case, the particle and field are in constant interaction and such qualities of the particle as energy and linear momentum are strongly dependent on the motion of the field.

Since the motion of particles should be completely determined by a knowledge of the field equations on any hypersurface surrounding the particle, the values of the sums of the two surface integrals in each of Eqs. (3.43) should not depend on the surfaces of integration chosen. The proof of this independence is most easily accomplished by showing that the three-dimensional divergence of the integrand of (3.43) vanishes when the field equations are satisfied. Then it immediately follows from Gauss' law that the integrals are independent of the surfaces of integration.

As a consequence of the strong conservation laws it is possible to show that when the field equations are satisfied

$$U_i^{[r\sigma]}{}_{,\sigma}=t_i^r+\dot{U}_i^{[4r]}. \tag{3.45}$$

The divergence of this expression certainly vanishes, and since the right-hand side is the integrand of (3.43), our proof is complete.

4. QUANTUM FIELD THEORY IN THE CANONICAL FORMALISM

In attempting to quantize covariant field theories, we have been guided by the assumption that the basic structure of the transformation group should remain unaffected by quantization. This assumption has been justified by the history of quantum theory to date. In every successful quantum theory all invariance properties, such as symmetry properties, Lorentz covariance, and gauge covariance have been the same as in the corresponding classical theory. This is true even for theories involving spinors. While the spin has, strictly speaking, no classical analog, the covariance group of the spin field is the same as that encountered in similar classical theories. Merely the representation is different. But that means that commutators and other combinations of individual transformations lead to the same transformations as they do in nonquantum theories. That is why we are convinced that it is at least reasonable to modify the classical results obtained in previous papers very slightly if at all, as far as the transformation theory is concerned.

Prior to the formal simplification of Feynman's Lagrangian quantization[6] by Schwinger,[7] we concentrated primarily on quantization through the canonical formalism. Whether direct quantization of the Lagrangian theory leads to an appreciable simplification remains to be seen.

In the classical theory, a covariant theory in the canonical formalism comprises a Hamiltonian and a number of constraints, classified as primary and secondary constraints. The group of invariant transformations is generated by functionals that are three-dimensional integrals over generating densities, the latter being linear combinations of the constraints. The constraints are multiplied by arbitrary functions, the *descriptors*, which characterize each individual transformation,[4] in such a manner that the highest-order constraints are multiplied by the undifferentiated descriptors, and the primary constraints by the highest time derivatives that occur. Under any of these invariant transformations, the Hamiltonian density remains unchanged in value, but it will add a linear combination of the primary constraints whose coefficients depend on the descriptors. The totality of the constraints by themselves form a system of involutions; together with the Hamiltonian they form a function group. For the transition to the quantum theory, it appears essential that Poisson brackets are not merely formal expressions

but that they have a natural group-theoretical significance; they represent the group-theoretical commutator of two infinitesimal transformations.

It may then be said that not only the Hamiltonian but each one of the constraints generates an infinitesimal canonical transformation which leaves the form of each constraint and of the Hamiltonian unchanged (modulo some constraints). Among these, the members of the original invariant transformation group form a subgroup which adds to the Hamiltonian only primary constraints. Furthermore, the primary constraints by themselves form another subgroup which, however, adds to the Hamiltonian higher-order constraints.

It is to be assumed, then, that the transformation theory of the quantized theory will run exactly along the same lines. Instead of with canonical transformations we shall have to deal with unitary transformations. Poisson brackets will have to be replaced by commutators of the corresponding Hermitian operators. In that respect, then, we must require that the commutation rules between the Hamiltonian density and the various constraints be exactly the same as between their nonquantum analogs.

In the full formulation of the quantized theory, there arises a well-known difficulty, which is somewhat more serious in an essentially nonlinear theory than in a theory like quantum electrodynamics. That difficulty is that there appears a discrepancy between the commutation relations on the one hand and the constraints on the other. Briefly, there are, classically speaking, variables that are canonically conjugate to constraints. Now it is a well-established principle that if two operators have a c-number commutator, then neither of them possesses discrete eigenvalues nor normalizable eigenfunctions. On the other hand, physical situations must be characterized by wave functionals (Hilbert vectors) that are eigenfunctions of every constraint, belonging to the eigenvalue 0.[12] A possible way out of this paradox is to build up the Hilbert space from only those states that satisfy all constraints and to make it, thus, deliberately, a small subspace of the functional space of all conceivable wave functionals without regard to constraints.

Clearly, this subspace contains all states that can possibly characterize a physical situation. It is also certain that the continuous unitary transformation generated by the Hamiltonian does not lead outside this subspace, though this operator induces some motion throughout the "big" functional space as well. All unitary transformations generated by any of the constraints map the Hilbert space on itself, and this includes those particular unitary transformations forming the group of transformations with respect to which the (quantized) theory is to be invariant.

But how does transition to the smaller space solve our difficulties? It does so by severely restricting the number of linear operations that may properly be called Hilbert operators. A Hilbert operator must map at least a dense set of states belonging to the Hilbert space into that same Hilbert space. But that will be the case only for such linear operations in the "big" space that commute with all constraints (modulo the constraints themselves). If we adopt this condition as a necessary property of all Hilbert operators (this condition can be sensibly formulated as a restriction only in the "big" space; operators not satisfying it will simply not be defined on the subspace), our difficulties will be removed for the simple reason that the troublesome operations canonically conjugate to constraints are not Hilbert operators in our sense! The constraints themselves reduce to zero operators. They do not represent significant physical quantities.

Our new convention saves us from formal embarrassment. Will the elimination of a large number of operations from consideration not embarrass us as physicists, by eliminating the mathematical description of physically meaningful quantities?

In answer, we find that the observables not ruled out are invariants, quantities that remain unchanged under all the infinitesimal transformations with respect to which the theory is assumed to be invariant. For electrodynamic quantities, for instance, commutability with the subsidiary conditions of quantum electrodynamics implies gauge invariance. And truly, any quantity that can be given a well-defined numerical value must be an invariant!

Frequently, it appears that we operate with noninvariant quantities as if they were directly observable, such as a particular component of a four-vector or tensor. On closer examination, we must admit that such a quantity has a meaning only with respect to a specified frame of reference. But how do we determine a particular frame of reference? Generally, we define a frame of reference in terms of physical realities; we speak of a "laboratory frame of reference," etc. A (local) frame of reference is, for instance, frequently defined in terms of a prevailing local velocity. This local velocity is, however, the time-like eigenvector of the matter tensor (if observed in a particular fashion). If we observe the scalar product of some four-vector (e.g., electric charge-current density) with this local velocity vector, we actually measure an invariant that depends in a complicated fashion, but uniquely, on both the matter tensor and the charge-current vector. We have gone through a number of examples to convince ourselves that any physically observable quantity

[12] The remark by G. Wentzel in his *Quantentheorie der Wellenfelder* (Franz Deuticke, Wien, 1943), p. 111, that while it is not permissible to set a constraint operator equal to zero outright, one may restrict oneself to Schrödinger functions which are made to vanish by the application of a constraint operator, refers to the general function space of all conceivable wave functionals, whether they satisfy the constraints or not, and holds, therefore, only without regard to normalizability. On the other hand, unless there exists a norm and with it the concepts of Hermiticity and unitariness, Dirac brackets are generally meaningless, and one cannot ascribe a precise meaning to the expectation value of a dynamical variable.

is an invariant, but this point is so obviously of major importance that it should be more fully investigated. Suffice it here to say that the point of view we have adopted is a generalization of and consistent with accepted practices in quantum electrodynamics and elsewhere.

So far, we have indicated the general form of a quantized covariant field theory. While we have not assumed the introduction of parameters, their introduction[2,3] does not lead to serious modifications. Most important, the Hamiltonian becomes itself a constraint. There is, therefore, no "motion." Any state that obeys all constraints is a solution of the Schrödinger equation, provided we do not permit it to change in the course of "time." This apparent freezing is, however, a purely formal result of the introduction of parameters. The Hilbert operators in the parameter formalism are perforce all constants of the motion, and the distinction between Schrödinger representation and Heisenberg representation disappears. In the parameter formalism the same physical quantity, observed at two different times, simply appears as two distinct operators.

A conjecture we made some time ago,[2] to the effect that the ordinary coordinates might turn into quantum-theoretical observables in a parameter formalism cannot be maintained. The coordinates do not commute with the "parameter constraints"[2] and are, therefore, not Hilbert operators. In fact, parametrization does not add to or subtract from the observables of the parameter-free theory.[13] It is a matter of purely formal convenience whether or not they should be used in any investigation.

Suppose a classical canonical covariant field theory is available. Can its quantum-theoretical analog be obtained by a definite algorithm? At present the answer is no. Primary constraints are generally of very simple structure, and it is possible to construct them by simple symmetrization with respect to the position of the momentum densities, which occur only linearly. They will satisfy among themselves the same commutation relations as their nonquantum analogs. The Hamiltonian is generally quadratic in the momentum densities, and so are the secondary constraints. It will be necessary to discover such an arrangement of factors in the Hamiltonian that the higher-order constraints, which are essentially defined as commutators between the primary constraints and the Hamiltonian, will in turn satisfy the correct commutation relations with the primary constraints and with the Hamiltonian. We have not yet carried out a specific example to show how difficult a problem it is to discover the right arrangement or whether this arrangement is in fact uniquely determined.[14]

[13] R. Penfield, Phys. Rev. **84**, 737 (1951).

[14] In informal discussion, J. L. Anderson has suggested that the sequence of factors be settled by the introduction of "locally geodesic" variables and retransformation to ordinary physical variables. This suggestion is closely related to a recent paper by B. S. DeWitt, Phys. Rev. **85**, 653 (1952).

5. LAGRANGIAN QUANTIZATION

One of the purposes of characterizing canonical transformations within the Lagrangian formalism in Sec. 3 was to prepare a formulation that would be sufficient to quantize in the Lagrangian formalism. We are here reformulating Schwinger's ideas[7] with this end in mind. In all that follows it is understood that equations involving operators are to be read as equations for the matrix elements leading from one fixed surface to another.

We shall assume that the elements of the unitary matrix $U(t_2, t_1)$ lead from one hypersurface in space-time belonging to the coordinate value t_1 to another hypersurface that belongs to the coordinate value $x^4=t_2$. In a parameter formalism, x^4 must be replaced by the parameter t. For any transformation, invariant or otherwise, we shall set

$$\delta' U=\frac{i}{\hbar}\delta' S=\frac{i}{\hbar}\int \delta' L d^4x. \tag{5.1}$$

We adopt $\delta' S$ rather than $\bar{\delta} S$ on the right-hand side, because all operators and matrix elements are defined in terms of "a complete set of commuting operators," by assumption the field variables $y_A(x^1, x^2, x^3)$ for any fixed x^4. For an invariant transformation, in which the Lagrangian as a function of its arguments, i.e., the form of the theory, does not change, the elements of the matrix U do not change, either.

Following closely the arguments of Sec. 3, we now set $\delta' L$ equal to

$$\begin{aligned}\delta' L&=Q^\rho{}_{,\rho}-\{\partial^A L\cdot f_A\}-\{\partial^{A\rho} L\cdot f_{A,\rho}\}\\&=[Q^\rho-\{\partial^{A\rho} L\cdot f_A\}]_{,\rho}-\{L^A\cdot f_A\},\\L^A&\equiv\partial^A L-(\partial^{A\rho} L)_{,\rho}.\end{aligned} \tag{5.2}$$

In this equation, "symbolic" products of operators are indicated by braces and dots and are to be understood so that the factor f_A is to be inserted in each product at the point where the partial derivative of L with respect to one of its arguments produces a vacancy. It follows that

$$\begin{aligned}\delta' U&=-\frac{i}{\hbar}\oint C^\rho d\sum_\rho-\frac{i}{\hbar}\int\{L^A\cdot f_A\}d^4x,\\C^\rho&\equiv\{\partial^{A\rho} L\cdot f_A\}-Q^\rho,\end{aligned} \tag{5.3}$$

if we make no assumptions concerning the field equations.

It is tempting to assume that for all conceivable transformations the volume integral on the extreme right-hand side must vanish and that this be the natural form of the quantized field equations, in view of Eqs. (3.31). But unless the choice of f_A is restricted, such a requirement is much too stringent. It would be equivalent to a "double-operator" equation at each space-time point. In other words, if we call an ordinary

operator a "Hilbert tensor of rank 2," then the requirement that the expression $(L^A \cdot f_A)$ should vanish for arbitrary f_A would represent a Hilbert tensor equation of rank 4. Such a theory would obviously have little in common with quantum field theory as we know it. (Exactly the same argument may be carried out, with the same results, in quantum mechanics.)

Instead, we propose to require that $(L^A \cdot f_A)$ vanish only for such choices of f_A that correspond to *invariant* transformations. This proposal can be justified as follows. First of all, this choice is itself an invariant requirement, since every invariant transformation maps the set of invariant transformations on itself. Second, with this mild requirement we obtain all the conservation laws that are associated with the invariant transformations of a given theory; thus, the major results of Schwinger's paper[7] will hold. Third, among the invariant transformations is, of course, the motion in the course of time, i.e., a coordinate transformation in which only x^4 (or t) changes. For this particular transformation, the generating density becomes directly the Hamiltonian density, and thus the Schrödinger equation is obtained.

Thus, for a theory that is generally covariant we should have

$$\{L^A \cdot \bar{\delta} y_A\} \equiv \{L^A \cdot (F_{A\mu}{}^{B\nu} y_B \xi^\mu{}_{,\nu} - y_{A,\mu} \xi^\mu)\} = 0. \quad (5.4)$$

In this expression, the choice of the "descriptors" (which we shall assume are c-numbers) is arbitrary.[1] We separate into a complete divergence and, in addition, a set of terms that are multiplied by undifferentiated descriptors,

$$\{L^A \cdot \bar{\delta} y_A\} \equiv \{L^A \cdot F_{A\mu}{}^{B\nu} \xi^\mu y_B\}_{,\nu} - \xi^\mu(\{L^A \cdot F_{A\mu}{}^{B\nu} y_B\}_{,\nu} + \{L^A \cdot y_{A,\mu}\}). \quad (5.5)$$

In view of the assumption that the theory is covariant, it follows from the structure of the Lagrangian alone that the expression computed must be a divergence, though it is not a consequence of the theory that it must vanish. However, we may infer that the second term vanishes, i.e., that the Bianchi identities are satisfied, purely as a result of the transformation properties of the Lagrangian:

$$\{L^A \cdot F_{A\mu}{}^{B\nu} y_B\}_{,\nu} + \{L^A \cdot y_{A,\mu}\} \equiv 0. \quad (5.6)$$

We may not infer, but we shall assume that Eq. (5.4) holds, and that means that the first term on the right-hand side of Eq. (5.5) must vanish. If we integrate this expression over a four-dimensional domain, we may convert it into a surface integral and find

$$\oint \xi^\mu \{L^A \cdot F_{A\mu}{}^{B\nu} y_B\} d\Sigma_\nu = 0, \quad (5.7)$$

Finally, we may choose $\xi^\mu(x^\rho)$ so that only a small (cap) surface element can contribute. We finally arrive at the result

$$\{L^A \cdot F_{A\mu}{}^{B\nu} y_B\} = 0. \quad (5.8)$$

More generally, we may conclude from Eq. (5.3) that for invariant transformations, where $\delta' L$ vanishes, our conjectured field equations,

$$\{L^A \cdot f_A\} = 0, \quad (5.9)$$

are equivalent to the requirement that the divergence $C^\rho{}_{,\rho}$ vanishes. In a covariant theory, in which C^ρ is given by an expression like (3.34), Eq. (5.9) leads to the requirement,

$$T_i{}^\rho - t_i{}^\rho = 0 = \{L^A \cdot c_{Ai}{}^\rho\}. \quad (5.10)$$

Furthermore, if the difference between the strong and the weak "stress tensor" vanishes, it follows that the weak stress tensor by itself satisfies a conservation law,

$$t_i{}^\rho{}_{,\rho} = 0. \quad (5.11)$$

In a simple theory like the theory of gravitation, where the C_{Ai} vanish, the weak stress tensor belonging to the coordinate descriptors is given by the expression

$$t_\mu{}^\rho = \{\partial^{A\rho} L \cdot y_{A,\mu}\} - L\delta_\mu{}^\rho. \quad (5.12)$$

We can now show that $t_4{}^4$ is the Hamiltonian density. If we carry out a coordinate transformation in which $\xi^4 = 1$ on one space-like three-dimensional surface (t_2), but vanishes on the other (t_1), we have, because of Eq. (5.3),

$$\delta' U = -\frac{i}{\hbar} \int_{x^4 = t_2} C^4 d^3x, \qquad C^4 = \{\partial^A \cdot L \cdot \dot{y}_A\} - L \equiv H. \quad (5.13)$$

This last equation is the Schrödinger equation. It shows at the same time how the Lagrangian and the Hamiltonian are related to each other, including the sequence of factors. The usual rule, that the time derivative of an observable is determined by its commutator with the Hamiltonian, also follows directly from Eq. (5.13).

With the assumptions made, it is possible to work out commutation relations. These commutation relations will be between the field variables and their time derivatives and do not involve by themselves momentum densities (which we have not introduced). These commutation relations are obtained as follows. We determine the generating functions for each of the invariant transformations of the theory and use them to calculate the changes in the various field variables. These changes will appear on both sides of the equation and will generally depend on the descriptors or on derivatives of the descriptors. The requirement that these equations should not lead to restrictions on the descriptors and their derivatives, nor permit a determination of the time derivatives of the field variables in terms of the field variables themselves, or some similar restriction, leads to the commutation relations.

Generally, there will be some relations that cannot be satisfied. In such cases, it will turn out invariably that the variables involved are "constraint variables"

and therefore not true observables. This circumstance shows that in the Lagrangian formalism the Hilbert space will be very similar to (and as involved as in) the Hamiltonian formalism described in the beginning of this section.

Two examples will suffice. First, consider a problem in ordinary quantum mechanics. Assume the problem possesses a mixed quadratic Lagrangian of the form,

$$L=\tfrac{1}{2}\dot{q}^k g_{kl}\dot{q}^l-V, \tag{5.14}$$

where g_{kl} and V are independent of the velocities. A brief calculation shows that the Hamiltonian will be:

$$H=\tfrac{1}{2}\dot{q}^k g_{kl}\dot{q}^l+V. \tag{5.15}$$

We now attempt to determine the velocities by the standard procedure. The resulting equation is

$$\dot{q}^m=\frac{i}{2h}([\dot{q}^k, q^m]g_{kl}\dot{q}^l+\dot{q}^l g_{kl}[\dot{q}^k, q^m], \tag{5.16}$$

$$[\dot{q}^k, q^m]\equiv[\dot{q}^m, q^k].$$

If the form g_{kl} is nonsingular, the last equation will lead to no algebraic restriction on the velocities only if we assume

$$\frac{i}{h}[\dot{q}^k, q^m]=g^{km}, \quad g^{km}g_{ml}=\delta_l{}^k. \tag{5.17}$$

This relationship is equivalent to the usual commutation relation between q_k and p_l. On the other hand, if g_{kl} is singular, then each of its null vectors corresponds to a "constraint variable," and the commutators involving them cannot be determined in a satisfactory manner.

As a second example take the commutation relations of the electromagnetic field in the vacuum. The generating function of a gauge transformation is

$$\bar{C}=\frac{1}{4\pi}\int \phi^{4\sigma}\xi_{,\sigma}d^3x. \tag{5.18}$$

We can derive the equation

$$\delta\phi_\rho(\mathbf{x})=\xi_{,\rho}$$

$$=\frac{i}{4\pi h}\int[\phi^{4\sigma}(\mathbf{x}'), \phi_\rho(\mathbf{x})]\xi_{,\sigma}(\mathbf{x}')d^3x', \tag{5.19}$$

which leads to

$$[\phi^{4\sigma}(\mathbf{x}), \phi_\tau(\mathbf{x}')]=\frac{4\pi h}{i}\delta_\tau{}^\sigma\delta(\mathbf{x}, \mathbf{x}'), \tag{5.20}$$

but does not lead to any definite commutation relation involving ϕ_4.

It appears very definitely that in the Lagrangian formalism, too, the quantum state of the system, or the matrix U, for that matter, must not depend on the "constraint variables," i.e., the variables canonically conjugate to the constraints. There is another argument which makes this result appear reasonable. It has been pointed out previously that the variables canonically conjugate to constraints will change in the face of one of the invariant transformations, the remainder not. That means that the value of one of the "canonical" variables, or, rather, its probability distribution at some time t_2, depends only on the state of the system at another time t_1, but the distribution of a "constraint" variable both on the state previously and on the frame of reference chosen. Since the choice of frame of reference in this context involves no physical activity on the part of the observer (such as modifications of his measuring instruments), but rather his "state of mind," the matrix U can hardly give information on "constraint variables." Thus, we come to the conclusion that our original assumption, that the field variables y_A represent a complete set of commuting operators, must be modified in that all those combinations of y_A that are canonically conjugate to the constraints must be excluded.

6. CONCLUSION

We have conjectured that the field equations of a covariant quantized theory are not simply the analogs of the Euler-Lagrange equations of the nonquantum theory, but of the form (5.9), where f_A stands for the most general invariant $\bar{\delta}y_A$ of the theory. If this conjecture should turn out to be correct, then the resulting Lagrangian quantum field theory will be equivalent to a canonical field theory (because there will exist a single "Hamiltonian" functional generating the motion), but possibly more manageable. The total number of algebraically independent "field equations" (5.9) is determined not by the number of field variables but by the structure of the transformation group of the theory. In the case of coordinate-covariant theories, we are led to the set of 16 equations (5.8); in theories of the electromagnetic field the gauge group generates 4 equations. In the case of the general theory of relativity and in the case of electrodynamics, it can be shown that in the classical limit these relations are exactly equivalent to the usual Euler-Lagrange field equations, but it is conceivable that in a theory in which the number of field variables greatly exceeds the number of field equations of the type (5.10) such a correspondence breaks down. We have not yet examined this question in any detail.

The significance of the conjectured equations (5.8) or (5.10) is closely related to the so-called secondary constraints. While in a Lagrangian theory the primary constraints are empty, the secondary constraints are not, but represent certain of the conjectured field equations, e.g., $\{L^A \cdot F_{A_B}{}^{B4}y_B\}$, which are free of second time derivatives. We may, conversely, obtain all of the Eqs. (5.8) from the secondary constraints simply by

giving the three-dimensional surface with respect to which they are formed every possible orientation.

In our Lagrangian theory, the commutation relations between the y_A and the $\dot{y}_A$ are not determined completely. As a result, the Hamiltonian, though formally it generates the motion, actually does not determine the time derivatives of all field variables. Preliminary examination shows, however, that the variables whose time derivatives remain indeterminate are precisely the ones whose time derivatives are also indeterminate in the classical theory, those which in the Hamiltonian theory are canonically conjugate to the primary constraints. In a nonlinear covariant theory, the separation of those variables whose time derivatives are indeterminate from those which are completely determined is a mathematical task of almost insurmountable difficulty. In all probability, the construction of the Hilbert space of permissible states and legitimate observables will be just as difficult in the Lagrangian formalism as it is in the canonical formalism (see Sec. 4).

In future work we plan to pursue the application of both the Hamiltonian and the Lagrangian theory to actual physical theories and to ascertain the usefulness of either.

PHYSICAL REVIEW VOLUME 89, NUMBER 1 JANUARY 1, 1953

Meson Theory of β-Decay and the ΔL-Forbidden Transitions

SEITARO NAKAMURA
Department of Physics, University of Tokyo, Tokyo, Japan
(Received April 21, 1952)

Existence of the β-meson of vector type which is neither a π- nor μ-meson and which transmits the β-decay of nuclei has been tantatively assumed, the results thus derived being compared with experiments on β-decay. The differences between the β-meson theory and the phenomenological Fermi theory lie in the natural deduction of the vector interaction as well as the introduction of new nuclear matrix elements which are characteristic of the meson dipole. The selection rules for the ΔL-forbidden transitions are involved in these matrix elements, the orders of which are expected to be that of the unfavored parity transitions in each degree of forbidden transitions. The observability of a free β-meson is also discussed.

1. THE MESON THEORY OF β-DECAY

THE theory of β-decay, originally formulated by Yukawa,[1] predicted the virtual emission and reabsorption of charged mesons in the β-decay of nucleons. After the two mesons, π and μ, were discovered, one was not successful in identifying either of them as an intermediary agent of nuclear β-decay, in spite of extensive analyses.[2-5] Recently, Friedman and Rainwater[6] showed that a free π-meson will not decay into an electron and neutrino with a probability more than 1/1419 times the probability of $\pi-\mu$ decay. Sasaki, Hayakawa, and the present author[7] once proposed the existence of a vector meson, which is neither π nor μ, and could be the agent of Yukawa's original idea, that of transmitting the nuclear force and β-decay. We have named it the β-meson. Tanikawa[8] and Caianiello[9] suggested the meson theory of β-decay through a τ-meson, the former assuming it to be pseudoscalar while the latter taking it to be vector. However, it is almost certain that the fate of these theories will primarily be dependent on the β-ray analysis. To clarify this point, we shall derive the β-meson theory in some detail.

For the purpose of this discussion, the β-meson is assumed to be of vector type, as in the Fermi theory the tensor interaction is indispensable in the explanation of the results of the recent experiments on the β-ray spectra and $\beta-\gamma$ angular correlations.[10] Its mass and coupling constants with nucleons and leptons will be tentatively taken arbitrary, not referring to those of any observed meson. Taking Konopinski's[11,12] Hamiltonian for the vector meson theory of β-decay, we have, in the case of an allowed transition, (as regards notation, see refer-

[1] H. Yukawa, Proc. Phys. Math. Soc. Japan **17**, 48 (1935), third series; S. Sakata, Proc. Phys. Math. Soc. Japan **23**, 291 (1941); **24**, 843 (1942); **25**, 86 (1943); H. A. Bethe and L. W. Nordheim, Phys. Rev. **57**, 998 (1940).
[2] Taketani, Nakamura, Ono, and Sasaki, Phys. Rev. **76**, 60 (1949); Nakamura, Fukuda, Ono, Sasaki, and Taketani, Prog. Theor. Phys. **5**, 740 (1950).
[3] H. Yukawa, Revs. Modern Phys. **21**, 474 (1949).
[4] J. Steinberger, Phys. Rev. **76**, 1180 (1949).
[5] M. Ruderman and R. Finkelstein, Phys. Rev. **76**, 1458 (1949).
[6] H. L. Friedman and J. Rainwater, Phys. Rev. **84**, 684 (1951).
[7] Sasaki, Nakamura, and Hayakawa, Prog. Theor. Phys. **3**, 454 (1948).
[8] T. Tanikawa, Prog. Theor. Phys. **3**, 315 (1948).
[9] E. R. Caianiello, Phys. Rev. **81**, 625 (1951).
[10] C. S. Wu, Revs. Modern Phys. **22**, 386 (1950); I. Shaknov, Phys. Rev. **82**, 333 (1951).
[11] E. J. Konopinski, Revs. Modern Phys. **15**, 209 (1945).
[12] E. J. Konopinski and E. Uhlenbeck, Phys. Rev. **60**, 308 (1941).

ences 11 and 12),

$$P(W)dW=\left(\frac{|\int 1|^2}{T_1}+\frac{|\int \beta\sigma|^2}{T_2}+\frac{|\mathbf{D}^{(0)}|^2}{T_2'}\right)\times F(\pm Z,W)(W_0-W)^2(W^2-1)^{\frac{1}{2}}WdW, \quad (1)$$

$$\frac{1}{T_1}=\frac{8}{\pi}\left(\frac{m}{m_\beta}\right)^5\left(\frac{g_1g_1'}{\hbar c}\right)^2\frac{m_\beta c^2}{\hbar}$$

$$\frac{1}{T_2}=\frac{32}{9\pi}\left(\frac{m}{m_\beta}\right)^5\left(\frac{f_1f_1'}{\hbar c}\right)^2\frac{m_\beta c^2}{\hbar}$$

$$\frac{1}{T_2'}=\frac{8}{\pi}\left(\frac{m}{m_\beta}\right)^5\left(\frac{f_1f_1'}{\hbar c}\right)^2\frac{m_\beta c^2}{\hbar}$$

$$\mathbf{D}^{(0)}=\frac{1}{\rho^2}\int\left\{\beta(\boldsymbol{\sigma}\cdot\mathbf{r})\mathbf{r}\right\}\times(m_\beta\gg m). \quad (2)$$

Here m_β, m are the rest mass of the β-meson and electron, respectively; g_1 and f_1 are the nuclear coupling constants, g_1' and f_1' the coupling constants with leptons; ρ is the nuclear radius. $\int 1$ and $\int\beta\sigma$ are the well-known nuclear matrix elements, the former corresponding to the Fermi selection rule, the latter to the Gamow-Teller selection rule. $\mathbf{D}^{(0)}$ is an entirely new matrix element, the selection rule of which is given as follows:

$\Delta J=0, \pm1$ (no $0\to0$),

$\Delta L=0, \pm1, \pm2$ (no $0\to0$, $1\leftrightarrow0$), parity change: no.

It is interesting to note that $\mathbf{D}^{(0)}$ directly allows the so-called ΔL-forbidden, ΔJ-allowed transition. The corresponding β-ray spectrum is of the allowed shape, as is seen in Eq. (1). The correction factors of the meson theory of β-decay in the forbidden transitions can be derived in the same way as in the case of the Fermi theory. The results are identical with those of the linear combination theory of the vector, V, and the tensor, T, Fermi-interactions, computed by Smith,[13] except for the following terms:

$$\left(\frac{1}{12}K^2L_0+\frac{3}{4}L_1\right)\sum_{ij}|D_{ij}^{(1)}|^2 \quad (3)$$

in the first forbidden transision, and

$$\frac{1}{72}\left(\frac{1}{15}K^4L_0+2K^2L_1+15L_2\right)\sum_{ijk}|D_{ijk}^{(2)}|^2 \quad (4)$$

in the second forbidden transition. Here

$$D_{ij}^{(1)}=\frac{1}{\rho^2}\int\beta(\boldsymbol{\sigma}\cdot\mathbf{r})(x_ix_j-\tfrac{1}{3}\delta_{ij}r^2), \quad (5)$$

$$D_{ijk}^{(2)}=\frac{1}{\rho^2}\int\beta(\boldsymbol{\sigma}\cdot\mathbf{r})\left(x_{(i}x_jx_{k)}-\frac{6}{5}\delta_{(ij}x_{k)}r^2\right). \quad (6)$$

[13] A. M. Smith, Phys. Rev. **82**, 955 (1951).

TABLE I. Selection rule derived from the meson dipole interaction.

Matrix elements	ΔJ	ΔL	Parity change	Spectrum correction factors
$\mathbf{D}^{(0)}$	$0, \pm1$ (no $0\to0$)	$0, \pm1, \pm2$ (no $0\to0$ $1\leftrightarrow0$)	no	1
$D_{ij}^{(1)}$	$\pm1, \pm2$ (no $1\leftrightarrow0$)	$\pm1, \pm2, \pm3$ (no $1\leftrightarrow0$ $2\leftrightarrow0$)	yes	'a' type
$D_{ijk}^{(2)}$	$\pm2, \pm3$ (no $2\leftrightarrow0$)	$\pm2, \pm3, \pm4$ (no $2\leftrightarrow0$ $3\leftrightarrow0$)	no	D_2 type

The selection rules of $D_{ij}^{(1)}$ and $D_{ijk}^{(2)}$ and the corresponding forbidden spectrum correction factors are listed in Table I.

Among the first forbidden, ΔL-forbidden cases, Pr^{142} [14] and Sb^{124} [15] are reported to show the 'a' type forbidden spectra. The orbital assignments, $(d_{5/2}, h_{9/2})$ for Pr^{142} and $(g_{7/2}, s_{1/2})$ for Sb^{124} are, however, not conclusive. If the super-allowed beta-decay $O^{14}\to N^{14*}$ is really a $0\to0$ (no) transition,[16] the vector or scalar interaction which enables us to derive the necessary matrix element $\int 1$ should be applied.

2. DISCUSSIONS

In comparing the results with experiments, no quantitatively definite conclusions could be obtained. But the following features are noted:

(1) The beta-decay in the ΔL-forbidden transitions, classified on the current version of the shell model by Mayer, Moszkowski, and Nordheim,[17] can be directly explained by the matrix elements $\mathbf{D}^{(0)}$ (ΔJ-allowed), $D_{ij}^{(1)}$ (ΔJ-first forbidden) and $D_{ijk}^{(2)}$ (ΔJ-second forbidden). There is some evidence that the ΔL-forbidden, ΔJ-allowed case has the allowed shape, and the ΔL-forbidden, ΔJ-forbidden case has 'a' type for the corresponding β-ray spectra.

Following Mayer, Moszkowski, and Nordheim,[14] $\log ft$ for the transition, $\Delta J=\pm1$, $\Delta L=\pm2$, no, covers the range from 4.9 up to 9.0 and the mean is about 6. From Eq. (2), we may expect that the order of the matrix element $\mathbf{D}^{(0)}$ is about that of the allowed unfavored parity transition. In this case, the higher orbital change might reduce the overlapping of the radial parts of the wave functions before and after the decay, compared to the case of the normal allowed transition. This may account for the above figures concerning the ft values. It must be borne in mind, however, with Brysk,[18] that the ΔL-forbidden transition may also be ascribed to the peculiar character of the nuclei. It may

[14] L. W. Nordheim, Revs. Modern Phys. **23**, 327 (1951), Table II, reference *hh*.

[15] L. M. Langer, Phys. Rev. **84**, 1059 (1951); Nakamura, Umezawa, and Takebe, Phys. Rev. **83**, 1273 (1951).

[16] J. D. Seagrave, Phys. Rev. **85**, 197 (1952).

[17] Mayer, Moszkowski, and Nordheim, Revs. Modern Phys. **23**, 315 (1951); L. W. Nordheim, Revs. Modern Phys. **23**, 322 (1951).

[18] H. Brysk, Phys. Rev. **84**, 362 (1951).

be worthwhile to mention that the final odd mass number nuclei of the ΔL-forbidden β-decay are almost about half-way between the two Schmidt limits.[19] As was suggested by Feenberg and Hammack,[20] a small admixture of the state having the orbital angular momentum which makes the transition in the allowed category for $\int\beta\boldsymbol{\sigma}$, ($\Delta L=\pm1$, 0), would be enough to explain the larger ft values of the ΔL-forbidden case. Emphasis should be laid on the fact that, in this case, one could expect, in principle, clear-cut distinction between meson theory and Fermi theory. Indeed, $\mathbf{D}^{(0)}$, $D_{ij}{}^{(1)}$ and $D_{ijk}{}^{(2)}$ cannot be derived from any of the five Fermi interaction or their linear combinations. However, the calculation of the nuclear matrix elements depends on the particular theory of nuclear structure. It may, therefore, be hard to draw any final conclusion.

(2) The need for the Fermi interaction $\int 1$ in addition to the Gamow-Teller interaction $\int\boldsymbol{\sigma}$ was discussed by Moszkowski,[21] and Horie and Umezawa,[22] in evaluating the matrix elements for light nuclei.[23] In the β-meson theory, the above is deduced as a matter of course.

(3) Apart from the ΔL-forbidden group as mentioned above, the spectrum correction factors in the forbidden transitions derived from the β-meson theory are essentially identical with the linear combination theory of V and T, except that the relative weight of V and T is now determined in (1). It is clear that, in a spectrum analysis of this type, we have to meet the most crucial test of the theory, since the difference between the meson and the Fermi theory is evident in the shape of the spectrum. Of course, it is easily seen that remarkable features of the forbidden spectra, i.e., 'a' type, D_2 type, etc., which revealed the success of the tensor Fermi interaction would not be devalued by our theory. However, the results will, in general, depend on the unknown ratios of the several matrix elements, which are understood from the equations of Konopinski and Uhlenbeck,[11,12] and Smith.[13]

For instance, it can be shown[24] that the β-meson theory predicts the approximate allowed spectrum or some appreciable deviation from it in the first forbidden transition, $\Delta J=\pm1$, 0, yes, depending on the unknown ratios of the several nuclear matrix elements. (See Appendix.) It must be admitted that there remain ambiguities concerning these ratios of the matrix elements.[25] Only systematic experimental investigations[23,26] will clarify the validity of the theory with regards to the spectrum shape.

(4) While the free β-meson is to be expected to decay into an electron and a neutrino in our theory, there has been no evidence to indicate its existence. However, if we take into account the fact that the predicted lifetime, τ_β,[27,28] for the β-decay of the β-meson is much shorter than that of any charged meson so far observed, it seems not at all absurd to deduce, with Caianiello, that the free β-meson might escape detection in the experiments now available.

The author would like to take this opportunity to thank Professor H. Yukawa for his kind information and encouraging discussions from abroad. He would like to thank Dr. M. Taketani and Messrs. M. Sasaki and M. Umezawa for their kind discussions throughout this work. The author is greatly indebted to Professors E. T. Konopinski, L. M. Langer, M. G. Mayer, S. A. Moszkowski, and L. W. Nordheim, for sending him their manuscripts before publication.

APPENDIX

If one puts

$$\int\boldsymbol{\alpha}=i\Lambda_1\frac{\alpha z}{2\rho}\int\mathbf{r},\qquad \int\beta\boldsymbol{\alpha}=i\Lambda_1{}^{\beta}\frac{\alpha z}{2\rho}\int\mathbf{r},$$

$$\int\beta\boldsymbol{\sigma}\times\mathbf{r}=ik^{\beta}\int\mathbf{r},\qquad \int\beta\gamma_5=i\Lambda_2{}^{\beta}\frac{\alpha z}{2\rho}\int\beta\boldsymbol{\sigma}\cdot\mathbf{r},\quad (7)$$

the spectrum correction factors, $C'(z, W)$, for the first forbidden transition derived from the vector and the

[19] Mayer, Moszkowski, and Nordheim, Revs. Modern Phys. **23**, 315 (1951), Table II; L. W. Nordheim, Phys. Rev. **75**, 1894 (1949), Figs. 1 (a) and (b).

[20] E. Feenberg and K. C. Hammack, Phys. Rev. **75**, 1877 (1949).

[21] S. A. Moszkowski, Phys. Rev. **82**, 118 (1951); see also reference 21.

[22] H. Horie and M. Umezawa, Phys. Rev. **83**, 1253 (1951).

[23] In an article by E. J. Konopinski and L. M. Langer, in *Annual Reviews of Nuclear Science*, Vol. 2, (Annual Reviews, Inc., Stanford) in press, all the possible linear combinations of the five Fermi interactions have been pinned down in the light of the newest spectrum analysis. Following them, the combination (V, T) should be ruled out by the evidence that the precision measurements of the first forbidden spectra give the allowed type, whereas the main terms in the (V, T) combination give spectrum correction factors which are energy dependent.

This conclusion is of great importance to our theory. However, if the following assumption is valid; (see Appendix)

$$\Lambda_1=1,\ \Lambda_1{}^{\beta}\neq k^{\beta}\quad\text{or}\quad \Lambda_1{}^{\beta}=k^{\beta},\quad \Lambda_1\neq1,$$

it may be possible to expect the main terms of the correction factor to be energy independent by cancelling out the $1/W$ term accidentally, as is mentioned in the text.

[24] S. Nakamura, Prog. Theor. Phys. (to be published).

[25] T. Ahrens and E. Feenberg, Phys. Rev. **86**, 64 (1952).

[26] If the pseudoscalar (P) Fermi interaction is really necessary, as has recently been shown in the attempt by Petschek and Marshak, to explain the first forbidden spectrum of RaE, we have to assume the pseudoscalar β-meson (rather than the π-meson), in addition to the vector meson. In this case, the spectrum formula (1) should be augmented by the $\int\beta\gamma_5$ interaction only, as was proved by Nelson, Miyazima, and Dyson. See A. G. Petschek and R. E. Marshak, Phys. Rev. **85**, 698 (1952); E. C. Nelson, Phys. Rev. **60**, 830 (1941); T. Miyazima, Proc. Phys. Math. Soc. Japan (in Japanese) **16**, 340 (1941); and F. J. Dyson, Phys. Rev. **73**, 929 (1948).

[27] $\tau_\beta\cong3\times10^{-11}$ sec, provided $m_\beta=1200$ m, $T_\beta=3\times10^{9}$ sec. $f_1{}^2/\hbar c=0.5$ and $g_1=0$. (See reference 9, and also H. A. Bethe and L. W. Nordheim, Phys. Rev. **57**, 998 (1940).)

[28] Gamma-instability of the free β-meson, that is, $\beta\rightarrow\pi+$photon, should be taken into consideration. See R. J. Finkelstein, Phys. Rev. **72**, 415 (1947); Fukuda, Hayakawa, and Miyamoto, Prog. Theor. Phys. **5**, 283, 352 (1950); Ozaki, Oneda, and Sasaki, Prog. Theor. Phys. **5**, 25, 165 (1950).

pseudoscalar β-meson theory will be formally expressed in terms of descending powers of $\alpha z/2\rho$.

$$C^1(Z,W)=\left(\frac{\alpha z}{2\rho}\right)^2(C_{V,T}+C_{T,P})-\frac{\alpha z}{2\rho}(C_{V,T}'+C_{T,P}')+(C_{V,T}''+C_{T,P}''+C_a), \tag{8}$$

$$C_{V,T}=\left|\int\mathbf{r}\right|^2[(1-\Lambda_1)^2/T_1+(\Lambda_1{}^\beta-k^\beta)^2/T_2-\{(1-\Lambda_1)(\Lambda_1{}^\beta-k^\beta)/T_1T_2\}\cdot(2/W)], \tag{9}$$

$$C_{T,P}=\left|\int\boldsymbol{\beta\sigma}\cdot\mathbf{r}\right|^2(1/T_2-\Lambda_2{}^\beta/T_3)^2, \tag{9'}$$

$$C_{V,T}'=\left|\int\mathbf{r}\right|^2\{[(1-\Lambda_1)/T_1+k^\beta(\Lambda_1{}^\beta-k^\beta)/T_2]\cdot(K+P^2/W)+([(\Lambda_1{}^\beta-k^\beta)-k^\beta(1-\Lambda_1)]/T_1T_2)\cdot(2K/3W)\}, \tag{10}$$

$$C_{T,P}'=\left|\int\boldsymbol{\beta\sigma}\cdot\mathbf{r}\right|^2(1/T_2)\cdot(1/T_2-\Lambda_2{}^\beta/T_3)\cdot\tfrac{2}{3}\cdot(K-P^2/W), \tag{10'}$$

$$C_{V,T}''=\left|\int\mathbf{r}\right|^2(1/T_1)\cdot[K^2/3+P^2/3+(2/9)\cdot KP^2/W]+\left|\int\boldsymbol{\beta\sigma}\times\mathbf{r}\right|^2(1/T_2)\cdot[K^2/6+P^2/6+(2/9)\cdot KP^2/W], \tag{11}$$

$$C_{T,P}''=\left|\int\boldsymbol{\beta\sigma}\cdot\mathbf{r}\right|^2(1/T_2)\cdot[K^2/9+P^2/9-(2/9)\cdot KP^2/W], \tag{11'}$$

$$C_a=(\sum|B_{ij}|^2\cdot 1/T_2+\sum|D_{ij}^{(1)}|^2\cdot 1/T_2')(K^2/12+P^2/12). \tag{12}$$

(This expression is a good approximation for the case $\alpha z\ll 1$.) Here T_3 is the characteristic time of the β-decay deduced from the pseudoscalar β-meson theory.

Except for the case, $\Delta J=\pm 2$, yes, the correction factors given by (8) depend upon the ratios, $(\Lambda_1,\ \Lambda_1{}^\beta,\ \Lambda_2{}^\beta)\alpha z/2\rho$, k^β, of the several matrix elements. (The phase of (7) was taken following the approximation of Ahrens and Feenberg.[22]) If $\alpha z/2\rho\gg 1$, one can easily infer the simple results, provided that the following special assumptions are valid.

(I) $(1-\Lambda_1)(\Lambda_1{}^\beta-k^\beta)\neq 0$.

The correction factors in the leading terms (9) and (9′) will take the form of $1-\mathfrak{L}/W$, where

$$\mathfrak{L}=\frac{2(1-\Lambda_1)(\Lambda_1{}^\beta-k^\beta)}{(1-\Lambda_1)^2/T_1+(\Lambda_1{}^\beta-k^\beta)^2/T_2+(1/T_2-\Lambda_2{}^\beta/T_3)^2\cdot|\int\boldsymbol{\beta\sigma}\cdot\mathbf{r}|^2/|\int\mathbf{r}|^2}.$$

(II) (a) $\Lambda_1=1$, and $\Lambda_1{}^\beta\neq k^\beta$ (or $1/T_2\neq\Lambda_2{}^\beta/T_3$),
(b) $\Lambda_1{}^\beta=k^\beta$, and $\Lambda_1\neq 1$ (or $1/T_2\neq\Lambda_2{}^\beta/T_3$).

The $1/W$ term in (9) will be canceled out, and the correction factors in (9) and (9′) become independent of w.

(III) $\Lambda_1=1$, $k=\Lambda_1{}^\beta$, and $\Lambda_2{}^\beta/T_3=1/T_2$.

The terms containing the factors, $(\alpha z/2\rho)^2$, and $(\alpha z/2\rho)$, in (8) will be all canceled out by themselves, and the smallest terms, (11), (11′), and (12), will determine the spectrum shape.

If $\mathfrak{L}>0$ in the case (I), a downward deviation of the Fermi plot is expected at the low energy region. Some indications of such a deviation were reported in the experimental spectra of Th^{233} [29] and Ru^{103}.[30] However, the evidence seemed not altogether unobjectionable. The attempts[31,32] to explain the first forbidden β-ray spectra by means of the large cancellation of the correction factors by assuming a suitable ratio of matrix elements should be compared to the case (III). For instance, in our theory, the spectrum of Tm^{170} [31] ($\Delta J=\pm 1$ (3→2), yes), is to be explained by (11) and that of RaE[32] ($\Delta J=0$ (0→0), yes) by (11′).

Actually, in the cases of Ru^{106}, Tm^{170}, RaE, and Th^{233}, the assumption $\alpha z\ll 1$ does not hold, and more elaborate discussions are required, which will be published later,[33] with the investigation of the second forbidden transition.

[29] Bunker, Langer, and Moffat, Phys. Rev. **80**, 468 (1950).
[30] E. Kondaiah, Arkiv Fys. **4**, No. 2 (1951).
[31] Nakamura, Umezawa, and Takebe, Phys. Rev. **84**, 865 (1951).
[32] A. G. Petschek and R. E. Marshak, Phys. Rev. **85**, 698 (1952).
[33] Taketani, Umezawa, Nakamura, and Ono, Prog. Theor. Phys. (to be published).

Light Emission Produced by Current Injected into a Green Silicon-Carbide Crystal*

K. LEHOVEC,† C. A. ACCARDO, AND E. JAMGOCHIAN
Signal Corps Engineering Laboratories, Fort Monmouth, New Jersey

(Received May 16, 1952)

This paper deals with the light emission, which arises from the passage of a current in the forward direction over a p-n-barrier in a transparent ("pure") silicon-carbide crystal. The results differ from previous results obtained on a dark blue (impure) silicon carbide crystal in several respects: The spectral distribution of light emission is found to be independent of current and temperature. Both the efficiency of light emission and the decay constant of light emission increase exponentially with decreasing temperature. This is explained by a nonradiative transition of excited electrons. In a dark blue (impure) silicon carbide crystal, the resistances in series with the p-n-barrier were largely eliminated, and light emission at a voltage of the same magnitude as $h\nu/e$, was observed.

1. INTRODUCTION

IN a previous paper, investigation of the light emission from blue SiC crystals excited by current flow was discussed.[1] The body of the crystals was of the p-type with occasional n-type surface layers.

Since the absorption edge of the SiC lattice lies at about 0.42 microns,[2] pure SiC should be colorless. The dark blue color of the crystals is indicative of lattice defects or high impurity content. The latter conclusion has now been confirmed by spectroscopic analysis (Table I). It is known that the spectral distribution, temperature dependence, and efficiency of light emission from phosphors depend on the impurity centers (activators, killers) present (e.g., in ZnS, Cu, and Ni, respectively). It is expected, therefore, that there should be differences in the injected light emission from SiC crystals which differ in impurity content. Pale greenish transparent SiC crystals have been obtained through the courtesy of Carborundum Company, Niagara Falls, New York. Such crystals are known to be of the n-type.[3] Spectroscopic analysis showed that they are of considerable purity, containing only traces of Al, Fe, Ti, Cu, and Mg. Four of the crystals emitted light with current passing. In this paper, experimental data will be presented on the light emission from one of these green SiC crystals. The intensity of the light emission as a function of current density, temperature, and wavelength was investigated. The response time of light emission to a current pulse was also measured. The technique is the same as reported previously.[1]

TABLE I. Spectroscopic analysis of a blue SiC crystal.

Al	0.1	Wt percent
Fe	0.05	Wt percent
Ti	0.002	Wt percent
Cu	Traces	
Mg	Traces	

2. DESCRIPTION OF THE CRYSTAL INVESTIGATED

The crystal under investigation was wedge shaped. An area contact was made on the base of the crystal. A well-defined area of about 1 mm² on one side of the crystal near the apex was found to emit green light when a current was passed through a catswhisker placed within this area (catswhisker negative).

Probe measurements were made to determine the potential distribution in the crystals. The potential distribution was very complex and indicated the presence of at least two barriers within the crystal. It was established that the boundaries of the green light emitting area coincide with a barrier, and that the green light appears when current passes the barrier in the forward direction.

It has been reported,[4] that SiC crystals which are phosphorescent under ultraviolet light also emit light when excited by current. We have found this technique helpful in selecting light emitting crystals. It should be noticed, however, that in the case of the crystal under discussion, the area which emits green light when current passes could not be distinguished by phosphorescence under ultraviolet from other parts of the crystal.

If the polarity of current was reversed (catswhisker positive), a yellow light emission with diffuse boundaries appeared. At higher voltages, a bright bluish-white light was superimposed at a few distinct spots.

The area emitting yellow light did not coincide with that emitting green light. Microscopic inspection indicated that each light came from a different depth in the crystal. It seems possible that the two types of light emissions are due to injection of carriers over two different barriers. The difference in color of the emitted light cannot be attributed to the different thicknesses that the light has to pass in order to reach the surface. In the locality of the light emission the crystal was about 1 mm thick. If absorption was an important factor, one would expect the intensity to be markedly

* Most of the data included in this paper were presented at the American Physical Society Meeting in New York, January 31, 1952, paper SC5.

† Now at Sprague Electric Company, North Adams, Massachusetts.

[1] Lehovec, Accardo, and Jamgochian, Phys. Rev. **83**, 603 (1951).

[2] O. Weigel, Nachr. Ges. Wiss. Göttingen, p. 264 (1915).

[3] G. Busch and H. Labhard, Helv. Phys. Acta **19**, 463 (1946).

[4] T. Tetzner, Z. angew. Phys. **1**, 153 (1948).

different when measured from each side of the wedge since the light had to pass through different thicknesses to reach each surface. The green and yellow light emissions were visible with about equal intensities both from the contact side of the crystal and the side opposite. It seems, therefore, that the different colors observed are to be ascribed to various activator (impurity) centers rather than to absorption.

The bright bluish-white spots which appear when the catswhisker is positive are located at the boundary of the area emitting green light at negative polarity of the catwhisker. These spots appear, therefore, when the current passes the barrier in the blocking direction. The current-voltage characteristic in the blocking direction showed a sharp break which corresponded to the initiation of the blue light spots. The current increased more rapidly with voltage after the break. It is suggested that the light spots arise from recombination of electron-hole pairs which have been created in the barrier by either a Zener effect or by ionization from electron collisions.

Parts of the crystal were found to phosphoresce under ultraviolet light. The color of the phosphorescence was reddish-yellow and about the same color as that of light emission caused by current flow with the point contact positive. A well-defined area of the crystal which included the area emitting yellow light under current flow was phosphorescent. There is one striking difference between the yellow phosphorescence and the yellow light emission under current flow, however. The yellow light emission under current flow decays instantaneously to the eye after interruption of current, whereas the phosphorescence decays gradually within several seconds after removal of the exciting ultraviolet light.

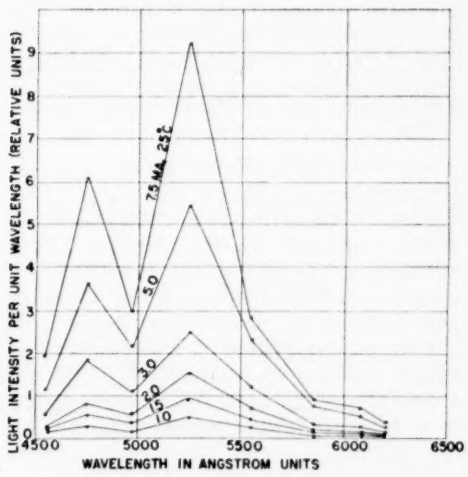

FIG. 1. Spectral distribution of the light emitted from a pale green SiC crystal as a function of the current passed through the crystal at room temperature.

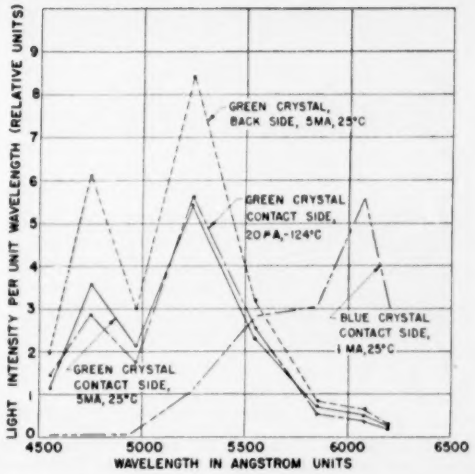

FIG. 2. Spectral distribution curves of the injected light emission from a pale green crystal taken from different sides of the crystal at the temperatures indicated. A spectral distribution curve of a blue SiC crystal is included for comparison (this curve depends on temperature). (See reference 1.)

3. EXPERIMENTAL RESULTS ON THE GREEN LIGHT EMISSION

(a) Spectral Distribution

The spectral distribution of the emitted light was measured by using a photomultiplier and various filters, as described previously.[1] Figures 1 and 2 show spectral distribution curves at room temperature and −124°C. The various curves in Fig. 1 refer to different currents passed through the crystal at room temperature. It is evident that spectral distribution of the emitted light does not change with the current passed through the crystal. In Fig. 2 spectral distribution curves which were taken (a) from different sides of the crystal, and (b) at room temperature and −124°C, are compared. Since the light emitting area was located close to the surface on which the catswhisker was placed, the light emission had to penetrate through a much thicker layer of the crystal in the case of the dashed-line curve than in the case of the solid-line curve. The fact that the spectral distribution is practically the same from either side of the crystal indicates that light absorption in the crystal is of little influence on the shape of the spectral distribution measured.[5]

Comparison of the spectral distribution curves at room temperature and at −124°C shows that spectral distribution of the green crystal does not depend on temperature in this range. In Fig. 2, the spectral distribution of light emission from a blue SiC crystal[1]

[5] R. W. Sillars [Phys. Rev. **85**, 136 (1952)] has recently suggested that the spectral distribution of the emitted light is modified by the absorption of the crystal. Sillars observed the light emitted at point contacts. We have selected for our measurements crystals with light emitting areas (due to *p-n*-boundaries) which were much larger than the point contacts.

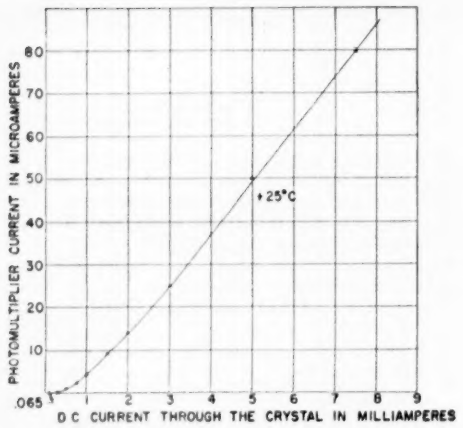

FIG. 3. Intensity of emission (expressed by the photomultiplier current) as a function of the current through the crystal at room temperature.

is included for comparison. The light emission in the blue crystal consisted of two bands, one with a maximum at 0.61 micron, the other with a maximum at 0.55 micron. When the temperature is lowered the emission band at 0.55 micron is enhanced more than that at 0.61 micron.

(b) Light Emission as a Function of the Current Passed

Since spectral distribution of the emitted light from the green crystal is independent of the current through the crystal and of the temperature (Figs. 1 and 2), the photomultiplier current is proportional to the intensity of the emitted light. Figure 3 shows the photomultiplier current as a function of the current passed through the crystal (catswhisker negative) at room temperature. For crystal currents larger than 1 ma, the light (as

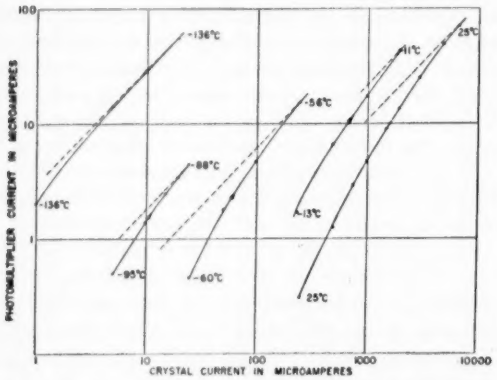

FIG. 4. Double logarithmic plot of the intensity of light emission (expressed by the photomultiplier current) as a function of the current passed through the crystal. Temperature of measurement is indicated in the figure. The dotted lines have a slope which corresponds to proportionality of the light intensity with the current passed through the crystal.

expressed by the photomultiplier current) can be approximated by the relation:[6] $i_{phot}=bi_{cryst}-a$, where a is of the order of 700 microamp and $b=1.2\times10^{-2}$. Thus for crystal currents larger than 1 ma the efficiency of light emission expressed by i_{phot}/i_{cryst} approaches a constant value b; whereas for crystal currents smaller than 1 ma the efficiency increases markedly with increasing current. This is seen more clearly from the double logarithmic plot of light intensity (expressed by photomultiplier current) *vs* crystal current (Fig. 4). The various curves refer to different temperatures. Since the curves were taken while warming up the crystal from −136°C to room temperature, the temperature of the crystal increased somewhat (as indicated in the figure) while taking the measurements for a

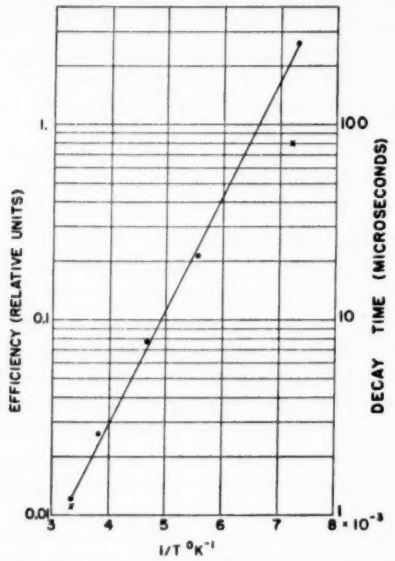

FIG. 5. Semilogarithmic plot of the values of efficiency corresponding to the dotted lines of Fig. 4 as a function of inverse absolute temperature. The straight line obtained indicates an exponential dependence with an activation energy of 0.118 ev. The two points marked by crosses are the time constants of the light emission.

particular curve. A slope of 45 degrees would indicate that the efficiency is independent of the current through the crystal. It seems that a slope of 45° is approached at higher current densities (the dotted lines have slopes of 45 degrees). At low current densities, the slopes become steeper. Relative values of efficiency have been calculated from the straight lines shown in Fig. 4. These values were plotted on a semilog scale against reciprocal absolute temperature (Fig. 5). A straight line is obtained which shows that the efficiency increases with decreasing absolute temperature by a Boltzmann factor $\exp(-T_0/T)$, with $T_0=1370$°K corresponding to an activation energy of $U=kT_0=0.118$ ev.

[6] A similar behavior has been found in the case of light emission from blue SiC crystals.

(c) Absolute Value of the Efficiency of Light Emission

The absolute value of efficiency is defined as the ratio: light quantum emitted per electron passed through the crystal. Knowing the spectral distribution of the emitted light and the spectral sensitivity of the photomultiplier, the absolute value of the efficiency can be calculated. The efficiency at room temperature for the particular crystal under investigation was found to be 2×10^{-6} quanta/electron. This value is of the same order of magnitude as that reported previously for a blue SiC crystal. This coincidence is accidential; at other temperatures the efficiencies differ in value. The efficiency of the pale green crystal under discussion increases with decreasing temperature (see Fig. 5) and reaches at $T=-134°C$ a value of about 2×10^{-4} quanta/electron. The temperature dependence of the efficiency of light emission intensity of the crystal under investigation can be written in the form $Ce^{1370/T}$, with $C=2\times10^{-8}$ quanta per electron in the temperature range $140°K<T<300°K$. Extrapolation to lower temperatures shows that an efficiency of about unity should be approached at $T\approx80°K$ (about liquid air temperature).

(d) Response Time

The response time of the light emission was investigated as follows: A square current pulse was passed through the crystal. The shape of the photomultiplier current caused by the light emitted from the crystal was inspected on an oscillograph. Figure 6 shows photographs of the pattern on the oscillograph corresponding to current pulses of different magnitude passed through the crystal. The temperature of the base plate on which the crystal was mounted was $-140°C$. The amplification of the photomultiplier current was adjusted to give traces of approximately the same height at the oscillograph. The shape of all traces is identical, independent of the magnitude of the current pulses used. The rise curves and the decay curves shown in the figure can be represented by functions $1-e^{-t/\tau}$ and $e^{-t/\tau}$, respectively, with $\tau=80$ microseconds. Measurements at room temperature also gave an exponential time dependence. Again the decay time was independent of the height of the current pulse. The decay time at room temperature was only 1.15 microseconds. The values of the decay time at room temperature and at $-140°C$ are plotted in Fig. 5, together with values of efficiency of light emission. It will be noted that the decay time shows a temperature dependence quite similar to that found for efficiency.

4. SOME ADDITIONAL DATA ON THE LIGHT EMISSION FROM A BLUE SiC CRYSTAL

The observations described in what follows were made on a blue SiC crystal. The crystal was of the p-type except for a thin n-type region of about 4 mm² area on one face. A yellow light was emitted with the passage of the current in the forward direction over the p-n-barrier. An effort was made to eliminate contact resistance in order to find the threshold voltage of the light emission for the intensity detectable by the eye. A nonrectifying base contact was made by plating zirconium on the base of the crystal by thermal dissociation of Zr hydride in a vacuum.[7] Probe measurements showed that the base contact resistance was less than 0.2 ohm (area of the contact about 0.5 cm²). The other contact consisted of four steel catswhiskers connected in parallel and placed on the n-type layer. The current-voltage characteristic of this arrangement is shown in Fig. 7. The voltage at which light emission visible to the eye begins is marked by an arrow. Notice the change in slope in the characteristic at this voltage. Such a change has been observed earlier by others.[8]

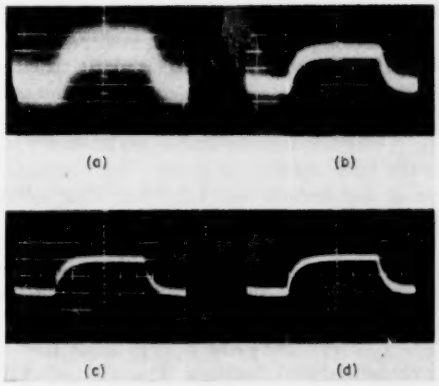

FIG. 6. Shape of the light pulse emitted from a green SiC crystal at $-140°C$ when passing a square current pulse: 900 microseconds duration, and 500 cps repetition rate. Amplitude of current pulse: (A): 3, (B): 8, (C): 12, (D): 17 microamps; dc bias current: 10 microamps. The vertical amplification was adjusted to obtain patterns of about the same height.

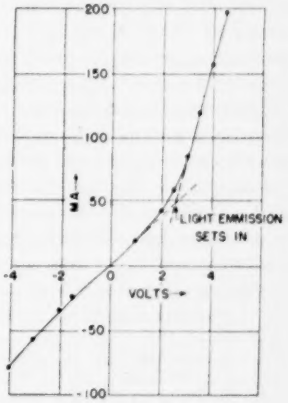

FIG. 7. Current voltage characteristic of a blue SiC crystal with p-n-barrier. The arrow marks the voltage between the electrodes of the crystal above which light emission is observed by the dark adapted eye.

[7] C. S. Pearsall and T. K. Zingeser, unpublished Massachusetts Institute of Technology Technical Report No. 104 (1949).
[8] O. Lossew, Physik. Z. 32, 695 (1931); B. Claus, Ann. Physik 11, 331 (1931); 14, 644 (1932).

A more exact determination of the threshold voltage for light emission at the barrier was made. A probe was placed on the light emitting surface and the area around the probe was inspected microscopically. The voltage between the current carrying contacts was increased until light emission became visible to the dark adapted eye in the area around the probe. The corresponding voltage at the contact was 1.8 volts. This voltage is less than that corresponding to the energy of the light quanta emitted (2 ev). The difficulties encountered in probing a *p-n* boundary grown under uncontrolled conditions do not permit one to put too much emphasis on this small difference. Any excess of energy emitted over energy supplied by the battery must have been taken up by lattice vibrations. This should lead to a cooling effect, as in the case of the well-known Peltier effect.

5. DISCUSSION

In the study of light emission one is concerned with (a) the excitation process (in our case, carrier injection) and (b) the emission process.

The carrier injection should not differ fundamentally from that known through studies of the transistor effect.[9] The emission process should not differ fundamentally from that occurring in ordinary phosphors.[10]

In what follows we shall discuss briefly some of our experimental results from the point of view of carrier injection and phosphorescence. Unfortunately, we are unable at present to produce artificial SiC crystals of known composition. Details of the barrier structure and of the activator centers in the crystals investigated are not known so that any interpretation is only tentative.

(a) Remarks on the Injection Process

The shape of the current-voltage characteristic (Fig. 7) suggests that the current over the barrier consists of two parts. One part is proportional to the voltage at the contact and passes the barrier layer essentially unrectified contributing nothing to the light emission. In the blocking direction at low voltages, this part constitutes the entire current. The other part which does lead to light emission sets in measurably above a threshold voltage in the forward direction and is absent in the blocking direction. We are inclined to ascribe the former to conduction on impurity levels[11] (or to some other process involving strongly disordered structure), and the latter, to carriers injected across the barrier. The presence of a current which does not lead to excitation and which at low current densities is a large fraction of the total current, may be one reason for the observed dependence of the efficiency on current density at low currents (Fig. 4).

(b) Remarks on the Emission Process

A dependence of efficiency on current density may be inherent also in the emission process. It is known from experiments on the luminescence of ZnS- and other phosphors that the efficiency of the emission process may increase with increasing intensity of excitation.[12] The dependence of the efficiency of excitation becomes more pronounced at lower intensities of excitation and at higher temperature and may be caused by the presence of so-called "killers."[13] "Killers" are centers which enable radiationless transitions of excited electrons. A well-known killer in ZnS-phosphors is Fe. Traces of Fe were present in the pale green crystal under investigation.

It is customary to consider the following processes when discussing the time dependence of emission of phosphors:

(1) The lifetime of the free electron before being captured; the capture may take place at traps (1a), at activator centers in an excited state (1b), or at killer centers (1c).

(2) The electron may be re-emitted into the conduction band from the traps (2a), or from the excited states of the activation centers (2b).

(3) The electrons captured in an excited state of the activator may transfer to the ground state under light emission (3a) or under dissipation of its energy in heat (3b). The electron captured at a "killer center" loses its energy into heat (definition of "killer").

Any one of these steps (1), (2), (3) may determine the decay time. Some of the steps (1b), (1c), (2b), (3a), (3b) account for the efficiency. In our case both efficiency and decay time are strongly temperature dependent. Only the processes (2a), (2b), and (3b) depend in general strongly on temperature. This suggests that at least one of the processes (2a), (2b), and (3b) are involved in the efficiency and decay time. We have observed that efficiency and decay time have about the same temperature dependence. This suggests that the same step is of importance for efficiency and decay. Trapping influences only decay but not efficiency tentatively and seems therefore of no importance. We conclude that either (3b) or (2b) (or both) account for the observations on efficiency and decay.

Let the relative probability of a free electron to be captured by an activator (instead of being captured by a killer) be f. Let the probability for a radiative transition per unit time of an electron from the excited state of the activator to the ground state (step 3a) be p, that of re-emission to the conduction band (step 2b) p', and that of nonradiative transitions to the ground

[9] W. Shockley, *Electrons and Holes in Semiconductors* (D. Van Nostrand and Company, Inc., New York, 1950).

[10] H. W. Leverenz, *Luminescence of Solids* (John Wiley and Sons, Inc., New York, 1950).

[11] Presence of such a current was suggested by G. Busch (Helv. Phys. Acta **10**, 167 (1946)) in order to explain measurements of the temperature dependence of thermoforce and of Hall effect in SiC crystals.

[12] N. Riehl, Z. Tech. Physik **20**, 152 (1939); J. H. Gisolf and F. A. Kröger, Physica **6**, 1101 (1939); Urbach, Urbach, and Schwartz, J. Opt. Soc. Am. **37**, 122 (1947); S. Robert and F. Williams, J. Opt. Soc. Am. **40**, 516 (1950).

[13] Urbach, Urbach, and Schwartz, J. Opt. Soc. Am. **37**, 122 (1947).

state (step 3b) p''. Both p' and p'' are of the type $s\exp(-E/kT)$ with different numerical values for s and E. In general, only one of the processes (2b) or (3b) will be of importance owing to differences in the numerical values of E. The efficiency is then[14] $\epsilon=fp/[p+s\exp(-E/kT)]$, and the decay time τ of phosphorescence: $1/\tau=p+s\exp(-E/kT)$. Our measurements covered a temperature range in which ϵ and $1/\tau$ were strongly temperature dependent. This implies that $p\ll s\exp(-E/kT)$. Thus $\epsilon\approx fp/[s\exp(-E/kT)]$, $1/\tau\approx s\exp(-E/kT)$, and $\epsilon/\tau=fp$.[15] Using the measured values $1/\tau\approx 10^6$ sec^{-1} at room temperature, $\epsilon=2\times10^{-6}$ quanta/electron at room temperature, and $E=0.114$ ev, we obtain $fp\approx 2$ sec^{-1} and $s\approx 10^8$ sec^{-1}. The value of s is of the same order of magnitude as that frequently obtained in other phosphors from glow and decay experiments.[16] Separation of f and p would be possible if efficiency and decay measurements were extended to sufficiently low temperatures where the factor $\exp(-E/kT)$ becomes negligibly small. Then efficiency and decay time should be independent of temperature: $\epsilon\approx f$ and $1/\tau\approx p$. Unfortunately with our present equipment we were not able to reach this temperature range.

The temperature U calculated from Fig. 5 is of the same order of magnitude as the ionization energy of conduction observed by G. Busch[17] for some pale green crystals (e.g., crystal 12a, $E_2=0.120$ ev in his Table I). It would be very interesting to investigate a possible relation between activation energy of conduction and that of efficiency of phosphorescence on the same crystal. Crystals with homogeneous impurity distribution would be necessary, however.

We are indebted to Mr. J. Mellichamp for performance of the spectroscopic analysis.

[14] Consideration of recapture of an electron of an activator after the release from an excited state introduces only a small modification of the equation, if $f\ll 1$.

[15] The close relationship between the temperature dependence of efficiency and that of decay time has been observed on Mn-activated zinc silicate phosphors by F. A. Kröger and W. Hoogenstraaten [Physica **14**, 425 (1948)].

[16] See, e.g., J. Randall and M. Wilkins, Proc. Roy. Soc. (London) **A184**, 366 (1945).

[17] G. Busch, Helv. Phys. Acta **10**, 167 (1946).

PHYSICAL REVIEW VOLUME 89, NUMBER 1 JANUARY 1, 1953

Diurnal Variations in the Intensity of Cosmic Rays Underground*

NOAH SHERMAN
H. M. Randall Laboratory of Physics, University of Michigan, Ann Arbor, Michigan

(Received August 6, 1952)

The number of coincidences between two trays of Geiger-counters located at a depth of 8.46×10^4 g cm^{-2} underground was recorded each hour, and these data were analyzed for variation of cosmic-ray intensity with solar and sidereal time. (A total of 7.4×10^6 μ-mesons was observed whose average energy is estimated to be 2×10^{11} ev.) In each case the standard deviation of the observed coincidence rates from the mean rate is not larger than the standard deviation expected from a normal distribution. The first harmonic amplitudes of the solar and sidereal variations indicate that the data are equally consistent with an assumed daily sinusoidal variation in the coincidence rates of $\sim$0.5 percent and with the absence of such variation. The difficulties involved in deducing directional properties of the primary cosmic radiation from harmonic analysis of variations in secondary radiation underground are discussed.

THE investigations of Elliot and Dolbear[1] indicate the existence of small solar and sidereal diurnal variations in the intensity of the hard component at sea level. They interpret these results as due to the non-isotropic incidence of primary cosmic rays. In the course of an investigation of the correlation between variations in atmospheric temperatures and variations in the intensity of high energy μ-mesons observed underground (to be reported at a later date), we have collected hourly counting rates for these particles which might be expected to reflect variations in the intensity of primaries of high energy.

The coincidences between two trays of Geiger counters (each tray 24 in.$\times$90 in.) located at a depth of 8.46×10^4 g cm^{-2} in a salt mine in Detroit, Michigan, were recorded each hour and analyzed for diurnal variations. An inch of Pb was placed between the trays to effectively eliminate coincidences due to local radioactivity and the accidental counting rate ($\sim$1.3 hr^{-1}) was measured periodically (showing negligible time variations) for use in correcting observed counting rates. During the year ending March 31, 1952, 7.4×10^5 counts were recorded with a mean corrected counting rate of 107.8 hr^{-1}. The average energy of μ-mesons observed at the depth of the mine has been estimated to be $\sim2\times10^{11}$ ev.[2]

The variation of intensity with solar time is shown in Fig. 1 and with sidereal time in Fig. 2. The errors are

* This work has been partially supported at different stages by the Air Force Cambridge Research Center and the joint program of the ONR and AEC.

[1] H. Elliot and D. W. N. Dolbear, J. Atmos. Terr. Phys. **1**, 205 (1951); H. Elliot, *Progress in Cosmic-Ray Physics*, edited by J. G. Wilson (North-Holland Publishing Company, Amsterdam, 1952), Chap. VIII.

[2] C. A. Randall, thesis, University of Michigan (1950) (unpublished).

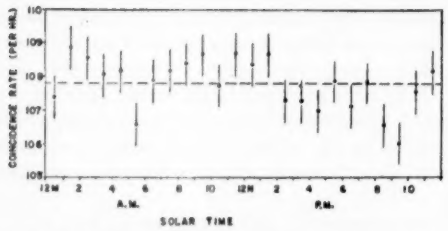

FIG. 1. Variation of cosmic-ray intensity with solar time at 8.46×10^4 g cm^{-2} depth. Errors are standard errors. The horizontal line represents the mean coincidence rate.

standard errors. In each case the standard deviation of the observed coincidence rates from the mean rate is not larger than the standard deviation expected from a normal distribution:

$$\sigma_{\text{solar}}=0.74\pm0.11,$$
$$\sigma_{\text{sidereal}}=0.64\pm0.10,$$
$$\sigma_{\text{normal}}=0.63.$$

Three different curves were drawn through each set of data, and a harmonic analysis was made for each curve. The mean amplitude of the first harmonic is 0.5 for the solar time curves and 0.2 for the sidereal time curves. The standard deviation of a normal distribution whose mean varies sinusoidally with time is expected to be $\sigma=(\sigma^2_{\text{normal}}+\sigma^2_{\text{sin}})^{\frac{1}{2}}$, where σ_{sin} is the root-mean-square amplitude of the sinusoidal variation. Using the first harmonic amplitudes given above, the standard deviations are 0.82 and 0.65 for the solar and sidereal variations, respectively, indicating that the data are consistent with either a daily sinusoidal variation in the coincidence rates of $\sim$0.5 percent or with the absence of diurnal variation. These results substantially agree with those of Barrett and Eisenberg,[3] who performed similar measurements at 16×10^4 g cm^{-2}.

If diurnal variations in the integral spectrum of μ-mesons are to be associated with anisotropic primary radiation whose direction of incidence depends on the position of the sun or galaxy (relative to the zenith), then the energy spectrum of the primaries and the processes involved in production of secondaries must be known in order to determine the contribution to meson intensity. Such knowledge is necessary since primaries with different zenith angles give rise to secondaries which traverse atmospheric matter of different density during their lifetimes (thus affecting the probability of nuclear interaction relative to decay into μ-mesons) and whose μ-meson decay products are subject to greater absorption in the greater amount of matter traversed at larger zenith angles. The lack of this detailed knowledge greatly limits the information concerning anisotropic incidence of primary radiation which can be deduced from the diurnal variation in μ-meson intensity. A further difficulty appears in the attempt to infer the peak value of the diurnal variation from the first harmonic of the analyzed data. An oversimplified model, in which a fraction of the observed μ-mesons is assumed to result from primaries emitted isotropically by the sun and traveling in straight lines to the earth and which constitutes the only contribution to the observed solar diurnal variation, will serve to illustrate the latter difficulty. If there were no intervening absorber between the sun and the detecting equipment, then the counting rate would vary sinusoidally, in accordance with the projected area of the counters on the plane normal to the direction of the radiation for twelve hours or less (beginning when the sun appears on the horizon), and then remain constant due to the earth's shielding. Harmonic analysis would then show a first harmonic whose amplitude is about half the peak variation, and the mean counting rate would be increased by about one-third of the peak contribution from the sun compared with the rate when the sun is below the horizon. Higher harmonics would be required to find the peak solar contribution. The existence of matter between the sun and the detector produces secondaries whose intensity must be expected to show a different variation from the situation in which primaries are detected directly.

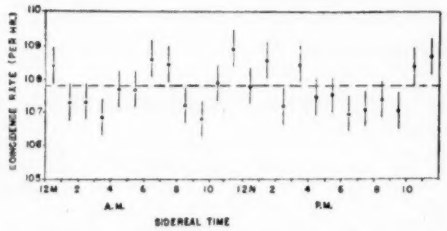

FIG. 2. Variation of cosmic-ray intensity with sidereal time at 8.46×10^4 g cm^{-2} depth. Errors are standard errors. The horizontal line represents the mean coincidence rate.

For academic interest, let us assume the simplified model above and, further, let us assume that primary radiation of solar origin has the same energy distribution as the isotropic primaries. Then the counting rate underground should depend on zenith angle θ of the sun in the same way as the intensity of secondaries of the isotropic radiation depends on their zenith angle[2] (*viz.*, $\sim\cos^{2.8}\theta$). Another $\cos\theta$ factor is introduced for the projected area of the counters, and the model indicates that the counting rate would vary as $\cos^{3.8}\theta$. Harmonic analysis of the function which varies as $\cos^{3.8}\theta$ over half the period and is zero over the other half, shows a first harmonic of $\sim$0.35 of the peak value. From the first harmonic of our experimental data the model does not exclude the possibility that about 1.7 percent of the μ-mesons observed underground are due to primaries emitted by the sun.

Most of the calculations were performed by A. E. Klickman. The collection of data is being continued with the same apparatus.

[3] P. H. Barrett and Y. Eisenberg, Phys. Rev. **85**, 674 (1952).

Masses of Light Atoms

K. OGATA AND H. MATSUDA
Department of Physics, Faculty of Science, Osaka University, Osaka, Japan
(Received June 30, 1952)

The mass differences of 33 doublets have been measured with a modified Bainbridge-Jordan type mass spectrograph, which has an experimental resolving power of about 60 000. In general, the values obtained are in good agreement with other mass spectroscopic data and with those calculated from nuclear disintegration energies. However, for the $C^{12}(H^1)_4-O^{16}$ doublet, the discrepancy between the present value 364.19 $\pm$0.06 ($\times10^{-4}$ amu) and the value 363.72$\pm$0.19 obtained from nuclear data does not seem to be negligible. The author calculated the atomic mass of C^{12}, one of the mass substandards, from the four different doublet sets, one with the $C^{12}(H^1)_4-O^{16}$ doublet and the others without. The four values of the C^{12} mass obtained were found to be in good agreement with one another, and their weighted average, 12.003844$\pm$6, was adopted as the atomic mass of C^{12}. Other mass substandards H^1 and D^2 were calculated from the $(H^1)_3-D^2$ doublet and the $(D^2)_2-\frac{1}{2}C^{12}$ doublet using the above C^{12} mass, and the atomic masses of H^1 and D^2 were obtained to be $H^1=1.008145\pm2$, $D^2=2.014741\pm3$. The atomic masses of other isotopes were determined by using these mass substandards.

I. INTRODUCTION

RECENTLY, Q-value determinations of many nuclear reactions have been made with great accuracy, especially for light nuclei, and in the low mass region, the atomic masses may be determined from the reaction data only without any mass spectroscopic data. The old mass difference values measured by the mass spectrograph were not in good agreement with those calculated from the nuclear reactions. For instance, Mattauch's value of the $(H^1)_2-D^2$ mass difference, 15.39$\pm$0.021 ($\times10^{-4}$ amu),[1] differs from the (1951) nuclear reaction value, 15.494$\pm$0.024.[2] The difference between the two values is about four times the probable error in the latter. As for the $(D^2)_2-He^4$ doublet, the Bainbridge-Jordan value, 256.1$\pm$0.4,[3] of 1937 is larger than the nuclear reaction value, 255.0 $\pm$0.23,[4] calculated from the available (1950) data by Bainbridge, by about four times the probable error in the latter value. (In the latter case improved Q determinations[2] brought agreement with the mass spectrographic value.) However, about two or three years ago mass difference redeterminations of light atomic mass doublets were started by Ewald,[5] Mattauch,[6] and Nier[7] and their collaborators, and the discrepancy between mass spectroscopic data and nuclear data has tended to become small, except for the $C^{12}(H^1)_4-O^{16}$ doublet.

In Osaka University, since 1939, mass determinations with the double-focusing mass spectrograph of the Bainbridge-Jordan type have been carried on for about thirty isotopes.[8] However, at that time, the experimental resolving power of the apparatus was about 7–8000, and close doublets, for example $(C^{12})_n(H^1)_m-(C^{12})_{n-1}C^{13}H_{m-1}$ ($n>2$), could not be resolved with it. So, since 1947, in order to obtain higher resolving power, the apparatus has been remodeled, and remeasurement of mass differences was started towards the end of 1950.

II. APPARATUS

A detailed description of the present modified Bainbridge-Jordan type mass spectrograph has been reported previously,[9] but the authors wish to introduce in this paper a brief description of the main points of the improvement. In Fig. 1, a schematic view of the

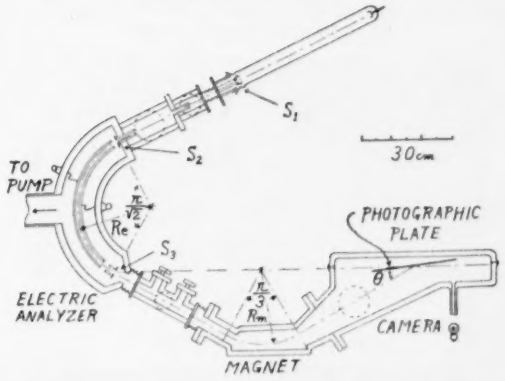

FIG. 1. Schematic drawing of modified Bainbridge-Jordan type mass spectrograph. The radius of the central beam in the electric and magnetic field, r_e and r_m, are both 25 cm. S_1 is a hole with a diameter of 0.5 mm, and S_2 is the principal slit, whose width is 0.005–0.008 mm and length about 0.2 mm, and the distance between them is about 45 cm. S_3 is the energy selecting slit with a width of about 0.08 mm. The inclination angle θ of the photographic plate relative to the central beam is about 24°.

[1] J. Mattauch, Physik. Z. **39**, 892 (1938).
[2] Li, Whaling, Fowler, and Lauritsen, Phys. Rev. **83**, 512 (1951).
[3] K. T. Bainbridge and E. B. Jordan, Phys. Rev. **51**, 384 (1937).
[4] K. T. Bainbridge, Phys. Rev. **81**, 146 (1951).
[5] H. Ewald, Z. Naturforsch. **5a**, 1 (1950); **6a**, 293 (1951).
[6] J. Mattauch and R. Bieri, Symposium on Mass Spectroscopy, National Bureau of Standards, 1951 (to be published in a bound volume of symposium papers).
[7] A. O. Nier and T. R. Roberts, Phys. Rev. **81**, 507 (1951); Collins, Nier, and Johnson, Phys. Rev. **84**, 717 (1951).
[8] Asada, Okuda, Ogata, and Yoshimoto, Nature **143**, 797 (1939); Proc. Phys.-Math. Soc. Japan **22**, 41 (1940); Okuda, Ogata, Aoki, and Sugawara, Phys. Rev. **58**, 578 (1940); Okuda, Ogata, Kuroda, Shima, and Shindo, Phys. Rev. **59**, 104 (1941); T. Okuda and K. Ogata, Phys. Rev. **60**, 690 (1941); K. Ogata, Phys. Rev. **75**, 200 (1949).
[9] K. Ogata and H. Matsuda, Symposium on Mass Spectroscopy, National Bureau of Standards (1951) (to be published).

(a)

(a) $(D^2)_2 - He^4$ doublet. (×20)

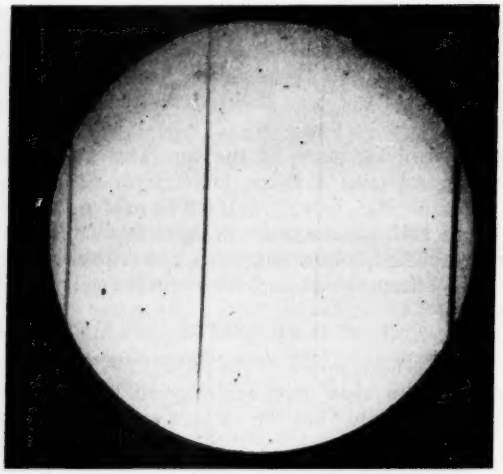

(b)

(b) $(D^2)_2O^{16} - Ne^{20}$ doublet. (×20)

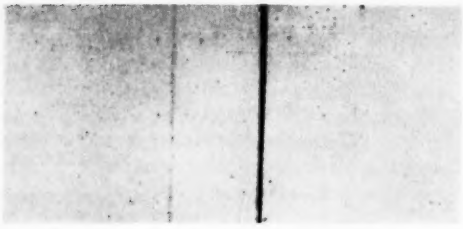

(c)

(c) $(H^1)_2 - D^2$ doublet. (×30)

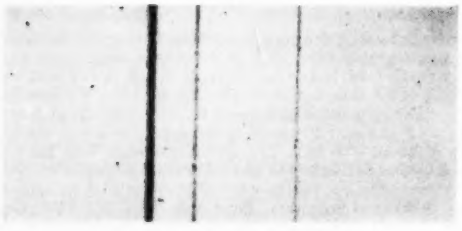

(d)

(d) $C^{13}(H^1)_4 - (N^{14})_2 - C^{13}O^{16}$ triplet. (×30)

FIG. 2. Some typical doublets.

apparatus is given. The main parts of the apparatus, electric field and magnetic field, are quite similar to those of the old Bainbridge-Jordan type; that is, the angle of the electric field and that of the magnetic field are $\pi/(2)^{\frac{1}{2}}$ and $\pi/3$, respectively, and the radius of the center beam is 25 cm in both fields. However, the collimating system and the location of the photographic plate were modified as shown in the figure. The collimating system consists of a hole S_1 and a slit S_2. The diameter of the hole S_1 is about 0.5 mm, the width of the slit S_2 is 0.005–0.008 mm, and the length 0.2 mm; and the distance between S_1 and S_2 is about 45 cm. S_3 is the energy selecting slit, whose width is 0.08–0.13 mm. Under these collimating conditions, the focal depth of the energy focusing is ten times greater than that of the direction focusing, and so the photographic plate is set along the directional focal plane, that is, at 24° to the central beam. Under this condition, the length of the sharp focusing region is about 6 cm on the photographic plate, and the center of the region is slightly on the lower mass side from the double focusing point.

The dry cells are used as the voltage supply to the electric field and their middle point is on the ground potential, and a 6–18 volt 100-amp hr storage battery is used as the magnetic field current supply. Their stability is completely sufficient during the exposure period, which is a few minutes in general. Under these conditions, a maximum experimental resolving power of about 60 000 was obtained.

The ion source is a discharge tube of ordinary Wien-type, whose diameter is 5 cm and length 50 cm, and whose discharge voltage is about 20 kv. The photographic plates now used are of Schumann-type prepared in our laboratory. In Fig. 2, some typical doublets are shown

III. DETERMINATION OF DOUBLET MASS DIFFERENCES

When the mass difference of a doublet is determined from its line separation, the following relation is as-

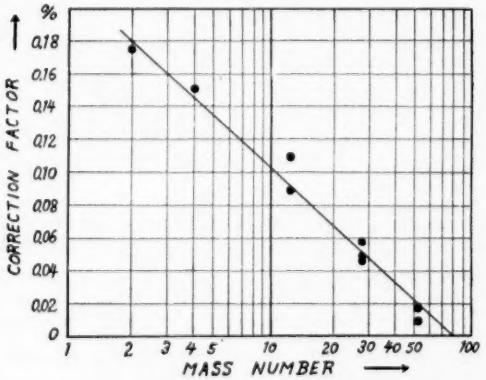

FIG. 3. Correction curve for mass dispersion referred to the Br—HBr line pair as the mass calibration standard.

TABLE I. Mass doublets.

Row	A	Doublet	No. of doublets (plates)	ΔM in 10^{-4} amu	Previous work
1	2	$(H^1)_2-D^2$	85(4)	15.492±0.008[a]	15.519±0.017[c]
					15.45 ±0.08[d]
					15.503±0.015[e]
					15.489±0.043[f]
2	4	$(D^2)_2-He^4$	36(3)	256.03 ±0.06	256.12 ±0.09[g]
					256.04 ±0.08[h]
3	6	$(D^2)_3-\frac{1}{2}C^{12}$	44(4)	423.01 ±0.09[a]	422.92 ±0.12[e]
4	10	$B^{10}-\frac{1}{2}Ne^{20}$	39(3)	167.22 ±0.08	
5	11	$B^{11}-\frac{1}{2}Ne^{22}$	18(2)	136.20 ±0.08	
6	11	$B^{10}H^1-B^{11}$	11(1)	114.47 ±0.14	
7	30	$B^{10}H^1F^{19}-B^{11}F^{19}$	18(2)	114.50 ±0.15	
		Weighted Average		114.48 ±0.10	
8	12	$B^{10}D^2-C^{12}$	16(2)	270.16 ±0.20	
9	12	$B^{11}H^1-C^{12}$	41(3)	171.15 ±0.06	
10	14	$C^{12}(H^1)_2-N^{14}$	36(4)	125.84 ±0.05[b]	125.97 ±0.21[g]
					125.64 ±0.10[e]
11	28	$(C^{12})_2(H^1)_4-(N^{14})_2$	37(4)	251.61 ±0.11[a]	251.70 ±0.25[g]
		Weighted Average		125.83 ±0.04	125.86 ±0.13[g]
12	15	$C^{12}(H^1)_3-N^{15}$	45(2)	233.77 ±0.06[b]	233.08 ±0.20[i]
13	16	$C^{12}(H^1)_4-O^{16}$	75(4)	364.15 ±0.08[b]	364.80 ±0.63[g]
14	28	$(C^{12})_2(H^1)_4-C^{12}O^{16}$	72(6)	364.23 ±0.08[a]	364.43 ±0.22[g]
		Weighted Average		364.19 ±0.06	363.71 ±0.12[e]
					364.52 ±0.10[f]
					364.27 ±0.08[j]
15	20	$(D^2)_2O^{16}-(H^1)_2O^{16}$	18(2)	83.09 ±0.18	83.12 ±0.12[e]
16	20	$(D^2)_2O^{16}-Ne^{20}$	31(3)	307.10 ±0.11	307.21 ±0.39[g]
					306.88 ±0.10[e]
17	20	$(D^2)_2O^{16}-\frac{1}{2}A^{40}$	24(2)	419.18 ±0.14	419.67 ±0.18[g]
					419.53 ±0.12[e]
18	27	$(C^{12})_2(H^1)_3-C^{12}C^{13}H^1$	20(2)	44.84 ±0.10	44.10 ±0.08[j]
19	27	$(C^{12})_2(H^1)_3-Al^{27}$	25(4)	420.14 ±0.18	
20	28	$(N^{14})_2-C^{12}O^{16}$	38(3)	112.54 ±0.09	112.73 ±0.14[g]
21	28	$C^{12}O^{16}-Si^{28}$	34(4)	180.18 ±0.14	180.15 ±0.30[e]
					180.6 ±0.8[k]
22	29	$C^{13}O^{16}-Si^{29}$	19(2)	218.00 ±0.17	
23	29	$B^{10}F^{19}-C^{13}O^{16}$	17(2)	130.49 ±0.15	
24	30	$B^{11}F^{19}-Si^{30}$	18(2)	339.48 ±0.20	
25	32	$(O^{16})_2-S^{32}$	88(5)	177.25 ±0.08[a]	177.16 ±0.20[e]
					177.64 ±0.07[j]
26	34	$S^{32}(H^1)_2-S^{34}$	64(5)	198.47 ±0.22[a]	
27	35	$S^{33}(H^1)_2-S^{34}H^1$	27(3)	113.77 ±0.32	
28	36	$(C^{12})_3-S^{34}(H^1)_2$	44(4)	165.45 ±0.22[a]	
29	36	$(C^{12})_3-H^1Cl^{35}$	21(2)	233.23 ±0.12	233.41 ±0.44[j]
30	37	$(C^{12})_3H^1-Cl^{37}$	22(2)	420.01 ±0.14	
31	38	$(C^{12})_3(H^1)_2-H^1Cl^{37}$	20(2)	420.03 ±0.14	420.14 ±0.46[j]
		Weighted Average		420.02 ±0.10	
32	40	$(C^{12})_3(H^1)_4-A^{40}$	22(3)	689.37 ±0.28	688.77 ±0.35[g]
33	48	$(C^{12})_4-S^{32}O^{16}$	32(4)	331.22 ±0.22[b]	331.32 ±0.13[j]

[a] The weighted average of the value determined by the new calibration method and that by the stray field correction on the previous data (see references 9 and 10).
[b] Determined by the stray field correction on the previous data (see references 9 and 10).
[c] T. R. Roberts, Phys. Rev. **81**, 624 (1951).
[d] Sommer, Thomas, and Hipple, Phys. Rev. **82**, 697 (1951).
[e] H. Ewald, Z. Naturforsch. **6a**, 293 (1951).
[f] See reference 6.
[g] A. O. Nier and T. R. Roberts, reference 7.
[h] H. Ewald, Z. Naturforsch. **5a**, 1 (1950).
[i] H. Ewald, Z. Naturforsch. **1**, 131 (1946).
[j] T. L. Collins, *et al.*, reference 7.
[k] H. E. Duckworth and R. S. Preston, Phys. Rev. **79**, 402 (1950).

sumed for a wider line pair (suffix 2) and a narrower doublet (suffix 1) corresponding to the required mass difference at its center:

$$\left(\frac{\Delta m_1}{m_1}\right)\Big/\Delta D_1=\left(\frac{\Delta m_2}{m_2}\right)\Big/\Delta D_2.$$

From this equation, if the fractional mass difference $\Delta m_2/m_2$ is known as the calibration standard, $\Delta m_1/m_1$ could be calculated by measuring the line separations ΔD_1 and ΔD_2.

In previous papers,[9,10] the Br−HBr line pair was used as the mass calibration standard. However, it was later found that with this mass calibration some systematic errors (about 0.2 percent at most) might be introduced to the mass differences of the doublets, especially in the light mass region. The cause of this systematic error may be attributed to the difference in the stray magnetic field, due to the difference between the field strength required for the calibration standard

[10] K. Ogata and H. Matsuda, Phys. Rev. **83**, 180 (1951).

and that for the doublet. In this case the above relation may not hold as accurately as it should, due to the difference in the dispersion constant for the doublet and for the standard line pair. Therefore, some corrections may be necessary for the mass differences previously reported.[9,10] The correction factor was obtained in the following way. First, two different sets of line pairs of the same fractional mass differences, such as $C_nH_m-C_nH_{m+1}$ and $C_{2n}H_{2m}-C_{2n}H_{2m+2}$ were recorded at the same position on a photographic plate by changing the magnetic field strength, and then the line separations for those two different sets were compared; from these the ratio of the dispersion constant could be obtained. Such an examination was performed for various fields, and the correction curve obtained is shown in Fig. 3, referring to the BrH−Br lines. The percentage correction read off from Fig. 3 should be reduced from the previous data.[9,10] The mass differences corrected with the above correction curve were found to be in good agreement with the mass differences obtained by the following calibration method.

In this paper, a new calibration method is described, in which complicated corrections such as those mentioned above are carefully avoided by using as the calibration standards the hydrocarbon lines which could be recorded with the same magnetic field strength as for the doublets to be measured. However, when the C_1-group is used for calibration standards, a correction of about +0.02 percent is necessary in the dispersion constant because of the wide separation. For the doublets of isotopes lighter than $M=12$, the above stray field correction may be necessary because no hydrocarbon lines could be used.

The systematic errors from other causes have been investigated; these are: (1) a possible effect of the shift of the center potential of the electric field from the ground potential, (2) an effect of the difference in line intensity of the doublet, (3) an effect depending on whether the atomic-molecular doublet or the molecular-molecular doublet is used. As already reported,[9] the errors of the above type have been proved to have no serious effects on the results for the conditions under which the measurements were made.

TABLE II. Zero cycles of mass doublets.

Cycle	$\Delta 10^{-4}$ amu
$(B^{10}D^2-C^{12})-(B^{10}H^1-B^{11})-(B^{11}H^1-C^{12})$ $+[(H^1)_2-D^2]$	+0.02±0.24
$[C^{12}(H^1)_2-N^{14}]+\frac{1}{2}[(N^{14})_2-C^{12}O^{16}]$ $-\frac{1}{2}[C^{12}(H^1)_4-O^{16}]$	0.00±0.07
$[(D^2)_3-\frac{1}{2}C^{12}]-\frac{3}{2}[C^{12}(H^1)_4-O^{16}]$ $-\frac{1}{2}[(O^{16})_2-S^{32}]+\frac{1}{2}[(C^{12})_4-S^{32}O^{16}]$ $+3[(H^1)_2-D^2]$	+0.18±0.16
$[C^{12}(H^1)_4-O^{16}]-[(C^{12})_4-S^{32}O^{16}]$ $-[S^{32}(H^1)_2-S^{34}]+[(C^{12})_3-S^{34}(H^1)_2]$	−0.05±0.32
$\frac{1}{2}[(D^2)_2O^{16}-Ne^{20}]-(B^{10}-\frac{1}{2}Ne^{20})+(B^{10}H^1-B^{11})$ $+(B^{11}H^1-C^{12})-\frac{1}{2}[C^{12}(H^1)_4-O^{16}]$ $+\frac{1}{2}[(C^{12})_2-S^{34}(H^1)_2]-\frac{1}{2}[S^{32}(H^1)_2-S^{34}]$ $-\frac{1}{2}[(O^{16})_2-S^{32}]+[(H^1)_2-D^2]$	+0.21±0.23
$(B^{10}-\frac{1}{2}Ne^{20})-\frac{1}{2}[(D^2)_2O^{16}-Ne^{20}]-(B^{10}D^2-C^{12})$ $+[(D^2)_2O^{16}-\frac{1}{2}A^{40}]-\frac{1}{2}[(C^{12})_2(H^1)_4-A^{40}]$ $+\frac{1}{2}[C^{12}(H^1)_4-O^{16}]$	+0.25±0.30
$[(D^2)_2O^{16}-\frac{1}{2}A^{40}]-\frac{1}{2}[(C^{12})_2(H^1)_4-A^{40}]$ $+2[(H^1)_2-D^2]-\frac{1}{2}[(H^1)_2S^{32}-S^{34}]$ $+\frac{1}{2}[(C^{12})_2-S^{34}(H^1)_2]-\frac{1}{2}[(O^{16})_2-S^{32}]$	+0.33±0.25

IV. DOUBLET MASS DIFFERENCE

The mass differences determined with particular attention to the above-mentioned points are summarized in Table I. In the table some of the values of the mass differences recently reported by others are also included for reference. The errors given in the table include not only the purely statistical errors and errors due to the deviation of the dispersion constant, about 0.03 percent, but also the errors due to the stray field correction, about 0.02 percent. In general, the present values are in good agreement with the recent values reported by others. However, for the $C^{12}(H^1)_4-O^{16}$ doublet the discrepancy between our present result and that of Ewald[5] is about five times as large as his error, and for the $(O^{16})_2-S^{32}$ doublet, the recent result of Collins *et al.*,[7] is greater than ours by six times their error. The mass difference for the $S^{33}(H^1)_2-S^{34}H^1$ doublet, calculated from the results obtained by Collins *et al.* for the $(C^{12})_4H^1-S^{33}O^{16}$ and $(C^{12})_4(H^1)_2-S^{34}O^{16}$ doublets, is 115.15±0.61, while the result obtained by the authors by direct measurement is 113.77±0.32.

In order to check the reliability of the results obtained, several zero-cycles were calculated, and are given in Table II. The consistency between the results obtained could be considered to be satisfactory.

In Table III(a), the present values are compared with the mass differences calculated from the Q-values of Li *et al.*'s table,[2] and in Table III(b), Q-values computed from our mass data are compared with those from nuclear reactions. As may be observed in Table III(a), the mass differences from the present mass spectroscopic measurements are in good agreement with those from nuclear reactions except for the $C^{12}(H^1)_4-O^{16}$ doublet, in which the difference is about two times as large as the error. In Table III(b), the Q-value, 3.116 ±0.004 Mev, for $O^{16}(d,\alpha)N^{14}$ is greater than that calculated from our mass data by about three times the error of the difference

V. ATOMIC MASS

To calculate the atomic masses from the doublets obtained above, the mass substandards H^1, D^2, and C^{12} must first be determined. These masses, in general, are computed from the so-called fundamental doublets, $(H^1)_2-D^2$, $(D^2)_3-\frac{1}{2}C^{12}$, and $C^{12}(H^1)_4-O^{16}$. However, the agreement between the mass spectroscopic value for $C^{12}(H^1)_4-O^{16}$ and the nuclear reaction value is not satisfactory, while for $(H^1)_2-D^2$ and $(D^2)_3-\frac{1}{2}C^{12}$ consistant values are obtained with either method. For

TABLE III. Comparison with nuclear reaction data.

(a) Doublet mass differences

Doublet	From Table I ΔM_1, 10^{-4} amu	Calculated from nuclear data ΔM_2, 10^{-4} amu[a]	$(\Delta M_2-\Delta M_1)$ in 10^{-4} amu
$(H^1)_2-D^2$	15.492±0.008	15.494±0.024	+0.002±0.025
$(D^2)_2-He^4$	256.03 ±0.06	255.96 ±0.08	−0.07 ±0.10
$(D^2)_3-\frac{1}{2}C^{12}$	423.01 ±0.09	423.02 ±0.16	+0.01 ±0.18
$B^{10}H^1-B^{11}$	114.48 ±0.10	114.66 ±0.09[b]	+0.19 ±0.14
$B^{10}D^2-C^{12}$	270.16 ±0.20	270.44 ±0.15[c]	+0.28 ±0.25
$B^{11}H^1-C^{12}$	171.15 ±0.06	171.27 ±0.11[d]	+0.12 ±0.13
$C^{12}(H^1)_2-N^{14}$	125.83 ±0.04	125.73 ±0.12[e]	−0.10 ±0.13
$C^{12}(H^1)_3-N^{15}$	233.77 ±0.06	233.68 ±0.11[f]	−0.09 ±0.12
$C^{12}(H^1)_4-O^{16}$	364.19 ±0.06	363.72 ±0.19[g]	−0.47 ±0.20
$(C^{12})_2(H^1)_3-C^{12}C^{13}(H^1)_2$	44.84 ±0.10	44.74 ±0.09[h]	−0.10 ±0.13

(b) Q-values.

Reaction	Q_1 calculated from Table I, in Mev[i]	Q_2 from nuclear reaction in Mev	(Q_1-Q_2) in Mev
$B^{10}(d,p)B^{11}$	9.217±0.014	9.234±0.009[j]	−0.017±0.017
$C^{12}(d,p)C^{13}$	2.733±0.009	2.723±0.004[j]	+0.010±0.010
$C^{13}(d,\alpha)B^{11}$	5.171±0.013	5.163±0.005[j]	+0.008±0.014
$N^{14}(d,p)N^{15}$	8.609±0.007	8.608±0.007[j]	+0.001±0.010
$N^{15}(p,\alpha)C^{12}$	4.957±0.008	4.961±0.005[j]	−0.004±0.009
$N^{15}(d,\alpha)C^{13}$	7.693±0.012	7.684±0.006[j]	+0.009±0.013
$O^{16}(d,\alpha)N^{14}$	3.088±0.009	3.116±0.004[j]	−0.028±0.010
$S^{32}(d,p)S^{33}$	6.445±0.036	6.422±0.011[k]	+0.023±0.038
$Si^{28}(d,p)Si^{29}$	6.254±0.023	6.246±0.008[k]	+0.008±0.024
$Si^{29}(d,p)Si^{30}$	8.379±0.030	8.388±0.013[l]	−0.009±0.033
$Si^{29}(d,\alpha)Al^{27}$	6.018±0.032	5.994±0.011[l]	+0.024±0.034

1 amu = 931.152 Mev.

[a] These mass differences are calculated from the Q-values listed in the paper of C. W. Li *et al.*, reference 2.
[b] $B^{10}(d,p)B^{11}$, $(2p-d)$.
[c] $C^{13}(d,p)C^{14}$, $C^{13}(d,\alpha)B^{11}$, $B^{10}(d,p)B^{11}$ and $(2d-\alpha)$.
[d] $C^{13}(d,p)C^{14}$, $C^{13}(d,\alpha)B^{11}$, $(2d-\alpha)$.
[e] $N^{14}(d,p)N^{15}$, $N^{15}(p,\alpha)C^{12}$, $(2p-d)$, $(2d-\alpha)$.
[f] $N^{15}(p,\alpha)C^{12}$, $(2p-d$, $(2r'-\alpha)$.
[g] $O^{16}(d,\alpha)N^{14}$, $N^{14}(d,p)N^{15}$, $N^{15}(p,\alpha)C^{12}$, $(2d-\alpha)$, $(2p-d)$.
[h] $C^{13}(d,p)C^{14}$, $(2p-d)$.
[i] Doublets used in the calculation:

Reaction	Row No. in Table I.
$B^{10}(d,p)B^{11}$	(1), (6), (7)
$C^{12}(d,p)C^{13}$	(1), (18)
$C^{13}(d,\alpha)B^{11}$	(1), (2), (9), (18)
$N^{14}(d,p)N^{15}$	(1), (10), (11), (12)
$N^{15}(p,\alpha)C^{12}$	(1), (2), (12)
$N^{15}(d,\alpha)C^{13}$	(1), (2), (12), (18)
$O^{16}(d,\alpha)N^{14}$	(1), (2), (10), (11), (13), (14)
$S^{32}(d,p)S^{33}$	(1), (26), (27)
$Si^{28}(d,p)Si^{29}$	(1), (18), (21), (22)
$Si^{29}(d,p)Si^{30}$	(1), (6), (7), (22), (23), (24)
$Si^{29}(d,\alpha)Al^{27}$	(1), (2), (13), (14), (19), (21), (22)

[j] See reference 2.
[k] E. N. Strait *et al.*, Phys. Rev. **81**, 747 (1951).
[l] D. M. Patter *et al.*, Phys. Rev. **85**, 142 (1952).

the determination of the C^{12} mass, the following four doublets sets could be used; one of these is the ordinary fundamental doublets, while the others do not contain the $C^{12}(H^1)_4-O^{16}$ doublet.

$$\left.\begin{matrix}(H^1)_2-D^2\\(D^2)_3-\frac{1}{2}C^{12}\\C^{12}(H^1)_4-O^{16}\end{matrix}\right\} \quad C^{12}=12.003840\pm 8 \quad (1)$$

$$\left.\begin{matrix}(O^{16})_2-S^{32}\\(C^{12})_4-S^{32}O^{16}\end{matrix}\right\} \quad C^{12}=12.003849\pm 6 \quad (2)$$

$$\left.\begin{matrix}B^{10}-\frac{1}{2}Ne^{20}\\(D^2)_2O^{16}-Ne^{20}\\B^{10}D^2-C^{12}\\(D^2)_3-\frac{1}{2}C^{12}\end{matrix}\right\} \quad C^{12}=12.003829\pm 27 \quad (3)$$

$$\left.\begin{matrix}(D^2)_2O^{16}-\frac{1}{2}A^{40}\\(C^{12})_3(H^1)_4-A^{40}\\(D^2)_3-\frac{1}{2}C^{12}\\(H^1)_2-D^2\end{matrix}\right\} \quad C^{12}=12.003827\pm 15 \quad (4)$$

Since the four different values of the C^{12} mass thus obtained were found to be in good agreement with one another, the weighted average of those four values was adopted as the atomic mass of C^{12}, and then the atomic masses of H^1 and D^2 were calculated from this C^{12} value and the mass differences of the $(H^1)_2-D^2$, $(D^2)_3-\frac{1}{2}C^{12}$ doublets. The masses of H^1, D^2, and C^{12} thus determined are given in Table IV together with those reported by others. The masses of other isotopes are computed from the doublet mass differences given in Table I with these masses of H^1, D^2 and C^{12} and are given in Table V.

In Table VI, some mass differences obtained in the

TABLE IV. Mass substandards.

	H^1	D^2	C^{12}
Ewald[a]	$1.008141 \pm 2\times10^{-6}$	$2.014732 \pm 4\times10^{-6}$	$12.003807\pm11\times10^{-6}$
Collins *et al.*[b]	$1.008146 \pm 3\times10^{-6}$	$2.014740 \pm 6\times10^{-6}$[e]	$12.003842\pm 4\times10^{-6}$
Li *et al.*[c]	$1.008142 \pm 3\times10^{-6}$	$2.014735 \pm 6\times10^{-6}$	$12.003804\pm17\times10^{-6}$
Bainbridge[d]	$1.0081386\pm3.2\times10^{-6}$	$2.0147252\pm5.7\times10^{-6}$	$12.003895\pm19\times10^{-6}$
Present work	$1.008145 \pm 2\times10^{-6}$	$2.014741 \pm 3\times10^{-6}$	$12.003844\pm 6\times10^{-6}$

[a] H. Ewald, Z. Naturforsch. **6a**, 293 (1951).
[b] T. L. Collins *et al.*, reference 7.
[c] See reference 2.
[d] See reference 4.
[e] Computed from H^1 and $(H^1)_3-D^2=15.519\pm0.017$ [T. R. Roberts, Phys. Rev. **81**, 624 (1951)].

TABLE V. Atomic masses.

C^{12}	$=12.003844\pm 6$
D^2	$=2.014741\pm 3$
H^1	$=1.008145\pm 2$
He^4	$=4.003879\pm 9$
B^{10}	$=10.016110\pm10$[a]
B^{11}	$=11.012811\pm 9$[b]
C^{13}	$=13.007505\pm12$
N^{14}	$=14.007550\pm 5$
N^{15}	$=15.004902\pm 9$
O^{18}	$=18.004883\pm20$
F^{19}	$=19.004444\pm22$
Ne^{20}	$=19.998772\pm13$
Ne^{22}	$=21.998382\pm24$
Al^{27}	$=26.990109\pm23$
Si^{28}	$=27.985825\pm16$
Si^{29}	$=28.985705\pm21$
Si^{30}	$=29.983307\pm31$
S^{32}	$=31.982274\pm8$[c]
S^{33}	$=32.981941\pm37$
S^{34}	$=33.978709\pm19$[d]
Cl^{35}	$=34.980064\pm22$
Cl^{37}	$=36.977675\pm21$
A^{40}	$=39.975148\pm24$[e]

[a] Weighted average of the masses from Row (4) and (8) in Table I.
[b] From (6) and (9).
[c] From (25) and (33).
[d] From (26) and (28).
[e] From (17) and (32).

above manner are compared with those calculated from recent nuclear disintegration data as well as with those from other mass spectroscopic data. The sulfur mass difference ratio, $(S^{32}-S^{32})/(S^{34}-S^{32})$, calculated from the present results is 0.500727 ± 20, which is in good agreement with the microwave value, 0.500714 ± 30;[11] while the value, 0.50082 ± 3, for the sulfur mass difference ratio is calculated from the data of Collins *et al.*[7] The mass ratio of Cl^{35}/Cl^{37} calculated from the present data is 0.9459779 ± 9, which is in agreement with the values obtained by others.[7]

The authors wish to express their sincere appreciation to Professor J. Mattauch for his valuable suggestions. It is also a pleasure to express their thanks to Dr. Asao Sugimoto for his kindly supplying us with the enriched sample of N^{15}. The authors are very greatly indebted to Mr. Y. Yoshikawa for preparing the BF_3 and SiF_4 sample, and to Mr. T. Nakatsuka for his laborious work in preparing Schumann plates. Also the authors acknowledge their gratitude to Professor T. Asada for his continuous interest in their mass determination work.

TABLE VI. Mass differences (amu) of nuclides comparing with other data.

	Present work (from Table V)	Previous work	Reference
$Si^{29}-Si^{28}$	$0.999880\pm26\times10^{-6}$	$0.99986 \pm16\times10^{-6}$	Duckworth[a]
		$0.999885\pm11\times10^{-6}$	Nuclear reaction[b]
$Si^{30}-Si^{29}$	$0.997602\pm36\times10^{-6}$	$0.99723 \pm21\times10^{-5}$	Duckworth[c]
		$0.997593\pm16\times10^{-6}$	Nuclear reaction[d]
$Si^{28}-Al^{27}$	$0.995717\pm28\times10^{-6}$	$0.995712\pm25\times10^{-6}$	Nuclear reaction[e]
$S^{33}-S^{32}$	$0.999667\pm38\times10^{-6}$	$0.99989 \pm 5\times10^{-5}$	Collins *et al.*[f]
		$0.999696\pm14\times10^{-6}$	Nuclear reaction[g]
$S^{34}-S^{32}$	$1.996435\pm21\times10^{-6}$	$1.99652 \pm 5\times10^{-5}$	Collins *et al.*[f]

[a] H. E. Duckworth and R. S. Preston, Phys. Rev. **79**, 402 (1950).
[b] From $Si^{28}(d,p)Si^{29}$ [E. N. Strait *et al.*, Phys. Rev. **81**, 747 (1951)], and H^1, D^2 (reference 2).
[c] Duckworth, Preston, and Woodcock, Phys. Rev. **79**, 188 (1950); and reference a.
[d] From $Si^{29}(d,p)Si^{30}$ [D. M. Patter *et al.*, Phys. Rev. **85**, 142 (1952)], and H^1, D^2 (reference 2).
[e] From $Al^{27}(\alpha,p)Si^{30}$, $Si^{28}(d,p)Si^{29}$ (E. N. Strait *et al.*, reference b), $Si^{29}(d,p)Si^{30}$ (D. M. Van Patter *et al.*, reference d) and H^1, $[(D^2)_3-He^4]$ (reference2).
[f] T. L. Collins *et al.*, reference 7.
[g] From $S^{32}(d,p)S^{33}$ (E. N. Strait *et al.*, reference b) and H^1, D^2 (reference 2).

[11] S. Geschwind and R. Gunther-Mohr, Phys. Rev. **81**, 882 (1951).

Alpha-Radioactivity in the 82-Neutron Region*

J. O. Rasmussen, Jr., S. G. Thompson, and A. Ghiorso
Department of Chemistry and Radiation Laboratory, University of California, Berkeley, California

(Received September 15, 1952)

In a survey for alpha-activity among cyclotron produced neutron deficient nuclides of the elements below lead, alpha-activity was detected in a number of rare earth nuclides with atomic number greater than 62, that of samarium, and in a gold and a mercury nuclide. A detailed study of the alpha-active nuclides of europium, gadolinium, terbium, and dysprosium was made.

The relationship between alpha-decay rates and energies in the rare earth region is examined. Calculations of the "effective nuclear radius for alpha-particles" were made using five different alpha-decay rate formulas.

The trends of the rare earth alpha-decay energies are discussed, particularly with respect to the discontinuity in neutron binding energies at the closed shell of 82 neutrons.

I. INTRODUCTION

RADIOACTIVE decay by emission of alpha-particles is a commonly observed mode of decay in the isotopes, both natural and artificial, of the elements of atomic number greater than 82, that of lead. However, with the lone exception of the alpha-emitting isotope of natural samarium ($Z=62$), discovered by Hevesy and Pahl[1] in 1933, alpha-decay in isotopes of elements below bismuth ($Z=83$) had not been reported prior to 1949.[2] At various times the problem of alpha-stability in these lighter elements has been considered.[3] It had been noted from observation of the general slope of the experimental mass defect curve that most isotopes of mass number greater than about 150 are energetically unstable toward alpha-decay. The fact that alpha-decay had not been observed (excepting in samarium) in the naturally occurring isotopes of the medium heavy elements could be adequately explained by the quantum mechanical consideration of the rate of penetration of the Coulombic potential barrier by escaping alpha-particles. The decay rate formulas developed by Gamow[4] and by Gurney and Condon[5] and verified by comparison with experimental alpha-decay data in the heavy elements showed the alpha-decay rate to be a very sensitive exponential function of decay energy. Thus, the naturally occurring isotopes of medium heavy elements might be unstable toward alpha-decay by energies up to about 2 Mev and still have unobservedly long alpha-decay half-lives (greater than $\sim 10^{16}$ years).

Kohman[6] has made an analysis of the binding energies for alpha-particles in medium heavy elements, based on the semi-empirical mass equation of Bohr and Wheeler[7] and the experimental mass defect curve. On this basis Kohman has predicted for the medium heavy elements that those nuclides sufficiently far to the neutron deficient side of the beta-stability region might exhibit observable alpha-decay. The mass defect curve is not well enough known in the regions of interest to make very exact predictions. A semi-empirical formula for alpha-decay energy developed by Feenberg,[8] taking into account the finite compressibility of nuclear matter, leads to the same general conclusions.

Studies[9] of the systematics of alpha-decay energy among the heavy elements have shown that, in accordance with the above mentioned theoretical predictions, for a series of isotopes (constant Z) the natural trend of alpha-decay energy is to increase as the number of neutrons is decreased, except for a large discontinuity at the closed shell of 126 neutrons. While alpha-decay energy generally increases with decreasing neutron number, the energy available for orbital electron capture or positron decay also generally increases (aside from fluctuations due to nuclear shell effects) and, consequently, half-lives for both modes of decay decrease. Whether or not by the removal of neutrons in the medium heavy elements, alpha-emission would become an important mode of decay before the half-lives became inconveniently short for detection had to be tested by experiments.

A survey was initiated in which targets of various medium heavy elements were subjected to high energy particle bombardments and then examined for alpha-radioactivity.

In 1949 Thompson and co-workers[2] reported some positive results of this survey, the discovery of alpha-radioactivity in neutron deficient isotopes of gold and

* Most of the material in this article is presented in greater detail in University of California Radiation Laboratory Report UCRL-1473 (1951) (unpublished); and J. O. Rasmussen, Jr., Ph.D. Dissertation, University of California (1952) (unpublished).

[1] G. Hevesy and M. Pahl, Nature **130**, 846 (1932).

[2] Thompson, Ghiorso, Rasmussen, and Seaborg, Phys. Rev. **76**, 1406 (1949).

[3] G. Gamow, Proc. Roy. Soc. (London) **A126**, 632 (1930); *Constitution of Atomic Nuclei and Radioactivity* (Oxford University Press, London, 1931), pp. 15–21; Z. Physik **89**, 592 (1934); *Structure of Atomic Nuclei and Nuclear Transformations* (Oxford University Press, London, 1937), pp. 7, 38–45, 48–52; W. Heisenberg, Z. Physik **77**, 1 (1932); A. Lande, Phys. Rev. **43**, 620, 624 (1933); E. D. Eastman, Phys. Rev. **46**, 1, 238 (1934); H. A. Bethe and R. F. Bacher, Revs. Modern Phys. **8**, 82, Secs. 8, 30 (1936); C. F. v. Weizsacker, *Die Atomkerne* (Akademische Verlagsgesellschaft, Leipzig, 1937), pp. 34–35, 101–102; A. J. Dempster, Phys. Rev. **53**, 869 (1938); Hahn, Flügge, and Mattauch, Physik. Z. **41**, 1 (1940).

[4] G. Gamow, Z. Physik **52**, 510 (1929).

[5] E. U. Condon and R. W. Gurney, Phys. Rev. **33**, 127 (1929).

[6] T. P. Kohman, Phys. Rev. **76**, 448 (1949).

[7] N. Bohr and J. A. Wheeler, Phys. Rev. **56**, 426 (1939).

[8] E. Feenberg, Revs. Modern Phys. **19**, 239 (1947).

[9] Perlman, Ghiorso, and Seaborg, Phys. Rev. **77**, 26 (1950).

TABLE I. Artificial alpha-activities in elements below lead.

Element	At. No.	Mass No.	Alpha-particle energy (Mev)	Measured half-life	Other modes	Branching ratio α/total	Partial alpha-decay half-life	Prepared by
Eu	63	147	$2.8_8\pm0.1$	24 days±2	*EC*	$\sim10^{-6}$	$\sim6\times10^{8}$ yr (within factor of 3)	$Sm^{147}(p,n)$8.5 Mev $Sm^{147}(d,2n)$19 Mev $Sm^{148}(d,3n)$19 Mev
Gd	64	148	$3.1_6\pm0.1$	>35 yr	···	···	$\sim1.4\times10^{2}$ yr (within factor of 3)	$Sm^{147}(\alpha,3n)$36 Mev $Eu^{151}(p,4n)$32 Mev
		149	3.0 ±0.15	9 days±1	*EC*	$\sim7\times10^{-6}$	$\sim4\times10^{8}$ yr (within factor of 3)	$Sm^{147}(\alpha,2n)$30 Mev
		150	2.7 ±0.15	(long)	···	···	···	$Eu^{151}(d,3n)$19 Mev
Tb	65	149	$3.9_5\pm0.04$ $3.9_5\pm0.02$[a]	4.1 hr±0.2	*EC*, prob. no β^+	···	···	$Eu^{151}(\alpha,6n)$60 Mev $Gd(p,xn)$32–200 Mev
	65	151	$3.4_4\pm0.1$	19 hr±1	···	···	···	$Gd(p,xn)$100 Mev $Eu^{151}(\alpha,4n)$45 Mev
Dy	66	$149\leq A\leq153$	$4.2_1\pm0.06$	7 min±2	···	···	···	$Tb^{159}(p,xn)$100 Mev
	66	$149\leq A\leq153$	$4.0_6\pm0.04$	19 min±4	···	···	···	$Tb^{159}(p,xn)$100 Mev
	66	$149\leq A\leq153$	$3.6_1\pm0.08$	2.3 hr±0.2	···	···	···	$Tb^{159}(p,xn)$100 Mev
Au	79	$183\leq A\leq187$	$5.0_7\pm0.1$	4.3 min±0.2	*EC*, β^+	α/K x-rays $\sim10^{-4}$	~30 days (within factor of 4)	$Au^{197}(d,pxn)$190 Mev $Pt(p,xn)$120 Mev
Hg	80	$A<195$	$5.6_0\pm0.1$	0.7 min±0.2	···	···	···	$Au^{197}(d,xn)$190 Mev

Note: No alpha-decay fine structure has been detected for any of the alpha-emitters listed above. Alpha-decay energies are from ion chamber pulse analysis unless otherwise noted.

[a] Energy determination in magnetic alpha-ray spectrograph by F. Asaro and J. O. Rasmussen (unpublished results), based on Ro^{226} energy standard, using $E_{\alpha_0}=4.777$ Mev from recent work of Rosenblum (private communication quoted in UPS Table of Isotopes to be published).

mercury and in isotopes of the rare earth elements containing a few more than 82 neutrons.

The present paper is concerned with the detailed study of the alpha-radioactive isotopes discovered in the survey, particularly in the heavy rare earth region. Also, several hitherto unreported alpha-active isotopes in the rare earth region are reported.

It may be worth mentioning at this point that with similar short, survey-type bombardments with 200-Mev protons on tungsten, tantalum, silver, palladium, samarium oxide, and tellurium (Te^{122}) oxide,[10] it was not possible with the techniques employed here to detect induced alpha-radioactivity other than that ascribable to heavy element contamination. The significance of these negative results is only qualitative; faster, more sensitive techniques may eventually uncover induced alpha-activity in the regions where initially negative results were obtained.

II. EXPERIMENTAL RESULTS

For each alpha-activity observed in the medium heavy elements, it would be desirable to obtain the following information: (1) alpha-particle energy, (2) half-life of activity, (3) atomic number of alpha-active nuclide (element assignment), (4) mass number of nuclide, and (5) other modes of decay, their accompanying radiations, and branching ratios between the decay modes of the nuclide. The experimental methods employed for obtaining such information are discussed in Appendix I.

A number of the alpha-emitting nuclides discovered among the neutron deficient nuclides of the medium heavy elements have been studied individually. Table I lists a number of these alpha-emitters with some of their properties. The ± sign with numerical data precedes the estimated limits of error, not the probable error. Experimental uncertainties in this work generally arise from so many sources as to render statistical evaluation of probable error impractical. Figure 1 shows the section of the isotope chart in which the rare earth alpha-emitters are situated.

A. Europium Isotope ($Z=63$)

In the first preliminary report[3] concerning this investigation it was stated that bombardment of samarium ($Z=62$) oxide with 200-Mev protons produced no significant amount of alpha-activity. This and other early proton bombardments of samarium for short periods of time (less than one hour), which also gave negative results, indicated that alpha-decay is not a prominent mode of decay among those neutron deficient isotopes of europium and samarium, whose half-lives are long enough (>3 minutes) to have been observed.

Later it was found possible by longer bombardments of samarium targets with protons or deuterons to produce enough of one europium isotope to observe its alpha-decay branching. Following bombardment of separated isotope $_{62}Sm^{147}$ oxide with 8.5-Mev protons and of natural samarium oxide with 19-Mev deuterons, there was observed a small amount of alpha-activity which decayed with about a three week half-life.

From the decay curve for the total count rate summed over the 2.8_8 Mev peak on the pulse analyzer, a value of 26±4 days was deduced for the half-life of the activity. The large limits of error on the half-life determined from this curve arise from the statistical uncertainties attending these determinations of such low counting rates and the fact that decay could only be followed through a decay factor of three.

A general study of the neutron deficient europium

[10] Electromagnetically enriched stable isotope. On loan from Oak Ridge Isotope Research and Development Division.

isotopes by Hoff, Rasmussen, and Thompson[11] has been recently made by proton and deuteron bombardments of isotopically enriched samarium oxide[10] targets. The isotope Eu^{147} was found to decay predominantly by electron capture with a half-life of 24 ± 2 days as determined from Geiger counter decay curves. None of the other neutron deficient europium isotopes with mass numbers between 144 and 150 have half-lives near 24 days. Hence, the observed alpha-activity in europium is evidently due to alpha-decay branching of Eu^{147}. Comparable amounts of Eu^{145}, Eu^{148}, and Eu^{149} have not shown detectable alpha-activity and are thus presumed to have alpha-decay rates less by at least a factor of five than that of Eu^{147}.

After these bombardments europium activities were separated from the samarium target material by means of the standard cation exchange column elutions described in Appendix I, E. The eluting agent for the 83°C separation was *p*H 3.4 citrate solution. Low energy alpha-activity was detected, following chemical separation, in the europium fraction, as mentioned. Further proof that it is a europium isotope will be given presently.

Energy determination for the europium alpha-activity was made by pulse analysis[12] of a thin vaporized sample, with Gd^{148} and Sm^{147} serving as alpha-energy standards. The alpha-particle energy for the standard Sm^{147} (a uniform, vaporized sample of Oak Ridge separated Sm^{147} oxide) was taken as 2.18 Mev from the work of Jesse and Sadauskis.[13] The energy for the standard Gd^{148} is taken as 3.16 Mev, the determination of which is mentioned in the following section, II B. By linear interpolation between the standards the alpha-particle energy of this europium activity is determined to be 2.8_8 Mev with estimated limits of error ±0.1 Mev.

Chemical proof that the 2.88-Mev alpha-activity is due to a europium nuclide and not to a gadolinium nuclide (which might conceivably have been produced by alpha-particles in the deuteron or proton beams of the 60-inch cyclotron) has been made by subjecting a mixture of a sample containing 2.88-Mev alpha-activity and Gd^{148} (3.16 Mev) alpha-tracer to a sodium amalgam reduction separation (Appendix I, E). Alpha-pulse analysis of activity in the reduced fraction and of activity not reduced showed the predominance of 2.88-Mev alpha-activity in the reduced fraction (europium) and of 3.1_6-Mev alpha-activity in that not reduced (gadolinium).

Determination of the branching ratio between alpha-decay and electron capture in Eu^{147} is difficult, since the detailed decay scheme for the electron capture process has not been determined yet and the counting yield of the Geiger-Mueller counter is not known. In order to make a rough estimate of the α/EC branching ratio in Eu^{147}, the decay of the 24-day activity was followed by counting the same thin vaporized sample in the alpha-pulse analyzer and in a windowless methane proportional counter (Nucleometer[14]) operated at 5 kev. The counting yield of the Nucleometer for electron capture decay is generally much higher than that of a conventional Geiger counter, since the Nucleometer counts Auger and conversion electrons of low energies which would be stopped by the window of a Geiger counter. It was found in this laboratory for a few heavy element electron capturing nuclides whose absolute disintegration rates could be calculated by observation of growth of their alpha-active daughters that the mean counting yield of 30 percent for the electron capture process in the Nucleometer is not greatly in error for any of the examples studied. Assuming 30-percent counting yield for the electron capture decay of Eu^{147} in the Nucleometer and a counting yield of 40 percent for the alpha-particles in the alpha-pulse analyzer, the branching ratio was calculated to be roughly $\alpha/EC\approx1\times10^{-5}$. With this branching ratio the partial half-life for alpha-decay is about 6×10^{8} years. The uncertainty of this partial alpha-half-life estimate is largely due to the counting yield assumption for *EC*, but the value is probably reliable within a factor of three.

B. Gadolinium Isotopes ($Z=64$)

1. 3.1₆-Mev Gd^{148}

After a bombardment of dysprosium oxide with 200-Mev protons a small amount of a long lived, low energy alpha-activity was found. Subsequent bombardments showed it to be produced in much larger yield by 38-Mev alpha-particle bombardment of natural samarium oxide or, in still greater yield, of samarium enriched[10] in Sm^{147}. Also this activity was produced in large yield by 50-Mev proton bombardment of europium oxide and in low yield with 32-Mev protons.

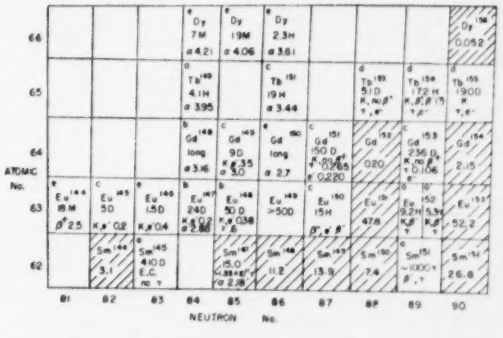

FIG. 1. Section of isotope chart showing the rare earth alpha-emitters. Mass numbers of dysprosium alpha-emitters are not known.

[11] Hoff, Rasmussen, and Thompson, Phys. Rev. **83**, 1068 (1951).
[12] Ghiorso, Jaffey, Robinson, and Weissbourd, *The Transuranium Elements: Research Papers* (McGraw-Hill Book Company, Inc., New York, 1949), Paper No. 16.8, National Nuclear Energy Series, Plutonium Project Record, Vol. 14B, Div. IV.
[13] W. P. Jesse and J. Sadauskis, Phys. Rev. **78**, 1 (1950).
[14] Manufactured by Radiation Counter Laboratories, Inc., Skokie, Illinois.

Bombarded material containing this activity was subjected to chemical separation by standard cation exchange column elutions and by sodium amalgam reduction, which procedures are described in Appendix I, E. In all these separations the long lived alpha-activity remained with the gadolinium fraction.

The alpha-particle energy of this long-lived gadolinium isotope was determined to be $3.1_6 \pm 0.1$ Mev by pulse analysis and comparison with many heavy element alpha-emitting standards of known energy. The conservatively large error limits are given because the alpha-energy standards were of much higher energy.

Counting data of the 3.1_6-Mev alpha-activity over a two year period established a lower limit of 35 years for the half-life.

The determination of mass number of the gadolinium isotope giving rise to this activity was made on the basis of the experimentally determined excitation function for its production by alpha-particle bombardment of enriched samarium (Sm^{147}) oxide, and by proton bombardment of natural europium. The alpha-particle excitation function, shown in Fig. 2, was determined by bombardment in the 60-inch cyclotron and the proton function by 31-Mev proton bombardment in the linear accelerator. In the transfer of bombarded oxides to platinum plates for counting, the oxides were dissolved in 12*N* HCl, precipitated as the hydroxides by addition of ammonia gas, washed with water, and slurried onto platinum plates for counting. The uncertainty in the ordinates of the points in Fig. 2 may be about 30 percent arising from uncertainties in chemical yield and self-absorption of alpha-particles in the relatively thick samples.

The element assignment of the 3.1_6-Mev alpha-activity to gadolinium reduced the mass assignment problem to that of deciding whether the excitation function of Fig. 2 with reaction threshold 28–30 Mev is that of an α,n, $\alpha,2n$, $\alpha,3n$, or $\alpha,4n$ reaction. The choice should be consistent with the observation in the proton excitation function of about a 30-Mev threshold for the $Eu^{151}(p,xn)Gd^{152-x}$ reaction. Since statistical theory predicts as bombarding energy is increased a very gradual onset of reactions in which several neutrons are evaporated, the actual energetic thresholds are probably below the estimates from these insensitive experiments. Theoretical estimates of α,xn and p,xn energetic thresholds were made by calculation from masses in the atomic mass table of Metropolis and Reitwiesner[15] (based on a semi-empirical mass formula of Fermi). Table II lists these values.

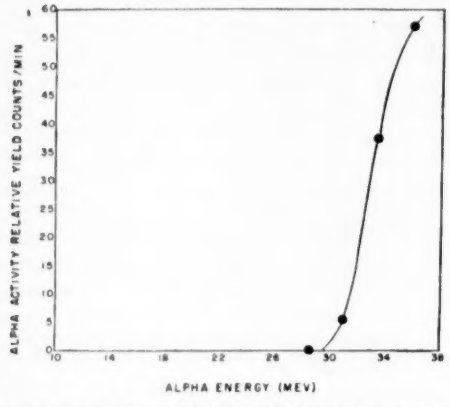

FIG. 2. Yield of 3.1_6-Mev gadolinium alpha-activity *versus* energy of alpha-particles bombarding Sm^{147}.

The comparison of the experimental and theoretical values in Table II indicate a probable mass assignment of the 3.1_6-Mev alpha-activity to Gd^{148}, although the possibility of an assignment to Gd^{147} is not too improbable, particularly when it is realized that the calculated thresholds would be lowered by a decrease in neutron binding energy that might be expected for several neutrons beyond the closed shell at 82 (see Harvey[16]). The mass assignment to 148 rather than to 147 seems more consistent with the long half-life (>35 years) of this activity, for the even-odd nuclide Gd^{147} should have considerable energy available for electron capture decay and consequently a much shorter half-life than 35 years.

It is possible to make a very rough estimate of the partial half-life for alpha-decay of Gd^{148} from the yield of 3.1_6-Mev alpha-activity produced in the excitation function bombardment of Sm^{147} with alpha-particles if an approximate value is assumed for the $\alpha,3n$ reaction cross section. From the observed yield for 36-Mev alpha-particles with a beam of measured intensity it was determined that,

$$T_{\frac{1}{2}\alpha}/\sigma(\alpha,3n) \approx 1.4\times 10^2 \text{ years barn}^{-1}.$$

The α,xn cross sections in the rare earth region are not known. If it is assumed that this cross section is about one barn, as was found for the $\alpha,3n$ reaction on Bi^{209} at the same energy above the $\alpha,3n$ threshold,[17] the estimate of the partial alpha-decay half-life of Gd^{148} would be 1.4×10^2 years. This estimate is probably reliable to a factor of three.

The presence of long lived electron capturing gadolinium isotopes in the samples containing Gd^{148} make it impossible at present by simple beta-gamma counting to set a significant lower limit on the branching ratio between alpha-decay and electron capture, if electron capture is a mode of decay. The possibility that Gd^{148} may be stable with respect to electron capture decay can neither be ruled out nor confirmed by present data.

2. *3.0-Mev* Gd^{149}

Following a bombardment of 200 mg of samarium oxide with 31-Mev alpha-particles, a chemical separa-

[15] N. Metropolis and G. Reitwiesner, *Table of Atomic Masses*, Atomic Energy Commission Unclassified Document NP-1980 (March, 1950), unpublished.
[16] J. A. Harvey, Phys. Rev. **81**, 353 (1951).
[17] E. L. Kelly and E. Segrè, Phys. Rev. **75**, 999 (1949).

tion by standard cation exchange column elution at room temperature (Appendix I, E) was made. A sample plate of the gadolinium and europium chemical fraction was prepared by vaporization. A small amount of 3.1_6-Mev Gd^{148} was observed in the sample; in addition there was some activity with alpha-energy of about 3.0 ± 0.15 Mev which decayed with a half-life of about a week. This 3.0-Mev activity was not observed following intensive deuteron (19 Mev) bombardments of of Sm_2O_3 and, hence, cannot be europium. The 3.0-Mev activity was assigned to Gd^{149}, which has been studied by Hoff *et al.*[11] and found to decay mainly by orbital electron capture with a half-life of 9 ± 1 days. The α/EC branching ratio is about 7×10^{-6} from comparison counting in the alpha-pulse analyzer and the methane proportional counter (Nucleometer) on the same counting yield assumptions as were made for the Eu^{147} α/EC estimation (i.e., α, 0.4; EC, 0.3). This branching ratio figure is probably good to within a factor of three. This branching ratio would correspond to a partial alpha half-life of about 4×10^{8} years.

3. 2.7-Mev Gd^{150}

It has been suggested by Kohman[18] that Gd^{150} might be stable with respect to electron capture although it is missing in nature. Thus, like Sm^{146}, Gd^{150} might be so missing because its alpha-decay half-life is much less than the age of the elements (i.e., $T_{\frac{1}{2}}\lesssim10^{8}$ years). In the hope that the alpha-half-life of Gd^{150} might be short enough to detect by cyclotron production, an intense irradiation of Eu_2O_3 with 19-Mev deuterons was made. Gd^{150} should have been produced in fair yield by the reaction $Eu^{151}(d,3n)Gd^{150}$.

Following bombardment the Eu_2O_3 target material was dissolved in 6N HCl, the rare earth hydroxides were precipitated with ammonia, and after redissolving with a minimum of 6N HCl a chemical separation of europium (and partially samarium) from gadolinium was made by the sodium amalgam procedure (Appendix I, E).

A thin uniform sample of part of the gadolinium fraction on a platinum plate was prepared by the volatilization technique (Appendix I, E). This sample exhibited a minute amount (0.45 alpha-disintegration/minute) of alpha-activity of 2.7 ± 0.15 Mev energy. The presence of short-range alpha-activity in the gadolinium fraction was further confirmed by Dunlavey,[19] who introduced some of the gadolinium fraction into the emulsion of an Ilford C2 photographic plate and allowed it to stand for several days before developing. Microscopic examination of the developed plate revealed a number of alpha-particle tracks with a mean range of about 9.7 microns. This range corresponds to an alpha-particle energy of 2.7_4 Mev on the range-energy curves of Rotblat.[20]

[18] T. P. Kohman, Phys. Rev. **73**, 20 (1948).
[19] D. C. Dunlavey, unpublished results.
[20] D. J. Rotblat, Nature **165**, 387 (1950).

TABLE II. Calculated reaction thresholds from Fermi semi-empirical mass equation.

Reaction	Threshold (Mev)
$Sm^{147}(\alpha,2n)Gd^{149}$	16.9
$(\alpha,3n)Gd^{148}$	24.5
$(\alpha,4n)Gd^{147}$	34.0
expt.	~28–30
$Eu^{151}(p,3n)Gd^{149}$	17.9
$(p,4n)Gd^{148}$	25.5
$(p,5n)Gd^{147}$	34.9
expt.	~30

The mass assignment of this alpha-activity to Gd^{150} should be considered tentative, since the assignment is based principally on semi-empirical considerations of the probable expected alpha-decay energy for Gd^{150}. Decay measurements over a one-year period show the activity to have a half-life of greater than two years, ruling out the possibility that this activity could arise from 155 day[21] Gd^{151}.

Sun *et al* [22] have reported observing an alpha-activity of 7.0-hour half-life from a bombardment of Sm_2O_3 with 30-Mev alpha-particles. This activity was assigned by them to gadolinium, since it was not produced by proton (8-Mev) and deuteron (15-Mev) bombardments on Sm_2O_3. They do not mention any alpha-particle energy measurements nor any chemical separations. In apparent contradiction to this it has not been possible here to detect any rare earth alpha-activity of half-life near seven hours following intense irradiations of Sm_2O_3 with 30-Mev alpha-particles. In nearly all bombardments here it is observed that some alpha-activity due to traces of heavy element (uranium, thorium, bismuth, or lead) impurities in the target materials is produced. It has generally been necessary to make alpha-energy measurements or chemical separations or both to make sure that observed alpha activity was due to rare earth nuclides and not to heavy element contaminants. For example, the 7.5-hour alpha-emitter At^{211} would be produced in good yield by 30-Mev alpha-particles on an extremely small amount of bismuth impurity by the reaction $Bi^{209}(\alpha,2n)At^{211}$. An alpha-particle energy measurement on any newly discovered alpha-emitter in the rare earth region needs to be made as proof in view of the probability of heavy element impurities in small amounts.

C. Terbium Isotopes ($Z=65$)

In a preliminary report[2] the discovery of rare earth alpha-emitters with alpha-particle energies of 4.2 and 4.0 Mev and half-lives of ~7 minutes and ~4 hours, respectively, was reported and their tentative assignment to terbium made. Subsequent work provided chemical proof for the assignment of the latter activity to terbium (3.9_5 Mev, 4.1 hour). The seven minute

[21] R. E. Hein and A. F. Voigt, Phys. Rev. **79**, 783 (1950).
[22] Sun, Pecjak, Jennings, Allen, and Nechaj, Phys. Rev. **82**, 772 (1951).

activity, whose half-life is too short for chemical identification of the element, was reassigned to dysprosium ($Z=66$) on the basis of later bombardment data. Its appearance in low yield after proton bombardments of gadolinium oxide in the first experiments was probably due to a small amount of terbium present in the target material. A second alpha-emitter in terbium (3.44 Mev, 19 hour) was also observed and studied.

1. 3.9$_6$-Mev Tb^{149}

This alpha-emitter of 4.1±0.1 hour half-life was the first of the artificial rare earth alpha-emitters to be observed, following a bombardment of gadolinium oxide with 200-Mev protons. Subsequently, the 4.1-hour alpha-activity was also produced by bombardment of terbium oxide with 120-Mev protons, of dysprosium oxide and ytterbium oxide with 200-Mev protons, and of europium oxide with alpha-particles of 90 Mev, 120 Mev, and (in ~3 percent of the 90-Mev yield) 60 Mev. It was produced in very low yield in a bombardment of gadolinium oxide with 31-Mev protons.

Following a number of these bombardments chemical separations of the rare earth products were made by the standard cation exchange column elutions described in Appendix I, E. The 4.1-hour alpha-activity was always observed exclusively in the terbium chemical fractions.

The alpha-particle energy was determined by pulse analysis to be 3.95±0.04 Mev. A recent energy measurement by Asaro and Rasmussen (Table I, reference a) using a magnetic alpha-ray spectrograph gave the more accurate result 3.9$_5$±0.02 Mev.

The mass number 149 was assigned to this activity on the basis of a mass spectrographic determination previously reported[23] by the authors in collaboration with F. L. Reynolds.

No positron activity with 4.1 hour half-life could be observed in samples containing Tb^{149}, but it has not yet been possible from direct counting data to make a significant estimate on the branching ratio between alpha-decay and electron capture, as there were present in all samples of Tb^{149} many other isotopes undergoing decay by electron capture and positron emission. A lower limit on the alpha-decay to electron capture branching ratio of about one percent was previously given.[2]

2. 3.4$_4$-Mev Tb^{151}

High energy (100–200 Mev) proton bombardments of gadolinium oxide, terbium oxide, and dysprosium oxide, and alpha particle-bombardments of europium oxide were observed to produce some alpha-activity of 19±1 hour half-life.

Following proton bombardments of gadolinium oxide and of dysprosium oxide, the terbium activities were separated from the gadolinium target material by means of the standard cation exchange column elutions described in Appendix I, E. For the 87°C separations *p*H 3.4 citrate solution was used as the eluting agent. This alpha-activity was found exclusively in the terbium chemical fraction. An average of several pulse analysis energy measurements gave an alpha-particle energy of 3.4$_4$±0.1 Mev.

Only a tentative mass assignment of the 19-hour activity can be made at present. The alpha-particle excitation work on europium oxide by Rollier and Rasmussen[24] indicated a probable mass assignment to 151, with 150 a possibility.

Theoretical half-life-energy relations for alpha-decay lead to the conclusion that the predominant mode of decay of the 19-hour terbium alpha-emitter must be orbital electron capture or positron emission. The presence of 17.2-hour Tb^{154}, however, which decays by electron capture and positron emission,[25] in all samples of the 19-hour terbium has hitherto made impossible any direct determination of the branching ratios between the expected modes of decay of the 19-hour terbium alpha-emitter, although the lower limit $\alpha/EC>4\times10^{-6}$ (probably much too low) can be set.[24]

D. Dysprosium Isotopes ($Z=66$)

The three dysprosium alpha-emitters listed in Table I were observed following high energy proton bombardments of several rare earth elements with atomic number greater than 64. They were also produced by 100 Mev C^{12} ion[26] bombardments of neodymium ($Z=60$) oxide by $Nd(C^{12},xn)Dy$ reactions. The alpha-energies and the half-lives of these isotopes were determined following bombardments of terbium ($Z=65$) oxide with protons of about 100-Mev energy.

With regard to the possible mass assignments of the three dysprosium activities of 4.2$_1$-, 4.0$_6$-, and 3.6$_1$-Mev energies, it is to be noted that all three are produced in good yield by 100-Mev protons on terbium. The 4.0$_6$ and 3.6$_1$-Mev activities are apparently produced in extremely low yield by 70-Mev protons on terbium. The cross sections for production of all three dysprosium alpha-emitters undergo large increases somewhere between 70 and 100 Mev. An approximate theoretical calculation similar to that outlined by Fermi[27] of the most probable number of neutrons to be evaporated from the compound nucleus Dy^{160}, ($Tb^{159}+H^1$), excited to a maximum of energy by 70- or 100-Mev protons is 6–7 or 9–10, respectively. The dysprosium alpha-emitters then would most likely be products of Tb^{159}-$(p,xn)Dy^{160-x}$ reactions with $7\leq x\leq 11$, allowing the limits $153\geq A\geq 149$ to be set on the mass numbers. Further studies of bombardment yields of these alpha-

[23] Rasmussen, Reynolds, Thompson, and Ghiorso, Phys. Rev. **80**, 475 (1950).

[24] M. A. Rollier and J. O. Rasmussen, Jr., unpublished results.

[25] G. Wilkinson and H. G. Hicks, Phys. Rev. **79**, 815 (1950).

[26] Miller, Hamilton, Putnam, Haymond, and Rossi, Phys. Rev. **80**, 486 (1950).

[27] E. Fermi, *Nuclear Physics* (University of Chicago Press, Chicago, 1950), p. 162.

emitters in the proton energy range between 70 and 120 Mev should enable one to set better limits on the individual mass numbers.

No information concerning other modes of decay, such as electron capture or positron emission, has been obtained yet for any of the three dysprosium alpha-emitters.

1. 4.2-Mev Dysprosium

Bombardments of terbium oxide with 100-Mev protons and bombardments of neodymium oxide with ~100-Mev C^{12} ions were observed to produce some alpha-activity with a seven minute half-life.

A probable element assignment is made by noting the bombardments in which this activity is produced and those in which it is not. Its production by protons on terbium and by carbon ions on neodymium ($Z=60$) restricts the atomic number of the seven-minute activity to 66 or less. Also, its atomic number must be greater than 65, for it was not produced by bombardments of europium oxide with alpha-particles at energies of 60, 90, or 120 Mev. Hence, the seven-minute activity is attributed to a dysprosium nuclide ($Z=66$).

The seven-minute alpha-activity is seen on the first two pulse analysis curves of Fig. 3. From these curves the alpha-particle energy of the seven-minute activity was determined as 4.21±0.06 Mev. The counting rates of this activity were calculated by the summation of the counts under the pulse analysis peak. The half-life of 7±2 minutes was determined from the slope of the decay curve. Other half-life determinations agree within these limits.

2. 4.0$_6$-Mev Dysprosium

Bombardments of terbium oxide with 100-Mev protons and of dysprosium oxide with 200-Mev protons were observed to produce alpha-activity with a 19-minute half-life.

The assignment of this activity of dysprosium is made on the basis of its appearance in the 100-Mev proton bombardment of terbium oxide and not in alpha-particle bombardments of europium oxide at energies of 60, 90, and 120-Mev. The alpha-particle energy of the 19-minute dysprosium activity is determined as 4.0$_6$±0.04 Mev by pulse analysis.

From several decay curves of this alpha-activity the half-life of 19±4 minutes was determined.

3. 3.6-Mev Dysprosium

Bombardments of terbium oxide with 100- and 120-Mev protons and bombardments of neodymium oxide with ~100-Mev C^{12} ions produced some alpha-activity of 2.3-hour half-life.

The element assignment to dysprosium was made on the basis of a chemical separation of the products of a 120-Mev proton bombardment of terbium oxide. The separation was made by standard cation exchange column elution at 78°C using *p*H 3.3 citrate solution as eluting agent, as described in Appendix I, E.

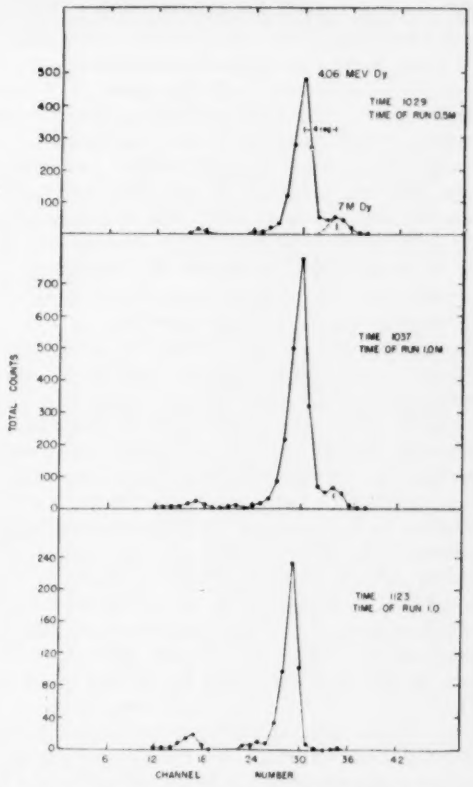

FIG. 3. Alpha-pulse analysis curves of a sample of dysprosium alpha-activities showing decay.

The alpha-particle energy was determined by pulse analysis to be 3.6$_1$±0.08 Mev. The half-life was determined from decay curves to be 2.3±0.2 hours.

E. Isotopes of Other Rare Earth Elements

There is good evidence of short half-life alpha-activities in rare earth elements with atomic number greater than 66, that of dysprosium, although no systematic study of them has yet been made.

A short bombardment of dysprosium oxide with 200-Mev protons produced, in addition to several activities in terbium and dysprosium which have been previously discussed (Secs. II, C and D), some alpha-activity with about a four-minute half-life and 4.2±0.15-Mev energy. This activity probably arises from a holmium ($Z=67$) isotope.

A short bombardment of samarium ($Z=62$) oxide with 100-Mev C^{12} ions was observed to produce some alpha-activity with about a 3.5-minute half-life. No energy measurement of the alpha-particles was made, so the possibility that this activity came from heavy element impurities in the target material cannot be

ruled out, but it seems probable that this activity was due to a holmium ($Z=67$) or an erbium ($Z=68$) nuclide.

It seems likely that some of the nuclides containing 84 or a few more neutrons of the elements of atomic number greater than 66 will exhibit appreciable decay by alpha-particle emission. It is to be expected, however, that the increased energies available to the various decay processes will result in very short half-lives for these isotopes. Those nuclides with half-lives greater than a few minutes in these higher elements are probably so many neutrons beyond the 84-neutron configuration favorable to alpha-decay that they will show unobservably low alpha-decay branching.

It appears that no appreciable alpha-branching is exhibited by neutron deficient nuclides of atomic numbers 67 to 69 with half-lives of intermediate length (>1 hour). A two-hour bombardment of erbium ($Z=68$) oxide with 200-Mev protons was made, and chemical separation by cation exchange column was completed two hours after the end of the bombardment. No alpha-activity was found in the fractions corresponding to elements with atomic number greater than 66 (dysprosium). (The 2.3-hour dysprosium alpha-activity and the 4.1-hour terbium activity were prominent in their respective chemical fractions.) In a search for long-lived alpha-activity a target of ytterbium oxide ($Z=70$) was given an intensive irradiation by protons of 150 and 250 Mev for a total of about forty hours. After several days a chemical separation by standard cation exchange column elutions was made. No alpha-activity in any of the rare earth elements was found except for the 3.1$_6$-Mev alpha-activity in gadolinium due to Gd^{148}.

No alpha-activities in nuclides with atomic numbers less than 63 (europium) have yet been observed in this investigation, excepting, of course, the natural alpha-emitting isotope Sm^{147}. Only a few short survey bombardments have been made in this region, so significant upper limits on alpha-half-lives cannot be set.

The best chance of observing alpha-activity in an artificially produced samarium isotope is probably in the 84-neutron isotope Sm^{146}, which is presumed beta-stable[18] but is missing in nature. Recently Long *et al.*[28] have reported discovery of alpha-activity attributable to Sm^{146} with a half-life of 10^4–10^6 years.

F. Gold Isotope ($A=79$)

1. 5.1-Mev Gold

Following bombardments of gold foils with 200-Mev protons or 190-Mev deuterons and of platinum foils with protons of as low energy as 100 Mev, an alpha-activity of 4.3-minute half-life was observed.[2]

This activity was assigned to gold on the basis of a chemical separation procedure utilizing extraction of the chloride into ethyl acetate as described in Appendix I, E. The alpha-activity in the gold fraction was counted within thirty seconds following chemical separation and no evidence of deviation from the simple 4.3-minute decay was found. From this evidence, it can be stated that the alpha-particles are emitted either by the 4.3-minute gold nuclide or by its platinum daughter nuclide (from positron or electron capture decay) with the half-life of the daughter less than 15 seconds, the latter possibility seeming unlikely.

By alpha-pulse analysis the energy of the 4.3-minute alpha-particles was determined as 5.07±0.1 Mev. Comparison standards Pu^{239} (5.14 Mev), Am^{241} (5.48 Mev), and Cm^{242} (6.11 Mev) were used in the determination.

The half-life of 4.3±0.2 minutes has been determined from alpha-decay curves extending through a decay factor of 100.

The limits set on the mass number of the gold alpha-emitter are rather indefinite, based on evidence concerning bombardment energies necessary for its production. Tentative limits of $183 \leq A \leq 187$ have been set.

Chemically separated samples containing the gold alpha-activity were counted with standard Geiger counters, with and without beryllium and lead absorbers. A component with approximately four-minute half-life can be resolved from the decay curves. From comparison of counting rates with different combinations of absorbers it was possible to determine an approximate figure for the abundance of electromagnetic radiation with four-minute half-life of about the energy of platinum K x-rays. The ratio of alpha-disintegrations to four minute K x-rays was about 10^{-4}. If both radiations arise from the same isotope and if roughly one K x-ray per electron capture disintegration is emitted, then the α/EC branching ratio would be 10^{-4} as reported in the 1949 paper.[2] This branching ratio should be regarded as uncertain.

G. Mercury Isotopes ($Z=80$)

1. 5.6-Mev Mercury

Following bombardments of gold foils with 190-Mev deuterons some alpha-activity of 0.7-minute half-life was observed. This activity was assigned to mercury on the basis of a chemical separation by volatilization (see Appendix I, E) from the gold foil. Its alpha-particle energy was determined to be 5.60±0.1 Mev by alpha-pulse analysis. Its half-life was determined to be 0.7±0.2 minute from decay curves of the 5.6-Mev alpha-peak from the pulse analyses.

No work to determine the threshold bombardment energy for production of this activity has been done besides the original 190-Mev deuteron bombardments; hence, no significant limits on the mass number can be set at this time.

[28] Long, Pool, and Kundu, Bull. Am. Phys. Soc. **27**, 20 (1952).

III. DISCUSSION

A. Alpha-Decay Rate

The alpha-emitters in the rare earth region are of special interest in that they provide data on the rate of alpha-decay in a region considerably removed from the heavy element alpha-emitters.

Of the rare earth alpha-emitters with known decay energies only the naturally occurring Sm^{147} has its alpha-decay rate well determined. The alpha-decay rates of Eu^{147}, Gd^{149}, and Gd^{148} are known approximately. Only upper limits can presently be set on the alpha-decay rates of the terbium and dysprosium alpha-emitters, since their alpha-to-electron capture decay branching ratios have not yet been determined experimentally

The correlations of alpha-decay rates and decay energies among the heavy element alpha-emitters show great regularity if nuclides of even-even nuclear type alone are included. The odd nucleon number alpha-emitters exhibit decay rates lower than the correlations of the even-even type nuclides would predict by factors as great as 1000.

If one knew which of several alpha-decay rate formulas that have been proposed most nearly represented the true physical situation, it would be possible by using the experimental alpha-decay of $_{64}Gd^{148}$ to calculate the value of the "effective nuclear radius for alpha-particles" or "alpha-particle penetration radius" for the daughter nuclide Sm^{144}. Alpha-decay rate formulas may generally be considered as the product of two factors, as $\lambda = f \cdot P$, where λ is the alpha-decay constant in seconds^{-1}. P represents the penetrability factor of the Coulombic potential barrier, and f, the hypothetical "decay constant in the absence of the potential barrier." The potential which the alpha-particle experiences is generally idealized as a pure coulombic potential at distances of the alpha-particle from the nucleus greater than an "effective nuclear radius" R, at which point there is assumed a sharp cutoff of the Coulombic potential to some low value. There is wide variation in the values estimated for f, the decay constant without barrier, depending upon the particular nuclear model chosen. The one body model as applied by Biswas and Patro[29] and by Perlman and Ypsilantis[30] leads to f values of the order of 2×10^{21} sec^{-1}, while at the other extreme the many-body model proposed by Bethe[31] leads to f values of the order of 1×10^{15} sec^{-1}. As a result, radius values determined from the experimental data on alpha-decay in the heavy region by the latter model exceed by 45 percent those determined by the former model. Other alpha-decay formulas lead to results between these extremes.

In view of the considerable variation in f estimates and some other details in various alpha-decay rate formulas, the R values (Sm^{144} daughter nucleus) were calculated from Gd^{148} data by five separate rate expressions. The first is the one-body formula used by Biswas and Patro[29] and by Perlman and Ypsilantis.[30] The second is a formula derived by one of the authors (J.O.R.).[32] The third is an approximate form of the one-body formula derived and applied by Preston[33] and also applied by Kaplan.[34] The fourth is a many-body expression of the same form as the second, but based on the procedure suggested by Cohen,[35] which uses alpha-penetration radii determined from alpha-particle bombardment excitation functions. The radii used were based on the (α, fission) cross-section measurements on Th^{232} by Jungermann.[36] The fifth decay expression used is the form of the many-body decay model proposed by Bethe.[31]

TABLE III. Alpha-particle penetration radius values calculated from alpha-decay rate data and corresponding constants for radius expressions.

Rate formula	Penetration radii (in 10^{-13} cm) Ra^{224}	Gd^{148}	Constants in radius expressions $aA^{\frac{1}{3}}+b$ a	b	Present's Eq.[a] a'	b'
1. BP and PY	8.70	7.55	1.46	−0.10	1.085	1.79
2. R	9.01	7.84	1.48	0.07	1.10	2.01
3. PK	9.25	8.00	1.58	−0.30	1.18	1.75
4. RCJ	10.16	9.10	1.34	2.07	1.00	3.80
5. BMB	12.60	11.78	1.04	6.32	0.77	7.70

[a] See reference 37.

The details of these five alpha-decay formulas can be found in Appendix II.

R values (Em^{220} daughter nucleus) from Ra^{224} data were also calculated by these expressions and are presented in Table III. From these R values in the two regions, constants "a" and "b" were determined to give agreement with the effective nuclear radius formula of type

$$R=(aA^{\frac{1}{3}}+b)\times10^{-13}\text{ cm},$$

where A is the mass number. The first term in the expression may be associated with the radius of the nucleus proper and the second term with the "radius of the alpha-particle" plus the range of nuclear forces. A radius expression in which the constant term might have greater physical significance was felt to be the following, employing Present's[37] nuclear radius formula which takes into account a finite compressibility of nuclear matter:

$$R=\{a'A^{\frac{1}{3}}[1+0.8(A-2Z)^2/A^2-0.3/A^{\frac{1}{3}}+0.010Z^2/A^{4/3}]+b'\}\times10^{-13}\text{ cm}.$$

The constants a, b, a', and b' are given in Table III with the five sets of R values.

[29] S. Biswas and A. P. Patro, Indian J. Phys. **22**, 540 (1948).
[30] I. Perlman and T. J. Ypsilantis, Phys. Rev. **79**, 30 (1950).
[31] H. A. Bethe, Revs. Modern Phys. **9**, 161 (1937).
[32] J. O. Rasmussen, Jr., Ph.D. Dissertation, University of California (1952), p. 65, unpublished.
[33] M. A. Preston, Phys. Rev. **71**, 865 (1947).
[34] I. Kaplan, Phys. Rev. **81**, 962 (1951).
[35] B. L. Cohen, Phys. Rev. **80**, 105 (1950).
[36] J. Jungermann, Phys. Rev. **79**, 640 (1950).
[37] R. Present, Phys. Rev. **60**, 28 (1947).

TABLE IV. Calculation of decay constants using nuclear radii fitting Gd^{148} decay.

Nuclide	Total[a] nuclear alpha-decay energy (Mev)	$\log_{10}\tau$ (τ is the mean life for alpha-decay in seconds, $\tau=1/\lambda$) Experimental	1 BP and PV 7.55[b]	2 R 7.84[b]	3 PK 8.00[b]	4 RCJ 9.10[b]	5 BMB 11.78[b]
Sm^{147}	2.26	18.79	19.89	19.87	19.74	19.88	19.77
Eu^{147}	2.98	11.42	11.98	11.98	11.91	12.01	11.94
Gd^{148} [b]	3.27	9.98	...	...	...	...	...
Gd^{149}	3.1	11.26	11.56	11.55	11.50	11.56	11.51
Gd^{150}	2.8	...	14.66	14.65	14.58	14.60	14.50
Tb^{149}	4.08	>4.33	4.66	4.64	4.64	4.68	4.73
Tb^{151}	3.56	>5.00	8.32	8.30	8.27	8.31	8.28
Dy	4.35	>2.84	3.62	3.61	3.53	3.63	3.69
Dy	4.20	>3.21	4.54	4.50	4.51	4.50	4.58
Dy	3.73	>4.08	7.68	7.68	7.66	7.64	7.64

[a] The "total nuclear alpha-decay energy" is the decay energy (alpha-particle plus recoil) that the nucleus stripped of electrons would exhibit. It is calculated by adding to the observed alpha-particle energy the recoil energy and an energy term equal to the electrostatic potential energy of the alpha-particle at the nucleus due to the electron cloud (see reference 32, Appendix II). This last correction amounts to 30 kev for uranium, 26 kev for polonium, and about 20 kev in the rare earth region. A graph of the correction term applied is shown in Fig. 4. This graph was plotted using the potential calculations of Dickinson [W. C. Dickinson, Phys. Rev. **80**, 563 (1950)].

[b] Radius values (in 10^{-13} cm) are based on the experimental decay rate of Gd^{148}.

The b' values for formulas (1), (2), and (3) seem to be reasonable physically, while the b' values for (4) and (5) seem too large. This comparison would favor the decay formulas (1), (2), and (3) with the higher f values over those with lower values. It should be borne in mind in this regard that the uncertainties in the experimental alpha-decay data for Gd^{148} suggest error limits on the calculated R values of about ± 5 percent. The constant terms b and b' in the radius expressions are very sensitive to the *difference* between the R values for Ra^{224} and Gd^{148}. A change of the Gd^{148} R value by ± 5 percent would cause a change in b and b' values of about ± 3. Alpha-decay formula (5) would still appear to be excluded by too large a value for b', but formula (4) could not be ruled out.

Using the R values for Gd^{148} the alpha-decay rates of the other rare earth alpha-emitters were calculated from the various decay expressions. Many of these alpha-emitters are not even-even nuclear type. From observations among the heavy elements one would expect the calculated rates to be merely upper limits for nuclei not of even-even type. Lower rates would not be surprising in view of the common occurrence of hindrance with odd nucleon type alpha-emitters. The calculations for the rare earth alpha-emitters are summarized in Table IV, as the logarithms to the base ten of the alpha-decay mean life τ in seconds ($\tau=1/\lambda$).

The decay rates calculated for each alpha-emitter by the various decay formulas are seen to differ very little. The different decay formulas evidently give about the same dependence of decay rate on decay energy, since no significant systematic differences from formula to formula are evident. As to the agreement with the experimental decay rates, it is seen that no disagreement occurs with the lower limits in the terbium and dysprosium nuclides, for which good α:*EC* branching ratios are not known. Note, however, that Gd^{149}, Eu^{147}, and Sm^{147} all exhibit progressively larger actual decay rates than are calculated. This discrepancy is of the opposite sign from the possible hindrance associated with odd nucleon nuclear types. Sm^{147} exhibits a decay rate ten times greater than predicted. The discrepancy may not be fundamental but may be due to experimental error in the alpha-particle energy value of 2.18 Mev used for Sm^{147}. This value was determined by Jesse and Sadauskis[13] in an argon filled ionization chamber. The assumption that total ionization in argon is strictly proportional to alpha-particle energy was tested and used in their Sm^{147} energy determination. If this assumption is not strictly true, and there is an "ionization defect," the energy value 2.18 Mev for Sm^{147} is too low.† So sensitive are the decay rate calculations in Sm^{147} to decay energy that an increase in decay energy of only 70 kev would remove the factor of ten discrepancy in the values of Table IV. The smaller discrepancies in

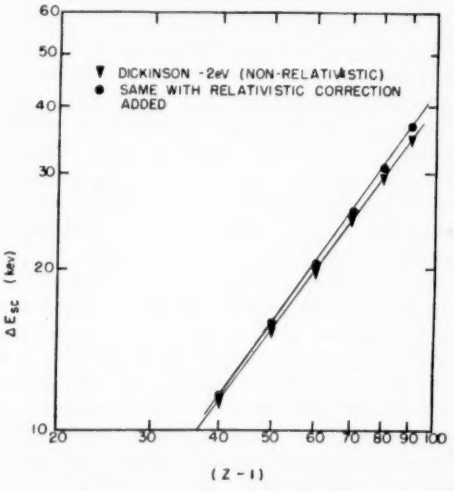

FIG. 4. The additive correction to the atomic alpha-decay energy to obtain the nuclear alpha-decay energy for decay rate calculations. The correction is in kev *versus* the atomic number minus one for the nucleus undergoing alpha-decay.

† *Note added in proof:*—It has come to the authors' attention that several investigators (Rhodes, Franzen, and Stephens, Phys. Rev. **87**, 141 (1952); G. C. Hanna, Phys. Rev. **80**, 530 (1950); T. E. Cranshaw and J. A. Harvey, Can. J. Research **A26**, 243 (1948)) have found a slightly nonlinear relationship between alpha-particle energy and total ionization in pure argon. If the empirical formula of Cranshaw and Harvey for the average energy to form an ion pair in argon is used to correct the Sm^{147} alpha-particle energy of 2.18 Mev, a corrected alpha-energy of 2.21 Mev is obtained. Applying the correction to the 3.16 Mev alpha-energy of Gd^{148}, an energy of 3.18 Mev is obtained. Such a correction partially removes the Sm^{147} decay rate anomaly.

Gd^{149} and Eu^{147} would be nearly corrected, too, by such a change, since their decay energy values are based on linear interpolation of ionization chamber measurements between the energy standards Gd^{148} and Sm^{147}.

In Table V the $\log_{10}\tau$ values for formula (2) in Table IV have been converted to half-life values and are compared with the experimental half-lives.

B. Rare Earth Alpha-Decay Energy Systematics and the Neutron Closed Shell of 82

With knowledge of the alpha-decay energies of many isotopes of the heavy elements and the beta-decay energies of a few, it has been possible to calculate the relative masses[39] of nuclides of given radioactive families with great accuracy by the method of closed decay cycles. The determination of a few neutron binding energies made it possible to relate the mass values between the various decay families and thus to calculate the relative masses of a very large number of heavy nuclides.

Before studying the systematics of alpha-decay energies in the rare earth region it would be well to attempt to calculate any unobserved alpha-energies possible by the method of closed decay cycle energy balances.[9] The application of such calculations to the rare earth alpha-emitters is unfortunately quite limited, since in the region where alpha-decay occurs the principal decay process is orbital electron capture, for which it is generally not possible to make direct experimental determinations of the decay energy. It is possible, though, to calculate the alpha-decay energies of Pm^{147} and Nd^{147} as follows: (The mass assignment of the samarium alpha-activity to 147 has been made by Weaver[40] and by Rasmussen *et al.*,[23] and the alpha-particle energy 2.18 Mev as determined in an argon filled ionization chamber by Jesse and Sadauskis[13] is used.)

TABLE V. Comparison of calculated and experimental alpha half-lives.

Nuclide	Total decay energy	Experimental alpha-half-life	Alpha-half-life (from formula 2)
Sm^{147}	2.26	1.35×10^{11} yr	1.6×10^{12} yr
Eu^{147}	2.98	$\sim6\times10^{8}$ yr	2.2×10^{4} yr
Gd^{148}	3.27	$\sim1.4\times10^{2}$ yr	...
Gd^{149}	3.1	$\sim4\times10^{2}$ yr	7.8×10^{3} yr
Gd^{150}	2.8	...	9.8×10^{6} yr
Tb^{149}	4.08	>4.1 hr	8.4 hr
Tb^{151}	3.56	≫19 hr	2.9 yr
Dy	4.35	>8 min	42 min
Dy	4.20	>19 min	6.2 hr
Dy	3.73	>2.3 hr	256 days

TABLE VI. Alpha-decay energies of rare earth nuclides.

Nuclide	N	E_α (Exp.) (Mev) including screening correction	"Normal" E_α (calc. from semi-emp. mass Eq.) Mev	Difference Mev
Sm^{147}	85	2.26	0.08	2.18
Eu^{147}	84	2.98	0.73	2.25
Gd^{148}	84	3.27	1.19	2.08
^{149}	85	3.1	1.01	2.1
^{150}	86	2.8	0.87	1.9
Tb^{149}	84	4.08	1.60	2.48
$^{(151)}$	(86)[a]	3.56	1.28	2.28
$Dy^{(150)}$	(84)[a]	4.35	2.05	2.30
$^{(151)}$	(85)[a]	4.20	1.87	2.33
$^{(152)}$	(86)[a]	3.73	1.73	2.00
Pm^{147}	86	1.56(calc.)	−0.59	2.15
Nd^{147}	87	1.04(calc.)	−1.28	2.32
^{144}	84	<2.0	−0.68	<2.68
Sm^{144}	82	<2.1	+0.64	<1.5
^{148}	86	<2.1	−0.07	<2.2
^{146}	84	>2.4	+0.28	>2.1

[a] ( ) indicates mass number not known but merely assumed for calculations.

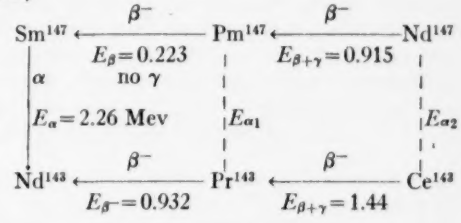

Conservation of energy requires that

$$E_{\alpha 1}=2.26+0.223-0.932=1.56 \text{ Mev};$$

$$E_{\alpha 2}=E_{\alpha 1}+0.915-1.44=1.04 \text{ Mev}.$$

(Beta-decay energies of Pm^{147} and Pr^{143} are from the NBS table.[41]) Nd^{147} decay energies are from the work of Emmerich and Kurbatov,[42] and Ce^{143} energies are from the work of Mandeville and Shapiro.[43] These alpha-decay energies correspond to alpha half-lives much too long for experimental detection.

The list of rare earth nuclides with known alpha-decay energies can be augmented for a study of decay energy trends by the addition of a few nuclides for which upper or lower limits on alpha-decay energy can be set by consideration of the relation between alpha-decay energy and rate. Approximate upper energy limits can be set for the naturally occurring rare earth nuclides not observed to undergo alpha-decay. Included in Table VI are Nd^{144}, Sm^{144}, and Sm^{148} for which upper energy limits have been set on the assumption that the half-lives for alpha-decay must be greater than 10^{14} years to have

[39] M. O. Stern, Revs. Modern Phys. **21**, 316 (1949); A. H. Wapstra, Physica **16**, 33 (1950); Huizenga, Magnussen, Simpson, and Winslow, AEC Declassified Document AECD-3150 (1951), unpublished; G. T. Seaborg, Phi Lambda Upsilon Lecture (III), Ohio State University (March, 1952), unpublished; M. O. Stern, University of California Radiation Laboratory Report UCRL-1728 (1952), unpublished.

[40] B. Weaver, Phys. Rev. **80**, 301 (1950).

[41] K. Way *et al.*, *Nuclear Data*, National Bureau of Standard Circular No. 499 (1950).

[42] W. S. Emmerich and J. D. Kurbatov, Phys. Rev. **83**, 40 (1951).

[43] C. E. Mandeville and E. Shapiro, Proc. Nat. Inst. Sci. India **17**, 45 (1951).

escaped experimental detection of decay.[44] The lower energy limit in Table VI for the presumably beta-stable Sm^{146} not present in nature was set on the assumption that its alpha-decay half-life must be less than 10^8 years to have decayed away since the formation of the elements.

Table VI also lists the alpha-decay energies calculated from the semi-empirical mass equation using the tables of Metropolis and Reitwiesner[15] and assuming a mass for He^4 of 4.00390 atomic mass units and the mass energy conversion factor of 931.4 Mev = 1 atomic mass unit.

In Fig. 5 the energy data of Table VI are plotted against neutron number.

The gadolinium isotopes constitute the only isotopic sequence for which the mass numbers are fairly certain. Mass assignments on the plot for the dysprosium isotopes are guesses based on the expectation that the various curves of Fig. 5 should be nearly parallel, as are those of Fig. 6, a plot of alpha-energies against mass number in the heavy region.

It is evident from Fig. 5 that a maximum in alpha-decay energy should occur for the samarium isotopes at 83 or 84 neutrons. In Sec. II A evidence was presented to show that Eu^{145}, Eu^{148}, and Eu^{149} must have alpha half-lives much longer than that of Eu^{147}, since no alpha-activity ascribable to them has been observed. In accordance with the relation between alpha-decay energy and decay rate it can, thus, be assumed that Eu^{147} with 84 neutrons, for which alpha-decay has actually been observed, has a greater alpha-decay energy than any of its neighboring europium isotopes (with the possible exception of Eu^{146}, for which a significant upper limit on the alpha half-life has not yet been determined). For the gadolinium and terbium isotopes, also, the maximum in alpha-decay energy probably occurs in the 84 neutron nuclides Furthermore, no alpha-activity ascribable to a nuclide with less than 84 neutrons has yet been observed.

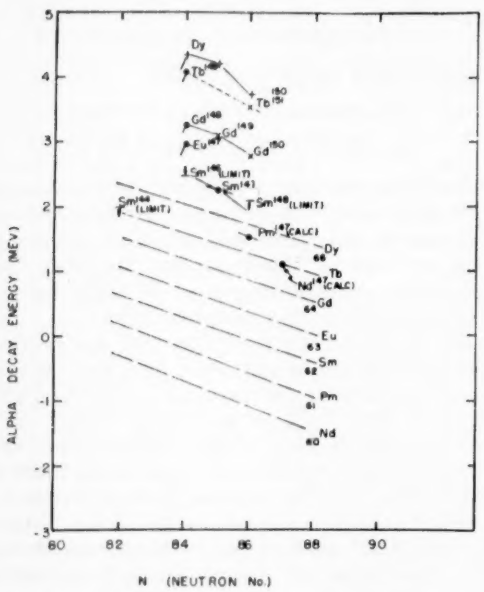

FIG. 5. Alpha-decay energy *versus* neutron number relationships of rare earth nuclides. The lower family of dashed lines is defined by the energies calculated from semi-empirical mass equation. —●— mass number certain. —×— mass number probable. —+— one of a few mass numbers.

[44] F. Bestenreiner and E. Broda, Nature **164**, 658 (1949); E. Broda and K. Jenkner, Experientia **7**, 121–127 (1951).

The normal trend for alpha-decay energy to increase with decreasing neutron number is seen from the family of parallel lines in Fig. 5 defined by the alpha-decay energies calculated from Fermi's semi-empirical mass equation in which no account is taken of fluctuations in nuclear binding energies caused by structural effects, such as those ascribed to nuclear closed shells. The true alpha-decay energies are not only greater than mass equation values by about 2 Mev, but exhibit a discontinuity in the normal trend, dropping to lower alpha-decay values for neutron numbers less than 84.

Although the neutron binding energies of these alpha-active rare earth nuclides cannot be calculated explicitly, as for the alpha-emitters in the neighborhood of 126 neutrons,[16] the analogy between the alpha decay energy curves in the two regions, with their maxima at 84 and 128 neutrons, respectively, would strongly suggest that the maxima at 84 neutrons in the rare earth alpha-decay energies are a consequence of the decreased neutron binding energies just beyond the closed shell[45] of 82 neutrons, in analogy to the maxima at 128 neutrons resulting from the abnormally low neutron binding energies just beyond the closed shell of 126 neutrons.

The effect on alpha-decay energies of the 82-neutron closed shell was early suspected after discovery of rare earth alpha-activity. Before any element or mass assignments had been made, the relationship to the closed shell was discussed by Thompson *et al.*[2] and by Perlman *et al.*,[9] and predictions of the probable mass numbers of alpha-active nuclides made. Subsequent experimental work has borne out these predictions to a remarkable degree.

The neutron binding energy comparisons of Harvey[16] show clearly an abnormal drop in the neutron binding energies just beyond 126 neutrons, and the few cases compared near 82 neutrons seem to indicate a like discontinuity.

From small extrapolations of the curves in Fig. 5 one might estimate the decay energies of a few nuclides, the alpha-activities of which have not yet been detected, such as, Sm^{146}, ~2.5 Mev, Sm^{148}, ~2.0 Mev, Pm^{145}, ~2.0 Mev. With such energies alpha-activity of Sm^{146} should be barely detectable and that of Sm^{148} and Pm^{145} undetectable by present techniques. Since the magni-

[45] M. G. Mayer, Phys. Rev. **75**, 1969 (1949).

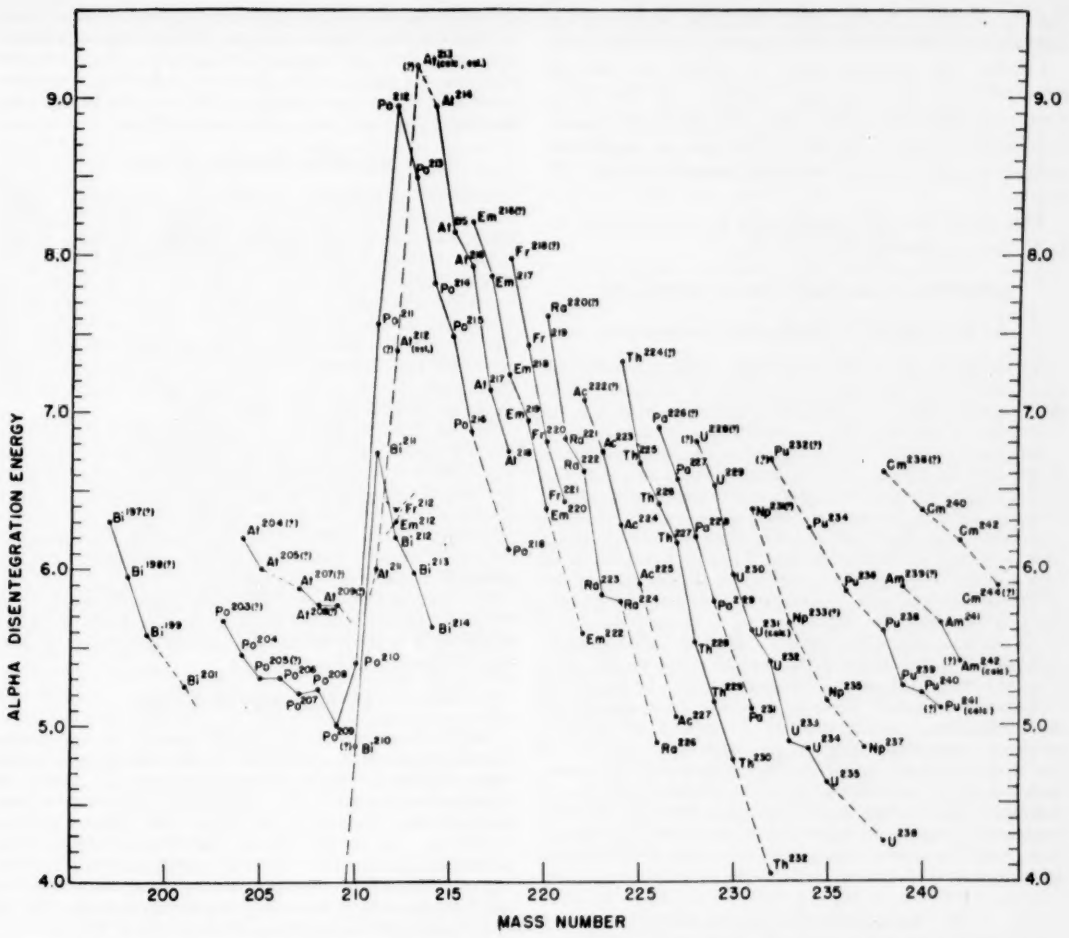

FIG. 6. Alpha-energy *versus* mass number relationships of the heavy nuclides. From Perlman, Ghiorso, and Seaborg (reference 9).

tude of the discontinuity in neutron binding energies at 82 neutrons is about 1.5 Mev,[16] the 83 and 82 neutron isotopes might be expected to have on the order of 1.5 and 3 Mev, respectively, less energy for alpha-decay than the 84 neutron nuclide of the same Z. This energy difference easily accounts for the undetectably low alpha-decay rate of Sm^{144} and indicates that the alpha-decay of nuclides with a few neutrons less than 84 may only become observable in elements with atomic number greater than 65, that of terbium.

It is interesting to note that as the atomic number is increased for the 84 neutron nuclides the increase in alpha-decay energy in going from atomic number 64 to 65 is much greater than that in going from 63 to 64. In Table VI, too, it is seen that the energy difference column shows the Tb^{149} alpha-energy to show the highest difference, some 0.3 Mev higher than the average of the lower elements. The observation might indicate that the 65th proton is less tightly bound than the general average in the region, that 64 might be a minor "magic number" proton configuration. A small splitting between the $2d_{\frac{5}{2}}$ and $2d_{\frac{3}{2}}$ levels on the Mayer[45] nuclear shell model could account for a slight extra stabilization of the 64 proton configuration.

It is a pleasure to acknowledge the constant interest and helpful suggestions of Professor G. T. Seaborg throughout this investigation. Discussions with Professor I. Perlman have been most helpful, particularly with regard to theoretical alpha-decay rate calculations.

The authors also gratefully acknowledge the cooperation of J. T. Vale and the crew of the 184-inch cyclotron, of Dr. J. G. Hamilton, T. M. Putnam, G. B. Rossi, and the crew of the 60-inch cyclotron, and of R. D. Watt and the crew of the proton linear accelerator.

The assistance of R. W. Hoff and D. C. Dunlavey with some of the later work is also greatly appreciated, as is the occasional help of other members of the chemistry group. Thanks are due J. G. Conway and

M. F. Moore for the spectrographic analyses for chemical identification of different rare earth elements.

Finally, the authors wish to thank the Isotope Research and Development Division of the Y-12 Research Laboratory, Oak Ridge, Tennessee, for making available the separated stable isotopes of samarium used as cyclotron target material in several bombardments.

This work was performed under the auspices of the U. S. Atomic Energy Commission.

APPENDIX I. EXPERIMENTAL METHODS

A. Production of Alpha-Active Isotopes

For the production of the alpha-active isotopes investigated, three-particle accelerators at the University of California Radiation Laboratory have been used: the 184-inch cyclotron, the 60-inch cyclotron, and the 32-Mev proton linear accelerator.

Rare earth elements were bombarded as the powdered oxides. Materials of the highest available chemical purity were generally used as target materials. Freedom from heavy element impurities (uranium, thorium, bismuth, and lead) was especially important in experiments on short-lived activities where rare earth chemical separations were not feasible. In the 184-inch cyclotron the oxides were generally bombarded in platinum or aluminum envelopes within the cyclotron tank. The probe could be positioned within the tank to expose the target material to bombardment at a radius corresponding to the desired bombardment energy. Where metal foils were bombarded in the 184-inch cyclotron, they were clamped to target holders at the end of the probe. In the 60-inch cyclotron alpha-particle, deuteron, or proton bombardments, the rare earth oxides were bombarded in the special target assembly developed for the transcurium isotope work at this laboratory and described in a recent article by Thompson *et al.*[46] This water-cooled assembly exposes the target to bombardment by the deflected beam of the 60-inch cyclotron. The C^{12} ion bombardments of rare earth oxides were made within the vacuum tank, with the oxides wrapped in envelopes of 0.00025-inch tantalum foil, which were in turn clamped to a probe.

B. Detection of Alpha-Activity

Alpha-activity was detected following bombardments by counting samples in argon filled ionization chamber counters adjusted with the aid of an oscilloscope such that they would count only the relatively large ionization pulses produced by alpha-particles and not the "pile-ups" due to beta-gamma-activity. Alpha-particles of the energies encountered in this work (2.9 to 5.7 Mev) rapidly lose energy by ionization in traversal of matter. Therefore, it was desirable that samples for alpha-counting be made as thin as possible. Samples were usually prepared by evaporation of active solutions on 5-mil thick platinum disks. The disks were heated to red heat in a flame to drive off all remaining moisture and to destroy organic material in order to minimize the self-absorption of alpha-activity in the sample. Despite the fact that target materials of good purity were used, there was often enough alpha-activity present from heavy element contamination that it was found desirable to use as the detection device the special argon-filled ionization chamber and 48-channel differential pulse-height analyzer.[12] By counting the alpha-radio activity in the pulse analyzer ion chamber, a measurement of the pulse height was obtained. The alpha-particle energy could then be calculated by comparison with the pulse heights produced by alpha-emitter standards of known energy. Since the nuclear coulombic potential barrier for alpha-particles is considerably lower for rare earth nuclides than for heavy element nuclides, the alpha-particles emitted by the rare earth alpha-emitters have energies less than those of any heavy element alpha-activities of comparable alpha-decay rates by at least 1 Mev. Thus, from the observation of alpha-particle energy and alpha-decay rate alone, an estimate of the atomic number of the alpha-active nuclide can be made with an uncertainty no greater than ten.

C. Alpha-Particle Energy

Alpha-particle energies were obtained by measuring the amount of ionization produced in an ionization chamber filled with purified argon. Pulse-height measurements were made by using the 48-channel differential pulse height analyzer described by Ghiorso *et al.*[12] The pulse height of the unknown alpha-activity was measured, and alpha-activity standards of known alpha-energy were also measured for comparison. The unknown alpha-energy was determined by linear interpolation or extrapolation from the standards. The linear dependence of total ionization in pure argon gas to alpha-particle energy over a wide range of energy has been shown by Jesse, Forstat, and Sadauskis.[47]

For the determination of the alpha-energies of the gold and mercury alpha-emitters, a special ionization chamber was used which had an arrangement for interposing a 5000-oersted magnetic field between the sample and the chamber. This device was made necessary because of the intense amount of beta- and gamma-radiation produced by other short lived nuclides which increased the "hash" or noise level in the ordinary grid chamber and thus prevented accurate alpha-pulse analysis.

For obtaining the best possible alpha-energy measurements thin, uniform samples were often prepared by vaporization in vacuum of the alpha-active material from a tungsten filament at white heat to a nearby platinum plate.

D. Half-Life of Activity

Half-life measurements were usually made by the conventional method of plotting the logarithm of the counting rate against time, with the half-life being determined from the slope of the straight line plot, after subtraction of contributions from other activities and from general background. This method was used in this work for the determination of half-lives ranging from 4 minutes to 24 days. The method is, of course, not applicable for the determination of extremely long half-lives. With long-lived Gd^{148}, for example, an estimate of the partial alpha half-life had to be made from bombardment yields.

In the work reported here it is not possible to rule out from experimental evidence alone the possibility that some of the activities are of the delayed alpha-emitter type, such as the beta-emitter Li^{8}. Theoretical considerations concerning alpha-decay rates as a function of decay energy make it unlikely that any of the medium heavy element alpha-emitters to be reported in this paper are of the delayed alpha-emitter type. The observed half-lives in decay of these activities are thus presumed to be the true half-lives of the alpha-active nuclides and not those of parent activities.

E. Atomic Number of Alpha-Active Nuclide

The determinations of atomic number were made by chemical means in the case of all activities where chemical separations could be made in a length of time comparable to the half-lives. For activities with half-lives too short to permit chemical element assignments it was necessary to resort to the physical arguments already given concerning the appearance or nonappearance of the activity in bombardments of different target materials.

Element assignments by chemical means were accomplished by making chemical separations on the bombarded material and observing in which chemical fraction the activity of interest appeared. By making adequate chemical separations the activity could be assigned to a single chemical element.

[46] Thompson, Ghiorso, and Seaborg, Phys. Rev. **80**, 782 (1950).

[47] Jesse, Forstat, and Sadauskis, Phys. Rev. **77**, 782 (1950).

It should be mentioned that such chemical assignments of atomic number do not necessarily determine the atomic number of the alpha-active nuclide. The possibility always exists as mentioned in Appendix I, D that the activity of interest is a short-lived activity in equilibrium with a longer-lived parent activity. In this case the activity of interest would appear in the chemical fraction of the longer-lived parent. Again it can only be said that theoretical alpha-decay half-life considerations make it unlikely that such is the situation with any of the alpha-emitters reported in this paper.

The rare earth elements (lanthanum through lutetium) present a special problem in chemical separation from one another, since they are very similar in chemical behavior.

The necessity of using thin samples for alpha-counting and alpha-energy measurement places a restriction on the amount of carrier material which may be added for the purpose of facilitating radiochemical separations. The cation exchange resin column separations to be mentioned below easily meet these requirements, since no added carrier is required.

The separation of the individual rare earth elements in small amounts in the work reported here was usually made by elution from cation exchange resin columns. Dowex-50 resin[48] (spherical fines) in the ammonium form was used exclusively in the columns. The eluting solutions of citric acid-ammonium citrate were always 0.25 *M* in total citrate with 1 g/l phenol added to prevent the growth of mold. Most of the separations were made in a jacketed column maintained at 78°, 83°, or 87°C. The apparatus and techniques employed in the column separations at elevated temperatures have been described in detail in a recent article.[46] Where speed in separation was unnecessary, the elutions were sometimes made at room temperature at a slower flow rate as described by Wilkinson and Hicks.[49]

Before several column separations small amounts of various rare earth elements were added, in order that positive chemical identification of elution peaks could later be made by spectrographic analysis.

Europium and gadolinium are not satisfactorily separated from one another by the cation exchange separations of the type described above. A sodium amalgam reduction procedure was employed as a means of effecting their separation. The zinc amalgam procedure described by Wilkinson and Hicks[49] for europium reduction was found to give extremely low yields unless europium carrier material was added in amounts too large for good alpha-counting. However, the sodium amalgam procedure described below was found to give a fair separation between europium and gadolinium. The reduction potential is sufficient to reduce samarium into the amalgam phase in low yield, and thus cannot be used effectively as the basis of a separation of europium from samarium. This procedure is essentially that used by Newton and Ballou for separation of samarium and europium fission products from other rare earths.[50]

Amalgam procedure: Dissolve the europium oxide or hydroxide (not more than 10 mg) in a minimum of hydrochloric acid. Dilute the solution to 15 ml with water, and add ten drops of glacial acetic acid. To the solution in a separatory funnel add 4 ml of 0.5-percent sodium amalgam. Shake for five seconds and transfer the amalgam layer to a second separatory funnel containing 30 ml of water. Again shake and transfer to a third funnel containing 30 ml of water. Finally, shake and transfer to a fourth funnel containing 20 ml 2*N* HCl. After the evolution of hydrogen has ceased, the europium fraction can be recovered by hydroxide precipitation of the aqueous phase in the fourth funnel, while the gadolinium can be recovered from the aqueous phase in the first funnel.

Following the deuteron bombardments of gold targets the radioactive mercury fraction was separated from the gold leaf by volatilization. Within a special steel chamber the gold was heated strongly under a platinum plate, which was cooled on the back by circulating water. The mercury condensed on the platinum plate.

A gold fraction was isolated from the gold or platinum targets by dissolving these metal targets in hot, concentrated aqua regia, diluting the solutions to about 6*N* in acid and extracting the gold chloride into ethyl acetate, which was then washed once or twice with 2*N* HCl. The gold was recovered by evaporating the ethyl acetate solution on a platinum plate.

F. Mass Number

Determinations of mass number of the alpha-active nuclides studied in this investigation were made by two methods: (a) deduction from production yields of activity as a function of energy of bombardment (excitation functions), and (b) mass spectrographic isotope separation with detection of alpha-activity by nuclear emulsion transfer plate.[23] A third possible method of mass assignment, the deduction from observation of daughter activities of known mass number, did not facilitate any mass assignments of the alpha-activities reported here.

For the alpha-active isotopes within a few mass numbers of the naturally occurring isotopes, the first method proved most convenient. For isotopes many mass numbers away from beta-stability, mass assignments cannot usually be made with certainty on the basis of excitation functions alone, although mass number limits can be set.

A mass spectrographic technique was used for the mass assignment of the Tb^{149} alpha-activity. This technique is described in the report by the authors in collaboration with Reynolds[23] on the mass assignment of the Tb^{149} and Sm^{147} alpha-activities. The mass spectrographic technique as applied to Tb^{149} is limited to activities of at least several hours half-life that can be produced in relatively large amounts.

G. Other Modes of Decay

Since the alpha-active nuclides studied here all lie to the neutron deficient side of beta-stability, it seems certain that all (with the exception of Gd^{150} and possibly Gd^{148}) will undergo decay by orbital electron capture, and some of the nuclides may exhibit positron emission also. These decay processes give rise to electron and electromagnetic radiation, referred to collectively as beta-gamma-activity.

The beta-gamma radiations were studied by standard techniques using argon filled or xenon filled Geiger counters, a windowless methane filled proportional counter, and a small beta-ray spectrometer of low resolution. Counting through various absorbers was done to give information on energies and relative abundances of various components of beta-gamma-radiations.

APPENDIX II. ALPHA-DECAY RATE FORMULAS

The five alpha-decay rate formulas used for the calculations in III-A will be discussed here in order of decreasing "frequency factor" f in the general rate expression, $\lambda = fP$.

The penetration factor P in all cases was calculated by the exponential expression (600)[51] of Bethe.[51] The reduced mass of the system and the total nuclear decay energy were used for the calculations.

The various decay formulas differ in the factor f multiplying the exponential factor P.

The first formula, used by Biswas and Patro[39] and by Perlman and Ypsilantis,[20] sets

$$f = v/R,$$

where v is the velocity of alpha-particle (center-of-mass system) and R is the nuclear radius.

[48] Dow Chemical Company, Midland, Michigan.

[49] G. Wilkinson and H. G. Hicks, Phys. Rev. **75**, 1370 (1949).

[50] A. S. Newton and N. Ballou, Chemical Procedure 62-1, University of California Radiation Laboratory Report UCRL-432 (1949), unpublished.

[51] A table has been prepared of Bethe's $\gamma(x)$ function to five-decimal places as a function of the argument $y=(1-x)^{\frac{1}{2}}$ over the range of y, 0.750(0.001)0.946. Copies of the table are available from the authors on request.

The second formula, derived by one of the authors (J.O.R.)[52] with a many-body model relating f to nuclear level spacing, gives f as

$$f=\frac{2D^*}{\pi\hbar}\left(\frac{E-U}{B-E}\right)^{\frac{1}{2}},$$

where E is the alpha-decay energy, B is the "barrier height" ($B=2Ze^2/R$), U is the "potential energy of the alpha-particle within the nucleus" (and is assumed equal to zero), and D^* is an energy presumably of the same order of magnitude as the average level spacing between nuclear levels of the same spin and parity as the alpha-emitting state.

In the case of even-even nuclides, whose ground states have zero spin and even parity, D^* might be estimated by the energy of the first excited state of zero spin and even parity. Experimental evidence from alpha-decay fine structure studies[52] indicates that this first excited $I=0,+$ state in heavy nuclides must have energy greater than 300 kev.

Thus, in the absence of direct experimental evidence by which to estimate D^*, the rough assumption was made that the first excited $I=0,+$ state has an energy corresponding to the first excited level of the nuclear "liquid drop" oscillation of lowest order ($n=2$). For this calculation the following equations of Bohr and Wheeler[53] were used:

$$\tfrac{1}{2}\hbar\omega_2=A^{-\frac{1}{3}}\{4\pi r_0^2O\cdot 2(1-x)\hbar^2/3M_Pr_0^2\}^{\frac{1}{2}}, \qquad \text{BW(26)}$$

where

$$4\pi r_0^2O\approx 14 \text{ Mev} \qquad \text{BW(12)}$$

and

$$x=\left(\frac{Z^2}{A}\right)\Big/\left(\frac{Z^2}{A}\right)_{\text{lim}}=\left(\frac{Z^2}{A}\right)\Big/47.8.$$

The calculations give for Ra^{224} the quantum of energy,

$$(\hbar\omega_2)_{Ra^{224}}=0.94 \text{ Mev},$$

and for Gd^{148},

$$(\hbar\omega_2)_{Gd^{148}}=1.43 \text{ Mev}.$$

These values of $\hbar\omega_2$ were substituted for D^* in the alpha-decay rate calculations by the second formula. In effect, this means assigning the same nuclear "frequency factor" to alpha-decay and to spontaneous fission. It is interesting in this connection to note Frenkel's discussion[54] of spontaneous fission and alpha-emission as closely related processes.

The third alpha-decay rate formula is an approximation to that derived by Preston[32] from a one-body model using the steepest descents method of approximating the Coulomb wave function. This formula was also used by Kaplan[34] in his correlation of even-even alpha-emitter data.

The Preston formula is given as two simultaneous equations from which one can solve for both the nuclear radius, R, and the "internal potential energy," U, of the alpha-particle within the nucleus.

$$\lambda=\frac{2v}{R}\frac{\mu^2\tan\alpha_0}{\mu^2+\tan^2\alpha_0}P,$$

and

$$\mu=-\tan\alpha_0\tan(\mu kR),$$

where R and P have their usual meanings defined earlier in this section, v is the alpha-particle velocity corresponding to the energy E, and k is its wave number.

$$\mu=(1-U/E)^{\frac{1}{2}},$$

and

$$\alpha_0=\text{arc}\cos(E/B)^{\frac{1}{2}}.$$

Now $\tan\alpha_0=\tan\text{ arc }\cos(E/B)^{\frac{1}{2}}=[(B-E)/E]^{\frac{1}{2}}$, and $v=(2E/m)^{\frac{1}{2}}$, so one obtains on substitution in the first equation

$$\begin{aligned}\lambda&=\frac{2^{\frac{1}{2}}E^{\frac{1}{2}}}{m^{\frac{1}{2}}R}\frac{(1-U/E)[(B-E)/E]^{\frac{1}{2}}}{(1-U/E)+(B-E)/E}P\\&=\frac{2^{\frac{1}{2}}}{m^{\frac{1}{2}}R}\frac{(E-U)(B-E)^{\frac{1}{2}}}{(E-U)+(B-E)}P.\end{aligned} \qquad (2.1)$$

The Preston equations can easily be put in a more convenient approximate form. Kaplan[34] showed from his correlation that

$$E-U\approx\pi^2\hbar^2/2mR^2; \qquad (2.2)$$

that is, that the kinetic energy of the alpha-particles within the nucleus in this one-body model nearly equals the energy of the $1S$ state of the alpha-particle in a spherical square potential well with radius R and with infinite walls. $E-U$ is about 0.52 Mev for the heavy element alpha-emitters correlated by Kaplan. Thus, if $E-U$ be neglected with respect to $B-E$, one obtains from Eq. (2.1),

$$\lambda=\frac{2^{\frac{1}{2}}(E-U)}{m^{\frac{1}{2}}R(B-E)^{\frac{1}{2}}}P. \qquad (2.3)$$

Finally, substituting for $E-U$ from (2.2) one obtains

$$\lambda=\frac{2^{\frac{1}{2}}\pi^2\hbar^2}{m^{\frac{1}{2}}R^3(B-E)^{\frac{1}{2}}}P, \qquad (2.4)$$

the expression used as formula (3) in the calculations of section III-A.

The fourth formula uses an f factor with the same energy dependence as the second formula.

$$f=f_0[E/(B-E)]^{\frac{1}{2}}. \qquad (2.5)$$

However, the numerical value of f_0 was taken as the mean of f_0 values calculated from heavy element even-even alpha-emitter data using the radius expression

$$R=(1.43A^{\frac{1}{3}}+1.48)\times10^{-13}\text{ cm}. \qquad (2.6)$$

The average of $\log f_0$ equals 19.10 from a correlation of Rasmussen.[55] This procedure follows Cohen's[35] correlation using penetration radius values determined from total nuclear absorption cross sections for bombarding alpha-particles. The radius expression used above is taken from the (α, fission) excitation function work of Jungermann[36] on Th^{232}, compared with Weisskopf's[56] theoretical calculations.

The fourth decay expression then is as follows:

$$f=1.26\times10^{19}[E/(B-E)]^{\frac{1}{2}}. \qquad (2.7)$$

The fifth decay expression is the form of the many body decay model proposed by Bethe,[31] where

$$f=6.2\times10^{14}E^{\frac{1}{2}},$$

with E in Mev, f in sec^{-1}.

[52] F. Asaro and I. Perlman, private communication.
[53] N. Bohr and J. A. Wheeler, Phys. Rev. **56**, 431 (1939).
[54] J. Frenkel, Academy of Science News X—1946—No. 4, Physics Series; J. Phys. U.S.S.R. **10**, 533 (1946).
[55] J. O. Rasmussen, Jr., Ph.D. Dissertation, University of California (1952), p. 54, unpublished.
[56] V. F. Weisskopf, AEC Declassified Document MDDC-1175 (1947), unpublished; *Lecture Series in Nuclear Physics*, p. 105.

The Relativity of Size

BANESH HOFFMANN
Queens College, Flushing, New York
(Received June 20, 1952)

A uniform change of size of all space-time intervals could not be detected, since the measuring instruments would be changed too. Therefore, a principle of similarity is proposed requiring that the equations of physics be invariant under such changes. This is shown to correspond to the principle that all units of interval are equivalent for expressing physical laws. It is pointed out that a given metrical tensor in the usual tensor calculus defines a specific unit of interval, so that the principle of similarity requires an enlargement of the tensor formalism and a corresponding change in the underlying geometry.

ACCORDING to the general theory of relativity, all (nonpathological) coordinate systems in space-time are equally suitable for the formulation of the general laws of nature, and therefore the equations expressing these laws must be invariant[1] under the group of continuous transformations.

If all space-time intervals were changed in the same ratio, there would be no way of detecting it since our measuring instruments would themselves be affected by the change.

Therefore, we may expect that, in addition to the above relativistic requirement of general invariance under continuous coordinate transformations, there should be a *principle of similarity* requiring that the equations of physics shall be invariant under any uniform change of over-all size. Such a change of scale, it will appear, is expressible analytically as a transformation on the metrical tensor of the type

$$g_{ab} \rightarrow g^*_{ab} = k^2 g_{ab}, \tag{1}$$

where k is independent of the coordinates x^a of space-time. This transformation is not a coordinate transformation, nor the result of a coordinate transformation. It can apply in the absence of a coordinate transformation, and it can apply independently of and in addition to any coordinate transformation that may be simultaneously applied. It is known as a similarity transformation. And it lies outside the formalism of the usual affine tensor calculus.

If we consider more fully the significance of the similarity transformations, Eq. (1), we shall see that they illuminate a curious limitation of the ordinary tensor calculus; for that calculus employs a particular unit of interval which cannot be changed unless one is prepared to go outside the tensor formalism. To see that this is so, let us begin by considering what happens in Cartesian vector analysis when the unit of length is changed. The length of a displacement dx^a is defined by

$$ds = \{\textstyle\sum_a (dx^a)^2\}^{\frac{1}{2}}. \tag{2}$$

If the components dx^a are measured in meters, then ds is also measured in meters. To go over to centimeters we use new components $d\bar{x}^a$ given by

$$d\bar{x}^a = 100 dx^a. \tag{3}$$

The length of the displacement is now given by

$$d\bar{s} = \{\textstyle\sum_a (d\bar{x}^a)^2\}^{\frac{1}{2}} = 100\{\sum_a (dx^a)^2\}^{\frac{1}{2}} = 100 ds, \tag{4}$$

and this, of course, is what one would expect.

In tensor analysis, however, the situation is different. The length is there defined by

$$ds = (g_{ab} dx^a dx^b)^{\frac{1}{2}}. \tag{5}$$

The change (3) from dx^a to $d\bar{x}^a$ arises because the coordinate net has been replaced by one a hundred times more closely woven. It is thus the result of a coordinate transformation $x^a \rightarrow \bar{x}^a = 100 x^a$. Under this coordinate transformation the components g_{ab} of the metrical tensor will be changed, the tensor law of transformation showing that

$$g_{ab} \rightarrow \bar{g}_{ab} = (100)^{-2} g_{ab}. \tag{6}$$

Consequently, the quantity

$$d\bar{s} = (\bar{g}_{ab} d\bar{x}^a d\bar{x}^b)^{\frac{1}{2}} \tag{7}$$

will have exactly the same value as the original ds instead of being a hundred times larger. While this result may strike one as unexpected, it should not be surprising since it merely testifies to the fact that ds is a scalar and thus cannot alter in value.

In what follows, it is important to distinguish between a metrical tensor and its components. Let us denote a metrical tensor by G and its components in a particular coordinate system by g_{ab}. Under a transformation of coordinates the values of the components of G change from g_{ab} to, say, $\bar{g}_{ab}$. But they still represent the same metrical tensor G.

Despite the changes in the values of the components, the metrical tensor G determines a unique unit of length. This is most easily explained in terms of rectilinear coordinates in a flat space. Suppose these coordinates are staked out in centimeters, and that when we place a certain rod in them the differences of the coordinates of its ends have the values dx^a. Then if the corresponding value of ds in (5) for this dx^a comes to unity, the length of this rod is the unit of length defined by G. And, although the coordinate mesh was staked

[1] The word *invariant* is used in its general sense, not as a synonym for *scalar*.

out in centimeters, this unit of length could be anything at all. It does not have to be a centimeter. It depends solely on G, since ds would have the same value no matter what coordinate mesh was used.

To go over to a new unit of length we must abandon the original metrical tensor G and start all over again with a new metrical tensor G^*, such that, if G has components g_{ab}, and G^* has components g^*_{ab} *in the same coordinate system*, then

$$g^*_{ab}=k^2g_{ab},$$

which is (1).

It was stated earlier that (1) was the analytical representation of a uniform change of size of space-time. We have just found, however, that it corresponds to a change in the unit of interval. To see how these two effects are related, and thus to see why the earlier assertion was valid, consider how a uniform change in size by a factor k would be treated analytically.

Let S be a given space in which is drawn a particular coordinate mesh, and let it have a metric G for which the length r of a certain rod is the unit of length. Let Σ be another space that is k times larger than (but is otherwise an exact replica of) S and all its contents, including the particular coordinate mesh, the metric, and the unit rod.

Then if x^a are the coordinates of any point in S and ξ^a are the coordinates of the corresponding point in Σ,

$$\xi^a=x^a. \tag{8}$$

The unit rod in Σ will be k times larger than that in S. Since the numerical values of lengths are the ratios of these lengths to the unit length being used, all distances between points in Σ will have the same numerical measure (relative to the unit kr) as the distances between the corresponding points in S have (relative to the unit r). Therefore, if in the given coordinate system the metrical tensor G of S has the components g_{ab}, while in the corresponding coordinate system the metrical tensor Γ of Σ has the components γ_{ab}, we must have, for all dx^a and corresponding $d\xi^a$,

$$g_{ab}dx^adx^b=\gamma_{ab}d\xi^ad\xi^b. \tag{9}$$

Therefore, by (8),

$$g_{ab}=\gamma_{ab}. \tag{10}$$

There is nothing intrinsic in Σ that shows it is k times the size of S. The change in size is relative. To express it we must refer all measurements to the same unit. Let us choose for this purpose the length r of the unit rod defined by G in S. Then we shall have to replace the metrical tensor Γ in Σ by a new metrical tensor Γ^* for which the unit of length is r instead of kr. If Γ^* has the components γ^*_{ab} in the given coordinate system, then

$$\gamma^*_{ab}=k^2\gamma_{ab}. \tag{11}$$

So, by (10),

$$\gamma^*_{ab}=k^2g_{ab}. \tag{12}$$

We can look on this in two ways. If we regard Σ as being truly k times the size of S, Eq. (12) results from our having used the same unit of length in S and Σ. However, we can alternatively map Σ on S by means of (8), points of Σ going over to the corresponding points of S. This is tantamount to a shrinking of Σ by a factor $1/k$, and this will shrink the unit of length in Σ to r/k in place of the r used formerly in both S and Σ. From this point of view, (12) corresponds to our merely changing the unit of length from r to r/k while remaining all the while in the one space S. Thus the principle of similarity is intimately related to our freedom to change the unit of interval, and we may state it in the alternative form: *All units of interval are equally suitable for the formulation of the general laws of nature.*

In the above discussion we used corresponding coordinate systems in S and Σ; otherwise, the values of the components of the metrical tensors would not have been directly comparable. A change of coordinates will alter the components of a metrical tensor but will not cause a change of size or a change of unit. Under the usual tensor law of transformation, a change of coordinates,

$$x^a\rightarrow\bar{x}^a=\bar{x}^a(x^b), \tag{13}$$

will cause

$$g_{ab}\rightarrow\bar{g}_{ab}=\frac{\partial x^c}{\partial\bar{x}^a}\frac{\partial x^d}{\partial\bar{x}^b}g_{cd}. \tag{14}$$

According to the principle of similarity, we must enlarge the basic formalism of the tensor calculus so as to have transformations of the type

$$g_{ab}\rightarrow\bar{g}_{ab}=k^2\frac{\partial x^c}{\partial\bar{x}^a}\frac{\partial x^d}{\partial\bar{x}^b}g_{cd}, \tag{15}$$

where k is a numerical parameter that is independent of the coordinate system used.

The existence of "fundamental lengths," such as the classical radius of the electron, the Compton radius of the electron, and the gravitational radius of the proton, does not contradict the principle of similarity, for a fundamental length is not in itself an absolute numerical quantity. It is a ratio. This ratio will have the value unity if the length in question is chosen to be the unit of length. But with many fundamental lengths to choose from, no particular length appears as the fundamental unit, and the multiplicity of available fundamental lengths in itself emphasizes the need for changes of unit and thus for the similarity transformations.

Neither a fundamental length nor the universe itself has an absolute size so far as giving this size a numerical value is concerned, which is all that concerns the equations of physics. All measurements of interval are ratios, and these ratios preserve their numerical values under any uniform over-all change in the "size" of the universe. The usual tensor calculus does not adequately take into account that size is not absolute. Because it

fixes a unit of interval, it lacks one of the most fundamental properties that one would require of a mathematical basis for physical theory. The relativity of size has hitherto been neglected in setting up the mathematical foundations of the theory of relativity and other parts of theoretical physics. The idea of this paper is that it should be made an explicit part of the fundamental mathematical structure.

In the general theory of relativity, as in other branches of theoretical physics, the unit of interval is changed by merely altering the numerical values of certain constants appearing in the equations. This *ad hoc* procedure obscures the fundamental fact that the original metrical tensor has been replaced by a different one, and thus that the underlying group is larger than that of the usual tensor calculus.

If no coordinate transformations were permitted, it would be necessary to recreate the equations of physics for each different type of coordinate system. The laws of transformation belonging to the usual tensor calculus permit us to build the equations once only, no matter how many different coordinate systems we propose to use. And the use of (15) instead of (14) extends this to changes of scale or of unit as well.

The principle of similarity and the consequent enlargement of the tensor formalism contained in the passage from (14) to (15) imply a corresponding enlargement of the underlying geometry from the affine to the similarity geometry. Because of the k^2 factor, (15) has more degrees of freedom than (14), and this should be reflected in the underlying geometrical structure rather than be treated as a minor formal modification of the usual tensor formalism. One could, of course, incorporate changes of size and unit in the general theory of relativity by simply replacing g_{ab} by $k^2 g_{ab}$ in the usual field equations. But this would be a purely symptomatic treatment of the problem. The above considerations suggest that the appropriate geometry for relativity is not the Riemannian geometry but some form of general similarity geometry.

To accomplish this enlargement of the underlying geometrical structure one can go over to a special case of the general conformal geometry. When I took this step in previous publications,[2] I had not clearly formulated in my mind the considerations set forth here. These considerations seem to have a significance independent of the particular mathematical device used in bringing them to bear on the problem of field theory and of any particular field equations that may be set up. Therefore, I have separated them from the specific developments reported in the following paper.

In his celebrated theory of 1918, Weyl introduced the conformal transformations

$$g_{ab} \rightarrow \rho^2 g_{ab},$$

where ρ is a function of position, these conformal transformations being linked to the electromagnetic potentials. In the presence of an electromagnetic field the transport of lengths was nonholonomic. Einstein pointed out serious physical objections to this theory; for example, the frequency of an atom would depend on its past history, and this would conflict with the existence of sharp spectral lines. It was evident that measuring rods do not behave in the way Weyl postulated.

If one gives up the nonholonomy associated with the existence of an electromagnetic field in Weyl's theory, one can always define a calibration that is everywhere the same by merely transporting a unit measuring rod from place to place. Thus, it appears that in avoiding the Einstein objections to Weyl's theory one not only loses the unification it promised of the gravitational and electromagnetic fields, but actually comes back to the Riemannian geometry and so to the gravitational theory of Einstein.

However, one does not have to retreat so far as this, for the similarity transformations are still permissible. Not only do they not succumb to the Einstein objections, but, as the present paper shows, they are physically essential. Since the similarity geometry has more degrees of freedom than the Riemannian there is room in it for further field quantities, and thus the possibility of achieving unification is not lost by the retreat from the Weyl to the similarity geometry, though it has to be achieved in a manner different from that of Weyl.

APPENDIX

The fact that a change in the unit of interval corresponds to a change from one metrical tensor to a different one has a bearing on the dimensionality of ds, g_{ab}, and dx^a which may not be out of place to discuss here. It is usual[3] to regard dx^a as having the dimensions of length. This is supported by the fact that if the coordinate mesh is staked out by a centimeter rod instead of a meter rod, the quantities dx^a will have values 100 times their former values. But the replacing of one coordinate mesh by another is only a coordinate transformation. Since ds is a scalar it will, under (14), remain unaltered in value, while the components g_{ab} will be changed to 100^{-2} times their former values. Thus ds should be a pure number, and g_{ab} should have the dimensions (length)$^{-2}$. However, one likes to think of ds as having the dimensions of a length. And if the dx^a are taken as lengths, this requires that the g_{ab} be pure numbers. They are usually so regarded in relativity (when the time coordinate x^4 is ct). Being pure numbers, they should retain the same values when the unit of length is changed. But this seems to contradict (14), and (15), too. Actually it conforms to (15) in the following way:

Staking out the coordinate mesh in centimeters instead of meters does not change the unit of length. If,

[2] B. Hoffmann, Phys. Rev. **72**, 458 (1947); **73**, 30 (1948); **73**, 1042 (1948).

[3] We ignore here the complications that arise when one uses such things as angle variables, as in spherical polar coordinates.

because dx^a changes to $100\,dx^a$, we wish to regard the quantities dx^a as lengths, we still have not made a change of unit. The change of unit will cause g_{ab} to be replaced by $100^2\,g_{ab}$, and this will exactly compensate the 100^{-2} factor caused by the change of coordinates, leaving the components of the new metrical tensor numerically equal to those of the old. In this sense g_{ab} does behave like a set of pure numbers. But this particular effect is due to our having combined the change of units with a corresponding change of coordinates.[4] Actually the two sets of numbers g_{ab} that have equal numerical values belong to different metrical tensors and to different coordinate systems. If whenever we make a change of units we make this corresponding change of coordinates, we can think of dx^a as lengths and g_{ab} as pure numbers, ds being a length. But there is no need to make this coordinate change, and when we refrain from making it we see that the dx^a are pure numbers, the g_{ab} have the dimensions (length)^2, and ds is a length.

[4] This is precisely the situation in Cartesian vector analysis. The transformation of coordinates given by (3) changes the components of the metrical tensor from δ_{ab} to $100^{-2}\delta_{ab}$. But the original metrical tensor δ_{ab} is changed to a new one $100^2\delta_{ab}$, and thus the final coefficients of the quadratic form for ds^2 are the same as the original.

PHYSICAL REVIEW VOLUME 89, NUMBER 1 JANUARY 1, 1953

The Similarity Theory of Relativity and the Dirac-Schrödinger Theory of Electrons

BANESH HOFFMANN
Queens College, Flushing, New York
(Received June 20, 1952)

The similarity theory of relativity is shown to contain the recent Dirac-Schrödinger theory of electrons as a special case. The variational principle is built on the curvature scalar formed from the basic symmetric similarity tensor $S_{\sigma\tau}$, and leads to a unified field theory of the gravitational field, the electromagnetic field, a scalar field of the sort used by Jordan in his theory of the variable gravitational constant, a charged scalar particle field, and a vector particle field.

I. THE DIRAC-SCHRÖDINGER EQUATIONS

RECENTLY Dirac has proposed[1] a new classical theory of electrons in which the usual Maxwell equations for free space are modified by a simple nonlinear condition on the electromagnetic potential four-vector A_a, which fixes the gauge.

Let $a, b, \cdots$ take on the range 1, 2, 3, 4, with 4 referring to the time. Also, let the metrical tensor g_{ab} have the signature $+++-$ (instead of the $---+$ used by Dirac). Then in the earlier form of Dirac's theory the nonlinear gauge-fixing condition may be written

$$A_a A^a = -m^2c^4/e^2, \tag{1}$$

where m and e are, respectively, the mass and charge of an electron. Later Dirac modified this, but the present paper has to do with the theory based on (1).

The Maxwell equations for free space can be derived from the variational principle

$$\delta \int \mathfrak{L}(-g)^{\frac{1}{2}}\, dx^1dx^2dx^3dx^4 = 0, \tag{2}$$

where

$$\mathfrak{L} = -\tfrac{1}{4}F_{ab}F^{ab} = \tfrac{1}{4}F^a{}_bF^b{}_a, \tag{3}$$

$$F_{ab} = \partial A_a/\partial x^b - \partial A_b/\partial x^a, \tag{4}$$

and

$$F^a{}_b = g^{ac}F_{cb}. \tag{5}$$

In Dirac's theory the restriction (1) is taken care of by replacing (3) by

$$\mathfrak{L} = \tfrac{1}{4}F^a{}_bF^b{}_a - \tfrac{1}{2}\lambda(A_aA^a + m^2c^4/e^2), \tag{6}$$

where λ is an unknown function. This leads to field equations consisting of (1) together with

$$F^{ab}{}_{,b} = j^a, \tag{7}$$

where

$$j_a = \lambda A_a, \tag{8}$$

and, as a consequence of (7),

$$j^a{}_{,a} = 0, \tag{9}$$

the comma denoting the covariant derivative with respect to g_{ab}. Thus a current four-vector j^a enters automatically, and Dirac showed that, without any further assumptions either as to the law of force or the structure of the electron, these equations correctly gave the nonvortical motion of beams of charged particles having m/e of electronic value.

The Dirac equations belonged to the special theory of relativity. They have been written here in general tensor form.

Schrödinger discovered[2] that these equations of Dirac

[1] P. A. M. Dirac, Proc. Roy. Soc. (London) **A209**, 291 (1951); Nature **168**, 906 (1951); Proc. Roy. Soc. (London) **A212**, 330 (1952).

[2] E. Schrödinger, Nature **169**, 538 (1952).

could be regarded as a limiting case of the Maxwell equations combined with the relativistic quantum-mechanical Gordon-Klein-Schrödinger wave equation for a scalar wave function representing charges. This wave equation can be written

$$g^{ab}\left(\partial_a-\frac{ie}{hc}A_a\right)\left(\partial_b-\frac{ie}{hc}A_b\right)\psi=\frac{m^2c^2}{h^2}\psi, \qquad (10)$$

where ∂_a denotes the covariant derivative operator and h is Planck's constant divided by 2π.

From (10) one obtains the following expression for the current four-vector

$$j_a=\frac{-ie}{2hc}(\psi^*\psi_{,a}-\psi\psi^*_{,a})-\frac{e}{hc}A_a\psi\psi^*. \qquad (11)$$

If, instead of the Dirac expression (8), one uses this value of j_a in (7), one has a theory of electric charges in an electromagnetic field in which the charges are represented by the quantum-mechanical scalar wave function ψ.

While Eqs. (7) and (11), are real, Eq. (10) is complex. Moreover, unlike the Dirac equations, the set (7), (10), (11) is gauge invariant and thus permits changes of gauge. Schrödinger discovered a particular choice of gauge that brings about a remarkable simplification. When this particular gauge is used, Eqs. (7), (10), (11) may be replaced by the real equations

$$F^{ab}{}_{,b}=j^a, \qquad (7)$$

$$j_a=-(e/hc)A_a\varphi^2, \qquad (12)$$

and

$$g^{ab}\varphi_{,ab}=\left(\frac{e^2}{h^2c^2}A_aA^a+\frac{m^2c^2}{h^2}\right)\varphi, \qquad (13)$$

in which only real quantities occur.

Equations (7) and (12) correspond to Dirac's Eqs. (7) and (8), with $-(e/hc)\varphi^2$ corresponding to Dirac's λ. Further, Schrödinger pointed out that, if one assumes that the wave amplitude φ does not vary appreciably in a distance comparable to the Compton wavelength of an electron, the left-hand side of (13) may be neglected and the equation then reduces essentially to the Dirac gauge-fixing Eq. (1).

The set of Schrödinger Eqs. (7), (12), (13) can be obtained from the variational principle (2) with

$$\mathfrak{L}=\tfrac{1}{4}F^a{}_bF^b{}_a+g^{ab}\varphi_{,a}\varphi_{,b}+\frac{e^2}{h^2}\left(A^aA_a+\frac{m^2c^4}{e^2}\right)\varphi^2. \qquad (14)$$

II. INADEQUACY OF THE PROJECTIVE THEORY

The fact that the Dirac Eqs. (1), (7), (8) are essentially five equations for the five field variables A_a, λ suggests a possible connection with the projective theory of relativity. Such a connection was found,[3] but in the projective theory there was no scalar field quantity directly corresponding to Dirac's field quantity λ.

The Schrödinger Eqs. (7), (12), (13) are also five equations for five field variables, namely, A_a and φ. And the possibility that these equations may belong to the projective theory of relativity is strengthened by the well-known fact[4] that the Gordon-Klein-Schrödinger scalar wave Eq. (10), as also the expression (11) for the current four-vector, may be obtained from a Lagrangian density

$$\mathfrak{L}=\gamma^{\alpha\beta}\psi_{,\alpha}\psi^*_{,\beta}, \qquad (15)$$

where α, β have the range 0, 1, 2, 3, 4 (with 0 referring to the gauge variable), $\gamma_{\alpha\beta}$ is the fundamental projective tensor of zero index,[5] and ψ is a projective scalar of index different from zero.

In the projective theory of relativity one starts out with a symmetric projective tensor $G_{\alpha\beta}$ of index $2N$. This has fifteen components, and from these one can construct a symmetric affine tensor g_{ab}, a projective vector φ_α of index zero and having $\varphi_0=1$, and a projective scalar Φ of index N. The quantities g_{ab}, φ_a have usually been identified, respectively, with the gravitational and electromagnetic potentials, the φ_a acquiring an added gradient under a gauge transformation. Thus one could expect that the projective scalar Φ might be identified with the projective scalar ψ in (15), and that one could construct out of $G_{\alpha\beta}$ a unified field theory of the gravitational, electromagnetic, and charge-scalar fields.

This, however, is not possible in a projective theory of the sort under discussion. For in such a theory $G_{\alpha\beta}$ is not of zero index and so only the ratios of its components are significant, and not the components themselves. This has to do with the nature of a projective theory and corresponds to the use of homogeneous coordinates in projective geometry. It is taken care of in the formalism by just the device of the index and the corresponding gauge transformations. Consequently, of the fifteen components of $G_{\alpha\beta}$ only fourteen are independent and there is not a fifteenth quantity available to play the part of the projective scalar ψ in (15). In field equations built in terms of the projective curvature tensor formed from $G_{\alpha\beta}$, the projective scalar Φ and the projective vector φ_a enter only in the gauge invariant combination

$$\theta_a\equiv\varphi_a-\frac{1}{N}\frac{\partial\log\Phi}{\partial x^a}. \qquad (16)$$

Thus the five quantities Φ, φ_a occur only in the four combinations θ_a.

If $G_{\alpha\beta}$ were of zero index it would have fifteen inde-

[3] B. Hoffmann, Phys. Rev. **87**, 703 (1952).

[4] O. Klein, Z. Physik. **37**, 895 (1926); **46**, 188 (1927).

[5] The gauge variable x^0 enters the components of a projective tensor only through a factor of the form $\exp(Kx^0)$ that is common to all the components. The constant K is called the index. Thus a projective tensor of zero index does not contain x^0. For further details of the projective formalism and references to the previous literature see the first paper listed in reference 7.

pendent components. But then the projective scalar Φ would be of zero index and so would not be suitable for the role of ψ in (15).

III. THE SIMILARITY THEORY

The principle of similarity discussed in the preceding paper[6] gives reasons for replacing the usual Riemannian geometry of the general theory of relativity by some form of general similarity geometry, so that the similarity transformations

$$g_{ab} \rightarrow \bar{g}_{ab} = k^2 g_{ab}, \tag{17}$$

where k is independent of the coordinates of space-time, will be reflected in the underlying geometrical structure.

In previous papers[7] I developed the similarity geometry as a special case of the general conformal geometry. The latter is characterized by transformations of the type

$$g_{ab} \rightarrow \bar{g}_{ab} = \rho^2 g_{ab}, \tag{18}$$

where ρ is any nonzero function of position. By specializing to the case where ρ is independent of the coordinates and is thus only a numerical parameter k, we obtain the similarity transformations (17).

There is an extensive literature dealing with the general conformal geometry. The classical conformal group in n dimensions has long been known to be related to the rotation group in $n+2$ dimensions, and the geometers have found that the appropriate mathematical tool for the study of the general conformal geometry is a conformal tensor calculus which employs entities $T_{\tau\ldots}{}^{\sigma\cdots}$, called conformal tensors, having $(n+2)^r$ components, where r is the number of indices. Thus in space-time, conformal tensors have 6^r components rather than the 4^r components of affine tensors or the 5^r components of projective tensors. The same is true of the similarity tensors in II.

There are many indications, in spinor theory, meson theory, and elsewhere, that entities having 6^r components are of significance for theoretical physics. Some are mentioned in the papers in reference 7. Schouten[8] has discussed this matter in detail from the point of view of conformal geometry, and his arguments equally support the similarity geometry used here, which may have a more plausible physical justification.

Weyl's theory, though conformal, did not employ the full resources of the general conformal geometry since it used tensors having only 4^r components. When one goes over to the general conformal geometry, the extra degrees of freedom release one from the necessity of bringing in the electromagnetic potentials as measures of a non-holonomy of length in parallel displacement. This removes a major physical difficulty in Weyl's theory. But there still remains the problem of finding an initial physical justification for the use of conformal geometry. The preceding paper gives physical reasons for the use of similarity transformations, but these reasons do not seem to extend beyond that. In the papers in reference 7 I was under the impression that one has to seek an affine metrical tensor g_{ab}. The preceding paper shows that this is not desirable, and the metrical tensor defined later in the present paper is one that undergoes similarity transformations. It is worth remarking that one can easily construct affine metrical tensors by simply dividing the metrical tensor used here by a suitable similarity scalar. This corresponds physically to fixing a particular unit of interval with reference to the physical quantity represented by the particular similarity scalar used in normalizing the metric. It thus corresponds to picking a "fundamental length" as the unit.

Let Greek letters $\sigma, \tau, \cdots$ from the later part of the alphabet have the range 0, 1, 2, 3, 4, 5, where 0 refers to the gauge variable, 1, 2, 3 to space, 4 to time, and 5 to a further variable associated with the ∞^1 transformations of the type (17). The basic definitions are given in II, and we repeat here merely that the variables x^σ transform as

$$\begin{aligned} x^0 &\rightarrow \bar{x}^0 = x^0 + N^{-1}\log k, \\ x^a &\rightarrow \bar{x}^a = \bar{x}^a(x^b), \\ x^5 &\rightarrow \bar{x}^5 = k^{-2}x^5, \end{aligned} \tag{19}$$

and that the field equations in II were built up from a symmetric second rank similarity tensor $S_{\sigma\tau}$ of index $2N$. Like all similarity tensors, $S_{\sigma\tau}$ is independent of x^5. It contains x^0 only in a multiplying factor $\exp(2Nx^0)$.

In II, for the sake of simplicity, the basic similarity tensor $S_{\sigma\tau}$ was subjected to the restrictions[9] that

$$S_{05} = 0 \tag{20}$$

and that

$$S_{55}/S_{00} \text{ be independent of } x^a. \tag{21}$$

The field equations built on the curvature scalar formed from this restricted $S_{\sigma\tau}$ were found to give a unified field theory of the gravitational, electromagnetic, and vector meson fields.

In the present paper these restrictions on $S_{\sigma\tau}$ are removed, so that $S_{\sigma\tau}$ is here taken to be a general symmetric similarity tensor of index $2N$. The physical identifications of various combinations of the components of $S_{\sigma\tau}$ that are made in the present paper correspond to those made in II, but minor adjustments are made in the light of the paper in reference 6.

The curvature scalar Z formed from the general symmetric similarity tensor $S_{\sigma\tau}$ is computed in the appendix to this paper, the result being given in (99). In the course of the computation quantities $g_{ab}, \psi_a, \theta_a, \varphi, \omega$ are defined, and Z is expressed in terms of them. Under coordinate transformations these quantities behave like

[6] B. Hoffmann, Phys. Rev. **89**, 49 (1953).

[7] B. Hoffmann, Phys. Rev. **72**, 458 (1947); **73**, 30 (1948); **73**, 1042 (1948). References to the previous literature given in these papers need not be repeated here. The second of these papers will here be referred to as II.

[8] J. A. Schouten, Revs. Modern Phys. **21**, 421 (1949).

[9] II, Eqs. (20) and (21). [Equation (22) in II contains a misprint. It should read $s_{\sigma\tau} = S_{\sigma\tau}/S_{00}$.]

ordinary affine tensors of ranks corresponding to their indices. Under similarity transformations they behave as follows:

$$g_{ab}\to k^2 g_{ab},\quad \psi_a\to k^2\psi_a,\quad \theta_a\to\theta_a,\qquad \varphi\to\varphi/k^2,\quad \omega\to\omega/k^2. \tag{22}$$

Since this is a four-dimensional theory, we consider a four-dimensional variational principle. The curvature scalar Z is independent of x^5, but contains x^0 in the initial factor Ψ^{-2}. So if we write

$$\bar{Z}=\Psi^2 Z, \tag{23}$$

$\bar{Z}$ will be independent of both x^5 and x^0.

The quantity $\bar{Z}$ contains the curvature scalar R formed from the g_{ab} in the term R/ω. In the general theory of relativity the Lagrangian density of the gravitational field is R. This suggests that the appropriate variational principle to use here is

$$\delta\int\omega\bar{Z}(-g)^{\frac{1}{2}}dx^1dx^2dx^3dx^4=0. \tag{24}$$

If we use this variational principle, however, we encounter difficulties in assigning numerical values to certain quantities. To avoid these difficulties it is necessary to alter the coefficient of R and to alter or remove the term $20N^2\omega$. To alter the coefficient of R we may add a term $(\alpha-1)R(-g)^{\frac{1}{2}}$ to the integrand, where α is a constant; and to remove the term $20N^2\omega$ we can simply subtract a term $20N^2\omega(-g)^{\frac{1}{2}}$ from the integrand. Thus, as variational principle, we take

$$\delta\int\{\omega(\bar{Z}-20N^2)+(\alpha-1)R\}(-g)^{\frac{1}{2}}dx^1dx^2dx^3dx^4=0, \tag{25}$$

where α is a numerical constant.

From (99) we see that (25) is the same as

$$\begin{aligned}\delta\int\Big[&\alpha R+\frac{2\omega}{(-g)^{\frac{1}{2}}}\frac{\partial}{\partial x^a}\Big(\frac{1}{\omega}g^{ab}(-g)^{\frac{1}{2}}\frac{\partial\log\omega}{\partial x^b}\Big)\\&+18g^{ab}\frac{\partial\log\omega}{\partial x^a}\frac{\partial\log\omega}{\partial x^b}-\omega\psi^a{}_b\psi^b{}_a\\&-\frac{1}{\omega}\Big(\theta^a{}_b\theta^b{}_a+g^{bd}\psi_a\theta^a{}_b\frac{\partial\varphi}{\partial x^d}\Big)\\&+\frac{1}{2\omega^2}g^{ab}\frac{\partial\varphi}{\partial x^a}\frac{\partial\varphi}{\partial x^b}\\&+\frac{10N}{\omega(-g)^{\frac{1}{2}}}\frac{\partial}{\partial x^a}\{\omega g^{ab}(-g)^{\frac{1}{2}}(\psi_b\varphi-\theta_b)\}\\&+20N^2\{g^{ab}(\theta_a-\psi_a\varphi)(\theta_b-\psi_b\varphi)+\varphi^2/\omega\}\Big]\\&\times(-g)^{\frac{1}{2}}dx^1dx^2dx^3dx^4=0.\end{aligned} \tag{26}$$

Let the metric be so chosen that the centimeter is the unit of length. Let c be such that the second is the unit of time. And let the gravitational constant be chosen so that the unit of mass is the gram.

Consider first the case where g_{ab} alone is significant; that is, where ω is constant and θ_a, ψ_a, φ are all zero. The variational principle then reduces to

$$\delta\int R(-g)^{\frac{1}{2}}dx^1dx^2dx^3dx^4=0,$$

which is that belonging to the general theory of relativity. This justifies the identification of g_{ab} with the gravitational-metrical tensor of Einstein's theory.

Next, keeping ω constant, but only θ_a and φ zero, we have

$$\delta\int(\alpha R-\omega\psi^a{}_b\psi^b{}_a)(-g)^{\frac{1}{2}}dx^1dx^2dx^3dx^4=0. \tag{27}$$

This is the variational principle for the gravitational and electromagnetic[10] fields in the general theory of relativity with the electromagnetic potential four-vector given by

$$\psi_a=-\frac{1}{c}\Big(\frac{2\kappa\alpha}{\omega}\Big)^{\frac{1}{2}}A_a, \tag{28}$$

where κ is the Einstein gravitational constant,

$$\kappa=8\pi\gamma/c^2, \tag{29}$$

and γ is the Newtonian gravitational constant.

When ω is allowed to be a function of x^a instead of being kept constant, we have further terms to consider in the variational principle. The significant point here is that, by (28), we have, in ω, a "variable gravitational constant" such as has been discussed by Jordan.[11] Some of the additional terms in the variational principle are analogous to those in Jordan's theory, so that his results may be applicable to the present theory.

Let us now go back to the case where ω is constant, and allow g_{ab}, ψ_a, and φ to enter, keeping θ_a zero. Then we have

$$\begin{aligned}\delta\int\Big\{&\alpha R-\omega\psi^a{}_b\psi^b{}_a+\frac{1}{2\omega^2}g^{ab}\frac{\partial\varphi}{\partial x^a}\frac{\partial\varphi}{\partial x^b}\\&+20N^2(1/\omega+g^{ab}\psi_a\psi_b)\varphi^2\Big\}(-g)^{\frac{1}{2}}dx^1dx^2dx^3dx^4=0,\end{aligned} \tag{30}$$

[10] In Eq. (79) the quantities ψ_{ab} are defined with a $\frac{1}{2}$ factor, so the $\frac{1}{4}$ factor in (3) is already included here.

[11] P. Jordan, Ann. Physik **I**, 15 (1947); Astron. Nachr. **276**, 13 (1948); *Schwerkraft und Weltall* (Vieweg, Braunschweig, 1952); G. Ludwig and C. Müller, Ann. Physik **2**, 76 (1948); Heckmann, Jordan, and Fricke, Astrophys. J. **28**, 113 (1951); G. Ludwig, *Fortschritte der Projectiven Relativitätstheorie* (Vieweg, Braunschweig, 1951); see also P. Bergmann, Ann. Math. **49**, 255 (1946).

where we have omitted the term

$$\frac{10N}{\omega(-g)^{\frac{1}{2}}}\frac{\partial}{\partial x^a}\{\omega g^{ab}(-g)^{\frac{1}{2}}(\psi_b\varphi-\theta_b)\}(-g)^{\frac{1}{2}},$$

which is a divergence when ω is constant and so contributes nothing to the field equations in the present case. This is precisely the Schrödinger variational principle, based on the Lagrangian density (14), extended to general relativity. Specifically, if Schrödinger's φ is denoted for the moment by $\bar{\varphi}$, we have

$$\varphi^2/2\alpha\omega^2=2\kappa\hbar^2\bar{\varphi}^2/e^2, \tag{31}$$

$$20N^2\varphi^2/\alpha\omega=2\kappa m^2c^2\bar{\varphi}^2/e^2, \tag{32}$$

and

$$(20N^2/\alpha)\psi^a\psi_a\varphi^2=(2\kappa/c^2)A^aA_a\bar{\varphi}^2. \tag{33}$$

From these we have

$$\omega\psi^a\psi_a=(e^2/m^2c^4)A^aA_a,$$

or, by (28),

$$\alpha=e^2/2\kappa m^2c^2, \tag{34}$$

α being a pure number.

If m is the electronic mass and e the electronic charge, α is of the order 10^{41}.

Finally, if we take g_{ab}, θ_a to be variable, ω constant, and ψ_a, φ zero, we have

$$\delta\int\left\{\alpha R-\frac{1}{\omega}\theta^a{}_b\theta^b{}_a+20N^2\theta^a\theta_a\right\}\times(-g)^{\frac{1}{2}}dx^1dx^2dx^3dx^4=0, \tag{35}$$

which corresponds to a combined gravitational and vector particle field, the latter having the same mass as the scalar field φ above.

When all quantities g_{ab}, θ_a, ψ_a, φ, ω are allowed to enter without restriction, various interaction terms appear linking these various fields.

We see, then, that the present theory contains the Dirac-Schrödinger equations as a special case. Since it has been built up in terms of tensors rather than spinors, there has been no possibility of its containing particles of spin $\frac{1}{2}$, so that electrons of the Dirac spinor type were excluded from the start. This raises a question as to the value of the mass m. If we take it to be the electronic mass, we have a unified field theory of the gravitational and electromagnetic fields containing scalar electrons of the sort described by the Dirac-Schrödinger equations; and alongside the scalar electron field there appears a vector particle field having the same mass but interacting differently with the Maxwellian part of the field. If we take m to be the mass of some meson, we have a unified theory of the gravitational, electromagnetic, vector meson, and charged scalar meson fields, the charge of the latter being taken equal to the electronic charge. And in either case we have in addition the further scalar field ω which belongs to the theory of Jordan.

APPENDIX

In this appendix we compute the value of the curvature scalar formed from the fundamental symmetric similarity tensor $S_{\sigma\tau}$. The aim of the computation is to express the curvature scalar in terms of certain combinations of the components $S_{\sigma\tau}$ that can be given immediate physical significance, and the mathematical definition of these combinations of the components goes hand in hand with the computation of the curvature scalar.

It is doubtful that the present computations could have been carried through without guidance from the analogous, though simpler, computations that have to be performed in the projective theory of relativity. The present computations are performed by the successive application of results known from the projective theory, and these will be stated shortly.

It is necessary to employ indices having various different ranges. The following conventions will therefore be employed consistently, and will be restated individually when first used:

Indices σ, τ, $\cdots$ from the middle of the Greek alphabet will have the range 0, 1, 2, 3, 4, 5.

Indices α, β, $\cdots$ from the beginning of the Greek alphabet will have the range 0, 1, 2, 3, 4 (as in projective relativity).

Indices p, q, $\cdots$ from the middle of the English alphabet will have the range 1, 2, 3, 4, 5.

Indices a, b, $\cdots$ from the beginning of the English alphabet will have the range 1, 2, 3, 4 (referring to space and time).

The index 4 will refer to time, and indices 1, 2, 3, to space. The index 0 will refer to the gauge, and the index 5 will correspond to the extra variable associated with the similarity transformations.

The components $S_{\sigma\tau}$ are independent of x^5 and contain x^0 only in the form of a common multiplying factor $\exp(2Nx^0)$, where N is a constant. Thus $S_{\sigma\tau}$ has the form $\exp(2Nx^0)f_{\sigma\tau}(x^1, x^2, x^3, x^4)$.

In the projective theory of relativity[12] one starts out from a symmetric projective tensor $G_{\alpha\beta}(\alpha, \beta=0, 1, 2, 3, 4)$ of the form $\exp(2Nx^0)f_{\alpha\beta}(x^1, x^2, x^3, x^4)$ and defines $\gamma_{\alpha\beta}$ by

$$\gamma_{\alpha\beta}=G_{\alpha\beta}/G_{00}, \tag{36}$$

so that $\gamma_{\alpha\beta}$ is independent of x^0 and

$$\gamma_{00}=1. \tag{37}$$

Then one writes

$$\varphi_\alpha=\gamma_{\alpha0} \tag{38}$$

and

$$g_{\alpha\beta}=\gamma_{\alpha\beta}-\varphi_\alpha\varphi_\beta. \tag{39}$$

Since

$$g_{a0}\equiv0, \tag{40}$$

the law of transformation shows that $g_{ab}(a, b=1, 2, 3, 4)$

[12] For references regarding the following details of the projective formalism, see II.

is an affine tensor; it is identified with the gravitational-metrical tensor of Einstein's general theory of relativity.

From (39) one has

$$\gamma_{\alpha\beta}=g_{\alpha\beta}+\varphi_\alpha\varphi_\beta. \tag{41}$$

Defining $\gamma^{\alpha\beta}$ by

$$\gamma^{\alpha\beta}\gamma_{\beta\gamma}=\delta^\alpha{}_\gamma, \tag{42}$$

one obtains, after a little computation,

$$\gamma^{ab}=g^{ab},\quad \gamma^{a0}=-g^{ab}\varphi_b,\quad \gamma^{00}=1+g^{ab}\varphi_a\varphi_b. \tag{43}$$

Also one finds that

$$\gamma=g, \tag{44}$$

where γ, g are, respectively, the determinants of $\gamma_{\alpha\beta}$ and g_{ab}.

The curvature scalar formed from $\gamma_{\alpha\beta}$ is denoted by B and turns out to have the form

$$B=R-\varphi^a{}_b\varphi^b{}_a, \tag{45}$$

where R is the curvature scalar formed from g_{ab},

$$\varphi^a{}_b=g^{ac}\varphi_{cb}, \tag{46}$$

and

$$\varphi_{cb}=\tfrac{1}{2}(\partial\varphi_c/\partial x^b-\partial\varphi_b/\partial x^c). \tag{47}$$

Finally, the curvature scalar formed from $G_{\alpha\beta}$ is denoted by $\bar{P}$ and turns out to have the form

$$\bar{P}=\Phi^{-2}\{B+2n\Phi^\alpha{}_{;\alpha}+n(n-1)\Phi^\alpha\Phi_\alpha\}, \tag{48}$$

where n is one less than the number of values that the indices α, β can take (and thus, in projective relativity $n=4$), the semicolon denotes the covariant derivative with respect to $\gamma_{\alpha\beta}$, indices are raised by means of $\gamma^{\alpha\beta}$, Φ is defined by

$$\Phi^2=G_{00}, \tag{49}$$

and Φ_α by

$$\Phi_\alpha=\partial\log\Phi/\partial x^\alpha. \tag{50}$$

We apply these various results, suitably modified, to the present problem of computing the curvature scalar formed from $S_{\sigma\tau}$.

We begin by writing

$$s_{\sigma\tau}=S_{\sigma\tau}/S_{00}, \tag{51}$$

so that $s_{\sigma\tau}$ is independent of x^0 (and, of course, of x^5 since $S_{\sigma\tau}$ is independent of x^5), and

$$s_{00}=1. \tag{52}$$

Denote the curvature scalar of $S_{\sigma\tau}$ by Z and that of $s_{\sigma\tau}$ by z. Then, from comparison with (36), (37), (48), (49), (50), we have (taking $n=5$ in (48))

$$Z=\Psi^{-2}\{z+10\Psi^\sigma{}_{/\sigma}+20\Psi^\sigma\Psi_\sigma\}, \tag{53}$$

where the solidus "/" denotes the covariant derivative with respect to $s_{\sigma\tau}$, indices are raised by $s^{\sigma\tau}$,

$$s^{\sigma\tau}s_{\tau\pi}=\delta^\sigma{}_\pi, \tag{54}$$

$$\Psi^2=S_{00}, \tag{55}$$

and

$$\Psi_\sigma=\partial\log\Psi/\partial x^\sigma. \tag{56}$$

To calculate z, the curvature scalar of $s_{\sigma\tau}$, we write

$$\varphi_\sigma=s_{\sigma 0}, \tag{57}$$

and then define $w_{\sigma\tau}$ by

$$w_{\sigma\tau}=s_{\sigma\tau}-s_{\sigma 0}s_{\tau 0}=s_{\sigma\tau}-\varphi_\sigma\varphi_\tau. \tag{58}$$

Thus

$$w_{\sigma 0}\equiv 0. \tag{59}$$

By (58)

$$s_{\sigma\tau}=w_{\sigma\tau}+\varphi_\sigma\varphi_\tau. \tag{60}$$

By comparison with (38) to (43) we see that if p, q, $\cdots$ have the range 1, 2, 3, 4, 5,

$$s^{pq}=w^{pq},\quad s^{p0}=-w^{pq}\varphi_q,\quad s^{00}=1+w^{pq}\varphi_p\varphi_q, \tag{61}$$

where

$$w^{pq}w_{qr}=\delta^p{}_r. \tag{62}$$

Also, by comparison with (44), we have

$$w=s, \tag{63}$$

where w, s are, respectively, the determinants of w_{pq} and $s_{\sigma\tau}$. And by comparison with (45) we have

$$z=W-\varphi^p{}_q\varphi^q{}_p, \tag{64}$$

where W is the curvature scalar of w_{pq},

$$\varphi^p{}_q=w^{pr}\varphi_{rq}, \tag{65}$$

and

$$\varphi_{rq}=\tfrac{1}{2}(\partial\varphi_r/\partial x^q-\partial\varphi_q/\partial x^r). \tag{66}$$

Next we have to compute W, the curvature scalar of w_{pq}. To do this we follow again the pattern of equations (38) to (48). Thus we write

$$w_{55}=\omega^2 \tag{67}$$

and

$$\bar{w}_{pq}=w_{pq}/\omega^2 \tag{68}$$

so that

$$\bar{w}_{55}=1. \tag{69}$$

Then we write

$$\psi_p=\bar{w}_{p5} \tag{70}$$

and

$$\bar{g}_{pq}=\bar{w}_{pq}-\psi_p\psi_q, \tag{71}$$

so that

$$\bar{g}_{p5}=0. \tag{72}$$

Then

$$\bar{w}_{pq}=\bar{g}_{pq}+\psi_p\psi_q, \tag{73}$$

and, defining $\bar{w}^{pq}$ by

$$\bar{w}^{pq}\bar{w}_{qr}=\delta^p{}_r, \tag{74}$$

we have

$$\bar{w}^{ab}=\bar{g}^{ab},\quad \bar{w}^{a5}=-\bar{g}^{ab}\bar{\psi}_b,\quad \bar{w}^{55}=1+\bar{g}^{ab}\bar{\psi}_a\bar{\psi}_b \tag{75}$$

and

$$\bar{w}=\bar{g}, \tag{76}$$

where $\bar{w}$, $\bar{g}$ are, respectively, the determinants of $\bar{w}_{pq}$ and $\bar{g}_{ab}$.

The curvature scalar $\bar{W}$ formed from $\bar{w}_{pq}$ is then

$$\bar{W}=\bar{R}-\bar{\psi}^a{}_b\bar{\psi}^b{}_a, \tag{77}$$

where $\bar{R}$ is the curvature scalar formed from $\bar{g}_{ab}$,

$$\bar{\psi}^a{}_b=\bar{g}^{ac}\bar{\psi}_{cb}, \tag{78}$$

and

$$\bar{\psi}_{cb}=\tfrac{1}{2}(\partial\bar{\psi}_c/\partial x^b-\partial\bar{\psi}_b/\partial x^c). \tag{79}$$

To obtain the curvature scalar W formed from w_{pq} we now apply (48). While Φ contained x^0, ω is independent of the corresponding variable x^5. Thus we obtain

$$W=\omega^{-2}\left\{\bar{W}+\frac{8}{(-\bar{w})^{\frac{1}{2}}}\frac{\partial}{\partial x^a}[\bar{w}^{ab}(-\bar{w})^{\frac{1}{2}}\partial\log\omega/\partial x^b]+12\bar{w}^{ab}\frac{\partial\log\omega}{\partial x^a}\cdot\frac{\partial\log\omega}{\partial x^b}\right\}. \tag{80}$$

Finally, we must define the metrical tensor g_{ab}. We want this to transform according to (17). From (58) we see that under transformations of the form (19) $w_{\sigma\tau}$ behaves like $s_{\sigma\tau}$. Thus w_{ab} is unaltered, w_{a5} acquires a factor k^{-2}, and $\omega^2(\equiv w_{55})$ acquires a factor k^{-4}. Then, by (68), $\bar{w}_{ab}$ acquires k^4 and $\bar{w}_{a5}$ acquires k^2. So, by (71), $\bar{g}_{ab}$ acquires k^4. Thus we are led to define g_{ab} as

$$g_{ab}=\omega\bar{g}_{ab}, \tag{81}$$

since under a transformation (19) this g_{ab} acquires a factor k^2, in conformity with (17).

From (81),

$$g=\omega^4\bar{g}, \tag{82}$$

where g is the determinant of g_{ab}.

Let R be the curvature scalar formed from g_{ab}. Then, from (48),

$$\begin{aligned}R&=\omega^{-1}\left\{\bar{R}+\frac{6}{(-\bar{g})^{\frac{1}{2}}}\frac{\partial}{\partial x^a}\left[\bar{g}^{ab}(-\bar{g})^{\frac{1}{2}}\frac{\partial\log\omega}{\partial x^b}\right]+6\bar{g}^{ab}\frac{\partial\log\omega}{\partial x^a}\frac{\partial\log\omega}{\partial x^b}\right\}\\&=\omega^{-1}\bar{R}+\frac{6\omega}{(-g)^{\frac{1}{2}}}\frac{\partial}{\partial x^a}\left[\frac{1}{\omega}g^{ab}(-g)^{\frac{1}{2}}\frac{\partial\log\omega}{\partial x^b}\right]+6g^{ab}\frac{\partial\log\omega}{\partial x^a}\frac{\partial\log\omega}{\partial x^b}.\end{aligned} \tag{83}$$

Also, by (75), (76), (81), and (82), the last two terms in (80) can be written

$$\begin{aligned}&\omega^{-2}\left\{\frac{8}{(-\bar{w})^{\frac{1}{2}}}\frac{\partial}{\partial x^a}\left[\bar{w}^{ab}(-\bar{w})^{\frac{1}{2}}\frac{\partial\log\omega}{\partial x^b}\right]+12\bar{w}^{ab}\frac{\partial\log\omega}{\partial x^a}\frac{\partial\log\omega}{\partial x^b}\right\}\\&=\frac{8}{(-g)^{\frac{1}{2}}}\frac{\partial}{\partial x^a}\left[\frac{1}{\omega}g^{ab}(-g)^{\frac{1}{2}}\frac{\partial\log\omega}{\partial x^b}\right]+\frac{12}{\omega}g^{ab}\frac{\partial\log\omega}{\partial x^a}\frac{\partial\log\omega}{\partial x^b}.\end{aligned} \tag{84}$$

Combining (77), (78), (83), and (84), and writing

$$\psi^a{}_b=g^{ac}\psi_{cb}=\frac{1}{\omega}\bar{g}^{ac}\bar{\psi}_{cb}=\frac{1}{\omega}\bar{\psi}^a{}_b, \tag{85}$$

we have

$$\begin{aligned}W&=\omega^{-1}R-\frac{6}{(-g)^{\frac{1}{2}}}\frac{\partial}{\partial x^a}\left[\frac{1}{\omega}g^{ab}(-g)^{\frac{1}{2}}\frac{\partial\log\omega}{\partial x^b}\right]+\frac{6}{\omega}g^{ab}\frac{\partial\log\omega}{\partial x^a}\frac{\partial\log\omega}{\partial x^b}\\&\quad+\frac{8}{(-g)^{\frac{1}{2}}}\frac{\partial}{\partial x^a}\left[\frac{1}{\omega}g^{ab}(-g)^{\frac{1}{2}}\frac{\partial\log\omega}{\partial x^b}\right]+\frac{12}{\omega}g^{ab}\frac{\partial\log\omega}{\partial x^a}\frac{\partial\log\omega}{\partial x^b}-\psi^a{}_b\psi^b{}_a\\&=\omega^{-1}R+\frac{2}{(-g)^{\frac{1}{2}}}\frac{\partial}{\partial x^a}\left[\frac{1}{\omega}g^{ab}(-g)^{\frac{1}{2}}\frac{\partial\log\omega}{\partial x^b}\right]+\frac{18}{\omega}g^{ab}\frac{\partial\log\omega}{\partial x^a}\frac{\partial\log\omega}{\partial x^b}-\psi^a{}_b\psi^b{}_a.\end{aligned} \tag{86}$$

To obtain the value of Z we must now compute the term $-\varphi^p{}_q\varphi^q{}_p$ in (64) and the terms $10\Psi^q{}_{/\sigma}$ and $20\Psi^\sigma\Psi_\sigma$ in (53).

Since φ_p does not contain x^5, we have, from (66),

$$\varphi_{5p}=-\varphi_{p5}=\tfrac{1}{2}\partial\varphi_5/\partial x^p,$$

or, if we write

$$\varphi=\varphi_5, \tag{87}$$

$$\varphi_{5p}=-\varphi_{p5}=\tfrac{1}{2}\partial\varphi/\partial x^p. \tag{88}$$

Then, by (65), (66), (68), (75), and (76), we have

$$
\begin{aligned}
-\varphi^{p}{}_{q}\varphi^{q}{}_{p} &= -w^{pr}w^{qs}\varphi_{rq}\varphi_{sp} \\
&= -w^{ac}w^{bd}\varphi_{cb}\varphi_{da} - 4w^{bc}w^{bd}\varphi_{cb}\varphi_{d\bar{a}} \\
&\quad -2w^{bc}w^{\bar{b}d}\varphi_{cb}\varphi_{d\bar{a}} - 2w^{b\bar{b}}w^{bd}\varphi_{\bar{b}b}\varphi_{da} \\
&= -\omega^{-4}\Big\{\bar{g}^{ac}\bar{g}^{bd}\Big[\varphi_{cb}\varphi_{da}+\psi_{a}\varphi_{cb}\frac{\partial\varphi}{\partial x^{d}} \\
&\qquad +\tfrac{1}{2}\psi_{a}\psi_{b}\frac{\partial\varphi}{\partial x^{c}}\frac{\partial\varphi}{\partial x^{d}}\Big] \\
&\qquad -\tfrac{1}{2}(1+\bar{g}^{ab}\psi_{a}\psi_{b})\bar{g}^{cd}\frac{\partial\varphi}{\partial x^{c}}\frac{\partial\varphi}{\partial x^{d}}\Big\} \\
&= -\omega^{-2}\Big\{g^{ac}g^{bd}\Big[\varphi_{cb}\varphi_{da}+\psi_{a}\varphi_{cb}\frac{\partial\varphi}{\partial x^{d}}\Big] \\
&\qquad -\frac{1}{2\omega}g^{ab}\frac{\partial\varphi}{\partial x^{a}}\frac{\partial\varphi}{\partial x^{b}}\Big\}. \qquad (89)
\end{aligned}
$$

In computing $\Psi^{\sigma}{}_{/\sigma}$ and $\Psi^{\sigma}\Psi_{\sigma}$ we shall need the values of s^{ab}, s^{a0}, and s^{00}. From (61), (68), (75), (76), and (87) we have

$$s^{ab}=w^{ab}=\omega^{-2}\bar{w}^{ab}=\omega^{-2}\bar{g}^{ab}=\omega^{-1}g^{ab}, \qquad (90)$$

$$
\begin{aligned}
s^{a0} &= -w^{ap}\varphi_{p} = -w^{ab}\varphi_{b} - w^{a\bar{b}}\varphi_{\bar{b}} \\
&= -\omega^{-1}g^{ab}\varphi_{b} - \omega^{-2}\bar{w}^{a\bar{b}}\varphi \\
&= -\omega^{-1}g^{ab}\varphi_{b} + \omega^{-1}\psi_{b}\varphi \\
&= -\omega^{-1}g^{ab}(\varphi_{b}-\psi_{b}\varphi), \qquad (91)
\end{aligned}
$$

and

$$
\begin{aligned}
s^{00} &= 1+w^{pq}\varphi_{p}\varphi_{q} = 1+\omega^{-2}\{\bar{g}^{ab}\varphi_{a}\varphi_{b} - 2\bar{g}^{ab}\psi_{b}\varphi_{a}\varphi \\
&\qquad +(1+\bar{g}^{ab}\psi_{a}\psi_{b})\varphi^{2}\} \\
&= 1+\omega^{-1}\{g^{ab}\varphi_{a}\varphi_{b} - 2g^{ab}\psi_{b}\varphi_{a}\varphi \\
&\qquad +(\omega^{-1}+g^{ab}\psi_{a}\psi_{b})\varphi^{2}\} \\
&= (1+\varphi^{2}/\omega^{2})+\omega^{-1}g^{ab}(\varphi_{a}-\psi_{a}\varphi)(\varphi_{b}-\psi_{b}\varphi). \qquad (92)
\end{aligned}
$$

Also

$$s=w=\omega^{8}\bar{w}=\omega^{8}\bar{g}=\omega^{4}g. \qquad (93)$$

We have now

$$
\begin{aligned}
\Psi^{\sigma}{}_{/\sigma} &= \frac{1}{(-s)^{\frac{1}{2}}}\frac{\partial}{\partial x^{\sigma}}\Big[s^{\sigma\tau}(-s)^{\frac{1}{2}}\frac{\partial\log\Psi}{\partial x^{\tau}}\Big] \\
&= \frac{1}{\omega^{2}(-g)^{\frac{1}{2}}}\frac{\partial}{\partial x^{a}}\Big[\omega^{2}(-g)^{\frac{1}{2}}\Big(s^{ab}\frac{\partial\log\Psi}{\partial x^{b}}+Ns^{a0}\Big)\Big] \\
&= \frac{1}{\omega^{2}(-g)^{\frac{1}{2}}} \\
&\quad \times\frac{\partial}{\partial x^{a}}\Big[\omega(-g)^{\frac{1}{2}}g^{ab}\Big(\frac{\partial\log\Psi}{\partial x^{b}}-N(\varphi_{b}-\psi_{b}\varphi)\Big)\Big], \qquad (94)
\end{aligned}
$$

and

$$
\begin{aligned}
\Psi^{\sigma}\Psi_{\sigma} &= s^{\sigma\tau}\frac{\partial\log\Psi}{\partial x^{\sigma}}\frac{\partial\log\Psi}{\partial x^{\tau}} = s^{\alpha\beta}\frac{\partial\log\Psi}{\partial x^{\alpha}}\frac{\partial\log\Psi}{\partial x^{\beta}} \\
&= s^{ab}\frac{\partial\log\Psi}{\partial x^{a}}\frac{\partial\log\Psi}{\partial x^{b}}+2Ns^{a0}\frac{\partial\log\Psi}{\partial x^{a}}+N^{2}s^{00} \\
&= \omega^{-1}g^{ab}\frac{\partial\log\Psi}{\partial x^{a}}\frac{\partial\log\Psi}{\partial x^{b}}-2N\omega^{-1}g^{ab}(\varphi_{b}-\psi_{b}\varphi) \\
&\quad \times\frac{\partial\log\Psi}{\partial x^{a}}+N^{2}(1+\varphi^{2}/\omega^{2}) \\
&\quad +N^{2}\omega^{-1}g^{ab}(\varphi_{a}-\psi_{a}\varphi)(\varphi_{b}-\psi_{b}\varphi) \\
&= N^{2}(1+\varphi^{2}/\omega^{2})+N^{2}\omega^{-1}g^{ab} \\
&\quad \times\Big(\varphi_{a}-\frac{1}{N}\frac{\partial\log\Psi}{\partial x^{a}}-\psi_{a}\varphi\Big) \\
&\quad \times\Big(\varphi_{b}-\frac{1}{N}\frac{\partial\log\Psi}{\partial x^{b}}-\psi_{b}\varphi\Big). \qquad (95)
\end{aligned}
$$

We note that, except for the initial factor Ψ^{-2}, the quantities φ_{a} and Ψ enter only in the combinations φ_{ab} and $\varphi_{a}-(1/N)(\partial\log\Psi/\partial x^{a})$. So we write

$$\theta_{a}=\varphi_{a}-\frac{1}{N}\frac{\partial\log\Psi}{\partial x^{a}}, \qquad (96)$$

$$\theta_{ab}=\tfrac{1}{2}(\partial\theta_{a}/\partial x^{b}-\partial\theta_{b}/\partial x^{a})=\varphi_{ab}, \qquad (97)$$

and

$$\theta^{a}{}_{b}=g^{ac}\theta_{cb}. \qquad (98)$$

Then, collecting the partial results (64), (86), (89), (94), (95), and substituting in (53), we have

$$
\begin{aligned}
Z=\Psi^{-2}\Big\{&\frac{1}{\omega}R+\frac{2}{(-g)^{\frac{1}{2}}}\frac{\partial}{\partial x^{a}}\Big[\frac{1}{\omega}g^{ab}(-g)^{\frac{1}{2}}\frac{\partial\log\omega}{\partial x^{b}}\Big] \\
&+\frac{18}{\omega}g^{ab}\frac{\partial\log\omega}{\partial x^{a}}\frac{\partial\log\omega}{\partial x^{b}}-\psi^{a}{}_{b}\psi^{b}{}_{a} \\
&-\frac{1}{\omega^{2}}\Big[\theta^{a}{}_{b}\theta^{b}{}_{a}+g^{bd}\psi_{a}\theta^{a}{}_{b}\frac{\partial\varphi}{\partial x^{d}}-\frac{1}{2\omega}g^{ab}\frac{\partial\varphi}{\partial x^{a}}\frac{\partial\varphi}{\partial x^{b}}\Big] \\
&+\frac{10N}{\omega^{2}(-g)^{\frac{1}{2}}}\frac{\partial}{\partial x^{a}}[\omega g^{ab}(-g)^{\frac{1}{2}}(\psi_{b}\varphi-\theta_{b})] \\
&+20N^{2}(1+\varphi^{2}/\omega^{2}) \\
&+\frac{20N^{2}}{\omega}g^{ab}(\theta_{a}-\psi_{a}\varphi)(\theta_{b}-\psi_{b}\varphi)\Big\}. \qquad (99)
\end{aligned}
$$

Gauge Invariance and Classical Electrodynamics

LLOYD MOTZ
Rutherfurd Observatory, Columbia University, New York, New York
(Received February 25, 1952; revised manuscript received September 30, 1952)

A Lagrangian for deriving the Maxwell-Lorentz field equations is obtained by starting from a general tensor of the second rank $\mathcal{G}_{\mu\nu}$, which is expressed as the sum of a symmetric and an antisymmetric part $\mathcal{G}_{\mu\nu}=\lambda g_{\mu\nu}+F_{\mu\nu}$. The symmetric part is identified with the metric tensor and the antisymmetric part with the electromagnetic field. A relationship between this second rank tensor and the gauge invariant Ricci-Einstein tensor is established by means of the gauge invariant theories of Weyl and Eddington. This relationship leads directly to the Klein-Gordon relativistic wave equation for a point charge moving in an electromagnetic field provided the function λ is properly chosen.

The Lagrangian density is defined as the quantity $(-|\mathcal{G}_{\mu\nu}|)^{\frac{1}{2}}$, where $|\mathcal{G}_{\mu\nu}|$ is the determinant associated with the tensor $\mathcal{G}_{\mu\nu}$. This choice is made for the Lagrangian density since $(-|\mathcal{G}_{\mu\nu}|)^{\frac{1}{2}}d\tau$ is the simplest generalized invariant volume element. Since the Lagrangian density is nonlinear and irrational as it stands, it is first rationalized by means of the Dirac matrices. If the Lagrangian that is obtained in this way is varied with respect to the vector and scalar potentials, one obtains a set of Maxwell-Lorentz equations for a charge-current distribution that is defined in terms of the field potentials. These equations are almost identical with those recently obtained by Dirac in his new classical electrodynamics. It is shown from the field equations that the velocity of the charge distribution is given by the relation

$$\mathbf{v}=(\mathbf{A}/\phi)c,$$

where $\mathbf{A}$ is the vector potential, ϕ is the scalar potential, and c is the speed of light. This is identical with the result obtained from the retarded potentials of a point charge. For the static case it is shown that the field equations lead to solutions for the fields and potentials that are finite everywhere, and the self-energy of the point charge is finite. The classical radius of the electron, the Compton wavelength and the fine structure constant come into the theory quite naturally.

INTRODUCTION

IT is generally believed that the infinity difficulties associated with the self-energy of the electron and the electromagnetic field are due to the fact that thus far it has been impossible to introduce into the theory a fundamental length of the order e^2/mc^2 in a satisfactory and relativistically invariant manner. Although recent developments in the quantum electrodynamics have produced a prescription for subtracting these infinities in an unambiguous way so that one is left with a result that is finite, the fundamental problem of accounting for the finite mass, charge, and self-energy of the electron still remains.

Since the introduction of a point charge (as demanded by the condition of relativistic invariance) already brings with it infinities in the classical electromagnetic theory, one should attempt to remove the infinity difficulties at this stage before passing over to a quantized theory. In the past a number of attempts have been made to achieve this result but without much success. Most of these older theories, of which that of Born and Infeld[1] is a good example, have led to nonlinear field equations which are extremely cumbersome and difficult to work with.

Recently Dirac[2] has introduced a new form of classical electrodynamics by adding to the old Lagrangian a term which is quadratic in the field potentials and has the effect of destroying the gauge invariance of the theory. Although Dirac is able to obtain the field equations for a charge-current distribution from this Lagrangian, the introduction of the additional term is performed rather artificially.

In the present paper, a new approach to this fundamental problem is suggested which enables one to obtain a new set of field equations which are linear and yet which lead to solutions for the field intensities which are everywhere finite. The charge-current distribution appears in a natural way, and for weak fields the Lagrangian and the Maxwell-Lorentz field equations reduce to those obtained by Dirac.

The essential departure from the Born-Infeld procedure that is taken in this paper is to replace the irrational Lagrangian they adopted, namely, the square root of a quadratic form, by a rational one that can be obtained from a tensor of the second rank by introducing the Dirac matrices. This second-rank tensor is not chosen arbitrarily but is determined from the condition of gauge invariance as introduced by Weyl and others. With this choice the charge-current distribution is automatically introduced and related in a simple way to the Gaussian curvature of the space or the mechanical density of the distribution. If the symmetric part of the second-rank tensor is properly chosen, the usual condition of gauge invariance of the electromagnetic potentials leads to the Klein-Gordon relativistic wave equation for the charge distribution.

THE GENERALIZED VOLUME AND THE LAGRANGIAN DENSITY

Since any tensor of the second rank can be written as the sum of a symmetric and an antisymmetric part, we shall take as the starting point of our theory the asymmetric second rank tensor

$$\mathcal{G}_{\mu\nu}=\lambda g_{\mu\nu}+F_{\mu\nu}, \tag{1}$$

where λ is some invariant function of the space-time coordinates which we shall specify later, $g_{\mu\nu}$ is to be identified with the metric tensor, and $F_{\mu\nu}$ is an anti-

[1] M. Born and L. Infeld, Proc. Roy. Soc. (London) **A144**, 425 (1934).
[2] P. A. M. Dirac, Proc. Roy. Soc. (London) **A209**, 291 (1951).

symmetric tensor that defines the electromagnetic field. The choice of (1) is not entirely arbitrary but is suggested by certain features of the gauge invariant theory developed by Weyl. We shall see, in particular, that the function λ can be chosen in such a way that one is led directly to the Klein-Gordon wave equation.

It is interesting to note that the property of gauge invariance is a feature not only of the electromagnetic potentials but also of the wave functions associated with particle fields. One might therefore expect that any theory which creates an electromagnetic potential by means of a gauge transformation should at the same time create a particle field. We shall see in what follows that this is true of the Weyl theory of gauge invariance. The possibility of deriving particle wave functions from the Weyl theory of gauge invariance was first investigated by London,[3] who identifies the integral of the four-vector obtained from Weyl's theory with the phase of the Schrödinger wave function.

The Weyl theory of gauge invariance is based on the notion that it is not possible to compare lengths at different places in space-time because the result of the comparison will depend on the path taken in bringing the two lengths together. In other words, if we consider the square of the line element $ds^2=g_{\mu\nu}dx_\mu dx_\nu$, only the relative values of $g_{\mu\nu}$ have physical significance. This theory has been criticized because it would seem to indicate that the natural frequency of an atom at a point in space-time should depend on the path taken by the atom to reach the point. This criticism can be answered in various ways.

It may, for example, be argued that although the frequency of an atom will depend on the path taken by the atom, the effect is so small as to be entirely beyond experimental verification for the conditions ordinarily met with in the laboratory. In other words, the effect may be of great theoretical significance and yet of no importance experimentally. The criticism may also be answered by stating that the comparison of lengths does not depend on the parallel displacement of the lengths from point to point but is a property of the geometry at the particular point where the lengths happen to be. This means that at each point of space-time a particular gauge exists which is determined only by the magnitude of the field intensities at that point. Whenever a particle reaches some point, it automatically adjusts its dimensions to the appropriate gauge regardless of the path it traversed to reach the point. As a final argument we note that ds is a complex quantity, in general, so that we may say that the variation in ds as one moves from point to point occurs in its phase and not in its absolute magnitude. Thus the physical quantities associated with the line element are independent of the path taken, and only the physically meaningless phase is altered.

If a small space-time interval at some arbitrary point (x_μ) is transferred by parallel displacement to a neighboring point $(x_\mu+dx_\mu)$, its length will change from a value l to a value $l+dl$ because of the change in gauge in going from the first point to the second. This change in length can be expressed by the formula

$$d(\log l)=\kappa_\mu dx_\mu, \tag{2}$$

where the κ_μ are the components of a four-vector. We note that these quantities have the dimensions of a reciprocal length. In the original form of the Weyl theory, these quantities were identified with the electromagnetic potentials, but we shall not do that at this stage.

Let us now consider a dimensionless invariant space-time function S which is so defined that $(\exp S)$ describes a new gauge system. This new gauge system is introduced by altering the length of our unit at each point in the ratio $(\exp S)$. We thus introduce into the theory a scalar field S in addition to the vector field κ_μ.

Let us now suppose that the gauge of our system is altered in the manner described above and consider what changes are introduced as a result of this. If the starred quantities represent the new values after the change of gauge, we obtain

$$\begin{aligned}&\text{line element:}\quad ds^*=ds(\exp S);\\ &\text{metric tensor:}\quad g^*_{\mu\nu}=g_{\mu\nu}(\exp 2S).\end{aligned} \tag{3}$$

We also have, from (2),

$$\begin{aligned}\kappa_\mu^* dx_\mu=d(\log l^*)&=d\log(l\exp S)\\ &=d(\log l)+(\partial S/\partial x_\mu)dx_\mu,\end{aligned} \tag{4}$$

or

$$\kappa_\mu^*=\kappa_\mu+(\partial S/\partial x_\mu).$$

If we now define the antisymmetric tensor $\mathfrak{F}_{\mu\nu}$ as the curl of the vector κ_μ,

$$\mathfrak{F}_{\mu\nu}=(\partial\kappa_\mu/\partial x_\nu)-(\partial\kappa_\nu/\partial x_\mu), \tag{5}$$

we see that $\mathfrak{F}_{\mu\nu}^*=\mathfrak{F}_{\mu\nu}$ so that $\mathfrak{F}_{\mu\nu}$ is independent of the gauge.

The idea behind the Weyl theory was to introduce into the formalism of general relativity only those tensors that are gauge invariant. Eddington calls these quantities in-tensors. Since the affine connections are functions of the metric tensor and its derivatives, it is clear that the physically important Riemann-Christoffel tensor is not an in-tensor. It is, however, fairly easy to generalize this tensor so that it is gauge invariant. If one does this and contracts it,[4] one obtains the second-rank in-tensor

$$\begin{aligned}{}^*G_{\mu\nu}=G_{\mu\nu}&-(\kappa^\alpha{}_{,\alpha}-2\kappa_\alpha\kappa^\alpha)g_{\mu\nu}-2\kappa_\mu\kappa_\nu\\ &-(\kappa_{\mu,\nu}-\kappa_{\nu,\mu})-2\mathfrak{F}_{\mu\nu},\end{aligned} \tag{6}$$

where $G_{\mu\nu}$ is the usual Einstein curvature tensor. The comma is used to denote the ordinary derivative, $\kappa_{\mu,\nu}=\partial\kappa_\mu/\partial x_\nu$.

[3] F. London, Z. Physik **42**, 375 (1927).

[4] A. S. Eddington, *The Mathematical Theory of Relativity* (Cambridge University Press, Cambridge, 1923) p. 204.

We see at once that the right-hand side of (6) is a sum of a symmetrical and an antisymmetrical part. It is quite natural, therefore, to identify the second-rank tensor (except for a scale factor) ${}^*G_{\mu\nu}$ with the tensor $\mathfrak{S}_{\mu\nu}$ introduced in (1). We shall therefore proceed by placing

$$ {}^*G_{\mu\nu}=Q\mathfrak{S}_{\mu\nu}, \tag{7}$$

where Q is a scale factor. On equating the symmetric and antisymmetric parts of (7) separately, we obtain

$$ -2\mathfrak{F}_{\mu\nu}=QF_{\mu\nu}, \tag{8}$$

$$ G_{\mu\nu}-(\kappa^{\alpha}{}_{,\alpha}-2\kappa_{\alpha}\kappa^{\alpha})g_{\mu\nu}-2\kappa_{\mu}\kappa_{\nu}-(\kappa_{\mu,\nu}+\kappa_{\nu,\mu})=Q\lambda g_{\mu\nu}, \tag{9}$$

or

$$ G_{\mu\nu}-2\kappa_{\mu}\kappa_{\nu}-(\kappa_{\mu,\nu}+\kappa_{\nu,\mu})=(\kappa^{\alpha}{}_{,\alpha}-2\kappa_{\alpha}\kappa^{\alpha}+Q\lambda)g_{\mu\nu}. \tag{10}$$

We shall now choose λ so that (10) will lead to the Klein-Gordon wave equation. We first place

$$ \kappa^{\alpha}{}_{,\alpha}-2\kappa_{\alpha}\kappa^{\alpha}+Q\lambda=k', \tag{11}$$

so that we obtain for λ the expression

$$ \lambda=(k'-\kappa^{\alpha}{}_{,\alpha}+2\kappa_{\alpha}\kappa^{\alpha})/Q, \tag{12}$$

and (10) becomes

$$ G_{\mu\nu}-(\kappa_{\mu,\nu}+\kappa_{\nu,\mu})-2\kappa_{\mu}\kappa_{\nu}=k'g_{\mu\nu}, \tag{13}$$

where k' is some universal constant, having the dimensions of the reciprocal of a length squared.

If we multiply both sides of (13) by $g^{\mu\nu}$ and make use of the index raising and lowering property of the metric tensor, we obtain

$$ G-2\kappa^{\nu}{}_{,\nu}-2\kappa^{\nu}\kappa_{\nu}=4k', \tag{14}$$

where G is the Gaussian curvature at a point and is equal to $8\pi\rho_0(dt/ds)^2\Gamma$. The quantities ρ_0 and Γ are the proper density of matter at the point and the Newtonian gravitational constant, respectively.

We shall now show that (14) leads to the Klein-Gordon equation. We first rewrite it in the form

$$ \kappa^{\nu}{}_{,\nu}+\kappa^{\nu}\kappa_{\nu}=\tfrac{1}{2}G-2k', \tag{15}$$

and note that κ_{ν} in this equation is defined except for a change of gauge. It follows, therefore, that (15) must still be valid if we replace κ_{ν} by $\kappa_{\nu}+\partial S/\partial x_{\nu}$, where S is the dimensionless function defined in (3). Since $\kappa^{\nu}{}_{,\nu}$ is equal to $\partial\kappa^{\nu}/\partial x_{\nu}$, we obtain from (15) the equation

$$ \frac{\partial}{\partial x_{\nu}}\left[\kappa^{\nu}+\frac{\partial S}{\partial x^{\nu}}\right]+\left[\kappa^{\nu}+\frac{\partial S}{\partial x^{\nu}}\right]\left[\kappa_{\nu}+\frac{\partial S}{\partial x_{\nu}}\right]=M, \tag{16}$$

where we have placed M equal to $\frac{1}{2}G-2k'$. It is now easy to see that (16) is identical with

$$ e^{-S}\left[\frac{\partial}{\partial x_{\nu}}+\kappa_{\nu}\right]\left[\kappa^{\nu}+\frac{\partial S}{\partial x^{\nu}}\right]e^{S}=M, \tag{17}$$

where the bracket on the left is to operate on everything that follows it. Multiplying through on the left by e^S and using the relation $(\partial S/\partial x_{\nu})e^S=(\partial/\partial x_{\nu})e^S$, we can write (17) as

$$ \left(\frac{\partial}{\partial x_{\nu}}+\kappa_{\nu}\right)\left(\kappa^{\nu}+\frac{\partial}{\partial x^{\nu}}\right)e^{S}=Me^{S}. \tag{18}$$

We shall now introduce the electromagnetic potentials by means of the relation

$$ \kappa_{\nu}=-iA_{\nu}\eta, \tag{19}$$

where η has the dimension of a reciprocal charge. We also substitute for S the quantity $-i\eta\chi$. If we now multiply both sides of (18) by $(e/c)^2$ and divide through by η, we obtain the result

$$ \left(\frac{e}{c\eta i}\frac{\partial}{\partial x_{\nu}}-\frac{e}{c}A_{\nu}\right)\left(\frac{e}{c\eta i}\frac{\partial}{\partial x^{\nu}}-\frac{e}{c}A^{\nu}\right)e^{-i\eta\chi}=-\frac{e^2}{c^2\eta^2}Me^{-i\eta\chi}. \tag{20}$$

If we now define $\eta=(1/\alpha e)$, where α is the fine structure constant, we can introduce Planck's constant by means of the relation $\hbar=(e/c\eta)$, and (20) becomes

$$ \left(\frac{\hbar}{i}\frac{\partial}{\partial x_{\nu}}-\frac{e}{c}A_{\nu}\right)\left(\frac{\hbar}{i}\frac{\partial}{\partial x^{\nu}}-\frac{e}{c}A^{\nu}\right)\exp\left(-i\frac{e}{c\hbar}\chi\right)$$

$$ =\hbar^2(2k'-\tfrac{1}{2}G)\exp\left(-i\frac{e}{c\hbar}\chi\right). \tag{21}$$

It is clear that we may identify this with the Klein-Gordon equation provided we identify the coefficient of the exponential on the right-hand side of (21) with the rest mass of the charge distribution by means of the equation

$$ \hbar^2(2k'-\tfrac{1}{2}G)=m^2c^2. \tag{22}$$

We shall see that this agrees with the result that we shall obtain in solving for the electrostatic case with gravitational effects neglected.

We shall return now to the determination of the function λ. From (5), (8), and (19) we obtain

$$ QF_{\mu\nu}=2i\eta(\partial A_{\mu}/\partial x_{\nu}-\partial A_{\nu}/\partial x_{\mu}). \tag{23}$$

If we now place $Q=2i\eta$, we obtain

$$ \lambda=i(k+\mu A_{\alpha}A^{\alpha}+\sigma A^{\alpha}{}_{,\alpha})\equiv i\Lambda, \tag{24}$$

where we have placed

$$ \mu=\tfrac{1}{2}\eta;\quad k=-k'/\eta;\quad \sigma=-\tfrac{1}{2}i. $$

The constant k is a universal constant whose value is very much larger than the electromagnetic field intensities usually met with in the laboratory. (This quantity plays a role here similar to that of the maximum field intensity introduced in the Born-Infeld theory.) We see that λ is both symmetric and invariant.

With the choice (24) of λ, we shall now make use of (1) to set up a Lagrangian function for the electromag-

netic field. We start by writing down the expression for the generalized volume element of our space. It has been shown by Eddington[6] that the simplest such volume element is given by the invariant,

$$dV=(-|\mathcal{G}_{\mu\nu}|)^{\frac{1}{2}}d\tau, \tag{25}$$

where $|\mathcal{G}_{\mu\nu}|$ is the determinant associated with the tensor $\mathcal{G}_{\mu\nu}$, and $d\tau=dx_1dx_2dx_3dx_4$.

It has been customary in the past to identify the components of the antisymmetric tensor $F_{\mu\nu}$ with the electromagnetic field strengths and to derive Maxwell's equations from a Lagrangian of the form

$$\tfrac{1}{4}F^{\mu\nu}F_{\mu\nu}(-g)^{\frac{1}{2}}d\tau,$$

where g is the determinant of the metric tensor.

Born and Infeld do not start from this form of the Lagrangian but instead use what is essentially the invariant integral (25) with λ taken equal to a constant. Since a Lagrangian function of this type is an irrational function of the field components, one is led to a set of nonlinear field equations.

In this paper we shall also start from the generalized volume element (25), but with λ defined by (24). If we identify the vector field A_μ with the electromagnetic potentials, then its curl [as defined by (23)] allows us to identify the components of $F_{\mu\nu}$ with the electromagnetic field intensities.

RATIONALIZING THE GENERALIZED VOLUME

If we neglect gravitational effects, we can choose a Galilean coordinate system and we obtain

$$\begin{aligned}|\mathcal{G}_{\mu\nu}|&=\begin{vmatrix}-\lambda & f_{21} & f_{31} & f_{41}\\ -f_{21} & -\lambda & f_{32} & f_{42}\\ -f_{31} & -f_{32} & -\lambda & f_{43}\\ -f_{41} & -f_{42} & -f_{43} & \lambda\end{vmatrix}\\ &=-\{\lambda^4+\lambda^2(f_{21}^2+f_{32}^2+f_{31}^2-f_{41}^2-f_{42}^2-f_{43}^2)\\ &\qquad-(f_{23}f_{41}-f_{31}f_{42}+f_{21}f_{43})^2\}\\ &\equiv-\mathcal{G}^2,\end{aligned} \tag{26}$$

where the f_{ij} are components of the antisymmetric tensor $F_{\mu\nu}$.

If we now introduce the conventional notation for the potentials and the field strengths, we obtain

$$\mathcal{G}^2=\lambda^4+(\mathbf{B}^2-\mathbf{E}^2)\lambda^2-(\mathbf{B}\cdot\mathbf{E})^2, \tag{27}$$

where

$$\begin{aligned}&\lambda=i[k+\mu(\mathbf{A}^2-\phi^2)+\sigma(\nabla\cdot\mathbf{A}+\dot{\phi}/c)],\\ &\mathbf{E}=-\nabla\phi-(1/c)\partial\mathbf{A}/\partial t,\quad \mathbf{B}=\nabla\times\mathbf{A}.\end{aligned} \tag{28}$$

$\mathbf{E}$ and $\mathbf{B}$ are the electromagnetic field strengths, $\mathbf{A}$ is the vector potential, and ϕ is the scalar potential. The dot signifies differentiation with respect to the time.

Instead of using the form (27) for $\mathcal{G}^2$, we shall transform it to the expression

$$\mathcal{G}^2=(\mathbf{E}\times\mathbf{B})^2+[\lambda^2+\tfrac{1}{2}(\mathbf{B}^2-\mathbf{E}^2)]^2-\tfrac{1}{4}(\mathbf{B}^2+\mathbf{E}^2)^2. \tag{29}$$

[6] A. S. Eddington, reference 4, p. 234.

In order to obtain $\mathcal{G}$ as a rational function of the field strengths, we shall introduce certain auxiliary field quantities in the form of fourfold row and column matrices which we define as follows:

$$\Psi=\begin{pmatrix}\psi_1\\ \psi_2\\ \psi_3\\ \psi_4\end{pmatrix};\quad \Psi^+=(\psi_1\psi_2\psi_3\psi_4). \tag{30}$$

The product of these two quantities is defined in the usual way by means of the relation

$$\Psi^+\Psi=\psi_1^2+\psi_2^2+\psi_3^2+\psi_4^2. \tag{31}$$

For the time being we shall make no assumptions about the ψ's, which may either be constants or space-time functions.

We now multiply the expression (29) on the left by the row matrix in (30) and on the right by the column matrix in (30). If we introduce Λ instead of λ as defined by (24), we obtain

$$\begin{aligned}\Psi^+\mathcal{G}^2\Psi=\Psi^+\{&(\mathbf{E}\times\mathbf{B})^2\\ &+[-\Lambda^2+\tfrac{1}{2}(\mathbf{B}^2-\mathbf{E}^2)]^2-\tfrac{1}{4}(\mathbf{B}^2+\mathbf{E}^2)^2\}\Psi.\end{aligned} \tag{32}$$

We can factor this expression in a manner similar to that used by Dirac in setting up his relativistic wave equation. We introduce the Dirac matrices γ_1, γ_2, γ_3, γ_4 and $\gamma_5=\gamma_1\gamma_2\gamma_3\gamma_4$. If we let $\boldsymbol{\gamma}$ represent the first three matrices, then it can be seen that (32) factors into the two expressions

$$\begin{aligned}\mathcal{G}\Psi=-\{&\boldsymbol{\gamma}\cdot(\mathbf{E}\times\mathbf{B})+\gamma_4[-\Lambda^2+\tfrac{1}{2}(\mathbf{B}^2-\mathbf{E}^2)]\\ &+\tfrac{1}{2}i\gamma_5(\mathbf{B}^2+\mathbf{E}^2)\}\Psi,\\ \Psi^+\mathcal{G}=-\Psi^+\{&\boldsymbol{\gamma}\cdot(\mathbf{E}\times\mathbf{B})+\gamma_4[-\Lambda^2+\tfrac{1}{2}(\mathbf{B}^2-\mathbf{E}^2)]\\ &+\tfrac{1}{2}i\gamma_5(\mathbf{B}^2+\mathbf{E}^2)\}.\end{aligned} \tag{33}$$

We shall now take for our Lagrangian density the quantity $\mathcal{G}\Psi$ and write

$$\begin{aligned}\mathfrak{L}=-\{&\boldsymbol{\gamma}\cdot(\mathbf{E}\times\mathbf{B})+\gamma_4[-\Lambda^2+\tfrac{1}{2}(\mathbf{B}^2-\mathbf{E}^2)]\\ &+\tfrac{1}{2}i\gamma_5(\mathbf{B}^2+\mathbf{E}^2)\}\Psi.\end{aligned} \tag{34}$$

We see that the Dirac matrices operate on Ψ in such a way as to replace the usual Lagrangian density by a fourfold Lagrangian density according to the following scheme:

$$\begin{aligned}\mathfrak{L}_1\equiv\mathcal{G}\psi_1=&-[(\mathbf{E}\times\mathbf{B})_z-i(\mathbf{E}\times\mathbf{B})_y]\psi_4-(\mathbf{E}\times\mathbf{B})_z\psi_3\\ &-[-\Lambda^2+\tfrac{1}{2}(\mathbf{B}^2-\mathbf{E}^2)]\psi_1-\tfrac{1}{2}(\mathbf{B}^2+\mathbf{E}^2)\psi_3,\\ \mathfrak{L}_2\equiv\mathcal{G}\psi_2=&-[(\mathbf{E}\times\mathbf{B})_x+i(\mathbf{E}\times\mathbf{B})_y]\psi_3+(\mathbf{E}\times\mathbf{B})_z\psi_4\\ &-[-\Lambda^2+\tfrac{1}{2}(\mathbf{B}^2-\mathbf{E}^2)]\psi_2-\tfrac{1}{2}(\mathbf{B}^2+\mathbf{E}^2)\psi_4,\\ \mathfrak{L}_3\equiv\mathcal{G}\psi_3=&-[(\mathbf{E}\times\mathbf{B})_x-i(\mathbf{E}\times\mathbf{B})_y]\psi_2-(\mathbf{E}\times\mathbf{B})_z\psi_1\\ &+[-\Lambda^2+\tfrac{1}{2}(\mathbf{B}^2-\mathbf{E}^2)]\psi_3+\tfrac{1}{2}(\mathbf{B}^2+\mathbf{E}^2)\psi_1,\\ \mathfrak{L}_4\equiv\mathcal{G}\psi_4=&-[(\mathbf{E}\times\mathbf{B})_x+i(\mathbf{E}\times\mathbf{B})_y]\psi_1+(\mathbf{E}\times\mathbf{B})_z\psi_2\\ &+[-\Lambda^2+\tfrac{1}{2}(\mathbf{B}^2-\mathbf{E}^2)]\psi_4+\tfrac{1}{2}(\mathbf{B}^2+\mathbf{E}^2)\psi_2.\end{aligned} \tag{35}$$

We may consider the ψ-quantities as additional degrees of freedom (additional fields of a nonelectromagnetic nature) that are introduced by the process of

rationalization. These fields factor out when one passes from the linear to the quadratic Lagrangian density.

Since the use of a Lagrangian density of the form (35) will give rise to a fourfold set of field equations, it may be argued that this will result in blackbody radiation intensities four times larger than those predicted by the Planck formula and therefore in disagreement with observation. That this is not the case can easily be seen from the fact that all the ψ's are not of the same order of magnitude. In fact it can be shown that for weak fields, that is, for fields that are small compared to k or to Λ, the quantities ψ_1 and ψ_2 are small compared to ψ_3 and ψ_4. From this it follows that for weak fields the Lagrangian density defined above reduces to that obtained by Dirac.[2] To see this we rewrite (35) in the form

$$\begin{aligned}
&\{\mathcal{G}+\lambda^2+\tfrac{1}{2}(\mathbf{B}^2-\mathbf{E}^2)\}\psi_1 \\
&\qquad=i[(\mathbf{E}\times\mathbf{B})_y+i(\mathbf{E}\times\mathbf{B})_x]\psi_4 \\
&\qquad\quad-[(\mathbf{E}\times\mathbf{B})_z+\tfrac{1}{2}(\mathbf{B}^2+\mathbf{E}^2)]\psi_3, \\
&\{\mathcal{G}+\lambda^2+\tfrac{1}{2}(\mathbf{B}^2-\mathbf{E}^2)\}\psi_2 \\
&\qquad=-[(\mathbf{E}\times\mathbf{B})_x+i(\mathbf{E}\times\mathbf{B})_y]\psi_3 \\
&\qquad\quad+[(\mathbf{E}\times\mathbf{B})_z-\tfrac{1}{2}(\mathbf{B}^2+\mathbf{E}^2)]\psi_4, \\
&\{\mathcal{G}-\lambda^2-\tfrac{1}{2}(\mathbf{B}^2-\mathbf{E}^2)\}\psi_3 \\
&\qquad=[i(\mathbf{E}\times\mathbf{B})_y-(\mathbf{E}\times\mathbf{B})_x]\psi_2 \\
&\qquad\quad-[(\mathbf{E}\times\mathbf{B})_z-\tfrac{1}{2}(\mathbf{B}^2+\mathbf{E}^2)]\psi_1, \\
&\{\mathcal{G}-\lambda^2-\tfrac{1}{2}(\mathbf{B}^2-\mathbf{E}^2)\}\psi_4 \\
&\qquad=-[(\mathbf{E}\times\mathbf{B})_x+i(\mathbf{E}\times\mathbf{B})_y]\psi_1 \\
&\qquad\quad+[(\mathbf{E}\times\mathbf{B})_z+\tfrac{1}{2}(\mathbf{B}^2+\mathbf{E}^2)]\psi_2,
\end{aligned} \tag{36}$$

and note that for small $\mathbf{E}$ and $\mathbf{B}$ we may place $\mathcal{G}$ equal to λ^2. If we do this and solve for ψ_1 and ψ_2, we obtain

$$\begin{aligned}
\psi_1&=\{[i(\mathbf{E}\times\mathbf{B})_y-(\mathbf{E}\times\mathbf{B})_x]\psi_4 \\
&\qquad-[(\mathbf{E}\times\mathbf{B})_z+\tfrac{1}{2}(\mathbf{B}^2+\mathbf{E}^2)]\psi_3\}/2\lambda^2, \\
\psi_2&=\{-(\mathbf{E}\times\mathbf{B})_x+i(\mathbf{E}\times\mathbf{B})_y]\psi_3 \\
&\qquad+[(\mathbf{E}\times\mathbf{B})_z-\tfrac{1}{2}(\mathbf{B}^2+\mathbf{E}^2)]\psi_4\}/2\lambda^2.
\end{aligned} \tag{37}$$

If we substitute these values of ψ_1 and ψ_2 into the last two equations of (36), we obtain the results

$$\begin{aligned}
&[\mathcal{G}-\lambda^2-\tfrac{1}{2}(\mathbf{B}^2-\mathbf{E}^2)]\psi_4 \\
&\qquad=[(\mathbf{E}\times\mathbf{B})^2-\tfrac{1}{4}(\mathbf{B}^2+\mathbf{E}^2)^2]\psi_4/2\lambda^2, \\
&[\mathcal{G}-\lambda^2-\tfrac{1}{2}(\mathbf{B}^2-\mathbf{E}^2)]\psi_3 \\
&\qquad=[(\mathbf{E}\times\mathbf{B})^2-\tfrac{1}{4}(\mathbf{B}^2-\mathbf{E}^2)^2]\psi_3/2\lambda^2.
\end{aligned} \tag{38}$$

If we now make use of the original definition of $\mathcal{G}^2$ as given in (29), we can substitute for the right-hand side of (38) and obtain

$$\begin{aligned}
&[\mathcal{G}-\lambda^2-\tfrac{1}{2}(\mathbf{B}^2-\mathbf{E}^2)]\psi_4=[\mathcal{G}-\lambda^2-\tfrac{1}{2}(\mathbf{B}^2-\mathbf{E}^2)] \\
&\qquad\times[\mathcal{G}+\lambda^2+\tfrac{1}{2}(\mathbf{B}^2-\mathbf{E}^2)]\psi_4/2\lambda^2, \\
&[\mathcal{G}-\lambda^2-\tfrac{1}{2}(\mathbf{B}^2-\mathbf{E}^2)]\psi_3=[\mathcal{G}-\lambda^2-\tfrac{1}{2}(\mathbf{B}^2-\mathbf{E}^2)] \\
&\qquad\times[\mathcal{G}+\lambda^2+\tfrac{1}{2}(\mathbf{B}^2-\mathbf{E}^2)]\psi_3/2\lambda^2.
\end{aligned} \tag{39}$$

From (39) we obtain at once the Lagrangian density for weak fields:

$$\mathcal{G}=-\Lambda^2-\tfrac{1}{2}(\mathbf{B}^2-\mathbf{E}^2). \tag{40}$$

For Λ different from zero this is the Lagrangian density used by Dirac, and for Λ equal to zero it reduces to the usual classical Lagrangian density. We see, then, that for the case of weak fields our theory gives the same result as that obtained with the classical theory.

If we now take (34) as our Lagrangian density, the Lagrangian becomes

$$L=\int \mathfrak{L}\,d\tau, \tag{41}$$

and the variational principle becomes

$$\delta\int \mathfrak{L}\,d\tau=0. \tag{42}$$

THE DERIVATION OF THE FIELD EQUATIONS

The variation of $\mathfrak{L}$ with respect to the electromagnetic field leads to the equation

$$\begin{aligned}
\delta\mathfrak{L}=-\{&\boldsymbol{\gamma}\cdot(\delta\mathbf{E}\times\mathbf{B})+\boldsymbol{\gamma}\cdot(\mathbf{E}\times\delta\mathbf{B}) \\
&+\gamma_4(-2\Lambda\delta\Lambda+\mathbf{B}\cdot\delta\mathbf{B}-\mathbf{E}\cdot\delta\mathbf{E}) \\
&+i\gamma_5(\mathbf{B}\cdot\delta\mathbf{B}+\mathbf{E}\cdot\delta\mathbf{E})\}\Psi.
\end{aligned} \tag{43}$$

If we now introduce the vector and scalar potentials from (28) and discard quantities that vanish at the integration limits, we find

$$\begin{aligned}
\delta\mathfrak{L}=\{&-\delta\mathbf{A}\cdot[\boldsymbol{\gamma}\times(\boldsymbol{\nabla}\times\mathbf{E})+\boldsymbol{\nabla}\times(\boldsymbol{\gamma}\times\mathbf{E}) \\
&+\gamma_4\{-4\mu\mathbf{A}\Lambda+\boldsymbol{\nabla}\times\mathbf{B}-(1/c)\partial\mathbf{E}/\partial t\} \\
&+i\gamma_5\{\boldsymbol{\nabla}\times\mathbf{B}+(1/c)\partial\mathbf{E}/\partial t\}]-\delta\phi[\boldsymbol{\gamma}\cdot(\boldsymbol{\nabla}\times\mathbf{B}) \\
&+\gamma_4(4\mu\phi\Lambda-\boldsymbol{\nabla}\cdot\mathbf{E})+i\gamma_5\boldsymbol{\nabla}\cdot\mathbf{E}]\}\Psi.
\end{aligned} \tag{44}$$

To obtain the field equations, we set the coefficient of $\delta\mathbf{A}$ and that of $\delta\phi$ separately equal to zero. After some trivial transformations, we obtain the equations of the electromagnetic field in the following form:

$$\boldsymbol{\nabla}\times\mathbf{E}+(1/c)\partial\mathbf{B}/\partial t=0,\quad \boldsymbol{\nabla}\cdot\mathbf{B}=0; \tag{45}$$

and

$$\begin{aligned}
&\boldsymbol{\nabla}\times[(\gamma_4+i\gamma_5)\Psi\mathbf{B}+(\boldsymbol{\gamma}\times\mathbf{E})\Psi] \\
&-(1/c)\frac{\partial}{\partial t}[(\gamma_4-i\gamma_5)\Psi\mathbf{E}+(\boldsymbol{\gamma}\times\mathbf{B})\Psi]=4\gamma_4\mu\Lambda\mathbf{A}\Psi,
\end{aligned} \tag{46}$$

$$\boldsymbol{\nabla}\cdot[(\gamma_4-i\gamma_5)\mathbf{E}+(\boldsymbol{\gamma}\times\mathbf{B})]\Psi=4\gamma_4\mu\Lambda\phi\Psi.$$

The first set is obtained from (28) and the second set from (42).

We now define the auxiliary field vectors

$$\begin{aligned}
\mathbf{D}&=(\gamma_4-i\gamma_5)\mathbf{E}\Psi+(\boldsymbol{\gamma}\times\mathbf{B})\Psi, \\
\mathbf{H}&=(\gamma_4+i\gamma_5)\mathbf{B}\Psi+(\boldsymbol{\gamma}\times\mathbf{E})\Psi.
\end{aligned} \tag{47}$$

In terms of these vectors the Lagrangian density takes on the simple form

$$\mathfrak{L}=\tfrac{1}{2}(\mathbf{D}\cdot\mathbf{E}-\mathbf{H}\cdot\mathbf{B})+\gamma_4\Lambda^2\Psi; \tag{48}$$

and the field equations become

$$\begin{gathered}\nabla\times\mathbf{E}+(1/c)\partial\mathbf{B}/\partial t=0;\quad \nabla\cdot\mathbf{B}=0,\\ \nabla\times\mathbf{H}-(1/c)\partial\mathbf{D}/\partial t=4\gamma_4\mu\Lambda\mathbf{A}\Psi;\\ \nabla\cdot\mathbf{D}=4\gamma_4\mu\Lambda\phi\Psi.\end{gathered}\tag{49}$$

We may note that in the Born-Infeld theory the auxiliary fields that are introduced also appear defined in terms of $\mathbf{E}$ and $\mathbf{B}$ but in a very complicated and irrational form.

As an immediate consequence of our field equations, we may note that the charge and current densities appear defined in terms of the electromagnetic potentials. For the charge and current densities, we obtain the expressions

$$4\pi\rho=4\gamma_4\mu\Lambda\Psi\phi,\quad (4\pi/c)\rho\mathbf{v}=4\gamma_4\mu\Lambda\Psi\mathbf{A},\tag{50}$$

where $\mathbf{v}$ is the velocity of the charge distribution. If we divide the second of these equations by the first, we obtain

$$\mathbf{v}=(\mathbf{A}/\phi)c.\tag{51}$$

We see that this is precisely the result obtained from the retarded potentials of a moving point charge in the usual theory. The retarded scalar and vector potentials for a moving point charge in the usual theory are given by

$$\begin{aligned}\phi&=e[\mathbf{r}+(1/c)\mathbf{v}\cdot\mathbf{r}]^{-1}|_{t-r/c},\\ \mathbf{A}&=(e\mathbf{v}/c)[\mathbf{r}+(1/c)\mathbf{v}\cdot\mathbf{r}]^{-1}|_{t-r/c},\end{aligned}$$

and their ratio leads to (51).

It has been shown that for the case of weak fields the Lagrangian density (34) reduces to the usual one. Using the same procedure it is possible to show that the field Eqs. (46) for the case of weak fields reduce to the usual set of Maxwell-Lorentz equations for a charge current distribution.

SOLUTION FOR THE STATIC CASE

For the electrostatic case $\mathbf{B}$ vanishes and the last equation in (49) becomes

$$(\gamma_4-i\gamma_5)\Psi\nabla\cdot\mathbf{E}=4\gamma_4\mu\Lambda\Psi\phi.\tag{52}$$

From this equation we now obtain the four equations

$$\begin{aligned}(\nabla^2\phi)(\psi_1-\psi_3)&=-4\Lambda\mu\phi\psi_1,\\ (\nabla^2\phi)(\psi_2-\psi_4)&=-4\Lambda\mu\phi\psi_2,\\ (\nabla^2\phi)(\psi_1-\psi_3)&=4\Lambda\mu\phi\psi_3,\\ (\nabla^2\phi)(\psi_2-\psi_4)&=4\Lambda\mu\phi\psi_4,\end{aligned}\tag{53}$$

where we have replaced $\nabla\cdot\mathbf{E}$ by $\nabla^2\phi$.

If we now add the first of these equations to the third one and the second to the fourth one, we obtain two identical differential equations for the potential ϕ,

$$\nabla^2\phi=-2\Lambda\mu\phi.\tag{54}$$

We can solve this equation for the case of spherical symmetry by successive approximations. Using the first equation in (28), we place Λ equal to $(k-\mu\phi^2)$ and rewrite (54) in the form

$$(d^2/dr^2)(r\phi)=-2\mu(k-\phi^2)(r\phi).\tag{55}$$

Since k is very much larger than ϕ^2 for ordinary fields, we neglect ϕ^2 on the right-hand side of (55) to a first approximation and obtain for ϕ the solution

$$\phi=(a/r)\exp[-(2|k|\mu)^{\frac{1}{2}}r],\tag{56}$$

where $|k|$ stands for the absolute value of k, which is a negative constant, and a is a constant of integration.

If we substitute this back into (55), we obtain the equation

$$(d/dr)(r^2d\phi/dr)=-2(\Lambda\mu ar)\exp[-(2|k|\mu)^{\frac{1}{2}}r],$$

or

$$(d/dr)(r^2E_r)=-2(\Lambda\mu ar)\exp[-(2|k|\mu)^{\frac{1}{2}}r].$$

If we again neglect ϕ^2 with respect to k on the right-hand side of this equation, we obtain

$$(d/dr)(r^2E_r)=(2|k|\Lambda\mu ar)\exp[-(2|k|\mu)^{\frac{1}{2}}r]$$

If we integrate this from zero to some finite value of r, we obtain the solution for the electrostatic field

$$E_r=(e/r^2)\{1-[(2|k|\mu)^{\frac{1}{2}}r+1]\exp[-(2|k|\mu)^{\frac{1}{2}}r]\},\tag{57}$$

where the constant a has been placed equal to $-e$.

We see that for large values of r Eq. (57) reduces to the ordinary expression for the electrostatic field of a point charge. For small values of r (57) becomes

$$E_r=(e/r^2)\{1-[1+(2|k|\mu)^{\frac{1}{2}}r][1-(2|k|\mu)^{\frac{1}{2}}r]\},\tag{58}$$

and we see that the field takes on a finite value at the origin, namely,

$$E_{0r}=2|k|e\mu.\tag{59}$$

We shall now make use of the result for the electrostatic case to determine the total energy contained in the electrostatic field of a point charge at rest at the origin. Since the energy density is given by $E_r^2/8\pi$, we write for the total energy in the field the integral

$$U=\frac{1}{2}\int_0^\infty E_r^2r^2dr=\frac{e^2}{2}\int_0^\infty\{1-[(2|k|\mu)^{\frac{1}{2}}r+1]\times\exp[-(2|k|\mu)^{\frac{1}{2}}r]\}^2\frac{dr}{r^2}.\tag{60}$$

On carrying out the integration, we obtain

$$U=\frac{e^2}{2}\left\{-\frac{1}{r}-\frac{(2|k|\mu)^{\frac{1}{2}}}{2}\exp[-2(2|k|\mu)^{\frac{1}{2}}r]+\frac{2}{r}\exp[-(2|k|\mu)^{\frac{1}{2}}r]-\frac{1}{r}\exp[-2(2|k|\mu)^{\frac{1}{2}}r]\right\}\Bigg|_0^\infty.$$

At the upper limit the entire expression vanishes; and we obtain the value at the lower limit by expanding the

exponentials to the first power in r. We thus find

$$U=\lim_{r\to 0}\frac{e^2}{2}\left\{\frac{1}{r}+\tfrac{1}{2}(2|k|\mu)^{\frac{1}{2}}-\frac{2}{r}[1-(2|k|\mu)^{\frac{1}{2}}r+\cdots]\right.$$
$$\left.+\frac{1}{r}[1-2(2|k|\mu)^{\frac{1}{2}}r+\cdots]\right\}.$$

On passing to the limit $r=0$, we finally obtain

$$U=\tfrac{1}{4}e^2(2|k|\mu)^{\frac{1}{2}}. \tag{61}$$

If we now equate the total energy in the field to the self energy mc^2 of the point charge, we obtain

$$\tfrac{1}{4}e^2(2|k|\mu)^{\frac{1}{2}}=mc^2. \tag{62}$$

From (62) we see that the classical radius of the electron, e^2/mc^2, enters into the theory quite naturally as the quantity $4/(2|k|\mu)^{\frac{1}{2}}$.

If we compare (62) with (22) we see that these two equations can be consistent only if

$$G=2(mc/\hbar)^2(32\alpha^2-1), \tag{63}$$

where α is the fine structure constant $\hbar c/e^2$. With this choice for G, we find that the constant $|k|$ has the value

$$|k|=8(mc/\hbar)^2\alpha^3 e. \tag{64}$$

We see from this that $|k|$ is indeed a very large constant, so that we are justified in neglecting ordinary fields compared with it.

If we substitute (64) into (59), we note that the electrostatic field at a point charge is just equal to $16(mc^2)^2/e^3$ or $2|k|/\alpha$.

THE HAMILTONIAN OF THE FIELD

To pass over to the Hamiltonian formalism, we introduce the momenta $\mathbf{p}_A$ and p_ϕ conjugate to the generalized coordinates $\mathbf{A}$, and ϕ, respectively, by means of the definitions:

$$p_{A^\mu}=\partial\mathfrak{L}/\partial\dot{A}^\mu, \quad p_\phi=\partial\mathfrak{L}/\partial\dot{\phi}. \tag{65}$$

We note that

$$\mathbf{p}_A=-(1/c)[(\gamma_4-i\gamma_5)\mathbf{E}+(\boldsymbol{\gamma}\times\mathbf{B})]\Psi=-\mathbf{D}/c, \tag{66}$$

and that

$$p_\phi=-\gamma_4 i\Lambda\Psi/c=-\gamma_4\lambda\Psi/c. \tag{67}$$

We now define the Hamiltonian density as

$$\mathfrak{IC}=\mathbf{p}_A\cdot\partial\mathbf{A}/\partial t+p_\phi\cdot\dot{\phi}-\mathfrak{L}. \tag{68}$$

If we make use of (48) for the Lagrangian density and place $\mathbf{D}=\mathbf{D}'\Psi$ and $\mathbf{H}=\mathbf{H}'\Psi$, the Hamiltonian density becomes

$$\mathfrak{IC}=\{\tfrac{1}{2}(\mathbf{D}'\cdot\mathbf{E}+\mathbf{H}'\cdot\mathbf{B})+\mathbf{D}'\cdot\boldsymbol{\nabla}\phi+\gamma_4\lambda[\lambda+(\dot{\phi}/c)]\}\Psi. \tag{69}$$

Since this Hamiltonian density contains no square roots or other irrational functions of the field variables, it should be possible to pass over to the quantum theory in the usual manner. The presence of the Dirac matrices in $\mathbf{D}'$ and $\mathbf{H}'$ in (69) should enable one to introduce the necessary spin into the theory.

DISCUSSION

There are a few points in connection with the theory developed above that are worth noting. The first point of interest concerns the manner in which the field equations and the Klein-Gordon equation enter into the theory. The former are obtained from a variational principle whereas the Klein-Gordon equation is introduced by means of a gauge transformation applied to a scalar equation. It would appear that the solution of the problem of the motion of an electron or a point charge involves the simultaneous solution of a set of field equations for the electromagnetic potentials and a set of wave equations. Since gravitational effects have been neglected, one may wonder whether a complete variational principle involving variation with respect to the gravitational as well as the electromagnetic potentials would not give both the field equations and the Klein-Gordon equation.

We have noted previously that the quantities ψ are not completely specified. In the present paper, we assumed them to be constants in dealing with the electromagnetic field equations. It is possible, however to allow the ψ's to enter the theory as space-time functions in which case the field equations would involve additional terms which depend on the derivatives of these quantities. In considering the nature of the Lagrangian density for weak fields, we do in fact tacitly assume that the ψ's are variable quantities such that for weak fields the first two components are small compared with the last two components.

We may finally note that the present theory does not suffer from the defect of having to introduce new arbitrary constants. The constants that do appear like k, G, and μ can all be expressed in terms of the fundamental constants of nature, e, m, h, and c.

In the summer of 1946, when the ideas developed in this paper first originated with the author, he had the pleasure of a number of stimulating discussions on the subject with Professor John A. Wheeler. It is also a pleasure to thank Peter G. Bergmann for suggesting some of the features of the arrangement of the material in the paper.

Localized Functions in Molecules and Crystals*

G. F. KOSTER
Physics Department, Massachusetts Institute of Technology, Cambridge, Massachusetts
(Received August 25, 1952)

The Wannier function in crystals is defined in terms of a differential equation and a variation procedure. This variation procedure is also used to define localized functions in molecules which can be used to build solutions of Schrödinger's equation. Illustrations of the procedure of building solutions of Schrödinger's equation from localized functions is given for examples taken from crystalline and molecular problems. Contact is made with Slater's work on the two-dimensional Mathieu problem. A numerical method of carrying out the variation procedure is discussed.

I. INTRODUCTION

IN the study of energy bands in solids, it is sometimes convenient to express the solutions of Schrödinger's equation in terms of Wannier functions.[1] These are functions constructed from the solutions of the periodic potential problem which are localized about a given atom in a crystal and are orthogonal to the same function about any other center. The purpose of this paper is first: define the Wannier function in terms of a differential equation, and second: find a variation procedure for finding the Wannier function. It will be seen that these two goals are most easily reached using the terminology of group theory[2] and that when phrased in this terminology the results can be generalized to define localized functions in molecules which have many of the desirable properties of Wannier functions in crystals.

Imagine a crystal which is periodic with respect to translations $\mathbf{R}_n$, where the $\mathbf{R}_n$ are expressible in the form

$$\mathbf{R}_n = n_1\mathbf{R}_1 + n_2\mathbf{R}_2 + n_3\mathbf{R}_3, \tag{1}$$

where $\mathbf{R}_1$, $\mathbf{R}_2$, and $\mathbf{R}_3$ form the edges of the unit cell in the crystal and the n's are integers. In the one-electron approximation, Schrödinger's equation (in atomic units)[3] takes the form

$$[-\nabla^2 + V(\mathbf{r})]\psi_l(\mathbf{k}, \mathbf{r}) = E_l(\mathbf{k})\psi_l(\mathbf{k}, \mathbf{r}). \tag{2}$$

Here $V(\mathbf{r})$ has the property that

$$V(\mathbf{r} - \mathbf{R}_n) = V(\mathbf{r}). \tag{3}$$

We specify the states $\psi_l(\mathbf{k}, \mathbf{r})$ in terms of a pseudomomentum $\mathbf{k}$ and the band to which the wave function belongs. The subscript l in Eq. (2) denotes the l^{th} band. The vector $\mathbf{k}$ specifies the translational properties of the wave function, and as Bloch has shown,[4] allows us to write the wave function in the form:

$$\psi_l(\mathbf{k}, \mathbf{r}) = e^{i\mathbf{k}\cdot\mathbf{r}}\mu_l(\mathbf{k}, \mathbf{r}), \tag{4}$$

where $\mu_l(\mathbf{k}, \mathbf{r})$ is periodic with respect to the translations $\mathbf{R}_n$.

In this notation, Wannier functions are defined as

$$a_l(\mathbf{r} - \mathbf{R}_n) = (1/N^{\frac{1}{2}})\sum(\mathbf{k})e^{-i\mathbf{k}\cdot\mathbf{R}_n}\psi_l(\mathbf{k}, \mathbf{r}), \tag{5}$$

where N is the number of unit cells in the macrocrystal over which ψ is normalized. The factor $(1/N^{\frac{1}{2}})$ normalizes $a_l(\mathbf{r})$. The summation extends over all $\mathbf{k}$ in the first Brillouin zone. Using the fact that

$$\sum(\mathbf{R}_n)e^{i(\mathbf{k}'-\mathbf{k})\cdot\mathbf{R}_n} = N\delta_{\mathbf{k},\mathbf{k}'}, \tag{6}$$

we can find by multiplying both sides of Eq. (5) by $e^{i\mathbf{k}'\cdot\mathbf{R}_n}$ and summing over $\mathbf{R}_n$ that

$$\psi_l(\mathbf{k}', \mathbf{r}) = (1/N^{\frac{1}{2}})\sum(\mathbf{R}_n)e^{i\mathbf{k}'\cdot\mathbf{R}_n}a_l(\mathbf{r} - \mathbf{R}_n). \tag{7}$$

From the orthogonality of the solutions of Schrödinger's equation and the fact that

$$\sum(\mathbf{k})e^{i\mathbf{k}\cdot(\mathbf{R}_m - \mathbf{R}_n)} = \delta_{m,n}, \tag{8}$$

it can be shown that

$$\int a_l(\mathbf{r} - \mathbf{R}_n)a_j(\mathbf{r} - \mathbf{R}_m)d\tau = \delta_{lj}\delta_{mn}. \tag{9}$$

It might be pointed out here that in the summation over $\mathbf{k}$ in Eq. (5), we could equally well have added up the wave functions from one band over part of the first Brillouin zone and wave functions from another band over the rest of the first zone without destroying the orthogonality properties of the Wannier function.

II. A DIFFERENTIAL EQUATION FOR THE WANNIER FUNCTION

Using the results of the preceding paragraphs, we can find a differential equation for the Wannier function. Let us apply the Hamiltonian operator $H = -\nabla^2 + V$ to both sides of Eq. (5):

$$Ha_l(\mathbf{r} - \mathbf{R}_n) = (1/N^{\frac{1}{2}})\sum(\mathbf{k})e^{-i\mathbf{k}\cdot\mathbf{R}_n}H\psi_l(\mathbf{k}, \mathbf{r}). \tag{10}$$

Using Eq. (2) we find that

$$Ha_l(\mathbf{r} - \mathbf{R}_n) = (1/N^{\frac{1}{2}})\sum(\mathbf{k})e^{-i\mathbf{k}\cdot\mathbf{R}_n}E_l(\mathbf{k})\psi_l(\mathbf{k}, \mathbf{r}). \tag{11}$$

A well-known property of energy bands is that the

* Supported by the ONR.

[1] G. H. Wannier, Phys. Rev. **52**, 191 (1937).

[2] For treatments of group theory see Eyring, Walter, and Kimball, *Quantum Chemistry* (John Wiley and Sons, Inc., New York, 1947), p. 172–189; E. Wigner, *Gruppentheorie* (Friedr. Vieweg und Sohn, Braunschweig, 1931); A. Speiser *Die Theorie der Gruppen* (Julius Springer, Berlin, 1927).

[3] The unit of length is the Bohr radius. The unit of energy is the Rydberg.

[4] F. Bloch, Z. Physik **52**, 555 (1928).

energy has the periodicity of the reciprocal lattices. By this we mean that

$$E_l(\mathbf{k}+\mathbf{K}_j)=E_l(\mathbf{k}), \tag{12}$$

where $\mathbf{K}_j$ are the primitive translations of the reciprocal space and are defined by the equations

$$\mathbf{R}_n\cdot\mathbf{K}_j=2\pi\times(\text{integer}). \tag{13}$$

We can, therefore, express $E_l(\mathbf{k})$ as a Fourier series:

$$E_l(\mathbf{k})=\sum(\mathbf{R}_j)e^{-i\mathbf{k}\cdot\mathbf{R}_j}\mathcal{E}_l(\mathbf{R}_j). \tag{14}$$

Substituting Eq. (14) in Eq. (11) and expressing $\psi_l(\mathbf{k},\mathbf{r})$ in terms of Wannier functions, we find that

$$Ha_l(\mathbf{r}-\mathbf{R}_n)=(1/N^{\frac{1}{2}})\sum(\mathbf{k})e^{-i\mathbf{k}\cdot\mathbf{R}_n}$$
$$\times\sum(\mathbf{R}_j)e^{-i\mathbf{k}\cdot\mathbf{R}_j}\mathcal{E}_l(\mathbf{R}_j)\sum(\mathbf{R}_m)e^{i\mathbf{k}\cdot\mathbf{R}_m}a_l(\mathbf{r}-\mathbf{R}_m). \tag{15}$$

By making use of Eq. (8) this reduces to

$$Ha_l(\mathbf{r}-\mathbf{R}_n)=\sum(\mathbf{R}_j)\mathcal{E}_l(\mathbf{R}_j)a_l(\mathbf{r}-\mathbf{R}_n-\mathbf{R}_j). \tag{16}$$

The set of Eqs. (16) for all values of $\mathbf{R}_n$ are the desired set of differential equations for the Wannier function. If we multiply (16) by $a_k(\mathbf{r})$ and integrate over all space, we find by use of (9) that

$$\int a_k(\mathbf{r})Ha_l(\mathbf{r}-\mathbf{R}_n)d\tau=\delta_{kl}\mathcal{E}_l(\mathbf{R}_n). \tag{17}$$

From Eqs. (16) and (17) we can see qualitatively how the width of the bands depends on the degree of localization of the Wannier function and how the Wannier functions approach the solutions of the Schrödinger one-electron equation for the isolated atoms which make up the crystal. Consider a crystal with an atomic like potential situated at each lattice point. We notice from Eq. (17) as the distance between lattice points increases that, because of the localization of $a_l(\mathbf{r})$, $\mathcal{E}_l(\mathbf{R}_n)$ approaches zero for $\mathbf{R}_n>0$. This means that $E_l(\mathbf{k})$ approaches $\mathcal{E}_l(0)$ for all values of $\mathbf{k}$. The bands become flat. As $\mathcal{E}_l(\mathbf{R}_n)$ approaches zero, Eq. (16) becomes

$$Ha_l(\mathbf{r}-\mathbf{R}_n)=\mathcal{E}_l(0)a_l(\mathbf{r}-\mathbf{R}_n). \tag{18}$$

As the distance between lattice points increases, the Hamiltonian approaches the isolated atom Hamiltonian over the region in which $a_l(\mathbf{r})$ has an appreciable value. The Wannier function approaches an atomic function about $\mathbf{R}_n$, and $\mathcal{E}_l(0)$ becomes the atomic level.

III. A VARIATION PROCEDURE FOR LOCALIZED FUNCTIONS

We shall now derive a variation procedure for localized functions in molecules and crystals.

Consider any Hamiltonian H which is invariant under some group of unitary operations G of order g. Let R represent any operation in this group and consider the following variation procedure for a function $a(\mathbf{r})$. Let us make

$$\int a(\mathbf{r})Ha(\mathbf{r})d\tau \tag{19}$$

have an extremum subject to the constraints

$$\int a(\mathbf{r})Ra(\mathbf{r})d\tau=d(R) \tag{20}$$

for all R in G, or for all R in any invariant subgroup[5] $\mathfrak{H}$ of G of order h. These constants $d(R)$ should be chosen to give the desired kind of localization to $a(\mathbf{r})$. In order to have these constraints be consistent, we must have

$$d(R)=d(R^{-1}), \tag{21}$$

since

$$\int a(\mathbf{r})Ra(\mathbf{r})d\tau=\int a(\mathbf{r})R^{-1}a(\mathbf{r})d\tau \tag{22}$$

because of the unitary nature of R. By using the method of Lagrangian multipliers, this problem is equivalent to taking the variation of[6]

$$\int a(\mathbf{r})[H-\sum'(R)\mathcal{E}(R)R]a(\mathbf{r})d\tau$$

and setting it equal to zero. Here $\mathcal{E}(R)$ are the Lagrangian multipliers for the constraints (20). This leads to the equation

$$Ha(\mathbf{r})-\sum'(R)\frac{\mathcal{E}(R)+\mathcal{E}(R^{-1})}{2}Ra(\mathbf{r})=0. \tag{23}$$

Since the constraint for R is exactly the same as that for R^{-1} we have that $\mathcal{E}(R)=\mathcal{E}(R^{-1})$; therefore

$$Ha(\mathbf{r})-\sum'(R)\mathcal{E}(R)Ra(\mathbf{r})=0. \tag{24}$$

If we take any other member R' of the subgroup $\mathfrak{H}$, and operate on Eq. (24) with it we get a differential equation involving $R'a(\mathbf{r})$:

$$HR'a(\mathbf{r})-\sum'(R)\mathcal{E}(R)R'Ra(\mathbf{r})=0. \tag{25}$$

Rewriting the summation as

$$\sum'(R)\mathcal{E}(R)R'RR'^{-1}R'a(\mathbf{r}), \tag{26}$$

and letting $R''=R'RR'^{-1}$ we have that

$$H[R'a(\mathbf{r})]-\sum'(R'')\mathcal{E}(R'^{-1}R''R')R''[R'a(\mathbf{r})]=0. \tag{27}$$

We can see how this yields Eq. (16) for a crystal. In this case, the subgroup is the group of translations in the crystal. All the elements of the translation group commute with one another, therefore, $R'^{-1}R''R'=R''$. If we consider R as being a translation through $\mathbf{R}_n$, then Eq.

[5] An invariant subgroup has the property that $R''=RR'R^{-1}$ is in $\mathfrak{H}$ for any R in G and R' in $\mathfrak{H}$.

[6] In this equation and the following $\Sigma'(R)$ means summation over $\mathfrak{H}$. $\Sigma(R)$ means summation over G.

(27) becomes

$$Ha(\mathbf{r}-\mathbf{R}_n)=\sum(\mathbf{R}_j)\mathcal{E}_l(\mathbf{R}_j)a_l(\mathbf{r}-\mathbf{R}_n-\mathbf{R}_j). \quad (16)$$

In this case, the constraints would be taken such that $d(R)=0$ except for the identity operation E, for which the constraint would be $d(E)=1$ in order to assure the normalization of $a(\mathbf{r})$. We see that for the case of crystals this variation procedure yields functions satisfying the same differential equation as the Wannier functions satisfy.

In the case of the crystal, we were able to express the coefficients $\mathcal{E}(\mathbf{R}_n)$ in terms of integrals involving Wannier functions and the Hamiltonian [Eq. (17)]. In the case of the general problem, we can do a similar thing: multiply Eq. (25) by $a(\mathbf{r})$ and integrate over all space. This yields

$$\int a(\mathbf{r})HR'a(\mathbf{r})d\tau=\sum(R)\mathcal{E}(R)d(R'R). \quad (28)$$

Since $R'R$ is also a member of the invariant subgroup $\mathfrak{H}$ we have a set of h simultaneous equations for $\mathcal{E}(R)$ which will express these quantities in terms of the constraints $d(R)$ and integrals of the form $\int a(\mathbf{r})HRa(\mathbf{r})d\tau$. The case of the crystal corresponds to the case $d(R'R)=0$ unless $R'R=E$, i.e., $R'=R^{-1}$. Therefore, Eqs. (28) reduce to

$$\int a(\mathbf{r})HR'a(\mathbf{r})d\tau=\mathcal{E}(R'^{-1})=\mathcal{E}(R'). \quad (29)$$

We know how to combine Wannier functions to give us a solution of Schrödinger's equation. Let us now see how we may combine the functions defined by Eq. (25) to give us solutions of Schrödinger's equation.

We know that the solutions of Schrödinger's equation of a given energy for a Hamiltonian which is invariant under a group G must form a basis for one of the irreducible representations of the group G. Let $\Gamma_l(R')_{mp}$ be the m, p^{th} matrix element in the matrix $\Gamma_l(R')$ which is equivalent to the operation R' in the l^{th} irreducible representation. Let g_l be the dimension of this representation. Let us multiply each of the Eqs. (25) by $\Gamma_l(R')_{mp}$ and sum over all R' in G.

$$H\sum(R')\Gamma_l(R')_{mp}R'a(\mathbf{r})=\sum'(R)\mathcal{E}(R)\sum(R')\Gamma_l(R')_{mp}R'Ra(\mathbf{r}). \quad (30)$$

Let us now expand $a(\mathbf{r})$ in terms of functions which transform according to the irreducible representations given by $\Gamma_i(R')$.

$$a(\mathbf{r})=\sum(ijk)c_{ijk}\varphi_j{}^{ik}. \quad (31)$$

Here $\varphi_j{}^{ik}$ transforms according to the j^{th} row of the i^{th} irreducible representation. The superscript k specifies which of the functions which transforms according to the j^{th} row of the i^{th} irreducible representations is specified in the summation. The $\varphi_j{}^{ik}$, therefore, have the property that

$$R\varphi_j{}^{ik}=\sum(j')\Gamma_i(R)_{j'j}\varphi_{j'}{}^{ik}. \quad (32)$$

Using this fact in Eq. (30) we find that

$$\sum(R')\Gamma_l(R')_{mp}R'Ra(\mathbf{r})=\sum(ijk)c_{ijk}\sum(j')\Gamma_i(R)_{j'j}\times\sum(j'')\sum(R')\Gamma_l(R')_{mp}\Gamma_i(R')_{j''j'}\varphi_{j''}{}^{ik}. \quad (33)$$

We also know that

$$\sum(R')\Gamma_l(R')_{mp}\Gamma_i(R')_{j''j'}=\frac{g}{\sqrt{g_i}\sqrt{g_l}}\delta_{il}\delta_{j'p}\delta_{j''m}, \quad (34)$$

where g_i is the order of the i^{th} irreducible representation. Using (34) in (33) we find that

$$\sum(R')\Gamma_l(R')_{mp}R'Ra(\mathbf{r})=(g/g_l)\sum(j)\Gamma_l(R)_{pj}\sum(k)c_{ljk}\varphi_m{}^{lk}. \quad (35)$$

For $R=E$, $\Gamma_l(E)_{pj}$ is the unit matrix, and we find that

$$\sum(R')\Gamma_l(R')_{mp}R'a(\mathbf{r})=(g/g_l)\sum(k)c_{lpk}\varphi_m{}^{lk}. \quad (36)$$

If we define

$$f_{mp}{}^{l}=\sum(k)c_{lpk}\varphi_m{}^{lk}, \quad (37)$$

substituting (37), (36), and (35) in Eq. (30) will yield

$$Hf_{mp}{}^{l}=\sum'(R)\mathcal{E}(R)\sum_{1}^{g_l}(j)\Gamma_l(R)_{pj}f_{mj}{}^{l}. \quad (38)$$

$f_{mp}{}^{l}$ transforms according to the m^{th} row of the l^{th} irreducible representations because of (32). The partners of this function in the same basis can easily be shown to be the functions $f_{j'p}{}^{l}$ $j'=1\cdots g_l$. Therefore, the functions $f_{11}{}^{l}$, $\cdots f_{g_l1}{}^{l}$, form a basis for the l^{th} irreducible representation as do the other sets:

$$\begin{matrix} f_{12}{}^{l}, & f_{22}{}^{l} & \cdots & f_{g_l2}{}^{l} \\ & & \vdots & \\ f_{1g_l}{}^{l} & \cdots & \cdots & f_{g_lg_l}{}^{l}. \end{matrix}$$

Equation (38) therefore expresses the function $f_{mp}{}^{l}$ as a linear combination of the other functions $f_{mj}{}^{l}$, $j=1\cdots g_l$, which transform according to the same row of the same irreducible representation but are in different bases.

Equations (38) can be expressed most easily in matrix form. Regard $f_{mj}{}^{l}$ for $j=1\cdots g_l$ as a column vector. Then Eqs. (38) become

$$H\begin{bmatrix} f_{m1}{}^{l} \\ \vdots \\ f_{mg_l}{}^{l} \end{bmatrix}=\left[\sum'(R)\mathcal{E}(R)\Gamma_l(R)\right]\begin{bmatrix} f_{m1}{}^{l} \\ \vdots \\ f_{mg_l}{}^{l} \end{bmatrix}. \quad (39)$$

To find the solutions of Schrödinger's equation, let us multiply both sides of this equation by a numerical matrix O

$$HO\begin{bmatrix} f_{m1}{}^{l} \\ \vdots \\ f_{mg_l}{}^{l} \end{bmatrix}=O\left[\sum'(R)\mathcal{E}(R)\Gamma_l(R)\right]O^{-1}O\begin{bmatrix} f_{m1}{}^{l} \\ \vdots \\ f_{mg_l}{}^{l} \end{bmatrix}. \quad (40)$$

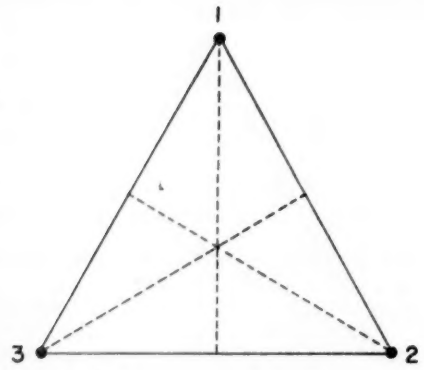

FIG. 1. A molecule whose symmetry is C_{3v}. Heavy dots represent the nuclei.

Clearly all we need to do to find the solutions of Schrödinger's equation is to find the matrix O which diagonalizes the matrix $\sum'(R)\mathcal{E}(R)\Gamma_l(R)$. The Eq. (40) will become

$$HO\begin{pmatrix} f_{m1}{}^l \\ \cdot \\ \cdot \\ \cdot \\ f_{mg_l}{}^l \end{pmatrix} = \begin{pmatrix} E_1 & & & 0 \\ & \cdot & & \\ & & \cdot & \\ 0 & & & E_{g_l} \end{pmatrix} O\begin{pmatrix} f_{m1}{}^l \\ \cdot \\ \cdot \\ \cdot \\ f_{mg_l}{}^l \end{pmatrix}. \quad (41)$$

The g_l functions given by

$$O\begin{pmatrix} f_{m1}{}^l \\ \cdot \\ \cdot \\ \cdot \\ f_{mg_l}{}^l \end{pmatrix}$$

are the solutions to Schrödinger's equation and the eigenvalues E_j of $\sum'(R)\mathcal{E}(R)\Gamma_l(R)$ are the corresponding energies. Clearly once we have solved for the matrix O we have solved the problem for all values of m in Eq. (39). In other words, we have found g_l sets of g_l functions which are solutions of Schrödinger's equation. The g_l functions $\sum(j)O_{nj}f_{mj}{}^l$, $m=1\cdots g_l$, all have the same energy E_n and form a basis for the irreducible representation l. The above procedure is essentially quite simple, but its simplicity may be obscured by the details necessary for the mathematical justification of the procedure. It is, therefore, profitable to state in words just how to go about finding solutions of Schrödinger's equation from the solution $a(\mathbf{r})$ of our variational procedure. If we seek functions which belong to the l^{th} irreducible representation and which solve the wave equations, we form the matrix $\sum'(R)\mathcal{E}(R)\Gamma_l(R)$. This matrix is of order g_l. Diagonalize this matrix by a unitary transformation O. The diagonal elements in this transformed matrix are the energies E_n of the g_l levels all of which have a degeneracy g_l, and each of these energies has functions associated with it which form a basis for the l^{th} irreducible representation. To find the g_l functions which have the energy E_n, form the $g_l{}^2$ functions $\sum(R)\Gamma_l(R)_{mp}a(\mathbf{r})=f_{mp}{}^l$. Then form the vectors

$$O\begin{pmatrix} f_{m1}{}^l \\ \cdot \\ \cdot \\ \cdot \\ f_{mg_l}{}^l \end{pmatrix}, \quad m=1\cdots g_l,$$

for all m. The n^{th} element in these vectors are the g_l functions belonging to the energy E_n.

There are a great many special cases in which we need not diagonalize $\sum'(R)\mathcal{E}(R)\Gamma_l(R)$. For all nondegenerate levels the matrices $\Gamma_l(R)$ are already diagonal since the matrices are all one-dimensional matrices. Another important case is the case in which we specify constraints for an abelian invariant subgroup of the total group. (An invariant subgroup in which all the elements commute.) In this case, all the matrices $\Gamma_l(R)$ for R belonging to the subgroup can all be chosen to be diagonal. $\sum'(R)\mathcal{E}(R)\Gamma_l(R)$ where the summation extends over the subgroup will be, therefore, diagonal. This is just the case we are confronted with in crystals and will be discussed in more detail later.

IV. EXAMPLES FROM MOLECULAR GROUPS

Consider the hydrogen molecule. The molecule is invariant with respect to a reflection in the plane passing midway between the nuclei and perpendicular to the line joining them. Let us call this operation σ. Let us look for a function $a(\mathbf{r})$ for which[7]

$$\int a(\mathbf{r})Ha(\mathbf{r})d\tau = \min, \quad (42)$$

with constraints

$$\int a(\mathbf{r})\sigma a(\mathbf{r})d\tau = 0, \qquad \int a(\mathbf{r})a(\mathbf{r})d\tau = 1. \quad (43)$$

We are, therefore, led to the equation

$$Ha(\mathbf{r}) - \mathcal{E}(E)a(\mathbf{r}) - \mathcal{E}(\sigma)\sigma a(\mathbf{r}) = 0. \quad (44)$$

There are two irreducible representations of this group; the symmetric representation with matrices $\Gamma_1(E)=(1)$, $\Gamma_1(\sigma)=(1)$; and the antisymmetric representation with matrices $\Gamma_2(E)=(1)$, $\Gamma_2(\sigma)=(-1)$. We can, therefore, form two molecular orbitals from our function $a(\mathbf{r})$. The symmetric molecular orbital is $\sum(R)\Gamma_1(R)Ra(\mathbf{r})=a(\mathbf{r})+\sigma a(\mathbf{r})$ with energy $\sum(R)\Gamma_1(R)\mathcal{E}(R)=\mathcal{E}(E)+\mathcal{E}(\sigma)$. The antisymmetric representation produces the molecular orbital $\sum(R)\Gamma_2(R)Ra(\mathbf{r})=a(\mathbf{r})-\sigma a(\mathbf{r})$ with energy $\mathcal{E}(E)-\mathcal{E}(\sigma)$. $a(\mathbf{r})$ will be a function localized about one nucleus and $\sigma a(\mathbf{r})$ will be a function localized about the other nucleus. $\mathcal{E}(E)$ is the average energy of the two states. One lies an energy $\mathcal{E}(\sigma)$ above this average, and the other an energy $\mathcal{E}(\sigma)$ below this average. Our Lagrangian multipliers $\mathcal{E}(E)$ and $\mathcal{E}(\sigma)$ can be expressed

[7] H in this integral is a one-electron Hamiltonian.

in terms of integrals by use of Eqs. (43) and (44)

$$\int a(\mathbf{r})Ha(\mathbf{r})d\tau=\mathcal{E}(E);\quad \int a(\mathbf{r})H\sigma a(\mathbf{r})=\mathcal{E}(\sigma). \quad (45)$$

The next special case we will consider is that of a system with a symmetry C_{3v}. Imagine a molecule consisting of three identical nuclei at the corners of an equilateral triangle (see Fig. 1). The symmetry operations of this group are σ_1, σ_2, σ_3 (reflections through planes perpendicular to the plane of the molecule and to the sides of the triangle passing through the points 1, 2, and 3, respectively) E, the identity operation and C_3 and C_3^2 (rotations clockwise through 120° and 240°, respectively). There are three irreducible representations to this group, two of them are one-dimensional and one of them is two-dimensional. Their matrices are given in Table I.[8] For arbitrary constraints the wave function for the representation Γ_1 will be [Eq. (38)]:

$$\psi_1=f_{11}{}^1=a(\mathbf{r})+\sigma_1a(\mathbf{r})+\sigma_2a(\mathbf{r})+\sigma_3a(\mathbf{r})+C_3a(\mathbf{r})+C_3^2a(\mathbf{r}), \quad (45)$$

with energy

$$E_1=\mathcal{E}(E)+\mathcal{E}(\sigma_1)+\mathcal{E}(\sigma_2)+\mathcal{E}(\sigma_3)+\mathcal{E}(C_3)+\mathcal{E}(C_3^2). \quad (46)$$

Similarly, for the representation Γ_2,

$$\psi_2=f_{11}{}^2=a(\mathbf{r})-\sigma_1a(\mathbf{r})-\sigma_2a(\mathbf{r})-\sigma_3a(\mathbf{r})+C_3a(\mathbf{r})+C_3^2a(\mathbf{r}), \quad (47)$$
$$E_2=\mathcal{E}(E)-\mathcal{E}(\sigma_1)-\mathcal{E}(\sigma_2)-\mathcal{E}(\sigma_3)+\mathcal{E}(C_3)+\mathcal{E}(C_3^2).$$

For the degenerate representation Γ_3 the energies will be obtained by diagonalizing the matrix

$$\sum(R)\Gamma_3(R)\mathcal{E}(R)=(c_{ij}). \quad (48)$$

This matrix has elements

$$\begin{aligned}
c_{11}&=\mathcal{E}(E)-\mathcal{E}(\sigma_1)+\tfrac{1}{2}\mathcal{E}(\sigma_2)+\tfrac{1}{2}\mathcal{E}(\sigma_3)-\tfrac{1}{2}\mathcal{E}(C_3)-\tfrac{1}{2}\mathcal{E}(C_3^2),\\
c_{12}&=(\sqrt{\tfrac{3}{2}})[-\mathcal{E}(\sigma_2)+\mathcal{E}(\sigma_3)+\mathcal{E}(C_3)-\mathcal{E}(C_3^2)],\\
c_{21}&=(\sqrt{\tfrac{3}{2}})[-\mathcal{E}(\sigma_2)+\mathcal{E}(\sigma_3)-\mathcal{E}(C_3)+\mathcal{E}(C_3^2)],\\
c_{22}&=\mathcal{E}(E)+\mathcal{E}(\sigma_1)+\tfrac{1}{2}[-\mathcal{E}(\sigma_2)-\mathcal{E}(\sigma_3)-\mathcal{E}(C_3)-\mathcal{E}(C_3^2)].
\end{aligned} \quad (49)$$

If we denote by $O=(o_{ij})$ the matrix which diagonalizes (c_{ij}), then the eigenfunctions corresponding to the two eigenvalues of (48) will be [see Eq. (41)] $o_{11}f_{11}{}^3+o_{12}f_{12}{}^3$ and $o_{11}f_{21}{}^3+o_{12}f_{22}{}^3$ corresponding to the first eigenvalue, and $o_{21}f_{11}{}^3+o_{22}f_{12}{}^3$ and $o_{21}f_{21}{}^3+o_{22}f_{22}{}^3$ corresponding to the second eigenvalue. Here

$$\begin{aligned}
f_{11}{}^3&=a(\mathbf{r})-\sigma_1a(\mathbf{r})+\tfrac{1}{2}[\sigma_2a(\mathbf{r})+\sigma_3a(\mathbf{r})-C_3a(\mathbf{r})-C_3^2a(\mathbf{r}),\\
f_{12}{}^3&=(\sqrt{\tfrac{3}{2}})[-\sigma_2a(\mathbf{r})+\sigma_3a(\mathbf{r})+C_3a(\mathbf{r})-C_3^2a(\mathbf{r})],\\
f_{21}{}^3&=(\sqrt{\tfrac{3}{2}})[-\sigma_2a(\mathbf{r})+\sigma_3a(\mathbf{r})-C_3a(\mathbf{r})+C_3^2a(\mathbf{r})],\\
f_{22}{}^3&=a(\mathbf{r})+\sigma_1a(\mathbf{r})+\tfrac{1}{2}[-\sigma_2a(\mathbf{r})-\sigma_3a(\mathbf{r})-C_3a(\mathbf{r})-C_3^2a(\mathbf{r})].
\end{aligned} \quad (50)$$

[8] These matrices are given in *Quantum Chemistry*, p. 179 (reference 2).

Thus, we see that from the one function $a(\mathbf{r})$ which is a solution to our variation problem we are able to construct two nondegenerate states and two sets of doubly degenerate states. We cannot always construct so many states from one function $a(\mathbf{r})$. Suppose we had chosen our constraints $d(E)=d(\sigma_1)=1$; $d(\sigma_2)=d(\sigma_3)=d(C_3)=d(C_3^2)=0$. In other words, so that $a(\mathbf{r})$ has the property that $\sigma_1a(\mathbf{r})=a(\mathbf{r})$, i.e., $a(\mathbf{r})$ is a symmetric function, which is localized about the point 1, with respect to the reflection σ_1. Under these conditions

$$\mathcal{E}(E)=\mathcal{E}(\sigma_1)\quad\text{and}\quad \mathcal{E}(\sigma_2)=\mathcal{E}(\sigma_3)=\mathcal{E}(C_3)=\mathcal{E}(C_3^2),$$

the last equality resulting from the fact that $\sigma_2a(\mathbf{r})=C_3a(\mathbf{r})=\sigma_3a(\mathbf{r})=C_3^2a(\mathbf{r})$ which is a consequence of $\sigma_1a(\mathbf{r})=a(\mathbf{r})$. Under these conditions, using Eqs. (45), (46), and (47):

$$\begin{aligned}
&\psi_1=a(\mathbf{r})+C_3a(\mathbf{r})+C_3^2a(\mathbf{r}); && E_1=2\mathcal{E}(E)+\mathcal{E}(C_3);\\
&\psi_2=0; && E_2=0.
\end{aligned} \quad (51)$$

For the degenerate representation, we note that the matrix (c_{ij}) is already diagonal ($c_{11}=c_{12}=c_{21}=0$; $c_{22}=2\mathcal{E}(E)-2\mathcal{E}(C_3)$. Therefore, we only have one doubly degenerate state with energy $2\mathcal{E}(E)-2\mathcal{E}(C_3)$ and wave functions

$$\begin{aligned}
f_{21}{}^3&=\sqrt{3}[-C_3a(\mathbf{r})+C_3^2a(\mathbf{r})],\\
f_{22}{}^3&=2a(\mathbf{r})-C_3a(\mathbf{r})-C_3^2a(\mathbf{r}).
\end{aligned} \quad (52)$$

For the other doubly degenerate state, $f_{11}{}^3=f_{12}{}^3=0$. We could equally well have adjusted the constraints so that $\sigma_1a(\mathbf{r})=-a(\mathbf{r})$. That is, so that $a(\mathbf{r})$ is antisymmetric with respect to σ_1. In this case, one doubly degenerate level would appear and the nondegenerate wave function forming a basis for Γ_2 would appear.

V. CRYSTALLINE GROUPS

Crystalline groups contain translations as well as the rotations, reflections, and inversions which appear in the study of molecules. It is convenient to introduce the notation used by Seitz,[9] in his series of papers on space groups, for the combined translations and rotations that appear in these groups. Let us denote the operation which consists of a rotation[10] α followed by a translation through $\mathbf{t}$ by

$$\{\alpha|\mathbf{t}\}. \quad (53)$$

TABLE I. Irreducible representations of the group C_{3v}.

Γ \ R	E	σ_1	σ_2	σ_3	C_3	C_3^2
$\Gamma_1(R)$	1	1	1	1	1	1
$\Gamma_2(R)$	1	−1	−1	−1	1	1
$\Gamma_3(R)$	$\begin{matrix}1&0\\0&1\end{matrix}$	$\begin{matrix}-1&0\\0&1\end{matrix}$	$\begin{matrix}\frac{1}{2}&-\sqrt{\frac{3}{4}}\\-\sqrt{\frac{3}{4}}&-\frac{1}{2}\end{matrix}$	$\begin{matrix}\frac{1}{2}&\sqrt{\frac{3}{4}}\\\sqrt{\frac{3}{4}}&-\frac{1}{2}\end{matrix}$	$\begin{matrix}-\frac{1}{2}&\sqrt{\frac{3}{4}}\\-\sqrt{\frac{3}{4}}&-\frac{1}{2}\end{matrix}$	$\begin{matrix}-\frac{1}{2}&-\sqrt{\frac{3}{4}}\\\sqrt{\frac{3}{4}}&-\frac{1}{2}\end{matrix}$

[9] F. Seitz, Z. Krist. **88**, 433 (1934); **90**, 289 (1935); **91**, 336 (1935); **94**, 100 (1936).

[10] Here the word rotation includes inversions and reflections.

By this we mean, the transformation from one rectangular coordinate system x_1, x_2, x_3 to another x_1', x_2', x_3' given by the equations

$$\begin{aligned} x_1' &= \alpha_{11}x_1+\alpha_{12}x_2+\alpha_{13}x_3+l_1, \\ x_2' &= \alpha_{21}x_1+\alpha_{22}x_2+\alpha_{23}x_3+l_2, \\ x_3' &= \alpha_{31}x_1+\alpha_{32}x_2+\alpha_{33}x_3+l_3. \end{aligned} \tag{54}$$

Here the matrix (α_{ij}) represents the rotational part of the operator (53) and l_1, l_2, l_3 are the components of the translation in the operator. $\{\epsilon|0\}$ denotes the identity operator, $\{\alpha|0\}$ a rotation about the origin, and $\{0|\mathbf{t}\}$ a pure translation. The symbols (53) have the property [using Eq. (54)]

$$\{\alpha|\mathbf{t}\}\{\beta|\mathbf{t}'\}=\{\alpha\beta|\alpha\mathbf{t}'+\mathbf{t}\}. \tag{55}$$

$\alpha\mathbf{t}'$ is the vector arising from operating on $\mathbf{t}'$ with the matrix α. From Eq. (55) we see that the inverse of $\{\alpha|\mathbf{t}\}$ is $\{\alpha^{-1}|-\alpha^{-1}\mathbf{t}\}$. We know from the results of Seitz that any operator R of the space group can be written in the form $\{\epsilon|\mathbf{R}_n\}\{\alpha|\mathbf{t}_\alpha\}$. In the case of no glide planes or screw axis, all the $\mathbf{t}_\alpha$ are zero and the set of operators $\{\alpha|\mathbf{t}_\alpha\}$ form a group called the point group of the crystal.

We set up our variation procedure as follows: We seek a function $a(\mathbf{r})$ for which

$$\int a(\mathbf{r})Ha(\mathbf{r})d\tau=\min, \tag{56}$$

subject to the constraints

$$\int a(\mathbf{r})\{\epsilon|\mathbf{R}_n\}a(\mathbf{r})d\tau=\delta_{\mathbf{R}_n,0}. \tag{57}$$

If we call $\mathcal{E}(\mathbf{R}_n)$ the Lagrangian multipliers corresponding to the constraints (57), Eq. (38) becomes in this case

$$\begin{aligned} H\sum(R)\Gamma(R)_{mp}a(r)=&\sum(\mathbf{R}_n)\mathcal{E}(\mathbf{R}_n) \\ &\times\sum(j)\Gamma(\{\epsilon|\mathbf{R}_n\})_{pj}\sum(R)\Gamma(R)_{mj}Ra(r). \end{aligned} \tag{58}$$

Here $\sum(R)$ denotes summation over all operations in the space group, $\sum(\mathbf{R}_n)$ denotes summation over just the pure translations in the space group, and $\sum(j)$ denotes summation over a row of the irreducible representation. The results of Seitz[11] on the reduction of space groups tells us how to find the matrices $\Gamma(R)_{mp}$ for a space group. In particular the matrices $\Gamma(\{\epsilon|\mathbf{R}_n\})$ are diagonal matrices. Equation (58) reduces to

$$\begin{aligned} &H\sum(R)\Gamma(R)_{mp}Ra(r) \\ &=[\sum(\mathbf{R}_n)\mathcal{E}(\mathbf{R}_n)\Gamma(\{\epsilon|\mathbf{R}_n\})_{pp}]\sum(R)\Gamma(R)_{mp}Ra(r). \end{aligned} \tag{59}$$

Therefore, $\sum(R)\Gamma(R)_{mp}Ra(r)$ for all m are eigenfunctions with eigenvalue $\sum(\mathbf{R}_n)\mathcal{E}(\mathbf{R}_n)\Gamma(\{\epsilon|\mathbf{R}_n\})_{pp}$. Since $\Gamma(\{\epsilon|\mathbf{R}_n\})_{pp}$ has the form $e^{i\mathbf{k}_p\cdot\mathbf{R}_n}$, the energy has the form $\sum(\mathbf{R}_n)\mathcal{E}(\mathbf{R}_n)e^{i\mathbf{k}_p\cdot\mathbf{R}_n}$. The eigenvectors can also be simplified.

$$\begin{aligned} &\sum(R)\Gamma(R)_{mp}Ra(\mathbf{r})=\sum(\mathbf{R}_n)\sum(\alpha) \\ &\quad\times[\Gamma(\{\epsilon|\mathbf{R}_n\})\Gamma(\{\alpha|\mathbf{t}_\alpha\})]_{mp}\{\epsilon|\mathbf{R}_n\}\{\alpha|\mathbf{t}_\alpha\}a(\mathbf{r}). \end{aligned} \tag{60}$$

Using the diagonal property of $\Gamma(\{\epsilon|\mathbf{R}_n\})$, we see that

$$[\Gamma(\{\epsilon|\mathbf{R}_n\})\Gamma(\{\alpha|\mathbf{t}_\alpha\})]_{mp}=e^{i\mathbf{k}_m\cdot\mathbf{R}_n}\Gamma(\{\alpha|\mathbf{t}_\alpha\})_{mp}.$$

The wave functions corresponding to the eigenvalue $\sum(\mathbf{R}_n)e^{i\mathbf{k}_p\cdot\mathbf{R}_n}\mathcal{E}(\mathbf{R}_n)$ are

$$\sum(\mathbf{R}_n)e^{i\mathbf{k}_m\cdot\mathbf{R}_n}\{\epsilon|\mathbf{R}_n\}\sum(\alpha)\Gamma(\{\alpha|\mathbf{t}_\alpha\})_{mp}\{\alpha|\mathbf{t}_\alpha\}a(\mathbf{r}),$$

$$m=1\cdots g_l, \tag{61}$$

where g_l is the order of the irreducible representation. Associated with the lattice point at the origin is the function $\sum(\alpha)\Gamma(\{\alpha|\mathbf{t}_\alpha\})_{mp}\{\alpha|\mathbf{t}_\alpha\}a(\mathbf{r})$. This function when translated through $\mathbf{R}_n$, multiplied by $e^{i\mathbf{k}_m\cdot\mathbf{R}_n}$ and summed over $\mathbf{R}_n$ gives the m^{th} wave function associated with the energy

$$\sum(\mathbf{R}_n)e^{i\mathbf{k}_p\cdot\mathbf{R}_n}\mathcal{E}(\mathbf{R}_n).$$

Before we go on to consider a special case of the application of the variation procedure to a crystal lattice, it will be necessary to review the results of Seitz[11,12] on the reduction of space groups. We observe, first of all, the effect of a general operator $R=\{\alpha|\mathbf{t}_\alpha+\mathbf{R}_n\}$ on a wave function whose $\mathbf{k}$ value is $\mathbf{k}_1$

$$\psi(\mathbf{k}_1,\mathbf{r})=\sum(\mathbf{R}_n)e^{i\mathbf{k}_1\cdot\mathbf{R}_n}\{\epsilon|\mathbf{R}_n\}a(\mathbf{r}).$$

Applying R to this wave function yields

$$\begin{aligned} R\psi&=\{\epsilon|\mathbf{R}_m\}\{\alpha|\mathbf{t}_\alpha\}\psi \\ &=\{\epsilon|\mathbf{R}_m\}\sum(\mathbf{R}_n)e^{i\mathbf{k}_1\cdot\mathbf{R}_n}\{\alpha|\mathbf{t}_\alpha\}\{\epsilon|\mathbf{R}_n\}a(\mathbf{r}) \\ &=\{\epsilon|\mathbf{R}_m\}\sum(\mathbf{R}_n)e^{i\mathbf{k}_1\cdot\mathbf{R}_n}\{\epsilon|\alpha\mathbf{R}_n\}\{\alpha|\mathbf{t}_\alpha\}a(\mathbf{r}). \end{aligned} \tag{62}$$

Since $\alpha\mathbf{R}_n$ is also an allowed translation, we can change the index of summation in (62) to $\alpha\mathbf{R}_n=\mathbf{R}_n'$:

$$\begin{aligned} R\psi&=\{\epsilon|\mathbf{R}_m\}\sum(\mathbf{R}_n') \\ &\qquad\times\exp(i\mathbf{k}_1\cdot\alpha^{-1}\mathbf{R}_n')\{\epsilon|\mathbf{R}_n'\}[\{\alpha|\mathbf{t}_\alpha\}a(\mathbf{r})] \\ &=\{\epsilon|\mathbf{R}_m\}\sum(\mathbf{R}_n') \\ &\qquad\times\exp(i\alpha\mathbf{k}_1\cdot\mathbf{R}_n')\{\epsilon|\mathbf{R}_n'\}[\{\alpha|\mathbf{t}_\alpha\}a(\mathbf{r})] \\ &=\exp(i\alpha\mathbf{k}_1\cdot\mathbf{R}_m)\sum(\mathbf{R}_n') \\ &\qquad\times\exp(i\alpha\mathbf{k}_1\cdot\mathbf{R}_n')\{\epsilon|\mathbf{R}_n'\}[\{\alpha|\mathbf{t}_\alpha\}a(\mathbf{r})]. \end{aligned} \tag{63}$$

We see that the effect of any space group operation whose rotational part is α is to transform $\psi(\mathbf{k}_1,\mathbf{r})$ to a wave function with wave vector $\alpha\mathbf{k}_1$. If $\alpha\mathbf{k}_1-\mathbf{k}_1\neq\mathbf{K}_j$, we see that we have generated a function which is orthogonal to $\psi(\mathbf{k}_1,\mathbf{r})$ and which has the same energy as $\psi(\mathbf{k}_1,\mathbf{r})$. (The same energy because the effect of any operator, which commutes with the Hamiltonian on a

[11] F. Seitz, Ann. Math. **37**, 17 (1936).

[12] Bouckaert, Smoluchowski, and Wigner, Phys. Rev. **50**, 58 (1936).

wave function, is to produce another function with the same energy.) The results of Seitz state that if for a wave function with wave vector $\mathbf{k}_1$, $\alpha\mathbf{k}_1-\mathbf{k}_1\neq\mathbf{K}_j$ for all α in the space group and any $\mathbf{K}_j$ then the functions

$$\psi_0(\mathbf{k}_1,r);\ \psi_1=\{\alpha_1|\mathbf{t}_{\alpha_1}\}\psi_0;\ \cdots\ \psi_n=\{\alpha_n|\mathbf{t}_{\alpha_n}\}\psi_0, \quad (64)$$

form a basis for an irreducible representation of the space group. If certain operators leave the wave vector unchanged, then we shall manufacture by this process different wave functions with the same value of $\mathbf{k}$ as $\mathbf{k}_1$. Seitz's results go on to state that the wave functions with a given value of $\mathbf{k}$ must form the basis for an irreducible representation of that subgroup to the total space group which leaves that value of $\mathbf{k}$ unchanged.

The other point that might also be mentioned here concerns the symmetry properties of a given band in reciprocal space. As can be seen from the previous paragraph, if there is an energy associated with some value of $\mathbf{k}$ in reciprocal space there must be an equal energy associated with all points generated from $\mathbf{k}$ by the operators α. Thus it is that the collection of all energies from all bands plotted in reciprocal space has all the symmetry properties of the reciprocal lattice. This would allow us to define bands which have all the symmetry properties of reciprocal space. Here, however, we shall define a band as that collection of energies arising from $E(\mathbf{k})=\sum(\mathbf{R}_n)\mathcal{S}(\mathbf{R}_n)e^{i\mathbf{k}\cdot\mathbf{R}_n}\mathcal{S}(\mathbf{R}_n)$ where $\mathcal{S}(\mathbf{R}_n)$ is given by our variational procedure. Let us see under what conditions a band defined in this manner has all the symmetry of $\mathbf{k}$ space. We notice from Eq. (63) if $\{\alpha|\mathbf{t}_\alpha\}a(\mathbf{r})=ca(\mathbf{r})$ for all α where $|c|=1$ then $E(\mathbf{k})=E(\alpha\mathbf{k})$ for all α. In the case of no glide planes or screw axis ($\mathbf{t}_\alpha=0$), $a(\mathbf{r})$ forms a basis of one dimension for an irreducible representation of the point group. If we desire to find a Wannier function which describes a band which is completely symmetric in $\mathbf{k}$ space, this Wannier function must have the property that any operation of the point group has the effect of multiplying it by a constant whose absolute value is one.

There is no reason to believe that our variation procedure will not admit solutions which have other symmetry properties than this simple one. In this case $\{\alpha|\mathbf{t}_\alpha\}a(\mathbf{r})$, is also a distinct solution to our variation problem. If we multiply Eq. (16) by $\{\alpha|\mathbf{t}_\alpha\}$, we get

$$\begin{aligned}H[\{\alpha|\mathbf{t}_\alpha\}a(\mathbf{r})]&=\sum(\mathbf{R}_n)\mathcal{S}(\mathbf{R}_n)\{\epsilon|\alpha\mathbf{R}_n\}\{\alpha|\mathbf{t}_\alpha\}a(\mathbf{r})\\&=\sum(\mathbf{R}_n)\mathcal{S}(\alpha^{-1}\mathbf{R}_n)\{\epsilon|\mathbf{R}_n\}\{\alpha|\mathbf{t}_\alpha\}a(\mathbf{r}).\end{aligned}\quad(65)$$

The constraints are also satisfied since

$$\begin{aligned}\int\{\alpha|\mathbf{t}_\alpha\}a(\mathbf{r})\{\epsilon|\mathbf{R}_n\}\{\alpha|\mathbf{t}_\alpha\}a(\mathbf{r})d\tau&=\int a(\mathbf{r})\{\alpha^{-1}|-\alpha^{-1}\mathbf{t}_\alpha\}\{\epsilon|\mathbf{R}_n\}\{\alpha|\mathbf{t}_\alpha\}a(\mathbf{r})d\tau\\&=\int a(\mathbf{r})\{\epsilon|\alpha^{-1}\mathbf{R}_n\}a(\mathbf{r})d\tau=\delta_{\mathbf{R}_n,0}.\end{aligned}\quad(66)$$

But if we have assumed $\{\alpha|\mathbf{t}_\alpha\}a(\mathbf{r})$ is not just a multiple of $a(\mathbf{r})$, then from (65) the energies associated with this Wannier function are $\sum(\mathbf{R}_n)\mathcal{S}(\alpha^{-1}\mathbf{R}_n)e^{i\mathbf{k}\cdot\mathbf{R}_n}$, where

$$\begin{aligned}\mathcal{S}(\alpha^{-1}\mathbf{R}_n)&=\int a(\mathbf{r})\{\epsilon|\alpha^{-1}\mathbf{R}_n\}Ha(\mathbf{r})d\tau\\&=\int\{\alpha|\mathbf{t}_\alpha\}a(\mathbf{r})\{\epsilon|\mathbf{R}_n\}H\{\alpha|\mathbf{t}_\alpha\}a(\mathbf{r})d\tau\\&\neq\int a(\mathbf{r})\{\epsilon|\mathbf{R}_n\}a(\mathbf{r})d\tau.\end{aligned}$$

Thus, the band of energies this Wannier function generates are distinct, at any point in reciprocal space, from those of $a(r)$ and, therefore,

$$\int a(\mathbf{r})\{\alpha|\mathbf{t}_\alpha\}a(\mathbf{r})d\tau=0, \quad (67)$$

by Eq. (9). We can, however, easily get the energy band associated with $\{\alpha|\mathbf{t}_\alpha\}a(\mathbf{r})$ from that of $a(\mathbf{r})$ by performing the operation α on $E(\mathbf{k})$, since

$$\begin{aligned}&\sum(\mathbf{R}_n)\mathcal{S}(\alpha^{-1}\mathbf{R}_n)\exp(i\mathbf{k}\cdot\mathbf{R}_n)\\&\quad=\sum(\mathbf{R}_n')\mathcal{S}(\mathbf{R}_n')\exp(i\mathbf{k}\cdot\alpha\mathbf{R}_n')\\&\quad=\sum(\mathbf{R}_n')\mathcal{S}(\mathbf{R}_n')\exp(i\alpha^{-1}\mathbf{k}\cdot\mathbf{R}_n')\\&\quad=\alpha E(\mathbf{k}).\end{aligned}\quad(68)$$

Thus we see that the symmetry properties of the band defined in terms of a Wannier function may be summed up by saying that if for any operation of the point group $\{\alpha|0\}a(\mathbf{r})=ca(\mathbf{r})$; $|c|=1$ then $\alpha E(\mathbf{k})=E(\mathbf{k})$. We shall now illustrate these general remarks with a special case.

Consider a two-dimensional cubic lattice [see Fig. 2(a)]. This space group has no glide planes or screw axes. The point group is the group C_{4v}. In Fig. 2(b) we have drawn reciprocal space. The dotted lines represent the edges of the first Brillouin zone. The operations of the point group are shown as well as points of special interest in reciprocal space. σ_{v1} and σ_{v2} are reflections through the X and Y axes, respectively. σ_{d1} and σ_{d2} are reflections through the 45-degree lines. The other operations of the point group are E, C_4, C_2, C_4^3, the identity and clockwise rotations through 90°, 180°, and 270°, respectively. Let us consider a wave function whose $\mathbf{k}$ vector reaches from the origin to the point a in Fig. 2(b). Let us find $\alpha\mathbf{k}_1$ for all α in the point group. Figure 3 shows the $\mathbf{k}$ values generated by this process. We notice that no two operators generate the same value of $\mathbf{k}$. Therefore, the functions

$$\psi_1;\quad \psi_2=\{\sigma_{d1}|0\}\psi_1;\quad\cdots;\quad\psi_8=\{C_4^3|0\}\psi_1$$

form a basis for an irreducible representation of the space group. Clearly the translations have for matrices

$$\Gamma(\{\epsilon|\mathbf{R}_n\})_{ij}=\delta_{ij}e^{i\mathbf{k}_i\cdot\mathbf{R}_n};\quad i,j=1\cdots8. \quad (69)$$

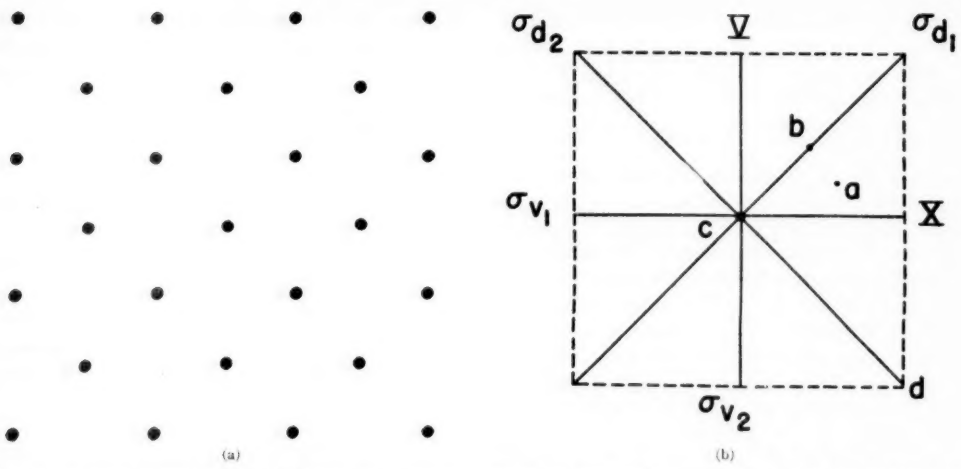

FIG. 2. (a) A two-dimensional lattice with square symmetry; (b) The first Brillouin zone for the two-dimensional square lattice, showing the operations of the point group and points of special interest in reciprocal space.

The matrix representing C_2 is an eight-by-eight matrix.

$$\Gamma(\{C_2|0\})=\begin{bmatrix}0&0&0&0&1&0&0&0\\0&0&0&0&0&1&0&0\\0&0&0&0&0&0&1&0\\0&0&0&0&0&0&0&1\\1&0&0&0&0&0&0&0\\0&1&0&0&0&0&0&0\\0&0&1&0&0&0&0&0\\0&0&0&1&0&0&0&0\end{bmatrix}. \tag{70}$$

This is merely a permutation matrix which is obtained by rotating Fig. 3 through 180° and writing in matrix form the permutation this induces on the numbers one through eight. We can similarly find matrices for all the operators of the point group. Using the matrices found in this way, let us construct our Bloch functions from Wannier functions by the use of Eq. (61). Let us assume that we have found a solution to our variation principle, $a_x(\mathbf{r})$, which has the same symmetry properties as a p_x-like atomic orbital under the point group, i.e., a function whose symmetry properties are like $xf(|\mathbf{r}|)$. Thus

$$\begin{aligned}&\sigma_{v1}a_x(\mathbf{r})=a_x(\mathbf{r}), &&\sigma_{v2}a_x(\mathbf{r})=-a_x(\mathbf{r}),\\&\sigma_{d1}a_x(\mathbf{r})=a_y(\mathbf{r}), &&\sigma_{d2}a_x(\mathbf{r})=-a_y(\mathbf{r}),\\&C_4a_x(\mathbf{r})=-a_y(\mathbf{r}), &&C_2a_x(\mathbf{r})=-a_x(\mathbf{r}).\\&C_4^3a_x(\mathbf{r})=-a_y(\mathbf{r}),\end{aligned} \tag{71}$$

Let us use the notation

$$\begin{aligned}E_x^{(j)}&=\sum(\mathbf{R}_n)e^{i\mathbf{k}_j\cdot\mathbf{R}_n}\mathcal{S}_x(\mathbf{R}_n),\\\mathcal{S}_x(\mathbf{R}_n)&=\int a_x(\mathbf{r})Ha_x(r-\mathbf{R}_n)d\tau.\end{aligned} \tag{72}$$

We see at once, from our discussion of the symmetry properties of energy bands, that

$$\begin{aligned}E_x^{(1)}=E_x^{(3)}=E_x^{(4)}=E_x^{(5)},\\E_x^{(2)}=E_x^{(3)}=E_x^{(6)}=E_x^{(7)}.\end{aligned} \tag{73}$$

Using Eqs. (61), (69), (70), and (71), we are able to construct Table II. The entries in the table denote the quantity $\sum(\alpha)\Gamma(\{\alpha|\mathbf{t}_\alpha\})_{mp}\{\alpha|\mathbf{t}_\alpha\}a(\mathbf{r})$, i.e., the function associated with each lattice point which when added up give the Bloch function [Eq. (61)]. The columns give all the Bloch functions which have the same energy, and the rows give all the Bloch functions with the same $\mathbf{k}$ value. Thus, if we wished to construct from this table a band which was completely symmetric and which had the energies of $a_x(\mathbf{r})$ in region I of Fig. 4, we would need to take $a_x(\mathbf{r})$ in regions I and VIII, $a_y(\mathbf{r})$ in regions II and III, $-a_x(\mathbf{r})$ in regions IV and V, and $-a_y(\mathbf{r})$ in regions VI and VII. If we wished to describe a band

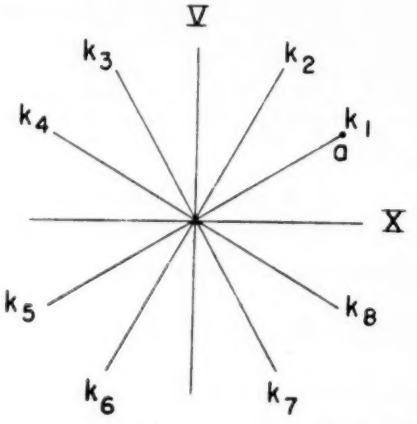

FIG. 3. $\mathbf{k}_1$ and all of the $\mathbf{k}$ vectors generated from it by the elements of the point group for the two-dimensional square lattice.

which was completely symmetric and had the energies of $a_y(\mathbf{r})$ in region I, we would need to take $a_y(\mathbf{r})$ in region I, $a_x(\mathbf{r})$ in region II, $-a_x(\mathbf{r})$ in region III, $a_y(\mathbf{r})$ in region IV, $-a_y(\mathbf{r})$ in region V, $-a_x(\mathbf{r})$ in region VI, $a_x(\mathbf{r})$ in region VII, and $-a_y(\mathbf{r})$ in region VIII.

We notice at once the similarity of these results to those of Slater[13] for the perturbed two-dimensional Mathieu problem. In his case he started out with Wannier functions, which were an exact solution to the two-dimensional Mathieu problem and had p_x-like and p_y-like symmetry. In order to construct bands that had the symmetry properties of reciprocal space, he was forced to make bands whose Wannier functions were p_x-like over part of momentum space and p_y-like over the rest of momentum space. A single Wannier function can describe the symmetric band in our case, just as a single Wannier function could describe the symmetric band in Slater's case. Thus, using column 1 of Table II, we see that our symmetric band, whose energies are those of $a_x(\mathbf{r})$ in region I, could be described in terms of the wave function

$$\psi(\mathbf{k},\mathbf{r})=\sum(\mathbf{R}_n)e^{i\mathbf{k}\cdot\mathbf{R}_n}[a(\mathbf{k})a_x(\mathbf{r}-\mathbf{R}_n)+b(\mathbf{k})a_y(\mathbf{r}-\mathbf{R}_n)], \quad (73)$$

where $a(\mathbf{k})$ is a function which is $+1$ in regions I and VIII, 0 in regions II, III, VI, and VII, and -1 in regions IV and V, and $b(\mathbf{k})$ is the same function rotated through 90°. Expanding $a(\mathbf{k})$ and $b(\mathbf{k})$ in Fourier series,

$$\begin{aligned} a(\mathbf{k})&=\sum(\mathbf{R}_n)e^{-i\mathbf{k}\cdot\mathbf{R}_n}c(\mathbf{R}_n),\\ b(\mathbf{k})&=\sum(\mathbf{R}_n)e^{-i\mathbf{k}\cdot\mathbf{R}_n}d(\mathbf{R}_n), \end{aligned} \quad (74)$$

we find that we can write $\psi(\mathbf{k},\mathbf{r})$ as

$$\begin{aligned}\psi(\mathbf{k},\mathbf{r})&=\sum(n,m)e^{i\mathbf{k}\cdot(\mathbf{R}_n-\mathbf{R}_m)}[c(\mathbf{R}_m)a_x(\mathbf{r}-\mathbf{R}_n)+d(\mathbf{R}_m)a_y(\mathbf{r}-\mathbf{R}_n)]\\ &=\sum(q)e^{i\mathbf{k}\cdot\mathbf{R}_q}\sum(m)[c(\mathbf{R}_m)a_x(\mathbf{r}-\mathbf{R}_m-\mathbf{R}_q)+d(\mathbf{R}_m)a_y(\mathbf{r}-\mathbf{R}_m-\mathbf{R}_q). \end{aligned} \quad (75)$$

The Wannier function describing the symmetric band (upper band in Slater's case) is thus

$$a'(\mathbf{r}-\mathbf{R}_q)=\sum(m)[c(\mathbf{R}_m)a_x(\mathbf{r}-\mathbf{R}_m-\mathbf{R}_q)+d(\mathbf{R}_m)a_y(\mathbf{r}-\mathbf{R}_m-\mathbf{R}_q)]. \quad (76)$$

The $c(\mathbf{R}_m)$ and $d(\mathbf{R}_m)$ we have here are exactly analogous to the c_{nm} which appear in Eqs. (52) and (53) of Slater's paper. The Wannier function forming the symmetric band whose energies are those of $a_y(\mathbf{r})$ in region I (Slater's lower band) can be described in a similar manner.

TABLE II. Wannier functions associated with the points of reciprocal space indicated in Fig. 3.

k \ $E_x^{(i)}$	$E_x^{(1)}$	$E_x^{(2)}$	$E_x^{(3)}$	$E_x^{(4)}$	$E_x^{(5)}$	$E_x^{(6)}$	$E_x^{(7)}$	$E_x^{(8)}$
$\mathbf{k}_1$	a_x	a_y	$-a_y$	$-a_x$	$-a_x$	$-a_y$	a_y	a_x
$\mathbf{k}_2$	a_y	a_x	$-a_x$	$-a_y$	$-a_y$	$-a_x$	a_x	a_y
$\mathbf{k}_3$	a_y	$-a_x$	a_x	$-a_y$	$-a_y$	a_x	$-a_x$	a_y
$\mathbf{k}_4$	$-a_x$	a_y	$-a_y$	a_x	a_x	$-a_y$	a_y	$-a_x$
$\mathbf{k}_5$	$-a_x$	$-a_y$	a_y	a_x	a_x	a_y	$-a_y$	$-a_x$
$\mathbf{k}_6$	$-a_y$	$-a_x$	a_x	a_y	a_y	a_x	$-a_x$	$-a_y$
$\mathbf{k}_7$	$-a_y$	a_x	$-a_x$	a_y	a_y	$-a_x$	a_x	$-a_y$
$\mathbf{k}_8$	a_x	$-a_y$	a_y	$-a_x$	$-a_x$	a_y	$-a_y$	a_x

[13] J. C. Slater, Phys. Rev. **87**, 807 (1952).

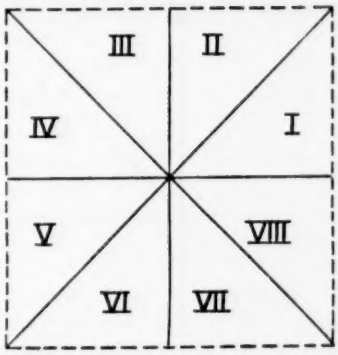

FIG. 4. Reciprocal space with various regions numbered.

We can gain some insight into what energies will be associated with the $a_x(\mathbf{r})$ Wannier function in our case by using the results of Slater's paper. In that paper we see that after perturbations of a general cubic nature are applied to the unperturbed two-dimensional Mathieu problem there are two symmetric bands, an upper one and a lower one, which touch only at the center and corners of the unit cell. In regions I and VIII, our p_x-like Wannier function has energies that are those of the upper band. In regions II and III they become those of the lower band with a discontinuous change along the 45° diagonal. In regions IV and V they are those of the upper band and in region VI and VII they are those of the lower band. Thus we see that our Wannier function $a_x(\mathbf{r})$ does indeed generate an energy surface which does not have all the symmetry of reciprocal space. We can also see that we may expect a general $a_x(\mathbf{r})$ to produce energy surfaces with discontinuities along the 45° diagonals.

Since the 45° diagonals in momentum space seem to be lines of special interest, as a final example of the application of our variation procedure let us find the Bloch functions constructed from $a_x(\mathbf{r})$ for a wave function with $\mathbf{k}$ vector at the point b of Fig. 2(b). In Fig. 5 we show all the wave vectors which arise from $\mathbf{k}_1$ by the operations of the point group. We notice that the operations E and σd_1, leave the vector $\mathbf{k}_1$ invariant. The wave functions with wave vector $\mathbf{k}_1$, must form a basis for an irreducible representation of the group consisting of E and σd_1. This group has a symmetric b_1 and an antisymmetric representation b_2. If we seek a representation of the space group whose wave function with $\mathbf{k}$

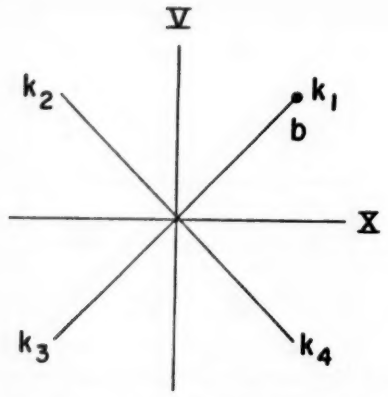

FIG. 5. $\mathbf{k}_1$ and all of the $\mathbf{k}$ vectors generated from it for the point b in reciprocal space.

value $\mathbf{k}_1$ forms a basis b_1, the matrices of the operations of the space group are

$$\Gamma(\{\epsilon|\mathbf{R}_n\})=\delta_{ij}e^{i\mathbf{k}_i\cdot\mathbf{R}_n},$$

$$\{C_2|0\}=\begin{bmatrix}0&0&1&0\\0&0&0&1\\1&0&0&0\\0&1&0&0\end{bmatrix},\quad \{C_4|0\}=\begin{bmatrix}0&1&0&0\\0&0&1&0\\0&0&0&1\\1&0&0&0\end{bmatrix},\text{ etc.}\quad(77)$$

If we carry out the procedure of Eq. (61) we can, in analogy to Table II, construct Table III. Notice all the wave functions corresponding to a given $\mathbf{k}$ value are the same, since $E_x^{(1)}=E_x^{(2)}=E_x^{(3)}=E_x^{(4)}$. If we carry out the procedure for the Bloch functions which are to form a basis for b_2, we must multiply the matrices of all the reflections of (77) by -1 and once again carry out the procedure of Eq. (61). This yields Table IV. Therefore, we see that at the boundary of regions I and II in momentum space the wave functions become the sum and difference of Bloch functions constructed from x and y like Wannier functions, which reflect the anomalous behavior of the energy at these points. Similar calculations to the above can easily be carried out for the other special points. The points c and d are of some interest because if we carry out our procedure for them we find that we can construct two wave functions with the same wave vector and energy, hence these are points at which bands "stick together."

From the discussion of the two-dimensional square net we see we can get a band of energies associated with a Wannier function $a_x(\mathbf{r})$ and another band associated with the Wannier function $a_y(\mathbf{r})$ whose energies are the same as for the band rotated through 90°. These two bands can be cut along the 45° diagonals and combined to form two symmetric bands with Wannier functions like (76) associated with them. Thus, there are two alternative ways of describing these two bands. If we describe them in terms of x-like and y-like Wannier functions as the atoms get further apart, these functions have symmetry properties which allow them to become solutions of Schrödinger's equation for one isolated atom. If we describe them in terms of functions like (76), since the value of $c(\mathbf{R}_n)$ or $d(\mathbf{R}_n)$ at any lattice point is independent of the nuclear separation, being given by symmetry properties, the Wannier functions will not reduce to a wave function about a single atom. This method of description, however, has the advantage of giving symmetric bands without any discontinuities along the 45° diagonals. For large internuclear distances, Wannier functions with x-like symmetry are clearly advantageous since they reduce to atomic wave functions. It may be, however, that at smaller internuclear distances the Wannier functions (76) will be an equally convenient way to describe energy bands since the atomic correspondence may be completely lost anyway. These alternative ways of describing energy bands will exist for all lattices in three dimensions as well, since none of the remarks we have made here made special use of a two-dimensional lattice.

VI. A NUMERICAL METHOD

The variation procedure outlined in this paper can, of course, be carried out numerically. We shall do it here for the calculation of Wannier functions in crystals.

Suppose we were to approximate our Wannier function for the crystal by a linear combination of functions which form a complete orthogonal set (for instance atomic orbitals),

$$a(\mathbf{r})=\sum(n)c_nu_n(\mathbf{r}).\quad(78)$$

Under these conditions

$$\int a(\mathbf{r})Ha(\mathbf{r})d\tau=\sum(n,m)c_nc_mH_{nm},$$
$$H_{nm}=\int u_n(\mathbf{r})Hu_m(\mathbf{r})d\tau,\quad(79)$$

and our constraints can be written

$$\int a(\mathbf{r})a(\mathbf{r}-\mathbf{R}_p)=\sum c_nc_mO_{nm}{}^p=\delta_{\mathbf{R}_p,0};$$
$$O_{nm}{}^p=\int u_n(\mathbf{r})u_m(\mathbf{r}-\mathbf{R}_p)d\tau.\quad(80)$$

Using the method of Lagrangian multipliers and varying

TABLE III. Wannier functions associated with the points of reciprocal space indicated in Fig. 5 (for a symmetric representation).

$\mathbf{k}$ \ $E_x^{(i)}$	$E_x^{(1)}$	$E_x^{(2)}$	$E_x^{(3)}$	$E_x^{(4)}$
$\mathbf{k}_1$	a_x+a_y	$-a_x-a_y$	$-a_x-a_y$	a_x+a_y
$\mathbf{k}_2$	$-a_x+a_y$	a_x-a_y	a_x-a_y	$-a_x+a_y$
$\mathbf{k}_3$	$-a_x-a_y$	a_x+a_y	a_x+a_y	$-a_x-a_y$
$\mathbf{k}_4$	a_x-a_y	$-a_x+a_y$	$-a_x+a_y$	a_x-a_y

the c's to make $\int a(\mathbf{r})Ha(\mathbf{r})d\tau$ a minimum, and using the orthogonality of the u's, we get the simultaneous equations

$$\sum(m)c_m[H_{mn}-\mathcal{E}(0)\delta_{mn}-\sum_{p>0}(p)O_{mn}{}^p\mathcal{E}(\mathbf{R}_p)]=0,$$
$$n=1,\cdots. \quad (81)$$

In order to find the solutions of these equations, we must set the determinant of the coefficients equal to zero.

$$|H_{mn}-\delta_{mn}\mathcal{E}(0)-\sum_{p>0}(p)\mathcal{E}(\mathbf{R}_p)O_{mn}{}^p|=0. \quad (82)$$

This equation merely determines a relation between the unknown quantities $\mathcal{E}(\mathbf{R}_n)$. Equation (82), coupled with the simultaneous Eqs. (81) and the constraints, however, is sufficient to determine the $\mathcal{E}(\mathbf{R}_n)$ and the c's. We can notice, however, that if we make our initial functions orthogonal, in the sense

$$O_{mn}{}^p=\delta_{mn}\delta_{po}, \quad (83)$$

our secular equation would reduce to

$$|H_{mn}-\delta_{mn}\mathcal{E}(0)|=0. \quad (84)$$

The orthogonality (83) means that we must combine the function $u_n(\mathbf{r})$ at the origin with other atomic functions about the other lattice points to produce a function $u_n'(\mathbf{r})$ with the necessary orthogonality. This could for example be carried out by the method of Löwdin.[14] The secular Eq. (84) could be solved directly for the average energy of the band. We could then proceed to compute the shape of the band by calculating the Fourier coefficients of the energy

$$\mathcal{E}(\mathbf{R}_n)=\int a(\mathbf{r}-\mathbf{R}_n)Ha(\mathbf{r})d\tau; \quad a(\mathbf{r})=\sum c_n u_n'(\mathbf{r}). \quad (85)$$

Löwdin carries out a discussion of the case where only one atomic orbital is used in this process.

[14] P. O. Löwdin, Phys. Rev. **18**, 365 (1950).

TABLE IV. Wannier functions associated with the points of reciprocal space indicated in Fig. 5 (for an antisymmetric representation).

$\mathbf{k}$ \ $E_x^{(i)}$	$E_x^{(1)}$	$E_x^{(3)}$	$E_x^{(2)}$	$E_x^{(4)}$
$\mathbf{k}_1$	a_x-a_y	a_x-a_y	$-a_x+a_y$	$-a_x+a_y$
$\mathbf{k}_2$	a_x+a_y	a_x+a_y	$-a_x-a_y$	$-a_x-a_y$
$\mathbf{k}_3$	$-a_x+a_y$	$-a_x+a_y$	a_x-a_y	a_x-a_y
$\mathbf{k}_4$	$-a_x-a_y$	$-a_x-a_y$	a_x+a_y	a_x+a_y

VII. CONCLUSION

In this paper we have been able to define the Wannier function in a crystal in terms of a differential equation and a variation procedure. These two methods of defining the Wannier function are methods that make no recourse to defining the Wannier function in terms of Bloch functions. We are thus able to find the Wannier function for a crystal without ever solving Schrödinger's equation. It is also seen that the methods used in this paper may also be used to advantage to actually compute energy bands in a solid.

Through the medium of group theory we have also been able to define localized functions in molecules which have many of the properties of Wannier functions in a solid. They have orthogonality properties. They also have the advantage that one of these localized functions can be operated on and combined with itself in many ways to give many solutions to Schrödinger's equation. In this sense, these functions relate the wave functions and energies of a great many states of the molecule or crystal. The localized functions are similar in many ways to the "equivalent orbitals" of Lennard-Jones.[15]

The author wishes to express his appreciation for the privilege of being a guest at the Brookhaven National Laboratory where this work was carried out. He also wishes to thank Professor J. C. Slater for many valuable discussions throughout the course of this work.

[15] J. E. Lennard-Jones, Proc. Roy. Soc. (London) **A198**, 14 (1949).

The Elastic Scattering of Protons from Helium 4

BRUCE CORK
Radiation Laboratory, Department of Physics, University of California, Berkeley, California
(Received August 25, 1952)

The absolute differential cross section has been measured for 31.6-Mev protons scattered elastically from helium. Seven increments of angles from 15° to 51° in the laboratory system of coordinates have been measured simultaneously, using proportional counters.

The observed nuclear scattering is approximately three times the calculated Rutherford scattering for a scattering angle of 17° in the center-of-mass system and approximately 100 times the calculated Rutherford scattering for an angle of 62° in the center-of-mass system. Also, the differential cross section for a center-of-mass angle 55° has been observed to be 59.1 millibarns/steradian for incident protons of 19.5 Mev in the laboratory system.

INTRODUCTION

THE elastic cross section for scattering of protons from He^4 has been measured at energies up to 9.5 Mev[1-5] and a phase shift analysis made for low energy protons.[6] The Berkeley proton linear accelerator has allowed the region of 32 Mev and below to be investigated. The apparatus which was used for proton-proton scattering[7] was used without modification to obtain data for elastic scattering of protons from helium 4 in the forward directions. An independent experiment giving the elastic and inelastic cross sections will also be reported in another paper.[8,9]

METHOD

The 31.6-Mev proton beam from the linear accelerator was deflected 12.6° in an analyzing magnet and a collimator 6 meters long gave a beam of 1-cm diameter, having a divergence of ±0.001 radian. The energy was calculated by measuring the deflection of the beam and the magnitude of the magnetic field along the trajectory. The beam entered the scattering chamber through a double 0.0002-in. Nylon foil and was scattered by helium at a pressure of slightly greater than one atmosphere. The scattered protons could be detected in either of nine proportional counters operated simultaneously. An additional counter detected only background neutrons and x-rays.

The fraction of the beam which was not scattered continued on through a 0.001-in. thick Duraluminum foil, and on into the Faraday cup, arranged as a charge integrator.

PROCEDURE

The scattering chamber was evacuated to a pressure of less than 10^{-5} mm of Hg and observed to be vacuum tight. Helium of greater than 99.5 percent purity (grade *A*), obtained from the Mathieson Company, was allowed to enter the scattering chamber through a

TABLE I. The differential cross section for the scattering of 31.6±0.3 Mev protons from helium 4. The tabulated counts are the actual counts divided by four and normalized to NTP and a collected charge of 306.9×10^{-12} coulomb. *T* and *B* refer to top and bottom halves of a given counter.

	Proton—He^4 scattering									Proton-proton scattering	
Mean angle (c.m.)	62.5°*T*	62.5°*B*	55.0°*T*	55.0°*B*	47.8°*T*	47.8°*B*	40.1°	24.8°	17.1°	102°–78°	90°–90°
Counts, run 1	352	337	474	469	···	657	1560	1554	1182	1.7	1.1
	365	350	512	474	···	668	1545	1490	1173	1.7	1.9
	386	314	509	479	···	618	1510	1520	1140	1.1	2.1
Counts, run 2	355	341	496	457	710	634	1498	1474	···	1.7	1.2
	350	385	447	480	666	658	1572	1530	···	1.9	1.2
	366	343	490	490	654	656	1546	1574	···	1.4	2.2
Total	2174	2070	2928	2849	2030	3891	9231	9142	3495	9.5	9.7
Total, both sectors		4244		5777		7851	9231	9142	6990	9.5	9.7
$(d\sigma/d\Omega)_{c.m.}$ mb/sterad		31.53		45.21		68.7	93.3	145.5	159.9	14.30	14.39
Prob. error		±0.8		±1.2		±1.8	±2.4	±3.8	±4.2	±0.15	±0.14
Calc. Rutherford cross section mb/sterad		0.315		0.503		0.847	1.65	10.75	47.1		

[1] J. Chadwick and E. S. Bieler, Phil. Mag. **42**, 923 (1921).
[2] N. P. Heydenburg and R. B. Roberts, Phys. Rev. **56**, 1092 (1939).
[3] N. P. Heydenburg and N. F. Ramsey, Phys. Rev. **60**, 42 (1941).
[4] Freier, Lamp, Sleator, and Williams, Phys. Rev. **75**, 1345 (1949).
[5] T. M. Putnam, Phys. Rev. **85**, 774 (1952).
[6] C. L. Critchfield and D. C. Dodder, Phys. Rev. **76**, 602 (1949).
[7] Cork, Johnston, and Richman, Phys. Rev. **79**, 71 (1950).
[8] J. Benveniste and B. Cork, Phys. Rev. **83**, 894 (1951).
[9] J. Beneveniste and B. Cork (to be published).

liquid nitrogen trap made of stainless steel. The impurities before trapping were reported to be mostly hydrogen.

It was possible to measure the amount of hydrogen impurity by detecting the 90° coincidence scattered protons in the scattering chamber (see below).

The helium was admitted to the scattering chamber at a constant rate of approximately one liter per minute and allowed to bubble out through an oil lock column of Litton oil 5 cm high. The number of scattering nuclei was determined by measuring the height of this column, the barometric pressure, and the temperature of the has in the scattering chamber.

The position of the beam and the amount of multiple scattering of the beam were detected by inserting a photographic emulsion at the charge integrator. The beam was observed to have a mean diameter of 2.4 cm at the charge integrator. The charge integrator had an aperture of 6 cm; thus, the amount of the beam lost was negligible.

The scattered protons were detected by the same proportional counters which were used for proton-proton scattering.[7] The counter plateaus were determined by adjusting the gas multiplication and amplifier gain, making a run, then a background run with the shutter closed, and then repeating the run with a higher value of gas multiplication. The number of protons plus background was recorded for each of the ten counters. Also, the number of 90° coincidence counts was measured in the 45°–45° counters and in the 51°–39° counters. This was a measure of the hydrogen contamination in the helium, plus accidental coincidence.

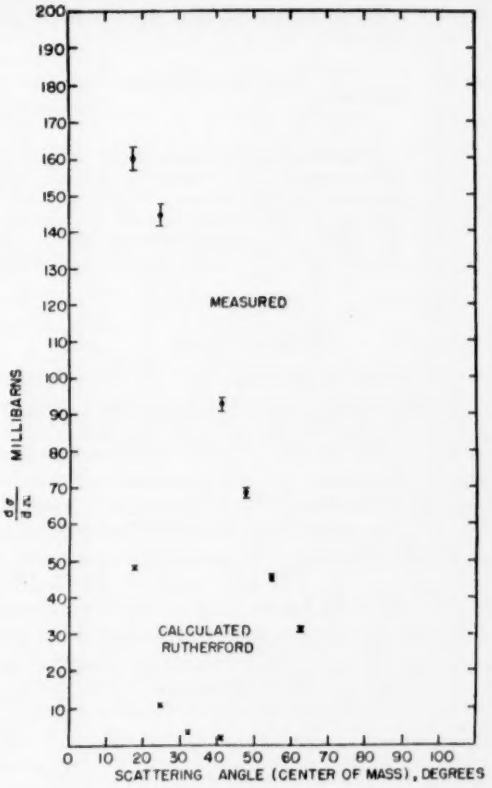
MEASURED
CALCULATED
RUTHERFORD
MILLIBARNS
$\frac{d\sigma}{d\Omega}$
SCATTERING ANGLE (CENTER OF MASS), DEGREES
0 10 20 30 40 50 60 70 80 90 100
10 20 30 40 50 60 70 80 90 100 110 120 130 140 150 160 170 180 190 200

FIG. 1. Absolute cross section for elastic scattering of 31.6-Mev protons from He^4.

RESULTS

The data for two series of runs are given in Table I. The number of counts for each angle measured is tabulated, corrected for background, counter resolving time, and normalized to NTP. The counting rate was sufficiently low so that the correction for counter resolving time was always less than 1 percent. The "plateau" was such that for the first group of runs, a 50-volt increase in potential of the proportional counter wire indicated a 0.3 percent decrease in the scattering cross section, while in the second group of runs, a 1.1 percent increase in the scattering cross section was indicated. The statistical fluctuation was ±1.3 percent.

The number of 90° coincidence counts is tabulated for each of two sets of counters. The pulse repetition rate of the linear accelerator was 15 pulses per record, 400 microsecond long pulses. The resolving time of the coincidence circuit was 1.0 microseconds, and from the observed counting rate, the calculated number of accidental coincidence counts is 1.5 (unscaled) per run. From these corrected data and the measured cross section for proton-proton scattering,[10] the amount of hydrogen impurity is determined to be 1.0±0.5 percent. The corrections have been made for each angle assuming 1 percent hydrogen contamination and no other contamination. The calculated cross section for each angle is given in Table I. The assigned probable errors include the following:

a. Collected charge: ±½ percent.
b. Mean energy: ±1 percent.
c. Measurement of temperature and pressure: ±½ percent.
d. Slope of plateau: +1.5 percent.
e. Rms deviation of counts: ±1.5 percent.
f. Calculated geometry: ±¾ percent.
g. Contamination scattering: ±1 percent.

The rms value of these probable errors is ±2.6 percent.

Figure 1 is a comparison of the observed cross section with the calculated Rutherford cross section at this energy. A further comparison will be made in a following paper.[9]

Protons of 19.5-Mev incident energy were obtained by adjusting the radio frequency voltage distribution of the linear accelerator cavity.[10] The differential cross section was then measured at a center-of-mass angle of 55.0 degrees and observed to be 59.1±1.6 millibarns/steradian.

It is a pleasure to acknowledge the help of Professor Luis W. Alvarez, who made these experiments possible. Also, the continued patience of the linear accelerator crew, under the supervision of Robert Watt, has greatly simplified the process of obtaining data.

[10] Bruce Cork, Phys. Rev. **80**, 321 (1950).

Formation of He^6 by 14-Mev Neutron Bombardment of Li and Be*

M. E. Battat and F. L. Ribe
University of California, Los Alamos Scientific Laboratory, Los Alamos, New Mexico
(Received September 25, 1952)

Formation of He^6 by bombardment of Li^6, Li^7, and Be^9 with 14-Mev neutrons has been observed. The He^6 was identified by its known half-life and the decay rate observed on a ten-channel time-delay analyzer. Beta-rays from the He^6 were detected by means of a thin-walled proportional counter, and the over-all counting efficiency was determined by using the $Cu^{63}(n,2n)Cu^{62}$ reaction. Cross sections determined for the $Li^6(n,p)$, $Li^7(n,d)$, and $Be^9(n,\alpha)$ reactions were 6.7 ± 0.8, 9.8 ± 1.1, and 10 ± 1 millibarns, respectively. The half-life of He^6 was found to be 0.83 ± 0.03 second.

INTRODUCTION

In the course of an investigation of the disintegration of Li^6 by 14-Mev neutrons[1] a large cross section was found for the sum of the (n,d) and (n,p) reactions. A large fraction of this cross section could be attributed to the (n,d) reaction, but it was impossible to obtain the magnitude of the smaller (n,p) cross section. Since the latter reaction yields beta-active He^6 (end point = 3.5 Mev, half-life ~0.82 sec),[2] it was feasible to measure its cross section by an activation method. The $Li^7(n,d)$ and $Be^9(n,\alpha)$ reactions, yielding the same radioactive nucleus, were also investigated. The $Be^9(n,\alpha)$ cross section has been measured for the neutron energy range from 2 to 4 Mev by Allen *et al.*[3] The $Li^6(n,p)He^6$ reaction for fast neutrons has been most recently observed by Poole and Paul.[4]

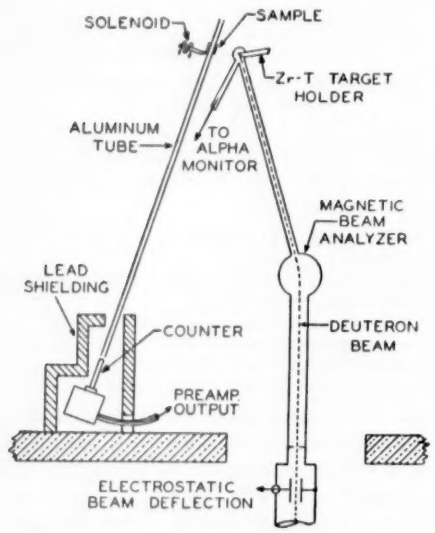

FIG. 1. Experimental arrangement for (n,He^6) cross-section measurements.

APPARATUS

The neutrons used in this experiment were obtained from the $H^3(d,n)He^4$ reaction, by bombarding a zirconium-tritium target[5] with the 250-kev diatomic deuteron beam of the Los Alamos Cockcroft-Walton accelerator. The angular position of the sample was 90 degrees with respect to the deuteron beam, corresponding to a neutron energy of 14.1 Mev. The number of neutrons from this reaction was measured by counting the accompanying alpha-particles emitted in a well-defined solid angle. For the He^6 activation it was necessary to know the instantaneous values of the neutron source strength Q. The Q values were obtained from a counting-rate meter, connected to the output of the alpha-monitor, calibrated under steady beam conditions, in terms of a known number of alphas emitted in a given time interval.

In order to determine the activation cross sections, it was necessary to identify the He^6 by means of its half-life and to determine the initial (saturated) activity of the irradiated samples at the instant the neutron irradiation stopped. Use was made of an automatic timing arrangement, consisting mainly of a time-delay analyzer. The time-delay analyzer, designed by C. W. Johnstone and O. L. Stone of this Laboratory, consisted of ten scales of 100 which were opened successively to the beta-ray pulses by means of a gate at intervals of 0.4 or 1.0 sec after initiation of the gate. Pulses derived by frequency division from a crystal-controlled 100-kc oscillator were used to control the timing of the gate. Such a gating arrangement was used earlier by Cassels and Latham[6] in their measurement of the He^6 half-life.

The He^6 beta-rays were detected by means of a thin-walled aluminum proportional counter filled to a pressure of 65 cm Hg with a Kr-CO_2 (7 percent CO_2) mixture. The normal lithium and beryllium samples were in the form of cylindrical shells which fitted closely around the counter, giving nearly 2π counting

* This work performed under the auspices of the AEC.
[1] F. L. Ribe, Phys. Rev. **87**, 205 (1952).
[2] Hornyak, Lauritsen, Morrison, and Fowler, Revs. Modern Phys. **22**, 303 (1950); R. K. Sheline, Phys. Rev. **87**, 559 (1952); Wu, Rustad, Perez-Mendez, and Lidofsky, Phys. Rev. **87**, 1140 (1952).
[3] Allen, Burcham, and Wilkinson, Proc. Roy. Soc. (London) **A192**, 114 (1948).
[4] M. J. Poole and E. B. Paul, Nature **158**, 482 (1946).
[5] Graves, Rodrigues, Goldblatt, and Meyer, Rev. Sci. Instr. **20**, 579 (1949).
[6] J. M. Cassels and R. Latham, Nature **159**, 367 (1947).

geometry. The counting system was biased to record pulses resulting from beta-ray energy losses in the counter of 0.3 kev or greater. With this bias the counter efficiency was approximately 100 percent.

EXPERIMENTAL PROCEDURE

The experimental arrangement is shown in Fig. 1. The sample was supported on an aluminum tube by means of a solenoid plunger about 15 cm from the neutron source. After an irradiation (to near saturation) of about 10 seconds, the deuteron beam was deflected and the solenoid energized, causing the sample to slide down the tube to a position around the counter. The counter was housed in lead shielding 150 cm from the neutron source.

Initiation of the first channel of the time-delay analyzer coincided with the deflection of the deuteron beam. It was not possible to observe the activity during the first second or so after the irradiation stopped; however, the number of channel intervals elapsed before useful counts were obtained provided a precise time interval for extrapolation to saturated activity. The initial decay of each sample was observed with channel widths of 0.4 and 1.0 sec, and further data were obtained by successively reinitiating the analyzer until the only counts obtained were due to normal background. Before and after each sample run, similar measurements were made with no sample to determine the background. These backgrounds were found to be quite reproducible.

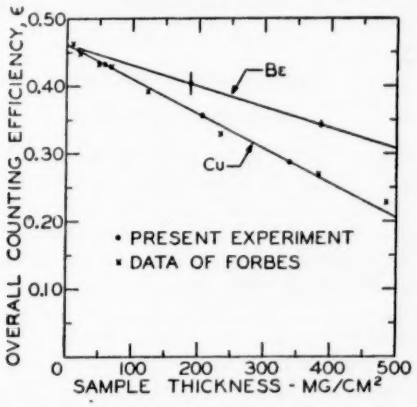

FIG. 2. Variation with sample thickness of the effects of self-scattering and absorption of beta-rays in copper and beryllium.

DETERMINATION OF THE CROSS SECTIONS

If one bombards a sample with a steady flux of f neutrons/cm²/sec, then the activity A at time t after the beginning of the irradiation is

$$A = f\sigma n[1-\exp(-\lambda t)], \qquad (1)$$

where σ is the activation cross section, n the number of atoms of the sample, and λ the disintegration constant of the resulting radioactive nucleus. For $t \gg 1/\lambda$ the cross section is given in terms of the counting rate N_0, corresponding to A, by

$$N_0 = f\sigma n\epsilon, \qquad (2)$$

where ϵ is a factor which takes into account geometry, self-scattering and absorption of the sample, and counter efficiency.

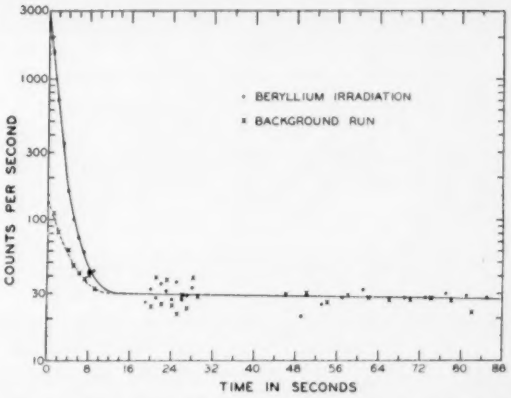

FIG. 3. Upper curve: Decay of He^6 activity induced in Be by 14-Mev neutrons, background included. Lower curve: Decay of background activity.

In order to determine the over-all counting efficiency ϵ, the 2.9-Mev, 10-minute beta-activity induced in copper by 14-Mev neutrons was used. The $Cu^{63}(n,2n)Cu^{62}$ cross section for normal copper as determined by Forbes[7] for 14-Mev neutrons is 350±25 millibarns. Cylindrical copper samples of thicknesses 56.9, 205, and 338 mg/cm² were bombarded for a few seconds with the 14-Mev neutrons, and the resulting activities were measured in the counting geometry which was used in the He^6 activation runs. In this case $t \ll 1/\lambda$, and the counting rate N_0 is given by

$$N_0 = (ft)\sigma n\lambda\epsilon. \qquad (3)$$

The integrated flux ft was known accurately from the total alpha-monitor count for the irradiation. The values obtained for ϵ are plotted in Fig. 2. Data obtained by Forbes for plane samples in 46-percent counting geometry are also given for comparison. The value of ϵ obtained for zero thickness of copper is assumed to apply also to the cases of lithium and beryllium, although a smaller slope of the curve of ϵ *versus* sample thickness is to be expected for the lighter elements and the He^6 beta-activity.

A. The $Be^9(n,\alpha)He^6$ Cross Section

Data were obtained for beryllium samples of thicknesses 189 and 385 mg/cm². Figure 3 shows the data for a typical run on the 189-mg/cm² sample using a 1.0-sec analyzer channel width. The background in this case is 5 percent of the initial activity, and it was of

[7] S. G. Forbes (private communication).

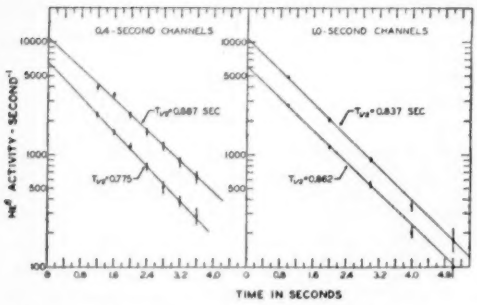

FIG. 4. Decay of He^6 activity induced in Be by 14-Mev neutrons.

roughly the same magnitude for all of the beryllium and lithium runs. He^6 decay curves for both beryllium samples are given in Fig. 4 (background subtracted). The lines drawn through the experimental points were fitted by the method of least squares, weighting the points inversely as their statistical errors. Values of ϵ for the two sample thicknesses, normalized to the value 0.463 for zero thickness are plotted in Fig. 2. This curve is taken, within the error of the present experiment, to apply also to lithium. The error in extrapolation of the values of ϵ to zero sample thickness is ± 5 percent. The data of Fig. 4 provided four determinations of the He^6 half-life which were 0.862, 0.837, 0.887, and 0.775 sec. The $Be^9(n,\alpha)$ cross section determined from these data is 10 ± 1 millibarn.

B. The (n,He^6) Cross Section for Normal Lithium

Three runs were made with a normal lithium sample of 191 mg/cm² thickness, two with 0.4-sec and one with 1.0-sec channels. The three values obtained for the He^6 half-life were 0.773, 0.811, and 0.822 sec. The cross section for the production of He^6 in normal lithium was determined as 9.5 ± 1.0 millibarn. This represents a combination of the $Li^6(n,p)$ and $Li^7(n,d)$ cross sections, weighted according to their normal isotopic abundances (92.6 percent lithium 7).

C. Ratio of the (n,He^6) Cross Sections of Li^6 and Li^7

Enriched samples of lithium 6 (90.94 percent) and lithium 7 (99.90 percent) in the form of cylindrical slugs 7.8 mm in diameter, of weights 0.793 and 0.964 gram, respectively, were used. These slugs were irradiated in turn in a thin polyethylene container which fitted around the counter. The He^6 activity from each slug was counted with the axis of the slug parallel to that of the counter. Since the activities were counted in identical geometry, the ratio of the $Li^6(n,p)$ and $Li^7(n,d)$ cross sections could be determined independently of the over-all counting efficiency. The background runs for this part of the experiment were made with the empty polyethylene container. There was no discernible contribution by the container to the background. Runs on each slug were made, using 0.4- and 1.0-sec channel widths. The four values obtained for the He^6 half-life were 0.806, 0.817, 0.830, and 0.911 sec, and the ratio of cross sections was found to be

$$\sigma_6(n,p)/\sigma_7(n,d)=0.69\pm 0.03.$$

D. The $Li^6(n,p)$ and $Li^7(n,d)$ Cross Sections

Combining the results of the measurements of $\sigma_6(n,p)/\sigma_7(n,d)$ and of the (n,He^6) cross section for normal lithium, one obtains for the isotopic cross sections: 9.8 ± 1.1 millibarn for $Li^7(n,d)He^6$ and 6.7 ± 0.8 millibarn for $Li^6(n,p)He^6$.

E. The He^6 Half-Life

The value of the He^6 half-life obtained from the 11 determinations of this experiment is 0.83 sec with an error of ± 0.03 sec, estimated from the statistical spread of the data.

EVALUATION OF ERRORS

A. Experimental Errors

Among the sources of experimental error in the determination of the cross sections were those arising from the flux measurements and the background determinations. In each of the measurements involving beryllium, normal lithium, and isotopic lithium the saturated activities were determined several times. In all cases, these measurements agreed among themselves to within ± 5 percent; this is taken as the error arising from both of the above sources. In addition, there was the 5 percent error in the extrapolation of the over-all counting efficiency to zero thickness, 7 percent error in the $Cu^{63}(n,2n)Cu^{62}$ cross section, and a 4 percent error in the calibration of the alpha-monitor. These errors account for the uncertainties quoted in the final cross section values.

B. Possible Formation of Li^8

If Li^8 (half-life = 0.83 sec)[2,8] were formed, either by the $Be^9(n,d)$ or the $Li^7(n,\gamma)$ reaction, its activity would not have been distinguished from that of He^6. The $Be^9(n,d)$ reaction, however, does not occur at 14-Mev neutron energy, since its threshold is 16.3 Mev. The $Li^7(n,\gamma)$ cross section for thermal neutrons is 33 millibarns.[9] Measurements made with a U^{235} fission chamber, at 15 cm from the neutron source, showed that the thermal and epicadmium (less than 14-Mev) neutron fluxes were 0.03 percent and ≤ 3 percent of the 14-Mev component, respectively. The activity of Li^8 due to

[8] W. Rall and K. G. McNeill, Phys. Rev. **83**, 1244 (1951). This paper also contains references to previous measurements of the Li^8 half-life.

[9] Hughes, Hall, Eggler, and Goldfarb, Phys. Rev. **72**, 646 (1947).

thermal and epithermal neutron capture was therefore negligible. It is reasonable to assume that the $Li^7(n,\gamma)$ reaction also gives a negligible contribution for 14-Mev neutrons, since at these energies particle emission from the compound nucleus is generally much favored over gamma emission. This assumption is borne out by the fact that even at the resonance peak of about 10 barns in the total cross section at 0.256-Mev neutron energy the $Li^7(n,\gamma)$ cross section is less than 0.1 millibarn.[10]

The authors are pleased to acknowledge the helpful interest of Dr. J. H. Coon and Dr. E. R. Graves throughout this investigation.

[10] Rose, Bayly, and Freeman, AERE, Harwell (private communication).

PHYSICAL REVIEW VOLUME 89, NUMBER 1 JANUARY 1, 1953

The Beta-Decay Interaction*

JOHN M. BLATT
University of Illinois, Urbana, Illinois
(Received September 12, 1952)

The recent identifications of two beta-decays as 0-to-0 transitions proves that the beta-decay interaction must contain a component obeying Fermi selection rules. Evidence is presented regarding the relative strengths of the Fermi- and Gamow-Teller interactions, and experiments are suggested to improve our knowledge of these strengths. It is pointed out that the He^6 *ft* value does *not* give significant information about the beta-decay interaction. An experiment is proposed to determine the nature (scalar or polar vector) of the Fermi interaction.

THERE are now two cases known of allowed and favored 0-to-0 transitions. One is a branch of the C^{10} decay;[1,2] the second is the decay of O^{14}.[1,3,4] Hence, the beta-decay interaction must contain a part leading to Fermi selection rules, i.e., an admixture of either the scalar or the polar vector interaction, or of both interactions.[5]

We wish to call attention to the fact that the O^{14} decay allows us to get more specific information about this Fermi component. First, we may ask for the relative strength of the Fermi and Gamow-Teller interactions. Let M_0^2 be the square of the nuclear matrix element for the Fermi interaction, M_1^2 be the corresponding quantity for the Gamow-Teller interaction (these quantities are often referred to as $(\int 1)^2$ and $(\int \boldsymbol{\sigma})^2$, respectively). We restrict ourselves to transitions for which these matrix elements can be computed theoretically without detailed knowledge of the nuclear wave functions.[6] For transitions within the same isotopic spin multiplet, between nuclei with neutron excesses T_ζ and T_ζ', respectively, we get

$$M_0^2 = T(T+1) - T_\zeta T_\zeta', \tag{1}$$

where T is the quantum number for the total isotopic spin. Formula (1) depends only upon the assumed charge independence of nuclear forces. In particular, it holds even in the presence of strong spin-orbit coupling, i.e., under conditions where the full supermultiplet theory of Wigner[7] is inapplicable.

Unfortunately, the determination of M_1^2 is not as clean-cut since the presence of spin-orbit coupling leads to appreciable corrections. For example, the 4 percent admixture of $^4D_{\frac{1}{2}}$ state to the $^2S_{\frac{1}{2}}$ ground state of H^3 leads to a 5 percent correction in M_1^2.[6,8,9] Since the D-state admixture is not very well known (it could be anywhere between 1 and 10 percent, if one takes into account the possibly quite large relativistic corrections to the magnetic moments of H^3 and He^3) the value of the beta-decay matrix element M_1^2 is correspondingly

* Work assisted by the joint program of the ONR and AEC.

[1] Sherr, Muether, and White, Phys. Rev. **75**, 282 (1949).

[2] R. Sherr and J. Gerhart, Phys. Rev. **86**, 619 (1952).

[3] Hornyak, Lauritsen, Morrison, and Fowler, Revs. Modern Phys. **22**, 291 (1950).

[4] The identification of the final state (a 2.3-Mev excited level of N^{14}) as having spin zero was made by Adair (private communication) by an ingenious application of the charge independence of nuclear forces, leading to a selection rule for the isotopic spin quantum number. In particular, Adair's argument shows that there cannot be an excited $^3S_1$ state of N^{14} close (in energy) to the $^1S_0$ "partner" of the O^{14} ground state. Previously the possibility (and even theoretical likelihood) of such a $^3S_1$ state close to the $^1S_0$ state had made it impossible to identify the beta-decay of O^{14} as a 0-to-0 transition. Dr. N. Kroll has kindly informed the writer that a weaker assumption about nuclear forces suffices to get the selection rule in the cases discussed by Adair. However, the identification of the 2.3-Mev level of N^{14} as a spin 0 state is not appreciably weakened by Kroll's argument; in particular, a $^3S_1$ state close by would have been observed in Adair's experiment even under Kroll's assumptions about nuclear forces.

[5] E. J. Konopinski, Revs. Modern Phys. **15**, 209 (1943).

[6] E. P. Wigner, Phys. Rev. **56**, 519 (1939); J. M. Blatt, Phys. Rev. **89**, 86 (1953), following paper.

[7] E. P. Wigner, Phys. Rev. **51**, 106 (1937).

[8] E. Gerjuoy and J. S. Schwinger, Phys. Rev. **61**, 138 (1942); and experimental evidence from the magnetic moments of H^3 and He^3. A recent theoretical calculation by Pease and Feshbach (private communication) indicates an admixture of 3 percent rather than 4 percent.

[9] E. Feenberg, quoted by G. Trigg, Phys. Rev. **86**, 506 (1952). An error of sign in the value quoted there was corrected in a private communication from Professor Feenberg to the writer. At the time Trigg's paper was written there was no experimental identification of the spins in the O^{14} decay. Thus Trigg's argument for the presence of a Fermi interaction was based primarily upon comparative half-lives rather than upon selection rules.

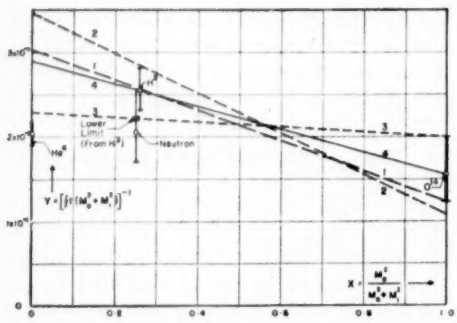

FIG. 1. Ordinate: $y=[ft(M_0^2+M_1^2)]^{-1}$, in (seconds)$^{-1}$. Abscissa: $x=M_0^2/(M_0^2+M_1^2)$. In principle, all points should lie on a straight line, with $y=G_1^2$ (strength of Gamow-Teller interaction) at $x=0$, and $y=G_0^2$ (strength of Fermi interaction) at $x=1$. The He^6 point is too low, indicating that the simple theoretical value $M_1^2=6$ is a bad overestimate. The H^3 value shown assumes a 4 percent admixture of ^4D state. Since the amount of this admixture is not well known at all, this point may be in error. However, M_1^2 for H^3 is certainly less than or equal to 3, giving the "lower limit" also indicated on the figure. Line 4 is considered the present "best" line, while lines 2 and 3 give reasonable extreme values of the ratio G_0^2/G_1^2.

uncertain. The situation is even worse in the He^6 decay, since the initial and final states do not even belong to the same isotopic spin multiplet. However, we can still use the H^3 and He^6 decays to establish upper limits for M_1^2ft, since in both cases M_1^2 is surely no larger than the theoretical value.[6] The only decay for which M_1^2 can be determined with high accuracy is the decay of the neutron.

A convenient way to plot the data is as follows: for each decay we determine (from theory) the nuclear matrix elements M_0^2 and M_1^2 and (from experiment) the comparative half-life (ft value). We then plot $y=[ft(M_0^2+M_1^2)]^{-1}$ against $x=M_0^2/(M_0^2+M_1^2)$. The result should be a straight line satisfying the equation

$$y=G_0^2x+G_1^2(1-x), \tag{2}$$

where G_0 and G_1 are the interaction constants for the Fermi and Gamow-Teller interactions, respectively. G_0^2 and G_1^2 can be read off directly as the values of y at $x=1$ and at $x=0$, respectively.

In order to minimize uncertainties arising from the theoretical calculation of matrix elements, we shall restrict ourselves to the simplest possible decays: those of the neutron, of H^3, of He^6, and of O^{14}. We shall adopt the following values for the lifetimes and maximum energies:

$$\text{Neutron: } E_0=0.783 \text{ Mev}, \quad t_{\frac{1}{2}}=12.5\pm2.5 \text{ minutes}; \tag{3}$$

$$\text{Triton: } E_0=18.0\pm0.5 \text{ kev}, \quad t_{\frac{1}{2}}=3.93\times10^8 \text{ sec}; \tag{4}$$

$$He^6\text{: } E_0=3.50\pm0.05 \text{ Mev}, \quad t_{\frac{1}{2}}=0.823 \text{ sec}; \tag{5}$$

$$O^{14}\text{: } E_0=1.8\pm0.1 \text{ Mev}, \quad t_{\frac{1}{2}}=76.5 \text{ sec}. \tag{6}$$

These values were taken primarily from the review article by Hornyak *et al.*[3] The lifetime of the neutron is not very well known, and the error stated here may be too optimistic. A recent measurement of the end-point energy in the triton decay by Langer (private communication) agrees with the value adopted here, but has a significantly smaller claimed error. No error is given here on the lifetimes of the triton, He^6, and O^{14}, since in all three cases the error in the ft value comes predominantly from the error in E_0. The end-point energy of He^6 differs from the value quoted in reference 3 because of two new measurements.[10]

The f values for all these decays were computed by numerical integration of the Fermi function; they check against previously stated values. The matrix element M_0^2 was taken from formula (1); the matrix element M_1^2 was taken to be 3 for the neutron, and 6 for the He^6 decay. The latter is probably an overestimate. In the case of H^3 we have used $M_1^2=2.84$, which follows if we assume a 4 percent admixture of the ^4D state. In view of the results of the following paper, however, we have also made use of the fact that M_1^2 cannot exceed 3. $M_1^2=0$ for O^{14}, of course.

The resulting plot of y *vs* x is shown in Fig. 1. In this figure we have also drawn in the lower limit for y determined from the H^3 decay by taking the values $M_1^2=3$ and $E_0=18.5$ kev. We see that this lower limit lies above the "best" value from the neutron decay. Hence it is very probable that the true lifetime of the neutron is somewhat less than 12.5 minutes. Next we observe that the dotted line number 3, drawn through the upper limit of the O^{14} point and the lower limit from H^3, falls above the He^6 point. We conclude that the matrix element of He^6 is almost certainly less than 6, and furthermore (since the matrix element is practically impossible to compute with any accuracy) that the *ft value of He^6 does not give any significant information about the beta-decay interaction.* This conclusion is sharply at variance with earlier work.[11] However, the difference is entirely due to the new value of the maximum energy in the He^6 decay. From the theoretical point of view the new value is much more acceptable, since the old ft value would have implied a practically perfect overlap between the wave functions of the $^1S_0$ ground state of He^6 and the $^3S_1$ ground state of Li^6. This was rather difficult to believe, especially since the magnetic moment of Li^6 deviates somewhat from the value expected for a pure $^3S_1$ state. While the situation now is more in accordance with theoretical expectations, it is of course unfortunate that the He^6 ft value no longer gives significant information.

If we accept Langer's measurement of the H^3 end point, the error on the H^3 point is decreased by a factor of 5, and the lower limit on the value of y at $x=0.25$ would move up to $y=2.42$, implying a neutron lifetime shorter than about 11 minutes.

[10] Dewan, Pepper, Allen, and Almquist, Phys. Rev. **86**, 416 (1952); Wu, Rustad, Perez-Mendez, and Lidofsky, Phys. Rev. **87**, 1140 (1952).

[11] S. A. Moszkowski, Phys. Rev. **82**, 155 (1951).

We now try to draw straight lines through the points of Fig. 1 (ignoring the He^6 point, of course). Dotted line number 1 is drawn as if the neutron lifetime were certainly longer than 10 minutes, and the value of E_0 for O^{14} certainly smaller than 1.9 Mev. Both assumptions are questionable at present, and we feel that a line such as dotted line number 2 gives a more adequate lower limit for the ratio G_0^2/G_1^2. An upper limit for this ratio is obtained from dotted line number 3, drawn as if E_0 of O^{14} were certainly greater than 1.7 Mev, and E_0 of H^3 less than 18.5 Mev. The latter of these assumptions is probably not too far off, but the former may be in error. Thus *it is not possible at present to exclude a ratio* $G_0^2/G_1^2=1$ (which corresponds to a horizontal straight line). However, a precision measurement of E_0 in the O^{14} decay would settle this question. The present "best" value of G_0^2/G_1^2 is derived from line 4. We thus obtain

$$G_0^2/G_1^2=0.54^{+0.5}_{-0.25}. \tag{7}$$

The best value of the ratio (7) agrees very well with Trigg's[9] best value; this agreement is somewhat fortuitous because Trigg based his best value in considerable part upon the old *ft* value of He^6. We also agree with other recent analyses of decays of mirror nuclei.[12] However, we feel that our decision not to incorporate decays for which the value of M_1^2 is doubtful allows us to fix more definite limits on the permissible range of the ratio (7) than can be obtained from a statistical analysis of a larger number of decays, all of which have uncertain matrix elements.

It might be worth while to point out that, in our opinion, a careful measurement of the lifetime of the neutron (with special attention given to establishing a *lower limit* for the lifetime) is more important than a measurement of the beta-neutrino angular correlation in the decay of the neutron.

The data discussed so far do not determine the nature of the Gamow-Teller or of the Fermi interaction. However, the decay of Cl^{36} strongly suggests the tensor interaction,[13] and so does the beta-neutrino angular correlation in He^6.[14] Thus, the Gamow-Teller part of the interaction is very probably of the tensor type. A theoretical conjecture can then be made as to the nature of the Fermi part, based upon the symmetry principle of Tolhoek and deGroot.[15] According to this symmetry principle, the Fermi interaction must be of the polar vector type.

We would like to point out that this theoretical conjecture can be checked experimentally by a measurement of the beta-neutrino angular correlation in the O^{14} decay.[16] This is a more unequivocal test than the beta-neutrino angular correlation in the neutron decay because, unlike the neutron decay, *only* the Fermi interaction is effective in O^{14}. While the 0-to-0 transition of C^{10} is equally good in principle, it is useless practically because it is only a minor branch.

At first sight, the beta-neutrino angular correlation in O^{14} seems hard to measure because the subsequent 2.3-Mev gamma-ray gives rise to a recoil momentum comparable to the recoil momentum from the beta-emission. However, we can use the gamma-ray to good advantage by requiring triple coincidences between positron, gamma-ray, and (delayed) recoil ion. Not only does this allow correction for the recoil momentum from the gamma-ray emission, but even more important, the experiment can be set up in such a way that observation of the gamma-ray limits the effective source volume. Since the gamma-ray is so energetic, it can be distinguished easily from the annihilation gamma-rays by pulse-height discrimination. Since the intermediate state has spin zero, there is no beta-gamma correlation[17] to confuse the beta-neutrino angular correlation.

Finally, Professor Teller has kindly pointed out to the writer that a beta-decay interaction which is a mixture of tensor and polar vector interactions is inconsistent with the view that the pi-meson (assumed to be pseudoscalar) appears in an intermediate state during the beta-decay. The absence of any direct interaction between pi-mesons and the electro-neutrino field had already been inferred from considerations based upon the lifetime of the pi-meson against μ-decay and electron decay and upon nuclear beta-decay lifetimes.[18]

We would like to thank Dr. Adair and Dr. Kroll for letting us see their work on isotopic spin selection rules before publication; Dr. Feenberg, Dr. Lauritsen, and Dr. Wu for calling to our attention the changed value of the He^6 end point, and Dr. Wu for communication of her recently determined value before publication; Dr. Teller and Dr. Lee for theoretical discussions; Dr. Allen for communication of results on the beta-neutrino angular correlation in He^6 prior to publications, and Dr. Allen, Dr. Frauenfelder, and Dr. Jentschke for discussions about the proposed beta-neutrino angular correlation experiment.

[12] R. Nataf and R. Bouchez, Phys. Rev. **87**, 155 (1952); R. Bouchez and R. Nataf, Compt. rend. **234**, 86 (1952); O. Kofoed-Hansen and A. Winther, Phys. Rev. **86**, 428 (1952), and unpublished work by the same authors.

[13] C. S. Wu and L. Feldman, Phys. Rev. **76**, 693 (1949); **82**, 457 (1951); H. W. Fulbright and J. C. D. Milton, Phys. Rev. **82**, 274 (1951). For the spin of Cl^{36} see: C. H. Townes and L. C. Aamodt, Phys. Rev. **76**, 691 (1949); Johnson, Gordy, and Livingston, Phys. Rev. **83**, 1249 (1951). The conclusion of Longmire *et al.*, Phys. Rev. **76**, 695 (1949) that the Cl^{36} spectrum *necessitates* a mixed interaction is no longer accepted.

[14] Allen, Paneth, and Morrish, Phys. Rev. **75**, 570 (1949) and later measurements by Professor Allen (private communication).

[15] S. R. deGroot and H. A. Tolhoek, Physica **16**, 456 (1950). However, a recent argument by Konopinski (to be published), based upon the spectrum shapes of once-forbidden beta-transitions, appears to rule out the tensor-polar vector combination.

[16] D. R. Hamilton, Phys. Rev. **71**, 456 (1947).

[17] D. L. Falkoff and G. E. Uhlenbeck, Phys. Rev. **79**, 334 (1950).

[18] J. Tiomno and J. A. Wheeler, Revs. Modern Phys. **21**, 144, 153 (1949); Lee, Rosenbluth, and Yang, Phys. Rev. **75**, 905 (1949).

The Beta-Decay of the Triton*

JOHN M. BLATT
University of Illinois, Urbana, Illinois
(Received September 12, 1952)

A general formula is derived for the beta-decay matrix elements in the decay of a nucleus into its mirror nucleus. This formula is specialized to the decay of H^3. Under the assumption of charge independence of nuclear forces, it is shown that the value $(\int\boldsymbol{\sigma})^2=3$ computed on the basis of a pure $^3S_1$ ground state is an upper limit for the true value of this matrix element, provided only that the $^3S_1$ state is present with a probability of at least 25 percent.

1. INTRODUCTION

MANY years ago Wigner[1] pointed out that the wave functions of mirror nuclei should be very similar to each other. Indeed, if neutron-neutron forces equal proton-proton forces, and if the Coulomb forces can be treated validly as a small perturbation which changes the energy of the state without appreciably changing the wave function, then the wave functions of mirror nuclei are identical. In that case, the matrix elements for the beta-decay of a nucleus into its mirror nucleus can be computed without detailed knowledge of the wave function.[2]

If we assume full charge independence of nuclear forces, i.e., equality of *nn*, *pp*, and *np* forces, then the total isotopic spin T is a good quantum number. It is then easy to show that the matrix element usually denoted[3] by $(\int 1)^2$ is given by

$$\left(\int 1\right)^2=T(T+1)-T_f T_f'. \tag{1.1}$$

This equals unity for mirror nuclei, for which $T=\frac{1}{2}$, $T_f=\frac{1}{2}$, $T_f'=-\frac{1}{2}$.

Unfortunately, no such simple result holds for the matrix element $(\int\boldsymbol{\sigma})^2$ which arises from the Gamow-Teller interaction.[4] If the forces are spin-independent in addition to being charge-independent, then the supermultiplet theory of Wigner[5] can be applied. In addition to the total angular momentum J and the total isotopic spin T, there are then the following additional good quantum numbers: the partition quantum numbers P, P', P'', the intrinsic spin of the nucleus S, and the orbital angular momentum of the nucleus L. The value of $(\int\boldsymbol{\sigma})^2$ under these assumptions has been calculated by Wigner.[2]

Unfortunately, the present evidence indicates that the nuclear forces are probably charge independent but are certainly not spin-independent. Trigg[6] has generalized Wigner's calculation to the extent that the orbital angular momentum L of the nucleus is no longer considered a good quantum number. However, Trigg assumes no appreciable admixtures of states belonging to partitions other than the dominant $(\frac{1}{2},\frac{1}{2},\pm\frac{1}{2})$. Since the tensor force leads to admixtures of other partitions,[7] and since the tensor force is probably the main spin-dependent force, we thought it worth while to calculate the effect of admixtures of states belonging to other partitions.

We first derive a general expression for $(\int\boldsymbol{\sigma})^2$ under the assumption of equal wave functions for the two mirror nuclei, i.e., equality of *nn* and *pp* forces, but no assumption about *np* forces. We then specialize the formula to the case of full charge independence by omitting all states with isotopic spin $T\neq\frac{1}{2}$. The application of these results to the decay of the triton is particularly simple because there are only three nucleons present. The permutation group on three variables has only three different irreducible representations (partitions); hence, all states which can be present in H^3 can be enumerated easily, and the relevant matrix elements can be calculated explicitly. When this is done, assuming charge independence of the nuclear forces, it turns out that there are only two states which would tend to make the value of $(\int\boldsymbol{\sigma})^2$ exceed 3. Since these states have to be present to at least 75 percent of the total wave function before $(\int\boldsymbol{\sigma})^2$ exceeds 3, we conclude that the true value of $(\int\boldsymbol{\sigma})^2$ for the decay of H^3 is less than or equal to 3.

The calculations reported here can also be used for the decay of other mirror nuclei, although they are not complete (i.e., not all possible partitions are enumerated) for nuclei of mass number greater than 3. In practice, however, the partitions $(\frac{1}{2},\frac{1}{2},\pm\frac{1}{2})$ and $(\frac{3}{2},\frac{1}{2},\mp\frac{1}{2})$ are surely the most important ones, and the results given here are sufficient for the computation of their effects in all mirror nuclei decays.

An appendix contains the explicit forms of the spin-isotopic-spin wave functions for all states of the triton.

2. A GENERAL EXPRESSION FOR $(\int\boldsymbol{\sigma})^2$

Consider a decay between two "corresponding" states of mirror nuclei, each with total angular momentum J. The initial nucleus has a neutron excess $T_f=\frac{1}{2}(N-Z)$

* This research was assisted by the joint program of the ONR and AEC.

[1] E. P. Wigner, as quoted in White, Delsasso, Fox, and Creutz, Phys. Rev. **56**, 512 (1939).
[2] E. P. Wigner, Phys. Rev. **56**, 519 (1939).
[3] E. J. Konopinski, Revs. Modern Phys. **15**, 209 (1943).
[4] G. Gamow and E. Teller, Phys. Rev. **49**, 895 (1936).
[5] E. P. Wigner, Phys. Rev. **51**, 106 (1937).
[6] G. L. Trigg, Phys. Rev. **86**, 506 (1952).
[7] A. M. Feingold, thesis, Princeton University (1952) (unpublished).

$=+\frac{1}{2}$, the final nucleus has $T_\xi'=-\frac{1}{2}$. The direction of the decay has no influence on the value of the matrix element. Let us define the "spherical components" of the Pauli spin vector $\boldsymbol{\sigma}^{(k)}$ for particle number k as follows:

$$\sigma_{+1}=-2^{-\frac{1}{2}}(\sigma_x+i\sigma_y),\quad \sigma_0=\sigma_z,\quad \sigma_{-1}=2^{-\frac{1}{2}}(\sigma_x-i\sigma_y). \tag{2.1}$$

The relevant operator for the allowed beta-decay with Gamow-Teller selection rules is the vector operator $\mathbf{Y}$ with the spherical components (A = mass number)

$$Y_\rho=\sum_{k=1}^{A}\sigma_\rho{}^{(k)}\tau_\xi{}^{(k)}, \tag{2.2}$$

where $\rho=1,\ 0,\ -1$, and τ_ξ is the conventional isotopic spin operator which changes a neutron into a proton and vice versa. Let the wave function of the initial state be Ψ_{JM}, the subscripts indicating the values of the total angular momentum and of its z component; the wave function of the final state is $\Phi_{JM'}$. Since the states are by assumption "corresponding" states, the value of J is the same, but M' may be any one of M, $M+1$, $M-1$. The quantity $(\int\boldsymbol{\sigma})^2$ is then defined as follows:

$$\left(\int\sigma\right)^2=\sum_{\rho=-1}^{+1}\sum_{M'=-J}^{+J}|(\Phi_{JM'},\,Y_\rho\,\Psi_{JM})|^2. \tag{2.3}$$

The value of this double sum is, of course, independent of M, since a different choice of M corresponds to a different choice of the z direction in space, which cannot affect the beta-decay probability.

To simplify expression (2.3), we observe that the matrix elements of a vector operator such as $\mathbf{Y}$ depend upon the magnetic quantum numbers M, ρ, and M' in the same way as the Clebsch-Gordan (vector addition) coefficients $(1J\rho M\,|\,1JJM')$.[8] We use the notation of Condon and Shortley.[9] Thus we may restrict ourselves to particular values of M, ρ, and M'. We shall pick $M=M'=J$ and $\rho=0$ for ease of computation. Thus

$$(\Phi_{JM'},\,Y_\rho\,\Psi_{JM})=(1J_\rho M\,|\,1JJM')\frac{(\Phi_{JJ},\,Y_0\,\Psi_{JJ})}{(1J0J\,|\,1JJJ)}. \tag{2.4}$$

When we square this and sum over ρ and M', the sum of the squares of the Clebsch-Gordan coefficients is unity, so that we get

$$\left(\int\sigma\right)^2=\left|\frac{(\Phi_{JJ},\,Y_0\,\Psi_{JJ})}{(1J0J\,|\,1JJJ)}\right|^2. \tag{2.5}$$

In order to get farther, we have to introduce a more detailed classification of the possible states. The states are linear superpositions of elementary states. Each elementary state has a definite orbital angular momentum L with z component m, a definite spin angular momentum S with z component μ, a definite isotopic spin quantum number T, and belongs to a definite row κ of some partition (P, P', P'') of the permutation group. For the sake of conciseness, we shall use the symbol P to denote all three quantities P, P', P''. We denote the space wave function belonging to row number κ of partition P and to an orbital angular momentum L, m by $\psi_{m\kappa}(L, P;\,\mathbf{r}_1\mathbf{r}_2,\,\cdots,\,\mathbf{r}_A)$. We denote the spin-isotopic-spin wave function belonging to row κ of the partition adjoint to P, to spin S with z component μ, to isotopic spin quantum number T, and neutron excess $T_\xi=+\frac{1}{2}$, by $V_{\mu\kappa}(P, T, S)$. Explicit expressions for the functions V in the case of three particles are contained in the appendix, and the reader unfamiliar with the representations of the permutation group is urged to read the appendix before proceeding with the rest of this paper. The spin-isotopic-spin wave functions for neutron excess $T_\xi'=-\frac{1}{2}$ will be denoted $U_{\mu\kappa}(P, T, S)$. They are obtained from the $V_{\mu\kappa}(P, T, S)$ by a systematic replacement of neutron wave functions by proton wave functions and vice versa (see the appendix).

We may now write the wave function Ψ_{JM} of the initial state as a linear superposition of wave functions $\Psi_{JM}(P, L, T, S)$ with definite values of the partition, orbital angular momentum, isotopic spin quantum number T, and spin quantum number S. We denote the probability amplitudes by α_{PLTS}:

$$\Psi_{JM}=\sum_{P,\,L,\,T,\,S}\alpha_{PLTS}\,\Psi_{JM}(P, L, T, S). \tag{2.6}$$

We shall normalize the functions $\Psi_{JM}(P, L, T, S)$ to unity; furthermore, they can be chosen in such a way that the coefficients α are all real numbers,[10] and we shall make such a choice. Thus, the quantities α are real and the sum of their squares is unity.

The functions $\Psi_{JM}(P, L, T, S)$ must be antisymmetric under the interchange of any two particles. Let f be the dimension of partition P. Then

$$\Psi_{JM}(P, L, T, S)=f^{-\frac{1}{2}}\sum_{\kappa=1}^{f}\sum_{m=-L}^{+L}\sum_{\mu=-S}^{+S}$$
$$\times(LSm\mu\,|\,LSJM)\psi_{m\kappa}(L, P)V_{\mu\kappa}(P, T, S). \tag{2.7}$$

We now turn to the wave function of the final state, $\Phi_{JM'}$. At this point we assume explicitly that neutron-neutron forces equal proton-proton forces, and that the effect of the Coulomb forces on the wave function is negligible (even though there may be a measurable effect on the energy of the state). This means that the probability amplitudes α are the same as in Ψ_{JM} (these amplitudes are, of course, independent of M in any

[8] E. P. Wigner, *Gruppentheorie und ihre Anwendung auf die Quantenmechanik der Atomspektren* (Vieweg and Son, Braunschweig, 1931, reprinted by Edwards Brothers, Ann Arbor, Michigan, 1944).

[9] E. U. Condon and G. H. Shortley, *Theory of Atomic Spectra* (Cambridge University Press, Cambridge, 1935). Unlike Condon and Shortley, the Clebsch-Gordan coefficients $(jj'mm'\,|\,jj'JM)$ used here are *defined* to vanish identically unless $m+m'=M$. Thus, a double summation over m and m', say, really reduces to a single sum.

[10] E. P. Wigner, Gött Nachr. **31**, 546 (1932).

case), and furthermore, that the space wave functions $\psi_{m\kappa}(L, P; \mathbf{r}_1, \mathbf{r}_2, \cdots, \mathbf{r}_A)$ are the same as the ones occurring in the initial state. Thus, the integrations over the space coordinates can all be reduced to the orthogonality and normalization integrals for the functions $\psi_{m\kappa}(L, P; \mathbf{r}_1, \mathbf{r}_2, \cdots, \mathbf{r}_A)$, which form an orthonormal set. Hence, we can compute the beta-decay matrix element without any detailed knowledge of the wave functions; indeed, all we shall need to know are the probability amplitudes α_{PLTS}.

We are interested in the matrix element $(\Phi_{JJ}, Y_0 \Psi_{JJ})$ which occurs in (2.5). The operator Y_0 does not involve any operations on space coordinates. Hence, this matrix element vanishes unless L and m are the same for the initial and final states. Furthermore, Y_0 is invariant under permutations of the particles [see (2.2)]. Thus, the matrix element vanishes unless the partition P and the row index κ are the same for the initial and final state. Since Y_0 is a component of a vector operator as far as the spin S is concerned, S' may differ from S by at most one unit. Similarly T' may differ from T by at most one unit. We, therefore, obtain

$$(\Phi_{JJ}, Y_0 \Psi_{JJ}) = \sum_P \sum_L \sum_{T'S'} \sum_{TS} \alpha_{PLT'S'} \alpha_{PLTS} \times (\Phi_{JJ}(PLT'S'), Y_0 \Psi_{JJ}(PLTS)), \quad (2.8)$$

where

$$(\Phi_{JJ}(PLT'S'), Y_0 \Psi_{JJ}(PLTS)) = f^{-1} \sum_{\kappa=1}^{f} \sum_{m=-L}^{+L} \sum_{\mu'=-S'}^{+S'} \sum_{\mu=-S}^{+S} (LS'm\mu' | LS'JJ) \times (LSm\mu | LSJJ) (U_{\mu'\kappa}(PT'S'), Y_0 V_{\mu\kappa}(PTS)). \quad (2.9)$$

One of the sums over μ and μ' is spurious, since μ must equal μ'.

Next we use the fact that the matrix element of a symmetric operator such as Y_0 is independent of the row index κ. Hence, we may omit the sum over κ provided we also omit the factor f^{-1} in front. Furthermore, Y_0 is the component with $\rho=0$ of a vector operator as far as the spin S is concerned. Thus, the dependence of the matrix element on the right side of (2.9) upon μ and μ' is given by the Clebsch-Gordan coefficients $(1S0\mu | 1SS'\mu')$. All these matrix elements may, therefore, be expressed in terms of the one with $\mu=\mu'=\frac{1}{2}$ (we recall that mirror nuclei beta-decays always involve odd mass number nuclei), as follows

$$(U_{\mu'\kappa}(PT'S'), Y_0 V_{\mu\kappa}(PTS)) = (1S0\mu | 1SS'\mu') \frac{(U_{\frac{1}{2}\kappa}(PT'S'), Y_0 V_{\frac{1}{2}\kappa}(PTS))}{(1S0\frac{1}{2} | 1SS'\frac{1}{2})}. \quad (2.10)$$

When we substitute (2.10) into (2.9), the sums over m, μ, and μ' can be evaluated explicitly by methods due to Racah.[11] We obtain

$$\sum_{m,\mu,\mu'} (LS'm\mu' | LS'JJ) (LSm\mu | LSJJ) (1S0\mu | 1SS'\mu') = (-1)^{J+S+L+1} (2J+1)^{\frac{1}{2}} (2S'+1)^{\frac{1}{2}} \times W(SJS'J, L1) (1J0J | 1JJJ), \quad (2.11)$$

where the W are the Racah coefficients defined in reference 11, and the last factor just cancels the Clebsch-Gordan coefficient which appears in Eq. (2.5). We define the following quantity:

$$Q(P, T'S', TS) = \frac{(2S'+1)^{\frac{1}{2}} (U_{\frac{1}{2}\kappa}(PT'S'), Y_0 V_{\frac{1}{2}\kappa}(PTS))}{(1S0\frac{1}{2} | 1SS'\frac{1}{2})}, \quad (2.12)$$

with the symmetry property

$$Q(P, TS, T'S') = (-1)^{S'-S} Q(P, T'S', TS). \quad (2.13)$$

$Q(P, T'S', TS)$ may be considered a matrix with rows labeled by $T'S'$ and columns labeled by T, S. There is one such matrix for every possible partition $P=(P, P', P'')$.

We now combine (2.5), (2.8), (2.9), (2.10), (2.11), and (2.12) to obtain the *final result:*

$$\left(\int \sigma\right)^2 = \left[\sum_P \sum_L \sum_{T'S'} \sum_{TS} (-1)^{J+S+L+1} \times (2J+1)^{\frac{1}{2}} \alpha_{PLT'S'} \alpha_{PLTS} \times W(SJS'J, L1) Q(P, T'S', TS)\right]^2. \quad (2.14)$$

We first show that this expression reduces to the one derived by Trigg[6] if we assume that there is no admixture of states belonging to partitions other than the dominant $P=(P, P', P'')=(\frac{1}{2}, \frac{1}{2}, \pm\frac{1}{2})$. That is, we assume that the probability coefficients α_{PLTS} are zero unless P is this particular partition. Since this partition contains only one multiplet, namely, $S=T=\frac{1}{2}$, the sums over P, T', S', T, and S in (2.14) all reduce to one term. Furthermore, for $S=\frac{1}{2}$ there are only two possible values of L, namely, $L=J+\frac{1}{2}$ and $L=J-\frac{1}{2}$. It is shown in the appendix that $Q=-\sqrt{6}$ for this partition, so that we get, with the notation $\alpha_{PL\frac{1}{2}\frac{1}{2}}{}^2=p_L$ (= the probability of finding orbital angular momentum L),

$$\left(\int \sigma\right)^2 = 6(2J+1)\left[\sum_{L=J-\frac{1}{2}}^{J+\frac{1}{2}} (-1)^L W(\tfrac{1}{2}, J, \tfrac{1}{2}J; L, 1) p_L\right]^2 = [J(J+1)]^{-1}\{\sum_{L=J-\frac{1}{2}}^{J+\frac{1}{2}} [J(J+1) + \tfrac{3}{4} - L(L+1)] p_L\}^2. \quad (2.15)$$

This result is the same as the one given by Trigg. As was

[11] G. Racah, Phys. Rev. **62**, 438 (1942).

mentioned in the introduction, the applicability of this formula is somewhat questionable. As long as the forces are both spin-independent and charge-independent, the orbital angular momentum L is a good quantum number and Wigner's calculation is applicable. It is believed at present that the forces are charge-independent to a good approximation, and that the main deviation from spin-independence is produced by the tensor force. Now, the tensor force has the property that its matrix elements are zero between states belonging to the partition $(\frac{1}{2}, \frac{1}{2}, \pm\frac{1}{2})$. Thus, the one additional state considered by Trigg is *not* admixed in first order by the tensor force. Rather, the tensor force admixes in first order a term belonging to partition $(\frac{3}{2}, \frac{1}{2}, \mp\frac{1}{2})$ with $T=\frac{1}{2}$ and $S=\frac{3}{2}$. For example, the main admixture to the dominant[12] $(\frac{1}{2}, \frac{1}{2}, -\frac{1}{2})$ $^2S_{\frac{1}{2}}$ state of H^3 is of type $(\frac{3}{2}, \frac{1}{2}, \frac{1}{2})$ $^4D_{\frac{1}{2}}$ (this is the state considered by Gerjuoy and Schwinger),[13] rather than of the type $(\frac{1}{2}, \frac{1}{2}, -\frac{1}{2})$ $^2P_{\frac{1}{2}}$ implied by the use of Trigg's expression (2.15). In this respect the triton is typical of all the mirror nuclei. Thus, Trigg's analysis of the data, which is based on Eq. (2.15), is open to some doubt.

We now proceed to give the values of Q, (2.12), for the partitions occurring in the wave function of the triton. The computation of these values of Q is outlined in the appendix. The dominant partition is $(\frac{1}{2}, \frac{1}{2}, -\frac{1}{2})$ corresponding to a completely symmetric space wave function and a completely antisymmetric spin-isotopic-spin wave function. This partition gives rise to only one multiplet, namely, $T=S=\frac{1}{2}$, and

$$Q(P, \tfrac{11}{22}, \tfrac{11}{22}) = -\sqrt{6} \quad \text{for} \quad P=(\tfrac{1}{2}, \tfrac{1}{2}, -\tfrac{1}{2}). \tag{2.16}$$

The next partition in order of importance is $(\frac{3}{2}, \frac{1}{2}, \frac{1}{2})$ with the three multiplets $T=S=\frac{1}{2}$; $T=\frac{1}{2}$, $S=\frac{3}{2}$; and $T=\frac{3}{2}$, $S=\frac{1}{2}$. We write Q as a matrix with rows labeled by $T'S'$ and columns labeled by TS:

Partition $(\frac{3}{2}, \frac{1}{2}, \frac{1}{2})$

$T'S'$ \ TS	$\frac{1}{2}\ \frac{1}{2}$	$\frac{1}{2}\ \frac{3}{2}$	$\frac{3}{2}\ \frac{1}{2}$
$\frac{1}{2}\ \frac{1}{2}$	$\sqrt{2}/3$	$4\sqrt{2}/3$	$-2\sqrt{2}/3$
$\frac{1}{2}\ \frac{3}{2}$	$-4\sqrt{2}/3$	$2\sqrt{5}/3$	$2\sqrt{2}/3$
$\frac{3}{2}\ \frac{1}{2}$	$-2\sqrt{2}/3$	$-2\sqrt{2}/3$	$-2\sqrt{2}/3$

(2.17)

If the forces are completely charge-independent (so far we have assumed only the equality of nn and pp forces), the total isotopic spin T is a good quantum number. In that case $T=T'=\frac{1}{2}$ and the last row and last column of the matrix (2.17) should be omitted.

The last partition which can occur in the triton is $(\frac{3}{2}, \frac{3}{2}, \frac{3}{2})$ which corresponds to a completely antisymmetric space function and a completely symmetric spin-isotopic-spin function. This partition gives rise to two multiplets, $T=S=\frac{1}{2}$ and $T=S=\frac{3}{2}$. Only the first of these occurs if the forces are charge-independent. The matrix Q is given by

Partition $(\frac{3}{2}, \frac{3}{2}, \frac{3}{2})$

$T'S'$ \ TS	$\frac{1}{2}\ \frac{1}{2}$	$\frac{3}{2}\ \frac{3}{2}$
$\frac{1}{2}\ \frac{1}{2}$	$5\sqrt{2}/3$	$-4\sqrt{1}/3$
$\frac{3}{2}\ \frac{3}{2}$	$4\sqrt{1}/3$	$-4\sqrt{(5/3)}$

(2.18)

The rest of this paper will be devoted to the triton decay. We would like to point out, however, that the partition $(\frac{3}{2}, \frac{1}{2}, \mp\frac{1}{2})$ is the dominant admixture produced by the tensor force in *all* mirror nuclei, so that (2.16) and (2.17) together with (2.14) give probably a more adequate description of mirror nuclei decays than Trigg's expression (2.15). Unfortunately, there are in general two or more states admixed in first order by the tensor force (the triton is an exception to this rule), making the analysis much more difficult in practice.

3. THE DECAY OF THE TRITON

We shall assume from the outset that the forces are charge-independent so that states with isotopic spin $T=\frac{3}{2}$ can be omitted. There are then the following states possible:[14]

$$\begin{aligned}
&\text{Partition } (\tfrac{1}{2}, \tfrac{1}{2}, -\tfrac{1}{2}): \quad {}^2S_{\frac{1}{2}} \quad {}^2P_{\frac{1}{2}}, \\
&\text{Partition } (\tfrac{3}{2}, \tfrac{1}{2}, \tfrac{1}{2}): \quad {}^2S_{\frac{1}{2}} \quad {}^2P_{\frac{1}{2}} \quad {}^4P_{\frac{1}{2}} \quad {}^4D_{\frac{1}{2}}, \\
&\text{Partition } (\tfrac{3}{2}, \tfrac{3}{2}, \tfrac{3}{2}): \quad {}^2S_{\frac{1}{2}} \quad {}^2P_{\frac{1}{2}}.
\end{aligned} \tag{3.1}$$

The first state listed is the dominant state, and is the only one present if the forces are spin- and charge-independent. The tensor force admixes in first order only the $(\frac{3}{2}, \frac{1}{2}, \frac{1}{2})$ $^4D_{\frac{1}{2}}$ state. In the next order all states are admixed, but states belonging to the completely antisymmetric partition $(\frac{3}{2}, \frac{3}{2}, \frac{3}{2})$ are high up in energy and consequently are not admixed to any appreciable extent.

For convenience of notation, we shall number the partitions by Roman numerals I, II, III. Since all states considered here have $T=\frac{1}{2}$ and $J=\frac{1}{2}$, we shall omit those symbols. Hence, the first state in (3.1) will be denoted by I^2S, the last state in the second line of (3.1) by II^4D, and so on. Their probability amplitudes will be denoted by $\alpha(\mathrm{I}^2S)$ and $\alpha(\mathrm{II}^4D)$, respectively, and their squares, the probabilities themselves, by $p(\mathrm{I}^2S)$ and $p(\mathrm{II}^4D)$. With this notation the matrix element $(\int\boldsymbol{\sigma})^2$ for the triton decay is

$$\begin{aligned}
\left(\int\boldsymbol{\sigma}\right)^2 = 3\{&p(\mathrm{I}^2S) - \tfrac{1}{3}p(\mathrm{I}^2P) - \tfrac{1}{3}p(\mathrm{II}^2S) \\
&+ \tfrac{1}{9}[p(\mathrm{II}^2P) - 5p(\mathrm{II}^4P) - 16\alpha(\mathrm{I}^2P)\alpha(\mathrm{II}^4P)] \\
&+ \tfrac{1}{3}p(\mathrm{II}^4D) \ - (5/3)p(\mathrm{III}^2S) \\
&+ (5/9)p(\mathrm{III}^2P)\}^2.
\end{aligned} \tag{3.2}$$

In the special case that the II^4D state is the *only* appreciable admixture, so that $p(\mathrm{I}^2S)=1-p(\mathrm{II}^4D)$, ex-

[12] The two superscripts on the term symbols denote the multiplicities $2T+1$ and $2S+1$, in this order.

[13] E. Gerjuoy and J. S. Schwinger, Phys. Rev. **61**, 138 (1942).

[14] The two superscripts on the left side of each state stand for the multiplicities $2T+1$ and $2S+1$, in that order.

pression (3.2) reduces to[15]

$$\left(\int\sigma\right)^2=3[1-\tfrac{8}{3}p(\mathrm{II}^4D)]^2. \tag{3.3}$$

This quantity is less than or equal to 3, no matter what the amount of admixture is. A D-state admixture of 4 percent follows from the measured magnetic moments of H^3 and He^3, if the exchange magnetic moments are assumed to be equal and opposite in these two nuclei, and if relativistic effects on the magnetic moments are ignored, the latter assumption being a rather doubtful one. If we assume a 4 percent D-state admixture for the sake of argument, the value of $(\int\sigma)^2$ is changed by roughly 5 percent, becoming 2.84 instead of 3.00. Such a 5 percent change is not much smaller than the experimental uncertainty in the ft value of the triton decay.[16] Since the amount of D-state admixture is by no means well known, and since other states may be admixed appreciably also, the value of $(\int\sigma)^2$ is quite uncertain.

We would like to point out that admixtures of $(\frac{3}{2}, \frac{1}{2}, \mp\frac{1}{2})$ states of the same order of magnitude, or even larger, may be expected in all mirror nuclei. It is quite likely that these are the dominant admixtures to the usually considered $(\frac{1}{2}, \frac{1}{2}, \pm\frac{1}{2})P$ states in the odd nuclei with mass numbers between 7 and 15. If this conjecture is correct, one should not attempt to make too detailed an analysis of the ft values of these mirror nuclei without taking this correction into account.[17] It is not apparent that the admixture correction is negligible even for those mirror nuclei which have one more or one less nucleon than some closed shell. Indeed, the triton satisfies this condition, yet the admixture correction to the matrix element is probably of the order of 5 percent, and may be a lot more than that if the magnetic moments of H^3 and He^3 are corrected for relativistic effects, which would change the D-state probability. Unfortunately, we do not know at this time how to make this correction, not even the direction of the relativistic effect; all we know is that the relativistic effect on the magnetic moment is *not* negligible compared to the admixture effect, which is not much consolation.

In view of the uncertainty in the actual value of $(\int\sigma)^2$, we think it may be useful to point out that, under very reasonable assumptions about the wave function of H^3, the true value of $(\int\sigma)^2$ is no larger than the elementary value 3. A look at expression (3.2) shows that there are only two states which can lead to larger matrix elements. One of them is the III^2S state, which would lead to $(\int\sigma)^2=25/3$ if it were the only state present. The other state is a linear combination of II^2P and II^4P obtained by diagonalizing the quadratic form in the brackets of (3.2). The eigenvalues of this quadratic form are (including the factor $\frac{1}{9}$ in front) $+0.727$ and -1.172. Only the latter of these is larger than unity. We clearly get the most unfavorable estimate if we assume that the two bad states are the *only* admixtures. Let p_1 stand for the probability of the particular mixture of II^2P and II^4P involved here, and denote $p(\mathrm{III}^2S)$ by p_2. Then $p(\mathrm{I}^2S)=1-p_1-p_2$ by assumption, and we get from (3.2)

$$\left(\int\sigma\right)^2=3(1-2.172p_1-2.667p_2)^2. \tag{3.4}$$

This can exceed 3 only if the following inequality is satisfied:

$$1.086p_1+1.333p_2\geqslant 1. \tag{3.5}$$

If p_1 is the only admixture (i.e., $p_2=0$), the state involved has to be present to the extent of at least 92 percent. The situation is a little more favorable for the III^2S state; it would have to be present to only (!) 75 percent. Conversely, *if the dominant* I^2S *state is present to at least 25 percent probability, the true value of* $(\int\sigma)^2$ *does not exceed 3.*

Because of this theorem it is very much worth while to measure the comparative half-life (ft value) of the triton decay with high accuracy, even though the true value of $(\int\sigma)^2$ is not known theoretically to anything like comparable accuracy. For such a measurement will allow us to put a very accurate *upper limit* on the product $(\int\sigma)^2ft$, which would help considerably in narrowing down the beta-decay interaction. This point is discussed in more detail in the preceding paper.

APPENDIX. SPIN- AND ISOTOPIC-SPIN FUNCTIONS FOR THE TRITON

Let α be the spin function for a particle with spin up, β the spin function for a particle with spin down. In accordance with expression (2.10) we may restrict ourselves to spin functions with $S_z=\mu=\frac{1}{2}$. There are three linearly independent functions, namely, $\alpha(1)\alpha(2)\beta(3)$, $\alpha(1)\beta(2)\alpha(3)$, and $\beta(1)\alpha(2)\alpha(3)$. These three functions form an orthonormal set. We now construct another orthonormal set with the property that members of the new set transform according to irreducible representations of the permutation group. These new functions are

$$\begin{aligned}
q_1&=6^{-\frac{1}{2}}[\beta(1)\alpha(2)+\alpha(1)\beta(2)]\alpha(3)\\
&\qquad -(2/3)^{\frac{1}{2}}\alpha(1)\alpha(2)\beta(3),\\
q_2&=2^{-\frac{1}{2}}[\beta(1)\alpha(2)-\alpha(1)\beta(2)]\alpha(3),\\
q_3&=3^{-\frac{1}{2}}[\alpha(1)\alpha(2)\beta(3)+\alpha(1)\beta(2)\alpha(3)\\
&\qquad +\beta(1)\alpha(2)\alpha(3)].
\end{aligned} \tag{A.1}$$

[15] This expression was first calculated by E. Feenberg (quoted in reference 6); a trivial mistake in sign in the formula quoted in reference 6 was corrected by Professor Feenberg in a private communication to the author.

[16] For references regarding the end-point energy and lifetime of the triton, see Hornyak, Lauritsen, Morrison, and Fowler, Revs. Modern Phys. **22**, 291 (1950).

[17] R. Nataf and R. Bouchez, Phys. Rev. **87**, 155 (1952); R. Bouchez and R. Nataf, Compt. rend. **234**, 86 (1952); O. Kofoed-Hansen and A. Winther, Phys. Rev. **86**, 428 (1952); and unpublished work by the same authors.

The function q_3 is completely symmetric under permutations of 1, 2, 3. It is the $S_z=\frac{1}{2}$ function belonging to the multiplet $S=\frac{3}{2}$ (quartet state). Since the completely symmetric representation of the permutation group is one-dimensional, there is only one such function, which transforms into itself under all permutations.

The functions q_1 and q_2 are necessary to describe the doublet ($S=\frac{1}{2}$) spin state with $S_z=\frac{1}{2}$. It should be noted that the complete doublet state for three particles cannot be written as the product of a space wave function and a spin wave function, but rather it is the sum of two such products. This should not be too surprising since, in the usual way of writing such states by means of Slater determinants, the wave function appears as a sum of even more products (the products are obtained by writing out the determinant explicitly). Under the permutation which exchanges coordinates 1 and 2, q_1 transforms into itself whereas q_2 transforms into its negative. But under all other permutations (except the identity, of course) q_1 and q_2 transform into linear combinations of each other. The matrices corresponding to the various permutations are given in Wigner's book[8] on page 63, with the notation given at the bottom of page 71.

There is no completely antisymmetric spin function among the set (A.1), corresponding to the fact that it is impossible to put three neutrons into the same space state (which would mean a completely symmetric space wave function).

If we were considering a nucleus containing three neutrons, say, the spin function q_3 would have to be multiplied by a completely antisymmetric space wave function to give an acceptable total wave function for the quartet spin state. To get a wave function for the doublet state of three neutrons, we would have to construct two space wave functions ψ_1 and ψ_2 which transform analogously to q_1 and q_2, and use them to construct a sum of two products of type $2^{-\frac{1}{2}}(\psi_1 q_2-\psi_2 q_1)$ which would then be completely antisymmetric also.

The situation is appreciably more complicated for the triton with its two neutrons and one proton. Let ν be the isotopic spin wave function for the neutron state, π be the isotopic spin wave function for the proton state. ν corresponds to $T_z=+\frac{1}{2}$, π to $T_z=-\frac{1}{2}$. We now construct three orthonormal base functions for the triton analogous to (A.1):

$$\begin{aligned} v_1&=6^{-\frac{1}{2}}[\pi(1)\nu(2)+\nu(1)\pi(2)]\nu(3)\\ &\qquad -(2/3)^{\frac{1}{2}}\nu(1)\nu(2)\pi(3),\\ v_2&=2^{-\frac{1}{2}}[\pi(1)\nu(2)-\nu(1)\pi(2)]\nu(3),\\ v_3&=3^{-\frac{1}{2}}[\nu(1)\nu(2)\pi(3)+\nu(1)\pi(2)\nu(3)\\ &\qquad +\pi(1)\nu(2)\nu(3)]. \end{aligned} \tag{A.2}$$

We must now find linear combinations of products of q's and v's which transform under permutations of the spin and isotopic spin coordinates *jointly* according to the three possible irreducible representations of the permutation group (two of these three representations are exemplified by the set (v_1, v_2) and by the one function v_3, respectively; the third representation is exemplified by a completely antisymmetric function).

We start with the completely symmetric spin-isotopic-spin functions which go along with completely antisymmetric space wave functions. Clearly one of these symmetric spin-isotopic-spin functions is the product v_3q_3 which corresponds to isotopic spin $T=\frac{3}{2}$ (because of v_3) and mechanical spin $S=\frac{3}{2}$ (because of q_3). The only other symmetric function is $2^{-\frac{1}{2}}(v_1q_1+v_2q_2)$, corresponding to isotopic spin $T=\frac{1}{2}$ (because of the occurrence of v_1 and v_2) and to mechanical spin $S=\frac{1}{2}$ (because of the occurrence of q_1 and q_2). Thus, the supermultiplet $(P, P', P'')=(\frac{3}{2}, \frac{3}{2}, \frac{3}{2})$ (meaning a completely antisymmetric space wave function) gives rise to two multiplets, namely, $T=S=\frac{3}{2}$ and $T=S=\frac{1}{2}$, with the spin-isotopic-spin wave functions $V_{\frac{1}{2},\kappa}(P, T, S)$:[18]

$$V(\mathrm{III};\tfrac{1}{2},\tfrac{1}{2})=2^{-\frac{1}{2}}(v_1q_1+v_2q_2), \tag{A.3}$$

$$V(\mathrm{III};\tfrac{3}{2},\tfrac{3}{2})=v_3q_3. \tag{A.4}$$

There is only one completely antisymmetric spin-isotopic-spin wave function, namely [we use the Roman numeral I for the partition $(\frac{1}{2}, \frac{1}{2}, -\frac{1}{2})$],

$$V(\mathrm{I};\tfrac{1}{2},\tfrac{1}{2})=2^{-\frac{1}{2}}(v_1q_2-v_2q_1). \tag{A.5}$$

It is easy to verify that this is indeed the properly normalized Slater determinant corresponding to three nucleons in the states $\nu\alpha$, $\pi\alpha$, and $\nu\beta$, respectively.

Finally, we write down the functions belonging to partition $(\frac{3}{2}, \frac{1}{2}, \frac{1}{2})$, which we shall denote by the Roman numeral II. There are two functions for each multiplet, which will be distinguished by the subscript $\kappa=1, 2$. The functions V_κ for the multiplet $T=S=\frac{1}{2}$ are

$$\begin{aligned} V_1(\mathrm{II};\tfrac{1}{2},\tfrac{1}{2})&=-2^{-\frac{1}{2}}(v_1q_1-v_2q_2),\\ V_2(\mathrm{II};\tfrac{1}{2},\tfrac{1}{2})&=2^{-\frac{1}{2}}(v_1q_2+v_2q_1). \end{aligned} \tag{A.6}$$

The signs are chosen in such a way that V_1 and V_2 transform into each other under permutations precisely in the same way as q_1 and q_2 of (A.1), or as v_1 and v_2 of (A.2).

The second multiplet in this partition is $T=\frac{1}{2}$, $S=\frac{3}{2}$ with the spin-isotopic-spin functions

$$V_1(\mathrm{II};\tfrac{1}{2},\tfrac{3}{2})=v_1q_3, \quad V_2(\mathrm{II};\tfrac{1}{2},\tfrac{3}{2})=v_2q_3. \tag{A.7}$$

Finally, we have the multiplet $T=\frac{3}{2}$, $S=\frac{1}{2}$ with the functions

$$V_1(\mathrm{II};\tfrac{3}{2},\tfrac{1}{2})=v_3q_1, \quad V_2(\mathrm{II};\tfrac{3}{2},\tfrac{1}{2})=v_3q_2. \tag{A.8}$$

Equations (A.3) through (A.8) contain nine different and mutually orthogonal functions. Since there are only nine linearly independent products v_iq_j we have exhausted all possibilities.

[18] We omit the common index $\mu=S_z=\frac{1}{2}$, and denote the partition $(\frac{1}{2}, \frac{1}{2}, \frac{1}{2})$ by the Roman numeral III for convenience as was also done in Sec. 3 of the paper. Since the representation is one-dimensional, we can omit the index κ.

We have written down these functions without indicating any method of constructing them systematically. The easiest way is by means of the Young symmetry operators (see Van der Waerden,[19] Sec. 129, or Weyl,[20] Chapter 5C). However, a detailed exposition of this method is beyond the scope of this appendix.

The spin-isotopic-spin functions U for the nucleus He^3 are obtained simply by replacing v_1, v_2, v_3 everywhere by u_1, u_2, u_3 which are defined analogously:

$$\begin{aligned} u_1 &= 6^{-\frac{1}{2}}[\nu(1)\pi(2)+\pi(1)\nu(2)]\pi(3) \\ &\qquad -(2/3)^{\frac{1}{2}}\pi(1)\pi(2)\nu(3), \\ u_2 &= 2^{-\frac{1}{2}}[\nu(1)\pi(2)-\pi(1)\nu(2)]\pi(3), \\ u_3 &= 3^{-\frac{1}{2}}[\pi(1)\pi(2)\nu(3)+\pi(1)\nu(2)\pi(3) \\ &\qquad +\nu(1)\pi(2)\pi(3)]. \end{aligned} \tag{A.9}$$

In order to calculate the matrix elements (U, Y_0V) which appear in the numerator of (2.12), we note first of all that Y_0 is a symmetric operator under permutations and, therefore, does not have matrix elements connecting different partitions. Within the same partition it connects only functions with the same value of κ, and furthermore (U_κ, Y_0V_κ) is independent of κ. As far as the z component of the mechanical spin is concerned, Y_0 connects only states with the same $S_z=\mu$, which we have chosen to be $+\frac{1}{2}$. From here on the calculation is trivial though slightly tedious, leading to the following matrices for (U, Y_0V):

Partition I: $(U, Y_0V)=1$

Partition II:

$T'S'$ \ TS	$\frac{1}{2}\,\frac{1}{2}$	$\frac{1}{2}\,\frac{3}{2}$	$\frac{3}{2}\,\frac{1}{2}$
$\frac{1}{2}\,\frac{1}{2}$	$-1/3$	$-4/3$	$2/3$
$\frac{1}{2}\,\frac{3}{2}$	$-4/3$	$-1/3$	$2/3$
$\frac{3}{2}\,\frac{1}{2}$	$2/3$	$2/3$	$2/3$

Partition III:

$T'S'$ \ TS	$\frac{1}{2}\,\frac{1}{2}$	$\frac{3}{2}\,\frac{3}{2}$
$\frac{1}{2}\,\frac{1}{2}$	$-5/3$	$8^{\frac{1}{2}}/3$
$\frac{3}{2}\,\frac{3}{2}$	$8^{\frac{1}{2}}/3$	$2/3$

(A.10)

Combination of (A.10) and (2.12) then gives the matrices $Q(P, T'S', TS)$ listed in Sec. 2 of the paper.

[19] B. L. Van der Waerden, *Moderne Algebra* (Julius Springer, Berlin, 1940); reprinted by F. Ungar Publishing Company, New York (1943).
[20] H. Weyl, *The Theory of Groups and Quantum Mechanics* (Methuen and Company, London, 1931).

PHYSICAL REVIEW VOLUME 89, NUMBER 1 JANUARY 1, 1953

The Lamb Shift for Hydrogen and Deuterium

E. E. SALPETER
Laboratory of Nuclear Studies, Cornell University, Ithaca, New York
(Received August 19, 1952)

Previous calculations of all second- and fourth-order radiative corrections, which contribute to the Lamb shift, are discussed. Further corrections to the Lamb shift in hydrogen and deuterium, resulting from the finite mass and internal structure of the nuclei, are calculated. The final theoretical results for the Lamb shift, excluding all sixth-order corrections, are (1057.19±0.16) Mc/sec for hydrogen and (1058.49±0.16) Mc/sec for deuterium. These values are about half a megacycle smaller than the corresponding experimental results

1. INTRODUCTION

THE accuracy of the experimental determination of the Lamb shift has improved considerably over the last few years. A detailed account of the experimental techniques and calculations involved in obtaining a precision measurement of the Lamb shift will be found in a series of papers entitled "Fine Structure of the Hydrogen Atom."[1-3] The total Lamb shift (denoted by S and expressed in megacycles per second) is the total energy difference between any $n\,^2S_{\frac{1}{2}}$ and $n\,^2P_{\frac{1}{2}}$ levels for a hydrogen-like atom, which coincide in the elementary Dirac theory for an electron in a Coulomb field. In the present paper we shall be mainly concerned with the case of $n=2$ for hydrogen and deuterium. For this case S is now known experimentally to within one-tenth of a megacycle.

The contributions of a large number of effects to the Lamb shift have by now been calculated by different authors. The main aim of the present paper is to summarize the results of these previous calculations and to calculate the contributions of a few more terms. Corrections to the Lamb shift of relative order α^2, $(\alpha m/M)$ and $(\alpha^{-1}m^2/M^2)$ and smaller corrections will not be treated in this paper.

The electromagnetic displacement of the energy levels of an electron bound in a fixed Coulomb potential involves an expansion in powers of α, the fine structure constant. All the terms of the lowest two orders in α

[1] W. E. Lamb and R. C. Retherford, Phys. Rev. **79**, 549 (1950); **81**, 222 (1951); **86**, 1014 (1952).
[2] W. E. Lamb, Phys. Rev. **85**, 259 (1952).
[3] Triebwasser, Dayhoff, and Lamb, Phys. Rev. **89**, 98 (1953).

have been calculated previously and the results are summarized in Sec. 2.

This electromagnetic displacement for a fixed Coulomb potential accounts for the main part of the Lamb shift. Corrections occur, however, to this displacement due to the finite mass and the internal structure of atomic nuclei. Some of the corrections due to the finite nuclear mass were calculated previously. The remaining mass corrections, to lowest order in α, are discussed in Sec. 3. Additional corrections are obtained for deuterium due to the finite size of the deuteron. These are discussed in Sec. 4. The effect of the internal structure of individual nucleons is discussed in Sec. 5. In Sec. 6 the results of these calculations are compared with the latest experimental results for the Lamb shift. A glossary of the terms discussed in the paper is given in the Appendix.

2. LAMB SHIFT FOR A FIXED COULOMB POTENTIAL

We summarize in this section the results of the calculations, carried out by various authors, of the electromagnetic level shift for a fixed Coulomb field, i.e., for an atom with an infinitely heavy nucleus without internal structure.

Two types of expansions occur in these calculations. The successive approximations in the treatment of the virtual radiation field of the elctron give an expansion in powers of α. Successive approximations made in the treatment of the Coulomb field give an expansion in powers of $Z\alpha$, where Z is the atomic number (unity in our case).

The result to lowest order, in both α and in $Z\alpha$, for a principal quantum number n of two and for unit charge Z is

$$S_\infty{}^{(1)}=\left(\frac{\alpha^3 Ry_\infty}{3\pi}\right)\left\{\left[\ln\frac{mc^2}{k_0(2,0)}-\ln 2+\frac{5}{6}\right]-\frac{1}{5}-\left[\ln\frac{Ry_\infty}{k_0(2,1)}-\frac{3}{8}\right]\right\}. \quad (1)$$

Ry_∞ is the Rydberg energy for infinite nuclear mass, m is the electronic mass and the two expressions k_0 are "average excitation energies," defined and calculated by Bethe, Brown, and Stehn.[4] The first term in square brackets in Eq. (1) comes from the shift of the $2S_{\frac{1}{2}}$ level, excluding the effect of vacuum polarization. The term involving $(-\frac{1}{5})$ is the contribution of vacuum polarization to the shift of the $2S_{\frac{1}{2}}$ level. The last term in square brackets comes from the shift of the $2P_{\frac{1}{2}}$ level.

In deriving Eq. (1), virtual photons of "low" and "high" momentum are treated in different ways. The low momentum part is calculated by means of the nonrelativistic method of Bethe,[5] using explicit atomic wave functions. These calculations[4] give

$$k_0(2,0)=(16.646\pm 0.007)Ry_\infty$$

and

$$k_0(2,1)=(0.9704\pm 0.0002)Ry_\infty.$$

For the high momentum part the electron is treated relativistically but plane wave approximations are used in intermediate states. This relativistic calculation, leading to Eq. (1), was carried out by various methods.[6,7]

Precision values for the fine structure constant α can now be obtained from measurements of fine structure[8] and of hyperfine structure. In view of the present uncertainty in the theoretical interpretation[9] of the hyperfine structure measurement, we write

$$1/\alpha=137.0360+\epsilon_\alpha. \quad (2)$$

The correction term ϵ_α should lie between ± 0.002.

Using a value of $(299{,}790.9\pm 1.0)$ km/sec for the velocity of light,[10] the value of the "Lamb constant" L, in frequency units, is

$$L\equiv(\alpha^3/3\pi)Ry_\infty c=(135.6431-3\epsilon_\alpha\pm 0.0005)\text{ Mc}. \quad (3)$$

The value[4] of the term in parenthesis in Eq. (1) is (7.7567 ± 0.0005). This gives for the Lamb shift to lowest order,

$$S_\infty{}^{(1)}=(1052.14-22\epsilon_\alpha\pm 0.07)\text{ Mc}. \quad (4)$$

This value of $S^{(1)}$ includes a contribution of -27.13 Mc from the vacuum polarization and $\frac{1}{2}L=+67.82$ Mc from the anomalous magnetic moment of the electron.

The next term in the expansion in powers of $Z\alpha$ (Coulomb potential acting twice, etc.) has been calculated by Baranger and others.[11] This term, including the effect of vacuum polarization, is $S^{(2,\,2)}=+7.14$ Mc. The The next term in the expansion in powers of α (two virtual photons) consists of three parts: (a) The fourth-order anomalous magnetic moment of the electron[12] contributes -0.94 Mc to S; (b) the fourth order vacuum polarization[13] contributes -0.24 Mc; and (c) the remaining fourth order radiative correction[14] terms $(+0.24\pm 0.10)$ Mc. The sum of these terms of order α and $Z\alpha$ times $S^{(1)}$ is then

$$S^{(2)}=(6.20\pm 0.10)\text{ Mc}. \quad (5)$$

No terms of relative order α^2, $Z\alpha^2$, $Z^2\alpha^2$ or of higher order have been calculated as yet. Since the term of

[4] Bethe, Brown, and Stehn, Phys. Rev. **77**, 370 (1950).
[5] H. A. Bethe, Phys. Rev. **72**, 339 (1947).
[6] N. M. Kroll and W. E. Lamb, Phys. Rev. **75**, 388 (1949); J. B. French and V. F. Weisskopf, Phys. Rev. **75**, 1240 (1949); J. Schwinger, Phys. Rev. **76**, 790 (1949).
[7] R. P. Feynman, Phys. Rev. **76**, 769 (1949).
[8] Dayhoff, Triebwasser, and Lamb, Phys. Rev. **89**, 106 (1953).
[9] R. Karplus and A. Klein, Phys. Rev. **85**, 972 (1952); N. M. Kroll and F. Pollock, Phys. Rev. **86**, 876 (1952); E. E. Salpeter and W. A. Newcomb, Phys. Rev. **87**, 150 (1952).
[10] J. W. M. DuMond and E. R. Cohen, Phys. Rev. **82**, 555 (1951).
[11] M. Baranger, Phys. Rev. **84**, 866 (1951); Karplus, Klein, and Schwinger, Phys. Rev. **86**, 288 (1952).
[12] R. Karplus and N. M. Kroll, Phys. Rev. **77**, 536 (1950).
[13] Baranger, Dyson, and Salpeter, Phys. Rev. **88**, 680 (1952).
[14] Bersohn, Weneser, and Kroll, Phys. Rev. **86**, 596 (1952).

relative order $Z\alpha$, $S^{(2,\,2)}$, is numerically much larger than might be expected, the term of order $Z^2\alpha^2$ may still be appreciable. We denote the contribution of this term to the Lamb shift by $S_Z{}^{(3)}$, that of the remaining terms which have not been calculated yet by S_R. The final result for the Lamb shift for a fixed Coulomb potential ($n=2$, $Z=1$) is then

$$S_\infty=(1058.34-22\epsilon_\alpha+S_Z{}^{(3)}+S_R\pm 0.12)\text{ Mc}. \quad (6)$$

3. MASS CORRECTIONS

Corrections to the fine structure of hydrogen of order $\alpha(m/M)(FS)$, due to the finite mass M of the proton, were calculated in a previous paper.[15] These terms are connected with Feynman diagrams (e.g., the exchange of two virtual photons between the electron and proton) which are quite different from the Feynman diagrams corresponding to the Lamb shift itself and to the effect of vacuum polarization. These terms have, however, different magnitudes for the $2S_{\frac{1}{2}}$ and $2P_{\frac{1}{2}}$ levels. They contribute therefore to the Lamb shift, as measured experimentally, and are of order $(m/M)S$. For hydrogen, these terms give a level shift of $+0.379$ Mc for the $2S_{\frac{1}{2}}$-state and -0.017 Mc for the $2P_{\frac{1}{2}}$-state. The contribution to the Lamb shift is thus $+0.396$ Mc. If the internal structure of the deuteron is neglected, then these terms are exactly half as big for deuterium as for hydrogen. Neglecting deuteron structure introduces an error of about ten percent for these terms.

We next have to apply reduced mass corrections to the expression (6) for S_∞ to correct for the finite mass of the nucleus. We shall only apply these corrections to the main term $S^{(1)}$, Eq. (4).

In principle these corrections could be obtained by calculating the Lamb shift as a whole by means of a four-dimensional covariant wave equation for the bound states of a two-body system, discussed previously.[16] This method would be similar to, but more complicated than, the Feynman method[7] for evaluating the Lamb shift. For instance, the operator, defined in Eq. (12) of reference 7, occurs in both methods. In the Feynman method the expectation value of this operator is taken, using the usual three-dimensional wave functions and the matrix elements of this operator are only required between states of the electron, which satisfy the Dirac equation (in a calculation to lowest order in $Z\alpha$). In the other method the expectation value of this operator is required using the four-dimensional wave functions of the two-body system, and matrix elements are also required for states not satisfying the Dirac equation.

But for the Lamb shift, in lowest order in $Z\alpha$, the nucleus interacts with the electron only once and no "energy denominators" involving the nucleus occur in the expression. Hence the mass of the nucleus enters only in a simple way and its effect can be obtained quite easily by analyzing the usual calculations for a fixed Coulomb potential.

We first consider Bethe's[5] nonrelativistic calculation for the "low momentum" part of the Lamb shift. Let M be the mass of the nucleus, m the electronic mass, and μ the reduced mass of the electron. We transform to the system in which the center of mass is at rest. In this system, the electron momentum $\mathbf{p}_e$ and the momentum of the nucleus $\mathbf{p}_N$ are equal and opposite. After the elimination of the center of mass, the Schrödinger equation involves the reduced mass μ and the "relative momentum" $\mathbf{p}$. Now $\mathbf{p}=\mu\mathbf{v}$, where $\mathbf{v}$ is the relative velocity. $\mathbf{p}_e$ is equal to m times the "absolute electron velocity," $(M/m+M)\mathbf{v}$. Thus $\mathbf{p}$ is exactly equal to $\mathbf{p}_e$.

In Bethe's calculation the Dirac matrix $\boldsymbol{\alpha}$ for the electron is replaced by the velocity of the electron, which is $\mathbf{p}_e/m$. The expression obtained is then proportional to [see Eq. (5) of reference 5]

$$\frac{1}{m^2}\int dk\sum_n \frac{|\langle 0|\mathbf{p}_e|n\rangle|^2(E_n-E_0)}{(E_n-E_0+k)}. \quad (7)$$

In Eq. (7) k is the energy of the virtual photon, E_0 is the energy eigenvalue of the Schrödinger equation (which involves the reduced mass μ and relative coordinates and momenta) for the state considered, E_n the energy for any other state.

Since $\mathbf{p}_e$ is equal to the relative momentum $\mathbf{p}$, all the quantities in the integral in Eq. (7), excluding the multiplying factor m^{-2}, refer to the Schrödinger equation involving the reduced mass μ. This integral is then exactly equal to the equivalent integral for a particle of mass μ in a fixed Coulomb potential. The value of this integral contains the cube of μ as a factor (this factor comes from the square of the atomic wave function). We therefore have to multiply the main (nonrelativistic) part of $S_\infty{}^{(1)}$ by the factor[16]

$$(\mu/m)^3\approx(1-3m/M). \quad (8)$$

The quantities Ry, $k_0(2,0)$ and $k_0(2,1)$ inside the parentheses in Eq. (1) also come from this nonrelativistic treatment and are all proportional to the first power of the mass. Hence these quantities have to be multiplied by (μ/m), i.e., the value of Ry for the reduced mass μ has to be taken. The remaining terms in the parenthesis in Eq. (1), including the quantity mc^2, come from the "high momentum" calculations.

In the Feynman method[7] these terms are evaluated by first calculating the Fourier transform, $A_\nu(\mathbf{q})$ of the electrodynamic potential of the nucleus for a momentum change $\mathbf{q}$. The radiative corrections to the scattering of an electron in such a potential are then evaluated, [see Eq. (24) of reference 7]. If the nucleus is given a finite mass the form of $A_4(\mathbf{q})$ is altered slightly and a small transverse component of the potential, $\mathbf{A}(\mathbf{q})$ is introduced. In Eq. (24) of reference 7 the true electron

[15] E. E. Salpeter, Phys. Rev. **87**, 328 (1952).

[16] In reference 4 this factor was given incorrectly as $(1-m/M)$.

mass m occurs, independent of the form of the potential and hence of the nuclear mass. For a fixed value of q the ratio of the radiative correction potential to $A_\nu(\mathbf{q})$ is proportional to q^2 and independent of the percentage of transverse component for all terms, except that due to the anomalous magnetic moment. For these main terms then the dependence of the atomic wave function and of $A_4(\mathbf{q})$ on the nuclear mass results in exactly the factor of Eq. (8) multiplying the Lamb shift expression for infinite mass. Furthermore the factor mc^2 inside the logarithm in the parenthesis in Eq. (1) comes from Eq. (24) of reference 7 and involves the true electron mass, whereas the factor $k_0(2, 0)$ involves the reduced mass μ, as discussed above. We therefore have to add to the parenthesis a term

$$\log(m/\mu)\approx(+m/M).$$

The contribution of $(\frac{1}{2})L$ to $S^{(1)}$ from the anomalous magnetic moment of the electron, on the other hand, depends in a more critical way on the small transverse component of A_ν and the factor of Eq. (8) does not apply to this term. The correct factor for this term has not yet been calculated, and we write it in the form[17]

$$[1-(1+\epsilon_\mu)m/M], \tag{9}$$

where ϵ_μ should be between ± 2. The total reduced mass correction to $S^{(1)}$ is then, to lowest order in m/M,

$$(m/M)[-3S^{(1)}+(2-\tfrac{1}{2}\epsilon_\mu)L]. \tag{10}$$

The reduced mass corrections to the fourth-order contributions to the Lamb shift, $S^{(2)}$, have not been calculated yet but should be between ± 0.030 Mc for hydrogen and ± 0.015 Mc for deuterium. The contribution of Feynman diagrams in which the nucleus (instead of the electron) emits and reabsorbs a virtual photon are of order $(m/M)^2S$ and hence negligible. Adding the terms calculated previously[15] and expression (10), the total correction to S due to the finite nuclear mass is, for hydrogen and deuterium, respectively,

$$\Delta S_H=-[1.175+0.037\epsilon_\mu\pm 0.030]\text{ Mc}, \tag{11a}$$

$$\Delta S_D=-[0.588+0.019\epsilon_\mu\pm 0.030]\text{ Mc}. \tag{11b}$$

4. EFFECT OF DEUTERON RADIUS

We consider next the effect of the finite size of the deuteron on the electrostatic, nonrelativistic, potential energy of the atomic states of deuterium. We first calculate this effect assuming the atomic electron to be centered on the center of mass of the deuteron and will justify this assumption later.

Let r be the distance of the proton from the center of mass of the deuteron ($2r$ is the relative distance) and γ^{-1} the "deuteron radius," $(4.314\pm 0.004)\times 10^{-13}$ cm. Let $\Phi(r)$ be r times the deuteron wave function, normalized such that $u(r)=e^{-2\gamma r}$ is its asymptotic expression. Let $\Delta V(r)$ be the difference between the electrostatic potential energy of an electron at a distance r from the center of the deuteron charge distribution and the equivalent energy for a point charge nucleus. This correction potential is

$$\Delta V(r)=+e^2N\int_r^\infty dy\Phi^2(y)[r^{-1}-y^{-1}];$$

$$N^{-1}=\int_0^\infty dr\Phi^2(r). \tag{12}$$

Since $\Delta V(r)$ is appreciable only for values of r very small compared with the atomic Bohr radius, a very accurate approximation to the expectation value $\langle\Delta V\rangle$ of this operator is obtained by replacing the atomic wave function $\psi(\mathbf{r})$ by its value at the origin $\psi(0)$,

$$\langle\Delta V\rangle=|\psi(0)|^2\int d^3r\Delta V(r)=(2\pi e^2/3)|\psi(0)|^2\langle r^2\rangle;$$

$$\langle r^2\rangle=N\int_0^\infty dr r^2\Phi^2(r). \tag{13}$$

Equation (13) and an approximation for $\langle r^2\rangle$ was derived previously by Karplus *et al.*[11] The normalization factor N is equal to $4\gamma(1-\gamma r_{0t})^{-1}$, where r_{0t} is a particular form of the effective range of the triplet neutron-proton potential which can be derived[18] from low energy experiments and depends slightly on the assumed shape of the nuclear potential. The integral in Eq. (13) has been calculated using various explicit deuteron wave functions corresponding to different potential shapes. Its value is equal to the "zero range value" (Φ replaced by u), $(1/8\gamma^2)$, times a factor F. F is very close to unity, since the integrand has its maximum outside the range of nuclear forces where Φ is nearly equal to its asymptotic expression u. The product $F(1-\gamma r_{0t})^{-1}$ was found to depend very little on the potential shape, being about 1.60 for a square well and 1.62 for a Yukawa potential. We adopt a value of (1.61 ± 0.05), the error comming from the uncertainty in r_{0t} and in the potential shape. Since $\langle\Delta V\rangle$, Eq. (13), is zero for the $2P$-state but not for the $2S$-state, it contributes to the Lamb shift in deuterium as measured experimentally an amount

$$\langle\Delta V\rangle=+(0.733\pm 0.025)\text{ Mc}. \tag{14}$$

We now have to justify the assumption, made in the derivation of (14), that the electron wave function can be considered to be centered on the center of mass of the deuteron instead of on the proton. We consider the problem in momentum space. Let $\varphi(\mathbf{p})$ be the atomic wave function in momentum space, i.e. the Fourier transform of $\psi(\mathbf{r})$, and a_0 the atomic Bohr radius. Then $\varphi(\mathbf{p})$ falls off rapidly, approximately as p^{-4}, with in-

[17] With $\epsilon_\mu=0$, Eq. (9) is the reduced mass factor for the fine structure, to which this term bears some similarity; G. Breit and G. E. Brown, Phys. Rev. **74**, 1278 (1949).

[18] J. M. Blatt and J. D. Jackson, Phys. Rev. **76**, 18 (1949); H. A. Bethe, Phys. Rev. **76**, 38 (1949); E. E. Salpeter, Phys. Rev. **82**, 60 (1951).

creasing p for $pa_0 \gg \hbar$. The Fourier-transform of the Coulomb potential for a momentum change $\mathbf{q}$ is proportional to q^{-2}. The Fourier transform $\Delta V(\mathbf{q})$ of $\Delta V(\mathbf{r})$ is proportional to a function of the order of magnitude of $(q^2+\hbar^2\gamma^2)^{-1}$, i.e., it is roughly constant up to momenta of the order of magnitude of $\hbar\gamma$ or about 50 Mev/c. The centering of the atomic wave function on the center of mass of the deuteron is a good approximation[19] for momenta p, such that the corresponding electron kinetic energy is very small compared with the deuteron binding energy, i.e., $p \ll 2$ Mev/c. The expression for $\langle \Delta V \rangle$ in momentum space is

$$\int\int d^3p d^3q \varphi^*(\mathbf{p}) \Delta V(\mathbf{q}) \varphi(\mathbf{p}+\mathbf{q}). \tag{15}$$

Since $p^2\varphi(p)$ decreases as p^{-2} for $p \gg \hbar/a_0 \sim 5$ kev, the main contribution to this integral comes from p, $q \lesssim \hbar/a_0 \ll 2$ Mev/c. The error involved in our assumption about the centering of the wave function is then only of the relative order of ($hc/a_0 2$ Mev) or less than one percent. In Eq. (15) $\Delta V(\mathbf{q})$ could be replaced by its value for $q=0$, which would lead exactly to Eq. (13). The conclusions in the present case are thus entirely different from those for the effect of deuteron radius on hyperfine structure.[19] In the latter case $\Delta V(\mathbf{q})$ is replaced by an *increasing* function of q and the main contribution to the equivalent integral comes from *large* values q, for which our centering approximation would not hold.

We have only calculated the expectation value of the correction potential $\Delta V(\mathbf{r})$ and have neglected radiative corrections to it. Working in momentum space and using Eq. (24) of reference 7 it can be shown that these radiative corrections are smaller than the expectation value by a factor of the order of $\alpha^2 \log\alpha$ and are thus negligible. As discussed previously,[15] the structure of the deuteron also affects the mass corrections to the fine structure slightly. These effects contribute the error of about ± 0.02 Mc to the deuterium Lamb shift mentioned in Sec. 3.

5. EFFECT OF INTERNAL STRUCTURE OF A NUCLEON

We have so far assumed neutrons and protons to be point-particles of the Fermi-Dirac type without any internal structure. In reality nucleons must behave rather differently, since they have a strong interaction with a virtual meson field. This interaction presumably gives rise to (a) the anomalous magnetic moment, (b) a spread of electric charge and magnetic moment over distances of the order of the meson Compton wave length, and (c) more complicated relativistic effects. In this section we discuss the order of magnitude of these structure effects without arriving at reliable quantitative results.

[19] F. Low, Phys. Rev. **77**, 361 (1950).

We first discuss effect (a), considering the anomalous magnetic moment μ_{an} of a nucleon as a given Pauli type moment, without considering the origin of this moment or its spatial spread. This moment of course gives a large, spin dependent, contribution to the hyperfine structure. But it was shown by Foldy[20] that such a moment produces an additional small potential, which is independent of spin direction. The additional potential energy operator $U(\mathbf{r})$, for the hydrogen atom, due to the anomalous proton moment $\mu_{p,\,an}$, is then

$$U(\mathbf{r}) = 4\pi\mu_{p,\,an}(e^2/4M_p^2)\delta^{(3)}(\mathbf{r}). \tag{16}$$

The level shift $\langle U \rangle$ due to this potential is zero for all states of nonzero orbital angular momentum and $+0.025$ Mc for the $2S$-state of hydrogen. Since the anomalous moments of the proton and neutron are almost equal and have opposite sign, the corresponding level shift in deuterium is negligible.

For hydrogen a potential similar to Eq. (16) is also produced by the Dirac part of the proton magnetic moment. This potential is the "Darwin term"[21,22] for a proton and would contribute 0.006 Mc to the $2S$-level shift. This term is of order $(m/M)^2\times$(fine structure) and is only one of several terms of this order, which have not been calculated yet and we omit it for the sake of consistency.

We consider next effects of type (b). The mesonic charge cloud around a nucleon is presumably spread over a radius of the order of the meson Compton wave length λ (about 10^{-13} cm). This spread of charge produces a small electrostatic correction potential (similar to that discussed in Sec. 4), which is appreciable only at distances of the order of λ or less. Foldy's term, Eq. (16), is a partial approximation to this potential. The Fourier transform of this potential for momentum changes q small compared with (meson mass)$\times c$ must be practically independent of q and proportional to the spatial volume integral of the potential. It is just this Fourier transform for small values of q which is measured in experiments on the electron-neutron interaction. The latest experimental value[23] for the spatial volume integral of this potential is

$$(4\pi r_0^3/3)(4100 \pm 1000) \text{ ev}. \tag{17}$$

Although Foldy's potential, Eq. (16), is only an approximation,[24] its volume integral agrees exactly with the experimental value, Eq. (17). Since this potential is appreciable only over distances much smaller than the atomic Bohr radius, the level shift due to it depends only on the volume integral (and not on the shape) of this potential and the value of 0.025 Mc calculated above should be a good approximation.

[20] L. L. Foldy, Phys. Rev. **83**, 688 (1951).
[21] C. G. Darwin, Proc. Roy. Soc. (London) **A118**, 654 (1928).
[22] L. L. Foldy and S. A. Wouthuysen, Phys. Rev. **78**, 29 (1950).
[23] Hamermesh, Ringo, and Wattenberg, Phys. Rev. **85**, 483 (1952).
[24] B. D. Fried, Phys. Rev. **86**, 434 (1952); S. Borowitz, Phys. Rev. **86**, 567 (1952).

If a reliable meson theory were available, effects on the atomic fine structure of type (*c*), (as well as of *b*), could be calculated. Such effects arise from processes in which a nucleon emits a virtual meson, which interacts electromagnetically with the atomic electron and is subsequently reabsorbed by the nucleus. These effects give rise to the anomalous nucleon magnetic moments and hence to the potential, Eq. (16), and to the spread of the charge. These effects could, however, also give rise to relativistic modifications, e.g., potentials whose Fourier-transforms are proportional to positive powers of the momentum q (up to $q\sim 100$ Mev/c). Such potentials would not be observed in the usual experiments on the neutron-electron interaction, since only very small (on a nuclear scale) values of q are involved. In an atom, however, the atomic electrons have a small, but finite, probability for having very large momenta. There is thus a possibility that such relativistic structure effects will contribute appreciably to the level shift, but contributions of more than a small fraction of a megacycle seem unlikely.

It seems likely that all structure effects (except for the Darwin term, which we neglect) will be of opposite sign and approximately equal for the neutron and proton. We therefore neglect nucleon structure effects for the Lamb shift in deuterium. In hydrogen we use a shift of $+(0.025+\epsilon_{st})$ Mc, where ϵ_{st} denotes the additional effects, mentioned but not calculated in this section.

6. RESULTS

The final results for the theoretical values for the Lamb shift in hydrogen and deuterium are

$$S_H=[1057.19-22\epsilon_\alpha+S_Z^{(3)}+S_R-0.04\epsilon_\mu+\epsilon_{st}\pm 0.13]\text{ Mc}, \quad (18a)$$

$$S_D=[1058.49-22\epsilon_\alpha+S_Z^{(3)}+S_R-0.02\epsilon_\mu\pm 0.13]\text{ Mc}, \quad (18b)$$

as compared with the latest experimental results.[3]

$$S_H=(1057.77\pm 0.10)\text{ Mc}, \quad (19a)$$

$$S_D=(1059.00\pm 0.10)\text{ Mc}. \quad (19b)$$

The theoretical value for the difference between the level shifts in deuterium and hydrogen is

$$S_D-S_H=(1.296+0.019\epsilon_\mu-\epsilon_{st}\pm 0.035)\text{ Mc}, \quad (20)$$

as compared with the experimental result[3]

$$S_D-S_H=(1.23\pm 0.15)\text{ Mc}. \quad (21)$$

There is thus a discrepancy of about half a megacycle between the present theoretical and experimental values for the Lamb shift, both in hydrogen and in deuterium. The present uncertainty in ϵ_α and ϵ_μ only increases the numerical error in Eqs. (18a) and (18b) to about ± 0.16 Mc. The good agreement between the theoretical and experimental values for (S_D-S_H), Eqs. (20) and (21), indicates that ϵ_{st} is not very large and that the discrepancy is probably not due to any effects which depend on the structure or mass of the nucleus.

This discrepancy between the theoretical and experimental level shifts is about three times the probable error and is as yet unresolved. It may (if not due to some theoretical or experimental error) be due to the sixth order corrections (the bulk of $S_Z^{(3)}+S_R$) being of the order of magnitude of $+\frac{1}{2}$ Mc, which would mean that some of these terms contain surprisingly large numerical coefficients. A precision measurement of the Lamb shift in singly ionized helium would throw some light on the charge dependence of any such large terms.

I am indebted to Professors H. A. Bethe, L. L. Foldy, R. Karplus, N. M. Kroll, and W. Lamb, and to Dr. S. Triebwasser for stimulating discussions and for the communication of unpublished results.

APPENDIX

For the convenience of the reader we give below a short glossary of the various terms discussed in this paper, the section in which they are defined and their contribution to the Lamb shift.

Section	Symbol	Meaning	Contribution to Lamb shift
2	$S_\infty^{(1)}$	All second-order radiative corrections for an infinitely heavy nucleus.	(1052.14±0.08) Mc
2	ϵ_α	Error in the value assumed for the fine structure constant.	±0.05 Mc
2	$S^{(2)}$	All fourth-order corrections.	(6.20±0.10) Mc
2	$S_Z^{(3)}$	Sixth-order corrections of highest order in Z.	unknown
2	S_R	All remaining radiative corrections for an infinitely heavy nucleus.	unknown
3	ΔS_H	Effect of nuclear mass on the level shift in hydrogen.	−(1.175±0.08) Mc
3	ϵ_μ	Error in the reduced mass correction factor for the contribution from the electron's anomalous magnetic monent.	±0.08 Mc (H) ±0.04 Mc (D)
4	ΔV	Effect of the finite deuteron radius.	(0.733±0.025) Mc
5	U	Effect of the electron-nucleon interaction for hydrogen.	(0.025±0.005) Mc
5	ϵ_{st}	Additional effects of the structure of a nucleon.	unknown

Fine Structure of the Hydrogen Atom. V* †

SOL TRIEBWASSER,‡ EDWARD S. DAYHOFF,§ AND WILLIS E. LAMB, JR.‖
Radiation Laboratory, Columbia University, New York, New York
(Received September 15, 1952)

Improvements in apparatus and techniques of measurement of the $2^2S_{\frac{1}{2}}-2^2P_{\frac{1}{2}}$ level shifts in hydrogen and deuterium are described. The more accurate results are $\$_H=1057.77\pm0.10$ Mc/sec and $\$_D=1059.00\pm0.10$ Mc/sec. These values are compared with results of quantum electrodynamic calculations.

The shape of the resonance curves has been examined in great detail and compared with theory. Assuming the theoretical value of the radiative width and hyperfine splittings, excellent agreement is obtained. Further, if only the radiative width is assumed, measurements on hydrogen reported here confirm theoretical hyperfine splittings to within 0.28 Mc/sec. Since contributions of the hyperfine structure of the $2S$ level have been measured to far greater accuracy, these results constitute a confirmation of the $2P$ hyperfine splittings to an accuracy of 1.0 percent.

INTRODUCTION

THIS is the fifth[114] paper of a series reporting on measurements[115] of the transition frequencies between the S and P states of the $n=2$ level of hydrogen and deuterium. The transitions with which we are concerned, from which the $2^2S_{\frac{1}{2}}-2^2P_{\frac{1}{2}}$ level shift $\$$ is found, are shown in Fig. 57.

It was estimated from the average deviations of the mean of individual runs reported in Part IV that, aside from possible uncertainties of theoretical corrections, the center of any resonance being observed could be measured to a precision of 1 part in 1000 of the line width. On the other hand, the disagreement among the various runs was well outside[116] of this accuracy. Due to the necessity of time consuming calculations of various corrections in Parts III and IV in order to evaluate $\$$ from the recorded data, a considerable amount of data had been accumulated before this situation became apparent.

Our initial efforts to resolve the discrepancy between internal and external consistency were directed toward a modification of the apparatus and the experimental procedure which would permit the elimination of some of the lengthy, and at times uncertain, corrections which previously were applied to the data. In addition, the problem of magnetic field calibration was examined for possible systematic or excessive random error.

R. MODIFICATIONS IN APPARATUS AND PROCEDURE

85. Rf Power and Frequency Stabilization

In the original technique for taking a run, the oscillator producing the transitions was allowed to drift slowly both in power and frequency, readings on both being taken at reasonable intervals. Corrections for these were applied to the data at some later time. For the present work a frequency regulator was developed[117] which kept the frequency within 5 kc/sec of the nominal value throughout the run. The power drift problem was solved simply by using a finely controlled attenuator of conventional design which was varied manually so as to keep constant the power monitor crystal current. Slow drifts in crystal calibration were observed but did not introduce any error as they were small and fairly uniform.

86. Elimination of "Soft" β-Component

The αe resonance was measured at a midfield of about 1159 gauss. This was sufficiently near to the βe crossing point (about 574 gauss) so that only a small percentage of the metastable atoms reaching the detector were in the β-state. Corrections discussed in Part IV, Sec. 73, were applied for residual β-state atoms. It was desired to eliminate this correction by removing even this small fraction of unwanted atoms. A small electric field in the proper direction was sufficient to quench the β-state atoms since the βf crossing point is very close (about 1190 gauss). As shown in Table VI of Part III, the electric field required lies in the z direction (π-polarization). To obtain this, a pair of plane electrodes was added between the bombarder and the rf interaction region.[118] All αe data were taken

* Work supported jointly by the Signal Corps and ONR.

† Submitted by Sol Triebwasser in partial fulfillment of requirements for the degree of Doctor of Philosophy in the Faculty of Pure Science, Columbia University.

‡ Present address: Watson Scientific Computing Laboratory, Columbia University, New York, New York.

§ Present address: National Bureau of Standards, Central Radio Propagation Laboratory, Microwave Standards Section, Washington, D. C.

‖ Present address: Department of Physics, Stanford University, Stanford, California.

[114] Paper I, Phys. Rev. **79**, 549 (1950); Paper II, Phys. Rev. **81**, 222 (1951); Paper III, Phys. Rev. **85**, 259 (1952); Paper IV, Phys. Rev. **86**, 1014 (1952). Frequent references to these papers are made. Chapters, sections, figures, equations, tables, appendices, and footnotes of Part V are numbered consecutively after those of I–IV. The designation of states by letters α, β, a, b, c, d, e, f is explained in Fig. 14 of Part I, partially reproduced in Fig. 57 for convenience.

[115] Earlier results were reported as follows: $\$=1000\pm100$ Mc/sec, W. E. Lamb, Jr., and R. C. Retherford, Phys. Rev. **72**, 241 (1947); $\$=1062\pm5$ Mc/sec, Phys. Rev. **75**, 1325 (1949); $\$_H=1058.27\pm1.0$ Mc/sec, $\$_D=1059.71\pm1.0$ Mc/sec in Part IV, Phys. Rev. **86**, 1014 (1952). Part II describes the apparatus used in the measurements reported here.

[116] See Table XVI, Part IV.

[117] E. S. Dayhoff, Rev. Sci. Instr. **22**, 1025 (1951).

[118] See Fig. 27, Part II.

in the presence of this "low voltage quenching" field. As described in Sec. 73 of Part IV, by measuring the quenching produced by these additional electrodes as a function of the applied field one can calculate the field required to quench adequately the "soft" β-component of the metastable beam. The electric field used in all of the αe runs taken was 4.6 volts/cm.

87. Rf Lines

The αf transition required an rf electric field with polarization perpendicular to the magnetic field. The earlier measurements were taken with a transmission line whose electric polarization was predominantly π, with σ-fields obtained only from the fringing of the field. In addition, the αf transition could not be taken at a sufficient separation in field from the αe peak to avoid overlap from that transition. The result was a line shape complicated by magnetic field inhomogeneity and relatively uncertain overlap. The measurements reported here were taken with transmission lines whose predominant polarizations were the desired ones for each of the transitions: σ for αf, π for αe.

The σ-polarization line is actually a modified coaxial cavity resonator in which the center conductor does not quite extend to the end plate, thereby leaving a gap through which the metastable atoms can pass. This arrangement is shown in Fig. 58. The cavity resonator is entirely inside the vacuum envelope and tuning is accomplished from the outside by means of an "O-Ring" sliding joint. The resonator part of the structure is entirely gold-plated to simplify the cleaning of surfaces exposed to the beam. This resonator has

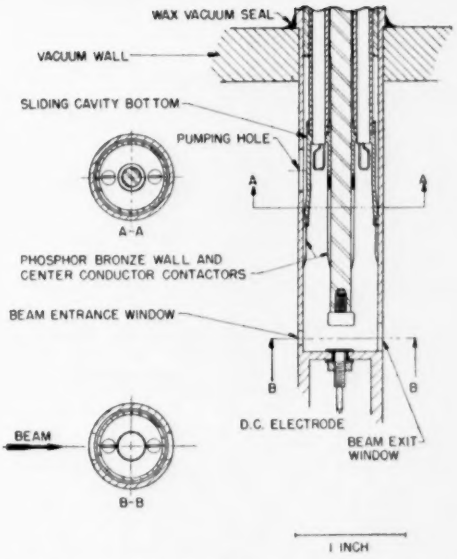

FIG. 58. Rf line used for the observation of σ-transitions. The static magnetic field is perpendicular to the plane of the drawing, while the beam of metastable atoms passes from left to right in the plane of the drawing.

a relatively high Q factor over the range from 1600 Mc/sec to 11,000 Mc/sec and consequently requires very little excitation power. The reduced power requirement in turn proved to be a major advantage at the higher frequencies where the other rf lines that had been constructed for this experiment were very inefficient. All of the αf data reported in this paper as well as the αa and αc data to be reported in Part VI were taken with this line.

The rf electric field of this line has a high degree of symmetry, possessing only the σ-components at all points along the center line of the beam. Atoms near the sides of the beam experience a small π-field component. From observations of the relative strengths of the αe and αf transitions at 1615 Mc/sec, it is estimated that the effective ratio of σ to π intensities is 10 to 1.

The π-polarization line shown in Fig. 59 was used for the αe measurements reported here. It differs only in detail from the line used for all measurements reported in Part IV. The rf and dc plates are equal in size and symmetrically placed about the axis of the rf line. The dc plate is provided with a solid metal back which is separated from the wall of the rf line by a 2-mil thick Teflon strip which has sufficient capacitance to act as a return path to ground for the rf current. The line is terminated below the interaction region in a crystal load whose current is used to monitor the rf power.

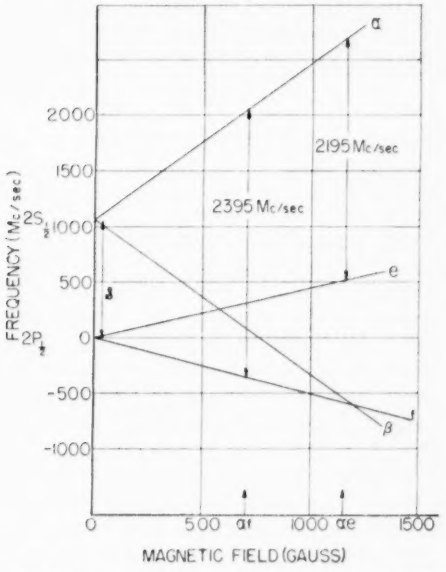

FIG. 57. Energy levels as a function of magnetic field for the $2^2S_{\frac{1}{2}}$ and $2^2P_{\frac{1}{2}}$ levels of hydrogen and deuterium. The letter designation of the states is as Fig. 14 of Part I.

88. Magnetic Field Measurement

Descriptions of the magnet, the magnet current regulator and the method of magnetic field measure-

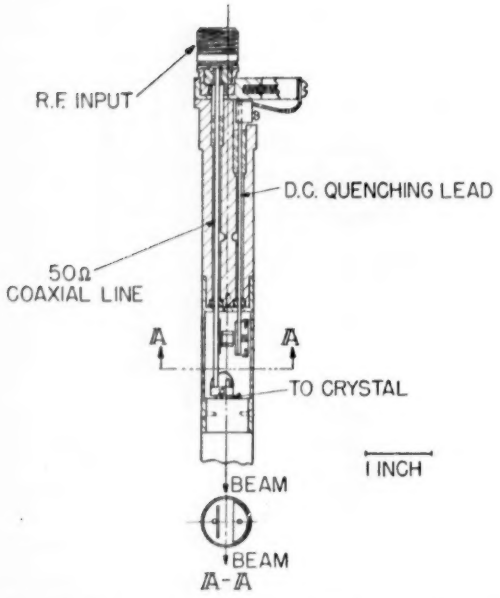

FIG. 59. Rf line used for the observation of π-transitions. The static magnetic field is horizontal in the plane of the drawing. The beam of metastable atoms is perpendicular to the plane of the drawing.

ment were given in Secs. 36, 38, and 39 of Part II. Briefly, the magnetic field is computed from Eq. 96a:

$$H = (\text{constant}) \times R, \tag{96a}$$

where R is the setting of an appropriate resistance box and the constant is measured at some known magnetic field. Improvements in the measurement of this magnetic field calibration constant are given in Sec. 100 of Part VI.[119]

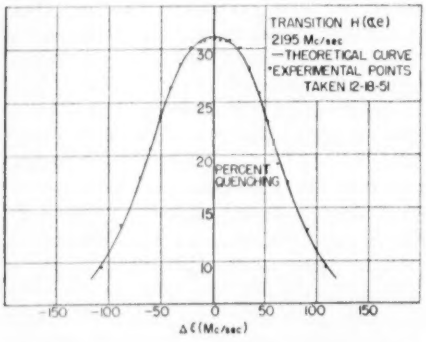

FIG. 60. H(αe) panoramic at 2195 Mc/sec, $H_0 = 1159.5$ gauss. Data are taken as a function of magnetic field H but plotted for convenience against a frequency variable ξ, using the conversion $(d\xi/dH) = 1.0204$ Mc sec^{-1} gauss^{-1}.

[119] Dayhoff, Triebwasser, and Lamb, Phys. Rev. 89, 106 (1953).

S. LINE SHAPE

89. Panoramics

The measurement of the center of a line to 0.1 percent of its width requires a careful study of the line shape and any possible asymmetries. The gross verification of the theory is achieved by plotting quenching as a function of magnetic field. Figures 60 to 63 show such curves except that the abscissa is plotted as "Mc/sec away from resonance" ξ. The effect of Zeeman curvature is too small to be seen on this scale, and the use of ξ as the abscissa is for convenience only. The solid line is a plot of

$$\varphi = \frac{\sum_m \int_0^\infty (1 - e^{-\psi_m/y}) \exp(-y^2) y^2 dy}{\sum_m \int_0^\infty \exp(-y^2) y^2 dy} \times 100, \tag{255}$$

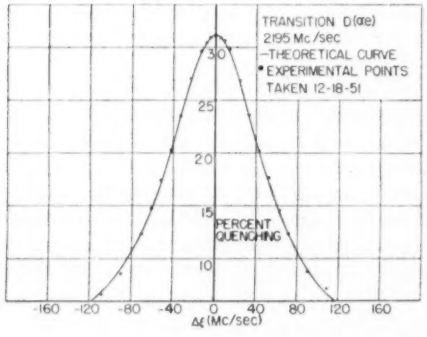

FIG. 61. D(αe) panoramic at 2195 Mc/sec, $H_0 = 1159.6$ gauss. Data are taken as a function of magnetic field H but plotted for convenience against a frequency variable ξ, using the conversion $(d\xi/dH) = 1.0207$ Mc sec^{-1} gauss^{-1}.

where

$$\psi_m = Ab^2/[(\xi - a_m)^2 + b^2]. \tag{256}$$

The only difference between (255), (256), and (197), (199) of Part III is the assumption of a $y^2 \exp(-y^2)$ distribution of metastable atoms rather than $y^3 \exp(-y^2)$. We again assume a $v^3 \exp(-v^2/U^2)$ distribution for atoms emerging from the hot tungsten oven,[120] but a $1/v$ dependence of the interaction time of the atoms with electrons in the bombarder[120] reduces the exponent of the velocity to 2. The parameter A is a measure of the effective rf power, b the theoretical lifetime of the $2P$ states, a_m the frequency displacement due to hyperfine structure of the component with $m_I = m$, ξ the number of Mc/sec away from the center of the composite resonance, and y is the dimensionless velocity variable, $v/(2kT/M)^{\frac{1}{2}}$. The simple velocity distribution assumed is, in fact, modified by motional Stark quenching[121]

[120] See Figs. 28 and 29, Part II.
[121] See appendices II and III, Part I.

and recoil in the bombarder.[121] Measurements described in Appendix VII do, however, indicate that $y^2 \exp(-y^2)$ is a good approximation to the actual velocity dependence of the distribution of metastable atoms leaving the bombarder.

The αf data were taken by starting on one side of the resonant magnetic field and moving in steps indicated by the experimental points until a curve was completed. The αe curve, on the other hand, was taken by starting at the peak of the resonance and taking points alternately on the two sides of the curve. The latter method eliminates asymmetry in the experimental points due to drift of power monitor calibration. The H(αf) panoramic shows a slight asymmetry in the peaks which is probably due to just this effect. Theoretical asymmetries discussed in Sec. 92 are too small to show up on the scale of this plot.

90. Line Widths

The line width may be subjected to a more careful check than the over-all shape because of the large amount of data accumulated at the working points. The procedure used consists of comparing the fractional quenching at the working points with that predicted theoretically.

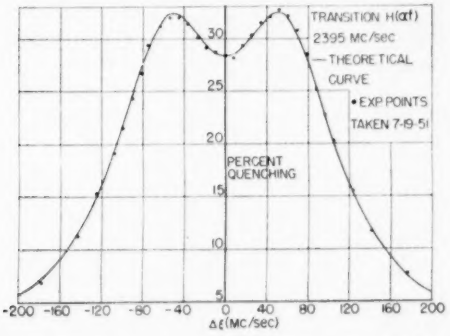

FIG. 62. H(αf) panoramic at 2395 Mc/sec, $H_0 = 703.77$ gauss. Data are taken as a function of magnetic field H but plotted for convenience against a frequency variable ξ, using the conversion $(d\xi/dH) = 1.9216$ Mc sec^{-1} gauss^{-1}.

The method of taking data outlined in Sec. 45 of Part II was followed. Details are given in Sec. 75 of Part IV. To recall the technique: A nominal resonant magnetic field H_0 was chosen on the basis of information from previous runs to be as near the true resonant magnetic field as possible. Then "working points" were selected above and below the resonant field to fall about at the points of inflection of the panoramic. The usual run consisted of 9 lines of data, 4 at one of the working points and 5 at the other, and two lines at H_0. The rf power was set for a previously selected peak quenching [31 percent for D(αf), H(αe), D(αe); 28.3 percent for H(αf)] at H_0. The measurements at H_0 were taken at the beginning and end of a run. A line of data at one of the working points consisted of three

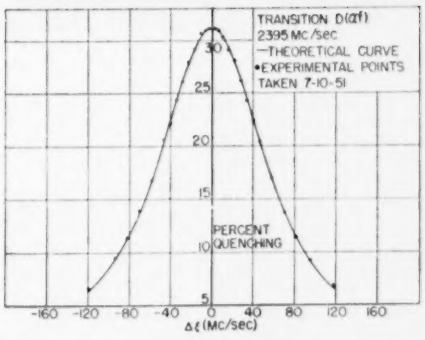

FIG. 63. D(αf) panoramic at 2395 Mc/sec, $H_0 = 704.57$ gauss. Data is taken as a function of magnetic field H but plotted for convenience against a frequency variable ξ, using the conversion $(d\xi/dH) = 1.9257$ Mc sec^{-1} gauss^{-1}.

measurements of the total beam size as measured by dc quenching of all the metastable α state atoms alternated with four measurements of the rf quenching for the previously set power and frequency. Tnis procedure compensates for a uniform drift of galvanometer and intensity of the metastable beam as discussed in Sec. 75 of Part IV.

Table XVII shows percent rf quenching at the working points for all runs. Each result was reduced to the nominal peak quenching as follows: Quenching at the

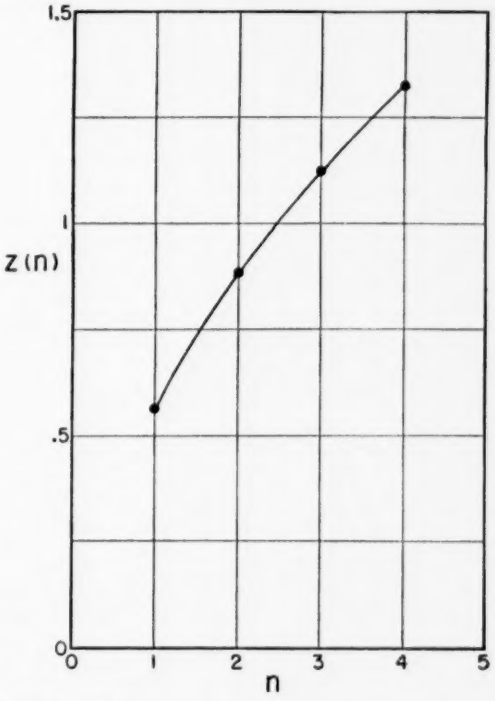

FIG. 64. $\Theta(n) = \left[\int_0^\infty \exp(-y^2) y^n dy\right] \Big/ \left[\int_0^\infty \exp(-y^2) y^{n-1} dy\right]$ plotted as a function of the velocity distribution index n.

TABLE XVII. Width data: Measured widths for all runs taken. Quenching is normalized to 31 percent at peak for H(αe), D(αe), D(αf), and 28.3 percent for H(αf) using measured quenching at peak associated with each run. Theoretical values are given for same peak quenching and actual operating points.

Runs H(αe) Date	Percent quenching at working points	Runs D(αe) Date	Percent quenching at working points
11/30/51	20.407	11/16/51	20.654
12/ 3/51	20.218	11/19/51	20.776
12/ 7/51	20.162	11/29/51	20.906
12/13/51	20.131	12/13/51	20.648
12/15/51	20.141	12/14/51	20.633
Average	20.212	Average	20.723
Av. dev.	0.085	Av. dev.	0.094
Theoretical for $\Delta H=\pm 60.054$ gauss	20.286	Theoretical for $\Delta H=\pm 40.040$ gauss	20.805

H(αf) Date	Percent quenching at working points	D(αf) Date	Percent quenching at working points
9/25/51	21.644	9/25/51	20.781
9/28/51	21.344	9/28/51	20.661
10/ 2/51	21.614	10/ 2/51	20.774
10/ 3/51	21.264	10/ 3/51	20.640
10/ 4/51	21.629		
Average	21.486	Average	20.714
Av. dev.	0.091	Av. dev.	0.064
Theoretical for $\Delta H=\pm 52.001$ gauss	21.497	Theoretical for $\Delta H=\pm 23.386$ gauss	20.734

working points and the peak of the curve was calculated for two slightly different values of A [Eq. (256)] and ($\Delta\varphi$ operating point)/($\Delta\varphi$ peak) evaluated. From the average percent quenching at the peaks, one can evaluate a correction to reduce the run to the nominal peak quenching for the particular transition. Since the peak quenching was set fairly carefully before the actual run data were taken, this never represented a correction of more than 0.5 percent in φ. Theoretical values were obtained from Eq. (255) modified as in Eq. (258) for motional Stark quenching and are seen to be consistent with the experimental values. The fact that the theoretical value is always higher may be an indication of the rf power narrowing discussed in Appendix IV of Part III.

If one assumes the theoretical value of the radiative width, the measurements summarized in Table XVII constitute a measurement of the a_m used in calculating the theoretical panoramics [Eqs. (255) and (256)]. The stated uncertainty in the observed "percent quenching at the working points" (0.085 percent in the case of the H(αe) transition) can be translated into an uncertainty in a_m. Following this scheme, we find that the results given for the H(αe) and H(αf) transitions confirm the hyperfine structure contributions to resonance width calculated from theoretical formulas given in Sec. 56 of Part III to within 0.20 Mc/sec in each case. Unpublished measurements of the sharp H($\alpha\beta$) transitions yield confirmation of the theoretical hyperfine structure of the $2S$ states to far greater accuracy, so we consider that the results being discussed here constitute a confirmation within 1.0 percent of the theoretical hyperfine structure splitting of the 2 P states. The absolute accuracy of the deuterium measurements is at least as good as the hydrogen results. Hyperfine splittings in the former, however, are much smaller.

TABLE XVIII. Slope measurement results (details explained in text, Sec. 91).

Transition	Date	Measured slope at working points $\Delta\varphi/\Delta\xi$	Number of measurements	Theoretical slope at working points $\Delta\varphi/\Delta\xi$
H(αe)	12/13, 15/51	0.3000±0.0084	4	0.3012
D(αe)	12/13, 14/51	0.3348±0.0018	4	0.3387
H(αf)	7/31/51	0.3090±0.0107	9	0.3023
D(αf)	7/27/51	0.3271±0.0086	9	0.3264

91. Slope at Operating Points

Since the exact resonant magnetic field H_0 was not known in advance, the runs did not have the fractional quenching exactly equal at the two working points. To arrive at this value, H_0, one must know $d\varphi/dH$ at the working points. This was calculated from the theoretical panoramic. In addition, measurements were made to verify the theoretical slopes. Table XVIII shows the results of these measurements. In the case of the αe transitions, two magnetic fields straddling a working point were chosen—in some cases 10 gauss apart and in others about 15 gauss apart. The rf power was set so as to give the correct quenching at the peak of the resonance. The galvanometer was then read as the magnetic field was alternated between the two values until a total of about 20 or 30 readings were taken. The average change in the galvanometer reading was computed. Then the measurements were repeated with rf power off to subtract any possible change in beam size with the relatively small change in magnetic field. At the beginning and end of this measurement the full size of the beam was measured by dc quenching. The average change in galvanometer reading with rf, minus the average without rf, divided by the total beam size, gave the change in fractional quenching. This procedure assumed only a small change in the beam size as the field was changed over the 10 or 15 gauss of the measurement, a condition satisfied with sufficient accuracy in the experiment. One could then calculate the slope of the quenching *vs* magnetic field curve. Each of the four measurements contributing to results in Table XVIII consisted of just such a measurement, two at each working point. Since the shift in the galvanometer reading was at most 6 cm, it was a difficult measurement to make with high precision. The small average deviation shown for D(αe) is probably accidental. Theoretical slopes were used in calculating the small corrections to the data of actual runs.

The αf slope was measured by selecting two magnetic field values straddling each of the original working points and taking alternate half-lines of data at these two points separated by about 6 gauss. These were taken on one day, 4 straddling one working point and 5 straddling the other. Again the measurements were in agreement with theoretical values. In none of the transitions was there any apparent asymmetry between the slopes at the two operating points. In all cases except the D(αe) transition, the measured slopes differ from the theoretical slopes by less than the average deviation.

T. RESULTS

92. Corrections Applied to Runs

The true resistances of the resistance boxes used in the magnetic field measurement, were found by correcting the nominal values of individual decades as measured against a precision resistor.[122] These values were then corrected for the temperatures of the boxes and the values at the working points corrected in this way were averaged. The result is the nominal resonant magnetic field resistance. Corrections were then applied for the difference in percent quenching at the working points yielding the corrected resonant magnetic field resistance [Eq. (252), Part IV].

$$\bar{R}=\tfrac{1}{2}(R_a+R_b)+\tfrac{1}{2}(\varphi_b-\varphi_a)/(d\varphi/dR). \qquad (252)$$

The calibration constant R/H was evaluated from the proton resonance data[119] corrected for temperature coefficients of the resistance boxes and frequency of the secondary standard as compared with the 5 Mc/sec standard frequency broadcasts of the National Bureau of Standards. The beat frequency was measured every day on which a run was taken. Interpolation for the magnet temperature was used to find R/H for the average temperature of the magnet for the run. Then H for the run is given by $\bar{R}/(R/H)$. Since the frequency of the rf used for the transitions is an integral multiple of the nominal 5.0 Mc/sec secondary standard, an additional correction must be applied for the true frequency of the oscillator. The resonant magnetic fields so calculated are given in Table XIX. The average deviation given for each run was computed from the square root of the sum of the squares of the average deviations of φ_a and φ_b in the run multiplied by $\frac{1}{2}(dH/d\varphi)$. Weights applied to individual runs are taken as $N/(\text{Av. dev.})^2$, where N is the number of lines of data taken at the working points.

93. Asymmetry and Shift Corrections

The asymmetry and shift corrections are shown in Table XX which is similar to Table XV of Part IV except for the assumption of a $y^2\exp(-y^2)$ velocity distribution and the inclusion of a correction for the "low voltage quencher" asymmetry in the case of αe transitions. Improved rf electric field polarization reduced "overlap" and "forbidden components" corrections sufficiently so that they may be neglected.

The Stark effect correction was calculated using the general technique applied to the other asymmetries, rather than by the method outlined in Sec. 57 of Part III. The velocity dependence of the Stark shift was inserted explicitly into Eq. (255) by modifying Eq. (256) as follows:

$$\psi_m=Ab^2/[(\xi-a_m-a_s y^2)^2+b^2], \qquad (257)$$

where a_s is the Stark shift in Mc/sec for an atom traveling at the velocity for which $y=1$. This was

TABLE XIX. Summary of runs: H_0 is the measured field at the center of the resonance after all corrections, but asymmetry and shift corrections common to all runs of a single transiton have been made.

Date	H_0 (gauss)	Av. dev. (gauss)	N	Relative weight
	H(αe) (2195 Mc/sec)			
11/30/51	1159.490	0.511	11	42
12/ 3/51	1159.511	0.229	9	173
12/ 7/51	1159.727	0.232	11	204
12/13/51	1159.485	0.182	11	332
12/15/51	1159.361	0.314	11	112
Average	1159.532±0.093			
	D(αe) (2195 Mc/sec)			
11/16/51	1159.397	0.245	9	150
11/19/51	1159.770	0.442	9	46
11/29/51	1159.486	0.223	9	181
12/13/51	1159.609	0.175	11	359
12/14/51	1159.584	0.160	9	352
Average	1159.555±0.073			
	H(αf) (2395 Mc/sec)			
9/25/51	703.669	0.125	11	70
9/28/51	703.624	0.135	9	49
10/ 2/51	703.688	0.198	11	28
10/ 3/51	703.750	0.142	5	25
10/ 4/51	704.082	0.298	5	6
Average	703.685±0.046			
	D(αf) (2395 Mc/sec)			
9/25/51	704.515	0.108	11	94
9/28/51	704.475	0.128	11	67
10/ 2/51	704.521	0.154	11	46
10/ 3/51	704.499	0.123	5	33
Average	704.503±0.017			

TABLE XX. Asymmetry and shift corrections: Corrections to ξ in Mc/sec calculated at the working points for peak quenching to which each transition is normalized.

Transition	H(αe)	D(αe)	H(αf)	D(αf)
Matrix element variation	−0.588	−0.366	−0.284	−0.125
Quenching asymmetry	−0.077	0.034	−0.133	0.012
Incomplete Back-Goudsmit effect and Zeeman curvature	−0.923	−0.105	−2.733	−0.195
Stark effect	0.308	0.150	−0.071	−0.033
Total correction	−1.280 Mc/sec	−0.287 Mc/sec	−3.221 Mc/sec	−0.341 Mc/sec

[122] Described in detail in reference 119, Sec. 98a.

TABLE XXI. Summary of results.

Transition	Frequency Mc/sec	$\overline{H_0}$ (gauss)	Av. dev. (gauss)	δ (Mc/sec)	Asymmetry and shift corrections	δ (Mc/sec) corrected	Av. dev. (Mc/sec)
H(αe)	2195	1159.532	0.093	1059.032	−1.280	1057.752	0.095
D(αe)	2195	1159.555	0.073	1059.344	−0.287	1059.057	0.074
H(αf)	2395	703.685	0.046	1061.016	−3.221	1057.795	0.089
D(αf)	2395	704.503	0.017	1059.291	−0.341	1058.950	0.033

$\delta_H = 1057.77 \pm 0.10$ Mc/sec
$\delta_D = 1059.00 \pm 0.10$ Mc/sec

calculated as described in Sec. 57 of Part III, except that the required matrix elements were taken from the intermediate field wave functions at the resonant magnetic field at which the transition was observed. Stark corrections given in Table XV of Part IV were calculated for the limiting case of small rf quenching and for the zero field matrix elements. The result of the sample calculation given in Sec. 57 of Part III is twice as large as the equivalent result of Part IV due to the incorrect velocity distribution assumed in the earlier calculations.

The only other substantial difference between Table XIX and Table XV is in the Zeeman curvature correction for the αf transition, where an incorrect sign was used in Part IV for the curvature of the transition frequency with respect to magnetic field.

The quenching asymmetry introduced by the additional β-state quencher mentioned above is calculated by a modification of Eqs. (203), (204), Part III as follows:

$$\varphi = \frac{\sum_m \int_0^\infty e^{-\rho v} e^{-r/v}(1-e^{-\psi_m/v})\exp(-y^2)y^3 dy}{\sum_m \int_0^\infty e^{-\rho v} e^{-r/v}\exp(-y^2)y^2 dy} \times 100, \quad (258)$$

where r is a measure of the decay rate of α-state atoms due to the additional electrodes computed from Eq. (42) of Part I. Only quenching due to αe coupling is taken into account. The parameter r is about $(\frac{1}{10})\rho$ in the experiment, so that the effect of αb quenching will surely be negligible in so far as any asymmetry is concerned.

94. Results

Table XXI gives the results for each of the transitions. The average deviations quoted were computed directly from the column labeled "H_0" in Table XIX, with weighting as given in the column labeled "Relative Weight" assigned to the deviations. The deviations in deuterium are smaller than those for hydrogen mostly due to the larger signal and reduced relative noise in the case of the heavier isotope. The smallness of the average deviation for the D(αf) is probably fortuitous. We consider that the average deviations for the hydrogen transitions and the D(αe) are representative of the ultimate accuracy inherent in the apparatus.

In estimating a limit of error, one must consider any residual systematic errors in the experimental technique and in the theoretical corrections applied to the results. Uncertainties of velocity distribution could lead at most to an additional correction of 0.02 Mc/sec. Due to the fact that the αf, αe Stark effects are opposite in sign, the average δ is affected less than either. The presence of unknown static electric fields would be a source of error, but it is felt that there are no residual effects of this kind near the stated accuracy in magnitude. An estimate of the effect of magnetic field inhomogeneity yields an error of less than 0.01 Mc/sec in the worst possible case.

From Table XXI, taking the average of αe and αf results for each of the isotopes considered, one arrives at $\delta_H = 1057.77$ Mc/sec for hydrogen and $\delta_D = 1059.00$ Mc/sec for deuterium with an accuracy of ± 0.10 Mc/sec for each. Weighted means are not used because it is felt that αe and αf measurements have equal inherent accuracies, fluctuations in the individual deviations being of a normal random nature. The precision stated is arrived at as follows: The average deviation of the mean for any individual run is of the order 0.10 Mc/sec. Then the average deviation of the mean for an individual transition would be 0.10 divided by $\sqrt{4}$ or $\sqrt{5}$ as the case may be for the number of runs in a transition, or about 0.05 Mc/sec. Finally, dividing 0.05 by $\sqrt{2}$ to take into account the two independent measurements represented by the αe and αf transitions, would yield the average deviation of the results stated. The accuracy given (0.10 Mc/sec) is, then, approximately 3× (average deviation of the mean).

It is worth noting that the magnitudes of average deviations as one progresses from "individual runs" to "average for a transition" to "average of different transitions," present a picture consistent with that to be expected from statistical theory. One would infer that the fluctuations in the measurements are probably random in nature.

V. EVALUATION

95. Comparison of Results with Theory

The present status of theoretical calculations of the level shift has been summarized in an accompanying paper by Salpeter.[123] He finds, apart from some specific contributions as yet uncalculated,

$$\delta_H = (1057.19 \pm 0.16)\text{Mc/sec};$$
$$\delta_D = (1058.49 \pm 0.16)\text{Mc/sec}.$$

These calculated values are about 0.5 Mc/sec smaller than the equivalent experimental results, although the $(\delta_D - \delta_H)$ values are in excellent agreement. This discrepancy between theoretical and experimental level

[123] E. E. Salpeter, Phys. Rev. 89, 92 (1953). See also Sec. 84 of Part IV. The authors are indebted to Dr. Salpeter for the communication of his unpublished results.

shifts is well outside the estimated error and is as yet unresolved.

The authors have benefited greatly from many valuable discussions of the theoretical aspects of this work with Professor N. M. Kroll. We wish to thank Messrs. J. Heberle and H. Reich and other members of the Columbia Radiation Laboratory staff for cooperation and assistance in the experimental work, and Messrs. A. H. Barrett and R. Herman for assistance in the computations.

APPENDIX VII. VELOCITY MEASUREMENTS

The motional electric field $\mathbf{E}=(\mathbf{v}/c)\times\mathbf{H}$ provides a means for measuring a suitably defined average velocity of metastable atoms in the beam since it produces a Stark quenching of the beam.[124] The measured average velocity can then be used as a verification of the velocity distribution assumed in the calculations of the various corrections. The measurement consists of applying to the atoms a uniform adjustable electric field along the direction of the motional field. The quenching of the beam by the resulting electric field will be at a minimum when the applied field neutralizes on the average the motional field for the beam.

For the purposes of this analysis, a satisfactory approximation may be obtained by starting with the assumption that the metastable atoms in the beam are distributed in velocity according to the law

$$f(v, n)=N\exp(-y^2)y^n, \tag{259}$$

where y is the previously defined dimensionless velocity variable, and N is a normalizing constant. The free parameter n is used to allow roughly for distortions of the distribution due to such causes as recoil, preferential scattering of slow atoms, motional Stark quenching of the faster atoms elsewhere in the beam, and the possible velocity dependence of the efficiency of the metastable atom detector. Excluding these effects, one would expect n to be 2 (Sec. 89).

The fractional quenching can be written as

$$\varphi=Z(E, n)/Z(\infty, n), \tag{260}$$

where the quenching function Z is given by

$$Z(E, n)=\int_0^\infty\left[1-\exp\left\{\frac{-a[E-(U/c)Hy]^2}{y}\right\}\right]\times\exp(-y^2)y^n dy. \tag{261}$$

The coefficient a is a constant for a fixed magnetic field, E is the applied electric field, U is $(2kT/M)^{\frac{1}{2}}$ and y is v/U. In the region of small quenching, the exponential function above can be expanded and the first nonzero term of Z retained. Z (and φ) will be a minimum when

$$dZ/dE=d/dE\int_0^\infty a\left[E-\left(\frac{UH}{c}\right)y\right]^2\exp(-y^2)y^{n-1}dy$$

$$=2a\left[E\int_0^\infty\exp(-y^2)y^{n-1}dy-\frac{UH}{c}\int_0^\infty\exp(-y^2)y^n dy\right]=0;$$

or, the value of E which leads to minimum quenching is given by

$$E_{\min}=(U/c)H\Theta(n), \tag{262a}$$

$$\Theta(n)=\left(\int_0^\infty\exp(-y^2)y^n dy\right)\Big/\left(\int_0^\infty\exp(-y^2)y^{n-1}dy\right). \tag{262b}$$

The function $\Theta(n)$ is plotted as a function of n in Fig. 64. Measured values of $E_{\min}/[(U/c)H]$ are given in Table XXII together with the graphically found value of n which would lead to the observed Θ. The measurement is made by substituting for the rf interaction region two round plates, 0.620 inches in diameter, 0.190 inches apart, parallel to and symmetrically placed about the plane determined by the magnetic field and the direction of the beam of atoms. To eliminate the effect of contact potentials, minima of φ as a function of E are taken for both polarities of the magnetic field. In the one case we observe $E+E_c$ and in the other, $E-E_c$; the average of the two observations eliminates E_c.

The theory given above assumes perfect uniformity of electric field in the interaction space. Fringing of this field will lead to an apparent value of the index n which is too high. The error to be expected for the actual geometry of the experiment has been estimated to be large enough to account for the observed deviation of n from 2.

The apparent decrease of n when the magnetic field is increased is interpreted as evidence for preferential

TABLE XXII. Observed velocity distribution indices for various magnetic fields.

Magnetic field (gauss)	$\Theta(n)$	n
	Deuterium	
575	1.007	2.5
705	0.945	2.2
1140	0.944	2.2
3670	0.793	1.7
	Hydrogen	
575	1.028	2.6
1140	0.994	2.4

[124] See Part I, Appendix II.

quenching by the motional electric field of the faster atoms before they enter the interaction space. Aside from the relatively slow variation with magnetic field of the denominator of the formula for the life time[125] of the α-state, this type of quenching varies directly with H^2.

Although this technique for measurement of n does not give much accuracy, the results may be taken to provide some confirmation of the assumed velocity distribution. Fortunately, as previously discussed (Sec. 93), the only correction sensitive to the value of n is that due to motional Stark effect. Uncertainty in this has been estimated at 10 percent of the correction itself and has been included in the estimate of error of the results.

[125] See Part I, Eq. (42).

PHYSICAL REVIEW VOLUME 89, NUMBER 1 JANUARY 1, 1953

Fine Structure of the Hydrogen Atom. VI*†

EDWARD S. DAYHOFF,‡ SOL TRIEBWASSER,§ AND WILLIS E. LAMB, JR.‖
Radiation Laboratory, Columbia University, New York, New York

(Received September 15, 1952)

Measurements of improved accuracy of transition frequencies from the $2^2S_{\frac{1}{2}}(m=+\frac{1}{2})$ state to several of the $2^2P_{\frac{1}{2}}$ magnetic sub-states in deuterium are presented and analyzed. The shape of the observed resonance curves is discussed and compared with theory.

The experimental result is given for the $2^2P_{\frac{1}{2}}-2^2S_{\frac{1}{2}}$ separation, $\Delta E_D-\$_D=9912.59\pm0.10$ Mc/sec, for deuterium. This is combined with the result for $\$_D$ from the preceding article to obtain the $2^2P_{\frac{1}{2}}-2^2P_{\frac{1}{2}}$ separation, $\Delta E_D=10{,}971.59\pm0.20$ Mc/sec for deuterium. From ΔE_D and the auxiliary constants R_D and c a new value is computed for the fine structure constant $\alpha=1/(137.0365\pm0.0012)$. The uncertainty stated is considered to be a limit of error for our experimental procedure without allowance for the uncertainty of the auxiliary constants.

INTRODUCTION

THE preceding articles of this series[128] have discussed the theory of measurement of the fine structure of hydrogen and have presented highly accurate results for the $2^2S_{\frac{1}{2}}-2^2P_{\frac{1}{2}}$ shift S for hydrogen and deuterium. On the basis of the foundation already laid, measurements of improved accuracy of transition frequencies from the $2^2S_{\frac{1}{2}}(m=+\frac{1}{2})$ state to several of the $2^2P_{\frac{1}{2}}$ magnetic sub-states in deuterium are here discussed. The improved accuracy results mainly from improved magnetic field measurement technique, the elimination of some experimental corrections, and better stability of the equipment. The splitting of the levels in a magnetic field H is shown in Fig. 65 together with the nomenclature used for the sub-levels. The transitions reported here are indicated.

* Work supported jointly by the Signal Corps and ONR.

† Submitted by Edward S. Dayhoff in partial fulfillment of requirements for the degree of Doctor of Philosophy in the Faculty of Pure Science, Columbia University.

‡ Present address: Central Radio Propagation Laboratory, Microwave Standards Section, National Bureau of Standards, Washington, D. C.

§ Present address: Watson Scientific Computing Laboratory, Columbia University, New York, New York.

‖ Present address: Department of Physics, Stanford University, Stanford, California.

[128] W. E. Lamb, Jr., and R. C. Retherford, Part I, Phys. Rev. **79**, 549 (1950); Part II, Phys. Rev. **81**, 222 (1951); Part III, Phys. Rev. **85**, 259 (1952); Part IV, Phys. Rev. **86**, 1014 (1952); Triebwasser, Dayhoff, and Lamb, Part V, Phys. Rev. **89**, 98 (1953). Frequent references to these papers are made. Chapters, sections, figures, equations, tables, appendices, and footnotes of Part VI are numbered consecutively after those of Parts I through V.

W. GENERAL PROGRAM

An inspection of the day to day variations of the results[129] obtained with the metastable beam electric resonance apparatus[130] prior to about a year ago suggested the possibility of systematic errors whose effect was judged to be somewhat less than 1 Mc/sec in the final result. On the other hand, the internal consistency of individual runs appeared to indicate a possible precision approaching 0.1 Mc/sec in the result. It thus appeared that a systematic attack on residual inadequacies in the procedure was in order. On the one hand, empirical corrections of observations were reduced in number and simplified in application; on the other, the experimental parameters of the measurement were determined in an improved manner.

96. Improvements

The chief empirical correction to be removed was the relatively uncertain one[131] for "soft" component[132] of the metastable beam which required a great deal of time consuming computation. New interaction spaces with essentially complete polarization of the rf[133] relieved the problem of overlapping resonances, since nearby resonances which might overlap the desired one usually require a different polarization. By this

[129] See Part IV, Sec. 84 and, in particular, Table XVI.
[130] Described in detail in Part II.
[131] See Part IV, Sec. 73.
[132] Atoms in β-state. See Part I, Sec. 16.
[133] Described in Part V, Sec. 87.

means, the overlap corrections which were necessary in Part IV have been avoided in Parts V and VI. Additional computational work arising from variations of oscillator frequency and interaction space power level during the course of a run has been eliminated by use of an automatic frequency stabilizer[134] and a finely adjustable attenuator.

An incidental, though quite important, result of this program has been earlier availability of the results of runs after taking data. Thus malfunctioning of the equipment could be noticed quickly, changes in the apparatus could be evaluated rapidly, and the ability to undertake developmental experiments was increased.

The phase of the improvement program directed toward the experimental parameters bore fruit chiefly in connection with the magnetic field measurements. Several sources of error in the rotating search coil device used for field measurement were located and removed and a more reliable method of calibration for this device was found. These improvements, discussed below, are felt to account for the major part of the improved accuracy reported in Parts V and VI of this series.

Other improvements in the equipment whose effect was to increase the constancy of the metastable beam and to extend the time between cleanings are described in Appendices IX and X.

X. MAGNETIC FIELD MEASUREMENT

97. Method of Observation

The magnetic field measuring device is described in Sec. 39 of Part II. Two search coils are mounted on a single shaft rotating at 30 rps. One is in the field to be measured while the other rotates in the field of a permanent magnet. The emf's due to the two coils are combined in a bridge (Fig. 31, Part II) whose unbalance signal is amplified by a 30-cps narrow band amplifier. At balance, where the output of the amplifier is zero, the field of the electromagnet is given simply by

$$H = (\text{constant}) \times R, \tag{96a}$$

where H is the field to be measured and R is the total resistance in one arm of the bridge containing a variable resistance box. The calibration constant is a function of the number of turns and the area of the two search coils, the resistance of the fixed arm of the bridge, and the field strength of the permanent magnet. In the present measurements, it is about 1/65 gauss per ohm.

98. Corrections to Rotating Search Coil Readings

(a) *Effects of Temperature*

The search coil resistances of about 110 ohms (copper wire) had to be added to the bridge arm resistances. Their resistance variations with temperature were about 0.4 ohm per degree. Since it was difficult to measure the coil temperatures with sufficient accuracy, the box resistances were increased by a factor of about 10 over the values used for the measurements of Part IV, reducing possible error from this source from 0.06 to 0.006 gauss per degree. Hence calibrating both before and after the day's run avoided the need for measuring the temperatures of the coils as the error due to nonuniform heating was negligible.

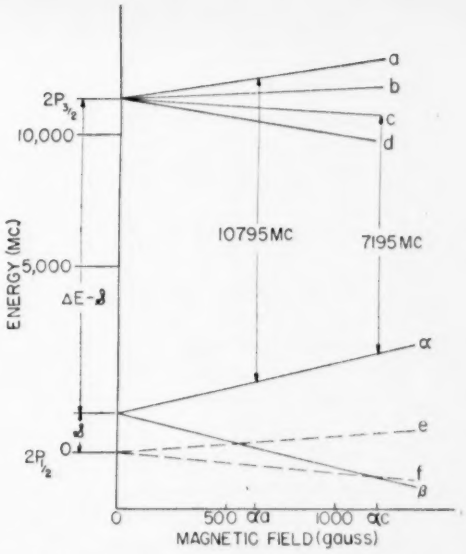

FIG. 65. Energy level splitting as a function of magnetic field for the $n=2$ levels of hydrogen, illustrating nomenclature of this paper and transitions reported.

Settings of the resistance box were standardized by intercomparison of the decade steps among themselves and with an external standard using a Wheatstone bridge arrangement with a sensitivity of a part in nearly 500 000 at a frequency near 30 cps. Repeating the measurements at several temperatures was sufficient to determine the temperature coefficients of the steps of the box. The absolute value of the standard resistance was unimportant since only ratios of resistances appeared in the results of the runs. The standard resistance and the resistance boxes contained low temperature coefficient precision resistors made by the General Radio Company. Their temperatures were monitored during runs with an accuracy sufficient to insure that error from this source would be less than one ohm.

It was found that the calibration constant depended on the temperature of the permanent magnet with a relative coefficient of 2.4×10^{-4} per degree. This variation was rather closely reproducible (Fig. 66) and results mainly from the reversible dependence of the magnetization of the permanent magnet on its temperature. Neglect of this is thought to be the most serious source of systematic error in the Part IV measurements

[134] See Appendix VIII.

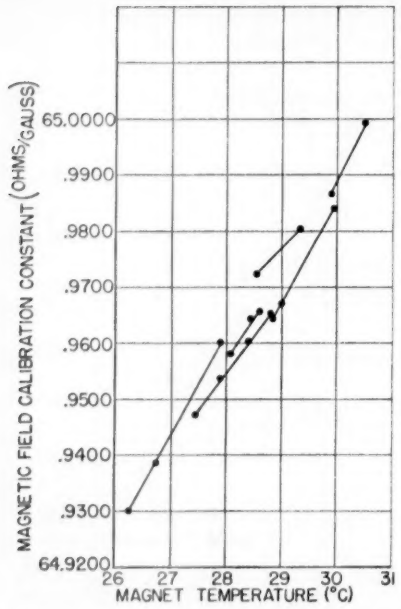

FIG. 66. Calibration constant of rotating search coil field measuring device as a function of temperature of the permanent reference magnet. Lines are drawn connecting points taken on the same day.

where the practice was to calibrate at the end of each day's run. The resultant errors were 0.25 Mc sec^{-1} $degree^{-1}$ for αe and 0.35 Mc sec^{-1} $degree^{-1}$ for αf. Since temperature in almost all cases increased nonuniformly several degrees during a run, the error would not be random. We have now thermally insulated the permanent magnet and improved the thermometry, greatly reducing the need for corrections. On most days on which runs were taken, the calibration constant was measured before and after the run. The magnet temperature was read at sufficiently frequent intervals to yield an average for each run accurate to 0.02 degree.

(b) Effect of 60 cps Field Component

It was observed that the calibration constant apparently depended on the relative phase of the 30-cps synchronous motor and the 60-cps power line. This dependence is associated with the 30-cps signal component generated in the search coil by a small 60-cps modulation of the magnetic field. Such 60-cps modulation is caused in our apparatus by the alternating currents used to heat the oven, bombarder cathode and plate heater. Equation (96a) is valid only if the 30-cps signals from the two coils are the induced emf's due to constant fields.

A loop of wire around a pole piece and fed from a variable amplitude source of 60-cps current was used to effect partial compensation of the field modulation of the electromagnet. In the runs of Part IV the degree of compensation was tested by observing the signal induced in an additional fixed coil placed nearby in the magnetic field. This method was later found to be inadequate, since the 60-cps component of the field was somewhat inhomogeneous. The error due to faulty compensation could easily have been 0.1 gauss at any magnetic field.

In the runs of Parts V and VI, the phase of the compensating field was made continuously adjustable and an improved test of the degree of compensation was developed. This test consisted of slipping the phase of the 4-pole, 30-cycle motor by 90 degrees (referred to the 60-cps power mains). Since the error due to the spurious 30-cps signal changes sign when this is done, adequate compensation existed when the above operation changed the balance point of the bridge less than ± 1 ohm in 80 000.

99. Calibration of Magnetic Field by αβ-Resonances

The calibration constant R/H is determined by observing the value of R for some known magnetic field H. The measurements of Part IV and the αc runs of Part VI used the sharp $\alpha\beta$-transition[135] for calibration. This is adequate when the π-polarization of rf electric field is used. Measurement at the βe crossing point (about 574 gauss and 1610 Mc/sec) then yields an accurate result. With the σ-polarization of rf electric field used in the αf, αa, and αc measurements, however, the situation is somewhat different and there is reason for expecting a genuine systematic disturbance of the resonance position.

The $\alpha\beta$-resonance as observed under these conditions (using the σ-polarized interaction space near the βe crossing point) is a second-order transition occurring both by way of the e state which is strongly coupled to the β-state by the motional Stark field and the f state which is coupled only by stray π-polarized fields. The f state, although far from resonance, is excited by the strong σ-radiation present while the e state, even though at exact resonance, is excited only by the π-polarized fringing rf fields of the interaction space and is relatively weak. Hence the observed $\alpha\beta$-resonance has a complicated shape, being a composite of the symmetrical e coupled shape and the very unsymmetrical f coupled shape.[136] The apparent center of the observed $\alpha\beta$-resonance is accordingly shifted from its expected position by an amount which depends critically on the stray fields in the interaction space. For this reason, the $\alpha\beta$-resonances are judged to be an unreliable method of calibration when observed with the σ-polarized interaction space. Experiments in which small electric fields which disturb the couplings of the various states are deliberately introduced show such shifts to be very real. As a result, it was decided that the proton reso-

[135] Theory in Chapter N of Part III.
[136] See Part II, Fig. 42; Part III, Fig. 52 and Chapter N.

nance[137] method of field calibration should be used for all precision measurements. Subsequent direct comparison of $\alpha\beta$- and proton resonances verified the highly variable nature of the $\alpha\beta$- with the σ-type interaction space. Differences of about 1 part in 10 000 sometimes were observed. These differences were of both signs, not randomly distributed, and usually showed drifts which apparently depended on the previous history of the apparatus. A group of $\alpha\beta$-runs could easily be in error by a part in 20 000. The π-type interaction space showed far less variation and better agreement between $\alpha\beta$- and proton calibration.

100. Calibration of Magnetic Field by Proton Resonance

A proton resonance probe was permanently mounted external to the vacuum envelope as near as possible to the interaction region. Resonances were observed near and corrected to 5.000 000 Mc/sec, for which $H = 1174.327 \pm 0.014$ gauss as computed from the results of Thomas, Driscoll, and Hipple.[138]

On four occasions when the vacuum system was opened for cleaning, a second probe was mounted in the center of the interaction region for the purpose of measuring the field inhomogeneity. The correction obtained on all occasions was 10 ± 1 parts in 80 000. A gradient of the strength of the magnetic field in the interaction space was found by moving the second probe along the path of the beam. The total field change in the interaction space was 12 parts in 80 000. Such a gradient might have required a correction to the mean field in the interaction space since the metastable beam was stronger on the entering side than on the exit side. This correction amounted to only $\frac{1}{2}$ part in 80 000 or 0.006 Mc/sec for the αa transition with 20 percent quenching and was neglected.

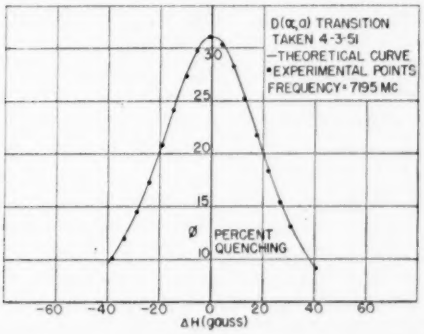

FIG. 67. Panoramic view of αa resonance curve. The abscissa is displacement from the resonant magnetic field $\bar{H}$ which is 630.68 gauss.

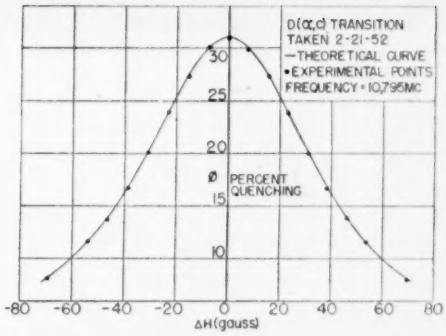

FIG. 68. Panoramic view of αc resonance curve. The abscissa is displacement from the resonant magnetic field $\bar{H}$ which is 1189.36 gauss.

To test the field measurement technique, calibrations were taken at 5.0 Mc/sec and 2.5 Mc/sec by zero-beating the proton resonance oscillator against a secondary standard at 5 Mc/sec in the former case and zero-beating its second harmonic against the same standard in the latter measurement. The ratio of resistance box readings with all corrections included was 2.0 to an accuracy of 1 part in 50,000. These two check points (1174 and 587 gauss) include about the full range of fields over which measurements in the experiment were made. To verify that the previous history of the iron was not significant, this test was done on two occasions with the same result. Additional evidence that effects due to the past history of the iron were negligible was provided by numerous measurements of the inhomogeneity correction mentioned in the paragraph above. In some cases deliberate efforts were made to induce irreversible changes in the inhomogeneity pattern (e.g., by reversing the field direction of the electromagnet), but in all cases the measured inhomogeneity was the same within expected error.

Y. LINE SHAPE

101. Panoramic Resonance Curves

Panoramic views of the αa and αc resonance curves are shown in Figs. 67 and 68. The αa transition was observed at 10,795 Mc/sec and the αc at 7195 Mc/sec, frequencies which center the αa at about 630 gauss (just above the crossing point of the β- and e states) and αc at about 1190 gauss (near the crossing field of the β- and f states). This choice of operating fields, together with the use of the low voltage quenching field[139] for the αc runs, insures that there will be no observable contribution to the quenching from atoms in the β-state. The solid lines labeled "theoretical

[137] R. V. Pound and W. D. Knight, Rev. Sci. Instr. **21**, 219 (1950).

[138] Thomas, Driscoll, and Hipple, J. Research Natl. Bur. Standards **44**, 569 (1950). Cylindrical probes of $\frac{1}{4}$ in. diameter, $\frac{5}{16}$ in. long, with a 0.2 normal solution of copper sulfate were used. Corrections for paramagnetic ions and diamagnetism of water are sufficiently small to be neglected.

[139] Described in Part V, Sec. 85. A small π-polarized electric field will aid in quenching β-state atoms near the βf crossing point.

curve" are plots of the fractional quenching, ϕ:

$$\phi = \frac{\sum_m \int [1-\exp(-\psi_m/y)]y^2 \exp(-y^2)dy}{\sum_m \int y^2 \exp(-y^2)dy}, \quad (263)$$

where

$$\psi_m = \frac{Ab^2}{(\xi-a_m)^2+b^2}$$

gives the shape of the absorption line, and

$$\xi = \Delta H \cdot (d\nu/dH)_{\text{res}}$$

converts frequency differences into magnetic field differences with sufficient accuracy for use with the panoramics. Here the summations are over the hyperfine components, the integrations are over the velocity distribution, y is a dimensionless velocity variable $v/(2kT/M)^{\frac{1}{2}}$, a_m is the hyperfine energy of the mth hyperfine state in frequency units, and b represents the natural radiative width of the line as given by theory.[140] It is sufficiently accurate to use Eq. (263) as the various small asymmetries significant in the precision results cannot be seen on the scale of the panoramics.

102. Gross Fit and Slopes

The data are fitted to the theoretical curves by applying a power level correction to the quenching so that the value at the center of the line is exactly 31 percent for which the theoretical curves were calculated. The origin of abscissas is chosen so that the curve is symmetrically placed. The fit is as close as could reasonably be expected, considering the manner of taking data. Each experimental point is the result of just one measurement of beam quenching by the rf and quenching of the total beam by a strong dc field. In view of the closeness of this fit, and the smallness of corrections which depend on slope, the slopes used for calculating the precision data were taken from the theoretical curves and no direct measurements of them were made.[141]

TABLE XXIII. Observed line widths. The ratio of quenching at working points to quenching at peak is a measure of line width.

Deuterium αa transition	
Run	$\phi_{\text{w.p.}}/\phi_{\text{peak}}$
1	0.7079
2	0.7147
3	0.7101
4	0.7073
5	0.7065
6	0.7080
Mean	0.7091
Average deviation	0.0022
Theoretical	0.7128
Difference	0.0037
Deuterium αc transition	
Run	$\phi_{\text{w.p.}}/\phi_{\text{peak}}$
10	0.6945
11	0.6940
12	0.6883
13	0.6930
14	0.6955
Mean	0.6930
Average deviation	0.0019
Theoretical	0.6972
Difference	0.0042

[140] See Part III, Sec. 62.

103. Line Width

A severe test of the quality of fit is provided by a close examination of the height of resonance curves at the "working points," using data obtained in the precision runs. The working points are two points chosen to lie approximately symmetrically above and below the apparent center of the resonance curve near its points of inflection. Thus, the ratio of the height of the curve at these points to the height at its center is a measure of the line width. This ratio, $\phi_{\text{w.p.}}/\phi_{\text{peak}}$, taken from the data of the precision runs is listed in Table XXIII. For the αa runs, the data indicate a small discrepancy from the theoretical expectation by 0.37 percent of the central height of the resonance with an Av. dev. of 0.22 percent. The αc runs show a similar condition, the discrepancy being 0.42 percent with an Av. dev. of 0.19 percent. In both cases, the lines are narrower than expected. As seen below, this discrepancy is easily understood and the fit is felt to be quite satisfactory.

In general, all effects which could possibly result in asymmetries or shifts significant at the level of accuracy of the precision runs have been included in the "theoretical" line widths used in this section, but terms which could only affect the lines symmetrically by small amounts have been dropped in the interest of simplifying the calculations. An omitted term which is known to have an appreciable influence on the line width is the power sharpening effect discussed in Appendix IV of Part III. This term would produce a lowering of the quenching at the operating points by an amount estimated at about 0.3 percent, which brings the experimentally observed and predicted line widths into reasonable agreement.

The low frequency transitions reported in Part V show a similar but less marked narrowing. Differences in degree of narrowing for various transitions stem from differences in the rf power level needed in each case. The effective power level depends on the average time of interaction of the beam and on the magnitude of the quenching observed for each hyperfine component of the resonance. The σ-polarized interaction space probably has a significantly shorter interaction time for αa and αc than for αf observations due to changes in the mode pattern occasioned by the short wavelength, since the diameter of the interaction space is

[141] Measurements of the slopes of the low frequency transitions are reported in Part V, Sec. 91. There the measured slopes were found to agree with the theoretical values.

about half a wavelength at 10 000 Mc/sec. At the lower frequencies, the π-polarization interaction space undoubtedly has a more uniform field distribution over the length of the beam, and consequently a longer average interaction time than the σ-polarized one. In addition, the peak quenching for a single hyperfine component is greater than the peak quenching for the composite resonance since the composite resonance is normalized to a predetermined height at its center.

The magnitude of the observed sharpening is in rough agreement with estimates of the effect of power sharpening. This explanation is thus not proven but made quite plausible. Since no appreciable shifts or asymmetries are introduced by this effect,[142] no detailed investigation of the phenomenon was attempted.

Z. RESULTS

104. Nature of Data

The taking of data for these runs follows fairly closely the plan previously described.[143] Briefly, this may be summarized as follows: The transition αa and αc in deuterium were studied at frequencies of 10,795 Mc/sec and 7195 Mc/sec, respectively. For the αa case, near the βe crossing point, the absence of β-state metastables is guaranteed by the motional electric field quenching, avoiding the necessity for a β-component correction.[144] For the αc transitions, near the βf crossing point, a small π-polarized electric field is introduced between the bombarder and the interaction region to insure the quenching of residual β-state atoms.[145]

A listing of dates of the runs is made is Table XXIV. Between runs number 2 and 3 on $D(\alpha a)$, the apparatus was opened and given a thorough cleaning. The $D(\alpha c)$ runs 1 through 9 are omitted since improvements were then made in the magnetic field calibration. Calibration was accomplished by means of the $\alpha\beta$ transition for the D(αc) runs while the proton resonance was used for the D(αa) data.

Each run usually contained four comparisons of the fractional quenching at the working points. Each quenching comparison consisted of two measurements of the quenching at one working point and one measurement at the other working point. The temporal sequence of these measurements was such that uniform drifts of the rf power level and beam strength did not influence the result. Each measurement of the fractional quenching at a working point consisted of four measurements of the rf quenching and three measurements of the quenching produced by a dc field sufficiently strong to quench essentially all metastables. These measurements were so arranged in time as to have eliminated any influence of uniform drifts in strength of metastable beam over the period of time needed for observing the rf and dc quenching twice each (60 seconds). In addition, at the beginning and end of each run, the fractional quenching at the nominal middle point of the resonance was measured (6 measurements of rf and 4 of dc quenching) for the purpose of normalizing the data to 31 percent quenching at the middle, the figure used in all of the asymmetry and shift calculations. For the αa runs numbered 5 and 6, the fractional quenching at the middle was also measured three times during the run but each measurement contained only 4 rf and 3 dc quenching values. This procedure was suggested by the tendency of the calibration of the rf power monitor crystal to drift during the run due to temperature effects. In extreme cases, the peak quenching might change from 30 percent to 32 percent during the run even though the crystal current was kept constant by continual readjustment of an attenuator in the rf line. The oscillator frequency was in all cases essentially constant during the run due to the use of the frequency stabilizer described in Appendix IX.

TABLE XXIV. Dates of runs.

Run No.	D(αa) Date	Run No.	D(αc) Date
1	2/21/52	10	6/21/51
2	2/22	11	6/25
3	2/26	12	6/26
4	2/27	13	6/27
5	2/28	14	6/29
6	2/29		

For the αa runs, the calibration of the rotating search coil used for measurement of the magnetic field was made before and after the run by means of the proton resonance. It is estimated that the maximum error of this technique was not more than 1 part in 40,000. With each measurement of the proton resonance field, the error due to possibly faulty compensation of the 60 cycle/sec ac component of the magnetic field was checked and maintained below 1 part in 80,000. The resistances of the rotating search coils were measured at the end of each run.

For the αc runs, the calibration was accomplished by measuring the resonant field of the $\alpha\beta$ resonance either at the end or the beginning of the run. The resonance frequency was nominally 1610 Mc/sec in all cases and was measured in the manner described below. The resonant field for the $\alpha\beta$ resonances was determined by a technique similar to that applied to the runs themselves, i.e., the quenching at a selected working point on one side was repeatedly compared with that at a point on the other side of approximately equal quenching. The central field was then calculated from these data using a slope measured near one or both of the selected points. Because of the sharpness of these resonances, it was unnecessary to make more than 5 or 6 comparisons in rapid succession.

[142] See Part III, Appendix IV.
[143] See Part IV, Sec. 75.
[144] β-component corrections are discussed more fully in Part IV, Sec. 73.
[145] This technique is discussed more fully in Part V, Sec. 86 and an additional correction of the results required by its use is calculated in Part V, Sec. 93, Eq. (258).

TABLE XXV. Summary of central fields.

Run	$\bar{H}$ gauss	Av. dev.	Residual	No. of items	Relative weight
Transition D(αa) (10,795.000 Mc/sec)					
1	630.655	0.029	0.024	4	48
2	630.655	0.086	0.024	6	8
3	630.676	0.115	0.003	4	3
4	630.752	0.057	0.073	4	12
5	630.845	0.093	0.166	4	5
6	630.663	0.043	0.016	4	22
Mean	630.679	0.071	0.035		
Transition D(αc) (7195.000 Mc/sec)					
10	1189.449	0.05	0.065	7	28
11	1189.275	0.06	0.109	4	11
12	1189.372	0.11	0.012	6	5
13	1189.308	0.08	0.076	6	9
14	1189.415	0.14	0.031	8	4
Mean	1189.362	0.080	0.068		

The use of the $\alpha\beta$ resonance taken with the σ-polarized interaction space, however, introduced the previously discussed possibility of systematic errors in the field calibration. In addition, at the time the αc runs were taken, the technique used for adjusting compensation of the 60-cps component of the magnetic field was somewhat defective, leading to an additional error, probably somewhat nonrandom in nature, perhaps as large as 5 parts in 80 000.

The following auxiliary data were collected in connection with each run: The frequency of beat note between the power oscillator and the appropriate harmonic of the crystal controlled secondary frequency standard was measured to about 0.001 Mc/sec by means of a calibrated auxiliary receiver. The frequency of the secondary standard was compared at the 5 Mc/sec level with the primary standard of frequency of this Laboratory to an accuracy no poorer than 5 cycles/sec. This primary standard of frequency was known to agree with the 5 Mc/sec broadcasts of the National Bureau of Standards to within 1 cps during all runs.

The temperature of the permanent reference magnet of the rotating search coil, read to 0.02°, was recorded after every two or three lines of data. The temperatures of the variable and fixed arms of the bridge of the rotating search coil, read to 0.1°, were recorded as needed, depending on their drift rates. Other information relating to the operating conditions and performance of the apparatus was recorded although not required in the analysis of the precision data.

105. Calculation of Central Fields

A preliminary value for the resistance corresponding to the central magnetic field of the resonance was obtained from Eq. (252).[146]

$$\bar{R}=\tfrac{1}{2}(R_a+R_b)+\tfrac{1}{2}(\bar{\phi}_b-\bar{\phi}_a)/|d\phi/dR|. \qquad (252)$$

Here R_a and R_b are the true resistances in the variable bridge arm for the working points at the mean temperature of the run, including adjustment for the temperature drift of the fixed resistance arm. The second term corrects for the unavoidable slight asymmetry of placement of the working points about the center of the resonance and seldom amounts to more than about 10 ohms out of 40 000 (80 000 for αc). In calculating $\bar{\phi}_b-\bar{\phi}_a$, the quenching at one of the two working points was obtained by averaging successive pairs of measurements so as to eliminate effects of uniform power drift. The slope $d\phi/dR$ was obtained from the calculated radiative line shape. To this preliminary $\bar{R}$ was added a correction for the measured difference between primary and secondary standards of frequency and for the day to day changes in the difference between the power oscillator frequency and the harmonics of the secondary standard. The αa results were corrected to a true frequency of 10 795.000 Mc/sec and αc to 7195.000 Mc/sec.

The mean temperatures of permanent magnet and resistance boxes during the run were calculated and the calibration data adjusted to these temperatures. With the αa runs, a linear interpolation between the proton resonance resistances before and after the run was made to obtain the proton resonance resistance at the mean temperature of the permanent magnet for the run.

A frequency correction was applied, since the proton resonance oscillator frequency was measured by comparison with the secondary frequency standard. An additional correction to the proton resonance field because of the inhomogeneity of the magnetic field and the spatial separation of the proton probe and the interaction space was included. With the αc runs, the $\alpha\beta$-transition was used for calibration either before or after the run and adjustment to the mean temperature of the run was made by means of previously measured average temperature coefficients.

The magnetic field of the line center was then obtained by dividing the resistance of the corrected center by R/H, the number of ohms per gauss obtained from the corrected calibration resonance resistance and field. The αa and αc central fields are listed by runs in Table XXV. That table gives for each run the central field of the resonance for the frequency indicated, the average of the deviations of individual determinations within the run, the residuals of all runs with respect to

TABLE XXVI. Summary of corrections to observed $\Delta E_D-\delta_D$. Units are Mc/sec.

Source of asymmetry or shift	Correction D(αa)	Correction D(αc)	Explanation section No.
Matrix element variation	0	−0.157	63
Quenching asymmetry	−0.038	−0.001	64
Incomplete Back-Goudsmit	0.138	0.077	65
Zeeman curvature	0	−0.015	65
Stark effect shift	0.005	0.005	57
Low voltage quenching field asymmetry	Not used	−0.005	86, 92
Total	0.105	−0.096	

[146] See Part IV, Sec. 77.

their mean, the number of separate determinations comprising each run, and the relative weight assigned to each run in calculating the means. Weights assigned to the various runs are in proportion to the number of determinations in the run divided by the square of the internal Av. dev. of the run.

An inspection of Table XXV shows that for the αa transition the average of the residuals is roughly equal to the mean Av. dev. divided by the square root of the number of determinations in a run. This situation is consistent with an assumption of general randomness in the errors causing the scatter and effective absence of day to day fluctuations other than those represented by the internal Av. dev.'s of the runs. For the αc results, the approximate equality of the mean Av. dev. and the average residual may be taken to indicate the presence of large day-to-day fluctuations.

106. Asymmetry and Shift Corrections

Corrections to the apparent position of the resonance have already received extensive treatment in these articles and need not be repeated in detail. For the transitions reported here, some of the corrections are considerably smaller than for transitions previously reported, the total amounting to -0.096 Mc/sec for the case of D(αc) and $+0.105$ Mc/sec for D(αa). Individual corrections are listed in Table XXVI.

It will be noted from the table that both the matrix element variation and the Zeeman curvature corrections are zero for the αa transition. This derives from the fact that the a state (for which $m=+\frac{3}{2}$) is not mixed with any other state by the Zeeman coupling. The low voltage field quenching asymmetry correction is required for the αc runs only.

107. Results

The observed positions of the resonances listed in Table XXV can be converted into values of the quantity $\Delta E_D - \delta_D$ by use of the Zeeman effect formulae (164–172).[147] After applying the corrections listed in Table XXVI, the final results for $\Delta E_D - \delta_D$ are in Table XXVII, 9912.59 Mc/sec from D(αa) and 9912.80 Mc/sec from D(αc).

The difference between the D(αa) and D(αc) results is 0.21 Mc/sec. This discrepancy is comparable to the mean average deviation of the D(αc) run results. It does not seem likely that its origin is to be found entirely or predominantly in fluctuations of a random nature since it is three times the sum of the technical probable errors of the αa and αc results. It is felt that this discrepancy is to be ascribed to systematic error arising in the $\alpha\beta$-resonance method of field calibration used for the αc runs. Reasons for expecting such a difficulty are set forth in Sec. 99 where it is indicated that an error of 1 part in 20 000 is likely. An error in the magnetic field of this magnitude amounts to 0.14 Mc/sec for $\Delta E_D - \delta_D$ which can quite satisfactorily account for the discrepancy. In view of this situation, it is felt that the αa runs alone should be used to obtain a final value for $\Delta E_D - \delta_D$.

[147] See Part III, Sec. 55.

TABLE XXVII. Summary of results.

	D(αa)	D(αc)	
Frequency	10 795.000	7195.000	Mc/sec
Magnetic field for resonance	630.679	1189.384	gauss
Preliminary $\Delta E_D - \delta_D$	9912.489	9912.899	Mc/sec
Corrections, Table XXVI	+0.105	−0.096	Mc/sec
Final $\Delta E_D - \delta_D$	9912.594	9912.803	Mc/sec
Mean residual	0.049	0.156	Mc/sec
Probable error	0.017	0.054	Mc/sec
Statistical limit of error (3 times probable error)	0.05	0.16	Mc/sec
Final limit of error estimate (see text)	0.10	···	Mc/sec

Reasons underlying the choice of operating conditions for the final high precision determination of $\Delta E_D - \delta_D$ include the following: The slope of the αa transition is about 1.4 Mc sec^{-1} gauss^{-1} which together with the choice of an operating field of only 630 gauss makes the Zeeman energy reasonably small without broadening the resonance in magnetic field too much. There is no Zeeman curvature or variation of the matrix element for this transition, facts which could be of some consequence should some omission in the theory later be uncovered. The operating frequency is chosen so that there will be no contamination of the beam by β-component at the operating fields. These reasons singly are not compelling but taken together indicate the extent to which ideal measurement conditions could be chosen.

108. Limit of Error of Result

This work has aimed throughout at a 0.1 Mc/sec limit of error, and consequently effects making contributions to the experimental result of order 0.01 Mc/sec have been investigated. The statistical probable error of the result is 0.017 Mc/sec. An error of more than three times this or 0.05 Mc/sec has a chance of only one in 100. To arrive at a reasonable limit of error, one must add to this an estimate of possible remaining systematic errors which will be taken as 0.05 Mc/sec. This figure is equal to the mean day-to-day scatter of the αa results. A systematic error whose nonrandom day-to-day changes were significantly larger than this amount would have been noticed whereas smaller effects would have been masked by the scatter. (An example of such an error would be possibly some effect due to the presence of charged insulating layers which could form on the inner walls of the apparatus. Presumably effects of this sort would change continuously with time except when the apparatus was cleaned.) An unvarying systematic effect or an omission in the theory by which the experimental results are interpreted would presumably spoil the consistency of values derived from different transitions. It is felt that the mutual con-

sistency of the results reported in Part V bears out the general reliability of the theory and method at least to this order of accuracy. The figure of $\pm(0.05+0.05)$ or ± 0.10 Mc/sec is therefore adopted to represent the range within which the authors believe the true value to lie.

109. The Fine Structure Constant

When the value of δ_D, 1059.00 ± 0.10 Mc/sec, reported in Part V is added to $\Delta E_D-\delta_D$, $\Delta E_D=10{,}971.58\pm0.20$ Mc/sec is obtained. This quantity leads to a value for the fine structure constant when inserted into the well-founded theoretical expression[148] for the fine structure separation

$$\Delta E=\frac{1}{32}\mu\alpha^4+\frac{5}{256}\alpha^6+\frac{1}{32\pi}\alpha^5\left[1-\frac{5.946}{\pi}\alpha\right]. \quad (135)$$

In ordinary units, for deuterium, this equation becomes

$$\nu_{\Delta E}=\frac{cR_D}{16}\alpha^2\left[1+\tfrac{5}{8}\alpha^2+\frac{\alpha}{\pi}-\frac{5.946}{\pi^2}\alpha^2\right]. \quad (264)$$

Actually, α is not determined from these measurements but rather the quantity α^2cR_D. For the auxiliary constants, the values $R_D=109{,}707.44$ cm^{-1} and $c=299{,}790.0$ km/sec given by Bearden and Watts[149] have been used. One obtains then $\alpha^{-1}=(137.0365\pm0.0012)$ for the value of the reciprocal of the fine structure constant as determined from the *fine structure* by this investigation.[150] The uncertainty quoted includes no allowance for uncertainty in the auxiliary constants. The uncertainty in c given by Bearden and Watts would add 0.0002 to the uncertainty in α^{-1}. A change in the value accepted for c by $+1$ km/sec would change α^{-1} by $+0.00023$.

It is of interest to compare this value with the most recently available value from measurements of the *hyperfine structure* of the ground state of hydrogen. Salpeter and Newcomb[151] discuss radiative corrections and find $\alpha^{-1}=(137.0355\pm0.0010)\cdot(1+\frac{1}{2}\delta)$ where the quantity δ is inserted to take account of effects as yet uncalculated due to departure of the proton magnetic field from that of a point dipole. The uncertainty given is a probable error. The value of δ may be greater than $\pm2\times10^{-5}$ according to Salpeter and Newcomb and consequently the small difference between their value and ours cannot be taken seriously at the present time. It should be noted that the comparison is not affected by the values used for the auxiliary constants.

The authors have benefited greatly from many valuable discussions of the theoretical aspects of this work with Professor N. M. Kroll. We wish to thank the members of the Columbia Radiation Laboratory staff for their wholehearted cooperation, and especially Messrs. J. Heberle and H. Reich for assistance with the taking of data, and Messrs. A. H. Barrett and R. Herman for assistance with the computation.

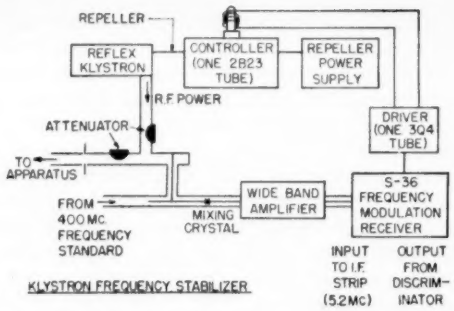

FIG. 69. Block diagram of frequency stabilizing arrangement used with reflex klystrons. The wide band amplifier is unnecessary when the beat note is strong.

APPENDIX VIII. OSCILLATOR FREQUENCY STABILIZER

Several of the reflex klystron oscillators showed rapid fluctuations in frequency of the order of several tenths of a megacycle. In addition to adding some degree of uncertainty to the frequency determination and requiring an extra set of corrections to the data, these fluctuations were reflected as power variations when the resonant interaction space was used. A block diagram of the frequency stabilizing arrangement constructed is shown in Fig. 69. The beat frequency between the Klystron and an appropriate harmonic of a crystal controlled standardized oscillator is amplified and used to provide an error signal to correct the Klystron frequency. The error signal is transferred to the dc level of the Klystron repeller by means of a 2B23 magnetically controlled diode.[152] The stabilization achieved in this way, even in the absence of additional dc amplification of the error signal, was adequate to confine the oscillator to a frequency band of width 5 kc/sec over a half-hour period.

APPENDIX IX. OVEN TEMPERATURE REGULATOR

Large fluctuations in beam size traceable to fluctuations in the temperature of the dissociating oven were observed on some occasions. Such fluctuations made it impossible to use the apparatus and since the cure for the source of the condition was usually replacement of the oven, which takes several days, a symptomatic cure in the form of a temperature regulator was tried. The regulator obtained its error signal from a photoelectric cell which monitored the light output of the hot oven. The amplified error signal was used to control

[148] See Part III, Sec. 53.
[149] J. A. Bearden and H. M. Watts, Phys. Rev. **81**, 73 (1951).
[150] Earlier results were reported as follows (Part IV): $\Delta E_D-\delta_D=9912.40\pm1.0$ Mc/sec, $\Delta E_D=10{,}972.11\pm1.0$ Mc/sec, $\alpha^{-1}=137.033\pm0.006$.
[151] E. E. Salpeter and W. A. Newcomb, Phys. Rev. **87**, 150 (1952).
[152] E. S. Dayhoff, Rev. Sci. Instr. **22**, 1028 (1951).

a variable impedance device put between the oven and the voltage regulated power line. This arrangement was able to reduce abnormal beam fluctuations by a factor of 5 or more in cases where such fluctuations were really due to variations in oven temperature. It did not cause more than a slight improvement in the beam steadiness on "quiet" days.

APPENDIX X. DETECTOR IMPROVEMENTS

An attempt was made to increase the time between overhauls[153] by making it possible to heat the detector strongly on occasions when it appeared to have become poisoned. Heating to a bright orange color seemed to be quite successful in restoring the beam to its initial strength. Generally, this procedure was necessary about once a month. Satisfactory running conditions could usually be maintained in this way for periods of three or four months before it became necessary to open the apparatus for cleaning.

Only rough qualitative observations of the effects of such heating can be reported here since this apparatus is not suited to quantitative measurements of this nature. In general, heating was followed immediately by a period of very low detection efficiency for metastable atoms and relatively high efficiency for background radiation.[154] Conditions gradually returned to normal after several hours of reconditioning by exposure to a normal flow of hydrogen gas. In the absence of hydrogen, apparently no reconditioning occurred over a 24-hour period. Replacement of the tungsten detector plate by activated thoriated tungsten, zirconium, and platinum has in each case resulted in a satisfactory beam and there appears to be no qualitative basis for choice among these metals.

[153] See Part II, Sec. 43.

[154] See Part III, Sec. 67.

PHYSICAL REVIEW VOLUME 89, NUMBER 1 JANUARY 1, 1953

The Canonical Transformation for an Electron-Positron Field Coupled to a Time-Independent Electromagnetic Field*

H. E. MOSES
Institute for Mathematics and Mechanics, New York University, New York, New York
(Received April 4, 1952)

The problem of the electron-positron field coupled to an unquantized electromagnetic field, constant in time, is solved in the Schrödinger picture by finding a suitable canonical transformation. It is shown that in the number representation this transformation satisfies an integro-difference equation which can be solved by means of a perturbation scheme in a manner analogous to the finding of one-particle canonical transformations. It is shown, moreover, that this canonical transformation can be expressed in terms of single-particle canonical transformations.

1. THE *N* REPRESENTATION OF THE ELECTRON-POSITRON FIELD

We consider the unperturbed energy representation of a single Dirac electron. A state is represented by a function of the momentum vector P, of the sign of the energy ϵ, and of the component of spin in the direction of momentum τ. These variables form a complete set of commuting variables. We shall designate this set of variables by the letter s and call s itself a "variable."

A state of the electron-positron field Φ is represented in the number representation (or Fock representation) by a set of functions $\psi_n(s)_n$, where $\psi_n(s)_n$ is an abbreviated expression for $\psi_n(s_1, s_2, \cdots, s_n)$ which is an antisymmetric function of the n variables $s_1, s_2, \cdots, s_n$. We call this representation "the N representation" and use the notation

$$\Phi \underset{N}{\leftrightarrow} \{\psi_n(s)_n\}. \tag{1}$$

The inner product of two states,

$$\Phi^{(1)} \underset{N}{\leftrightarrow} \{\psi_n{}^{(1)}(s)_n\}, \quad \Phi \underset{N}{\leftrightarrow} \{\psi_n(s)_n\},$$

is given by

$$(\Phi^{(1)}, \Phi) = \sum_{n=0}^{\infty} \int \cdots \int_{n\text{-fold}} \bar{\psi}_n{}^{(1)}(s_1, s_2, \cdots, s_n) \times \psi_n(s_1, s_2, \cdots, s_n) ds_1 ds_2 \cdots ds_n$$

$$\equiv \sum_{n=0}^{\infty} \int \bar{\psi}_n{}^{(1)}(s)_n \psi_n(s)_n (ds)_n, \tag{2}$$

where the integration over the variables $s_1, s_2, \cdots, s_n$ means integration over the continuous variables and summation over the discrete variables. The bar represents the complex conjugate. The annihilation operator $A^-(s')$ and creation operator $A^+(s')$ are defined by

* This work is an extract of a report for a project supported by the ONR and the Air Force Cambridge Research Center.

(see, e.g., Friedrichs[1])

$$A^-(s')\Phi \underset{N}{\leftrightarrow} \{(n+1)^{\frac{1}{2}}\psi_{n+1}(s)_n(s')\}, \tag{3}$$

where

$$\psi_{n+1}(s)_n(s') \equiv \psi_{n+1}(s_1, s_2, \cdots, s_n, s')$$

and

$$A^+(s')\Phi \underset{N}{\leftrightarrow} \{(n)^{\frac{1}{2}} \operatorname*{Asy}_{s_1, \cdots s_n} \psi_{n-1}(s)_{n-1}\delta(s_n; s')\}, \tag{4}$$

where

$$\operatorname*{Asy}_{s_1, \cdots s_n} f(s_1, s_2, \cdots, s_n)$$

means the sum of all terms $(-1)^p f(s_a, s_b, \cdots s_r)/n!$, with $s_a, s_b, \cdots s_r$ being a permutation of the variables $s_1, s_2 \cdots s_n$ and p being the number of interchanges required to effect this permutation.

The function $\delta(s; s')$ is a generalized δ-function defined by

$$\int_I f(s')\delta(s; s')ds' = \begin{cases} f(s) \text{ if } I \text{ includes } s, \\ 0, \text{ otherwise,} \end{cases} \tag{5}$$

I being the range of integration.

The number operator is defined by

$$N = \int A^+(s')A^-(s')ds', \tag{6}$$

and is represented by

$$N\Phi \underset{N}{\leftrightarrow} \{n\psi_n(s)_n\}. \tag{7}$$

The electron number operator is given by

$$N_+ = \int A^+(s')A^-(s')\delta_{\epsilon', +}ds', \tag{8}$$

while positron number operator is given by

$$N_- = \int A^+(s')A^-(s')\delta_{\epsilon', -}ds', \tag{9}$$

where

$$\delta_{\epsilon, +} = \begin{matrix} 1, & \epsilon > 0, \\ 0, & \epsilon < 0, \end{matrix} \tag{10}$$

$$\delta_{\epsilon, -} = \begin{matrix} 0, & \epsilon > 0, \\ 1, & \epsilon < 0. \end{matrix} \tag{11}$$

2. THE X REPRESENTATION

Consider the Hamiltonian of the Dirac electron

$$H = H^{(0)} + eH^{(1)}, \tag{12}$$

where $H^{(0)}$ is the unperturbed operator and $H^{(1)}$ is the perturbation.

$$H^{(0)} = i\sum_i \alpha_i \partial/\partial x_i - \beta m, \quad (h=c=1). \tag{13}$$

$$H^{(1)} = \sum_i \alpha_i A_i(X) + \varphi(X). \tag{14}$$

$A_i(X)$ and $\varphi(X)$ are the vector and scalar potentials and are functions of the position X only.

Let us denote the eigenfunctions of $H^{(0)}$ by $\chi^{(0)}(X, \mu; s)$, μ being the spinor index which runs from 1 to 4. We define the operators $\Xi^{\mp}(X, \mu)$ by

$$\Xi^-(X, \mu) = \int \chi^{(0)}(X, \mu; s)A^{-\epsilon}(s)ds,$$

$$\Xi^+(X, \mu) = \int \bar{\chi}^{(0)}(X, \mu; s)A^{+\epsilon}(s)ds, \tag{15}$$

or from the orthogonality of the eigenfunctions,

$$A^{-\epsilon}(s) = \sum_\mu \int \Xi^-(X, \mu)\bar{\chi}^{(0)}(X, \mu; s)dX,$$

$$A^{+\epsilon}(s) = \sum_\mu \int \Xi^+(X, \mu)\chi^{(0)}(X, \mu; s)dX, \tag{15a}$$

where $A^{-\epsilon}(s)$ is $A^-(s)$ for values of s in which $\epsilon > 0$, and $A^{-\epsilon}(s)$ is $A^+(s)$ for values of s in which $\epsilon < 0$. The operator $A^{+\epsilon}(s)$ is defined analogously. In the integrations of (15), $A^{\pm\epsilon}(s)$ are considered as "functions" of ϵ in terms of the superscript as well as through the variable s.

In the Heisenberg picture operators $\Xi^{\mp}(X, \mu)$ satisfy the Dirac equation and its adjoint, respectively.

3. THE M REPRESENTATION

The M representation is obtained by expanding $\Xi^{\pm}(X, \mu)$ in terms of the eigenfunctions of H, rather than in terms of those of $H^{(0)}$.

Let us assume that the spectrum of H is the same as that of $H^{(0)}$. (This assumption is not necessary, but it simplifies the discussion. If the spectrum of H differs from that of $H^{(0)}$, much of what follows is still valid.) Then the single-particle state in the representation of the operator H will be a function of a complete set of commuting variables v, of which some are analogous to the momentum, one of which is the sign of the energy which we designate by ι, and one of which is analogous to τ.

In the M representation the operators $B^{\pm\iota}(v)$ are defined by

$$B^{-\iota}(v) = \sum_\mu \int \Xi^-(X, \mu)\bar{\chi}(X, \mu; v)dX,$$

$$B^{+\iota}(v) = \sum_\mu \int \Xi^+(X, \mu)\chi(X, \mu; v)dX, \tag{16}$$

where $\chi(X, \mu; v)$ are the eigenfunctions of H. We define

[1] K. O. Friedrichs, Communications on Pure and Applied Mathematics, **4**, 1 (1951).

the annihilation and creation operators B^-, B^+ by

$$B^-(v)=\delta_{s,+}B^{-s}(v)+\delta_{s,-}B^{+s}(v),$$
$$B^+(v)=\delta_{s,+}B^{+s}(v)+\delta_{s,-}B^{-s}(v), \tag{17}$$

and introduce the modified number operator M,

$$M=\int B^+(v)B^-(v)dv. \tag{18}$$

The representation in terms of this operator is called the M representation. In a manner analogous to the use of the N representation we represent a state Φ in the M representation as follows:

$$\Phi\underset{M}{\leftrightarrow}\{\zeta_n(v)_n\}. \tag{19}$$

The advantage of the M representation is that the solution of the Schrödinger equation $\Phi(t)$ has a simple form in the M representation, namely,

$$\Phi(t)\underset{M}{\leftrightarrow}\left\{\exp\left[-it\sum_{i=1}^{n}|E(v_i)|\right]\zeta_n(v)_n\right\}\equiv\{\zeta_n(v)_n(t)\}, \tag{20}$$

where $E(v)$ is the energy corresponding to the value v of the quantum variable and where

$$\Phi(0)\underset{M}{\leftrightarrow}\{\zeta_n(v)_n\}. \tag{21}$$

Actually, one is more interested in the N representation of $\Phi(t)$,

$$\Phi(t)\underset{N}{\leftrightarrow}\{\psi_n(s)_n(t)\}. \tag{22}$$

Our objective is to find the transformation between the M representers and the N representers of an arbitrary state Φ. Having this transformation we can find the functions $\psi_n(s)_n(t)$ in terms of

$$\zeta_n(v)_n(t)=\exp\left[-it\sum_{i=1}^{n}|E(v_i)|\right]\zeta_n(v)_n.$$

This transformation is obtained through our knowledge of the relations between the operators $B^\pm$ and $A^\pm$, which from (15) and (16) are

$$B^{-s}(v)=\int u(v;s)A^{-s}(s)ds,$$
$$B^{+s}(v)=\int\tilde{u}(v;s)A^{+s}(s)ds, \tag{23}$$

or equivalently,

$$A^{-s}(s)=\int\tilde{u}(v;s)B^{-s}(v)dv,$$
$$A^{+s}(s)=\int u(v;s)B^{+s}(v)dv, \tag{23a}$$

where

$$\tilde{u}(v;s)=\sum_{\mu}\int\chi(X,\mu;v)\tilde{\chi}^{(0)}(X,\mu;s)dX, \tag{24}$$

so that $\tilde{u}(v;s)$ is the eigenfunction of H in the representation of the unperturbed Hamiltonian.

If instead of considering an electron-positron field we consider an electron field only, Eqs. (23) and (24) are replaced by

$$B^-(v)=\int u(v;s)A^-(s)ds,$$
$$B^+(v)=\int\tilde{u}(v;s)A^+(s)ds, \tag{25}$$

and

$$A^-(s)=\int\tilde{u}(v;s)B^-(v)dv,$$
$$A^+(v)=\int u(v;s)B^+(v)dv. \tag{26}$$

We shall use these relations to illustrate a point later.

4. THE SINGLE-PARTICLE CANONICAL TRANSFORMATION

Consider the single-particle Dirac theory. Let a state be represented in the H representation by a function $g(v)$ and the same state in the $H^{(0)}$ representation by $f(s)$, then we have

$$g(v)=\int u(v;s)f(s)ds,$$
$$f(s)=\int\tilde{u}(v;s)g(v)dv, \tag{27}$$

that is, $u(v;s)$ is the kernel of the canonical transformation of the single-particle theory. The functions $u(v;s)$ satisfy the following orthogonality conditions:

$$\int\tilde{u}(v;s)u(v';s)ds=\delta(v;v'),$$
$$\int\tilde{u}(v;s)u(v;s')dv=\delta(s;s'). \tag{28}$$

There are many such transformations $u(v;s)$ corresponding to the fact that the eigenfunctions $\chi(X,\mu;s)$ are not unique but must have boundary conditions assigned to them. The most interesting functions $u(v;s)$ are those two for which $\chi(X,\mu;s)$ have radially outgoing or incoming parts for $|X|$ large. The equation

which such functions $u(v;s)$ satisfy are[2,3]

$$u(v;s)=\delta(v;s)+e\Big[i\pi\delta(E(v)-E(s))+\frac{p}{E(v)-E(s)}\Big]\int H^{(1)}(s';s)u(v;s')ds', \quad (29)$$

and

$$u(v;s)=\delta(v;s)+e\Big[-i\pi\delta(E(v)-E(s))+\frac{p}{E(v)-E(s)}\Big]\int H^{(1)}(s';s)u(v;s')ds', \quad (30)$$

where $p/(\xi-\eta)$ means that in integrations over η the principal part of the integral is to be taken and

$$H^{(1)}(s';s)=\sum_{\mu}\int\bar{\chi}^{(0)}(X,\mu;s')H^{(1)}\chi^{(0)}(X,\mu;s)dX. \quad (31)$$

Equations (29) and (30) are usually solved by expansions in the parameter e:

$$u(v;s)=\sum_{r=0}^{\infty}e^r u^{(r)}(v;s). \quad (32)$$

By substituting in (29) or (30) one obtains $u^{(r)}$ in terms of u^{r-1} and

$$u^{(0)}(v;s)=\delta(v,s). \quad (33)$$

We assume in what follows all $u^{(r)}$ have been found. It will also be useful to substitute the expansion (32) into the orthogonality relations (28). One obtains conditions on $u^{(r)}(v;s)+\bar{u}^{(r)}(s;v)$ in terms of the functions $u^{(r-1)}$. These relations will be useful to us later. Such relations are independent of the explicit form of $u^{(r)}$. In particular,

$$u^{(1)}(v;s)+\bar{u}(s;v)=0. \quad (34)$$

5. THE CANONICAL TRANSFORMATION IN THE ELECTRON-POSITRON FIELD

We now wish to introduce the transformation which relates the representers in the M representation to those in the N representation. If we have the M and N representations for an arbitrary state vector Φ, we write

$$\Phi\underset{M}{\longleftrightarrow}\{\zeta_n(v)_n\} \quad \text{and} \quad \Phi\underset{N}{\longleftrightarrow}\{\psi_n(s)_n\}.$$

We introduce the transformation in the form

$$\zeta_n(v)_n=\sum_{n'}\int T_{n;n'}(v)_n:(s)_{n'}\psi_{n'}(s)_{n'}(ds)_{n'}, \quad (35)$$

where $(ds)_{n'}$ means an integration over the variables $s_1, s_2, \cdots, s_{n'}$. For convenience we use the notation $T_{n;n'}(v)_n:(s)_{n'}$ to be a function of the variables $v_1, v_2, \cdots, v_n$ and of the variables $s_1, s_2, \cdots, s_{n'}$. It is seen that this function is separately antisymmetric in $v_1, v_2, \cdots, v_n$ and $s_1, s_2, \cdots, s_{n'}$.

In order that the length of Φ be preserved we have the orthogonality conditions for the functions $T_{n;n'}(v)_n:(s)_{n'}$, namely,

$$\left.\begin{aligned}\sum_n\int\bar{T}_{n;n'}(v)_n:(s')_{n'}T_{n;n''}(v)_n:(s'')_{n''}(dv)_n&=\delta_{n';n''}\operatorname*{Asy}_{\substack{s_1'\cdots s_{n'}'\\ s_1''\cdots s_{n''}''}}\delta(s';s'')_{n'},\\ \sum_{n'}\int\bar{T}_{n;n'}(v)_n:(s)_{n'}T_{n'';n'}(v'')_{n''}:(s)_{n'}(ds)_{n'}&=\delta_{n;n''}\operatorname*{Asy}_{\substack{v_1\cdots v_n\\ v_1''\cdots v_{n''}''}}\delta(v;v'')_n,\end{aligned}\right\} \quad (36)$$

where

$$\delta(s';s)_n=\delta(s_1';s_1)\cdot\delta(s_2';s_2)\cdots\delta(s_n';s_n), \quad (37)$$

and

$$\delta(s';s)_0=1.$$

Here $\delta_{n;n'}$ is the Kronecker delta. We use the notation

$$\operatorname*{Asy}_{\substack{v_1\cdots v_n\\ s_1\cdots s_{n'}}}f(v_1\cdots v_n:s_1\cdots s_{n'})$$

to mean that $f(v_1\cdots v_n:s_1\cdots s_{n'})$ is to be antisymmetrized with respect to the two sets of variables $v_1\cdots v_n$ and $s_1\cdots s_{n'}$ separately.

It should be noted that the set of functions $T_{n;n'}(v)_n:(s)_{n'}$ is analogous to the function $u(v;s)$ used in the one-electron problem which transforms functions in the s to the v representation. The whole point of what follows is to press this analogy.

For any operator Λ we define operators $\Lambda^{v,n}$ and $\Lambda^{s,n}$ by

$$\Lambda\Phi\underset{M}{\longleftrightarrow}\{\Lambda^{v,n}\zeta_n(v)_n\}, \quad \Lambda\Phi\underset{N}{\longleftrightarrow}\{\Lambda^{s,n}\psi_n(s)_n\}.$$

That is to say, $\Lambda^{v,n}\zeta_n(v)_n$ is the n-particle component of $\Lambda\Phi$ in the M representation and $\Lambda^{s,n}\psi_n(s)_n$ is the n-particle component of $\Lambda\Phi$ in the N representation.

Now

$$\Lambda^{v,n}\zeta_n(v)_n=\sum_{n'}\int T_{n;n'}(v)_n:(s)_{n'}\Lambda^{s,n'}\psi_{n'}(s)_{n'}(ds)_{n'}. \quad (38)$$

If we have two state vectors $\Phi^{(1)}$ and Φ and write the inner product $(\Phi^{(1)},\Lambda\Phi)$ in terms of the N representation we should have

$$(\Phi^{(1)},\Lambda\Phi)=\sum_n\int\bar{\psi}_n{}^{(1)}(s)_n\Lambda^{s,n}\psi_n(s)_n(ds)_n.$$

But since (by definition) the operator adjoint to Λ,

[2] K. O. Friedrichs, Comm. Pure and Appl. Math., **1**, 361 (1948).

[3] C. Møller, Kgl. Danske Videnskab. Selskab. Mat-fys. Medd. **23**, 1 (1945).

which we denote by Λ_a, satisfies

$$(\Lambda_a\Phi^{(1)}, \Phi) = (\Phi^{(1)}, \Lambda\Phi),$$

we have

$$\sum_n \int \bar{\psi}_n{}^{(1)}(s)\Lambda^{s,n}\psi_n(s)_n(ds)_n = \sum_n [\bar{\Lambda}_a{}^{s,n}\bar{\psi}_n{}^{(1)}(s)_n]\psi_n(s)_n(ds)_n. \quad (39)$$

Hence, we can write (38) as

$$\Lambda^{v,n}\zeta_n(v)_n = \sum_{n'} \int [\bar{\Lambda}_a{}^{s,n'}T_{n;n'}(v)_n : (s)_{n'}]\psi_{n'}(s)_{n'}(ds)_{n'}, \quad (40)$$

where $\Lambda_a{}^{s,n'}$ operates on the variables $s_1 \cdots s_{n'}$. But we also have

$$\Lambda^{v,n}\zeta_n(v)_n = \sum_{n'} \int \Lambda^{v,n}T_{n;n'}(v)_n : (s)_{n'}\psi_{n'}(s)_{n'}(ds)_{n'}, \quad (41)$$

where the operator $\Lambda^{v,n}$ operates on the variables $v_1 \cdots v_n$ of the functions $T_{n;n'}(v)_n : (s)_{n'}$.

Now since the state and, hence, the set of functions $\psi_n(s)_n$ is arbitrary we have from (40) and (41)

$$\Lambda^{v,n}T_{n;n'}(v)_n : (s)_n = \Lambda_a{}^{s,n'}T_{n;n'}(v)_n : (s)_{n'}. \quad (42)$$

If we took Λ to be the energy operator of the field, Eq. (42) for $T_{n;n'}(v)_n : (s)_{n'}$ would be analogous to the equations for $u(v; s)$. It is simpler, however, to take Λ to be one of the creation or annihilation operators $B^-(v)$, $B^+(v)$, $A^-(s)$, $A^+(s)$, all choices leading to the same result, as is required by a consistent theory. We take Λ to be the operator $B^-(v)$ and Λ_a to be $B^+(v')$ since the creation operator is the adjoint of the annihilation operator.

The left-hand member of (42) is then

$$(n+1)^{\frac{1}{2}}T_{n+1;n'}(v)_n(v') : (s)_{n'}.$$

The right-hand member of (42) is obtained in the following way. We can express the operator $B^+(v')$ in terms of $A^{\pm}(s)$ from (23) as

$$\begin{aligned}\bar{B}^+(v') &= \bar{B}^{+\epsilon'}(v')\delta_{\epsilon',+} + \bar{B}^{-\epsilon'}(v')\delta_{\epsilon',-} \\ &= \int u(v'; s')\bar{A}^{+\epsilon'}(s')ds'\delta_{\epsilon',+} + \int \bar{u}(v'; s')\bar{A}^{-\epsilon'}(x')ds'\delta_{\epsilon',-} \\ &= \int [u_{++}(v'; s') + \bar{u}_{--}(v'; s')]\bar{A}^+(s')ds' + \int [u_{+-}(v'; s') + \bar{u}_{-+}(v'; s')]\bar{A}^-(s')ds', \quad (43)\end{aligned}$$

where

$$\left.\begin{aligned}u_{++}(v'; s') &= u(v'; s')\delta_{\epsilon',+}\delta_{\epsilon',+} \\ u_{+-}(v'; s') &= u(v'; s')\delta_{\epsilon',+}\delta_{\epsilon',-}, \quad \text{etc.}\end{aligned}\right\} \quad (44)$$

Then we have

$$\begin{aligned}\bar{B}^{+s,n'}T_{n;n'}(v)_n : (s)_{n'} &= (n')^{\frac{1}{2}}\int [u_{++}(v'; s) + \bar{u}_{--}(v'; s)] \operatorname*{Asy}_{s_1, s_2, \cdots, s_{n'}} \cdot T_{n;n'-1}(v)_n : (s)_{n'-1}\delta(s_{n'}; s)ds \\ &\quad + (n'+1)^{\frac{1}{2}}\int [u_{+-}(v'; s) + \bar{u}_{-+}(v'; s)]T_{n;n'+1}(v)_n : (s)_{n'}(s)ds. \quad (45)\end{aligned}$$

In (42) replacing n by $n-1$ and replacing v' by v_n, we are led to our fundamental equation for $T_{n;n'}(v)_n : (s)_{n'}$ which is

$$\begin{aligned}(n)^{\frac{1}{2}}T_{n;n'}(v)_n : (s)_{n'} &= \left\{ \operatorname*{Asy}_{s_1 \cdots s_{n'}} (n')^{\frac{1}{2}}T_{n-1;n'-1}(v)_{n-1} : (s)_{n'-1}[u_{++}(v_n; s_{n'}) + \bar{u}_{--}(v_n; s_{n'})] \right\} + (n'+1)^{\frac{1}{2}}\int [u_{+-}(v_n; s') \\ &\quad + \bar{u}_{-+}(v_n; s')] \cdot T_{n-1;n'+1}(v)_{n-1} : (s)_{n'}(s')ds'. \quad (46)\end{aligned}$$

Equation (46) together with the orthogonality conditions (36) are our basic equations for finding the functions $T_{n;n'}(v)_n : (s)_{n'}$.

Equation (46) is a difference equation with respect to the subscripts n and an integral equation with respect to the variables s. We are thus led to an interesting integro-difference equation. To get some insight into the nature of the solution we shall consider a pure electron field, where we obtain a difference equation which can be solved explicitly.

In the case of the electron field where the M and N creation and annihilation operators are related by (25), the equation which replaces (46) is

$$(n)^{\frac{1}{2}}T_{n;n'}(v)_n : (s)_{n'} = (n')^{\frac{1}{2}} \operatorname*{Asy}_{s_1 \cdots s_{n'}} T_{n-1;n'-1}(v)_{n-1} : (s)_{n'-1}u(v_n; s_{n'}). \quad (47)$$

The orthogonality conditions (36) are valid for the electron field.

To solve (47) it is convenient to think in terms of the $n-n'$ plane (see Fig. 1).

It is seen that if the functions $T_{n;n'}(v)_n : (s)_{n'}$ are prescribed on the n and n' axes, the functions can be found anywhere in the $n-n'$ plane. It is further seen that the value of $T_{n;n'}(v)_n : (s)_{n'}$ at any point (n, n') depends only on the value of the function at the point

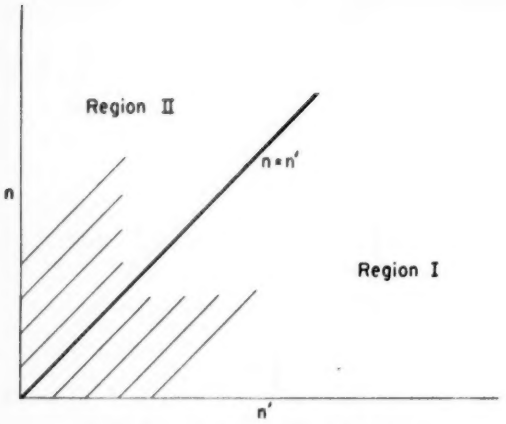

FIG. 1. Integro-difference equation for the canonical transformation.

on the axis at which a 45° line from (n, n') intersects the axis (see diagram). In region II of the $n-n'$ plane, i.e., the region for which $n>n'$, Eq. (47) can be solved immediately, because the values of the functions $T_{n;n'}(v)_n:(s)_{n'}$ on the n axis can be found from (47), except for the value $n=0$. From (47) it is clear that

$$T_{n;0}(v)_n:(s)_0=0,$$

so that

$$T_{n;n'}(v)_n:(s)_{n'}=0, \quad \text{for} \quad n>n'. \tag{48}$$

In order to find the functions for $n'\gtrless n$ we must know these functions on the n' axis. For this we use the orthogonality conditions (36).

Setting $n'=n''=0$ in the first of the Eqs. (36) and using (48) we have

$$|T_{0;0}(v)_0:(s)_0|^2=1, \tag{49}$$

or, within an arbitrary but unimportant phase factor,

$$T_{0;0}(v)_0:(s)_0=1. \tag{50}$$

Setting $n=n''=0$ in the second of Eqs. (36) and using (49), we have

$$\sum_{n'>0}\int \bar{T}_{0;n'}(v)_0:(s)_{n'}T_{0;n'}(v)_0:(s)_{n'}(ds)_{n'}=0$$

$$=\sum_{n'>0}\int |T_{0;n'}(v)_0:(s)_{n'}|^2(ds)_{n'},$$

from which it follows that

$$T_{0;n'}(v)_0:(s)_{n'}=0, \quad \text{for} \quad n'>0. \tag{51}$$

Hence, it follows that in region I in the $n-n'$ plane (i.e., for $n<n'$)

$$T_{n;n'}(v)_n:(s)_{n'}=0, \quad n<n'. \tag{52}$$

Therefore, it is only for $n'=n$ that transformation functions are not identically zero. From (47) and (50) we have

$$T_{n;n}(v)_n:(s)_n=\underset{s_1\cdots s_n}{\text{Asy}}\, u(v_1;s_1)u(v_2;s_2)\cdots u(v_n;s_n)$$

$$=\underset{\substack{s_1\cdots s_n\\ v_1\cdots v_n}}{\text{Asy}}\prod_{i=1}^{n}u(v_i;s_i), \tag{53}$$

where the second equation follows from the first by virtue of the properties of the asymmetrizing operator.

Thus, the only transformation functions which do not vanish are these which take an n-particle state in the N representation to an n-particle state in the M representation. This result could have been anticipated because, for the electron field,

$$M=N, \tag{54}$$

as follows from (25). It should also be noted that the nonvanishing transformation function consists of appropriately symmetrized products of the single-particle transformation functions. Again this fact could have been anticipated.

The greater complexity in the treatment of the electron-positron field arises from the fact that $M\neq N$ in this case.

6. SOLUTION OF THE INTEGRO-DIFFERENCE EQUATION

We shall now solve Eq. (46) to the second order in the electron charge by a perturbation procedure.

In (46) we set up the expansion

$$T_{n;n'}(v)_n:(s)_{n'}=\sum_{r=0}^{\infty}e^rT^{(r)}{}_{n;n'}(v)_n:(s)_{n'}, \tag{55}$$

and substitute (55) and expansion (32) in (46). As the zero-order equation we find, using (33) for $u^{(0)}$,

$$(n)^{\frac{1}{2}}T^{(0)}{}_{n;n'}(v)_n:(s)_n$$

$$=\underset{s_1\cdots s_{n'}}{\text{Asy}}\,(n')^{\frac{1}{2}}T^{(0)}{}_{n-1;n'-1}(v)_{n-1}:(s)_{n'-1}\delta(v_n;s_{n'}). \tag{56}$$

The orthogonality conditions (36) give the results

$$\sum_n\int T^{(0)}{}_{n;n'}(v)_n:(s')_{n'}T^{(0)}{}_{n;n''}(v)_n:(s'')_{n''}(dv)_n$$

$$=\delta_{n';n''}\underset{\substack{s_1\cdots s_{n'}\\ s_1''\cdots s_n''}}{\text{Asy}}\,\delta(s';s'')_{n'}, \tag{57}$$

and

$$\sum_{n'}\int \bar{T}^{(0)}{}_{n;n'}(v)_n:(s)_{n'}T^{(0)}{}_{n'';n'}(v'')_{n''}(s)_{n'}(ds)_{n'}$$

$$=\delta_{n;n'}\underset{\substack{v_1\cdots v_n\\ v_1''\cdots v_n''}}{\text{Asy}}\,\delta(v;v'')_n. \tag{58}$$

In a manner similar to the manner of solving for $T_{n;n'}(v)_n:(s)_{n'}$ in the case of the electron field, we have

for $T^{(0)}$

$$T^{(0)}{}_{n:n'}(v)_n:(s)_{n'}=\delta_{n:n'}\operatorname*{Asy}_{\substack{v_1\cdots v_n\\ s_1\cdots s_n}}\delta(v;s)_n. \tag{59}$$

Thus the zero-order term gives an identity transformation, as is to be expected.

The first-order terms from (46) are, on substituting (59) for $T^{(0)}$,

$$\begin{aligned}(n)^{\frac{1}{2}}&T^{(1)}{}_{n:n'}(v)_n:(s)_{n'}\\ &=\operatorname*{Asy}_{s_1\cdots s_{n'}}(n')^{\frac{1}{2}}T^{(1)}{}_{n-1:n'-1}(v)_{n-1}:(s)_{n'-1}\delta(v_n;s_{n'})\\ &\quad+\operatorname*{Asy}_{s_1\cdots s_{n'}}(n')^{\frac{1}{2}}\delta_{n:n'}\delta(v;s)_{n'-1}[u_{++}{}^{(1)}(v_{n'};s_{n'})\\ &\quad+\bar{u}_{--}{}^{(1)}(v_{n'};s_{n'})]+\operatorname*{Asy}_{\substack{v_1\cdots v_{n'+1}\\ s_1\cdots s_{n'}}}(n'+1)^{\frac{1}{2}}\delta_{n:n'+2}\delta(v;s)_{n'}\\ &\quad\times[u_{+-}{}^{(1)}(v_{n'+2};v_{n'+1})+\bar{u}_{-+}{}^{(1)}(v_{n'+2};v_{n'+1})].\end{aligned} \tag{60}$$

The orthogonality relations also give a relation for $T^{(1)}$, namely,

$$\bar{T}^{(1)}{}_{n:n'}(v)_n:(s)_{n'}+T^{(1)}{}_{n':n}(s)_{n'}:(v)_n=0. \tag{61}$$

To solve (60) it is again useful to think in terms of the $n-n'$ plane (see Fig. 1). The value of $T^{(1)}$ depends on the values of this function on the n and n' axes. First, let us consider the solution of (60) in region II, where $n>n'$. We can obtain the values of $T^{(1)}{}_{n:n'}$ on the n axis from (60) by setting $n'=0$. It is seen that

$$\begin{aligned}&T^{(1)}{}_{n:0}(v)_n:(s)_0=0,\quad n>0,\quad n\neq 2,\\ &T^{(1)}{}_{2:0}(v)_2:(s)_0=2^{-\frac{1}{2}}[u_{+-}{}^{(1)}(v_2;v_1)+\bar{u}_{-+}{}^{(1)}(v_2;v_1)],\\ &\qquad=-(2)^{\frac{1}{2}}\operatorname*{Asy}_{v_1,v_2}u_{+-}{}^{(1)}(v_1;v_2),\end{aligned} \tag{62}$$

using the fact that $\bar{u}^{(1)}(v;s)=-u^{(1)}(s;v)$. Hence, for $n>n'$ the only functions $T^{(1)}{}_{n:n'}(v)_n:(s)_{n'}$ which do not vanish are those for which $n=n'+2$.

The solution of (60) in region II can be obtained by induction. The result is

$$\begin{aligned}T^{(1)}&{}_{n+2:n}(v)_{n+2}:(s)_n\\ &=-((n+1)(n+2))^{\frac{1}{2}}\operatorname*{Asy}_{\substack{v_1\cdots v_{n+2}\\ s_1\cdots s_n}}\delta(v;s)_n\\ &\quad\times u_{+-}{}^{(1)}(v_{n+1};v_{n+2}).\end{aligned} \tag{63}$$

Having found $T^{(1)}{}_{n:n'}(v)_n:(s)_{n'}$ in the region II of the $n-n'$ plane where $n>n'$, we can easily find this function in region I of the plane, i.e., for $n<n'$ by using the orthogonality relation (61). The result is

$$\begin{aligned}&T^{(1)}{}_{n:n'}(v)_n:(s)_{n'}=0,\quad (n<n',\quad n\neq n'-2),\\ &T^{(1)}{}_{n-2:n}(v)_{n-2}:(s)_n=+(n(n-1))^{\frac{1}{2}}\operatorname*{Asy}_{\substack{v_1\cdots v_{n-2}\\ s_1\cdots s_n}}\delta(v;s)_{n-2}\\ &\quad\times u_{-+}{}^{(1)}(s_{n-1};s_n).\end{aligned} \tag{64}$$

To find $T^{(1)}{}_{n:n}(v)_n:(s)_n$ we find $T^{(1)}{}_{0:0}(v)_0:(s)_0$ from (61) and $T^{(1)}{}_{n:n}(v)_n:(s)_n$ for $n>0$ from (60). Thus, we see that

$$RT^{(1)}{}_{0:0}(v)_0:(s)_0=0, \tag{65}$$

where R stands for the real part of the function. Thus, $T^{(1)}{}_{0:0}$ is purely imaginary. The phase of the representers can always be so chosen that the imaginary part contributes nothing.

$$T^{(1)}{}_{0:0}(v)_0:(s)_0=0. \tag{66}$$

From (60) it can be proved by induction that

$$\begin{aligned}T^{(1)}&{}_{n:n}(v)_n:(s)_n=n\operatorname*{Asy}_{\substack{v_1\cdots v_n\\ s_1\cdots s_n}}\delta(v;s)_{n-1}[u_{++}{}^{(1)}(v_n;s_n)\\ &\quad+\bar{u}_{--}{}^{(1)}(v_n;s_n)].\end{aligned} \tag{67}$$

In the same way the higher orders $T^{(p)}$ can be obtained. In fact, it appears possible to obtain a general expression for $T^{(p)}{}_{n:n'}(v)_n:(s)_{n'}$, though the expression would be complicated. We shall indicate the results for $T^{(2)}{}_{n:n'}(v)_n:(s)_{n'}$.

$$\begin{aligned}T^{(2)}&{}_{n:n'}(v)_n:(s)_{n'}=\delta_{n-4:n'}T^{(2)}{}_{n'+4:n'}(v)_{n'+4}:(s)_{n'}\\ &\quad+\delta_{n-2:n'}T^{(2)}{}_{n'+2:n'}(v)_{n'+2}:(s)_{n'}\\ &\quad+\delta_{n:n'}T^{(2)}{}_{n':n'}(v)_{n'}:(s)_{n'}\\ &\quad+\delta_{n+2:n'}T^{(2)}{}_{n'-2:n'}(v)_{n'-2}:(s)_{n'}\\ &\quad+\delta_{n+4:n'}T^{(2)}{}_{n'-4:n'}(v)_{n'-4}:(s)_{n'},\end{aligned} \tag{68}$$

where

$$\begin{aligned}T^{(2)}&{}_{n'+4:n'}(v)_{n'+4}:(s)_{n'}\\ &=\tfrac{1}{2}((n'+1)(n'+2)(n'+3)(n'+4))^{\frac{1}{2}}\operatorname*{Asy}_{\substack{v_1\cdots v_{n'+4}\\ s_1\cdots s_{n'}}}\delta(v;s)_{n'}\\ &\quad\cdot u_{+-}{}^{(1)}(v_{n'+1};v_{n'+2})u_{+-}{}^{(1)}(v_{n'+3};v_{n'+4}),\end{aligned} \tag{69}$$

$$\begin{aligned}T^{(2)}&{}_{n'+2:n'}(v)_{n'+2}:(s)_{n'}=-((n'+1)(n'+2))^{\frac{1}{2}}\\ &\quad\times\operatorname*{Asy}_{\substack{v_1\cdots v_{n'+2}\\ s_1\cdots s_{n'}}}\Big\{\delta(v;s)_{n'}\Big[u_{+-}{}^{(2)}(v_{n'+1};v_{n'+2})\\ &\quad+\int u_{+-}{}^{(1)}(v_{n'+1};s')\bar{u}_{--}{}^{(1)}(v_{n'+2};s')ds'\Big]\\ &\quad+n'\delta(v;s)_{n'-1}u_{+-}{}^{(1)}(v_{n'};v_{n'+1})\\ &\quad\times[u_{++}{}^{(1)}(v_{n'+2};s_{n'})+\bar{u}_{--}{}^{(1)}(v_{n'+2};s_{n'})]\Big\},\end{aligned} \tag{70}$$

$$T^{(2)}{}_{n':n'}(v)_{n'}:(s)_{n'} = \underset{\substack{v_1\cdots v_{n'}\\ s_1\cdots s_{n'}}}{\text{Asy}} \Big\{ \delta(v;s)_{n'} T^{(2)}{}_{0:0}(v)_0:(s)_0$$

$$+\frac{n'(n'-1)}{2}\delta(v;s)_{n'-2}[u_{++}{}^{(1)}(v_{n'-1};s_{n'-1})$$

$$+\bar{u}_{--}{}^{(1)}(v_{n'-1};s_{n'-1})]\cdot[u_{++}{}^{(1)}(v_{n'};s_{n'})$$

$$+\bar{u}_{--}{}^{(1)}(v_{n'};s_{n'})]-n'(n'-1)\delta(v;s)_{n'-2}$$

$$\times u_{+-}{}^{(1)}(v_{n'-1};v_{n'})u_{-+}{}^{(1)}(s_{n'-1};s_{n'})$$

$$+n'\delta(v;s)_{n'-1}[u_{++}{}^{(2)}(v_{n'};s_{n'})+\bar{u}_{--}{}^{(2)}(v_{n'};s_{n'})]$$

$$+n'\delta(v;s)_{n'-1}\int[u_{+-}{}^{(1)}(v_{n'};s')\bar{u}_{+-}{}^{(1)}(s_{n'};s')$$

$$+\bar{u}_{-+}{}^{(1)}(v_{n'};s')u_{-+}{}^{(1)}(s_{n'};s')]ds'\Big\}, \quad (71)$$

with

$$T^{(2)}{}_{0:0}(v)_0:(s)_0 = -\tfrac{1}{2}\int\int |u_{+-}{}^{(1)}(s_1;s_2)|^2 ds_1 ds_2, \quad (72)$$

$$T^{(2)}{}_{n'-2:n'}(v)_{n'-2}:(s)_{n'}$$

$$=(n'(n'-1))^{\frac{1}{2}}\underset{\substack{v_1\cdots v_{n'-2}\\ s_1\cdots s_{n'}}}{\text{Asy}}\Big\{\delta(v;s)_{n'-2}\Big[u_{-+}{}^{(2)}(s_{n'-1};s_{n'})$$

$$+\int u_{--}{}^{(1)}(s_{n-1};s')\bar{u}_{+-}{}^{(1)}(s_n;s')ds'\Big]$$

$$+(n'-2)\delta(v;s)_{n'-3}[u_{++}{}^{(1)}(v_{n'-2};s_{n'-2})$$

$$+\bar{u}_{--}{}^{(1)}(v_{n'-2};s_{n'-2})]\cdot u_{-+}{}^{(1)}(s_{n'-1};s_{n'})\Big\}, \quad (73)$$

$$T^{(2)}{}_{n'-4:n'}(v)_{n'-4}:(s)_{n'}$$

$$=-\tfrac{1}{2}((n'-3)(n'-2)(n'-1)n')^{\frac{1}{2}}\underset{\substack{v_1\cdots v_{n'-4}\\ s_1\cdots s_{n'}}}{\text{Asy}}\delta(v;s)_{n'-4}$$

$$\cdot u_{-+}{}^{(1)}(s_{n'-3};s_{n'-2})u_{-+}{}^{(1)}(s_{n'-1};s_{n'}). \quad (74)$$

There are several interesting results which should be particularly noted. Most important is that, while from the basic equation (46) it is by no means obvious that the functions $T_{n:n'}(v)_n:(s)_{n'}$ are antisymmetric in the variables $v_1\cdots v_n$, the solution has indeed these antisymmetry properties. This gratifying result is due to the fact that our choice of the functions $u(v;s)$ guarantees that $B^{\pm}(v)$ satisfy the commutation rules for annihilation and creation operators when the operators $A^{\pm}(s)$ do, and also that we have used a consistent perturbation procedure.

Secondly, we ought to observe that in the zeroth order $n=n'$ for nonvanishing transformation functions, whereas for first-order $|n-n'|=0, 2$ and second-order $|n-n'|=0, 2, 4$ give nonvanishing functions. Generally, in the pth order nonvanishing transformation functions occur for $|n-n'|=0, 2, 4, \cdots, 2p$. It can be shown that this result corresponds to the possibility of creating 0, 1, 2, $\cdots$, p electron-positron pairs.

Another important consequence of the way the theory is set up is that the theory is *a priori* gauge invariant up to this point. This result is an immediate consequence of the gauge invariance of the Dirac Hamiltonian.[4]

One might ask the question as to whether the transformation exists. It can be seen that this transformation exists to the second order if $T^{(2)}{}_{0:0}$, as given by (72), is finite. It can be shown that if the vector potential is identically zero $T^{(2)}{}_{0:0}$ is finite for a large class of electrostatic potentials. However, $T^{(2)}{}_{0:0}$ is infinite if the vector potential is not identically zero. This point will be discussed elsewhere.[4]

The author wishes to express his indebtedness to Professor K. O. Friedrichs for numerous helpful discussions.

[4] Since the expectation value of N to the second order in e is proportional to $T^{(2)}{}_{0:0}$ if one starts initially with no particles present, we come to the somewhat surprising conclusion that for suitable electrostatic fields the expectation value of the number of particles is finite to the second order. No renormalization is required. The present author's proof is quoted in Part V of K. O. Friedrichs' papers on quantum field theory to appear shortly in Comm. Pure and Appl. Math., where the present problem is treated in a different manner.

Bremsstrahlung Cross Section of 60-Mev Electrons in Lead*

C. D. CURTIS†
University of Illinois, Urbana, Illinois
(Received May 12, 1952)

Sixty-Mev electrons from a pulsed betatron passed through lead foils of thicknesses 0.001, 0.005, and 0.015 inch placed in a magnetic cloud chamber. Measurements of approximately 1100 large energy losses gave the differential bremsstrahlung cross section as a function of x-ray energy for the high energy portion of the x-ray spectrum. Corrections were applied for instrumental discrimination and for multiple radiation and ionization energy losses in the foils. While the shape of the top 30 percent of the x-ray spectrum agreed with the theory within experimental uncertainty, the magnitude of the cross section was about 7 percent lower than theory.

INTRODUCTION

IN 1934 Bethe and Heitler[1,2] developed a theory for bremsstrahlung production by relativistic electrons. They made calculations using as targets a bare nucleus and a nucleus screened by the electrons of the Thomas-Fermi atom. Use of the Born approximation required that $Ze^2/hv \ll 1$ before and after collision of the electron with the nucleus, where v is the electron speed. Even when the speeds approach that of light, however, Ze^2/hv becomes approximately 0.6 for lead. In this case Parzen[3] has pointed out that any error in the cross section integrated over all angles of the emergent electron and quantum should be no greater than $(\mu/E_0)^{\frac{1}{2}}$, where μ and E_0 are, respectively, the rest and total energy of the incident electron. Schiff[4–6] obtained an analytic expression for a differential energy spectrum for a thin target. In the worst case of large Z and partial screening this was no more than 4 percent higher than the numerical calculations of Bethe and Heitler.

Measurements[7–14] of the total radiation energy loss by electrons of various energies from a few tenths to 13.5 Mev have yielded rather inconsistent results, from approximately 15 percent lower to at least 40 percent higher than those predicted by the Bethe-Heitler theory. One of the difficulties in the measurement of energy loss of electrons passing through foils has been that of interpretation because of multiple scattering within the foils.[12]

Measurements[15,16] of the energy loss of cosmic-ray electrons with energies up to 200 Mev passing through lead plates in a cloud chamber have confirmed the theory within an uncertainty of approximately 20 percent.

Lanzl[17] found the total radiation cross section of 17.6-Mev electrons in high Z elements to be 10 percent lower than theory with an uncertainty of about 10 percent.

The experimental shape of the x-ray energy spectrum from monokinetic electrons is in general agreement with theory at energies of 20 and 300 Mev.[18–20]

The present paper describes a measurement of the differential bremsstrahlung cross section for 60-Mev electrons in lead. When the electrons passed through lead foils in a magnetic cloud chamber, the energies for the x-ray quanta which were emitted were determined for the top 30 percent of the x-ray spectrum. The difference observed between the incident and emergent energies of an electron thus gave approximately the quantum energy $h\nu = E_0 - E$.

EXPERIMENTAL ARRANGEMENT

A. Source of Electrons

Electrons were accelerated to an energy of 82.5 Mev in a pulsed betatron.[21] No special device was used to extract the electron beam, although this would be desirable to obtain a monoenergetic beam with maximum intensity. For cloud-chamber operation, however, the electrons which normally emerged through the vacuum chamber wall after expansion of the electron orbit gave far more than sufficient intensity. Although the betatron operated at 82.5 Mev, the electrons escaping from the vacuum chamber were greatly degraded by scattering from the injector structure and by passing through the chamber wall. The mean energy of

* Assisted by the joint program of the ONR and AEC.
† Now at Argonne National Laboratory, Chicago, Illinois.
[1] H. Bethe and W. Heitler, Proc. Roy. Soc. (London) **146**, 83 (1934).
[2] H. Bethe, Proc. Cambridge Phil. Soc. **30**, 524 (1934).
[3] G. Parzen, Phys. Rev. **81**, 808 (1951).
[4] L. I. Schiff, Phys. Rev. **83**, 252 (1951).
[5] L. Katz, Can. J. Phys. **29**, 518 (1951).
[6] G. D. Adams, Phys. Rev. **74**, 1707 (1948).
[7] H. Klarman and W. Bothe, Z. Physik **101**, 489 (1936).
[8] J. J. Turin and H. R. Crane, Phys. Rev. **52**, 63 (1937).
[9] L. J. Laslet and D. G. Hurst, Phys. Rev. **52**, 1035 (1937).
[10] A. J. Ruhlig and H. R. Crane, Phys. Rev. **53**, 618 (1938).
[11] W. A. Fowler and J. Oppenheimer, Phys. Rev. **54**, 320 (1938).
[12] M. M. Slawsky and H. R. Crane, Phys. Rev. **56**, 1203 (1939).
[13] Ivanov, Walther, Sinelnikov, Taranov, and Abramovich, J. Phys. (U.S.S.R.) **4**, 319 (1941).
[14] Van Atta, Petrauskas, and Myers, Am. J. Roentgenol & Radium Therapy **50**, 803 (1943).
[15] P. M. S. Blackett, Proc. Roy. Soc. (London) **165**, 11 (1938).
[16] C. D. Anderson and S. H. Neddermeyer, Phys. Rev. **50**, 263 (1936).
[17] L. H. Lanzl and A. O. Hanson, Phys. Rev. **83**, 959 (1951).
[18] H. W. Koch and R. E. Carter, Phys. Rev. **77**, 165 (1950).
[19] Powell, Hartsough, and Hill, Phys. Rev. **81**, 213 (1951).
[20] J. W. Dewire and L. A. Beach, Phys. Rev. **83**, 476 (1951).
[21] Kerst, Adams, Koch, and Robinson, Rev. Sci. Instr. **21**, 462 (1950).

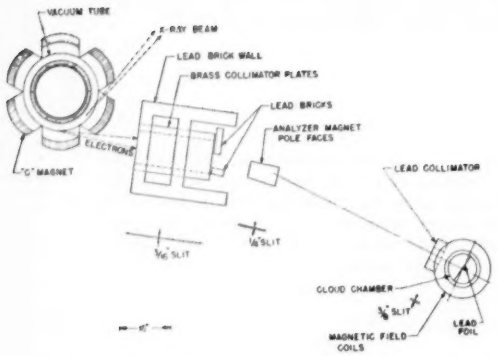

FIG. 1. Experimental layout.

the electrons entering the cloud chamber was approximately 60 Mev. Most of them had traveled a slanting path through the wall much longer than the wall thickness. Figure 1 is a diagram of the experimental arrangement. Parallel brass plates two ft long, which were imbedded in lead bricks, collimated electrons from the betatron into a sheet $\frac{3}{16}$ in. thick. The electrons then passed between the plates of a permanent magnet with a field strength of approximately 2500 gauss. The magnet effected some energy analysis of the electrons and separated them from any x-rays present. The remaining electrons with a limited energy spread entered a cloud chamber 8 in. in diameter through a $\frac{3}{8}$-in. lead collimator slit to produce tracks spread over a width of 4 in. in the chamber.

B. Detection of Radiation Straggling

For the high energy end of the x-ray spectrum, an especially thin target foil is desired to insure measurement of very low energy straggled electrons whose energies will permit an accurate energy determination of the x-rays emitted. This will be the case only if the target is thin enough to render multiple radiation losses negligible and ionization loss very small. Of particular concern is the energy loss experienced by the straggled electron through excessive multiple scattering after the large radiation loss has occurred. One is limited, however, in the minimum thickness practicable by the need for keeping the number of cloud-chamber photographs necessary for reasonable statistics from becoming prohibitive, particularly in terms of time required for analysis. A total of 20 400 pictures were taken, with and without lead foils of varying thicknesses. Of these, 1700 were taken at various times during the experiment with no foils in the cloud chamber. These pictures furnished data for calibration of the primary electron energies. Some 4900 pictures were taken with a foil thickness of 0.005 in. Five parallel foils were placed perpendicular to the path of the electrons to increase the chance of a radiation event for each picture. This arrangement permitted measurement of straggled electron energies up to a few Mev. However, with the available field strength, the spacing was too close for accurate measurement of more than about 10 Mev. For observation of higher energy straggled electrons and for greater ease of analysis, 11 200 pictures were taken using one foil 0.015 in. thick across the center of the cloud chamber. On these pictures, radii were measured up to 25 cm corresponding to a maximum energy of about 21 Mev. Corrections for energy loss by the straggled electrons in foils 0.015 and 0.005 in. thick were necessary. Still thinner foils of 0.001 in. were used to reduce further the necessary corrections. The radiation events occurred very infrequently in these foils, particularly quite near the high energy tip of the x-ray spectrum. Only 2600 pictures were taken with five such foils in the chamber; therefore, the statistics were very poor indeed. The data from these pictures serve only as a rough check on the results from the other foil arrangements.

The number of electron tracks passing through the foils varied from picture to picture, but from six to ten tracks for each provided a good distribution without bunching.

The cloud-chamber magnetic field was produced by current from a pulsed generator.[22] A timing circuit triggered the betatron at the peak of the current pulse which had a duration of about 350 milliseconds. The cloud chamber and betatron were operated once every 30 seconds. Because of a slow variation of the field current with time, it was regularly monitored.

The average value of the peak magnetic field strength was approximately 3100 gausses with the value at a specified time determined to within 2 percent. The calibration of the field current meter in terms of steady field strength was accomplished with a proton magnetic moment detector. The strength of the pulsed field was then determined from the relative values of the voltages induced in a rotating coil placed in the fluxes of the steady and pulsed fields. A second method of obtaining the pulsed field strength used a General Electric fluxmeter which integrated the time rate of change of magnetic flux.

The cloud chamber had an air filling to approximately 26 lb per sq in. absolute. The condensing vapor was an ethyl alcohol-water mixture of 3:1. Two General Electric FT-422 lamps illuminated a region $\frac{3}{4}$ in. deep in the chamber. They were singly pulsed for photography and multiply pulsed 60 times per second for visual observation.[22]

The cloud-chamber tracks were photographed stereoscopically by a single camera and two mirrors.[18] For best sensitivity and contrast most pictures were taken on Eastman Kodak linograph-ortho film which was processed in D-11 developer.

C. Analysis of Tracks

All pictures were scanned for events on plane projection tables which used lenses matched to the one in

[22] C. D. Curtis, Ph.D. thesis, University of Illinois (1951, unpublished).

the camera. Radii of tracks projected into the horizontal plane to original size were measured on these tables. For the radiation events, radii of the straggled electrons were included up to 25 cm on the one-foil pictures and up to 17 cm on the five-foil pictures, although the latter limit was reduced later in evaluation of the data. All tracks penetrating the foils were counted as traversals with the exception of a very few low energy tracks which could be detected as having less than a fixed minimum radius. This limit was 30 cm for the five-foil pictures and 45 cm for the one-foil pictures, corresponding to about 27.4 and 41.3 Mev, respectively. An occasional picture was discarded because of an excessive number or bunching of the tracks. A first glance could determine without discrimination the condition of the picture. Data were also collected on events such as secondary electrons and electron created pairs. A few large electron energy losses occurred in the cloud-chamber gas and one electron created pair was observed there. All pictures were scanned a second time for radiation events with special attention given to short chord length tracks. In the case of one-foil pictures, an attempt was made to miss none of the 25-cm radius straggled tracks with a chord length ≥ 3.5 cm. Later in the treatment of corrections to the data, a longer minimum chord length was used.

Another examination of the pictures was made by projection through the original camera-mirror system used for the photography. A stereo-projection table[18] provided flexibility for measuring all angles necessary to describe a track in three dimensions. The dip angles made by the incident and emergent tracks with the horizontal plane and the angles between their projections in this plane were measured. The dip angle was necessary for determining the electron energy, and the angular distributions were used in making corrections to the data.

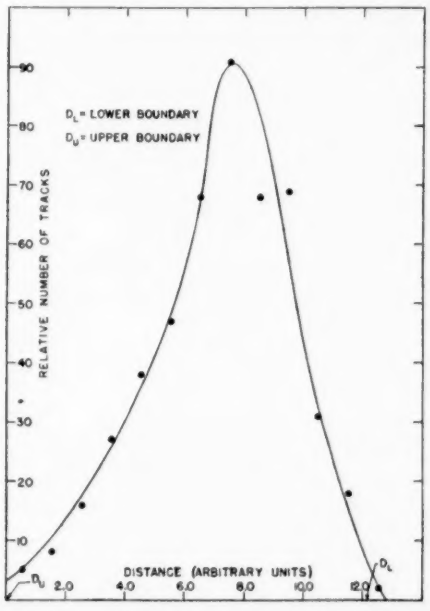

FIG. 2. Vertical position distribution of tracks at the 15-mil foil.

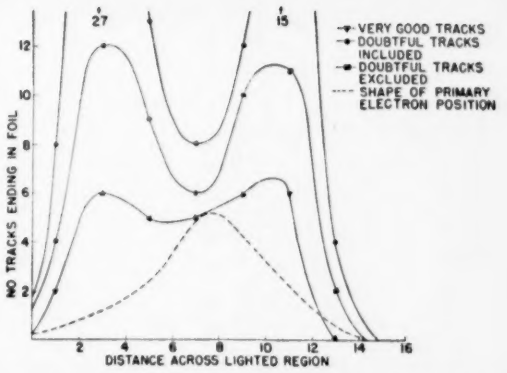

FIG. 3. Position distribution of tracks ending at a foil. They are classified according to their appearance. Shape of the incident electron distribution shows that many of the terminating tracks do not correspond to stopped electrons.

Some scattering of the incoming electrons occurred as they passed through the $\frac{1}{8}$-in. glass wall of the cloud chamber and through the successive lead foils. Consequently, a few tracks passed out of the lighted region and appeared near the foils only as faint tracks. The track counting was thus susceptible to error. For example, one could mistake a secondary electron knocked from a foil for a straggled electron following radiation. The policy established was to discard faint tracks consistently whether or not there appeared to be straggling. The lighted region in the chamber was 1.7 cm deep and fairly well-defined. Also the distribution of incident electrons across this region, as exemplified in Fig. 2, had few tracks near the boundaries. The possible error in observation, therefore, would be small.

A few tracks ended at the foils. One would expect an occasional electron to lose all or nearly all of its energy in a foil so that no straggled electron track could be seen. Also an electron may undergo elastic or inelastic scattering in a foil through an angle near 90 degrees and show very faintly or not at all. One wonders, therefore, how many terminated tracks to count as stopped electrons. A conscientious examination of these tracks was taken for part of the pictures. They were classified according to certainty, and their positions across the lighted region of the chamber were plotted. Figure 3 reveals that even among the best appearing events more terminated tracks appeared near the boundaries of the lighted region than in the middle. A comparison between the terminated track and incident electron track distributions indicates that scattering is responsible for the difference between them. The number of stopped electrons was assumed to correspond to the area under the

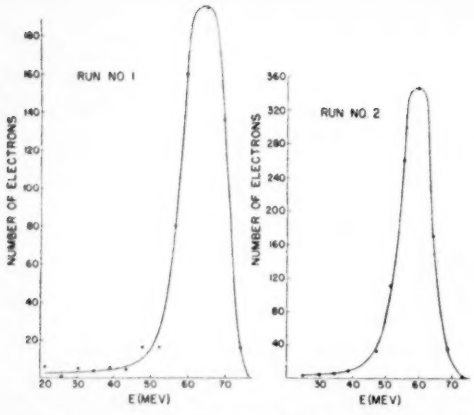

FIG. 4. Energy distribution of primary electrons. The mean energies of run 1 and run 2 are 62.5 and 57.8, respectively.

dashed curve. This number was then used as a contribution to the highest energy interval of the x-ray spectrum.

TREATMENT OF DATA

A. Calculation of the Cross Section

The experiment was performed with two energy distributions of the primary electrons. Figure 4 gives the two distributions with mean energies of 62.5 and 57.8 Mev, respectively. The corresponding widths at half-maximum intensity are roughly 13 and 10 Mev. The experimental results were determined separately for each distribution and then weighted results for the combined distributions were computed.

For convenience of presentation, the x-ray spectrum was calculated in terms of one maximum energy which was the arithmetic mean energy of the primary electrons. One minus the ratio of straggled electron to mean primary electron energy gave the fractional energy carried off by a quantum. A plot of the number of straggled electrons per Mev of energy *versus* the fractional energy loss so defined gave an experimental number spectrum of x-ray quanta. The corresponding theoretical spectrum was obtained by averaging over the primary energy distribution the cross section for production of each of a number of fixed, straggled electron energies. The slight distortion of this theoretical spectrum from that for monokinetic electrons of the mean energy is shown in Fig. 5.

The straggled electron energies were grouped in intervals of width equal to 0.05 of the mean energy. The atomic cross section for one interval in units of cm^2/Mev is

$$\phi_k = n/NWm, \qquad (1)$$

where n is the number of straggled electrons in the interval, N the number of primary or incident electrons, m the number of target atoms per cm^2 of foil, and W the width of the energy interval in Mev.

Of the number of observed straggled electrons, a few were classified as doubtful. Because of occasional close spacing of primary tracks, imperfect stereoscopic images, etc., they could not be classified with certainty as events in question. The doubtful events constituted 3 percent of the total number of events in all energy intervals from both five-mil and fifteen-mil foil data. Only half the doubtful events were retained. The number of doubtful tracks was quite small in all energy intervals except the one at the tip of the spectrum in which 10 of 84 tracks were in doubt. Retaining half the doubtful ones then left 79 events to be used.

B. Corrections

Two major corrections were applied to the data. One was a geometry correction. The other accounted for energy loss of electrons in the foils by multiple radiative and ionizing collisions.

The geometry correction resulted because many electrons, after traversing the lead foils, passed out of the lighted region in the cloud chamber without leaving sufficient track length for measurement of the energy loss. Because of the difficulty of making an accurate correction, several methods were used and compared.

The first method of correction retained tracks in a specified interval only with a chord length greater than a chosen minimum. Corresponding to a given minimum chord length was a maximum dip angle that the emergent track made with the horizontal plane, which was parallel to the boundaries of the lighted region. The magnitude of this angle depended upon the vertical position of the track at the foil in the lighted region. In general, the angle was double valued because of possible deflection up or down.

Corresponding to a minimum chord length K is a

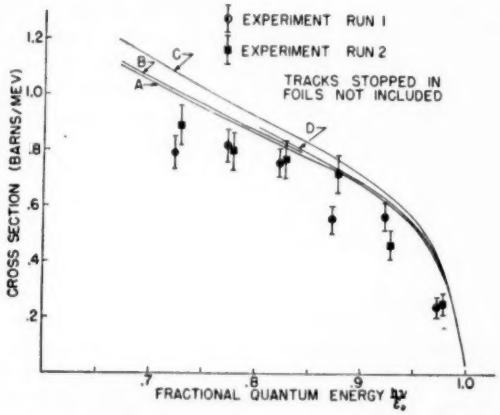

FIG. 5. Theoretical cross section and uncorrected results for two separate runs. $\mathcal{E}_0$ is the mean incident electron energy, and equals 62.5 Mev and 57.8 Mev, respectively, for runs 1 and 2. Correspondingly, curves B and C are the theory averaged over the two incident electron energy distributions above 38.9 Mev. Curve D is the average over energies above 27.5 Mev for run 1. Curve A is the theory for monoenergetic electrons of 62.5 Mev.

minimum ratio $\lambda_m = K/R$ with R the track radius. In determining the maximum dip angle α_M, a value of λ_m was chosen for each energy interval which was considerably greater than the smallest λ-value recorded. The particular value was such that it gave in the worst instance a probable error in measured radius corresponding to half the width of the energy interval. The radius of curvature of a track was measured by comparison of its arc with standard arcs scribed on a thin sheet of Lucite. The value of λ_m varied slowly with energy and had an approximate value of 0.29.

The use of λ_m together with the angular distribution of emergent tracks scattered out of the horizontal plane determined the fraction of events eliminated by the λ_m selection. The correct angular distribution of dip angles was inferred from the observed angular distributions and the assumption of angular symmetry about the incident direction. Figure 6 is an example of angular distributions that existed with respect to perpendicular planes. The ratio of the total area under the true dip angle curve to the area for angles less than α_M gave the correction factor to apply to the number of events in a given energy interval having $\lambda \gtrsim \lambda_m$. Since not all stragglings occurred at the same vertical position in the lighted region, an integration was carried out over the incident electron position distribution.

A correction based on the angular symmetry method alone is independent of chord lengths, position distribution, and lighted region boundaries. It requires only that the angular distribution of straggled electrons be symmetrical in space about the incident electron direction. This should be true if there is no polarization of the incident electrons. The angular distribution should be circular on a polar coordinate graph, when no discrimination correction is necessary, and with adequate statistics. The observed angular distributions proved to be approximately elliptical.

Another method of correction consisted in retaining only those events for which the emergent tracks were deflected toward the central plane of the lighted region. Since straggled electrons should be deflected up and down in equal numbers, the same number should be

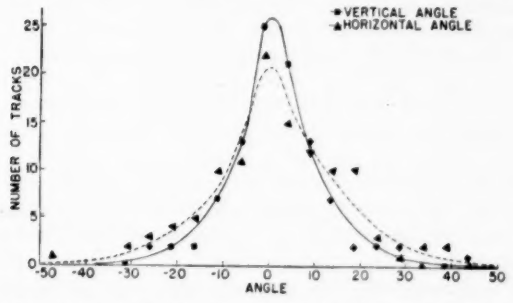

FIG. 6. Angular distribution of straggled electron tracks from 15-mil foil. Electrons have lost 0.875 times initial energy. The vertical and horizontal angles are angles made respectively with the horizontal plane and the vertical plane containing the primary electron direction at the foil.

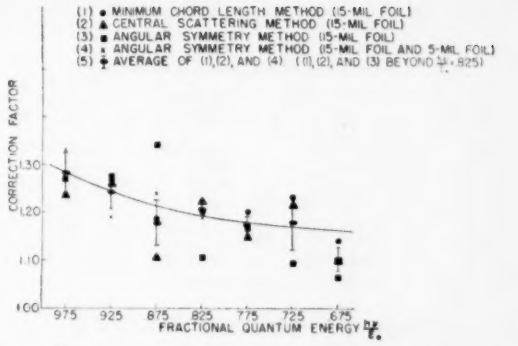

FIG. 7. Geometry correction to account for straggled electron tracks leaving the lighted region too abruptly for measurement.

deflected toward as away from the central plane of the lighted region. However, one can observe relatively more of the centrally deflected tracks for a given magnitude of deflection because of their greater lengths. In addition, the minimum chord length correction already described was applied to the centrally deflected tracks. This was smaller than that applied to all observed tracks. Retention of only the centrally deflected tracks appreciably reduces the statistics.

The three methods of correction described were used in correcting the one-foil data. Only the angular symmetry method was used for the five-foil data since not all the information necessary for the other methods was collected for these data. Figure 7 shows the correction for each method and the average correction to the total observed number of events as a function of energy. These corrections do not account for the number of electrons that may have stopped in the foils and which have already been discussed.

Because of the thickness of a foil, an electron may undergo successive radiation events while passing through it. Part of the energy loss will result also from ionizing collisions. Ionization after a large radiation loss may remove a straggled electron from one energy interval to another. This effect is increased by multiple scattering of the electron, particularly at low energy. To obtain an accurate bremsstrahlung cross section, the observed cross section must be corrected to that for an infinitely thin foil. The correction for multiple radiation loss is greater than that for ionization loss at all energies except for those near the tip of the x-ray spectrum. The net effect of the energy losses is to produce an increase in the observed cross section over the true cross section for most x-ray energies.

An electron of energy E_0 may lose energy by one or more successive radiative collisions down to an energy E' while passing through a foil. Unless the foil is very thick, the number of electrons emerging can be determined with sufficient accuracy by considering at most two successive radiation events. If η electrons of energy E_0 strike a foil of thickness t and n atoms per unit volume,

TABLE I. Energy loss correction. $\mathcal{E}_0 = 60.4$ Mev = primary electron energy. The calculations are first-order approximations for monokinetic electrons.

		435.9-mg/cm² foil			145.3-mg/cm² foils		
$\mathcal{E}$ (Mev)	$h\nu/\mathcal{E}_0$	Radiation correction	Ionization correction	Total correction	Radiation correction	Ionization correction	Total correction
1.51	0.975	−13.2%	−12.0%	−23.0%	−7.5%	−4.0%	−11.2%
4.53	0.925	−14.4	−1.8	−15.9	−8.2	≃0.6	−8.7
7.55	0.875	−11.7	−1.5	−13.0	−6.5	≃0.5	−6.9
10.57	0.825	−5.6	−1.7	−7.2	−3.2	≃0.6	−3.8
13.59	0.775	−2.6	−1.8	−4.3			
16.61	0.725	−1.8	−1.8	−3.6			
19.63	0.675	−4.7	−1.8	−6.4			

the number emerging with energy E' will be

$$N(E', t) \simeq \eta n^2 \frac{t^2}{2} \int_{E'}^{E_0} \phi(E_0, E)\phi(E, E')dE + n\eta\left[t - \frac{nt^2}{2}\int_0^{E_0} \phi(E_0, E)dE\right]\phi(E_0, E'), \quad (2)$$

where $\phi(E, E')$ is the cross section per unit energy range. The two terms represent, respectively, the numbers of two collision events and one collision events. The two integrals diverge for the range of E near E_0; however, their difference remains finite there.

The number of electrons leaving energy E' while passing through the foil is approximately

$$\eta n^2 \frac{t^2}{2} \phi(E_0, E') \int_0^{E'} \phi(E', E)dE. \quad (3)$$

The difference of (2) and (3) gives the number of straggled electrons emerging from the foil with energy E'. Division by ηnt gives the observed atomic cross section

$$\phi_t \simeq \phi_{t0} + \frac{nt}{2}\left\{\int_{E'}^{E_0} \phi(E_0, E)[\phi(E, E') - \phi_{t0}]dE - \phi_{t0}\int_0^{E'} \phi(E', E)dE - \phi_{t0}\int_0^{E'} \phi(E_0, E)dE\right\}, \quad (4)$$

where the cross section for an infinitely thin foil is $\phi_{t0} = \phi(E_0, E')$. The first two integrals diverge for the range of E near E'; however, their difference remains finite.

TABLE II. Uncorrected number of radiation events.

Foil thickness in mg/cm²	No. of foil traversals	No. of events for $h\nu/\mathcal{E}_0$ values 0.975	0.925	0.875	0.825	0.775	0.725	0.675
29.92	66016	5[a]	4	10	20			
145.9	97268	36[a]	66	79	88			
435.9	46628	43[a]	93	111	138	141	149	131[b]

[a] Does not include electrons stopped in a foil.
[b] Energy bin width is 0.79 times other bin widths, which are approximately 3 Mev wide.

From (4) the correction term to be applied to the observed cross section is proportional to the foil thickness to a first-order approximation. The correction was evaluated assuming the theoretical value for the cross section to be valid and using for E_0 the mean primary electron energy. Integration over the primary energy distribution would have appeared as a second-order effect and was not made. The first-order correction was less than 15 percent for all straggled electron energies for the thickest foil.

The straggled electrons emerge from a foil with a spread in angular distribution because of multiple scattering in the foil and because of a transverse component of momentum received in the bremsstrahlung process. The effective path length traversed by the straggled electrons after radiation has occurred is consequently increased. The increase is more pronounced for the lower energy electrons. This effect was included in an approximate manner by multiplying the correction term in Eq. (2) by $\sec\bar{\theta}$, where $\bar{\theta}$ was the observed mean angle that the emergent straggled electrons for each energy interval made with the incident direction.

There were five parallel foils across the cloud chamber for collection of the five-mil foil data. The effective value of t in Eq. (2) was increased a little over the five-mil thickness to account for some electrons undergoing two successive radiations in separate foils and not losing enough energy during the first collision for the resulting change in radius to be detected between foils. For this calculation the maximum energy which could be detected was taken as 30 Mev. The effective value of t was not critically dependent upon this choice.

Energy loss of the straggled electrons by ionization in the foils of thickness t was calculated by assuming the effective path length to be $\frac{1}{2}t\sec\bar{\theta}$ and by using Bloch's well-known formula for collision loss. The shape of the x-ray spectrum and the slow variation in amount of ionization with energy result in more straggled electrons entering than leaving a given energy interval. For the lowest electron energy interval there can be a flux of electrons only into the interval.

The results of the two types of energy loss corrections are tabulated in Table I. All energies listed are for the mid-points of energy intervals. The correction to the observed cross section is negative for both energy loss effects.

RESULTS AND CONCLUSIONS

Table II and Figs. 8–10 contain the most significant data and results for the bremsstrahlung cross section. The cross sections are in units of barns (10^{-24} cm^2) per nucleus per Mev of straggled electron or x-ray energy. $h\nu/\mathcal{E}_0$ is the ratio of radiation quantum energy to the mean kinetic energy of the primary electrons. The point spreads on the graphs are probable errors resulting from the statistics and the uncertainties in the geometry corrections. A substantial part of the uncertainty in the five-mil foil results arose through the geometry corrections based on only the angular symmetry method.

Because of the poor statistics, no attempt was made to correct the one-mil foil results. The uncorrected total cross section for the top four energy intervals of the spectrum is 6.8 barns compared with the theoretical value of 7.78 barns. Both the negative energy loss correction and the positive geometry correction should

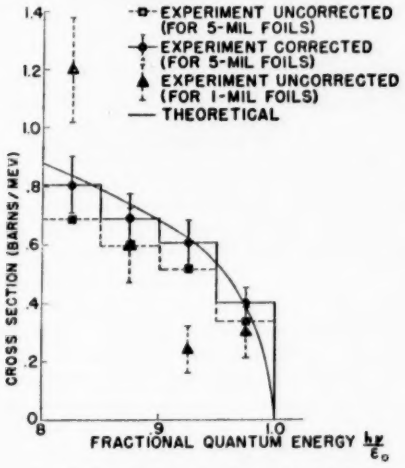

FIG. 8. Results from 5-mil and 1-mil foils.

be smaller than for the five-mil and fifteen-mil foil results because of the thinner foils and less multiple scattering.

The total cross section for the five-mil foil data for the top of the x-ray spectrum from 50 to 62.8 Mev is 7.8 $\pm$0.5 barns compared with 8.07 barns from theory. The combination of fifteen-mil and five-mil foil results represents better statistics and gives for the top 12.28-Mev energy range of the spectrum a total cross section of 7.5$\pm$0.3 barns compared with 8.00 barns from theory. The total cross section for the top 20.48 Mev of the spectrum determined from the fifteen-mil foil data is 15.2$\pm$0.6 barns compared with 16.52 barns from theory or 8 percent lower. The theoretical values here do not include the contribution from bremsstrahlung production in the field of orbital electrons. This correction would be no more than 1 percent.

Within experimental uncertainties, the top 30 percent of the x-ray spectrum agrees with the Bethe-Heitler

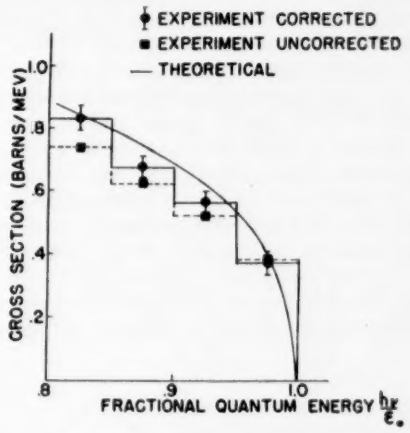

FIG. 9. Combined results from 5-mil and 15-mil foils.

theory in shape. However, the magnitude of the bremsstrahlung cross section appears a few percent lower than theory.

The pair production process is much like the reverse of bremsstrahlung production. Many x-ray absorption and pair production experiments[6,23–26] have indicated that the cross section for pair production in heavy elements relative to that in light elements is lower than that given by the Bethe-Heitler theory using the Born approximation. For example, Emigh[26] gives a pair cross section for gold relative to aluminum 7.9$\pm$1.5 percent lower than theory for x-rays in the range 50 to 300 Mev from a 300-Mev betatron.

The present experiment was in part an exploratory study of a method for obtaining an absolute bremsstrahlung cross section and spectral shape. There is room for improvement of the statistics and of the experimental techniques to reduce the uncertainties. Among the most

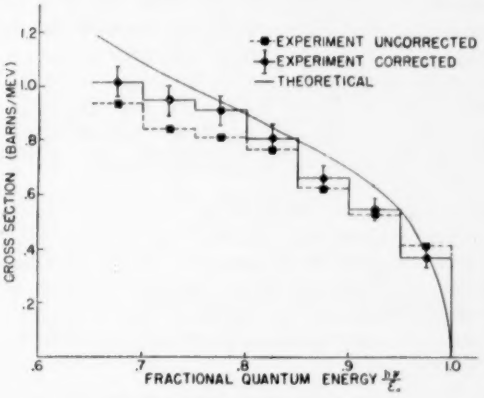

FIG. 10. Results from 15-mil foils.

[23] R. L. Walker, Phys. Rev. **76**, 527 (1949).
[24] J. L. Lawson, Phys. Rev. **75**, 433 (1949).
[25] Dewire, Ashkin, and Beach, Phys. Rev. **83**, 505 (1951).
[26] C. R. Emigh, Phys. Rev. **86**, 1028 (1952).

important improvements in further work of this type would be the use of a nearly monokinetic electron beam obtained directly from the accelerator or with the aid of a larger analyzer magnet. The electron beam should be well centered in a deeply lighted region with little vertical spread. A long entrance window would minimize scattering of the primary electrons. The chamber should be larger and have a stronger magnetic field applied than in the present experiment if more of the spectrum were to be examined at the same primary energy. In this connection, the problem caused by a wide angular distribution of straggled electrons would become less acute for a given point on the spectrum. The use of higher primary electron energies would permit examination of the high energy end of the spectrum in more detail.

The author wishes to acknowledge with gratitude the advice, suggestions, and encouragement of Professor Donald W. Kerst, who directed this work. He also wishes to express his appreciation to Dr. H. W. Koch who designed much of the cloud-chamber equipment. This experiment was in part a culmination of early interest stimulated in radiation straggling by Dr. L. S. Skaggs. The collection and analysis of data were carried forward with the able assistance of P. C. Fisher, J. W. Henderson, G. Modesitt, and J. H. Malmberg.

PHYSICAL REVIEW VOLUME 89, NUMBER 1 JANUARY 1, 1953

Effect of Equatorial Ring Current on Cosmic-Ray Intensity*

S. B. Treiman†
Institute for Nuclear Studies, University of Chicago, Chicago, Illinois
(Received August 25, 1952)

The equatorial ring current postulated by Chapman and Ferraro to explain the main phase of terrestrial magnetic storms is analyzed with respect to its effect on the intensity of the cosmic radiation. For mathematical convenience, the ring current is replaced by a current sheet located on the surface of a sphere concentric with the earth, in accordance with a suggestion due to Chapman. A simple expression is then obtained relating the variations in magnetic field at the equator with the corresponding variations to be expected in the intensity of cosmic radiation measured by an arbitrary detector located at any latitude and atmospheric depth.

I. INTRODUCTION

IT is well known that terrestrial magnetic storms are due, in part, to current systems located above the surface of the earth. In particular, Chapman and Ferraro[1] have postulated the existence of a westward-flowing ring of current which encircles the earth in the magnetic equatorial plane and which has a radius several times that of the earth. It is supposed that the current decays slowly during the periods between storms but that it is enhanced from time to time by corpuscular beams from the sun, the resulting current variations giving rise to the magnetic disturbances observed on the earth during the main phase of magnetic storms.

Now one can, of course, imagine an infinite number of current systems which could produce the magnetic disturbances observed on the earth's surface. In order to provide an independent test of the ring current theory, therefore, Chapman[2] has suggested that it would be profitable to study the effect of such a current system on the cosmic radiation.

In the following, an attempt is made to determine the variations in cosmic-ray intensity that would be expected to accompany variations in the intensity of the postulated ring current. The calculations are carried out in the approximation corresponding to the Stoermer theory of allowed cones in the field of a simple dipole, i.e., the effect of the ring current on the Stoermer cones is calculated and the assumption is then made that all directions within the modified cones are "allowed." Considerations of the earth's shadow and of the finer details of the Lemaitre-Vallarta theory are neglected. Although we speak here of a "ring" current, the calculations are actually carried out for a simpler current system which approximates the effect of a ring current.

II. DETERMINATION OF THE ALLOWED CONES

We consider the motion of a particle of charge e in the combined magnetic fields of the earth's dipole and of a ring current encircling the earth in the magnetic equatorial plane. The coordinate system is shown in Fig. 1. The positive z axis points toward the earth's magnetic north. The earth's dipole M_e is located at the origin and is directed along the negative z axis. The earth's radius is designated by ρ, and the radius of the ring is taken to be $a\rho$; θ is the angle between the velocity vector of the particle and the meridian plane, where θ is positive if the particle crosses the meridian plane from east to west.

* Assisted by the Air Research and Development Command, USAF.
† Now at Palmer Physical Laboratory, Princeton University, Princeton, New Jersey.
[1] S. Chapman and V. Ferraro, Terr. Mag. Atmos. Elec. **45**, 245 (1940), and references therein.
[2] S. Chapman, Nature (London) **140**, 423 (1937).

For a magnetic field possessing axial symmetry, as in the case under consideration, the vector potential is independent of the azimuthal angle ω and can be represented by $\mathbf{A}=A\mathbf{i}_\omega$, where $\mathbf{i}_\omega$ is a unit vector pointing from east to west. It is readily shown then that the following expression is an integral of the motion:

$$pr\cos\lambda\sin\theta+A(e/c)r\cos\lambda, \tag{1}$$

where the particle momentum p is, of course, a second integral of the motion.

The vector potential due to the earth's dipole moment is given by

$$A_e=M_e\cos\lambda/r^2. \tag{2}$$

The vector potential due to a ring of current is a complicated expression and depends on the assumed cross-sectional radius. However, if we assume that the latter is small compared to $a\rho$, then we can write

$$(r\ll a\rho)\quad A_r=M_r r\cos\lambda/(a\rho)^3, \tag{3}$$

$$(r\gg a\rho)\quad A_r=M_r\cos\lambda/r^2, \tag{3'}$$

where M_r is the equivalent dipole moment of the ring. We now make the approximation, suggested by Chapman,[2] that these limiting equations hold for all values of r, in the first case for $r\leqslant a\rho$ and in the second case for $r\geqslant a\rho$. This is equivalent to replacing the ring by a current sheet located on the surface of a sphere of radius $a\rho$, where the current density is proportional to $\cos\lambda$. We will continue to speak of a "ring" current, however, as a matter of convenience.

Introduce the Stoermer variable R, defined by the equation

$$R=r(cp/eM_e)^{\frac{1}{2}}. \tag{4}$$

The earth's radius, in Stoermer units, is given by

$$R_e=\rho(cp/eM_e)^{\frac{1}{2}}; \tag{5}$$

and the radius of the ring, in Stoermer units, is

$$R_a=aR_e. \tag{6}$$

From Eq. (1) we then obtain the following relations:

$$(R\leqslant R_a)\quad R\cos\lambda\sin\theta+\cos^2\lambda/R+KR^2\cos^2\lambda/R_a^3=\alpha, \tag{7}$$

$$(R\geqslant R_a)\qquad R\cos\lambda\sin\theta+(1+K)\cos^2\lambda/R=\alpha, \tag{7'}$$

where α is the constant of the motion and $K\equiv M_r/M_e$.

One can now proceed in the same way as in the derivation of the allowed Stoermer cones in the field of a simple dipole. (Notice that these equations reduce to the Stoermer equation when K vanishes.) For any choice of α one can plot the allowed regions in the meridian $(R-\lambda)$ plane from the requirement $|\sin\theta|\leqslant 1$. When α is larger than a certain value $\bar{\alpha}$, the allowed region breaks up into two parts, the outer part extending to infinity, the inner part being insulated from infinity by forbidden regions. The qualitative features are the same as in ordinary Stoermer theory; but $\bar{\alpha}$ now depends on the parameters K and R_a, whereas in ordinary Stoermer theory it has the fixed value two.

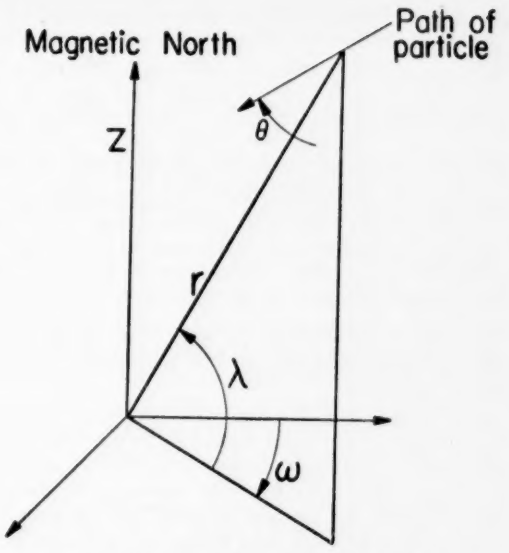

FIG. 1. Illustration of coordinate system used.

Our object is to find the minimum momentum for which a particle coming from infinity can arrive at the earth's surface at latitude λ and at angle θ with respect to the meridian plane. Setting $R=R_e$ in Eq. (7), we can solve for R_e in terms of λ and θ for any choice of α. If α is larger than $\bar{\alpha}$, the smaller of the two roots puts the earth's surface in the inner allowed region, and the earth cannot be reached by particles coming from infinity. In this way we find the minimum value of R_e, hence the minimum momentum, for the arrival of a particle from infinity. Denoting this minimum by $\bar{R}_e$, we find

$$\bar{R}_e=\frac{2(1+K/a^3)\cos^2\lambda}{\bar{\alpha}+[\bar{\alpha}^2-4(1+K/a^3)\cos^3\lambda\sin\theta]^{\frac{1}{2}}}. \tag{8}$$

There remains now to determine $\bar{\alpha}$ as a function of the parameters K and R_a. Let $\sin\theta=\cos\lambda=1$ in Eqs. (7) and (7'); and denote the resulting functions of R on the left-hand sides of these equations by $F_1(R)$ and $F_2(R)$, respectively. Consider the equation

$$F(R)=\alpha, \tag{9}$$

where

$$F(R)=\begin{cases}F_1=R+1/R+KR^2/R_a^3, & \text{for } R\leqslant R_a;\\ F_2=R+(1+K)/R, & \text{for } R\geqslant R_a.\end{cases} \tag{10}$$

As in ordinary Stoermer theory, $\bar{\alpha}$ is that value of α for which Eq. (9) has only a single positive root; since for larger values of α the equation clearly has two positive roots and the allowed region in the meridian plane then splits up into two parts, the inner part being insulated

TABLE I. Maximum values of $(-k)$.

λ	10°	20°	30°	40°	50°
$-k$	3.7	2.4	2.6	3.8	7.8

TABLE II. Maximum values of $(-H\delta C/C\delta H)$ for total cosmic-ray intensity at sea level.

λ	10°	20°	30°	45°
$-H\delta C/C\delta H$	0.4	0.4	1.0	~ 0

from infinity by forbidden regions. In effect then, $\bar{\alpha}$ is equal to the smallest value of $F(R)$ for positive values of the argument R.

Let α_1 and α_2 be the respective minimum values of $F_1(R)$ and $F_2(R)$; and let R_1 and R_2 be the values of R which produce these minima: $F_1(R_1)=\alpha_1$, $F_2(R_2)=\alpha_2$. It can be seen from Eq. (10) that $R_1<R_2$. Hence, (a) if $R_a<R_1$, the smallest value of $F(R)$ is given by $\bar{\alpha}=\alpha_2$; (b) if $R_a>R_2$, then $\bar{\alpha}=\alpha_1$; (c) if $R_1<R_a<R_2$ then $\bar{\alpha}$ is equal to the smaller of the two minima, α_1 and α_2.

From Eq. (10) we find

$$\alpha_2=2(1+K)^{\frac{1}{2}}; \quad R_2=(1+K)^{\frac{1}{2}}; \tag{11}$$

and if we make the reasonable assumption that K is small compared to unity, then for $R_a \gtrsim 1$ it is easily shown that

$$\alpha_1 \approx 2(1+K/2R_a^3); \qquad R_1 \approx (1+2K/R_a^3)/(1+3K/R_a^3). \tag{12}$$

Recalling our assumption that K is small, we see that $\alpha_1=\alpha_2$ when $R_a \approx 1$. From the discussion of the preceding paragraph it therefore follows that

$$\bar{\alpha}=\begin{cases}\alpha_2, & \text{for } R_a \lesssim 1;\\ \alpha_1, & \text{for } R_a \gtrsim 1.\end{cases} \tag{13}$$

The allowed cones in the presence of the "ring" current can now be obtained by substituting these results into Eq. (8).

In particular, we want to find the minimum value of R_e for arrival of a particle from the vertical direction $(\sin\theta=0)$. This minimum is designated by $\bar{R}_{ev}$. From Eqs. (6), (8), and (13) we find

$$(\bar{R}_{ev} \lesssim 1/a) \quad \bar{R}_{ev}=\cos^2\lambda(1+K/a^3)/2(1+K)^{\frac{1}{2}}; \tag{14}$$

$$(\bar{R}_{ev} \gtrsim 1/a) \quad \bar{R}_{ev}=\cos^2\lambda(1+K/a^3)/2(1+K/2a^3\bar{R}_{ev}^3). \tag{14'}$$

Equation (14′) has yet to be solved for $\bar{R}_{ev}$. Since $K/a^3 \ll 1$, however, a very good approximation is obtained by setting $\bar{R}_{ev}=\frac{1}{2}\cos^2\lambda$ on the right-hand side of Eq. (14′).

The minimum momentum for vertical arrival, designated by $\bar{p}_v$, can now be found from Eq. (5). Neglecting terms higher than the first order in $K=M_r/M_e$, we arrive at the following results:

$$(\cos^2\lambda \lesssim 2/a) \quad \bar{p}_v=B\cos^4\lambda[M_e-(1-2/a^3)M_r]; \tag{15}$$

$$(\cos^2\lambda \gtrsim 2/a) \quad \bar{p}_v=B\cos^4\lambda[M_e-(4\cos^{-6}\lambda-1)(2M_r/a^3)]; \tag{15'}$$

where $B=e/4c\rho^2$.

III. RELATION BETWEEN COSMIC-RAY AND MAGNETIC VARIATIONS

Equations (15) and (15′) give the vertical cutoff momentum as a function of geomagnetic latitude λ. Consider now a cosmic-ray detector located at λ and at a depth x below the top of the atmosphere; and for simplicity, suppose that it is a "vertical" detector; i.e., that it responds only to particles which are incident from the vertical direction within a small solid angle. The counting rate C arises from the primary radiation, either directly or through secondary particles. If we assume that the latter maintain the direction of travel of the primaries, then the counting rate will be a function of the vertical flux of primaries, hence a function of $\bar{p}_v$:

$$C=C(\bar{p}_v). \tag{16}$$

If the detector is a nondirectional device (e.g., an ionization chamber), the vertical flux of radiation can be obtained from the observed counting rate by a Gross transformation.

Let H be the total magnetic field intensity at the geomagnetic equator. This contains a term H_e due to the earth's dipole and a term H_r due to the extraterrestrial current system, where

$$H_e=M_e/\rho^3; \qquad H_r=-2M_r/(a\rho)^3. \tag{17}$$

Suppose now that M_r changes by δM_r. This produces directly a change in H; and indirectly, by inducing currents below the earth's surface, it produces effectively a change δM_e in the earth's dipole moment.[2] Assuming that a fraction f of the observed change in H is due to this secondary process, we can write

$$f\delta H=\delta H_e=\delta M_e/\rho^3; \qquad (1-f)\delta H=\delta H_r \doteq -2\delta M_r/(a\rho)^3. \tag{18}$$

From Eq. (16) we obtain the relation

$$\partial C/\partial H=(\partial C/\partial\lambda)\frac{\partial\bar{p}_v/\partial H}{\partial\bar{p}_v/\partial\lambda}. \tag{19}$$

Evaluating the derivatives in Eq. (19), and making use of the fact that $H \approx H_e \gg H_r$, we obtain the following results:

$$\frac{\delta C}{C}=\frac{1}{C}\left(\frac{\delta C}{\delta\lambda}\right)k\frac{\delta H}{H}; \tag{20}$$

where

$$(\cos^2\lambda \lesssim 2/a) \quad k = -[(a^3-2)(1-f)+2f]/8\tan\lambda; \quad (20')$$

$$(\cos^2\lambda \gtrsim 2/a) \quad k = -[f+(1-f)(4\cos^{-6}\lambda-1)]/4\tan\lambda. \quad (20'')$$

These equations give the changes in cosmic-ray intensity that would be expected to accompany changes in the intensity of the extra-terrestrial current system. It should be pointed out that the derivative $\delta C/\delta\lambda$ involves the measurement of λ in radians. The discontinuity at the value $\cos^2\lambda \approx 2/a$ arises from the peculiarity of the current system considered. For a true ring current the function k would show a smooth transition at $\cos^2\lambda = 2/a$. The results obtained here are fairly exact (within the limits of the Stoermer approximation) for the current sheet that has been considered. They are only approximate if the current system is more nearly represented by a ring, although the approximation improves as $\cos^2\lambda$ becomes increasingly larger or smaller than $2/a$.

The effect on the cosmic radiation of a true ring current (taken to have a negligibly small cross-sectional radius) has been calculated by Hayakawa *et al.*[3] However, these authors have considered the effects only for a particular primary momentum (15 Bev/c) at a particular latitude (0°).

Following Chapman,[2] we assume that the fraction f has the value one-third. Equations (20′) and (20″) then reduce to the following:

$$(\cos^2\lambda \lesssim 2/a) \quad k = -(a^3-1)/12\tan\lambda; \quad (21')$$

$$(\cos^2\lambda \gtrsim 2/a) \quad k = -(8\cos^{-6}\lambda-1)/12\tan\lambda. \quad (21'')$$

The most significant feature of these results is the algebraic sign of the cosmic-ray effect. It is seen that a decrease in magnetic field intensity at the equator should correspond to an increase in cosmic-ray intensity, contrary to some of the qualitative arguments which have appeared in the literature. If the radial distance of the "ring" current is small, k is given by Eq. (21′), and it is seen that $|k|$ decreases rapidly with decreasing radius. For sufficiently large values of a, however, k is given by Eq. (21″), and it attains its maximum value, independent of a. In Table I we list the maximum value of $|k|$ for several latitudes.

[3] Hayakawa, Nishimura, Nagata, and Sugiura, J. Sci. Res. Inst. Tokyo **44**, 121 (1950).

In order to indicate the magnitude of the cosmic-ray variations to be expected, we can take as an example the total intensity of ionizing radiation at sea level, using for the latitude effect, $\delta C/\delta\lambda$, the values given in the paper by Johnson.[4] The maximum value of $|H\delta C/C\delta H|$ is given in Table II. For the nucleonic component, which shows a larger latitude effect,[5] these values would be considerably larger. During large magnetic storms, $\delta H/H$ may be as large as $\frac{1}{2}-1$ percent. Thus, unless the radius of the ring is assumed to be very small, the cosmic-ray variations should be detectable at intermediate latitudes. Above the knee of the latitude curves, however, the effect should vanish. Finally, it should be observed that our results cannot be used at very small latitudes, because of the inadequacy there of the Stoermer approximation. In this approximation k approaches infinity as λ becomes very small, but $\delta C/\delta\lambda$ approaches zero; and the problem becomes indeterminate.

It is perhaps most often the case that magnetic storms are not accompanied by detectable cosmic-ray disturbances, or that if they are, the cosmic-ray and magnetic variations do not show a detailed correspondence in time.[6] If the theory of the ring current is to be retained, it is necessary to suppose that the radius of the ring at such times is very small—and possibly the currents actually flow in the ionosphere. In other cases there does exist a detailed correlation between cosmic-ray and magnetic field variations, but the algebraic sign of the effect is the opposite of that predicted by the ring current theory.[7,8] Correlations with the proper algebraic sign and reasonable order of magnitude have, however, been reported[9]; but the statistical uncertainties make it difficult to determine whether or not the cosmic-ray and magnetic field variations show the detailed correspondence in time which would be required by the ring current theory.

The author wishes to express his thanks to Professor J. A. Simpson for several valuable discussions on the observational data of cosmic-ray time variations.

[4] T. H. Johnson, Terr. Mag. Atmos. Elec. **43**, 1 (1938).
[5] J. A. Simpson, Phys. Rev. **81**, 895 (1951).
[6] S. E. Forbush, Terr. Mag. Atmos. Elec. **43**, 203 (1938); J. A. Simpson (to be published).
[7] S. E. Forbush, Phys. Rev. **51**, 1108 (1937).
[8] V. F. Hess and A. Demmelmair, Nature (London) **140**, 316 (1937).
[9] See, e.g., Hess, Demmelmair, and Steinmaurer, Terr. Mag. Atmos. Elec. **43**, 7 (1938).

Electrical Fields in the Crookes Dark Space of a Low Pressure Glow Discharge in Air and N_2*

ROBERT P. STEIN†
Department of Physics, University of California, Berkeley, California
(Received July 8, 1952)

Application of a 20 000-volt electron beam probe to the study of the fields in the Crookes dark space of normal and abnormal glow discharges in air and N_2 from 50 to 400 microns pressure and current densities from 3 to 20 $\mu a/cm^2$ were made. In general agreement with Aston's low pressure study of 1911, the fields generally dropped in a linear fashion from cathode to negative glow. Fields ranged from 600 volts/cm on down at the cathode. Over-all accuracy was 10 percent or better. These fields, together with known variations of ion drift velocity and approximate Townsend second coefficients γ, allow the ionization per cm along the axis to be computed as a function of position in the dark space. While accuracy of fields at the cathode are not such as to allow of positive statement, the nature of errors present strongly indicate the ionization function in the dark space to be of the type deduced by Morton under similar conditions in coaxial cylindrical geometry.

INTRODUCTION

THE fields in the Crookes dark space of glow discharges have been studied in the past by methods utilizing an electron beam probe,[1] foreign body probes, and the Stark effect. The published studies using the beam probe have been confined to a limited range of operating conditions owing to the inadequate research facilities at the time they were done. The results obtained by the use of a probe in the Crookes dark space cannot be considered reliable, and the Stark effect studies were confined to abnormal discharges having appreciable light emission from the dark space. Thus, although studies have been conducted on this subject, it was considered important to measure the fields anew utilizing the electron beam probe method with the benefit of modern techniques extending the range of discharges which can be investigated far beyond the few points obtained by Aston.[1] With the equipment developed air and N_2 were investigated in the pressure range 25–150 microns and 30–500 microns, respectively, over the current range of 0–2 milliamperes and current densities from 3 to 20 $\mu a/cm^2$.

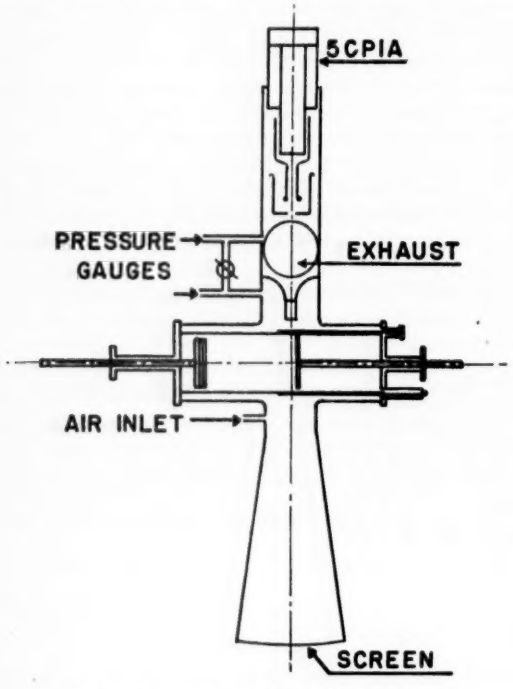

FIG. 1. Cross section of the discharge tube and measuring beam.

EQUIPMENT AND PROCEDURE

The apparatus used is schematically sketched in Fig. 1. It is to be described in detail in another paper. In principle, it consists of two separate glass chambers connected by a 0.10-mm hole through which the electron beam generated in the evacuated gun chamber could pass so as to traverse a glow discharge contained in the other chamber. The electron gun was that of a 5CP1 cathode-ray tube with an auxiliary high voltage lens attached so that 20 000-volt electron beams could be generated. The glow discharge itself was contained in inner glass cylinder with an inside diameter of 6 cm, which was about 2 mm greater in diameter than the flat Dural electrodes used. The length of the discharge was restricted from 9 to 14 cm. The Dural electrodes were mounted on Wilson seals so that any desired portion of the discharge could be moved in front of the fixed probing beam. The motion was accomplished by micrometer screws. The beam entered the inner cylinder through a one-mm hole and left through an adjustable one-mm slit. The potential of the plane of the discharge which was opposite these holes was adjusted so that a minimum current leaked to the surrounding grounded chamber. The beam after leaving the discharge was detected on a fluorescent screen after traversing a field

* This project has been supported by the ONR.
† Currently at U.S. Naval Ordnance Test Station, Inyokern, California.
[1] F. W. Aston, Proc. Roy. Soc. (London) **A84**, 526 (1911).

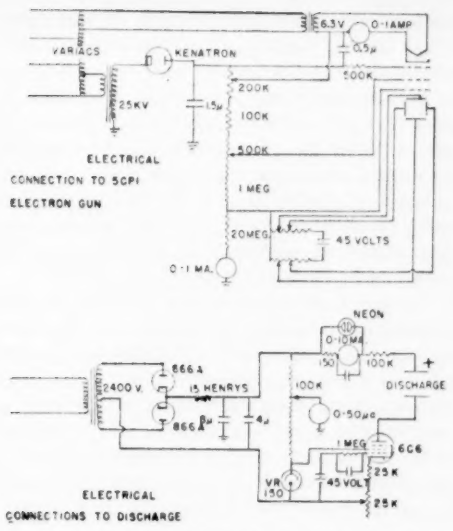

FIG. 2. Diagram of electrical connections to the gun and discharge.

free drift space. Its deflection could be read to 0.1 mm equivalent to a field of 1 volt-cm. The electrical connections are shown in Fig. 2. The beam deflection was calibrated by passing it through a uniform field consisting of a second parallel plane just behind the cathode and integral with it.

In order to calculate the field in terms of the measured deflection a theory was developed assuming that all field lines were parallel with the axis of the discharge, correcting to a first approximation for the fact that the probing beam will experience different fields as it is deflected in traversing the discharge. Elaborate precautions were taken to prevent deflection or disturbance of discharge and beam by charge accumulations at any point.

Gaseous purity was that for a chamber with Aquadag and Glyptal inside and that could not be beaked out but gave a vacuum of 10^{-6} mm. As constant pumping was needed during a measurement purity in some measure was assured by the flow of fresh gas. The air was dried over suitable refrigerants to remove Hg, CO_2, and water vapor. The N_2 was tank gas purified by standard techniques proven in this laboratory to be more than adequate.

Because of the necessity of maintaining a low pressure in the electron gun and with limitations in pumping speed the range of values of pressure over which measurement could be made was restricted. This precluded studies in H_2 because of its rapid diffusion. The discharge tube length could be varied from 14 cm on down. Most convenient operation with the power source used was found to be at 9-cm length. Figures 3 and 4 give the range of current densities and pressures at which measurements could be carried out in air and N_2 relative to the normal and absnormal glow regions. The region covered by Aston's data, which are the only comparable data on hand, is shown relative to this study as far as it could be determined from his article. Further data typical of the discharge investigated are presented in Fig. 5 showing current-potential characteristics at several pressures. The crosses on the curves indicate points at which field strength studies were made. In many of the lower pressure discharges studied, in both air and N_2, no anode spot was present. Curves for potential plotted against electrode spacing are seen in Figs. 6 and 7. The separation shown in Fig. 6 where the discontinuity is noted is that at which the anode spot abuptly appeared. This was accompanied by a decrease in the uniform luminosity spread over the low field region and an increase in intensity of the negative glow with appearance of a Faraday dark space. Below 100 microns pressure the anode spot could not form. No fully developed positive column was present in any of the discharges. At the higher pressures in N_2 there was a column which, however, never exceeded 4 cm in length. There were no appreciable oscillations up to 10^5 cycles present in these discharges.

Prior to field strength measurement the discharge was kept running for at least 2 hours to stabilize pressure, current, and potential. Curves for potential plotted against electrode separation were run at one or more current values. Curves were also determined for current at various potentials for the 9-cm electrode separation used. A current was chosen and data were taken on the deflection of the beam relative to beam distance from the cathode. At constant pressure other currents were chosen and further measurements were made. To check these data the current was measured as a function of the beam deflections at various positions of the beam. The curves for deflection relative to position were then evaluated by cross plotting. Good agreement between both methods of taking data were obtained.

SOURCES OF ERROR

Despite all precautions sources of error could not be eliminated.

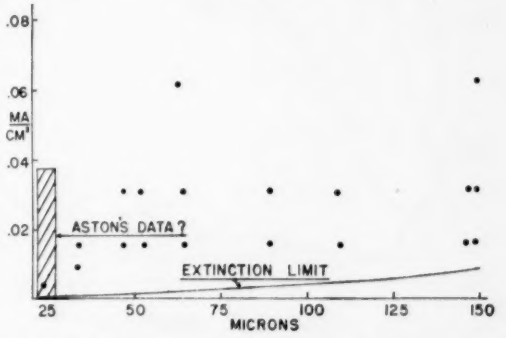

FIG. 3. Range of current densities and pressure for measurement in air. Dural electrodes, diameter = 5.4 cm; gap = 9.1 cm.

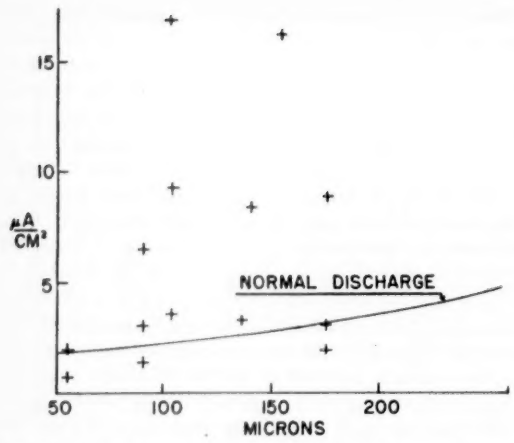

FIG. 4. Range of current density and pressure for measurements in nitrogen. Electrode diameter 5.4 cm; gap 9.0 cm.

1. It was difficult to obtain exact parallellism between cathode surface and beam. Angles between cathode surface and beam could at times have been 0.025 radian. At an extreme the error in the calculated fields, which ranged from 600 volts/cm down to small values near the negative glow, could have been 15 volts/cm. In the high field regions of the dark space such an error is not serious, but it reaches values of the order of 100 percent error near the negative glow at high pressures and high current densities. The error is systematic and constant, yielding a value too high or too low by the same amount under any given set of conditions. If the beam is directed toward the cathode, there is a sharp corner in the field strength curve at the negative glow. If the beam is directed away the sharpness of transition is reduced. A survey of the data indicates that, in general, these errors were not very serious. Velocity fluctuations of the probe beam were always small and either could be compensated or were negligible.

2. Another troublesome feature was the dependence of discharge potential on the position of the discharge relative to the entrance and exit holes for the probing beam. The effect was greatest in gases at low pressure. It was significant only below 50 microns where it was 2.8 percent and became 0.5 percent at 100 microns. It probably came from the conductivity of the forks holding the glass cover plates defining the slits. These acted as extra cathodes because of their conducting coating of glyptal. They therefore drew some discharge current when the plasma near the cathode diffused through the holes at low pressures. This altered the economy of the glow.

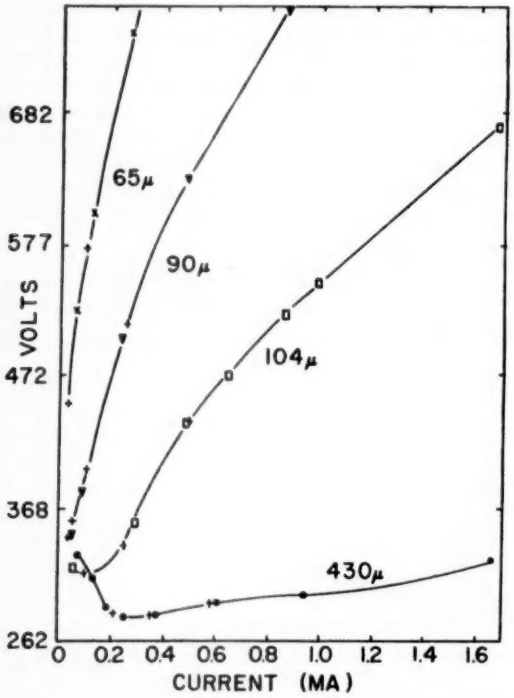

FIG. 5. Potential current characteristics for N_2 at pressures indicated.

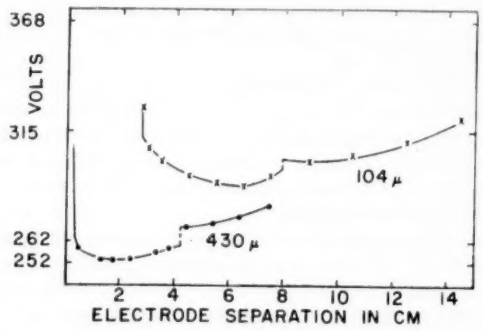

FIG. 6. Curves for potential plotted against Dural electrode separation in nitrogen at pressures indicated. Current density $=3.7\times10^{-6}$ amp/cm².

3. A third source of error, the consequences of which will later be discussed, arose when it was discovered on dismantling the tube that the cathode had been cleaned by the discharge over all of its surface except for an annular ring of some 6-mm width at the outer edge of the cathode. The ring was covered with a gray coating of sputtered material. This indicated that the diameter of the discharge used in calculation of the deflections near the cathode was too large. Probably a more serious aspect of this same situation lies in the deviation of the field lines from parallelism with the axis of the discharge near the cathode. The effect was caused by potentials on the glass wall which was close to the cathode in order to reduce edge effects in the reverse sense.

4. Measurement of field strengths was carried out along the whole gap in a number of cases. To test the validity of the measurements, these fields were inte-

grated across the gap. In many instances the total potential drops so obtained were *less* than the applied potential. The integrated potentials ranged down to values as low as half of the applied potential. This discrepancy is, however, not as serious as it seems. Actually most of the applied potential drop is across the Crookes dark space and integration of the field confirms this. Thus, in the short length of some centimeter or so of dark space the fields are very high and drop to zero by the time the glow is reached. From there on the fields are weak and extend some eight or more centimeters to the anode. It was observed in curves of field strength across the gap that from the beginning of the negative glow on the measured fields had negative values of varying small amounts. The integral of these negative fields over the negative glow and column to the anode reduced the total integrals across the gap to potentials that were lower than applied potentials. The error is an edge effect in which a negative deflection is imparted to the beam in passing

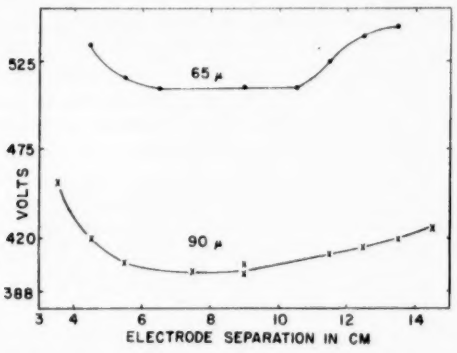

FIG. 7. Curves of potential plotted against electrode separation for N_2 at pressures indicated.

through the exit or entrance hole to the discharge. The more "abnormal" the discharge, i.e., the lower the pressure and smaller the current, the greater this deflection appeared to be. This can be associated with the so-called lack of parallelism of beam and cathode referred to earlier and appears as a constant factor in a given discharge. While negative fields in the region of the negative glow might in this discharge be expected, it is not likely that they are as great or extend the length of the discharge. Thus, all the field strength curves plotted across the gap and shown in Figs. 8 to 11 inclusive for N_2 have been "corrected" by raising the field strength values by a constant amount along the whole discharge so that the integrated field equals the applied potential. The correction amounts to some 6 volts at 440 microns, which is about 2.5 percent of the maximum field, ten volts at 100 microns, or about 6 percent, and about 15 volts at 50 microns which is about 10 percent of the maximum field. The fields of Figs. 12 to 14 for air have not been corrected. Since the

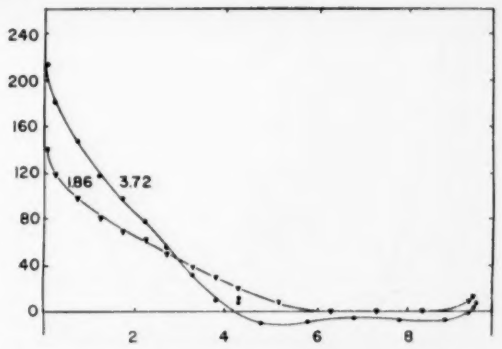

FIG. 8. Field strength, volts/cm, observed at various distances in cm from the cathode for nitrogen at .55 microns at 1.86 and 3.72 μ amp/cm^2. This curve has been corrected for field distortion.

purpose of this study was to investigate the fields in the Crookes dark space as to magnitude and variation across the dark space, the errors indicated are not compromising. However, they reduce the accuracy of the absolute values observed at worst to 10 percent rather than the 1 percent to be expected from the resolving power of the method for such beams. The trends of the fields can be considered as correct except to distances within about one tenth of the length of the dark space from the cathode and near the end of the dark space where fields are low.

RESULTS AND THEIR INTERPRETATION

As indicated in Figs. 8 to 14 inclusive the fields in the dark space fall off nearly linearly with the distance from the cathode as initially reported by Aston.[1] The irregularities as well as curvatures noted other than at the cathode or near the glow can well be real. However, even accepting those, it seems clear that in these dis-

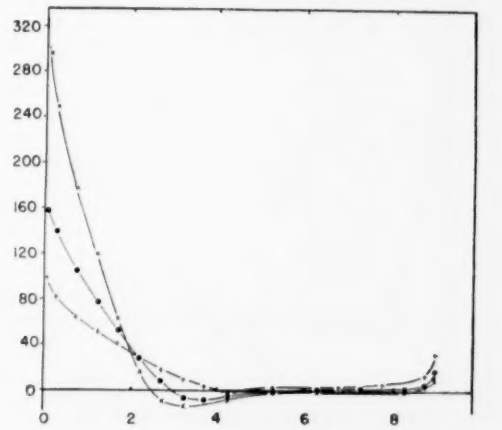

FIG. 9. Field strength, volts/cm, observed at various distances in cm from the cathode for nitrogen at 90 microns and 9.33, 3.72, and 1.86 μ amp/cm^2 reading from top to bottom curve. This curve has been corrected for field distortion.

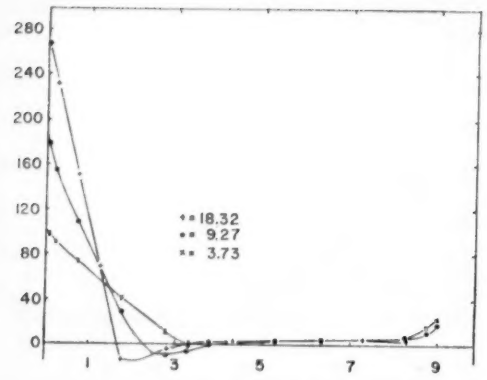

FIG. 10. Field strength, volts/cm, observed at various distances in cm from the cathode for nitrogen at 104 microns and indicated current densities in μ amp/cm^2. This curve has been corrected for field distortion.

charges the field declines nearly in a linear fashion with the distance from the cathode.

This observation on the part of Aston has caused some concern ever since it was known. The reason for this stems from the fact that if the electrons be ignored as contributing to the dark space field because of their scarcity, the field gradient cannot be attributed to any distribution of the space charge consequent to known ionic drift velocities. Numerous investigators have attempted to derive a suitable mathematical theory for the Crookes dark space. Some of the more successful of these are summarized by Penning and Druyvesteyn[2] in their excellent article of 1940. Probably one of the more significant earlier theories was that of Compton[3] and Morse. It leads to the fields indicated by curves A of Fig. 15. The latter theory uses the conventional Townsend ionization function α as represented by the generalized Townsend equation for α/p as a function of the field strength to pressure ratio E/p. Even though the theory yielded reasonable values for the length of the dark space d, and of the second Townsend coefficient γ, it gives a fall of potential at variance with those observed here. In its use of Townsend's functions it is contrary to the more recent indications of Druyvesteyn and Penning[2] and Morton[4] and Johnson[5] that the Townsend functions are not applicable to the Crookes dark space with its high E/p ratios.

Von Engel and Steenbeck[6] accepted the linear fall as given by Aston as an observed fact. Assuming that the velocity of the positive ions is proportional to the field strength and that the first Townsend coefficients α apply in these fields, they derived a relation based on the condition that $\gamma[\exp(\int \alpha dx)-1]=1$ for a self-sustaining discharge. Here γ is the fraction of positive ions incident on the cathode leading to electron emission, and $[\exp(\int \alpha dx)-1]$ is the number of electrons created in the dark space by impact. The theory derived on this basis appeared to give satisfactory results in neon, which Druyvesteyn[7] later showed to be fortuitous. Actually the drift velocity is not proportional to the field at high E/p,[8–10] and the Townsend functions cannot be applied to high E/p ratios, a fact unknown to von Engel and Steenbeck.

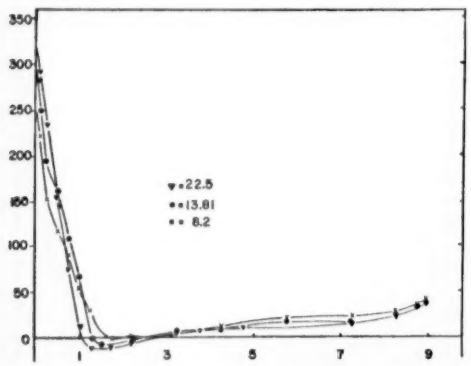

FIG. 11. Field strength, volts/cm, observed at various distances in cm from the cathode for nitrogen at 430 microns and indicated current densities in μ amp/cm^2. This curve has been corrected for field distortion.

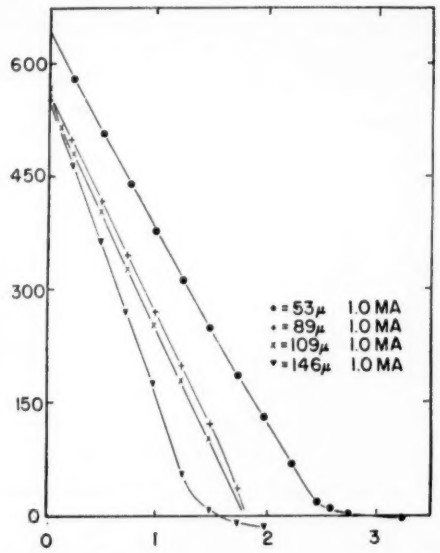

FIG. 12. Field strength, volts/cm, at various distances in cm from the cathode in air for various pressures in microns. These data have not been corrected for distortion as in nitrogen.

[2] M. J. Druyvesteyn and F. M. Penning, Revs. Modern Phys. **12**, 87 (1940).
[3] K. T. Compton and P. M. Morse, Phys. Rev. **30**, 305 (1927).
[4] P. L. Morton, Phys. Rev. **70**, 358 (1946).
[5] G. W. Johnson, Phys. Rev. **73**, 284 (1947).
[6] A. von Engel and M. Steenbeck, Electrichen Gasentladung **2**, 26–31 (1934).
[7] M. J. Druyvesteyn, Physica **5**, 875 (1938).
[8] A. V. Hershey, Phys. Rev. **56**, 908 (1939).
[9] J. A. Hornbeck, Phys. Rev. **84**, 393 (1951).
[10] C. H. Wannier, Phys. Rev. **83**, 281 (1951).

As indicated by Penning and Druyvesteyn[2] and in view of Morton[4] and Johnson's[5] studies, which make the ionization functions over much of the Crooks dark space unknown, a different procedure is suggested. Thanks to studies of Hershey,[8] and later studies of Hornbeck[9] and Wannier,[10] it is quite certain that in the regions of E/p covered in these studies the ion drift velocity varies as about $(E/p)^{\frac{1}{2}}$ near the cathode in the negative glow. Much work has been done in recent years giving a fair knowledge of the order of magnitude to be expected for secondary emission coefficients γ_i of positive ions at the cathode. It is then possible to set up the differential equations for the processes involved in the Crookes dark space and assuming a linear fall of potential to solve for the ionization function α at various points of the field required to satisfy these conditions.

Let α be the number of ions created by a secondary electron emitted from the cathode per cm advance at any point in the dark space. This will vary with the distance from the cathode. Let K be the mobility of the positive ions. The number of ionizations per second which occur as a result of electron impacts in an element of length dx along the field at any distance x from the cathode may be written as $j_e^{\alpha dx}$, where j_e is the electron current density. The number of ionizing acts per second must be equal to the divergence per second of positive ions from the element dx. In other words, the divergence of the positive ion current at x must equal the ion production, so that α equals the divergence of positive ion current divided by j_e. This divergence may be taken as $nedv/dx+vedn/dx$, if diffusion to the walls is neglected in a uniform field between parallel planes. Here v is the average velocity of the positive ions at x, and $n(x)$ is the density of the positive ions at x. The electron current density is given by $j-nve$. If the contribution of the few mobile electrons to the space charge in the Crookes dark space be neglected, $dE/dx=4\pi ne$. If n is constant, it then follows that E decreases linearly with x. Represent the drift velocity of the positive ions by $v=KE^S$, where K is a constant and S has an arbitrary positive value limited by $0<S\leq 1$. This assumption is made since E/p ranges from 10^4 to 0 volts/cm per mm Hg for abnormal discharges and from 10^3 to 0 for normal glow discharges. It can be assumed that for high E/p, $S\sim\frac{1}{2}$ and for low E/p, $S=1$. Actually the field is changing very rapidly, and it is doubtful whether a proper value for "mobility" can be assigned as equilibrium with the field is never obtained. The value of S is thus not assured, but its range of variation is limited, lying between the values indicated. If E_c is the cathode field, then K may be eliminated by noting that $j/(1+\gamma)=nKE_c^S$. This assumption is justified if the mobility law remains valid for values of x so near the cathode that no appreciable electron ionization occurs between the point of departure and the cathode. The resulting equations may then be solved for α as a function of x for various reasonable values of γ and S. This leads to the set of curves of Fig. 16.

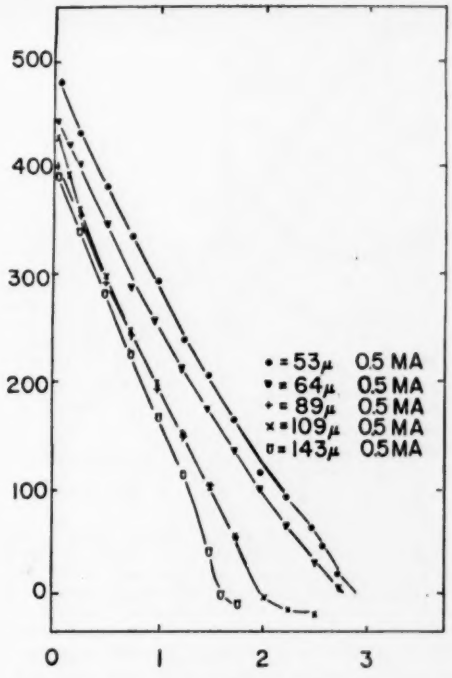

FIG. 13. Field strength, volts/cm, at various distances in cm from the cathode in air at various pressures in microns. These data have not been corrected for distortion as in nitrogen.

In this diagram α is plotted as a function of x, the

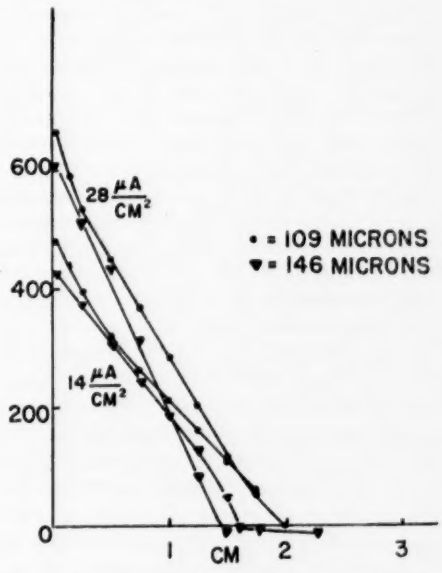

FIG. 14. Field strength, volts/cm, at various distances in cm from the cathode in air at various pressures and currents. These data have not been corrected for distortion as in nitrogen.

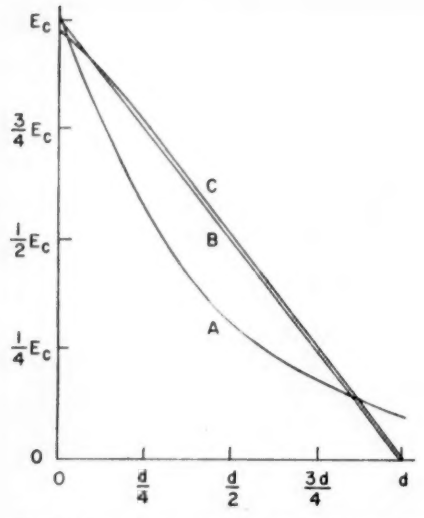

FIG. 15. Electrical fields plotted against distance from the cathode under various conditions. These curves are plotted as fractions of the cathode field against fractions of the length of the dark space. Curve (A) from Compton and Morse's theory. Curve (B) linear decrease of field observed. Curve (C) minor alteration of linear field due to distortion near cathode indicated by observed errors.

distance from the cathode. The two sets of curves shown are for positive ion mobilities varying as E and E^1 (i.e., $S=1$ and $S=\frac{1}{2}$) at different values of γ. It is seen that with this field distribution the values of α depend quite strongly on γ, especially near the surface of the cathode. If a transition in the mobility law occurs, as it must with a large range of E/p, say from E to E^1, the value of α does not shift for the curve $S=\frac{1}{2}$, $\gamma=a$ to the curve $S=1$, $\gamma=a$. This follows since the boundary conditions of both these curves are applied at the cathode—because the transition of the curve for a given γ and S occurs at a lower value of E or x. Instead some sort of a smooth transition must occur at the transition distance x, or field E, from the $S=\frac{1}{2}$, $\gamma=a$ curve to a curve similar in shape to the $S=1$ curves. Transitions cannot be plotted since the boundary conditions for the $S=1$ curves are unknown. The transition probably occurs in the range $E/p\sim100$ and therefore occurs close to the negative glow for the discharges investigated.

While it may be concluded that an approach of this type is suggestive and fruitful more discussion of the influence of errors is needed before conclusions may be drawn. It happens that the curves computed for α near the cathode are very sensitive to variations in field gradient there. If the gradient decreases by 10 percent in the first 20 percent of the dark space adjoining the cathode, the values of α there will shrink towards zero since the drift velocity in that region will vary closely as E^1. This region is, however, one where a 10 percent change in gradient is near the known limits of accuracy for the more abnormal discharges in air and N_2. However, there are other sources of error that cannot be neglected. These stem from the unknown distortion of the fields and equipotentials near the cathode. That some distortion takes place is indicated by the annulus of no discharge around the rim of the cathode. This requires that some consideration be given to the contributing causes, notably to radial diffusion of carriers and wall potentials. The walls adjoining the cathode receive predominatingly positive ions by diffusion. They should thus be quite positive. An estimate of this field was made by assuming that an axial field builds up to cancel the diffusion of positive ions from the dark space. Thus $Ddn/dr=nKdv/dr$, where r is the distance from the discharge axis. Solution yields a positive wall potential in volts which is given roughly by $\Delta V=(D/K)\log n$. Here n is the positive ion density, and D/K is nearly half the average energy of positive ions divided by the electron. If $n\simeq10^8$ as here indicated, then ΔV in volts is roughly $\Delta V\simeq18\bar{E}/2=9\bar{E}$, with $\bar{E}$ the average electron energy in volts. The energy near the anode in the Crookes dark space varies with discharge conditions. It has been estimated at various times and lies in the order of 10 ev. If the energy $\bar{E}$ chosen under the local discharge conditions is 8 ev, then ΔV is 72 volts. This would readily account for the ring on the cathode. At some half to three quarters the length of the dark space from the cathode, electrons and positive ions reach the walls in equal numbers, and at the negative glow there is a plasma to which ambipolar diffusion processes apply. The ion energies are

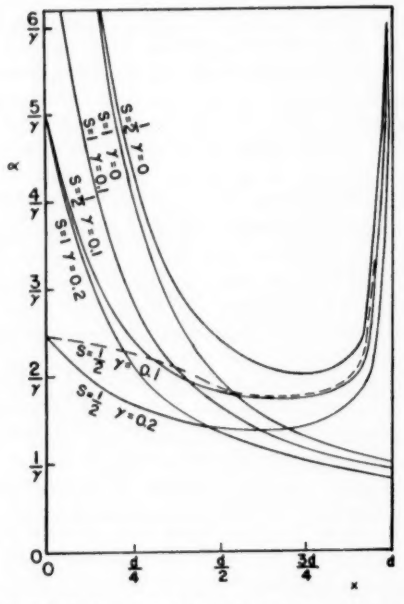

FIG. 16. Calculation of the ionization function α plotted against distance x from the cathode as fractions of the Crookes dark space d, assuming various values for the exponent for ion drift velocity as a function of the field and various values of the second coefficient γ for electron liberation by positive ion bombardment.

nearly thermal, but there are many electrons with 40 to 50 volts of energy. Thus, opposite the negative glow wall potentials will be perhaps several volts negative. Figure 17 shows the possible potential distribution in perhaps exaggerated form. Study with tubes of varying diameter and with different distances between tube and rim of the electrode would give some indication of the effect.[11] That it is of no serious consequence in regard to the major portion of the data is indicated since Aston's fields with a tube of twice the diameter as the one used in the most abnormal discharge are quite consistent with the present data. The effect is, however, quite important at the cathode.

Before further discussion the direct "wall effect" should be considered. Drift velocity calculations assumed no discontinuity at the cathode surface. Diffusive motion with zero molecules or ions behind the cathode surface leads to a net loss of carriers from that region by diffusion along the axis superposed on the field action. On the other hand, the accommodation coefficient of the cathode for positive ions is certainly not unity and some ion reflection occurs. This would tend to counteract the loss by diffusion. It is not likely that even with the relatively low pressures these effects, which extend only a few ionic free paths, are too significant especially since they tend to cancel each other.

Thus, the radial field deviations are probably the important factors. If the fields are as indicated, the values of α computed by the uniform field theory must be raised in regions where the carrier and electron loss to wall current is large, while it does not alter α much where the radial field components are small. The converging lines or increased fields near the cathode will alter the solution of the relations affecting α near the cathode. The net result of these factors will be to reduce α near the cathode and increase it near the negative glow.

Taking into account the existing indicated radial components in the field form, which were not included in the reduction of the data, requires that the fields calculated on the assumption of beam-cathode parallelism and field uniformity must be corrected. Thus, if a linear field is computed from the beam indications, the form of the true existing field along the axis of the discharge could well be that shown by curve C of Fig. 15 instead of curve B as deduced from the data. The effect of such a change as between curves C and B of Fig. 15 on α cannot accurately be computed. Rough computation yields the dashed curve of Fig. 16, corresponding to values of $S=\frac{1}{2}$ and $\gamma=0.1$. If the second derivative of the altered field curve of Fig. 15 had its negative value doubled with a resultant decrease of the cathode field of 2 percent, α would become zero near

[11] The diameter of the electrode relative to that of the wall was chosen for the purpose of reducing divergence of the field lines from the axis in areas traversed by the beam. It was not until all the data were reduced that the present considerations were recognized. Thus, it was too late to carry on measurements varying the elaborate tube design in this investigation.

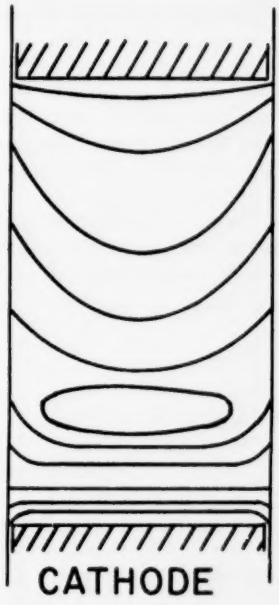

FIG. 17. Possible potential distribution estimated for the nitrogen discharge at 175 microns. It is the distribution that leads to curve (C) of Fig. 15.

the cathode. This would give curves for α, as a function of distance from the cathode, of sensibly the same shape as those calculated by Morton.[4] In studying the ionization by electrons in nonuniform fields with coaxial cylindrical geometry in regions of p and E/p analogous to those applying to these discharges, Morton observed values of an ionization indicating that the values of α as defined here deviated materially from those observed for uniform field geometry. Using the Smit[12] approach, he calculated the ionization as a function of distance from the cathode with a step-by-step process and obtained curves for ionization which start near zero at the cathode and rise in a fashion to be expected from the α values of Fig. 16 corresponding to curve C of Fig. 15.

While field geometry differs in the Crookes dark space and in Morton's study, the variation of α and of ionization across the dark space must be analogous. Both variations of α and of ionization are consistent with the characteristic luminosities in the dark space which is not the case for the Townsend function.

CONCLUSION

It may be concluded from these studies that the field distribution in the Crookes dark space of a discharge extending into the normal glow discharge regions in clean N_2 up to some 0.4-mm pressure are in agreement with the form observed under different conditions by Aston.[1] The data are good to 10 percent and cover a rather extensive range of discharge conditions. The data disagree with those of Brown and Thompson[13] in N_2 as yielded by a shadow probe as well as those obtained by

[12] J. A. Smit, Physica **3**, 543 (1937).
[13] W. L. Brown and E. E. Thompson, Phil. Mag. **8**, 919 (1929).

Brose[14] from the Stark effect studies which perforce covered a different range of discharge conditions. It has further been shown that such a general linear distribution of field, if analyzed in terms of a proper variation of ion drift velocity with E/p and using appropriate values of the second Townsend coefficient, enables a calculation of α, the ionization per unit length along the axis. While accuracy of the data at the cathode do not permit a positive statement, the nature of the inherent errors strongly suggest that the α will be low near the cathode and rise as the negative glow is approached. This yields the type of ionization across the dark space indicated by Morton[4] and Johnson[5] to be probable in this E/p and p range.

[14] E. Brose, Ann. phys. **58**, 731 (1919).

The writer wishes to acknowledge his indebtedness to Professor Leonard B. Loeb, at whose suggestion and under whose guidance this study was made, for his not inconsiderable assistance. Special thanks are also due Dr. Wulf B. Kinkel for his aid in the development of the apparatus and his ingenuity and help in overcoming the many difficult technical problems involved. The writer wishes to express his thanks to Professor A. von Engel of Oxford for his many useful suggestions.

PHYSICAL REVIEW VOLUME 89, NUMBER 1 JANUARY 1, 1953

Antiferromagnetic Resonance above the Curie Temperature*

ROALD K. WANGSNESS
United States Naval Ordnance Laboratory, White Oak, Maryland
(Received September 23, 1952)

The role of short-range order in effecting the disappearance of absorption as the Curie temperature is approached is discussed. The prediction of a simple theory of the effect agrees very well with experimental results from MnO. Consideration is also given to the relation of resonance experiments and studies made by neutron diffraction.

I.

THE first overt experimental study of magnetic resonance in an antiferromagnetic substance was made on Cr_2O_3 and gave the surprising result that as the material was cooled below its Curie temperature T_c the absorption suddenly and almost completely disappeared.[1] A curve showing the temperature dependence of the magnitude of the absorption at resonance (the "peak height" h) is a convenient way of partially presenting the data. A series of such curves giving h as a function of T/T_c for several materials is given in Fig. 1 which is due to Maxwell and McGuire.[2] The extinction of the resonance near T_c is a general feature of all these curves. The decline is less abrupt, however, for the compounds MnO, MnS, and MnTe, and the relative temperature range involved becomes smaller as one goes down the column of the periodic table containing the elements of negative valence. Because of the theory reviewed below and the difficulty of preparing the samples, it is felt that the residual absorption at T_c is due to impurities. Therefore, this residuum will have been subtracted from the data discussed below, and additional corrections will have been made by dividing each reading by a factor which approximately accounts for the temperature variation of the properties of the apparatus. These questions are discussed in more detail by Maxwell and McGuire.[2]

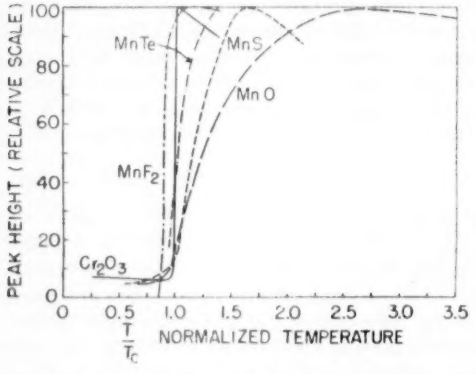

FIG. 1. Peak height of resonance absorption *vs* temperature for several antiferromagnetic materials.

Present views on the vanishing of the absorption are due to Nagamiya and Kittel[3] and ascribe it to a combined effect of anisotropy and exchange. Because of the increasing anisotropy as T falls below T_c, the actual resonance frequency will no longer coincide with the applied microwave frequency and, in fact, generally

* Supported in part by the ONR.
[1] Trounson, Bleil, Wangsness, and Maxwell, Phys. Rev. **79**, 542 (1950).

[2] All data except MnF_2 from L. R. Maxwell and T. R. McGuire (to be published in Revs. Modern Phys.). MnF_2 results due to C. A. Hutchison, Jr. (private communication to L. R. Maxwell).

[3] T. Nagamiya, Prog. Theoret. Phys. **6**, 350 (1951); C. Kittel, Phys. Rev. **82**, 565 (1951). See also: F. Keffer and C. Kittel, Phys. Rev. **85**, 329 (1952); R. K. Wangsness, Phys. Rev. **86**, 146 (1952); J. Ubbink, Phys. Rev. **86**, 567 (1952).

increases rapidly to the millimeter wave region. The basis of the derivation of the resonance conditions is the division of the magnetic atoms into sublattices whose resultant magnetizations are then discussed by using the classical equations of motion. Although this treatment is commonly used in the theories of antiferromagnetism, its dynamical validity is questionable near and above the Curie temperature since a meaningful division into such sublattices requires the existence of appreciable long-range order in the magnetic lattice.

For most materials of interest, T_c is so large that the difficulty of working in the required frequency region has prevented the observation of the resonance predicted for the antiferromagnetic state, although an actual antiferromagnetic resonance has apparently been observed in $CuCl_2 \cdot 2H_2O$ for which T_c is only a few degrees K.[4] Thus, it is desirable that we be able to learn as much as possible from those experiments which can be conveniently performed and which do yield results, namely, those done in the paramagnetic region above T_c.

The peak height for a paramagnetic material can be expected to be proportional to the total resultant moment and hence to the susceptibility χ.[5] That this is not the only effect which must be considered is most clearly shown by the contrast between the curve for MnO in Fig. 1 and the steady increase of χ to its maximum as T decreases to T_c.[6]

A clue to another feature which may affect the dependence of h on T is provided by neutron diffraction results. At room temperature (which is about 2.5 T_c) a residual coherence was observed in the pattern from MnO which indicated the existence of short-range order.[7] It is noteworthy that the decline in h of MnO begins at about this point and, at the same time, is the most gradual of any of those shown in Fig. 1. Accordingly, it seems worth while to attempt to assess the influence of short-range magnetic order upon the resonance absorption.

II.

The concept of the average short-range order, or order of neighbors, is familiar in the theory of alloys and gives a measure of the effectiveness of interactions in producing a nonrandom distribution of neighbors about a central atom.[8] For AB type alloys, the short-range order parameter σ is defined as the fractional excess of unlike over like nearest neighbor pairs. Above the Curie temperature where long-range order is absent, σ is still different from zero and increases with decreasing temperature until a critical value σ_c is reached. Below this temperature, there is a marked change in the dependence of σ upon T, with a concomitant appearance of long-range order.

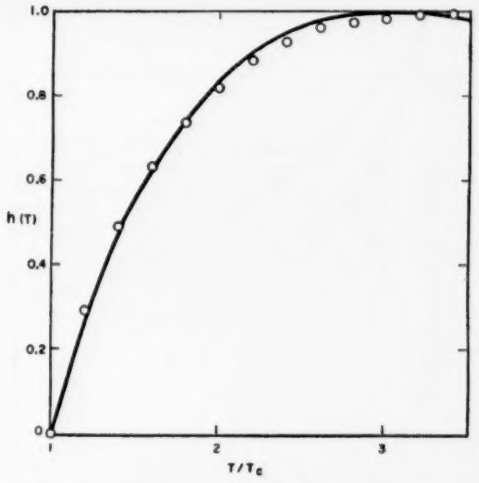

FIG. 2. Peak height *vs* temperature for MnO. Solid curve was calculated from Eq. (1). Open circles are experimental values.

The discussion of order in binary alloys is similar to that appropriate to the Ising model which, however, does not take into account the vectorial character of angular momentum which is requisite for a dynamical theory of resonance. Moreover, it is not likely that antiferromagnetic ordering can be adequately described by a single parameter; for example, one may need to consider the ordering within the shells of more remote neighbors. We shall, however, assume a description in terms of σ, defined as the average fractional excess of antiparallel over parallel nearest neighbor pairs, to be sufficiently accurate for our present purposes.

One simple possibility which suggests itself is that at temperatures not too far above T_c, for which the average short-range order is less than the critical value, varying local conditions may result in actual values of the short-range order in various separate regions which are greater than σ_c. Correspondingly, one would expect the material in these regions to be essentially antiferromagnetic, although the sample as a whole could not be said to be so. The disparity between the resonance frequencies of these regions and the applied frequency would then be so great, as discussed above, that they would effectively be excluded from the material for which the normal resonance could be obtained. The result is that the total absorption above T_c would be less than that anticipated from the usual arguments; this agrees qualitatively with Fig. 1.

We already expect h to be proportional to the susceptibility $\chi(T)$. Recognition of the possible effect of ordering now leads us to expect h to be further proportional to a function of σ, $w(\sigma)$, such that $w(\sigma_c)=0$ and $w(0)=1$. A definite dependence of h upon σ can be obtained by expanding $w(\sigma)$ about σ_c; in first approxi-

[4] Poulis, van den Handel, Ubbink, Poulis, and Gorter, Phys. Rev. **82**, 552 (1951).
[5] M. H. L. Pryce and K. W. H. Stevens, Proc. Phys. Soc. (London) **A63**, 36 (1950).
[6] H. Bizette, Ann. phys. **1**, 295 (1946).
[7] Shull, Strauser, and Wollan, Phys. Rev. **83**, 333 (1951).
[8] F. C. Nix and W. Shockley, Revs. Modern Phys. **10**, 1 (1938).

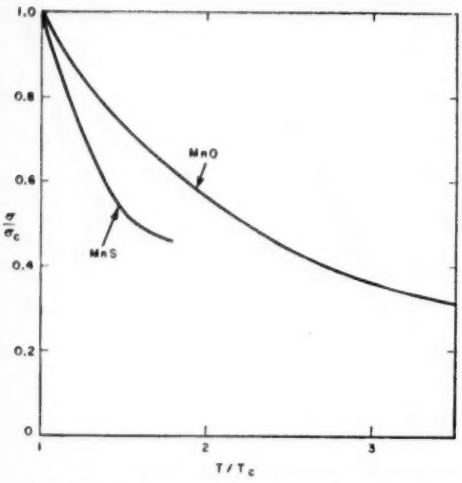

FIG. 3. Relative short-range order *vs* temperature. MnO curve is that used for Fig. 2. MnS curve from resonance and susceptibility measurements.

mation, this results in h being proportional to $(\sigma_c-\sigma)$. Combining these considerations, we can write an expression for h in the following convenient form

$$h(T)=P[1-(\sigma/\sigma_c)][\chi(T)/\chi(T_c)]. \qquad (1)$$

For now, we shall treat P as a normalization constant for the purpose of comparison with experiment; later, we shall briefly consider the factors one can expect to be involved in P.

The quantities $\chi(T)/\chi(T_c)$ and $\sigma(T)$ have been calculated by Li[9] for a simple cubic lattice of moments of spin $\frac{1}{2}$. Keeping in mind these limitations on their applicability, we can use his values to evaluate (1); the result is shown together with the experimental data from MnO in Fig. 2. The agreement between the two curves in this case is surprisingly good. It should be noted that no experimental determination of theoretical parameters has been made, nor has the curve given by (1) been otherwise adjusted except for normalization.

III.

It seems safe to conclude from Fig. 2 that the effects of antiferromagnetic interactions upon the resonance are noticeable at temperatures for which the material would ordinarily be described as paramagnetic. The temperature range over which Eq. (1) is useful is also much greater than might be anticipated from its derivation.

There are several possible reasons for the slight discrepancies in the two curves other than those discussed by Li concerning the validity of his calculations of σ and χ. Li's values of σ were obtained for zero applied field, and if an external field were present, σ could be expected to be decreased because of the tendency toward greater parallelism of the spins. This would in turn increase the values of h given by (1); for the initial regions, this is the correct direction to improve the agreement between the curves. If the residual absorption is of paramagnetic origin, its value would decrease at higher temperatures rather than remaining constant as was assumed in treating the experimental data. This would increase the agreement at higher temperatures by raising the experimental values. Although P was treated as a constant, a correct expression for it should involve the relaxation times of the system. These in turn will depend upon the temperature due to the effects of thermal agitation, and their value may well be influenced by the existing average short-range order. Other cases may require an expansion of w beyond the first two terms, resulting in a direct dependence of P upon σ.

If we assume the general validity of (1), it is then possible to invert our procedure and use the results of resonance experiments and susceptibility measurements to learn something about the short-range order in other materials. We have thus the possibility of a fruitful relation between the work on neutron diffraction and that on antiferromagnetic resonance; for example, the MnS curve in Fig. 1 would then indicate that short-range ordering effects are not as pronounced as in MnO for comparable values of T/T_c. Equation (1), unfortunately, enables us to obtain only the ratio σ/σ_c rather than the absolute value of σ; this ratio has been calculated for MnS by using the experimental values[6] of χ and is shown in Fig. 3 with the theoretical values which were previously used for MnO. These curves confirm the qualitative expectations of the relative values of the short-range order; the experimental data do not suffice to extend the curve to larger values of T/T_c in order to see if the value of the ratio for MnS does become greater than that ascribed to MnO at sufficiently great temperatures as the trend of the curve suggests.

I wish to thank Dr. L. R. Maxwell, Dr. T. R. McGuire, and Dr. J. S. Smart for many helpful discussions of this work.

[9] Y. Y. Li, Phys. Rev. **84**, 721 (1951).

The Electronic Emission Spectrum of $C^{13}O^{16}$†

K. E. McCulloh and George Glockler*
Department of Chemistry, State University of Iowa, Iowa City, Iowa
(Received August 25, 1952)

That part of the emission spectrum of $C^{13}O^{16}$ occurring between 1900 and 6500A has been obtained in an uncondensed discharge under conditions of low current density. A rotational analysis of the 0–1, 0–2, 0–3, 0–4, 0–5, and 1–1 Angstrom bands has been made. The molecular constants derived therefrom agree closely with those calculated for $C^{13}O^{16}$ from spectroscopic data pertaining to $C^{12}O^{16}$. The behavior, with respect to isotopic substitution, of the first vibrational quantum in the $B\,^1\Sigma^+$ electronic state suggests the possibility of rapid convergence of the levels. In the fourth positive group of $C^{12}O^{16}$, thirty-five band heads have been measured, involving nine v'' progressions and twelve v' progressions, each including at least two measured bands. Band origins calculated from these data agree closely with those represented by term formulas herein proposed. Vibrational constants for the ground electronic states of the two isotopic species, consistent with the theory of the isotope effect and with existing experimental data are, in cm^{-1},

	ω_e	$\omega_e x_e$	$\omega_e y_e$
$C^{12}O^{16}$	2169.84	13.301	0.0123
$C^{13}O^{16}$	2121.47	12.715	0.0115

INTRODUCTION

BECAUSE of the present availability of C^{13}, enriched in excess of 50 atom percent, it has become possible to observe spectra of isotopic modifications of carbon-containing molecules without resorting to extreme or unusual experimental methods. Investigation of such spectra is especially important in those cases where studies of the spectra of the ordinary isotopic species have failed to provide sufficient data for complete and unambiguous determination of structure or other molecular properties.

In this respect carbon monoxide is of interest because of a number of spectroscopic constants which remain to be determined, in spite of numerous investigations, the subject of which has been the $C^{12}O^{16}$ spectrum. The present work is concerned with application of the results of an investigation of the electronic emission spectrum of $C^{13}O^{16}$ to the problem of evaluating some of these constants. To be considered are the vibrational constants for the $X\,^1\Sigma^+$ state (ground electronic state and lower state of the fourth positive group) and for the $B\,^1\Sigma^+$ state (upper state of the Angstrom bands), as well as the constants T_e for the $A\,^1\Pi$ (lower state of the Angstrom bands and upper state of the fourth positive group) and $B\,^1\Sigma^+$ electronic states.

Existing reports of the spectrum of $C^{13}O^{16}$ have been confined to absorption. Birge,[1] in 1929, reported observation of the main absorption progression in the fourth positive group of $C^{13}O^{16}$, but no wave numbers were published. More recently, the infrared fundamental[2] and first overtone[3] have been observed. These infrared data, together with measurements of the fourth positive group herein reported, serve as experimental verification for vibrational constants to be proposed.

Of the vibrational formulas derived by a number of investigators for the ground electronic state of $C^{12}O^{16}$, three merit consideration in the light of the existing body of spectroscopic data. The first of these, obtained by Read[4] as a result of measurements of the fourth positive group, is most successful in expressing the relative positions of the higher vibrational levels. Inconsistency of this formula with the newer, more accurate infrared measurements[2,3,5] can apparently be traced to inaccuracies in data for vacuum ultraviolet fourth positive bands.

The second of these formulas was proposed by Rao[6] on the basis of an analysis of the Cameron bands. While this formula fits Rao's experimental values for the lowest few vibrational quanta very closely, it cannot be extended to represent the higher levels. The levels thus computed differ from the experimentally-determined term values in the vicinity of $v=20$ by more than 150 cm^{-1}.

Recently, vibrational constants based on precise infrared measurements have been proposed by Plyler, Benedict, and Silverman.[3] When their formula is extrapolated in the direction of higher vibrational states, the difference between calculated and observed term value in no case exceeds 10 cm^{-1} where reliable data are available. In view of statements by these investigators concerning the sensitivity of the constants (especially $\omega_e y_e$) to slight changes in the infrared data, it is believed that reasonable estimates of experimental uncertainty allow for minor alteration of the formula, in order to

† Based in part on a dissertation submitted in partial fulfillment of the requirements for the degree of Doctor of Philosophy, in the Department of Chemistry and Chemical Engineering, in the Graduate College of the State University of Iowa, June, 1951. (K.E.M.)

* On leave of absence from the State University of Iowa during the academic year 1952–1953. Present address: Office of Army Ordnance Research, Box CM, Duke Station, Durham, North Carolina.

[1] R. T. Birge, Phys. Rev. **34**, 379 (1929).

[2] Lagemann, Nielsen, and Dickey, Phys. Rev. **72**, 284 (1947).

[3] Plyler, Benedict, and Silverman, J. Chem. Phys. **20**, 175 (1952).

[4] D. N. Read, Phys. Rev. **46**, 571 (1934).

[5] G. Herzberg and K. N. Rao, J. Chem. Phys. **17**, 1099 (1949).

[6] K. N. Rao, Astrophys. J. **110**, 304 (1949).

TABLE I. Angstrom bands of $C^{13}O^{16}$.

Band	ν_0 (obs) cm^{-1}	ν_0 (calc) cm^{-1}
0-1	20712.5	20712.4
0-2	19297.1	19296.5
0-3	17913.5	17913.6
0-4	16563.6	16563.7
0-5	15246.8	15246.8
1-1	22749.9	22749.7

bring it into agreement with term values for the higher levels obtained from measurements of the fourth positive group.

When the present authors examined the available data for the fourth positive[7] and infrared bands, it appeared that some of the vacuum ultraviolet measurements were subject to a systematic error of about 2 cm^{-1}. This error, most apparent in the case of the two v' progressions with $v''=0, 1$ in the fourth positive group, has the effect that Read's constant $T_e=65074.3$ cm^{-1} for the $A\ ^1\Pi$ electronic state[4] is too low by about 2.2 cm^{-1}. By making this correction, still retaining Read's vibrational constants for the $A\ ^1\Pi$ state, but altering slightly the ground-state term formula given by Plyler, Benedict, and Silverman, a set of molecular constants, representing satisfactorily both the infrared and the fourth positive band systems, is obtained. The constants so derived appear in Table IV. It will be shown that this term formula, together with the ratio of reduced masses $C^{12}O^{16}:C^{13}O^{16}=0.955913$ obtained from the isotope masses $C^{12}=12.00382$, $C^{13}=13.00751$, $O^{16}=16$,[8] constitutes a satisfactory basis for calculating constants to represent the vibrational structure of the $C^{13}O^{16}$ fourth positive group. These constants are also listed in Table IV.

For the $B\ ^1\Sigma^+$ electronic state of $C^{12}O^{16}$, since only the first vibrational quantum is available from analysis of the Angstrom bands,[9] ω_e and $\omega_e x_e$ have not been known. In the present work approximate values for these constants have been obtained from a study of the isotope effect in the Angstrom bands.

EXPERIMENTAL DETAILS

The emission spectrum of $C^{13}O^{16}$ was excited under conditions of low rotational temperature in the positive column of an end-on discharge tube of 1-cm internal diameter, with aluminum electrodes in side arms spaced 30 cm apart. Power was supplied by a 60-cycle, 8000-volt, 25-milliampere luminous tube transformer. The tube was filled with carbon dioxide, 53 atom percent C^{13}, prepared by the method of Zwiebel, Turkevitch, and Miller[10] from enriched barium carbonate obtained from Eastman Kodak Company. Spectrograms were obtained with the discharge tube operating at pressures between 0.2 and 0.4 mm Hg. The spectrograph was a 3-meter grating instrument with a dispersion of 5.6A per mm in the first order. Spectra were photographed in the first order, using Eastman 103a-0 plates below 5000A, and Eastman 103-F3 above this wavelength. Exposures varied from five minutes to two hours.

TABLE II. Rotational constants of $C^{13}O^{16}$.

Electronic state	v	B (obs) cm^{-1}	B (calc) cm^{-1}
B	0	1.861	1.862
B	1	1.836	1.837
A	1	1.509	1.509
A	2	1.489	1.488
A	3	1.468	1.467
A	4	1.446	1.445
A	5	1.424	1.423

All of the band systems of $C^{13}O^{16}$, analogous to those of $C^{12}O^{16}$ occurring between 1900 and 6500A under similar conditions, were observed. These systems include the fourth positive group, the "3A" bands, the third positive group, the Herzberg bands, and the Angstrom bands. However, because of the limited dispersion employed, only the rotational fine structure of the Angstrom bands and the band heads of the fourth positive group were well enough resolved from $C^{12}O^{16}$ bands to justify their measurement. For the remaining systems, the directions of degradation and of isotope shift were generally such that most of the $C^{13}O^{16}$ band heads fell within the relatively close structures of their $C^{12}O^{16}$ counterparts. Measurements were made against iron comparison spectra, except in the extreme ultraviolet region, where copper lines were taken as standards. A comparator of the type described by Glockler and Fullerton[11] was employed. Wave numbers were converted to vacuum with data from Kayser's *Tabelle der Schwingungszahlen*.

EXPERIMENTAL RESULTS AND DISCUSSION

The rotational structures of the 0-1, 0-2, 0-3, 0-4, 0-5, and 1-1 Angstrom bands of $C^{13}O^{16}$ have been analyzed insofar as rotational temperature, resolution, and overlapping $C^{12}O^{16}$ bands permit. In all, 263 lines have been measured and assigned. Wave numbers of individual lines, together with discussion of perturbations affecting these bands, are available elsewhere.[12] In Table I, observed origins of these bands are listed and compared with values computed from molecular constants listed in Table IV. The absence of systematic discrepancies between observed and calculated origins in the $v'=0$ progression is an indication of the reliability of these constants. It should be emphasized that the vibrational constants for the $A\ ^1\Pi$ state of $C^{13}O^{16}$ were not obtained directly from the spectrum, but rather from Read's[4] values for $C^{12}O^{16}$ and the ratio of reduced masses.

For the $B\ ^1\Sigma^+$ state, approximate values for the

[7] L. Gerö, Z. Physik **100**, 374 (1936).
[8] Hornyak, Lauritsen, Morrison, and Fowler, Revs. Modern Phys. **22**, 291 (1950).
[9] R. Schmid and L. Gerö, Z. Physik **93**, 656 (1935).
[10] Zwiebel, Turkevitch, and Miller, J. Am. Chem. Soc. **71**, 376 (1949).
[11] G. Glockler and F. W. Fullerton, Rev. Sci. Instr. **4**, 530 (1939).
[12] K. E. McCulloh, Ph.D. dissertation, State University of Iowa, June, 1951 (unpublished).

vibrational constants were obtained from Schmid and Gerö's[9] first vibrational quantum for $C^{12}O^{16}$, together with the value for the corresponding quantum in $C^{13}O^{16}$, as determined in the present work. This quantity was evaluated by subtracting the wave number of the 0–1 Angstrom band origin from that of the 1–1 band. By neglecting $\omega_e y_e$ and higher constants, and assuming that the ratio of corresponding constants for the two isotopic species is equal to the appropriate power of the inverse ratio of reduced masses, the values appearing in Table IV were obtained. The resulting constants would appear to suggest fairly rapid convergence of the vibrational levels, but an experimental test of this point is impossible because of the predissociation affecting all levels of this electronic state above $v=1$.

The rotational constants derived in the analysis of these bands are listed in Table II. Combination differences $R(J)-P(J)$ were averaged for the $v'=0$ progression. From these combination differences the constant B for the upper state was evaluated, taking the effect of centrifugal stretching into account. The remaining constants were determined from this value, together with data from Q-branches. Calculated constants appearing in Table II were obtained from Schmid and Gerö's[9,13] constants for $C^{12}O^{16}$ and the ratio of reduced masses. Agreement between observed and calculated values is generally within ± 0.001 cm^{-1}, corresponding to the limits of experimental error.

In the vibrational analysis of the fourth positive group, measurements and assignments have been obtained for a total of thirty-five band heads appearing at wavelengths above 1900A. In order to determine wave numbers of the origins, $C^{13}O^{16}$ rotational constants computed from Schmid and Gerö's[13] values for $C^{12}O^{16}$ were used in the head-origin separation formula,

$$\nu_h-\nu_0=(B'+B'')^2/(4B''-4B').$$

These heads and origins are listed in Table III, together with their assignment and a comparison with corresponding wave numbers computed from the constants appearing in Table IV. The agreement between observed and calculated origins of the fourth positive bands of $C^{13}O^{16}$ is within the limits of experimental error, approximately ± 1 cm^{-1} for accurately measured bands. This agreement offers additional confirmation of the reliability of the vibrational constants for the ground electronic state. Another test of these constants is provided by isotope shifts in the infrared bands. Calculated shifts, $C^{12}O^{16}-C^{13}O^{16}$ for the 1–0 and 2–0 infrared band origins, 47.16 and 93.23 cm^{-1}, respectively, compare favorably with the observed values, 47.11[2] and 93.27[3] cm^{-1}.

In general, the consistency of the isotope theory with the spectra of $C^{12}O^{16}$ and $C^{13}O^{16}$ has been demonstrated for the vibrational levels of the ground electronic state and the $A\ ^1\Pi$ state. With regard to rotational constants, experimental limitations do not permit a test of the theory within the accuracy to be expected thereof.

The vibrational constants herein proposed are believed to be more reliable than other values which have been published previously. The constants for the ground electronic state fit both the infrared vibration-rotation and fourth positive band systems of $C^{12}O^{16}$, as well as the spectrum of $C^{13}O^{16}$. The new vibrational formula for the $B\ ^1\Sigma^+$ electronic state, while going beyond previously available information, can be accepted only with reservation until further experimental work is possible. Most useful in this connection would be investigation of the spectrum of still another isotopic species of the carbon monoxide molecule.

TABLE III. The fourth positive group of $C^{13}O^{16}$.[a]

Band	ν_h (obs) cm^{-1}	ν_0 (obs) cm^{-1}	ν_0 (calc) cm^{-1}
2–9	49674.5	49662.1	49661.7
2–10	47803	47790	47791.1
3–9	51056.7	51045.6	51044.6
3–10	49186.4	49174.5	49174.0
3–11	47340.4	47327.7	47328.1
4–10	50535.2	50524.6	50523.9
4–11	48689.5	48678.3	48678.0
4–12	46868.6	46856.5	46856.7
4–13	45073.2	45060.2	45060.0
4–14	43302.2	43288.1	43287.8
4–15	41555.9	41540.4	41540.0
5–11	50005.2	49995.1	49994.9
5–12	48184.2	48173.5	48173.6
5–13	46388.2	46376.8	46376.9
5–14	44616.7	44604.4	44604.7
5–15	42870.2	42856.8	42856.9
5–16	41148.0	41133.4	41133.5
6–12	49469.	49459	49457.6
6–13	47672.3	47662.1	47660.9
6–14	45900.0	45889.2	45888.7
6–15	44153.4	44141.8	44140.9
6–16	42431.3	42418.7	42417.5
6–17	40733.4	40719.7	40718.3
6–18	39058.8	39043.7	39042.4
7–14	47148.9	47139.2	47139.6
7–15	45402	45391	45391.8
8–16	44896.2	44886.5	44886.4
8–17	43197	43187	43187.2
8–19	39873.4	39861.3	39861.6
8–20	38247.3	38234.1	38234.9
9–18	42707	42697	42697.3
9–20	39431.4	39420.0	39419.9
10–19	42211	42202	42198.6
10–20	40586	40576	40571.9
10–21	38982	38972	38969.2

[a] Band heads listed to only five significant figures represent bands for which accurate measurement was impossible because of overlapping or perturbation.

TABLE IV. Molecular constants of carbon monoxide.

Electronic state	Isotopic species	T_e cm^{-1}	ω_e cm^{-1}	$\omega_e x_e$ cm^{-1}	$\omega_e y_e$ cm^{-1}
X	$C^{12}O^{16}$	0	2169.84	13.301	0.0123
X	$C^{13}O^{16}$	0	2121.47	12.715	0.0115
A	$C^{12}O^{16}$	65076.5	1515.61[a]	17.250[a]	0
A	$C^{13}O^{16}$	65076.5	1481.82	16.490	0
B	$C^{12}O^{16}$	86927.6	2160.7	39.3	0[b]
B	$C^{13}O^{16}$	86927.6	2112.2	37.6	0[b]

[a] See reference 4.
[b] Assumed value.

[13] R. Schmid and L. Gerö, Z. Physik **101**, 343 (1936).

The Decay of V^0 Particles*

R. B. LEIGHTON, S. D. WANLASS, AND C. D. ANDERSON
California Institute of Technology, Pasadena, California
(Received September 15, 1952)

In a set of 23,000 cloud-chamber photographs taken in a study of penetrating showers, 134 examples of the decay of neutral V-particles, and 18 of the decay of charged V-particles, were observed. An analysis of the 152 examples leads to the following principal conclusions: (1) V-particles result from the impact of mesons and probably also of nucleons, upon nuclei. (2) V-particles are generally produced singly and not in pairs. (3) Two independent kinds of data, one based on measurements of angles and other purely spatial relationships, and the other based on measurements of momentum and specific ionization, lead to the conclusion that more than 80 percent of these neutral V-particles decayed by the production of a heavy positive and a light negative particle. The mass of the heavy positive particle in most instances was consistent with that of a proton, but in a few cases may have been somewhat less. The negative particle appeared most often to be a π-meson, although in a few cases a μ-meson was indicated. In about 7 percent of the cases, the positive particle was light and had a mass consistent with that of a π- or μ-meson. In these cases the mass of the negative particle was not well determined. So far, therefore, in these investigations, there is no direct evidence that a neutral V-particle decays into two π-mesons, or into a positive π-meson and a negatively charged proton, although a few cases may be so interpreted. (4) The data are consistent with the assumption of a two-body decay for a majority of the neutral V-particles, and therefore a rather extensive analysis is given based upon this assumption. (5) The energy release, or Q-value, of the decay of neutral V-particles was computed, on the assumption of a two-body decay, for those cases in which the production of a heavy positive particle was clearly indicated, and where momentum measurements were possible. On the assumption of a decay into a proton and a π^- meson, the Q-values obtained ranged from 10 Mev to about 100 Mev. The great majority of cases however, may be described in terms of discrete Q-values at 35 ± 3 Mev, and 75 ± 5 Mev, although, of course, the data are consistent with distributions about these values. For the same set of cases, if the positive particle is assumed to be as light even as $1250m_e$, and/or the negative particle is assumed to be a μ-meson, the distribution of Q-values is not greatly changed, and the apparent necessity for at least two different Q-values remains. In those few cases mentioned in (3) above, in which the positive particle was light, and in which the mass of the negative particle was undetermined, the energy release, computed on the basis of a two-body decay, depends upon the assumed identity of the decay products, and is about 100–130 Mev for the assumption that two π-mesons are produced, about 50–80 Mev for a positive π-meson and a negative τ-meson, and about 30–80 Mev for a positive π-meson and a negative proton. (6) The rest mean lifetime of V^0 particles, which appear to yield protons and π^--mesons as decay products, was found to be 1.6×10^{-10} sec for 26 cases having Q-values greater than 50 Mev, and 2.9×10^{-10} sec for 48 cases having Q-values less than 50 Mev, on the assumption of a two-body decay. In view of the rather poor statistics, the above two lifetimes are consistent with a single value, and lead to an average of $2.5\pm0.7\times10^{-10}$ sec. The above lifetimes are not appreciably changed if a multibody decay of the neutral V-particle is assumed. (7) The data are not adequate to distinguish conclusively between a two-body and a multi-body decay, and, therefore, a discussion is also given in terms of a variety of possible decay schemes of the neutral V-particle.

I. INTRODUCTION

IN the few years since V-particles were first observed[1] in cosmic-ray penetrating showers, their existence has become firmly established,[2] and some of their properties have been determined.[2–7] The present paper reports some of the results of an analysis of an additional 134 cases of the decay of neutral V-particles and 18 cases of the decay of charged V-particles which occurred in a set of 23,000 cloud-chamber photographs. These results seem to indicate a rather great complexity in the phenomena associated with the decay of V-particles, and do not provide complete answers even to such obvious questions as those concerning the number and identity of the decay products. In some respects they substantiate conclusions drawn from previous observations, and in other respects they do not. Oftentimes an unambiguous choice between various alternatives of interpretation is precluded by the rather large inherent errors in some of the measurements and by the statistical character of the available information. An attempt has been made throughout to allow properly for these limitations in the data.

II. APPARATUS

The apparatus used in these experiments was a counter-controlled double cloud chamber operated in a magnetic field. Each chamber was rectangular in shape, approximately 33 cm wide, 19 cm high, and of 12 cm illuminated depth. Between the two chambers was a space approximately 2.5 cm high, which was occupied by a lead plate of that thickness; the total amount of absorber between the chambers, including the brass chamber walls, was 34 g/cm^2. The chambers were illuminated from the side by light, from a linear quartz flashtube, which passed through a glass cylindrical lens system; the energy used per exposure was about 500 joules. Stereoscopic exposures were made on 70 mm Kodak Linagraph Pan film using a lens opening of $f/11$ and a magnification of 6.3× from film to cloud chamber. The centers of the lenses were 14 cm apart, and 93 cm from the rear plane of the cloud chambers. The cham-

* Supported in part by the joint program of the ONR and AEC.
[1] G. D. Rochester and C. C. Butler, Nature **160**, 855 (1947).
[2] Seriff, Leighton, Hsiao, Cowan, and Anderson, Phys. Rev. **78**, 290 (1950).
[3] Armenteros, Barker, Butler, Cachon, and Chapman, Nature, **167**, 501 (1951).
[4] Thompson, Cohn, and Flum, Phys. Rev. **83**, 175 (1951).
[5] W. B. Fretter, Phys. Rev. **82**, 294 (1951).
[6] Leighton, Wanlass, and Alford, Phys. Rev. **83**, 843 (1951).
[7] Armenteros, Barker, Butler, and Cachon, Phil. Mag. **42**, 113 (1951).

bers were filled with pure argon gas, and a saturated mixture of 65 percent ethyl alcohol and 35 percent water, to a total gauge pressure of 20 cm of Hg. The expansion ratio was about 1.07.

The magnet, of pole diameter 45 cm, was operated at an induction of 5000 gauss at a power of 13 kw. The rectangular pole faces, between which the chambers were situated, were thermostatted within approximately $\pm 0.1°C$, as were the copper-lined walls of an insulated box which surrounded these pole faces and the cloud chambers. In spite of these precautions, distortions were sometimes present, so that the maximum detectable momentum for long tracks varied from about 2 Bev/c to about 5 Bev/c.

The arrangement of counters and lead around the chambers is shown in Fig. 1. The lead blocks were placed as close as possible above the upper chamber, in order to minimize the loss of V-particles through decay. The rectangular shape of the chambers was well suited to this purpose. The top tray of six 1 in.$\times$12 in. counters was well shielded against soft radiation by 10 cm of lead above, 5 cm of lead below, and by the magnet windings at front and rear. The lower tray of six 1 in.$\times$12 in. counters was located immediately below the lower chamber and was shielded only by the chambers and magnet windings.

A pulse-height-discrimination-coincidence circuit was used to select events in which any n or more counters of the upper tray, and any m or more of the lower tray, were discharged simultaneously. Such an event is here called an $n-m$ coincidence. In part of the experiment the apparatus was situated at 220 m elevation, where 1–3 coincidences were used; in another part it was located at 1750 m elevation, where 1–3 coincidences, and later 2–3 coincidences, were used. The 1–3 counting rate at 220 m elevation was about 4 hr^{-1}, and at 1750 m, about 12 hr^{-1}. At 1750 m the 2–3 counting rate was about 3.5 hr^{-1}.

The chamber was allowed about two minutes for recovery after each expansion, during which time a coincidence could not actuate it. Thus the rate at which the chamber operated was somewhat less than the above counting rates.

The results to be described are based upon a total of 23,000 photographs of which 14,000 were taken at 220 m elevation with 1–3 coincidences, 7000 at 1750 m with 1–3 coincidences, and 2000 at 1750 m with 2–3 coincidences. At 220 m, about 8 percent of the photographs, and at 1750 m, about 20 percent of the 1–3 photographs and about 40 percent of the 2–3 photographs, showed penetrating showers (i.e., two or more collimated, time associated, nonelectronic particles). The figures here given represent lower limits to the percentage of cases in which the chamber was actuated by a penetrating shower, for many additional photographs showed slow protons and mesons, or other evidences of a penetrating shower.

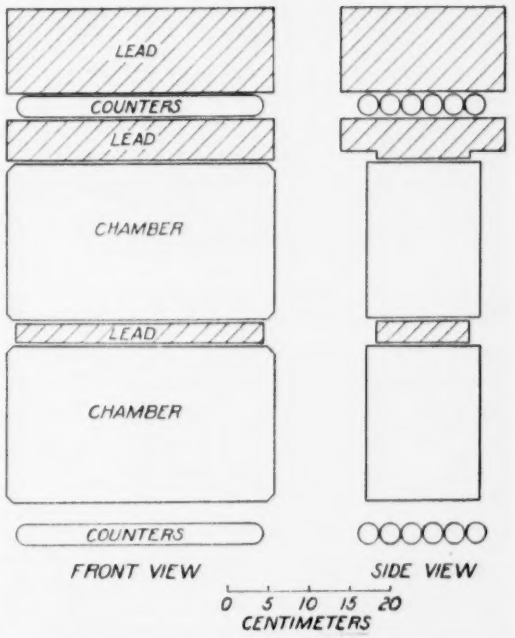

FIG. 1. The arrangement of counters and lead blocks around the cloud chambers. Only the inner walls of the chambers are indicated; the pole structure, yoke and magnet windings, which constituted additional absorber, are not shown.

III. THE PRODUCTION OF V-PARTICLES

In this set of photographs, a total of 134 V^0 particles, 7 V^+ particles, and 11 V^- particles were observed to decay. Ten photographs showed more than one V-particle: in 3 cases, two V^0 decays; in 1 case, three V^0 decays; in 4 cases, one V^0 decay and one $V^\pm$ decay; and in 2 cases, two $V^\pm$ decays. Only in three of these cases, however, did the V-particles appear to be produced in the same nuclear event. Examples of V-particle decay are shown in Figs. 2–5.

In order to investigate the manner in which V-particles are produced, it is useful to classify them according to the circumstances of their occurrence. Considering first the neutral V-particles, one finds that 72 occurred in penetrating showers whose origins were in the lead blocks above the chambers, 37 were produced in nuclear interactions (or stars) in the lead plate between the chambers, and 25 occurred alone in the chamber, or were not clearly associated with any nearby event. Of the 37 stars in the lead plate from which V^0 particles emerged, 27 were produced by charged particles which were themselves penetrating shower secondaries from a nuclear collision somewhere above the chamber,[8] 6 were produced by single charged particles, unaccompanied by

[8] In order to be sure that an event was actually initiated by a charged particle, it was required that this particle should have been visible in the lower chamber, had it traversed the plate without deflection, and that it actually be deflected by at least five degrees at a point coinciding, within the accuracy of measurement, with the nuclear event in question.

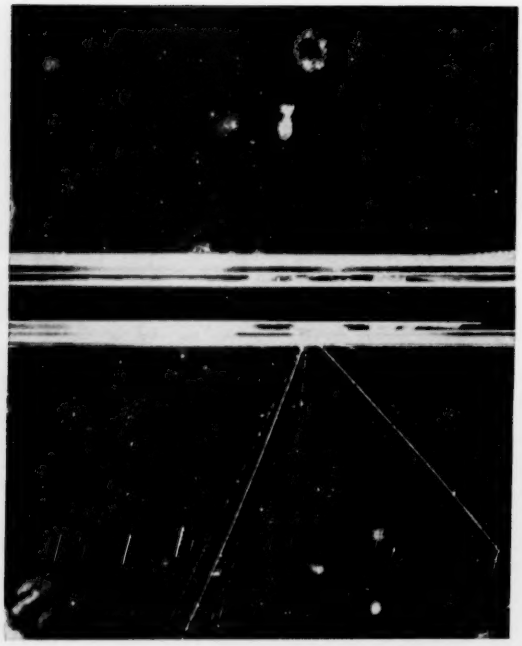

FIG. 2. Example of the production of a V^0 particle by a single charged particle. The initiating particle enters the lead plate between the chambers almost vertically from above and slightly to the right of the center of the chamber. In the lead plate it undergoes a nuclear collision, from which six charged particles, the V^0 particle, and an unknown number of neutral particles emerge. The V^0 particle decays near the bottom of the lower chamber into a heavily-ionizing positive particle and a negative particle of about minimum ionization. These products are probably a proton and a π^- meson, respectively. The shortness of the tracks does not permit accurate measurements of the momenta.

a shower or other indication of nearby nuclear events, and 4 were apparently produced by neutral particles. A similar classification of the charged V-particles showed that: 9 of these occurred in penetrating showers whose origins were above the chamber, and 9 were produced in stars in the lead plate. Of the 9 stars in the lead plate yielding charged V-particles, 8 were initiated by charged penetrating-shower secondaries, and 1 was produced by a single charged particle. None of these stars was produced by a neutral particle.

It has been generally supposed that V-particles are produced in energetic nucleon-nucleon collisions, presumably with about equal cross-section in $n-n$, $n-p$, or $p-p$ collisions. The above observations indicate, however, either (1) that protons are many times more effective in producing both charged and neutral V-particles than are neutrons, (2) that energetic protons are many times more numerous than energetic neutrons, or (3) that *meson*-nucleon collisions can result in V-particle production. Of these alternatives, the last appears to be the most acceptable in view of the large body of experimental evidence in favor of charge-independence of nuclear forces.

It would thus appear that in this experiment the great majority of both the neutral and charged V-particles were produced by mesons. However, this result does not necessarily indicate a larger cross section for V-particle production by mesons than for production by nucleons, since the number of high energy mesons present in a penetrating shower is known[9] to be much greater than the number of high energy nucleons. Also, V-particle production by mesons does not necessarily imply production by π-mesons, or by π-mesons alone, since it is now thought[10] that, at the very high energies prevailing in the original nuclear collisions with which we are here concerned, other heavier mesons may be produced about as copiously as are π-mesons.

A second conclusion regarding V-particle production,

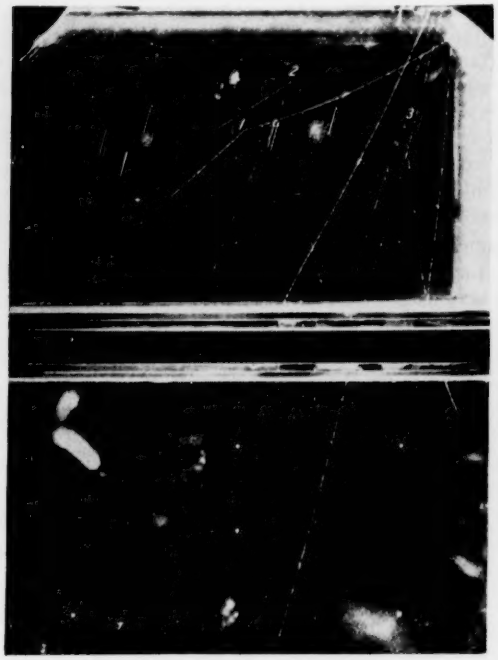

FIG. 3. A rare example of the production of several V^0 particles in a single nuclear event. Most of the tracks in the upper chamber are those either of secondary particles from a nuclear event in the lead blocks above the chamber, or of V^0 particle secondaries. Two of the three V^0 decays (Nos. 2 and 3) are in excellent alignment with the origin of the nuclear event, while No. 1, both of whose decay particles are heavily ionizing, is not aligned with this origin. This indicates either that this last decay yields three or more secondary particles, or that the assumed line of flight of the V^0 particle is not the correct one for this case. All of the decay tracks are consistent with the assumption that the negative particles are π-mesons, and that the positive particles are protons. The energies released in these three cases, assuming two-body decay, are $Q_1=41\pm7$ Mev, $Q_2=51\pm8$ Mev, and $Q_3=34\pm7$ Mev. Unfortunately, the distortions in the upper chamber were unusually severe.

[9] Camerini, Davies, Fowler, Franzinetti, Muirhead, Lock, Perkins, and Yekutieli, Phil. Mag. 42, 1241 (1951).

[10] Bristol Conference on V-particles and Heavy Mesons, December, 1951 (unpublished).

namely, that they are probably not always produced in pairs, can be deduced from the number of multiple V-particle decays that were observed in this series of photographs. For, if V-particles were always produced in pairs, one would expect to have seen many more cases than were observed in which two V-particles decay inside the cloud chamber. Consider, for example, V-particles that are produced in collisions in the lead plate between the chambers. Assuming a mean rest lifetime of 3×10^{-10} sec[2], and a time dilation factor of 5 (as a reasonable upper limit), one can calculate a probability of approximately 0.2 as a lower limit that the decay of such a V-particle would occur in the lower chamber. For slower speeds of travel, the probability of decay inside the lower chamber is greater than this, except for speeds less than about $\beta=0.1$, which seem quite unlikely to occur in view of the high energies in these events. Thus one would expect that, in at least 7 of the 37 cases in which V^0 particles were produced in the lead plate and were observed to decay in the lower chamber, a second V^0 particle or a $V^\pm$ particle would have been observed also. This is to be compared with the single such case in which a V^0 particle and a V^+ particle, produced in the same star in the lead plate, both decayed inside the chamber. This result alone strongly suggests that V-particles are not produced in pairs; a less direct suggestion follows from the fact that the number of double V^0 decays, in which the origins of the two particles are different, actually exceeds the number in which both proceed from the same origin. The possibility is not excluded, of course, that a V-particle may be produced along with another particle whose mean rest lifetime is either much longer or much shorter than 3×10^{-10} sec.†

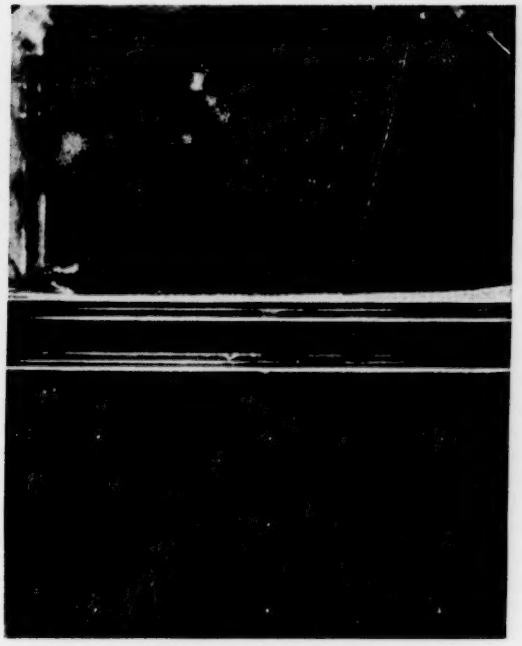

FIG. 4. Example of a V^0 particle produced in a nuclear event in the lead blocks above the chambers. The decay track on the left corresponds to a negative particle, of momentum 207 ± 10 Mev/c, which is probably a π-meson. The decay track on the right corresponds to a positive particle, of momentum 700 ± 150 Mev/c, and is probably a proton, but in the lower chamber its ionization and momentum indicate a somewhat lower mass. The energy release, assuming the products to be a π-meson and a proton, is $Q=42\pm6$ Mev.

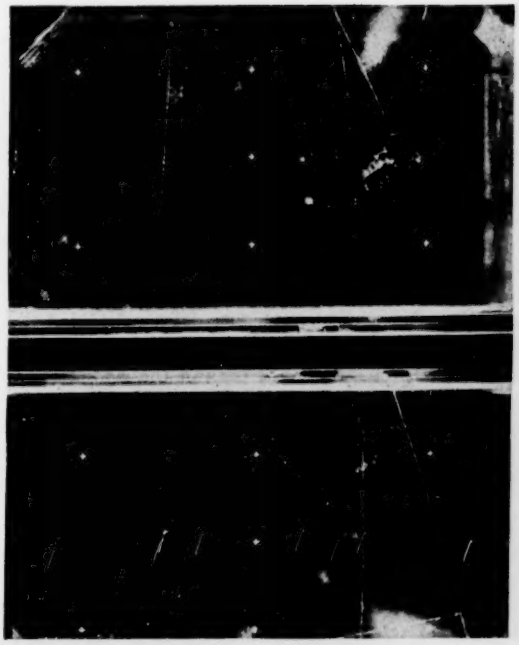

FIG. 5. Example of unrelated V^0 decays. One V^0 decay occurs very near the top and somewhat to the left of the center of the upper chamber, yielding a heavily ionizing positive particle which travels downward and toward the camera, and a lightly ionizing negative particle whose tracks is very short. This V^0 particle is probably produced in the same nuclear event, in the lead blocks above the chamber, that gives rise to the penetrating shower to the right. One of these shower particles in turn undergoes a nuclear collision in the lead plate between the chambers, from which a second V^0 particle emerges. This V^0 particle decays above the center of the lower chamber, and similarly yields a heavily ionizing positive particle which travels almost vertically downward, and a lightly ionizing negative particle whose track length is short. Both of the negative particles in these decays are ejected at such angles that they pass out of the front or rear wall of the chamber after traveling only a short distance. The positive particles in both of these decays are probably protons, although that of the lower decay may be somewhat lighter than a proton. The energy release of the lower decay is $Q=37\pm5$ Mev. That of the upper decay is not known, since the meson track was not measurable.

IV. THE PRODUCTS OF NEUTRAL V-PARTICLE DECAY—COPLANARITY

Before discussing the more complicated measurements that can be used to study the products of V^0 decay, we shall first derive some information concerning the

† Of course, if a substantial fraction of the neutral V-particles were to decay into neutral particles, the above conclusion would be weakened.

number and identity of these products by making use of certain purely geometrical properties of the decay. One of these properties is the so-called "coplanarity" of the decay, i.e., the angular relationship between the line of travel of the V^0 particle and the "decay-plane" defined by the tracks of its two charged decay products; another is the angular relationship of each charged particle track to the line of travel of the V^0 particle.

To measure the angular deviation from coplanarity for a given decay, one must know the path of the V^0 particle as well as the paths of its two charged decay products. This information is available in those cases where the event in which the V^0 particle originated also yielded a number of charged particles whose tracks appear in the chamber. The path of the V^0 particle is then taken to be along the straight line connecting this origin (located by backward extrapolation of the charged particle tracks) with the point at which the decay occurred.

In these experiments the numerical data required for calculating the orientations of the decay-plane and the path of the incident V^0 particle were obtained in each case from a graphical construction. A sheet of tracing paper was placed on a viewing screen upon which the two sets of track images from the stereoscopic photographs were projected. Careful pencil traces were then made of the two track-images of the V-particle and of other particles on the photographs. The additional required graphical constructions were also made on the same sheet of paper.

Figure 6 illustrates schematically the reprojection system used. In this system, which was optically identical to the camera system, the surface of the viewing screen was made to correspond to the rearmost interior surface of the cloud chamber. Fiducial marks, scribed on this cloud chamber surface and present on each photograph, were brought into register on the screen—thus assuring the spatial correspondence of these surfaces. A point, P, in the interior of the cloud chamber thus appeared upon reprojection as two points separated by a distance Δx given by the formula,

$$\Delta x = zS/(D-z), \tag{1}$$

where the symbols are defined in Fig. 6. In the present experiment the quantities S and D were, respectively, 14 cm and 93 cm.

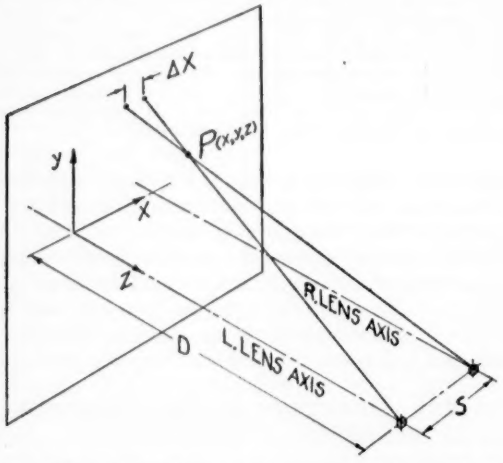

FIG. 6. Perspective diagram of the geometry of the reprojection system. The two stereoscopic views were reprojected through the same optical system as was used in the original camera, onto a screen perpendicular to the two camera axes. A point P, which lay at the point (x, y, z) when photographed, thus reprojects into two points on the screen. These two points are separated by an amount Δx, given by Eq. (1) of the text.

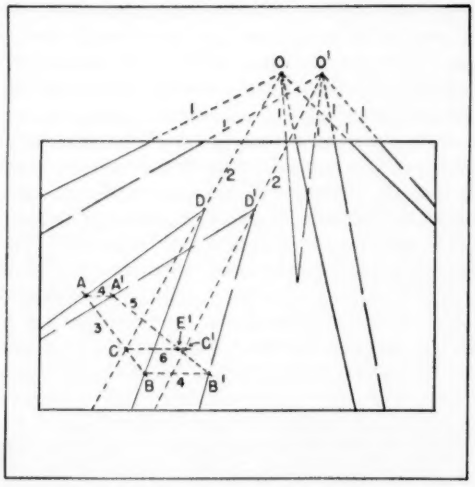

FIG. 7. Schematic diagram of the coplanarity test. The larger rectangle represents the screen, the smaller one the boundaries of the visible region of the cloud chamber. The two sets of tracks resulting from projection through the left and right lenses are shown dashed and solid, respectively. If the V^0 path (DC, $D'C'$) lay in the decay-plane (ADB, $A'D'B'$), the two points E' and C' would coincide.

The construction by which the deviation from coplanarity was measured is represented schematically in Fig. 7. The two sets of track images resulting from projection through the left and right lenses are shown dashed and solid, respectively. In the case of V-particle secondaries, tangents to the tracks at the apex of the decay were used, instead of the tracks themselves. Auxiliary lines are shown dotted and are numbered in the order of their construction. First, the tracks radiating from the origin of the V-particle are projected backward to their intersection point (O, O'). Next, the path of the V^0 particle (OD, $O'D'$) is constructed and extended beyond the decay point (D, D'). The problem now consists in determining the angle that this extended line makes with the decay-plane, namely, the plane formed by the two lines (DA, $D'A'$) and (DB, $D'B'$). To accomplish this, an arbitrarily chosen sloping line (AB, $A'B'$), lying in the decay-plane is drawn as indicated. (Note how points A' and B' are found by construction lines 4 drawn parallel to DD'.) Upon the

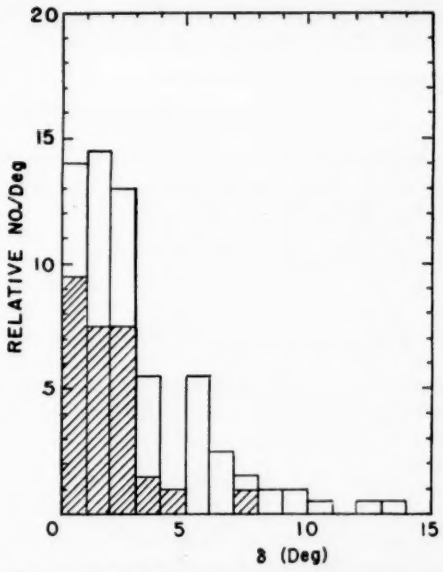

FIG. 8. Distribution of angular deviation δ from coplanarity for 60 cases. The cross-hatched portion of the distribution represents the contribution of the 28 cases whose estimated errors of measurement were 2° or less.

completion of lines 5 and 6, two points appear which are of particular importance, i.e., a point (C, C') on the extended V^0 path, and a point (C, E') in the decay-plane. The horizontal distance $E'C'$ on the diagram can readily be converted by Eq. (1) into a difference in depth of these two points. This in turn is then readily converted into an angle δ between the line $(DC, D'E')$ and the V^0 path $(DC, D'C')$ and thence to the angle δ_1 between the V^0 path and the decay-plane. The last step was rarely taken, since δ is always larger than δ_1, and thus provides a sharper test of coplanarity.

The accuracy with which it is possible to carry out the above construction varies from case to case for several reasons: The accuracy with which an origin can be located depends upon the number of tracks available for the backward extrapolation, and the distance of the extrapolation (sometimes as great as 20 cm); the angular accuracy with which the V^0 path can be drawn depends upon the distance from the V^0 particle decay-point to the origin; the accuracy with which tangents to the decay-tracks can be drawn depends upon the length of the tracks; and the sensitivity of the coplanarity test depends upon the orientation of the V^0 decay, it being most sensitive when the decay-plane is seen edgwise in one camera view. The over-all accuracy with which the coplanarity could be measured thus varied from about 1° to about 10°, but was usually in the range 2°–4°. This accuracy represents a significant improvement over that of a previously reported result.[2]

Sixty of the 134 V^0 decays exhibited origins and thus could be analyzed for coplanarity. Of these, 37 had origins in the lead plate between the chambers, and the remaining 23 had origins in the lead blocks above the chambers. The distribution of δ for these 60 cases is shown in Fig. 8. The cross-hatched portion of the diagram represents the 28 most accurate cases obtained by eliminating all those whose estimated error of measurement is greater than 2°. It appears from this distribution that almost all of the decays could have been exactly coplanar, and hence could have been two-body decays.

Perhaps a more meaningful test of coplanarity is a comparison of the measured deviation δ with the smaller of the two angles, θ_+ or θ_-, (see Fig. 10) between the charged particle tracks and the V^0 path, since in any case δ cannot exceed the smaller of these angles. The ratio $\sin\delta/\sin\theta_s$ (where θ_s denotes the smaller of the two angles) is a quantity which compares approximately the components, perpendicular to the decay-plane, of the momentum of the V^0 particle, with the component, perpendicular to the V^0 path, of the momentum of one of the charged products. The distribution of $\sin\delta/\sin\theta_s$ is shown in Fig. 9. Again almost all of the decays could have been coplanar, and hence could have been two-body decays. However, we cannot rule out any type of decay in which the transverse momentum carried by a third decay particle is on the average less than about 50 percent of that carried by one of the charged particles. Several decay processes can be imagined which would satisfy this condition. Some of these will be discussed later.

Since the observed distributions of δ and $\sin\delta/\sin\theta_s$ are wholly consistent with a two-body mode of decay for at least a large fraction of the V^0 particles, we shall continue our analysis, for the time being, under the assumption of a two-body decay, and then later consider the data in terms of possible multibody decay schemes.

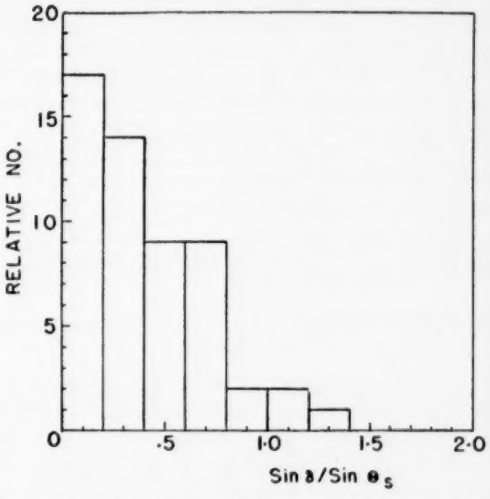

FIG. 9. The distribution of $\sin\delta/\sin\theta_s$ for 54 cases. The entire width of this distribution could have been due to errors of measurement or to scattering of the V^0 particle before decay, so that almost all of the decays could have been exactly coplanar.

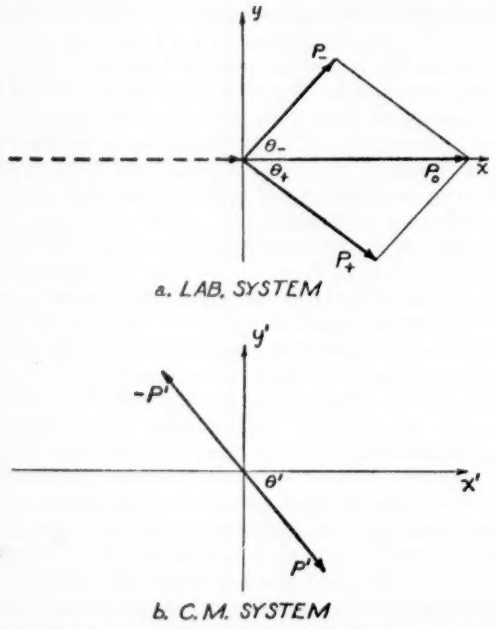

FIG. 10. Momentum diagrams of the decay $V^0 \rightarrow M_+ + M_- + Q$ as seen in the laboratory system (cloud chamber) and in the center-of-mass system moving with the V^0 particle.

V. THE PRODUCTS OF NEUTRAL V-PARTICLE DECAY —FURTHER GEOMETRICAL CONSIDERATIONS

A second property of V^0 decay which provides information concerning the decay products is the size of θ_+ relative to θ_-. Consider the two-body decay of a V^0-particle of mass M_0 into charged particles of mass M_+ and M_- (Fig. 10). In the center-of-mass system (henceforth denoted by c.m.) each particle has a momentum of magnitude P', and the positive particle is emitted at an angle θ' with respect to the direction of travel of the V^0 particle. In the laboratory system, moving with speed $-\beta c$ along the x axis relative to the c.m. system, the momenta are $\mathbf{P}_+$ and $\mathbf{P}_-$, at angles θ_+ and θ_- with the path of the V^0 particle. The transformation equations between the laboratory system and the c.m. system can be written in the form

$$\text{(a)}\quad P_{+x}=\frac{P_0P'\cos\theta'}{M_0\beta}+\frac{P_0}{2M_0^2}[M_0^2+(M_+^2-M_-^2)],$$

$$\text{(b)}\quad P_{+y}=P'\sin\theta',$$

$$\text{(c)}\quad P_{+z}=0,$$

$$\text{(d)}\quad P_{-x}=\frac{-P_0P'\cos\theta'}{M_0\beta}+\frac{P_0}{2M_0^2}[M_0^2-(M_+^2-M_-^2)], \qquad (2)$$

$$\text{(e)}\quad P_{-y}=-P'\sin\theta',$$

$$\text{(f)}\quad P_{-z}=0,$$

where P_{+x} is the x component of $\mathbf{P}_+$, etc., P_0 is the magnitude of the momentum of the V^0 particle, and

$$P'=[M_0^2-(M_+-M_-)^2]^{\frac{1}{2}}\times[M_0^2-(M_++M_-)^2]^{\frac{1}{2}}/2M_0, \quad (3)$$

all momenta, masses, and energies being written in energy units. From the momentum parallelogram of Fig. 10, using the law of cosines,

$$\text{(a)}\quad P_{+x}=P_+\cos\theta_+=(P_0^2+P_+^2-P_-^2)/2P_0,$$

and (4)

$$\text{(b)}\quad P_{-x}=P_-\cos\theta_-=(P_0^2+P_-^2-P_+^2)/2P_0.$$

Inserting these expressions in Eq. 2(a) and 2(d), subtracting 2(d) from 2(a), and dividing by P_0, we obtain

$$\frac{P_+^2-P_-^2}{P_0^2}=\frac{M_+^2-M_-^2}{M_0^2}+\frac{2P'\cos\theta'}{M_0\beta}. \qquad (5)$$

The value of the quantity on the left has been used by the Manchester workers[7] as a criterion for the classification of V^0 decays into two groups, into which they assume that all V^0 particles must fall. We shall adopt their notation and designate the quantity α to be

$$\alpha=\frac{P_+^2-P_-^2}{P_0^2}=\frac{\sin^2\theta_--\sin^2\theta_+}{\sin^2\theta_T}=\frac{\sin(\theta_--\theta_+)}{\sin(\theta_-+\theta_+)}, \qquad (6)$$

where the second equality follows from the law of sines applied to the momentum parallelogram, and θ_T is the total angle between the secondary tracks. Equation (5) indicates that, for a given mode of two-body decay, a given speed βc, and an isotropic distribution in the c.m. system, the quantity α has an average value equal to $(M_+^2-M_-^2)/M_0^2$, and is uniformly distributed, with amplitude $2P'/M_0\beta$, on either side of the average. The actual distribution of α for a given two-body decay scheme is the result of a number of such uniform distributions, each having the same average value but a different amplitude, because of the different speeds βc of the various cases. The total distribution thus should have a maximum at the value $(M_+^2-M_-^2)/M_0^2$ and should be symmetrical about this maximum. Thus by evaluating α for those cases in which θ_+ and θ_- can be

TABLE I. Central values of α and minimum amplitudes of the α-distribution for various decay products.

No.	Decay products $M_+(m_e)$	Decay products $M_-(m_e)$	Q Mev	Central value $(M_+^2-M_-^2)/M_0^2$	Amplitude $2P'/M_0$
1	276	276	120	0	0.71
2	276	210	120	0.06	0.73
3	500	276	50	0.22	0.44
4	1000	276	50	0.49	0.32
5	1837	276	35	0.69	0.17
6	1837	210	35	0.74	0.19

measured, one can hope to gain some information as to the relative masses of the decay products.

The values of α were computed for the 60 cases for which origins were available. The distribution of those values is shown in group I of Fig. 11. On the figure are drawn several vertical lines, which correspond to the expected average values of α for the various decay schemes indicated in Table I. The energy release or Q-value was assumed to correspond roughly to those obtained by direct calculation from the data. (A detailed discussion of Q-values will be given in Sec. IX.) The average value of α is not very sensitive to the assumed Q-value, but the width of the α-distribution ($2P'/M_0\beta$), which varies approximately as $Q^{\frac{1}{2}}$, is. From the great preponderance of positive values of α it is immediately apparent that at least a large majority of these decays, if not all of them, yielded a relatively heavy positive particle and relatively light negative one. (Negative values of α are quite possible, even for a large positive average value of α, if the V^0 is moving sufficiently slowly when it decays.) The position of the rather sharp peak of the distribution at a value of α corresponding to a decay into a proton and a negative π- or μ-meson, leads one to conclude that a great majority of the decays are probably of this type.[11] However, since the distribution is not symmetrical about this peak, and since the selection of cases could hardly have been biased against large positive values of α, we conclude, on the other hand, that some of the decays are probably of another type.

It has been postulated that V^0-particles exist which decay into two π-mesons. However, the number of negative values of α (some of which will later be shown to correspond to a decay into a heavy and light particle) suggests that at least very few, if any, of the decays yielded particles of equal, or nearly equal, mass.[7] For, even if one takes all of the negative α-values, and an equal number of the positive values, as corresponding to a decay into particles of equal mass, one obtains only about 20 percent which could possibly be of this type.

There are, of course, other possible two-body decay schemes that would lead to the observed α-distribution, such as, for example, a decay in which the product particles are of unequal mass, the heavier of mass about 500–1200m_e, perhaps a τ- or κ-meson, and the lighter of π- or μ-meson mass. Most of the negative values of α might, then logically be interpreted in terms of a decay into the corresponding anti-particles.

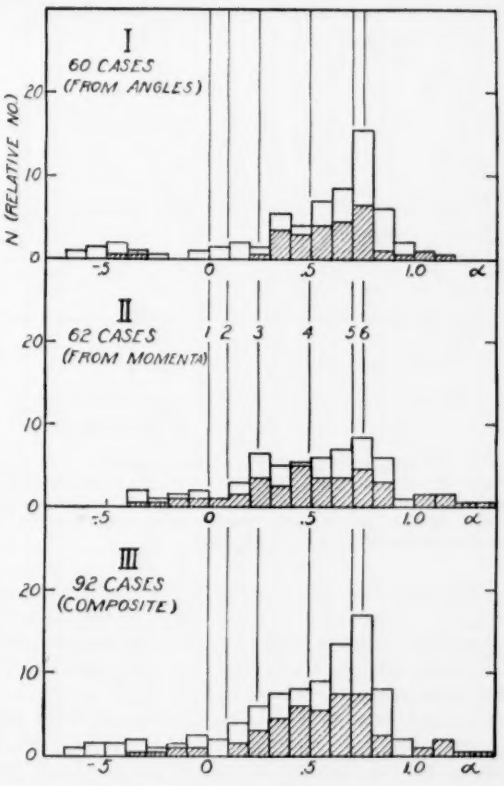

FIG. 11. Distribution of α for V^0 decay. The quantity α is defined by Eq. (6) of the text. For a given two-body decay scheme, given speed βc for the V^0 particle, and isotropic decay in the c.m. system, this quantity has an average value equal to $(M_+^2-M_-^2)/M_0^2$ and is uniformly distributed about this average with an amplitude $2P'/M_0\beta$ (see Eq. (5) of the text).

Group I is the distribution of those values of α that were derived from the angles θ_+ and θ_-.

Group II is a similar distribution, but in this case the values of α were evaluated from the measured momenta only.

Group III is a composite distribution.

The cross-hatched portion of each distribution indicates the contribution made by cases whose positive particles, being heavily ionizing, were known to be much heavier than π-mesons. Vertical lines extending through all three distributions identify the average values of α to be expected for decay of a V^0 particle into particles whose masses are indicated in Table I.

These distributions give clear indication of the existence of V^0 decays leading to a proton and a π- or μ-meson, and strongly suggest the existence of at least one other type of V^0 decay scheme, but do not serve to identify clearly the nature of this latter scheme.

VI. NATURE OF DECAY PRODUCTS—MOMENTUM MEASUREMENTS

Additional information about the decay products can be gained from measurements of their momenta. We shall consider first a new distribution of the quantity α, calculated now from the measured momenta of the decay products. (It will be recalled that α can be expressed in terms of the momenta of the particles as well as in terms of angles as was done previously [Eq. (6), Sec. V].)

[11] It is interesting to note that one can estimate a Q-value from the half-width of this distribution peak. Assuming a decay into a proton and a π-meson, and taking $\beta\approx 1$, $M_0=M_p+M_\pi+Q\approx M_p+M_\pi=1079$ Mev, the half-width of the peak equal to 0.15, and assuming that the π^- meson is nonrelativistic, one obtains

$$0.15=2P'/M_0=2P'/1079,$$

and

$$Q\approx\frac{P'^2(M_p+M_\pi)}{2M_\pi M_p}=\frac{0.15^2\times 1079^2}{8\times 141\times 0.87}=26 \text{ Mev}.$$

This value agrees surprisingly well with actual measurements (see references 4, 6, and 7) of the energy release.

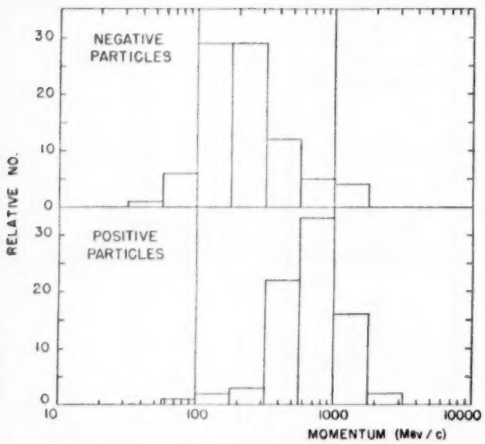

FIG. 12. Distribution of momentum of 79 positive and 86 negative V^0-decay secondaries. Only those particles whose momenta were measurable, or derivable from momentum balance, are included. Particles whose tracks were too short or too straight for accurate measurement are thus omitted.

The momenta of the decay products were determined from measurements of the curvatures of the tracks in the magnetic field. In order to make these measurements sufficiently precise, it was necessary to incorporate certain refinements which have been neglected in previous cloud chamber work. It has usually been assumed that the magnetic field, although not constant in strength throughout the chamber, is at least unidirectional, and that the radius of curvature of a track on the film corresponds to the radius of curvature of a helix whose axis is parallel to the magnet axis. Neither of these assumptions is strictly correct, for actually the field may have sizable components transverse to the magnet axis, and also the track image on the film is not an orthogonal projection of a helix onto a plane, but is rather a projection through a point (i.e., through the lens aperture) onto a plane. An exact expression, which takes both of these effects into account, has been derived relating the true momentum of a particle to the measured curvature of its track on the film. To make use of this exact relationship it was necessary to measure the three rectangular components of the magnetic field throughout the chamber, and thus to make allowance for the direction of the magnetic field as well as for the variation in its axial component. In the application of this formula to the track measurements, the only assumption involved is that the measured average radius of curvature over the length of the track is equal to the true radius of curvature at the center of the track. The correction arising from the use of this more exact formula was found usually to be about 5–10 percent, but in some cases was as great as 20 percent.

The curvature of a track was measured on each stereoscopic view, and a value of the momentum was calculated from each measurement. In each case an uncertainty was assigned whose size was appropriate to the length and quality of the track. These two values of the momentum were then combined to obtain the final measured momentum. The final uncertainty was taken to be somewhat less than that of either of the individual uncertainties, but was always large enough to include both measured values, and was never taken to be less than the error to be expected from multiple scattering or less than $P/40$ percent (P in Mev/c).

In a few cases the momentum of one of the decay particles was computed from a knowledge of the momentum of the other particle and the angle that each made with the V^0-path, using conservation of momentum, with the assumption of a two-body decay of the V^0-particle.

The momenta carried by the positive and negative decay-particles are shown in Fig. 12, and the momenta of the V^0 particles, themselves, obtained by vector addition of the momenta of the positive and negative particles for each case, are shown in Fig. 13. All of these histograms represent only those cases in which the momenta could be measured with reasonable accuracy, so that those decays whose tracks inside the chamber were very short, and those whose tracks, although long, were too straight for measurement, are not represented. The dotted lines of Fig. 13 represent approximately the contribution that might be expected from the unmeasurable cases. This contribution was obtained by assigning to each unmeasurable case a momentum calculated on the assumption that the observed angle, θ_T, corresponded to the maximum possible angle. It must be remembered, of course, that these distributions, even when corrected for the observed but unmeasurable cases, do not correctly describe the momentum distribution of all the V^0 particles actually produced. This results from the fact that the probability that a V^0 particle will decay in the cloud chamber depends upon its velocity as well as upon its mean life.

An α-distribution, computed only from measured momenta, is shown in Fig. 11, group II. This distribution is seen to be somewhat similar to that of group I, which was obtained only from geometrical data. The peak corresponding to a decay into a proton and a π- or μ-meson is not as pronounced as that of group I, but occurs at about the same value of α.

The difference in the shapes of the α-distributions of groups I and II can be explained by the difference in the selection of the measurable cases included in the two groups. The sole criterion for the inclusion of a case in group I was that it possess an origin so that the angles θ_+ and θ_- could be measured. This distribution is, therefore, unbiased, since the value of α depends only upon the speed of the V^0 particle and upon the orientation of the decay in the c.m. system. On the other hand, the criterion for the inclusion of a case in group II was that *both* decay particles have measurable momenta. This criterion tends to exclude decays in which the V^0 particle, and hence at least one of its decay particles,

possesses a very high momentum. These excluded decays, for the most part, will be those for which the momentum of the heavier particle would have been unmeasurable no matter in what direction it might have been ejected in the c.m. system, but some borderline cases will also be excluded in which the momentum of the heavy particle was unmeasurable only because it was ejected in a forward direction in the c.m. system. Thus the sharp peak would be less pronounced, and the center of gravity of the distribution would be shifted toward smaller values of α.

A composite α-distribution is shown in Fig. 11, group III. This distribution was constructed by combining groups I and II. In the 30 cases in which α was known both from angle division and from momenta, that value was used that was considered to be the more accurate.

The cross-hatched portions of the three α-distributions represent the contribution of those cases whose positive particle was identifiable as being much more massive than a π- or μ-meson. An analysis similar to that outlined above can be used to explain the differences between the sub-distributions and the total ones: The cases in which the positive particle is heavily ionizing will tend more often to be those in which the positive particle is ejected in a backward direction in the c.m. system and is therefore moving more slowly in the laboratory system. These cases correspond to *negative* values of $\cos\theta'$ and hence to *smaller* values of α than the average for the particular type of decay in question.

A slightly sharper upper limit upon the number of cases that can be interpreted as decaying into two equally massive, relatively light particles, can now be made. If one removes from the negative α-values of group III those that are cross-hatched, and then doubles the remaining number from symmetry considerations, it appears that no more than about 15 percent of those

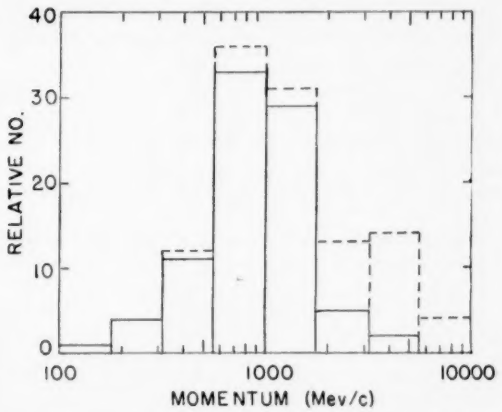

FIG. 13. Distribution of momenta of 85 V^0 particles. The momenta were determined by vector addition of the momenta of the decay particles. As in the preceding figure, cases whose decay tracks were unmeasurable are not included. The dotted distribution represents an estimate of the contributions that might have been made by the unmeasurable particles, based upon an assumed relationship between θ_T and the V^0 particle momentum.

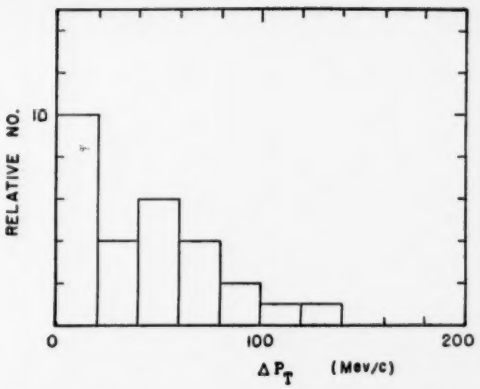

FIG. 14. The distribution of $\Delta P_T = |P_+ \sin\theta_+ - P_- \sin\theta_-|$ for 28 cases. This quantity represents the "missing" transverse momentum in the plane of the decay. The width of this distribution could be due entirely to errors in measurement, but is also not inconsistent with the distribution to be expected for certain types of multibody decay.

decays included on these α-distributions could be of the above type.

Further evidence as to the number of particles resulting from the decay of a V^0 particle can be obtained by testing the balance of the components of momentum transverse to the V^0 path in those cases where θ_+ and θ_- and also P_+ and P_- are known independently. The difference $\Delta P_T = |P_+ \sin\theta_+ - P_- \sin\theta_-|$ is a measure of this balance, and should have the value zero if momentum transverse to the direction of the V^0 particle is conserved. The distribution of this quantity is shown in Fig. 14. It is seen that almost all of the decays could have satisfied the condition of transverse momentum balance, but, as in the discussion of coplanarity, we cannot exclude certain types of multibody decay in which the transverse momentum of an unseen neutral particle is small on the average compared to the transverse momenta of the visible particles. The restriction that can be placed upon this "missing" transverse momentum is about the same as in the case of the coplanarity test—namely that it be less than about 50 percent of the transverse momentum of the visible particles.

For comparison with Fig. 14, the distribution of the transverse momentum of the negative particles, $P_- \sin\theta_-$, is given in Fig. 15.

It should be emphasized that the assumption of a two-body decay underlies the whole discussion of the distributions of the quantity, α, in this section of the paper, and that the presence of a substantial fraction of multibody decays would alter considerably the significance of these distributions.

VII. NATURE OF DECAY PRODUCTS—SPECIFIC IONIZATION

Further information as to the character of the decay products is provided by a determination of their specific

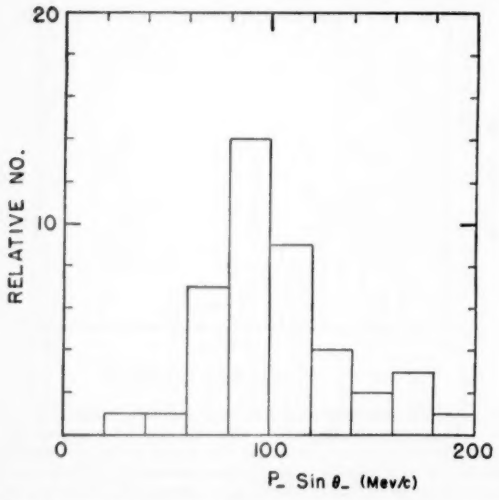

FIG. 15. The distribution of $P_-\sin\theta_-$ for 42 cases. This quantity is equal to transverse momentum $P'\sin\theta'$ if the decay is a two-body decay. The sharp peak in this distribution falls at about 95 Mev/c, the limiting value to be expected for a two-body decay into a proton and a π-meson with an energy release of 35 Mev. The presence of transverse momenta substantially greater than this limiting value strongly suggests the presence either of two-body decays, or of multibody decays, with energy releases greater than 35 Mev.

ionization. The accurate measurement of ionization is exceedingly difficult, even in cases where the droplets along the track are actually resolved. Fortunately, a considerably larger error can be tolerated in the ionization than in the momentum (for ionizations greater than twice minimum) to obtain a mass measurement of given accuracy. In the present experiment, the specific ionizations for individual tracks were estimated independently by two or more observers, and were evaluated a second time by the same observers several weeks later. The estimates were made by visual comparison with other tracks on the same photograph whose ionizations were considered known. For example, a straight penetrating shower-particle track (>1000 Mev/c) was taken to be at minimum ionization, while an electron track (50–100 Mev/c) was assumed to be 1.3 times minimum. If a track appeared indistinguishable from such comparison tracks, it was assigned an ionization less than 1.5 times the minimum value.

In some cases a track appeared definitely heavier than a track of minimum ionization, and yet not as heavy as one of twice minimum; in such a case a value of 1.1–1.8 times minimum might be assigned. A track whose ionization was above twice minimum could often be compared with heavily ionizing mesons and protons of known momenta and therefore of known specific ionizations. In all cases a range of ionization was determined within which all observers could agree that the actual value almost surely lay, and outside of which it was very unlikely to lie. This range of values thus does not represent a "probable error" or "standard deviation" in the usual sense.

Inasmuch as the mass of a particle of unit charge is determined from the momentum and ionization by an equation of the form

$$M=P\cdot f(I), \tag{7}$$

where P is the momentum and $f(I)$ is a function of the specific ionization only, it follows that the error in the mass value that arises from errors in momentum and ionization is approximately

$$\frac{\Delta M}{M}=\frac{\Delta P}{P}+\frac{f'(I)\Delta I}{f(I)}. \tag{8}$$

It can be assumed that the errors in the estimate of ionization, while perhaps rather large and not subject to direct statistical treatment, are at least independent of the identity of the particle. Thus it was possible to evaluate the accuracy with which ionization can be estimated by calibrating on heavily ionizing π-mesons, for which the momenta could be measured very accurately.

VIII. NATURE OF DECAY PRODUCTS—MEASURED MASSES

In 87 of the 134 V^0 decays it was possible to measure the momentum of at least one of the decay particles. Some of these particles were also heavily ionizing so that estimates of their masses could be made. Many of the particles, on the other hand, were essentially at minimum ionization so that only upper limits could be placed upon their masses. These limits often served to distinguish between "heavy" and "light" particles, and thus permitted a rough classification of the decays according to the relative masses of the secondaries, as shown in Table II. In each of the 42 cases of group 1*b* the positive particle, because of its ionization and momentum, is definitely known to be heavier than the negative particle. One can conclude in addition that the majority of the 29 positive particles of group 1*c*, which are at minimum ionization, must also be more massive than their companion negative particles. This conclusion follows from the relative populations of groups 3*a* and 1*c*, which would be expected to be equal for any

TABLE II. Classification of secondary particles in V^0 decay.

M_+ \ M_-	1 $M_-<700m_e$	2 $M_->700m_e$	3 M_- indeterminate	Total
a $M_+<700m_e$	2	1	4	7
b $M_+>700m_e$	42	0	3	45
c M_+ indeterminate	29	0	6	35
Total	73	1	13	

decays which yield positive and negative particles of equal mass. Thus the direct mass determinations tend to support the conclusion previously drawn that probably not over 15 percent of these decays could yield particles of equal mass.

Three of the cases appearing in Table II are of special interest. Group 1*a* seems to indicate the existence of decays, of the type postulated by the Manchester Group, in which the two products have equal mass, while the single case in group 2*a* seems to indicate the existence of decays leading to a light positive particle and a heavy negative one. These three interesting cases will now be discussed.

Let us first consider the two cases in group 1*a* in order to determine whether a decay into two π-mesons is indeed indicated. The first of these cases may not be a V^0 decay at all. The apex of the V^0-particle, while in the gas of the cloud chamber, was just outside the visible region, so that it may actually represent a chance coincidence of two unrelated tracks. In addition, the momentum and ionization of the positive particle restrict M_+ to be less than $700\text{-}300m_e$, and thus a π^+ meson is not necessarily indicated. Finally, additional doubt is cast upon this case because of the lack of transverse momentum balance with respect to an assumed line of flight from a nearby origin.

The second case is certainly a V^0 decay. In this case, the momentum of the positive particle was about 295 Mev/c, and its ionization was less than 1.5 times minimum, and thus its mass was less than about $500m_e$. The track of the negative particle, however, was so short that its curvature could not be measured. The momentum of this particle was evaluated from transverse momentum balance with respect to an assumed line of flight from a clearly defined nearby origin. Although this procedure is probably permissible statistically, it must be used with caution in individual cases, since the identification of an origin is not always trustworthy, and in any case the V^0 particle might have been appreciably scattered before decay. We therefore conclude that there is little direct evidence in these data that indicates the existence of decay into equal particles, but that a few of the decays (groups 1*a* and 3*a* and four or five of 1*c*) might be interpreted as being of this type.

The single case in group 2*a* is especially interesting. It is shown in Fig. 16. The momentum of the positive particle is 190 ± 20 Mev/c, and its ionization is less than 1.5 times minimum. This restricts its mass to be less than about $350m_e$. The momentum of the second particle (which is negative if it is going away from the apex of the V and positive if going toward it) is 210 ± 40 Mev/c. Its ionization is estimated to be 2–4 times minimum, which indicates that its mass lies in the range $450\text{–}1000m_e$. Thus, even if one allows for extreme errors in the determination of both the curvature and the ionization, it is extremely difficult to interpret this particle as a π-meson.

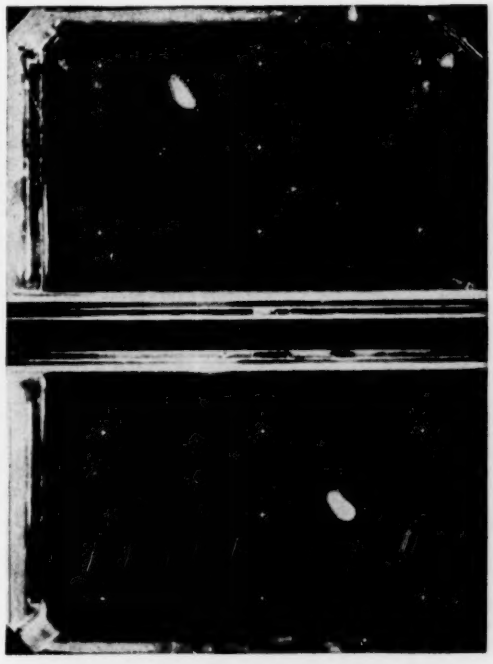

FIG. 16. Example of V^0 decay leading to a positive meson (presumably a π-meson) and a negative particle whose mass is considerably greater than that of a π-meson. The decay is in the upper left part of the upper chamber; the positive particle proceeds downward from the decay point, and the negative, toward the right and slightly downward.

The positive particle enters the lead plate but passes outside the visible region of the lower chamber; the negative particle passes through the front wall of the upper chamber after traveling about 8 cm through the chamber. This decay is described further in the text.

This decay is in general alignment with the two high momentum tracks that traverse both chambers, but there is no identifiable origin with which it is associated. On the other hand, this can also be said of many of the V^0 decays. If it were to be interpreted as a V^+ decay or a κ^+ meson decay, the particle would have been traveling upward, and would similarly not have been proceeding from an identifiable origin. Of the 18 V^+ particles observed in the present experiment, none were traveling upward, and all were clearly associated either with a penetrating shower or with a nuclear interaction origin in the lead plate between the cloud chambers. Furthermore, the kinetic energy of the π- or μ-meson in the center-of-mass system of an assumed V^+ or κ^+-decay is greater than 200 Mev, a value considerably higher than is now thought to be associated with either of these types of decay. Thus this case most probably represents a V^0 decay.

Therefore, this case appears to support an alternative hypothesis suggested above to explain the appearance of the α-distribution, i.e., that V^0 particles may exist that decay into a $\pi^\pm$ or $\mu^\pm$ meson and a particle of mass 500–

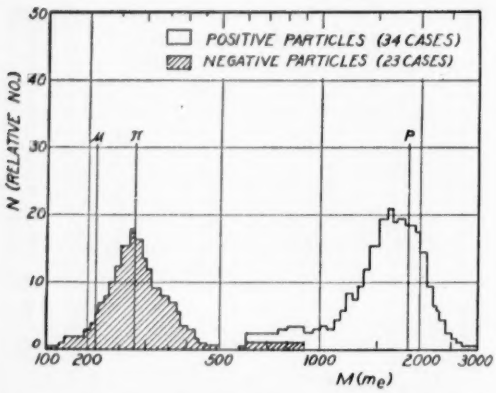

FIG. 17. The measured masses of V^0 particle secondaries. In this diagram each measurement is represented by a rectangular area whose width corresponds to the mass limits determined by the limits of the estimated ionization and by the central value of the measured momentum, and whose height is adjusted to give equal area to each rectangle. The ordinate at a given mass value is thus the sum of the heights of the rectangles containing that value, with a weight for each measurement inversely proportional to the range of values (on the logarithmic scale) covered by that measurement. The broken curve so obtained therefore represents a weighted frequency curve for the mass measurements. This procedure was used in order to allow for the widely varying accuracy of the individual measurements.

The results indicate that almost all of the negative particles were probably π-mesons, but that a few might have been μ-mesons and a few others were probably heavier than π-mesons; likewise, almost all of the positive particles were probably protons, but they could all have been somewhat lighter than protons, and a few seem to be considerably lighter than protons. The greater spread of the frequency curve of the positive particles may result entirely from greater errors in momentum measurement, but would also be consistent with a mixture of protons and lighter particles amongst the decay products.

$1200m_e$, the heavier particle being possibly a τ- or κ-meson, or a somewhat lighter particle.[12]

The measured masses of the secondary particles, as determined by their measured momenta and estimated ionizations are shown in Fig. 17. Only those cases in which a particle was heavily ionizing are represented. All cases represented in the diagram are plotted as rectangles of the same area, whose widths correspond to the mass ranges derived from the central values of the measured momenta and the extreme limits of the ionization estimates.

The most striking feature of the diagram is the peak corresponding to the mass of a π-meson. As was pointed out in Sec. VII, the error in the mass measurement of a light particle is determined almost entirely by the error in the ionization estimate. The sharpness of this peak thus indicates, not only that the negative particles are most probably π-mesons, but also that the estimates of ionization were sufficiently reliable, statistically, to distinguish π-mesons from μ-mesons.

Although the mass distribution indicates that almost all of the light particles are π-mesons, there were five cases, two heavily ionizing and three at minimum ionization, whose measured masses or upper mass limits were too low to reconcile with the mass of a π-meson. This number of cases suggests that μ-mesons may sometimes be produced in V^0 decay, but is surely too small to permit any strong conclusions as to decay schemes with which they may be associated. For these five decays, however, it can be stated that (1) four exhibited heavy positive decay-particles, presumably protons, but possibly τ- or κ-mesons. In the remaining decay the mass of the positive particle was indeterminate. (2) Three, with which points of origin could be associated, were consistent with "coplanarity," and hence with a two-body decay. (3) Four of the decays seemed to lead to an energy release or "Q-value" of about 40 Mev, but one, which might possibly be a κ^- meson traveling upward, required a Q-value of 11 ± 3 Mev. If it were a κ^- meson decay, the energy of the μ-meson in the center-of-mass system of the decay would be about 44 Mev, a value not inconsistent with other observed cases[12,13] (see Fig. 19).

The spread in the measured masses of the positive particles is broader than that of the negative particles, because of the greater difficulty of measuring the higher values of momenta here involved. The distribution reaches a maximum at a value somewhat lower than a proton mass; after considerable study of the measurement technique that was used, it was concluded that this does not necessarily indicate a mass lower than that of a proton for all of these particles, but that a few τ- or κ-mesons could have been present. The positive particles of Figs. 4 and 5 are examples of the few whose masses seemed too low to be protons.

In addition to the case shown in Fig. 16 and discussed above, one or two further examples of slow heavy decay particles were found whose measured masses seemed to lie in the range 600–$1200m_e$. A few cases were also found whose upper mass limit was sufficiently low to exclude a proton, and whose accompanying particle was apparently a π-meson. (Some of these cases are included in groups 1*c* and 3*a* of Table II, since the arbitrary division at $700m_e$ classifies as "indeterminate" a few cases whose upper mass limits lie between $700m_e$ and about $1000m_e$.) None of these slow particle tracks was of sufficiently high quality to yield a reliable mass determination, so that these data must be regarded only as supporting evidence for, but not conclusive proof of, the hypothesis advanced above regarding the possible existence of a second type of V^0 decay in which a τ- or κ-meson may be produced.

Finally, before leaving this discussion of the nature of V^0 decay products, it should be pointed out that there is no evidence, either from the α-distributions of Fig. 11 or from actual mass measurements, that requires the presence of V^0 particles whose decay leads to a positive meson and a negative proton, although a small number of the decays might have been of this type.

[12] R. B. Leighton and S. D. Wanlass, Phys. Rev. **86**, 426 (1952).

[13] C. O'Ceallaigh, Phil. Mag. **42**, 1032 (1951).

IX. ENERGY RELEASE IN V^0 DECAY

The energy release, or Q-value, of the two-body decay of a neutral V-particle can be determined from the momenta of the two decay-particles and the included angle between their paths, if the masses of the decay-particles are known. In the decay described by Fig. 10, we have, in the laboratory system,

$$E_0=E_++E_-=(P_+^2+M_+^2)^{\frac{1}{2}}+(P_-^2+M_-^2)^{\frac{1}{2}},$$

and

$$P_0^2=P_+^2+P_-^2+2P_+P_-\cos\theta_T,$$

so that

$$M_0^2=E_0^2-P_0^2=M_+^2+M_-^2+2E_+E_--2P_+P_-\cos\theta_T$$
$$=(M_++M_-)^2+2E_+E_--2M_+M_-$$
$$-2P_+P_-\cos\theta_T; \quad (9)$$

we have therefore

$$Q=M_0-(M_++M_-)$$
$$=(M_++M_-)\left(\left[1+\frac{2Q_1}{M_++M_-}\right]^{\frac{1}{2}}-1\right) \quad (10)$$
$$=Q_1-\frac{Q_1^2}{2(M_++M_-)}+\cdots, \quad (11)$$

where

$$Q_1=\frac{E_+E_--M_+M_--P_+P_-\cos\theta_T}{M_++M_-}$$
$$=\frac{M_+T_-+E_-T_+-P_+P_-\cos\theta_T}{M_++M_-},$$

and E_+, T_+ and E_-, T_- are the total and kinetic energies, respectively, of the product particles in the laboratory system, the remaining quantities having the same significance as in Eqs. (2)–(6). The quantity Q_1 was introduced in order to simplify the computation of Q; it will be noted that $Q\approx Q_1$ for small values of Q.

The decays for which sufficient data were available to permit the calculation of a Q-value were classified into three groups according to their decay products.

Group A consists of those decays which clearly yielded a light negative and a heavy positive particle. The 38 decays in this group constitute practically the entirety of class 1*b* of Table II. A Q-value was calculated for each of these, assuming a two-body decay yielding a negative π-meson and a proton. The Q-values so obtained ranged from 10±3 Mev to 87±15 Mev, and were distributed within this range as indicated by the cross-hatched portion of the histogram of Fig. 18.[14]

Group B consists of those remaining cases in which there was no evidence against the assumption of decay into π-mesons and protons, and in which the α-values, in being greater than +0.5, actually gave some support for this assumption. The 25 decays in this group constitute practically the entirety of class 1*c* of Table II. Q-values were calculated for these decays assuming two-body decay into a π-meson and a proton. The Q-values so obtained ranged from 10±5 Mev to 97±30 Mev, and were distributed within this range as is indicated by the unshaded portion of the histogram of Fig. 18. The contributions of groups A and B to the total distribution are seen to be quite similar, within reasonable statistical fluctuation.

Group C consists of seven decays that seemed to exhibit properties which would preclude an interpretation in terms of a decay into a negative π-meson and a proton. These decays were those of classes 1*a*, 2*a*, and 3*a* of Table II. Q-values were calculated for various possible two-body decay schemes chosen to fit the observed properties of each individual case, with the following results: (1) Three of the decays, which could have yielded a positive and a negative π-meson, gave Q-values of about 110 Mev for this decay scheme. (2) Two of the above three decays might alternatively have

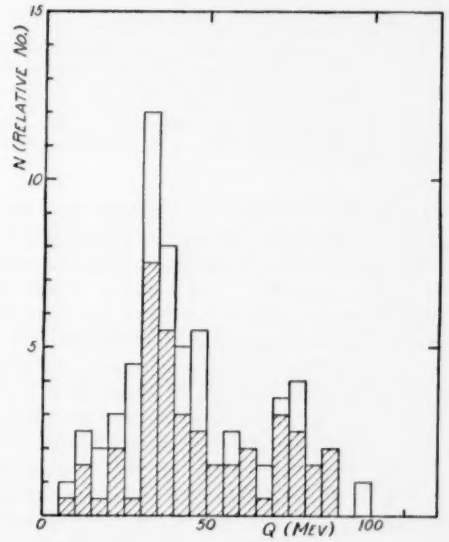

FIG. 18. The distribution of measured Q-values for 63 cases in which the decay $V^0\rightarrow p+\pi^-$ was indicated. The cross-hatched portion of this histogram represents those cases in which the positive particle was surely much heavier than a π-meson, and the unshaded portion, those of the remaining cases, whose α-values were greater than +0.5, and in which there was no evidence against the assumed decay scheme.

[14] In three of these decays the lighter particle seemed too light to be a π-meson, and in five other decays the heavier particle seemed too light to be a proton. Q-values were therefore recalculated for these eight decays assuming in the first three cases a two-body decay yielding a μ-meson and a proton, and in the latter five cases a two-body decay yielding a π-meson and a τ-meson of mass $975m_e$ or a κ-meson of mass $1250m_e$. These alternative Q-values were approximately equal to the Q-values calculated for $\pi+p$ decay, and were spread over a comparable range. In view of the small number of these "anomalous" cases and the large inherent errors in an individual mass measurement, particularly in the case of a massive positive particle, these cases, calculated for $\pi+p$ decay, were included in the histogram along with the "genuine" $\pi+p$ decays.

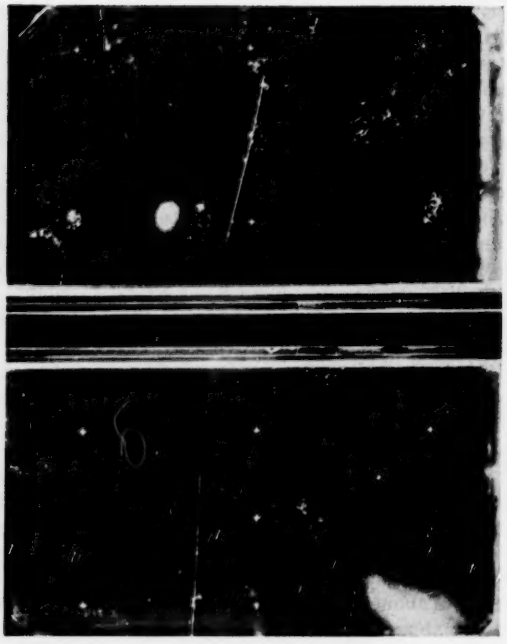

FIG. 19. A probable V^0 decay which has a very low Q-value. The decay occurs near the middle of the lower chamber. The negative meson, in this case probably a μ-meson, curves downward and to the right, and the proton goes almost straight downward, from the decay point. The data for this case are given in column 1 of Table III. The Q-value for this case is 10 ± 3 Mev. This decay may be alternatively interpreted as the decay of a negative κ-meson entering the chamber from the bottom. This interpretation seems rather unlikely, however.

yielded a negative π-meson and a positive τ- or κ-meson. One of the other decays (see the previous discussion in connection with Table II) seemed to yield a positive π-meson and a negative τ- or κ-meson. These three decays, interpreted in terms of a decay into a $\pi^{\pm}$ and a $\tau^{\mp}$ meson, all gave Q-values of about 60 Mev. (3) The remaining three decays were of much poorer quality and could be interpreted in terms of either of the above decay schemes, but the Q-values did not seem to agree with those indicated above or with one another.

It is clear that many more of these "anomalous" decays will be required before an assignment of decay scheme can be made. For that reason, the remainder of the present discussion will concern only the results of the Q-value calculations for groups A and B.

The histogram of Fig. 18 was constructed by counting the number of Q-values within each 5 Mev range, without regard to the errors involved in the individual measurements. This histogram strongly suggests the existence of at least two Q-values, one at about 35 ± 3 Mev, another at about 75 ± 5 Mev, and possibly a third near 45 Mev, although a continuous distribution with or without one or more discrete values would also be consistent with the observed distribution. Armenterous *et al.*[7] obtained Q-values for twelve cases which were distributed in excellent agreement with the above histogram. These authors concluded, however, that their data indicated a single Q-value at 46 ± 6 Mev. In order to determine whether the present results will support such a conclusion, it is necessary to investigate the errors involved in the Q-value determination.

The accuracy with which the Q-value may be determined from the measured momenta and the angle depends upon the accuracy with which these three quantities are known. The error in Q-value is often much more sensitive to the error in a certain one of the quantities, usually the momentum of the lighter particle, than to errors in the other quantities. This can be seen by evaluating the derivatives

$$\text{(a)}\quad \frac{\partial Q}{\partial P_+}=\left(\frac{E_-P_+}{E_+}-P_-\cos\theta_T\right)\Big/(M_++M_-+Q);$$

$$\text{(b)}\quad \frac{\partial Q}{\partial P_-}=\left(\frac{E_+P_-}{E_-}-P_+\cos\theta_T\right)\Big/(M_++M_-+Q); \tag{12}$$

$$\text{(c)}\quad \frac{\partial Q}{\partial \theta_T}=(P_+P_-\sin\theta_T)/57.3(M_++M_-+Q)(\text{Mev}\cdot\text{deg}^{-1}).$$

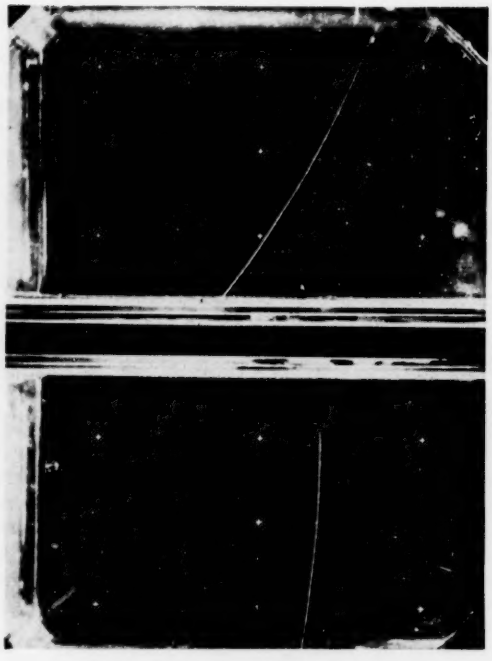

FIG. 20. A V^0 decay which has an intermediate Q-value. The decay occurs near the top of the lower chamber, and slightly to the right of the center. The positive particle, which is very heavily ionizing, travels almost straight downward, and the lightly ionizing negative particle travels downward and to the left from the decay point. The data for this case are given in column 4 of Table III. The Q-value for this case is 37 ± 3 Mev.

The numerical values that were commonly found for these derivatives were, for $\pi+p$ decay,

(a) $\partial Q/\partial P_+ = -0.1$ to $+0.2$ (usually about $+0.07$);

(b) $\partial Q/\partial P_- = 0.3$ to 1.0 (usually about 0.6);

(c) $\partial Q/\partial \theta_T = 0.5$ to 3.0 Mev/deg (usually about 1.5).

To each Q-value an uncertainty was assigned whose magnitude was derived from the estimated errors in the momenta and the included angle, using the partial derivatives of Eq. (12) for this purpose. The absolute uncertainty tended to be smaller, the lower the Q-value, whereas the percentage error was roughly independent of the Q-value. The estimated errors were about ± 30 percent on the average, and about ± 15 percent in several of the best cases. Thus the average estimated uncertainty in the Q-value might be large enough to permit an interpretation in terms of a single Q-value at 46 ± 6 Mev. However, if this were the case one would expect that the distribution would, within a reasonable statistical fluctuation, show a maximum near 46 Mev; also, those Q-values having small estimated uncertainties should be distributed more closely about this value than are those of large estimated uncertainty so that the few best cases should give Q-values very close to 46 Mev.

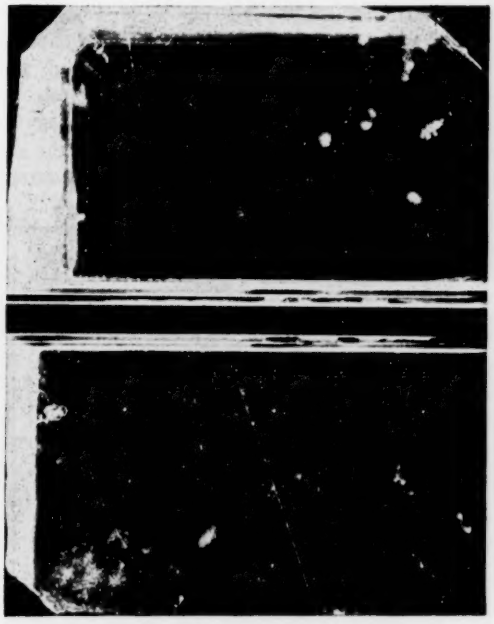

FIG. 21. A V^0 decay which has a high Q-value. The decay occurs near the top center of the lower chamber. The positive particle is heavily ionizing, and moves downward and slightly toward the right from the decay point, while the negative particle is near minimum ionization and travels diagonally downward and to the right from the decay point. The data for this case are given in column 7 of Table III. The Q-value calculated for this case is 72 ± 10 Mev.

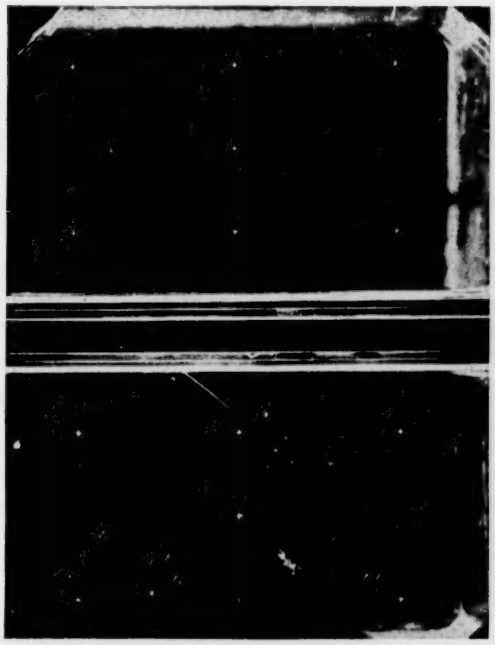

FIG. 22. A V^0-decay which has a high Q-value. The V^0 particle, which is produced in the nuclear interaction in the lead plate between the chambers, decays immediately below the top of the lower chamber. The positive particle appears to be slightly above minimum ionization, and travels downward and toward the right from the decay point. The negative particle is heavily ionizing and travels toward the left and somewhat downward from the decay point. The data for this case are indicated in the last column of Table III. The Q-value calculated for this case is 79 ± 15 Mev. This is in many respects the most convincing example of a high Q-value decay so far observed, both because of the internal checks upon the momenta that are afforded by the heavy ionization of both decay-particles, and because the Q-value cannot be reduced below about 65 Mev even by assuming quite large errors in the momenta and ionizations.

To illustrate the above point, photographs of some of the best cases are shown in Figs. 19 to 22, and the measured quantities bearing upon the Q-value calculations for these cases are indicated in Table III. It would appear to be very difficult to reconcile these cases with a single Q-value.

X. DISCUSSION

In the preceding sections of this paper it was shown that the great majority of V^0 decays ($\sim$80 percent) yield a heavy positive and a light negative particle as decay products, which in most instances are best interpreted as a proton and a π^- meson. These decays were rather extensively analyzed on the assumption that they all were two-body decays, an assumption that was quite consistent with the data up to that point. However, the apparent existence of an non-unique Q-value suggests the presence, either of more than one mode of

TABLE III. Q-values for eight examples of V^0-decays that yield a proton and a meson.

Quantity	25686 (Fig. 19)	14539	31044	31817 (Fig. 20)	19063 (1) [Fig. 3 (1)]	30514	19955 (Fig. 21)	28167 (Fig. 22)
P_+(Mev/c)	375±100	390±50	660±100	72±20	400±50	510±50	500±50	800±150
I_+(×min)	4–8	3–4	1.5–3	>15	3–6	2.5–4	2–4	1.5–2
$M_+(m_e)$	1600–2400	1350–1650	1200–2300	>700	1400–2200	1500–2100	1300–2200	1500–1900
P_-(Mev/c)	67±7	150±10	205±10	125±5	60±5	130±5	300±25	77±7
I_-(×min)	1.5–3	1–2	<1.5	1.5–3	3–6	1.5–2.5	<1.5	3–4
$M_-(m_e)$	130–230	<370	<380	230–430	205–330	240–380	<550	265–310
θ_+(deg)	—	—	8	—	—	14	—	9.5
θ_-(deg)	—	—	24	—	—	56	—	104.5
θ_T(deg)	53±1	45±1	32±1	52±1	151±2	70±1	19±1	114±1
$\partial Q/\partial P_+$	0.015	−0.025	−0.027	0.061	0.10	0.043	−0.11	0.11
$\partial Q/\partial P_-$	0.19	0.42	0.35	0.51	0.68	0.50	0.42	0.77
$\partial Q/\partial\theta_T$	0.29	0.65	1.1	0.11	0.19	0.97	0.80	0.82
Q(Mev)	10±3	33±5	36±5	37±3	41±7	46±4	72±10	79±15

two-body decay, or of multibody decay. It seems appropriate, therefore, to discuss these data in terms of various alternative modes of decay, a few of which will now be considered in relation to the present measurements of coplanarity, Q-value, decay product mass, and lifetime[15]:

(A) $$V^0\rightarrow p+\pi^-+E.^{16} \quad (1)$$

As previously shown this hypothesis, which assumes a unique mass of the V^0 particle, is consistent with the measurements of coplanarity. However, if all V^0 particles which seem to yield protons and π^- mesons were of this type, then the entire spread in Q-values would have to be ascribed to errors of measurement, a possibility which is considered to be quite unlikely, but which cannot, of course, be completely excluded.

(B) $$V^0\rightarrow p+\pi^-+\nu+E, \quad (2)$$

$$V^0\rightarrow p+\pi^-+\pi^0+E. \quad (3)$$

The above three-body decay schemes, one yielding a neutrino and the other a neutral π-meson, have been considered by Brueckner and Thompson.[17] Under the assumption that the emission of the particles in the c.m. system is governed only by statistical factors, these authors have calculated two distribution curves for each of these decay schemes. The first, which can be compared with the observed values of δ, is a distribution of $\gamma\beta\delta$, where $\gamma=(1-\beta^2)^{-\frac{1}{2}}$ and βc is the speed of the V^0-particle. The second is a distribution of Q-values, where Q is the apparent energy release calculated on the assumption of a two-body decay as in Sec. IX of this paper. In these distributions a value for the true energy release, E, was assumed such that the most probable Q-value appears at 35 Mev. The true energy release then corresponds to 130 Mev for decay (2), and 70 Mev for decay (3). Even though these distributions are based on several simplifying assumptions, a considerable significance may be attached to them.

In Fig. 23 the distribution of $\gamma\beta\delta$, for the 50 observed cases in which both δ and β are known, is plotted as a histogram, and is compared with the corresponding distributions calculated by Brueckner and Thompson. The observed distribution of $\gamma\beta\delta$, allowing for statistical fluctuations, is not inconsistent with either of the calculated distributions, although the observed cases occur more often at the smaller values of $\gamma\beta\delta$. A somewhat sharper comparison is obtained if one selects only those cases in which the estimated error in $\gamma\beta\delta$ is relatively small. Thirty-two cases, in which the error is less than 2.5°, are plotted in Fig. 24. Again, in view of the small number of cases, the observed distribution cannot be

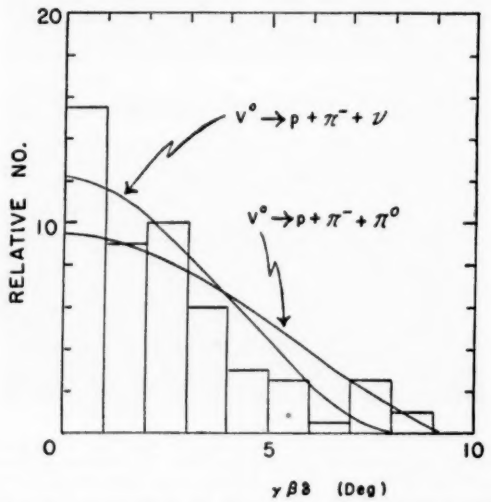

FIG. 23. A comparison of the measured deviations from coplanarity with those to be expected on the basis of a three-body decay of the V^0 particle. The quantity $\gamma\beta\delta$, whose distribution is here given, is defined in the text.

[15] Tentative results of measurements of lifetimes of V^0 particles will be used. The details of the lifetime measurements will be reported elsewhere.

[16] The symbol E is used to denote the *true* energy release associated with a decay scheme. The term Q-value refers to the energy release calculated upon the assumption that the charged secondaries are the only secondaries produced in a decay. If no neutral particles are produced in a decay then the Q-value is of course identical with the true energy release, E. If one or more neutral particles are also produced the Q-values are distributed up to a maximum value equal to the true energy release, E.

[17] K. A. Brueckner and R. W. Thompson, Phys. Rev. **87**, 390 (1952).

said to be inconsistent with either of the calculated distributions, although it now shows a still greater proportion of cases corresponding to small values of $\gamma\beta\delta$. Inasmuch as the errors of measurement will tend to broaden the observed distributions, the large number of cases at small values of $\gamma\beta\delta$ suggests that an appreciable fraction, if not all, of the V^0 decays may be of a two-body type.

In Fig. 25 the distribution of 63 observed Q-values, plotted as a histogram, is compared with the corresponding calculated distributions. The observed distribution does not appear to correspond closely to the calculated distribution for the decay scheme in which a π^0 meson is produced. It cannot, however, be said to be inconsistent with the calculated distribution for the decay scheme in which a neutrino is produced, although the rather sharp peak suggests the presence of a discrete Q-value at about 35 Mev, and is an indication again that a substantial fraction of the V^0 particles may undergo two-body decay.

For both of the three-body decay schemes here considered, the V^0-decays of high Q-value, corresponding to low kinetic energies of the neutral particle, should, on the average, show smaller deviations from coplanarity than the decays of low Q-value. That such a correlation is not indicated in the present observations can be seen in Fig. 26, in which the deviation from coplanarity is plotted *versus* the observed Q-values. Of course, in view of the small number of cases and the magnitude of the errors of measurement, the data cannot be said to be inconsistent with either of the three-body decays here under discussion. However, the apparent concentration of points in the region of Q-value near 35 Mev and $\gamma\beta\delta$ near zero again suggests that a substantial fraction of the V^0 particles may undergo two-body decay with an

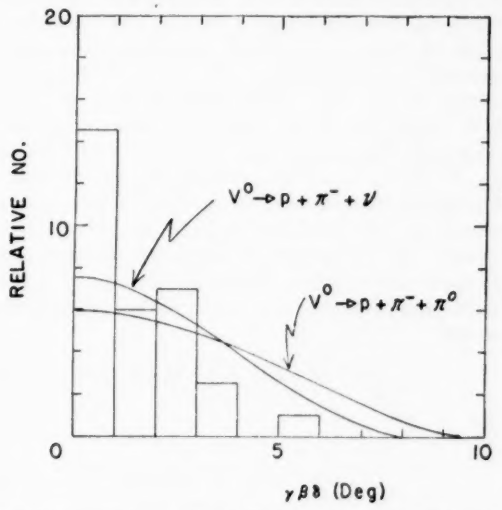

FIG. 24. A comparison similar to Fig. 23, except that all $\gamma\beta\delta$ values whose estimated errors are greater than 2.5° are omitted.

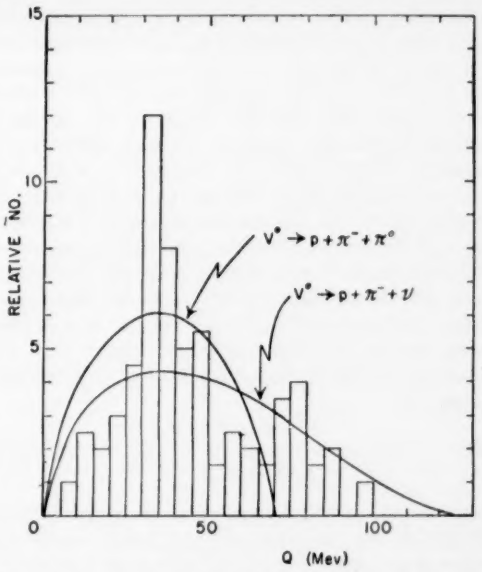

FIG. 25. A comparison of calculated Q-values with the distributions to be expected on the basis of three-body decay of the V^0 particle.

energy release of about 35 Mev.

$$\text{(C)}\qquad V^0 \begin{cases} \nearrow\ p+\pi^-+E_1 & \text{(a)}, \\ \searrow\ p+\mu^-+\nu+E_2 & \text{(b)}. \end{cases} \qquad (4)$$

A branching decay scheme, such as the above, in which a unique V^0 particle decays by either of two alternative modes, would lead both to a unique Q-value and to a distribution. The decay (a) would not show deviation from coplanarity, and would correspond to a unique Q-value, E_1, which might be associated with the observed peak at 35 Mev. The decay (b) would show deviations from coplanarity and a distribution in Q-value up to a limiting value, E_2. One sees that E_2-E_1 should equal 33 Mev, the difference in mass of the π- and μ-mesons. Such a relationship is not completely excluded by the data in Fig. 18, inasmuch as the larger errors are associated with the higher Q-values.

Furthermore, according to this hypothesis, π^- mesons should be associated with the unique Q-value (i.e., 35 Mev) and μ^- mesons with the distributed Q-values, Such a correlation, however, is not indicated in Fig. 27. in which the measured masses of the decay products are plotted *versus* the measured Q-values; in fact, the few μ^- mesons, whose presence seems to be indicated, are found for the most part in the region near 40 Mev, whereas the π^- mesons are distributed over all values of Q.

$$\text{(D)}\qquad V_n^0 \rightarrow p+\pi^-+E_n. \qquad (5)$$

According to this hypothesis the V^0 particle occurs in more than one energy state, E_n, and undergoes two-body decay. All decays would then be exactly coplanar, and thus in this respect would be consistent with the observations. The discrete Q-values, E_n, might be correlated with the observed Q-values. However, the measured mean lifetimes of V^0-particles with low Q-value (less than 50 Mev) and high Q-value (greater than 50 Mev) differ from one another by less than a factor of two, and, in fact, are consistent with a single mean value of $2.5\pm0.7\times10^{-10}$ sec, within expected fluctuations. Upon this hypothesis it would thus be necessary to assign comparable lifetimes to V^0-particles in different energy states, whereas one might expect very wide differences in the lifetimes associated with the different states.

$$\text{(E)} \qquad \begin{aligned} V^0 &\rightarrow p_n + \pi^- + E_n; \\ p_n &\rightarrow p + h\nu_n. \end{aligned} \qquad (6)$$

According to this hypothetical decay of a unique V^0 particle, the resulting proton is left in one or more states of excitation, p_n, and subsequently returns to its ground state, e.g., by the emission of a photon. If the mean lifetime associated with the transition of the excited proton to its ground state is very short compared with the mean lifetime (2.5×10^{-10} sec) of the V^0 particle itself, then one would expect to find a distribution of Q-values corresponding to each state of excitation of the proton, where the breadth of the distribution would be determined by the energy of the photon, $h\nu_n$. This follows from the fact that the proton would have decayed to its ground state before producing the track in the cloud chamber. Furthermore, deviations from coplanarity would be expected if an excited proton were produced, although these deviations would be small if the energies of the photons were small.

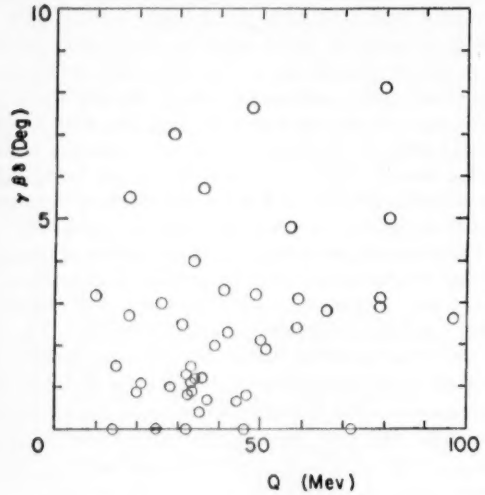

FIG. 26. A plot of observed deviations from coplanarity *vs* calculated Q-value for 44 cases.

Only in those cases where the V^0 decay results in a proton already in its ground state would one expect a discrete Q-value. Such decays would show no deviation from coplanarity and should correspond to the high Q-values. Such a correlation is not borne out by the observations (see Fig. 26), but in view of the statistical nature of the observations, such a mixture of cases, some of which are coplanar and correspond to a unique Q-value, and others which show slight deviations from coplanarity and correspond to a distribution of Q-values, can be said to be consistent with the present data. Of course, there is no evidence at present for the existence of excited protons, nor is there evidence that photons accompany V^0 decay. On the other hand, there is no evidence against the existence of such photons, for photons of energies of a few tens of Mev might very easily escape detection.

While it is true that this hypothesis circumvents the difficulty associated with assigning two nearly equal lifetimes to different particles (or different degrees of excitation), it does imply the production of comparable numbers of excited and unexcited protons.

$$\text{(F)} \qquad \begin{aligned} V^0 &\rightarrow X_n^0 + h\nu_n; \\ X_n^0 &\rightarrow p + \pi^- + E_n. \end{aligned} \qquad (7)$$

A non-unique Q-value associated with an apparently unique lifetime might also be explained in terms of a branching and cascade two-body decay scheme involving an intermediate particle. For example, a unique V^0 particle decays by photon emission into a secondary particle, X_n^0, which subsequently undergoes a two-body decay into a proton and π^- meson. If the lifetime associated with the decay of the secondary particle is very short ($<10^{-12}$ sec) compared with that ($\sim2.5\times10^{-10}$ sec) associated with the incident V^0 particle, then the X_n^0 particle would not move an appreciable distance in the cloud-chamber before it decays, and the point of origin of the proton and π^- meson tracks would be essentially the point of decay of the incident V^0 particle. Decays of this type would therefore show deviations from coplanarity of an amount corresponding to the energies of the photons $h\nu_n$. A set of discrete Q-values, E_n, would be expected corresponding to the various degrees of excitation of the secondary particle. A decay scheme such as the above could be considered as consistent with the present measurements of coplanarity, Q-values and lifetime. However, this decay scheme again implies comparable probabilities for competing decays.

$$\text{(G)} \qquad V^0 \begin{cases} \nearrow\ X^0 + \mu^0 + E_1, \quad X^0 \rightarrow p + \pi^- + E_3; & (8a) \\ \searrow\ X^+ + \pi^- + E_2, \quad X^+ \rightarrow p + \mu^0 + E_4. & (8b) \end{cases}$$

Another hypothetical decay scheme leading to a non-unique Q-value and an apparently unique lifetime, is the

one represented above, in which there are two alternate modes of decay of the V^0-particle, each of which results in the production of an intermediate unstable particle, X^0 or X^+. If the mean lifetimes of the intermediate particles are both very short compared with the mean lifetime of the V^0-particle, then deviations from coplanarity would be expected for both modes (a) and (b), if the coplanarity measurements are made in the usual manner on the proton and π^- meson tracks. The Q-value measurements, however, if also carried out in the usual manner, would lead to a unique value for mode (a) and to a distribution for mode (b). As is apparent from the previous discussion a decay scheme of this type could also be consistent with the present data, but would imply again comparable probabilities for decay by modes (a) and (b).

The foregoing decay schemes have all been chosen to yield a proton and a π^- meson as the visible (i.e., charged) products of V^0 decay. It should be recalled, of course, that the experimental evidence does not require that the heavy particles actually be protons, or that all of them be protons. In addition, the few cases in which the negative particle seems to be a μ^- meson have largely been ignored; and the few decays whose positive decay-particle seems to be a π^+ or μ^+ meson have not been considered because of the lack of information as to the nature of the negative particles for these latter cases. Many decay schemes could probably be imagined that would fit all of the data so far obtained, if some specific assumption were to be made as to the nature of these negative decay particles, but to discuss them at the present time seems rather premature. It is at least clear that much remains to be learned about almost all aspects of V-particle decay, and that much more data, of much better quality than is at present available, will be needed to establish clearly the nature of V-particles.

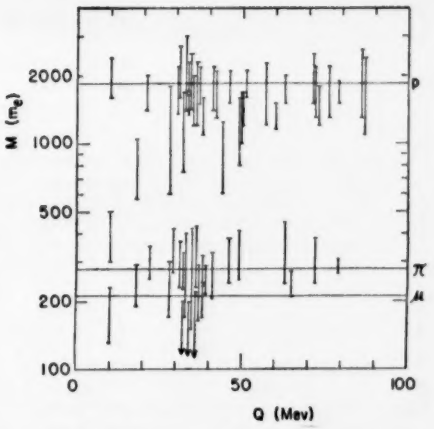

FIG. 27. A plot of the measured masses of the secondary particles of V^0 decay *vs* the calculated Q-value. Each particle is represented on this diagram by a vertical line which extends over the range of mass values defined by the limits of the estimated ionization and the central value of the measured momentum. Only heavily ionizing particles, for which upper and lower mass limits could be estimated, are shown, except for three negative particles of minimum ionization whose upper mass limits seemed too low to reconcile with the mass of a π-meson. All of the particles whose upper mass limit is less than $500m_e$ are negative particles, the remainder positive.

We take pleasure in acknowledging the able assistance of Dr. E. W. Cowan and of Mr. William L. Alford and Mr. Frank H. Shelton. Our thanks are also due the Carnegie Institution of Washington for laboratory space on Mount Wilson, California.

A Study of Neutral V Particles*

W. B. FRETTER, M. M. MAY, AND M. P. NAKADA
Department of Physics, University of California, Berkeley, California
(Received September 15, 1952)

The V particles produced in penetrating showers have been studied in a cloud chamber containing lead plates. The results can be interpreted in terms of two types of neutral unstable particles, $V_1^0 \rightarrow p+\pi$ and $V_2^0 \pi+\pi$, although other possibilities are not excluded by our data. Analysis of the dynamics of three-particle decay indicates that such a process must still be considered as possible. The lifetimes of the particles have been calculated, taking into account the bias introduced by the finite size of the cloud chamber. If we use average values for the masses of the unstable particles, the lifetime for the V_1^0 is $(10\pm7)\times10^{-10}$ sec and for the V_2^0 is $(4\pm3)\times10^{-10}$ sec.

INTRODUCTION AND APPARATUS

THE unstable particles produced in penetrating showers, first discovered by Rochester and Butler in 1947,[1] have now been observed in several laboratories.[2-6] A large cloud chamber formerly used for studies of penetrating showers[7] was arranged for detection of these unstable neutral particles, called V^0 particles, and has been operated at Berkeley since February, 1950 and at Lake Sabrina, California (9000 feet elevation) during the summer of 1951. We are reporting on about 75 V^0 particles that have been observed to date in this cloud chamber, which has no magnetic field but contains lead plates.

Although the arrangement of the lead plates was changed from time to time, many of the pictures were taken with seven ½-inch lead plates in the chamber. The plates were spaced about 2 inches apart to allow room for observation of the decaying particles. The arrangement of apparatus is shown in Fig. 1. The chamber was expanded when one and only one of the counters above the chamber triggered in coincidence with both the counters below the chamber. During most of the time there was only a thin roof above the apparatus and nearly all the V^0 particles were created in the material in the chamber. At sea level the counting rate is 2 per hour, with about 2 or 3 penetrating showers per day. The anticoincidence arrangement of the upper counters eliminated many low energy showers which otherwise would have counted in the rather loose selection of events. It seems important not to require very high energy penetrating showers, since the tracks of V^0 particles often may be lost in the large electronic cascades usually accompanying such events.

Stereoscopic pictures were taken with a double lens camera 220 cm in front of the cloud chamber. The lenses were 11.5 cm apart and set at angles of 3° to converge on the chamber. The pictures were searched for unstable particles in a stereoscopic viewer, and if one was found, measurements on it were made in a reprojection apparatus made especially for the purpose. Examples of V^0 particles photographed with our apparatus have been published.[8]

MEASUREMENTS

The reprojector was designed to give a three-dimensional reproduction of events as they actually took place in the cloud chamber. The same camera that took the pictures was used as a projector, and the film was placed in the same orientation that it had when the pictures were taken. A ground glass plate 60 cm in diameter was used for a screen. A glass plate similar to the front glass of the cloud chamber was mounted in front of the screen to compensate for distortions introduced by photographing through the front plate of the cloud chamber. The screen could be moved toward or away from the camera. It was mounted on swivels so that it could be moved to any possible plane with the center of the screen remaining fixed as the screen was tilted. Because the center of the screen was the fixed reference point in reprojection, the camera mounting was made so that the camera could be moved vertically and horizontally. This allowed the operator to bring any image point within the cloud chamber to focus at the center of the screen.

In reprojecting pictures the following procedure was used. The screen was brought to a position corresponding to the front of the plates of the cloud chamber, and the film was adjusted until the two images of the plates coincided on the screen. The penetrating shower was located and the center of the shower was brought to focus at the center of the screen. This involved motion of the camera vertically and horizontally, motion of the screen toward and away from the camera, and the superposition of the images of penetrating particle tracks which emerged from the penetrating shower center. The latter operation required the tilting of the plane of the screen. With the center of the shower at the

* Assisted by the joint program of the ONR and AEC.
[1] G. D. Rochester and C. C. Butler, Nature **160**, 855 (1947).
[2] Armenteros, Barker, Butler, and Cachon, Phil. Mag. **62**, 1113 (1951).
[3] Seriff, Leighton, Hsiao, Cowan, and Anderson, Phys. Rev. **78**, 290 (1950).
[4] Thompson, Cohn, and Flum, Phys. Rev. **83**, 175 (1951).
[5] H. S. Bridge and M. Annis, Phys. Rev. **82**, 445 (1951).
[6] W. B. Fretter, Phys. Rev. **83**, 1053 (1951).
[7] W. B. Fretter, Phys. Rev. **76**, 511 (1949).
[8] C. C. Butler, "Unstable Heavy Cosmic Ray Mesons," in J. G. Wilson, *Progress in Cosmic Ray Physics* (North-Holland Publishing Company, Amsterdam, 1952).

center of the screen, an attempt was next made to orient the plane of the screen to see if it could be made to coincide with the plane of the V^0 particle. Sometimes the plane of the V^0 particle did not include the penetrating shower center. In such noncoplanar cases, no angle measurements could be made. When the plane of the V^0 particle contained the center of the penetrating shower, angle measurements were made as follows.

A line through the penetrating shower origin and the apex of the V^0 particle was used as reference, and the angles that the decay products made with this line were measured. The distance between the origin of the penetrating shower and the apex of the V^0 particle was measured, and the maximum available distance in the cloud chamber for the detection of each V^0 particle was measured along the same reference line. The position of the event within the chamber was noted. The angle between the initiator of the penetrating shower and the reference line was measured. The angle between the plane containing the V^0 and the plane containing the reference line and the initiating particle was estimated. Figure 2 shows the most important quantities measured.

The ionization of the tracks was estimated by making comparisons with minimum ionizing particle tracks. Scattering of tracks in the plates of the chamber was also measured. Ionization and scattering were also observed with the viewer and from positive enlarged photographs.

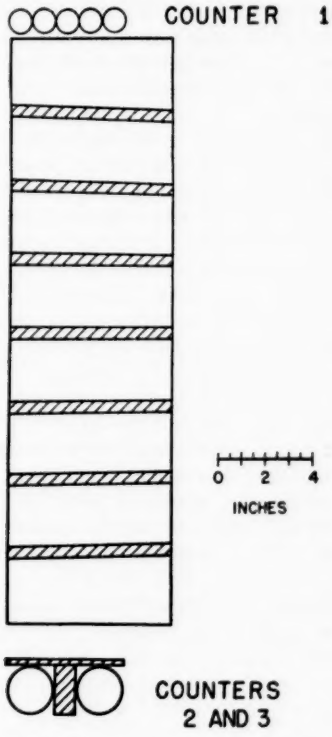

FIG. 1. Schematic diagram of the cloud chamber and counter arrangement.

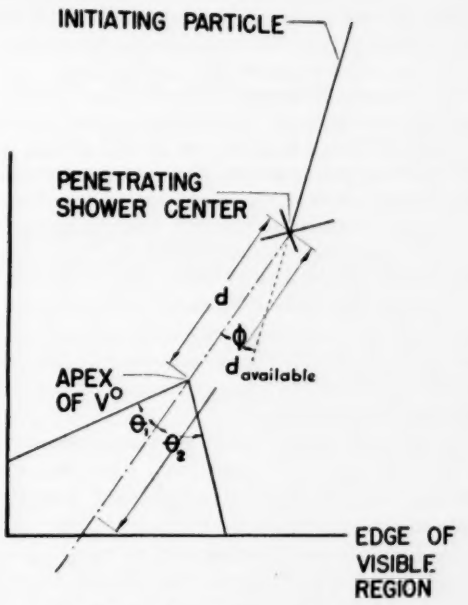

FIG. 2. Sketch showing some of the quantities measured in a picture of a V^0 particle.

Repeated measurements of the depth position of a penetrating shower center fell within a range of 0.4 cm. Horizontal and vertical positions of the penetrating shower center could usually be located to ± 0.1 and ± 0.2 cm, respectively, depending on the number and geometry of unscattered penetrating particles in the penetrating shower. The accuracy of measurements on particles depended on the orientation of the event, the distance from and orientation with respect to the penetrating shower center, and the lengths of unscattered track available for measurement. Measurements on how closely the plane of the V^0 event contained the penetrating shower center were made as follows. The penetrating shower center was moved to different off-coincidence positions, and the plane of the screen was reoriented to see if the V^0 images could be made to coincide. Then, with the origin of the penetrating shower in coincidence, different screen orientations were tried to determine when the V^0 event went out of coincidence. With certain events 2° shifts in the plane would result in noncoincidence. Most events were such that 5° shifts in planes would result in noncoincidence.

IDENTIFICATION OF V PARTICLES

Although it seems well established now that most V events are caused by unstable heavy particles, we have made a statistical study of V^0 events that occurred in the gas and in the lead plates of the cloud chamber in a series of 16,570 pictures taken when the chamber contained seven ½-inch lead plates. A total of 855 pene-

trating showers occurred in this series, two of which originated in the gas. The number expected to originate in the gas, assuming geometric cross sections, was 1.8.

The V^0 events observed in the gas fell into two sharply distinguished categories. Thirty-eight events were seen in which at least one of the tracks was at four times minimum ionization or less. No track from events in this category terminated in the gas of the chamber. Four events were seen in which both tracks were at least ten times minimum ionization. All but one track from events in this category terminated in the gas.

There was one neutral produced 5-prong star in the gas. There were two stars produced by charged particles in the gas, one with two prongs and one with five prongs, and there was one ten-prong star in which the producer could not be identified.

A total of 26 nonelectronic V^0 events were observed in the lead, and 14 V events, i.e., a charged particle entering the plate and two nonelectronic charged particles leaving the plate. A very large number of electronic V events and Y events were, of course, observed coming from the lead. Events were called nonelectronic only if the particles penetrated further lead plates without multiplication.

Events whose cross sections are proportional to the geometrical cross section should occur about 500 times more frequently in the lead than in the argon gas. Thus, one would expect $26/500=0.05$ V^0 events and $14/500=0.03$ V events of this kind in the gas. It is probable, however, that the four very low energy V events are actually neutron stars. No comparison with similar events in the lead can be made in this case, since the particles would not have emerged from the lead plates. It seems clear, however, that the 38 V^0 events of higher energy must originate in decay rather than collision processes. Some of the V events occurring in the lead must also be true V^0 particles, but these have not been included in the analysis.

TABLE I. Statistics of V^0 particle penetrating showers.

	V^0 producing showers	Percent	All showers	Percent
Charged primary	35	55	620	72
Neutral primary	3	5	46	5
Unknown primary	25	40	192	23
Multiplicities of penetrating particles	4.9 ± 1.2		4.4 ± 1.0	
Large showers	16%		14%	
Showers with only one penetrating particle	14%		5%	
Number of penetrating particles per V^0			80 ± 24	
Number of penetrating showers per V^0			18 ± 3	
Number of V^0's per calendar month				
Lake Sabrina			16	
Berkeley			2	
Penetrating particles per penetrating shower				
Lake Sabrina			4.4 ± 1.0	
Berkeley			4.3 ± 1.0	

COPLANARITY

It was possible to determine the coplanarity of 63 V^0 particles observed during the course of the experiment. Of these, 43 were coplanar as determined from the reprojector, 13 looked coplanar in the stereoscopic viewer (for various reasons they could not be reprojected) and 7 events were noncoplanar. Only those events were used where the penetrating shower origin was obvious.

If one assumes that all events are due to two-particle decay but that scattering might have taken place before decay to produce the noncoplanar events, a scattering mean free path can be estimated. The total amount of lead traversed by all V^0's is 1416 g/cm² of lead. If the coplanar events did not scatter and the noncoplanar events experienced single scattering only, a scattering mean free path of 200 ± 90 g/cm² of lead is calculated. In estimating the amount of lead traversed by noncoplanar V^0's, a most likely path with scattering in lead was assumed. Estimated angles of scatter were 10, 20, 30, 45, 70, 90, and 90 degrees.

Various three-particle decay schemes have been suggested.[9] These would require the decay into two oppositely charged particles and a neutral particle. The most easily identifiable neutral particle is the neutral meson. Its rapid decay into photons of high energy would result in the development of electron showers in the lead plates of the cloud chamber. No showers that might have been the result of the neutral meson were seen, although the usual electronic component in penetrating showers often made the observation uncertain.

From observations of scattering in the lead plates, ionization, and range, it is sometimes possible to make tentative identification of the decay products.[10] As is generally the case in such identification, errors in ionization estimates and poor statistics on scattering measurements combine to make the estimate of mass in an individual case quite uncertain. However, it is usually possible to distinguish a proton from a meson when they are above minimum ionization. In three pictures both tracks could be identified by the above procedures. These were all proton+meson decay events. In other pictures, only one of the particles could be identified: 4 were protons and 7 were mesons.

The penetrating showers in which V^0's were produced were examined and compared with all penetrating showers detected with the present apparatus to see if any trends could be noticed. The results are given in Table I.

Large showers have been arbitrarily defined as having 8 or more penetrating particles. The corresponding entries mean that, for example, 16 percent of the V^0 producing showers were large showers. Detection efficiency has been ignored, but it is obviously easier to see

[9] Leighton, Wanlass, and Alford, Phys. Rev. **83**, 843 (1951).
[10] W. M. Powell, Phys. Rev. **69**, 385 (1946).

V particles in small showers than in complicated large showers.

There seem to be no definite trends. Neutral as well as charged primaries produce events that yield V^0's. Both large and small showers give rise to V^0's. In two nuclear interactions that gave rise to V^0's, no penetrating particles were produced directly. In two other pictures, V^0's were accompanied by one other penetrating track. Nothing else of the same age as the V^0 track appeared in the chamber.

THE DYNAMICS OF DECAY

Before we proceed to an analysis of the data obtained, we will discuss briefly the dynamics of two-particle and three-particle decay in terms of our measurable quantities, which are somewhat different than those measured when the cloud chamber is in a magnetic field. The nature of the unstable neutral particle and the characteristics of the decay products are still not known exactly, and various possibilities must be considered.

The simplest types of decay schemes that may be assumed are the following:

$$V^0 \rightarrow (1)+(2), \qquad \text{(A)}$$

where (1) and (2) are charged particles of opposite signs and of mesonic mass or heavier; and

$$V^0 \rightarrow (1)+(2)+\nu, \qquad \text{(B)}$$

where ν is a neutrino, so chosen because the near coplanarity of the V^0 with its decay products would seem to rule out the emission of a heavier neutral particle, and the emission of a γ-ray is rendered unlikely by the lack of such observed secondary interactions as would normally accompany it. Of course, there may well be several different V^0's and several competing modes of decay. As a matter of fact, it is necessary to make an assumption of this kind to interpret existing data.

A. Two-Particle Decay

The dynamics of the two-particle decay process (A) are very simple and have already been discussed extensively in print.[2,8] The three particles involved must lie in a plane for momentum to be conserved, and, in the rest system of the V^0, the angle ϕ^* which the (equal and opposite) momenta of particles (1) and (2) make with the direction of the V^0 must be sinusoidally distributed:

$$F(\phi^*)d\phi^* = \sin\phi^* d\phi^*.$$

For completeness, and in order to fix the nomenclature, we list the conservation equations (the velocity of light $c=1$ throughout this paper). m and p refer to the mass and momentum of the V^0.

(1) In the center-of-mass system of the V^0:

$$p_1^* = p_2^* = p^*; \quad m = (m_1^2+p^{*2})^{\frac{1}{2}}+(m_2^2+p^{*2})^{\frac{1}{2}}.$$

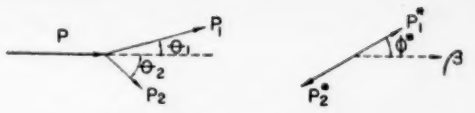

FIG. 3. Momentum vectors in two-particle decay.

(2) In the laboratory system:

$$p = p_1\cos\theta_1 + p_2\cos\theta_2; \quad p_1\sin\theta_1 = p_2\sin\theta_2;$$
$$(m^2+p^2)^{\frac{1}{2}} = (m_1^2+p_1^2)^{\frac{1}{2}}+(m_2^2+p_2^2)^{\frac{1}{2}}.$$

See Fig. 3. Once values for the masses are chosen, there are only two independent variables, which may be taken to be p_1, p_2, or θ_1, θ_2 or ϕ^*, γ, where $\gamma=(1-\beta^2)^{-\frac{1}{2}}$, β = velocity of the V^0. The relativistic transformation equations for the angles are

$$\cot\theta_1 = \gamma\left(\cot\phi^* + \frac{\beta}{\beta_1^*}\csc\phi^*\right);$$

$$\cot\theta_2 = \gamma\left(-\cot\phi^* + \frac{\beta}{\beta_2^*}\csc\phi^*\right).$$

These equations underlie much of the development which is to follow (they are valid, of course, no matter what the decay scheme). They can also give some insight into the behavior of θ_1 and θ_2, which are important quantities for our analysis.

It is also seen that, if $\beta>\beta_1^*$, then θ_1 is acute for all values of ϕ^*, its maximum value being

$$\cot\theta_1 = (\gamma\beta/\beta_1^*)(1-\beta_1^{*2}/\beta^2)^{\frac{1}{2}},$$

which is near the most probable value for $\beta \gg \beta_1^*$. Similar considerations apply to β_2^* and θ_2. The total opening angle θ is also restricted in range for certain β's, and curves exhibiting its variation with ϕ^* are given by Butler.[8]

In order to discuss what use may be made of those results, the experimental apparatus must be considered. The apparatus now in use in various laboratories differs as follows: (1) a magnetic field may or may not be present; (2) the initial event giving rise to the V^0 can or cannot be located. If a magnetic field is present, (Leighton *et al.*;[9] Manchester group[2]), independent estimates of m_1 and m_2 can be made, using track ionizations. Those estimates are usually compatible with the identification of (1) and (2) with known particles (protons and π-mesons), within the error inherent in the ionization measurements. One can then obtain the mass of the V^0 in terms of p_1, p_2, and θ.[2] *If the initial event can be located*, the two-particle decay assumption may be tested directly by checking the coplanarity of the V^0 with the center of the initial event, as well as the transverse momentum balance.

Granting that the observations are found to be at least partially fitted by one or more two-particle decay

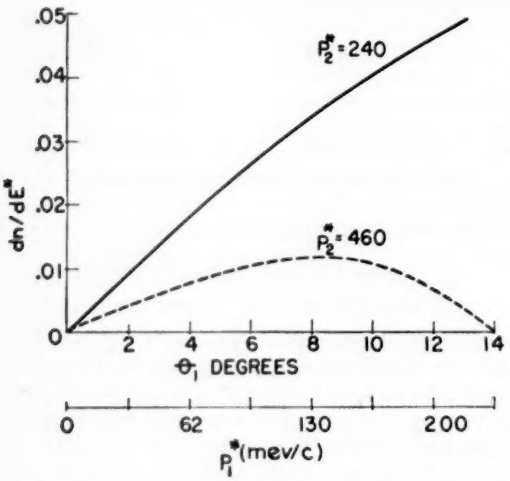

FIG. 4. Distribution functions for the momentum of the proton in three-particle decay.

schemes, the distribution in ϕ^* may be obtained and compared with the theoretical sinusoidal distribution. If the initial event is not located (θ_1, θ_2 not known), one may use

$$\sin\phi^* = p_1 p_2 \sin\theta / pp^*.$$

If there is no magnetic field, but the initial event can be located, the only measurable quantities of the ones which occur in the conservation equations are θ_1 and θ_2. One must therefore assume, *a priori*, one or more reasonable decay processes. The number of such processes is restricted by the coplanarity property and by the characteristics of the decay tracks (penetration, ionization, etc.). If one makes the simplest plausible assumption of a V^0 decaying into two known charged particles only, the V^0 mass becomes the only adjustable parameter, and one has two criteria with which to make the adjustment: the distribution in ϕ^* and the observed ionizations of the decay tracks. In terms of θ_1 and θ_2, these quantities are given by[11]

$$\cos^2\phi^* = \frac{1+\delta^2+1/\sigma^2-[(1+\delta^2+1/\sigma^2)^2-4\delta^2]^{\frac{1}{2}}}{2},$$

where

$$\delta = \frac{1/\beta_2^* - K/\beta_1^*}{1+K}, \quad K = \frac{\tan\theta_1}{\tan\theta_2}, \quad \sigma = \frac{\cot\theta_1+\cot\theta_2}{1/\beta_1^*+1/\beta_2^*},$$

and the sign of $\cos\phi^*$ is the same as the sign of δ;

$$\beta_1 = \frac{\sin\phi^*/\sin\theta_1}{[m_1^2/p^{*2}+\sin^2\phi^*/\sin^2\theta_1]^{\frac{1}{2}}} \text{ (similarly for } \beta_2).$$

β_1^*, β_2^* and p^* are, of course, functions of m, m_1, m_2 only.

[11] M. M. May, Ph.D. thesis, University of California, 1952 (unpublished).

In addition, the decay tracks may undergo ionization changes, scattering, and other significant interactions. In particular, a track may stop within a known thickness of lead, thus allowing an upper limit to be set on p_1 or p_2 as the case may be. The other momentum is then obtained from transverse momentum conservation, and an upper limit for m, the V^0 mass, can be calculated by the formula given above. If the track penetrates one or more plates before stopping (but suffers no nuclear interactions), both an upper and a lower limit for m may be found.

B. Three-Particle Decay

One is led to the assumption of three-particle decay for the V^0 mainly by the impossibility of explaining the experimental data by means of a single two-particle decay process, since the energy available in the center-of-mass system of the V^0 does not have a unique value. As an alternative to postulating the existence of two types of V^0's, with what turns out to be similar lifetimes and frequency of production but different masses, decay products, and possibly different spins, the hypothesis of a single V^0 with a single three-particle decay has been advanced.[12] The third particle is taken to be a neutrino. The particular decay scheme,

$$V^0 \rightarrow p + \mu^- + \nu,$$

may be thought attractive in the light of the fact that a lifetime of 10^{-10} second yields very closely the coupling constant for Fermi interactions,[6] and this scheme has been used as a numerical example in what follows. Replacing the μ^- means by a π^- makes very little difference quantitatively.

We consider first the general process

$$V^0 \rightarrow (1) + (2) + \nu,$$

(1) and (2) being massive particles. Obviously, it is impossible to draw exact conclusions as to angular and momentum spectra without a detailed interaction theory. Still, one may expect to observe any sharply varying functional dependences of the phase space factor in the transition rate formula on observable quantities:

$$\frac{dn}{dE} = \frac{2}{\pi\hbar^3} \frac{p_1^2 dp_1 p_2^2 dp_2}{dE} d\Omega_1 d\Omega_2.$$

We proceed to look for such variations. We shall work first in the center-of-mass system of the V^0, where we note that (a) there are two independent variables relevant to the decay process, as the momentum triangle can be specified by three variables and the energy equation makes one of them a function of the other two; we choose for these variables p_1^* and p_2^*, the momenta of (1) and (2) in the center-of-mass system; (b) in the

[12] K. A. Brueckner and R. W. Thompson, Phys. Rev. **87**, 390 (1952). T. D. Lee, private communications.

elements of solid angle $d\Omega_1 d\Omega_2$, there is only one angle which affects physically significant quantities in the center-of-mass system; the others specify the position of the momentum triangle in space; we choose for that angle θ^*, the angle between p_1^* and p_2^*, and lump the others into the symbol $d\Omega'$, so that $d\Omega_1 d\Omega_2 = \sin\theta^* d\theta^* d\Omega'$.

The conservation equations for energy and momentum yield

$$\cos\theta^* = [(E^* - E_1^* - E_2^*)^2 - p_1^{*2} - p_2^{*2}]/2p_1^* p_2^*,$$

where

$$E_1^* = (m_1^2 + p_1^{*2})^{\frac{1}{2}}; \quad E_2^* = (m_2^2 + p_2^{*2})^{\frac{1}{2}}.$$

E^*, the total energy available, $= m$, the V^0 mass. Then

$$d(\cos\theta^*)/dE^* = (E^* - E_1^* - E_2^*)/p_1^* p_2^*,$$

and

$$\frac{dn}{dE^*} = \frac{2}{\pi\hbar^3} p_1^* p_2^* (E^* - E_1^* - E_2^*) dp_1^* dp_2^* d\Omega'.$$

As a function of p_1^*, this expression vanishes at $p_1^* = 0$ and at $E_1^* = E^* - E_2^*$. The latter limit corresponds to the largest value which p_1^* can take on for any p_2^*. However, p_2^* is an independent variable, and, for a given p_2^*, p_1^* can only range from 0 to

$$[(E^* + p_2^* - E_2^*)^2 - m_1^2]/2(E^* + p_2^* - E_2^*).$$

Thus, if we plot a set of curves of dn/dE^* *vs* p_1^*, each curve corresponding to one value of p_2^*, dn/dE^* is seen not to vanish when p_1^* reaches its upper limit as determined by the conservation equations, except on the curve defined by

$$p_2^* = \left[\frac{(m^2 - m_1^2 - m_2^2)^2 - 4m_1^2 m_2^2}{4m^2}\right]^{\frac{1}{2}}.$$

For that case, in the upper limit $p_1^* = p_2^*$, no neutrino is emitted, and the momenta of both (1) and (2) reach their largest possible values. Such a curve is plotted in Fig. 4 (dotted line) for a plausible set of values of m, m_1, m_2. A curve corresponding to a lower, and more probable value of parameter p_2^* is also shown (full line). For that case, we see that not only does dn/dE^* not vanish when p_1^* reaches its upper limit, but the upper limit is reached before dn/dE^* passes through its maximum, a maximum which occurs when p_1^* satisfies

$$E_1^* + p_1^{*2}/E_1^* = E^* - E_2^*.$$

We proceed to use these results to obtain a distribution in θ_1, the angle which the proton in the laboratory system makes with the V^0 (see Fig. 5). For not too slow V^0's, this angle is expected to be small, because p_1^*, p_2^*, and p_ν^* will tend to be approximately equal (on the basis of phase space considerations only), making the velocity of the proton in the center-of-mass system, β_1^*, small, and its (vector) velocity in the laboratory system, β_1, not very different from the velocity of the

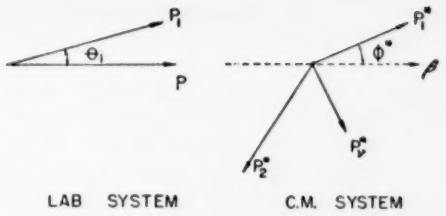

FIG. 5. Momentum vectors in three-particle decay.

V^0, β. The Lorentz transformation on angles gives

$$\tan\theta_1 = \frac{p_1^* \sin\phi^*}{\gamma(p_1^* \cos\phi^* + \beta E_1^*)} = \frac{\sin\phi^*}{\gamma(\cos\phi^* + \beta/\beta_1^*)},$$

where the nomenclature is taken over unchanged from the discussion of two-particle decay (see Fig. 3). We note again that $\tan\theta_1$ increases monotonically with β_1^*, but, as a function of ϕ^*, reaches a maximum at $\cos\phi^* = -\beta_1^*/\beta$. Since, as we have seen, β_1^* possesses an upper limit corresponding to $E_1^* = E^* - E_2^*$ and depending only on the values of the masses, there exists a similar upper limit to $\tan\theta_1$. Choosing $m = 2400$ electron masses (on the high side of the plausible range), $m_1 = 1836$ and $m_2 = 210$ gives

$$\tan\theta_1 \leq \frac{0.25}{\gamma\beta} \frac{1}{(1 - (0.25/\beta)^2)^{\frac{1}{2}}}.$$

At this point, we introduce a nonrelativistic approximation for p_1^* and E_1^*, since all evidence points to a disintegration energy small (10–20 percent) compared with the proton mass. In order to obtain the distribution function in terms of θ_1 and ϕ^*, it must be noted that five independent variables are needed to specify the momenta and the angles between them in the laboratory system. Those variables may be taken to be p_1^*, p_2^* (or alternately θ_1, p_2^*), β, ϕ^*, and ψ, where ψ is the angle between the plane containing p_1^*, p_2^*, and p_ν^* and the plane containing p_1^* and β. The symbol $d\Omega'$ which occurs in the expression for dn/dE^* can be written out explicitly:

$$d\Omega' = 2\pi \sin\phi^* d\phi^* d\psi,$$

where the 2π comes from integration over an angle expressing rotation of the entire figure about the direction of the V^0 as an axis. We then have

$$\frac{dn}{dE^*} = \frac{4}{\hbar^3}\gamma^2\beta^2 m_1^2 p_2^* \frac{\tan\theta_1 \sec^2\theta_1 \sin^2\phi^*}{(\sin\phi^* - \gamma \tan\theta_1 \cos\phi^*)^3} \times\left[E^* - E_2^* - m_1 - \tfrac{1}{2}m_1\left(\frac{\gamma\beta \tan\theta_1}{\sin\phi^* - \gamma \tan\theta_1 \cos\phi^*}\right)^2\right] \times d\theta_1 d\phi^* dp_2 d\psi.$$

The corresponding relativistic expression has been calculated.[11] A representative plot may perhaps be ob-

TABLE II. Observed and calculated data for 34 coplanar measurable V^0 decays.

$p+\pi$ $m=2210$	No.	θ_1	θ_2	$I_{1\,obs}/I_{min}$	$I_{2\,obs}/I_{min}$	Identification (1)	(2)	d cm	d_a cm	ϕ	ϕ^*	$I_{1\,calc}/I_{min}$	$I_{2\,calc}/I_{min}$	γ	$t\times10^{10}$	$t_a\times10^{10}$
	38,789	9	27	2	1	p		13.0	24	13	116	2.5	1.5	1.3	5.2	10.2
	41,596	0	44	1	1			4.0	37	40	0	...	...	...	...	...
	46,386	23	42	4	1			6.8	13		117	12	2	1.0	7.1	12.5
a	48,580	5	22	1	1			11.5	25	35	96	1.5	1	1.7	2.7	5.8
	51,313	10	30	3	1			6.5	42		114	3	1.5	1.2	3.0	20.0
	51,689	9	34	4	1			4.0	30	30	98	2.5	1.5	1.3	1.7	12.8
	56,318	37	81	10	3			1.9	10		90	20	2	1.0	4.0	21.3
a	56,611	5	21	1	1	p	π	5.4	25	42	100	1.5	1	1.7	1.2	5.8
	57,384	12	28	3	1			5.3	7		126	5.5	1.5	1.1	3.2	4.2
a	57,424	2	9	1	1			1.5	26	26	99	1	1	3.7	0.14	2.4
	60,186	14	61	5	2			5.5	7	24	80	4.5	2	1.1	3.9	5.0
	60,484	15	54	4	2			2.8	10		90	5	2	1.2	5.1	11.3
	61,331	13	27	4	1			1.1	7		130	6	1.5	1.1	0.73	4.6
a	61,582	2	10	1	1		π	13	16		90	1	1	3.7	1.2	1.5
	61,759	10	35	3	1	p		2.7	7		102	3	1.5	1.2	1.2	3.2
	62,220	22	54	2	1.5			3.7	8		99	9.5	2.5	1.1	3.7	8.0
a	62,419	5	15	1.5	1.5		π	23	45		128	2	1	1.6	6.5	9.5
b	73,834	3	32	1	1			4.1	40		46	1.5	2	1.8	0.90	8.7
	75,535	8	23	2	1	p		5.0	9	47	122	2.5	1	1.3	2.0	3.6
	77,217	14	32	3	1			13.2	18		119	5.5	1.5	1.1	8.6	11.7
	77,242	6	8	10	1.5			2.8	7	149	166	12	1.5	1.1	2.2	5.5
	77,771	18	52	4	1.5			2.8	11		98	7	2	1.1	2.3	9.2
	80,322	26	32	6	1			11.2	22	34	137	20	2	1.0	13.5	26.5
$\pi+\pi$ $m=800$																
	38,385	12	21	1	1.5			14.2	23.5	24	68	1	1	2.6	2.0	3.2
	38,521	14	19	1	1			13	22	13	78	1	1	2.6	1.8	3.1
	40,881	25	45	1	1			4.3	24	35	68	1	1.5	1.4	1.4	7.8
	41,610	20	72	1	4	π		17.6	43	15	46	1	1.5	1.3	7.4	18.1
	43,891	5	6	1	1			12.3	30	39	83	1	1	7.4	0.66	1.4
	47,698	12	38	1	2		π	2.6	15	34	48	1	1.5	1.8	0.57	3.3
a	48,580	5	22	1	1			11.5	25	35	33	1	1.5	2.9	1.4	3.1
	49,310	9	12	1	1		π	3.7	14	13	79	1	1	3.9	0.33	1.2
a	56,611	5	21	1	1	p	π	5.4	25	42	35	1	1.5	3.1	0.61	2.8
a	57,424	2	9	1	1			1.5	26	26	30	1	1	6.3	0.08	1.4
	58,647	10	29	1	1		π	3.5	40		52	1	1.5	2.2	0.61	7.0
a	61,582	2	10	1	1		π	13	16		24	1	1	5.3	0.84	1.0
a	62,419	5	15	1.5	1.5		π	23	45		47	1	1	4.1	1.9	3.8
	72,699	8	18	1	1			10.6	21	29	58	1	1	3.5	1.1	2.2
	73,548	6	12	1	1			8.8	22	33	63	1	1	4.5	0.67	1.7
b	73,834	12	28	1	1		π	9.0	30		58	1	1	2.2	1.5	5.1

[a] These observations could be either $p+\pi$ or $\pi+\pi$ decays from the standpoint of ionizations.
[b] These observations form a V^0 pair.

tained by setting $\phi^*=\pi/2$, $\gamma\beta=1$, and choosing for p_2^* the value which it has when $p_1^*=p_2^*=p_\nu^*$. For the masses listed above, that value is 240 electron masses. Such a plot is given in Fig. 4. Note that the conservation requirements impose a cutoff on θ_1 (i.e., on β_1^*) before $dn/dE^*(\theta_1)$ reaches its maximum. Also shown in a similar plot for $p_2^*=460$ electron masses, the largest value it can take on. It is clear that the most likely values of $\tan\theta_1$ are of the same order of magnitude as its upper limit.

Since that upper limit corresponds to two-particle decay ($p_\nu^*=0$), the range of most probable values of θ_1 determined by a certain V^0 momentum under the assumption of three-particle decay lies close to the value of θ_1 determined by the same V^0 momentum under two-particle decay. Thus, a given experimental θ_1 distribution gives similar V^0 momentum distributions under both assumptions, and consequently, similar spreads in the angles and ionizations of the decay tracks. Hence, it would be difficult to use θ_1 measurements to differentiate between the two assumptions.

Another distribution of interest which may be obtained is the distribution in p_ν^*, the momentum of the neutrino in the center-of-mass system. If a three-particle decay process is interpreted as two-particle decay and one attempts to determine the V^0 mass from the experimentally measurable quantities p_1, p_2, and θ (the angle between p_1 and p_2), one obtains instead of the true V^0 mass m, a relativistically invariant expression m'[9]:

$$\begin{aligned} m'^2&=(E_1+E_2)^2-(p_1+p_2)^2\\ &=(E_1^*+E_2^*)^2-(p_1^*+p_2^*)^2\\ &=m^2-2mp^*. \end{aligned}$$

Since actually, if a three-particle decay does exist, with a disintegration energy of order $m/10$ to $m/5$, p_ν^* will be of the order $m/10$ or smaller, and, to a first approxi-

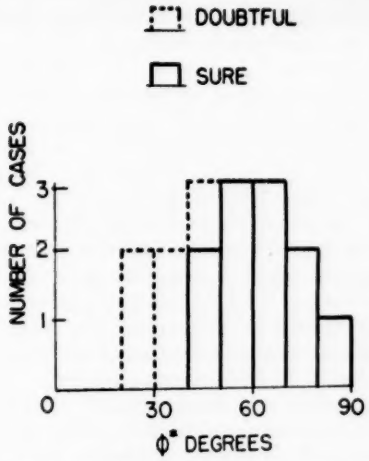

FIG. 6. Distribution in ϕ^* for $\pi+\pi$ cases.

mation, we will have

$$m'=m(1-2p_\nu^*/m)^{\frac{1}{2}}\cong m-p_\nu^*.$$

Since histograms of m' (or rather of its equivalent $Q'=m'-m_1-m_2$) are available, the p_ν^* distribution is therefore of some interest. We have

$$\frac{dn}{dE^*}=\frac{2}{\pi\hbar^3}p_1^*p_\nu^*(E^*-E_1^*-p_\nu^*)dp_1^*dp_\nu^*d\Omega''.$$

Thus, p_ν^* ranges from 0 to $E^*-E_1^*(=m-E_1^*)$ and maximizes dn/E^* at $(m-E_1^*)/2$. This is the usual result to be expected in any three-particle decay process involving a neutrino.

Brueckner and Thompson[12] have investigated the distribution in δ, the angle which the V^0 makes with the plane of the proton and meson ($\delta\leqslant\theta_1$) (an angle which would vanish under the assumption of two-particle decay), and have found a broad maximum at $\delta=0$. A study of the dependence of dn/dE^* upon the other angles and the momenta has failed so far to reveal any striking characteristics such as might be used to distinguish between two-particle and three-particle decay. In particular, there seems to be no correlation between the directions of the three decay particles in the center-of-mass system if, as indicated by phase space arguments, their momenta tend to be equal in that system. Thus, if one expresses dn/dE^* as a function of θ^* and, say p_2^*, even assuming particle (1) to be very heavy in comparison with particle (2), the distribution in θ^* is not sharp except in the (unlikely) case that p_1^* and p_2^* are much larger than p_ν^*; then, dn/dE^* is maximum at $\theta^*=180°$. Similar conclusions can be drawn for the other angles.

RESULTS

The data, together with quantities calculated from the data in terms of various decay schemes, are presented in Table II. We concern ourselves now with the 34 coplanar measurable cases, omitting those where the measurements were uncertain or impossible. In 16 cases the slower particle came off at the smaller angle and therefore, must, have been heavier. Since the particles are not electrons and have a lifetime of order 10^{-8} second or longer (this is deduced from the dimensions of the chamber and the lack of observed decays), the decay particles are either hitherto unknown particles or else must be identified as a proton and a meson (π or μ), respectively. We shall assume a π-meson rather than a μ-meson, because $\pi-\mu$ decays have been observed and π-mesons, as distinguished from μ-mesons, have been identified in a few similar cases elsewhere.[2,9] We therefore postulate

$$V_1^0\rightarrow p+\pi. \qquad \text{(C)}$$

Observed ionizations in 16 cases then lead to a V_1^0 mass between 2200 and 2400 electron masses. This hypothesis also leads to agreement with observed ionizations in 7 more cases, in all of which both particles travel at minimum ionization. In the remaining 11 cases, however, the hypothesis leads to disagreement with observed ionizations well outside experimental error. All but 2 of those 11 cases involve minimum ionization particles only, and could be accounted for by decay scheme (C) with a V^0 mass of order 2700–2800. The 2 exceptions involve a slower particle (which comes off at the larger angle), and decay scheme (C) cannot explain them at all. We have not attempted to use the ionization estimates in an accurate way. If the observed and calculated ionizations agree to a factor of two, this is considered satisfactory. When an ionization is listed as 1.5 $I_{\min}$, it means only that the track looked slightly above minimum, and probably not as much as 3 $I_{\min}$, for example.

Following a suggestion due to the Manchester group,[2] we attempt to explain these 11 cases by postulating a second decay scheme:

$$V_2^0\rightarrow\pi^++\pi^-. \qquad \text{(D)}$$

A V_2^0 mass of 700 to 900 electron masses can then account for the observed ionizations in all 11 cases, as well as 5 of the 7 minimum ionization cases which could also be accounted for by decay scheme (C). Thus, we have in all 18 cases which can only be explained by scheme (C), 11 cases which can only be explained by scheme (D), and 5 cases which can be explained by either.

We next attempt to determine the V^0 masses more closely. Given any mass value, we can compute a ϕ^* distribution. However, except for 8 cases where one of the decay particles stops in the chamber, we cannot measure masses directly. Other experimental groups,[2,4,9] working with magnetic fields, have measured them, and we shall begin by using the values which they obtained and by examining the corresponding ϕ^* distribution.

For decay processes (D), the Manchester group[2]

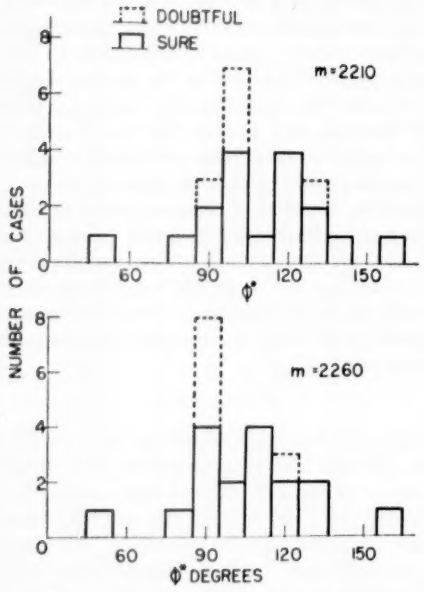

FIG. 7. Distribution in ϕ^* for $p+\pi$ cases.

obtains a V_2^0 mass of 800 electron masses. This value yields the ϕ^* histogram shown in Fig. 6. We have plotted both the 11 cases which can only be explained by decay scheme (D) (solid line) and those 11 plus the the 5 which can be explained by either scheme (dotted line). While there are too few observations for the result to be very significant, it can perhaps be concluded that most if not all of the 5 doubtful cases should be accounted for by scheme (C), where, as we shall see, they lead to more probable values of ϕ^*. It should be noted that, since we cannot differentiate between positive and negative decay products, we cannot tell whether ϕ^* is greater or less than 90°. Little more can be said about these data other than that they are compatible with the Manchester assumption. Observed and calculated ionizations, together with the measured angles θ_1 and θ_2 are shown in Table II.

For decay process (C), the Manchester group obtains a V_1^0 mass of 2210 electron masses.[2] The corresponding ϕ^* histogram is shown in Fig. 7 (dotted line graph includes doubtful cases), and the observed and calculated ionizations are compared in Table II. It is seen that the calculated ionizations are on the whole larger than the observed values (although not outside experimental error; the two worst cases, 46,386 and 62,220, are both "borderline" events so far as accuracy of measurement is concerned) and that an excess of protons seems to be emitted backward in the center-of-mass system of the V_1^0. Both conditions can be remedied by increasing the V_1^0 mass. Leighton *et al.*[9] quote two measured mass values for process C, 2170 and 2260. The former leads to somewhat worse disagreement with our data than does the Manchester figure. The latter improves the situation only slightly (see Fig. 7). Calculations based on a V_1^0 mass of 2350 electron masses have also been carried out for purposes of comparison. This last value is in outright disagreement with the experimental results of all other groups and results are not shown for that reason. A more nearly normal ϕ^* distribution was indeed obtained, however, and the calculated ionizations, although on the light side, agreed with the observed values within the experimental error.

This excess of type (C) decays for which $\phi^*>90°$ for accepted values of the V_1^0 mass is somewhat puzzling. The cloud chamber tends to select low energy V_1^0's, since the initial event and the decay must both be contained within a limited volume. However, two independent variables are needed to specify the process in the laboratory system, and we may choose ϕ^* and γm, the V_1^0 energy, to be those two variables. Therefore, for any given V_1^0 energy, the distribution in ϕ^* should still be sinusoidal. It is certainly true that if the V_1^0 is of high energy, and it is required that the proton be above minimum ionization for identification, the distribution will be biased toward events where the proton came out backwards. But, since most of our V^0's are low energy and in addition, the 5 uncertain cases (all of which involve minimum ionization particles only) are included with the 18 "sure" type (C) decays (16 of which involve protons at heavier than minimum ionization), we cannot invoke a bias toward slow protons which would tend to be emitted backwards in the center-of-mass system. Including these 5 cases, we have 17 events with $\phi^*>90°$ *vs* 6 events with $\phi^*\leqslant 90°$ for $m=2210$ and 16 events with $\phi^*>90°$ *vs* 7 events with $\phi^*\leqslant 90°$ for $m=2260$. If anything, adding the 5 uncertain events makes the

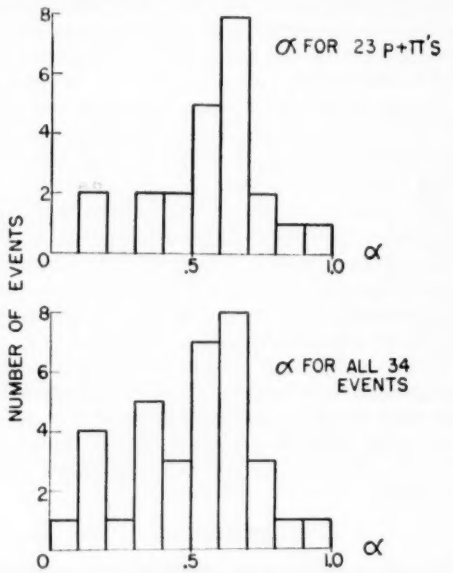

FIG. 8. Distribution in $\alpha=\sin(\theta_2-\theta_1)/\sin(\theta_2+\theta_1)$.

distribution worse (see Fig. 7). Poor statistics or some unknown systematic error in measurement of the angles (e.g., overestimating both θ_1 and θ_2) might explain the asymmetry.

For completeness, we have plotted in Fig. 8 the distribution in α, where[2]

$$\alpha=\frac{\sin(\theta_2-\theta_1)}{\sin\theta}=\frac{m_1^2-m_2^2}{m^2}+\frac{2p^*\cos\phi^*}{\beta_m}.$$

Since the average and most probable value of $\cos\phi^*$ is zero, the distribution should center about $(m_1^2-m_2^2)/m^2$. This is 0.65 for $m=2260$ and 0.67 for $m=2210$. Instead, as seen in Fig. 8, the lower values of α predominate and, since θ_1, θ_2, and θ are measured quantities, we have thus a fairly direct confirmation of the ϕ^* histograms.

In 8 cases, one or both secondary particles stop within one of the lead plates in the chamber. This allows us to set an upper limit on its momentum, and thereby also on the mass m of the V^0, by means of transverse momentum considerations and the formulas developed previously. The results are shown in Table III. It is seen that, in 4 of the 8 cases, the maximum V^0 mass is of order 2200 electron masses (only two figures are significant) in agreement with the work of other experimenters referred to above. One of these cases, 56 611, is listed as uncertain on the basis of ionization evidence. However, scattering measurements seem to identify it as a $p+\pi$ decay. Another event, 80,322, is also of some interest, as particle (2), presumably a π-meson traveling at or near minimum ionization, also stops. Its range is no more than 1.4 cm of brass. This would put its momentum at 120 Mev or less, while the transverse momentum balance yields $p_2=434$ Mev. Since the particle does not leave the chamber, one is led to the conclusion that some nuclear interaction must have taken place in the brass. This would tend to indicate that particle (2) is indeed a π-meson rather than a μ-meson.

Finally, the momentum distribution for both types of V^0's have been plotted (Fig. 9). The peak for the V_1^0 with $m=2210$ comes near $\beta\gamma=0.6$, and for the V_2^0, near 2. Since, however, the former is nearly 3 times as heavy as the latter, the actual most likely momenta in Mev are the same for both particles and of the order 600–800 Mev. The momentum distribution for V_1^0 with $m=2260$ can be obtained from the plotted distribution for V_1^0's with $m=2210$ by multiplying the scale figures by 1.2.

TABLE III. Determination of V^0 mass from range of secondary particle (all cases assumed $p+\pi$).

Observation number	Particle measured	Maximum range cm of Pb	Maximum V^0 mass $\times 10^2 m_e$
46,386	proton	1.5	2.3
51,313	proton	1.5	2.2
56,611	meson[a]	4.0–5.3	2.2
61,331	proton	1.6	2.2
77,217	proton	1.8	2.2
77,242	proton	1.3	2.3
77,771	proton	1.3	2.3
80,322	proton	2.1[b]	2.5

[a] Identified from scattering. [b] Cm of brass.

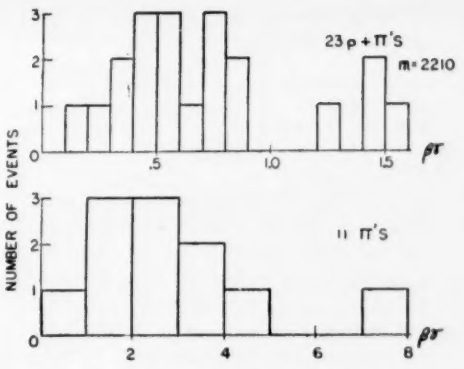

FIG. 9. Distribution in $\beta\gamma$ for all events.

LIFETIMES

The apparatus used required that both the initial event and the decay of the V^0 be contained within the illuminated volume of the cloud chamber before measurements could be carried out. The time of decay in the rest system of the V^0, t, was given by the measured distance d from initial event to apex of V and by the velocity of the V^0, which was derived from the angles and depended therefore on the mass and decay scheme assumed: $t=d/\beta\gamma c$, $\gamma=1/(1-\beta^2)^{\frac{1}{2}}$. Similarly, the "available decay time" t_a was defined by $t_a=d_a/\beta\gamma c$, where d_a was a distance measured from the initial event along the line of flight of the V^0 to the furthest point where the decay event could have been observed and identified. The ith observation could therefore be characterized by two numbers t_i and t_{ai}, and since necessarily $t_i>t_{ai}$, our selection of data was biased and the mean life, calculated from

$$\bar{t}=\sum_{i=1}^{N} t_i/N \qquad (1)$$

(N = total number of observations), was expected to be smaller than the true value τ.

A first-order correction can be worked out as follows. For every observed decay occurring before t_{ai}, there will be, on the average,

$$\frac{e^{-t_{ai}/\tau}}{1-e^{-t_{ai}/\tau}}$$

particles decaying after t_{ai}. These unobserved particles will have a mean decay time $\tau+t_{ai}$, and the sum over t_i's in Eq. (1) should therefore be replaced by

$$\sum_{i=1}^{N}\left[t_i+(\tau+t_{ai})\frac{e^{-t_{ai}/\tau}}{1-e^{-t_{ai}/\tau}}\right].$$

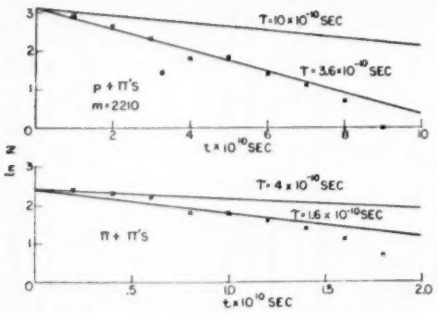

FIG. 10. Plot of measured and corrected lifetimes.

Similarly, the total number of observations is not N, but is

$$N+\sum_{i=1}^{N}\frac{e^{-t_{ai}/\tau}}{1-e^{-t_{ai}/\tau}}=\sum_{i=1}^{N}\frac{1}{1-e^{-t_{ai}/\tau}}.$$

Hence,

$$\tau=\sum_i\left[t_i+(\tau+t_{ai})\frac{e^{-t_{ai}/\tau}}{1-e^{-t_{ai}/\tau}}\right]\Big/\sum_i\frac{1}{1-e^{-t_{ai}/\tau}}$$

$$=\frac{1}{N}\sum_i\left[t_i+\frac{t_{ai}}{e^{t_{ai}/\tau}-1}\right]. \tag{2}$$

The same formula is obtained[13] by considering the probability density function for observing N decays occurring at t_i, $i=\cdots N$, observation being conditioned on $t_i\leqslant t_{ai}$:

$$P(\tau)=\prod_{i=1}^{N}\frac{e^{-t_{ai}/\tau}}{\tau(1-e^{-t_{ai}/\tau})},$$

and then making a maximum likelihood estimate of τ, i.e., solving the equation

$$-(\partial/\partial\tau)\ln P(\tau)=0.$$

By this method, one can also obtain an estimate of the variance

$$\sigma^2=\left\{\sum_{i=1}^{N}\left[\frac{1}{\tau^2}-\frac{e^{t_{ai}/\tau}}{\tau^4}\left(\frac{t_{ai}}{e^{t_{ai}/\tau}-1}\right)^2\right]\right\}^{-1}. \tag{3}$$

Equation (3) neglects errors in d and in $\beta\gamma c$, the latter being much larger than the former. Taking these errors into account leads of course to a larger variance, as does taking into account the fact that these errors are not the same in all cases. The details have been worked out,[13] but they are not reported here since it is felt that they cannot have much significance at this time in view of the tentative nature of our conclusions. As seen below, even the minimum statistical variance (3) is sufficiently large so that taking experimental error into account will not make it much larger. Since the plates were only one-half inch thick, we have not corrected for particles decaying before they leave the plate in which they were created. We have also neglected the intervening plates since during most of the experiment they were evenly spaced and thus introduce no bias.

For decays of type C, including both sure and uncertain cases, the average decay time in the center-of-mass system, $\bar{t}$ was 3.6×10^{-10} second if $m=2210$ electron masses, and 3.0×10^{-10} second if $m=2260$ electron masses. The corresponding corrected mean lifetimes τ, obtained by Eq. (2), were 10×10^{-10} second and 8×10^{-10} second with statistical variance of $\pm7\times10^{-10}$ second and $\pm6\times10^{-10}$ second, respectively. These variances are larger by a factor of three than the statistical error based solely on the limited number of observations, and the large factor is due to the strong bias introduced by the limited size of the cloud chamber. For decays of type D, we include only the 11 sure cases since it was felt that most or all of the 5 uncertain cases were $p+\pi$ decays. The uncorrected average decay time was 1.6×10^{-10} second, and the corrected lifetime was 4×10^{-10} second with a variance of 3×10^{-10} second. A semilogarithmic plot of number of particles not decayed *vs* time is shown in Fig. 10. The conclusions which can safely be drawn from the data are, therefore, (1) the decays postulated have mean lifetimes of order 10^{-10} to 10^{-9} second; and (2) the lifetime against type C decays may be different from the lifetime against type D decays by a factor which seems to be of order 2, but which may be as large as order 10.

Knowledge of the t_i's and the t_{ai}'s may also cast some light on the hypothesis of the creation of V^0's in pairs,[14] which was put forth in an attempt to explain the long V^0 lifetimes by means of universal nuclear coupling constants. If a second V^0 has certainly been created whenever one is observed, the probability for observing the second one is

$$P\left(\frac{T_a}{\tau}\right)=\frac{1}{\tau}\int_0^{T_a}e^{-t/\tau}dt=1-e^{-T_a/\tau},$$

where T_a is some average time available for decay in the center-of-mass system. Let us assume that both members of any pair have the same lifetime, the same T_a and are emitted on the average with the same energy. The uncorrected average decay time for either member of the pair is

$$\bar{t}=\int_0^{T_a}te^{-t/\tau}dt\Big/\int_0^{T_a}e^{-t/\tau}dt,$$

or

$$\bar{t}=\frac{\tau}{1-e^{-T_a/\tau}}\left[1-e^{-T_a/\tau}\left(1+\frac{T_a}{\tau}\right)\right]. \tag{4}$$

We have seen that for either decay scheme

$$\bar{t}/\tau=\tfrac{1}{2}\quad\text{to}\quad\tfrac{1}{4}.$$

[13] B. Rankin (private communication).

[14] A. Pais, Phys. Rev. 86, 663 (1952).

Substituting into (4) and solving for T_a/τ gives 1.25 to 0.55. As would be expected, this is approximately the value obtained for the ratio of the average of the actual t_{ai}'s to τ. Putting it into $P(T_a/\tau)$ gives 0.71 to 0.42, i.e., pairs should be observed in 42 to 71 percent of all cases. Actually 3 pairs were observed in 65 cases. One involved one type C decay and one type D decay. Another involved a type C decay and an unmeasurable event, and the third involved an uncertain case and an unmeasurable event. In at most 10 other pictures, pairs could have occurred and escaped detection, owing to heavy electronic showers, etc. Hence, experimentally, pairs occurred in no more than 20 percent of the cases. This corresponds to $T_a/\tau=0.22$. Since the available decay time is inversely proportional to the $\beta\gamma$ of the V^0 ($t_{ai}=d_{ai}/\beta\gamma c$), we can estimate that the more energetic member of the pair must have a $\beta\gamma$ larger than the observed member by a factor ranging from $0.55/0.22=2.5$ to $1.25/0.22=5.7$. If pairs actually are only seen in 10 percent of the pictures, the two values of $\beta\gamma$ differ on the average by a factor ranging from 5.5 to 13. Whether this is a likely or an unlikely situation cannot be said at present.

It has also been proposed[15] that the events which cannot be $p+\pi$ decays should be accounted for by the process

$$V^0\rightarrow x+\pi, \quad \text{with} \quad m_x=1000 \text{ electron masses.}$$

The disintegration energy associated with this decay would have to be approximately 175 Mev to agree with observed ionizations. The only known particles with which x might be identified are K or τ-mesons, both of which are thought to have lifetimes of about 10^{-9} second. The question is whether such a short lifetime is compatible with the absence of observed secondary particle decays, at least in the 11 cases which are surely not $p+\pi$ decays. To decide it, we first seek to estimate the time available to particle x for its decay (measured in its own center-of-mass system). This can be done by calculating the average difference between t_{ai} and t_i for the events in question, assuming the above decay scheme, and one obtains about 8×10^{-10} second. Particle x is moving very slowly in the center-of-mass system of the V^0 ($\sim0.16\ c$), and hence this value remains practically unchanged in its own center-of-mass system. If its lifetime is τ_x, the probability of observing 1 decay in 11 events is

$$P=1-\exp(-8\times10^{-10}/\tau_x)=1/11;$$

hence, $\tau_x\geqslant8\times10^{-9}$ second. Hence, the possibility $V^0\rightarrow K$ (or τ)$+\pi$ cannot be ruled out as an alternative to decay scheme D. However, it cannot account for all measurable events, for then we would have $P\sim1/34$ and $\tau_x\geqslant2\times10^{-8}$ second.

[15] R. B. Leighton, private communication.

C. Analysis of Data Assuming Three-Particle Decay

The identification of some secondary particles as π-mesons makes the process

$$V^0\rightarrow p+\mu^-+\nu$$

untenable as an explanation of all events. It might still account for some of the events. If there is an elementary fermion with a lifetime 10^{-10} second against decay into a proton and a π-meson, and if there exists a universal four-fermions interaction, it may not be unreasonable to expect $V^0\rightarrow p+\mu^-+\nu$ decay as a competing process.

One might also advance the single process

$$V^0\rightarrow p+\pi^-+\nu$$

as a possible explanation for all events. We have seen that five independent variables are needed to specify any such three-particle decay in the laboratory system and, since we only measure two (θ_1 and θ_2), we cannot expect our data to provide any thoroughoing test of the hypothesis. However, we might expect two quantities, the departure from coplanarity and the spread in V^0 mass values, to behave differently under two- and three-particle decay. So far as the first one is concerned, the angle which the V^0 makes with the $p-\pi$ plane, δ, is less than θ_1, and therefore less than 20° in nearly all cases. Since, furthermore, its theoretical distribution[12] shows a broad maximum at $\theta=0$ and since our coplanarity measurements are only accurate within 5°, our results (34 coplanar cases *vs* 7 noncoplanar ones) cannot be used to differentiate between two- and three-particle decay.

CONCLUSIONS

Our conclusions may be summarized as follows:

(1) If the 34 coplanar cases are interpreted as two-particle decays, one particle was heavier than the other in 18 cases, and the measurements on angles, ionizations, and scattering agreed best with the assumption of a $p+\pi$ decay with a disintegration energy of 50–100 Mev. In 11 more cases, angles and ionizations precluded that possibility, but interpretation on the basis of a $\pi+\pi$ decay seemed permissible. Five cases lent themselves to either interpretation from the standpoint of angle-ionization measurements.

(2) The assumption of masses of 2210 and 2260 for the V_1^0 which decays into a proton and a π-meson led to calculated ionizations on the whole too high, but not outside experimental error, and to values of ϕ^* predominantly larger than 90°. Assuming a mass of 800 for the V_2^0 which decays into two π-mesons led to ionizations in agreement with experiment. The ϕ^* distribution was not significant.

(3) A search for experimental bias failed to turn up any decisive reasons for the anomalous ϕ^* distribution. Statistics are poor, however.

(4) The lifetime of the V_1^0 is $(10\pm7)\times10^{-10}$ second and the lifetime of the V_2^0 is $(4\pm3)\times10^{-10}$ second. The errors given are statistical variances, not probable errors, and the calculated values depend quite strongly on the assumed mass of the unstable particle. If the V_2^0 actually decays into a π-meson and a meson of intermediate mass,[15,16] which would be quite consistent with our data, the lifetime would of course be different.

(5) Three pairs were observed. Only one allowed classification of both its members, one of which turned out to be a V_1^0 and the other a V_2^0. This frequency of observation contradicts the hypothesis that V^0's are created only in pairs, unless one V^0 usually has a value of $\beta\gamma$ from 5 to 10 times as large as the other.

(6) The data do not preclude interpretation by means of a three-particle decay scheme, one of which would be a neutrino.

It was not possible to deduce from the angle between the decay plane and the plane of the V^0 and the primary whether or not the V^0 was consistently emitted with a high angular momentum. Nor was it possible to connect the type of V^0 emitted with the type of primary causing the initial event.

[16] Report from Copenhagen Conference, June, 1952.

PHYSICAL REVIEW VOLUME 89, NUMBER 1 JANUARY 1, 1953

Enhancement of the Green Continuum of Hg by a Rare Gas

C. KENTY AND D. A. LARSON*
Lamp Development Laboratory, General Electric Company, Nela Park, Cleveland, Ohio
(Received September 5, 1952)

The green continuum of Hg vapor in a low current, positive column discharge has been found to be greatly enhanced by the presence of a considerable pressure of a rare gas (e.g., 50-mm argon). The effect is most striking for lower Hg pressures (e.g., at 50°C). At 215°C the light efficiency of the continuum reaches 41 lu/w. The continuum extends from 4000 to 6400A; its maximum occurs at 5130A at 115° and shifts toward the violet at higher temperatures. Very small amounts of gas impurity, e.g., 40 parts per million of N_2 increase the brightness and also the voltage; larger amounts, e.g., 150 ppm N_2, quench the brightness almost completely.

THE green and ultraviolet continua of Hg as excited in a low current discharge were first studied by Rayleigh.[1] Volkringer[2] excited the bands with an electrodeless discharge. The requisites for strong continua are a low current (~1 ma) and an elevated Hg pressure (e.g., 200°C).

We have found that the addition of a rare gas (e.g., 43-mm argon) brings out the green, so-called 4850, band strongly at as low as 60°C (hot cathode, ½-ma positive column, 1½-inch tube). At 100°C the line spectrum is nearly gone (see Fig. 1, curve *A*). Without the argon, curves *B* and *C* show that the continuum is very weak relative to the lines at 100°C and only moderately strong at 180°. 4916 and 5770-90 tend to persist. Curve *D* shows the continuum excited optically.

Approximately true light intensity distributions for two different temperatures are shown by Fig. 2. They agree sufficiently with Volkringer's[2] distribution, and show the band extending from 4000 to 6400A, much further than is commonly recognized. At 115° the maximum is at 5130A and shifts toward the blue at higher temperatures.

The brightness of the continuum increases rapidly with Hg temperature up to ~210°, where arc constriction sets in and the lines appear. Thus with 55-mm argon the brightness of a 0.25-ma discharge increased 250-fold from 75 to 215°. Meanwhile the voltage rose from 115 to 470 (arc length 10 cm). The light efficiency of the discharge at the higher limit was measured as 41 lu/w.

From 10 to 60 mm argon and, e.g., at 160°C, the brightness and voltage increase roughly in proportion to p; below 10 mm the brightness decreases rapidly.

The other rare gases yielded qualitatively similar results; Xe in particular gave about the same efficiencies as argon.

The brightness is very sensitive to impurities. So far, and unless otherwise stated, all results deal with "spectroscopically pure" argon containing 30–50 parts per million of N_2. Removal of most of this N_2 was found to lower the brightness to less than half and decrease the voltage 25 percent. Maxima in both brightness and voltage occur around 50 ppm N_2; beyond this the brightness drops rapidly to a few percent at 150 ppm N_2. A drop in voltage beyond the maximum may be due to one or more of several causes not discussed here. The initial rise in brightness is closely related to the increase in voltage whatever the impurity (e.g., H_2O, CO_2).[3]

With a well-developed continuum (100°C), strong

* Now of Research Laboratory, Westinghouse Electric Corporation, Bloomfield, New Jersey.
[1] Lord Rayleigh, Proc. Roy. Soc. (London) **A114**, 620 (1927).
[2] H. Volkringer, Ann. phys. **10**, 14, 15 (1930).
[3] C. Kenty, Phys. Rev. **80**, 95, 96 (1950).

irradiation[3] with visible Hg lines had a negligible effect on voltage. Also the discharge showed negligible absorption[3] for 5461. These results indicate negligible concentrations of metastable Hg atoms.[3]

With commutator and sectored disk, the continuum was found to decay with a half-life of ~2 msec (55 mm argon, 100°C) in agreement with results of Rayleigh[1] and Holstein, Alpert, and McCoubrey.[4] Such a decay time and the measured brightness yield a relatively high concentration of emitters, 5×10^{11} cm^{-3}. Mobility considerations indicate ~10^9 electrons cm^{-3}.

According to Mrozowski[5] the emitters are $A^3\Sigma_u^-$ Hg_2 molecules ($6^3P_0+6^1S_0$). The upper metastable state

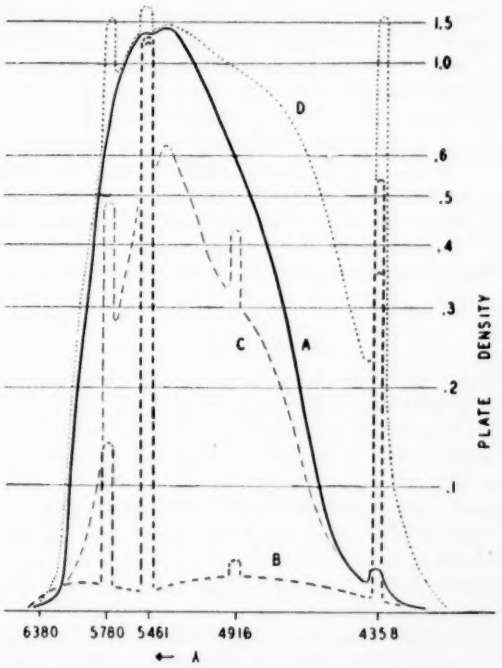

FIG. 1. Densitometer traces of panchromatic film spectrograms of green continuum. *A*, 43 mm argon, 100°C, 0.5 ma; *B*, no argon, 100°C, 0.5 ma; *C*, no argon, 180°C, 0.3 ma; *D*, no argon, 270°C, optically excited through quartz by low pressure Hg lamps. The curves have no absolute significance.

[4] Holstein, Alpert, and McCoubrey, Phys. Rev. **76**, 1259 (1949); Alpert, McCoubrey, and Holstein, Phys. Rev. **76**, 1257 (1949).

[5] See, for example, W. Finkelnburg, *Kontinuerliche Spectren* (Verlag. Julius Springer, Berlin, 1938), Sec. 60.

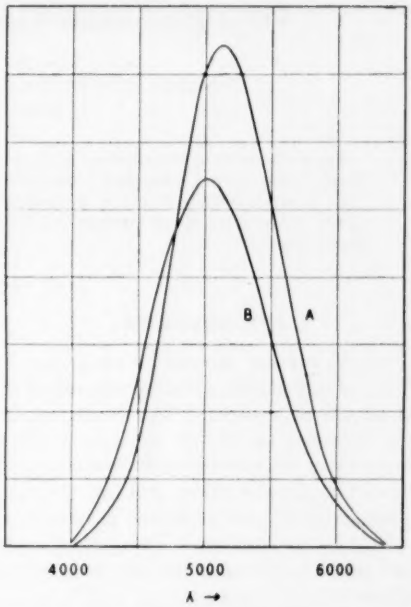

FIG. 2. G.E. recording microphotometer tracings of green continuum with 55 mm argon. *A*, 0.5-ma discharge at 115°C; *B*, 0.25-ma discharge at 200°C.

(6^3P_2) forms $B^3\Pi_u$ and $B^3\Sigma_u^-$ molecules,[5] the latter of which is metastable. The initial increase of voltage due to impurity would indicate, following earlier results,[3] that the ionization is largely two-stage and that these molecules from 6^3P_2, especially $B^3\Sigma_u^-$ (and possibly to some extent 6^3P_2 itself), figure importantly in the two-stage process, being destroyed[3] by N_2. The increase in brightness, as in earlier experiments,[3] could then be due to enrichment by N_2 of $A^3\Sigma_u^-$ from 6^3P_2 and its molecular states and also[6] 6^3P_1. A lot of N_2 evidently destroys[7] $A^3\Sigma_u^-$.

With 50 ppm N_2 the ionization is assumed to be two-stage involving almost entirely $A^3\Sigma_u^-$. Very few electrons evidently reach the 7.74 v energy necessary to excite 7^3S_1 from normal. Evidently also this state is hardly produced from $A^3\Sigma_u^-$ by electron collision.

It is assumed that the argon functions by reducing loss of Hg_2 molecules to the walls, and possibly assisting in their formation.

[6] E.g., G. A. Rosselot, Phys. Rev. **49**, 871 (1936).

[7] See Foote, Ruark, and Chenault, Phys. Rev. **37**, 1685 (1931).

The Alpha-Gamma Angular Correlation in Radiothorium*

JAMES BATTEY, L. MADANSKY, AND F. RASETTI
Department of Physics, The Johns Hopkins University, Baltimore, Maryland
(Received September 23, 1952)

The alpha-decay of radiothorium is followed by an 83.3-kev gamma-ray whose angular correlation with the alpha-particle was investigated, using scintillation counters and fast coincidence circuits. The correlation curve does not agree with any of the theoretical ones derived under the assumption that the angular momenta of the three states involved are $0-J-0$. Possible reasons for this somewhat unexpected result are discussed.

I. INTRODUCTION

THE alpha-gamma correlation occurring in the decay of radiothorium has been examined by two different groups of workers.[1,2] The earlier experiment cannot be regarded as reliable, since no attempt was made to separate the radiothorium from its daughters. This present work was under way at the time the second measurement was reported. Inasmuch as the results of the latter experiment were rather surprising, it seemed worth while to carry this present work to its conclusion.

For some time it has been supposed that the energy levels of ThX consisted of an 86.8-kev and a 3.5-kev excited state in addition to the ground state. This was based on the report of two gamma-rays by Surugue and Tsien-San-Tsiang[3] and by Riou,[4] and also from the study of the alpha-fine structure by Rosenblum,[5] who indicated a possible slight broadening of the ground state alpha-group consistent with the existence of a 3.5-kev excited state.

However, a more recent study of the gamma-rays by Riou[6] based on a more careful separation of the decay products of radiothorium indicates that only the 83.3-kev gamma-ray is to be attributed to radiothorium decay, the 86.8-kev gamma occurring in the derivatives. The results of the present work tend to confirm this contention. It is then assumed that only one excited state of ThX occurs with an appreciable intensity in the alpha-emission of radiothorium, and that this 83.3-kev excited state decays to the ground state by the emission of one gamma-ray. It is hoped that the study of the angular correlation between the short-range alpha and the 83.3-kev gamma will shed some light on the angular momentum of the nuclear levels involved.

II. PREPARATION OF SOURCES

Radiothorium was separated from its decay products by alternate hydroxide precipitations of radiothorium, which left ThX in solution, and sulfide precipitations which removed ThB and ThC. The purified radiothorium plus the carrier was made into a suitable alpha-source by a modification of a technique described by Tödt,[7] in which radiothorium and thorium are electrolytically deposited onto a rhodium foil from an acid solution at high current density. In the region of the cathode where the solution has become alkaline due to a vigorous evolution of hydrogen, the thorium forms a hydroxide and is deposited as such on the cathode. A rhodium foil of one-half mil thickness was selected as a cathode since it does not absorb the gamma-radiation too severely and serves as a suitable backing material.

III. APPARATUS

The source was placed in a vacuum chamber. The alphas were detected by a three-mil thick anthracene flake mounted in the chamber with the source and observed by the phototube through a Lucite window. The gammas were detected with a sodium iodide crystal. Both detectors showed good energy resolution. A pulse-height spectrum of the alpha- and gamma-counters showed 20 percent and 16 percent resolution, respectively, at half-maximum for the radiations observed.

The pulses from both phototubes were sent through fast amplifiers to a fast coincidence circuit (resolution about 1.5×10^{-8} sec), and also through linear amplifiers to channel discriminators. A relatively slow coincidence circuit (7 μsec resolution) was fed from the output of the channel discriminators. And finally, a coincidence between the output of the fast coincidence circuit and the coincidence between the channel discriminators was recorded. In this way an energy criterion was imposed on both radiations while good time resolution was maintained. The accidental coincidence rate was determined by the introduction of sufficient lengths of delay line in the fast circuit to remove all true coincidences and provided a background correction.

IV. RESULTS

The experiments performed were originally based on the older assumption of the presence of two gamma-rays

* This investigation was supported by the AEC.
[1] Kilchitsky, Latishev, and Buliginsky, Doklady Akad. Nauk, S.S.S.R. **64**, 57 (1949).
[2] Beling, Feld, and Halpern, Phys. Rev. **84**, 155 (1951).
[3] J. Surugue and Tsien-San-Tsiang, Compt. rend. **213**, 172 (1941)
[4] M. Riou, J. phys. et radium **11**, 185 (1950).
[5] Rosenblum, Valadares, and Perey, Compt. rend. **228**, 385 (1949).
[6] M. Riou, private communication.
[7] F. Tödt, Z. physik. Chem. **113**, 331 (1924).

of 86.8 kev and 83.3 kev, each in coincidence with the same short range alpha. Angular correlation data were taken with the source alone, and then approximately equal amounts of data were taken with a thallium absorber interposed in the gamma-ray beam. An 86.8-kev gamma has sufficient energy to eject the K electrons of thallium and is severely absorbed, whereas an 83.3-kev gamma does not have sufficient energy for this process and is not so severely absorbed. Thus, two correlation curves are obtained which would have the two alpha-gamma processes present in appreciably different proportions. Hence the knowledge of the attenuation of the two gamma-rays in the thallium absorber is sufficient to isolate the two alpha-gamma-processes.

Inasmuch as the geometry involved in an angular correlation is far from ideal for the measurement of absorption coefficients, it was decided that an experimental measurement of the attenuation of the two gamma-rays was preferable to a computed attenuation based on tabulated absorption coefficients. An 86.8-kev gamma-ray was simulated by an 87.8-kev gamma-ray occurring in the K capture in Cd^{109}, and an 83.3-kev gamma by an 84.1-kev gamma occurring in the beta-active thulium^{170}, where appropriate corrections were made for the bremsstrahlung continuum from the beta-decay.

Considerable care was expended in lapping the thallium absorber to a thickness of 0.241 g/cm^2 uniform to 2 percent, so that the measurements would be independent of the exact area of the absorber used. The absorber was made somewhat larger than the minimum size necessary to cover the detector as insurance against imperfect alignment.

Values for the attenuation of the assumed radiothorium gamma-rays in the thallium absorber were then obtained by appropriate corrections for the small differences in energy between the radiothorium gamma-rays and the gamma-rays used for calibration. The attenuation for an 83.3-kev gamma-ray was found to be 0.622 ± 0.009. This corresponds to an absorption coefficient that is somewhat smaller than the tabulated value, due primarily to imperfect geometry. The attenuation for an 86.8-kev gamma-ray was found to be 0.279 ± 0.004. This corresponds to an absorption coefficient that is appreciably smaller than the tabulated value, due primarily to the detection of the fluorescent K-radiation from the thallium absorber, again because of the poor geometry.

Assuming that there are two gamma-rays following the short-range alpha of radiothorium, the relative intensities of these two transitions can be directly obtained from the correlation data with and without absorber and from the values of the gamma-ray attenuations. The experimental value of the attenuation of the coincidence rate, integrated over all angles, is 0.646 ± 0.017. This coincides with the value for the 83.3-kev gamma-ray of 0.622 ± 0.009, within the experimental error. This is consistent with Riou's result that there is only one gamma-ray present in the decay of radiothorium, that is, the 83.3-kev gamma-ray.

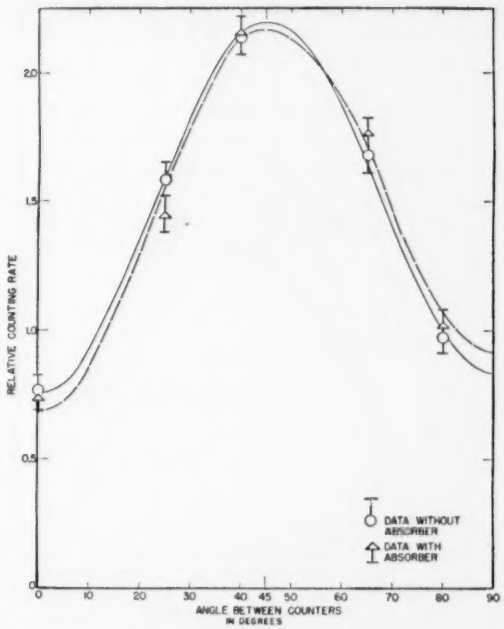

FIG. 1. Experimental data with and without absorber. The solid curve represents the least square fit to the experimental angular correlation data without absorber, the dotted curve with absorber. The solid angles of both counters are a 3×10^{-3} fraction of the total sphere. The curves are normalized to the same area, where the correlation with absorber is $W(\theta)=0.91+5.37\cos^2\theta-5.60\cos^4\theta$, and the correlation without absorber $W(\theta)=0.83+5.55\cos^2\theta-5.63\cos^4\theta$.

A separate experiment designed to detect gamma-gamma coincidences in the 80- to 90-kev range was also performed with a circuit of 2 μsec resolution. No coincidences were detected, in agreement with the findings of Beling *et al.* This result, however, is also in agreement with the assumption of only one gamma-ray.

The growth of the decay products of radiothorium is controlled by the 3.64-day half-life of its first daughter, ThX. The angular correlation data were taken with radiothorium sources that were not more than sixteen-hours old. Although the single channel rates increased continuously throughout the experiment, the coincidence rate did not, indicating that the decay products were not contributing any coincidences to the correlation. The data are shown in Fig. 1. These were taken with the counter solid angles equal to a 3×10^{-3} fraction of the total sphere. The curves represent a least square fit to the data. Within the experimental error, the two curves may be regarded as representing the same correlation, which is again consistent with the assumption of only one gamma-ray.

As Beling *et al.* point out, lifetime arguments exclude the possibility of the gamma-radiation being of higher

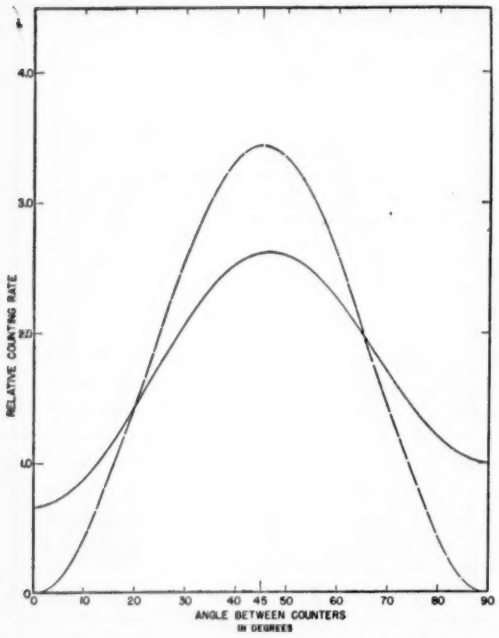

FIG. 2. The solid angular correlation curve represents the average, after reduction to zero solid angle, of the least square fit to the data with and without absorber. The dotted curve corresponds to a $0-2-0$ sequence and is plotted for comparison. The curves are normalized to the same area.

multipolarity than quadrupole. This in turn limits the complexity of the distribution to $\cos^4\theta$. The argument is even stronger with our shorter resolving time of 1.5×10^{-8} sec. The presence of the large $\cos^4\theta$ term indicates that the gamma-radiation is at least quadrupole.

If the least square curves are corrected to zero solid angle, the angular correlation without absorber becomes $W(\theta)=1.00+7.27\cos^2\theta-7.48\cos^4\theta$, and the angular correlation with absorber becomes $W(\theta)=1+6.39\cos^2\theta-6.76\cos^4\theta$. The average of these two curves weighted equally is $W(\theta)=1+6.83\cos^2\theta-7.12\cos^4\theta$. This agrees rather closely with the results of Beling *et al.* for their correlation without absorber, that is $W(\theta)=1+6.90\cos^2\theta-7.07\cos^4\theta$. Our curve is shown in Fig. 2.

CONCLUSIONS

Inasmuch as the nuclei involved have an even number of neutrons and protons, it might be expected that the ground states would have zero angular momentum. If the gamma-radiation is quadrupole, then the sequence of angular momentum states would be $0-2-0$. However, the experimental data do not fit $W(\theta)=\cos^2\theta-\cos^4\theta$, the correlation shown in Fig. 2, which corresponds to this sequence, nor does it fit any other $0-J-0$ sequence. Some general remarks should be made in this connection.

1. The possibility of impurities from other disintegration series in the radiothorium sources, that could contribute false coincidences, was rejected as highly improbable, because the radiothorium supply was separated from MsTh I some months in advance of taking any correlation data. The only contaminant that is usually found with MsTh I is radium, and this would be removed from the radiothorium with MsTh I. The decay products of radium which would give coincidences would have died out before the correlation data were taken. On the other hand, if the decay products of radiothorium are changing the correlation, then the coincidence rate should increase and the shape of the correlation change with time. Neither of these things occurred.

2. It is possible that an atomic magnetic field could alter the population of the magnetic substates of the intermediate nucleus and thus change the correlation. However, it is difficult to believe that there are magnetic fields of electronic origin in the solids used, which are strong enough to reorient the nucleus in 10^{-8} sec. The value 10^{-8} sec is used as an upper limit for the lifetime, since no coincidences above the accidental rate were observed when a delay line of 2×10^{-8} sec was introduced in one of the channels. It is also interesting to note that our source was composed of thorium hydroxide, and the source prepared by Beling *et al.* was iron chloride as a carrier for thorium. Hence, it appears that similar results were obtained with different solid compounds, which provides an additional argument against reorientation.

3. There still remains the possibility that the proposed disintegration scheme is not correct. However, at the present time there is no direct evidence for other modes of decay. It would therefore be of considerable interest to determine whether other gamma-rays whose energy is very close to 83 kev exist and are in coincidence with the short-range alpha.

4. If it is assumed that the disintegration scheme is simple, that is, having one gamma-ray, that no impurities are contributing coincidences, and that the intermediate state is not being reoriented, then the assumption that the angular momenta of both ground states are zero must be rejected. However, none of the angular momentum assignments in which the selection rules operate to limit the alpha-particles to one angular momentum group followed by quadrupole gamma-radiation seem to fit the data very well. An example which is not too remote from a fit but nevertheless outside the probable error, is the sequence $1-2-1$ with $L=2$ in both transitions. This gives $W(\theta)=1+5\cos^2\theta-5.33\cos^4\theta$. In computing alpha-gamma correlations, mixtures of the different alpha-angular momentum groups that are consistent with angular momentum and parity selection rules must be considered.[8] This introduces the parameters of the relative intensities of the different alpha-angular momentum groups and the phase angles between their matrix

[8] S. P. Lloyd, Phys. Rev. **85**, 904 (1952).

elements into the correlation expression. The systematic investigation of assignments using mixtures of alpha-angular momentum groups involves much computation. None of the cases that involve mixtures of angular momentum groups for the alpha-particle have been computed here; however, Beling[9] has considered a few without finding a convincing fit with the data.

[9] J. K. Beling, dissertation, Massachusetts Institute of Technology (1951), unpublished.

We are indebted to Professor I. Halpern and his colleagues for communicating to us the results of their investigation. We also wish to thank Professor M. Riou for sending us his most recent unpublished results on the gamma-radiation from the decay of radiothorium.[10]

[10] *Note added in proof.*—A recent paper by Rosenblum, Valadares, and Guillot (Compt. rend. **235**, 238 (1952)) reports measurements of the internal conversion lines of radiothorium, which confirm the existence of one gamma-ray of 83.4 kev as assumed in the interpretation of our data.

PHYSICAL REVIEW VOLUME 89, NUMBER 1 JANUARY 1, 1953

Entropies of Activation in Metallic Diffusion*

G. J. DIENES
Brookhaven National Laboratory, Upton, New York
(Received September 15, 1952)

The various contributions to the entropy of activation for metallic diffusion are examined theoretically. In particular, the entropy contribution arising from the altered vibrational frequencies around the saddle point is estimated. It is concluded that negative over-all entropies of activation are theoretically permissible and are likely to arise when the over-all activation energy is small.

I. INTRODUCTION

THE temperature dependence of volume diffusion is accurately described by the simple exponential relation

$$D=D_0e^{-E/RT}, \tag{1}$$

where D=diffusion constant; D_0=constant; E=activation energy; R=gas constant; T=temperature in °K. The activation energy E may be estimated theoretically in simple cases.[1] It is much more difficult to give a sound theoretical interpretation to D_0, the so-called frequency factor, although many attempts have been made in the past to derive theoretical expressions for this quantity.[2]

This problem was attacked again in the last few years with clarification of some of the puzzling features. The writer proposed an empirical correlation which related D_0 to the quantity E/T_m, where T_m is the melting point in °K, and suggested that E/T_m be identified with the entropy of activation.[3] Zener[4] proposed a theory for D_0, which seemed to account at least partly for the above correlation, in which only positive experimental entropies of activation ΔS, calculated as

$$\Delta S/k=\ln(D_0/\nu a^2), \tag{2}$$

were permitted (ν=Debye frequency, a=lattice parameter). In Zener's theory, the origin of the entropy contribution is traced to the temperature coefficient of the work required to produce a given distortion within the lattice. Finally, this was traced to the temperature coefficient of the elastic moduli, which is negative, yielding a positive ΔS. Zener suggested that experimentally observed negative entropies of activation are to be attributed to experimental inaccuracies or to the presence of short-circuiting diffusion paths.

The writer pointed out[5] that Zener's theory is unable to account for the large negative entropies of activation for self-diffusion in tin as calculated from Fensham's excellent experimental data on single crystals.[6] At about the same time Nowick[7] published an article in which intermetallic diffusion experiments were reinterpreted on the basis of Zener's theoretical expression for D_0. Nowick argues that this theoretical D_0 is correct at least to order of magnitude and suggests that many experimental activation energies are greatly in error at any but the highest temperatures because of diffusion along internal surfaces or "short circuiting paths" and that the writer's earlier correlation reflects essentially this inaccuracy. Nowick is certainly correct in calling attention again to the well-known poor quality of most diffusion data. However, he offers no explanation for the behavior of tin. Further, recent researches by Smoluchowski and co-workers[8,9] indicate strongly that dis-

* Research carried out under contract with the AEC.

[1] See for example the recent review by F. Seitz in *Phase Transformations in Solids* (John Wiley & Sons, Inc., New York, 1951), pp. 77–149.

[2] See for example A. D. LeClaire, section on "Diffusion of Metals" in *Progress in Metal Physics I* (Interscience Publishers, Inc., New York, 1949), pp. 306–379.

[3] G. J. Dienes, J. Appl. Phys. **21**, 1189 (1950).

[4] C. Zener, J. Appl. Phys. **22**, 372 (1951); *Theory of Diffusion*, "Imperfections in Nearly Perfect Crystals," (John Wiley and Sons, Inc., New York, 1952), pp. 289–314.

[5] G. J. Dienes, J. Appl. Phys. **22**, 848 (1951).

[6] P. J. Fensham, Australian J. Sci. Res. **A3**, 91 (1950); **A3**, 105 (1950).

[7] A. S. Nowick, J. Appl. Phys. **22**, 1182 (1951).

[8] R. Smoluchowski, Phys. Rev. **87**, 482 (1952).

[9] R. Flanagan and R. Smoluchowski, J. Appl. Phys. **23**, 785 (1952).

TABLE I. Values of γ for different lattices.[a]

Lattice	γ
Face-centered cubic	2
Body-centered cubic	4/3
Hexagonal close packed, $\parallel C$	1.0
Hexagonal close packed, $\perp C$	1.0
Tetragonal tin lattice, $\parallel C$	1/3
Tetragonal tin lattice, $\perp C$	2/3

[a] γ defined here is not quite the same as Zener's γ since the jump distance λ rather than the lattice parameter a is used here. λ is a more convenient quantity whenever noncubic lattices are considered.

locations and mosaic block boundaries cannot serve as short-circuiting paths. Only high angle grain boundaries could act as short circuits.

In view of the rather unsatisfactory state of affairs discussed above, the writer felt that it was worthwhile to investigate in somewhat more detail the various contributions to the entropy of activation. In particular, it is important to find out whether negative entropies of activation be theoretically permissible. The purpose of this note is to describe some of the results of this theoretical study.

II. THE ENTROPY OF ACTIVATION

The vacancy mechanism of diffusion will be assumed as operative throughout since this mechanism is probably the most prevalent one in metals.[1] Rather obvious modifications, which would not influence the final conclusions, are required if other mechanisms are dominant. The complete expression for D as a function of temperature may be written as[4]

$$D=\gamma\nu\lambda^2 e^{\Delta S/R}e^{-(E_v+E_m)/RT}, \tag{3}$$

where γ = geometrical constant, entirely determined by the lattice geometry of the atomic jump; ν = vibrational frequency of atom in the equilibrium position $\cong$ Debye frequency; λ = jump distance; ΔS = over-all entropy of activation; E_v = energy required to create vacancy at 0°K; and E_m = energy required to move vacancy at 0°K. The values of γ for typical lattices are listed in Table I.

Equation (3) is based on the well-known transition state theory of reaction rates. The fundamental assumption of this theory is that the activated complexes are always in equilibrium with the initial reactants.[10] This fundamental assumption, as applied to solid state diffusion, has not yet been critically examined.[11] In this paper the entropies of activation are examined within the framework of the transition state theory.

The value of ΔS in Eq. (3) is a composite quantity. As a first approximation, the following processes contribute to the over-all ΔS.

(1) The variation of the over-all activation energy with temperature. As the lattice expands with increasing temperature, the energies needed to create and move a vacancy will decrease. That is,

$$E=E_v'+E_m'=E_0-\delta T=E_v+E_m-\delta T, \tag{4}$$

where δ is inherently positive. The corresponding entropy $\Delta S_1=\delta/R$ is inherently positive. For convenience it has been assumed that these temperature effects may be expressed through the same δ for both E_v' and E_m'. As long as Eq. (4) is valid one always measures E_0 experimentally. E_0 already includes the contribution to the energy originating in displacements (relaxation) of the atoms around the vacancy and the saddle point, respectively.

(2) The altered vibrational frequencies around a vacancy. The neighboring atoms of a vacancy possess vibrational frequencies different from normal atoms. This effect introduces a constant factor in Eq. (3) which shows up as a contribution to the entropy ΔS_2.

(3) The altered vibrational frequencies around the saddle point. The atoms constituting the configuration of the saddle point possess vibrational frequencies different from normal atoms. As in (2) a constant factor is introduced which appears as an entropy contribution ΔS_3.

In the following, an attempt is made to estimate theoretically each of these contributions to the entropy.

(1) Mott and Gurney[12] and Frenkel[11] have made estimates of ΔS_1. A derivation somewhat different in technique but not in concept is given here. From the rapid decrease of interatomic forces with increasing atomic separation, one may assume that E of Eq. (4) depends on the interatomic distance r in an exponential manner. Thus

$$E(r)=Ae^{-\alpha r}. \tag{5}$$

Then

$$\begin{aligned} dE/dT&=Ae^{-\alpha r}(-\alpha)dr/dT \\ &=-\alpha(dr/dT)E. \end{aligned} \tag{6}$$

Letting $dr/dT=r_0\beta$, where β = coefficient of linear expansion, gives

$$dE/E=-\alpha r_0\beta dT. \tag{7}$$

Integration gives

$$E=E_0e^{-\alpha r_0\beta T}, \tag{8}$$

or within the range of linearity of Eq. (4), certainly valid over limited temperature ranges,

$$E=E_0(1-\alpha r_0\beta T), \tag{9}$$

which corresponds to an entropy contribution

$$\Delta S_1=\alpha r_0\beta E_0. \tag{10}$$

ΔS_1 is inherently positive and may be quite large depending on the magnitude of the various quantities in Eq. (10). Further, ΔS_1 may vary a great deal from material to material, primarily through E_0 and α.

[10] Glasstone, Laidler, and Eyring, *The Theory of Rate Processes* (McGraw-Hill Book Company, Inc., New York, 1941), pp. 184–201, 477–552.

[11] In this connection see the qualitative discussion in reference 2 and that by J. Frenkel in *Kinetic Theory of Liquids* (Oxford University Press, London, 1946), pp. 17–37.

[12] N. F. Mott and R. W. Gurney, *Electronic Processes in Ionic Crystals* (Oxford University Press, London, 1946), pp. 26–36.

(2) Mott and Gurney[12] have estimated the contribution to the entropy ΔS_2 arising from the altered vibrational frequencies around a vacancy. They assume that the vibrational frequencies of the X neighbors of a vacancy are ν as before in the two directions perpendicular to the line joining the neighbor to the vacancy, but some smaller value ν' parallel to this line. Under these conditions the contribution to the entropy of activation ΔS_2 is

$$\Delta S_2 = XR \ln(\nu/\nu'). \tag{11}$$

ΔS_2 is positive if the assumption $\nu' < \nu$ is valid.[13] It is difficult to assign a value to ΔS_2, but Mott and Gurney estimate that it may be of the order of 6 entropy units. This figure may be a considerable overestimate. The atoms surrounding a vacancy tend to move in toward the vacancy.[14,15] It was pointed out to the writer by LeClaire[16] that this relaxation restricts the movement of these atoms tangential to the sphere on which their centers lie. It is probable that ΔS_2 remains positive, but it may be considerably smaller than originally estimated by Mott and Gurney.

(3) The third important factor contributing to the over-all entropy of activation, which has not been considered by previous workers, arises from the altered vibrational frequencies of the atoms constituting the saddle point configuration. Physically, one anticipates that the situation existing at the saddle point is somewhat analogous to that around an interstitial atom. The volume available to the atoms has been decreased by moving an atom to the saddle point, and consequently the vibrational frequencies have been increased. Consequently one expects ΔS_2 to be negative. Any sort of exact calculation is difficult particularly if the relaxation of the atoms is to be taken into account. An order of magnitude calculation is possible, however, and will be described in this section.

It will be assumed that the vibrational frequency, ν, may be expressed as an inverse power function of the volume.[17] Thus

$$\nu = C/V^{\gamma}, \tag{12}$$

where V is the volume, C is a constant and γ is Grüneisen's constant. In terms of the interatomic distance, Eq. (12) may be written

$$\nu = C'/(r)^{3\gamma}, \tag{13}$$

where all constant factors have been absorbed in C'. A change in the vibrational frequency of an atom from ν to ν' corresponds to an entropy change (per mole of that atom) of

$$\Delta S_i = R \ln(\nu_i/\nu_i') = R \ln[r_i'/r_i]^{3\gamma} = 3R\gamma \ln(r_i'/r_i). \tag{14}$$

Analogous to the procedure of Mott and Gurney for vacancies, it is assumed that the neighbors of the atom at the saddle point vibrate with the altered frequency in the direction of the line connecting them to the moving atom, but that their frequencies are not altered in the two directions perpendicular to this line. Thus, each altered vibrational frequency corresponds to one degree of freedom. The contribution to the entropy of activation of N neighbors of an atom at the saddle point is given by

$$\Delta S = 3R\gamma \sum_{i=1}^{N} \ln \frac{r_i'}{r_i}. \tag{15}$$

It is somewhat more difficult to estimate the altered vibrational frequencies of the atom at the saddle point in the two directions perpendicular to the jump direction. As a crude approximation, this contribution may be taken as the average of ΔS in Eq. (15) with two degrees of freedom. The final expression for ΔS_3 is then given by

$$\Delta S_3 = 3R\gamma \sum_{i=1}^{N} \ln \frac{r_i'}{r_i} + \frac{6R\gamma}{N} \sum_{i=1}^{N} \ln \frac{r_i'}{r_i}. \tag{16}$$

Equation (16) forms the basis of the present calculation. The procedure may be illustrated for a simple face centered cubic lattice. Let the vacancy be situated at (110) (in units of $a/2$) and let the diffusing atom be located at (000). Assume that the saddle point is halfway along the line from (000) to (110), i.e., at $(\frac{1}{2}\ \frac{1}{2}\ 0)$. If the nearest neighbors around both (000) and (110) are taken into account, care being taken not to count the common neighbors twice, it is found that for these 18 neighbors

$$\sum_{i=1}^{N} \log_{10} \frac{r_i'}{r_i} = -0.286,$$

and ΔS_3 for this system is, therefore,

$$\Delta S_3 = 2.3(3R\gamma)[-0.286-(2/18)(0.286)] = -4.36\gamma.$$

If one takes 2 as a representative value for Grüneisen's constant, this contribution to the entropy of activation amounts approximately to

$$\Delta S_3 \sim -8.7 \text{ eu}.$$

Similar calculations were made for other crystal lattices with the results shown in Table II. The results indicate that in the lattices considered here the effect of decreased interatomic distances outweighs the effect of increased distances leading to a net "tightening" of the lattice and a corresponding net negative contribution to the entropy of activation. It is difficult to say what influence the relaxation of the atoms may have on ΔS_3. In the present order-of-magnitude calculation, this

[13] It should be pointed out that ΔS_2 is expected to be negative when an interstitial rather than a vacancy is created in the lattice (see reference 12).

[14] H. B. Huntington and F. Seitz, Phys. Rev. **61**, 315 (1942).

[15] G. J. Dienes, Phys. Rev. **86**, 228 (1952).

[16] A. D. LeClaire (private communication, May, 1952).

[17] See for example J. C. Slater, *Introduction to Chemical Physics* (McGraw-Hill Book Company, Inc., New York, 1939), pp. 215–221.

TABLE II. Contribution to the entropy of activation from altered vibrational frequencies of atoms in the saddle point configuration. Vacancy mechanism.

Crystal lattice	Vacancy at	Saddle point at	No. of neighbors considered	$\sum_{i=1}^{N} \log_{10}\frac{r_i'}{r_i}$	$\frac{2}{N}\sum_{i=1}^{N} \log_{10}\frac{r_i'}{r_i}$	ΔS_3	ΔS_3 in entropy units for $\gamma=2$
Face-centered cubic	110	$\frac{1}{2}\frac{1}{2}0$	18	−0.286	−0.032	-4.36γ	−8.72
Body-centered cubic	111	$\frac{1}{2}\frac{1}{2}\frac{1}{2}$	20	−0.269	−0.027	-4.06γ	−8.12
Hexagonal close packed, $\parallel C$ $C/a=1.633$	$0\frac{1}{\sqrt{3}}\frac{1}{2}$	$0\frac{1}{2\sqrt{3}}\frac{1}{4}$	18	−0.286	−0.032	-4.36γ	−8.72
Hexagonal close packed, $\perp C$ $C/a=1.633$	100	$\frac{1}{2}00$	18	−0.286	−0.032	-4.36γ	−8.72
Hexagonal, Zn $C/a=1.862$, $\parallel C$	$0\frac{1}{\sqrt{3}}\frac{1}{2}$	$0\frac{1}{2\sqrt{3}}\frac{1}{4}$	18	−0.308	−0.034	-4.69γ	−9.38
Hexagonal, Zn $C/a=1.862$, $\perp C$	100	$\frac{1}{2}00$	18	−0.272	−0.030	-4.14γ	−8.28
Tetragonal, Sn lattice, $\parallel C$	001	$00\frac{1}{2}$	26	−0.309	−0.012	-4.40γ	−8.80
Tetragonal Sn lattice, $\perp C$	$\frac{1}{2}0\frac{1}{4}$	$\frac{1}{4}0\frac{1}{8}$	26	−0.298	−0.011	-4.23γ	−8.46

effect was neglected. In one respect the magnitudes given in Table II have been probably underestimated. The initial frequencies were assumed to be the normal frequencies corresponding to the normal interatomic distance, r_i. If the decreased frequencies around the vacancy had been used, the relative change, and therefore ΔS_3, would have been greater in magnitude. The total entropy of activation is given by

$$\Delta S=\Delta S_1+\Delta S_2+\Delta S_3. \tag{17}$$

The first two terms are positive while the last term is negative according to the calculations presented in this section. The final sign and magnitude of ΔS is determined by the relative importance of these three factors.

III. DISCUSSION

The results described in the previous section seem to indicate that negative entropies of activation are theoretically permissible. ΔS_1 in Eq. (17), the contribution arising from a decrease in activation energy with increasing temperature due to the expansion of the lattice, is always positive. It is proportional to the energy of activation and for small energies of activation may become quite small. Thus, it is precisely for low energies of activation that the negative contribution to ΔS is expected to outweigh the positive contribution leading to a net negative ΔS. This trend is in agreement with experimental observations.[3,5] ΔS_2 is probably positive but may, in many cases, be considerably smaller than the 6 eu estimated by Mott and Gurney. The results of Table II indicate that in many cases ΔS_3 may be considerably larger than ΔS_2. ΔS, therefore, may be negative for small values of ΔS_1.

It is concluded that, contrary to Zener's views,[4] negative entropies of activation for solid state diffusion are theoretically permissible. It also follows that, at least in some cases, Nowick's[7] reinterpretation of activation energies for intermetallic diffusion based on Zener's theory for D_0 may be incorrect.

It must be re-emphasized, as many have pointed out before, that for further progress accurate diffusion data over wide ranges of temperature are required so that the various critical quantities may be evaluated with a high degree of reliability. Fortunately, new techniques are coming into use,[18,19] following the work of Zener and co-workers,[20,21] which will permit diffusion measurements at much lower temperatures than hitherto possible. Further, since solid state diffusion is not a single process but depends on the creation and motion of vacancies, it is important that the energies and entropies of activation of each process be established independently. Anelasticity studies offer some hope of accomplishing this.[18]

[18] A. S. Nowick, Phys. Rev. **82**, 551 (1951).
[19] A. D. LeClaire, Phil. Mag. **42**, 672 (1951).
[20] C. Wert and C. Zener, Phys. Rev. **76**, 1169 (1949).
[21] C. Wert, Phys. Rev. **79**, 601 (1950).

PHYSICAL REVIEW VOLUME 89, NUMBER 1 JANUARY 1, 1953

The Mesonic Auger Effect

G. R. BURBIDGE,* *University of London Observatory, London, England*

AND

A. H. DE BORDE, *University College, London, England*

(Received September 17, 1952)

A simplified nonrelativistic theory of the mesonic Auger effect is presented and discussed. Comparison is made between the predicted and observed numbers of Auger electrons emitted in μ^- meson capture processes.

I. INTRODUCTION

NEGATIVE mesons of low energy may be captured by atoms or molecules into stable states of motion by processes of the type

$$A+\mu^-\rightarrow A^*+e, \quad (1)$$

where A refers to an atom or molecule and A^* to the same molecule with an electron replaced by the negative meson μ^-. The interaction of mesons of low energy with atoms and molecules has been the subject of several theoretical papers.[1-4] Unfortunately the capture process (1) probably occurs at energies where standard approximations are unreliable. The problem has been investigated by one of the authors[5] using both heavy and light particle approximations, but difficulties have arisen and it is hoped to report on this work at a later date.

Owing to its large mass compared with that of an electron, it is anticipated that in general a meson will first be captured into a state of high excitation in the atomic or molecular field. For example, if it is captured into an atomic state with a mean distance from the nucleus equal to that of a K shell electron, its ionization energy will then be equal to that of a K electron, but the corresponding total quantum number will be about 15 for a μ-meson or 17 for a π-meson.

In such a state, the wave function at the nucleus will be very small, and the probability of interaction with the nucleons, therefore, negligible. The meson, however, can make transitions to states of lower excitation both by radiative and radiationless (Auger) processes, until it eventually reaches its $1s$ state. Here the meson spends an appreciable fraction of its time within the nucleus,[6] particularly for atoms of medium or high atomic number, so that interaction with nucleons may occur.

Support for this picture of the processes involved in the capture of negative mesons is now available from several experiments. Thus, Chang[7] and Hincks[8] have observed gamma-rays associated with the capture of μ^--mesons by nuclei. In the latter experiments an estimate of about 9-Mev energy emitted per stopped meson in lead was made, compared with an estimated ionization energy for the $1s$ level of 9.56 Mev, after allowance for the finite size of the nucleus has been made. This is consistent with the interpretation that the rays arise from the radiative transitions of the captured μ^--meson in the atomic field.

Slow electrons associated with μ-meson capture have been observed by Cosyns, Dilworth, Occhialini, Schoenberg, and Page,[9] and by Fry,[10] while similar electrons associated with π-meson capture have been observed by Menon, Muirhead, and Rochat.[11] These have been interpreted as Auger electrons ejected in radiationless transitions in the atomic field.

In the present work, the time required for transitions of the meson from an initial state of high excitation to its $1s$ state is estimated, as well as the number and energy distribution of the Auger electrons ejected. In making these calculations, pending a fuller analysis of the capture process, some assumption has to be made about the initial state of atomic capture. It has been pointed out by Bohr[12] that for a given total quantum number, n, the meson is probably most likely to be captured into a circular orbit ($l=n-1$) owing to the greater statistical weight of this orbit. This assumption is made, thereby greatly simplifying the problem as the only significant transitions are then radiative and Auger transitions of the type $(n, n-1)\rightarrow(n-1, n-2)$. In the following, transitions of this type, and of the type $(n, n-2)\rightarrow(n-1, n-2)$ are considered.

For radiative transitions the selection rule $\Delta l=\pm 1$ applies. For Auger transitions the electron can be ejected into states with $l=0$, 1, 2, etc., but estimates of the transition rates for the higher values of l show these to be appreciably smaller. Throughout these calcula-

* Present address: Yerkes Observatory, University of Chicago, Williams Bay, Wisconsin.

[1] B. Ferretti, Nuovo cimento **5**, 325 (1948).
[2] R. Huby, Phil. Mag. **40**, 685 (1949).
[3] R. L. Rosenberg, Phil. Mag. **40**, 759 (1949).
[4] A. S. Wightman, Phys. Rev. **77**, 521 (1950).
[5] G. R. Burbidge, Ph.D. thesis, London (1951), (unpublished).
[6] J. A. Wheeler, Revs. Modern Phys. **21**, 133 (1949).
[7] W. Y. Chang, Revs. Modern Phys. **21**, 166 (1949).
[8] E. P. Hincks, Phys. Rev. **81**, 313 (1951).
[9] Cosyns, Dilworth, Occhialini, Schoenberg, and Page, Proc. Phys. Soc. (London) **A62**, 801 (1949).
[10] W. F. Fry, Phys. Rev. **83**, 594 (1951).
[11] Menon, Muirhead, and Rochat, Phil. Mag. **41**, 583 (1950).
[12] N. Bohr, quoted by B. Bruno, Arkiv Mat., Astron. Fysik, **36A**, No. 8, 44 (1948).

tions the mass of the μ-meson has been put equal to $210m_e$.

II. AUGER TRANSITION PROBLEM

The initial state of the system consists of an electron in its ground state ψ_i and a meson in an excited state χ_i (quantum numbers, n_1, l_1, m_1). The final state consists of an electron in a positive energy state ψ_f, (quantum numbers, l, m) and a meson in a lower excited state $\chi_f(n_2, l_2, m_2)$. Hydrogen-like wave functions will be assumed (the Bohr radius a_0 being replaced by $a'=a_0/\mu$ for the meson, where μ is the meson mass in atomic units).

We have[13]

$$\psi_f=\left\{\frac{m_e}{\hbar}\frac{2l+1}{4\pi}\frac{(l-|m|)!}{(l+|m|)!}\right\}^{\frac{1}{2}}2^{l+1}\kappa^{l+1}e^{i\kappa r_2}r_2{}^l \times{}_1F_1(l+1-iy;2l+2,-2i\kappa r_2)|\Gamma(l+1-iy)|e^{\frac{1}{2}\pi y} \times P_l{}^{|m|}(\cos\theta_2)e^{im\varphi_2}/(2l+1)!,$$

$$\chi_i=\left\{\frac{2l_1+1}{4\pi}\frac{(l_1-|m_1|)!}{(l_1+|m_1|)!}\frac{(n_1-l_1-1)!}{2n_1[(n_1+l_1)!]^3}\right\}^{\frac{1}{2}}\left(\frac{2\mu Z_1}{n_1a_0}\right)^{l_1+\frac{1}{2}} \times r_1{}^{l_1}\exp\left(-\frac{\mu Z_1}{n_1a_0}r_1\right)L_{n_1+l_1}{}^{2l_1+1}\left(\frac{2\mu Z_1}{n_1a_0}r_1\right) \times P_{l_1}{}^{|m_1|}(\cos\theta_1)e^{im_1\varphi_1},$$

χ_f being the same as χ_i apart from change of suffix. Here $y=Z/\kappa a_0$, m_e is the electronic mass, Z and Z_1 are the effective nuclear charges experienced by the electron and meson, respectively, and κ is the momentum of the ejected electron. The associated Legendre polynomials are those defined by Rodrigue's formula. The meson and electron coordinates are, respectively, $(r_1, \theta_1, \varphi_1)$, $(r_2, \theta_2, \varphi_2)$.

The number of transitions per second is given by[14]

$$P_A=\left|\frac{1}{\hbar}\int\int\chi_f{}^*\psi_f{}^*\frac{e^2}{r_{12}}\chi_i\psi_i d\tau_1 d\tau_2\right|^2. \tag{2}$$

The angular integrations are easily performed by expanding $1/r_{12}$ in spherical harmonics:

$$\frac{1}{r_{12}}=\sum_{N=0}^{\infty}\sum_{M=-N}^{N}\frac{(N-|M|)!}{(N+|M|)!}P_N{}^{|M|}(\cos\theta_1) \times P_N{}^{|M|}(\cos\theta_2)e^{iM(\varphi_2-\varphi_1)}\begin{cases}r_1{}^N/r_2{}^{N+1} & (r_2\geq r_1)\\ r_2{}^N/r_1{}^{N+1} & (r_1\geq r_2).\end{cases} \tag{3}$$

Since the total transition rate must be independent of m_1, the integration is simplified by choosing $m_1=0$. Performing the integrations, squaring, and summing over final values of m_2, we get the following contributions from all angular parts:

S transitions ($l=0$, $l_1=l_2$): 1

P transitions ($l=1$, $l_1=l_2+1$): $l_1/3(2l_1+1)$.

The radial integrals are best performed separately for the S and P transitions.

A. *P* Transitions

The only nonvanishing term of (3) is the term $N=1$. For $l_1=n_1-1$, we have

$$L_{n_1+l_1}{}^{2l_1+1}=-(2n_1-1)!,\quad L_{n_2+l_2}{}^{2l_2+1}=-(2n_1-3)!.$$

Hence, apart from a numerical factor, the required integral is

$$I=\int_0^{\infty}dr_2\,{}_1F_1(2+iy;4;2i\kappa r_2)e^{-Br_2} \times\left\{\int_0^{r_2}dr_1r_2r_1{}^{2n_1}e^{-Ar_1}+\int_{r_2}^{\infty}dr_1r_2{}^4r_1{}^{2n_1-3}e^{-Ar_1}\right\},$$

where

$$A=\frac{\mu Z_1}{a_0}\left(\frac{1}{n_1}+\frac{1}{n_1-1}\right),\quad B=\frac{1}{a_0}(Z+i\kappa a_0).$$

The integration over r_1 may be carried out by parts, and the integrations over r_2 (following Burhop[15]) by use of the relation

$$\int_0^{\infty}r^pe^{-qr}\,{}_1F_1(a;b;cr)dr=\frac{\Gamma(p+1)}{q^{p+1}}\,{}_2F_1(a,p+1;b;c/q).$$

We find $I=I_1+I_2+I_3$, where I_1, I_2 are finite series,

$$I_1=\sum_{N=1}^{2n_1+1}\frac{(2n_1)!N}{(A+B)^{N+1}A^{2n_1+2-N}} \times{}_2F_1\left(2+iy,N+1;4;\frac{2i\kappa}{A+B}\right),$$

$$I_2=\sum_{N=1}^{2n_1-2}\frac{(2n_1-3)!N(N+1)(N+2)(N+3)}{(A+B)^{N+4}A^{2n_1-1-N}} \times{}_2F_1\left(2+iy,N+4;4;\frac{2i\kappa}{A+B}\right),$$

and

$$I_3=\frac{(2n_1)!}{\kappa^2A^{2n_1+1}}\frac{1}{(i+y)^2}\,{}_2F_1\left(2+iy,2;4;\frac{2}{1-iy}\right).$$

Since $|A|\gg|B|$, the major contribution to I arises from I_3. This may be evaluated explicitly by successive

[13] W. Gordon, Z. Physik **48**, 180 (1928).

[14] P. A. M. Dirac, Proc. Roy. Soc. (London) **A114**, 243 (1927).

[15] E. H. S. Burhop, Proc. Roy. Soc. (London) **A148**, 272 (1935).

use of the relations[16]

$$\frac{\Gamma(a)\Gamma(b)}{\Gamma(c)}\,{}_2F_1(a,b;c;z)$$

$$=\frac{\Gamma(a)\Gamma(b-a)}{\Gamma(c-a)}(-z)^{-a}\,{}_2F_1(a,1-c+a;1-b+a;z^{-1})$$

$$+\frac{\Gamma(b)\Gamma(a-b)}{\Gamma(c-b)}(-z)^{-b}\,{}_2F_1(b,1-c+b;1-a+b;z^{-1}),$$

$$(|\arg(-z)|<\pi),$$

and

$${}_2F_1(a,b;c;z)=(1-z)^{c-a-b}\,{}_2F_1(c-a,c-b;c;z),$$

which give

$$I_3=\frac{3}{\kappa^2}\frac{(2n_1)!}{A^{2n_1+1}}\frac{1}{1+y^2}\exp[y(2\tan^{-1}y-\pi)].$$

An approximate evaluation of the series terms I_1 and I_2 may be made since $|2i\kappa/(A+B)|\ll 1$ and, usually, $|B|<|A|$, by putting each hypergeometric function equal to 1, and ignoring B by comparison with A. The series may then be summed to give

$$I_1=-C_1(2n_1+2)!/2,\quad I_2=+C_2(2n_1+2)!/5,$$

where C_1, C_2 are correction factors of order 1. A graphical method of determining C_1, C_2 has been described in the thesis of one of the authors.[5] In general C_1, C_2, have been found to be less than 1, and a convenient method of estimating the error involved in the approximation is by putting both C_1 and C_2 equal to 1 and 0 in turn. The correct value should lie between these two limits.

B. *S* Transitions

The particular transition considered is that in which $l_1=l_2=n_1-2$, $n_2=n_1-1$. For this case we have

$$L_{n_1+l_1}{}^{2l_1+1}=(2n_1-2)!\left\{\frac{2Z_1\mu r_1}{n_1a_0}-(2n_1-2)\right\}.$$

The integrations over r_1 and r_2 may be performed as before. It is found however that the two terms arising at the lower limit of the integration over r_1 cancel. These are the equivalent of I_3 in the P transitions integral, and in the absence of cancellation would be expected to give the major contribution. Thus, the S transition rates are, in general, smaller than the corresponding rates for P transitions.

After some simplification the remaining terms in the radial integral give

$$I=\sum_{N=1}^{2n_1-2}\frac{(2n_1-2)!}{2n_1-1}\frac{N(N+1)}{A^{N+2}(A+B)^{2n_1-1-N}}\times{}_2F_1\left(1+iy;N+1;2;\frac{2i\kappa}{A+B}\right)$$

$$=C_3\frac{(2n_1-2)!(2n_1-2)(2n_1)}{3}\frac{1}{A^{2n_1+1}},$$

where C_3 is a correction factor of the same type as C_1, C_2.

C. Radiative Transitions

The radiative transition rate is given by

$$P_R=\frac{4}{3}\frac{(2\pi\nu)^4\epsilon^2}{h\nu c^3}\left|\int\chi_f^*\mathbf{r}_1\chi_i d\tau_1\right|^2,$$

where ν is the frequency of the emitted quantum.

The integral has been evaluated in general form by Gordon.[17] The only amendments required are a summation over all possible final states, the substitution of the mesonic mass for the electron mass, and the substitution of the Bohr value for the frequency of the emitted quantum,

$$\nu=\frac{2n_1-1}{n_1^2(n_1-1)^2}\frac{Z_1^2\epsilon^2\mu}{2a_0h}.$$

III. RESULTS AND DISCUSSION

Collecting together all factors, the following formulas are found to the relevant transition rates.

P Auger Transitions: $(n_1,n_1-1)\rightarrow(n_1-1,n_1-2)$

$$P_A=\frac{1}{3}\left(\frac{Z}{Z_1}\right)^2C^2\frac{\pi m_e\epsilon^4}{\mu^2\hbar^3}\frac{2^{4n_1+6}n_1{}^{2n_1+2}(n_1-1)^{2n_1+4}}{(2n_1-1)^{4n_1+2}(1+y^2)}\times\frac{y^2\exp\{y(4\tan^{-1}y-\pi)\}}{\sinh\pi y},\quad(4)$$

where

$$C=1-\left(\frac{Z}{Z_1}\right)^2\frac{(2n_1+1)(2n_1+2)n_1^2(n_1-1)^2(1+y^2)}{3(2n_1-1)^2\mu^2y^2\exp\{y(2\tan^{-1}y-\pi)}\times\left(\frac{C_1}{2}-\frac{C_2}{5}\right).$$

S Auger Transitions: $(n_1,n_1-2)\rightarrow(n_1-1,n_1-2)$.

$$P_A=\left(\frac{Z}{Z_1}\right)^4\frac{\pi m_e\epsilon^4}{\mu^4\hbar^3}\frac{2^{4n_1+6}n_1{}^{2n_1+4}(n_1-1)^{2n_1+5}}{9(2n_1-1)^{4n_1+2}}\frac{e^{\pi y}}{\sinh\pi y}C_3^2.\quad(5)$$

[16] E. T. Whittaker and G. N. Watson, *A Course of Modern Analysis* (The Macmillan Company, New York, 1946), fourth edition, Chapter 14.

[17] W. Gordon, Ann. Physik **2**, 1031 (1929).

TABLE I. Auger and radiative transition rates/sec (P_A and P_R) for elements in photographic emulsions together with energy, E, of emitted Auger electron in kev.

Element		Transition $(n_1, n_1-1) \rightarrow (n_1-1, n_1-2)$ $n_1=2$	3	4	5	6	7	8
C	P_A	2.07×10^{11}	6.08×10^{12}	3.88×10^{13}	1.31×10^{14}	3.15×10^{14}	6.11×10^{14}	1.02×10^{15}
	P_R	1.71×10^{14}	1.76×10^{13}	3.76×10^{12}	1.53×10^{12}	4.48×10^{11}	2.02×10^{11}	1.01×10^{11}
	E	76.6	14.0	4.8	2.1	1.0	0.6	0.3
N	P_A	2.24×10^{11}	6.54×10^{12}	4.12×10^{13}	1.39×10^{14}	3.33×10^{14}	6.43×10^{14}	1.07×10^{15}
	P_R	3.16×10^{14}	3.26×10^{13}	6.96×10^{12}	2.15×10^{12}	8.30×10^{11}	3.74×10^{11}	1.88×10^{11}
	E	104.3	19.1	6.5	2.9	1.4	0.7	0.4
O	P_A	2.38×10^{11}	6.89×10^{12}	4.33×10^{13}	1.45×10^{14}	3.47×10^{14}	6.66×10^{14}	1.11×10^{15}
	P_R	5.39×10^{14}	5.57×10^{13}	1.19×10^{13}	3.66×10^{12}	1.42×10^{12}	6.38×10^{11}	3.21×10^{11}
	E	136.2	24.9	8.5	3.7	1.8	0.9	0.5
Br	P_A	3.18×10^{11}	9.02×10^{12}	5.53×10^{13}	1.81×10^{14}	4.23×10^{14}	7.90×10^{14}	1.27×10^{15}
	P_R	1.98×10^{17}	2.04×10^{16}	4.35×10^{15}	1.34×10^{15}	5.19×10^{14}	2.34×10^{14}	1.17×10^{14}
	E	2601	471	156.8	65.9	30.0	13.1	4.0
Ag	P_A	$3.25\times10^{11}-$ 3.29×10^{11}	$9.24\times10^{12}-$ 9.40×10^{12}	$5.63\times10^{13}-$ 5.78×10^{13}	$1.84\times10^{14}-$ 1.92×10^{14}	$4.28\times10^{14}-$ 4.58×10^{14}	$7.97\times10^{14}-$ 8.86×10^{14}	$1.27\times10^{15}-$ 1.48×10^{15}
	P_R	6.43×10^{17}	6.63×10^{16}	1.41×10^{16}	4.36×10^{15}	1.69×10^{15}	7.60×10^{14}	3.82×10^{14}
	E	4698	848	281	171.1	52.5	22.0	5.8

Radiative Transitions:

$$P_R=\left(\frac{\epsilon^2}{hc}\right)^6\frac{\mu m_e c^3}{3\epsilon^2}Z_1{}^4\frac{2^{4n_1}n_1{}^{2n_1-4}(n_1-1)^{2n_1-2}}{(2n_1-1)^{4n_1-1}}. \quad (6)$$

A factor of 2 has been incorporated in the Auger transition rates to allow for the 2 electrons in the K shell. In numerical work, since C is almost independent of Z, it has been computed for one element only. Values of the K shell ionization potential from the tables of Compton and Allison[18] have been taken, the ionization potential corresponding to $Z=Z_1-1$ being used to allow for screening by the meson. In Table I, Auger and radiative rates for some elements are presented, together with the energy of the ejected electron.

Table I enables an estimate of the total time of transition from a level $n_1=8$ to the $1s$ state to be made for a μ-meson. For bromine the estimated time is 4×10^{-15} sec, while for carbon the time is 9×10^{-14} sec. The time for carbon may be lengthened if the atom becomes completely ionized through earlier Auger transitions, but allowing for radiative transitions only, the time required is as short as 2×10^{-11} sec. These times are all very much less than the life time of a μ-meson, 2.15×10^{-6} sec, and strongly confirm previous conclusions that the majority of μ^- meson decays observed will take place when the meson has spent almost its entire life in a $1s$ state. The weakness of the interaction between μ-mesons and nucleons is thus demonstrated.

As the P transitions are apparently more important than the S transitions, no S transitions have been calculated. The exceptional case of the $2s\rightarrow1s$ transition, where the only other possible transition is the $2s\rightarrow2p$ radiative transition calculated by Wheeler,[6] for which the rate is very small for light elements, has been considered. It will be seen that for y small, (4) reduces to the formula quoted by Wheeler except for the Z dependence. The argument of Wheeler that the S transitions should be more probable than the P transitions, in view of the greater magnitude of the S electronic wave functions in the region of energy transfer, does not appear to be valid.

[18] A. H. Compton and S. K. Allison, *X-Rays in Theory and Experiment* (D. Van Nostrand and Company, Inc., New York, 1935).

IV. EXPERIMENTAL COMPARISON

Auger electrons accompanying stopped μ-mesons have been observed by Cosyns *et al.*,[9] 1949, and Fry,[10] 1951, and the number of electrons per stopped meson deduced. The results for the heavy elements, silver and bromine, may be separated from those for the lighter elements by the use of Wheeler's Z^4 law for nuclear absorption by which decay electrons should rarely be emitted for elements of atomic number appreciably greater than 11. Cosyns deduced a frequency of 20 percent for Auger electrons of energy greater than 20 kev in silver bromide, but commented that the rigorous criterion adopted for the recognition of Auger electrons may have excluded as many as had been accepted. No conclusions were reached concerning the lighter elements but out of 53 negative meson decays he observed two cases in which both Auger and decay electrons were emitted. This suggests an Auger frequency of the order of 4 percent.

The experiments of Fry were based on a somewhat smaller number of tracks and gave a frequency for emission of Auger electrons in silver bromide of energy between 15 and 70 kev of 0.34 ± 0.06 when appropriately weighted cases of double emissions were included.

The predicted and experimental results for the heavy elements (assuming the probability of capture independent of Z) are shown in Table II. The predicted

results are rather high, even after allowance has been made for the fact that the observations must be regarded as a lower limit. It is possible that the discrepancy may be removed by consideration of transitions between noncircular orbits. Calculations concerning such transitions and those involving the emission of L shell electrons are proceeding. Also no allowance has been made for the reduction of the Auger transition rate caused by the ejection of K shell electrons by earlier Auger transitions.

For the light elements, assuming relative abundances of H:C:N:O of 340, 170, 36, 90, the computed Auger frequency is 1.6 percent. However, since almost every meson passing through the $2s$ state of carbon, nitrogen, and oxygen might be expected to emit an Auger electron, this figure is certainly an underestimate. To account for the observed number, a very small proportion of mesons would be required to pass through the $2s$ state.

These results are also based on a hydrogenic approximation for the atom and have been extrapolated to include the heavy elements of the emulsion. The effect of the finite size of the nucleus on the energy levels, as discussed by Wheeler,[6] has been ignored.

The simple picture must be qualified by further consideration.[5] In atoms containing many electrons, a large number of Auger electrons are probably emitted in the first transitions, and the atom may become highly ionized. Inside the orbit defined for the μ-meson by $n=15$, the K electrons will first be ejected, and the rate of Auger transition may then depend upon the rate at which the K shell is replenished from the outer shells. The alternative to this is the direct Auger ejection of outer shell (L, M, etc.) electrons, and these rates are probably much smaller than the K shell ejection rates. It may be, however, that the atom has been completely stripped of electrons by the first transitions—this is clearly possible for light atoms. In this case the rate of descent of the meson towards the nucleus will depend on the rate of recombination of the system, and the radiative transition rate. The possibility of electron recombination can be ruled out for hydrogen by the calculations of Wightman[4] and Fermi and Teller,[19] which show that an electron cannot be bound to the proton-meson system which has a separation less than $0.64\ a_0$, corresponding to a meson orbit $n\approx 12$. For nuclei of higher atomic number than hydrogen the electron will have stable orbits whatever the value of the nucleus-meson separation. Thus electron recombination is possible in principle even for close orbits. From Table I, however, it is seen that for close orbits radiative transitions dominate, so this effect would not be important. The calculation of the critical separation for the meson-proton system leads to an interesting conclusion. The loss of energy of such a system to surrounding atoms or molecules will depend on the velocity of the system and the material through which it is moving. But the time taken for the meson to descend by radiative transitions to its K orbit, if there is no interaction with other particles, is calculated to be 2×10^{-7} sec,[5] which is about one-tenth of the natural lifetime of the μ-meson. Thus, if there are conditions in which collisional de-excitation is negligible, it is possible that in some cases a μ-meson may decay before reaching the K orbit.

Fermi and Teller and Frank[20] pictured the meson-proton system in its ground state as effectively neutral. In this state Frank suggested that the system would not have any interaction with electrons, and that, consequently, it would be able to penetrate easily the electron shells of a heavy atom, perhaps Ag, in an emulsion. If the system could get inside the atomic K orbit and still remain bound, it would appear that the meson might be absorbed by the nucleus and the proton repelled by it. Alternatively, there should be a finite probability that the proton will be captured by the nucleus. Frank showed that capture of the proton is probable if the nucleus is a deuteron but not if it is a heavy nucleus. For such a heavy nucleus it is to be expected that when the proton is ejected electrons will be scattered out. In the light of later calculations[4,5] it would appear that the dipole system of meson and proton will not be neutral with respect to electrons in the shells. In this case the initial stages in the process of Frank would not take place; the meson-proton system might dissociate in the outer electronic shells, or, much more probably, remove electrons. The absorption of the meson and the repulsion of the proton scattering out more electrons could then take place. The calculation of the energies of the ejected electrons using this mechanism would be extremely complicated.

TABLE II. Predicted and observed numbers of slow electrons per negative μ-meson stopped in silver bromide.

	Energy range						
	15–70 kev	10–20 kev	20–40 kev	40–60 kev	60–100 kev	>100 kev	>20 kev
Predicted	0.64	0.39	0.48	0.10	0.06	0.03	0.67
Observed by Cosyns *et al.*	...	...	...	...	...	...	0.20
Observed by Fry	0.34	...	...	...	...	...	...

We are deeply indebted to Professor H. S. W. Massey for introducing us to this problem and for stimulating discussion, and also to Dr. E. H. S. Burhop for many discussions on the Auger transition problem. The majority of the work was done at University College, London. The authors wish to acknowledge grants from the D.S.I.R. and the Ministry of Education.

[19] E. Fermi and E. Teller, Phys. Rev. **72**, 399 (1947).

[20] F. C. Frank, Nature **160**, 525 (1947).

Characteristics of Br^{87}, a Delayed Neutron Activity*†

ANDREW F. STEHNEY,‡ *Argonne National Laboratory, Chicago, Illinois and Department of Chemistry and Institute for Nuclear Studies, University of Chicago, Chicago, Illinois*

AND

NATHAN SUGARMAN, *Institute for Nuclear Studies, University of Chicago, Chicago, Illinois*

(Received September 25, 1952)

The energies of the beta-rays of Br^{87} were determined to be 2.6 and 8.0 Mev by aluminum absorption measurements. Gamma-radiation was observed, and from the absorption curve of the secondary Compton electrons, the maximum energy of the gamma-radiation was found to be 5.4 Mev. Most of the gamma-rays have energies in the range 2 to 4 Mev. Coincidences were observed between the weaker beta-ray and the gamma-rays. Gamma-gamma coincidences were also noted.

The fission yield of Br^{87} was found to be 3.1 percent.

I. INTRODUCTION

SOON after the discovery of fission in U^{235} by Hahn and Strassmann,[1] it was found that neutron activity persisted for several minutes after the fission process stopped.[2,3] Furthermore, it was shown that these neutrons were not produced by photodisintegration from gamma-rays of the fission products.[4] Studies on U^{235} have shown that delayed neutrons are emitted with several decay periods,[5–7] and the same decay periods are found in the thermal fission[6,8] of Pu^{239}, and in fast fission[9] of U^{238} and Th^{232}. Table I lists the half-lives, energies, and yields of the delayed neutrons from U^{235} obtained by Hughes, Dabbs, Cahn, and Hall.[7]

An explanation for delayed neutron emission was given in the fission mechanism proposed by Bohr and Wheeler.[10] Calculations using the nuclear drop model showed that some of the short-lived fission products may be expected to have available beta-decay energies greater than the binding energy of a neutron in the product nucleus, and that there would be an appreciable probability of cases of beta-decay leading to levels of the product nucleus from which a neutron might be emitted. According to this theory, the decay periods observed for the delayed neutrons would be those of the beta-ray emissions.

TABLE I. Data on delayed neutrons in fission of U^{235}.

Half-life, sec	Ave. kinetic energy, kev	Yield per fission neutron, $\times 10^4$	Fission yield,* %
55.6	250	2.5	0.063
22.0	560	16.6	0.42
4.51	430	21.3	0.53
1.52	620	24.1	0.60
0.43	420	8.5	0.21
0.05		2.5	0.063

* Fission yields are calculated using a value of 2.5 for the number of fission neutrons per fission.

Snell and co-workers[11] chemically identified the 55.6-sec and 22.0-sec neutron activities as bromine and iodine, respectively, and tentatively assigned them to Br^{87} and I^{137}. Later, mass assignments of 87 to the 55.6-sec Br delayed neutron emitter and of 137 to the 22.0-sec I delayed neutron emitter were made by Sugarman[12] in his work on the short-lived halogen fission products.

Alvarez[13] showed that neutrons are emitted following beta decay, as proposed by Bohr and Wheeler, in experiments on the 4.2-sec N^{17} delayed neutron activity. Coincidences were observed between beta-rays and O^{16} fragments recoiling from neutron emission.

Snell and co-workers[11] pointed out that the Bohr-Wheeler mass equation predicts the beta-decay energies of the halogens to be less than the neutron binding energies of their rare gas daughters for masses 87 and 137. Mayer[14] suggested that these energy discrepancies might be explained through the shell model of nuclear structure. Since Kr^{87} and Xe^{137} each has one neutron in excess of a shell number, the excitation energy which the rare gas nuclides receive in beta decay from the halogens would be sufficient to evaporate a neutron if the binding energy of the extra neutron were exceptionally low. The work of Hanson *et al.*[15] and of Harvey[16] indeed showed that for nuclides having 51 neutrons, the neutron binding energy is smaller than that calculated from the

* This document is based on work performed at the Argonne National Laboratory, Chicago, Illinois.

† Presented in partial fulfillment for the Ph.D. degree in the Department of Chemistry, University of Chicago, by A.F.S.

‡ Now at Argonne National Laboratory, Chicago, Illinois.

[1] O. Hahn and F. Strassmann, Naturwiss. **27**, 11 (1939).

[2] Roberts, Meyer, and Wang, Phys. Rev. **55**, 510 (1939).

[3] Booth, Dunning, and Slack, Phys. Rev. **55**, 876 (1939).

[4] Roberts, Hafstad, Meyer, and Wang, Phys. Rev. **55**, 664 (1939).

[5] Snell, Nedzel, Ibser, Levinger, Wilkinson, and Sampson, Phys. Rev. **72**, 541 (1947).

[6] W. C. Redman and D. Saxon, Phys. Rev. **72**, 570 (1947).

[7] Hughes, Dabbs, Cahn, and Hall, Phys. Rev. **73**, 111 (1948).

[8] F. deHoffman and B. T. Feld, Phys. Rev. **72**, 567 (1947).

[9] Sun, Charpie, Pecjak, Jennings, Nechaj, and Allen, Phys. Rev. **79**, 3 (1950).

[10] N. Bohr and J. A. Wheeler, Phys. Rev. **56**, 426 (1939).

[11] Snell, Levinger, Meiners, Sampson, and Wilkenson, Phys. Rev. **72**, 545 (1947).

[12] N. Sugarman, J. Chem. Phys. **17**, 11 (1949).

[13] L. W. Alvarez, Phys. Rev. **75**, 1127 (1949).

[14] M. G. Mayer, Phys. Rev. **74**, 235 (1948).

[15] Hanson, Duffield, Knight, Diven, and Palevsky, Phys. Rev. **76**, 578 (1949).

[16] J. A. Harvey, Phys. Rev. **81**, 353 (1951).

semi-empirical mass equation by several tenths of an Mev. It also appeared probable that the decay energies of Br^{87} and of I^{137} would be greater than those calculated from the mass equation because of closed shell effects.

In the work reported here, the energies of the beta- and gamma-radiations of Br^{87} were measured, and the relationship between them investigated. The total energy of decay was found to be about 8 Mev. In addition, the fission yield of Br^{87} in U^{235} was found to be 3.1 percent, in good agreement with the value of 3.0 percent predicted from the smooth yield-mass curve[17] of the fission products. A comparison of the fission yield of Br^{87} with that for delayed neutron emission from Br^{87} shows that neutron emission occurs in only 2.0 percent of the disintegrations of Br^{87}.

Neutron emission from Kr^{87} was not investigated in this work.

II. CHEMICAL SEPARATION OF BROMINE

The method of Strassmann and Hahn[18] was used to obtain a fast separation of active bromine from fission material. Solid uranyl nitrate was irradiated in the "rabbitt" of the Argonne heavy-water pile. The irradiated salt was dissolved in hot $6N$ H_2SO_4, and carrier bromine was added as Br^- and BrO_3^-. Air was drawn through the solution to sweep evolved Br_2 into a $1N$ HNO_3 solution containing Ag^+ and Fe^{++}, where bromine was immediately precipitated as AgBr.

The precipitate was collected on a filter-paper disk using vacuum. After being washed and dried by sucking alcohol and ether through it, the precipitate was mounted on a card and counted. Counting was usually started 75 to 90 sec after the end of the irradiations.

The only fission product likely to interfere in this procedure is iodine. Strassmann and Hahn[18] stated that, in the absence of weighable amounts of iodine, there was no interference from iodine activity. In the experiments reported here, it was found that less than 1 percent of the iodine activity came over when air was swept through the solution for 20 sec, but as much as 3 percent came over in 60 sec. Accordingly, air sweepings were limited to about 15 sec. Furthermore, for every determination of the Br^{87} activity, a decay plot was made, and the only decay periods observed were those of bromine nuclides and a krypton decay product, namely, 55.6-sec Br^{87}, 3-min Br^{85}, 30-min Br^{84}, and 75-min Kr^{87}. The relative activities of these nuclides varied for different absorber thicknesses, but the 55.6-sec activity always predominated at the start of the counting. One of the decay curves is given in Fig. 1 which shows the decay of activity from a precipitate of AgBr measured through 86 mg/cm² of aluminum in which the decay periods of Br^{87}, Br^{85}, and Kr^{87} were observed.

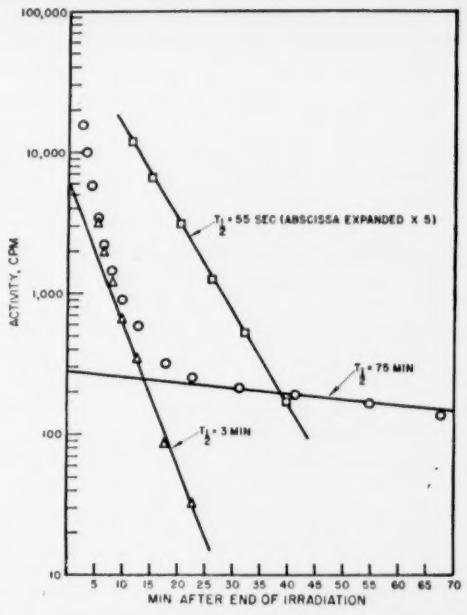

FIG. 1. Decay curve of bromine activity through 86 mg/cm² of aluminum. ○, original points; △, 75-min component subtracted; □, 75-min and 3-min components subtracted.

III. COUNTING APPARATUS AND PROCEDURES

Three types of measurements were made: (1) absorption measurements with a single counter for determination of beta-ray and gamma-ray energies; (2) coincidence measurements for clarification of the decay scheme; and (3) absorption of secondary electrons from gamma-rays for measurement of the gamma-ray energies.

The technique used to obtain the absorption curve of the 55.6-sec Br^{87} activity in a single counter was the same as that used by Stanley and Katcoff[19] in their work on 86-sec I^{136}, and by Sugarman[12] on 3.00-min Br^{85}. A portion of the absorption curve was constructed by following the decay of a sample through four different absorbers which were successively placed in position, repeating the absorbers of the set until only the longer-lived activities were left. After corrections were made for dead-time losses of the counter tube, the decay curve through each absorber was plotted and the curve was resolved. The next portion of the absorption curve was obtained with a newly prepared sample and another set of four absorbers. One of the four absorbers used in the previous set was used again, so that the activity of the second sample could be normalized to that of the first. Different amounts of uranyl nitrate were irradiated for the various samples to provide an initial counting rate of 10 000 to 15 000 counts per minute (cpm) for each set of absorbers.

The 55.6-sec Br^{87} activity was read from the resolved

[17] *Radiochemical Studies: The Fission Products* (McGraw-Hill Book Company, Inc., New York, 1951), National Nuclear Energy Series, Vol. 9, Div. IV.

[18] F. Strassmann and O. Hahn, Naturwiss. **28**, 817 (1940).

[19] C. W. Stanley and S. Katcoff, J. Chem. Phys. **17**, 653 (1949).

decay curve for each absorber at 3 min after the end of irradiation, although decay measurements were started before this time. A plot of the activity of the Br^{87} *vs* absorber thickness resulted in an absorption curve for the radiations of Br^{87}.

Since an error in one of the normalizing points for a set of absorbers would have been carried through in all of the succeeding points, the curve was checked, after it had been determined, by making several runs using other absorbers as normalization points. In addition, this "interlocking" absorption curve was shown to agree with the aluminum absorption curve of the singles count obtained in the coincidence work discussed later. In this case, the gamma-ray counting rate was used as the monitor of the disintegration rate of the source.

Rapid changing of the absorbers was accomplished by a specially designed absorber wheel. Openings for twelve absorbers were equally spaced along the circumference of the wheel which passed through a lead shield between an end-window Geiger-Mueller tube above, and a set of shelves below. Turning of the wheel was controlled by an automatic timer which could be set to hold each absorber in place from 3 sec to 3 min.

The scaling circuit was a Nuclear Instruments and Chemical Corporation Model No. 165. During the decay of the 55.6-sec activity, register pulses from the scaler were recorded on an Esterline-Angus chart.

In the coincidence work, two Victoreen end-window counters were arranged opposite each other, 2 cm apart. The source was mounted midway between the counters between two lead sheets $\frac{1}{8}$-in. thick with $\frac{3}{16}$-in. holes at the source position. Each source consisted of AgBr precipitated onto a filter paper circle of $\frac{1}{8}$-in. diameter. Placing the counters at right angles would have been preferable in order to reduce the possibility of spurious coincidences from photons scattered in the Compton process or from annihilation radiation resulting from pair formation. Since only a few coincidence counts were obtained for each source, because of the short life of the activity, the lower geometry factor of the right-angle arrangement would have resulted in so low a number of coincidences that the analysis would not have been feasible. Measurements made on coincidences in Na^{24} and Co^{60} showed that the number of spurious coincidences did not contribute noticeably to the true coincidence rate. The counter in which only gamma-rays were counted was surrounded by graphite to prevent coincidences from beta-particles which were scattered after being counted in the other counter.

The pulses from each counter were passed into a mixing circuit which had a resolving time of 0.3 μsec to record the coincidences. The single counts from each counter were also recorded by separate scalers. In operation, the register pulses from the single scalers were recorded on Esterline-Angus charts during the decay of the 55.6-sec activity, in the same way as described for the singles absorption work, whereas the coincidence counts were read visually at regular intervals.

A copper absorber of 5.7 g/cm^2 thickness was positioned between one counter (gamma-counter) and the source during all the coincidence measurements to absorb the beta-particles on that side. Varying thicknesses of absorber were placed against the window of the other counter (beta-counter) to measure the coincidence counting rate as a function of absorber. Only 1700 mg/cm^2 of aluminum could be fitted into the space available between the lead sheet and the window of the counter, so copper absorbers were used in measuring the coincidences for large absorber thicknesses.

Varying amounts of uranyl nitrate were irradiated to provide about 15 000 cpm initially in the beta-counter through each absorber used. This gave a total coincidence count ranging from about 50 through the thin absorbers, to about 20 through the thicker absorbers, during the decay of the 55.6-sec activity in a given source. The coincidences were observed to decay with a half-life of about 1 min, but with such a small number of counts an accurate decay plot of the coincidences could not be made. The procedure adopted was to record the total number of coincidence counts for the first six minutes, during which time 99 percent of the coincidences for Br^{87} could be expected. Corrections were made for dead-time losses caused by high singles rates in the two counters, the number of chance coincidences, the coincidences from the longer-lived activities present, and the cosmic-ray coincidence background in the 6-min counting period.

The coincidence counting rate, A^0, at the start of the counting period, was then calculated from the corrected number of coincidence counts, ΔC, obtained during the counting time, t, by the expression:

$$\Delta C = (A^0/\lambda)(1-e^{-\lambda t}),$$

where λ is the disintegration constant for Br^{87}. The decay curves of the single counts in the two counters were resolved for the Br^{87} activity. Since the interpretation of the coincidence data involved ratios of coincidence to single counting rates, the disintegration rates of the various samples were thus normalized.

Gamma-ray energies were determined by measuring the ranges of the secondary electrons from the gamma-rays.[20] Beta-rays from the source were removed by a thick aluminum absorber, and coincidence counts from secondary electrons were recorded in two counters, mounted one behind the other, as a function of the thickness of absorber placed between the two counters.

The counter arrangement of Fowler, Lauritsen, and Lauritsen[21] was used in studying the absorption of the

[20] W. Bothe and W. Kolhorster, Naturwiss. **17**, 271 (1929); Curran, Dee, and Petrzilka, Proc. Roy. Soc. (London) **169**, 269 (1938); H. Becker and W. Bothe, Z. Physik **76**, 421 (1932); E. Bleuler and W. Zünti, Helv. Phys. Acta **19**, 376 (1946); Bennett, Bonner, Hudspeth, Richards, and Watt, Phys. Rev. **59**, 781 (1941).

[21] Fowler, Lauritsen, and Lauritsen, Revs. Modern Phys. **20**, 236 (1948).

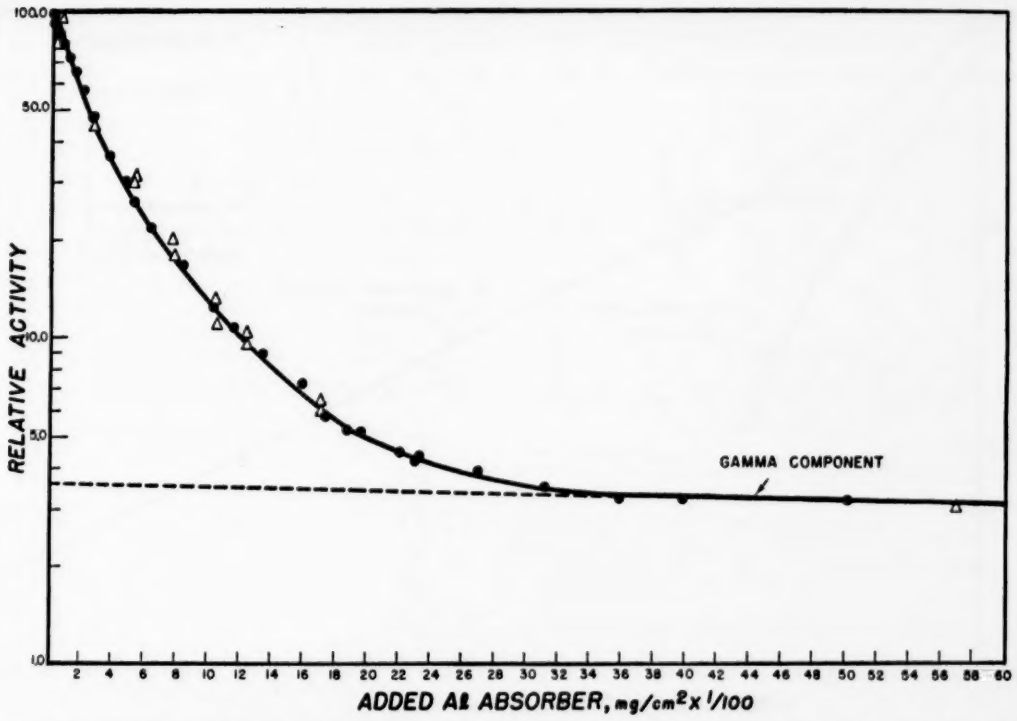

FIG. 2. Aluminum absorption curve of 55.6-sec Br^{87}. ●, interlocking absorbers technique; △, $\beta-\gamma$ coincidence work using gamma-ray counter as monitor.

secondary electrons from Br^{87}. The absorption data of Fowler *et al.*[21] on gamma-rays of high energy could then be used in interpreting the observations on Br^{87}. The rear counter consisted of two counters placed side by side which increased the number of counts observed, and thus, improved the statistical accuracy of the measurements. The counters were Eck and Krebs type cylindrical counters, with glass walls of about 30 mg/cm² thickness over the sensitive region of the counter. The coincidence circuit used in the other coincidence work was used here.

Each absorption point of the secondary electrons was obtained with a freshly prepared source. Corrections were made for chance coincidences, background counts, and dead-time losses. Decay curves of the coincidences and of the activity in the front counter were analyzed for the 55.6-sec activity, and the counting rates of the various sources were normalized to the same disintegration rate by using ratios of the coincidence rate of Br^{87} at a given time to the activity of Br^{87} in the front counter at the same time. The absorption curve of the secondary electrons from Br^{87} was then determined by plotting these ratios *vs* the thickness of aluminum absorber.

IV. BETA-RAY ENERGIES

The aluminum absorption curve of the 55.6-sec activity, determined in a single counter with the revolving wheel apparatus, is given in Figs. 2 and 3. The absorption points obtained with the coincidence apparatus are also given in Fig. 2 for comparison. The curve was resolved into a gamma-ray, whose counting rate was about 3.5 percent of the initial activity, and two beta-activities. Range determinations of the beta-radiation were made by the comparison method of Feather,[22] using UX_2 as the standard beta-ray emitter. Feather's value of 1105 mg/cm² of aluminum was used for the range of the beta-radiation from UX_2. The Feather range of the more energetic beta-ray (β_1) of Br^{87} was found to be about 4200 mg/cm² of aluminum. Beta-rays of known energies greater than 3 Mev were not available for comparison of ranges in our apparatus. However, according to published range-energy curves,[23] the observed range of β_1 corresponds to a maximum beta-energy of 8.0 Mev.[24] The range of the less energetic beta-radiation (β_2) was found to be 1260 mg/cm² of aluminum, corresponding to a maximum beta-energy of 2.6 Mev.

Since the initial portion of the absorption curve for the harder beta-ray was drawn in somewhat arbitrarily,

[22] N. Feather, Proc. Cambridge Phil. Soc. **34**, 599 (1938).

[23] L. E. Glendenin, Nucleonics **2**, No. 1, 12 (1948); L. Katz and A. S. Penfold, Revs. Modern Phys. **24**, 28 (1952).

[24] As described later, the visual ranges of secondary electrons from gamma-rays agreed with the extrapolated Glendenin curve to within 10 percent for electron energies as high as 17 Mev.

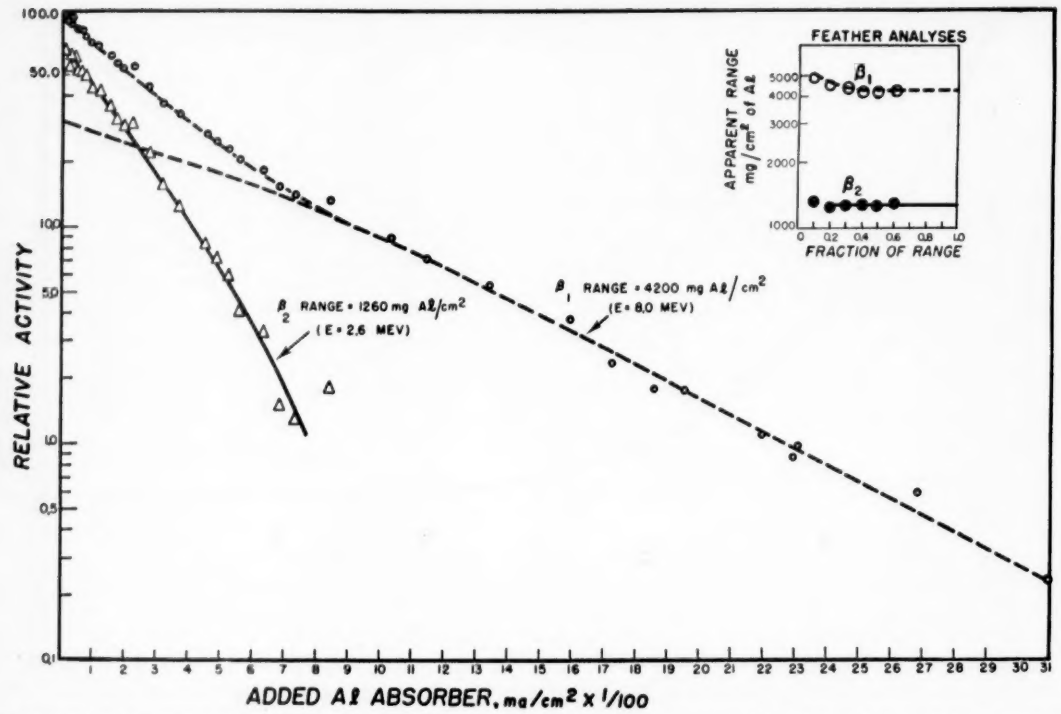
FEATHER ANALYSES
APPARENT RANGE mg/cm² of Al
FRACTION OF RANGE
β1
β2
β2 RANGE = 1260 mg Al/cm² (E = 2.6 MEV)
β1 RANGE = 4200 mg Al/cm² (E = 8.0 MEV)
RELATIVE ACTIVITY
ADDED Al ABSORBER, mg/cm² x 1/100

FIG. 3. Analyzed aluminum absorption curve of Br^{87} after subtraction of gamma-ray component. Feather analysis made by comparison with UX_2. ○, gamma-component of Fig. 2 subtracted; △, β_1-component subtracted.

the exact ratio of intensities of the two beta-rays cannot be given, but it appears that the weaker beta-ray is present in about twice the intensity of the harder beta-ray.

Some consideration was given to the possibility that the hard beta-ray component might be soft electromagnetic radiation of high counting efficiency. The half-thickness in aluminum of this component over a considerable portion of the curve was about 370 mg/cm², which would correspond to a photon of 25-kev energy.[23] The half-thickness of a 25-kev photon in lead would be about 15 mg/cm². The absorption curve of Fig. 4 shows that the observed half-thickness in lead of this component is about 220 mg/cm², which corresponds to an energy of 70 or 120 kev for photons. Photons of these energies would be counted with less than 0.2 percent efficiency. Furthermore, the observed reduction in range of the hard beta-ray of Br^{87} in lead compared to that in aluminum is similar to the reduction obtained when absorption curves through aluminum and lead were made for RaE (1.17-Mev β), UX_2 (2.32-Mev β), and Pr^{144} (3.1-Mev β). Thus the component in question is a beta-ray and not a photon.

V. GAMMA-RAY ENERGIES

Absorption in lead did not provide much information about the energy of the gamma-rays. A half-thickness of 19.8 g/cm² was obtained for the gamma-rays, consistent with a photon energy of 3 Mev or greater, where the half-thickness value for absorption is at a maximum.[21] Although only one gamma-ray component was apparent, a soft gamma-ray might have been masked by the hard gamma-ray of high counting efficiency.

The energies of the gamma-rays were determined by aluminum absorption of their secondary electrons. The method was tested with gamma-rays of known energies. The end point of the secondary electrons was chosen from a linear plot of the absorption curve as the intersection of the absorption curve with the background of scattered radiation.[25] The corresponding energy value for the most energetic electrons was calculated from the end-point value by Glendenin's range-energy relationship[23] for beta-particles, i.e., $E=1.85R+0.245$, where R is in g/cm² of aluminum, and E is in Mev. In addition, a small correction was made for the energy lost to the photons scattered backward. This procedure was applied to the secondary-electron absorption curves of Co^{60} (1.32 Mev), ThC″ (2.62 Mev), Na^{24} (2.76 Mev), and combined sources of Co^{60} and Na^{24}. Values of 1.3, 2.6, 2.7, and 2.6 Mev, respectively, were

[25] Although corrections were made for coincidences due to cosmic rays and for chance coincidences, a flat "tail" was always obtained in the absorption curves. This "tail" was probably due to scattering of radiation from the walls of the rear counter and, in some cases, to coincidences between gamma-rays emitted in cascade from the source.

obtained from these four curves. Evidence that this procedure was valid for gamma-rays of higher energy was obtained by applying it to the absorption curves of Fowler and co-workers[21] for the gamma-rays from ThC″ (2.62 Mev) and from the reactions F^{19} $(p, \alpha\gamma)$, (6.3 Mev), and Li^7 (p, γ), (17.5 Mev), for which 2.7, 6.5, and 19.0 Mev, respectively, were obtained.

The range of the secondary electrons from the gamma-rays of Br^{87} corresponded to a photon energy of 5.4 Mev (Fig. 5). It was observed that the intensity of the electrons decreased much more rapidly in the region from 0 to 1 g/cm² of aluminum than expected for 5.4-Mev photons. This is illustrated in Fig. 6 in which a curve of the shape expected for 5.4-Mev photons from our calibration runs and from the data of Fowler *et al.*[21] has

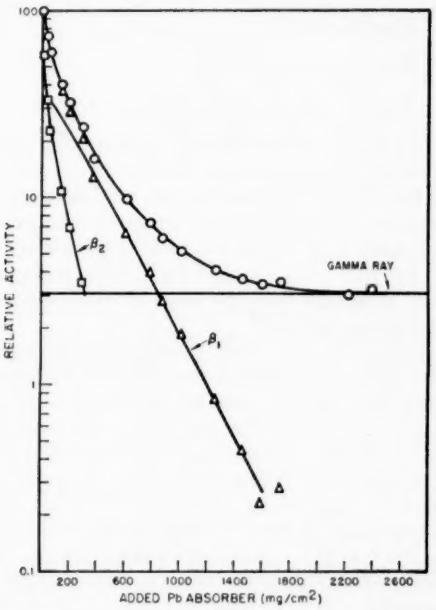

FIG. 4. Lead absorption curve of Br^{87}. ○, original points; △, gamma-ray subtracted; □, gamma-ray and β_1-component subtracted.

been fitted to the experimental curve at large absorber values. The difference between the curves at smaller absorber thicknesses is plotted and is a measure of the abundance of softer photons. It is estimated that more than 80 percent of the total number of photons are in the energy range 2 to 4 Mev.

VI. COINCIDENCE STUDIES

A proposed decay scheme for Br^{87} is given in Fig. 7 which relates the radiations detected in the absorption measurements in a manner consistent with the coincidence data to be described below. The counting rates expected[26] from a source disintegrating with this decay

[26] A. C. G. Mitchell, Revs. Modern Phys. **20**, 296 (1948).

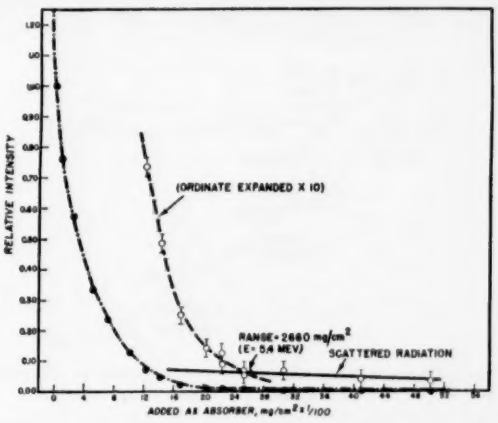

FIG. 5. Aluminum absorption curve of secondary electrons from gamma-rays of Br^{87} (linear plot). Two counter wall thicknesses equal to 60 mg/cm².

scheme at a rate, N_0, are as follows:

$$N_\beta = N_0\omega_\beta(\alpha_1 F_1 S_1 + \alpha_2 F_2 S_2), \quad (1)$$

$$N_\gamma = N_0\alpha_2\omega_\gamma[\pi_1 G_1\epsilon_1 + \pi_2(G_2\epsilon_2 + G_3\epsilon_3)], \quad (2)$$

$$N_{\beta\gamma} = N_0\alpha_2\omega_\beta\omega_\gamma F_2 S_2[\pi_1 G_1\epsilon_1 + \pi_2(G_2\epsilon_2 + G_3\epsilon_3)], \quad (3)$$

$$N_{\gamma\gamma} = 2N_0\alpha_2\omega_\beta\omega_\gamma\pi_2 G_2\epsilon_2 G_3\epsilon_3. \quad (4)$$

In these equations, the counting rates are designated by N with the subscript to denote the type of measurement.

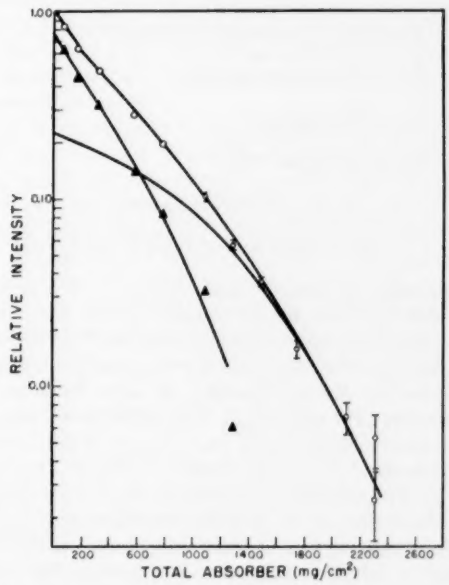

FIG. 6. Aluminum absorption curve of secondary electrons from Br^{87} after subtraction of scattered radiation compared with curve expected from 5.4-Mev photon. ○, experimental points; ▲, 5.4-Mev photon curve, drawn in, subtracted from experimental points.

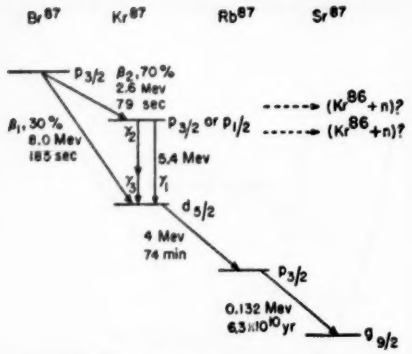

FIG. 7. Proposed decay scheme for Br^{87} in relation to succeeding members of chain.

The numerical subscript refers to the radiation correspondingly labeled in Fig. 7, and the other symbols are defined as follows: α = fraction of disintegrations of a given beta-ray; F = fraction of beta-rays passing through a given absorber; G = fraction of gamma-rays passing through a given absorber; ϵ = counting efficiency of photons; π = branching ratio of gamma-rays; ω = geometry factor; S = scattering and self-absorption factors for beta-rays. The source was symmetrically placed between the counters, so that ω_β equals ω_γ and both are henceforth designated by ω.

The following ratios of the counting rates were used in interpreting the coincidence data on Br^{87}:

$$N_{\beta\gamma}/N_\gamma=\omega F_2 S_2, \tag{5}$$

$$\frac{N_{\beta\gamma}}{N_\beta}=\frac{\alpha_2\omega F_2 S_2[\pi_1 G_1\epsilon_1+\pi_2(G_2\epsilon_2+G_3\epsilon_3)]}{(\alpha_1 F_1 S_1+\alpha_2 F_2 S_2)}, \tag{6}$$

$$\frac{N_{\gamma\gamma}}{N_\gamma}=\frac{2\omega\pi_2 G_2\epsilon_2 G_3\epsilon_3}{\pi_1 G_1\epsilon_1+\pi_2(G_2\epsilon_2+G_3\epsilon_3)}$$

$$=\frac{2\pi_2(\omega G_2\epsilon_2)(\omega G_3\epsilon_3)}{(1-\pi_2)(\omega G_1\epsilon_1)+\pi_2(\omega G_2\epsilon_2)+\pi_2(\omega G_3\epsilon_3)}. \tag{7}$$

According to Eqs. (5) and (6), a plot of $N_{\beta\gamma}/N_\gamma$ *vs* absorber thickness for Br^{87} should provide the absorption curve of β_2, whereas a similar plot for $N_{\beta\gamma}/N_\beta$ should decrease from the value $\alpha_2\omega S_2[\pi_1 G_1\epsilon_1+\pi_2(G_2\epsilon_2+G_3\epsilon_3)]/(\alpha_1 S_1+\alpha_2 S_2)$ for no absorber, to zero for absorbers thicker than the range of β_2. The experimental ratios of the total coincidence rate, $N_{\beta\gamma}+N_{\gamma\gamma}$, to N_γ are plotted *vs* thickness of aluminum absorber in Fig. 8. The values of $N_{\beta\gamma}/N_\gamma$, obtained by subtracting $N_{\gamma\gamma}/N_\gamma$, determine the absorption curve of a beta-ray having a Feather range of 1440 mg/cm² of aluminum, corresponding to an energy of 2.9 Mev. This value is somewhat larger than that of 2.6 Mev obtained in the singles absorption work of Fig. 3. The plot of $N_{\beta\gamma}/N_\beta$ (Fig. 9) also showed that the gamma-rays of Br^{87} follow a beta-ray whose energy is less than 3 Mev, since there is a sharp reduction in this ratio from zero absorber to about 1200 mg/cm² of aluminum. Beyond this thickness, the ratio of $N_{\beta\gamma}$ to N_β is essentially zero, being $(0.17\pm0.27)\times10^{-3}$. This ratio, if greater than zero, would be equal to the counting yield of gamma-rays following β_1. From the calibration curve of counting yield *vs* photon energy described later, the upper limit of 0.44×10^{-3} corresponds to about 0.7 Mev as the maximum energy of gamma-radiation following β_1.

In order to evaluate the results of the $\gamma-\gamma$ coincidences observed for Br^{87}, it was necessary to perform calibration runs on species of known decay scheme, such as Co^{60} and Na^{24}. The following ratios of counting rates were expected for the latter two nuclides, each of which decays by a single beta-ray followed by 2 gamma-rays in cascade:

$$N_{\beta\gamma}/N_\gamma=\omega FS, \tag{8}$$

$$N_{\beta\gamma}/N_\beta=\omega G_1\epsilon_1+\omega G_2\epsilon_2, \tag{9}$$

$$N_{\gamma\gamma}/N_\gamma=2(\omega G_1\epsilon_1)(\omega G_2\epsilon_2)/(\omega G_1\epsilon_1+\omega G_2\epsilon_2). \tag{10}$$

The plot of $N_{\beta\gamma}/N_\gamma$ *vs* thickness of aluminum absorber gave the absorption curve of the beta-ray in each case. The plots were extrapolated to zero total absorber using self-absorption and self-scattering corrections given by Engelkemeir *et al.*,[27] and values of 0.081 for Co^{60} and 0.083 for Na^{24} were obtained for ω. This was in satisfactory agreement with the value of 0.085 obtained in the same way with Br^{87}.

Equation (9) was used to estimate the counting yields, $\omega G\epsilon$, of the gamma-rays through 5.7 g/cm² of copper. For Co^{60}, $N_{\beta\gamma}/N_\beta$ was 1.57×10^{-3}. Assuming that the 1.16- and 1.32-Mev gamma-rays were equivalent to two 1.25-Mev gamma-rays, the counting yield for each was 0.78×10^{-3}. The value of $N_{\beta\gamma}/N_\beta$ for Na^{24} was 2.69×10^{-3}; this led to a value of 1.8×10^{-3} for the counting yield of the 2.76-Mev gamma-ray of Na^{24}, when the 1.38-Mev gamma-ray was assumed to have a counting yield slightly greater than that of a 1.25-Mev gamma-ray.

Substituting the above counting yields into Eq. (10) showed that spurious $\gamma-\gamma$ coincidences were negligible for Co^{60} and Na^{24}, because the calculated values of $N_{\gamma\gamma}/N_\gamma$ were 0.78×10^{-3} and 1.19×10^{-3} for Co^{60} and Na^{24}, respectively, and the corresponding experimental values were 0.81×10^{-3} and 1.08×10^{-3}.

For Br^{87}, $N_{\gamma\gamma}/N_\gamma$ was $(1.5\pm0.2)\times10^{-3}$ when copper absorbers 5.7 g/cm² thick were between each counter and the source. The factors in Eq. (7) were estimated in order to determine the value of $N_{\gamma\gamma}/N_\gamma$ expected for the decay scheme proposed in Fig. 7. Counting yields for the gamma-rays were estimated by fitting to the values for 1.25 Mev and 2.76 Mev a curve of the shape calculated by Fowler *et al.*,[21] for the counting efficiency of gamma-

[27] Engelkemeir, Seiler, Steinberg, and Winsberg, *Radiochemical Studies: The Fission Products* (McGraw-Hill Book Company, Inc., New York, 1951), Paper No. 4, National Nuclear Energy Series, Vol. 9, Div. IV.

rays in thick aluminum counters as a function of photon energy. The aluminum absorption curve of the secondary electrons (Fig. 6) indicated that the energy of γ_1 was 5.4 Mev, that 2.0 and 3.4 Mev would be reasonable energies for γ_2 and γ_3, and that π_2 was about 0.8. Substitution of this value of π, and the values of $\omega G\epsilon$ corresponding to these photon energies into Eq. (7), results in a calculated value of 1.3×10^{-3} for $N_{\gamma\gamma}/N_\gamma$.

Three possible mechanisms by which spurious $\gamma-\gamma$ coincidences could be produced were examined in order to find out how seriously they might contribute to the observed $\gamma-\gamma$ coincidence rate. Spurious coincidences from the Compton process, in which the Compton electron is counted in one counter and the scattered photon in the other, are estimated as contributing at most 0.03×10^{-3} to the value of $N_{\gamma\gamma}/N_\gamma$. Similar calculations on annihilation radiation from pair formation yields a maximum contribution of about 0.06×10^{-3}. The contribution to the observed $\gamma-\gamma$ coincidence rate by bremsstrahlung is estimated to be about the same order. Thus, it would appear that the spurious $\gamma-\gamma$ coincidences are less than 10 percent of the observed rate.

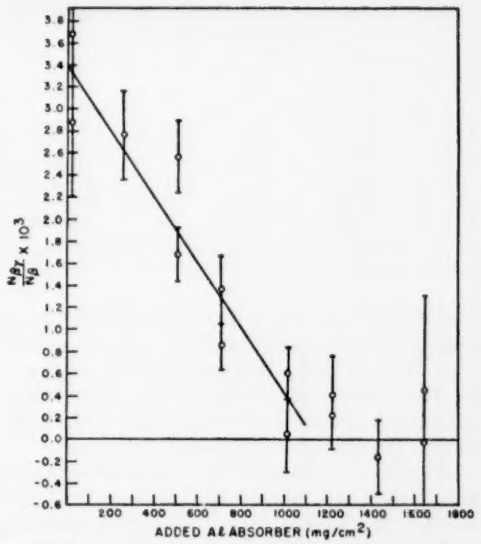

FIG. 9. Aluminum absorption curve of ratio of $\beta-\gamma$ coincidences to β-counting rate, $N_{\beta\gamma}/N_\beta$.

VII. DISCUSSION OF THE DECAY SCHEME OF Br^{87}

The aluminum absorption curve of radiations from Br^{87} (Fig. 3) showed that there are two beta-rays, 70 percent of 2.6 Mev and 30 percent of 8.0 Mev. From the aluminum absorption curve of secondary electrons from the gamma-rays of Br^{87}, (Figs. 5 and 6), gamma-rays of 5.4 Mev energy were detected in about 20 percent branching ratio. The gamma-rays in large abundance were found to be less energetic, in the energy range 2 to 4 Mev. The relationships between these radiations were established by coincidence measurements from which the following information was obtained: (1) all, or almost all, of the gamma-radiation follows the 2.6-Mev beta-ray; (2) if any gamma-rays follow the 8.0-Mev beta-ray, they have an upper energy limit of 0.7 Mev; and (3) cascading gamma-rays occur in the decay of Br^{87} giving rise to $\gamma-\gamma$ coincidences. This information is summarized in the proposed decay scheme for Br^{87} given earlier in Fig. 7.

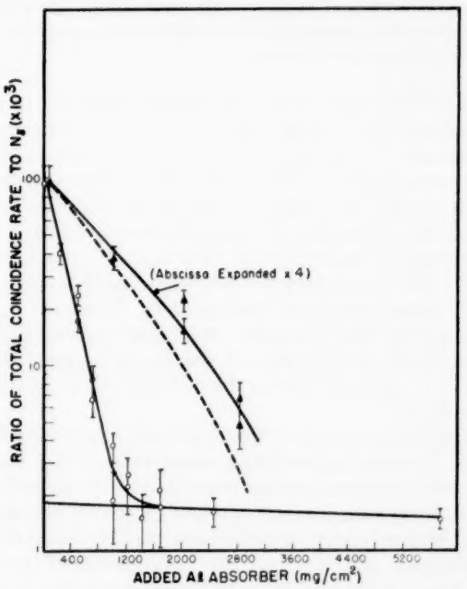

FIG. 8. Aluminum absorption curve of coincidences in beta- and gamma-counter. ○, $(N_{\beta\gamma}+N_{\gamma\gamma})/N_\gamma$; ▲, $N_{\gamma\gamma}/N_\gamma$ subtracted from original points, $N_{\beta\gamma}/N_\gamma$. Absorption curve of 2.6-Mev β-ray (β_2) taken from Fig. 3 is given by dashed line.

The spins assigned to Br^{87} and the excited state of Kr^{87} were selected to conform to transition rules for beta- and gamma-decay and to nuclear shell models.[28] Table II lists Nordheim's[29] beta-transition rules for odd A nuclides and the $\log_{10}(ft)$ values corresponding to each type of transition. From the maximum kinetic energy of the beta-rays and the half-lives of the decays, $\log_{10}(ft)$ values were obtained for beta-decays of nuclides of mass 87 using tables and graphs calculated by Moszkowski.[30] A summary of the data and the expected transitions is given in Table III. According to nuclear shell models,[28] the ground level of Kr^{87} should be a $d_{\frac{5}{2}}$ state. The $\log_{10}(ft)$ value for the decay of Br^{87} by β_1 of 7.4, corresponds to a first forbidden transition, so the decay is accompanied by a change of 1 in orbital angular momentum and a spin change of 0 or 1. This agrees with the assignment of $p_{\frac{3}{2}}$ for Br^{87} which is expected from nuclear shell theory.

[28] Mayer, Moszkowski, and Nordheim, Revs. Modern Phys. **23**, 315 (1951).
[29] L. W. Nordheim, Phys. Rev. **78**, 294 (1950).
[30] S. A. Moszkowski, unpublished work, Institute for Nuclear Studies, University of Chicago (1950).

TABLE II. Summary of Nordheim's rules for transitions of odd A nuclides.

Transition type	$\log_{10}(ft)$	ΔL	ΔI	Nature of transition
I	4.8–5.5	0	0, 1	$G-T$ allowed
II	(~6–7)	2	1	$G-T$ allowed (l-forbidden)[a]
III	6.5–7.5	1	0, 1	1st forbidden
IV	~8–9	1	2	1st forbidden[a]
V	>9			≥2nd forbidden

[a] See reference 28.

The decay of Br^{87} by β_2 has a $\log_{10}(ft)$ of 4.7, corresponding to an allowed transition with no change of orbital angular momentum and a change of 0 or 1 in spin. Thus, the excited level of Kr^{87} could be either a $p_{\frac{1}{2}}$ or $p_{\frac{3}{2}}$ state. A $p_{\frac{1}{2}}$ state is favored because of the observation that the gamma-ray transition is complex.

The total decay energy of Br^{87} was found to be about 8 Mev in these experiments. If allowance is made for the possibility that gamma-rays with a maximum energy of 0.7 Mev follow the more energetic beta-ray, then the decay energy may be as high as 9 Mev. Also, because of the uncertainty of determining beta-ray energies from absorption curves analyzed by the Feather method, the error in the beta-ray energy from this source may be of the order of 0.5 Mev. An estimate of 6.8 Mev for the total decay energy was made by Coryell[31] from a modified mass equation which takes account of the discontinuities in the Z_A parameter at the shell edges.

The excitation energy of the state from which the gamma-rays are emitted was determined as 5.4 Mev. Although it is difficult to estimate the error in this value, it is not likely that it would exceed 0.4 Mev. Since no measurements were made on beta-neutron coincidences, one cannot assign the state from which the neutrons are emitted. If the neutrons come off of the 5.4-Mev excited state of Kr^{87}, in poor competition with the gamma-rays, then the neutron binding energy would be about 5.2 Mev. On the other hand, a weak beta-ray of 2 percent branching ratio may exist which decays to a more excited state of Kr^{87} from which the neutrons are emitted. Such a beta-ray would not have been detected in the beta-ray absorption curve. An estimate of 5.7 to 6.0 Mev for the neutron binding energy can be made from the semi-empirical mass formulas including the shell effect. This estimate tends to support the existence of a third beta-ray branch in low yield.

VIII. FISSION YIELD OF Br^{87}

It has been shown[32] that the same yield of Br^{87} is obtained by dissolving irradiated uranyl nitrate in an acid solution of carrier BrO_4^- and reducing with Br^-, as by reducing the BrO_3^- with H_2S or by irradiating uranium metal and dissolving in HCl. The fastest of these procedures was used here for the fission-yield determination. An aliquot of a standard uranyl nitrate solution was pipetted into a small lusteroid tube and frozen in a dry-ice bath. After irradiation for 45 sec in the Argonne heavy-water pile, the uranium solution was melted and poured into a solution containing 5 ml $0.05M$ KBr and 5 ml $6N$ H_2SO_4. Then, 2 ml of $0.01M$ $KBrO_3$ were added. After stirring for 15 sec, I^- carrier was added, followed by 15 ml of $0.5M$ $KMnO_4$ to oxidize the excess Br^- to Br_2 and I^- to IO_3^-. The bromine was distilled into 10 ml of $0.3M$ H_2SO_3, and precipitated as AgBr after the solution was acidified and boiled to remove SO_2. Oxidation of excess Br^- by $KMnO_4$ was used rather than equivalent amounts of BrO_3^- and Br^-, because only part of the bromine was collected in the distillation, and this portion may not have been in equilibrium with all of the carrier bromine present, if bromine were swept out as it was formed. The Br_2 was collected in H_2SO_3 because there was some evidence that direct precipitation in a Ag^+-Fe^{++} solution resulted in a chemically contaminated precipitate which would lead to spuriously high chemical yields.

TABLE III. Spin changes of mass 87 isobars deduced from values of $\log_{10}(ft)$.

Nuclide	E_β^{max}(Mev)	$T_{\frac{1}{2}}$	$\log_{10}(ft)$[a]	Transition type	Transition
Sr^{87}		Stable			($Sr^{87}g_{9/2}$)
Rb^{87}	0.132	6.3×10^{10} yr	16.0	V	$Rb^{87}p_{3/2}\rightarrow Sr^{87}g_{9/2}$
Kr^{87}, grd.	4	74 min	7.3	III	$Kr^{87}d_{5/2}\rightarrow Rb^{87}p_{3/2}$
Br^{87}, grd.?	8.0, 30%	185 sec	7.4	III	$Br^{87}p_{3/2}\rightarrow Kr^{87}d_{5/2}$
	2.6, 70%	79 sec	4.7	I	$Br^{87}p_{3/2}\rightarrow Kr^{87}p_{1/2}$ or $p_{3/2}$

[a] $\log_{10}(ft)$ values are for t in sec.

The fission yield of Br^{87} was calculated relative to that of 85-min Ba^{139} whose yield in U^{235} was taken as 6.3 percent.[17] Two aliquots of the uranyl nitrate solution were irradiated for analysis of barium together with the aliquot for the measurement of bromine activity. Analysis for barium was delayed about 2 hr after the irradiation in order to allow for decay of 9.7-min Cs^{139} to Ba^{139}, which was then isolated as $BaCl_2\cdot H_2O$ using the HCl–ether procedure developed by Glendenin.[33] Decay curves and aluminum absorption curves showed that all of the activity was due to Ba^{139} except for a small amount of 12.8-day Ba^{140}, for which a correction was made.

Counting was done with the absorber wheel apparatus used to obtain the aluminum absorption curve of Fig. 3. In order to eliminate interference from Br^{85}, the activity of Br^{87} was measured through 1222 mg/cm² of aluminum and extrapolated to zero total absorber by means of the absorption curve of Fig. 3. Ba^{139} was measured through 47.6 mg/cm² of aluminum and an extrapolation to zero

[31] C. D. Coryell (private communication).
[32] A. F. Stehney and N. Sugarman, J. Chem. Phys. **20**, 629 (1952).
[33] L. E. Glendenin, *Radiochemical Studies: The Fission Products* (McGraw-Hill Book Company, Inc., New York, 1951), Paper 288, National Nuclear Energy Series, Vol. 9, Div. IV.

TABLE IV. Fission yield of Br^{87} from U^{235}.

Run	Fission product isolated	Reference time, min	Activity, cpm $\times 10^{-3}$	Correction factors: Parent-daughter	Saturation	Decay	Absorption	Chemical yield	Corrected activity, cpm $\times 10^{-3}$	Fission yield, %
1	Br^{87}	5.00	2.53	1.00	2.34	42.0	10.2	3.22	8.15	3.04
	Ba^{139}	300	2.53	0.89	163	11.6	1.62	2.56	17.6	(6.3)
	Ba^{139}	300	1.86	0.89	163	11.6	1.62	3.20	16.2	
2	Br^{87}	5.00	5.12	1.00	2.34	42.0	10.2	2.99	15.35	3.22
	Ba^{139}	250	9.00	0.89	163	7.69	1.62	1.86	30.3	(6.3)
	Ba^{139}	250	4.93	0.89	163	7.69	1.62	3.34	29.7	

total absorber was made using an aluminum absorption curve for Ba^{139}. The bromine sources were about 8 mg/cm^2 in thickness, and the barium sources varied from 5 to 8 mg/cm^2. For both, the active precipitates were collected on filter paper and mounted on cardboard under Cellophane. From the results of Engelkemeir *et al.*,[27] it seemed reasonable to assume that the Cellophane, the source thickness, and the backing would have about the same effect on Br^{87} as on Ba^{139}, so corrections were made only for absorption by the window of the counter (3.7 mg/cm^2) and by the air space (6 mg/cm^2) between the source and the window. Accordingly, the aluminum absorption curves of Ba^{139} and Br^{87} were extrapolated 9.7 mg/cm^2 from zero added absorber to true zero absorber for the comparison of yields.

Some doubt of the validity of absorption corrections of Ba^{139} and Br^{87} was raised by the observation that the absorption curve for Ba^{139} dropped sharply from zero to about 50 mg/cm^2 of added absorber, whereas the absorption curve for Br^{87} was almost exponential from zero to more than 300 mg/cm^2 of added absorber. However, the decay curves of these activities indicated that no contaminating activities were present other than those for which corrections had been made, so the absorption curves were extrapolated to zero total absorber by following the experimental points as closely as possible without assuming any required shape for the curves.

The results obtained for the fission yield of Br^{87} are given in Table IV. The activity values of column 4 were taken from decay curves at the reference times given in column 3. A factor of 0.89 (column 5) was applied to the activity of Ba^{139} in order to correct for the hold-up of decay of Ba^{139} by its parent, 9.7-min Cs^{139}, and the half-life of Se^{87} was assumed to be very small so that no parent-daughter correction was used for Br^{87}. Corrections for unsaturated irradiations of 45 sec duration are given in column 6. The activities were corrected for decay from the end of irradiation and to zero total absorber using the factors of columns 7 and 8. Column 9 gives the ratio of the amount of carrier added to the amount of carrier recovered for each sample. The product of the activity values in column 4 by the correction factors give the corrected activities of column 10. An average value of 3.13 percent for the fission yield of Br^{87} was obtained from the data of Table IV. This agrees with the chain yield of 3.0 percent for mass 87 which is obtained by interpolation of the smooth yield-mass curve[17] of the fission products of U^{235}.

An upper limit for the half-life of Se^{87} was obtained by the following experiment. Uranyl nitrate was irradiated for 45 sec, and dissolved in an acid solution containing Br^- carrier. An equivalent amount of BrO_3^- was added and the solution was boiled vigorously for one minute to drive off Br_2. Additional Br^- carrier was added and stirred for one minute, then BrO_3^- was added and bromine swept out, precipitated as AgBr, and counted. For each of two runs, a value of 13 sec was calculated for the half-life of Se^{87} from the amount of Br^{87} activity recovered. This limiting half-life is the value which would be obtained if 2 percent of the bromine were retained after the first sweeping process. A value of about 2 percent for the bromine left behind was actually observed in preliminary experiments. Even if as little as 0.1 percent of the bromine were retained, the smallest limiting half-life that could be determined is 8 sec because of the long time elapsed between sweepings.

This work was assisted by the grant of a predoctoral fellowship to one of us (A.F.S.) from the U. S. Atomic Energy Commission.

The Total n-p Scattering Cross Section at 4.75 Mev*

E. M. Hafner, W. F. Hornyak, C. E. Falk, G. Snow, and T. Coor
Brookhaven National Laboratory, Upton, New York

(Received September 9, 1952)

Attenuation measurements in good geometry on polyethylene and graphite scatterers with transmissions from 0.30 to 0.65 have been made. A thin-walled gas target was used, producing forward d-d neutrons at a mean energy of 4.749±0.009 Mev. Care was taken to minimize uncertainties arising from neutrons of other energies, from unshadowed background, and from impurities in the samples. The geometry was such that multiple scattering-in contributed no more than 0.12 percent to the total uncertainty. Checks against rate-dependent sensitivity of the detector revealed no effects greater than 0.15 percent. The total n-p scattering cross section deduced from the measurements is $1.690\pm0.006_4$ barns, where the probable error has been increased from the statistical error of 0.002_4 barn to include the energy uncertainty and estimates of possible systematic effects. Values of $r_{0s}^{(n-p)}$, the singlet effective range of the n-p interaction, obtained from this result for several potential shapes, are compared with corresponding values of $r_{0s}^{(p-p)}$. The validity of the hypothesis of charge independence is found to depend on the potential shape assumed.

I. INTRODUCTION

A STUDY of the scattering of neutrons by protons and a comparison with the scattering of protons by protons can yield fundamental information about the nature of nuclear forces. The effective range theory[1,2] of nuclear scattering shows that the neutron-proton scattering cross section is approximately determined up to 10 Mev by four parameters: the triplet and singlet scattering amplitudes, a_t and a_s, and the triplet and singlet effective ranges, r_{0t} and r_{0s}. The first three of these parameters have been determined with good precision from measurements of the deuteron binding energy and of neutron-proton scattering cross sections at thermal energies. Measurements of the neutron-proton scattering cross sections at higher energies serve as the most promising method of determining the fourth parameter, r_{0s}. A comparison of the n-p singlet effective range with the measured value of the p-p singlet effective range then serves as a most critical test of the hypothesis of charge independence of nuclear forces.

Salpeter[3] has pointed out that the three parameters a_t, a_s, r_{0t} are known with sufficient accuracy so that a measurement of the total n-p cross section at energies greater than ~2 Mev can yield information about the shape of the neutron-proton interaction potential in addition to the value of r_{0s}. Since the singlet n-p cross section contributes only one quarter of the total cross section, a very precise scattering experiment is needed to obtain the value of r_{0s}. An interpretation[3] of the most recent medium energy cross-section measurements[4] assigns the value $2.6\pm0.5\times10^{-13}$ cm to the effective singlet range in the shape independent approximation, and concludes that the experimental results are not sufficiently accurate to yield information about the shape of the nuclear potential. This result implies charge independence of effective range to an accuracy of 25 percent.

The present experiment is an attempt to provide a more accurate cross section in the medium energy region, that is, at an energy high enough to bring in a significant dependence of cross section on range and low enough to avoid complications introduced by the contributions of angular momenta greater than zero and of relativistic effects. The importance of the shape dependent terms increases in direct proportion to the energy. At the beginning of this work we had been informed[5] that an accurate measurement at 1.3 Mev was in progress. We decided to work at a somewhat higher energy, 5 Mev, principally to obtain a separate evaluation of the singlet effective range, and also in the hope of combining the results to obtain a more definite clue to the potential shape than has hitherto been given.

The measurements were made in the forward beam of neutrons from the $H^2(d,n)He^3$ reaction. Three scatterer diameters were used, the smallest requiring a scattering-in correction of 0.6 percent. The thin-walled target contained deuterium gas in which the energy loss was 195 kev, separated from the accelerator vacuum system by a nickel foil in which the energy loss was 161 kev. Recoil scintillation neutron counters of approximately one percent efficiency were used as detector and monitor. Each counter amplifier fed two independent discriminators and scalers, operating at different counting rates, as a check against scaler pile-up, dead-time effects, and drift of bias. Transmission runs at alternately high and low neutron flux were taken as an additional check against any possible rate dependence. Scatterers were made of polyethylene and graphite, with transmissions between 0.30 and 0.65. The mean effective neutron energy of 4.75 Mev was chosen primarily on the basis that it permitted accurate foil and gas-thickness calibrations to be made, using sharp proton resonances at approximately half the deuteron energy.

The effect of axial neutrons not originating in the target gas was measured by transmission runs under

* Research carried out under contract with the AEC.

[1] H. A. Bethe, Phys. Rev. **76**, 38 (1949).
[2] J. M. Blatt and J. D. Jackson, Phys. Rev. **76**, 18 (1949).
[3] E. E. Salpeter, Phys. Rev. **82**, 60 (1951).
[4] Lampi, Freier, and Williams, Phys. Rev. **80**, 853 (1950).
[5] D. H. Frisch (private communication).

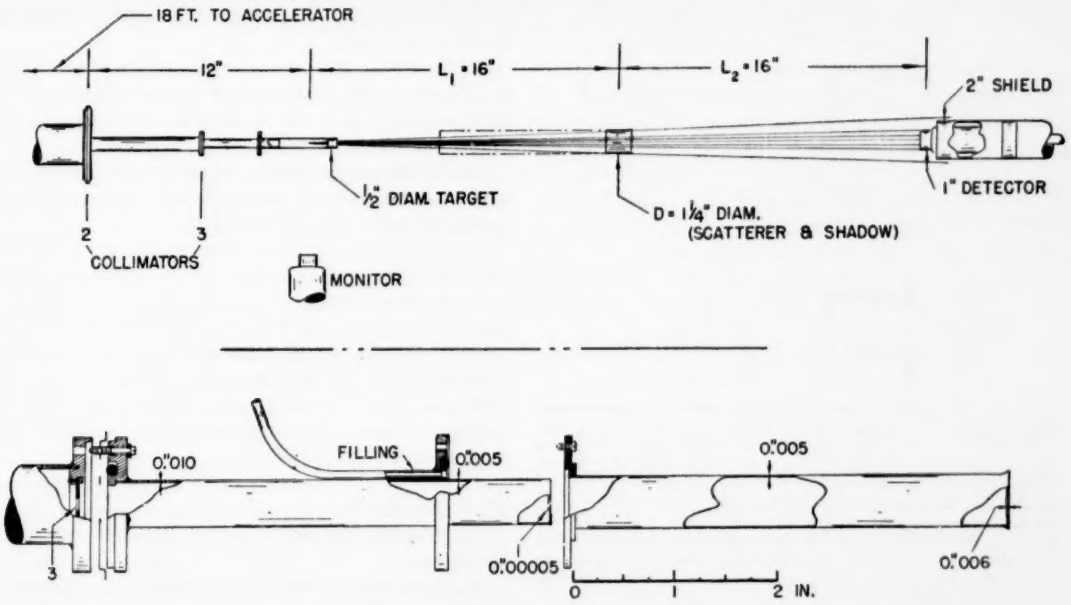

FIG. 1. Geometry of the experiment and exploded view of target assembly. The beam collimators, 2 and 3, are preceded by another aperture 48 in. away, backed by a solid cylinder to scatter out neutrons produced in the slit surface. The minimum scatterer and shadow diameter is shown; the margin of safe shadowing around the detector shield is ¼ in. The detector is fitted with an axial viewing tube for line-up. Target is made of brass, with entrance window of Ni and end-foil of Au. There is also a liner of 0.002-inch Au.

hydrogen filling, and the correction was, on the average, about 0.5 percent of the cross section. The shadow background of 1.5 percent was measured with nickel cylinders of computed transmission 0.0003. Upper limits to scattering-in effects of order higher than the first were estimated and found to be small. An analysis of a total of 209 runs, each with a statistical probable error of about 0.6 percent, at the various diameters and transmissions, checked this estimate and yielded the cross sections quoted in Sec. V.

The design of the experiment involved a number of considerations which are, it is felt, essential to the success of any precise transmission measurement. In the belief that many of these factors have been treated here with greater care than in previous determinations, a fairly detailed discussion of the method is carried out in Sec. II following the order of the summary just given.

II. EXPERIMENTAL METHOD

A. Geometry

The proper choice of geometry in this experiment represents a compromise between two sets of conflicting factors:

(1) In order to obtain a small scattering-in effect, D/L should be small, where D is the scatterer diameter and $L=L_1+L_2$ is the distance from source to detector (see Fig. 1).

(2) From the standpoints of background and intensity, L should be small. If a quantity β be defined as the fraction of unattenuated detectable flux that is not shadowed, it has been observed that β increases roughly as L^2. It is also clear that, if the ion current is fixed and the primary neutron flux at the detector is to be held at a reasonable value, the target thickness and hence the uncertainty in mean neutron energy must increase approximately as L^2.

As a result of first-order scattering-in effects apparent cross sections are lowered by an amount

$$\frac{\Delta\sigma}{\sigma}=\frac{f}{16}\left(\frac{DL}{L_1L_2}\right)^2, \tag{1}$$

where L_1 and L_2 are the distances shown in Fig. 1, and

$$f=\frac{4\pi}{\sigma}\left(\frac{d\sigma}{d\omega}\right)_0 \tag{2}$$

is a measure of the predominance of forward scattering. In the case of scattering by hydrogen, isotropic in the center-of-mass coordinates, a simple calculation shows that in the laboratory frame $f_{\text{lab}}=4$. The function $\Delta\sigma/\sigma$ has a minimum at $L_1=L_2=L/2$. The over-all detector diameter, with adequate margin of safety, that must be shadowed is 2½ inches (Sec. IIC). Therefore, the smallest scatterer diameter that can be used under the above optimum selection of L_1 and L_2 is 1¼ inch. Our estimate of the probable error of the scattering-in correction (Sec. IV) is one-fifth of the full value of the effect at best geometry. From these considerations it

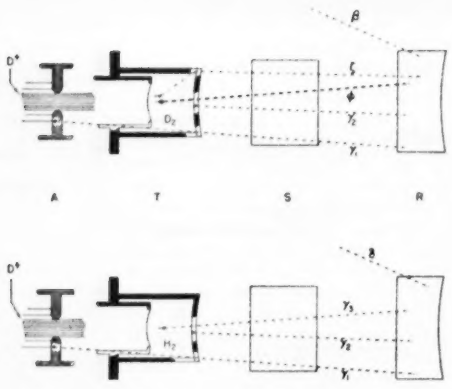

FIG. 2. Schematic view of neutron components with deuterium filling (upper) and hydrogen filling (lower). φ is the primary flux. γ_1 is the forward flux from the surfaces of apertures (A); γ_2 from the Au end-wall of target (T); γ_3 from traces of D_2 with the H_2 filling. ζ is due to wall scattering of primary neutrons. β is the off-axis flux detected by the recoil unit (R) but not shadowed by the scatterer (S), that occurs with D_2 filling; δ is the corresponding flux with H_2 filling. In this experiment, under the geometry of Fig. 1, the components had the following approximate magnitudes relative to φ: $\gamma_1+\gamma_2\simeq 0.02$; $\gamma_3\simeq 0.01$; $\zeta\simeq 0.003$; $\beta\simeq 0.015$; $\delta=0.0025$.

follows that an error less than 0.0015 results from a detector distance greater than 25 inches.

It has been found under the prevailing background conditions at this laboratory that $\beta\simeq 1.2\times 10^{-5}L^2$, where L is in inches. The effect of β (Sec. IIG) is to lower apparent cross sections by an amount

$$\frac{\Delta\sigma}{\sigma}=\frac{(1-T)}{T\ln(1/T)}\beta. \tag{3}$$

The estimated uncertainty in this correction assigns a probable error which is one-tenth of its full value. It follows that the detector distance can be increased to 30 inches before the error exceeds 0.0015. It was found when set up at this distance that an unattenuated detector counting rate of 300/sec was obtained with a gas thickness such that the uncertainty in effective neutron energy was 9 kev. This geometry, shown in Fig. 1, was taken to represent the compromise sought.

B. Target Design

The greatest demand on the neutron source is that it be essentially monoenergetic, since no fast neutron detector combining reasonable sensitivity with high energy resolution is available for measurements in good geometry. For detailed knowledge of the spectrum of the neutron beam, one is therefore forced to depend upon an ion-beam calibration and the calculated kinetics of the primary reaction. In such a procedure, errors of the following four types are introduced.

(1) *Inaccuracy of accelerator energy.* Reliance was made upon the absolute voltage scale established by the Wisconsin group,[6] and to some extent, on the linearity and stability of an electrostatic deflector working on the diatomic beam.

(2) *Inaccuracy of target calibration.* By a proper choice of technique, this measurement can be referred to the same scale on which the incident energy is based.

(3) *Inaccuracy of Q value.*

(4) *Superfluous neutrons.* An uncertainty arises from neutrons differing in energy from forward neutrons produced in the primary reaction.

Errors of type (1) and (2) are small (Sec. II E), and the small Q value uncertainty can be reduced by future measurements. By far the most serious uncertainty is found in category (4). It is to be understood that here concern is with neutron sources that are wholly or partially shadowed by the scatterer (Fig. 2). The classification that has been adopted for the shadowed neutron components, measured as fractions of the total detectable flux, is as follows:

φ: forward d-d neutrons produced in the target gas ("primary flux").

γ_1: forward d-d neutrons produced in collimating apertures.

γ_2: forward d-d neutrons produced in end-wall of target.

ζ: neutrons produced in the primary reaction that scatter into the forward direction from the walls of the target structure. Since the angular variation of the energy in the d-d reaction at the beam energy used here is large, many of these scattered neutrons are of considerably lower energy than $\bar{E}_n$, the mean energy of the primary flux.

The source γ_1 is likely to be large in measurements with a deuteron beam. Carbon layers depositing on the apertures produce a broad distribution of low energy neutrons with high yield at our bombarding energy, and deuterium occluded in depth on these surfaces produces a distribution extending from about 3 Mev to the energy of the primary flux. The effective strength of this source has been maintained at a low value by means of the arrangement of collimators shown in Fig. 1 and by using a detector whose efficiency for the lower energies is relatively poor.

Neutrons γ_2 are the result of d-d interactions below the surface of the end wall in which the beam stops. The end wall was made of gold; a material of high atomic number was selected to reduce the possibility of producing (d,n) neutrons in the wall material itself. The mean energy of the γ_2 neutrons is estimated to be approximately 0.5 Mev less than the energy of the primary flux under the conditions of this experiment. The γ_1 and γ_2 sources, with attendant corrections, are discussed in Sec. II F.

In order to keep the strength ζ of the scattering in the target walls small, a thin-walled target was built as shown in Fig. 1. The outer wall of the target was machined from brass stock to a thickness of 0.005 inch on a diameter of $\frac{1}{2}$ inch and over a length of 4 inches. This wall thickness is computed to be close to the

[6] Herb, Snowdon, and Sala, Phys. Rev. **75**, 246 (1949).

collapse limit of the target under one atmosphere pressure. The end wall was 0.006-inch gold foil, rim-soldered to a thin flange. A small gasket sealed the gas cylinder to an intermediate thin-walled (0.010-inch) section which supported the entrance foil and filling line. The entrance foil was of 0.00005-inch nickel mounted on an opening $\frac{1}{4}$ inch in diameter, and was required to withstand a pressure of 25 cm for bombardment times of the order of 50 hours at a maximum current of 2 microamperes. The section supporting the entrance foil in turn was sealed with an "O" ring to a heavier tube, on which the last two collimating apertures were mounted. The assembly was attached to the beam tube by means of Marman[7] clamp and flanges. The design is such that only thin walls subtend significant solid angles at the source. To prevent deuterons scattered in the entrance foil from striking the brass side wall of the target, a lining of 0.002-inch gold foil was used.

A particularly important feature of this target design is the foil mounting. In order to reduce the solid angle subtended by the gasketed flange at the neutron source, the foil was situated on a short re-entrant tube with 0.005-inch walls and end. The end was drilled to $\frac{1}{4}$-inch diameter, leaving a margin for mounting of about 0.090 inch. The foil could be waxed to this mount, but it was found that the temperature rise in foils under bombardment was too great to permit this unless a retaining ring was added, which, however, undesirably increased the mass. It was found that foils could be successfully soldered to the mounting, using the following technique. The mounting is warmed on a hot plate and covered with a thin layer of high-tin solder. The foil is cut oversize and laid on a clean aluminum surface that has been brought just above the solder point. The mounting is quickly inverted on the foil, and is lifted when solder begins to flow well. In almost every trial this procedure led to a good bond that outlived the foil itself.

The total wall scattering for the target was estimated on the basis of the known reaction kinetics, angular distribution of the *d-d* reaction, detector efficiency as a function of energy, and reasonable assumptions concerning the differential cross section for scattering of neutrons in the walls. Results of the calculation are shown in Fig. 3. The effect of this flux on the apparent cross section of polyethylene of transmission 0.50 has been calculated to be 0.03 percent.

C. Detection and Monitoring

The detector used in this experiment was of the recoil type consisting of a ZnS and Lucite molded detector[8] developed in this laboratory. The recoil unit was a cylinder one inch in diameter and $\frac{5}{8}$ inch high, mounted on an RCA type C 7151 experimental photomultiplier whose photocathode diameter is $1\frac{1}{4}$ inch and whose over-all diameter is $1\frac{1}{2}$ inch. This detector is comparatively insensitive to gamma-rays, has a short rise time and pulse duration, and has an efficiency of the order of one percent at the discriminator levels and neutron energy used in this experiment.

The response of the detector to primary neutrons and to background of types γ and δ (Sec. II F, G) is shown in Fig. 4. It is clear that the component δ, which includes photons and neutrons originating in the accelerator, is less than 1 percent of the total flux for all bias settings above 3 volts. At 15 volts, the lower of the two settings used, it contributes 0.2 percent. It also appears that the neutrons comprising γ are, on the average, slightly lower in energy than the primary beam, as expected. This was confirmed by measurements on the background and from transmission data taken on the γ component (Sec. II F).

Define as a rate effect any behavior of the detector system that produces observed counting rates not proportional to the incident flux over the range of rates involved in the transmission runs. Such an effect leads to a systematic error in transmissions measured in the conventional way, that is, from the ratio of attenuated to unattenuated counting rate at constant source intensity. If the effects are small, if n and n^0 denote the incident and observed counting rates, and if T and T^0 the true and observed transmissions, the unattenuated count can be written as

$$n^0=n(1+a_1n+a_2n^2+\cdots), \tag{4}$$

and the attenuated count as

$$T^0n^0=Tn(1+a_1Tn+a_2T^2n^2+\cdots). \tag{5}$$

From these definitions and the fact that

$$d\sigma/\sigma=(1/\ln T)(dT/T),$$

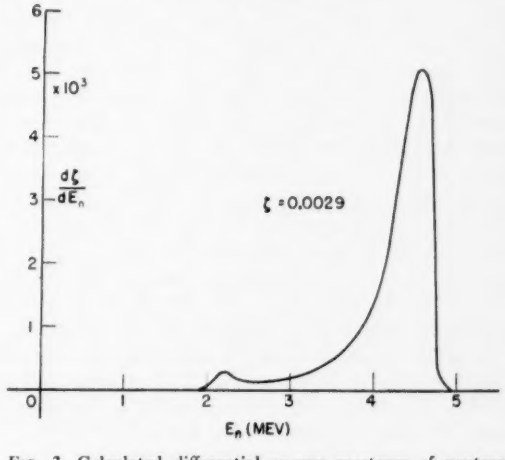

FIG. 3. Calculated differential energy spectrum of neutrons scattered into the forward beam by the walls of target shown in Fig. 1. Integration of the spectrum yields the value $\zeta=0.0029$. This flux raises the apparent cross section of a CH_2 scatterer of transmission 0.5 by less than 0.03 percent.

[7] Manufactured by Marman Products Company, Inc., Inglewood, California.

[8] W. F. Hornyak, Rev. Sci. Instr. **23**, 264 (1952).

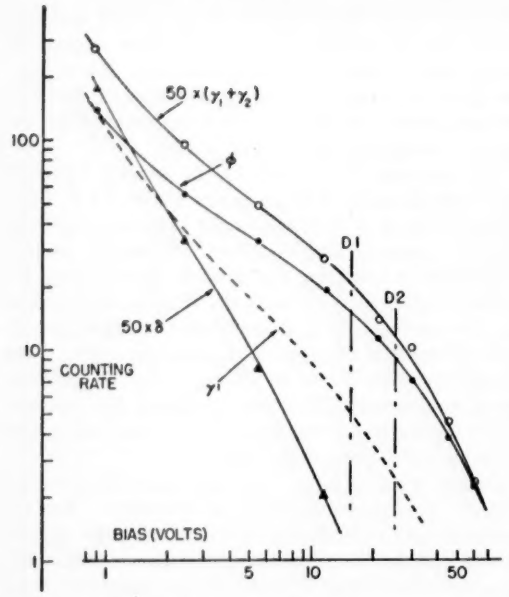

FIG. 4. Integral bias spectra of forward neutrons, φ is the spectrum of d-d neutrons of energy 4.75 Mev. $(\gamma_1+\gamma_2)$ was taken with$^{\text{r}}$target at vacuum, δ with evacuated target shadowed. γ' is obtained by subtracting the full-energy spectrum from the slit spectrum, normalized for largest pulses, and suggests a low energy component at about 2 Mev. D1 and D2 are the settings on channels 1 and 2 in transmission measurements.

the shift in apparent cross section up to effects of second order is

$$\Delta\sigma/\sigma=-(1/\ln T)[a_1 n(1+a_1 n)(1-T)+a_2 n^2(1-T^2)]. \tag{6}$$

The effect is positive when the coefficients are positive.

The probability of superposition of two pulses of finite duration gives a shift whose magnitude and sign depend upon the pulse-height spectrum and operating bias. The effect is of first order. In Appendix I, a_1 is calculated as a function of bias for a spectrum closely resembling the observed curve, and it is shown that there is a setting for which the gain of counts due to pile-up of small pulses is compensated by loss of counts due to pile-up of large pulses. In this experiment one scaler was operated at this setting and the other at a bias such as to give approximately half as great a counting rate. It was therefore possible to look for significant discriminator and scaler rate effects by a comparison of transmissions taken on the two channels.

A total of about 2.6×10^7 unattenuated detector counts was taken on channel 1, at an average rate of 200 cps. The mean value of the quantity T_1/T_2 deduced from the data was found to be 1.00023 ± 0.00021, the probable error being computed externally from a treatment of the counting statistics of the measurements. The error computed internally from the deviations of 20 subgroupings of the data was 0.00019. This effect was considered to be not significant, and no correction has been made for it.

An additional check on rate effects was obtained by dividing the runs into two groups, one being taken at twice the incident beam current of the other. The two rates worked with were about 150 and 300 cps on channel 1. All cross sections were corrected as well as possible for other effects (Sec. III B). The analysis of about 75 runs at low flux and 100 at high flux, each run having 0.58 percent statistical accuracy, gave a mean value for the quantity $T_{\text{high}}/T_{\text{low}}$ of 1.0012 ± 0.0008. The probable error is statistical and is the same when computed externally and internally. An estimate of systematic error in the current dependence of background (Sec. IV) must be added to this error. The result is to raise the probable error to 0.0014. Since an effect larger than this was not uncovered in the data quoted above, no attempt has been made to correct the results.

Monitoring of the neutron source was accomplished by using a recoil unit of the same type as the detector but mounted on a 5819 phototube. The monitor saw neutrons at 90° to the incident deuteron beam and with such geometry that its counting rate increased by an amount calculated to be less than 0.03 percent due to backscattering from samples in the forward beam. As seen in the block diagram (Fig. 5), the detector and monitor systems were essentially identical. The nonoverload feature of the detector amplifier was added in order to eliminate widening and to reduce overshoot and ringing of occasional large pulses. The total pulse duration (including a small overshoot) was observed to be less than 5 microseconds at the output of the amplifier. A Model 1030 (Atomic Instrument Company) scaler was used on detector channel 1 with a 1-microsecond resolving time. The remaining three scalars had 5-microsecond resolving times. The stability of this system against time and variation of ion current is shown in Fig. 6, which displays the first section of data taken on a polyethylene scatterer of transmission 0.523. The detector-to-monitor ratios on single runs, with scatterer out and in, are given for two pairings of the

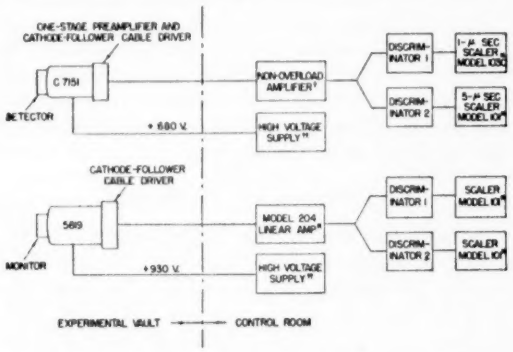

FIG. 5. Schematic of electronics. *Atomic Instrument Company; † Chase and Higinbotham, Rev. Sci. Instr. **23**, 34 (1952); †† W. A. Higinbotham, Rev. Sci. Instr. **22**, 429 (1951).

four channels used. The statistical probable errors of the runs, taken from the deviations, are approximately 1.5 times the error deduced from the number of counts, indicating that electronic jitter in these runs was competing with counting statistics. During subsequent measurements, the stability improved. Corresponding analysis of all runs (Sec. V) gave a ratio 1.1 of observed to computed statistical error.

The design of the detector preamplifier assembly deserves note. It was found in preliminary runs that unshadowed masses adjacent to the recoil unit can scatter a significant fraction of the neutron flux into the detector. Such an effect makes the background β a function of shadow diameter and position, and increases the uncertainty of its measurement. The difficulty was avoided with an in-line design such that the entire assembly was shadowed, with a safety margin, by scatterers of smallest diameter. Furthermore, in order to facilitate alignment of scatterer and detector, the axis of the assembly was kept open and a thin tube inserted from front to back. When the phototube was removed, the target and scatterer were visible and accurate alignment was easily accomplished.

D. Scatterers

In this experiment, scatterers of polyethylene $(CH_2)_n$ and graphite were used to determine cross sections which, upon appropriate subtraction, yielded the hydrogen cross section. Such measurements involve determinations of length, density, and deviations from purity of the scatterers. The extent to which uncertainties in the carbon cross section enter the determination of σ_H required that the accuracy of the constants for graphite samples had only to be about one-third of that for polyethylene.

Uncertainty of length measurement is a constant linear amount and sets an upper limit to transmissions that can be used. If an error of 0.0003 inch is not to produce an error in cross section greater than 0.05 percent, the minimum scatterer length is 0.6 inch, corresponding to a polyethylene transmission of 0.75. Consideration of statistical uncertainty in a measurement of reasonable duration sets a slightly lower transmission limit. A lower limit to transmission is set by the uncertainty of background measurement at 0.30 or a length of 2.5 inches. Polyethylene scatterers of these two limiting lengths were used, together with a set of three more at an intermediate length. Table I lists as l_0 the micrometer readings averaged over the proper central region of the scatterers, that is, the region that shadows the sensitive volume of the detector. Owing to imperfections in machining the scatterers, l_0 usually differed from the average lengths $\bar{l}$ taken over the entire scatterer. For graphite, l_0 was taken equal to $\bar{l}$. Diameters and vacuum weights are also listed in Table I.

Polyethylene may be expected to yield slightly under the pressure of a micrometer. This effect was checked by independent measurements of sample E, using an accurate shadow comparator and a Pratt-Whitney supermicrometer set to two pressures and extrapolated to zero. The results are shown in Table I. The values of $\bar{l}$, D, and M permit the density ρ_1 to be computed. The mean value for the five polyethylene samples is 0.9221 ± 0.0003 g/cm³.

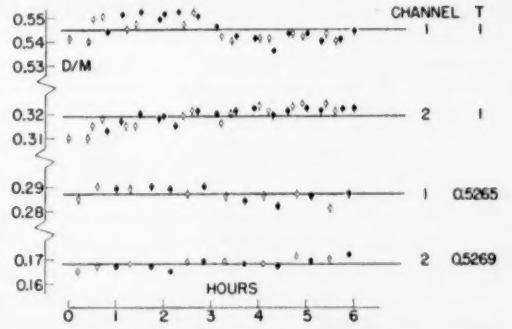

FIG. 6. Record of first six-hour run on the system of Fig. 5. Each point represents 64 000 counts in detector channel 1 and about half that number in channel 2. The two upper sets were obtained with no attenuation in the neutron beam; the lower two with scatterer B (Table I) in the beam. Open circles represent data taken at beam current 2.0 microamperes; solid circles at 1.0 microampere. The statistical probable error of the resulting transmission values is about 0.0010.

It was found that a more precise determination of density follows from measurement of buoyancy is distilled water, if care is taken to eliminate effects of surface tension, air bubbles, and failure of surfaces to wet. The results of this measurement, corrected to 22°C, are given in Table I as ρ_2. The mean value and temperature coefficient from the buoyancy method are

$$\rho_2=(0.9214\pm0.0001)(1-0.00065\Delta T)\ \text{g/cm}^3. \quad (7)$$

The discrepancy between density values by the two methods is somewhat outside probable error, and may indicate unknown systematic effects. In calculating the results, Eq. (7) has been applied.

It is clear from an inspection of Table I that the polyethylene is extremely homogeneous. It is well known, however, that bulk graphite is not, and that its density is considerably lower than that of the pure crystal (2.25 g/cm³). Thus, there is a need to estimate the effect of both microscopic and macroscopic inhomogeneities in the graphite on the cross-section determination.

Assuming that the process of compressing microcrystalline powder into graphite stock leaves spherical holes, all of equal radius r and randomly distributed through the sample, it can then be shown that an apparent cross section is lower than a true cross section by an amount

$$\frac{\Delta\sigma}{\sigma}=\frac{2}{3}\left(1-\frac{\sigma}{\rho_0}\right)\frac{r}{\lambda}, \quad (8)$$

where ρ is the observed bulk density, ρ_0 the crystalline

TABLE I. Properties of scatterers at 22°C.

Sample	Material	l (inches)	l_0 (inches)	D (inches)	M_{vac} (grams)	ρ_1 (g/cm³)	ρ_2 (g/cm³)	a (barns)
A	$(CH_2)_n$	0.9114	0.9119	1.2502	16.895	0.9214	0.9214	25.126
B	$(CH_2)_n$	1.3722	1.3719	1.2363	24.891	0.9220	0.9214	16.701
C	$(CH_2)_n$	1.3686	1.3680	1.6226	42.822	0.9228	0.9214	16.749
D	$(CH_2)_n$	1.3707	1.3683	1.9896	64.396	0.9220	0.9213	16.745
E	$(CH_2)_n$	2.5063[a]	2.5059	1.2057[b]	43.228	0.9223	0.9214	9.1432
F	C	2.0796		1.2519	72.177	1.721		5.052
G	C	2.0808		1.6247	121.911	1.725		5.034
H	C	2.0810		2.0005	184.855	1.727		5.028
J	C	4.0350		1.2519	141.267	1.736		2.578

[a] 2.5064 by shadow; 2.5066 by supermicrometer.

[b] 1.2056 by shadow.

density, and λ the mean free path for scattering in the actual bulk sample. For holes of radius 0.010 inch (considerably greater than the size of cavities visible on the surface), this effect is less than 0.1 percent. The effect therefore has been ignored in the results.

The macroscopic variation in density requires, however, that the number used in computing cross sections be the mean density over only the proper central region of the scatterer. Thus, at the completion of the runs, all graphite samples were machined to the diameter of that region and the densities remeasured. In most cases the change was negligible; the later values are listed as ρ_1 in Table I.

It is convenient to define for a given scatterer a constant a given by

$$a=\frac{A\ \ln 10}{Nl_0\rho}\times 10^{24}\ \text{barns}, \tag{9}$$

where N is Avogadro's number, A the molecular weight, and ρ the density. In obtaining the values listed in Table I, $N=6.0254\times 10^{23}$ was used, and the assumption was made that the scatterers are chemically perfect samples of CH_2 and C. ($A_{CH_2}=14.0317$; $A_C=12.0151$). Since a is proportional to D^2, a temperature correction amounting to $\frac{2}{3}$ of the polyethylene coefficient [Eq. (7)] must be applied. No temperature corrections were made for graphite. The constant then conveniently relates transmissions to cross sections through

$$\sigma=a\log_{10}(1/T)\ \text{barns}. \tag{10}$$

The polyethylene scatterers were machined from commercial[9] stock. A macrochemical analysis of this material by the Bureau of Standards has yielded the following analysis: percent by weight of H=14.37 ±0.01, C=85.57±0.03, O=0.07±0.02, residue=0.007 ±0.002. The oxygen content revealed here is consistent with the assumption that each polymer chain of approximate length equal to 1500 carbon atoms, as determined by infrared spectroscopy on one of these samples, is terminated by an oxygen atom.

[9] Plax Corporation, Hartford, Connecticut, who supplied the stock, fabricates it from pure bulk ethylene resin obtained from the Bakelite Company.

The net correction given by the chemistry to the hydrogen cross section, taking into account H, C, and O observed in polyethylene, is readily calculated to be −0.1 millibarn, and an upper limit for the effect of the residue to be −0.3 millibarn. The uncertainty introduced by the chemistry into the hydrogen cross section is 0.07 percent.

The graphite samples were cut from material of 99.98 percent purity, and unless the contaminants have cross sections exceeding 5 barns their effect on σ_C is negligible. The possibility that water is absorbed in this material has been removed by observing no loss of mass on baking.

The effects of neutrons scattered out by air displaced by the scatterers, and scattered in by the thin blades used to support the samples, have been estimated and found to be negligible.

E. Neutron Energy

The arguments connected with the significance and straightforward interpretation of the cross section (see Sec. I) have indicated a choice of energy close to 5 Mev. Consideration of the upper voltage limit of the electrostatic accelerator at this laboratory led to the $H^2(d,n)$-He^3 reaction with a gaseous target as the most convenient neutron source. The highest reliably attainable bombarding voltage of 1.8 Mev was used principally for the following reasons:

(1) It permits the most accurate determination of the energy loss of the deuteron beam in the target and entrance foil since this energy is closest to twice the proton energy at which sharp and intense resonances occur that are convenient for such calibrations.

(2) It gives the smallest energy loss for a fixed physical thickness of foil and gas.

(3) Finding that prior work on the scattering cross section of carbon is not quite detailed enough to reveal structure that would affect the measurements, careful runs through the usable neutron energy region were made, resulting in the data shown in Fig. 7. The energy region in the vicinity of 1.8 Mev is seen to be free from such structure.

(4) It was found that at 1.8 Mev, carbon gives the

smallest relative contribution to the cross section of polyethylene (refer Fig. 7).

(5) Backgrounds of type γ and δ increase with bombarding voltage, because of the relatively large thicknesses of the sources involved, and because C−d neutrons are more efficiently detected at higher energies. At voltages much above 1.8 Mev, these backgrounds become excessive.

The energy of the incident beam was thus chosen as 1800 kev. Electrostatic analysis of the D_2^+ beam was used for control and stabilization of the accelerator voltage. The energy scale was established, and linearity and stability checked, by adopting as standards[6] the values 873.5 kev for resonance in $F^{19}(p,\alpha\gamma)O^{16}$, 993.3 kev for resonance in $Al^{27}(p,\gamma)Si^{28}$, and 1882 kev for threshold in $Li^7(p,n)Be^7$. Many runs on these reactions have allowed us to arrive at a limit of uncertainty of 0.1 percent in the voltage scale. The assumption was made that a fixed analyzer voltage focuses D_2^+ and H_2^+ ions of exactly the same energy.

Forward neutrons produced in the target cover an interval of about 200 kev, due primarily to energy loss of deuterons in the gas. The knowledge of the functional form of the dependence of total n-p cross section on energy permits the definition of an effective mean neutron energy $\bar{E}_n$ in such a way that the observed cross section corresponds to neutrons of this energy alone.

The necessary accuracy in the target and foil energy losses can be achieved by making direct measurements on the energy loss of protons of approximately half the deuteron energy. Using the fact that deuterons and protons of equal velocities have equal rates of energy loss, the initial and final energies of deuterons in the gas were found with essentially the same precision as that obtained in the measurements of proton energy loss. The energy loss of protons was determined by measuring the mid-points of thick-target resonances after the proton beam had traversed the Ni foil alone, and the foil and gas combined.

When observed through the foil, the $Al^{27}(p,\gamma)Si^{28}$ resonance at 993.3 kev showed a width of about 20 kev, as compared with a width of 5 kev for measurements in the direct beam. A similar result was obtained with the fluorine resonance. The increase in width is much larger than the straggling and is probably due to nonuniformities in foil thickness. This width contributes the largest source of error to the energy-loss determinations. The reproducility of resonance mid-points suggests an error of 2 kev, but the possibility of a nonsymmetrical distribution of fluctuations in foil thickness increases the uncertainty to 4 kev.

Since the deuteron energy in the foil and gas was not exactly twice the proton resonance energies, extrapolations of the proton energy losses, amounting to approximately 15 percent, were necessary. They were made with the aid of the Bethe-Bloch formula with corrections for the K electrons,[10] using $I=300$ ev[11] as the ionization potential of Ni. It was thus determined, for example, that the deuteron energy loss in one of the two foils used in this experiment was 160.6 ± 4.6 kev, giving as the deuteron energy leaving the foil $1.639_4\pm0.005$ Mev.

Since the gas target thickness was known (i.e., length 8.14 ± 0.16 cm and 250 ± 1 mm Hg pressure), the resonance measurement on protons that had penetrated the foil and gas could be used to find the ionization potential for H_2 and D_2. The value obtained, including the C_k correction, is $I=20\pm2.5$ ev. A recent analysis by Bogaardt and Kondijs[12] of all range-energy data obtained with natural alpha-emitters yields $I=17.1\pm0.4$ ev, which is in agreement with the less accurate result obtained here. It was decided to use the value for I obtained here in calculating the deuteron energy loss, since it tends to remove certain systematic errors (in length and pressure measurements, for example) from the determination of mean deuteron energy. The energy loss in the gas thus obtained is $195._4\pm7$ kev, which results in a mean deuteron energy in the target of $\bar{E}_d=1.541_7\pm0.006$ Mev.

From the kinematics of the $H^2(d,n)He^3$ reaction including a small relativistic correction, and the Q value of 3.268 ± 0.004 Mev,[13] the corresponding mean neutron energy emitted in the forward direction is $\bar{E}_n=4.749\pm0.009$ or $4.749(1\pm0.0019)$ Mev.

The energy dependence of the total n-p cross section is such that, at this energy, $\Delta\sigma/\sigma=-0.70\Delta E/E$. Therefore, the 0.19 percent uncertainty in $\bar{E}_n$ is equivalent to an uncertainty of 0.13 percent in the cross section.

It is necessary to consider three sets of effects that tend to make the mean neutron energy, as measured above, depart from the true effective mean neutron energy, defined as the single energy for which the total

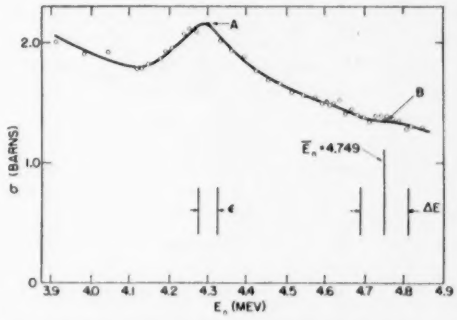

FIG. 7. Total cross section of carbon *vs* mean energy in a target of thickness ϵ. The target thickness and mean energy (ΔE and $\bar{E}_n$) used in the transmission runs are also shown. The solid points, A and B, have probable errors of about 0.5 percent.

[10] M. S. Livingston and H. A. Bethe, Revs. Modern Phys. **9**, 261 (1937).

[11] $I_{Ni}=(28/29)I_{Cu}$, where $I_{Cu}=310$ ev from R. Mather and E. Segrè, Phys. Rev. **84**, 191 (1951).

[12] M. Bogaardt and B. Kondijs, Physica **18**, 249 (1952).

[13] Whaling, Li, Fowler, and Lauritsen, Phys. Rev. **83**, 512 (1951).

n-p cross section is identical with the cross section observed with the finite energy width of the mean in the target. The effects are

(1) reduction of mean energy due to departure of the angle between the direction of an incident deuteron and the direction of the corresponding detectable neutron from zero.

(2) Shift of effective mean energy due to variation of σ_H over the energy interval, and to the variation of d-d yield and detector solid angle through the depth of the target.

(3) Corresponding shift due to resonance structure of σ_C within the interval.

An estimate from formulas[14] of the multiple Coulomb scattering of deuterons gives the rms angle of scattering in the Ni foil as about 2° and the angle in the D_2 gas as considerably less. The finite angle subtended by the recoil detector is less than 1°. These angular departures from zero produce a negligible reduction (i.e., 0.02 percent) in the mean neutron energy.

The effects grouped as (2) above produce an over-all effect which is of second order in the deviation of deuteron energy in the target from the mean energy. The linear terms drop out since they arise from an integration of an odd function over a symmetric interval. The numerical values indicate an effect of 3×10^{-5}, which can be neglected. The calculated effect is very small as a result of a fortuitous cancellation of terms. A conservative upper limit to the uncertainty resulting from error in the terms involved is 0.03 percent.

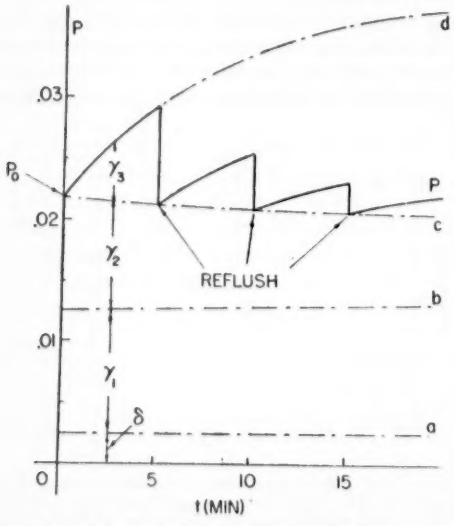

FIG. 8. Schematic short-time behavior of detector count with hydrogen filling, relative to count with deuterium filling. Deuterium is removed at time zero, and the solid curve p represents observed fluctuations of count for subsequent running and refilling cycles. The dashed curves represent the components believed to contribute to p (see text).

[14] W. T. Scott, Phys. Rev. 85, 245 (1952).

A similar calculation has been carried out in order to estimate the shift due to possible resonance structure in the carbon cross section. The effect is again of second order in the relative energy deviation, and it has been found that any structure consistent with the data of Fig. 7 produces a negligible shift in cross section. The observed hydrogen cross section is therefore essentially identical with the cross section for a hypothetical homogeneous neutron beam of energy $\bar{E}_n$.

F. Hydrogen Background

For the purposes of this discussion, background is defined as any component of the unattenuated neutron flux that does not originate in the d-d reaction in the gas volume of the target, or, if it does so originate, does not pass without scattering into the detector. Referring, then, to Fig. 2, one sees that the total flux consists of the primary component φ and three essentially distinct types of background. Neutrons ζ, which arise from target-wall scattering of d-d neutrons, were considered in Sec. II B, where it was shown that the cross section shift resulting from them is negligible. Neutrons β are the result of scattering from the room walls and other remote masses, and are discussed in Sec. II G. Concern here is with the components γ_1 and γ_2 produced in beam-defining apertures and the Au end wall of the target, respectively. These neutrons have a significantly lower mean energy than the primary neutrons and, since they are produced on the axis of the experiment, are geometrically indistinguishable from them. In Appendix II it is shown that

$$T=T^0+(\gamma_1+\gamma_2)(T-T_{12})-(1-T)\beta, \qquad (11)$$

where T is the true transmission of a given scatterer for the component φ, and T_{12} is its transmission for the components γ_1 and γ_2 combined. In order to make the correction for this background, both its magnitude and its transmission must be known.

Direct measurements of the necessary quantities are in principle possible when D_2 in the target is completely replaced by H_2 at the same pressure. Under this condition the deuteron beam current and energy at all surfaces in question are exactly reproduced. After subtraction of shadow background (Sec. II G), the unattenuated counting rate (relative to the rate with deuterium filling) gives $(\gamma_1+\gamma_2)$, and the rate with scatterer in gives T_{12}.

Experience showed that this procedure must be examined more carefully. It was found that a significant rate of ion exchange occurred at the walls of the target during bombardment, so that deuterium which had been occluded during previous running reappeared in the target volume during hydrogen runs. Also, the strength of γ_2 was found to diminish slowly during hydrogen runs, again as the result of the diffusion of deuterium out of the Au surface into the gas. The time-dependence of the detector count, as observed in many runs, is shown schematically in Fig. 8. The shadow count

δ is very steady at 0.0025. The count at time zero, which is called p_0, is the sum $(\delta+\gamma_1+\gamma_2)$ and is assumed to represent the state of the system in the deuterium runs just preceding the hydrogen background run. After a few minutes of running, the exchange of hydrogen with deuterium in the target walls has released an amount of deuterium gas producing the component γ_3; these neutrons are presumably of the same energy as the primary neutrons φ, and therefore correspond to transmission T. A complete reflushing of the target with H_2 removes this D_2 fraction and reduces the count rate, which then builds up again as more gas is exchanged, and subsequent flushings finally remove most of the D_2. Meanwhile, the component γ_2 is steadily falling as the end wall exchanges gas, and γ_1 is rising very slowly as carbon and deuterium continue to build up on apertures in the beam. The net effect of these two drifts is to make the initial count after successive flushings diminish until all the D_2 has been lost from the end wall. Bombardment of the Ni window does not contribute to γ_1 or γ_2, presumably because it runs too hot to retain contamination layers.

Although the details of this picture of the hydrogen background are not essential to a proper correction, it is of interest to note that they have been confirmed by many observations. It was found, for instance, that when the target after running with deuterium was evacuated and then sealed off, the variations of γ_2 and γ_3 under continued bombardment disappeared, and that the target pressure did not rise, thus indicating that the appearance of D_2 during hydrogen runs was the result of exchange and not simply of outgassing due to warm-up. Cleaning apertures and replacing the target end wall with fresh gold reduced p_0 in the expected way, and an inverse-square study of $(\gamma_1+\gamma_2)$ as a function of detector distance showed that γ_1 came mostly from collimators 2 and 3 (Fig. 1). The long-time behavior of p_0, which is shown in Fig. 9, is also understandable. The slits started clean at time zero. During the first 47 hours of beam time the hydrogen runs were brief (20–30 min), and $(\gamma_1+\gamma_2)$ rose steadily to 0.028. At this point an extended H_2 run of 310 min removed most of γ_2, giving $\gamma_1\sim0.015$ and $\gamma_2\sim0.013$ at about 50 hours. At 83 hours collimators 2 and 3 were cleaned, removing most of γ_1. The subsequent low count indicated that just before cleaning γ_1 had risen to 0.022, and that γ_2 had again built up to 0.014 in the second half of the runs. It is therefore clear that the two components grow at about equal rates.

Finally it should be noted that, in addition to measuring p_0 directly, one can deduce it from measurements in the presence of γ_3. From the discussion of Appendix II, it is seen that

$$p(T-T_p^0)=(\gamma_1+\gamma_2)(T-T_{12})-(1-T)\delta, \quad (12)$$

where p is the entire hydrogen background count $(\delta+\gamma_1+\gamma_2+\gamma_3)$, and T_p^0 is the uncorrected in-out ratio for the given scatterer in this flux. The fact that

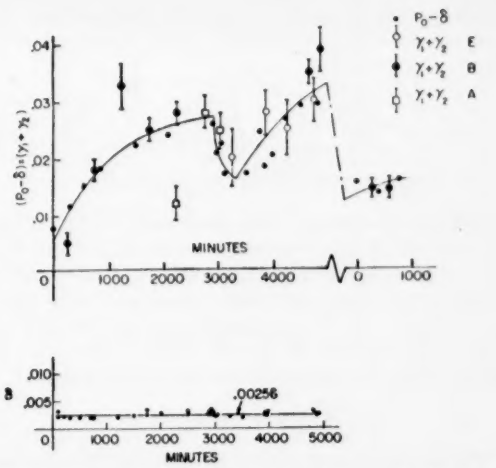

FIG. 9. Observed long-time variation of hydrogen backgrounds $(\gamma_1+\gamma_2)$ and δ, covering period of transmission measurements. The measurements are relative to count with deuterium filling. Time is taken as minutes of beam after cleaning aperture surfaces. The points labeled $(p_0-\delta)$ are the directly observed initial count (Fig. 8); other points are deduced through Eq. (12) from transmission measurements on scatterers *A*, *B*, *E*. These are somewhat less precise than the direct measurements, which are used to determine the curve. The dip at 3000 minutes is the result of extended running with hydrogen filling, which replaces deuterium in end-wall of target. δ is the corresponding shadow background. Since its source is within the accelerator, where the accumulation of carbon and deuterium layers has been progressing for a much longer time, the background is expected to be constant over this interval.

$(\gamma_1+\gamma_2)$ is essentially constant during a hydrogen run implies then that, as p rises rapidly due to the growth of γ_3, T_p^0 must approach T at such a rate as to maintain invariance of the product $p(T-T_p^0)$. Use has been made of Eq. (12) to compute $(\gamma_1+\gamma_2)$ from measurements of T_p^0 as a check against the direct measurements of p_0, and the points are shown in Fig. 9. The agreement between the background deduced by this method, and p_0 as directly measured, is good. The transmissions T_{12} (Table II) needed here and in Eq. (11) were obtained from poor-geometry high rate measurements with the target at vacuum. It was assumed that the energy distribution of γ_1 and γ_2, and hence of T_{12} for a given scatterer, were independent of time. Now the measured background would be expected to be an upper limit to p_0, since γ_3 may not be exactly zero; on the other hand, values of $(\gamma_1+\gamma_2)$ deduced through Eq. (12) should represent a lower limit, since the end wall tends to lose deuterium during the measurement. Thus, the agreement between the two methods lends confidence to the belief that this background has been correctly treated.

It is interesting to attempt to describe the transmission of scatterers, with hydrogen filling, in terms of the observed integral bias spectrum of the neutrons involved (Fig. 4). It is assumed that the spectrum can be approximated by two groups, one just below the energy of the primary neutrons and the other at con-

TABLE II. Observed transmissions with hydrogen filling.

Sample	Material	T	T_{12}
A	CH_2	0.6509	0.575±0.012
B	CH_2	0.5225	01441±0.003
E	CH_2	0.3053	0.230±0.005
J	C	0.300	0.214±0.005

siderably lower energy. This grouping of energies is to be expected if the neutrons arise from *d-d* and C-*d* sources in the slit and end-wall surfaces. If the relative strengths of higher and lower energy groups is taken to be about 3-to-1, as suggested by the spectra, the calculated behavior of the transmission data can be shown to be in agreement with the data of Table II.

G. Shadow Background

The neutron component to be discussed here consists of the flux entering the detector along paths that do not traverse the scatterer; it is denoted by β (Fig. 2) and is measured in units of the total unattenuated count rate with deuterium filling. From Eq. (11) one sees that, for this component alone,

$$T=T^0-(1-T)\beta, \tag{13}$$

where T^0 is the observed in-out ratio for a scatterer whose true transmission of the direct beam is T. For proper correction of observed transmissions, β must be accurately known in magnitude; its spectrum is of no importance.

The background β was measured by using nickel shadows 10 inches long with a computed transmission of 0.0003. This value was based on a transmission measurement which gave 3.07±0.03 cm as the mean free path for the neutron energy used in this experiment. It was assumed that the computed shadow transmission is in error due to multiple scattering by no more than its full value. The shadows were cylinders of $1\frac{1}{4}$ and 2 inches in diameter to match the smallest and largest scatterers. No measurable diameter dependence of β was found, but nevertheless, the shadow geometry of Fig. 1 was used under the assumption that extension of source diameter (owing to production and scattering at points near the axis of the experiment) was more likely than corresponding extension of the detector, since all masses near the detector were known to be completely shadowed. This choice of geometry minimizes the difference between the flux attenuated by the scatterer and the flux removed by its shadow.

Most of the neutrons involved in the shadow background originate in the target and scatter from the walls and floor of the room. The small remainder, denoted by δ, come directly and by wall scattering from the accelerator, 19 feet or more ahead of the target. δ was measured frequently throughout our runs by means of shadow measurements with hydrogen filling. These data are given in Fig. 9, where it is seen that δ was essentially constant at 0.0025 through the experiment. This is to be expected, since the sources giving rise to it have been building up to their present thicknesses over a period of years.

Since β is normalized to the primary flux φ, the component of β originating in the target is independent of ion current. On the other hand, since the sources of δ are approximately independent of focus and deflection conditions, the counting *rate* of these neutrons is constant, and δ is therefore inversely proportional to the ion current. This accounts for the fact that β, measured as a function of ion current (Fig. 10), is a good fit to the curve

$$\beta=0.0127+0.0024/\bar{I}, \tag{14}$$

where $\bar{I}$ is the average ion current, in microamperes, reaching the target gas. As a result, the values of β to be used for correcting data taken at the high and low currents of the transmission runs differed by 0.0010.

H. Scattering-In Problems

In a measurement with finite geometry, a fraction of the attenuated count is attributable to neutrons that are detected in spite of having undergone one or more scatterings in the sample. This effect is called the "scattering-in." The first-order effect of scattering-in, due to single scattering, for a scatterer centered on the axis of the measurement, is

$$\Delta\sigma/\sigma=-fG, \tag{15}$$

where f is the anisotropy parameter defined in Eq. (2), and $G=(D/L)^2$. Denoting by f_h, f_c, and f_p the values of f for H, C, and CH_2, respectively, at the mean neutron energy $\bar{E}_n$, it is then easily shown that

$$f_h\sigma_H=\tfrac{1}{2}(f_p\sigma_p-f_c\sigma_c), \tag{16}$$

and that

$$\sigma_H=(\sigma_p{}^0-\sigma_c{}^0)/[2(1-f_hG)], \tag{17}$$

where $\sigma_p{}^0$ and $\sigma_c{}^0$ are observed cross sections, uncorrected for the effect, for CH_2 and C scatterers of equal diameter D. For isotropic n-p scattering in center-of-mass coordinates, $f_h=4$. Consequently, Eq. (17) gives the true cross section, corrected for single scattering, in terms of known or measured quantities, without requiring knowledge of f_p or f_c. Note that, since the length of scatterer does not enter Eq. (15), the choice of transmissions of CH_2 and C is immaterial.

A number of estimates based on various models for the scatterers indicated that the contribution of multiple scattering to the scattered-in flux is less than $\frac{1}{5}$ of the single scattering effect. Thus, the error arising from multiple scattering for the smallest diameter scatterer, where the total effect is 0.60 percent, cannot exceed 0.12 percent.

Both the length and the diameter of the polyethylene scatterers were varied in this experiment to establish the freedom from multiple scattering error suggested above. The five scatterers of Table I were made to

dimensions that would give scattering-in effects from 0.006 to 0.015 at transmissions from 0.30 to 0.65.

One criterion for freedom of the method from an uncertainty due to multiple scattering is given by the internal consistency of two computed cross sections: one obtained by extrapolating the diameter function, the other from the slope of $\ln T$ *vs* l_0. The results of this study are shown in Fig. 11. The cross sections deduced from them are $\sigma_p=4.734\pm0.003$ (diameter extrapolation) and $\sigma_p=4.728\pm0.003$ (transmission slope), where only the statistical probable errors are given. The conclusion drawn from this test is that multiple scattering does not produce effects greater than 0.12 percent in cross sections deduced from transmission measurements carried out in the geometry of this experiment.

III. DESCRIPTION OF RUNS

A. Schedule of Runs

The runs were scheduled for convenience in counting, the scaler on channel D1 being used to start the entire system and to stop it after a predetermined register count. Each run consisted of 64 000 counts unattenuated, followed by the same number with scatterer in, and finally by another out count of the same number. This in-out distribution is found to correspond closely to the most effective use of a given total time interval considering the statistics, background, and the range of scatterer transmissions. Such an optimization of time is desirable primarily to minimize electronic drift and time dependence of background. Runs at low beam current were alternated with runs at high current for a number of runs sufficient to give statistical significance to the pile-up study. A total of 209 runs were made on the CH_2 and C samples of Table I. Shadow and hydrogen background were measured frequently, and foil thicknesses checked for stability several times. Again from the standpoint of optimizing the use of the time, about one-quarter of the total time was devoted to the graphite measurements.

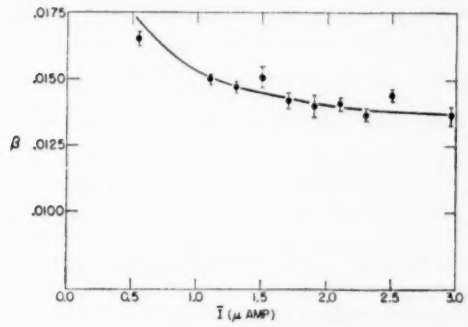

FIG. 10. Dependence of shadow background, measured with deuterium filling and normalized to the unattenuated flux, on average ion current at target. The rise at low current arises from the contribution of δ (see text), and fits Eq. (14), plotted here as the solid line.

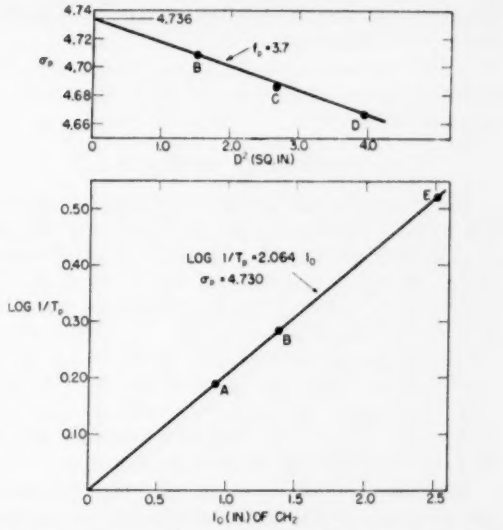

FIG. 11. Internal consistency check against multiple scattering-in, using diameter and length variation of polyethylene. The best line through the diameter plot is taken without regard to the f-value of hydrogen, and the scattering-in effect thus observed for scatterer B is used for A, B, and E in the second plot. The cross section obtained from the best fit (including the origin) of the length function is found to agree with the extrapolation of the diameter function to within 0.12 percent.

B. Computations and Corrections

For each run, the D/M ratio (detector count relative to monitor count) with scatterer in was divided by the average of the two unattenuated D/M ratios to give T^0, the uncorrected transmission. There were two such values from each run, derived from the two pairs of channels in the detection system (Fig. 5). The results from channel 2 were used only to show that, over the experiment as a whole, there was no significant deviation of T_2^0/T_1^0 from unity and hence no significant rate effect; all final cross sections were then deduced from the data obtained from channel 1 alone.

The shadow background correction was made to T^0 by using Eq. (11) and the curve of Fig. 10, read at the appropriate beam current. The hydrogen background correction was made, also using Eq. (11), from the T_{12} data of Table II and the curve of Fig. 9, read at the appropriate time. The a values of Table I were then used (after temperature correction) with Eq. (10) to give σ^0, the cross section uncorrected for scattering-in.

The entrance foil of the target had to be changed about halfway through the experiment, after 42 hours of beam time; and the second foil was found to be several kilovolts thinner than the first. The difference was accounted for by a small correction to all the later cross sections using the known energy dependences of C and H. Thus, all data refer to a mean neutron energy of 4.749 Mev computed for the first foil.

Finally, a scattering-in correction was applied to each value of σ^0 in order to provide sets of completely cor-

rected cross sections for studies of internal consistency. These corrections were derived from f_p and f_e values obtained from best fits to the polyethylene and graphite diameter studies consistent with the value $f_h=4$, as discussed in Sec. V.

IV. SOURCES OF ERROR

The discussion of this section evaluates the contributions to the total probable error of the n-p cross section from all significant sources of which we are aware. We shall consider two sets of estimates; the first in most cases is based on observations of the stability of measurements, while the second is our opinion regarding the extent to which additional systematic errors may have entered the data. In some cases, the second value contains only the systematic estimate; in others, this estimate is combined with the first, as the square root of the sum of squares.

Table III lists twelve sources of error with the two sets of estimates of their magnitudes, given in parts per thousand of hydrogen cross section. The errors in hydrogen background correction are given, first, by the statistics of p_0 and T_{12} measurements (Fig. 9 and Table II) and, second, by combining with this an estimate of uncertainty due to loss and exchange of deuterium in the target end wall during the hydrogen runs. The estimate follows from the observation that the duration of a single run was at most 70 min, while the drop in p_0 indicated in Fig. 9 required bombardment for 220 min. The probable error from rate effects is given as the full effect observed by comparison of data at high and low beam current. The error in neutron energy contains an uncertainty of 4 kev in the Q value[13] of the primary reaction; the remainder, in the first estimate, includes the errors in target length and the fluctuations in resonance mid-points in successive foil calibrations. The second estimate takes into account the possibility that non-uniformities of the entrance foil produce asymmetries in the resonance data. The contribution of counting statistics in measurements of T^0 is given; the first estimate is the error for the experiment as a whole, and the second is the error for any one of the scatterer geometries taken alone. The statistical error in shadow background is deduced from the data shown in Fig. 10, while the second estimate allows for systematic uncertainties in this measurement of $\frac{1}{10}$ of its full value. The uncertainty due to multiple scattering is taken from the transmission-diameter inconsistency (Sec. II H); this is covered by the second estimate which is taken as $\frac{1}{5}$ of the full scattering-in effect for the smallest diameter scatterer. Observations on the limitations of the line-up procedure were used to deduce the error due to axial misalignment of scatterers. The uncertainty in composition of the polyethylene is taken from the chemist's quotations (Sec. II D). The error in scatterer dimensions is taken from the data pertinent to Table I, and the temperature of the polyethylene samples is assumed to be uncertain by 1°C. The effect of degradation by wall scattering is taken as the full computed effect. Finally, an estimate of the effect of the finite interval in neutron energy is included, taking into account all effects discussed in Sec. II E. In each of the two over-all estimates, the total error is taken as the square root of the sum of squares.

TABLE III. Breakdown of the total probable error (parts/1000).

Source	First	Second
H_2 background	0.5	2.1
Rate effects	1.5	1.5
Neutron energy	1.3	1.4
Counting statistics	0.7	1.4
Shadow background	0.4	1.3
Multiple scattering	1.2	1.2
Misalignment	1.0	1.0
Chemistry of CH_2	0.7	0.7
Dimensions	0.4	0.4
Temperature of CH_2	0.3	0.3
Degradation	0.3	0.3
Finite energy interval	0.1	0.1
Total	2.8	3.9

An inspection of Table III shows that in this experiment there are seven effects contributing approximately the same magnitude of error, and hence any attempt to reduce significantly the total error of 0.39 percent would necessitate improvements in most of these factors.

Since the purpose of the experiment is to obtain knowledge of the singlet potential, it is necessary to combine the total probable error of the cross-section measurement with the errors in other measured quantities entering the relation between cross section and the singlet parameters. The situation is at present such that the uncertainties in other experiments (see Sec. V B) correspond to a cross-section uncertainty of 0.3 percent. Thus, if the other parameters are treated as exact, the probable error of this determination must be increased to 0.5 percent. Note that a significant improvement in the precision of the cross-section measurement must be accompanied by better data on other parameters if the singlet parameters are to be more closely defined.

V. EXPERIMENTAL RESULTS AND INTERPRETATION

A. Examination of Cross-Section Data

The final cross sections of all scatterers, computed and corrected according to the procedures of Sec. III B, are given in Table IV. The scatterers are listed as in Table I; their transmissions and diameters are given here as nominal values. The column σ^0 represents cross sections corrected for shadow background, hydrogen background, temperature, and variation of foil thickness, but not for scattering-in effects. A best value for the hydrogen cross section, corrected for scattering-in, can now be computed, if it be assumed that multiple scattering can be ignored and that the n-p scattering

TABLE IV. Final cross sections for all scatterers.

Scatterer	Material	T	D (in)	σ^0 (barns)	σ (barns)
A	CH_2	0.65	1.25	4.686	4.713
B	CH_2	0.52	1.25	4.702	4.728
B	CH_2	0.52	1.25	4.715	4.741
C	CH_2	0.52	1.63	4.687	4.732
D	CH_2	0.52	2.00	4.667	4.735
E	CH_2	0.30	1.25	4.707	4.731
$(CH_2)_{Av}$					4.730±0.007
F	C	0.54	1.25	1.349	1.355
G	C	0.54	1.63	1.339	1.350
H	C	0.54	2.00	1.332	1.348
J	C	0.30	1.25	1.339	1.345
$(C)_{Av}$					1.350±0.003
A, B, E, F, J	H		1.25	1.679	1.689
C, G	H		1.63	1.674	1.691
D, H	H		2.00	1.667	1.693
$(H)_{Av}$					1.690±0.003

is isotropic. At each of the three scatterer diameters, σ^0 for hydrogen is obtained by subtraction of graphite from polyethylene, the weight of each value being determined by the number of runs taken at that diameter. For example, σ^0 for hydrogen at diameter 1.25 inch is half the difference between the mean of A, B, and E and the mean of F and J, and has four times the weight of the other two diameters. The three values thus obtained are fitted by least squares to the function $\sigma^0=\sigma(1-0.00384D^2)$, which takes into account the first-order scattering-in effect in the geometry of this experiment, with $f_h=4$. As pointed out in Sec. II H, this treatment does not require knowledge of f_p and f_c. It yields 1.690 barns for the corrected cross section of hydrogen, which we adopt as our final value.

The data can be examined from several distinct points of view, each of which tends to provide a test of internal consistency of the results. Such a test has already been described in connection with multiple scattering (Sec. II H), where it was pointed out that the best fit to the diameter function is consistent, to about 0.1 percent, with the best fit to the transmission function. It is appropriate to point out that certain systematic effects other than multiple scattering would also be expected to show up in this comparison. The background corrections fall into this class, since they are functions of transmission, Eq. (11). According to Eq. (6), pile-up is also expected to vary with transmission, as would the effect of a significant amount of low energy flux not accounted for by the hydrogen background correction.

A second consistency test is given by the statistical behavior of the results. For this purpose, fully corrected cross sections are obtained from σ^0 values by deducing the most probable scattering-in corrections for polyethylene and graphite. This is done by fitting the σ^0 data of Table IV to linear functions of D^2 that are consistent with $f_h=4$. The corrected cross sections are then listed as σ in Table IV. Each entry in the polyethylene data of this table represents the mean of a number of runs sufficient to give a probable error of 0.006 barn due to counting statistics; each graphite entry has a corresponding error of 0.003 barn. The mean values $(CH_2)_{Av}$ and $(C)_{Av}$ in Table IV are given with probable errors computed, for *any one* of the entries, from the observed deviations of single values. These are then reflected as an error of 0.003 barn in the n-p cross section $(H)_{Av}$. The agreement between observed statistical error and prediction from number of counts indicates consistency of cross sections over the range of transmissions and diameters used in the experiment.

Temperature drift, fluctuation of backgrounds, changes in foil thickness and accelerator calibration, and other slow time variations, are expected to show up in a time-sequential breakdown of corrected cross sections. All of the runs on polyethylene are studied in this way in Fig. 12, each point representing the mean of eight consecutive runs. The total probable error, estimated as in Table III, is also shown. Since corrections were made from smoothed data, the fluctuations of these points should reveal whatever significant effects are superimposed on counting statistics. The external probable error of the mean in Fig. 12, computed from the number of counts, is 0.0023 barn; the observed internal error is 0.0026 barn. The points are therefore consistent with a constant cross section of 4.730 barns.

Finally, the distribution of the errors of individual runs on polyethylene is compared with the normal distribution. In Fig. 13 integral plots are made for the three transmissions separately, and a differential plot for the entire set normalized to transmission 0.52. Agreement with normal distributions is satisfactory. Recalling the two tests against rate effects in the detector, described in Sec. II C, we have given a total of five checks against systematic errors of certain types. If no other errors have entered the measurement, the first estimate of Table III applies, and the probable error of the hydrogen cross section is 0.004_7 barn. Adopting the second estimate, we have the final value $1.690\pm0.006_6$ barns.

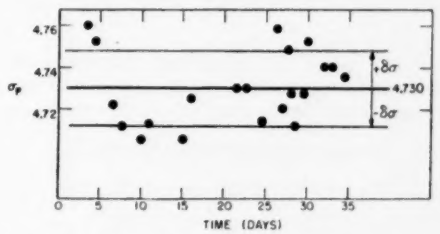

FIG. 12. Sequential breakdown of polyethylene cross sections, including all corrections, showing statistical consistency with a constant cross section. $\delta\sigma$ is the total probable error for polyethylene analogous to the error for hydrogen deduced from Table III.

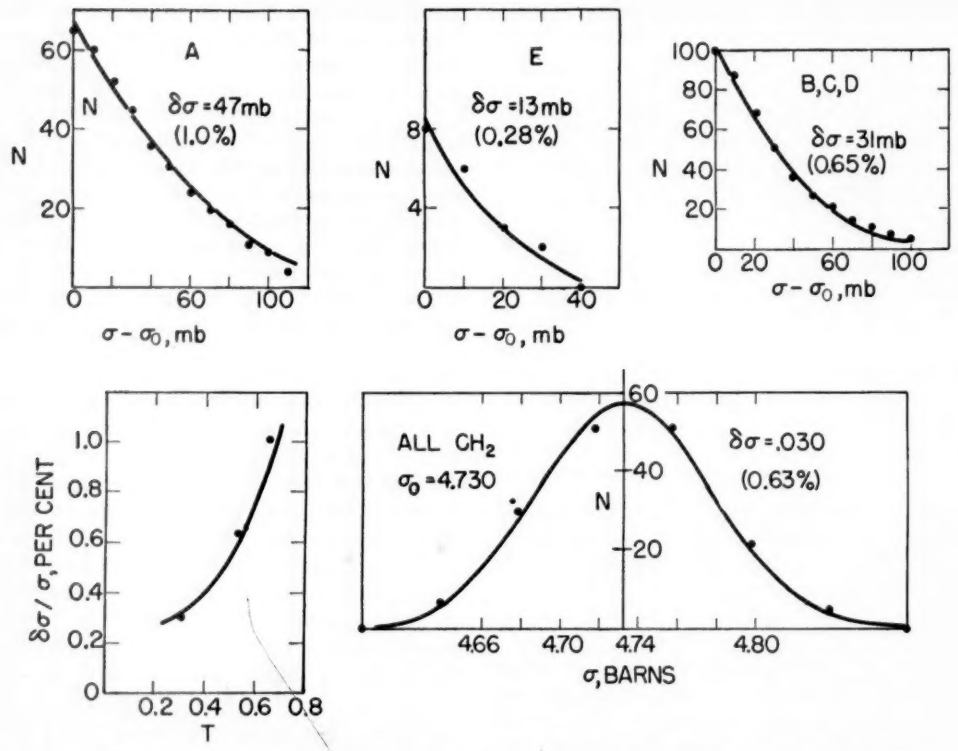

FIG. 13. Distributions of deviations of corrected individual runs on polyethylene around the mean value 4.730 barns. The three upper curves are integral plots for single transmissions compared with integrals of Gaussian functions (solid curves). The points on the lower left plot are the statistical probable errors per run at each transmission, read from the upper curves and compared with the prediction from counting statistics (solid curve). The final curve is the differential distribution of all runs, normalized to transmission 0.52, where the predicted statistical probable error per run is 0.58 percent.

B. Interpretation

From the theory of effective range,[1-3] the total n-p scattering cross section for angular momentum $l=0$ can be written

$$\sigma=\sigma_t+\sigma_s=\frac{3\pi}{k^2+[1/a_t-\frac{1}{2}\rho_t(0,E)k^2]^2}+\frac{\pi}{k^2+[1/a_s-\frac{1}{2}\rho_s(0,E)k^2]^2}, \quad (18)$$

where $k^2=ME/2\hbar^2$, and E=energy of incident neutron in the laboratory system. The subscripts t and s denote triplet and singlet states, respectively. In this notation,

$$\rho_t(0,E)\cong r_{0t}[1-2P_t r_{0t}^2k^2];$$

a_t=triplet scattering amplitude at zero energy;
r_{0t}=triplet effective range at zero energy;
P_t=small coefficient that depends on the shape of the triplet potential well. Such coefficients are tabulated in reference 2 as a function of (r_0/a).

The singlet parameters are defined analogously.

The contributions of higher angular momenta to the total n-p cross section are negligible below 5 Mev, so that σ of Eq. (18) represents the experimental total scattering cross section.

From measurements of the binding energy of the deuteron,[13] the epithermal n-p total cross section,[15] and the coherent scattering amplitude,[16] the three parameters a_t, a_s, and $\rho_t(0,-\epsilon)$ are determined:[17]

$$\begin{aligned} a_t&=5.378(1\pm0.0039)\times10^{-13}\text{ cm},\\ a_s&=-23.69(1\pm0.0024)\times10^{-13}\text{ cm},\\ \rho_t(0,-\epsilon)&=r_{0t}(1+2P_t\gamma^2r_{0t}^2)\\ &=1.702(1\pm0.017)\times10^{-13}\text{ cm}, \end{aligned} \quad (19)$$

where $\gamma^2=M\epsilon/\hbar^2$, ϵ=binding energy of the deuteron.

In the shape independent approximation ($P_t=P_s=0$), the total n-p cross section, $\sigma^{(S.I.)}$, is a function of the one unknown r_{0s} for a given energy. A plot of $\sigma^{(S.I.)}$

[15] E. Melkonian, Phys. Rev. **76**, 1744 (1949).
[16] Burgy, Ringo, and Hughes, Phys. Rev. **84**, 1160 (1951).
[17] For a list of the experimental values used, together with a discussion of the contributions of their experimental errors to the uncertainties in a_t, a_s, and $\rho_t(0,-\epsilon)$, see G. Snow, Phys. Rev. **87**, 21 (1952).

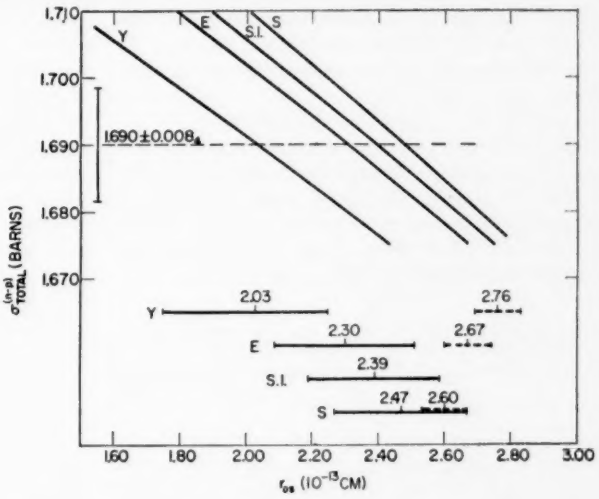

FIG. 14. Theoretical total n-p cross sections as a function of effective singlet range r_{0s} for the well shapes: Square (S), "Shape Independent" (S.I.), Exponential (E), and Yukawa (Y). Resultant values of $r_{0s}^{(n-p)}$ are shown and compared with $r_{0s}^{(p-p)}$ for each well shape.

versus r_{0s} at $E_n=4.749$ Mev, using the parameters of Eq. (19), yields $r_{0s}^{(S.I.)}=(2.39\pm0.20)\times10^{-13}$ cm for $\sigma=1.690\pm0.008_4$b.[18] This is illustrated in Fig. 14.

To consider shape dependent effects, we have plotted σ *versus* r_{0s} in Fig. 14 for the three potential well shapes: square (S), exponential (E), and Yukawa (Y). For simplicity we have assumed the same well shape for singlet and triplet potentials. The experimental result for σ then determines r_{0s} for each well shape, as shown in Fig. 14, and listed in Table V. In all cases σ is quite insensitive to r_{0s}; $(r_{0s}/\sigma)(\partial\sigma/\partial r_{0s})\simeq1/18$. Nevertheless, the experimental error in σ yields an uncertainty in r_{0s} for each shape that is smaller than or comparable to the differences between the values of r_{0s} for different shapes. Therefore, this experiment yields information about the singlet effective range coupled with the potential shape.

In Table V and Fig. 14, the values[19] of the proton-proton effective singlet range $r_{0s}^{(p-p)}$ are listed and compared with $r_{0s}^{(n-p)}$ for each potential well shape. The following results are found: for a Yukawa well, $r_{0s}^{(n-p)}$ is definitely smaller than $r_{0s}^{(p-p)}$; for an exponential well, $r_{0s}^{(n-p)}$ is smaller than $r_{0s}^{(p-p)}$ with errors that almost overlap; and for a square well, $r_{0s}^{(n-p)}$ is slightly smaller than $r_{0s}^{(p-p)}$ with errors that completely overlap.

A more rigorous test of the hypothesis of charge independence than the comparison of the quantities $r_{0s}^{(n-p)}$ and $r_{0s}^{(p-p)}$ is the comparison of the corresponding values of the singlet intrinsic range b_s defined by Blatt and Jackson.[20] The parameters b_s are more appropriate than r_{0s} since they characterize the range of the specifically nuclear potential, excluding the Coulomb potential. The values of $b_s^{(n-p)}$ obtained from this experiment are listed in Table V along with the more accurate values of $b_s^{(p-p)}$. The same conclusion follows from the comparison of b_s as for r_{0s}. Hence, a square well is compatible with charge independence, a Yukawa well is not compatible, and the exponential well is a borderline case.

For completeness, we have also listed in Table V the well depth parameter s (defined by Jackson and Blatt[19]) for the n-p and p-p singlet interactions. We see that $s^{(n-p)}$ is a few percent larger than $s^{(p-p)}$ for all three potential well shapes. This result reiterates with slightly more force the same result already obtained by Bethe[1] from a comparison of $a_s^{(n-p)}$ and $a_s^{(p-p)}$ assuming equal singlet n-p and p-p intrinsic ranges.

TABLE V. The singlet effective range r_{0s}, intrinsic range b_s, and well depth parameter s, for the n-p singlet interaction (obtained from this experiment) and for the p-p singlet interaction (Jackson and Blatt).

Well shape	$r_{0s}^{(n-p)}$ (10^{-13} cm)	$r_{0s}^{(p-p)}$ (10^{-13} cm)	$b_s^{(n-p)}$ (10^{-13} cm)	$b_s^{(p-p)}$ (10^{-13} cm)	$s^{(n-p)}$	$s^{(p-p)}$
Square	2.47±0.20	2.60±0.07	2.37±0.19	2.58±0.06	0.926±0.006	0.889±0.003
Exponential	2.30±0.21	2.67±0.07	2.17±0.20	2.51±0.06	0.937±0.006	0.907±0.003
Yukawa	2.03±0.23	2.76±0.07	1.90±0.21	2.47±0.06	0.953±0.006	0.922±0.003

[18] For the purposes of this interpretation, the probable error of σ has been increased by an amount that reflects the present experimental uncertainties in a_s, a_t and r_{0t}.

[19] J. D. Jackson and J. M. Blatt, Revs. Modern Phys. **22**, 77 (1950).

[20] See reference 2. Blatt and Jackson also give formulas with which $b_s^{(n-p)}$ can be computed from the values of r_{0s} and a_s for each of the assumed well shapes.

Schwinger[21] has given a possible explanation of this small difference in potential well depth in terms of the different electromagnetic interactions that are present in the n-p and p-p systems.

It is profitable at this point to dwell upon the dependence of the cross section on shape. The shape dependence is manifested through the triplet and singlet parameters P_t and P_s (the shape dependent terms in the expansion of $k\cot\delta$ of order k^6 or higher can be neglected at $E_n=4.75$ Mev). These parameters as obtained from the formulas of Blatt and Jackson[2] are as follows:

Well shape:	S	S.I.	E	Y
P_t:	−0.040	0	+0.029	+0.137
P_s:	−0.03	0	+0.010	+0.055

Most of the shape dependence of σ comes from the parameter P_t rather than P_s since $\sigma_t \simeq 3\sigma_s$. Note that a positive value of P decreases the triplet cross section but increases the singlet cross section as compared to $P=0$, since the triplet and singlet scattering amplitudes have opposite signs. Hence, it follows that a pure Yukawa well shape for the triplet potential coupled with any of the shapes other than Yukawa for the singlet potential will imply a value for $r_{0s}{}^{(n-p)}$ even smaller than the one given in Table I, which assumed Yukawa shapes for both singlet and triplet interactions. Stated in another way, this experiment indicates that the Yukawa well value of $P_t=0.137$ coupled with any reasonable value of P_s implies that $r_{0s}{}^{(n-p)}<r_{0s}{}^{(p-p)}$; hence, that charge independence is not valid.

Since the hypothesis of charge independence has the great virtue of simplicity and is at least qualitatively valid, and since the Yukawa form for the nuclear potential is the most satisfying from the meson theoretic point of view, it seems pertinent at this point to ask whether both ideas can be maintained without contradicting the results of this experiment. One simplification of the theoretical analysis of this experiment is the omission of tensor forces in the triplet interaction. The influence of tensor forces on the shape dependent factor P_t has recently been investigated[22] for a particular choice of central and tensor Yukawa potentials. The potential parameters were chosen from the tables of Feshbach and Schwinger[23] so that all low energy parameters including the deuteron quadrupole moment were given correctly, and so that the ratio of tensor range to central range was a maximum. The shape dependent coefficient was found to be 0.14 ± 0.04 as compared with 0.137 for a pure central Yukawa well. Hence, the triplet shape-dependent parameter P_t does not appear to be sensitive to the presence of tensor forces.†

Next we have considered the effect of a repulsive core on the value of the parameter P_t. The idea of a repulsive core was introduced by Jastrow[24] in an attempt to preserve the hypothesis of charge independence while comparing high energy n-p and p-p scattering, and therefore it seemed plausible to inquire whether the repulsive core could accomplish the same purpose of 4.75 Mev. For ease of computation a Hulthén potential displaced from the origin by a repulsive core of variable width b_c was used. The results for a displaced Yukawa well will certainly be similar. The potential had the form

$$V(r)=\begin{cases}+\infty, & r<b_c;\\ -W\dfrac{e^{-\xi(r-b_c)}}{1-e^{-\xi(r-b_c)}}, & r>b_c.\end{cases} \tag{20}$$

For each value of b_c the parameters W and ξ were chosen so as to fit the experimental values of the deuteron binding energy and the effective range $\rho_t(0,-\epsilon)$; $\rho_t(-\epsilon,-\epsilon)$ was evaluated from its definition[3] in terms of the simple bound state wave function for this potential. Next one can define P_t by the equation

$$\rho_t(-\epsilon,-\epsilon)=\rho_t(0,-\epsilon)+2P_t r_{0t}{}^3\gamma^2, \tag{21}$$

where terms of higher order in $(\gamma r_{0t})^2$ have been dropped. One then obtains P_t as a function of the size of the repulsive core b_c. This is shown in Fig. 15. At $b_c=0$, i.e., no repulsive core, $P_t=+0.11$ as compared with +0.137 for a pure Yukawa well. P_t falls steeply to 0 at $b_c=0.28\times10^{-13}$ cm, and then approaches its limiting[25] value of −0.049 at the maximum repulsive core ($b_c=1.06\times10^{-13}$ cm) consistent with the low energy scattering parameters. As the size of the repulsive core increases, the depth of the Hulthén potential increases, and the parameter $1/\xi$ decreases, so as to maintain the values of ϵ and $\rho_t(0,-\epsilon)$. This calculation shows that a small repulsive core, $b_c\simeq0.3\times10^{-13}$ cm, which decreases the parameter $1/\xi$ by two thirds, can reduce a large positive value of P_t to zero. Such a reduction in P_t and correspondingly in P_s would yield a value for $r_{0s}{}^{(n-p)}=2.4\pm0.22$, which is smaller than, but certainly not inconsistent with, the corresponding value of

[21] J. Schwinger, Phys. Rev. **78**, 135 (1950).
[22] W. C. Guindon and G. Snow (private communication).
[23] H. Feshbach and J. Schwinger, Phys. Rev. **84**, 194 (1951).
† *Note added in proof:*—J. Blatt has kindly informed us that L. Biedenharn has calculated the shape coefficients for three other choices of tensor and central Yukawa potentials. The value obtained for P_t varied from 0.053 to 0.096. More extensive calculations are clearly necessary in order to determine the importance of tensor forces with respect to the shape dependent coefficients.
[24] R. Jastow, Phys. Rev. **81**, 165 (1951).
[25] These limiting values for b_c and P_t are valid for any well shape displaced from the origin by an infinite repulsive core. Such a limit corresponds to assigning the value of the logarithmic derivative of the wave function at a finite distance as discussed by Breit and Bouricius [Phys. Rev. **75**, 1029 (1949)] for the singlet interaction. The maximum value of b_c can be derived from the general formulas that relate (a, r_0), the scattering amplitude and effective range for a given potential displaced by a repulsive core, to (a', r_0') the same quantities for the given potential without repulsive core. One can show that

$$a=a'+b_c;\quad r_0=r_0'\left(\frac{a'}{a}\right)^2 2b_c+\left(\frac{1-b_c+b_c^2}{a\quad 3a^2}\right).$$

$r_{0s}^{(p-p)}$. Since the limiting value of P_t is negative and only slightly larger in magnitude than the square well value for P_t, all values of b_c larger than 0.3×10^{-13} cm will also be consistent with the hypothesis of charge independence. Hence, we see that the Yukawa-type shape and charge independence can both be maintained if we assume a repulsive core. This should not be construed as definite evidence for a repulsive core, since either the hypothesis of charge independence or the assumption of a Yukawa tail may be wrong.

A recent measurement of the total n-p cross section at 14 Mev by Poss *et al.*[26] led[17] to a mean effective range $r_{0s}^{(n-p)}=2.2\pm0.35\times10^{-13}$ cm. At this energy, the values of $r_{0s}^{(n-p)}$ for the three well shapes (S), (E), and (Y) differ from each other by much less than the probable error. Another pertinent experiment in progress is a measurement[27] of the total n-p cross section at 1.32 Mev. They obtain the tentative result $r_{0s}^{(n-p)}=2.2\pm0.3\times10^{-13}$ cm in the shape independent approximation. These measurements, as well as the present measurement, are consistent with the less accurate results[3] obtained from the experiment of Lampi *et al.*[4]

Measurements by Poss and Storrs seem to imply a failure of the hypothesis of charge independence of nuclear forces. A repetition of the 14-Mev experiment and the completion of the 1.3-Mev experiment may well serve as definitive tests of this hypothesis. Unfortunately, the more or less shape-insensitive value for $r_{0s}^{(n-p)}$ obtained so far from these two experiments falls just in the middle of the range of values obtained for $r_{0s}^{(n-p)}$ from the present experiment. Hence, as the matter now stands, all three potential well shapes, (S), (E), and (Y), as well as all shapes that give equivalent P values, are consistent with all the medium energy n-p data. Finally, it is possible that the value of $r_{0s}^{(n-p)}$ will eventually be measured in a way that is more independent of shape parameters. If so it will, when combined with the measurement reported here, yield an approximate value of the parameter characteristic of the shape of the triplet n-p potential.

We are indebted to Professor D. H. Frisch for his collaboration in the early stages of the experiment, and thereafter for many invaluable suggestions and criticisms. The assistance of Dr. H. L. Poss in the initial phases was also considerable. We are grateful to Dr. E. O. Salant for originally suggesting this experiment, to Dr. H. S. Snyder for discussions about calculations with a repulsive core, to Dr. C. P. Baker for discussion of the entire problem, to Dr. R. Davis, Jr., for the evaporation of CaF_2 targets, to Dr. G. J. Dienes for extensive discussion of the properties of polyethylene, to Mr. R. G. Fulton of the Bakelite Company for infrared spectroscopy, to Dr. R. A. Paulson of the Bureau of Standards for chemical analysis, to Miss Jean Snover for numerical calculations, and to Mr. Frank Marder for construction of the thin-walled target.

[26] Poss, Salant, Snow, and Yuan, Phys. Rev. **87**, 11 (1952).
[27] C. L. Storrs and D. H. Frisch, Massachusetts Institute of Technology Progress Report, May 21, 1952 (unpublished).

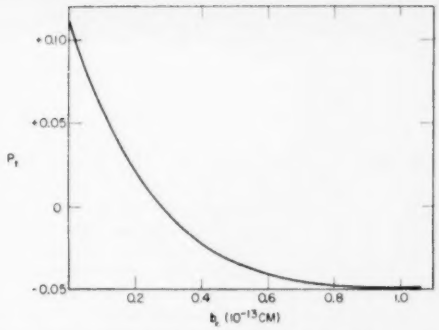

FIG. 15. Shape dependent coefficient P_t for a Hulthén potential displaced from the origin by a repulsive core of width b_c (10^{-13} cm), as a function of b_c. The potential is always adjusted to give correct ϵ and a_t (see text).

APPENDIX I. PILE-UP CALCULATION

Assume that the differential pulse-height spectrum at the discriminator of the detector system can be represented by a distribution of the form

$$f(E)=A(E+\epsilon)^{-\eta}, \tag{22}$$

where E is the pulse height and A, ϵ, and η are arbitrary constants. The integral counting rate *vs* bias is then

$$n(E)=\int_E^\infty f(E)dE=[A/(\eta-1)](E+\epsilon)^{1-\eta}, \tag{23}$$

where, if N is the counting rate at the bias setting E_0, $A=N(\eta-1)(E_0+\epsilon)^{\eta-1}$. Now the rate of pile-up of two pulses smaller than E_0 and of duration τ is

$$P_1=\tau\int_0^{E_0}\int_{E_0-x}^{E_0}A(x+\epsilon)^{-\eta}A(y+\epsilon)^{-\eta}dydx. \tag{24}$$

The integral bias curve observed with our system, Fig. 4, is a good fit to the function (23) if one takes $\epsilon=10.5$ volts and $\eta=2.8$. In order to perform the integrations indicated in (24), we have taken, $\eta=3$ and obtained

$$P_1=\tau N^2\left\{1+2\frac{(k+1)^2}{(k+2)^4}[6\ln(k+1)-(k+2)(4+k-2k^2)]\right\},$$

where $k=E_0/\epsilon$. The rate of pile-up of two pulses larger than E_0 is simply $P_2=\tau N^2$, and the net effect is therefore

$$P=P_1-P_2$$
$$=2\tau N^2\frac{(k+1)^2}{(k+2)^4}[6\ln(k+1)-(k+2)(4+k-2k^2)]. \tag{25}$$

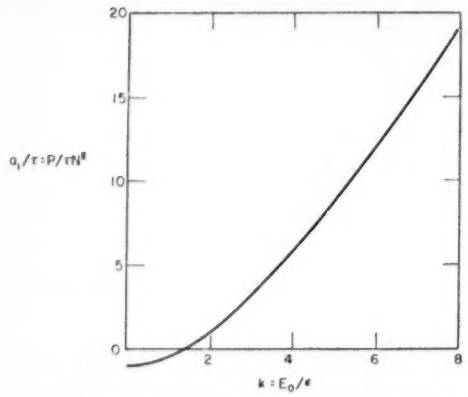

FIG. 16. Rate of pile-up of two pulses, as a function of discriminator bias, for the pulse-height spectrum of neutrons detected in this experiment.

The quantity P/N^2, which can be identified with the coefficient a_1 of Eq. (4), is roughly quadratic in k, rising from the value $-\tau$ at $k=0$ through zero at $k=1.4$ to $+\tau$ at $k=2$ (see Fig. 16). Transmission measurements on channel D1 were made at $E_0=15$ volts, $k=1.4$; pile-up of this type is therefore not expected to enter the experiment.

APPENDIX II. CORRECTION FOR HYDROGEN BACKGROUND

Using the notation of Fig. 2, adopt the following definitions:

A. With deuterium in the target chamber, let

U = unattenuated total count rate,
φU = unattenuated count rate from d-d neutrons produced in the gas,
βU = total count rate with perfect shadow,
$T^0 U$ = total count rate with a scatterer whose true transmission for the component φ is T and whose true transmission for the components $(\gamma_1+\gamma_2)$ is T_{12},
$\gamma_1 U$ = unattenuated count rate for neutrons produced in collimating slits,
$\gamma_2 U$ = unattenuated count rate for neutrons produced in gold end-wall of target.

B. With hydrogen in the target chamber, assume that γ_1 and γ_2 are the same in intensity and in energy as they were in A. Then, with reference to the same scatterer, let

pU = unattenuated total count rate,
$\gamma_3 U$ = unattenuated count rate from d-d neutrons produced in traces of D_2 arising from exchange of H_2 in target walls,
δU = total count rate with perfect shadow,
$pT_p^0 U$ = total count rate with scatterer in.

According to the definitions,

$$\gamma_1+\gamma_2+\varphi+\beta=1, \quad \text{and} \quad \gamma_1+\gamma_2+\gamma_3+\delta=p. \tag{26}$$

Now $T^0=\varphi T+(\gamma_1+\gamma_2)T_{12}+\beta$, implying, together with (26), that

$$T=T^0+(\gamma_1+\gamma_2)(T-T_{12})-(1-T)\beta. \tag{27}$$

The hydrogen background correction is contained in the second term and can be made from direct measurement of γ_1, γ_2, and T_{12}, using a first approximation for T. However, it is important to note that the correction can be made in the presence of an arbitrary amount of γ_3. Observe that

$$pT_p^0=(\gamma_1+\gamma_2)T_{12}+\gamma_3 T+\delta. \tag{28}$$

Using (26) and (28), consider

$$p(T-T_p^0)=(\gamma_1+\gamma_2)(T-T_{12})-(1-T)\delta. \tag{29}$$

Subtracting (29) and (27), one obtains

$$T=T^0+p(T-T_p^0)-(1-T)(\beta-\delta). \tag{30}$$

Thus, the correction can be made from the total hydrogen count p and the corresponding transmission T_p^0. It has been assumed here that the neutrons involved in γ_3 have the same mean energy as those in φ. This is true to the extent that the deuterium fraction entering the hydrogen filling is uniformly distributed through the target volume.

PHYSICAL REVIEW VOLUME 89, NUMBER 1 JANUARY 1, 1953

Barrier Penetration Effects for Light Nuclei*†

B. E. FREEMAN‡ AND J. L. MCHALE
Yale University, New Haven, Connecticut

(Received August 11, 1952)

The penetration parameters F_L^2/ρ, ρ/G_L^2, and ρ/A_L^2 have been compared as functions of energy for a number of reactions induced by proton or alpha-particle bombardment of light nuclei. It was found that these parameters behaved quite similarly in the energy range considered, particularly for $L>0$. The limitations on the applicability of barrier "penetration factors" in the treatment of reaction cross sections are investigated by computing a number of typical cases, making use of the one-body model with allowance for absorption of the incident wave. Several sets of values of nuclear radius and well depth were used. The relation between the one-body cross section without absorption and the channel penetration parameters, f_L^2/ρ and ρ/g_L^2, is treated in some detail for the $Li^7(p,\alpha)\alpha$ reaction. Breit's consideration of the case of very strong absorption $\sigma_L \propto 1/A_L^2$, is also presented. The connection between the one-body model without absorption and a one-level dispersion formula in the vicinity of sharp resonance is used to tabulate the properties of a number of one-body resonances. In a number of cases resonances were found to be broadened markedly by the absorption of the incident wave in nuclear matter.

I. INTRODUCTION

IN the past, "penetration factors" have been applied extensively to study nuclear reactions involving the absorption or emission of charged particles. Such a factorization is supposed to split off the barrier dependence of the damping constant Γ which characterizes the prescribed disintegration channel. The residual factor contained in Γ is then to depend only on the behavior of the compound nucleus in releasing disintegration products in the absence of the barrier.

With the exception of certain limiting cases, however, this procedure is incompatible with evidence obtained on the basis of simplified models of the nucleus. In the general case it is found that barrier effects cannot be separated from those of specifically nuclear origin. Excitation functions calculated for such models provide a useful measure of barrier penetration and resonance effects, but it is not intended to substitute them for more complete considerations of many-body features of the reactions.

Various combinations of the regular and irregular Coulomb functions, F_L and G_L, evaluated at the nuclear surface, have been proposed as penetration parameters. The form $\Gamma \propto F_L^2/\rho$ is perhaps the most widely employed penetration parameter. As will be seen later, it represents a limiting case of the one-body model of the nucleus. Konopinski and Bethe[1] used the relation $\Gamma \propto \rho/G_L^2$, suggested by Kapur and Peierls,[2] to study several reactions with light nuclei. Christy and Latter,[3] guided by the considerations of Wigner[4] and Wigner and Eisenbud,[5] applied the penetration parameter ρ/A_L^2 to the study of a number of reactions with light elements. The damping constant Γ is also expressible in terms of the quantities f_L^2/ρ or ρ/g_L^2 under special conditions. Here, $f_L=F_L\cos K_L+G_L\sin K_L$ and $g_L=G_L\cos K_L-F_L\sin K_L$ are Coulomb functions corrected for the presence of an average nuclear potential, which produces a phase shift K_L. Breit[6] obtained the relation $\Gamma \propto f_L^2/\rho$ for a weakly coupled resonating nuclear element under the idealization of sharp localization in space; a similar result is obtained in his schematic treatment of nuclear resonances.[7] For a strong repulsive interaction in a large region, however, the result $\Gamma \propto \rho/g_L^2$ is obtained. The reason for considering all these possibilities is that for different nuclear models one or another penetration parameter can be used in a simple formula. The parameters listed above apply to limiting cases of the more general conditions determined by the location of resonating elements in the compound nucleus, the competition from other channels, and other factors.

The publication of extended tables of the Coulomb functions[8] eliminates the uncertain and possibly large errors introduced by the employment of the J.W.B.K. approximation to the square of the Coulomb functions. But the absence of a unique definition of a penetration parameter emphasizes the uncertainties and need for caution in the application of "penetration factors."

In some cases, such as the escape of α-particles from radioactive nuclei, the main interest has been in the approximate energy dependence of the mean life. Here it does not matter much how the barrier penetration effects are treated, nearly equivalent results being obtained by different methods. For light nuclei, however, one can obtain appreciable differences depending on which of the current conventions is used. The main

* Part of a dissertation submitted by Burton E. Freeman for the degree of Doctor of Philosophy at Yale University.
† Assisted by the joint program of the ONR and AEC.
‡ Now at the Los Alamos Scientific Laboratory, Los Alamos, New Mexico.
[1] E. J. Konopinski and H. A. Bethe, Phys. Rev. **54**, 130 (1938).
[2] P. R. Kapur and R. Peierls, Proc. Roy. Soc. (London) **A166**, 277 (1938).
[3] R. F. Christy and R. Latter, Revs. Modern Phys. **20**, 185 (1948).
[4] E. P. Wigner, Phys. Rev. **70**, 15 (1946); Phys. Rev. **70**, 606 (1946).
[5] E. P. Wigner and L. Eisenbud, Phys. Rev. **72**, 29 (1947).
[6] G. Breit, Phys. Rev. **58**, 506 (1940).
[7] G. Breit, Phys. Rev. **69**, 472 (1946).
[8] Bloch, Hull, Broyles, Bouricius, Freeman, and Breit, Revs. Modern Phys. **23**, 147 (1951).

distinction between these problems is the fact that in studies of reactions of the lighter nuclei one is concerned with relatively wide resonances and with the interpretation of yield *versus* bombarding energy data. A variation of a coefficient by a factor 2 or 4 can be of considerable interest if one tries to test different hypotheses regarding the location of virtual energy levels. Such problems did not arise in the work of Gamow[9] and of Condon and Gurney[10] on the original explanation of the Geiger-Nuttall relation. It has been shown by Ostrofsky, Breit, and Johnson[11] that the nuclear model used and the barrier effects can combine themselves in such a way that the simple application of a barrier "penetration factor" can be seriously in error. This fact is obvious through an inspection of their graphs which give very different yield curves depending on the model used.

In the present paper, the mutual consistency of the penetration parameters is tested, and their applicability is determined by computing theoretical yield-energy curves making use of simplifying assumptions somewhat similar to those of OBJ. Only one reaction is studied from the point of view of comparison with experiment. In other cases, the object is to enable an experimental worker to form a reasonably immediate judgment regarding the effect of a change in the model on the shape of the cross section-energy curve. In many cases below, the words "penetration parameter" are used in preference to "penetration factor" so as to emphasize the fact that a potential barrier affects the cross section in a somewhat more complicated manner than through the application of a factor. On the other hand, it will be seen that in some cases "penetration factors" give a good representation of the more accurate relations.

For the sake of simplicity, the calculations on the energy dependence of cross sections are confined to the one-body model, with the inclusion of effects of absorption of the incident wave. The phase shift K_L contained in the definition of f_L and g_L is therefore determined by a one-body approximation. The variety of situations covered has turned out to be so great that only a small fraction of the available material could be prepared for publication.[12] On the other hand, some of the penetration parameters studied below have a general significance also in a many-body approach as has been shown by Breit.[7] On the whole, the study indicates that less care has to be exercised regarding the choice of the penetration parameter when barrier effects are pronounced.

[9] G. Gamow, Physik. Z. **32**, 651 (1931); Z. Physik **52**, 510 (1929); Nature **122**, 805 (1929).
[10] E. U. Condon and R. U. Gurney, Phys. Rev. **33**, 127 (1929).
[11] Ostrofsky, Breit, and Johnson, Phys. Rev. **49**, 22 (1936). This paper is referred to as OBJ in the text.
[12] With the exception of certain representative cases, space limitations prevent the inclusion in this paper of the curves obtained. The unpublished plots can be procured from G. Breit, Sloane Physics Laboratory, Yale University, New Haven, Connecticut.

Notation and Symbols[8]

F_L=regular Coulomb function: $F_L \sim \sin(\rho - \frac{1}{2}L\pi - \eta(\ln 2\rho) + \sigma_L)$. G_L=irregular Coulomb function: $G_L \sim \cos(\rho - \frac{1}{2}L\pi - \eta(\ln 2\rho) + \sigma_L)$. A_L, φ_L=phase amplitude variables: $A_L = |F_L^2 + G_L^2|^{\frac{1}{2}}$ with $F_L = A_L \sin\varphi_L$ and $G_L = A_L \cos\varphi_L$; and $\varphi_L = 0$ when $\rho = 0$. $\rho = kr$, where r is the interparticle separation and $k = \mu v/\hbar = 2\pi/\Lambda$. The quantity μ is the reduced mass and v is the relative velocity of the colliding particles.

$\eta = ZZ'e^2/\hbar v$, where Z and Z' are the atomic numbers of the collision partners. $\mathfrak{F}_L$=solution of the one-body radial equation,

$$[d^2/dr^2 + (2\mu/\hbar^2)\{E' - V + (ih/2)P - L(L+1)/r^2\}]\mathfrak{F}_L = 0.$$

$V(r)$ and $P(r)$ are real quantities such that $V(r) = ZZ'e^2/r$ and $P(r) = 0$ for $r > r_0$; r_0 is the radius of the compound nucleus; E' is the energy of relative motion. For $r > r_0$,

$$\mathfrak{F}_L = e^{iK_L}(F_L \cos K_L + G_L \sin K_L).$$

$$z^2 = (2\mu/\hbar^2)[E' - V + (ih/2)P]r^2 = (k'r)^2 = (k_0' + ik_1')^2 r^2 = (\alpha + i\beta)$$

where k_0', k_1', α, and β are all real quantities. They satisfy

$$(2\mu/\hbar^2)(E' - V)r^2 = (k_0 r)^2 = (k_0' r)^2 - (k_1' r)^2 = \alpha,$$
$$(\mu/\hbar)Pr^2 = 2k_0' k_1' r^2 = \beta.$$

The symbol k_1' is called the absorption coefficient.

In the cross-section formulas, the following symbols and abbreviations are used:

σ_L=partial cross section for a reaction.
$\delta_L = dF_L/F_L d\rho - d\mathfrak{F}_L/\mathfrak{F}_L d\rho$;
$\rho\delta_L = (\rho dF_L)/(F_L d\rho) - (z d\mathfrak{F}_L/\mathfrak{F}_L dz)$.
$u_L = \mathfrak{F}_L(r)/\mathfrak{F}_L(r_0)$.
$s = \sin(2k_0' r)$; $c = \cos(2k_0' r)$; $sh = \sinh(2k_1' r)$; and $ch = \cosh(2k_1' r)$. The abbreviation Re stands for the real part; Im stands for the imaginary part.

Guide to Figures

The following symbols and abbreviations have been used to simplify the labeling of the figures:

E_{Mev}=energy of incident particle in Mev.
E'_{Mev}=relative energy of motion in Mev.
$U = |V|$ where V is the real part of the nuclear potential.
$k'_1 = 0$ denotes the case of vanishingly small absorption.
$\mathfrak{L}_1 = \log_{10}\Pi_1 = \log_{10}(F_L^2/\rho)$.
$\mathfrak{L}_2 = \log_{10}\Pi_2 = \log_{10}(\rho/G_L^2)$.
$\mathfrak{l}_1 = \log_{10}\pi_1 = \log_{10}(f_L^2/\rho)$.
$\mathfrak{l}_2 = \log_{10}\pi_2 = \log_{10}(\rho/g_L^2)$.
$\mathfrak{L} = \log_{10}[10^{39}(\sigma_L v/2\pi P)\ \text{cm}^2]$.
$\mathfrak{P} = \log_{10}[10^{39}(2L+1)r_0^2(F_L/\rho)^2\ \text{cm}^2]$.

Incident channels for proton and alpha-particle bombardment are designated by $Z^A(p,\ )$ and $Z^A(\alpha,\ )$, respectively, where Z^A is the target isotope.

II. SCOPE OF CALCULATION

Under simplifying assumptions discussed in a later section, reaction cross sections have been calculated for the following conditions: (a) Incident particle: proton or alpha-particle; (b) Target nucleus: the elements from lithium to silicon; (c) Energy: from 0.5 to 5.0 Mev; (d) Relative angular momentum: from $L=0$ to $L=4$. Although these target elements and energies present no difficulty for proton bombardment, certain combinations of element and energy must be omitted for alpha-particles. The target element Si is the heaviest element for which Coulomb functions are available[8] with incident alpha-particles. The calculations have been made for values of the nuclear radius, r_0, given by

$$r_0=CA^{\frac{1}{3}},\quad C=1.6\times10^{-13}\quad\text{or}\quad 2.1\times10^{-13}\text{ cm},\quad (1)$$

where A is the mass number of the compound nucleus. The smaller of the two values of C corresponds approximately to some of the nuclear data in conventional interpretations. The larger value was used for two reasons: (a) it was desired to ascertain the effect of a change in r_0; (b) when a nucleus is bombarded by deuterons one has, in general, a variety of processes taking place, starting with a typical Oppenheimer-Phillips transfer and ending with the formation of a compound nucleus; a somewhat intermediate stage consists in the formation of a compound nucleus having a loose structure, with the deuteron being attached to the main body of the bombarded nucleus through the tail of either the neutron or the proton wave function.

The masses of the target nucleus and incident particle were approximated as integral multiples of the proton mass. The Coulomb parameter[8] η, which is large at low energies, is slightly in error because of the latter approximation. This means that the calculations apply to slightly lower energies than intended. But even for alpha-particle bombardment, the correction is only 0.6 percent, an amount which is negligible in comparison with the uncertainties of the one-body model.

III. COMPARISON OF BARRIER PENETRATIONS

The parameters $\Pi_1=F_L^2/\rho$ and $\Pi_2=\rho/G_L^2$ have been calculated for the reactions of protons on Li^7, B^{11}, N^{14}, Ne^{20}, Mg^{24} and Si^{28}, and compared with the results obtained by Christy and Latter,[3] who used a form proportional to $\Pi_3=\rho/A_L^2$. In the low energy limit these forms become equivalent, since for this limit $F_LG_L\propto\rho$ and $F_L\ll G_L$. Therefore, all three reduce to the limiting form $\exp\{-2\pi\eta\}$. Since the principal energy dependence of the partial cross section σ_L is given by the factor $(1/v^2)e^{-2\pi\eta}$ at sufficiently low energies, $\sigma_L\propto\Gamma/E$ in the low energy limit.

For the six target elements employed, the parameters

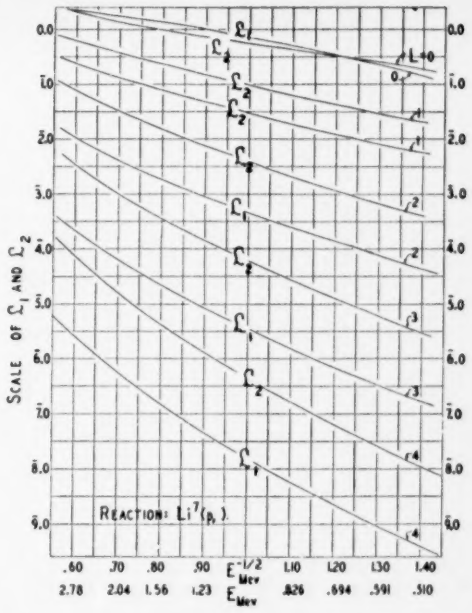

FIG. 1. Comparison of penetration parameters for $Li^7(p,\ )$: $\mathfrak{L}_1$ *vs* $E_{Mev}^{-\frac{1}{2}}$ and $\mathfrak{L}_2$ *vs* $E_{Mev}^{-\frac{1}{2}}$. The curves were normalized by fitting the $L=0$ pair at $E=3$ Mev. $r_0=1.6\times10^{-13}A^{\frac{1}{3}}$ cm.

Π_1 and Π_2 showed closely similar behavior as functions of energy. For large L the ratio Π_1/Π_2 is practically independent of energy in the range from $E=0.5$ to 3.0 Mev.

The comparison of Π_1 and Π_2 is illustrated[12] for proton bombardment of Li^7 in Fig. 1. It is seen that the curvatures of the two parameters differ markedly for $L=0$. For example, the Li^7 curves intersect at $E=0.62$ Mev when fitted at 3.0 Mev. The relative curvature of the $L=0$ parameters exhibited an interesting variation as a function of the atomic number Z' of the target nucleus. For Li^7, the curve ρ/G_0^2 is concave upward; this curvature decreases with increasing Z' until, for Si^{28}, it has reversed, and the curve for ρ/G_0^2 is everywhere above the F_0^2/ρ curve.

The curves[12] computed for the radius $r_0=2.1\times10^{-13}A^{\frac{1}{3}}$ cm agreed qualitatively with the results obtained for the smaller radius with minor exceptions. For example, using the same normalization employed for the smaller radius, the second intersection of Π_1 and Π_2 for $L=0$ is shifted to an energy less than 0.5 Mev.

Konopinski and Bethe[1] obtained a remarkable fit to the $Li^7(p,\alpha)\alpha$ experimental yield[13] up to $E=1$ Mev by assuming that $\Gamma\propto\Pi_2$ with $L=1$ and $r_0=1.65\times10^{-13}(A-1)^{\frac{1}{3}}$ cm. They also showed, in accordance with the selection rule corresponding to a spin $I=\frac{3}{2}$ and odd parity for the ground state of Li^7, that the data could not be fitted to a penetration parameter Π_2

[13] Rumbaugh, Roberts, and Hafstad, Phys. Rev. **54**, 657 (1938). Herb, Parkinson, and Kerst, Phys. Rev. **48**, 118 (1935).

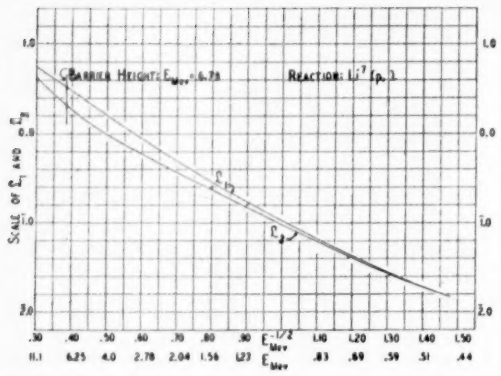

FIG. 2. Comparison of the penetration parameters F_1^2/ρ and G_1^2/ρ for $Li^7(p,\ )$ over an extended energy range: Ω_1 and Ω_2 *vs* $E_{Mev}^{-\frac{1}{2}}$ for $r_0=1.6\times10^{-13}A^{\frac{1}{3}}$ cm and $L=1$. The curves were fitted at 0.5 Mev.

with $L=0$. The results of the preceding paragraph indicate that their fit can be duplicated quite closely with a Π_1 parameter for $L=1$. In Fig. 2 these parameters are compared over an extended energy range. It is seen that the greatest disparity occurs roughly in the vicinity of the top of the potential barrier, $E=6.78$ Mev. The intersection phenomenon noted earlier for the $L=0$ case is apparently present here also, occurring off scale beyond $E=11$ Mev. In Sec. VI, the $Li^7(p,\alpha)\alpha$ reaction will be discussed on the basis of the one-body model of the nucleus.

Christy and Latter calculated Π_3 for protons incident on some light nuclei up to F^{19}, using the constant nuclear radius $e^2/mc^2\approx1.3\times10^{-13}$cm. A qualitative comparison of their curves from 0.5 to 3.0 Mev with those described here shows that they are similar functions of energy to within the estimated variation due to the different choice of radius. A more quantitative comparison is illustrated in Table I for $Li^7(p,\ )$ with $r_0=1.6\times10^{-13}A^{\frac{1}{3}}$ cm. For $L>1$ in the energy interval considered, the difference between A_L and G_L is completely negligible because of the high barrier and, thus, $\Pi_2=\Pi_4$. Since the minimum barrier occurs for $L=0$, the disparity between Π_2 and Π_3 is greatest here at a given energy. It is seen that $\Pi_2=\Pi_3$ in the $L=0$ case up to about 1 Mev, and $\Pi_2=\Pi_3$ up to about 2 Mev for $L=1$. In the latter case, moreover, the two parameters only differ by 3 percent at 3.0 Mev.

A comparison of the energy dependence of the penetration parameters with that of the collision cross section will be discussed later in connection with Fig. 6. The shape of the curve for parameter Π_1 will be seen to be similar to that of the curve for the log of the yield calculated for a special choice of the potential energy well. An inspection of Figs. 1 and 3 of OBJ shows, however, that a considerable variation in the shapes of (σ, E) curves is obtained as a result of varying the assumed potential wells. If one wishes to determine the value of L from the experimental data one is confronted therefore with the necessity of eliminating the influence of these variations. While it is true that the data can be fitted by means of $L=1$, it is hardly possible to consider them as a proof that $L=1$. The actual situation does not consist in accounting for the data without a partial influence of resonance as might perhaps be concluded from a cursory examination of the paper of Konopinski and Bethe. It is also necessary to eliminate the variations in shape which can arise as a result of varying assumptions regarding the interactions inside the nucleus. These variations have been referred to in the OBJ paper in terms of a partial approach to resonance so as to correlate the curves more vividly with the assumed changes in potential wells. On the other hand, the assignment of $L=1$ to this reaction is highly probable as has been brought out by Breit[14] and by Konopinski and Bethe.[1] It has been pointed out by Breit in the same connection that the distinction between different values of L becomes artificial because one has to consider the possibility of perturbations from such configurations as p^2s and p^2d of the Li^7 nucleus which can react with incident s-particles without violation of the parity rule. The perturbations are considered to arise as a result of the incidence of the proton so that one has a compound nucleus in an even state even though one is dealing with an s-proton. For this reason the effect of the partial wave $L=0$ cannot be excluded by parity considerations alone and conclusions regarding which of the partial waves is dominant are more difficult than simple sticking probability considerations would lead one to believe.

An incident p-wave can cause the appearance of a perturbing configuration in a distant collision and the perturbing configuration can then interact with the s-wave. The energy dependences of distant p-wave collisions and close s-wave collisions are somewhat similar and an appreciable range of energies within which the two interactions can take place may be expected to exist. The $Li^7(p,\alpha)\alpha$ reaction will be discussed briefly again in connection with the work of Inglis and collaborators.[15]

IV. SUMMARY OF THE ONE-BODY MODEL

The calculations in the present paper are arranged along lines similar to those of Ostrofsky, Breit, and

TABLE I. Energy dependence of the penetration parameters Π_2 and Π_3 for $Li^7(p,\ )$ with $r_0=1.6\times10^{-13}A^{\frac{1}{3}}$ cm.

	$L=0$		$L=1$	
E	Π_2	Π_3	Π_2	Π_3
0.5	0.1806	0.1804	0.01844	0.01844
1.0	0.5227	0.5202	0.09604	0.09601
1.5	0.8761	0.7679	0.2106	0.2102
2.0	1.280	1.001	0.3545	0.3524
3.0	2.305	1.357	0.6560	0.6408

[14] G. Breit, Rev. Sci. Instr. **9**, 63 (1938).
[15] Heydenburg, Hudson, Inglis, and Whitehead, Phys. Rev. **73**, 241 (1948); Phys. Rev. **74**, 405 (1948); D. R. Inglis, Phys. Rev. **74**, 21 (1948).

Johnson, who made use of an absorption coefficient for the incident wave in the nuclear matter in order to account for the conversion of the wave from the incident channel to disintegration channels. The same device has been used later by Feshbach, Peaslee and Weisskopf[16] and by Serber *et al.*[17] It is realized that the formation of compound states owing their stability essentially to the participation of many nucleons is not taken account of in such a treatment. On the other hand, corrections for the formation of such states can be made in a number of ways as is well-known.

In the one-body model, the real potential $V(r)$ is replaced by the complex potential $V(r)-(ih/2)P(r)$ for $r<r_0$. The introduction of a negative imaginary potential within the nuclear radius r_0 provides for absorption of particles from the beam at a rate $P|\Psi|^2$ per unit time per unit volume, where Ψ is the complete wave function, i.e., an incident plane wave of unit density modified by the Coulomb and nuclear potentials.

The partial reaction cross section without spin is obtained in the usual way. There results,

$$\sigma_L=(\Lambda^2/\pi v)(2L+1)|\mathfrak{F}_L(r_0)|^2\int_0^{r_0}P(r)|u_L|^2dr. \quad (2)$$

This formula differs from a corresponding one in OBJ only through the use of P which is a function of r rather than a constant. The formula can be expressed in terms of the wave function and its logarithmic derivative at the nuclear surface by noting that

$$\int_0^{r_0}P(r)|u_L|^2dr=-v\,\mathrm{Im}(d\mathfrak{F}_L/\mathfrak{F}_L d\rho)_{r=r_0}. \quad (3)$$

Since at the nuclear surface $\mathfrak{F}_L$ must satisfy the usual one-body conditions[6]

$$\mathfrak{F}_L=F_L/[1-F_LG_L\delta_L-iF_L^2\delta_L], \quad (4)$$
$$\delta_L=dF_L/(F_Ld\rho)-d\mathfrak{F}_L/(\mathfrak{F}_Ld\rho),$$

the partial reaction cross section can be written as

$$\sigma_L=(\Lambda^2/\pi)(2L+1)\{(F_L^2\,\mathrm{Im}\delta_L)/|1-F_LG_L\delta_L-iF_L^2\delta_L|^2\}, \quad (5)$$

an equation which can be derived by an application of Green's theorem in a well-known manner. Since the cross section must vanish when P vanishes, $\mathrm{Im}\delta_L$ is different from zero only if the potential has an imaginary part.

The condition on $\mathfrak{F}_L$ at the nuclear surface in Eqs. (4) determines the one-body phase shift K_L:

$$\tan K_L=(\mathfrak{F}_LF_L'-\mathfrak{F}_L'F_L)/(\mathfrak{F}_L'G_L-\mathfrak{F}_LG_L'), \quad (6)$$

where a prime indicates differentiation with respect to ρ. The penetration parameters $\pi_1=f_L^2/\rho$ and $\pi_2=\rho/g_L^2$ and then given by

$$\pi_1=(F_L^2/\rho)/|1-F_LG_L\delta_L-iF_L^2\delta_L|^2, \quad (7)$$
$$\pi_2=1/[(A_L^2/\rho)-\pi_1].$$

The physical implications of the reaction cross section given by Eq. (5) are most easily seen for the special case of vanishingly small absorption. Equation (5) then reduces to one of the OBJ results:

$$\sigma_L=(4\pi Pr_0^3/v)(2L+1)\{(F_L/\rho)^2\langle u_L^2\rangle/[(1-F_LG_L\delta_L)^2+F_L^4\delta_L^2]\}, \quad (8)$$

where

$$\langle u_L\rangle^2=\int_0^{r_0}w_L|u_L|^2dr;\quad \int_0^{r_0}w_L(r)dr=1. \quad (9)$$

The quantity $w_L(r)dr$ is the relative intrinsic probability of inducing the reaction in the interval dr at r. For equal probabilities in equal intervals, $w_L(r)$ reduces to the constant $1/r_0$. It is seen in Eq. (8) that, in the limit of very small absorption, σ_L is a function of real quantities only, proportional to P and containing a resonance denominator. The resonance property, which arises from the junction of the internal and external wave functions at the nuclear surface, is also present in very modified form for the case of nonvanishing P.

Since resonances may be defined in various ways the term 90° resonance will be reserved for describing the condition in which $K_L=90°$. For a 90° resonance, $\mathfrak{F}_L=e^{iK_L}\ (F_L\cos K_L+G_L\ \sin K_L)=iG_L$, $d\mathfrak{F}_L/(\mathfrak{F}_Ldr)=dG_L/(G_Ldr)$ and so $(1-F_LG_L\delta_L)=0$. This condition corresponds to a maximum of σ_{sc}/Λ^2 with respect to variations of K_L, where σ_{sc} denotes the partial elastic scattering cross section. It can be shown with the help of Eqs. (4) that the maximum of the wave function inside the nucleus is not reached at the same energy as the maximum of σ_{sc}/Λ^2. For high barriers, however, σ_{sc}/Λ^2 and $|\mathfrak{F}_L(r_0)|^2$ are nearly proportional to one another.[6]

It is of interest to note that the "no-absorption" formula can be written as

$$\sigma_L=(4\pi Pr_0^3/v)(2L+1)\langle u_L^2\rangle(\pi_1/\rho), \quad (10)$$

where π_1 is the penetration parameter defined by Eqs. (7). If $\langle u_L^2\rangle$ is practically independent of energy then $\sigma\propto\pi_1/E$ for this special case.

In order to apply the one-body formula to study various reactions, the internal potential $V-(ih/2)P$ has been put equal to a constant. The internal radial wave function is then

$$\mathfrak{F}_L(z)=(\pi z/2)^{\frac{1}{2}}J_{L+\frac{1}{2}}(z), \quad (11)$$

where $J_{L+\frac{1}{2}}(z)$ is the Bessel function of half integral order. The derivative, $d\mathfrak{F}_L/dz$, which occurs in δ_L, is evaluated by the well-known recurrence relation;

$$d\mathfrak{F}_L/dz=(L+1)\mathfrak{F}_L/z-\mathfrak{F}_{L+1}=-(L\mathfrak{F}_L)/z+\mathfrak{F}_{L-1}. \quad (12)$$

[16] Feshbach, Peaslee, and Weisskopf, Phys. Rev. **71**, 145 (1947).
[17] Fernbach, Serber, and Taylor, Phys. Rev. **75**, 1352 (1949).

The calculation of the cross section thus reduces to the problem of evaluating the Coulomb and complex Bessel functions at the nuclear radius, r_0. The required separation of $\mathfrak{F}_L(z)$ into real and imaginary parts is effected in principle by expressing $\mathfrak{F}_L(z)$ in terms of the trigonometric and hyperbolic functions. In practice this is quite tedious for $L>0$. Using this separation procedure, OBJ derived the partial cross section for s-waves:

$$\sigma_0=\frac{(2\pi P/v)(sh/k_1'-s/k_0')}{|k'|^2(F_0^2+G_0^2)(ch+c)+k^2(F_0'^2+G_0'^2)(ch-c)-2k(k_0's+k_1'sh)(F_0F_0'+G_0G_0')-2k(k_1's-k_0'sh)}. \tag{13}$$

The abbreviations employed here are listed under Notation and Symbols in the Introduction. It is interesting to note that the Coulomb functions occur in combinations which make the introduction of the phase amplitude variables, A_0 and φ_0, convenient.

For calculational purposes, the partial inelastic cross section is expressed in terms of its real and imaginary parts:

$$\sigma_L=(\Lambda^2/\pi)\frac{(2L+1)(F_L^2/\rho)\ \mathrm{Im}(\rho\delta_L)}{[1-F_LG_L\{\mathrm{Re}(\rho\delta_L)/\rho\}+F_L^2\{\mathrm{Im}(\rho\delta_L)/\rho\}]^2+[F_L^2\ \mathrm{Re}(\rho\delta_L)/\rho+F_LG_L\{\mathrm{Im}(\rho\delta_L)/\rho\}]^2}. \tag{14}$$

V. APPROXIMATIONS TO THE REACTION CROSS-SECTION FORMULA

It was seen in the preceding section that the primary difficulty in obtaining an exact and convenient expression for the one-body cross section was due to the presence of complex Bessel functions in Eq. (14). This difficulty is circumvented in practice by appropriate approximations.

If P is small, for example, the quantity $Y(z)=(zd\mathfrak{F}_L)/(\mathfrak{F}_Ldz)$ can be expanded in a Taylor series about the real point k_0r. Thus,

$$Y(z)=Y(k_0r)+\tfrac{1}{2}i\hbar P\left[\frac{\partial}{\partial(\frac{1}{2}i\hbar P)}Y(z)\right]_{P=0}+\cdots. \tag{15}$$

It is observed that Eq. (15) gives the real and imaginary parts of Y as a sum of even and odd powers of P, respectively.

The differential coefficients in Eq. (15) can be evaluated by a method employed by Breit, Thaxton, and Eisenbud.[18] Their procedure determines the coefficient of $\frac{1}{2}i\hbar P$ to be

$$\left[\frac{\partial}{\partial(\frac{1}{2}i\hbar P)}Y(z)\right]_{P=0}=-[(2\mu r/\hbar^2)/\mathfrak{F}_L^2(k_0r)]\int_0^r\mathfrak{F}_L^2(k_0\xi)d\xi$$
$$=-(\mu r^2/\hbar^2)(1-\mathfrak{F}_{L-1}\mathfrak{F}_{L+1}/\mathfrak{F}_L^2). \tag{16}$$

Coefficients of higher powers of $\frac{1}{2}i\hbar P$ are increasingly difficult to evaluate in closed form.

For P very small it is sufficient to keep only the first two terms in the expansion (15). Substitution of this approximation into Eq. (14) yields the cross-section formula,

$$\sigma_L=(4\pi Pr_0^3/v)\frac{(2L+1)(F_L/\rho)^2\langle u_L^2\rangle}{[1-F_LG_L\delta_L+(P\mu r_0/\hbar)F_L^2\langle u_L^2\rangle]^2+[F_L^2\delta_L+(P\mu r_0/\hbar)F_LG_L\langle u_L^2\rangle]^2}, \tag{17}$$

where $\langle u_L^2\rangle$ is defined by Eq. (9). If the terms in the denominator of Eq. (17) containing P are put equal to zero, the OBJ cross-section formula Eq. (8) for vanishingly small absorption is obtained.

Since the expansion for $Y(z)$ is not convergent for all values of P and the calculation of the higher order differential coefficients is quite tedious, an alternative method has been adopted. In this approach a series expansion of $\mathfrak{F}_L(z)$ is made which converges for all finite values of z, namely,

$$\mathfrak{F}_L(z)=\frac{z^{L+1}}{1\cdot3\cdot5\cdots(2L+1)}\left[1-\frac{z^2}{2(2L+3)}+\frac{z^4}{8(2L+3)(2L+5)}-\frac{z^6}{48(2L+3)(2L+5)(2L+7)}+\cdots\right]$$
$$=\frac{z^{L+1}}{1\cdot3\cdot5\cdots(2L+1)}\Omega_L. \tag{18}$$

The corresponding series for $Y(z)$ may be written in the form

$$Y(z)=-L+\frac{(2L+1)\{1-z^2/[2(2L+1)]+z^4/[8(2L+1)(2L+3)]-\cdots\}}{\Omega_L}, \tag{19}$$

[18] Breit, Thaxton, and Eisenbud, Phys. Rev. **55**, 1018 (1939).

by employment of the recurrence relation (12). It is seen that the series (19) is an even function of z. The identification of the real and imaginary parts of $\Omega_L(z^2)$ is facilitated by defining

$$\mathrm{Re}(z^2)=\alpha=(k_0r)^2;\quad \mathrm{Im}(z^2)=\beta=\mu P/\hbar. \tag{20}$$

The quantity α is therefore the square of the wave number for the nuclear region when $P=0$, and β is proportional to P. One may expand therefore as follows:

$$\Omega_L(\alpha+i\beta)=\sum_0^\infty a_n(\alpha, L)(i\beta)^n;\quad a_0(\alpha, L)=\Omega_L(\alpha), \tag{21}$$

where the zeroth coefficient, $a_0(\alpha, L)$, is given by

$$\begin{aligned}a_0(\alpha, L)&=1-\alpha/[2(2L+3)]+\alpha^2/[8(2L+3)(2L+5)]\\&\quad-\alpha^3/[48(2L+3)(2L+5)(2L+7)]+\cdots\\&=1\cdot3\cdot5\cdots(2L+1)\mathfrak{F}_L(k_0r)/(k_0r)^{L+1}.\end{aligned} \tag{22}$$

The second equality sign in Eq. (22) results from the relation of $\Omega_L(\alpha)$ and the spherical Bessel function of real argument.

The coefficients $a_n(\alpha, L)$ in the series (21) for $\Omega_L(\alpha+i\beta)$ can now be expressed in terms of the real functions $\Omega_{L+n}(\alpha)$ by noting that Eq. (21) can be written in the alternative form,

$$\begin{aligned}\Omega(\alpha+i\beta)&=\Omega(\alpha)+(i\beta)[\partial\Omega_L/\partial(i\beta)]_{\beta=0}\\&\quad+[(i\beta)^2/2!][\partial^2\Omega_L/\partial(i\beta)^2]_{\beta=0}+\cdots\\&=\Omega_L(\alpha)+(i\beta)[\partial\Omega_L(\alpha)/\partial\alpha]\\&\quad+[(i\beta)^2/2!][\partial^2\Omega_L(\alpha)/\partial\alpha^2]+\cdots.\end{aligned} \tag{23}$$

The second equation in (23) is a consequence of the symmetry of Ω_L in α and $i\beta$. Employment of the Bessel function identity,

$$2[d/d(x^2)][J_n(x)/x^n]=-J_{n+1}(x)/x^{n+1}, \tag{24}$$

yields the series,

$$\begin{aligned}\Omega_L(\alpha+i\beta)&=\Omega_L(\alpha)-(i\beta)\Omega_{L+1}(\alpha)/[2(2L+3)]+\cdots\\&\quad+(-i\beta)^n\Omega_{L+n}(\alpha)/[n!2^n(2L+3)\cdots\\&\quad\times(2L+2n+1)]+\cdots.\end{aligned} \tag{25}$$

Since Eq. (19) can be written as

$$Y(z)=-L+[(2L+1)\Omega_{L-1}(\alpha+i\beta)]/\Omega_L(\alpha+i\beta), \tag{26}$$

the series (25) permits the calculation of the change of $Y(z)$ with respect to E, V or P in a straightforward manner. In terms of the $\mathfrak{F}_{L+n}(\alpha)$, Eq. (26) becomes

$$Y(z)=-L+\frac{k_0r[\mathfrak{F}_{L-1}(\alpha)+\cdots\langle(-1)^n(i\beta)^n\mathfrak{F}_{L+n-1}(\alpha)/n!2^n(k_0r)^n\rangle+\cdots]}{[\mathfrak{F}_L(\alpha)+\cdots\langle(-1)^n(i\beta)^n\mathfrak{F}_{L+n}(\alpha)/n!2^n(k_0r)^n\rangle+\cdots]}, \tag{27}$$

with the aid of Eq. (18). The quantity $Y(z)$ is expressed in terms of real Bessel functions by means of Eq. (27) and is much more convenient for numerical work than Eq. (19).

There is a third method for obtaining the real and imaginary parts of $Y(z)$ which utilizes the recurrence relation

$$[Y(z)-(L+1)][Y(z)+(L+1)]=-z^2=-\alpha-i\beta, \tag{28}$$

obtainable with the help of Eq. (12). Separation of Eq. (28) into real and imaginary parts gives

$$\begin{aligned}\mathrm{Re}[Y_{L+1}(z)+L+1]&=-\frac{\alpha[\mathrm{Re}Y_L(z)-(L+1)]+\beta\,\mathrm{Im}Y_L(z)}{[\mathrm{Re}Y_L(z)-(L+1)]^2+[\mathrm{Im}Y_L(z)]^2},\\ \mathrm{Im}Y_{L+1}(z)&=\frac{\alpha\,\mathrm{Im}Y_L(z)-\beta[\mathrm{Re}Y_L(z)-(L+1)]}{[\mathrm{Re}Y_L(z)-(L+1)]^2+[\mathrm{Im}Y_L(z)]^2}.\end{aligned} \tag{29}$$

Since the real and imaginary parts of $Y(z)$ for $L=0$ may be determined by the relation $J_0(z)=\sin z$, which was used to obtain the zeroth partial cross section (13), values of these quantities for $L>0$ are determined by repeated application of Eqs. (29).

There are two objectionable features of the recurrence method (29). First, Eqs. (29) obscure the physical origin of the quantities calculated. In this respect, the series calculation of $\mathfrak{F}_L(z)$ is superior, since the latter shows clearly the dependence of $Y(z)$ on P, V and E, and its rate of change with respect to these parameters. The second objection to the recurrence method is that Eqs. (29) require, for given L, the calculation of all values of $z\mathfrak{F}_{L'}/\mathfrak{F}_{L'}dz$ between $L'=L$ and $L'=0$. Therefore, the chance for errors is correspondingly large, and their detection correspondingly difficult. The recurrence method is most useful when z is so large that the series calculation requires the evaluation of an inconvenient number of terms.

It is of interest now to consider another limiting form of the total reaction cross-section formula (14), namely, the case of very strong absorption, P. The consequences of this condition have been examined by Breit, who derived the result reported below in connection with the present work. The result but not the derivation has been stated in another connection.[8]

For strong absorption the wave function is strongly damped in the nuclear region, since the probability is great that a particle will be absorbed from the beam before penetrating the nucleus appreciably. Since

$$k_1'\approx k_0'\approx[\mu P/2\hbar]^{\frac{1}{2}} \tag{30}$$

for P very large, the real and imaginary parts of z are unbounded as P increases. It is therefore permissible to employ the asymptotic form of $\mathfrak{F}_L$,

$$\mathfrak{F}_L\sim\sin[z-(L\pi/2)]. \tag{31}$$

The function u_L which is normalized to unity at the nuclear radius, r_0, is approximately given by

$$u_L \sim [\sin(z - L\pi/2)]/[\sin(z_0 - L\pi/2)]. \quad (32)$$

Since $\sinh(k_1'r)$ and $\cosh(k_1'r)$ have the common asymptotic form $\exp[k_1'r/2]$, Eq. (32) can be written as

$$u_L \sim \exp\{-k_1'(r_0 - r)\} \exp\{ik_0'(r_0 - r)\}. \quad (33)$$

Thus, the normalized interior solution u_L decays exponentially towards the center of the nucleus as was expected, and is independent of L in the limiting case of strong absorption. In this limit,

$$\rho\delta_L \sim -r(du/udr) \sim ik_0'r - k_1'/r. \quad (34)$$

Substitution of Eq. (34) into the cross-section formula (14) yields

$$\sigma_L \sim (\Lambda^2/\pi) \frac{(2L+1)F_L^2 k_0' r_0/\rho}{[1 + F_L G_L k_1' r_0/\rho + F_L^2 k_0' r_0/\rho]^2 + [F_L G_L k_0' r_0/\rho - F_L^2 k_1' r_0/\rho]^2}. \quad (35)$$

The neglect of unity in the denominator of Eq. (35) and the use of the asymptotic forms in Eq. (30) for k_1' and k_0' give the final result,

$$\sigma_L = 2(2L+1)\Lambda\Lambda_0/A_L^2, \quad (36)$$

where $\Lambda_0 = (h/2\mu P)^{\frac{1}{2}}$. It is seen that the dependence of $\sigma_L v$ in Eq. (36) on the Coulomb functions is the same as that of the "penetration factor" employed by Christy and Latter. The quantity Λ_0 is proportional to the particle wave number in the nuclear region. As $P \to \infty$, $\Lambda_0 \to 0$ and σ_L vanishes. This paradox may be explained as follows: the wave function is so strongly damped by the presence of large P that the probability of finding the particle in the nucleus decreases faster than P increases, causing a decreasing cross section.

The simplicity of the result owes its origin to the fact that the wave function decreases at the surface of the nucleus in a thin layer. Within the layer which forms a kind of a skin around the body of the nucleus, the decay of the wave amplitude is given by a simple exponential function provided the skin thickness is small in comparison with the nuclear radius. This situation is very similar to that arising in the familiar case of "skin effect" for high frequency electric currents. Here also the case of small skin thickness gives an especially simple answer.

TABLE II. Values of the depth of the potential well.[a]

Target nucleus	A	B
1. Incident protons		
Li^7	40.00	31.7
C^{12}	17.6	11.06
O^{16}	13.4	8.07
Na^{23}	21.00	16.79
Si^{28}	10.86	7.73
2. Incident alpha-particles		
He^4	10.0	5.80
Li^6	11.55	8.55
Be^8	13.10	10.71
B^{11}	15.48	13.61
C^{12}	11.40	9.63
N^{14}	8.13	6.56
O^{16}	8.17	6.75
F^{19}	14.38	13.12

[a] The symbol A indicates that the radius is $1.6 \times 10^{-13} A^{\frac{1}{3}}$ cm. The symbol B indicates that the radius is $2.1 \times 10^{-13} A^{\frac{1}{3}}$ cm.

VI. CROSS SECTIONS FOR VANISHINGLY SMALL ABSORPTION

It was seen in Secs. IV and V that the one-body model gives a formula for the reaction cross section which admits factorization in terms of a penetration parameter only in certain limiting cases. In this section the one-body cross section without absorption, Eq. (8), is applied to the study of some of the reactions listed in Sec. III.

For the rectangular well, Eq. (9) becomes

$$\langle u_L^2 \rangle = (1/r_0)\int_0^{r_0} u_L^2 dr = (1 - \mathfrak{F}_{L-1}\mathfrak{F}_{L+1}/\mathfrak{F}_L^2)/2, \quad (37)$$

where $\mathfrak{F}_L$ is a function of the real argument $k_0 r_0$, and is related to the Bessel function $J_{L+\frac{1}{2}}(k_0 r_0)$ by

$$\mathfrak{F}_L = (\pi k_0 r_0/2) J_{L+\frac{1}{2}}. \quad (38)$$

Since the depth $U = |V|$ of the one-body well is subject to considerable uncertainty, several values of U, in conjunction with the two nuclear radii selected in III, have been employed. These are designated the binding energy,[19] "zero," and special Van Vleck[20] well depths, respectively. As the name implies, the second named well depth simply corresponds to the case $U = 0$. The special Van Vleck well depth is the ordinary Van Vleck well depth evaluated for zero bombarding energy. This device removes the small velocity dependence of the latter well. The values of the binding energy well depth are listed in Table II.

For small values of P it is convenient to make use of Eq. (8) and to tabulate the quantity $\sigma_L v/(2\pi P)$. This procedure leaves the absolute magnitude of the cross section unspecified, but permits comparisons of the yield curves for different assumptions about the potential well. The factor $v/2\pi$ has been inserted in order to deal directly with a quantity proportional to the number of incident particles inside the nucleus, for a unit flux of incident particles.

In order to show details of the cross section away from resonance, a logarithmic scale was adopted for $\sigma_L v/2\pi P$. For proton bombardment, the quantity

[19] See Appendix.

[20] J. H. Van Vleck, Phys. Rev. **48**, 467 (1935); Ostrofsky, Bleick, and Breit, Phys. Rev. **49**, 352 (1936). See Appendix.

$\mathfrak{L}=\log_{10}[(\sigma_L v/2\pi P)\times 10^{39}\ \text{cm}^3]$ was plotted against $E_{\text{Mev}}^{-\frac{1}{2}}$, and, for alpha-particles, $\mathfrak{L}$ was plotted against E_{Mev}.

If $\delta_L=0$ and $\langle u_L^2\rangle=\frac{1}{2}$ in Eq. (8), then $\sigma_L v/2\pi P=(2L+1)r_0^2(F_L/\rho)^2$. The quantity on the right side, which is proportional to Π_1/ρ and has the same low energy dependence as $\sigma_L v$ in Eq. (8), namely, $\sigma_L v \propto e^{-2\pi\eta}/v$. It may be used as a "penetration factor" measure of the one-body cross section, but it is seen that the only justification for such a terminology is in the relation of the "penetration factor" to $\sigma_L v$.

Some[12] representative results are displayed in Figs. 3–5. Comparison of the $\mathfrak{L}$ and $\mathcal{P}=\log_{10}[(2L+1)r_0^3\times(F_L/\rho)^2 10^{39}\ \text{cm}^3]$ curves in Figs. 3 and 4 show that their large structural differences are by no means localized in the immediate vicinity of the one-body resonances. These differences persist both above and below resonance. Both $\mathfrak{L}$ and $\mathcal{P}$, however, show the same rapid increase in the low energy region as E_{Mev} increases, since the major energy dependence here is due to the factor $(F_L/\rho)^2$.

Many of the calculated one-body cross sections exhibited no resonance in the energy interval plotted. The presence of a resonance just outside the interval however, decidedly altered the shape of $\mathfrak{L}$ in comparison with $\mathcal{P}$. As has been shown by OBJ, conclusions drawn from fitting nonresonant excitation functions to various

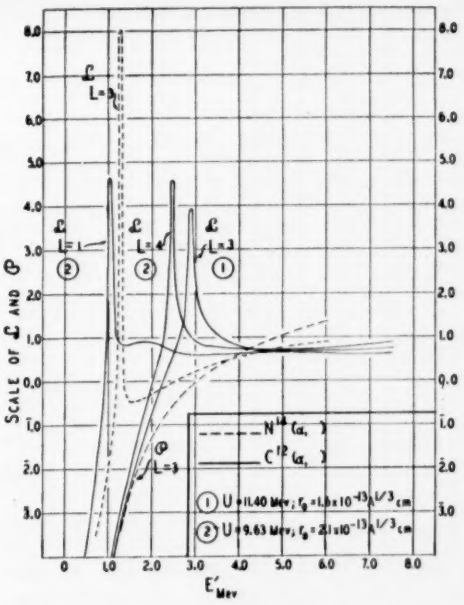

FIG. 4. The "no-absorption" cross sections for $N^{14}(\alpha,\ )$ and $C^{12}(\alpha,\ )$. Dashed curves: $\mathfrak{L}$ vs $(E_{\text{Mev}}')^{-\frac{1}{2}}$ and $\mathcal{P}$ vs $(E'_{\text{Mev}})^{-\frac{1}{2}}$ for the reaction $N^{14}(\alpha,\ )$ with $r_0=2.1\times10^{-13}A^{\frac{1}{3}}$ cm and $U=6.56$ Mev. Solid curves: $\mathfrak{L}$ vs $(E_{\text{Mev}}')^{-\frac{1}{2}}$ for $C^{12}(\alpha,\ )$ with parameters as stated. For $N^{14}(\alpha,\ )$, $E_{\text{Mev}}'=(7/9)E_{\text{Mev}}$; for $C^{12}(\alpha,\ )$, $E_{\text{Mev}}'=(3/4)E_{\text{Mev}}$.

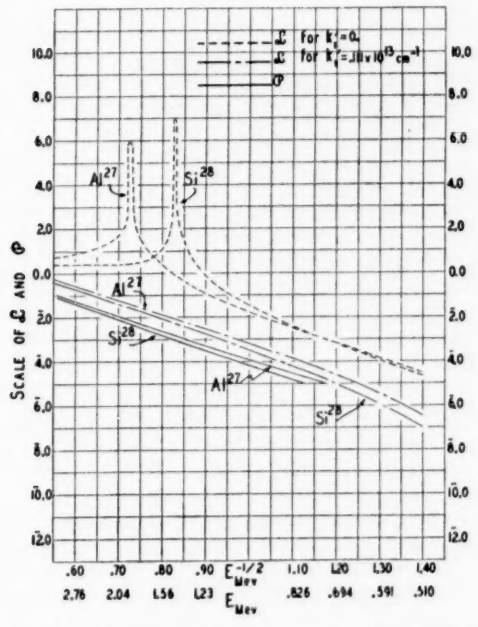

FIG. 3. One-body cross sections for $Al^{27}(p,\ )$ and $Si^{28}(p,\ )$, compared with a "penetration factor" cross section. Dashed lines: $\mathfrak{L}$ vs $(E_{\text{Mev}})^{-\frac{1}{2}}$ for $k_1'=0$; long-short dashed lines: $\mathfrak{L}$ vs $(E_{\text{Mev}})^{-\frac{1}{2}}$ for $k_1'=0.111\times10^{13}\ \text{cm}^{-1}$; solid lines: $\mathcal{P}$ vs $(E_{\text{Mev}})^{-\frac{1}{2}}$. All curves were computed for $L=3$, $U=28.63$ Mev, and $r_0=1.6\times10^{-13}A^{\frac{1}{3}}$cm.

"penetration factors" may diverge widely from those deduced from a potential well calculation.

The regularities, as a function of the atomic number, which appeared in the penetration parameter curves of Sec. III should be absent in the reaction cross sections computed with the binding energy well depths since the latter are not smooth functions of Z'. For the special Van Vleck and zero well depths, however, these regularities should persist since these well depths are independent of Z'. This expectation is confirmed in Fig. 4 for the triad C^{12}, N^{14}, and O^{16} under proton bombardment and with the two special Van Vleck well depths corresponding to the two choices of radius. It is seen that the energy of a particular resonance decreases as Z' increases. The relatively depressed values of $\mathfrak{L}$ for Si^{28} at low energies are effected by the Coulomb barrier.

An apparent difficulty in evaluating the cross-sectional formula (8) occurs when the quantity δ_L becomes infinite. This situation arose in the course of the calculations whenever $\mathfrak{F}_L$ vanished. The vanishing of $\mathfrak{F}_L$ causes no anomaly in the cross section, however, as the following argument shows.

If in Eq. (8) $\mathfrak{F}_L$ approaches zero, then δ_L becomes very large, and so unity can be neglected in comparison with $F_L G_L \delta_L$ in the denominator. The resulting partial cross section is then

$$\sigma_L=(4\pi P r_0^2/v)(2L+1)\langle u_L^2\rangle/(\rho A_L\delta_L)^2. \qquad (39)$$

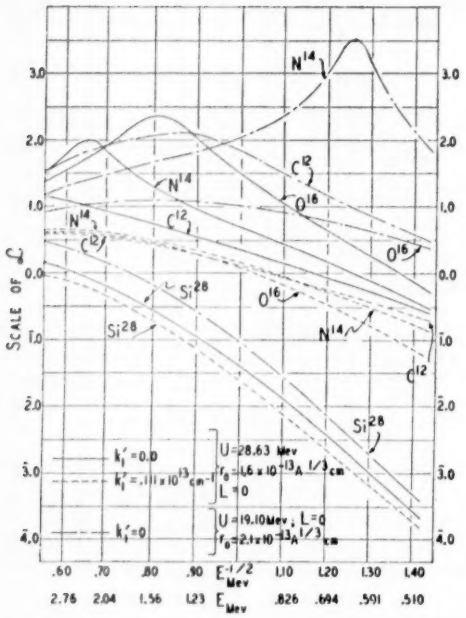

FIG. 5. One-body reaction cross sections for $N^{14}(p,\ )$, $O^{16}(p,\ )$, $Si^{28}(p,\ )$, and $C^{12}(p,\ )$. Solid lines: $\mathfrak{L}$ *vs* $(E_{\text{Mev}})^{-\frac{1}{2}}$ for $U=28.63$ Mev, $r_0=1.6\times10^{-13}A^{\frac{1}{3}}$ cm, and $k_1'=0$; Long-short dashed lines: $\mathfrak{L}$ *vs* $(E_{\text{Mev}})^{-\frac{1}{2}}$ for $U=19.10$ Mev, $r_0=2.1\times10^{-13}A^{\frac{1}{3}}$ cm, and $k_1'=0$; Dashed lines: $\mathfrak{L}$ *vs* $(E_{\text{Mev}})^{-\frac{1}{2}}$ for $U=28.63$ Mev, $r_0=1.6\times10^{-13}A^{\frac{1}{3}}$ cm and $k_1'=0.111\times10^{13}$ cm^{-1}. For all curves, $L=0$.

If the terms in Eq. (39) not containing $(\mathfrak{F}_L)^{-1}$ are neglected, Eq. (39) can be written as

$$\sigma_L\approx-(2\pi P r_0^3/v)(2L+1)\mathfrak{F}_{L+1}/[(k_0r_0)^2A_L^2\mathfrak{F}_{L-1}]. \quad (40)$$

with the aid of Eq. (37). Hence, the cross section is finite and changes smoothly in the neighborhood of a zero of $\mathfrak{F}_L$.

The analysis of the $Li^7(p,\alpha)\alpha$ reaction illustrates some of the limitations of the one-body model. The yield[21] of this reaction exhibits a broad maximum at $E=3$ Mev and theoretical fits[15] to the angular distribution ascribe this condition to two levels of the compound nucleus Be^8. The first level, approximately 1 Mev wide, occurs at $E=3$ Mev with $I=2$ and even parity; the second level, approximately centered on 3 Mev, with a width of several Mev, is supposed to have $I=0$ and even parity, and be excited by both p and f protons.

In Fig. 6 the behavior of the one-body cross section for the $Li^7(p,\alpha)\alpha$ reaction is shown. The well depth, $U=19.52$ Mev, was chosen to give a resonance of σ_1 at about 3 Mev. It should be noted that the quantity plotted, $\mathfrak{L}$, is a function of $\sigma_1 v$. With the other parameters equal to those of Fig. 6, the value $U=18.6$ Mev satisfies the 90° resonance condition at $E=3$ Mev. But the maximum of σ_1 is then shifted up to about $E=3.2$ Mev.

No attempt is being made here to consider the effect of different relative spin orientations. Such considerations can presumably be carried out best in the framework of a "dispersion theory" representation. The problem has been considered from this viewpoint by Inglis *et al.*[15] On the other hand, calculations of the present paper show that the experimental resonance is much narrower than that indicated by the "one-body" treatment as would be expected on most theories of many-body effects.

The logarithms of the penetration parameters $\pi_1=f_L^2/\rho$ and $\pi_2=\rho/g_L^2$ for the $Li^7(p,\ )$ reaction have also been plotted in Fig. 6. Comparison of the $\mathfrak{L}$ and $\mathfrak{l}_1=\log_{10}\pi_1$ curves shows that they have similar shapes, but that the maximum value of $\mathfrak{l}_1$ occurs at a slightly higher energy. This shift is due to the energy dependence of the factor $\langle u_L^2\rangle/\rho$ in Eq. (10), which is important for a broad resonance. In this quantity in the present case the factor $1/\rho$ accounts for most of the variation as E is varied from 1 to 2 Mev. But for a sharp resonance $\mathfrak{L}$ and $\mathfrak{l}_1$ will be similar functions of energy, with their maxima occurring for the same value of E. Away from resonance the factor F_L^2/ρ in $\mathfrak{L}$ and $\mathfrak{l}_1$ contains the principal energy dependence of these two functions. The reason for the presence of the sharp maximum in the $\mathfrak{l}_2=\log_{10}\pi_2$ function can be seen with the help of Eqs. (7) which define the barrier parameters π_1 and π_2

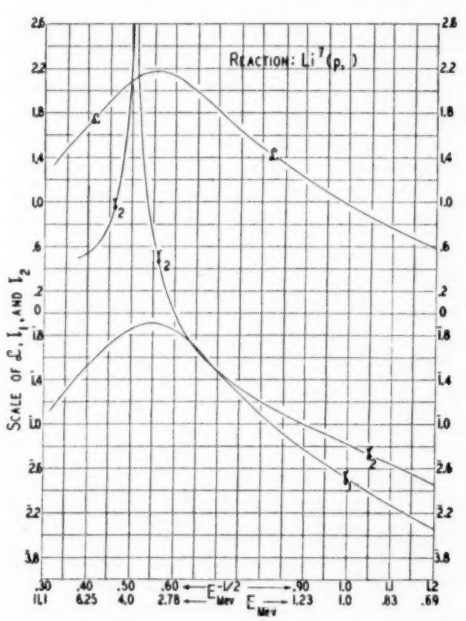

FIG. 6. Comparison of one-body cross section with the channel penetration parameters for $Li^7(p,\ )$: $\mathfrak{L}$, $\mathfrak{l}_1$ $\mathfrak{l}_2$ *vs* $E_{\text{Mev}}^{-\frac{1}{2}}$; $\mathfrak{l}_1$ and $\mathfrak{l}_2$ were normalized at 2.04 Mev. $L=1$ and $r_0=1.6\times10^{-13}A^{\frac{1}{3}}$ cm. The well depth $U=19.52$ Mev was chosen to give a one-body resonance at about 3 Mev.

[21] Hornyak, Lauritsen, Morrison, and Fowler, Revs. Modern Phys. **22**, 291 (1950).

in terms of the one-body model. Since $f_L^2+g_L^2=A_L^2$, π_1 always must satisfy the condition $\pi_1 \leq A_L^2/\rho$, the case of equality representing a singular point of π_2. For a broad, flat resonance π_1 varies slowly over a wide range of energy values, while A_L^2/ρ decreases rapidly as E increases from 0. These circumstances provide an opportunity for A_L^2/ρ to "catch up" with π_1, as is exemplified by l_2 in Fig. 6. The singular point of l_2, i.e., the point at which $A_L^2=\pi_1$, cannot occur on the low energy side of the resonance of l_1 in Fig. 6 because the quantity A_L^2/ρ is decreasing monotonically as E increases.

The half-widths of the one-body resonances depend strongly on the energy and angular momentum for which they occur. In general, the half-width decreases with increasing angular momentum and decreasing energy. To obtain a quantitative estimate of this dependence, the half-widths were calculated from the curves by treating the resonances in a way similar to that of Breit and Yost.[22]

The one-level dispersion formula near sharp resonance suggests that the partial cross section may be written as

$$\sigma_L=A/[(E-E_0)^2+B], \tag{41}$$

where A and B are almost constant functions of E in the vicinity of resonance, and E_0 is the energy at which the resonance peak occurs. Since the quantity $(1-F_LG_L\delta_L)$ is very nearly a linear function of energy in the range of interest, it is assumed that it can be approximated near E_0 in the form $C(E-E_0)$, where C is energy independent. The quantity B is identified as $(F_L^2\delta_L/C)^2$ by comparison with (8). The value of $E-E_0=\Delta E$ for which Eq. (8) has a value equal to one-half of the maximum value, A/B, is given by $\Delta E=\pm|B|^{\frac{1}{2}}$, so that the width at half-maximum is $2\Gamma=2|B|^{\frac{1}{2}}$.

The values of $F_L^2\delta_L$ and C at $E=E_0$ have been calculated for a number of resonances together with the corresponding half-widths; some of the results are listed in Table III. The table illustrates the rapid decrease in the half-width for decreasing energy and increasing angular momentum. It should be noted that in the transition from a one-body resonance to the corresponding many-body resonance, the resonance may be sharpened appreciably.

The principal energy dependence in the expression for the half-width is contained in the factor F_L^2. The maximum variation of C is roughly an order of magnitude, while the quantity δ_L at resonance varies by only a factor of four or five at most. These circumstances provide a convenient method for investigating the energy dependence of the half-width: for a particular element, small changes in the depth of the potential well are made, thus shifting the resonance peak. Since only small variations in δ_L and C result from the altered well depths, a constant factor times F_L^2 yields a qualitative estimate

[22] G. Breit and F. L. Yost, Phys. Rev. **48**, 204 (1935).

TABLE III. Half-widths of resonances for incident protons.[a]

Isotope	r_0	L	U(Mev)	E_0(Mev)	2Γ(Mev)
N^{14}	A	2	28.63	0.67	0.0006
C^{12}	A	2	28.63	2.75	0.3
Be^{9}	B	2	19.10	2.6	0.5
B^{11}	B	2	19.10	0.83	0.01
Al^{27}	A	3	28.63	1.9	0.002
Si^{28}	A	3	28.63	1.45	0.0002
F^{19}	B	3	19.10	2.7	0.08
Na^{23}	B	3	19.10	0.85	0.00006
Al^{27}	B	1	19.10	2.00	0.4
Si^{28}	B	1	19.10	1.72	0.1
Ne^{20}	B	0	0.00	2.20	2
Mg^{24}	B	0	0.00	2.10	1
Al^{27}	B	0	0.00	2.04	0.7
Si^{28}	B	0	0.00	2.10	0.6

[a] The symbol A indicates the radius is $1.6\times10^{-13}A^{\frac{1}{3}}$ cm. The symbol B indicates the radius is $2.1\times10^{-13}A^{\frac{1}{3}}$ cm.

of the dependence of the half-width on energy. The behavior of the one-body cross section as a function of well depth for constant energy of relative motion is shown in Fig. 7 for the $B^{11}(\alpha,)$ reaction.

Another interesting feature is the dependence of the resonance height on energy. At a 90° resonance, the partial cross section is given by

$$(\sigma_L)_{\text{res}}=(4\pi Pr_0^3/v)(2L+1)\langle u_L^2\rangle/(\rho F_L\delta_L)^2. \tag{42}$$

Since the half-width is given by $2|F_L^2\delta_L/C|$, it can be concluded that the area under the resonance curve is roughly constant, i.e., independent of the energy at which the peak is located.

The occurrence of F_L^2 in the expression for the half-width indicates that the penetration parameter containing F_L^2 is in some degree applicable to this model. The assumptions which led to this identification were that: (1) the resonance is sharp, (2) the quantity $(1-F_LG_L\delta_L)$ is a linear function of the energy in the resonance region, and (3) δ_L is a constant near resonance. These approximations are not completely valid, but, in many cases, the penetration parameter Π_1 should suffice in getting orders of magnitude.

Figure 8 consists of contour plots of the cross section as a function of bombarding energy and well depth for the $C^{12}(p,)$ reaction. These curves confirm the expectation that increasing the depth of the potential well decreases the energy at which the resonance occurs, and indicate how the shape of the resonance peak depends on its energy level.

A single resonance is represented by a contour ridge —a line of slowest descent—running approximately along the $E+U=$const line[23] in the (U, E) plane, since k_0 and, hence, $d\tilde{\delta}_L/[\tilde{\delta}_L d(k_0r_0)]$ are constant along this line. Near resonance the latter quantity is by far the most rapidly varying function of energy in the expression $(1-F_LG_L\delta_L)$, which itself varies slowly with energy in the region of resonance.

In the limit of zero energy the cross section contains

[23] It should be noted that the horizontal and vertical scales in Figs. 8 and 9 are unequal.

singularities along the U axis. As is expected, however, these singular points are removed by the introduction of a finite damping coefficient.

VII. EFFECT OF ABSORPTION ON THE CROSS SECTION

Within the limitations of the one-body model, the results presented in the preceding section should be valid whenever the inelastic cross section of a scattering process is small. But, for reactions of high yield, formula (8) is not applicable. The partial cross section σ_L is no longer proportional to the imaginary part of the potential, but, as a function of P, reaches a maximum and finally decreases to zero as P becomes very large.

For finite absorption the sharp resonances which were prominent features of the "no-absorption" calculations are modified appreciably. This modification of the resonance shapes and the variation of the cross section with P have been investigated for some of the reactions of Sec. VI with the aid of the general one-body formula (14) for the reaction cross section. The lengthy calculations required to evaluate Eq. (14) restricted the scope of this study. For the case of incident protons with the special Van Vleck interaction, reaction cross sections have been computed for the isotopes C^{12}, N^{14}, O^{16}, Al^{27} and Si^{28}, employing $L=0$, 1, 2, 3, 4 and $r_0=1.6\times10^{-13}A^{\frac{1}{3}}$ cm; and the isotopes Be^{9}, B^{11}, C^{12}, N^{14}, F^{19}, Na^{23}, Al^{27} and Si^{28} with $r_0=2.1\times10^{-13}A^{\frac{1}{3}}$ cm and the same range of L. In addition, the $B^{11}(\alpha,)$ reaction was investigated for various combinations of U, r_0, and L.

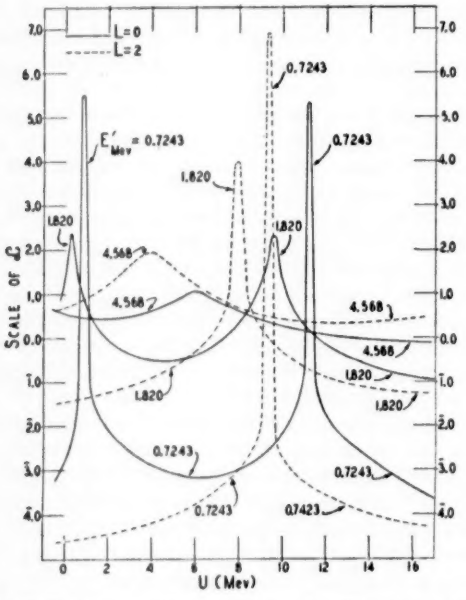

FIG. 7. Resonances of the cross section for $B^{11}(\alpha,)$ as a function of the well depth U at a constant energy of relative motion E_{Mev}'. Each curve is a plot of $\mathfrak{L}$ *vs* U for the constant values of L and E_{Mev}' shown. For all curves, $r_0=1.6\times10^{-13}A^{\frac{1}{3}}$ cm. $E_{Mev}'=0.733E_{Mev}$.

The absorption coefficient used in the evaluation of Eq. (14) was obtained from Fernbach, Serber and Taylor's[17] analysis of total cross sections of nuclei to high energy neutrons. The value which has been found is $k_1'=0.111\times10^{13}$ cm^{-1}.

Two methods have been used to calculate the real and imaginary parts of $(zd\mathfrak{F}_L)/(\mathfrak{F}_L dz)$ which appear in Eq. (14). The major portion of the calculations was performed using Eq. (27) of Sec. V. This method gave values to three significant figures with the neglect of all terms beyond the fourth or fifth in the series defined by Eq. (27). The other method utilized the recurrence relation for the Bessel function as given by Eqs. (29).

Some[12] results of these calculations, shown in Figs. 3 and 5, are compared directly with the corresponding "no-absorption" curves. It is seen in Fig. 3 that the introduction of absorption drastically modifies the sharp resonances which occur for large L in the "no-absorption" case.

The contours of the quantity $\mathfrak{L}$ for the $C^{12}(p,)$ reaction with absorption are shown in Fig. 9. It is seen that the cross section now goes to zero at $E=0$, in contrast to the case of "no-absorption" in Fig. 8. In fact, the introduction of absorption modifies the contour ridges to such an extent that, for $L>0$, the cross section does not increase at all with decreasing E. For $L=0$ the cross section rises to a peak value—a maximum of a function of two variables—the location of the peak being at $E\approx2.2$ Mev, $U=2.0$ Mev.

The variation of $\mathfrak{L}$ with k_1' is illustrated in Fig. 10 for the $O^{16}(p,)$ reaction. It is seen that increasing k_1' decreases the maximum and increases the half-width of the resonance. Since this effect is very pronounced even for small values of k_1', the resonance peak is barely detectable when k_1' has increased to the Serber value, $k_1'=0.111\times10^{13}$ cm^{-1}. Nevertheless, the resonance may still be identified by noting the steeper slope on the low energy side of the resonance "peak," and the more gentle slope on the high energy side in comparison with the case of no resonance. Thus, the cross section is greater than its value would be if there were no resonance in the energy interval considered.

VIII. SUMMARY

In the energy interval from 0.5 to 3.0 Mev it was noted that the principal deviation in the energy dependences of the penetration parameters F_L^2/ρ and ρ/G_L^2 occurred for $L=0$, and that this deviation almost vanished for large L. This situation is illustrated in Fig. 1 for the $Li^7(p,)$ reaction. The difference, $\log_{10}(\rho/G_0^2)-\log_{10}(F_0^2/\rho)$, of the curves for $L=0$ passes through a sequence of values from 0.112 to -0.106 and then rises to zero as E increases to 3 Mev. The absolute change of this difference over the whole energy interval is 0.149 for $L=1$ and only 0.007 for $L=4$, so that the

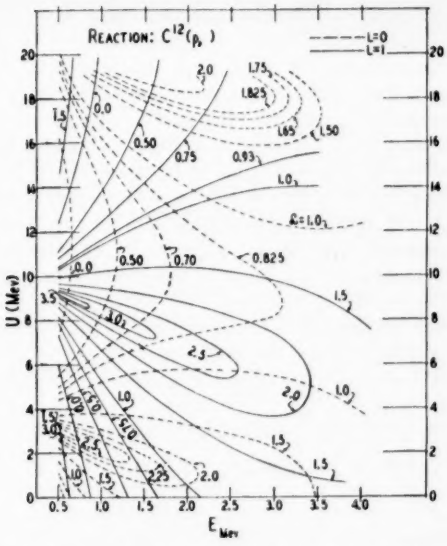

FIG. 8. Contours in the (U, E_{Mev}) plane of the reaction cross section for $C^{12}(p,\ )$ with $k_1'=0$. The curves are plots of U *vs* E_{Mev} for the constant value of $\mathfrak{L}$ shown; $r_0=2.1\times10^{-13}A^{\frac{1}{3}}$ cm.

cumulative correction to the almost constant ratio of the penetration parameters is a factor of 1.41 in the former case, and 1.02 in the latter. In Fig. 2 the comparison of the logarithms of the penetration parameters is carried out over an extended energy scale for $L=1$. With the curves fitted at 0.5 Mev, their difference slowly increases with E and reaches a maximum of about 0.226 near the height of the potential barrier. The difference then decreases with the indication of a second intersection of the curves beyond the high energy side of the scale. Table I shows the closely parallel behavior of the parameters ρ/G_L^2 and ρ/A_L^2 in regions where the barrier is high.

The OBJ one-body model was used to test the reliability of these parameters in representing barrier penetration effects, and special limiting cases, in which the barrier dependence of the resonance half widths could be identified as "penetration factors," were discussed. In particular it was shown that the penetration parameter ρ/A_L^2 could be identified with the case of very strong absorption of the incident wave. Figures 3, 4, and 5 present a selection of one-body cross sections with and without absorption, compared in certain cases with a "penetration factor" derived from the one-body model. Figures 4 and 5 indicate how the potential well can drastically modify the energy dependence of the yield expected from a "penetration factor" analysis, even at energies considerably removed from the virtual resonance level. Figures 3 and 5 show the effect that absorption has on the one-body cross sections. The absorption coefficient, k_1', which was derived from the analysis of high energy scattering data, is so large that the resonance features of the "no-absorption" model are practically obliterated. In Fig. 6 the channel penetration parameters, f_L^2/ρ and ρ/g_L^2, are applied to the study of the $Li^7(p,\ )$ reaction, and compared with the OBJ cross section without absorption. For a sharp resonance it was seen that f_L^2/ρ is by far the major energy dependent factor in the one-body cross section formula, and, thus, in this case the barrier dependence of the damping constant is not separable from purely nuclear effects. Figures 7, 8, and 9 illustrate how the one-body resonances depend on the parameters which describe the compound nucleus, namely, the nuclear radius, well depth, bombarding energy, angular momentum, and absorption coefficient. The $O^{16}(p,\ )$ reaction in Fig. 10 has been selected to investigate the variation of the cross section as a function of the absorption coefficient.

The many body features of nuclear reactions are included in the present study only to the degree of taking into account schematically the absorption of the incident wave in nuclear matter.

We are greatly indebted to Professor G. Breit who initiated and guided this work. In particular, we wish to thank him for supplying us with the result for the case of very strong absorption. To Professor Breit and Professor C. Kittel, we extend our thanks for the use of some unpublished work which influenced the course of the present calculations.

We are grateful to Mr. Harrison M. Jones and Mr. John L. Johnson for their help in various phases of this work. Mr. Johnson has in addition read the manuscript

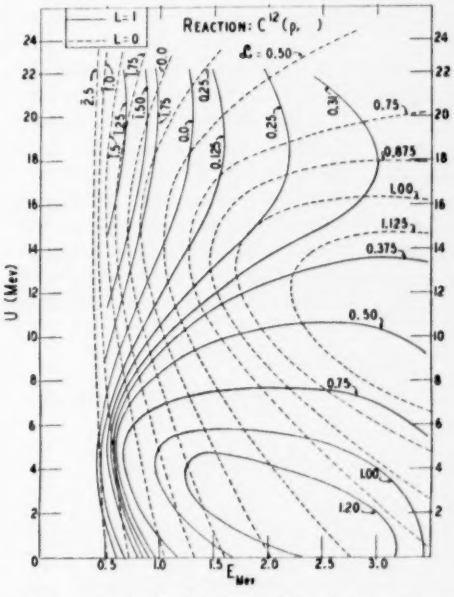

FIG. 9. Contours in the (U, E_{Mev}) plane of the reaction cross section with absorption for $C^{12}(p,\ )$. The curves are plots of U *vs* E_{Mev} for the constant value of $\mathfrak{L}$ shown. For all curves, $k_1'=0.111\times10^{13}$ cm^{-1}, and $r_0=1.6\times10^{-13}A^{\frac{1}{3}}$ cm.

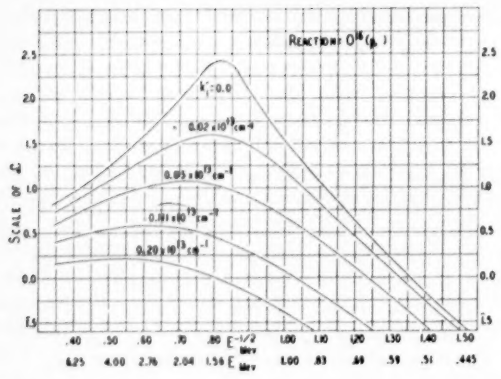

FIG. 10. Effect of absorption on the one-body resonance of $O^{16}(p,)$: $\mathcal{L}$ *vs* $E_{\text{Mev}}^{-\frac{1}{2}}$ for constant k_1'. For all curves $U=28.63$ Mev, $r_0=1.6\times10^{-13}A^{\frac{1}{3}}$ cm, and $L=0$.

critically, and checked the formulas. We also wish to thank Mr. James F. Bartram, Mrs. Martha C. Meeker, Mrs. Carolyn Arfken, Mrs. Dorothea Bone, and Miss Jacqueline Gibson for assistance with the calculations and preparation of the figures.

APPENDIX

1. *Binding energy well depth:* This estimate is provided by the binding energy of the incident particle in the compound nucleus. The kinetic energy in the ground state of the last bound particle is estimated by assuming that r times the radial wave function is a sine wave which vanishes at the nuclear boundary. Large binding energies and large extra-nuclear Coulomb barriers suppress the tail of the wave function and hence, improve the approximation. For these assumptions the well depth is related to the binding energy by $U=B+(h\pi)^2/(2\mu r_0^2)$, where B is the absolute value of the binding energy, and the second term on the right is the ground state kinetic energy. The well depth computed from this formula, using the correct binding energy, may be much too small for the heavier elements because of the action of the exclusion principle in requiring the last bound particle to occupy an excited state.

2. *Van Vleck well depth:* Van Vleck considered the case of incident neutrons, and Ostrofsky, Bleick, and Breit made application to the case of incident protons. It was assumed by Van Vleck that the interaction between all pairs of nucleons is of the Majorana exchange type, and that the nucleons are distributed according to the Thomas-Fermi statistical model. Additional approximations similar to those made in the Hartree-Fock treatment are also required. Surface effects are eliminated by assuming that the range of the force is small compared with the nuclear radius. The well depth resulting from this calculation depends slightly on the energy of the incident particle. In the present application the velocity dependence has been neglected, and the depth at zero energy used. The latter well depth is called the special Van Vleck well depth in the text.

The Van Vleck formula for the potential well is

$$V=-A\{E(W_+)\mp E(W_-)+2[\alpha/(\pi k_P^2)]^{\frac{1}{2}}[e^{-W_+^2}-e^{-W_-^2}]\},$$

where the sign is negative if $k_P>k$, and positive if $k_P<k$. Here,

$$W_\pm=|k_P\pm k|/(2\alpha^{\frac{1}{2}}); \quad E(W)=(2\pi^{-\frac{1}{2}})\int_0^W e^{-t^2}dt;$$

and

$$k=[(9\pi N)/(4r_0^3)]^{\frac{1}{2}}$$

with N equal to the number of neutrons; k_P is 2π times the wave number of the proton inside the nucleus and the neutron-proton potential is $Ae^{-\alpha r^2}$. In order to evaluate V from the above formula, a method of successive approximations was used. The value of N was placed equal to one-half of the mass number, so that with the radius convention employed in Sec. III, k and V become independent of target element. Use of the values obtained from proton-proton scattering, $\alpha=1.23\times10^{24}$ cm^{-2} and $A=100$ Mev, determined the value of the Van Vleck well depth at zero bombarding energy as follows:

$$V=-28.63 \text{ Mev} \quad \text{for} \quad r_0=1.6\times10^{-13}A^{\frac{1}{3}} \text{ cm},$$

and

$$V=-19.10 \text{ Mev} \quad \text{for} \quad r_0=2.1\times10^{-13}A^{\frac{1}{3}} \text{ cm}.$$

Electronic Energy Bands in Metals

G. PARZEN
University of Notre Dame, Notre Dame, Indiana
(Received July 30, 1952)

A method is presented for calculating the energy levels of a crystal. The method is based on finding a variational principle for the energy levels in terms of the Wannier functions instead of the usual Bloch wave functions. The variational principle does not give the energy $E(\mathbf{k})$ directly, but if $E(\mathbf{k})$ for a particular band is expanded in a Fourier series in $\mathbf{k}$, then the variational principle gives the Fourier coefficients of $E(\mathbf{k})$ in this expansion. The maxima and minima properties of the variational principle are investigated. The variational principle is properly modified for application to valence bands. The types of trial functions that will arise is discussed, and the method is applied to a one-dimensional crystal. Our results are compared with the results of the method of orthogonal plane waves for the same problem.

I. INTRODUCTION

THE most direct method available for the calculation of the energy levels of an electron moving in a periodic potential is the cellular method; that is, we solve Schrödinger's equation within one of the atomic polyhedra for that solution which satisfies the proper boundary conditions on the surface of the polyhedron. This method is difficult to apply in practice because of the awkward shape of the surfaces of the atomic polyhedra. Slater[1] has given an approximate way of satisfying these boundary conditions, and several metals have been treated in this way.

The idea behind our approach is to find a variational principle for the energy levels of a crystal which involves only the Wannier functions instead of the usual Bloch wave functions. The hope is that such a variational principle will avoid the difficulties of having to fit the boundary conditions on the surface of the atomic polyhedra, and at the same time, the integrals arising will extend over a few cells of the crystal rather than over the entire crystal.

In the following paragraphs, such a variational principle is presented. The variational principle does not give the energy directly, but if $E(\mathbf{k})$ for a particular band is expanded in a Fourier series in $\mathbf{k}$, then our variational principle allows us to calculate the Fourier coefficients of $E(\mathbf{k})$ in this expansion.

We have applied the method to a one-dimensional crystal chosen to resemble lithium, and we have compared our results with those obtained by the method of orthogonal plane waves[2,3] when applied to the same problem.

II. THE WANNIER FUNCTION AND ITS PROPERTIES

Since we are interested in obtaining a variational principle for the energy levels of a crystal in terms of the Wannier functions, our immediate problem is to find a set of equations for the energy levels of the crystal which involve just the Wannier function; that is, the usual wave function does not occur.

For the sake of simplicity, we shall prove all our results for the one-dimensional crystal. For the most part, our results can easily be transferred to the three-dimensional crystal.

Before proceeding further, we would like to give here the definition and some of the properties of the Wannier function.

Let us consider a one-dimensional crystal whose atoms are separated by the distance a and are located at the points $x_n=na$. Let $V(x)$ be the periodic potential due to the atoms, and let $\psi_k(x)$ be the eigenfunctions of an electron moving in this potential and having the energy levels $E(k)$. Then

$$\mathfrak{H}\psi_k(x)=E(k)\psi_k(x), \tag{2.1}$$

$\mathfrak{H}$ being the Hamiltonian for an electron moving in a periodic potential $V(x)$.

The energy levels of the electron will occur in bands, and to each band we associate a set of Wannier functions according to the definition,

$$U_n(x)=N^{-\frac{1}{2}}\sum_k e^{-ikx_n}\psi_k(x). \tag{2.2}$$

N is the total number of atoms in the crystal and the sum over k is only over those values of k which corresponds to the particular band we are considering. For the lowest band k would go from $-\pi/a$ to $+\pi/a$.

The Wannier functions defined by (2.2) can be obtained from each other by a simple displacement,

$$U_n(x)=U_0(x-x_n), \tag{2.3}$$

and they form an orthonormal set,

$$\int dx U_0(x-x_m)U_0(x-x_n)=\delta_{nm}. \tag{2.4}$$

The Wannier function of a free particle can be easily calculated. Here $\psi_k=\exp(ikx)/L^{\frac{1}{2}}$, where $L=Na$ is the length of the crystal. Equation (2.2) gives

$$U_0=\frac{1}{\sqrt{a}}\frac{\sin(\pi x/a)}{\pi x/a} \tag{2.5}$$

[1] J. C. Slater, Phys. Rev. **45**, 794 (1934).
[2] C. Herring, Phys. Rev. **57**, 1169 (1940); C. Herring and A. G. Hill, Phys. Rev. **58**, 132 (1940).
[3] R. Parmenter, Phys. Rev. **86**, 552 (1952).

as the Wannier function of the lowest band of a free particle.

The type of asymptotic behavior indicated by (2.5) is characteristic of the Wannier function. As x becomes large, it oscillates while its amplitude decreases like $1/x$.

It should be noted that (2.2) may be turned around and solved for $\psi_k(x)$ in terms of $U_0(x-x_n)$,

$$\psi_k(x)=N^{-\frac{1}{2}}\sum_n e^{ikx_n}U_0(x-x_n). \tag{2.6}$$

This expression may be interpreted in the following way. If we consider $\psi_k(x)$ within a single band, then within that band we can represent $\psi_k(x)$ by a Fourier series in k. Equation (2.6) is just this Fourier series for $\psi_k(x)$ and the Wannier functions $U_0(x-x_n)$ are the Fourier coefficients of the series.

Having defined the Wannier function $U_0(x)$, we may ask now for the differential equation that it must obey. This equation can be obtained from Schrödinger's equation (2.1). We substitute for $\psi_k(x)$ using Eq. (2.6) and then sum over k, which varies over a band.

We get

$$\mathcal{H}U=\sum_n \epsilon_{-n}U(x-x_n). \tag{2.7}$$

Here ϵ_n is the Fourier coefficient in the Fourier series of $E(k)$:

$$E(k)=\sum_n \epsilon_n e^{ikx_n}, \tag{2.8}$$

and

$$\epsilon_n=N^{-1}\sum_k e^{-ikx_n}E(k). \tag{2.9}$$

We have dropped the subscript zero on $U(x)$.

The variational principle we will soon derive will not give $E(k)$ directly but will be an expression for these Fourier coefficients ϵ_n. We would like to point out that ϵ_n can be expressed simply in terms of the Wannier functions,

$$\epsilon_n=\int dx U^*(x+x_n)\mathcal{H}U(x). \tag{2.10}$$

This is obtained by multiplying both sides of (2.7) by $U(x+x_n)$ and using the orthogonality property of $U(x+x_m)$.

We would like now to re-express our problem of finding the energy levels of the crystal just in terms of the Wannier functions alone, that is, to eliminate the wave function $\psi_k(x)$ entirely.

It is clear, however, that Eq. (2.7) cannot be regarded as an equivalent equation to the Schrödinger equation (2.1) for determining the energy levels of the crystal. Equation (2.7) contains a great number of unknown constants, the ϵ_n, and they cannot all be determined by a single equation.

The extra conditions on $U(x)$, which are not contained in Eq. (2.7) and which we must add so that the ϵ_n shall be completely determined, are the orthogonality conditions $\int dx U_n^* U_m=\delta_{nm}$.

A set of equations which involve only the Wannier functions and which are equivalent to the Schrödinger equation for determining the energy levels of the crystal are the following:

$$\mathcal{H}U=\sum_n \epsilon_n D^n U, \tag{2.11a}$$

$$\int dx U^*U=1, \tag{2.11b}$$

and

$$\int dx U^* D^n U=0, \quad n=\pm1, \pm2\cdots. \tag{2.11c}$$

Here D is the displacement operator, $D^{\pm n}f(x)=f(x\pm na)$, and has been introduced to make clear that there is but one function, $U(x)$, involved in the set of Eqs. (2.11).

In order to see that the ϵ_n are now determined, we can imagine the following procedure in solving the above equations. We can regard Eq. (2.11a) as an eigenvalue equation for ϵ_0 in which $\epsilon_{\pm1}, \epsilon_{\pm2}, \cdots, \epsilon_{\pm n}\cdots$ occur as parameters. Then we can solve (2.11a) to find $\epsilon_0=\epsilon_0(\epsilon_{\pm1}, \epsilon_{\pm2}, \cdots, \epsilon_{\pm n}, \cdots)$, and $U=U(x; \epsilon_{\pm1}, \epsilon_{\pm2}, \cdots)$. And we can take $U(x; \epsilon_{\pm1}, \epsilon_{\pm2}, \cdots)$ and put it into $\int dx U^* D^n U=0$ and thus get a set of equations for $\epsilon_{\pm1}, \epsilon_{\pm2}, \cdots$.

III. THE VARIATIONAL PRINCIPLE

We will now find a variational principle for the Wannier function $U(x)$ which will yield the Eqs. (2.11).

Consider the integral

$$I_0=\int dx U^*\mathcal{H}U, \tag{3.1}$$

where the function U is restricted by the conditions

$$\int dx U^*U=1 \tag{3.2a}$$

and

$$\int dx U^* D^n U=0. \tag{3.2b}$$

We will prove that the requirement that I_0 be an extremum will yield the Eqs. (2.11), that I_0 takes on a minimum value, and that this minimum value is ϵ_0. In other words, the above equations will give a variational principle for ϵ_0.

First let us prove the extremum property of I_0. Introduce the Lagrangian multipliers λ_n, $n=0, \pm1\cdots$ for the restrictions (3.2) and compute δI_0. We get

$$\int dx\{\delta U^*(\mathcal{H}U-\sum_n \lambda_n D^n U) + ((\mathcal{H}U)^*-\sum_n \lambda_n D^{-n})\delta U\}=0, \tag{3.3}$$

so that we have

$$\mathcal{H}U=\sum_n \lambda_n D^n U, \tag{3.4}$$

which is the desired equation for U. It is clear that the Lagrangian multipliers λ_n are just the Fourier coeffi-

cient ϵ_n in the Fourier expansion of $E(k)$. Also the extremum value of I_0 is obtained when U is the Wannier function satisfying (3.4), and thus the extremum value of I_0 is ϵ_0, according to Eq. (2.10).

In the same way we can form the integrals

$$I_n = \int dx U^* \mathcal{H} D^{-n} U, \tag{3.5}$$

and with the same side conditions on U given by (3.2), these integrals have extremums when U is the Wannier function satisfying Eqs. (2.11) and the extremum value of I_n is ϵ_n.

We have therefore obtained a variational principle for the Fourier coefficients, ϵ_n, of the energy $E(k)$. We have not so far demonstrated whether the I_n have minima or not. We will do this in the next section.

It might be noted here that our variational principle seems clumsy because of the many conditions (3.2) which must be satisfied by the trial function. Actually, it is only necessary to satisfy these conditions for the first few values of n, $n=0, 1, 2\cdots$. For higher values of n, the conditions will be automatically fulfilled because the overlap between $U(x)$ and $U(x-x_n)$ will get smaller as x_n get larger.

IV. THE MINIMA PROPERTIES OF I_n

We wish to establish now the minima properties of I_n.

First let us treat I_0. To show that I_0 has a minimum, it is only necessary to show that I_0 has a lower bound; that is, that is always larger than some definite quantity when the trial function U obeys the proper restrictions.

Consider the integral

$$I = \int dx \psi^* \mathcal{H} \psi, \tag{4.1}$$

where ψ must satisfy

$$\int dx \psi^* \psi = 1. \tag{4.2}$$

By the usual Rayleigh-Ritz principle, I has a minimum value and this minimum value is simply the lowest level $E(0)$ of the Hamiltonian $\mathcal{H}$.

Now consider the integral I_0. It is similar to the integral I, except that the class of functions which may be used in computing I_0 is more restrictive. We have the added restrictions $\int dx U^* D^n U = 0$. Since $I \geq E(0)$, then $I_0 \geq E(0)$ also. Thus, I_0 has a minimum value, and this minimum value is larger than $E(0)$; that is, we have not only shown that ϵ_0 is the minimum value of I_0 but also that $\epsilon_0 \geq E(0)$.

We have shown that ϵ_0 is the minimum value of I_0, if U obeys the restrictions (3.2), but this is not true of $I_{\pm 1}$, $I_{\pm 2}\cdots I_{\pm n}\cdots$. These last integrals have neither minimum nor maximum. (See Appendix I, for proof.)

However, we can establish the following integrals which do not have minima:

$$I_0 + \tfrac{1}{2}(I_1 + I_{-1}) \geq \epsilon_0 + \tfrac{1}{2}(\epsilon_1 + \epsilon_{-1}), \tag{4.3}$$

$$I_0 + \tfrac{2}{3}(I_1 + I_{-1}) + \tfrac{1}{3}(I_2 + I_{-2}) \geq \epsilon_0 + \tfrac{1}{2}(\epsilon_1 + \epsilon_{-1}) + \tfrac{1}{3}(\epsilon_2 + \epsilon_{-2}), \tag{4.4}$$

and quite generally,

$$I_0 + \frac{m-1}{m}(I_1 + I_{-1}) + \frac{m-2}{m}(I_2 + I_{-2}) \cdots + \frac{1}{m}(I_m + I_{-m}) \geq \epsilon_0 + \frac{m-1}{m}(\epsilon_1 + \epsilon_{-1}) \cdots + \frac{1}{m}(\epsilon_m + \epsilon_{-m}). \tag{4.5}$$

We shall prove (4.3) and the rest follow in the same way. We have only to prove that $I_0 + \frac{1}{2}(I_1 + I_{-1})$ have a lower bound. Now $I = \int dx \psi^* \mathcal{H} \psi$, where $\int dx \psi^* \psi = 1$ does have a lower bound; in fact, $\int dx \psi^* \mathcal{H} \psi \geq E(0)$.

Therefore, let

$$\psi = (1/\sqrt{2})(1+D)U, \tag{4.6}$$

where U obeys at least the first two of the conditions (3.2). Then, we get for I,

$$I = \int dx U^* [1 + \tfrac{1}{2}(D^1 + D^{-1})] U = I_0 + \tfrac{1}{2}(I_1 + I_{-1}). \tag{4.7}$$

Thus, $I_0 + \frac{1}{2}(I_1 + I_{-1}) \geq E(0)$, and it has a lower bound and also a minimum value, which must be $\epsilon_0 + \frac{1}{2}(\epsilon_1 + \epsilon_{-1})$.

V. THE VARIATIONAL PRINCIPLE FOR THE VALENCE BANDS

The variational principle that we have derived will give the energy levels of the lowest band. However, in practice, we are interested in finding the valence bands.

For example, suppose we wish to find the energy levels of the second band which lies above the first or lowest band. What restrictions must be put on the trial function $U(x)$ so that I_0 as calculated by Eq. (3.1) will converge to the ϵ_0 of the second band and not to the ϵ_0 of the first band?

We might guess that the trial function $U(x)$ should be orthogonal to the Wannier function $U^{(1)}(x)$ of the lowest band; that is, we should require that

$$\int dx U^* U^{(1)} = 0. \tag{5.1}$$

This turns out not to be sufficient. What is required is that U should be orthogonal to *all* the Wannier functions of the lowest band, that is,

$$\int dx U^* D^n U^{(1)} = 0. \tag{5.2}$$

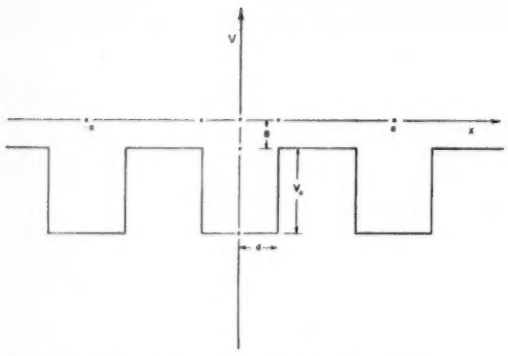

FIG. 1. The shape of the potential assumed for our one-dimensional calculation.

This result is suggested by the following. Let us expand U in the wave functions $\psi_k(x)$ of our Hamiltonian $\mathfrak{H}$,

$$U=\sum_k a_k\psi_k(x). \tag{5.3}$$

Then

$$I_0=\sum_k |a_k|^2E(k). \tag{5.4}$$

If we wish (5.4) to yield the ϵ_0 of the second band, Eq. (5.4) suggests that we require $a_k=0$ for all values of k which lie in the first band; that is, $U(x)$ should be orthogonal to all the wave functions of the first band. This actually is the case and is proved in Appendix I.

Now the requirement that $a_k=0$ in the first band is equivalent to Eq. (5.2), because, as

$$U^{(1)}=\frac{1}{\sqrt{N}}\sum_{k \text{ in first band}}\psi_k(x), \tag{5.5}$$

then Eq. (5.2) gives

$$\frac{1}{\sqrt{N}}\sum_{k \text{ in first band}}a_ke^{ikx_n}=0. \tag{5.6}$$

Equation (5.6) says that the Fourier coefficients of the function a_k, where k is restricted to the lowest band, are all zero. Thus, it follows that $a_k\equiv 0$ for k is the lowest band.

VI. ON THE CHOICE OF TRIAL FUNCTIONS

Having the variational principle, we are now faced by two problems. How good is the variational principle, and what sort of functions shall we use as true functions?

Such questions cannot be answered very well without considerable calculation for the case of an actual metal. Nevertheless, we thought it might be worth while to apply our variational principle to a one-dimensional crystal which was so chosen as to resemble the metal lithium. We believe that this simple calculation will tell us how the calculation will proceed for an actual metal.

We chose our crystal potential to be made up of square wells as shown in Fig. 1. We chose the parameters, the internuclear distance a, the potential depth V_0, and the well width d, so that the first band is very narrow. An electron whose state is in the first band is essentially bound to the atom with an "orbit radius" of about d.

The ratio $a/2d$, which is the ratio of the internuclear distance to the radius of the inner a lowest band was taken fairly large; we let $a/2d=3$, 4, 5, 7, and 10. The corresponding ratio for lithium is about 15. We will see that the larger this ratio is, the better will be the trial function we will use.

Now our trial function must be orthogonal to the Wannier functions of the lowest band, as we are trying to locate the second band. Thus, if we denote by $\varphi(x)$ the Wannier function of the lowest band, we will write our trial function as

$$U(x)=u(x)-\sum_n c_n\varphi(x-x_n); \tag{6.1}$$

and we will chose c_n so as to make $U(x)$ orthogonal to $\varphi(x-x_n)$, as is required by (5.2).

Since the lowest band is very narrow, the Wannier function $\varphi(x)$ of this band is given to a good approximation by just the atomic wave function, that is, by just the bound state wave function for a well of depth V_0 and width d. (See Appendix II for discussion of this point.) Further, we also assume that the functions overlap very little and are mutually orthogonal. Thus, the coefficients c_n in (6.1) are given by

$$c_n=\int dx\varphi^*(x-x_n)u(x). \tag{6.2}$$

The only quantity as yet undetermined in our trial function (6.1) is the function $u(x)$. Now as we are finding the energy levels of a valence band, we expect the wave function of the particle to be fairly close to the free-particle wave function. Thus, we expect that $u(x)$ should resemble the free-particle Wannier function given by (2.5), that is,

$$u(x)\simeq\frac{1}{\sqrt{a}}\frac{\sin(\pi x/a)}{\pi x/a}. \tag{6.3}$$

Now, we will construct the simplest possible trial function out of (6.1), (6.2), and (6.3) by considering the case where the ratio of the interatomic distance to the radius of the inner orbit of the electrons is large. For our problem this ratio is $a/2d$. For actual metals this ratio is quite large.

From (6.2) and (6.3) one can see that the coefficient c_n decrease as n increases. In fact, as we can expect $\varphi(x)$ to have the general form $\varphi(x)\simeq\exp(-x^2/d^2)$, the c_n will decrease very fast. We will suppose that our ratio $a/2d$ is large enough so that c_1 and c_{-1} are already quite small and just the c_0 term in (6.1) is sufficient. Our trial function is then

$$U(x)=u(x)-c_0\varphi(x). \tag{6.4}$$

Now in our choice of $u(x)$, we must keep in mind that the trial function must satisfy the conditions (3.2), $\int dx U^* D^n U = 0$. We see that if we choose $u(x)$ as given by the free-particle Wannier function, then (6.4) will automatically satisfy the conditions (3.2), in the sense that $c_1, c_2, \cdots$ are considered small. For since $\int dx u^* D^n u = 0$, then

$$\int dx U^* DU = -(c_0^* c_1 + c_0 c_{-1}^*), \tag{6.5a}$$

and

$$\int dx U^* D^n U = -(c_0^* c_n + c_0 c_{-n}^*), \tag{6.5b}$$

and the right band sides of (6.5) are nearly zero.

Thus, the trial function used in our calculation is

$$U = A\left\{\frac{1}{\sqrt{a}}\frac{\sin(\pi x/a)}{\pi x/a} - c_0\varphi(x)\right\}, \tag{6.6a}$$

where A is the normalization constant,

$$A = 1/(1-c_0^2). \tag{6.6b}$$

There are no parameters left in (6.6) to vary. We will simply use (6.6) to calculate ϵ_n, the Fourier coefficients of the energy, according to $\epsilon_n \simeq \int dx U^* \mathcal{H} D^{-n} U$; and having ϵ_n, we can find the energy

$$E(k) = \sum_n \epsilon_n \exp(ikx_n).$$

There are some properties of ϵ_n and $E(k)$ we can foresee immediately. We will write

$$\epsilon_n = \tilde{\epsilon}_n + \Delta\epsilon_n, \tag{6.7}$$

where the $\tilde{\epsilon}_n$ are the Fourier coefficients of a free particle, that is,

$$\hbar^2 k^2/2m = \sum_n \tilde{\epsilon}_n e^{ikx_n}. \tag{6.8}$$

Then the $\tilde{\epsilon}_n$ are given by

$$\tilde{\epsilon}_0 = (\hbar^2/2ma^2)\cdot(\pi^2/3), \tag{6.9a}$$

and

$$\tilde{\epsilon}_n = \tilde{\epsilon}_0((-1)^n/n^2)\cdot(3/\pi^2), \tag{6.9b}$$

for the lowest band.

Now the ϵ_n do not decrease very fast, since $\tilde{\epsilon}_n$ goes like $1/n^2$; but it seems very likely that the $\Delta\epsilon_n$ do decrease very fast, and our calculation seems to verify this behavior. In fact, according to our trial function (6.6), as $a/2d$ gets larger, $c_0 \to 0$ and U approaches the free Wannier function, and $\Delta\epsilon_n \to 0$.

We have supposed that our $a/2d$ is large enough so that only $\Delta\epsilon_0$ and $\Delta\epsilon_1$ are significantly different from zero. We believe this to be consistent with the approximations already made relative to $c_1, c_2 \cdots c_n \cdots$.

Thus, $E(k)$ is given by

$$E(k) = (\hbar^2 k^2/2m) + \Delta\epsilon_0 + 2\Delta\epsilon_1 \cos ka. \tag{6.10}$$

Note that ϵ_1 and ϵ_{-1} are real and equal in our problem.

The position of the lowest level of the band is

$$E(0) = \Delta\epsilon_0 + 2\Delta\epsilon_1, \tag{6.11}$$

and the width of the band is

$$\Delta E = (\hbar^2\pi^2/2ma^2) - 4\Delta\epsilon_1. \tag{6.12}$$

Using our trial function (6.6), $\Delta\epsilon_0$ and $\Delta\epsilon_1$ are found to be

$$\Delta\epsilon_0 = (A^2-1)\tilde{\epsilon}_0 + A^2[V_{Av} - c_0^2 E_b], \tag{6.13a}$$

and

$$\Delta\epsilon_1 = (A^2-1)\tilde{\epsilon}_1. \tag{6.13b}$$

Here E_b is the energy of the narrow inner band, and we have dropped terms which seemed of the same order as c_1. V_{Av} is the average value of V over a cell.

VII. COMPARISON WITH THE METHOD OF ORTHOGONAL PLANE WAVES

In the above we have presented what seems to be a suitable, yet simple, trial function for the valence band. We though it would perhaps be worthwhile to compare our results with those of some other method. We chose to compare our results with those of the method of orthogonal plane waves, because this method seems capable of some accuracy and because with our choice of trial function there is a close connection between the two methods. (See Appendix III.)

In the method of orthogonal plane waves,[4] the wave function $\psi_k(x)$ is expanded in a set of plane waves made orthogonal to wave functions of the inner bands.

For our problem, let the orthogonal plane wave ϑ_k be defined by

$$\vartheta_k(x) = e^{ikx}/L^{\frac{1}{2}} - c_k\phi_k(x), \tag{7.1a}$$

where

$$\phi_k = N^{-\frac{1}{2}}\sum_n e^{ikx_n}\varphi(x-x_n), \tag{7.1b}$$

and

$$c_k = \frac{1}{a^{\frac{1}{2}}}\int dx\varphi^*(x)e^{ikx}. \tag{7.1c}$$

Then our trial function is

$$\psi_k = \sum_n A_n\vartheta_{k+k_n}(x), \tag{7.2}$$

where $k_n = 2\pi n/a$.

For purposes of comparison with our method, we took just one term in (7.2), since with one term the amount of labor involved in both methods will be about the same.

Thus, the orthogonal plane wave trial function was taken as

$$\psi_k = A\{e^{ikx}/L^{\frac{1}{2}} - c_k\phi_k\}, \tag{7.3}$$

where

$$A^2 = 1/(1-c_k^2).$$

With this trial function, $E(k)$ is given by

$$E(k) = \frac{1}{1-c_k^2}\left\{\frac{\hbar^2k^2}{2m} + V_{Av} - c_k^2 E_b\right\}. \tag{7.4}$$

[4] See references 2 and 3 for the details of this method.

TABLE I. A comparison of the results obtained for the valence band of a one-dimensional crystal. $E(0)$ is the lowest level of the band, and ΔE is the width of the band. Units of energy are $\hbar^2/2md^2$.

$a/2d$		Exact	Our method	OPW method
3	$E(0)$	1.00	1.06	1.24
	ΔE	0.40	0.39	0.031
4	$E(0)$	1.00	1.08	1.15
	ΔE	0.20	0.198	0.087
5	$E(0)$	1.00	1.003	1.10
	ΔE	0.12	0.12	0.049
7	$E(0)$	1.00	1.05	1.07
	ΔE	0.06	0.06	0.04
10	$E(0)$	1.00	1.04	1.04
	ΔE	0.03	0.03	0.02

VIII. THE CALCULATION AND RESULTS

For the actual calculation we chose $V_0=(\pi/2)^2\hbar^2/2md^2$, and we rather arbitrarily put $B=1\cdot\hbar^2/2md^2$. The narrow lowest band was located at $E_b=-1.59\hbar^2/2md^2$.

The atomic wave function $\varphi(x)$ associated with the lowest band was approximated by a Gaussian,

$$\varphi(x)=(2\alpha/\pi)^{\frac{1}{4}}\exp(-\alpha x^2), \tag{8.1}$$

and α was chosen by minimizing the energy of a particle in a square well of depth V_0 and width d. We found $\alpha=0.510/d^2$.

The results of the calculation are given in Table I. The lowest level $E(0)$ and the width ΔE of the valence band were calculated exactly, by our method and by the method of orthogonal plane waves. The calculation was repeated for different values of $a/2d$ ($a/2d=3$, 4, 5, 7, and 10).

When $a/2d$ gets very large, our results and those of the method of orthogonal plane waves approach the correct results. However, as $a/2d$ gets smaller, it would seem that our method gives considerably better results.

The calculation was done rather roughly; the last decimal place given is somewhat uncertain. However, the accuracy is sufficient for the main purpose of this one-dimensional problem, *viz.*, to gain some understanding as to how the method is applied and what sort of trial functions should be chosen. It shows that one can expect to attain accuracy without too much labor in the three-dimensional problem, and it indicates some superiority over the method of orthogonal plane waves.

We are planning to apply our method to the calculation of the energy levels of lithium.

We would like to thank Professor Charles Mullin, Professor Eugene Guth, and Mr. Thomas Wainwright for their help and for their discussion of the problem.

APPENDIX I. THE MINIMAL PROPERTIES OF U

We will present here a different proof that I_0 has a minimum, because this proof can be easily extended to the valence or higher bands.

We wish to show that the Wannier function of the lowest band,

$$U(x)=N^{-\frac{1}{2}}\textstyle\sum_k \psi_k(x), \tag{I.1}$$

is the function that minimizes the integral

$$I_0=\int dx U^*\mathfrak{C}U,$$

subject to the restrictions

$$\int dx U^*U=1 \tag{I.2a}$$

and

$$\int dx U^*D^nU=0, \quad n=\pm1, \pm2\cdots. \tag{I.2b}$$

If we expand U in $\psi_k(x)$, $U=\sum_k a_k\psi_k(x)$, then

$$I_0=\textstyle\sum_k |a_k|^2E(k), \tag{I.3}$$

and $\sum_k |a_k|^2=1$. It is clear that to get the lowest possible value of I_0, we should make the a_k for high k equal zero. We are restricted in this by the conditions $\int dx U^*D^nU=0$. Since there are N such conditions to fulfill, N of the a_k must be different from zero. As we wish the lowest value of a_k, we will make the a_k of the N states of the lowest band different from zero, and all the other a_k equal to zero.

Condition (I.2b) now says

$$\sum_{k \text{ in lowest band}} |a_k|^2e^{ikx_n}=0, \quad n\neq0. \tag{I.4}$$

This means that $|a_k|^2$ is a constant independent of k, for k is the lowest band, since all its Fourier coefficients except the first are zero. Therefore, $|a_k|^2=1/N$, in the first band, will minimize I_0, and the minimum value of I_0 is

$$\epsilon_0=\frac{1}{\sqrt{N}}\sum_{k \text{ in lowest band}} E(k). \tag{I.5}$$

It is clear that the Wannier function (I.1) will make I_0 give this minimum value.

The above proof can be easily adapted to show that to make I_0 converge to the ϵ_0 of the second band the necessary restriction is $a_k=0$ in the first band.

To show that I_n, $n\neq0$, has no maximum nor minimum, we simply calculate I_n using as trial functions the Wannier functions of a free particle, particularly those of the higher bands. The I_n so calculated can be made as large as we please, both positively and negatively.

APPENDIX II. THE WANNIER FUNCTION OF A NARROW BAND

In Sec. VI we said that for the narrow inner bands, the Wannier function is the isolated atomic wave function $\varphi(x)$. This is a little surprising, as $\varphi(x)$ does

not have the correct oscillating asymptotic behavior for a Wannier function.

A more accurate expression for the Wannier function of a narrow band is the following:

$$U=\varphi(x) \quad \text{in the first cell,} \tag{II.1a}$$

$$U=0\ \varphi(x-x_n) \quad \text{in the } n\text{th cell.} \tag{II.1b}$$

To obtain (II.1), let us solve for the $\psi_k(x)$ of the narrow band by the cellular method. Within the first cell of the crystal, we will find $\psi_k(x)=\varphi(x)$, independent of k, because it is a narrow band. Also $\varphi(x)$ will be very nearly the isolated atomic wave function. In any other cell we can obtain $\psi_k(x)$ from its value in the first cell. Thus, in the nth cell, $\psi_k(x)=\exp(ikx)\varphi(x-x_n)$.

Now since $\psi_k(x)$, in this approximation, is given by

$$\psi_k(x)=\varphi(x) \quad \text{in the first cell,} \tag{II.2a}$$

$$\psi_k(x)=e^{ikx_n}\varphi(x-x_n) \quad \text{in the } n\text{th cell,} \tag{II.2b}$$

we can now use the definition of the Wannier function to find and obtain Eqs. (II.1).

APPENDIX III. CONNECTION WITH THE ORTHOGONAL PLANE WAVE METHOD

There is a close connection between our method and the orthogonal plane wave method. To make this connection clearer, let us take the trial function used in the OPW (orthogonal plane waves) method, and let us compute from it the Wannier function which corresponds to it and compare this result with our Wannier function.

According to (7.1), the trial function is

$$\vartheta_k=A_k(e^{ikx}/L^{\frac{1}{2}}-c_k\phi_k), \tag{III.1}$$

where $A_k=(1-c_k^2)^{-\frac{1}{2}}$.

The Wannier function which corresponds to this trial function is obtained by

$$U=N^{-\frac{1}{2}}\textstyle\sum_k \vartheta_k(x). \tag{III.2}$$

The sum over k cannot be easily done. However, there is one limit where it can be done, and this is when $a/2d\to\infty$, when the ratio of the interatomic distance to the radius of the inner orbit becomes very large. In this limit c_k becomes very small, and we will put $A_k^2=1$ independent of k. Substituting into (III.1) the proper expressions for c_k and for ϕ_k according to (7.1), and doing the sum over k in (III.2), we get

$$U=\frac{1}{a^{\frac{1}{2}}}\frac{\sin(\pi x/a)}{\pi x/a}-\sum_n c_n\varphi(x-x_n). \tag{III.3}$$

Since, when $a/2d$ is very large, only the c_0 term is significant, we see that in this limit both methods correspond to the same trial function and should lead to the same results. This is borne out by our calculation.

Of course, that the two methods become the same for very large $a/2d$ is only true for our particular choice of trial function.

Electron Ejection from Mo by He^+, He^{++}, and He_2^+

HOMER D. HAGSTRUM
Bell Telephone Laboratories, Murray Hill, New Jersey
(Received September 25, 1952)

Total yield and kinetic energy distribution have been measured for electrons ejected from atomically clean and gas covered molybdenum by the ions He^+, He^{++}, and He_2^+ in the kinetic energy range 10 to 1000 ev. Evidence is presented that one electron is excited into the kinetic energy continuum for each incident He^+ ion and that the electrons so excited are partially internally reflected at the potential barrier of the metal. The slowest ions observed were found to eject 0.25, 0.72, and 0.13 electron per ion for He^+, He^{++}, and He_2^+, respectively. Total electron yield is found to be nearly independent of ion kinetic energy up to 1000 ev. This observation and that of the kinetic energy maximum for slow ions indicate that the electrons are released in an Auger type process for which the energy is supplied by the potential and not the kinetic energy of the ion (potential ejection). Electrons of kinetic energy greater than the upper limit predicted by present theory are observed for faster ions and are accounted for by the shift of the energy levels of the bombarding particle when it is near the metal surface. Some conclusions concerning reflection processes at a metal surface and the nature of electron ejection by the alpha-particle (He^{++}) and the molecular helium ion (He_2^+) come out of this work.

I. INTRODUCTION

EJECTION of an electron from a metal by a positive ion proceeds by the excitation of an electron into the kinetic energy continuum above the surface potential barrier. The energy for this transition may come either from the kinetic or potential energy of the ion. These two possibilities have been distinguished as *kinetic* and *potential ejection*, respectively. Depending upon the kinetic energy range of the ion, kinetic ejection may involve the acceleration by impact inside the metal of free and/or bound electrons some of which escape through the surface,[1,2] or the release of bound electrons from surface atoms.[3,4] The evidence is that kinetic ejection predominates for all ions of kinetic energy greater than a few thousand electron volts and at all speeds in the event potential ejection is energetically impossible.

Potential ejection, on the other hand, involves electronic interaction between the incoming ion and the conduction electrons of the metal while the ion is still outside the metal surface. It can occur when the potential energy recovered on neutralization of the ion is sufficient both to extract the neutralizing electron and to excite a second metal electron to a level above the potential barrier at the surface of the metal. Potential ejection is thus expected to be the predominant mechanism for the case of slow ions of the noble gases incident upon metal surfaces.

Detailed mechanisms of potential ejection have been proposed and investigated theoretically by Oliphant and Moon,[5] Massey,[6] Shekhter,[7] and Cobas and Lamb.[8] Experimental investigations of potential ejection for slow ions of the noble gases include those of Penning,[9,10] Oliphant,[11] Rostagni,[12] and D'Ans, DaRios, and Malaspina.[13] Oliphant[14] and Greene[15] have studied the related ejection of electrons by metastable atoms of the noble gases.

This paper is the report of a study of the secondary electron emission from molybdenum produced by the ions He^+, He^{++}, and He_2^+. The measurements were made with an instrument which provides a focused beam of ions, homogeneous in constitution and energy, whose energy at the target surface can be varied over a wide range. The state of the target surface has been investigated by observation of the rate of adsorption of gas upon it. In this study of potential ejection, it has thus been possible, perhaps for the first time, to meet the rather basic experimental requirement of known ions of known kinetic energy incident upon a target surface demonstrably free from adsorbed atoms. Measurements are reported of total electron yield and of distribution in kinetic energy of the ejected electrons. The dependence of these characteristics on kinetic energy of the incident ion has also been investigated. Discussion of the results in the light of theory is included and comparison with previous experimental results is made.

Notation used in this paper is defined in Table I. Relevant energy constants are listed in Table II.

[1] A. Becker, Ann. Physik **75**, 217 (1924).
[2] G. Schneider, Ann. Physik **11**, 357 (1931).
[3] M. E. Gurtovoy, J. Exptl. Theor. Phys. (U.S.S.R.) **10**, 483 (1940).
[4] W. Ploch, Z. Physik **130**, 174 (1951).
[5] M. L. E. Oliphant and P. B. Moon, Proc. Roy. Soc. (London) **A127**, 388 (1930).
[6] H. S. W. Massey, Proc. Cambridge Phil. Soc. **26**, 386 (1930); **27**, 460 (1931).
[7] S. S. Shekhter, J. Exptl. Theor. Phys. (U.S.S.R.) **7**, 750 (1937).
[8] A. Cobas and W. E. Lamb, Phys. Rev. **65**, 327 (1944).
[9] F. M. Penning, Physica **8**, 13 (1928); Proc. Roy. Acad. Sci. (Amsterdam) **31**, 14 (1928).
[10] F. M. Penning, Proc. Roy. Acad. Sci. (Amsterdam) **33**, 841 (1930).
[11] M. L. E. Oliphant, Proc. Roy. Soc. (London) **A127**, 373 (1930).
[12] A. Rostagni, Z. Physik **88**, 55 (1934); Ricerca sci. **9**, 633 (1938).
[13] D'Ans, DaRios, and Malaspina, Nuovo cimento **5**, 394 (1948).
[14] M. L. E. Oliphant, Proc. Roy. Soc. (London) **A124**, 228 (1929).
[15] D. Greene, Proc. Phys. Soc. (London) **B63**, 876 (1950).

II. THEORETICAL PREDICTIONS CONCERNING POTENTIAL EJECTION

The process of electron ejection by the potential energy recovered when an ion is neutralized at a metal surface is a form of collision of the second kind because in it internal energy is converted to kinetic energy. It is also recognizable as an Auger process in which the excited system metal-ion, on decaying to its ground state, ionizes itself with the ejection of an electron.

Two detailed mechanisms of the electronic transitions involved in potential ejection have been proposed and treated theoretically. One of these is a two-stage process, illustrated in Fig. 1, in which the ion is first neutralized to an excited state by resonance capture of a metal electron, from which state the atom subsequently decays to the ground state with the excitation of a second electron into the kinetic energy continuum. In the case of He^+ incident on Mo, resonance capture occurs to the ^3S metastable level of He, the only excited state isoenergetic to a filled level in the metal (see Fig. 1)

Quantum-mechanical calculations made to date agree in predicting that neutralization by resonance capture (stage 1 of Fig. 2) will occur before the ion can approach the metal surface much closer than several Angstrom units. Shekhter[7] concludes that the probability reaches unity at 3.5A for a 25-ev H^+ ion. Sternberg[16] has recently calculated 4 to 5A as the distance where it becomes highly probable that a 10-ev He^+ ion will be neutralized.

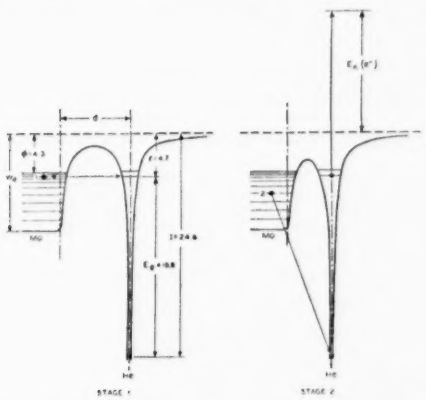

FIG. 1. Electronic transitions characteristic of the so-called two-stage process of potential ejection illustrated for the case of He^+ incident on Mo. Stage 1 consists of the resonance capture by tunneling through the barrier of a conduction electron (1) into the ^3S metastable state of the He atom. In stage 2 the excited atom thus formed is de-excited by capture of second metal electron (2) with the simultaneous excitation of the "metastable" electron into the continuum. State 2 as illustrated here involves electron exchange between metal and atom. Decay of the excited atom without electron exchange (dropping of the "metastable" electron to the ground state and exciting of the second metal electron) is possible but less probable (see text). $E_k(e^-)$ is the kinetic energy the excited electron possesses if it leaves the metal.

[16] D. Sternberg (private communication).

TABLE I. Definitions of notation.

	Particles
e^-	electron
He	normal helium atom
He^M	^3S metastable helium atom
He^+, He^{++}	atomic helium ions
He_2^+	diatomic molecular helium ion
	Energies
I_1	first ionization energy of He ($\rightarrow He^+$)
I_2	second ionization energy of He ($\rightarrow He^{++}$)
I^v	vertical ionization energy of He_2[a]
ϵ	ionization energy of He^M
E_e	electronic excitation energy
E_k	kinetic energy
ϕ	work function
W_i	width of conduction band
W_a	$W_i+\phi$
	Voltages and Currents
V_{ST}	voltage between electrodes S and T (positive when T positive re: S)
V_r	retarding potential, V_{ST}, corrected for contact potential
I_S, I_T	positive currents to electrodes S and T, respectively
	Particle Currents[b]
I^i	primary ionic current entering electrode S
I_i^e	secondary electron current ejected by I^i at T
I_i^i	secondary ionic current from partial reflection of I^i at T
I_i^m	secondary current of metastable atoms from partial reflection of I^i as metastable atoms at T
I_{ii}^e	tertiary electron current ejected from S by I_i^e
I_{ii}^e	tertiary electron current ejected from S by I_i^i
I_{im}^e	tertiary electron current ejected from S by I_i^m
I_r	$I_i^i+I_{ii}^e+I_{im}^e$
	Ejection Coefficients
γ_i, γ_i'	number of electrons ejected per incident ion at T and S, respectively
γ_m, γ_m'	number of electrons ejected per incident metastable atom at T and S, respectively
δ, δ'	number of electrons ejected per incident electron at T and S, respectively
	Reflection Coefficients[c]
R_{ii}	fraction of I^i reflected as ions at T
R_{im}	fraction of I^i reflected as metastable atoms at T
R	$R_{ii}+\gamma_i'R_{ii}+\gamma_m'R_{im}$
	Other Special Symbols
f_k	fraction of electrons comprising I_i^e having kinetic energies $>E_k$
ρ	$I_S/(I_T+I_S)$
z	number of electronic charges carried by primary ion
$z\rho$	$-\gamma_i$ for V_r sufficiently negative
Δp	rise in pressure on target flash
Δt_c	target cold interval
d	distance of ion or atom from metal surface
P	probability that an electron excited into the kinetic energy continuum escapes from the metal.

[a] This quantity is defined and evaluated in reference c of Table II.
[b] The particle currents here defined may or may not involve transport of electric charge. When they do, the symbol also stands for the absolute magnitude of the electric current (see Fig. 4).
[c] These definitions apply only to the case of singly charged ions incident on the target surface.

According to Cobas and Lamb's calculation[8] the decay of He^M by the electron exchange and excitation process (stage 2 of Fig. 1) should proceed with unity probability much nearer the metal surface. Shekhter[7] showed the decay of an excited atom at the metal

TABLE II. Energy constants.

$I_1(\mathrm{He}) = 24.58$ ev[a]	$\epsilon = I(\mathrm{He}^M) = 4.77$ ev[d]
$I_2(\mathrm{He}) = 78.98$ ev[b]	$\phi(\mathrm{Mo}) = 4.27$ ev[e]
$I^s(\mathrm{He_2}) \cong 16.8$ ev[c]	$W_i(\mathrm{Mo}) \cong 6.5$ ev[f]
$E_e(\mathrm{He}^M) = 19.81$ ev[a]	$W_a(\mathrm{Mo}) \cong 10.8$ ev

[a] C. E. Moore, *Atomic Energy Levels*, Vol. I, National Bureau of Standards Circular 467 (1949).
[b] $I_2(\mathrm{He}) = I_1(\mathrm{He}) + I_1(\mathrm{He}^+) = 24.58 + 54.403 = 78.98$ from reference a.
[c] This is the energy liberated in the transition following electron capture from the stable $\mathrm{He_2}^+$ state to the repulsive $\mathrm{He_2}$ state at constant nuclear separation. The value is that quoted by R. Meyerott, Phys. Rev. **70**, 671 (1946), based on observations by O. S. Duffendack and H. L. Smith, Phys. Rev. **34**, 68 (1929) of spectral enhancement in the $A^2\Pi \rightarrow X^2\Sigma$ system of CO^+ by the molecular ion $\mathrm{He_2}^+$.
[d] $\epsilon = I_1(\mathrm{He}) - E_e(\mathrm{He}^M) = 24.58 - 19.81 = 4.77$ ev.
[e] H. B. Michaelson, J. Appl. Phys. **21**, 536 (1950).
[f] This value is taken to be approximately the same as W_i(W) since W and Mo have the same number of valence electrons and essentially the same lattice constant. M. F. Manning and M. I. Chodorow, Phys. Rev. **56**, 787 (1939) obtained $W_i(\mathrm{W}) = 0.47R = 6.4$ ev from their calculated state density for the six lowest bands of tungsten. This value is in good agreement with the experimental values for the width of the valence band in W of 7.0 ± 0.5 and 6.5 ± 0.5 ev determined by J. A. Bearden and T. M. Snyder, Phys. Rev. **59**, 162 (1941) from transitions from the $5d$, $5s$ band to L_{II} and L_{III}, respectively.

surface without electron exchange (the alternative to stage 2 of Fig. 1; see figure caption) to be much less probable, calculating 0.05 for the probability of the process occurring during transit of the ion to and away from the metal.[17]

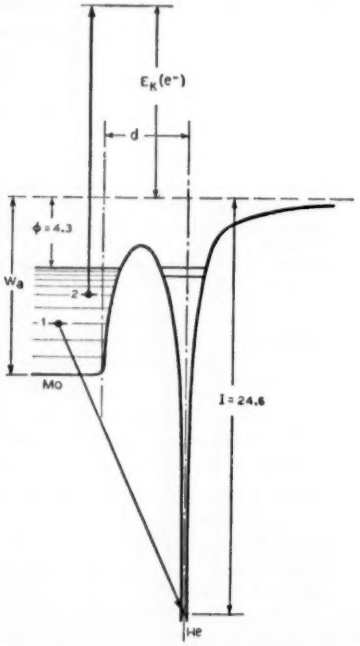

FIG. 2. Electronic transitions involved in the so-called direct process of potential ejection illustrated for He^+ on Mo. The ion is neutralized directly to the ground state with the simultaneous excitation of a second metal electron into the continuum. The metastable levels play no role.

[17] Because of rather drastic simplifying assumptions, calculations of total probabilities, or of the position at which a process proceeds with high probability, should perhaps be trusted only as to relative order of magnitude. Cobas and Lamb, as well as Massey in an earlier calculation (reference 6), used wave functions for the metal electrons which are taken to be zero outside the metal surface. Thus perhaps the most important part of the interaction is neglected. Shekhter used functions which extend outside the metal but found it necessary to simplify the calculations in other ways. Cobas and Lamb have pointed out an error in the matrix element used by Massey.

Theory of the two-stage electron ejection process by He^+ ions on Mo thus indicates that one electron should be excited into the continuum for each ion which strikes the metal surface and that electrons appearing outside the metal should have kinetic energies within the limits specified in Table III.

Shekhter has proposed the so-called direct process of potential ejection illustrated in Fig. 2. His calculation of the total probability of this process gave 0.1. Thus it is much less probable than the two-stage process which presumably predominates when neutralization by resonance capture can occur ($\phi < \epsilon < W_a$). The direct process is of considerable interest for ion-metal combinations for which $\epsilon < \phi$ where it is the only potential ejection process possible. The kinetic energy limits predicted by the direct process for He^+ incident on Mo are included in Table III and indicated on Fig. 13 even though the process is most likely not the predominant one in this case.

Oliphant and Moon[5] discussed neutralization of an ion on the basis of field emission induced by the ion and made the original proposal of the tunneling mechanism of resonance capture as an alternative. Shekhter[7] showed that neutralization of an ion to the ground state accompanied by radiation is very improbable ($\sim 5 \times 10^{-7}$). There have been no theoretical considerations of potential ejection mechanisms for He^{++} or He_2^+.

TABLE III. Kinetic energy limits of ejected electrons according to mechanisms of Figs. 1 and 2 evaluated for He^+ on Mo.

	Two-stage process (Fig. 1)	Direct process (Fig. 2)
$E_k(e^-)_{\min}$	$I - \epsilon - W_a = 9.0$ ev	$I - 2W_a = 3.0$ ev
$E_k(e^-)_{\max}$	$I - \epsilon - \phi = 15.5$ ev	$I - 2\phi = 16.0$ ev

III. EXPERIMENTAL APPARATUS AND PROCEDURE[18]

The apparatus with which the present experiment was conducted is depicted in Fig. 3. The instrument produces an ion beam, homogeneous in constitution, of total energy spread less than one electron volt. The kinetic energy of the beam at the target surface may be varied conveniently from 10 to 1000 ev. Beam currents are of the order of 5×10^{-10} amp of He^+, 2×10^{-11} amp of He^{++}, and 1×10^{-12} amp of He_2^+ over most of the kinetic energy range.[19]

It is essential to the success of the experiment that no ions strike the edges of the apertures in electrodes M_1, M_2, N, and S and that all ions strike only the target T inside the sphere. For this reason great care

[18] A more detailed account of the experimental apparatus and procedure than that given here is in preparation for submission to *The Review of Scientific Instruments*.

[19] The He_2^+ ions were produced in the ion source at high pressures by the secondary process investigated by J. A. Hornbeck and J. P. Molnar, Phys. Rev. **84**, 621 (1951).

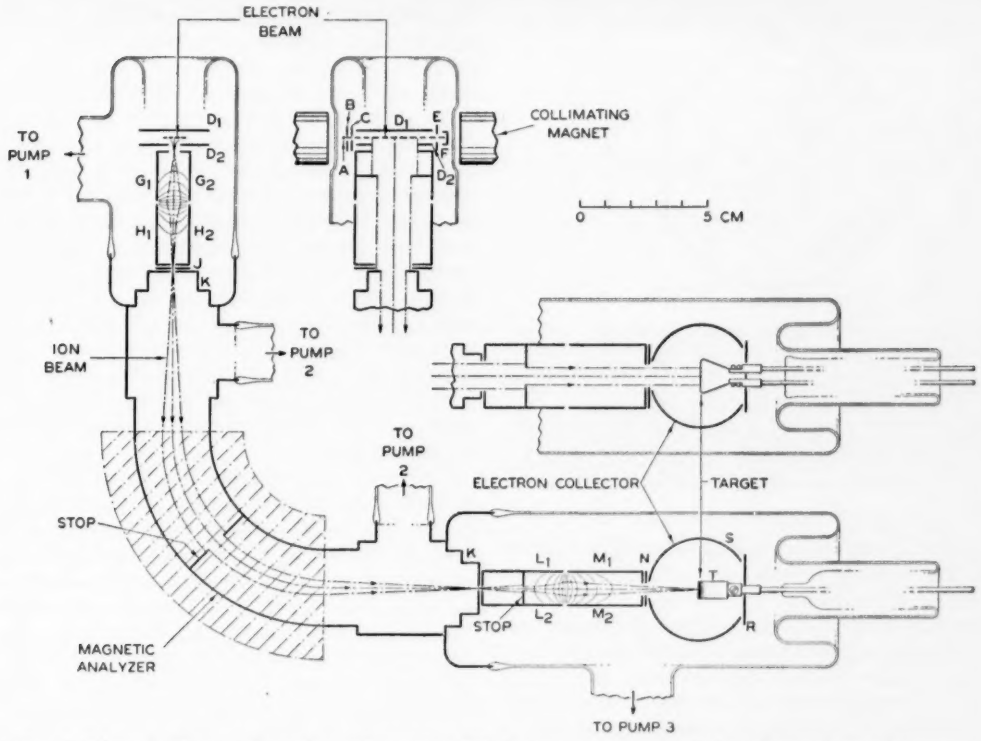

FIG. 3. Schematic diagram of experimental apparatus. The instrument is composed of an electron impact ion source (electrodes A to F), electrostatic ions lenses (G–H and L–M), a magnetic analyzer (K), the target (T), and the spherical electron collector (S). Equipotential lines are indicated in the G–H and L–M lenses. Views of ion source and target-collector ends at 90° from principal view are also shown.

was taken in the design of the $L-M$ lens and the stop between electrodes L_1 and L_2 to see that these conditions were met. Measurements in an auxiliary test apparatus[20] showed the focus to be such that 99.9 percent of the beam strikes within an area 0.2×0.8 cm at the target surface. Since the flat face of the target in the present instrument has the dimensions 0.7×1.4 cm, it is clear that the fraction of the ion beam which misses the target is entirely negligible. That the ion beam is considerably narrower than the target is further demonstrated by the constancy of the currents to S and T (with the current to electrode R equal to zero) for considerable sideways deflection of the beam in either direction by a cross voltage between electrodes M_1 and M_2. This cross voltage was always adjusted so that the beam passed through the center of the entrance aperture in S to strike the center of the target.

The target used in the present experiment was a Mo ribbon 0.0015 in. thick, formed as shown in Fig. 3. It could be heated to 1750°K in a time of the order of one second. Thus desorption of adsorbed gas directly from the target could be accomplished rapidly enough to make adsorption rate studies possible. The size of the target relative to the sphere was made as small as possible, consistent with the requirement that all ions strike it, so that the target-collector geometry would be suitable for determination of electron energy distribution functions by retardation between T and S.

The apparatus is evacuated by three independent two-stage mercury diffusion pumps through traps cooled by liquid nitrogen. Vacuum processing consisted of long periods of pumping with filaments and target hot, heating of the ionization manometer electrodes to red heat by bombardment, and torching of auxiliary glass parts. This was followed by extended pumping with the target cold except for the flashes of short time duration needed to clean it and to make the adsorption rate measurements. After starting the pumps several weeks of processing were needed before data taking commenced. Background pressures were then less than 4×10^{-9} mm Hg as measured with an ionization manometer of the type described by Bayard and Alpert.[21]

[20] Specifications on focus and energy homogeneity of the ion beam quoted here were determined with an apparatus like that of Fig. 3 except that the sphere and target are replaced by a slit system and plane parallel retardation chamber placed at the target position. This apparatus is to be reported on elsewhere (reference 18). It is in fact that used in the study of dissociative ionization by electron impact shown in Fig. 3 of H. D. Hagstrum, Revs. Modern Phys. **23**, 185 (1951).

[21] R. T. Bayard and D. Alpert, Rev. Sci. Instr. **21**, 571 (1950).

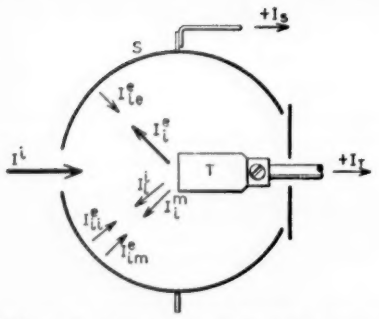

FIG. 4. Schematic diagram of target, T, and electron collector, S, showing primary, secondary, and tertiary particle currents which need to be considered in interpreting retarding potential measurements. The letters e, i, and m in sub- and super-scripts stand for electron, ion, and metastable atom, respectively. The superscript indicates the nature of the particle. For a secondary current the single subscript indicates the primary particle; for a tertiary current the subscripts indicate the primary and secondary particles, respectively. See explicit definitions of each symbol given in Table I.

Always the measured rate of adsorption of gas on the target was taken as the final test of the vacuum and target surface conditions.

Contact potential between target and electron collector was determined by retardation of the thermionic electron current emitted directly from the heated target. In making these measurements, the heating current was pulsed, and measurements made of thermionic current passed between the heating pulses in the manner described by Germer.[22] The primary, secondary, and tertiary currents which flow between S and T are depicted schematically in Fig. 4; the symbolic designations are defined in Table I.

IV. STATE OF THE TARGET SURFACE

For a surface sensitive phenomenon like potential ejection it is essential that one know the state of the target surface. This is emphasized by the observation that a monolayer of nitrogen forms on a tungsten surface in $\frac{2}{3}$ second at 10^{-6} mm Hg pressure.[23] It is clear that specification of evacuation procedure and target processing alone is not sufficient to demonstrate an atomically clean surface. Means for such demonstration is afforded, however, by the measurement of the rate of adsorption of gas upon the target surface.[24]

The measurement consists in observing the rise in pressure, Δp, accompanying sudden heating of the metal as a function of previous cold interval, Δt_c, during which the adsorption took place. The flashing of the target at the end of one cold interval and the beginning of another consisted of a 30-second flash followed by two 5-second flashes with one and two minutes cold interval between the first and second and the second and third of these flashes, respectively. This procedure was found to prevent the readsorption of desorbed gas by the target before such gas could be pumped out of the system. Δp was read on the first flash and the instant of cooling after the third flash marked the beginning of the next cold interval. Occasionally, the target was heated for longer periods, particularly after prolonged exposure to the residual gases, to remove absorbed gas and to degas the target supporting leads.

The result of adsorption rate measurements made with the instrument set up for γ_i measurements (He gas being admitted; ion source filament on) is shown in the lower graph of Fig. 5. The Δp *vs* Δt_c curve is seen to pass through a maximum just short of two hours after which the curve levels off to an adsorption rate (slope of the $\Delta p - \Delta t_c$ curve) much smaller than the initial rate. This result is interpreted as indicating the formation in 1.5 to 2 hours of a monoloayer by adsorption from the adsorbable gas component present in the instrument.[23] Simultaneous measurement of γ_i, plotted at the top of Fig. 5 shows a reduction of γ_i for 200-ev He^+ ions as gas covers the surface. The effect saturates when the surface is completely covered as indicated by the adsorption rate measurements. In obtaining these data, the Mo target was flashed to 1500°K.

The data of Fig. 5 were taken with He in the apparatus and the ion source filament on. The pressure of He in the target chamber (about 1/100 of that in the ion source chamber) was about 1×10^{-7} mm Hg. The adsorption rate therefore is determined by the amount of adsorbable impurity introduced with the He as well as the adsorbable component in the residual gas which is slowly desorbed from the internal parts and walls of the instrument itself. An adsorption rate about 20 percent less (monolayer adsorption time about 20 percent greater) was measured with no He being admitted and the ion source filament unheated. An order of magnitude calculation shows that this observation can be accounted for by the introduction with the helium of about 0.3 percent impurity, a not unreasonable amount.

The maximum in the $\Delta p - \Delta t_c$ curve was observed in all measurements in this work when the monolayer adsorption time was greater than about half an hour. This experimental result indicates that if the layer is left on the surface a longer time its later removal results

[22] L. H. Germer, Phys. Rev. **25**, 795 (1925).

[23] The term "monolayer" is used in this paper to denote the surface coverage at which the adsorption rate is observed to decrease from a relatively high constant value to a relatively low value. The time required to reach this condition from an atomically clean condition is termed the "monolayer adsorption time." The example quoted here is based on data of J. A. Becker and C. D. Hartman (private communication; paper submitted to J. Phys. Chem.). The monolayer adsorption time is determined by the kinetic theory rate at which molecules strike the surface, the observed initial sticking probability of 0.5, and the result that the sticking probability begins to fall from this initial constant value when the surface concentration of N atoms reaches 2.5×10^{14} per cm^2.

[24] L. Apker, Ind. Eng. Chem. **40**, 846 (1948). The method was brought to the author's attention in a public discussion of it by W. B. Nottingham in 1948. The author is indebted to his colleagures J. P. Molnar, J. A. Becker, and C. D. Hartman for helpful discussions concerning the adsorption rate measurements.

in a smaller number of gas atoms reaching the ionization gauge. Under these circumstances the remainder of the layer may possibly come off in a form more readily adsorbed or otherwise removed from the gas phase during the many collisions with the walls of the apparatus before reaching the ionization gauge. The effect may perhaps be the result of relatively slow surface migration and chemical rearrangement in the surface layer of more than one adsorbed molecular species. Or it may indicate the slow interaction of the surface layer with a second molecular species arriving at the surface from the surrounding gas. At these low pressures it is difficult to specify the nature of the adsorbable gas component. Earlier in the evacuation procedure, however, the residual gases present in the apparatus, as determined by m/e analysis, were found mainly at $m/e=28$ and 18 (presumably CO and H_2O) in about equal proportions. No ion current was detectable at $m/e=32$ (O_2).

The question remains whether the procedure adopted results in fact in an atomically clean Mo surface. Evidence already presented shows that a flash to 1500°K certainly removes adsorbed gas. To remove more tenaciously held atoms, if any were present, the target was heated to 1750°K for short intervals (minutes) periodically throughout the experiment. This treatment is held adequate to assure an atomically clean Mo surface on the following grounds: it is assumed that flashing to a temperature high enough to remove adsorbed oxygen cleans the metal of any contaminant likely to be present. Unfortunately there are no direct determinations of the temperature needed to remove oxygen from Mo. It is possible, however, to obtain a good estimate from the similar data for W and the observations of the relative temperatures of Mo and W at which several other surface phenomena take place. Langmuir's conclusion is that heating to 2200°K removes oxygen from W.[25] Measurements of degassing rate,[26] nitrogen desorption,[27] thorium evaporation,[28] and mobility of surface atoms[29] all show rates for Mo comparable to those for W when the Mo temperature is about 0.8 that of W. Finally, the work of Gulbransen and Wysong[30] on the evaporation of molybdenum oxides shows that the oxides can be removed readily by heating and that one need not fear a situation for molybdenum like that obtaining for aluminum whose oxides have a lower vapor pressure than the metal itself. For these reasons it was thought safe to conclude that oxygen will be removed from Mo at about 0.8 $\times 2200°K \cong 1750°K$ and that this temperature is sufficiently high to remove any other impurity atom from the Mo surface in this experiment. The value of γ_i measured immediately after a target flash (Fig. 5) is thus taken to be characteristic of the atomically clean metal.

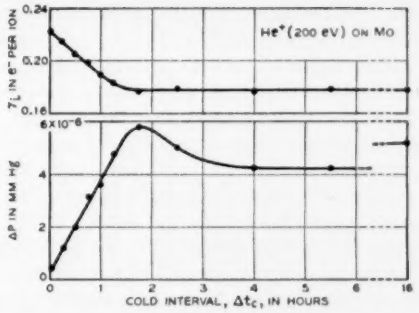

FIG. 5. Plots of γ_i (top) and Δp observed at flash (bottom) for the Mo target as a function of cold interval, Δt_c. He^+ ions of 200-ev kinetic energy were used in obtaining the γ_i data. The target was flashed to 1500°K. Both curves give evidence of a monolayer adsorption time of 1.5 to 2.0 hours. The γ_i value measured within a minute after flash is characteristic of atomically clean Mo, that observed after 2 hours characteristic of Mo with a monolayer of gas adsorbed upon it.

No polishing of the target ribbon was undertaken. The surface on inspection after removal appeared to be thermally etched, clean, and polycrystalline in nature.

V. ELECTRON YIELD (γ_i) AND ITS DEPENDENCE ON THE KINETIC ENERGY

The measurement of total electron yield, γ_i, is made with $V_{ST}=-5$ v. This assures collection of all ejected electrons since electrons are then accelerated to the electron collector. The results are plotted as functions of ion kinetic energy in Fig. 6. Measurements are reproducible to within 5 percent and it is believed that no systematic error of greater than this amount is present in the data.

There are several important features of the results of Fig. 6 to be discussed. First, the fact that γ_i is essentially independent of ion kinetic energy in the range 10 to 1000 ev is to be noted. This is a strong indication of the essential correctness of the potential ejection mechanism for ejection by each of the ions He^+, He^{++}, and He_2^+. The data lead one to expect that very slow ions,

[25] O_2 was found to affect thermionic emission from W at $T<2200°K$ [I. Langmuir, J. Am. Chem. Soc. **35**, 105 (1913)]. An oxygen film was removed at 2070°K at a rate such that half disappeared in 20 seconds [I. Langmuir and D. S. Villars, J. Am. Chem. Soc. **53**, 495 (1931)]. See also I. Langmuir, *Phenomena, Atoms and Molecules* (Philosophical Library, New York, 1950), p. 35 ff.

[26] F. J. Norton and A. L. Marshall, Trans. Am. Inst. Mining Met. Engrs. **156**, 351 (1944), report that with similar previous treatment the degassing rate of Mo at 2100°K is comparable to that of W near 2650°K.

[27] J. A. Becker and C. D. Hartman, private communication, observe that adsorbed nitrogen is completely removed at and above 1500°K from Mo, above 1800°K from W.

[28] M. Benjamin and R. O. Jenkins, Proc. Roy. Soc. (London) **A180**, 225 (1942), report that thorium starts to evaporate from Mo at 1700°K, from W at 2100°K. See also R. O. Jenkins, Rep. Prog. Phys. **9**, 177 (1942–43).

[29] From observations with the field emission microscope Benjamin and Jenkins (reference 28) find Mo atoms becoming mobile on Mo at 770°K, W on W at 1170°K. E. W. Müller, Z. Physik **108**, 668 (1938) quotes 1100°K for this latter temperature.

[30] E. A. Gulbransen and W. S. Wysong, Trans. Am. Inst. Mining Met. Engrs. **175**, 628 (1948).

of thermal velocities perhaps, would eject electrons with efficiencies comparable to those measured in this experiment. In this respect the present data agree with the results of previous workers. However, the results of Oliphant,[11] Rostagni,[12] and D'Ans, DaRios and Malaspina,[13] indicating a rise of $\gamma_i(He^+)$ to near unity or above in the vicinity of 1000-ev kinetic energy are not supported by the present results. The present results are more in agreement with the results of Penning[10] concerning the dependence of γ_i on ion kinetic energy for noble gas ions. The value of 0.17 for $\gamma_i(He^+)$ on Mo at low velocities obtained in previous studies[11-13] agrees well with the value obtained here (Fig. 6) for gas covered molybdenum. This is most likely an indication that the surfaces used in the earlier work were contaminated as the experimental procedure used would also lead one to expect.

A second feature of the data of Fig. 6 is the dependence of γ_i on the nature of the incident ion. Taking the data at low ion energies as representative of pure potential ejection it is seen that $\gamma_i(He^{++}):\gamma_i(He^+):\gamma_i(He_2^+)=0.72:0.25:0.13=2.9:1:0.52$. It is of interest to compare these ratios to the relative magnitudes of potential energy made available by the ion after its neutralization. Using the data of Table II one finds:

$$[I_2(He)-2\phi]:[I_1(He)-\phi]:[I^v(He_2)-\phi]$$
$$=[79.0-2\times 4.3]:[24.6-4.3]:[16.8-4.3]$$
$$=3.5:1:0.62.$$

This sequence of γ_i magnitudes, together with the observation that the average electron ejected by He^{++} is not much more energetic than that ejected by He^+ (Sec. VI), suggests that an ion ejects electrons at a metal surface by potential ejection approximately in proportion to the potential energy it can make available at the metal surface on neutralization. This would follow in the case of the doubly charged ion if the decay to the ground state were to proceed through a series of excited states of the singly charged ion and the neutral atom, one electron being excited into the continuum at each step. Sternberg[16] has pointed out that the spread of the wave function of an electron in a high lying excited state will make neutralization to such a state more probable than to a lower state thus favoring the "cascade" type of ejection mechanism for multiply charged ions.

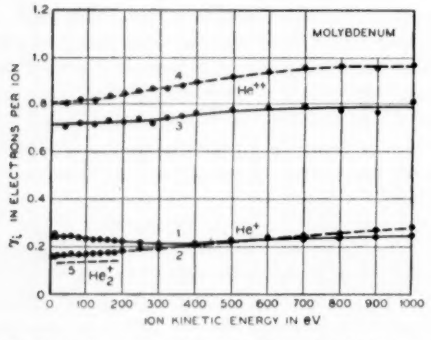

FIG. 6. Plot of experimental data giving total electron yield, γ_i, as a function of ion kinetic energy for the ions He^+ (curves 1 and 2), He^{++} (curves 3 and 4), and He_2^+ (curve 5) on Mo. Curves 1 and 3 are for atomically clean Mo, curves 2, 4, and 5 for Mo covered with a monolayer of gas. Data for He_2^+ lie within 30 percent of line 5.

There remains the possibility, however, that ejection by He^{++} consists of excitation of a single electron which then divides its energy among several other electrons as occurs in secondary emission by incident electrons. Under these circumstances one would expect $\gamma_i(He^{++})=\delta(70.4\text{ ev})$ since the electron formed by absorption of all the potential energy of He^{++} is the equivalent of a 70.4-ev electron entering from outside the metal surface. Bruining[31] has published data of Copeland on δ for Mo which show $\delta(70.4\text{ ev})\cong 0.7$. Thus, as far as magnitude is concerned, $\gamma_i(He^{++})$ could be explained in this way. However, in view of the results for He^+, one should perhaps expect at least a measurable proportion of the electrons excited inside the metal with maximum kinetic energy to be observed outside the metal. The fact that no electrons of energies greater than about 40 ev are observed from He^{++} in this work (Fig. 11) militates against this mechanism of potential ejection by multiply charged ions.

A third point of interest is the magnitude of $\gamma_i(He^+)=0.25$ for slow ions and what it means in view of the theoretical conclusion that one electron is excited into the kinetic energy continuum for each incident He^+ ion. First it should be pointed out that this conclusion is supported by the observation that the quantity R is small, indicating that few ions incident normally to the surface are reflected as ions or metastable atoms. Since radiative neutralization has also been shown to be small,[7] it is difficult to escape the conclusion that one electron is in fact excited into the kinetic energy continuum by each incident ion. The value of γ_i which results depends then solely on the probability, P, that the excited electrons will escape from the metal. We shall assume throughout this discussion that the velocity vectors of the excited electrons are randomly directed.

If the excited electrons start from a point outside the metal surface, as the representation of stage 2 in Fig. 1 suggests, the probability of escape, P, should be at least 0.5 since the electrons which enter the metal may be partially reflected or may excite other electrons which escape. If the electrons were freed inside the potential barrier at the metal surface the possibility of internal reflection at the barrier would reduce P below 0.5.

It can be shown that an electron of total kinetic energy E_k inside the metal incident on a barrier of

[31] H. Bruining, *Die Sekundär-Elektronen-Emission fester Körper* (Springer-Verlag, Berlin, 1942), Fig. 30, p. 22. The author is indebted to his colleague K. G. McKay for a helpful discussion of this point.

height W_a will be internally reflected if its velocity vector makes an angle, θ, with the surface normal greater than $\theta_c=\cos^{-1}(W_a/E_k)^{\frac{1}{2}}$ (see Fig. 7). An electron incident at $\theta<\theta_c$ can escape. The probability of escape can be determined by integration over the solid angle included in the cone of semi-angle θ_c about the surface normal. Thus

$$P=(1/4\pi)\int_0^{\theta_c} 2\pi \sin\theta d\theta=\tfrac{1}{2}(1-\cos\theta_c)=\tfrac{1}{2}[1-(W_a/E_k)^{\frac{1}{2}}].$$

For the two stage process of Fig. 1 electrons could be excited inside the metal to total kinetic energies, E_k, in the range $I-\epsilon$ to $I-\epsilon+W_i$. Using the constants characteristic of He^+ and Mo, the probability P ranges from 0.13 to 0.18. γ_i, which represents an average of P over all possible excited electrons, would lie somewhere within this range if all electrons start inside the metal. The experimental observation of $\gamma_i=0.25$ then suggests that the excited electrons start from a point only part way inside the potential barrier of the metal. This conclusion is compatible with the process of Fig. 1 if the second stage occurs when the atom has penetrated into the potential barrier.

The mechanism proposed above which reduces γ_i below the value 0.5 is internal reflection of electrons incident on the barrier at greater than a critical angle to the surface normal. The quantum-mechanical reflection of electrons incident normally to the barrier and having kinetic energy greater than the barrier height is negligible for the 20-ev electrons encountered here.[32] The above picture of release of the ejected electron inside the metal barrier is not to be confused with the suggestion of Oliphant and Moon[5] that ions may be neutralized inside the metal surface nor with Massey's conjectures[6] (later disputed by Cobas and Lamb[8]) concerning emission of electrons in a cone at the metal surface. Shekhter's objection[7] to the unity transition probability calculated for the potential ejection process of Fig. 1 on the grounds that the measured γ_i is much less than unity appears not to be valid.

The transit time for an ion through the experimental apparatus from ion source to target is about 0.5 microsecond. Any excited ion would certainly decay to its ground state by radiation early in its transit through the instrument. Thus no effect on γ_i of excited ions or radiation from such ions is expected.

The potential ejection by He_2^+ is conceived to proceed by neutralization of He_2^+ resulting in dissociation to two normal He atoms. The energy by which the ground state of He_2^+ lies above the repulsive potential curves of He_2 at the same nuclear separation is recovered and used to extract the neutralizing electron and to excite a second electron (see reference c of Table II).

[32] L. A. MacColl, Bell System Tech. J. **30**, 888 (1951), Fig. 4. See discussion in C. Herring and M. H. Nichols, Revs. Modern Phys. **21**, 185 (1949), Sec. IV. 4.

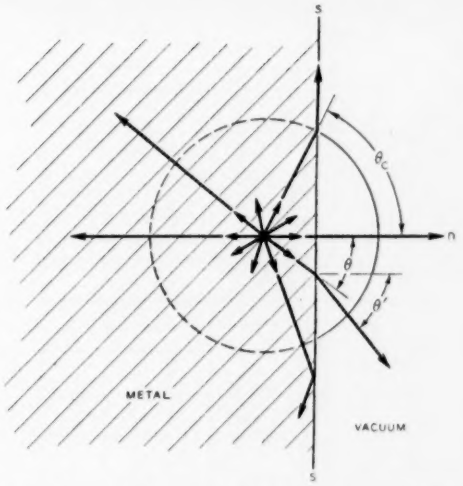

FIG. 7. Schematic diagram of refraction and internal reflection at a metal surface (S–S) of electrons excited into the kinetic energy continuum inside the metal surface barrier with velocity vectors randomly directed. The figure holds for any plane containing a normal (n) to the surface. θ_c is the critical angle for total reflection inside the metal. An electron directed at an angle θ to the surface normal will escape at an angle $\theta'>\theta$ if $\theta<\theta_c$.

VI. ELECTRON ENERGY DISTRIBUTIONS

The kinetic energy distributions of ejected electrons have been determined in this work by applying retarding potentials between target and electron collector. Retarding potential curves for electrons ejected by He^+ ions of 40-, 200-, and 1000-ev energy are plotted in the top graphs of Figs. 8, 9, and 10, respectively. In the lower graphs of these figures are plotted the slopes of the retarding potential curves giving the energy distribution functions. Data are given for atomically clean Mo and for Mo covered with a monolayer of gas. Corresponding retarding potential and energy distribution curves for electrons ejected by 80-ev He^{++} ions are shown in Fig. 11.

The retarding potential curves are plots of the quantity $\rho=I_S/(I_T+I_S)$ *versus* V_r, the retarding potential between electrodes S and T corrected for the contact potential as determined by retardation of thermionic electrons emitted from the heated target (see Fig. 12). Satisfactory interpretation of the $\rho(V_r)$ curves demands consideration of the behavior with respect to V_r of the various space currents which may flow between electrodes S and T. These are the currents defined under the heading "Particle Currents" in Table I and depicted in Fig. 4.

We consider first singly charged ions ($z=1$). For V_r sufficiently negative (S positive re: T) the current I_i^e is collected at S *in toto*, but the currents I_i^i, I_{ie}^e, I_{ii}^e, and I_{im}^e are completely suppressed making $I_S=-I_i^e$ and $\rho=-\gamma_i=-I_i^e/I^i$. On the other hand, for V_r sufficiently positive, I_i^e is retarded out leaving only the secondary and tertiary currents which result from

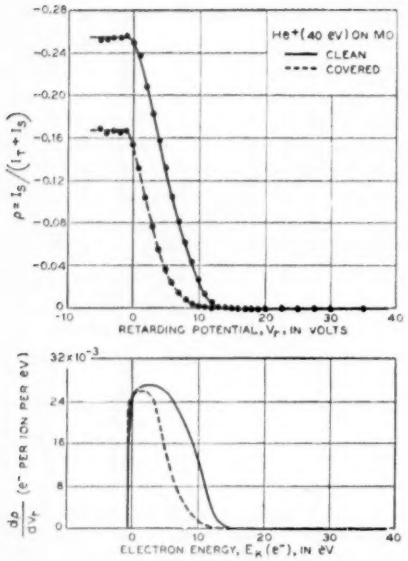

FIG. 8. Retarding potential curves (top) and electron energy distribution functions derived from them (bottom) for electrons ejected by 40-ev He^+ ions from clean Mo and from Mo covered with a layer of adsorbed gas.

reflection of primary ions as ions or metastable atoms. Thus, for singly charged ions $I_S = I_i^i + I_{ii}^e + I_{im}^e$ and $\rho = R = R_{ii} + \gamma_i' R_{ii} + \gamma_m' R_{im}$. These extreme values of ρ are indicated in Fig. 10 where R has the largest observed value.

Between the extremes of V_r discussed above, $\rho \cong -f_k\gamma_i + R$. The approximate equality in this expression is necessary because ρ is distorted by other effects such as the variability of δ' with V_r, the loss of electrons through the entrance aperture, and the distortion resulting from the failure of the target-collector geometry to meet the point-sphere ideal. The first two of these effects are small in this experiment, of the order of a few percent at most, and will not be discussed further here. The third effect represents a possibly more serious distortion of the energy distribution function. It is introduced by the fact that the target, though small relative to the collector sphere, is nevertheless plane. This tends to make electrons appear to

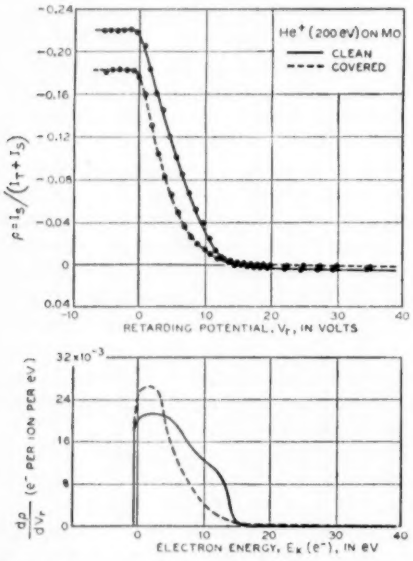

FIG. 9. Retarding potential curves (top) and energy distribution functions derived from them (bottom) for electrons from 200-ev He^+ ions on clean and covered Mo.

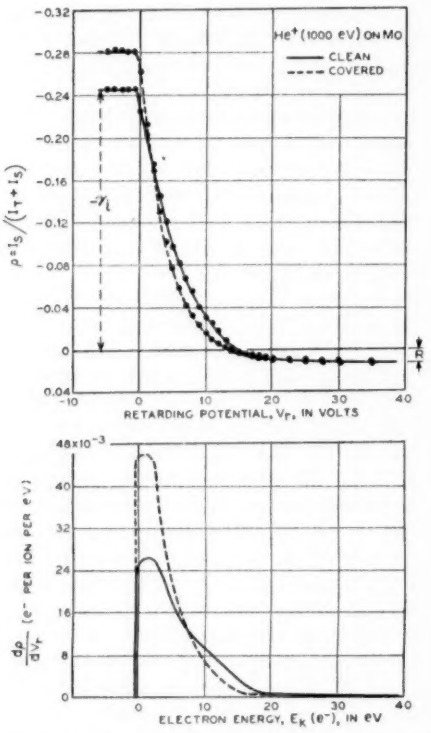

FIG. 10. Retarding potential curves (top) and energy distribution functions (bottom) for electrons from He^+ ions of 1000-ev energy at the target.

have smaller energies than they really do since the plane parallel retardation near the target operates only on the normal component of the electron's velocity. Electrons for which θ' (Fig. 7) is near 90° will be returned to the metal at much smaller V_r than $E_k(e^-)$. An energy distribution may thus appear to include electrons of zero energy even though, in fact, it does not. To the extent this limitation can be neglected the energy distribution function is $d\rho/dV_r = -\gamma_i(df_k/dV_r)$ for $V_r > 0$ since in this region R is constant.

ρ *versus* V_r does not saturate at $V_r = 0$, resulting in $d\rho/dV_r$ having a value for a limited range with $V_r < 0$, because of retardation of the secondary ionic and

tertiary electronic currents in this region and the acceleration to S of electrons lost through the entrance aperture when the field is zero or retarding (see Fig 12). The rapid saturation of ρ with decreasing V_r, however, indicates that the tertiary electronic currents soon have difficulty in finding the small target against a retarding field and that the reflected ions are of low velocity. R is constant for $V_r>0$ because the secondary ionic and tertiary electronic currents are then accelerated from one electrode to the other.

For doubly charged ions $z=2$ and γ_i expressed in electrons per incident ion is equal to $z\rho=2\rho$ for V_r sufficiently negative. Secondary and tertiary currents can flow when the current I_i^e is suppressed in this case also. These currents result from reflection of the doubly charged ion as a doubly charged ion, a singly charged ion, or a neutral atom, the latter two possibly excited. They were found to be very small in this experiment (Fig. 11).

No significant change in the form of the kinetic energy distribution function for electrons from He^+ is seen to occur with increasing ion energy (Figs. 8, 9, and 10). This is to be expected from the theory of

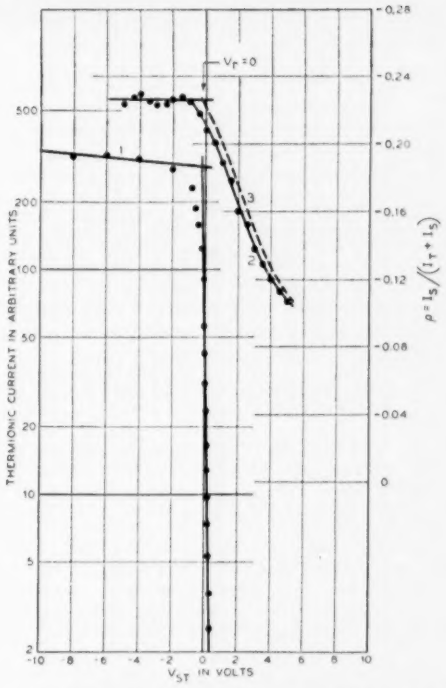

FIG. 12. Data for determination of contact potential between target and electron collector (electrodes T and S, respectively) in the experimental apparatus. Curve 1 shows the variation with V_{ST} of the current of thermionic electrons emitted from the heated target. The crossing of the extrapolated straight line portions of this curve determines the point of zero field at $V_{ST}=-0.2$ volt. Curve 2 is a part of the retarding potential curve for electrons from 200-ev He^+. Why it saturates at negative values of the corrected retarding potential $V_r(=V_{ST}+0.2$ ev in this case) is explained in Sec. VI of the text. Curve 3 is representative of the curve as it would appear if the effects of secondary and tertiary currents and electron loss through the entrance aperture in S could be corrected for.

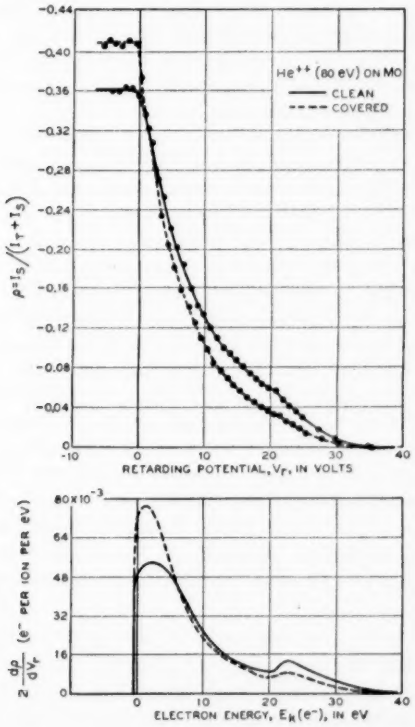

FIG. 11. Retarding potential curves (top) and electron energy distribution functions derived from them (bottom) for He^{++} ions of 80-ev energy incident upon clean Mo and upon Mo covered with a layer of adsorbed gas. Note that the energy distribution in number of electrons per incident ion per electron volt energy range is $2(d\rho/dV_r)$ for He^{++} since the ion is doubly charged ($z=2$).

potential ejection although kinetic ejection might conceivably result in a similar independence of distribution function and ion energy. The theory of potential ejection has not been developed to the point where a reliable distribution function can be derived. However, the two stage process of Fig. 1, which theory indicates is the predominant one, should yield the same electron energy distribution function for He^+ ions incident on a metal surface as is observed for the metastable atoms, He^M.[33] The distributions observed for He^+ are in approximate agreement with the distributions observed by Oliphant[14] and Greene[15] for electrons from He^M. In particular, in agreement with Greene, it seems difficult to account for the observed distribution for He^+ as being Maxwellian and resulting from thermal emission of the electrons.[34] There are serious discrepancies be-

[33] This conclusion is supported by the Townsend discharge measurements of J. P. Molnar, Phys. Rev. **83**, 940 (1951), which show $\gamma_i(A^+)$ and $\gamma_m(A^M)$ on several targets to be closely equal.

[34] A theory of thermal emission of electrons from a spot on the target surface heated by dissipation of the ion's *kinetic* energy

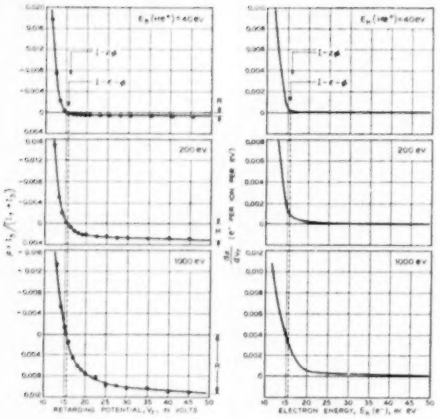

FIG. 13. Portions of the retarding potential curves of Figs. 8, 9, and 10 near the upper electron energy limit plotted (left) to an extended ordinate scale and the corresponding portions of the energy distribution functions (right). Energy limits predicted by the two potential ejection mechanisms discussed in the text in Sec. II are indicated above the top curves. Definition of the quantity R in terms of ejection and reflection coefficients is given in Table I. Note the agreement of the upper limit with theory at low $E_k(\mathrm{He}^+)$, and the increase in R and the appearance of electrons of energies beyond the theoretical limits with increase in $E_k(\mathrm{He}^+)$.

tween the distributions of electrons ejected by He^+ observed by Oliphant[11] and those observed in this work, however.

The effect of a layer of adsorbed gas atoms on the target surface is seen to reduce the number of fast electrons relative to the number of slow electrons. It appears to be true at ion energies for which γ_i increases or decreases from clean to covered target. The adsorbed layer does not appreciably shift the break in the retarding potential curves near $V_r=0$. A careful measurement shows the shift of the break and hence the variation of target work function to be no more than a few tenths of an electron volt.

In the distribution of electrons from He^{++} (Fig. 11), there is evidence of electrons having energies beyond 30 ev but none detectable which received all the energy available by neutralization of He^{++} directly to the ground state of He. On the other hand the mean energy of about 8 ev for electrons from He^{++} (compare the approximate 6-ev mean for electrons from He^+) would indicate sharing of the potential energy with several electrons as discussed in Sec. V. The structure observed in the distribution function of Fig. 11 remains unexplained.

was proposed by P. L. Kapitza, Phil. Mag. **45**, 989 (1923) and discussed further by N. D. Morgulis, J. Exptl. Theor. Phys. (U.S.S.R.) **4**, 449 (1934); **9**, 1484 (1939); **11**, 300 (1941), and by S. V. Izmailov, J. Exptl. Theor. Phys. (U.S.S.R.) **9**, 1473 (1939). The theory does not account for the observed dependence of kinetic ejection on work function [H. Paetow and W. Walcher, Z. Physik **110**, 69 (1938)] nor the dependence on ion mass of kinetic ejection by isotopic ions [W. Ploch, reference 4].

VII. LIMITS OF KINETIC ENERGY OF EJECTED ELECTRONS

It is the purpose in this section finally to discuss the observed limits of ejected electron energy in the light of the predictions of theory.

All experimental observations of the lower energy limit show it to be zero. As has been pointed out this can result, in part at least, from the plane geometry of the target surface. Calculation of the apparent energy distribution function as would be measured in plane parallel geometry for the case represented in Fig. 7 indicates that this effect alone cannot account entirely for the experimentally observed form of the distribution function. It seems further necessary to assume that electrons suffer energy losses on leaving the metal, a conclusion perhaps not at variance with the observation that adsorbed gas on the surface decreases the relative number of fast electrons.

The present work agrees with Greene's observation[15] of electrons of zero energy released by He^M. Of Greene's four possible reasons for this observation, those attributing it to incorrect values of W_a or of contact potential can no longer be entertained. No serious error in the value of W_a given in Table II seems possible. Contact potential was measured in this experiment. The behavior of γ_i with $E_k(\mathrm{He}^+)$ makes improbable the third reason attributing the electrons near zero to kinetic ejection. Energy loss at the metal surface remains the most probable explanation.

Oliphant's conclusion[14] that no electrons of energy less than 1.9 ev are ejected by He^M is most likely to be attributed to a failure of his method of determining the contact potential between target and electron collector. Oliphant's energy distributions for electrons from He^+ on Mo[11] show electrons of zero energy but possess other characteristics very difficult to explain. Evidence is presented by Oliphant of electrons in quantity having energies in excess of 20 ev. To account for these electrons, Oliphant and Moon[5] proposed the possibility of ions being neutralized inside the potential barrier of the metal where they could eject electrons of maximum energy $I-\phi=20.3$ ev. Theory of the predominant two stage process predicts a maximum energy of 15.5 ev (Table III). The present results do not support the view of Oliphant and Moon. It is perhaps possible to explain Oliphant's result if his ion beam (not m/e analyzed) contained an appreciable admixture of He^{++} ions.

In Fig. 13 retarding potential data in the vicinity of maximum electron energy are plotted to an extended ordinate scale. From these graphs three interesting conclusions may be drawn: (1) At low $E_k(\mathrm{He}^+)$ a rather well defined upper limit of $E_k(e^-)$ is observed agreeing well with the predictions of theory. (2) As $E_k(\mathrm{He}^+)$ is increased the quantity R ($=\rho$ at large positive V_r) is seen to increase indicating greater reflection of ions as ions and metastable atoms at higher

ion energies. (3) Small numbers of electrons possessing energies in excess of the theoretical limits are produced as the incident ion energy is increased. This last conclusion is based on the assumption that R is independent of V_r in this region. This is eminently reasonable since the incident ion energy at the target surface is independent of V_r and all secondary and tertiary currents resulting from reflection of ions as ions or metastable atoms are then accelerated by V_r. Changes in slope of the $\rho(V_r)$ curve are thus attributed to retardation of the electron current (I_i^e) ejected by the primary ion current. It should be noted that the number of electrons observed beyond $V_r=15.5$ v is very small representing at most only about 1 percent of all electrons ejected by 1000-ev He^+.

In view of all other aspects of the phenomenon, the electron current observed at $V_r>15.5$ v is most probably the result of potential ejection occurring when the incoming atom is very close to the metal surface where the atomic energy levels are shifted by the proximity of the metal. The theories discussed in Sec. II all assume the energy levels of the atomic particle to be undisturbed on approach to the metal surface. Considerations of the potential energy of interaction of the particles He, He^M, and He^+ with the surface atoms of a metal show that the levels must shift and that electrons faster than the limits $I-\epsilon-\phi$ could be produced by final decay of the metastable atom very close to the metal surface. The effect would be expected to become more pronounced at higher ion energies because the probability of decay at greater distances from the metal is reduced in inverse proportion to the ion's velocity.

Another possible explanation of the electrons having $E_k(e^-)>I-\epsilon-\phi$ attributes them to kinetic ejection by the incident ions or by the normal atoms resulting from ion neutralization. The probability of ejection by this mechanism would also be expected to increase with increasing ion energy as is observed.

The maximum energy of electrons produced by ions incident on a gas covered surface appears, in Fig. 8 for example, to be less than that for a clean surface. This is not the case; the appearance of the curves of Fig. 8 results from the much smaller number of faster electrons produced at the gas covered surface. If the data are plotted to relative ordinate scales which make the slopes of the curves appear equal at $V_r=10$ v, breaks like those at the upper left of Fig. 13 appear in both curves at the same energy. This is in agreement with the observation recorded above that the adsorbed layer changes the work function of the target by at most a few tenths of an electron volt.

The author wishes to express his gratitude to his colleagues C. Herring, J. A. Hornbeck, J. P. Molnar, G. H. Wannier, and A. H. White for helpful discussions during the course of the work; to H. W. Weinhart under whose supervision the experimental tube was constructed; and to F. J. Koch for technical assistance.

Paramagnetic Resonance Absorption in Salts of V and Mn†

CLYDE A. HUTCHISON, JR., AND LEONARD S. SINGER*
Institute for Nuclear Studies and Department of Chemistry, University of Chicago, Chicago, Illinois
(Received July 29, 1952)

Paramagnetic resonance absorptions in tetravalent, trivalent, and divalent salts of V and in a divalent salt of Mn have been investigated at room temperature and at a frequency of 9.2×10^9 sec^{-1}. A detailed study has been made of the absorption in single crystals of the Tutton salt of V^{+2} as a function of orientation. The results have been interpreted on the basis of crystalline electrostatic fields.

INTRODUCTION

WE have carried out an investigation of paramagnetic resonance absorption at a frequency of 9.2×10^9 sec^{-1} and at room temperatures in tetravalent, trivalent, and divalent salts of V and in a divalent salt of Mn. We have studied in particular detail the case of the Tutton salt of divalent V. During the preparation of our results for publication there appeared the work of Bleaney, Ingram, and Scovil[1] on this same salt at a frequency of 2.3×10^{10} sec^{-1}. We consequently present here an abbreviated account of our work.[2]

EXPERIMENTAL WORK

Preparation of Powders

The tetravalent salt of V studied was a commercial product labeled cp, G. Frederick Smith and Company $VOSO_4\cdot2H_2O$, which was dried at 110°C for 24 hr. Analysis showed that this salt contained no other transition elements and no other valence states of V, but did contain small amounts of $(NH_4)_2SO_4$ and H_2SO_4.

TABLE I. Description of cylindrical crystals.

Crystal No.	Weight g	Density g cm^{-3}	% V	% of metal atoms which are V	Angle between cylindrical axis and a-axis	b-axis (Symmetry axis)	c-axis
1							
Outer section	0.2554	···	4.64	36.1	···	···	···
Middle section	0.3307	···	4.54	35.3	···	···	···
Inner section	0.1709	···	4.81	37.4	···	···	···
Whole crystal	0.8217	1.898	4.66	36.3	0.500π	0.000	0.500π
2	0.6009	1.894	4.66	36.3	0.068π	0.500π	0.524π
3	0.5559	1.894	4.66	36.3	0.068π	0.500π	0.524π
4	0.8080	1.895	4.52	35.2	0.568π	0.500π	0.024π

† Assisted by the ONR.
* Now at the Naval Research Laboratory, Washington, D. C.
[1] Bleaney, Ingram, and Scovil, Proc. Phys. Soc. (London) **A64**, 601 (1951).
[2] For detailed paper (or extended version or material supplementary to this article) order Document 3731 from American Documentation Institute, 1719 N Street, N.W., Washington 6, D. C., remitting $2.30 for microfilm (images 1 inch high on standard 35-mm motion picture film) or $22.80 for photocopies (6x8 inches) readable without optical aid.

Two trivalent salts of V were prepared[3] by reduction of a solution of cp V_2O_5 in H_2SO_4 to the tetravalent state with SO_2 followed by electrolytic reduction to the trivalent form and precipitation with concentrated H_2SO_4. This produced a salt which analysis showed to have composition very close to $V_2(SO_4)_3\cdot2H_2SO_4\cdot6H_2O$ and to contain no other valence states of V. Heating of this salt under reduced pressure produced a second material containing 19.7 percent V instead of 14.8 percent which the initial preparation contained.

The divalent Tutton salt, $V(NH_4)_2(SO_4)_2\cdot6H_2O$ was prepared in solution by a method similar to that of Meyer and Aulich.[4] The solution was evaporated on a vacuum line to give a solid product which analysis showed to have the composition V, 13.1 percent; SO_4, 51.2 percent; mole SO_4/mole V, 2.07. The theoretical composition is V, 13.2 percent; SO_4, 49.2 percent; mole SO_4/mole V, 2.00. Successive oxidations with $KMnO_4$ and reduction with SO_2 showed that of the total V, a maximum of 11 percent V^{+3} or 6 percent V^{+4} or 4 percent V^{+5} or some equivalent combination of the three was present.

Preparation of Crystals

Single crystals of $V(NH_4)_2(SO_4)_2\cdot6H_2O$ were prepared from aqueous solution by the method of Holden.[5] Since V^{+2} reduces H_2O, it was necessary to add amalgamated Zn to the solutions from which the crystals were grown in order to keep the V in the divalent state for the several weeks required for growth. This introduced Zn^{+2} into the crystals. The monoclinic Tutton salts of V^{+2} and Zn^{+2} are isomorphous. The descriptions of four such mixed crystals of the Tutton salts of Zn and V, after grinding to right circular cylinders are given in Table I.

Goniometric measurements on the mixed monoclinic crystals gave a value of 106° 16′ for the β-angle between the a and c axes and 0.737:1.000:0.496 for the axial ratios, $a:b:c$. These are very close to the values found for the Tutton salts of Ni, Mg, Zn, and Fe.[6] The a, b,

[3] A. Stahler and H. Wirthwein, Ber. deut. chem. Ges. **38**, 3978 (1905).
[4] J. Meyer and M. Aulich, Z. anorg. u. allgem. Chem. **194**, 278 (1930).
[5] A. N. Holden, Disc. Faraday Soc. No. 5, 312 (1949).
[6] *Strukturbericht*, edited by C. Hermann *et al.* (Becker and Eiler, Leipzig), Vol. 2 (1928–32), p. 436.

and c axes will throughout this paper be taken as forming a right-hand set.

After goniometric alignment a surface grinder was employed to produce a plane surface on the crystal normal to the desired direction of the cylindrical axis. This plane surface was then cemented to a holder and a right circular cylindrical surface was ground. At least one crystal edge was left on the end opposite the plane. This was employed to mount the cylindrical crystal on a crystal holder at a known angle of rotation about the axis with respect to the graduated head of the holder. The dial reading of the crystal holder could thus be correlated with the angles between axes of the crystal and the direction of the alternating and the static magnetic fields. The maximum error in the determination of angles throughout this work is approximately 0.010π.

Crystals of $Mn(NH_4)_2(SO_4)_2 \cdot 6H_2O$ were prepared and mounted in the same manner as described for the case of the V salt. Crystal 1 was the pure Mn salt with the cylindrical axis parallel to the b axis.

Apparatus

The right circular cylindrical crystals were mounted in a transmission cavity in the form of a rectangular box operated in the TE_{102} mode at a frequency of approximately 9×10^9 sec^{-1}. The cylindrical axis was maintained parallel to the broad face of the guide and perpendicular to the narrow face and the longitudinal axis of the guide. The holder was graduated and rotatable so that the crystal could be rotated through known angles about its axis.

The klystron was modulated at an audiofrequency with a square wave and the detected transmitted microwave power was amplified with a tuned amplifier. The detected output of the amplifier was either read from a meter or recorded with a recording potentiometer. The magnetic field was measured as a function of current using the proton resonance. Magnetic fields as determined by measurement of the current were reproducible to 0.1 percent.

RESULTS

Tetravalent V

This powder showed a single strong resonance absorption with a maximum corresponding to a g factor of 1.96 and a width at half-maximum absorption of 180 gauss.

Trivalent V

No magnetic resonance absorption was observable in either of the two preparations.

Divalent V

The powder gave the rather complicated absorption shown in Fig. 1.

Crystal 1 was oriented such that the a axis, c axis, direction of propagation of microwaves and direction of static field were coplanar. In Fig. 2 are shown the absorptions for various values of ψ. ψ is the angle of rotation of the c axis away from the direction of propagation of microwaves in the sense in which a right hand screw would be turned to advance it along the b axis of the crystal. Plotted on the vertical axis is the quantity $(B-A)/(B-Z)$, in which A is amplifier output at field strength H; B is amplifier output at very high field strength; Z is amplifier output with infinite attentuation in microwave transmission line. A second crystal cut in the same manner and not described in Table I gave results in agreement with those of Fig. 2.

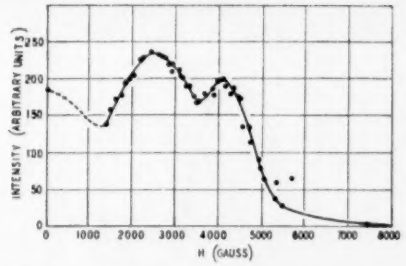

FIG. 1. Experimental intensity of absorption as a function of magnetic field strength.

Crystal 3, cut as stated in Table I, was examined at 26 different values of the angle η between the b axis and the direction of the static magnetic field. The absorptions were recorded by a recording potentiometer. Measurements on crystal 2 were in agreement with those on crystal 3.

Absorptions due to crystal 4 at 23 different values of the angle σ, between the b axis and the direction of propagation of microwaves in the wave guide were recorded.

A crystal in which only 7.4 percent of the metal ions were V gave, when rotated about its b axis, essentially the same absorption curves as crystal 1.

Mn

Crystal 1 gave the absorptions shown in Fig. 3.

INTERPRETATION OF RESULTS

Powders

The observations on the paramagnetic resonance absorption of the various oxidation states of V are consistent with the rule of Kramers.[7]

Crystals

a. Calculations

We have employed for the interpretation of the data the model employed by Hebb and Purcell;[8] Weiss, Whitmer, Torrey, and Hsiang;[9] Whitmer, Weidner,

[7] H. A. Kramers, Proc. Roy. Acad. Amsterdam **4**, 871 (1937).
[8] M. H. Hebb and E. M. Purcell, J. Chem. Phys. **5**, 338 (1937).
[9] Weiss, Whitmer, Torrey, and Hsiang, Phys. Rev. **72**, 975 (1947).

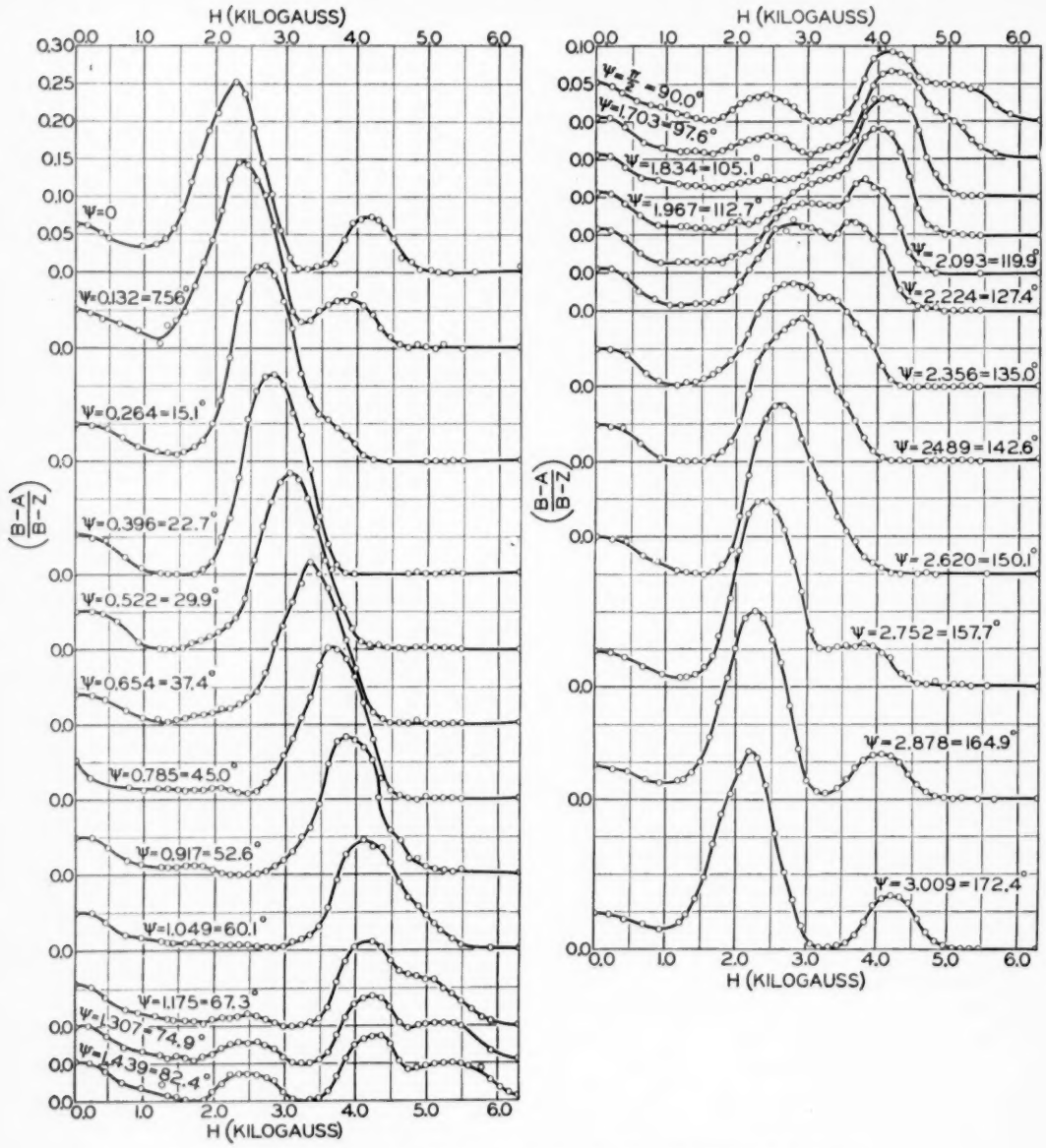

FIG. 2. Experimental intensity of absorption as a function of magnetic field strength.

and Weiss;[10] Bleaney, Penrose, and Plumpton[11] and others in the interpretation of the magnetic properties of alums and Tutton salts. The Hund ground state of V^{+2} is ^4F. The crystalline structure is assumed similar to that known for the Mg salt,[12] and the space group is assumed to be C_{2h}^5. The large electric field of the nearly octahedral arrangement of H_2O dipoles results in a Γ_2 ground state with only spin degeneracy.[13] A small axial electric component, due to distortion of the octahedron, combined with spin-orbit coupling is assumed to result in a further splitting of the Γ_2 state by an amount δ with only the Kramers degeneracy remaining to be removed by the static magnetic field. There are two inequivalent V^{+2} ions per unit cell. The axial electric fields for these two ions differ only with respect to the angle which they make with the b axis of the monoclinic

[10] Whitmer, Weidner, and Weiss, Phys. Rev. **73**, 1468 (1948).
[11] Bleaney, Penrose, and Plumpton, Proc. Roy. Soc. (London) **A198**, 406 (1949).
[12] W. Hoffman, Z. Krist. **78**, 279 (1931).
[13] H. A. Bethe, Ann. Physik **3**, 133 (1929).

crystal, the one being a reflection of the other in a plane perpendicular to the b axis. The secular equation[9,10,14] of the combined axial electric-spin-orbit and magnetic perturbations is

$$\epsilon^4-\tfrac{1}{2}\epsilon^2(1+20x^2)+4\epsilon x^2(1-3\cos^2\theta)+1/16+9x^4+\tfrac{1}{2}x^2-3x^2\cos^2\theta=0.$$

In this equation $x=g\beta H/2\delta$, $\epsilon=E/\delta$, θ is the angle between the magnetic field and the electric axis, and E is the eigenvalue of the energy. For three values of θ, 0, $\cos^{-1}(1/\sqrt{3})$, and $\pi/2$, this equation factors into two quadratics. For other values of θ, since the equation is quadratic in x^2, we may easily calculate the eigenvalues of the energy *versus* static field strength in terms of the one parameter δ. We calculated such energy level curves (ϵ *versus* x) for θ ranging from 0 to $\pi/2$ at intervals of about every $\pi/24$. We have also graphed the $\Delta\epsilon$'s *versus* x and the values of H for maximum absorption (resonance) *versus* δ for the same values of θ as an aid in the interpretation of the results. Moreover, we have also calculated the perturbed eigenstates and the matrix elements of J_z and of $J_+=J_x+iJ_y$ as functions of x, where the z axis is the axis of the axial electric perturbation.[14] From these we have calculated for several values of the angle θ, the value of

$$\begin{aligned}|(M'|J_{z'}|M)|^2=&(M'|J_z|M)\cos^2\xi\\&+\tfrac{1}{4}\cos^2\xi\cot^2\theta[(M'|J_+|M)+(M'|J_+|M')]^2\\&+\tfrac{1}{4}\cos^2\beta\csc^2\theta[(M'|J_+|M)-(M|J_+|M')]^2\\&-(\cos^2\xi)(\cot\theta)(M'|J_z|M)[(M'|J_+|M)\\&+(M|J_+|M')]\end{aligned}$$

as a function of x. This is the square of the matrix element of the component of the angular momentum along the z' axis in a new system of coordinates oriented as follows with respect to the set x, y, z (in which J was expressed): z' is the direction of the high frequency magnetic field, y' is the direction of the static magnetic field and x' is the direction of propagation of microwave energy along the wave guide. The x and y axes being arbitrary are so chosen that the projection of y' on the x, y plane lies along x. ξ is the angle between z and z', β the angle between z and x' and θ the angle between z and y' (this is the same θ as previously defined). Hence $|(M'|J_{z'}|M)|^2$ is proportional to the intensity of the absorption due to the transition $M'\rightarrow M$. Graphs of $|(M'|J_{z'}|M)|^2$ *versus* x were employed in the comparison of the experimental relative intensities with the model.

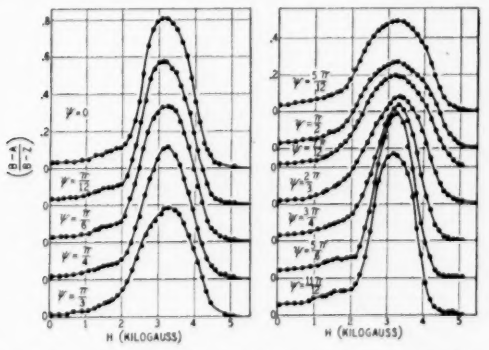

FIG. 3. Experimental intensity of absorption as a function of magnetic field strength.

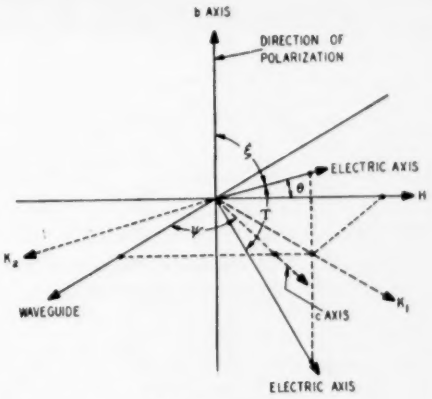

FIG. 4. Orientation of crystal.

b. *The Orientation of the Electric Axes*

It is clear that in the measurements on V^{+2} crystal 1 (see Table I, Fig. 2), oriented as shown in Fig. 4 the electric axes of the two inequivalent V^{+2} ions have the same value of $\cos^2\theta$. Hence since θ enters into the secular equation only as $\cos^2\theta$ the resonance pattern is thereby simplified. In Fig. 5(a) are shown the peak positions as a function of ψ as determined from Fig. 2. Examination of this plot showed that there were two stationary points $\pi/2$ apart, one at $\psi=0.476\pi$ and one at $\psi=0.976\pi$. It was therefore concluded that at one of these angles the plane of the electric axes was perpendicular to and at the other parallel to the magnetic field corresponding to the two points of symmetry in the function $\cos^2\theta$ occurring in the secular equation. Consequently the orientations of the principal axes, K_1, K_2, of susceptibility shown in Fig. 4 (K_1 is in the plane of the electric axes and bisects the angle between them and K_2 is perpendicular to their plane) are known except for a rotation of $\pi/2$ in the a, c plane. It was assumed (this assumption will later be seen to be correct) that when $\psi=0.976\pi$ the plane of the electric axes, and hence K_1, was perpendicular to the magnetic field.

In order to test this assumption crystals 2 and 3 (see Table I) were cut so that their cylindrical axes were perpendicular to this assumed plane of the electric axes. The required angles were those listed in Table I. The crystal was oriented in the wave guide as shown in Fig. 6. In Fig. 7(a) are shown the experimental peak positions as determined from the recorded absorption

[14] C. Kittel and J. M. Luttinger, Phys. Rev. **73**, 162 (1948).

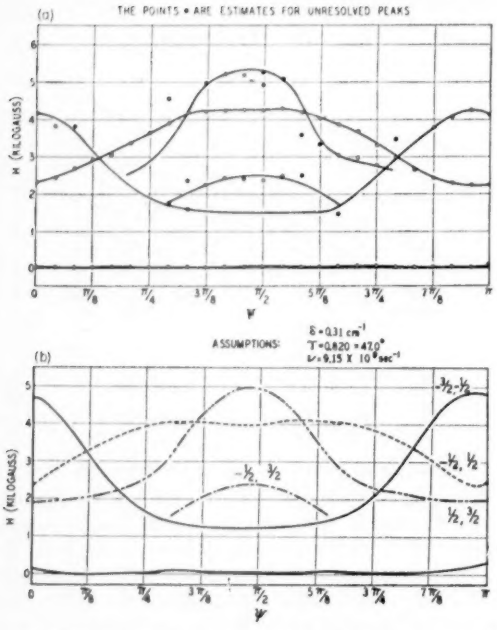

FIG. 5. Field strength for maximum absorption as a function of ψ. (a) Experimental; (b) Theoretical.

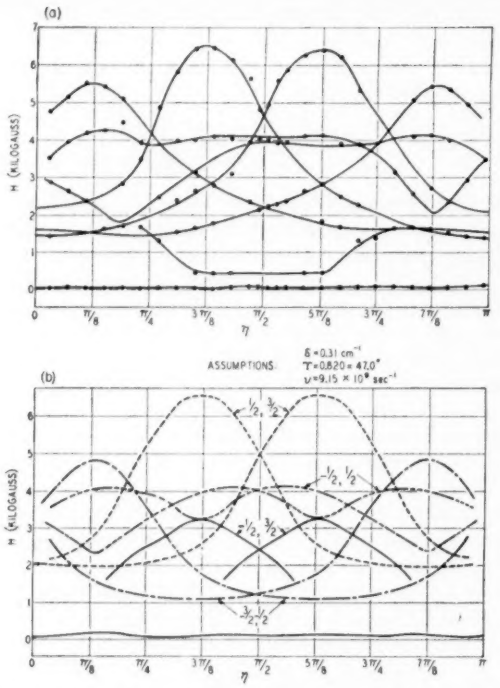

FIG. 7. Field strength for maximum absorption as a function of η. (a) Experimental; (b) Theoretical.

curves. Examination of this plot showed that there were four stationary points, two of them 0.261π apart and located symmetrically about $\eta=0.500\pi$, and the other two $\pi(1-0.261)$ apart located symmetrically about $\eta=0.500\pi$. This then is seen to determine the acute angle Υ, between the electric axes as 0.261π and they consequently make angles of 0.369π and -0.369π with the b axis.

As a check on this hypothesis crystal 4 (see Table I) was cut so that its cylindrical axis was the K_1 axis (the bisector of the acute angle made by the electric axes). The required angles were those listed in Table I. The crystal was oriented as shown in Fig. 8. In Fig. 9(a) are shown the experimental peak positions as determined from the recorded absorption curves. Examination of this plot showed that the cylindrical axis of this crystal was in fact K_1. Since there are only two stationary points, it is indicated that the electric axes associated with the inequivalent ions made angles θ and $-\theta$ with the static magnetic field, and that both kinds of ions gave rise to the same absorption spectrum, as was to be expected.

c. *The Magnitude of the Electric Field Splitting* δ

Knowing that the angle Υ between the electric axes was 0.261π, it was then desired to adjust the parameter

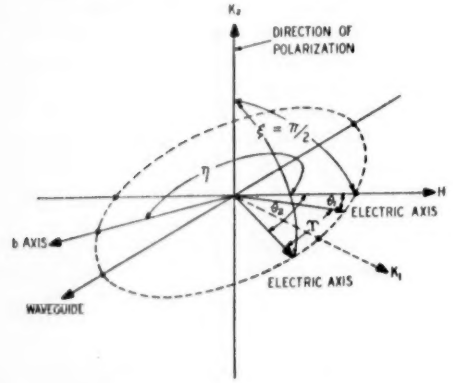

FIG. 6. Orientation of crystal.

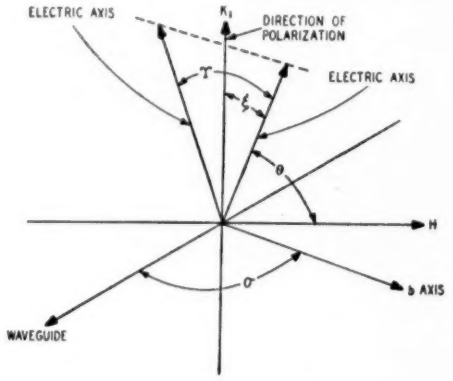

FIG. 8. Orientation of crystal.

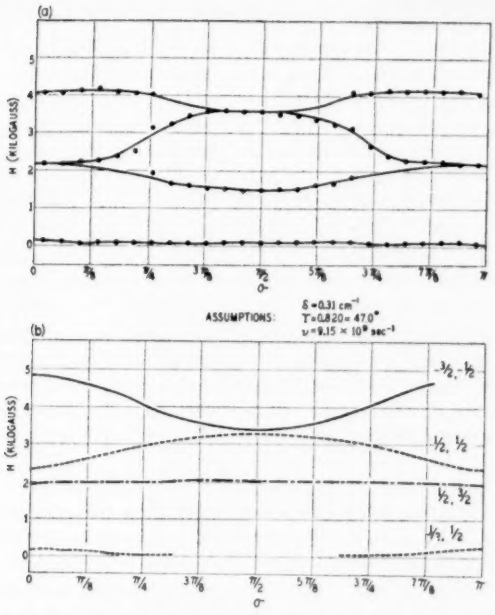

FIG. 9. Field strength for maximum absorption as a function of σ. (a) Experimental; (b) Theoretical.

δ so that the best fit of the experiments with the theory could be obtained. As a first step the calculated graphs of peak positions and intensities *versus* field strength as described in Sec. *a* were employed to construct theoretical resonance absorption curves for several values of θ. In constructing these curves the shapes were assumed Gaussian and the experimental widths were employed as these were substantially larger than the theoretical ones. The theoretical and experimental curves for $\delta=0.31\ \text{cm}^{-1}$ are compared for $\theta=0.131\pi$, $\theta=\cos^{-1}(1/\sqrt{3})$, and $\theta=\pi/2$ in Figs. 10, 11, and 12, respectively. The strong field quantum numbers are employed for the labeling of these figures. The experimental curves were taken from those on crystal 1 shown in Fig. 2 since in this orientation (see Fig. 4) both axes have the same

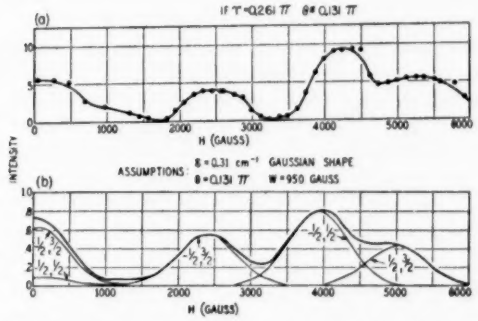

FIG. 10. Intensity of absorption as a function of field strength for $\psi=\pi/2$. (a) Experimental; (b) Theoretical.

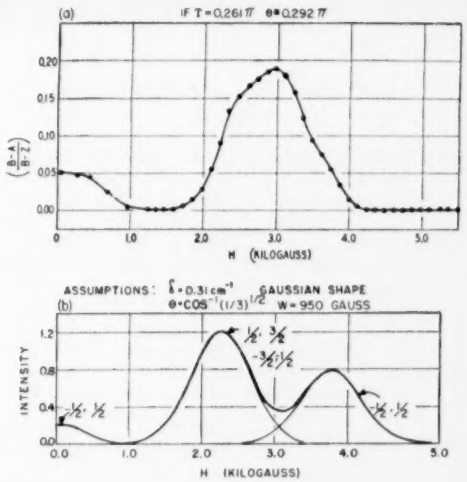

FIG. 11. Intensity of absorption as a function of field strength for $\psi=0.794\pi$. (a) Experimental; (b) Theoretical.

value of $\cos^2\theta$ and hence both inequivalent ions give rise to the same absorption pattern. It was found that any value of δ less than the microwave quantum, 0.306 cm^{-1}, yielded curves with very intense absorptions near zero magnetic field, in disagreement with the experimental observations. For values of δ above 0.306 cm^{-1} the disagreement between theory and experiment increased with increasing δ. In view of an insensitivity in the choice of δ of about 0.01 cm^{-1} the value $\delta=0.31\pm0.01\ \text{cm}^{-1}$ was chosen.

As a second step this value of δ was employed in

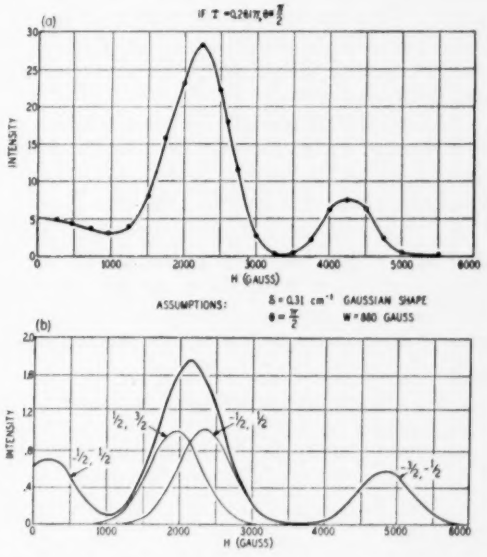

FIG. 12. Intensity of absorption as a function of field strength for $\psi=0$. (a) Experimental; (b) Theoretical.

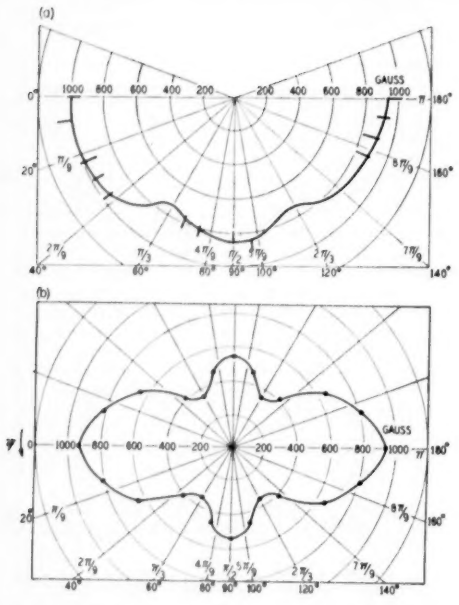

FIG. 13. Width at half-maximum absorption as a function of ψ. (a) Experimental; (b) Theoretical.

conjunction with the previously determined values, 0.261π for Υ, and 0.024π for the dihedral angle between the plane of the electric axes and the b, c plane (i.e., between K_1 and c axis) to construct theoretical curves of field strengths for maximum absorption *versus* angle of rotation. These curves are shown in Figs. 5(b), 7(b), and 9(b) for the angles $\theta=0.131\pi$, $\theta=\cos^{-1}(1/\sqrt{3})$, and $\theta=\pi/2$, respectively. The strong field quantum numbers are employed for the labeling of these figures. The corresponding Figs. 5(a), 7(a), and 9(a) are the experimental curves for the same angles obtained from crystal 1 for which both inequivalent ions gave rise to the same absorption curve.

Positions of peaks and relative intensities are seen to be in essential agreement with the theoretical results. The rather large discrepancy in the appearance of the experimental and theoretical absorption curves at $\theta=\cos^{-1}(1/\sqrt{3})$ is seen on examination of Fig. 2 to occur in a region where the appearance is changing extremely rapidly with rotation of the crystal and hence is very sensitive to choice of angles. The theoretical curve is not constructed for exactly the experimental angle.

d. Width

In Fig. 13 the experimental widths at half-maximum absorption are plotted *versus* the angle of rotation ψ for the experiments using crystal 1. The theoretical curve calculated from the theory of Van Vleck[15] assuming Gaussian shape and the data of Hoffman for the pure V salt are also shown in Fig. 13. For the concentrations of V employed, the theoretical widths are considerably less than this being 330 gauss when the c axis is parallel to the magnetic field. Thus, the dipole-dipole interactions alone are not sufficient to account for the observed widths. Also, as has been stated previously, a considerably more dilute crystal (by a factor of about 5) showed essentially the same widths as those for the more concentrated crystals. These abnormal widths are presumably due to nuclear interactions leading to unresolved hyperfine structure.

CONCLUSIONS

The results of the measurements of the resonance absorptions in the V Tutton salt are in essential agreement with a model based on the known structure of the Tutton salts. Small axial electric fields superposed on the large cubic fields about the two inequivalent V^{+2} ions lead to this agreement when the axial splitting parameter δ is taken to be 0.31 ± 0.01 cm^{-1}; the smaller angle Υ between the electric axes is taken to be 0.261π; and the dihedral angle between the plane of the electric axes and the b, c plane (i.e., the angle between K_1 and the c axis) is taken to be 0.024π. K_1 lies within the angle β between the a and c axes. The small discrepancies which exist between this simple model and the observations are undoubtedly due to the actual rhombicity of the electric field as discussed by Bleaney, Ingram, and Scovil.[1] These authors employed a much more dilute salt, one V ion per 1000 metal ions, than was used in our experiments (see Table I). They made their measurements at 1.2 cm wavelength and 20° or 90°K whereas our observations were at 3 cm and room temperature. However, they obtained 0.244π for the angle between electric axes to be compared with our value, 0.261π; and 0.01π for the angle between K_1 and the c axis to be compared with our value, 0.024π. Their axial splitting parameter $2D=0.316\pm0.01$ cm^{-1} is to be compared with our value, 0.31 ± 0.01 cm^{-1}.

We thank Philip Shevick for the design and construction of electronic equipment and Hans Riehm and Jay S. Hitchcock for the construction of apparatus.

[15] J. H. Van Vleck, Phys. Rev. **74**, 1168 (1948).

PHYSICAL REVIEW VOLUME 89, NUMBER 1 JANUARY 1, 1953

Strong Conservation Laws and Equations of Motion in Covariant Field Theories*

JOSHUA N. GOLDBERG†
Department of Physics, Syracuse University, Syracuse, New York
(Received September 11, 1952)

The relationship between the covariance of a field theory and the equations of motion is discussed in both the Lagrangian and the Hamiltonian formalism. All theories whose field equations are derivable from a variational principle and are covariant under arbitrary (curvilinear) coordinate transformations possess Bianchi identities and, hence, "strong" conservation laws. Because the strong conservation laws are ordinary divergences equal to zero, whether or not the field equations are satisfied, there exist certain skew-symmetric expressions whose divergences yield the components of the energy-momentum tensor. These superpotentials, as the skew-symmetric expressions are called, enable us to write the energy and momentum content of the field as two-dimensional surface integrals. Also, by using the superpotentials together with the field equations, one can find certain surface integrals which are independent of the surface of integration and which yield the equations of motion for the singularities enclosed by the surface. If the Einstein-Infeld approximation method is applied in the general theory of relativity, the above surface integrals reduce to integrals which are equivalent to those used by Einstein and Infeld to obtain the equations of motion for the field sources.

In the Hamiltonian formalism the covariance of the theory is revealed in the existence of a number of constraints between the momenta and the field variables. Therefore, we examine the relationship between the constraints and the Bianchi identities, which lead to the strong conservation laws. We find that the first time derivative of the constraints leads to the existence of four linear combinations of field equations which are free of the time derivatives of the canonical field variables. These four expressions are the "secondary" constraints. The second time derivative of the primary constraints leads to the Bianchi identities in terms of the canonical field variables. Thus, we are able to establish the existence of the strong conservation laws in the Hamiltonian formalism and by the same arguments as in the Lagrangian formalism establish the existence of the superpotentials. The superpotentials are written out only for the gravitational theory.

I. INTRODUCTION

IN this paper we shall discuss the relationship between the transformation properties of a covariant field theory and the equations of motion for the field sources in both the Lagrangian and Hamiltonian formalisms. All theories whose field equations are derivable from a variational principle and are covariant with respect to transformation groups involving arbitrary *functions* possess "strong" conservation laws. These strong laws are certain (ordinary) divergences which vanish whether or not the field equations are satisfied. The existence of such strong conservation laws enables us to set up certain two-dimensional surface integrals which yield the "equations of motion." These equations will be the ponderomotive laws only when the covariant transformation group under consideration is that of arbitrary (curvilinear) coordinate transformations. In any case, the type of covariant group possessed by a given field theory will determine what is conserved "strongly," and hence what kind of "motion" is determined by the field equations alone.

Maxwell's theory of electromagnetism is covariant with respect to the Lorentz group which depends only on arbitrary *parameters*. One can construct conservation laws for the Maxwell field, but these laws will hold only when the field equations are satisfied. Furthermore, the Maxwell equations do not contain the mass of the charged particles in the field; therefore, the ponderomotive laws—the Lorentz equations—represent an assumption distinct from and outside the framework of the field equations. On the other hand, the field equations of the electromagnetic theory are also covariant with respect to the gauge group, which depends on one arbitrary *function*. There exists, therefore, one strong conservation law for the Maxwell field and that is the conservation law for charge. This conservation law tells us that the charged particles producing the field must move so that the total charge is conserved. Beyond this statement, the field equations by themselves leave the motion of the particles arbitrary. Moreover, it is well known that the total charge in a given region of space may be calculated by means of a two-dimensional surface integral over a surface which encloses that region. Thus, the time rate of change of the charge enclosed by a surface may also be calculated by means of a surface integral. If the field equations are satisfied on that surface (i.e., if the charge and current distributions are zero on the surface), then the total charge enclosed is constant in time.

In a similar fashion, theories which are covariant with respect to coordinate transformations possess four strong conservation laws as they involve four arbitrary functions. These laws are the conservation laws for energy and momentum. Because these are strong laws, the energy and momentum can be calculated by means of two-dimensional surface integrals, and the equations of motion for the particles enclosed by the surface can also be calculated by means of surface integrals. The methods we use to prove this result can be applied to more general transformations to obtain corresponding conservation laws and equations of motion. However, in this paper we shall restrict our attention to coordinate transformations.

The general theory of relativity is the only significant field theory known today whose field equations deter-

* This work was supported by the ONR. This paper includes the results of a dissertation submitted in partial fulfillment of the requirements for the degree of Doctor of Philosophy at Syracuse University.
† Now at Armour Research Foundation, Chicago, Illinois.

mine the equations of motion of the particles producing the field.[1–3] As a result of the covariance of the theory of gravitation under arbitrary coordinate transformations, the field equations are nonlinear and, moreover, the field equations satisfy four differential identities (the Bianchi identities). The nonlinearity of the field equations is essential for the explicit description of the interactions between particles. If we have linear field equations, then the sum of any number of solutions is again a solution of the field equations while the world lines of the particles producing the fields are unaffected by the summation process. The role played by the Bianchi identities is very complex, but for our purposes it is sufficient that the existence of the Bianchi identities guarantees the existence of the strong conservation laws.[4] As we have noted above, the existence of these strong conservation laws permits us to determine the equations of motion from the field equations by means of surface integrals.

In their solution of the problem of motion in the gravitational theory, Einstein and Infeld also use surface integrals to obtain the equations of motion.[1–3] However, in order to set up their surface integrals they separate the gravitational metric into the metric for flat space, which is assumed to be the exact field at spatial infinity, and a part representing the deviation from flat space. With this substitution certain of the field equations consist of linear terms which may be written as the spatial divergence of an antisymmetric form, plus a form containing primarily nonlinear terms. Because of the skew-symmetry of the linear form, the two-dimensional surface integral of the nonlinear form vanishes whenever the field equations are satisfied on the surface of integration according to Stokes' theorem. These surface integrals yield the equations of motion. This derivation of the surface integrals depends on the specific structure of the gravitational field equations. There is no indication as to how these surface integrals are related to the covariance of the theory.

Bergmann has shown that any field theory whose field equations are derivable from a variational principle and whose field equations are covariant under arbitrary coordinate transformations will possess Bianchi identities and, hence, strong conservation laws.[5] Because of the existence of the strong conservation laws there exist certain skew-symmetric forms, which we shall call "superpotentials." These superpotentials enable us to find linear combinations of the field equations which may be written as the spatial divergence of an antisymmetric form, plus other terms. Both types of terms are related to the energy and momentum of the field. Thus, the surface integrals can be set up independently of any splitting-up of field variables or approximation methods. Furthermore, the fact that these surface integrals can be related to the energy-momentum tensor adds to their significance in determining the equations of motion. If we apply the Einstein-Infeld approximation, our surface integrals are equivalent to theirs.

The usual approach in quantizing a field theory is first to cast the classical theory into the Hamiltonian formalism. From the Poisson brackets of the field variables one obtains the commutation relations to be obeyed by the quantum-mechanical operators. That is why we have formulated the strong conservation laws and the surface integrals for the equations of motion also in terms of the canonical variables. Inasmuch as covariance in the canonical formalism expresses itself through the primary and secondary constraints, it is to be expected that the canonical constraints are related directly to the conservation laws. We shall show this relationship explicitly.

II. THE LAGRANGIAN FORMALISM

2.1 Strong Conservation Laws

In this section we shall summarize previous results (I) needed here. The field equations are assumed to be derivable from a variational principle whose Lagrangian density is a function of the field variables and their first derivatives,

$$\text{(I-2.1)} \qquad \delta I=0, \quad I=\int_V L(y_A, y_{A,\mu})d^4x. \tag{2.1}$$

The field variables y_A are assumed to transform under arbitrary coordinate transformations according to the law

$$\text{(I-2.3)} \qquad \delta y_A=F_{A\mu}{}^{B\nu}y_B\xi^\mu{}_{,\nu}-y_{A,\mu}\xi^\mu, \tag{2.2}$$

where the ξ^μ are the descriptors of the transformation (for a coordinate transformation they are merely the infinitesimal changes of the coordinates) and the $F_{A\mu}{}^{B\nu}$ are certain constants in any given theory. If the field equations,

$$\text{(I-2.2)} \qquad \begin{gathered} L^A\equiv\partial^A L-(\partial^{A\rho}L)_{,\rho}=0, \\ \partial^A L\equiv\partial L/\partial y_A, \quad \partial^{A\rho}L\equiv\partial L/\partial y_{A,\rho}, \end{gathered} \tag{2.3}$$

are to be covariant under the above transformations, the density function, L, must transform at most by the addition of a total divergence. In order to satisfy this condition on the Lagrangian density, the field equations must satisfy the four Bianchi identities,

$$\text{(I-3.3)} \qquad (F_{A\mu}{}^{B\nu}y_BL^A)_{,\nu}+y_{A,\mu}L^A\equiv 0. \tag{2.4}$$

From the Bianchi identities one immediately obtains the

[1] Einstein, Infeld, and Hoffman, Ann. Math. **39**, 66 (1938).
[2] A. Einstein and L. Infeld, Ann. Math. **41**, 455 (1940).
[3] A. Einstein and L. Infeld, Can. J. Math. **1**, 209 (1949).
[4] There is only one case where this is not so. If the infinitesimal transformation of the field variables does not involve derivatives of the "descriptors" of the transformation, then there will exist Bianchi identities but no conservation laws. This case is of no interest to us and we shall not consider it further.
[5] P. G. Bergmann, Phys. Rev. **75**, 680 (1949). This paper will be referred to as I and references to equations in this paper will be made as (I-2.1), etc.

strong conservation laws:

$$\text{(I-3.11)} \qquad \begin{aligned} &T_{\mu}{}^{\nu}{}_{,\nu}\equiv 0, \\ &T_{\mu}{}^{\nu}=-F_{A\mu}{}^{B\nu}y_B L^A-\delta_{\mu}{}^{\nu}L+\partial^{A\nu}Ly_{A,\mu}. \end{aligned} \tag{2.5}$$

When the field equations are satisfied, $L^A=0$, these strong laws reduce to the usual "weak" conservation laws found in all field theories derived from a variational principle:

$$\text{(I-3.8)} \qquad \begin{aligned} &t_{\mu}{}^{\nu}{}_{,\nu}=0, \\ &t_{\mu}{}^{\nu}=-\delta_{\mu}{}^{\nu}L+\partial^{A\nu}Ly_{A,\mu}. \end{aligned} \tag{2.6}$$

All of the above results, with minor changes, hold equally as well for the gauge transformation in the theory of electromagnetism. In that case we have

$$\bar{\delta}\varphi_{\rho}=\xi_{,\rho}, \tag{2.7}$$

and the "Bianchi" identity and the strong conservation law are one:

$$T^{\rho}{}_{,\rho}\equiv L^{\rho}{}_{,\rho}\equiv 0. \tag{2.8}$$

Equation (2.8) leads directly to the conservation law for charge.

2.2 Superpotentials

Although we ordinarily confine our attention to those domains where the field equations are satisfied, the existence of the strong conservation laws is of great importance. It is well known that whenever the complete divergence of a "tensor" form[6] vanishes, then the form itself may be represented as the complete divergence of an antisymmetric form whose rank is higher by one. (This corresponds to writing B as the curl of a vector potential A in the electromagnetic theory.) Therefore, we may write

$$T_{\mu}{}^{\nu}=U_{\mu}{}^{[\nu\sigma]}{}_{,\sigma}. \tag{2.9}$$

The square brackets around the superscripts ν and σ indicate that $U_{\mu}{}^{[\nu\sigma]}$ is antisymmetric in these indices. The existence of these "superpotentials," as we shall call this antisymmetric tensor-form, will enable us to obtain the surface integrals for the equations of motion.

Before we go into a discussion of the equations of motion, it is interesting to note that the superpotentials permit us to write the total energy and momentum in the field as surface integrals. As was mentioned in the introduction, this possibility corresponds to Gauss' law in electromagnetic theory. The total energy and momentum density in the field is represented by $T_{\mu}{}^{4}$. From Eq. (2.9) we find that

$$T_{\mu}{}^{4}=U_{\mu}{}^{[4s]}{}_{,s}, \quad (s=1, 2, 3). \tag{2.10}$$

[6] By a tensor-form we mean a set of quantities whose components are distinguished by indices but which may not have simple transformation properties, e.g., the ordinary divergence of a tensor.

If P_{μ} is the total energy and momentum in a given three-dimensional volume V with the surface S, then

$$P_{\mu}=\int_V T_{\mu}{}^{4}dV=\oint U_{\mu}{}^{[4s]}n_s dS, \tag{2.11}$$

where the n_s are the components of the unit normal vector to the surface S. The significance of this statement is that one need not integrate across the singular regions of the field in order to calculate the energy and momentum content of the field including the singularities. Thus the total energy and momentum of the field, including the particles in the field may be calculated without the necessity of making an arbitrary separation of the total field into external and self-fields as is necessary in the theory of electromagnetism. Clearly, the time rate of change of energy and momentum contained in a volume V is also given, from Eq. (2.11), by a surface integral:

$$dP_{\mu}/dt=\oint U_{\mu}{}^{[4s]}{}_{,4}n_s dS. \tag{2.12}$$

This result is of interest in the investigation of (gravitational) radiation.

2.3 Equations of Motion

In the theory of gravitation the problem of motion was solved by means of a particular approximation method which allows certain of the field equations to be written as the sum of two terms, one of which is the spatial divergence of an antisymmetric form.[1-3] We shall now find those linear combinations of the field equations having this form, without splitting the field variables or applying an approximation procedure.

From Eqs. (2.5), (2.6), and (2.9) we find that the following linear combinations of field equations may be written in terms of the superpotentials:

$$F_{A\mu}{}^{B\nu}y_B L^A\equiv U_{\mu}{}^{[\sigma\nu]}{}_{,\sigma}+t_{\mu}{}^{\nu}=0. \tag{2.13}$$

Let us set ν equal to s, $(1, \cdots, 3)$, and in the potentials separate the derivative with respect to x^4 from the spatial derivatives:

$$F_{A\mu}{}^{Bs}y_B L^A\equiv U_{\mu}{}^{[rs]}{}_{,r}+U_{\mu}{}^{[4s]}{}_{,4}+t_{\mu}{}^{s}=0. \tag{2.14}$$

It is evident that these linear combinations of field equations have just the required property. If we now take the divergence of Eq. (2.14), the first term vanishes identically because of the anti-symmetry of r and s in $U_{\mu}{}^{[sr]}$, and because of the symmetry of r and s in the derivatives. Thus the divergence reduces to

$$(F_{A\mu}{}^{Bs}y_B L^A)_{,s}\equiv(U_{\mu}{}^{[4s]}{}_{,4}+t_{\mu}{}^{s})_{,s}=0. \tag{2.15}$$

Equation (2.15) tells us that the closed-surface integral over $(U_{\mu}{}^{[4s]}{}_{,4}+t_{\mu}{}^{s})$ will be independent of the surface

as long as the field equations are satisfied at least on the surface of integration.

Therefore, we form the two-dimensional surface integral over Eq. (2.14):

$$\oint F_{A\mu}{}^{Bs}y_B L^A n_s dS \equiv \oint U_\mu{}^{[rs]}{}_{,r} n_s dS$$

$$+ \oint (U_\mu{}^{[4s]}{}_{,4} + t_\mu{}^s) n_s dS = 0. \quad (2.16)$$

Here, the first integral vanishes identically because of what Einstein calls "the lemma."[1-3] The essential argument is that the spatial divergence of any antisymmetric form, whose antisymmetric indices are spatial, may always be represented as the curl of a vector, the remaining indices being disregarded. The integral of a curl over a closed surface always vanishes. Thus, from Eq. (2.16) we are left with

$$\oint F_{A\mu}{}^{Bs}y_B L^A n_s dS \equiv \oint (U_\mu{}^{[4s]}{}_{,4} + t_\mu{}^s) n_s dS = 0. \quad (2.17)$$

If the surface does not enclose any singularities, then this result is trivial. Applying Gauss' theorem, and remembering Eq. (2.15), the surface integrals give an identically vanishing result. When singularities are enclosed by the surface, however, Gauss' theorem cannot be applied to yield this trivial result. The surface integrals need no longer vanish identically. Equation (2.15) tells us that no surface integral of the form (2.17) can depend on the shape of the surface as long as the field equations are satisfied on that surface. If two different surfaces enclose the same singularities, then Gauss' theorem applied to the region between the surfaces will give an identically vanishing result. Therefore, the surface integrals (2.17) can be functions only of the coordinates and the time derivatives of the coordinates of any singularities enclosed by the surface. Hence, these surface integrals must yield the equations of motion for the singularities enclosed.

It is important to remember that the surface integrals, Eq. (2.17), would have no meaning were it not for the existence of the strong conservation laws. A surface integral taken over a linear combination of the full field equations would vanish on a cap, as well as on a closed surface, as long as the field equations are satisfied on the surface of integration. By means of the strong conservation laws, and the consequent skew-symmetric superpotentials, we have shown that the closed surface integral over a quantity which is not a linear combination of the full field equations vanishes. Moreover, the existence of the superpotentials enabled us to prove that these closed surface integrals are independent of the surface of integration in the sense of the previous paragraph.

Indeed, one can obtain these surface integrals directly from the statement of the strong conservation laws by making use of the existence of the superpotentials and the condition that the field equations be satisfied on the surface of integration. Separating the derivative with respect to x^4 in the strong conservation laws, Eq. (2.5), we have:

$$T_\mu{}^4{}_{,4} + T_\mu{}^s{}_{,s} \equiv 0. \quad (2.18)$$

Taking the volume integral of the above equation and applying Gauss' theorem to the second term, we find that,

$$\int_V T_\mu{}^4{}_{,4} dV + \oint T_\mu{}^s n_s dS \equiv 0. \quad (2.19)$$

We can now substitute for T^4 from Eq. (2.10) and thus obtain an expression involving only a surface integral:

$$\oint (U_\mu{}^{[4s]}{}_{,4} + T_\mu{}^s) n_s dS \equiv 0. \quad (2.20)$$

If the field equations are satisfied on the surface of integration, then Eq. (2.20) reduces to (2.17). The only advantage of the original derivation of the surface integrals is in proving that these integrals really give the equations of motion and for comparison with the method of Einstein and Infeld.

The surface integrals can be generalized to the case where matter is represented by a tensor field P^A rather than by singularities in the field. The P^A become the right-hand sides of the field equations; that is,

$$L^A = P^A. \quad (2.21)$$

In this case, Eqs. (2.15) and (2.17) are replaced by

$$(U_\mu{}^{[4s]}{}_{,4} + t_\mu{}^s)_{,s} = (F_{A\mu}{}^{Bs}y_B P^A)_{,s}, \quad (2.15')$$

and

$$\oint (U_\mu{}^{[4s]}{}_{,4} + t_\mu{}^s) n_s dS = \oint F_{A\mu}{}^{Bs}y_B P^A n_s dS. \quad (2.17')$$

Clearly these integrals are no longer independent of the surface. If the distribution of matter is not zero on the surface, then changing the surface will in turn change the amount of matter enclosed by the surface. In this case, the equations of motion cannot be independent of the surface. These surface integrals depend on the distribution of matter through the field variables themselves as well as through the P^A explicitly. The dependence of the field variables on the distribution of matter is determined by the field equations, Eq. (2.21), and thus by the distribution of matter throughout all space. The explicit dependence of the equations of motion on the P^A, however, is determined solely by the distribution of matter on the surface. This situation is to be expected as the change in the energy and momentum contained within the surface will depend on

the flux through the surface. The analogous situation occurs in the theory of electromagnetism with respect to the conservation law for charge.

It is easy to see that no new information can be obtained from Eq. (2.13) by setting ν equal to 4. The same surface integrals result after taking a time derivative and substituting from the strong conservation laws for those terms which are not a spatial divergence. Thus, once having satisfied the surface integrals (2.17), these additional relations are empty.

2.4 Theory of Gravitation

In the theory of gravitation, Eq. (2.14) becomes

$$-2(-g)^{\frac{1}{2}}G_\mu{}^\nu \equiv U_\mu{}^{[\tau\nu]}{}_{,\tau} + U_\mu{}^{[4\nu]}{}_{,4} + t_\mu{}^\nu = 0, \quad (2.22)$$

where[7,8]

$$U_\mu{}^{[\nu\lambda]} = \tfrac{1}{2}(-g)^{\frac{1}{2}}\{\delta_\mu{}^\nu(g^{\lambda\tau}g^{\rho\sigma} - g^{\lambda\sigma}g^{\rho\tau}) - \delta_\mu{}^\lambda(g^{\nu\tau}g^{\rho\sigma} - g^{\nu\sigma}g^{\rho\tau}) + \delta_\mu{}^\rho(g^{\nu\tau}g^{\lambda\sigma} - g^{\lambda\tau}g^{\nu\sigma})\}g_{\rho\sigma,\tau}. \quad (2.23)$$

Following Einstein and Infeld, we write the gravitational metric as the sum of the metric for flat space and a term representing the deviation from flat space:

$$g_{\mu\nu} = \eta_{\mu\nu} + h_{\mu\nu}, \qquad \eta_{44} = 1, \quad \eta_{mn} = -\delta_{mn}, \quad \eta_{4m} = 0. \quad (2.24)$$

It is convenient to introduce a linear combination of the $h_{\mu\nu}$ as the field variables,

$$\gamma_{\mu\nu} = h_{\mu\nu} - \tfrac{1}{2}\eta_{\mu\nu}\eta^{\rho\sigma}h_{\rho\sigma}. \quad (2.25)$$

Substituting Eqs. (2.24) and (2.25) into (2.23) we find that $U_\mu{}^{[\tau\sigma]}{}_{,\tau}$ becomes

$$U_\mu{}^{[\sigma\tau]}{}_{,\tau} = (\gamma_{\mu\tau,\,\nu} - \gamma_{\mu\nu,\,\tau} + \delta_{\mu\tau}\gamma_{\nu m,\,m} - \delta_{\mu\nu}\gamma_{\tau m,\,m})_{,\tau} + (\delta_{\mu\nu}\gamma_{4\tau,\,4} - \delta_{\mu\tau}\gamma_{4\nu,\,4})_{,\tau} + \text{nonlinear terms}. \quad (2.26)$$

The first group of linear terms on the right-hand side of Eq. (2.26) are just those terms which Einstein and Infeld separate from the field equations in order to obtain their surface integrals. The second group is not separated out because in their approximation procedure these terms behave like the nonlinear terms. Therefore, if we apply the Einstein-Infeld approximation procedure, in each step of the approximation we obtain the same surface integrals modulo terms which vanish because of "the lemma." The reason we do not obtain the identical surface integrals right away is that Einstein and Infeld only separate out linear terms, whereas we separate out all the terms in the field equations which are the spatial divergences of skew-symmetric expressions. Thus, one sees that these surface integrals, which result from the covariance of the theory, really give the equations of motion for the field sources.

[7] P. Freud, Ann. Math. **40**, 417 (1939).
[8] H. Zatskis, Phys. Rev. **81**, 1023 (1951).

III. THE HAMILTONIAN FORMALISM

3.1 Primary Constraints

In order to show the relationship between the constraints and the strong conservation laws in the Hamiltonian formalism, we shall require an explicit expression for the Hamiltonian so that we may calculate Poisson brackets of the constraints and the Hamiltonian. Such relations are meaningless without definite expressions for the Hamiltonian and the constraints. Therefore, in what follows we shall assume that our Lagrangian is an integral over a density function L which is homogeneous quadratic in the first derivatives of the field variables:

$$L = \Lambda^{A\rho B\sigma}(y_C)y_{A,\,\rho}y_{B,\,\sigma}. \quad (3.1)$$

The covariance of the theory under arbitrary coordinate transformations leads to the Bianchi identities, Eq. (2.4), which place certain restrictions on the coefficients $\Lambda^{A\rho B\sigma}$. After substituting the above expression for the Lagrangian into Eq. (2.4) and separately considering the coefficients of various differential orders, we find that

$$\begin{aligned}
&\text{(a)}\quad u_{\mu A}{}^\rho L^{AC\sigma\tau} + u_{\mu A}{}^\sigma L^{AC\tau\rho} + u_{\mu A}{}^\tau L^{AC\rho\sigma} \equiv 0,\\
&\text{(b)}\quad \delta_\mu{}^\sigma L^{AC\rho\tau} + \partial^C(u_{\mu B}{}^\sigma L^{AB\rho\tau}) - u_{\mu B}{}^\tau\Gamma^{\rho\sigma B,\,AC} - u_{\mu B}{}^\rho\Gamma^{\tau\sigma B,\,AC} \equiv 0,\\
&\text{(c)}\quad \delta_\mu{}^\tau\Gamma^{\rho\sigma C,\,AB} + \delta_\mu{}^\sigma\Gamma^{\tau\rho B,\,CA} + \delta_\mu{}^\rho\Gamma^{\sigma\tau A,\,BC} + \partial^C(u_{\mu D}{}^\tau\Gamma^{\rho\sigma D,\,AB}) + \partial^B(u_{\mu D}{}^\sigma\Gamma^{\tau\rho D,\,CA}) + \partial^A(u_{\mu D}{}^\rho\Gamma^{\sigma\tau D,\,BC}) \equiv 0.
\end{aligned} \quad (3.2)$$

$$u_{\mu A}{}^\tau \equiv F_{A\mu}{}^{B\tau}y_B,$$

$$L^{AB\rho\sigma} \equiv \Lambda^{A\rho B\sigma} + \Lambda^{A\sigma B\rho},$$

$$\Gamma^{\rho\sigma B,\,AC} \equiv \partial^B\Lambda^{A\rho C\sigma} - \partial^A\Lambda^{B\rho C\sigma} - \partial^C\Lambda^{A\rho B\sigma}.$$

These three sets of relations will be frequently used in the following calculations.

One can consider the transition to the Hamiltonian formalism as a Legendre transformation.[9] Therefore, the following two equations are valid whether or not the field equations are satisfied:

$$\pi^A = \partial L/\partial y_{A,\,4}, \quad (3.3)$$

$$y_{A,\,4} = \partial H/\partial\pi^A. \quad (3.4)$$

Equation (3.3) is merely the definition of the momenta canonically conjugate to the field variables y_A; on the

[9] The function $L(q_k, \dot{q}_k)$ is considered as the generator of the transformation to the coordinates q_k and p_k by defining p_k as $\partial L/\partial\dot{q}_k$. One then asks for that function $H(q_k, p_k)$ which generates the inverse transformation $\dot{q}_k\partial H/\partial p_k$. By considering the total differential dL, or dH, one finds that $H = \sum_k p_k\dot{q}_k - L$ which is the usual definition of the Hamiltonian.

other hand, Eq. (3.4) is one-half of the Hamiltonian field equations. In the Lagrangian formalism, when we consider situations in which the field equations are not satisfied, we set the right-hand sides of the field equations equal to expressions P^A, which represent the distribution of matter. When we pass to the Hamiltonian formalism, the number of field equations is doubled. The question arises whether all of them may be considered eligible for nonvanishing right-hand sides. Setting up the Hamiltonian formalism through a Legendre transformation shows that only half of the field equations may acquire right-hand sides:

$$-(\dot{\pi}^A+\delta H/\delta y_A)=P^A. \tag{3.5}$$

Setting $\rho=\sigma=\tau=4$ in Eq. (3.2a), one finds that the $u_{\mu A}{}^4$ are null vectors of Λ^{A4B4}. Because of the existence of these null vectors, there are four linear combinations of field equations in the Lagrangian formalism that are free of second time derivatives of the field variables. This situation is reflected in the Hamiltonian formalism in the existence of the primary constraints which are four linear combinations of the momenta and field variables not involving the $y_{A,4}$. Multiplying Eq. (3.3) by the $u_{\mu A}{}^4$ we have

$$g_\mu\equiv u_{\mu A}{}^4\bar{\pi}^A=0, \quad \bar{\pi}^A=\pi^A-2\Lambda^{A4B\nu}y_{B,\nu}. \tag{3.6}$$

Thus, although the π^A are uniquely defined in terms of the field variables and their derivatives, the $y_{A,4}$ are not uniquely determined by the canonical field variables. They are determined only up to a linear combination of the null vectors $u_{\mu A}{}^4$. This lack of uniqueness in the $y_{A,4}$ is reflected in the corresponding lack of uniqueness of the Hamiltonian. All generally covariant theories possess this property. The Hamiltonian density (if we do not introduce parameters) is,[10]

$$H=\tfrac{1}{4}E_{AB}\bar{\pi}^A\bar{\pi}^B-\Lambda^{A\tau B\nu}y_{A,\tau}y_{B,\nu}+w^\rho g_\rho, \tag{3.7}$$

where the w^ρ are four arbitrary functions of the field variables. E_{AB} is the quasi-inverse of Λ^{A4B4} and is defined by the relationship

$$E_{AC}\Lambda^{C4D4}E_{DB}=E_{AB}. \tag{3.8}$$

Therefore,

$$E_{AC}\Lambda^{C4B4}=\delta_A{}^B-v^{B\mu}u_{\mu A}, \tag{3.9}$$

where

$$E_{AB}v^{B\mu}=0,$$

and

$$u_{\mu A}v^{A\nu}=\delta_\mu{}^\nu.$$

Since the E_{AB} is only a quasi-inverse, it is not quite uniquely determined by the defining relation above. Therefore, the last term in Eq. (3.7) is redundant. However, in practice one chooses a particular form for the quasi-inverse and any further changes in the Hamiltonian are then represented as linear combinations of primary constraints as indicated in Eq. (3.7). The null vectors $v^{A\mu}$ exhibit a corresponding lack of uniqueness, although for a particular choice of inverse the null vectors are uniquely defined by the relations (3.9). In the following, we assume that a particular choice of E_{AB} has been made. Therefore, there is no redundancy in Eq. (3.7) and the null vectors are unique.

[10] R. Penfield, Phys. Rev. **84**, 737 (1951).

3.2 Secondary Constraints

Since we are looking for the strong conservation laws, which are satisfied even when the field equations are not, we must use the field equations with right-hand sides. In order to set these up consistently, we shall redefine the Lagrangian density as

$$L^*=L-y_AP^A, \tag{3.10}$$

where L is the usual density function. In the variational principle the P^A are considered given and are not to be varied. The transformation law for the y_A is unaffected by this change and that of the P^A is,

$$\bar{\delta}P^B=-F_{A\mu}{}^{B\nu}P^A\xi^\mu{}_{,\nu}-(P^B\xi^\mu)_{,\mu}. \tag{3.11}$$

If one carries out the argument normally leading to the Bianchi identities, one finds that the requirement that $\bar{\delta}L^*$ be a divergence leads to the usual identities without P^A appearing at all. The terms involving the P^A either cancel outright or go together to form a total divergence. Clearly, the definition of the momenta, π^A, is not altered and, therefore, the primary constraints are the same as in the usual case. However, the Hamiltonian density is changed by the addition of the term y_AP^A:

$$H^*=H+y_AP^A. \tag{3.12}$$

In this Hamiltonian the P^A are not dynamical variables, and thus this theory does not by itself lead to differential equations for the P^A. It is clear that the new Hamiltonian density H^* is determined, as is the old one, up to a linear combination of the primary constraints.

Following Anderson and Bergmann[11] we introduce the function space whose "points" are arbitrary sets of functions $y_A(x^1, \cdots, x^4)$ and call it the "configuration" space of the Lagrangian theory, Σ_c. If we double the dimensionality of this space by adjoining to it the second set of arbitrary functions $\pi^A(x^1, \cdots, x^4)$, we get the phase space of the corresponding canonical formalism, Σ. However, because ofthe existence of the primary constraints, not all points of Σ correspond to possible situations in the Lagrangian theory. We must restrict ourselves to that sub-space Σ_l of Σ where the primary constraints, Eq. (3.6) are satisfied. The fact that the primary constraints are satisfied in Σ_l for all time places certain restrictions on the field equations which are called "secondary" constraints. The question arises as to how many such secondary constraints exist. In

[11] J. Anderson and P. G. Bergmann, Phys. Rev. **83**, 1018 (1951). This paper will be referred to as II and reference to equations in this paper will be made as (II-3.2), etc.

general, the answer depends on the transformation law for the field variables. For the case which we consider there are only four secondary constraints. We shall delay the proof of this statement until the next section. Here we shall calculate the secondary constraints.

Consider a three-dimensional integral over the primary constraints g_μ with arbitrary weight functions σ^μ. Obviously, this integral vanishes in the space Σ_l,

$$\mathcal{G}=\int \sigma^\mu g_\mu d^3x \overset{l}{=} 0, \tag{3.13}$$

and, conversely, if it vanishes for all possible σ^μ, then automatically the primary constraints are required to be satisfied. (The symbol l above an equal sign means that the relationship is valid in Σ_l.) Since the primary constraints are satisfied in Σ_l for all time, it follows that the time derivatives of the g_μ must also vanish in Σ_l. Thus the time derivatives of $\mathcal{G}$ must likewise vanish in Σ_l. Because of the field equations, Eqs. (3.4) and (3.5), we have:

$$\frac{d\mathcal{G}}{dt}=\frac{\partial \mathcal{G}}{\partial t}+(\mathcal{G},\mathcal{H}^*)\overset{l}{=}0, \tag{3.14}$$

where

$$\mathcal{H}^*=\int H^* d^3x.$$

$(\mathcal{G},\mathcal{H}^*)$ is the Poisson bracket of the two functionals $\mathcal{G}$ and $\mathcal{H}^*$.[12]

From Eq. (3.12) it is evident that if $\mathfrak{F}(y_A, \pi^A)$ is an arbitrary functional, then

$$(\mathfrak{F},\mathcal{H}^*)=(\mathfrak{F},\mathcal{H})-\int \frac{\delta \mathfrak{F}}{\delta \pi^A} P^A d^3x. \tag{3.15}$$

Using the above relation, Eq. (3.14) becomes

$$\int\left\{\dot\sigma^\mu g_\mu+\sigma^\mu\left[(g_\mu, H)-\frac{\partial g_\mu}{\partial \pi^A}P^A\right]\right\}d^3x\overset{l}{=}0. \tag{3.16}$$

Since the weight functions σ^μ are arbitrary, the coefficients of the differentiated and the undifferentiated weight functions must vanish separately. Clearly, the coefficient of $\dot\sigma^\mu$ vanishes in Σ_l. In order to identify the terms multiplied by σ^μ, we must evaluate the Poisson bracket (g_μ, H), which we shall denote by L_μ. We have:

$$\begin{aligned}L_\mu\equiv&(u_{\mu A}{}^s\bar\pi^A)_{,s}+\delta_\mu{}^4 H+\delta_\mu{}^s y_{A,s}\pi^A\\&+\delta_\mu{}^4\Lambda^{AmBn}y_{A,m}y_{B,n}-2\delta_\mu{}^m\Lambda^{A4Bn}y_{A,m}y_{B,n}\\&+u_{\mu C}(\Gamma^{nmC,AB}y_{A,n}y_{B,m}-2\Lambda^{AnCm}y_{A,mn})\\&+f_\mu(g_\rho).\end{aligned} \tag{3.17}$$

[12] For the definition of the Poisson brackets of functionals see P. G. Bergmann and J. H. M. Brunings, Revs. Modern Phys. **21**, 480 (1949).

In L_μ, above, $f_\mu(g_\rho)$ represents many factors of g_ρ and $g_{\rho,s}$. We have chosen to write them in this way because in Σ_l these terms make no new contribution and in taking further time derivatives of $\mathcal{G}$ these terms will never contribute anything new. Therefore, the coefficient of σ^μ in Eq. (3.16) is,

$$(g_\mu, H^*)\equiv L_\mu-u_{\mu A}{}^4 P^A\overset{l}{=}0. \tag{3.18}$$

By a direct comparison with the field equations, Eq. (3.5), we find that

$$L_\mu\equiv -u_{\mu A}{}^4(\delta H/\delta y_A+\dot\pi^A)+\dot g_\mu. \tag{3.19}$$

From the above, it is evident that there exist four linearly independent combinations of the field equations which are free of the $\dot\pi^A$ and $\dot y_A$. These four equations correspond to the four linear combinations of field equations in the Lagrangian formalism which are free of second time derivatives of the field variables. Because the L_μ are four expressions involving the momenta and the field variables, but no time derivatives, the relationships (3.18) are called "secondary" constraints.

In the theory of the electromagnetism a similar situation arises. There the primary constraint is $\pi^4=0$, and the secondary constraint is $\pi^s{}_{,s}+c\rho=0$, where ρ is the charge density. π^s is equal to the negative of the electric field strength divided by $4\pi c$, and therefore the secondary constraint corresponds to the Lagrangian field equation $\operatorname{div}\mathbf{E}=4\pi\rho$.

3.3 The Bianchi Identities

Before proceeding to take further time derivatives, we shall stop to examine how far this process need be carried. According to II the number of secondary constraints in any theory is P times the number of arbitrary functions in the transformation law for the field variables, where P is the highest order of differentiation occurring in the transformation law. Therefore, we should expect to find only four secondary constraints in a coordinate covariant theory such as we are considering. Our case differs from the situations considered in II in that we are dealing with the possibility that the field equations may not be satisfied. However, the argument is not altered by this fact and, therefore, we shall not repeat the whole argument. Instead we shall merely indicate where changes need to be made in order to include the possibility that the field equations need not be satisfied. We shall continue to restrict our discussion to coordinate transformations, although the extension to the more general transformations considered in II is trivial. In order to facilitate comparison with II, we shall place the number of the equation in II which corresponds to the equations we write to the left of our equations.

In II it was shown that the generating density function for an infinitesimal invariant transformation

can be brought into the particularly simple form,

(II-5.4) $$C={}^1A_\mu\xi^\mu-{}^0A_\mu\xi^\mu. \tag{3.20}$$

If the Lagrangian, and therefore the Hamiltonian, explicitly describes the possibility that the field equations may not be satisfied, then the coefficients ${}^nA_\mu$ may depend on the P^A, which are a measure of the amount by which the field equations are not satisfied, as well as on the canonical field variables. The group character of the transformation law is not altered by the introduction of the P^A into the theory. Therefore, in this case as well, the ${}^nA_\mu$ form a function group.

The investigation of the Poisson bracket relations of the ${}^nA_\mu$ with the Hamiltonian proceeds in the same fashion as in II. Because of the covariance of the theory under arbitrary coordinate transformations, the Hamiltonian can change as a function of its arguments only by adding a linear combination of primary constraints. Furthermore, this change is given by the total time derivative of the generating functional of the transformation.[13]

Therefore, we have

(II-5.8) $$(\mathfrak{C},\mathfrak{H}^*)+\frac{\partial\mathfrak{C}}{\partial t}\equiv\int\delta' w^\rho g_\rho d^3x. \tag{3.21}$$

As a result it follows that

(II-5.12) $$g_\mu\equiv{}^1A_\mu, \tag{3.22}$$

and[14]

(II-5.13) $$\frac{\partial\,{}^1A_\mu}{\partial t}+({}^1A_\mu, H^*)={}^0A_\mu\equiv a_\mu{}^\nu g_\nu, \tag{3.23}$$

$$(g_\mu, H^*)-{}^0A_\mu\equiv a_\mu{}^\nu g_\nu,$$

$$\frac{\partial\,{}^0A_\mu}{\partial t}+({}^0A_\mu, H^*)\equiv b_\mu{}^\nu g_\nu. \tag{3.24}$$

The $a_\mu{}^\nu$ and $b_\mu{}^\nu$ are certain functions of the field variables which are determined by the transformation properties of the Hamiltonian. The only difference between the above relations and the corresponding relations in II is the occurrence of the partial derivative with respect to t on the left-hand side of the above equations. This additional term results from the fact that the ${}^nA_\mu$ can depend on the time through the P^A as well as through the field variables.

[13] A canonical transformation produces the following changes in value:

$$\delta q_k=\partial C/\partial p_k,\quad \delta p_k=-\partial C/\partial q_k,\quad \delta H=\partial C/\partial t.$$

Therefore,

$$\delta' H=H(q_k, p_k)-H(q_k', p_k')+\partial C/\partial t$$
$$=(C, H)+\partial C/\partial t.$$

[14] The Poisson bracket $({}^nA_\mu, H^*)$ is to be calculated as follows:

$$\left(\int\sigma^\mu\,{}^nA_\mu d^3x, \mathfrak{H}^*\right)=\int\sigma^\mu({}^nA_\mu, H^*)d^3x,$$

where the σ^μ are arbitrary weight functions.

Comparing Eq. (3.23) with (3.18) we find that, modulo the primary constraints, the ${}^0A_\mu$ are equal to the secondary constraints. In fact, by considering the transformation law for the y_A, one can show that

$${}^0A_\mu\equiv L'_\mu-u_{\mu A}{}^4P^A, \tag{3.25}$$

where

$$L'_\mu\equiv L_\mu-f_\mu(g^\rho).$$

Equation (3.24) tells us, therefore, that the total time derivative of the secondary constraints does not lead outside the function group composed of the g_μ and ${}^0A_\mu$. Hence, the four secondary constraints are the only conditions imposed on the field equations by the existence of the primary constraints.

From the above it is evident that the second time derivative of the primary constraints should vanish identically modulo the primary and secondary constraints. This condition yields the Bianchi identities in the canonical formalism. Let us consider

$$\mathfrak{A}=\int\sigma^\mu\,{}^0A_\mu d^3x=\int\sigma^\mu(L'_\mu-u_{\mu A}{}^4P^A)d^3x\overset{I}{=}0. \tag{3.26}$$

Equation (3.16) shows that we need only consider $d\mathfrak{A}/dt$ in order to obtain all the interesting information from $d^2\mathfrak{S}/dt^2$:

$$\frac{d\mathfrak{A}}{dt}=\int\left\{\dot\sigma^\mu\,{}^0A_\mu+\sigma^\mu\left[({}^0A_\mu, H^*)+\frac{\partial\,{}^0A_\mu}{\partial t}\right]\right\}d^3x\overset{I}{=}0. \tag{3.27}$$

Again we consider the coefficients of σ^μ and $\dot\sigma^\mu$ separately. The coefficient of $\dot\sigma^\mu$ is merely the secondary constraint and, therefore, gives no new information. From the previous argument concerning the function group, the coefficient of σ^μ is equal to a linear combination of primary constraints and, hence, vanishes in Σ_I. Let us calculate this term explicitly:

$$\begin{aligned}(L'_\mu, H^*)\equiv{}&\partial^A L'_\mu\frac{\partial H}{\partial\pi^A}+\partial^{A\,s}L'_\mu\left(\frac{\partial H}{\partial\pi^A}\right)_{,\,s}\\&+\partial^{A\,rs}L'_\mu\left(\frac{\partial H}{\partial\pi^A}\right)_{,\,rs}-\left(u_{\mu A}{}^s\frac{\delta H^*}{\delta y_A}\right)_{,\,s}\\&-\left(\delta_\mu{}^4\frac{\partial H}{\partial\pi^A}+\delta_\mu{}^s y_{A,\,s}\right)\frac{\delta H^*}{\delta y_A}\\\equiv{}&B_\mu-(u_{\mu A}{}^s P^A)_{,\,s}\\&-\left(\delta_\mu{}^4\frac{\partial H}{\partial\pi^A}+\delta_\mu{}^s y_{A,\,s}\right)P^A.\end{aligned} \tag{3.28}$$

Therefore, we obtain

$$\begin{aligned}\partial\,{}^0A_\mu/\partial t+({}^0A_\mu, H^*)\equiv{}&B_\mu-(u_{\mu A}{}^\nu P^A)_{,\,\nu}\\&-(\delta_\mu{}^4\partial H/\partial\pi^A+\delta_\mu{}^s y_{A,\,s})P^A\overset{I}{\equiv}0.\end{aligned} \tag{3.29}$$

The symbol l above an identity sign means that the relationship is an identity modulo the primary constraints (but not involving time derivatives of primary constraints). The secondary constraints are satisfied only as long as we remain in Σ_l. However, the relation (3.29) are satisfied, in the above sense, throughout Σ; i.e., Eq. (3.24) is valid throughout Σ. Furthermore, since Eq. (3.29) must be satisfied identically in Σ, whether or not P^A is zero, the terms containing P^A and those not containing P^A must vanish separately. Hence, we have

$$(u_{\mu A}{}^{\nu}P^A)_{,\nu}-(\delta_\mu{}^4\partial H/\partial\pi^A+\delta_\mu{}^\alpha y_{A,\alpha})P^A\overset{l}{\equiv}0, \quad (3.30)$$

and

$$B_\mu\overset{l}{\equiv}0. \quad (3.31)$$

Comparing Eq. (3.30) with the Bianchi identities, Eq. (2.4), we see that this identity must be satisfied by the P^A, if they are to be the right-hand sides of covariant field equations.

The B_μ can also be written in the same form and are, therefore, the Bianchi identities in terms of the canonical variables. By using the relations given in Eq. (3.2) one can show that

$$\frac{\partial L'_\mu}{\partial\pi^A}\dot\pi^A+\frac{\partial L'_\mu}{\partial\pi^A{}_{,\alpha}}\dot\pi^A{}_{,\alpha}-(u_{\mu A}{}^\alpha\dot\pi^A)_{,\alpha}$$
$$-\left(\delta_\mu{}^4\frac{\partial H}{\partial\pi^A}+\delta_\mu{}^\alpha y_{A,\alpha}\right)\dot\pi^A\equiv0. \quad (3.32)$$

Adding the above identity to B_μ we have

$$B_\mu\equiv L'_{\mu,4}-\left[u_{\mu A}{}^\alpha\left(\frac{\delta H}{\delta y_A}+\dot\pi^A\right)\right]_{,\alpha}$$
$$-\left(\delta_\mu{}^4\frac{\partial H}{\partial\pi^A}+\delta_\mu{}^\alpha y_{A,\alpha}\right)\left(\frac{\delta H}{\delta y_A}+\dot\pi^A\right)\overset{l}{\equiv}0. \quad (3.33)$$

If we remember Eq. (3.19), we see that the above is just what one would expect the Bianchi identities to become in the Hamiltonian formalism.

3.4 Strong Conservation Laws

As has been pointed out previously, the strong conservation laws are certain ordinary divergences which vanish whether or not the field equations are satisfied. Furthermore, they are a result of the existence of the Bianchi identities. Having already obtained the Bianchi identities in the canonical formalism we are prepared to derive from them the strong conservation laws.

The first two terms of B_μ, Eq. (3.33) can easily be put into the form of a divergence:

$$L'_{\mu,4}-\left[u_{\mu A}{}^\alpha\left(\frac{\delta H}{\delta y_A}+\dot\pi^A\right)\right]_{,\alpha}$$
$$\equiv\left\{\delta_4{}^\nu L'_\mu-\delta_\alpha{}^\nu u_{\mu A}{}^\alpha\left(\frac{\delta H}{\delta y_A}+\dot\pi^A\right)\right\}_{,\nu}. \quad (3.34)$$

The remaining two terms require a little manipulation, but without difficulty one can show that,

$$\delta_\mu{}^\alpha y_{A,\alpha}\left(\frac{\delta H}{\delta y_A}+\dot\pi^A\right)$$
$$\equiv\left\{\delta_\alpha{}^\nu\left[\delta_\mu{}^\alpha\left(H-\pi^A\frac{\partial H}{\partial\pi^A}\right)-\delta_\mu{}^\nu y_{A,\nu}\partial^{A\alpha}H\right]\right.$$
$$\left.+\delta_\mu{}^\alpha\delta_4{}^\nu y_{A,\alpha}\pi^A\right\}_{,\nu}, \quad (3.35)$$

$$\delta_\mu{}^4\frac{\partial H}{\partial\pi^A}\left(\frac{\delta H}{\delta y_A}+\dot\pi^A\right)$$
$$\equiv\left\{\delta_\mu{}^4\delta_4{}^\nu H-\delta_\mu{}^4\delta_\alpha{}^\nu\frac{\partial H}{\partial\pi^A}\partial^{A\alpha}H\right\}_{,\nu}. \quad (3.36)$$

Substituting from the above three relations, Eq. (3.33) becomes

$$T_\mu{}^\nu{}_{,\nu}\overset{l}{\equiv}0,$$
$$T_\mu{}^\alpha=u_{\mu A}{}^\alpha\left(\frac{\delta H}{\delta y_A}+\dot\pi^A\right)+\delta_\mu{}^\alpha\left(H-\pi^A\frac{\partial H}{\partial\pi^A}\right), \quad (3.37)$$
$$T_\mu{}^4=-L'_\mu+\delta_\mu{}^4H+\delta_\mu{}^\nu y_{A,\nu}\pi^A.$$

The above is just the statement of the strong conservation laws.

One should not expect the Bianchi identities and hence the strong conservation laws to hold in the total phase space Σ. The covariance of the Lagrangian theory, which is responsible for both the Bianchi identities and the conservation laws, is reflected in the canonical formalism by the existence of the primary constraints. Since the constraints are satisfied only in Σ_l, it would be unrealistic to expect to find identities and conservation laws, resulting from the covariance of the theory, which are valid in regions of Σ where the constraints are not satisfied.

3.5 Surface Integrals

The arguments leading up to the surface integrals for the equations of motion are the same here as in the Lagrangian case, Sec. II. Formally the surface integrals are the same. Unfortunately, however, although the superpotentials may be found in principle, even the

restriction to a quadratic Lagrangian does not permit their explicit calculation. Bergmann and Schiller, by making a specific assumption about the transformation properties of the Lagrangian density, are able to derive expressions for the superpotentials.[15] In their formulation the superpotentials are easily carried over into the Hamiltonian formalism. However, in any case the determination of the Bianchi identities follows from similar arguments to those presented in this paper.

In a particular theory, such as the theory of gravitation, the calculation of the superpotentials should not lead to any serious difficulties. From Eqs. (3.19) and (2.13) with $\nu=4$, one sees that modulo the primary constraints

$$L_\mu' = U_\mu{}^{[s4]}{}_{,s} + t_\mu{}^4. \tag{3.38}$$

Therefore, in the theory of gravitation one can show that,[16]

$$U_\mu{}^{[s4]} = u_{\mu A}{}^s \bar{\pi}^A - \tfrac{2}{3}(u_{\mu A}{}^4 L^{ABns} - u_{\mu A}{}^s L^{ABn4}) y_{B,n}. \tag{3.39}$$

If we substitute for the π^A from Eq. (3.3), the above expression for $U_\mu{}^{[s4]}$ agrees with that obtained from Eq. (2.23). The antisymmetry in s and 4 can be shown explicitly by making use of Eq. (3.9) and dropping extra factors containing g_μ:

$$U_\mu{}^{[s4]} = \tfrac{1}{3}(u_{\mu A}{}^s L^{AC4t} - u_{\mu A}{}^4 L^{ACts}) E_{CB} \bar{\pi}^B + \tfrac{2}{3}(u_{\mu A}{}^s L^{ABn4} - u_{\mu A}{}^4 L^{ABns}) y_{B,n}. \tag{3.40}$$

Thus, for the theory of gravitation we can write out the surface integrals explicitly.

IV. DISCUSSION

As a result of the existence of strong conservation laws in a generally covariant field theory, there exist superpotentials whose divergences yield the components of the energy-momentum tensor, $T_\mu{}^\nu$. We have shown that by means of these superpotentials the total energy and momentum contained in a three-dimensional region of space can be calculated by a two-dimensional surface integral taken over the boundary of that region. Furthermore, we were able to set up certain two-dimensional surface integrals which were independent of the surface of integration and which yielded the equations of motion for any singularities (particles) enclosed by the surface. In the canonical formalism the fact that the constraints together with the Hamiltonian form a function group enabled us to obtain the Bianchi identities and, hence, the strong conservation laws in terms of the canonical variables. Thus, the superpotentials and the surface integrals can be found in the Hamiltonian formalism.

Up to now the investigation of gravitational radiation has been unsuccessful because of the necessary restriction to small particle velocities (compared with the velocity of light) in the Einstein-Infeld approximation method.[17,18] If this restriction to slow motion is removed, then the field equations cannot be integrated beyond the first order without knowledge of the motion of the particles in advance. However, by using the Hamiltonian formalism, one can build up a solution of the field equations as a Taylor series with respect to time. Since the constraints and Hamiltonian form a function group, one need only choose the initial conditions such that the primary and secondary constraints are satisfied. Having done so, one then proceeds as though there were no constraints. Thus, the problem of investigating gravitational radiation is reduced to the choice of initial conditions and the evaluation of certain surface integrals.

Since the energy and momentum of the field can be calculated by means of surface integrals, there is no need to separate the self-field of a particle from the total field. Indeed, because of the nonlinearity of the field equation one cannot make this separation. It appears conceivable that when the gravitational field is quantized the usual renormalization of the mass and charge may not be necessary. The role played by the equations of motion in a quantized theory is still open to question. There seems to be no way of interpreting equations of motion within the framework of quantum mechanics as it exists today. However, this question will have to be investigated further.

In conclusion, I wish to express my appreciation to Dr. Peter G. Bergmann for many valuable discussions.

[15] P. G. Bergmann and R. Schiller, Phys. Rev. **89**, 4 (1952).

[16] The definition of $A^{\rho B\sigma}$ in the theory of gravitation is given by Bergmann, Penfield, Schiller, and Zatzkis, Phys. Rev. **80**, 81 (1950).

[17] L. Infeld and A. E. Scheidegger, Can. J. Math. **3**, 195 (1951).

[18] A. E. Scheidegger, Phys. Rev. **82**, 883 (1951).

Symmetry Requirements in Electron Scattering by an Atom

L. E. H. TRAINOR* AND TA-YOU WU
Division of Physics, National Research Council, Ottawa, Canada
(Received September 15, 1952)

It is pointed out that in the treatment of the problem of electron scattering by an atom including the effect of the Pauli principle, the use of unsymmetrized wave function and asymptotic conditions in one electron does not ensure the required asymptotic conditions in the other electron. However, the use of symmetrized wave functions automatically ensures symmetrical asymptotic conditions in both electrons.

IN a recent note[1] the treatment of electron scattering by hydrogen-like atoms by Mott and Massey[2] is discussed. At the end of the second section, the possibility of simultaneously satisfying the symmetry requirements and the asymptotic conditions as they are stated by Mott and Massey is questioned. The purpose of the present note is to point out that the implication of symmetrized wave functions in their treatment insures symmetrized asymptotic conditions, and hence, their scheme is consistent from the point of view of symmetry requirements.

Since the Hamiltonian of the system under discussion is symmetric in the two electrons, it is evident that if a set of asymptotic conditions uniquely determines a solution of the Schrödinger equation, then the solution so determined has the same symmetry properties as are expressed in the asymptotic conditions. Conversely, if one assumes symmetrized solutions, one implies symmetrized asymptotic conditions. The treatment of Mott and Massey serves as an illustration.

Let $\Psi(1,2)$ be any solution whatsoever of the Schrödinger equation for the two-electron atomic system, and let it be expanded as a function of the coordinates of one electron in terms of the complete set of hydrogenic functions,

$$\Psi(1,2)=\Sigma\int\varphi_n(1)\Phi_n(2), \tag{1}$$

where the expansion coefficients Φ_n are functions of the coordinates of the second electron. On substitution of (1) into the Schrödinger equation, one obtains

$$(\Delta_2+k_n^2)\Phi_n(2)=\int\varphi_n^*(1)\left[-\frac{2z}{r_2}+\frac{2}{r_{12}}\right]\Psi(1,2)d\mathbf{r}_1, \tag{2}$$

which is an infinite system of differential equations. If one requires the asymptotic conditions

$$\Phi_n(2)\longrightarrow\begin{cases}\delta_{n0}e^{i\mathbf{k}_0\cdot\mathbf{r}_2}+\dfrac{e^{ik_nr_2}}{r_2}\xi_n(\vartheta_2,\varphi_2), & k_n^2>0,\\ \text{exponentially decreasing function of } r_2, & k_n^2<0,\end{cases} \tag{3}$$

the system (2) can be put in the form

$$\Psi(1,2)=\varphi_0(1)e^{i\mathbf{k}_0\cdot\mathbf{r}_2}+\Sigma\int\varphi_n(1)\int\int\frac{\exp(ik_n|\mathbf{r}_2-\mathbf{r}_2'|)}{4\pi|\mathbf{r}_2-\mathbf{r}_2'|}\times\varphi_n^*(1')\left[-\frac{2z}{r_2'}+\frac{2}{r_{12}'}\right]\Psi(1',2')d\mathbf{r}_1'd\mathbf{r}_2'. \tag{4}$$

It is generally assumed that the conditions (3) uniquely determine the solution $\Psi(1,2)$. In this case, namely, if $\Psi(1,2)$ in (1) is any solution not necessarily symmetrized, there is no assurance of an asymptotic form corresponding to outgoing waves of electron 1 in the alternative expansion

$$\Psi(1,2)=\Sigma\int\varphi_n(2)\chi_n(1).$$

In the particular case in which $\Psi(1,2)$ is required to be a symmetrized solution, let

$$\begin{aligned}\Psi^{\pm}(1,2)&=\Sigma\int[\varphi_n(1)F_n(2)\pm\varphi_n(2)F_n(1)],\\&=\Sigma\int[\varphi_n(1)F_n(2)\pm\varphi_n(1)G_n(2)],\\&=\Sigma\int\varphi_n(1)\Phi_n^{\pm}(2)=\pm\Sigma\int\varphi_n(2)\Phi_n^{\pm}(1).\end{aligned} \tag{5}$$

It is evident from (5) that the asymptotic conditions (3) now apply to the coordinates of both electrons in a symmetrical manner, and are expressed in the "solution" (4)[3] by virtue of the symmetrized function $\Psi^{\pm}(1',2')$ in the integrand.

This theory is satisfactory, except that, in view of the form of the asymptotic conditions (3) imposed, no allowance has been made for finding the cross sections corresponding either to both electrons being ejected into definite directions, or to both electrons being left in a doubly excited state of the two-electron system, i.e., the

* National Research Laboratories Post-doctoral Fellow, now at Queens University, Kingston, Ontario, Canada.

[1] T. Y. Wu, Phys. Rev. **87**, 1012 (1952).

[2] N. F. Mott and H. S. W. Massey, *Theory of Atomic Collisions* (Oxford University Press, London, 1949), pp. 140, 215, 258.

[3] In the sense of a solution of the integral equation, by iteration, for example.

inverse Auger or auto-ionization transition. In the case of electron scattering by the hydrogen atom, this corresponds to a doubly excited state of the negative hydrogen ion which can undergo auto-ionization.

In actual calculations, one usually replaces $\Psi^{\pm}(1, 2)$ in the integrand of (4) by the single term corresponding to one electron in the atom and an incident plane wave (Oppenheimer approximation), or by a finite number of terms from (5).[1,4] In either case, the use of symmetrized approximation wave functions in (4) implies symmetrized asymptotic conditions in the manner discussed above.

[4] G. A. Erskine and H. S. W. Massey, Proc. Roy. Soc. (London) **A212**, 512 (1952).

PHYSICAL REVIEW VOLUME 89, NUMBER 1 JANUARY 1, 1953

Luminescence and Photoconductivity in Cadmium Sulfide at the Absorption Edge

CLIFFORD C. KLICK
Crystal Branch, Metallurgy Division, Naval Research Laboratory, Washington, D. C.
(Received August 4, 1952)

Measurements of optical transmission, photoconductive response, luminescent edge emission, and excitation spectrum for edge emission have been made on single crystal specimens of CdS at 77°K and 4°K. At the lowest temperature there is an energy gap of more than 0.1 electron volt between the absorption edge and the onset of emission. Coupled with information from the emission spectrum and the infrared properties of CdS, this observation suggests that edge emission in this material may occur at a special center and not be characteristic of the pure lattice.

INTRODUCTION

LUMINESCENT edge emission occurs in cadmium sulfide at the long wavelength side of the absorption edge when the material is cooled to liquid nitrogen temperature (77°K) and excited with ultraviolet light.[1] At liquid helium temperatures (4°K) the emission spectrum of single crystal materials sharpens into a series of equally spaced "lines" with a width at half-maximum of approximately 10A.[2] This luminescent emission is less broad than that of impurity activated materials with the exception of activators, such as the rare earths, in which the electronic transition occurs in an inner electronic shell.[2] One explanation is that either free electrons and holes or excitons recombine in the pure lattice so that this emission is "lattice" emission. The successive luminescent peaks would correspond to the excitation of increasing numbers of vibrational quanta, and the spacing of the peaks would correspond in energy to the principal infrared vibrational frequency. This simple explanation faces theoretical objections since the probability of electron-hole or exciton recombination in the pure material is relatively small.

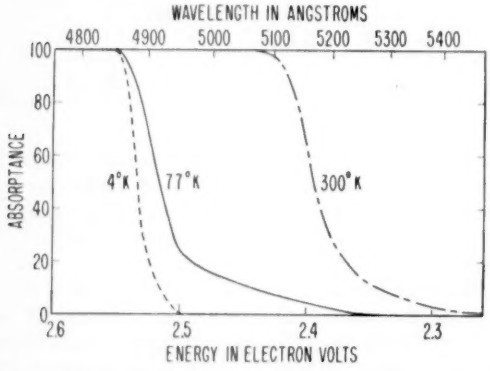

FIG. 1. Absorptance (100 minus percent transmission) of CdS as a function of wavelength for temperatures of 4°K, 77°K, and 300°K. The sample is approximately 0.004 cm thick.

[1] F. A. Kröger, Physica **7**, 1 (1940).
[2] C. C. Klick, J. Opt. Soc. Am. **41**, 816 (1951).

The experiments on the electrical and optical properties of CdS at the absorption edge was undertaken primarily to investigate whether edge luminescence was characteristic of the pure lattice. Also, since the large photoconductivity in CdS is technically and scientifically of great interest,[3] it was felt that the measurements would aid in understanding this phenomenon. Finally, an understanding of edge emission in CdS might suggest explanations of edge emission in such varied materials as the silver halides[4] and germanium.[5]

EXPERIMENTAL ARRANGEMENT

The cadmium sulfide investigated here was single crystal material grown from the vapor by the Frerichs technique.[6] Photoconductivity was measured on a rod-like specimen approximately 1 mm in diameter and 4 mm long. The other measurements were on thin flaked specimens approximately 4 mm×1 mm×0.1 mm. For the emission and excitation measurements the samples were held between quartz plates. Because of this, the

[3] See, for instance, A. Rose, RCA Rev. **12**, 362 (1951) for an introduction to this subject.
[4] Farnell, Burton, and Hallama, Phil. Mag. **41**, 157 (1950).
[5] J. R. Haynes and H. B. Briggs, Phys. Rev. **86**, 647 (1952).
[6] R. Frerichs, Naturwiss. **33**, 381 (1946).

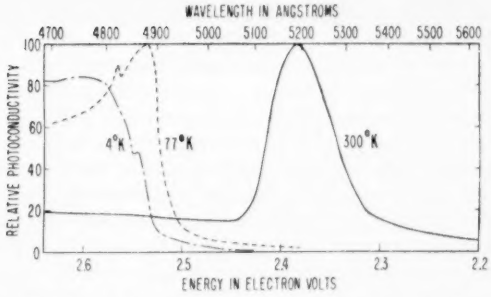

FIG. 2. Relative photoconductivity of CdS as a function of wavelength. The ordinate scale for each curve is set independently.

flakes broke into smaller pieces; there was, however, no grinding of the material. Although excitation and emission measurements were made on the same specimens, other samples were used for the photoconductivity and transmission measurements. In order to minimize effects due to inclusion of silver in the material, specimens whose luminescence was low at room temperature were chosen.

In all measurements temperature control was obtained by immersing the samples directly in either liquid nitrogen (77°K) or liquid helium (4°K) exposed to atmospheric pressure.

All optical measurements were made with the same monochromator and the same slit widths in order to facilitate comparison of the various data. The trace of the emission spectrum of the mercury 5461A line given in Figs. 4, 5, and 6 indicates that the energy band pass of the instrument at its half-maximum points is 0.015 electron volt. The change in dispersion with wavelength of the monochromator is such as to maintain this band width approximately constant over the narrow wavelength range investigated. In each measurement the monochromator was motor-driven and a continuous record obtained.

EXPERIMENTAL RESULTS

A. Absorption

Figure 1 presents the results of measurements on the absorptance (100 minus percent transmission) of a flake of CdS 0.004 cm thick. An absorptance of 90 in this case corresponds to an absorption coefficient of 600 cm^{-1} neglecting reflection losses; an absorptance of 10 corresponds to an absorption coefficient of 25 cm^{-1}. Between 300°K and 77°K the absorption edge shifts to the short wavelength by about 1A/°K; between 77°K and 4°K the shift continues at a slower rate—approximately 0.5A/°K. It also appears that the absorption edge is sharper at 4°K than at the higher temperatures. Both the 300°K and the 77°K curves show a decided long wavelength tail; the 4°K curve is drawn without this tail, but the data here is not conclusive because of the light scattering in the arrangement used. Data from measurements on photoconductivity and excitation indicate that there is probably also a long wavelength tail in the 4°K absorptance curve.

B. Photoconductivity

The photoconductivity of a single crystal of CdS as a function of the wavelength of the incident light is given in Fig. 2 for temperatures of 300°K, 77°K, and 4°K. The curves are drawn for equal numbers of incident quanta. For 50 volts applied to the crystal, the photocurrents at 4700A were 2.5×10^{-10} amp at 300°K, 1.5×10^{-9} amp at 77°K, and 2.5×10^{-10} amp at 4°K. At all temperatures the growth and decay of the photocurrent was slow with as much as a minute being required for equilibrium to occur. Point-by-point measurements were used to check the results of a continuous record.

At 300°K the well-known photoconductivity peak appears at the absorption edge. The peak shifts to shorter wavelengths as the temperature is decreased and is reduced in size relative to the short wavelength response until at 4°K the peak essentially disappears.

C. Emission

The emission spectrum of single crystal CdS is presented in Fig. 3 where the results are given in units of relative number of emitted quanta as a function of wavelength. Although excitation was by the 3650A Hg line, the emission spectrum has been found to be independent of the exciting wavelength. In going from 77°K to 4°K, the main portion of the emission shifts to long wavelengths and small emission bands appear at short wavelengths. These small bands were also found at 77°K by Kröger[1] in powdered materials prepared in the usual way by firing with flux. Since they appear to the short wavelength side of the absorption edge, Kröger attributed them to surface emission. At the lowest temperature there is a considerable sharpening of the main emission peaks; spectra taken with higher resolution[2] indicate that the width at half-maximum is 10A. The spacing of the main emission lines is uniform in energy and the energy difference between two suc-

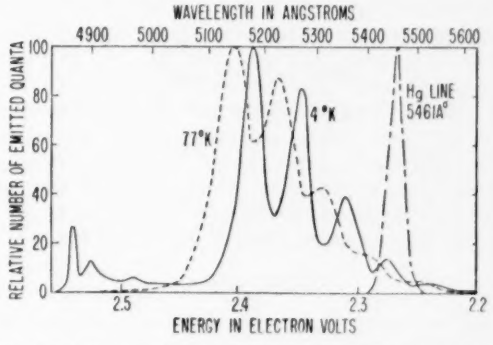

FIG. 3. Relative number of emitted quanta of CdS as a function of wavelength. Excitation is by the Hg 3650A line.

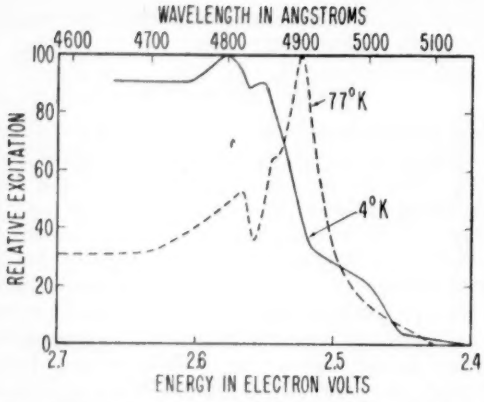

FIG. 4. Relative quantum efficiency of excitation for edge emission in CdS as a function of wavelength. Emission filtered through Corning No. 3484 glass transmitting wavelengths longer than 5300A.

cessive peaks corresponds to a quantum of infrared light with a wavelength of 32 microns.

D. Excitation

Relative quantum efficiency for the excitation of the main edge emission is shown as a function of the wavelength of the exciting light in Fig. 4 for temperatures of 77°K and 4°K. As in the photoconductivity and absorptance results there is a shift to short wavelengths as the temperature decreases. At 77°K there is a large peak in the excitation spectrum as there is in photoconductivity at the same temperature; in both measurements these peaks disappear at 4°K. In contrast with the photoconductivity measurements, however, the rise and decay of luminescence with the application or removal of excitation occurs in less than a second.

E. Summary of Experimental Results

In order to facilitate comparison of the data taken at each temperature, the results for 4°K have been collected in Fig. 5 and those for 77°K in Fig. 6. At 4°K the excitation spectrum has a peak at 2.48 ev which is approximately 0.1 ev below the highest points of the photoconductivity and excitation spectra. This peak is not accompanied by a photoconductivity maximum. In general, the absorptance and excitation edges at 4°K are found on the long wavelength side of the photoconductivity edge. At 77°K the separation of these curves is less than at 4°K. The distinct gap between the absorption edge and the onset of emission at 77°K is increased to more than 0.1 ev at 4°K.

DISCUSSION

As mentioned above, the uniform spacing of the emission lines in CdS is suggestive of interaction with a vibrating system the frequency of which corresponds to a 32 micron infrared quantum. It has been found by Plyler[2] that an absorption band at 34μ exists at room temperature. The absorption coefficient at the peak of this band is only of the order of 100 cm^{-1} and cannot correspond to the main infrared absorption peak. From data on the infrared absorption of ZnS, it is possible to estimate that the main CdS band is in the range of 40–45 microns; experimentally, it is found not to be less than 37 microns. These results suggest that the vibration system with which the electronic transition responsible for edge emission is coupled is not characteristic of the pure lattice. Further evidence is found in the data of Fig. 5 discussed above. The energy gap between the absorption edge and the onset of emission also implies that this is not a case of simple lattice emission corresponding to some type of resonance radiation.

One explanation of these experiments is that the emission corresponds to electron-hole or exciton recombination but that two effects occur. First, the emitting system is coupled closely enough to the lattice so that

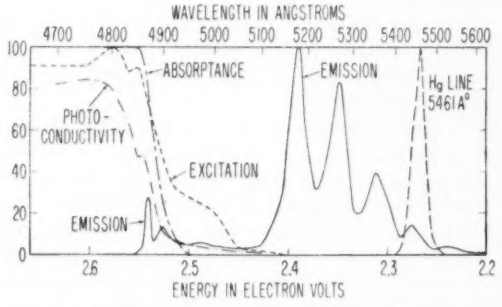

FIG. 5. Absorptance, photoconductivity, emission, and excitation of CdS at 4°K.

there is observed the normal Stokes' shift in absorption and emission wavelengths. Second, the coupling of the emitting system with the lattice causes an increase in the lattice vibrational frequency near the emitting system.

Another explanation is that edge emission in CdS occurs at points in CdS containing specific lattice defects. The emission energy would then be characteristic of the defect as would be the vibrational frequency. A conclusive choice between these explanations is not possible at present. However, there appear to be several arguments which favor the second explanation. First, the probability of an exciton radiating appears to be small compared with the probability that it will be annihilated at a lattice defect. Second, the change in lattice frequency appears to be quite large to be caused by an electrically neutral system of coupled hole and electron. Calculations of this effect would, of course, be instructive. Finally, the observed infrared band at 34μ is understood as arising from the vibrational frequency of the defect in its ground state on the second

explanation above. The first explanation of edge emission offers no interpretation of this band which is observed under conditions where neither free electrons nor holes are formed.

If defects are responsible for edge emission in CdS, their nature is unknown, but they are almost certainly not due to the inclusion of foreign ions. The commonly known activators for CdS give an emission to the long wavelength side of the edge emission both at high and low temperatures. Also the intentional inclusion of impurities tends to weaken the edge emission rather than enhance it. Finally, it seems improbable that a trace of impurities could produce as bright and consistent a luminescence as is observed. From the infrared data it is apparent that the vibrational frequency of the luminescent center is higher than that of the pure material. This suggests that the center is in a region of lattice compression as may occur near an interstitial atom or ion.

There are two explanations for the excitation peak which is not accompanied by photoconductivity and occurs at 2.48 ev in the 4°K curve. The first is that this is an exciton level. A relation derived by Seitz[7] predicts that the lowest exciton level for CdS would be 0.17 ev below the conduction band. Since the approximations used in deriving this expression are worst for the lowest level, the difference between the theoretical value of 0.17 ev and the experimental value of approximately 0.10 ev may not be significant. The second explanation is that the excitation peak corresponds to absorption directly in the luminescent center so that luminescence occurs without the transport of charge. Supporting evidence for this view is the low value of the absorptance in this region as contrasted with high values in bands normally ascribed to excitons.

This investigation touches upon the complicated problem of conductivity in CdS in two respects. The first is that the large peak in conductivity occurring at the absorption edge at 300°K is reduced in size as the temperature decreases and finally disappears at 4°K. Thus it is distinctly a temperature dependent phenomenon. The second is the general similarity of the wavelength response of excitation and photoconductivity coupled with their widely different response times. It has been suggested that the large photoconductivities observed in the sulfides originate in small

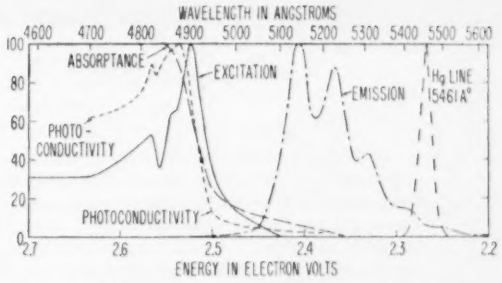

FIG. 6. Absorptance, photoconductivity, emission, and excitation of CdS at 77°K.

special volumes of the crystal such as n-p junctions,[8] n-p-n junctions,[9] or surface layers.[10] The data here is consistent with this view if the luminescence originates throughout the crystal. A model in which both the slow response photoconductivity and fast response luminescence are characteristic of the whole crystal has been suggested by Kallman and Kramer.[11]

The emission spectrum of CdS is also of considerable interest because it presents evidence for the interaction of the electronic transition with only a single mode of vibration of the luminescent center. Should there be more than one vibrational mode of importance or a spectrum of interactions, one would expect a smearing out of the lines in the long wavelength side of the emission or at least a distinct loss of resolution. That this is not apparent lends support to the procedure used in computing configurational coordinate curves for luminescent impurities[12,13] where interaction is considered with only a single mode of vibration. A detailed discussion of the approximations involved in this procedure is contained in recent work by Lax.[14]

The single crystal CdS was kindly prepared by Mr. William Zimmerman III of the Crystal Preparations Section, Crystal Branch at the Naval Research Laboratory. The author also wishes to express his thanks to Dr. James H. Schulman, Dr. Earle K. Plyler, and Dr. David L. Dexter for stimulating discussions.

[7] F. Seitz, Phys. Rev. **76**, 1376 (1949).

[8] E. S. Rittner, Science **111**, 685 (1950).
[9] K. G. McKay, Phys. Rev. **84**, 833 (1951).
[10] R. H. Bube, Phys. Rev. **83**, 393 (1951).
[11] H. Kallman and B. Kramer, Phys. Rev. **87**, 91 (1951).
[12] F. E. Williams, Phys. Rev. **82**, 281 (1951).
[13] C. C. Klick, Phys. Rev. **85**, 154 (1952).
[14] M. Lax, Phys. Rev. **86**, 640 (1952); **86**, 660 (1952).

Electric Resonance Transitions in a Tapered Electric Field*

JOSHUA N. GOLDBERG,† JOHN W. TRISCHKA, AND PETER G. BERGMANN
Department of Physics, Syracuse University, Syracuse, New York
(Received August 20, 1952)

In this paper we investigate the broadening of the spectral lines produced by small inhomogeneities in the homogeneous C-field of the molecular beam electric resonance apparatus. To do so, we represent the inhomogeneities as an arbitrary function of time because of the flight of the molecules through the field. The transitions which we investigate occur between states which are the instantaneous solutions of the Stark effect problem in which we neglect the effects of nuclear molecular interactions. We obtain a solution for the probability amplitudes for a transition such that $\Delta J=0$ and $\Delta m=\pm 1$ by considering a linear combination of the solutions for the case in which there are no inhomogeneities. As an example, we consider the inhomogeneity of the C-field as represented by a linear taper. In this case the amount of line broadening depends on the ratio of the amplitude of the taper to the amplitude of the radio frequency field which induces the transitions. Because under optimum operating conditions the product of the rf field and the homogeneous field is kept constant, the inhomogeneities have a greater effect in strong than in weak C-fields. The line broadening, however, is considerably smaller than one might estimate from the energy level difference computed for two perfectly hodogeneous fields having respectively field intensities equal to the two extreme values of the tapered field.

IN the electric resonance method of molecular beam spectroscopy,[1] broadening of the spectral lines has been observed in strong fields. This broadening has been attributed to small inhomogeneities in the homogeneous field (C-field) of the molecular beam apparatus.[2] Inasmuch as the determination of the physically interesting parameters of a molecule—electric dipole moment, moment of inertia, nuclear quadrupole moments, etc.—depends on the resolution of the fine and hyperfine structure of the broad lines observed, we have attempted to obtain quantitative information on the degree of broadening of the line profile on account of inhomogeneities in the C-field. In our calculations we have represented this inhomogeneity as a change in the C-field *with time*, because of the flight of the molecule through the field. To simplify matters, we have neglected the effects of the nuclear quadrupole moment; our methods can be modified to include such effects, but the calculations become considerably more laborious. In our opinion, this simplification does not destroy the essentials of the situation.

If a molecule is in a constant electric field $\mathcal{E}$, the separation of its energy levels remains fixed. If we impose an oscillating field $\mathcal{E}_x \cos\omega t$ at right angles to $\mathcal{E}$, such that $h\omega$ is equal to the energy separation of two states with different spatial quantization, transitions will be induced between these states in a regular and predictable manner.[1] If a small inhomogeneity $f(t)$ is added to the constant field, the energy levels will shift adiabatically as long as df/dt is sufficiently small. A molecule exposed to this field for a time τ will no longer be near resonance for the entire time of exposure. Moreover, since the resonance frequency changes in time, the molecule will be near resonance (at least for a small interval of time) over a greater range of frequencies of the oscillating field than is the case in a perfectly homogeneous field. Therefore, one would expect, even without detailed calculations, that the peaks of the spectral lines should be decreased as well as their widths broadened by the presence of a small inhomogeneity.

To show these effects explicitly, we must solve the time dependent Schrödinger equation,

$$[J^2\hbar^2/2I-\mu_z(\mathcal{E}+f(t))-\mu_x\mathcal{E}_x\cos\omega t]\Psi=ih\partial\Psi/\partial t, \quad (1)$$

where J is the total angular momentum, μ is the effective molecular dipole moment, and I is the moment of inertia of the molecule. In the absence of an oscillating field, the last term in the Hamiltonian does not appear. Therefore, transitions will occur between those states which are instantaneous solutions of the Stark effect problem,

$$[J^2\hbar^2/2I-\mu_z(\mathcal{E}+f(t))]\psi_{Jm}=E_{Jm}\psi_{Jm}, \quad (2)$$

provided the selection rules are satisfied. The first index refers to the rotational quantum state and the second to the space quantization of the molecule.

In order to solve the full time dependent problem stated in Eq. (1), we expand Ψ in terms of the ψ_{Jm} with time dependent coefficients:

$$\Psi=\sum_{J'm'} a_{J'm'}(t)\psi_{J'm'}(t)\exp\left[-\frac{i}{\hbar}\int E_{J'm'}dt\right]. \quad (3)$$

By substituting the expansion (3) into Eq. (1), we obtain

* This paper incorporates the major results of a Master's dissertation by one of us (JNG), which was accepted by the Graduate School of Syracuse University in 1950.

† Now at Armour Research Foundation, Chicago, Illinois.

[1] H. K. Hughes, Phys. Rev. **72**, 614 (1947).

[2] J. W. Trischka, Phys. Rev. **74**, 718 (1948).

differential equations for the coefficients a_{Jm}:

$$\dot{a}_{Jm}=\sum_{J'm'}\left\{\langle Jm|\mu_x\mathcal{E}_x|J'm'\rangle\cos\omega t - i\hbar\left\langle Jm\left|\frac{\partial}{\partial t}\right|J'm'\right\rangle\right\}a_{J'm'}\times\exp\left[\frac{i}{\hbar}\int(E_{Jm}-E_{J'm'})dt\right]. \quad (4)$$

The instantaneous Stark effect wave functions, ψ_{Jm}, are linear combinations of ordinary states of a rigid rotator belonging to different values of the quantum number J. If we continue to label stationary levels with a quantum number J, then this quantum number is not quite identical with the usual one describing the total angular momentum of the molecule. As a result, transitions with $\Delta J=0$ and $\Delta m=\pm1$ are permissible. Therefore, we shall consider the case where ψ_{Jm} is the initial state and $\hbar\Omega=E_{Jm}-E_{Jm+1}-\hbar\omega\approx0$. All terms in Eqs. (4) which do not have Ω in the exponent may be neglected as they contribute little to the result. Equations (4) thereby reduce to a pair of simultaneous differential equations. Dropping the subscript J, they are:

$$i\hbar\dot{a}_m=\tfrac{1}{2}h_{10}a_{m+1}\exp\left(i\int\Omega dt\right),$$
$$i\hbar\dot{a}_{m+1}=\tfrac{1}{2}h_{10}a_m\exp\left(-i\int\Omega dt\right), \quad (5)$$

where

$$h_{10}=\langle J, m+1|\mu_x\mathcal{E}_x|Jm\rangle. \quad (6)$$

If the degenerate states with m equal to ±1 are involved, both must be taken into account as transitions can occur to either from the state with $m=0$. The only resulting change in Eqs. (5) is that the right-hand side of the first of these equations is multiplied by 2. Hereafter we shall consider m unequal to zero unless otherwise specified.

If $f(t)$ is sufficiently small, one would not expect the line shape to be seriously affected. Since this condition is satisfied in the experimental set-up, we shall look for a solution as a linear combination of the instantaneous solutions of Eq. (5). These solutions are of the form:

$$a_m\sim c_0\exp\left[\tfrac{1}{2}i\int(\Omega\pm R)dt\right],$$
$$a_{m+1}\sim c_1\exp\left[\tfrac{1}{2}i\int(-\Omega\pm R)dt\right], \quad (7)$$

where $R=(\Omega^2+h_{10}^2/\hbar^2)^{\frac{1}{2}}$. Each probability amplitude, in the homogeneous case, is the sum of two exponential terms, differing by the sign of R in (7). In this case, each exponential would satisfy Eq. (5) separately. However, in the presence of inhomogeneities the two terms will combine. There are two linearly independent solutions of the homogeneous case which separate these different exponentials explicitly:

$$\Psi^+=c_0^+\exp\left[\tfrac{1}{2}i\int(\Omega+R-E_m/\hbar)dt\right]\psi_m + c_1^+\exp\left[\tfrac{1}{2}i\int(-\Omega+R-E_{m+1}/\hbar)dt\right]\psi_{m+1},$$
$$\Psi^-=c_0^-\exp\left[\tfrac{1}{2}i\int(\Omega-R-E_m/\hbar)dt\right]\psi_m + c_1^-\exp\left[-\tfrac{1}{2}i\int(\Omega+R+E_{m+1}/\hbar)dt\right]\psi_{m+1}. \quad (8)$$

The coefficients c_0^+, c_0^-, c_1^+, and c_1^- are determined by Eqs. (5) and the requirement that Ψ^+ and Ψ^- be normalized:

$$c_0^+=h_{10}[h_{10}^2+\hbar^2(\Omega+R)^2]^{-\frac{1}{2}},$$
$$c_0^-=h_{10}[h_{10}^2+\hbar^2(\Omega-R)^2]^{-\frac{1}{2}},$$
$$c_1^+=-\hbar(\Omega+R)[h_{10}^2+\hbar^2(\Omega+R)^2]^{-\frac{1}{2}},$$
$$c_1^-=-\hbar(\Omega-R)[h_{10}^2+\hbar^2(\Omega-R)^2]^{-\frac{1}{2}}. \quad (9)$$

We now write the solution of Eq. (1) as a linear combination of Ψ^+ and Ψ^- with time dependent coefficients:

$$\Psi=b_1(t)\Psi^++b_2(t)\Psi^-. \quad (10)$$

A comparison of Eqs. (10) and (8) with Eq. (3) shows that the probability amplitudes a_m and a_{m+1} are related to the coefficients b_1 and b_2 as follows:

$$a_m=b_1c_0^+\exp\left[\tfrac{1}{2}i\int(\Omega+R)dt\right]+b_2c_0^-\exp\left[\tfrac{1}{2}i\int(\Omega-R)dt\right],$$
$$a_{m+1}=b_1c_1^+\exp\left[\tfrac{1}{2}i\int(-\Omega+R)dt\right]+b_2c_1^-\exp\left[-\tfrac{1}{2}i\int(\Omega+R)dt\right]. \quad (11)$$

Substituting Eq. (10) into (1), we obtain a pair of differential equations for b_1 and b_2:[3]

$$\dot{b}_1=-b_2(c_0^+\dot{c}_0^-+c_1^+\dot{c}_1^-)\exp\left(-i\int Rdt\right),$$
$$\dot{b}_2=b_1(c_0^+\dot{c}_0^-+c_1^+\dot{c}_1^-)\exp\left(i\int Rdt\right). \quad (12)$$

[3] These equations have been simplified by means of the orthonormality conditions of Ψ^+ and Ψ^-. These conditions result in the following relations for the coefficients:

$$(c_0^+)^2+(c_1^+)^2=1,$$
$$(c_0^-)^2+(c_1^-)^2=1,$$
$$c_0^+c_0^-+c_1^+c_1^-=0.$$

The above equations show clearly that when $f(t)$ is identically zero b_1 and b_2 do indeed vanish. That is, the solution would reduce to that for a constant field, as it should. Since $f(t)$ is much smaller than the steady field, we say that b_1 and b_2 will not differ much from the homogeneous field solution. Therefore, we can apply the method of successive approximations to obtain a solution of Eqs. (12). We shall let $b_1(0)=b_2(0)=1$ and apply the initial conditions later. Thus we obtain:

$$b_1(t)=1-\int_0^t RA\exp\left(-i\int_0^{t'}Rdt''\right)dt',$$
$$b_2(t)=1+\int_0^t RA\exp\left(i\int_0^{t'}Rdt''\right)dt', \tag{13}$$

where

$$A=(c_0^+\dot{c}_0^-+c_1^+\dot{c}_1^-)/R.$$

To evaluate the integrals which appear in the above equations, we hold A fixed and so obtain:

$$b_1(t)=1-iA\left[\exp\left(-i\int_0^t Rdt'\right)-1\right],$$
$$b_2(t)=1-iA\left[\exp\left(i\int Rdt'\right)-1\right]. \tag{14}$$

This solution will be valid only if $A\ll 1$. A should be evaluated at the mean value of the static field, so that as little asymmetry as possible will be introduced by means of the approximation method.

Applying the initial conditions $a_m(0)=1$ and $a_{m+1}(0)=0$ in Eqs. (10), we find for the probability amplitudes the following expressions:[3]

$$\begin{aligned}a_m(t)=&\left[1-iA\left\{\exp\left(-i\int Rdt\right)-1\right\}\right]\\&\times c_0^+(0)c_0^+(t)\exp\left[\tfrac{1}{2}i\int(\Omega+R)dt\right]\\&+\left[1-iA\left\{\exp\left(i\int Rdt\right)-1\right\}\right]\\&\times c_0^-(0)c_0^-(t)\exp\left[\tfrac{1}{2}i\int(\Omega-R)dt\right],\end{aligned}$$

$$\begin{aligned}a_{m+1}(t)=&\left[1-iA\left\{\exp\left(-i\int Rdt\right)-1\right\}\right]\\&\times c_0^+(0)c_1^+(t)\exp\left[\tfrac{1}{2}i\int(-\Omega+R)dt\right]\\&+\left[1-iA\left\{\exp\left(i\int Rdt\right)-1\right\}\right]\\&\times c_0^-(0)c_1^-(t)\exp\left[-\tfrac{1}{2}i\int(\Omega+R)dt\right].\end{aligned} \tag{15}$$

Thus, the probability $P(m, m+1)$ of a transition from the state ψ_m to the state ψ_{m+1} after a time τ is given by[4]

$$\begin{aligned}P(m,m+1)=&\tfrac{1}{2}[(1+\delta^2(0))(1+\delta^2(\tau))]^{-\frac{1}{2}}\\&\times\Big\{[(1+\delta^2(0))(1+\delta^2(\tau))]^{\frac{1}{2}}-\delta(0)\delta(\tau)\\&-\cos\int_0^\tau Rdt-2A[\delta(\tau)(1+\delta^2(0))^{\frac{1}{2}}\\&-\delta(0)(1+\delta^2(\tau))^{\frac{1}{2}}]\sin\int_0^\tau Rdt\Big\},\end{aligned} \tag{16}$$

where we have used the abbreviation

$$\delta(t)=h\Omega(t)/h_{10}. \tag{17}$$

It is evident that if $f(t)$ vanishes, Eq. (16) reduces to the usual expression for the transition probability,[5]

$$P_0(m,m+1)=(1+\delta^2)^{-1}\sin^2(\tfrac{1}{2}R\tau). \tag{18}$$

If we evaluate the matrix elements involved and neglect second-order terms in $f(t)$, we find that

$$\Omega(t)=\omega_0-\omega+2K\mathcal{E}f(t), \tag{19}$$

where

$$K=3(2m+1)/[J(J+1)(2J-1)(2J+3)],$$

and $\omega_0=K\mathcal{E}^2$ is the frequency separation of the energy levels at the mean field value. We also have

$$h_{10}=-\tfrac{1}{2}Kh\mathcal{E}\mathcal{E}_x[(J-m)(J+m+1)]^{\frac{1}{2}}. \tag{20}$$

For optimum operating conditions, one chooses

$$h_{10}/h=-\pi/\tau. \tag{21}$$

Hence, one can write[6]

$$\delta(t)=\frac{(\omega-\omega_0)\tau}{\pi}-\frac{4f(t)}{\mathcal{E}_x[(J-m)(J+m+1)]^{\frac{1}{2}}}. \tag{22}$$

Up to now we have represented the inhomogeneity of the C-field as an arbitrary function $f(t)$. For most functions, however, the integration over R cannot be carried out easily. A particularly simple example for which this integration can be carried out in closed form is that in which the inhomogeneity is represented as a linear taper:

$$f(t)=\Delta\mathcal{E}(t/\tau-\tfrac{1}{2}). \tag{23}$$

In this case we have

$$\delta(t)=\frac{(\omega-\omega_0)\tau}{\pi}-\frac{4\Delta\mathcal{E}(t/\tau-\tfrac{1}{2})}{\mathcal{E}_x[(J-m)(J+m+1)]^{\frac{1}{2}}}, \tag{24}$$

[4] When $m=0$, $P(0, 1)$ is equal to one-half the expression given in Eq. (16) and $\delta(t)=h\Omega/\sqrt{2}h_{10}$. Similarly for $P(0, -1)$.

[5] H. C. Torrey, Phys. Rev. **59**, 293 (1941).

[6] If the initial state is one with $m=0$, the fact that the transition can take place to either of the two states with $m=\pm 1$ introduces a factor of 2 multiplying h_{10}^2 in R. The definition of optimum operating conditions is then altered by a factor of $\sqrt{2}$. Thus

$$\delta(t)=\frac{(\omega-\omega_0)\tau}{\pi}-\frac{2\sqrt{2}f(t)}{\mathcal{E}_x[J(J+1)]^{\frac{1}{2}}}.$$

and[7]

$$\int_0^\tau R dt = -\frac{\pi \mathcal{E}_x[(J-m)(J+m)]^{\frac{1}{2}}}{8\Delta\mathcal{E}}\Big\{\delta(\tau)[1+\delta^2(\tau)]^{\frac{1}{2}} - \delta(0)[1+\delta^2(0)]^{\frac{1}{2}} + \ln\frac{\delta(\tau)+[1+\delta^2(\tau)]^{\frac{1}{2}}}{\delta(0)+[1+\delta^2(0)]^{\frac{1}{2}}}\Big\}. \quad (25)$$

It is clear from Eq. (23) that the effect of the taper is completely determined by $\Delta\mathcal{E}/\mathcal{E}_x$. By choosing optimum operating conditions the product $\mathcal{E}\mathcal{E}_x$ was set equal to a constant. Hence, if $\mathcal{E}$ is increased $\mathcal{E}_x$ must be decreased in order to maintain optimum operating conditions. Therefore, the inhomogeneities will have the greatest effect on the line shape in strong C-fields where they were first observed by Trischka.[2] The fact that a given ratio $\Delta\mathcal{E}/\mathcal{E}$ has a greater effect when the C-field is relatively strong than when it is weak may seem paradoxical. However, it is well known[1,8] that the line width is proportional to the product $\mathcal{E}\mathcal{E}_x$. On the other hand, the energy level perturbation due to the taper is proportional to $\mathcal{E}\Delta\mathcal{E}$. Thus the shift in energy levels due to the inhomogeneities is small in weak and large in strong C-fields, compared with the line width in a homogeneous field. Therefore, one should expect the inhomogeneities of the C-field to produce greater broadening of the line profile in strong fields.

In Fig. 1(a) we have plotted the probability that a molecule initially in a state with $J=1$ and $m=0$ will undergo a transition to a state with $J=1$ and $m=\pm 1$. The curves are drawn for both a homogeneous field and a field with a linear taper. (In both of these cases the specific molecular parameters drop out of the expression for the transition probability.) The field values represented by the curves are such that $\Delta\mathcal{E}/\mathcal{E}_x=0.625$. For such field values we have:[9]

$$A=(\Delta\mathcal{E}/\pi\mathcal{E}_x)[1+\delta^2(\tau/2)]^{-\frac{1}{2}}\leqslant 0.20.$$

[7] For $m=0$, the factor outside the brackets becomes

$$-\pi\mathcal{E}_x[J(J+1)]^{\frac{1}{2}}/(4\sqrt{2}\Delta\mathcal{E}).$$

[8] The dependence of the line width on the product $\mathcal{E}\mathcal{E}_x$ can easily be verified if one examines the transition probability for the homogeneous case, Eq. (18), using the fact that $\mathcal{E}\mathcal{E}_x\sim 1/\tau$.

[9] The general relation is

$$A=\frac{4f(t)}{K\mathcal{E}\mathcal{E}_x^2(J-m)(J+m+1)}[1+\delta^2(\tau/2)]^{-\frac{1}{2}}.$$

For the case $m=0$, the numerator is divided by 2.

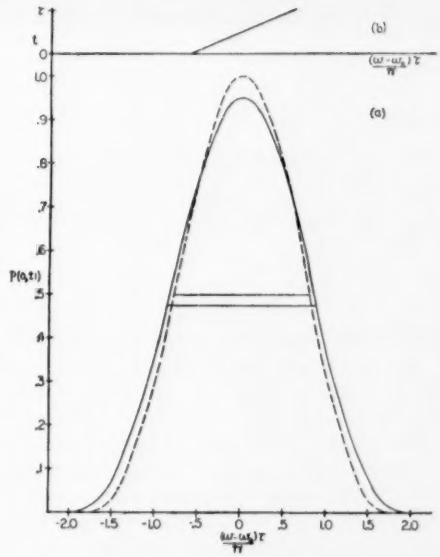

FIG. 1. (a) compares the line profiles for a transition occurring from the state $J=1$, $m=0$ to the state $J=1$, $m=\pm 1$ in a homogeneous field (broken curve) and in a field with a linear taper (solid curve). The taper has produced a 13 percent increase in half-width and a 5 percent decrease in peak. (b) shows the instantaneous resonance position as a function of time.

Thus, these field values represent the limit of our approximation method. Figure 1(b) shows that the instantaneous resonance frequency sweeps over nearly the entire range of frequencies included within the half-width of the homogeneous field curve. Following the, conservative method of estimating the broadening,[2] one would expect the half-width to be nearly doubled. However, the taper increases the half-width by only 13 percent and decreases the peak by 5 percent.

If one attempts to use a larger ratio of $\Delta\mathcal{E}/\mathcal{E}_x$, the curve becomes double peaked, dipping at resonance. Because the approximation breaks down first in the immediate vicinity of resonance (since A achieves its maximum value at resonance), this result may well be spurious. For points off resonance, however, one should still get a reasonable picture of the broadening as long as $A\leqslant 0.20$.

PHYSICAL REVIEW VOLUME 89, NUMBER 1 JANUARY 1, 1953

A Theory of the Deviation from Close Packing in Hexagonal Metal Crystals*

JOHN B. GOODENOUGH†
Department of Physics, University of Chicago, Chicago, Illinois
(Received September 11, 1952)

A mechanism is proposed to show how the Fermi surface interacts with the Brillouin zone boundaries. The direction and relative magnitude of the variation of the c/a ratio for hexagonal crystals from the ideal value for close packing are predicted as a function of the electron-atom ratio, and these predictions are compared with values of lattice parameters which are reported in the literature.

I. INTRODUCTION

WHEN the metallurgist discusses crystal structure in metals, he usually thinks in terms of the packing of hard "spheres," and yet it is a long known fact that often the lattice axial ratio c/a shows variations from the value to be expected from this ideal model. The reason for these variations, at least at low temperatures, lies presumably in the origins of the cohesive binding energy of these metals since nature demands that the crystal assume that configuration which gives rise to a minimum crystal free energy or, at absolute zero, to a maximum cohesive binding energy. The customary cohesive energy calculation for metals is the cellular method of Wigner and Seitz.[1] In this method, however, one requires the one-electron wave functions which describe the valence electrons to be spherically symmetric about any nucleus. Bardeen[2] maintains this restriction in his correction for the effective mass of the binding electrons in the Fermi energy term. Unless an angular dependence is introduced into the valence electron wave functions, however, this method is unable to investigate how a variation in the axial ratio from the ideal value can lower the total free energy of the crystal.

Jones[3] has considered these distortions for the case of h.c.p. crystals with an electron-atom ratio, hereafter designated z in this paper, greater than 1.75, i.e., for the divalent metals and the ϵ- and η-phases of the β-brass type alloys. In these crystals the ideal axial ratio for the close-packing of "spheres" is $c/a=1.633$. He argued that when the Fermi surface of the valence electrons overlaps a Brillouin zone boundary in a particular direction in reciprocal space, the electrons with wave numbers corresponding to the overlapping region exert a force to expand the lattice in the corresponding direction in the lattice space. Jones took the zone shown in Fig. 3 as the first Brillouin zone for the h.c.p. lattice and therefore argued that since overlap must occur through the A faces when $z>1.75$, the ϵ-phase ($c/a<1.633$) is to be expected whereas for values of z approaching two the η-phase ($c/a>1.633$) may appear due to overlap through the B faces.

This explanation, if correct, is only applicable to metals and alloys whose electron-atom ratios are large enough for overlap to occur through at least one set of zone faces. There are, however, many hexagonal metals with low z whose axial ratios show similar variations from their ideal value. Barrett and Trautz[4] have reported a low temperature h.c.p. phase in lithium where $z=1$. They found that lithium transforms martensitically from the b.c.c. phase to a f.c.c. phase if cold worked at low temperatures, or spontaneously to an h.c.p. phase with axial ratio[5] $c/a=1.563$ at lower temperatures. Among the transition metals and rare earths there are many instances of h.c.p. structures all of which have axial ratios which are less than the ideal value 1.633. Due to a demotion of the outer s-electrons in the formation of the crystal lattice, the value of z in these metals is approximately one. Since the density of states in the unfilled d- or f-bands of these metals is much larger than that in the s-band, it is difficult to determine how the s electron-atom ratio is varying as these elements are alloyed with one another. Although there are no definitive experiments as to the variation of the axial ratio with z in these h.c.p. lattices with low z, one nevertheless wonders by what mechanism the axial ratio should be less than the ideal value for all the h.c.p. lattices with approximately one valence electron per atom. Since the Fermi surface is completely contained within the first Brillouin zone, Jones's ideas are not applicable.

Owen and Edmunds[6] have examined the ζ-phase of the silver-zinc system and found it to be complex hexagonal with an axial ratio which varies from 0.7450 to 0.7383 as z increases from 1.46 to 1.5. Since the surface of the Brillouin zone for this structure is not reached until $z=1.56$, the variation in c/a with z cannot be explained by zone overlap.

Several alloys with z-values in the neighborhood of $\frac{3}{2}$ have h.c.p. structures. In Table I are listed some of the experimentally recorded axial ratios. It is at once noted

* This paper was written as a Ph.D. thesis for the Department of Physics, University of Chicago.
† Now at Massachusetts Institute of Technology Digital Computor Laboratory, Cambridge, Massachusetts.
[1] E. Wigner and F. Seitz, Phys. Rev. **43**, 804 (1933); **46**, 509 (1934); and E. Wigner, Phys. Rev. **46**, 1002 (1934).
[2] J. Bardeen, J. Chem. Phys. **6**, 367 (1938).
[3] H. Jones, Proc. Roy. Soc. (London) **A147**, 396 (1934).
[4] C. S. Barrett and O. R. Trautz, Am. Inst. Mining Met. Engrs. **175**, 579 (1948).
[5] C. S. Barrett, *Phase Transformations in Solids* (John Wiley & Sons, Inc., New York, 1951), p. 343. Edited by R. Smoluchowski *et al.*
[6] E. A. Owen and I. G. Edmunds, J. Inst. Metals **63**, 291 (1938).

that there is a progressive contraction of the symmetry axis with increasing electron-atom ratio. For values of z in the range $1.2 \leq z \leq 1.4$ the axial ratio is greater than 1.633 and decreases relatively slowly with increasing z. The axial ratio continues to decrease continuously to values of $c/a < 1.633$ for $z > 1.4$. In this range of z, therefore, the crystal transforms continuously from an η-brass phase to an ϵ-brass phase as z increases. When h.c.p. alloys with z values approaching two change from the ϵ-brass phase to the η-brass phase, on the other hand, the phase change is discontinuous and a mixture of the two phases can appear simultaneously in the same lattice. Is it possible for the same mechanism to cause a continuous change from the η-brass to the ϵ-brass phase when $z = 1.4$ and a discontinuous change from the ϵ-brass to the η-brass phase for higher electron-atom ratios? Again Jones' ideas cannot apply, at least for values of $z < 1.4$, since any overlap of the A faces, according to his mechanism, would force a distortion to $c/a < 1.633$.

The seemingly anomalous value of c/a in the gold-mercury system has been reported by two independent investigators. Pabst[7] first reported a narrow, homogeneous h.c.p. β-phase about $z = 1.25$ with $c/a = 1.647$. He found that as z varied from 1.2 to 1.34, the axial ratio increased from 1.638 to a maximum value of 1.647 in the neighborhood of $z = 1.25$, and then decreased slowly to 1.645 at $z = 1.34$. Stenbeck,[8] on the other hand, reported a practically constant value of $c/a = 1.647$ for values of z from 1.19 to 1.33. He was unable to find the maximum value in the c/a ratio at $z = 1.25$ reported by Pabst. According to his measurement, the homogenous β-phase extends from $z = 1.21$ to $z = 1.27$. He was not able to detect any ordering in his sample.

Typical of the measurements on alloys which show a discontinuous change from an ϵ-brass to an η-brass phase at high values of z are those of Owen and Pickup[9] on the copper-zinc system. They found that as z varies from 1.76 to 1.87, the axial ratio of the ϵ-brass phase decreases linearly from 1.570–1.554, that as z varies from 1.87–1.91 the axial ratio remains constant, that in the range $1.91 \leq z \leq 1.96$ both the ϵ- and the η-phase are present, and that as z increases from 1.97 to 2.0, the axial ratio of the η-phase increases linearly from 1.804 to 1.856. It will be seen that the forces which are responsible for these distortions are considerably more complex than the simple considerations of Jones.

Hume-Rothery and Raynor[10] have pointed out three of the experimentally important factors in any consideration of crystal structure in metal alloys, *viz.*, size factor, electro-chemical factor, and electron-atom ratio.

[7] A. Pabst, Z. physik. Chem., **B3**, 443 (1929).
[8] S. Stenbeck, Z. anorg. u. allgem. Chem. **214**, 16 (1933).
[9] E. A. Owen and L. Pickup, Proc. Roy. Soc. (London) **A140**, 179 (1933).
[10] W. Hume-Rothery and G. V. Raynor, J. Inst. Metals **66**, 191 (1940).

TABLE I. Experimentally recorded axial ratios of some h.c.p. alloys.

Alloy	z	c/a
Ag Al	1.45–1.85	1.625–1.588[a, b]
Ag Cd	1.46–1.55	1.619–1.608[c]
Ag Sn	1.43–1.59	1.630–1.616[d]
Ag Hg	1.44–1.45	1.630–1.617[e]
Ag Sb	1.4 –1.64	1.634–1.617[f]
Cu Si	1.35–1.4	1.635–1.633[g]
Au Hg	1.21–1.25–1.27	1.638–1.647–1.645[h] 1.647–1.647–1.647[e]

[a] A. Westgren and A. J. Bradley, Phil. Mag. **6**, 280 (1928).
[b] W. Hofman and K. E. Volk, Metallwirtschaft **15**, 699 (1936).
[c] H. Astrand and A. Westgren, Z. anorg. u. allgem. Chem. **175**, 90 (1928).
[d] Niel, Almin, and Westgren, Z. physik. Chem. **14**, 81 (1931).
[e] See reference 8.
[f] Westgren, Hagg, and Eriksson, Z. physik. Chem. **B6**, 40 (1929).
[g] A. G. H. Anderson, Trans. Am. Inst. Mining Met. Engrs. **137**, 334 (1940).
[h] See reference 7.

Recently Zener[11] has pointed out the importance of the d-shell electrons in determining crystal structure in the transition metals. This paper will be concerned with variations in the axial ratio which appear to be predominantly determined by the electron-atom ratio. The Bloch[12] model is employed to investigate how the valence electrons of metals and their alloys can force distortions in a lattice from the packing of "spheres" in order to increase the cohesive binding energy of the lattice. Those lattices which have axial ratios which differ from the ideal value as a result of an ordering of atoms of different size are omitted from the discussion.

II. GENERAL THEORY

In order to understand the role of the valence electrons in determining crystal structure or crystal distortion, it is necessary to have a knowledge of the various factors which contribute to the binding energy of the crystal. The calculation of the internal energy of a metal compared with the energy of the widely separated individual atoms which compose it is usually made in two steps. First, the energy of the lowest level of the valence electrons is computed by some method such as that of Wigner and Seitz, and then the whole energy of the electrons referred to this lowest level, the Fermi energy, is calculated. Though the energy of the lowest level is sensitive to changes in atomic volume, it is not very sensitive to changes in crystal structure for a given atomic volume. Fuchs[13] has shown that the difference in energy of the lowest level of the valency electrons between the b.c.c. and the f.c.c. structures having the atomic volume of copper is only 10^{-3} ev per atom. The calculated energy difference between the b.c.c. and f.c.c. phases for copper of 0.1 ev per atom is due to the interaction of the closed d-shells which just touch in the noble metals. In this paper the d-electron contributions are neglected except in so far as they

[11] C. Zener, Phys. Rev. **81**, 440 (1951).
[12] F. Bloch, Z. Physik **52**, 555 (1928).
[13] K. Fuchs, Proc. Roy. Soc. (London) **A151**, 585 (1935).

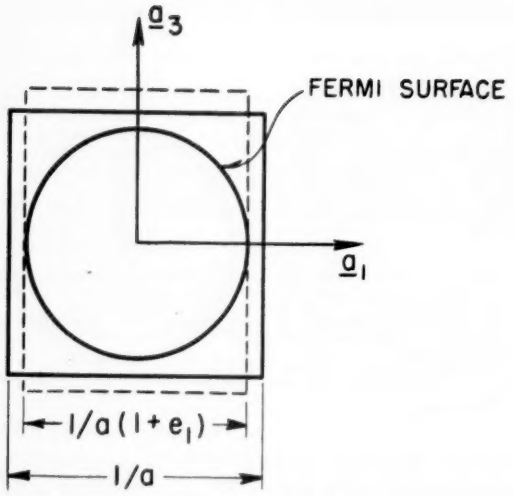

FIG. 1. Brillouin zone for a two-dimensional square lattice before and after distortion.

contribute to the elastic constants of the metal or metal alloy. The Fermi energy, on the other hand, is sensitive to changes in structure even when the volume remains unchanged since the kinetic energy of the electrons which move in a periodic potential is not proportional to the square of the wave number, as in the case of free electrons, but depends upon the period of the lattice. It is assumed, therefore, that the lowest level of the valence electrons remains constant during a small distortion from the packing of "spheres" in any given phase. Consideration is given only to how changes in the Brillouin zone boundaries should effect the Fermi energy.

Brillouin[14] has shown that due to the perturbations inherent in the restrictions of a lattice on the otherwise freely moving electrons, the electron energy *vs* wave number curve in any direction in reciprocal space is not a parabola, as in the case of free electrons, but shows discontinuities at certain sets of planes in the lattice which are determined by the lattice configuration. The regions in reciprocal space which are enclosed by these energy discontinuity surfaces are the Brillouin zones of the lattice. When the crystal is subject to a shear which alters the lattice configuration, the positions of the Brillouin zone boundaries must also change. In order to study the effect of a change of shape alone on the binding energy of a crystal, only those distortions of the lattice which do not involve a volume change should be considered. If a crystal distorts without a volume change, then some of the Brillouin zone surfaces must move toward the center of the zone while others move away. In order to understand how the electron energy will change with movements of the energy discontinuity surfaces, consider a two-dimensional square lattice. The Brillouin zone for this lattice is a square of side $1/a$, where a is the lattice parameter. Figure 2 (a) represents, schematically, the electron energy *vs* wave number curve for the direction $\mathbf{a}_1$ of Fig. 1 and Fig. 2 (b) the electron energy *vs* wave number curve for the direction $\mathbf{a}_3$. If the lattice is given a positive strain e_1 and a negative strain e_3 subject to the constraint $(1+e_1)(1+e_3) = 1$, then the Brillouin zone will shear in the opposite direction as shown in Fig. 1. This means that the wave number corresponding to the surface of energy discontinuity will move to smaller absolute values in the $\mathbf{a}_1$ direction and larger absolute values in the $\mathbf{a}_3$ direction as shown in Fig. 2. Since the crystal volume remains constant during the distortion, the density of energy states in k-space remains constant. The Fermi surface will, therefore, remain stationary through the distortion if no redistribution of electrons takes place and if it does not intersect a zone boundary. A redistribution of the electrons will cause the Fermi surface to bulge slightly in the direction of the approaching surfaces.

It is now apparent that if the Fermi surface is close to but does not yet intersect or touch a particular energy discontinuity surface, a movement of that surface towards the Fermi surface, as in Fig. 2 (a), will lower the average electron energy due to the shift in the position of the energy gap. The Fermi surface exerts, as it were, a force of attraction on the energy discontinuity surface. This force will be greater the larger the energy discontinuity across the surface, the smaller their distance of separation, and the larger the energy of the Fermi surface. The last dependence results from the fact that the larger the energy of the Fermi surface, the smaller the curvature of the surface and therefore the larger the area of Fermi surface within a given distance from the energy discontinuity surface. The energy levels which are most affected by the movement of the Brillouin surface correspond to those values of k in the immediate neighborhood of the surface. Therefore, as the Fermi surface of a crystal approaches, as the electron-atom ratio is increased, the surface of a Brillouin zone, there will be an increasing opportunity for the crystal to lower its average electron energy by a distortion which will cause the zone surface to move in the direction of the closest element of area of the Fermi surface. Since the Fermi surface, before it intersects any boundaries, is approximately spherical, this direction of motion will be normal to the zone surface toward the center of the zone.

If the electron-atom ratio is so large that the Fermi surface intersects the Brillouin zone surface, any movement of the zone surface toward the center of the zone will result in two opposing energy changes. There will be a decrease in the energy *vs* wave number surface due to the change of position of the energy gap which will tend to lower the average electron energy. There will also, however, be an increase in the energy of the Fermi surface due to a redistribution of the electrons which are displaced by the movement to unoccupied energy

[14] L. Brillouin, *Quantenstatistik* (Julius Springer, Berlin, 1931).

states. This latter effect, which will tend to increase the average electron energy, will begin abruptly so that the force of attraction between the Fermi surface and the energy discontinuity surface should show a sharp maximum at that value of z for which the two surfaces just touch. If the energy discontinuity across the Brillouin zone surface is large so that overlap of the zone surface does not take place, the repulsive force between the two surfaces may dominate as z is increased further so that the Fermi surface now pushes the energy discontinuity surface away from the center of the Brillouin zone.

When the Fermi surface begins to overlap the energy discontinuity surface, the repulsive force between the two surfaces will be partially relieved since not all of the electrons which are displaced by a movement of the energy discontinuity surface toward the center of the zone are forced to energy states which increase the energy of the Fermi surface. Some of the displaced electrons are forced to energy states which, though greater in energy by the magnitude of the energy gap, are still of lower energy than the Fermi surface. Although the total force between the Fermi and Brillouin surfaces may be repulsive, the decrease in the repulsive force between the two surfaces because of zone face overlap can be considered to contribute an effective partial pressure against the zone boundary to push it toward the center of the zone. This partial pressure will begin abruptly at that value of z for which overlap of the Brillouin zone surface begins.

Finally it should be noted that when there is complete overlap of an energy discontinuity surface, a movement of this surface toward or away from the center of the Brillouin zone will have little effect on the average valence electron energy. The perturbation of the electron energy *vs* wave number curve in any direction through the energy discontinuity surface is of equal magnitude on either side of the surface. The average electron energy, when the perturbed states on each side of the energy discontinuity are included, is therefore the same as it would be were there no surface of energy discontinuity present.

We can qualitatively conclude, therefore, that as the Fermi surface of a metal approaches, with increasing z, a Brillouin zone energy discontinuity surface, there will be a force of attraction between the two surfaces. Once the Fermi surface intersects an energy discontinuity surface, there will be two opposing forces between the surfaces. The repulsive force between the two surfaces will increase with increasing intersection of the surfaces, or with increasing z. The rate of increase with z of this repulsive force will decrease when overlap of the zone surface by the Fermi surface begins as a result of what may be thought of as a partial pressure of the overlapping electrons to push the Brillouin zone surface toward the center of the zone. The maximum repulsive force between the two surfaces should occur at that z for which the low energy side of the energy discontinuity surface is just completely intercepted by the Fermi surface, since the number of electrons which are displaced by a movement of the zone surface cannot increase for larger values of z whereas the partial pressure due to the overlapping electrons does increase. If the electron-atom ratio is increased beyond this, therefore, the total force on the energy discontinuity surface will decrease toward zero.

Any Brillouin zone is composed of several energy discontinuity surfaces of different orientation, and there will be similar forces of interaction between each of these faces and the Fermi surface. From Fig. 1 it is apparent that if the Fermi surface exerts a force of attraction on all the Brillouin zone surfaces, then though some of the faces will move in the direction of the attractive force in a constant volume deformation, the other faces will be forced to move against this force. There results a competition among the zone faces for movement toward the center of the zone. The type of distortion to be expected in a crystal will therefore depend upon the relative magnitudes of the forces between the Fermi surface and the various energy discontinuity surfaces. In cubic crystals the Brillouin zones are composed of families of energy discontinuity surfaces which are symmetrical with respect to the origin in reciprocal space and therefore equidistant from the Fermi surface.

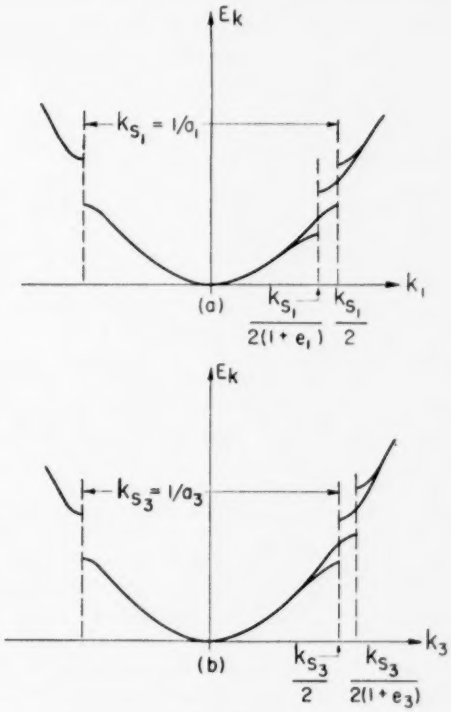

FIG. 2. Schematic representation of variations in the electron energy *vs* wave number curves for different directions in a metal lattice under strain.

The energy gap across each equivalent face is the same, and therefore each equivalent face is subject to an identical force of attraction toward or repulsion from the center of the zone. Since the restoring forces possess the same cubic symmetry in a cubic lattice, there is no preferred direction of shear as a result of the force of interaction between the Brillouin zone surfaces and the Fermi surface. Also, since the equivalent Brillouin surfaces in cubic crystals are sets of $\{n, n, m\}$ planes, the linear coefficients of the strains in the expression for the change of average electron energy due to a movement of each equivalent face are the same. If, therefore, the distortion is without a volume change, the resulting restraint on the strains will cause the linear term to vanish in the expression for the total change in the average electron energy with distortion. Any contribution to the energy change with distortion due to a redistribution of the electrons among the energy states will also be of second order in the strains, since both the number of electrons which would redistribute themselves and the amount of energy change of each in any redistribution are proportional to the strains. In cubic crystals, therefore, any increase in binding energy with distortion due to the "electron energy anisotropy"

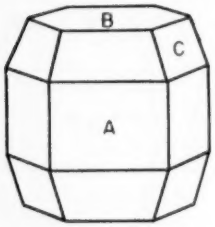

FIG. 3. First Brillouin zone for the h.c.p. lattice. It is bounded by the 20 planes $\{1\bar{1}0, 0\}$, $\{1\bar{1}0, 1\}$, $\{000, 2\}$.

effect, to name the mechanism under discussion, can be only a second-order effect. Nevertheless, this effect should be considered in any quantitative calculation of the elastic constants in cubic crystals since here one is interested in the second derivative of the energy change with respect to the strains.

When the lattice structure is noncubic, however, the "electron energy anisotropy" effect is a first-order effect, and the directions of the resulting distortions of the lattice should be predictable. In the hexagonal lattices, for example, the sets of Brillouin zone faces parallel to the symmetry axis will be reached by the Fermi surface, as it expands with increasing electron-atom ratio, at a different time than the faces perpendicular to the axis or sets of faces intersecting the axis at acute angles so that there is an uneven competition for contraction perpendicular and parallel to the axis. There results a decrease in the average electron energy with distortion which is to the first order in the strains whereas the restoring force is to the second order in the strains, and distortions of the lattice result.

As is evident from the discussion of the single energy discontinuity surface, not only is the shape of the Brillouin zone an important factor in determining distortion to tetragonality in crystals, but also its fullness, or the electron-atom ratio z. If the zone is nearly empty so that only those energy states are occupied which are closely proportional to the square of the wave number, there will be practically no change in the Fermi energy as a result of a constant volume lattice distortion. The curvature of the electron energy *vs* wave number surface which pertains to the occupied energy states is not appreciably altered, and the electrons are free to minimize their kinetic energy by a redistribution among the energy states. If z is increased so that the Fermi surface approaches the set of equivalent energy discontinuity planes closest to the center of the Brillouin zone, the Fermi surface will exert an increasing force of attraction on the zone surfaces. In crystals with hexagonal symmetry all the bounding surfaces of an equivalent set cooperate to cause a similar distortion parallel to the symmetry axis as they respond to the attractive force of the Fermi surface. The crystal will therefore prefer to suffer a shear in which the nearest set of zone surfaces move closer to the center of the zone. For values of z such that the Fermi surface intersects the nearest set of cooperating faces but has not yet reached the competing set of zone surfaces, the crystal may prefer to shear in the opposite direction. If z is further increased, the relative magnitudes of the various competing forces will determine the direction of crystal shear.

III. BRILLOUIN ZONE CONSIDERATIONS

Before the general considerations just discussed are applied to the particular examples of distortion in metals and metal-alloys which were previously cited, it is necessary to first examine the Brillouin zones for the h.c.p. lattice and for the ζ-phase of the silver-zinc system. It will also be instructive to consider briefly the zone for the f.c.c. lattice.

In Fig. 3 is shown the first Brillouin zone for the h.c.p. lattice.[15] The number of energy states per atom included within a Brillouin zone, according to the Pauli principle and the periodic boundary conditions for the Bloch electronic wave function, is given by twice the product of the atomic volume and the Brillouin zone volume. The number of energy states per atom in the first zone of the ideal h.c.p. lattice is, therefore, 1.75. In Fig. 4 is pictured the zone for the h.c.p. lattice which just contains two energy states per atom. Consider now what might be expected to happen as these zones are filled up by an increase of the electron atom ratio z. It is assumed, for convenience, that the Fermi surface is a sphere. This is a good approximation only when the first zone is partially filled. It will, however, serve as a first approximation. If there were no distortion from the close-packing of hard spheres, i.e., if $c/a = 1.633$, and if there were no energy discontinuity across the zone surfaces, then the Fermi surface would just touch the

[15] Refer to Appendix I

surface A when $z_A=(2\pi/9)(c/a)=1.14$, the surface B when $z_B=(2\pi/\sqrt{3})(a/c)^2=1.36$, and the surface C when $z_C=(2\pi/9)(c/a)\{1+\frac{3}{4}(a/c)^2\}^{\frac{1}{2}}=1.67$. If the magnitude of the energy discontinuity across face A is 1 ev when the lattice parameter is $a=3$A, then overlap of the A faces will occur when $z_A'=1.45$, and the Fermi surface will just touch the respective zone surfaces when $z_A=1.14$, $z_B=1.32$, $z_C=1.57$. If an h.c.p. lattice has $c/a=1.633$ when $z=0$ and z is increased, then as z approaches 1.14 there will be an increasing tendency for the lattice to distort in such a way that the zone surfaces A are brought closer to the center of the zone. The average electron energy is lowered if electrons occupy the energy states which are depressed by the perturbation in the vicinity of the zone surfaces. Such a distortion would decrease the c/a ratio found in the real lattice. Since the two B faces, which would favor a distortion in the opposite sense, are farther from the center of the zone than are the A faces, and since there are only two B faces compared with six A faces, their competing influence will be smaller than that of the A faces provided the energy gaps of the two sets of zone faces are of similar magnitude. It is concluded, therefore, that when $z\leq 1.14$, the valence electron pressure for distortion in h.c.p. crystals is in such a direction as to favor $c/a<1.633$. The change in valence electron energy will be to the first order in the lattice strains while the restoring force is of second order so that a finite distortion should take place. Although the maximum distorting force before distortion will be at $z=1.14$, the maximum distortion should occur at that z for which the distorting force is a maximum after distortion. For a distortion to $c/a=1.563$, the Fermi surface will just touch the A faces when $z_A=1.09$.

If $z=1.32$, there is sufficient intersection of the A faces by the Fermi surface for the repulsive force between these surfaces to nearly overbalance the attractive force. The B faces, on the other hand, will be experiencing a maximum force of attraction toward the center of the zone. The net interaction between the Fermi surface and the A and B faces, therefore, would produce a distortion to a $c/a>1.633$. Because there are only two B faces, the maximum attractive force between the Fermi surface and the B faces will be smaller than that between the Fermi surface and the six A faces if the energy discontinuities across these faces are of similar magnitude. There will also be an attractive force between the Fermi surface and the twelve C faces which will work against a distortion to $c/a>1.633$. If, therefore, a distortion to $c/a>1.633$ occurs for values of z in the neighborhood of 1.32, it should be small compared to the maximum distortions to $c/a<1.633$ at other z values.

Since only half of any C face will be interacting with the Fermi surface if A face overlap has not yet begun, and since the angle with which these surfaces intersect the symmetry axis is defined by $\tan\theta=(\sqrt{3}/2)(a/c)$, the total effect of the C faces will be roughly the same as 2.6 C faces parallel to the symmetry axis at the same distance from the center of the zone. As z increases beyond 1.32, the attractive forces acting on the C faces will be increasing rapidly along with the repulsive component of the interaction force on the B faces. These increases will be counterbalanced by the increase of repulsive force on the A faces before A face overlap begins. A slow variation in the total shearing force with z in the region $1.3\leq z\leq 1.45$ should not, therefore, be surprising. According to the simple model of a spherical Fermi surface, the maximum attractive force acting on

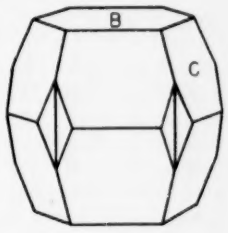

FIG. 4. The Brillouin zone for the h.c.p. lattice which contains just two valence electrons per atom. It is bounded by the planes $\{1\bar{1}0, 0\}$, $\{1\bar{1}0, 1\}$, $\{000, 2\}$.

the B faces after a distortion to $c/a=1.647$ will occur at a $z_B=1.29$.

After A face overlap occurs, the rate of increase with z of the repulsive force on the A faces will diminish while that on the B faces will increase. The increasing attractive force between the Fermi surface and the twelve C faces will therefore cause the axial ratio for any given alloy to decrease continuously with increasing z. Since the Fermi surface will not reach both halves of a C face at the same time because of the energy discontinuity across the A faces, there will be a broad maximum in the attractive force between the Fermi and zone

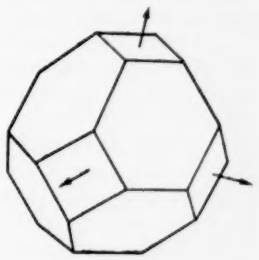

FIG. 5. First Brillouin zone for the f.c.c. lattice.

surfaces in the range $1.6<z<1.8$. The axial ratio will, however, continue to decrease in this range due to the increasing force of repulsion on the B faces. The actual rate of variation will depend upon the elastic constants of the particular alloy, the magnitude of the respective energy discontinuities, and the atomic volume. Figure 9 shows how the various contributions of the different faces to the total shearing force combine.

For values of z close to two, the A faces will be largely overlapped so that their interaction with the Fermi surface will be relatively small. The repulsive forces

between the Fermi surface and the B and C faces will predominate. If no overlap of the zone boundaries takes place, the repulsive forces will make the zone of Fig. 4 as "round" as possible so as to lower the energy of the Fermi surface. This means that the shearing force due to the repulsive forces will vanish if the B faces are equidistant with the C faces from the center of the zone. This occurs only if there is a distortion to $c/a<1.633$. In fact, $k_B=k_C$ when $c/a=1.50$. If there is no overlap, therefore, there will be a force to shear the crystal to an axial ratio $c/a=1.50$. Since this force will decrease with the distortion while the reactive forces which resist distortion increase with the strains, the maximum distortion to be anticipated in any divalent h.c.p. metal should be about midway between these extremes, or to a $c/a\cong1.56$. If, on the other hand, B face overlap does take place, then the repulsive force on the B face will be reduced by the effective partial pressure of the overlapping electrons. If B face overlap is occurring, however, the repulsive force on the C faces will continue to increase rapidly with increasing z. There may, therefore, be some value of z for which the repulsive forces on the C faces will predominate so that distortions to $c/a>1.633$ result. Since the repulsive force on the twelve C faces

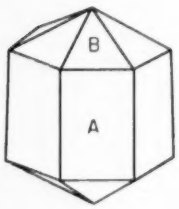

FIG. 6. Probable first Brillouin zone for the complex h.c.p. ζ-phase of the silver-zinc system.

will increase rapidly with small changes in z near to two, a gradual change from the ϵ- to the η-brass phase cannot occur. The crystal will be at a lower energy if it forms two distorted phases than if it forms one homogeneous phase with no distortion. The reason for the continuous change of axial ratio in the neighborhood of $z=1.4$ would appear to be the slowness of the variation in the total distorting forces in the transition region from one phase to another and the smallness of the maximum force distorting the crystal to axial ratios greater than 1.633. If z is close to two and the zone is nearly full, the interface between the Fermi surface and the twelve C faces comprises a large fraction of the total Fermi surface. Any displacement of the C faces towards the center of the zone, therefore, displaces a large number of electrons while the available non-intersecting Fermi surface to which they may be displaced is small. There results a large change in the energy of the non-intersecting Fermi surface with a small change in the position of the C faces. The respulsive force between the Fermi surface and the twelve C faces increases rapidly, therefore, with z approaching two. If the electron-atom ratio is so large that only the η-brass phase is present, the axial ratio should increase rapidly with increasing z due to the increasing force of repulsion on the C faces. These features of the h.c.p. lattice are summarized in Fig. 9.

In Fig. 5 is shown the form of the first Brillouin zone for the f.c.c. lattice. The number of states in the inscribed sphere of this zone is $\sqrt{3}\pi/4=1.36$. It is therefore expected that as z approaches 1.36, there will be a decrease in the stability of the cubic configuration and an increasing likelihood that a f.c.tet. phase appear. Due to the symmetry of the zone structure, there is no preferred axis for elongation. Also the eight faces which are met when $z=1.36$ compete equally for opposing distortions so that any lattice shear will only be accompanied by a decrease in the valence electron energy which is of second order smallness. Therefore, although alloys with a f.c.c. structure with $z\cong1.36$ are in the optimum range for distortion to tetragonality, it is not surprising that there are no known instances of f.c.tet. crystals as a result of the interaction of the valence electrons with the crystal lattice.

Consider, finally, the complex h.c.p. ζ-phase of the silver zinc system. Owen and Edmunds[6] have proposed an hexagonal structure for this phase with 54 atoms to the unit cell. For an electron-atom ratio of 1.48, they give values of c and a of 5.646A and 7.615A, respectively, or an axial ratio $c/a=0.742$. To construct the probable first Brillouin zone for this phase, note that if k_0 is the radius in k space of the Fermi sphere corresponding to z electrons per atom and Ω is the atomic volume, then

$$k_0=[(3/4\pi)\cdot(z/2\Omega)]^{\frac{1}{3}}=0.224\text{A}^{-1},$$

for the values quoted above for which x-ray data was published. The x-ray measurements showed two lines of very strong intensity corresponding to the hexagonal Miller indices (3, 0, 0) and (2, 0, 2). Since the distance between parallel reflection planes in the hexagonal lattice is given by

$$d=\{(4/3a^2)(h^2+k^2+hk)+l^2/c^2\}^{-\frac{1}{2}},$$

the two very strong lines appear to be composed of overlapping reflections from the set of six $\{3\bar{3}0, 0\}$ and the set of twelve $\{2\bar{2}0, 2\}$ planes which are at distances from the origin in k-space of 0.228A^{-1} and 0.233A^{-1}, respectively. These two sets of planes form the zone shown in Fig. 6. For an axial ratio $c/a=0.742$, the Fermi sphere will just touch the zone surfaces marked A in Fig. 6 when $z=1.56$ and the zone surfaces B when $z=1.67$. If the Fermi surface does not intersect any of the zone boundaries, the force of attraction on the A faces favors a contraction in reciprocal space perpendicular to the symmetry axis, or a decrease in the axial ratio c/a, while the force of attraction on the B faces, since they intersect the symmetry axis at an angle $\theta>45°$, favors an opposite distortion. Since the A faces exert their maximum influence when $z=1.56$ and the B faces when $z=1.67$, it is predicted that as z

approaches the value 1.50, the c/a ratio will decrease with increasing z.

IV. ORDERS OF MAGNITUDE

The average energy per atom of the valence electrons whose wave numbers are defined by any volume Ω_k of k space is

$$U=2\Omega\int_{\Omega_k}E_k d^3\mathbf{k}, \tag{1}$$

where Ω is the atomic volume of the metal. If z is the number of electrons per atom which have wave numbers within the volume Ω_k, then

$$z=2\Omega\int_{\Omega_k}d^3\mathbf{k}. \tag{2}$$

Since the number of valence electrons remains constant during a distortion of the lattice, $\partial z/\partial e=0$, where e is the lattice strain, and

$$\partial U/\partial e=-z'E_k'(\tfrac{1}{2}k_s)\{\alpha-\beta+\gamma\}, \tag{3}$$

where $z'=2\Omega\cdot(4\pi/3)k_0^3$, $E_k'(k)=h^2k^2/2m$, and α, β, γ are dimensionless parameters. The parameters α and β have been calculated for the simple model of Fig. 7.[16]

With $\mu=k_s/2k_0$, $Q=|V_s|/2E_k'(\tfrac{1}{2}k_s)$, and $\cos^{-1}\lambda$ the angle between the normal to a Brillouin zone surface and the line joining the center of the zone to the mean edge of that surface, the calculation gives $\alpha=\alpha(\lambda,\mu,Q)$ arising from the attractive force between the two surfaces and $\beta=\beta(\mu,Q)$ from the repulsive force between the two surfaces if they intersect one another. $\beta=0$ if $\mu\geq 1$. The dimensionless parameter γ is zero unless there is zone overlap. If the valence electrons see a coulombic potential about each lattice site, $|V_s|\propto 1/k_s^2$ and

$$\partial|V_s|/\partial e=-k_s\partial|V_s|/\partial k_s=2|V_s|. \tag{4}$$

Although there is, therefore, an increase of the energy gap with contraction of a zone surface to decrease γ, the parameter will nevertheless be positive.

For all three sets of faces in the h.c.p. lattice, the parameter λ is nearly $\sqrt{3}/2$. In Fig. 8 the dimensionless coefficient α is plotted as a function of Q. The attractive force between the Fermi energy and the Brillouin zone surface increases rapidly for larger Q, or for larger energy discontinuities. If the energy gap across the A faces is $2|V_s|=1$ ev, then $Q=0.005a^2$ where a is the lattice parameter in Angstrom units.

If σ is the stress in dynes per square centimeter producing the strain e, then

$$\sigma=-\frac{1}{\Omega}\frac{\partial U}{\partial e}=\frac{1}{\Omega}\cdot z'E_k'\left(\frac{k_s}{2}\right)\{\alpha-\beta+\gamma\}. \tag{5}$$

In the case of a uniform lateral stress acting in all directions at right angles to the z axis,

$$\sigma_1=-\frac{1}{\Omega}\frac{\partial U}{\partial e_A},$$

where $(1+e_A)=(1+e_1)^2\cong 1+2e_1$, and therefore the strain e_1 to be expected in an h.c.p. crystal is

$$e_1=\frac{1}{2\Omega}(S_{11}+S_{12})z'\sum_{(1)}E_k'\left(\frac{k_s}{2}\right)\{\alpha-\beta+\gamma\}$$
$$+\frac{1}{\Omega}S_{13}z'\sum_{(3)}E_k'\left(\frac{k_s}{2}\right)\{\alpha-\beta+\gamma\},$$

where the first summation is taken over all pairs of faces which contribute to stresses perpendicular to the symmetry axis and the second summation refers to all pairs of faces which contribute to stresses parallel to the symmetry axis. The S_{ij} are the elastic constants of the metal. Since all of the elastic constants for hexagonal crystals are not customarily known, Young's modulus E is used to give an order of magnitude estimate. In Fig. 9 is plotted

$$2\Omega E_1e_1\cong z'[\textstyle\sum_{(1)}E_k'(\tfrac{1}{2}k_s)\{\alpha-\beta+\gamma\}$$
$$-\textstyle\sum_{(3)}E_k'(\tfrac{1}{2}k_s)\{\alpha-\beta+\gamma\}] \tag{6}$$

as a function of z under the assumption that $a=3$A and $Q_A=0.05$, $Q_B=0.08$, $Q_C=0.06$ where Q_i refers to the ith face. This gives a qualitative picture of the expected variation of the strain e_1 with z for a given crystal. The choice of $Q_A=0.05$ is arbitrary. It represents an energy

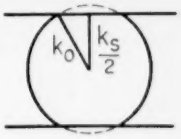

FIG. 7. Cross section of Fermi sphere intersecting pair of Brillouin zone surfaces.

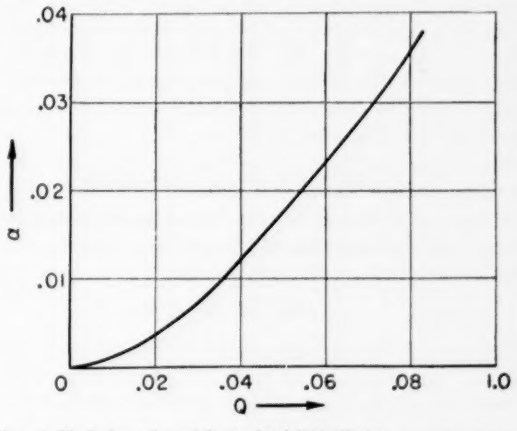

FIG. 8. Variation of α with $Q=|V_s|/2E_k'(\tfrac{1}{2}k_s)$ for a pair of zone surfaces when $\mu=1$, $\lambda=\lambda'=\tfrac{1}{2}\sqrt{3}$.

[16] Refer to Appendix II.

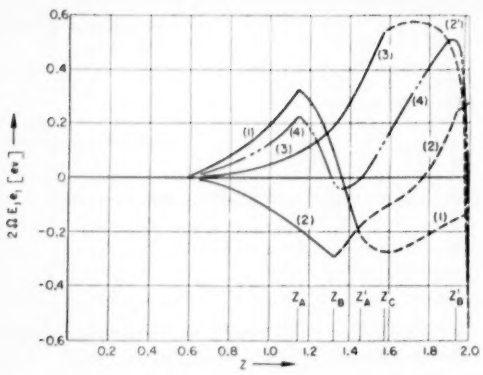

FIG. 9. Contributions to initial electron energy change per atom with strain in h.c.p. lattice with $a=3$A for distortions to $c/a<1.633$ by (1) A faces; (2) B faces; (3) C faces. (4) is the resultant contribution. The solid curves are calculated from Eq. (6) with $Q_A=0.05$, $Q_B=0.08$, $Q_C=0.06$. The dashed lines are conjectured extrapolations. (2') is conjectured B face contribution if there is no B face overlap.

gap of $10/a^2$ ev across the A faces if a is expressed in Angstrom units. Since,[17] however, the energy discontinuity can be expressed in terms of the nuclear charge Z, the atomic scattering factor F_s, and the structure amplitude S_s as

$$2|V_s|=\frac{2e^2}{\pi\Omega|k_s|^2}\{Z-F_s\}S_s, \tag{7}$$

and since $E_k'(\frac{1}{2}k_s)\propto k_s^2$, the Q_i's should be in the approximate ratio

$$Q_A:Q_B:Q_C=\frac{S_{100}(Z-F_{100})}{k_A^4}:\frac{S_{002}(Z-F_{002})}{k_B^4}:\frac{S_{101}(Z-F_{101})}{k_C^4}$$
$$\cong 1:1.6:1.2.$$

The expression for α breaks down for large values of z where the Fermi surface is intersecting most of the Brillouin surface. The curves are therefore only qualitatively extrapolated for these larger z values. The relatively broad maximum for the C face contribution arises from the fact that the Fermi surface does not reach both halves of the C faces at the same time, that part of the C face which bounds the second zone being reached at a greater z-value.

V. COMPARISON WITH EXPERIMENT

The axial ratio for the h.c.p. lattice which is distorted from the ideal packing of spheres by a strain e_1 perpendicular to the symmetry axis is

$$c/a=1.633/(1+e_1)^3.$$

From Fig. 9 it is apparent that e_1 is positive for values of $z<1.14$ and therefore that the transition and rare-earth metals which have h.c.p. structures should have a $c/a<1.633$. The actual value of the valence electron-atom ratio in these elements is difficult to determine due to an uncertainty in the amount of demotion of the s-electrons to the d- or f-shell. Measurements of the saturation magnetization of cobalt, however, indicate that this element has 0.7 valence electrons per atom. Since $E_1=2.07\times10^{12}$ dynes/cm^2 and $2\Omega=22\times10^{-24}$ cm^3, if $Q_A=0.05$, $Q_B=0.08$, $Q_C=0.06$, then $e_1=0.001$ and the axial ratio for cobalt should be $c/a=1.628$. The experimentally measured value for the axial ratio is 1.623, a value corresponding to $e_1=0.002$. It should be noted that if one wanted to use a knowledge of the axial ratio and elastic constants to estimate the number of valence electrons in the metal, it would be necessary to know the magnitude of the energy discontinuity across the various faces.

In the case of the low temperature h.c.p. phase of lithium, $z=1$ and $2\Omega=40\times10^{-24}$ cm^3. If $E_1=0.5\times10^{12}$ dynes/cm^2 and $Q_A=0.05$, $Q_B=0.08$, $Q_C=0.06$ are assumed to be the appropriate values for the lithium h.c.p. structure, then $e_1=0.013$ and $c/a=1.570$ as against the experimentally reported value 1.563. It appears, therefore, that the "electron energy anisotropy" effect is of sufficient magnitude to cause the observed distortions from the ideal packing of "spheres" in hexagonal crystals.

Figure 9 also predicts that $e_1<0$ if $1.29\leq z\leq1.46$. The exact range of z for which $e_1<0$ and the magnitude of e_1 depend upon an arbitrary assignment of the magnitude of the energy discontinuities across the various Brillouin zone surfaces. There are three qualitative features which are important, however. First, there is the existence of a range of z for which $c/a>1.633$; second, the magnitude of the maximum distortions to $c/a>1.633$ in this range should be smaller than the maximum distortions to $c/a<1.633$ on either side of this range; and third, the rate of change of distortion with z in this range should be small. From Table I it is observed that experimentally one finds distortions to $c/a>1.633$ which are small in magnitude and vary slowly with z in the range $1.21\leq z\leq1.4$. Pabst[7] has even reported observation of a maximum in the axial ratio at $z=1.25$ in the gold-mercury system. The qualitative features of Fig. 9 for $1.29\leq z\leq1.45$ are in general accord with the observed variations of the axial ratio with electron-atom ratio. Whereas the qualitative curve predicts a maximum axial ratio for $z=1.29$ when $c/a=1.647$, the observed maximum appears to be at about $z=1.25$, a discrepancy which could well be due to the simplified model of a spherical Fermi surface.

Figure 10 indicates how the "electron energy anisotropy" effect is dependent upon the magnitude of the energy gaps and the lattice parameter. The ratio $Q_A:Q_B:Q_C$ is held constant. If the lattice parameter is fixed and the energy gaps are increased, the magnitude of the maximum distortion to $c/a>1.633$ is decreased while the z-value at which it occurs is increased. For fixed energy gaps $c/a>1.633$ occurs for a lower range of

[17] A. H. Wilson, *The Theory of Metals* (Cambridge University Press, Cambridge, 1936), p. 78.

z-values and has a larger maximum value if the lattice parameter is decreased.

The qualitative arguments of the interaction of the Fermi surface with all of the zone faces also predict a nearly linear decrease in the axial ratio with z in the range $1.45 \leq z \leq 1.85$ in agreement with measurements given in Table I and those of Owen and Pickup[9] on ϵ-brass. They also show the possibility of a phase change to the η-brass phase for values of z close to two if there is sufficient B-face overlap.

Finally, consider the complex h.c.p. ζ-phase in the silver-zinc system. This phase also has a single symmetry axis so that the variations with z in the axial ratio should be predictable. It was predicted in the general discussion of the Brillouin zone for this phase that as z increased towards 1.50, the c/a of the crystal should decrease. This is in agreement with the measurements of Owen and Edmunds.[6]

VI. SUMMARY

In summary, a mechanism has been considered whereby the valence electrons in hexagonal metallic crystals can influence the lattice structure due to a change in their average energy with variation of the lattice axial ratio. It was shown how the Fermi surface for the metallic binding electrons interacts with surfaces of energy discontinuity which constitute the Brillouin zone boundaries. Before the Fermi surface reaches the energy discontinuity surface, there exists a force of attraction between them which depends upon their distance of separation, the magnitude of the energy discontinuity across the zone surface, and the energy of the Fermi surface. If the two surfaces intersect one another but do not overlap, there is also a repulsive force between the two surfaces which depends upon the area of interface between the two surfaces and the area of Fermi surface which is not a common interface with some other zone boundary. After overlap of a zone boundary by the Fermi surface, the amount of unoverlapped interface no longer increases so rapidly with increasing z. The resulting relief in the rate of increase of the repulsive forces between the two surfaces with increasing z has been thought of as an effective partial pressure of the overlapping electrons to push the zone surface toward the center of the zone. Finally, if a zone surface is completely overlapped, there is no interaction between the two surfaces.

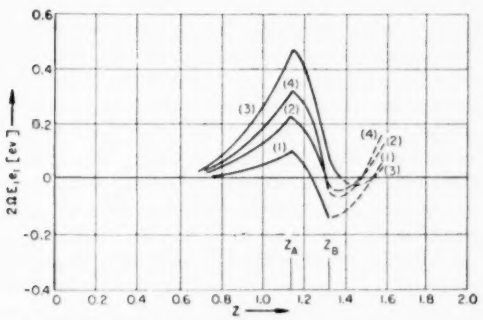

FIG. 10. Initial electron energy change per atom with strain in h.c.p. lattice for distortion to $c/a < 1.633$ for an A face energy discontinuity of (1) 0.62 ev with $a = 3$A; (2) 1.0 ev with $a = 3$A; (3) 1.6 ev with $a = 3A$; and (4) 1.6 ev with $a = 2.5$A, when $Q_A : Q_B : Q_C = 1 : 1.6 : 1.2$.

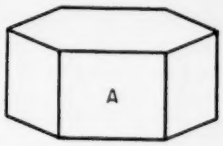

FIG. 11. First Brillouin zone for the h.c.p. lattice after Brillouin and Seitz.

The Brillouin zones for two hexagonal lattices were considered, and it was shown how the forces of interaction between the Fermi and energy discontinuity surfaces could qualitatively explain the observed variations of the axial ratio from the ideal value for the close packing of spheres. A semiquantitative calculation for the axial ratio variation in cobalt and lithium indicate that the interactive forces under consideration are of sufficient magnitude to cause the distortions which are observed in these lattices.

Finally, it was shown that the Brillouin zone structure for the cubic crystals have such a symmetry that the "electron energy anisotropy" effect can be only of second-order magnitude. This would explain why the variations of the axial ratio with electron-atom ratio is peculiar to noncubic crystals.

The author wishes to express his sincere gratitude to his sponsor Dr. C. Zener for initially interesting him in this problem and for his many helpful criticisms and suggestions during the development of the work. He would also like to thank the Westinghouse Electric Corporation for the support it gave to the work.

APPENDIX I

In Fig. 3 is shown the first Brillouin zone for the h.c.p. lattice. Brillouin[18] and Seitz,[19] on the other hand, have taken the zone of Fig. 11 to be the first Brillouin zone for the h.c.p. lattice. In order to investigate which of these two is the correct zone, it is first noted that the h.c.p. lattice is made up of four interpenetrating orthorhombic lattices with unit vectors $A_1 = a$, $A_2 = \sqrt{3}a$, $A_3 = c$. Since the h.c.p. lattice, with two atoms α and β in the unit cell, consists of two simple hexagonal lattices with corresponding atoms at $(0, 0, 0)$ and $(\frac{1}{2}, \frac{1}{6}, \frac{1}{2})$, the potential at any point $\mathbf{r}$ may be expanded as the Fourier series

$$V = V_0 + \sum_s V_s e^{2\pi i \mathbf{k}_s \cdot \mathbf{r}},$$

where $\mathbf{k}_s$ is a vector denoting one of the points of the

[18] L. Brillouin, *Wave Propagation in Periodic Structures* (McGraw-Hill Book Company, Inc., New York, 1946).

[19] F. Seitz, *Modern Theory of Solids* (McGraw-Hill Book Company, Inc., New York, 1940).

reciprocal lattice such that $\mathbf{k}_s \cdot \mathbf{r} = (s_1/A_1)x + (s_2/A_2)y + (s_3/A_3)z$ and the Fourier coefficient of the potential may be written

$$V_s = V_{s\alpha} + V_{s\beta} e^{\pi i(s_1 + s_2 + s_3)},$$

where, since each of the simple lattices is described by (0, 0, 0) and $(\frac{1}{2}, \frac{1}{2}, 0)$,

$$V_{s\alpha,\beta} = A_{\alpha,\beta}\{1 + e^{\pi i(s_1+s_2)}\}.$$

According to the well-known degenerate perturbation calculation,[14] the magnitude of the energy discontinuity across the planes defined by

$$\mathbf{k}_s \cdot \mathbf{k} + \tfrac{1}{2}|k_s|^2 = 0$$

is given by $2|V_s|$. Therefore, if

$$V_s = 2A_\alpha \cos^2\frac{\pi}{2}(s_1+s_2)\left\{1 + \frac{A_\beta}{A_\alpha} e^{\pi i(s_1+s_2+s_3)}\right\} \qquad \text{(i)}$$

vanishes for a given (s_1, s_2, s_3), there can be no energy discontinuity corresponding to this set of integers. In Fig. 4 is shown the second Brillouin zone for the h.c.p. lattice. A comparison of Fig. 11 and Fig. 4 with the zone

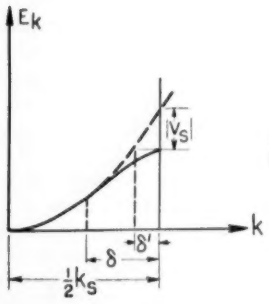

FIG. 12. Geometric relation between $|V_s|$ and δ.

of Fig. 3 reveals at once that the zone of Fig. 3 is what one would obtain if the Fourier coefficient for the surfaces {000, 1} vanish whereas Fig. 11 is the zone one would obtain if this Fourier coefficient does not vanish. According to Eq. (i),

$$V_{001} = 2A_\alpha\{1 - A_\beta/A_\alpha\}. \qquad \text{(ii)}$$

Mott and Jones[20] assume that the scattering coefficients A_α and A_β of the two atoms in the unit cell are identical and therefore take $V_{001} = 0$. Brillouin, on the other hand, has pointed out that the atomic potential about atom α by which the valence electrons are scattered is a planar reflection of the atomic potential about atom β. For an appropriate choice of axis, therefore, $V_\beta(x, y, z) = V_\alpha(x, -y, z)$, so that for the {000, 1} planes

$$\frac{A_\beta}{A_\alpha} = \frac{\int_{-\infty}^{\infty}\int\int e^{-2\pi i \mathbf{k}_s \cdot \mathbf{r}}[V_\beta(x, y, z) - V_0]dxdydz}{\int_{-\infty}^{\infty}\int\int e^{-2\pi i \mathbf{k}_s \cdot \mathbf{r}}[V_\alpha(x, y, z) - V_0]dxdydz}$$

$$= \frac{\int_{-\infty}^{\infty}\int\int e^{-2\pi iz/c}[V_\alpha(x, -y, z) - V_0]dxdydz}{\int_{-\infty}^{\infty}\int\int e^{-2\pi iz/c}[V_\alpha(x, y, z) - V_0]dxdydz}. \qquad \text{(iii)}$$

If $y' = -y$ is substituted into the numerator of Eq. (iii), however, it is at once apparent that $A_\beta = A_\alpha$ and therefore that $V_{001} = 0$. Figure 3 should, therefore, be the correct first Brillouin zone for the h.c.p. lattice.

APPENDIX II

In the calculation of the parameters α and β, a simplified model is used in which it is assumed that (1) the Fermi surface is spherical except when it intersects a Brillouin zone boundary, (2) the electrons which contribute appreciably to the "electron energy anisotropy" effect are included within the solid angle formed by a rotation of a 30° plane angle about the k-vectors to the center of the respective faces (i.e., $\lambda = \sqrt{3}/2$), (3) the magnitude of the energy gap remains constant during a movement of any energy discontinuity surface, and (4) the energy discontinuity is constant over the discontinuity surfaces. In order to justify the 30° angle of rotation of assumption (2), it is necessary to estimate δ, the largest distance in k space from the Fermi surface to the energy discontinuity surface at which the electron energy is appreciably affected by movements of the discontinuity surface. Although all of the valence electron energies are affected by the movement of each face, nevertheless it will be sufficient to consider only those electrons whose wave numbers lie in a region of k space near to the moving face as contributing appreciably to the "electron energy anisotropy" effect. It should be noted that cobalt, which is assumed to have 0.7 valence electrons per atom, is h.c.p. with $c/a = 1.623$ while the h.c.p. form of nickel, with 0.6 valence electrons per atom, shows practically no distortion. It appears, therefore, that when the h.c.p. lattice has 0.7 electrons per atom, the Fermi surface is just close enough for movements of the Brillouin zone surfaces to appreciably affect the electron energies. Since the Fermi surface is approximated by a sphere, $z = 2\Omega \cdot (4\pi/3)k_0^3$, where Ω is the

[20] N. F. Mott and H. Jones, *The Theory of the Properties of Metals and Alloys* (Oxford University Press, London, 1936), Chap. V.

atomic volume, and the radius of the Fermi sphere, when $z=0.7$, is $k_0=0.491/a$. Since $\frac{1}{2}k_s(A)=0.578/a$ is the distance from the center of the zone to an A face, $\delta=0.087/a$. If, therefore, the Fermi surface is just touching an A face, the critical plane angle is given by $\theta=\cos^{-1}[1-2/k_s(A)]=31°$. To avoid an overlap of solid angles for the different zone faces for the h.c.p. lattice, the value $\theta=30°$ is taken. The approximation $\lambda=\sqrt{3}/2$ becomes increasingly poor as the Fermi surface intersects more and more of the Brillouin zone surface.

The geometric correlation between δ and $|V_s|$ can be seen from Fig. 12. Geometrically,

$$\frac{|V_s|}{\delta'}=\left[\frac{d(h^2k^2/2m)}{dk}\right]_{k_s/2}=\frac{2E_k'(\frac{1}{2}k_s)}{\frac{1}{2}k_s},$$

$$Q=\frac{|V_s|}{2E_k'(\frac{1}{2}k_s)}=\frac{\delta'}{\frac{1}{2}k_s}.$$

If $\delta'=\frac{1}{3}\delta$, then $Q_A=0.05$, which is the value taken for Q in the calculations of Fig. 9. This means that all the electrons whose k vectors lie within a distance $3\delta'$ of the zone surface are considered in the estimation of the "electron energy anisotropy" effect. Geometrically, it appears reasonable that all the electrons which contribute appreciably to this effect have k vectors in this volume of k space.

Assumption (3) is employed in the evaluation of the term $z\langle\partial E_k/\partial e\rangle$ of $\partial U/\partial e$. Since $\langle\partial E_k/\partial e\rangle=0$ if there is no energy discontinuity, the term $z\langle\partial E_k/\partial e\rangle$ can be expressed as a series of terms to the first and higher powers of the energy discontinuity $2|V_s|$. From Eq. (4), a change in magnitude of the energy discontinuity with distortion is proportional to the strains. Any contribution to $\langle z\delta E_k\rangle$ due to a change in the magnitude of the energy gap with distortion will, therefore, be only of second order in the strains.

From the energy equation of the degenerate perturbation calculations in which the potential for the free electrons is expressed as

$$V(r)=V_0+\sum_s V_s e^{2\pi i\mathbf{k}_s\cdot r},$$

the kinetic energy of an electron of wave number k is given by[14]

$$E_k=\frac{h^2}{2m}(k^2+\mathbf{k}\cdot\mathbf{k}_s+\tfrac{1}{2}k_s^2)$$
$$-\frac{1}{2}\frac{h^2}{2m}\{[k_s^2+2(\mathbf{k}\cdot\mathbf{k}_s)]^2+4(2m/h^2)^2|V_s|^2\}^{\frac{1}{2}}.$$

This expression is used in Eq. (1) for the evaluation of $\partial U/\partial e$.

APPENDIX III

Jones[21] has recently measured the lattice parameters for the ζ-phase of the silver-zinc system with $z=1.5$. He finds $c=2.816$A and $a=7.639$A, with nine atoms to the unit cell. This is in agreement with recent measurements by Edmunds and Qurashi,[22] who found $c=2.8197$A and $a=7.6360$A. Jones found a first strong doublet corresponding to the Miller indices (1, 1, 1) and (0, 3, 0). From these figures the Fermi surface, after account is taken of intersection with the B faces, has a radius $k_0=0.226\text{A}^{-1}$ while the B faces are found at $k_B=0.220\text{A}^{-1}$ and the A faces at $k_A=0.227\text{A}^{-1}$. The probabel Brillouin zone would be as shown in Fig. 13. The decrease in the axial ratio as z varies from 1.46 to 1.5 would be due to an increasing repulsive force between the Fermi surface and the B faces where the two surfaces intersect and an increasing attractive force on the A faces which are not yet reached.

APPENDIX IV

Although there is no distortion to tetragonality in cubic crystals as a result of the "electron energy anisotropy" effect, nevertheless the interactive forces between the Fermi and zone surfaces exist. They are just those forces which Jones[23] has suggested are responsible for the Hume-Rothery[24] electron-atom ratio rules for phase changes in binary substitutional alloys. It should, therefore, be instructive to estimate the ratio of the Fermi energies for the f.c.c. and b.c.c. structures.

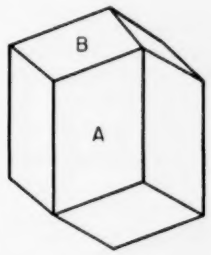

FIG. 13. Probable first Brillouin zone of silver-zinc ζ-phase after measurements of R. Jones.

The total valence electron energy referred to the lowest electron energy state is the Fermi energy. If there is but one pair of zone faces separated a distance k_s in wave number space, and if the Fermi surface is approximated by a sphere, or portions of a sphere, then the Fermi energy is given by

$$U=2\Omega 4\pi\left\{\int_0^{\mu}\int_0^{k_s} E_k k^2 dk d(\cos\theta)\right.$$
$$\left.+\int_{\mu}^{1}\int_0^{k_s/2\cos\theta} E_k k^2 dk d(\cos\theta)\right\}=\beta_k U_0, \quad \text{(i)}$$

[21] Richard Jones (private communication).

[22] E. A. Edmunds and Qurashi (private communication to R. Jones by H. Lipsom).

[23] H. Jones, Proc. Roy. Soc. (London) **144**, 225 (1934); **147**, 396 (1934). N. F. Mott and H. Jones, p. 170 of reference 20.

[24] W. Hume-Rothery, J. Inst. Metals **35**, 295 (1926); *The Metallic State* (Oxford University Press, London, 1931), p. 328.

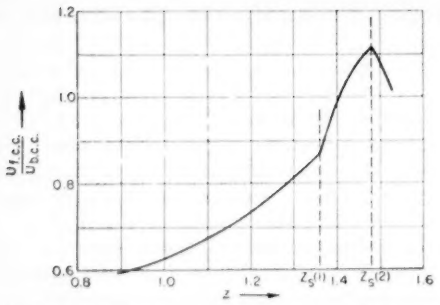

FIG. 14. Ratio of Fermi energies for a f.c.c. and b.c.c. lattice calculated from Eq. (v) with $Q_1=Q_2=0.05$.

where $U_0=\frac{3}{5}zE_k^f(k)$, $z=2\Omega\cdot(4\pi/3)k^3$, and $\beta_k=(k_s/2k)^5\cdot f(\mu, Q)$ is a dimensionless parameter.

The volume enclosed by the Fermi surface in wave number space, Ω_k, can always be expressed as

$$\Omega_k=\alpha_k\cdot(4\pi/3)(k_s/2)^3, \qquad \text{(ii)}$$

where α_k is a dimensionless parameter. Since the electron-atom ratio z is conserved in a phase transformation,

$$(k_s/2k)^3=1/\alpha_k=z_s/z,$$

where $z_s=2\Omega\cdot(4\pi/3)(k_s/2)^3$. Since $\alpha_k=\alpha_k(\mu, Q)$ and z_s is known, there is the functional relation between z and μ for any given phase

$$z=\alpha_k(\mu, Q)\cdot z_s. \qquad \text{(iii)}$$

For a single pair of faces

$$\Delta U=U-U_0=U_0(\beta_k-1).$$

In the f.c.c. lattice there are four pair of nearest zone faces, and in the b.c.c. lattice six pair of zone faces. If the influence of the six small next-nearest zone faces of the f.c.c. lattice is neglected, and if the influence of each zone face is assumed to be that of an infinite plane, then

$$U_{f.c.c.}=U_0+4\Delta U=U_0(4\beta_k-3),$$
$$U_{b.c.c.}=U_0+6\Delta U=U_0(6\beta_k-5),$$

and

$$U_{f.c.c.}/U_{b.c.c.}=[4\beta_k(1)-3]/[6\beta_k(2)-5], \qquad \text{(iv)}$$

where $\beta_k(1)$ refers to the f.c.c. lattice and $\beta_k(2)$ refers to the b.c.c. lattice.

For the simple model of a spherical Fermi surface, it is readily shown that

$$\alpha_k(1)=(6\mu^{-2}-3\mu^{-3}-2), \quad \alpha_k(2)=(9\mu^{-2}-5\mu^{-3}-3).$$

If the constants Q_1 and Q_2 are taken for a measure of the energy gaps across the f.c.c. and b.c.c. zone faces respectively, then the respective values $\mu_1(z)$ and $\mu_2(z)$ for a given value of z can be calculated from relation (iii). Since $z_s(1)=1.362$ and $z_s(2)=1.480$, relation (iv) can then be written as

$$\frac{U_{f.c.c.}}{U_{b.c.c.}}=\frac{4(1.362/z)^{5/3}\cdot f(\mu_1(z), Q_1)-3}{6(1.480/z)^{5/3}\cdot f(\mu_2(z), Q_2)-5}. \qquad \text{(v)}$$

Figure 14 shows a plot of $U_{f.c.c.}/U_{b.c.c.}$ *vs* z for $Q_1=Q_2=0.05$. The perturbation value for E_k given in Sec. IV was used in the calculation of β_k to give

$$f(\mu, Q)\cong\begin{cases}\mu^{-4}-5Q^2\mu^{-2}\left[\frac{1}{4}\log\left(\frac{2}{Q}\right)-\frac{1}{3}\right] & \text{for } \mu\geq 1\\ \frac{1}{4}(5\mu^{-4}-1)+5Q^2\left[\left(5-3\log\left(\frac{2}{Q}\right)\right)\frac{\mu^{-2}}{6}\right. & \\ \qquad\left.+\frac{1}{2}\left(\log\left(\frac{2}{Q}\right)-1\right)\right] & \text{for } \mu\leq 1.\end{cases}$$

This calculation shows that if the Fermi energy alone is used as a criterion for the relative stability of the f.c.c. and b.c.c. phases in a metal alloy, the f.c.c. phase has the lower Fermi energy and therefore is the more stable for $z<1.4$. For larger values of z, however, there is a range in which the b.c.c. phase is the more stable. This range corresponds to the β-phase region in the β-brasses.

The Hall Effect of Copper-Nickel Alloys*

ALBERT I. SCHINDLER† AND EMERSON M. PUGH
Department of Physics, Carnegie Institute of Technology, Pittsburgh, Pennsylvania
(Received September 11, 1952)

The ordinary and extraordinary Hall effects have been measured at room temperatures for the Ni–Cu series of alloys. The number of conduction electrons calculated from $n^*=1/R_0Ne$ (where R_0 is the "ordinary" constant measured at high fields) agrees fairly well with the number of 4*s* electrons predicted for the alloys from the simple band model. It is shown that the agreement for these alloys should improve at lower temperatures. Results in pure nickel and copper do not agree so well. A two-band model is invoked to explain the ordinary effect in pure nickel. Since in pure copper the 4*s* band is half-full, the simple approximation, valid for nearly empty bands, should not be expected to hold. No explanation is offered for the extraordinary Hall effect in any of the samples.

A. INTRODUCTION

IT has been shown,[1–4] that the Hall emf in ferromagnetics can be separated into two distinct parts, one proportional to H (the ordinary Hall effect) and one proportional to M (the extraordinary Hall effect). It has been proposed[3] that e_H, the ferromagnetic Hall electric field per unit current density be written as

$$e_H=E_H/ib=R_0(H+\alpha 4\pi M), \qquad (1)$$

where E_H = the Hall emf, R_0 = the ordinary Hall constant, i = the current density in the ferromagnetic sample, b = the width of the sample between the Hall probes, M = the intensity of magnetization, and H = the magnetic field corrected for demagnetization. Values of R_0 and α have been determined previously for nickel.[3] This paper reports experimentally determined values of R_0 and α for the nickel-copper alloy system at room temperatures.

The nickel-copper system was chosen for several reasons. First, copper alloyed with nickel forms a homogeneous single-phase substitutional solid-solution over the entire range of composition. Second, the nickel-copper system saturates at low magnetic fields, and only those materials having saturation magnetizations smaller than the field of the magnet used could be investigated. Third, the number of holes in the 3*d* band of this alloy system and, consequently, the number of electrons in the 4*s* band have been quite accurately determined from measurements of the saturation magnetization.[5,6] One expects the ordinary Hall constant to be a measure of the number of electrons taking part in conduction processes. According to the simple band model, the addition of copper to nickel should increase the number of electrons in the 3*d* band until this band is filled, and, thereafter, should increase the number of electrons in the 4*s* band.

The Hall constant may be defined by $R=\partial e_H/\partial B$, where R is independent of B in most materials but not in the ferromagnetic materials. The R_0 which is independent of B in ferromagnetic materials can be obtained from the slope of the e_H *vs* B curve at high fields where $M=M_s$ = constant. From Eq. (1), since $H=B-4\pi M$,

$$\partial e_H/\partial B=R_0\{1+4\pi(\alpha-1)\partial M/\partial B\}, \qquad (2)$$

which gives $R_0=\partial e_H/\partial B$ when $\partial M/\partial B=0$. If B_s is the smallest value for B for which $M=M_s$, then above B_s the e_H *vs* B curve is a straight line. Extrapolating this straight line back to $B=0$ gives $4\pi(\alpha-1)R_0M_s$, from which α can be obtained provided M_s is known. Thus, R_0 is obtained from measurements of the change of E_H with incremental changes in field above saturation and α is obtained from measurements of the change in E_H on reversal of any given field above $B=B_s$.

B. METHOD OF MEASUREMENT

Measurements were made on nickel-copper alloys containing 0, 10, 20, 30, 40, 50, 60, 80, 90, 95, and 100 percent copper. Each sample was measured in the unannealed state and after it had been annealed for two hours. The samples were 4.5 cm×2.0 cm×0.1 cm and were mounted in the holder shown in Fig. 1. They were hard soldered into two copper electrodes, which were fastened to micarta strips for added rigidity. The Hall

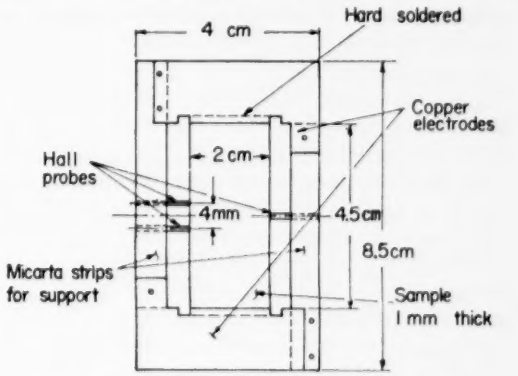

FIG. 1. Sample holder for Hall emf measurements.

* This research was supported by the ONR.
† Now at the Naval Research Laboratory, Washington, D. C.
[1] A. W. Smith and R. S. Sears, Phys. Rev. **34**, 1466 (1929).
[2] Emerson M. Pugh, Phys. Rev. **36**, 1503 (1930).
[3] Pugh, Rostoker, and Schindler, Phys. Rev. **80**, 688 (1950).
[4] N. Rostoker and E. M. Pugh, Phys. Rev. **82**, 125 (1951).
[5] C. Sadron, Ann. Physik **17**, 371 (1932).
[6] H. Krutter, Phys. Rev. **48**, 664 (1935).

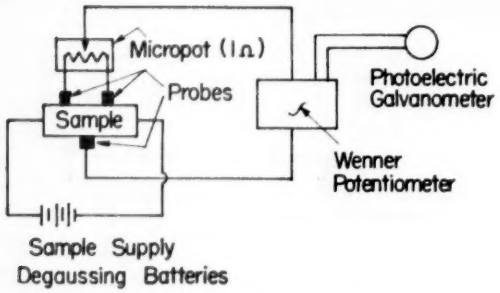

FIG. 2. Circuit diagram for Hall emf measurements.

probe connections shown in Fig. 2 were adapted from a method originated by Kolacek.[7] One probe on one side and two probes (4 mm apart) on the other side of the samples were used. The two probes on the same side were connected to a 1-ohm Micropot, used as a voltage divider. The center tap of this Micropot and the remaining Hall probe were then connected to a Wenner potentiometer with a Rubicon photoelectric galvanometer which has a linear response for small deflections. The Wenner potentiometer is graduated into steps of 10^{-7} volt, but interpolations can be made with the galvanometer deflections to $\pm 5 \times 10^{-9}$ volt.

Copper-constantan thermocouples were connected to each Hall probe to determine the temperature of the sample and to determine the corrections for the Ettingshausen effect. The field was measured with a flat spiral shaped flux coil in contact with the sample and connected to a greatly overdamped high sensitivity galvanometer operating as a fluxmeter. The sample with flux coil and thermocouples was placed between the poles of the electromagnet, with the flat surface perpendicular to the field. Glass wool wrapped around the whole assembly prevented air currents from disturbing the thermal equilibrium. To change the magnetic field without disturbing the temperature equilibrium, a method previously devised by one of us[8] was adapted for use with the available Kohl magnet. By reversing the direction without changing the magnitude of the current in a selected coil the field was changed without affecting the Joule heating. This greatly improved the stability of the readings. Since the four coils of the Kohl magnet had approximately equal numbers of turns it was necessary to shunt three coils with different resistors to insure that different field changes would be produced by reversing different coils. The resistors were chosen to provide five convenient steps in magnetic field above the saturation of the samples for the R_0 determinations. To avoid breaking the current during these reversals, each coil reversing switch was made to produce a temporary short instead of an open circuit across the coil at the mid-point in its reversal. Since the four coils were in series, one coil could be temporarily shorted without causing difficulty.

To insure sufficient stability for the required accuracy good thermal equilibrium was essential. The magnet and sample currents were turned on for three hours before measurements were to be made. High stability during measurements was also required for these currents. For the magnet current, a 120-volt storage battery was floated across a 220-volt dc line. Four Navy degaussing type batteries in parallel supplied the large sample current that was required and maintained it quite steady for several hours.

To make certain that the true Hall effect is measured, one must eliminate all thermal emf's, especially those due to the Ettingshausen effect. Most of the thermal emf's were eliminated by maintaining temperature equilibrium throughout the measuring circuit and then observing the changes produced by changes in the magnetic field. However, the Ettingshausen effect causes changes in the temperatures at the Hall probes with changes in the magnetic field. The thermocouples connected to the Hall probes were used to determine these field dependent temperature changes. In all cases the corrections were small.

C. RESULTS AND DISCUSSION

The curves in Fig. 3(a) and 3(b) show the variation in Hall voltage with the magnetic induction (beyond

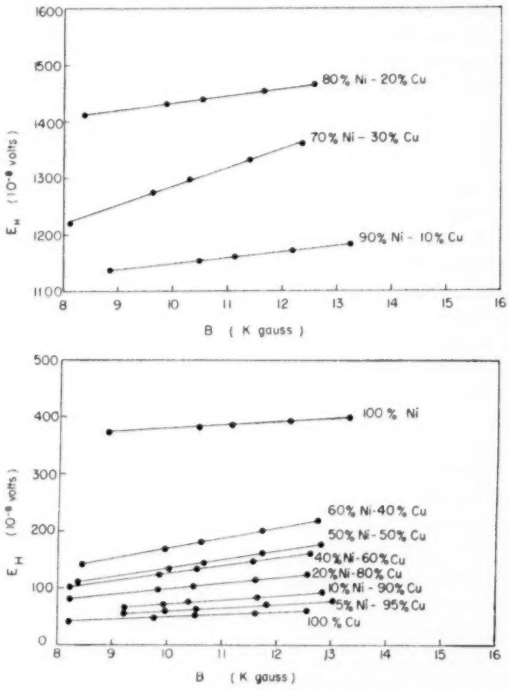

FIG. 3. (a) Hall emf *versus* magnetic induction, using 10 amp through 0.1-cm thick samples of Ni—Cu alloys at 20°C. (b) Hall emf *versus* magnetic induction, using 10 amp through 0.1-cm thick samples of Ni—Cu alloys at 20°C.

[7] F. Kolacek, Ann. Physik **39**, 1491 (1912).
[8] See reference 2, p. 1506.

saturation) for the different alloys of copper and nickel using a 10-amp sample current at 20°C. Each point on the curves represents an arithmetical average of five runs. Figure 4 illustrates the variation of R_0 with copper content, while Fig. 5 shows the variation of n^* ($n^*=1/NR_0ec$) with copper content. Values for the field parameter α at 25°C are plotted *versus* copper content in Fig. 6. The spread of the data is such that the standard deviations in the R_0's are in the neighborhood of 2 percent, except for the 30 percent Cu alloy. For this alloy the spread is greater because its Curie point is very close to the temperature of the measurements.

The values of n^*, as shown in Fig. 5, are close to the number, n_s, of electrons in the 4*s* conduction band predicted from magnetic measurements[5,6] using the simple band model. The predicted values of n_s are shown in Fig. 5 by the dotted line. According to these predictions, adding copper to nickel adds electrons to the 3*d* band and not to the 4*s* band until the 3*d* band is filled at 60 percent copper. From this point on the extra electrons fill up the 4*s* band.

When values of R were determined from measurements at low fields as they have been in the past, the values of $n=1/NRec$ differed in order of magnitude from predicted values of n_s, for most ferromagnetic materials. Here, with R_0 obtained from high field measurements, the calculated values of n^* do not differ from the predicted values of n_s by as much as a factor of 2. In some of the alloys the agreement is quite striking. The agreement is even more striking when it is realized that the measurements on the alloys containing 20 and 30 percent copper were measured at room temperatures which are close to their Curie points where $\partial M/\partial B\neq 0$ at the highest fields available. If a correction[9] is made for this, the experimental values for these two alloys move up toward the theoretical curve. Unfortunately, the values of $\partial M/\partial B$ are not known for these alloys at the temperatures of these measurements. It is known, however, that the correction due to this factor is of the right magnitude[9] to improve this agreement for these alloys.

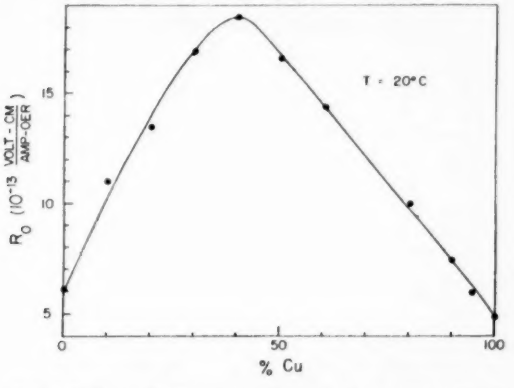

FIG. 4. Ordinary Hall constant, R_0, *versus* Cu content in Ni–Cu alloys at 20°C. Not corrected for the fact that $\partial M/\partial B\neq 0$ above technical saturation.

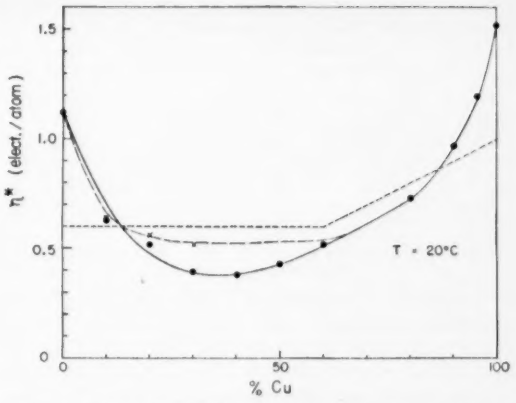

FIG. 5. Values of $n^*(1/NR_0ec)$ *versus* Cu content in Ni–Cu alloys at 20°C. Values taken directly from the slopes of the lines in Fig. 3 are shown as circles connected with a solid line. Values obtained by correcting for the fact that $\partial M/\partial B\neq 0$, even at high fields, are shown as crosses connected by a line of long dashes; which is extended smoothly through the 40 percent and the 50 percent Cu alloys, since corrections of similar magnitude but of unknown value should be made for them also. The numbers of 4*s* electrons per atom, predicted by simple band theory, are indicated by the line of short dashes.

The study made by Rostoker[4] and one of us of the Hall effect measurements on Ni made by Smith[10] at temperatures above and below its Curie point, suggests that similar corrections should be applied for the alloys having 40 and 50 percent Cu. A correction here would also improve the agreement between theory and experiment for these alloys. With the 60, 80, and 90 percent copper alloys the agreement between theory and experiment is fairly good. Low temperature measurements now being made on this series of alloys may clear up these discrepancies.

The field parameter α can be calculated from the data for those samples that are ferromagnetic at room

[9] Since the completion of the experimental part of this paper, the order of magnitude of this correction has been determined by Norman Rostoker and Simon Foner by assuming that $M/M_s=f(T/T_c, \mu H/kT)$ has the same form for all ferromagnetics.

The saturation magnetizations, M_s, and the Curie temperatures, T_c, are known for all of the alloys and for pure nickel. Since accurate measurements of M in nickel have been made by P. Weiss and R. Forrer [Ann. phys. 5153 (1926)] for a wide range of values of T and H, empirical values for $f(T/T_c, \mu H/kT)$ could be obtained from the nickel data and applied to the alloys. Values of M *versus* H (therefore, M *versus* B) for the alloys at the temperature of the measurements were estimated from the nickel data. From these, values of $\partial M/\partial B$ were obtained and used in Eq. (2) to obtain corrected values of R_0 from the high field data. The corrected values of n^* are shown in Fig. 5 by crosses connected with a dashed line. The nickel measurements of M do not extend to sufficiently high temperatures to make it possible to use this method for obtaining the corrections for the 40 percent and 50 percent copper alloys, whose Curie temperatures are below the temperature of these measurements. However, the smooth behavior of R_0 and α in nickel (see reference 4) when passing through the Curie point appears to justify drawing the dashed line smoothly to the nonmagnetic alloy (60 percent Cu, 40 percent Ni).

[10] A. W. Smith, Phys. Rev. **30**, 1 (1910).

TABLE I. Values of R_0 and α for those alloys that are ferromagnetic at 20°C. The right-hand columns of both R_0 and α are corrected for the fact that $\partial M/\partial B \neq 0$ even at high fields.

Alloy comp % Cu	$R_0\alpha\left(10^{-12}\frac{\text{volt-cm}}{\text{amp-oer}}\right)$	$R_0\left(10^{-12}\frac{\text{volt-cm}}{\text{amp-oer}}\right)$		α	
		Uncorr.	Corr.	Uncorr.	Corr.
0	60.7	6.07	6.07	10.0	10
10	235	11.0	10.8	21.4	22
20	396	13.4	12.3	29.6	32
30	795	16.9	12.9	47	62

temperatures; namely, the alloys containing 0 percent, 10 percent, 20 percent, and 30 percent Cu. The product $R_0\alpha$ for each alloy is obtained from the intercept of its straight line with the $B=0$ axis in Fig. 3 and its saturation magnetization. These values are shown in Table I. The value calculated for α then depends upon the value of R_0 chosen. Table I shows two values of R_0; the first has been obtained directly from the slopes of the lines in Fig. 3 and the second has been corrected[9] for the fact $\partial M/\partial B \neq 0$ even at high fields. Table I also show values of α obtained both with the corrected and the uncorrected values of R_0.

Since the n^* curve crosses the predicted curve of n_s fairly close to the alloy concentration at which this series changes from being paramagnetic to being diamagnetic, one is tempted to speculate on the possibility that a correction of the opposite sign due to a change in the sign of $\partial M/\partial B$ would improve the agreement for pure copper. However, for such a correction to account for the fact that in copper $n^*=1.48$ would require an α of the order of 10^5. This does not seem likely.[11] A more plausible explanation is that, since in copper the 4*s* band is half-full, the simple approximation of the spherical Fermi surface implicit in $R_0=1/Nnec$, which is valid for nearly empty bands, does not hold.

Two possible explanations have been proposed[3] for the large value of n^* (or small value of R_0) in pure nickel. One of these assumes that R_0 is reduced by conduction in the 3*d* band. This 3*d* conduction would tend to produce a positive R_0 while the 4*s* conduction produces a negative R_0. This explanation seems plausible, since $R_0\alpha$ is known, from experiments of Smith[10] and others, to be positive for both cobalt and iron. $R_0\alpha$ passes through zero at some alloy of cobalt and nickel. If this point of view is adopted, then

$$R_0=-(\sigma_s^2/n_s\sigma^2-\sigma_d^2/n_d\sigma^2)/Nec,$$

and the ratios of the conductivities due to the 3*d* and 4*s* bands can be determined. For pure nickel $\sigma_d/\sigma_s=0.3$ and, for Ni 90 percent and Cu 10 percent, $\sigma_d/\sigma_s=0.03$. This appears to be the most logical explanation for the large value of n^* in nickel.

No satisfactory explanation for the value of α is available. A paper by Rostoker[12] and one of us reviews the various attempts to explain the values for α, which are strongly dependent on temperature, and points out the inadequacies of each of them.

The authors are indebted to the ONR for funds to carry on this research. They are also indebted to J. Goldman, R. Smoluchowski, N. Rostoker, and Simon Foner for assistance and stimulating discussions. They wish to thank the International Nickel Company for furnishing the nickel-rich alloys and the Westinghouse Manufacturing Company for furnishing the copper-rich alloys.

[11] It is interesting to notice that n^* from Hall measurements is generally less than expected in paramagnetic elements (e.g., Li, Na, Mg) and greater than expected in diamagnetic elements (e.g., Cu, Ag, Au). The values of α required to account for these discrepancies are very large.

[12] Presented to the Conference on Magnetism at the University of Maryland, September 2 to 6, 1952. It is planned that the papers from this conference will appear in the *Reviews of Modern Physics*.

Angular Distribution of Gamma-Rays and Short-Range Alpha-Particles from $N^{15}(p,\alpha\gamma)C^{12}$†

ALFRED A. KRAUS, JR., A. P. FRENCH,* WILLIAM A. FOWLER, AND C. C. LAURITSEN
Kellogg Radiation Laboratory, California Institute of Technology, Pasadena, California

(Received August 13, 1952)

Measurements of the angular distributions of gamma-rays and alpha-particles from the reaction $N^{15}(p,\alpha\gamma)C^{12}$ indicate that the 4.432-Mev excited state of C^{12} is 2^+ or >4, that the 12.51-Mev level of O^{16} is 2^- or >5, that the 12.95-Mev level is 2^- or >5, and that the 13.24-Mev level is 4^+ or >5.

THE reaction $N^{15}(p,\alpha\gamma)C^{12}$, in which the gamma-ray energy is 4.432 ± 0.010 Mev, exhibits strong resonances[1] at 429, 898, and 1210 kev, and we have measured the angular distribution of gamma-rays and alpha-particles relative to the protons at these resonances.

Protons from the 1.6-Mv electrostatic generator of the Kellogg Radiation Laboratory were magnetically analyzed and used to bombard a titanium nitride (TiN) target prepared using nitrogen enriched to 31 percent N^{15}. The emitted gamma-rays were detected by a scintillation counter consisting of a glass cell, containing about 100 cc of a solution of terphenyl in xylene, cemented to a 5819 photomultiplier tube. The center of the phosphor was 9.5 cm from the target. The amount of absorbing material between target and phosphor was small, and the symmetry of the arrangement was tested with natural sources of Co^{60} and ThC'' and with the isotropic gamma-rays from the 935-kev resonance in $F^{19}(p,\alpha\gamma)O^{16}$.

The angular distribution curves from gamma-rays from the 429- and the 898-kev resonances in $N^{15}(p,\alpha\gamma)C^{12}$ are shown in Figs. 1 and 2, respectively. The points plotted are the measured values corrected for background and absorption. The absorption corrections averaged about one percent and in no case exceeded four percent.

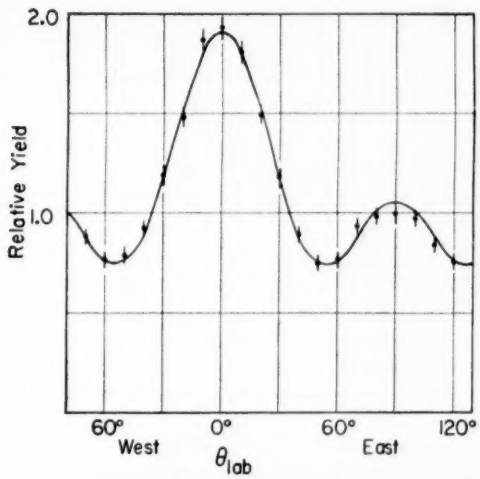

FIG. 1. Angular distribution of gamma-rays at the 429-kev resonance. The theoretical curve is for $x=0.82$.

It may be seen that the two angular distributions are very similar, and analysis shows that they may be accounted for under the following assumptions: (a) the ground state of N^{15} has spin $\frac{1}{2}$ and odd parity (denoted $\frac{1}{2}^-$), the proton being $\frac{1}{2}^+$; (b) the O^{16} compound states formed at 429 and 898 kev are both 2^- and are formed by d wave protons; (c) the O^{16*} breaks up by emission of p wave alpha-particles, leading to a 2^+ state of C^{12} which decays to the ground state 0^+ by emission of electric quadrupole gamma-rays.

The proton and N^{15} may collide with parallel or antiparallel spin orientations. If we suppose that in a fraction x of all cases the O^{16} is formed from the antiparallel configuration, the relative probability for emission of a gamma-ray at an angle θ to the proton beam is given by

$$W(\theta)=\left(\frac{1}{2}+\frac{5}{2}\cos^2\theta-\frac{8}{3}\cos^4\theta\right)+\frac{x}{1-x}(1-3\cos^2\theta+4\cos^4\theta).$$

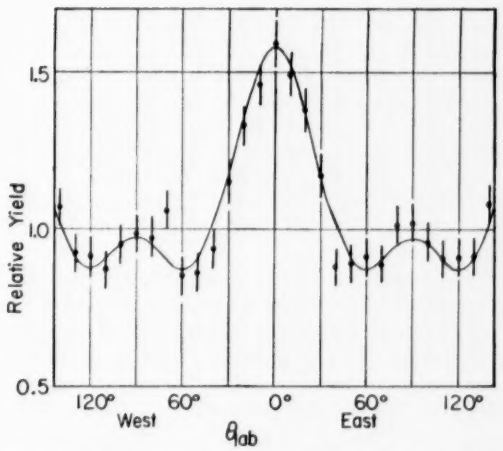

FIG. 2. Angular distribution of gamma-rays at the 898-kev resonance. The theoretical curve is for $x=0.58$.

† This work was assisted by the joint program of the ONR and AEC.

* On leave of absence from Cavendish Laboratory, Cambridge, England.

[1] Schardt, Fowler, and Lauritsen, Phys. Rev. **86**, 527 (1952).

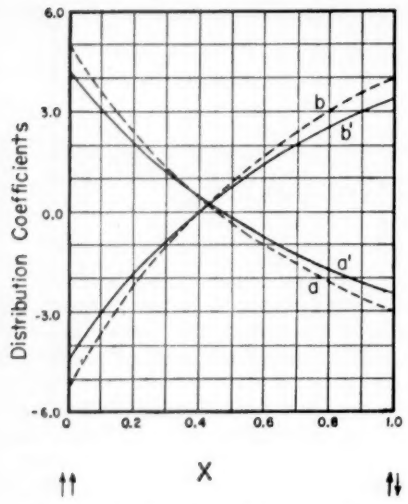

FIG. 3. Angular distribution coefficients for the assignment ($2\,2^-\,1\,2^+$). The dashed curves are theoretical values. The solid curves are corrected for the gamma-ray detector solid angle.

In obtaining this expression we ignore any possible contribution from f wave alpha-particles in the break-up of the O^{16}, on the grounds that they are strongly discouraged by the potential barrier. If the theoretical distribution function is normalized to the form

$$W(\theta)=1+a(x)\cos^2\theta+b(x)\cos^4\theta,$$

a and b can be plotted as functions of x. These functions are shown as dashed curves in Fig. 3.

The finite solid angle subtended by the gamma-ray detector modifies the ideal pattern somewhat. Its effect is to replace a and b in the above formula by different values a' and b'. These are plotted as the solid curves in Fig. 3. The experimental data of Fig. 2 (898 kev) were analyzed by an approximate least squares method and gave $a'(x)\simeq-0.927$ and $b'(x)\simeq1.471$. These correspond to $x\simeq0.62$ and $x\simeq0.60$, respectively. The actual least square error is obtained, however, with $x=0.58$; the estimated probable error on this value is ±0.03. The theoretical distribution for $x=0.58$ is shown as the solid curve in Fig. 2, and it can be concluded that the experimental results conform to our initial assumptions about the spins and parities of the nuclear states involved. The result obtained at the 429-kev resonances can be fitted in a similar way by putting $x=0.82\pm0.04$ (solid curve of Fig. 1).

Our assumption that the 4.432-Mev level of C^{12} is 2^+ is supported by studies[2] of the reaction $B^{11}(p,\gamma\gamma)C^{12}$ and is in agreement with nearly all theoretical models of this nucleus. The 898-kev gamma-ray distribution indicates that the 12.95-Mev level of O^{16} is 2^- or greater than five, and that the 4.432-Mev state of C^{12} is 2^+ or greater than four. The 429-kev distribution indicates that the 12.51-Mev level of O^{16} is 2^- or greater than five.

[2] Hubbard, Nelson, and Jacobs, Phys. Rev. **87**, 378 (1952).

Figure 4 shows the angular distribution of alpha-particles at the 898-kev resonances as measured by the $10\frac{1}{2}$-inch variable angle (0°–160°) proton spectrometer of the Kellogg Radiation Laboratory. The target was evaporated KNO_3 (enriched to 61 percent N^{15}). The points plotted are the measured points corrected for a small background, for the fact that some of the alpha-particles leave the target singly charged, for the change in solid angle due to the motion of the center of mass, and for the fact that some of the particles are slowed down by irregularities in the target. The theoretical curve shown in Fig. 4 is

$$W(\theta)\sim7-6\cos^2\theta,$$

obtained from the assignment ($2\,2^-\,1\,2^+$) with $x=0.60$.[3] The agreement with the experimental points is considered satisfactory in view of the number of corrections applied to the original data. The point at 117° is high, because near this angle the scattered protons have the same energy as the alpha-particles and were not separated from the alpha-particles by the spectrometer. This distribution is in agreement with the assignments made on the basis of the gamma-ray distribution.

We have also measured the gamma-ray distribution at the 1210-kev resonance, but in preliminary measure-

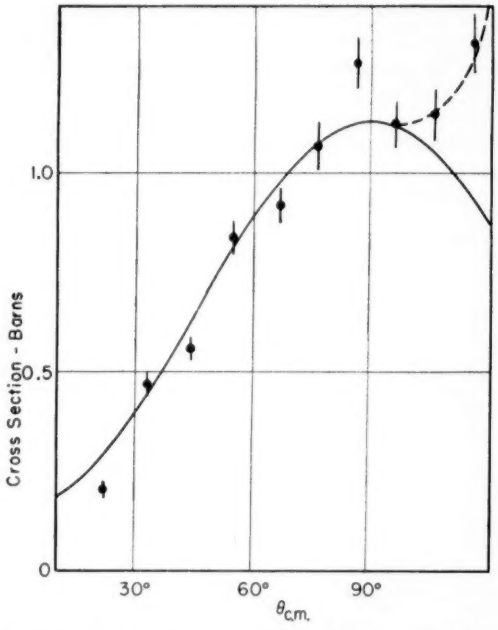

FIG. 4. Angular distribution of short-range alphas from the 898-kev resonance. The solid curve represents $W(\theta)\sim7-6\cos^2\theta$. The dashed line indicates the scattered protons. The probable error of the cross section is ±20 percent.

[3] In the assignment ($lJ^{\pm}l'J'^{\pm}$), the first number describes the angular momentum of the proton wave; the second, the spin and parity of the state in O^{16}; the third, the relative angular momentum of the emitted alpha-particles; and the fourth, the spin and parity of the 4.432-Mev excited state of C^{12}.

ments we were unable to determine uniquely the spin and parity of the excited state of O^{16} since the theoretical distributions for the assignments 3^-, 4^+, and 5^- differ only by small amounts. The short-range alpha-particle distribution was then measured at this resonance. The

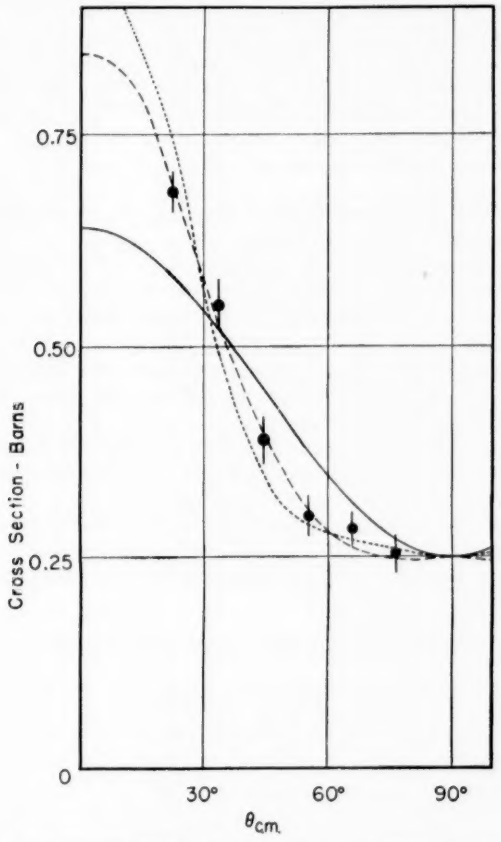

FIG. 5. Angular distribution of short-range alphas from the 1210-kev resonance. The solid curve is for ($2\,3^-\,1\,2^+$), the curve of long dashes is for ($3\,4^+\,2\,2^+$), and the dotted curve is for ($4\,5^-\,3\,2^+$).

points are plotted in Fig. 5. The solid curve is for ($2\,3^-\,1\,2^+$); the dashed curve is for ($3\,4^+\,2\,2^+$); and the dotted curve is for ($4\,5^-\,3\,2^+$). From this distribution we can conclude that the state is not 3^-. The final measurement was a more accurate gamma-ray distribution.

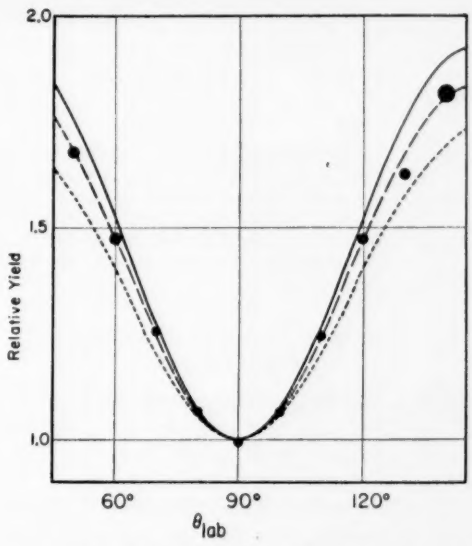

FIG. 6. Angular distribution of gamma-rays at the 1210-kev resonance. The curves correspond to the assignments in Fig. 5.

During this experiment the target was set at 45° with respect to the proton beam. The gamma-rays were measured at angles such that they did not pass through the target material, so there were no absorption corrections. Statistical errors were minimized by taking on the order of 10^4 counts at each point. The results are shown in Fig. 6. From this curve we conclude that the excited state is 4^+. The gamma-ray distribution at this resonance enables one to show, independently of the results at the other resonances, that the excited state of C^{12} is 2^+ or greater than four.

In each case for an assignment in O^{16}, states of spin up to but not always including six were considered in the theoretical calculations. States with such high angular momentum would require proton waves of orbital angular momentum greater than five, and the barrier factors for such waves make the formation of such states highly improbable. In all cases we have considered only the minimum allowed l values for the incoming protons and outgoing alpha-particles.

The authors would like to express their thanks to Professor R. F. Christy and Professor Thomas Lauritsen for their help and advice in this work.

The Radiations of Th^{231}(UY)

MELVIN S. FREEDMAN, ARTHUR H. JAFFEY, FRANK WAGNER, JR., AND JACK MAY
Chemistry Division, Argonne National Laboratory, Chicago, Illinois

(Received September 15, 1952)

β-ray spectrum studies on a double-lens spectrometer of the electron spectrum of UY revealed a complex spectrum with three beta-components of 302 kev (44 percent), 216 kev (11 percent), and 94 kev (45 percent), and numerous conversion lines assignable to gammas of 22, 59, 63, 85, 122, 167, and 208 kev, each of these except the 122 kev also observed directly as gammas in a scintillation spectrometer. There is also evidence for a 107- and for a 230-kev gamma-ray. The samples were separated carrier-free from isotopically pure U^{235} (99.86 percent) by solvent extraction. A decay scheme is presented which gives a total disintegration energy of 324 kev.

INTRODUCTION

ONE of the naturally-known beta-emitters is Th^{231} (or UY), being the daughter by alpha-decay of U^{235}. It has also been formed by the reactions $Th^{230}(n,\gamma)Th^{231}$ [1] and $Th^{232}(n,2n)Th^{231}$.[2]

Most of the previous measurements of the radiations of UY which have been reported were performed on samples milked from the U^{235} present in natural uranium. Due to the decay $U^{238}\xrightarrow{\alpha}UX_1(Th^{234})$, the milked UY samples contained large amounts of both UX_1 and its daughter $UX_2(Pa^{234})$. The presence of these interfering activities greatly complicated experiments on UY radiations, since the isotopic abundance of U^{235} is only 0.7 percent. The availability of enriched U^{235} with attendant reduction of the UX_1 content, made possible more clear-cut measurements. UY from such sources has been investigated by absorption techniques,[3,4] with the relatively poor resolution of such methods. The results indicated that the radiations of UY included: (1) a single beta-ray of about 0.2 Mev; (2) *L* x-rays, presumably from conversion of low energy gamma-rays; (3) a very soft component presumably due to *M* x-rays and low energy conversion electrons; (4) several gamma-rays, whose energies were 35 kev, 65 to 75 kev, and 100 kev. The last two gamma-rays were uncertain as to energy.

More recently, the radiations from UY extracted from natural uranium have been examined with a beta-ray spectrometer.[5] The results indicated the presence of gamma-rays at 59, 63, 82, and 120 kev; the beta-ray end point was found to be 390 kev, with some indication of lower energy branches with 190- and 100-kev maximum energies.

In the work reported here,[6] an enriched U^{235} sample was used to supply the UY source. The radiations were examined with a magnetic beta-ray spectrometer and a gamma-ray scintillation spectrometer. Sufficient information was secured to make possible the proposal of a decay scheme which fits the measurements reasonably well.

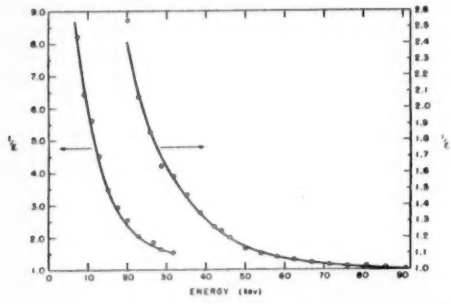

FIG. 1. Efficiency (ϵ) of anthracene scintillation counter as a function of energy.

EXPERIMENTAL—ELECTRON SPECTROMETRY

A double lens spectrometer adjusted for a transmission of *ca* 2 percent with a resolution of *ca* 3 percent was used to examine the electron spectrum of UY. The spectrometer calibration was based on a value of 624 kev[7] for the *K* conversion line of Ba^{137}.

An anthracene scintillation counter served as a detector, the scintillations being detected by a 1P21 photomultiplier at liquid nitrogen temperature, located in a magnetic shield outside the magnetic field of the spectrometer lens coils. The light flashes from the 1 mm thick by 8 mm diameter anthracene crystal were piped to the photomultiplier through a 20 inch long$\times\frac{3}{4}$ inch diameter clear quartz light guide, to which the crystal was cemented.

The efficiency of this system for detection of electrons fell below 100 percent for energies less than 80 kev. A determination of the efficiency correction applicable to the counting data was made by a comparison of the Kurie plot of an experimental spectrum of Pm^{147} to the known allowed shape. A very thin ($<10\ \mu g/cm^2$) sample of Pm^{147}, prepared by vacuum volatilization of the

[1] A. H. Jaffey and E. K. Hyde, Argonne National Laboratory Report ANL-4249 (1949) (unpublished).
[2] Nishina, Yasaki, Kimura, and Ikawa, Nature **142**, 874 (1938).
[3] Jaffey, Lerner, and Warshaw, Phys. Rev. **82**, 498 (1951). Includes survey of previous work.
[4] G. B. Knight and R. L. Macklin, Phys. Rev. **75**, 34 (1949).
[5] Stoker, Hok, and Sizoo, Physica **17**, 164 (1951).
[6] Freedman, Jaffey, May, and Wagner, Argonne National Laboratory Report ANL-4613, 67 (1951) (unpublished); Phys. Rev. **86**, 633 (1952).
[7] L. Langer and R. D. Moffat, Phys. Rev. **78**, 74 (1950).

trifluoro-acetylacetonate compound onto a *ca* 10 $\mu g/cm^2$ LC-600 film, gave a Kurie plot linear to *ca* 80 kev, but dropped below the linear extrapolation at lower energies, down to <8 kev. Such thin samples have been shown[8] to give an allowed shape down to *ca* 8 kev. A graph of the efficiency correction factor is given in Fig. 1.

Counting data was recorded automatically on a chart recorder by a logarithmic counting rate meter, as the spectrometer coil current was swept continuously over the necessary range. The counting rate was determinable to ±1 percent from the chart trace, and the current at any chart position to within ±0.1 percent.

The spectrographic data reported here are the results of several experiments made on separate samples, each the product of an individual chemical separation. The UY samples were prepared by chemically isolating the UY (in radioactive equilibrium) from a stock solution of 25 grams of U^{235} [9] in HNO_3. The chemical separation, carried out for us by Paul Fields, Gray Pyle, and Ruth Sjoblom of this Laboratory, was designed to yield samples without carrier and with a minimum of massive impurities present. The thorium was separated from the uranium, as well as from impurities, by making use of the formation of a complex with thenoyl-trifluoro-acetone (TTA) in benzene solution. The thorium was further purified by usual well-known chemical procedures, with particular attention to the purity of the reagents involved, and to the thorough destruction of residual organic matter. The purified thorium was obtained as a minute dry deposit of the chloride in a platinum crucible.

TABLE I. UY—Beta-components.

Maximum energy of beta (kev)	Relative intensity (%)
302±2	44
216±5	11
94±2	45

The almost invisible deposit was taken up in 5λ of pure 3*N* HCl solution and deposited on a thin (<20 $\mu g/cm^2$) film of LC-600 on a circle of *ca* 5 mm diameter. The amount of impurity coming through the chemical procedure varied among the several experiments performed; the spectrometer results clearly showed the presence of impurities which increased the source self-absorption in terms of a broadening of the conversion line peaks, becoming worse with decreasing energy. The best experiments were done with samples estimated to be of average thickness 20 $\mu g/cm^2$, fairly uniformly spread over the sample area. Similar sources were used in the scintillation gamma-spectrometer experiments described below.

[8] Langer, Motz, and Price, Phys. Rev. **77**, 798 (1950).

[9] Obtained from Union Carbon and Carbide Corporation, Oak Ridge National Laboratory. Isotopic analysis—99.86 percent U^{235}; 0.07 percent U^{238}; 0.07 percent U^{234}.

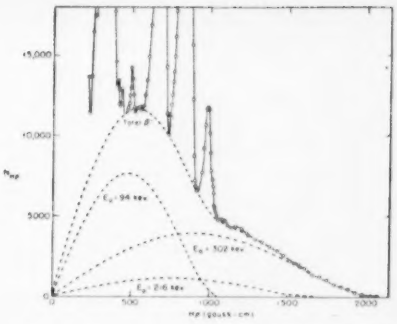

FIG. 2. Momentum spectrum of Th^{231} (UY).

From the amassed data the three runs which clearly gave the best results were taken as a basis for computation. Figure 2 presents an over-all momentum spectrum and Fig. 3 a Kurie analysis. Corrections for counting efficiency and for decay of the sample have been applied.

Successive subtractions of apparentiy linear components from the Kurie curve indicated beta-continua (Table I) of energies $E_0=302\pm2$ kev (44 percent relative abundance), $E_0=216\pm5$ (11 percent) and 94 ± 2 kev (45 percent). No beta of intensity >2 percent of the 302-kev beta and of substantially higher energy was observed, in contradiction to the results of Stoker *et al.*[5] The relative abundance of the low beta-component is subject to considerable error, inasmuch as imperfectly resolved conversion lines overlie the major portion of the spectrum. A short section of the curve between 23 and 28 kev [between lines $N_{IV}(1)$ and $L_I(2)$] seems well resolved from the tail of line $L_I(2)$ and to have no other lines on it, and so was considered as reliable to guide the drawing in of the low beta; similarly for the regions at 45 kev and 70 kev. A further indication of the correctness of this subtraction is had from Fig. 4, where the profiles of the conversion lines are shown on a momentum plot after subtracting the 94-kev beta. The line shapes are similar to those normally obtained with this instrument, especially in their low energy tails; subtraction of a beta of much

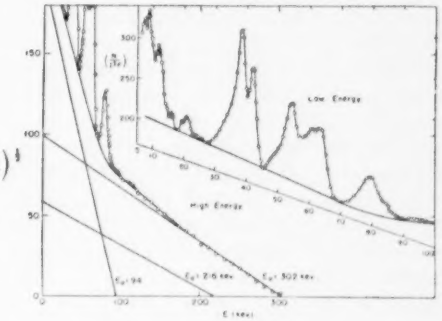

FIG. 3. Kurie plot for Th^{231} (UY).

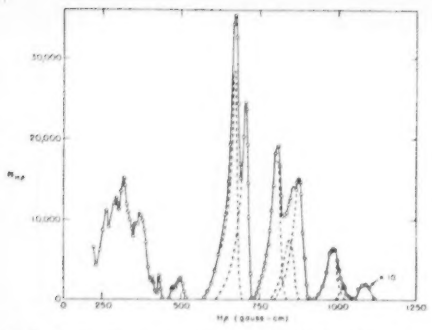

FIG. 4. Momentum plot of conversion lines of Th^{231} (UY); beta-continue subtracted off.

lower intensity would result in excessively large base widths of the lines, compared to their half-widths [3.6 percent for line $L_I(2)$]. However, as will be seen in the discussion below, a major difficulty with our interpretation of the experimental results is associated with an apparently too high branching ratio for the low energy beta.

Table II summarizes the information on the conversion lines. Many of the lines are low in intensity, and lie in an energy region where the counter efficiency is low. To distinguish statistical fluctuations from true lines, each of three selected data charts was examined. Only lines which appeared on all three were considered.

The unfolded shapes of incompletely resolved lines were obtained by construction, using leading and trailing edge profiles of nearby resolved lines as a guide. From these shapes the relative line intensities and peak locations were obtained graphically. No attempt was made to resolve the group below 14 kev completely, except to obtain a rough value for the relative intensity of line $K(5)$, which is an upper limit estimate. No lines were observed at 98 or 115 kev, contrary to the observations of Stoker *et al.*[5]

In columns I, IV, and V of Table II are given the line assignments. The shell binding energies were obtained by a Moseley law interpolation from data[10] for neighboring elements. Of the 18 lines definitely observed, the assignment of eight seems certain (labeled *) and of nine, probable (labeled ↑). One line (**) was not assigned. In some cases the same line is assigned to two levels, using the intensities and provisional assignments of other lines and the results of the gamma-ray spectroscopy (see below) as a guide. Where a line is so assigned, the major component of course determines the observed line energy, and a small unresolved component may be assigned with some latitude on the energy scale; the actual peak values were used in the assignments and perhaps account for some of the disagreements in energy between various conversion lines assigned to one level.

[10] A. H. Compton and S. R. Allison, *X-Rays in Theory and Experiment* (D. Van Nostrand and Company, Inc., New York, 1935), second ed., p. 794.

Line $K(6)$ was assigned to a 208-kev transition on the basis of the results of gamma spectroscopy. Some of the lines assigned to the 22-kev gamma could equally well have been allotted to gammas of 26 or 28 kev; 22 kev was chosen as giving the best energy balance in the proposed decay scheme, and in agreement with the results of gamma-ray spectroscopy (see gamma-ray measurements, below). In fact, the relative intensities of lines $M_I(1)$, $M_{III}(1)$, and $N_{IV}(1)$ suggest that the assignment may not be correct, and that 25–26 kev would be more reasonable. Lines A_1, A_2, A_3, and A_4 agree satisfactorily with predicted Auger transition energies, although considering the poor resolution and the large number of possible Auger transitions in this energy region such allocations are not very significant. Line $K(5)$ was ascribed to a cross-over transition of 122 kev spanning the 59-kev and 63-kev transitions and $K(7)$ is ascribable, as a small fraction of line $M_{II}(2)$, to a cross-over of the 63-, 85-, and 22-kev gammas.

In column VII of Table II are listed the intensities of the conversion lines relative to the intensity of the beta plus gamma and internal conversion transitions assumed to feed the emitting level in question, according to the decay scheme proposed in Fig. 7 (see discussion below). The conversion line intensities relative to the sum of all beta transitions appear in column VI.

TABLE II. UY conversion lines and gammas.

I	II	III	IV	V	VI	VII
Line	Energy (kev)	Binding (kev)	Gamma (kev)	Gamma best value (kev)	Line or gamma-intensity relative to total beta intensity	Line or gamma-intensity relative to intensity of betas feeding level
$L_{III}(1)$ ↑	6.0	16.8	22.8			
$M_I(1)$ ↑	16.0	5.4	21.4			
$M_{III}(1)$ ↑	17.6	4.2	21.8			
				22	$0.80-[0.5(\gamma)+0.3(L$ x-rays)]	
$L_I(2)$*	38.2	21.2	59.4		0.094	0.209
$M_{II}(2)$*	54.3	5.1	59.4		<0.066	<0.147
$N(2)$*	59.6	1.	60.6			
				59.4	0.063	0.15
$L_I(3)$*	41.9	21.2	63.1		0.083	0.184
$M_{IV}(3)$*	59.6	3.6	63.2		0.031	0.069
$N(3)$*	63.7	1.	64.7			
				63.1	0.126	0.28
$L_I(4)$*	63.7	21.2	84.9		0.060	0.107
$M_I(4)$*	79.4	5.4	84.8		0.026	0.046
$N_{IV}(4)$*	84.0	0.7	84.7		0.004	0.008
				84.8	0.44 (normalized)	0.79
				107		
$K(5)$ ↑	8.7	113.1	121.8		<0.06	<0.13
				121.8	0.008	0.018
$K(6)$*	94.9	113.1	208.0		0.0007	0.002
				208	0.0009	0.002
$K(7)$ ↑	54.3	113.1	167.4		≪0.066	≪0.147
				167.4	0.0066	0.014
				230	0.0004	0.001
**	10.9	(Unassigned)				
			Possible Auger transitions			
A_1 ↑	7.6	$L_{III}-M_I-M_{IV}=7.7$; $L_{III}-M_{II}-M_{III}=7.5$				
A_2 ↑	9.9	$L_{II}-M_I-M_{II}=10.0$; $L_{II}-2M_I=9.6$; $L_{III}-M_{III}-M_V=10.1$				
A_3 ↑	11.9	$L_I-M_I-M_{III}=11.6$; $L_I-M_I-M_{IV}=12.2$; $L_I-M_{II}-M_{III}=12.0$; $L_{II}-M_{II}-M_{IV}=11.8$; $L_{II}-2M_{III}=12.1$; $L_{III}-2M_V=11.8$				
A_4 ↑	14.7	$L_I-M_{III}-M_V=14.6$; $L_{II}-M_{IV}-M_V=14.3$.				

* Denotes line assignment considered certain.
↑ Denotes line assignment considered provisional.

From the conversion lines it was clear that there existed gamma-rays of 85, 63, 59, and 22 kev in considerable abundance. In addition, there was a very low intensity 95-kev conversion line $K(6)$, ascribed to K conversion of a 208-kev gamma-ray. These gamma-rays fitted into a consistent decay-scheme, since the differences in the beta-ray energies (maximum energies 93, 216, 302 kev) corresponded (Fig. 7) to the gamma-ray energies.[11] Most of the possible cross-over gamma-rays were not observed; the intensities of the conversion lines were either too low or the conversion lines resulting were hidden under the conversion lines of the more intense gamma-rays.

EXPERIMENTAL—GAMMA-SPECTROSCOPY

A search for unconverted gamma-rays was made, using the conventional photoelectric method with the beta-ray spectrometer. The results were negative because of low intensity resulting from weakness of sample activity and low conversion efficiency in the thin converters necessary at such low gamma-ray energies.

Since it was evident from preliminary measurements that a simple absorption counting technique could not handle the complex gamma-mixture involved, a NaI(Tl) crystal spectrometer[12,13] was used. A crystal $1\frac{1}{4}$ inches in diameter and $\frac{1}{2}$ inch thick was hermetically enclosed in an 0.030-inch thick aluminum cup (206 mg/cm^2) with a Pyrex glass disk sealed on the side facing the 5819 photomultiplier. An electrical tape (*ca* 50 mg/cm^2) light shield covered the entire crystal-photomultiplier combination. The sample was as close to the crystal as possible, at a geometry of about 30 percent. The output of the photomultiplier was linearly amplified and analyzed with a single channel differential pulse-height selector, with variable channel width. The channel-width was less than 10 percent of any peak width, and hence had a negligible effect upon the resolution.

Preliminary examination of a UY source (Fig. 5c) showed that while most of the activity lay in two peaks at 22 and 85 kev, there was evidence of the presence of gamma-rays at other energies, although these were not resolved. The shape of the low energy side of the 85-kev peak indicated that there might be a gamma-ray in this region, while the tailing off of the high energy side went far beyond the expected straggling of a single peak.

In order to decrease the relative concentration of the 85-kev peak, the peaks were differentially attenuated, by placing absorbers between sample and crystal. Appropriate absorbers were chosen in the following manner: A plot of half-thickness *vs* quantum energy for any particular absorber material characteristically has an increasing slope above the K-edge for some range of energy, followed by a decreasing slope. The maximum discrimination between two gamma-rays (for a given residual intensity) is achievable with the absorber

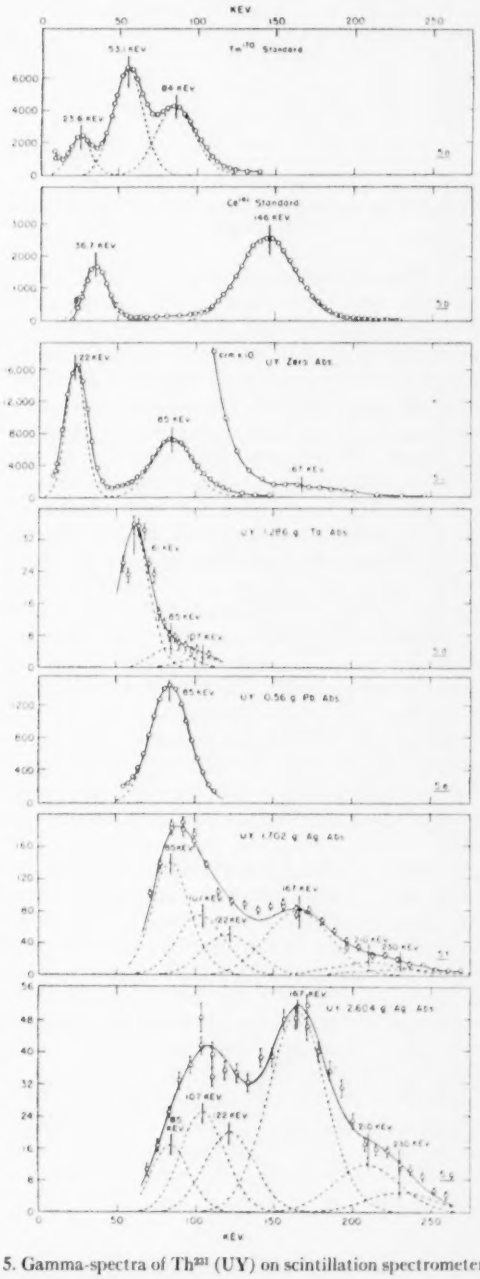

FIG. 5. Gamma-spectra of Th^{231} (UY) on scintillation spectrometer.

[11] 216−93=123; 63+59=122; 302−216=86; 302−93=209.

[12] This was an instrument developed by R. Swank of this laboratory [R. K. Swank, Argonne National Laboratory Report ANL-4303 (1949) (unpublished); R. K. Swank and J. S. Moenich, Rev. Sci. Instr. (to be published)], and was essentially similar to published versions (see reference 13) of NaI(Tl) gamma-ray spectrometers. We wish to thank Mr. Swank for the preparation of the NaI(Tl) crystal and for the design and construction of the amplifier and pulse-height analyzer circuits.

[13] S. A. E. Johannson, Nature **165**, 396 (1950); R. W. Pringle, Nature **166**, 11 (1950); Bell, Cassidy, and Kelley, Phys. Rev. **82**, 103 (1951); R. Hofstadter and J. McIntyre, Phys. Rev. **78**, 617 (1950); **80**, 631 (1950); Nucleonics **7**, 32 (September, 1950).

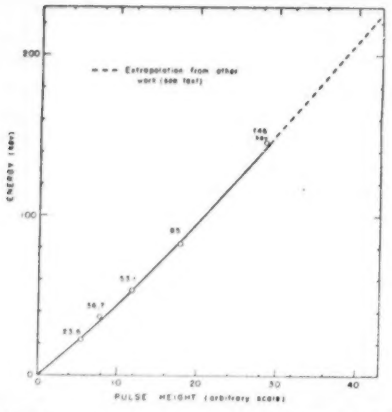

FIG. 6. Pulse amplitude *vs* energy for gammas on NaI(Tl) scintillation spectrometer.

material having the largest slope in the energy region of interest, and hence whose K-edge lies considerably below this region. Of the absorbers available, it was calculated that silver would give the best discrimination between an 85-kev gamma-ray and one with an energy somewhat above 100 kev, although a copper absorber would not be much worse. Using some estimates as to energies and relative intensities derived from the absorption measurements, it was calculated that a 1.7-g/cm^2 absorber would give the best discrimination. The pulse analysis is shown in Fig. 5f. It was evident that the 85-kev gamma-ray had not been discriminated against sufficiently, and a heavier (2.6-g/cm^2) silver absorber was used (Fig. 5g). Although the resolution was improved in this measurement, still greater discrimination would have been possible with a thicker absorber; unfortunately, the sample intensity was too low to allow still further attenuation.

Both curves clearly show the presence of two gamma-rays at about 100 kev and 165 kev, with some indication of at least one lower-intensity peak above 200 kev. The detailed analysis of the two curves is discussed below.

In order to examine the region covering the low energy wing of the 85-kev peak, preferential absorption was again used. This involved absorption by an element whose K-edge lay below 85 kev, since the smallest half-thickness (or greatest absorption) occurs just above the K-edge. The shape of the curve in Fig. 5c indicates the possible presence of the 59- and 63-kev gamma-rays indicated in the β-spectrometer curves; thus the best discrimination would not occur with the elements whose K-edge lies just below 85 kev [mercury, $K=83.2$ kev and gold, $K=80.9$ kev[10]] since the half-thickness decreases very rapidly below the K-edge. Of the easily available elements, tantalum was chosen as the best material, and Fig. 5d shows a curve taken with a 1.3-g/cm^2 tantalum absorber.[14] Very good discrimination was achieved, with a 61-kev gamma-ray dominant and only a small tail resulting from the 85-kev (and higher) gammas. The resolution was too poor to separate 59- and 63-kev gamma-rays, if both were present.

A lead absorber (K-edge$=88.2$ kev) did not attenuate the 85-kev gamma-ray very much, but did attenuate the gamma-rays above and below it in energy, so that Fig. 5e shows a practically "clean" peak at 85 kev.

Standardization of pulse height in terms of energy was achieved by the use[15] of Ce^{141} and Tm^{170} as standards (Figs. 5a and 5b).

The energy of the Ce^{141} gamma-ray is 146 kev,[16] while that of Tm^{170} is 85 kev.[17] In addition to the gamma-rays, the K x-rays of the daughter elements, praseodymium (Ce^{141} decay) and ytterbium (Tm^{170} decay) were observed, since both gamma-rays are partially converted. Since the scintillation spectrometer does not resolve the K_α and K_β lines, averaged[18,19] values for the effective K x-ray energies were taken, 36.7 kev for Pr and 53.1 kev for Yb.

For softer quantum radiation, the stopping power of NaI is so great that the absorption occurs close to the surface of the crystal; some of the iodine K x-rays following the photoelectric process escape backwards through the crystal surface, resulting in the formation of the "escape peak."[20] This peak occurs at an energy corresponding to the difference between the quantum radiation energy and that of the iodine K x-rays (suitably averaged). The effect is small at higher energies—only 6 percent at 85 kev,[21] so that the only escape peak observable was that due to the Yb K x-rays, at 23.6 kev. The escape peak (55.8 kev) from the Tm^{170} 85-kev gamma-ray occurred at the high energy side of the Yb K x-ray peak and hence was unobservable. The two gamma-ray lines, the two K x-rays and the escape peak were used to construct a pulse-height-energy calibration curve (Fig. 6).

Examination of the high energy tail of the UY curves (Figs. 5f and 5g) showed some high energy components beyond the highest point (146 kev) on the calibration curve; their energies were evaluated using other calibration curves measured in this laboratory,[22] normalized to our curve. The calibration curve in Fig. 6 shows a distinct curvature indicating higher efficiency at lower photon energies. This characteristic has been observed

[14] Ta, K edge$=67.5$ kev.

[15] We wish to thank Donald Englekemeir and Theodore Novey for providing us with samples of these activities.

[16] H. B. Keller and J. M. Cork, Phys. Rev. **84**, 1079 (1951); M. Freedman and D. Engelkemeir, Phys. Rev. **79**, 897 (1950).

[17] J. S. Fraser, Phys. Rev. **76**, 1540 (1949); D. Saxon and J. Richards, Phys. Rev. **76**, 186 (1949); H. Agnew, Phys. Rev. **77**, 655 (1950); R. Caldwell, Phys. Rev. **78**, 407 (1950).

[18] The energies (see reference 19) of the most prominent K x-rays of Pr are: $K\alpha_2=35.6$ kev; $K\alpha_1=36.1$ kev; $K\beta_1=40.8$ kev, while the relative intensities are approximately (see reference 19) 3:6:2, respectively. Constructing Gaussian curves with suitable half-widths, and adding them, an approximate Gaussian results with its peak at 36.7 kev.

[19] A. H. Compton and S. K. Allison, reference 10, pp. 640–1, 785.

[20] West, Meyerhof, and Hofstadter, Phys. Rev. **81**, 141 (1951).

[21] F. K. McGowan, Phys. Rev. **85**, 151 (1952).

[22] D. W. Engelkemeir (private communication).

by others,[22,23] but does not seem to be characteristic of NaI(Tl), since other laboratories[24] have found NaI(Tl) spectrometers to be linear to quite low energies. The reasons for the different results are not clear.

Due to the limited resolving power of scintillation spectrometers in this low energy region, the overlapping peaks were most conveniently resolved by constructing individual components with "ideal" shapes. An examination of the Ce^{141} curve (Fig. 5b) showed the 146-kev gamma-ray and Pr K x-ray peaks to be almost pure Gaussian curves, with half-widths proportional to (pulse-height)$^{\frac{1}{2}}$. The 85-kev UY peak examined through a lead absorber (Fig. 5e) was similarly found to be reasonably "clean" Gaussian curve, with the expected half-width. The more complex curves were analyzed by constructing individual Gaussian curves of assumed energies and intensities and suitable half-widths.

While most of the UY gamma-rays reported here were observed as separate peaks, some of the ones listed in Table III were presumed to be present only as a result of analysis of the complex curves. Thus, there is little doubt concerning the existence of gamma-rays at 22, "61," 85, and 167 kev and with somewhat less certainty, at 107 kev; some of these lines may, of course, be composites. As mentioned below, there may also be unresolved K x-rays at about 93 kev. Using these energies and "ideal" curves with appropriate half-widths, it was not found possible to account for the shape of the experimental curves without assuming that another gamma-ray was present at 122 kev. Of course, the energy and intensity assumed for this component were quite arbitrary; the energy was chosen to fit the proposed decay scheme (Fig. 7). This component would then match a K-conversion line observed in the magnetic spectrometer at 9 kev. The tail at the high energy side of the 167-kev peak (Fig. 5f and 5g) was too wide to be accounted for by only one peak of Gaussian shape, and hence the assumption that both 210- and 230-kev gamma-rays were present. Here too, the choice of energies and intensities was somewhat arbitrary.

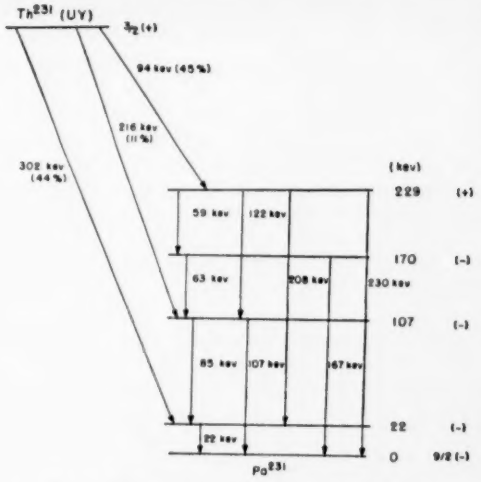

FIG. 7. Suggested decay scheme for Th^{231} (UY).

TABLE III. Experimental data on relative gamma-ray intensities.

Absorber	Gamma-ray energy	Absorption correction factor	Relative intensity
Al	22	1.46	1.7
0.2 g/cm²	85	1.00	1.00
Ta	59	137.	
1.29 g/cm²	63 } Av = 61*	65.4	0.40
Pb			
0.56 g/cm²	85	3.0	0.70
Ag	85	81.	0.78
1.70 g/cm²	107	10.	0.06
	122	4.9	0.021
	167	2.2	0.016
	210	1.6	0.003
	230	1.5	0.001
Ag	85	850.	1.15
2.60 g/cm²	107	34.	0.075
	122	11.5	0.022
	167	3.3	0.019
	210	2.0	0.003
	230	1.9	0.001

* Assumed to have a 63/59 intensity ratio of 2.

Although previous work[3] had indicated the presence of L x-rays, these were not resolved in the present measurements, and presumably appeared only as a widening of the 22-kev peak. Analysis of the peak shows that it must be, in the main, a gamma-ray of 22 kev (the energy uncertainty predominantly positive due to possible peak shift by L x-rays). The intensity of the gamma-ray itself is less than that indicated in Table IV; however, it seems unlikely that the L x-rays contribute more than about 30 percent.

The very high efficiency of the NaI(Tl) crystal for gamma-rays of low energy made possible semiquantitative estimates of relative intensities. Up to 200 kev, over 80 percent of the photons entering the crystal should have interacted with it. Up to 100 kev most of the interaction is photoelectric absorption and, were it not for the escape peak, the main peak intensity would fairly well measure relative intensity in the source. Even above 100 kev, the observed peak represents more than the photoelectric absorption, due to reabsorption of Compton-scattered photons in the crystal.[25] For example, Fig. 5b shows that at 146 kev, most of the gamma-ray pulses lie in the peak. At lower energies

[22] R. W. Pringle and S. Standil, Phys. Rev. **80**, 762 (1950).
[24] V. O. Eriksen and G. Jenssen, Phys. Rev. **85**, 150 (1952); West, Meyerhof, and Hofstadter, Phys. Rev. **81**, 141 (1951); Jentschke, Eby, Taylor, Remley, and Kruger, Phys. Rev. **83**, 170 (1951); **84**, 1034 (1951) (for electrons).
[25] J. A. McIntyre and R. Hofstadter, Phys. Rev. **78**, 617 (1950); R. Hofstadter and J. A. McIntyre, Phys. Rev. **80**, 631 (1950).

TABLE IV. Averaged values for relative gamma-ray intensities.

Gamma-ray energy	Relative intensity
22 (+ L x-rays)	1.7
61 {59 63	0.40*
85	1.00
105	0.06_5
122	0.02
167	0.018
210	0.003
230	0.001

* May be too high.

the escaping I K x-ray reduces the efficiency but even at 60 kev the effect is no larger than 10 percent.[26]

The relative intensities of the gamma-rays were calculated by multiplying the peak heights by (pulse height)$^{\frac{1}{2}}$,[27] and by the appropriate absorption correction factor.[10,28] The accuracy of the latter correction factor was poor for some of the gamma-rays, due to the large attenuations used, with attendant accentuation of the errors in values of the absorption coefficients. In Tables III and IV are listed the observed relative intensities, after correction. Escape peak corrections or corrections for crystal stopping power were not made; the resulting errors were probably less than 20 percent. In most cases, the absorption correction was probably the most serious source of error. The abundance of the 61-kev component is quite uncertain. The absorption correction (Ta curve) is quite large, and its average magnitude depends upon the intensity division between the 59 and 63 kev components. The ratio (59:63 intensity) was assumed to be 1:2, in order to equalize the transition intensities (conversion electrons+gamma-rays). An examination of Fig. 5c, taken with no added absorber, would indicate the 61:85 ratio to be of the order of 1:10 rather than the 0.4 of Table III. This evidence, however is not reliable, since a relatively small shift in the construction of the 85-kev peak would increase the intensity available to the 61 kev component.

In addition to absorption correction errors, as mentioned above, the construction of the 122-, 230-, and 210-kev peaks involved some arbitrariness in choice of intensity. The uncertainty in the intensity of the 22-kev peak was increased by the presence of unresolved L x-rays. The intensity discrepancy (0.70:1.00) in the 85-kev lines observed with and without Pb absorber (Table III) may indicate the presence of an unresolved component between 85 and 107 kev, since the Pb absorber would attenuate such a component (K-edge = 88 kev). K x-rays (93 kev) are known to be present to a small extent due to conversion of the 167- and 208-kev transitions and to a possibly larger extent due to 122-kev conversion [Table II, $K(5)$].

[26] F. K. McGowan (private communication).
[27] For a Gaussian curve, area $\propto$ peak height $\times$ half-width.
[28] M. T. Jones, Phys. Rev. **50**, 110 (1936).

DISCUSSION

It did not appear possible to construct a decay scheme for UY consistent with all the experimental facts. The scheme we present (Fig. 7) is in the main a consequence of the observed energy balances between the major and most convincingly assigned gamma-rays, the 59, 63, and 85 kev, and the beta-energy differences. To these are added the well established (Fig. 5g) though less accurately measured 167-kev gamma and the 22-kev gamma (Fig. 5c and Table II).

As was discussed in the gamma-ray experimental section, the precise allocation of energies and relative intensities of the remaining gammas, 107, 122, 208, and 230 kev, was guided by the level structure of this decay scheme, though in each case the gamma-ray spectrometer results seemed to require the presence of more than one gamma in the energy range 90–130 and similarly for the range 200–240 kev. Supporting evidence for the existence of the 122-kev gamma is derived from the most prominent low energy conversion line $K(5)$; and no assignment for line $K(6)$ other than as the K line of a 208-kev gamma seems reasonable.

The absence of an L conversion line for the 122-kev gamma at *ca* 102 kev (present to <0.02 percent of total beta) implies an unacceptably large K/L conversion ratio; this must be regarded as one of the inconsistencies in the picture.

No concern need be given to the absence of an L conversion line for the 208-kev gamma as it is expected to be of lower intensity than the K line which is barely observable. As for the L line of the 167-kev gamma, it too may be expected to be weaker than the K line which constitutes only a fraction of the line $M_{II}(2)$, $K(7)$. These considerations are strengthened by reference to the low intensities of the unconverted gammas (Table IV).

The intensity of the gammas was related to the intensity of the betas and conversion electrons by normalizing the 85-kev gamma to match the sum of the intensities of the two weaker betas, correcting for the small branching by way of the 107-kev gamma. The one glaring inconsistency in the proposed scheme is associated with intensity considerations of the weak (94-kev) beta and the 59-kev—63-kev gamma-sequence. Referring to Fig. 7 and Tables I, II, and IV, it will be seen that, since the intensities of the 122-, 208-, and 230-kev transitions are low, the 59-kev gamma plus conversion electron intensities should be nearly equal to the intensity of the weak beta; and since the 167-kev transition is weak compared to the 63-kev transition, the latter should be comparable to the 59-kev total intensity. Therefore, it is reasonable to divide the observed gamma-intensity of the "61-kev" line between the 59- and 63-kev gammas so as to equate their total (gamma plus conversion electron) intensities. Using the most favorable (largest) value for the total intensity of the 61-kev gamma (40 percent of that of the 85-kev

gamma) and accounting for the conversion of the 85-kev transition, for the small branches by way of the 107-, 122-, and 167-kev gammas, and for the contribution of the 216-kev beta, one obtains the intensity figures summarized in Table II.

The necessary subdivision of the "61-kev" gamma into 59-kev and 63-kev components (1:2) is not in conflict with the fact that the gamma-peak was found at 61 kev, instead of *ca* 62 kev, in consideration of the accuracy of the gamma-measurements. The burden of the discrepancy is, in these calculations, placed entirely on the 59-kev and 63-kev transitions, which are seen to be too low by about a factor of 2, comparing the 50 percent intensity of the latter with the 80 percent figure for the sum of the 85-kev plus 167-kev transitions fed by the softest beta [11/(45+11)=20 percent contribution of the 216-kev beta subtracted off]. A reduction of the relative intensity of the 94-kev beta by a factor of *ca* 3 is, however, required if the intensities of the two low energy betas and the gammas of 59, 63, and 85 kev are to be brought into agreement. So great a reduction appears irreconcilable with the Kurie analysis (see discussion in experimental section). That the low energy beta is present in substantial abundance is also consistent with the experimental results of Stoker *et al.*[5] who found, with sources probably thicker than were used in the work reported here, betas of energy 390, 190, and 100 kev in relative intensities 1:2:2.

Based on the experimental beta branching ratios, the logft values for the beta-transitions are 6.2 (302 kev), 6.0 (216 kev), and 4.3 (94 kev). The low value for logft for the 94-kev beta is exceptional for such high Z; the only other value below 5.0 for $Z \geq 74$ is that for Pb^{214} (4.70). This may be taken as further evidence that the experimental value for the intensity of the 94-kev beta may be too high; a threefold reduction in the intensity would result in a logft=4.9.

It is also possible that the low intensity of the 59 kev–63 kev sequence is due to a higher intensity of the 122-kev cross-over transition than observed. Analysis of the 85-kev gamma-ray line (Figs. 5c, e, and Table III) indicates a maximum possible (though unlikely) intensity of K x-ray (*ca* 93 kev) of about 30 percent of that of the "85-kev peak." This figure would be sufficient to account for most of the intensity misfit. However, so large a K conversion coefficient would aggravate the already too high K/L conversion ratio limit discussed above. Also the intensity of K electrons would then exceed the *ca* 13 percent figure set as a rough upper limit (Table II) for $K(5)$.

There is only a slight broadening of the 22-kev gamma-peak, (Fig. 5c), insufficient to resolve any L x-rays. If an average value for the fluorescent yield of all L vacancies of 40 percent is assumed[29] a conversion coefficient of unity for the 22-kev transition is required to match the observed intensity of the 22-kev gamma (plus its conversion electrons, of which only the relatively weak L_{III} and higher energy lines were observed) to the sum of the beta-intensities.

Sufficient evidence is available to allow plausible guesses as to spin and parity assignments of the levels of the Th^{231} and Pa^{231} nuclei. However, such arguments depend intimately on the validity of the decay scheme assumed, and this is considered to be too uncertainly established to warrant extensive discussion. In Fig. 7 we indicate spins and parities for the levels consistent with the ft values and transition probabilities observed, and with the predictions of the strong spin-orbit coupling nuclear shell model.[30]

We wish to acknowledge the aid of Paul Fields, Gray Pyle, and Ruth Sjoblom for carrying out the chemical separations, and of Drs. Theodore Novey, Donald W. Engelkemeir, and Mr. Jerome Lerner for helpful discussions of the scintillation spectrometer measurements.

[29] B. B. Kinsey, Can. J. Research **26A**, 404 (1948).
[30] M. G. Mayer, Phys. Rev. **78**, 16 (1950).

Luminescence and Thermionic Emission of Barium Oxide*

VIRGIL L. STOUT†
Department of Physics, University of Missouri, Columbia, Missouri
(Received June 13, 1952)

The cathodoluminescent spectrum of BaO samples has been studied as a function of the state of thermionic activity and the temperature of the samples.

In order to conduct these measurements a vacuum tube was designed which allowed a sealed-off oxide sample to be studied at temperatures both above and below room temperature.

Two of the six luminescent bands identified were found to vary in intensity as the thermionic emission of the sample changed. A luminescent band at 345 mμ increased in intensity with increasing thermionic activity; a luminescent band at 465 mμ decreased with increasing thermionic activity. The peak intensity of both bands was found to vary inversely with temperature. Speculations concerning possible luminescence mechanisms are presented.

INTRODUCTION

BARIUM oxide is of commercial importance as it is capable of copious electron emission when heated to elevated temperatures. Because of this, many experimental investigations have been carried out in an attempt to explain its electrical properties.[1] Most of these investigations were conducted by studying only processes involving thermal excitation thus leaving the electronic energy level structure of crystalline BaO in doubt.

Recently, extensive studies have been made on BaO using other methods of investigation. Optical absorption, photoelectric emission, photoconductivity, and dielectric-constant measurements have been reported within the last few years. Tyler and Sproull[2] determined the short wavelength absorption edge to be at 3.8–4.0 ev and found radiation of this energy to produce photoconductivity. Apker, Taft, and Dickey[3] made photoelectric emission studies that indicated the top of the valence band to be 5.0–5.2 ev below the vacuum potential. Bever and Sproull[4] have measured the low frequency dielectric constant as being about 34 over a wide frequency range. Combined reflectivity, photoconductivity, photoelectric emission, and thermionic emission measurements were made by DeVore and Dewdney[5] that corroborate the previously mentioned energy of the absorption edge and indicate a temperature dependence of the forbidden gap to be 7×10^{-4} ev/deg.

Luminescence measurements have been made upon BaO by various investigators. Ewles[6] reported peaks of cathodoluminescent bands at 465, 572, and 597 mμ.

This study was undertaken in an effort to correlate luminescent and thermionic emission measurements, and to study the luminescent properties of barium oxide in hopes of learning more about its energy-level scheme.

EXPERIMENTAL

Barium oxide samples were prepared by decomposing $BaCO_3$ that was obtained from two sources. A high purity $BaCO_3$ was prepared by a process involving the triple recrystallization of barium nitrate.[7] The other carbonate source was Mallinckrodt's ultra pure $BaCO_3$.[8] These carbonates in a nitrocellulose binder were sprayed upon previously vacuum fired base metal cathode structures of 1001 Ni[9] or a W-Ni[9] to form a sample cathode. These cathodes were mounted in vacuum tubes described below.

Two types of vacuum tubes were used in the course of this investigation. Tube Type I used a target cathode that was cylindrical in form, and its temperature was measured using a Mo-Ni thermocouple. For thermionic emission measurements, a cylindrical sliding anode could be placed over the sample cathode; for luminescent measurements the anode was slid down over the cathode-to-press leads. Luminescence was induced by bombarding the sample with 1500 volt electrons at a beam current of up to 50 μa. This electron bombardment of the target raised its temperature by about 50°C above room temperature. The insulating particles of BaO were probably raised to an even higher temperature. With this tube, studies could be made of the effect of activation and the effect of variation of temperature, above room temperature, upon the luminescence of barium oxide. It was soon found that the temperature range above room temperature is not of particular interest due to the poor resolution of the multiple band spectrum of the oxide.

To permit studies of a sample at reduced temperatures, a second vacuum tube, Type II, was designed. Figure 1 shows a drawing of this tube. In this tube the BaO sample was located on a nickel cathode button that was attached to a hollow Kovar rod ¼ inch in diameter and 2½ inches long. The flat tantalum anode was positioned for thermionic emission measurements,

* Supported in part by the ONR.
† Now at the Stanford Research Institute, Stanford, California.
[1] A. S. Eisenstein, *Advances in Electronics* (Academic Press, Inc., New York, 1948), Vol. 1, pp. 1–64.
[2] W. W. Tyler and R. L. Sproull, Phys. Rev. **83**, 548 (1951).
[3] Apker, Taft, and Dickey, Phys. Rev. **76**, 453 (1949).
[4] R. S. Bever and R. L. Sproull, Phys. Rev. **83**, 801 (1951).
[5] H. B. DeVore and J. W. Dewdney, Phys. Rev. **83**, 801 (1951).
[6] J. Ewles, Proc. Roy. Soc. (London) **A167**, 34 (1938).
[7] C. D. Prather, N.D.R.C., Report 518 Div. 14 (1945).
[8] Mallinckrodt Chemical Works, St. Louis, Missouri.
[9] 1001 Ni—Pure electrolytic nickel. W-Ni—4.66 percent tungsten-nickel alloy. Both base metals obtained from E. M. Wise, International Nickel Company.

as shown in the drawing. For luminescent studies, the anode was swung back toward the wall of the tube. Electrons from the Raytheon 2K33 electron gun were focused by a magnetic lens and deflected to the sample with a permanent magnet. The geometrical arrangement of the electron gun and the target prevented material evaporated from and light emitted by the electron-gun cathode from reaching the sample. Thermionic emission measurements were made with a tungsten coil heater inserted into the Kovar rod and with a vacuum of about 10^{-6} mm of Hg in the ground-glass joint-enclosed chamber. Reduced temperatures were obtained by placing liquid air in the rod or by blowing refrigerated nitrogen gas into the cathode.

The processing of both tubes of Type I and Type II was normal, except that with tubes of Type II certain extra steps were taken. During bakeout, the ground-glass joint was disassembled and a tube conducting dry nitrogen gas into the Kovar cup was inserted in its place. This gas prevented excessive oxidation of the Kovar. Also, after Type II tubes were processed and activated, thermionic emission measurements were made before the tube was sealed off of the exhaust system. This eliminated the necessity of further heating of the Kovar cup.

The state of thermionic activation was measured by making retarding potential plots of the thermionic emission current at five temperatures in the temperature range of about 650 to 1000°K. From each retarding potential plot the zero-field emission current was obtained. A Richardson plot was constructed from the five values of the zero field emission currents and their corresponding temperatures. The state of activation is designated here by stating the work function and zero-field current density at 1000°K as obtained from the Richardson plot. Different states of activation were obtained by (1) using cathodes of inherently different activity, (2) drawing emission current from a cathode in a low state of activation to increase the activity, and (3) by exposing an activated cathode to carbon dioxide gas at about 900°K to reduce the state of activation. This gas was admitted through glass break-off tips after the tube was resealed to the exhaust manifold. At no time was the sample exposed to a pressure in excess of 10^{-7} mm of other than the gas to be admitted.

Most of the luminescent spectra intensities were measured with a recording spectrophotometer. Light emitted at the luminescent surface was focused by a fused quartz lens onto the entrance slit of a Perkin-Elmer model 83 monochromator which used crystalline quartz optics. Directly in front of the entrance slit was located a rotating disk which served to interrupt the light beam entering the monochromator 23.3 times per second. Light from the exit window of the monochromator was focused by a front surface aluminum mirror system upon the cathode of a 1P28 photomultiplier. The signal output from the 1P28 was fed into a two-stage 23.3-cycle parallel "*T*" network

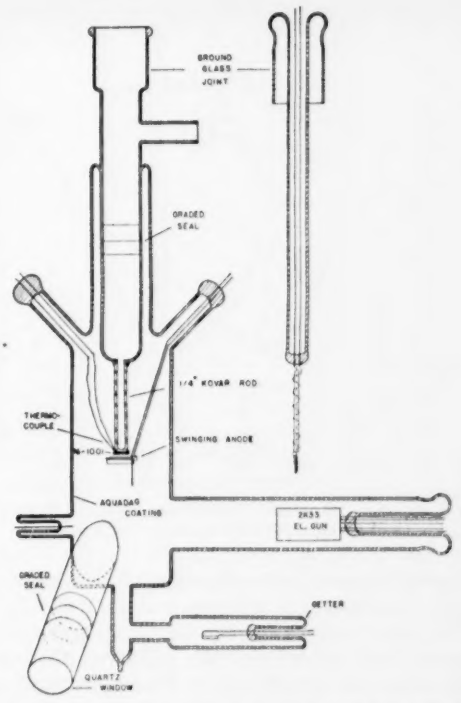

FIG. 1. Experimental vacuum tube Type II, designed so that thermionic emission and luminescence could be studied on the same BaO sample.

amplifier.[10] From the amplifier the signal was fed into a phase sensitive rectifier and then to a Speedomax recorder. A 1000 volt battery supply was used for the 1P28. The maximum band pass of the instrument used was 3 mμ at 300 mμ and 24 mμ at 560 mμ. In all cases light intensities were extremely low.

The spectral response of the detector was determined by measuring the emission spectrum of a stable light source, first with a thermistor bolometer and then with the 1P28. The Servotherm thermistor bolometer type BG-1 was assumed to be a blackbody receiver. From a plot of wavelength *versus* wavelength drum setting, a dispersion curve was obtained for the monochromator. All recorder readings were corrected to relative intensity values using the spectral response and dispersion information. The absorption coefficient of quartz and the reflectivity of aluminum were taken to be constant in the wavelength range investigated, 300 to 600 mμ.

A few relative intensity measurements were made by the photographic technique using Eastman 103F and I-N plates in an Adam Hilger spectrograph. The photographic method had the advantage of permitting measurements of very weak luminescent intensities, and the wavelength range available for investigation was 300 to 850 mμ. This method of recording data was

[10] J. M. Sturdevant, Rev. Sci. Instr. **18**, 124 (1947).

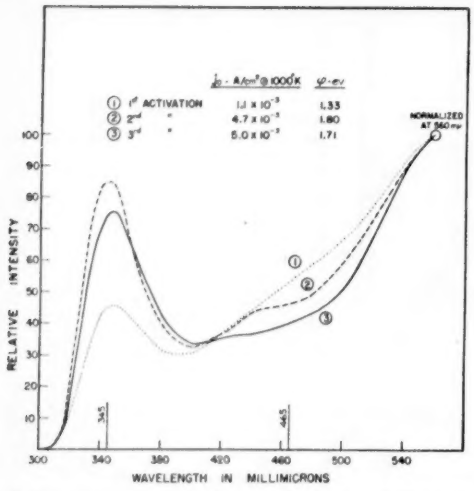
j_0 - A/cm² @ 1000°K
φ - ev
① 1st ACTIVATION 1.1 x 10⁻³ 1.33
② 2nd " 4.7 x 10⁻³ 1.80
③ 3rd " 5.0 x 10⁻² 1.71
NORMALIZED AT 560 mμ
RELATIVE INTENSITY
WAVELENGTH IN MILLIMICRONS

FIG. 2. Luminescent spectra observed from Tube 3, Type II for three different states of thermionic activation.

discarded because plate calibration for wavelength and density was extremely laborious.

The luminescent afterglow was examined using an electron pulse technique. The resulting luminescent light pulse was detected by a 931A photomultiplier, amplified with a video amplifier, and observed on a Sylvania type P4 synchroscope.

RESULTS

From the photographic and spectrophotometric studies, six bands were identified as belonging to the luminescent spectrum of BaO. These are listed according to wavelength in millimicrons and energy in electron volts in Table I.

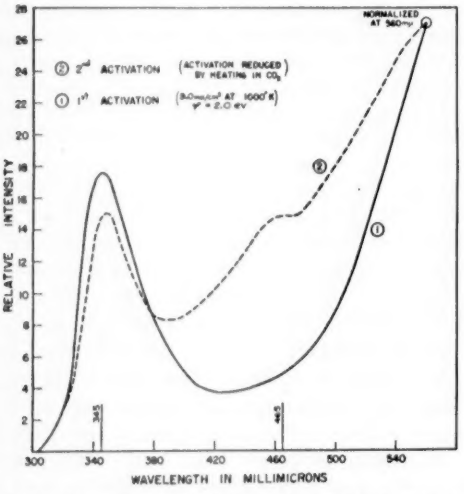
NORMALIZED AT 560 mμ
② 2nd ACTIVATION (ACTIVATION REDUCED BY HEATING IN CO_2)
① 1st ACTIVATION
RELATIVE INTENSITY
WAVELENGTH IN MILLIMICRONS

FIG. 3. Luminescent spectra observed from Tube 3, Type I for two different states of thermionic activation.

Spectrophotometric studies show that the luminescent spectrum depends upon the state of thermionic activation; Figs. 2, 3, and 4 demonstrate this to be the case. Figure 2 shows various luminescent spectra emitted by Tube 3, Type I for which the state of thermionic activation was varied by drawing emission current. The original state of activation was achieved by heating only. Since it was necessary that the tube be moved between spectrophotometric measurements, the different curves were normalized at 560 mμ. Figure 3 shows the luminescence in two states of activation for Tube 3, Type II. The first state of activation was produced by the activation procedure conducted while the tube was on the exhaust manifold; and, the second state of activation resulted when the tube was deactivated slightly by heating the active BaO cathode at 900°K for a short time in CO_2 at a pressure of a few mm of Hg. Figure 4 shows the luminescence of a very inactive cathode produced accidentally by heating a BaO cathode in a poor vacuum.

These plots show that the general changes in the luminescent spectrum with increasing activation are (1) an increase in the intensity emitted in the 345 mμ band, and (2) a decrease in intensity emitted in the 465 mμ band.

TABLE I. Peaks in the luminescent spectrum of BaO.[a]

Wavelength in mμ	Energy in ev
345	3.6
465[b]	2.7
550[b]	2.3
595[b]	2.1
650	1.9
700	1.8

[a] Temperature about 350°K.
[b] These bands were previously identified by Ewles (reference 6).

The temperature dependence of luminescence was investigated in the temperature range of 90 to 475°K. The results of these measurements are exemplified quite well by Figs. 4, 5, and 6 which show the cathodoluminescent spectra emitted by BaO in the temperature range 90 to 390°K. At higher temperatures further flattening of the spectrum is observed. The predominant effect of reducing the temperature is (1) a moderate increase of 345 and 550 mμ peak intensities, and (2) marked increase of the 465 mμ peak intensity.

When the 1500-volt electron beam was modulated at 60 pps with a square one-microsecond pulse in a tube of Type I, the luminescent light pulse was found to decay in the order of or less than one microsecond. These measurements were made at about 350°K.

INTERPRETATION OF RESULTS

In order to interpret the results of these experiments, certain fundamental assumptions are necessary. Since two types of base metals and barium oxide samples of

different origins produce similar results, it is assumed that the luminescence and thermionic emission are characteristic of pure BaO with a stoichiometric excess of Ba. This is an assumption frequently made in discussing thermionic activation alone. The excess of Ba may be thought of in terms of interstitial Ba or may be associated with oxygen ion voids in the BaO crystalline matrix. It is possible for voids of both oxygen and barium to exist in the matrix, thus providing both donor and acceptor levels. Ion voids associated with lattice defects at crystal surfaces may also be present.

It is further assumed that the largest part of the energy absorbed from electron bombardment produces free electrons in the conduction band and leaves holes in the filled band, which come into thermal equilibrium with the lattice in a very short time.

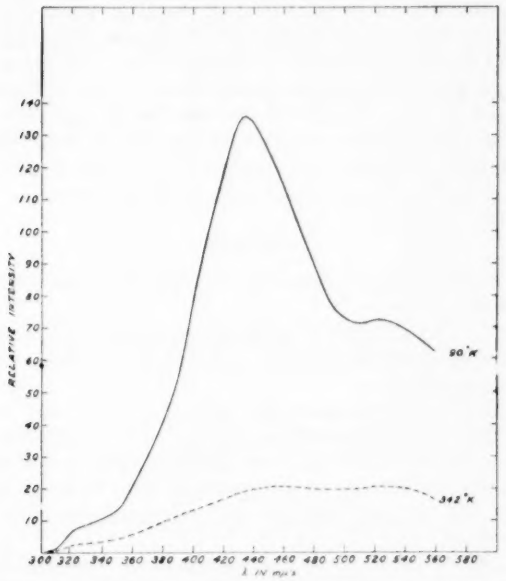

FIG. 4. Luminescent spectra from a very inactive cathode of Tube 2, Type II at two different temperatures.

Since the luminescence of the 345 mμ band in all cases increases in intensity with increasing thermionic activity, one is lead to the hypothesis that the 345 mμ band results from the presence of donor-type sites. These sites (e.g., O-ion voids) must contribute levels close to the bottom of the conduction band since the observed luminescence maximum at 3.6 ev is nearly the observed band-to-band energy gap of 3.8–4.0 ev.

If the 345 mμ band results from donor levels, a possible mechanism for the luminescent act is radiative capture of a donor-level electron by a hold in the valence band.

The luminescent intensity expected if such a mechanism occurs can be expressed in equation form as:

$$I \propto N_p N_d \sigma n l,$$

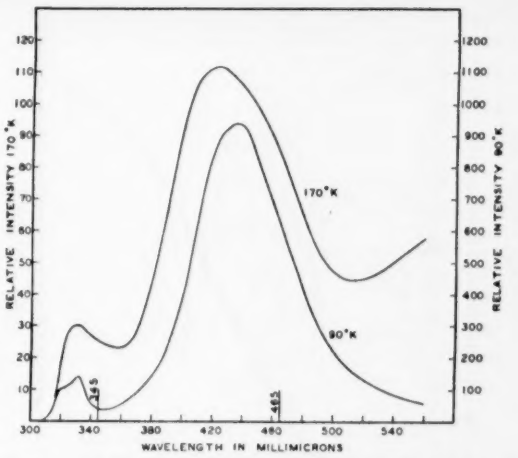

FIG. 5. Luminescent spectra from Tube 3, Type II (Activation No. 1) for temperatures 90 and 170°K.

where N_p is the number of holes produced per unit volume per unit time, N_d is the number of donor centers per unit volume, σ is the capture cross section of a hole by a donor-level electron, n is the mean number of lattice collisions during the life of a hole, and l is the mean free path of a hole. From the equation it appears that the temperature dependence of luminescence will be supplied by the mean free path and to some extent by the collision cross section. Although the mean free path for holes in ionic crystals is approximately exponentially related to the reciprocal temperature[11] it does not seem wise to pursue the temperature dependence more precisely at the present time. However, it is interesting to note that the peak intensity of the 345 mμ band does show an exponential relation to reciprocal temperature over a considerable temperature range as seen in Fig. 7.

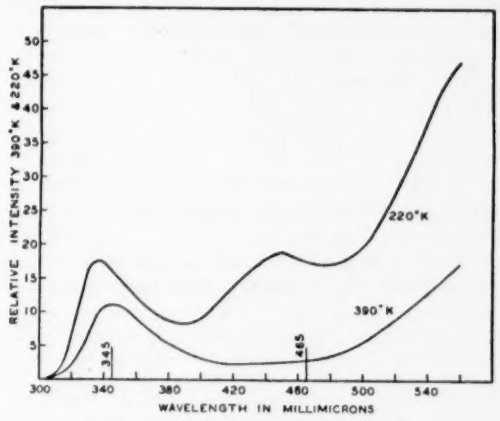

FIG. 6. Luminescent spectra from Tube 3, Type II (Activation No. 1) for temperatures 220 and 390°K.

[11] N. F. Mott and R. W. Gurney, *Electronic Processes in Ionic Crystals* (Oxford University Press, London, 1948), p. 104.

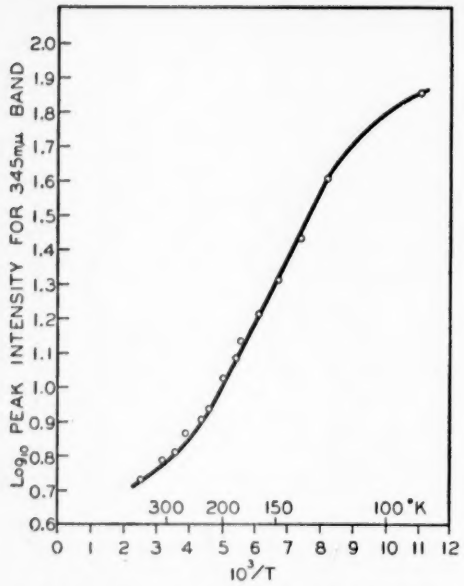

FIG. 7. Peak luminescent intensity of the 345 mμ luminescent band as a function of reciprocal temperature.

An alternate explanation of the 345 mμ band is that it arises from edge emission. The mechanism of edge emission has been ascribed to a radiative transition made by a conduction band electron falling into a hole in the valence band. This act presumably must occur as a three-body collision where the three bodies are (1) a conduction band electron, (2) a hole in the valence band, and (3) the crystalline lattice. If it is assumed that the luminescence occurs within a layer not more than 10^{-5} cm thick, absorption within the crystal has a negligible effect on the short wavelength cut off of the luminescence spectra. The observed luminescence maximum at 3.6 ev differs sufficiently from the band to band gap of 3.8–4.0 ev to make this mechanism questionable.

Although the 465 mμ band decreases in intensity with increasing thermionic activity, it may be due to either donor or acceptor sites. When acceptor sites (e.g., Ba voids) are present they will probably introduce acceptor levels just above the valence band. Luminescence at 2.67 ev might easily result from downward transitions from an excited level to the ground state of this center. If this process does take place, the acceptor levels must then lie at least 2.67 ev below the bottom of the conduction band. The increasing luminescence intensity with decreasing temperature can also be explained qualitatively with this model.

Since O is divalent one might suppose that donor sites may accept one or two electrons corresponding to the F and F′ centers of the alkali halides. The first electron will be closely bound and occupies an energy level well below the conduction band, whereas, the second electron will be released with relative ease and contribute a level just below the conduction band. Samples of BaO which are thermionically inactive will contain relatively few donor sites, most of which will contain only one electron because of the presence of lower lying acceptor states. Luminescence at 2.67 ev might result from hole capture of single electrons bound at these donor centers. With increasing thermionic activity the density of donor sites as compared with acceptor sites will increase and thus nearly all donor centers will be occupied by two electrons. When this occurs, luminescence at 2.67 ev will decrease, while that at 3.6 ev will increase, as is observed. If this mechanism is present, the temperature dependence of the 465 mμ band should be similar to that for the 345 mμ band. The much greater temperature dependence observed for the 465 mμ band seems to indicate that hole capture is probably not responsible for both of these bands.

SUMMARY

(1) Six cathodoluminescent bands were observed for BaO.

(2) The afterglow of luminescence at room temperature was found to be of the order of, or less than, one microsecond.

(3) The luminescent spectrum was found to vary as a function of thermionic activation. The luminescent intensity of the 345 mμ band increased with increasing thermionic activity, while the luminescent intensity of the 465 mμ band decreased with increasing thermionic activity.

(4) By reducing the temperature of the luminescent sample, the radiation in the 345 mμ and 465 mμ bands was greatly enhanced.

(5) If the mechanism of luminescent emission in the 345 mμ band is correctly described as being the result of electron capture from a donor level by a hole in the valence band, the donor level must lie at least 3.6 ev above the upper edge of the valence band.

The author wishes to express his indebtedness to Professor A. S. Eisenstein who suggested and supervised this problem.

Letters to the Editor

PUBLICATION of brief reports of important discoveries in physics may be secured by addressing them to this department. The closing date for this department is five weeks prior to the date of issue. No proof will be sent to the authors. The Board of Editors does not hold itself responsible for the opinions expressed by the correspondents. Communications should not exceed 600 words in length and should be submitted in duplicate.

F-Center Wave Functions and Electronic *g*-Values in KCl Crystals*

ARNOLD H. KAHN† AND C. KITTEL
Department of Physics, University of California, Berkeley, California
(Received November 14, 1952)

RECENTLY Hutchison and Noble[1] have observed electronic spin resonance in a KCl crystal colored with excess K. The resonance is believed to be associated with *F*-centers, but one cannot without confirmatory experiments exclude the possibility of contributions from other types of centers.[2] They observed the splitting factor $g=1.995\pm0.001$, which differs from the free electron $g=2.0023$ by $\Delta g=-0.007\pm0.001$. This shift, although small, has significant implications for the angular dependence of the ground state of the *F*-center electron. We show below that it is not possible to account for the order of magnitude of the shift using the standard theoretical model[3] of an *S*-electron in a central field. The shift Δg may, however, be explained approximately if the ground state has predominantly *G*-character, or if we use a molecular orbital wave function representing the excess electron as shared among the cations which bound the vacancy. The two models are closely related, but the molecular orbital viewpoint is perhaps more attractive on general grounds.

The spin-orbit interaction to the first order of perturbation theory gives $\Delta g=0$ if the ground state has *S*-character. The nonspherical components of the potential energy arise in large part from the charges of the six K^+ ions adjacent to the vacancy; these components mix the ground state with functions having $L=4$ and higher. Writing the additions as $\psi_G{}^M$, an improved ground-state function may be written

$$\psi'=\psi_S'+b(\psi_G{}^4+\psi_G{}^{-4}), \tag{1}$$

and the lowest excited state of interest here is expected to have the form

$$\psi''=\psi_S''+c(\psi_G{}^4-\psi_G{}^{-4}). \tag{2}$$

We neglect $\psi_G{}^0$ and terms with $L>4$. Both ψ' and ψ'' have $\Delta g=0$.

The spin-orbit interaction $\lambda\mathbf{L}\cdot\mathbf{S}$ will mix some ψ'' in ψ'. If for simplicity we set $b=c$, then for the perturbed ground state

$$\Delta g\cong-\frac{64b^2}{(1+2b^2)^2}\cdot\frac{\lambda}{\Delta}, \tag{3}$$

where Δ is the energy separation between the two states considered. We may safely assume that Δ is of the order of 1 ev, but it is more difficult to estimate λ. If we suppose that the $\psi_G{}^4$ function is chiefly concentrated about a circle passing through four of the K^+ ions surrounding the vacancy, we estimate $\lambda\approx10^{-17}$ erg, where the effective potential is taken as e^2/r with r measured from the center. Then $\lambda/\Delta\approx10^{-5}$, and in the limit $b\gg1$ we have $\Delta g\approx-2\times10^{-4}$. For $b=0.1$, $\Delta g\approx-6\times10^{-5}$, which is much too small.

We must thus suppose that there is a strong mixture of *G*-function in the ground state; there is no other possibility of accounting for the observed Δg value. The difference between the calculated maximum $\Delta g\approx-2\times10^{-4}$ and the observed $\Delta g\approx-7\times10^{-3}$ may not be significant in view of the considerable uncertainties surrounding the estimate of λ made above. The estimate using Eq. (7) below is closer, however.

It thus appears that we might use a *G*-function as a starting approximation rather than an *S*-function. The lowest energy *G*-function[4] in the cubic potential of the six K^+ ions is nondegenerate and transforms as $x^4+y^4+z^4$, as does also the molecular orbital,

$$\Psi=\sum_{i=1}^{6}\psi_i, \tag{4}$$

proposed by Muto,[5] and Inui and Uemura,[6] for the *F*-center ground state. Here ψ_i is the wave function of the valence electron when on the ith of the six neighboring K^+ ions.

On the molecular orbital model the important spin-orbit effects arise through the electrostatic polarization of the K atoms by the vacancy. The ground state of the valence electron on the K atom is normally pure $4s$, but the unsymmetrical electrical field associated with the vacancy will polarize the K atom, thus mixing a large amount of $4p$ function into the ground state. The polarized ground-state function for the atom on the positive x side of the vacancy is

$$\psi_1=\psi_S-(\epsilon/\sqrt{2})(\psi_P{}^1-\psi_P{}^{-1}). \tag{5}$$

The axis of quantization is taken along the $z$axis. The other ψ_i will be composed of similar mixtures of $4s$ and $4p$ functions, taken in such a way as to possess electric dipole moments in the direction of the vacancy. Spin-orbit interaction with the other $4p$ states will partially lift the quenching of the angular momenta of the atoms in the $x-y$ plane. In the presence of spin-orbit interaction $\lambda\mathbf{L}\cdot\mathbf{S}$, we have to first order

$$\psi_1=\psi_S-\frac{\epsilon}{\sqrt{2}}\psi_P{}^1\left(1+\frac{\lambda}{2\Delta}\right)+\frac{\epsilon}{\sqrt{2}}\psi_P{}^{-1}\left(1-\frac{\lambda}{2\Delta}\right). \tag{6}$$

The change in the g-factor for the *F*-center will then be

$$\Delta g=-\frac{4}{3}\frac{\lambda}{\Delta}\cdot\frac{\epsilon^2}{1+\epsilon^2}. \tag{7}$$

From the $4p$ doublet splitting of the K atom we obtain $\lambda=38\ \mathrm{cm}^{-1}$. For Δ we use the $4s-4p$ separation, which is close to the *F*-band energy. With hydrogenic wave functions we estimate $\epsilon=0.9$, which is consistent with an estimate on the basis of polarizability of a K atom. We find $\Delta g=-1.7\times10^{-3}$, of the correct order of magnitude, but somewhat too small. It would be raised somewhat by considering higher states.

We are indebted to Professor Hutchison for advance communication of his results.

* This work has been assisted in part by the U. S. Office of Naval Research.
† National Science Foundation Fellow.
[1] C. A. Hutchison, Jr., and G. A. Noble, Phys. Rev. **87**, 1125 (1952); for earlier work see C. A. Hutchison, Jr., Phys. Rev. **75**, 1769 (1949); M. Tinkham and A. F. Kip, Phys. Rev. **83**, 657 (1951).
[2] *V*-centers may probably be excluded, as they might be expected to have a g larger than the free electron value; because of the strong spin-orbit interaction in a chlorine atom, we estimate $\Delta g\approx0.1$ for a *V*-center in KCl.
[3] S. R. Tibbs, Trans. Faraday Soc. **35**, 1471 (1939); J. H. Simpson, Proc. Roy. Soc. (London) **A197**, 269 (1949); L. Pincherle, Proc. Phys. Soc. (London) **A64**, 648 (1951).
[4] H. A. Bethe, Ann. Physik **3**, 133 (1929); see p. 166.
[5] T. Muto, Prog. Theoret. Phys. **4**, 243 (1949).
[6] T. Inui and Y. Uemura, Prog. Theoret. Phys. **5**, 252, 395 (1950).

A Suggested Scheme for Meson Production

H. MESSEL AND H. S. GREEN
University of Adelaide, Adelaide, South Australia
(Received July 24, 1952; revised manuscript received November 24, 1952)

A MASS of facts[1-8] is rapidly accumulating concerning the existence of two classes of particles, the first with masses intermediate between the π-meson and the proton, and the second with masses greater than the proton. Unsystematized, these facts tend to present a confusing appearance to a casual inspection. The purpose of this note is to suggest a classification of all observed particles, based on the properties of first-order wave equations, and the existence, already suggested from several quarters,[9] of isobaric excited states of the nucleon, and to propose a model for the structure of the nucleon.

The meson field (φ) for particles with integral spin is supposed to be determined by a wave equation of the type

$$(i\beta^\lambda\partial_\lambda - m)\varphi = \text{const} \times \Sigma_{i,j}(\bar{\Psi}_i\Psi_j + \bar{\Psi}_j\Psi_i), \quad (1)$$

where the Ψ_i are nucleon wave functions, and m is a multiple of the π-meson mass. Bhabha and others[10–13] have shown that relativistic restrictions imposed on the matrices β^λ require that they should satisfy

$$[\beta^\lambda, [\beta_\mu, \beta_\nu]] = \delta_\mu{}^\lambda\beta_\nu - \delta_\nu{}^\lambda\beta_\mu. \quad (2)$$

The masses of particles derived from nucleon interactions would then be simple multiples of the π-meson mass. The lowest spin state of such particles would be spin 0. These particles of zero spin may decay by neutrino emission to particles of spin $\frac{1}{2}$, of which the μ-meson is the representative of lowest (nonvanishing) mass. Another mode of decay is possible in which one or more mesons of spin 0 are created, with a Q-value which is either very small, or a multiple of m_π.

The classification of mesons with mass less than the proton mass is therefore as follows:

	Charged	Uncharged	Spin $\frac{1}{2}$
1.	$\pi^\pm \to \mu^\pm + \nu$	$\pi^0 \to 2\gamma$	$\mu^\pm \to e^\pm + 2\nu$
2.	$\zeta^\pm \to \pi^\pm + \pi^0$	$\zeta^0 \to \pi^+ + \pi^-$	
3.	$\tau^\pm \to \pi^\pm + \pi^- + \pi^+$(?)	$\tau^0(V_1{}^0) \to \pi^+ + \pi^-$ or $\zeta^\pm + \pi^\mp$ or $\pi^+ + \pi^- + \pi^0$	
4.	$\psi^\pm \to \pi^\pm + \zeta^0$(?)		$\kappa^\pm \to \mu^\pm + \pi^+ + \pi^-$ or $\mu^\pm + 2\nu$
5.	$\chi^\pm \to \pi^\pm + \tau^0$	$\chi^0 \to \pi^+ + \pi^-$ or $\psi^\pm + \pi^\mp$	

Most of these reactions are given in the Report of the International Physics Conference, Copenhagen, June, 1952, except $V^\pm$, as it was called there, has been identified with the spin-$\frac{1}{2}$ $\kappa^\pm$, since its mass would otherwise not fall in with this scheme.

It remains to account for those particles whose masses are greater than the proton mass. It seems that there is a "mass barrier" at the proton mass which is necessary to ensure the stability of the proton, and prevents the decay of isobaric states to particles whose masses are *all* below the proton mass. We assume the nucleon may be regarded as consisting of two particles, one a massive core of spin zero and the other of spin one-half, bound together by the meson forces, which lead to the existence of one or more energy levels, excited states corresponding to the possibly observed isobaric states of the nucleon.[1,6] To account for the existence of charged as well as neutral mesons of zero spin, it is necessary to suppose that the core (denoted by F) may be positively charged or neutral. If the spin-$\frac{1}{2}$ particle is identified with either an electron, or a neutrino, a simple explanation of β decay can be given:

$$N = F^0 + \nu \to F^0 + \nu + e^+ + e^- \to P + \nu + e^- \quad (P = F^0 + e^+)$$

or

$$N = F^+ + e^- \to F^+ + e^- + \nu + \nu \to P + \nu + e^- \quad (P = F^+ + \nu).$$

In the real excited state recognized as a $V_1{}^0$ particle, a μ^- meson may replace the electron.

Thus, the structure of the nucleon is in some ways comparable with that of the hydrogen atom, but in this instance there are no definite selection rules and the quanta may correspond to mesons of various masses. In the interaction of two nucleons, either or both may transit to excited states, through the exchange of spin-$\frac{1}{2}$ particles. These excited states may be real or virtual. As an example of a process in which virtual intermediate states are important, we cite the interaction of a π^- with a proton:

$$\begin{aligned} P + \pi^- &= (F^+ + \nu) + \pi^- \\ &\to (F^0 + \nu) \text{ excited} \\ &\to (F^0 + \nu) + (\pi^0 \text{ or } \gamma) \\ &\to N + (\pi^0 \text{ or } \gamma). \end{aligned}$$

We do not, however, suppose that nuclear forces are due directly to meson coupling, but rather to exchange between the spin-$\frac{1}{2}$ particles, which are actually coupled to the core by the meson field.

Most of the real excited states have short lives, decaying to the ground state with meson emission. In case both nucleons are excited, as is likely at high energies, two but not more than two mesons of the various species will be created in a nucleon-nucleon interaction. At low energies only π-mesons could be emitted; but at higher energies, there is an increasing probability for mesons of greater mass to result; and, as the experimental evidence suggests,[6,8] the proportion of heavier mesons may be quite high. This model of meson production is intermediate between the multiple[14–16] and plural[17] models which have hitherto been advanced. Obviously a succession of real transitions between excited states is possible. Possible observed reactions[1,6,7] are

$$V_1{}^0 \to P + \pi^-,$$
$$V_1{}^\pm \to V_1{}^0 + \pi^\pm.$$

A further feature of this model is the resolution of the anomaly of the copious production of $v_1{}^0$ mesons in spite of their relatively long lifetimes. Since they mostly appear in real states as the result of nuclear collisions and not through the absorption of mesons, (though this is possible in principle), the coupling constant which characterizes the decay does not have to be as large as other theories would require. The interaction of the spin-zero mesons with the nucleon must clearly be quite strong, at least at low energies, on this model; however, as has been shown, there is no need to postulate any additional coupling to account for β-decay.

We wish to acknowledge discussions with Professor Fermi and Professor Wentzel on the above topics and also to thank Professor Wentzel for pointing out that a somewhat similar model for the nucleon had been discussed by him[18] in 1936.

[1] C. C. Butler, *Progress in Cosmic Ray Physics* (North Holland Publishing Company, Amsterdam, 1951), Vol. I.
[2] C. O. O'Ceallaigh, Phil. Mag. **42**, 1032 (1951).
[3] Danysz, Lock, and Yekutieli, Nature **169**, 364 (1952).
[4] R. B. Leighton and S. D. Wanlass, Phys. Rev. **86**, 426 (1952).
[5] Daniel, Davies, Mulvey, and Perkins, Phil. Mag. **43**, 753 (1952).
[6] Armenteros, Barker, Butler, Cachon, and York, Phil. Mag. **43**, 597 (1952).
[7] Proceedings of the Rochester Conference on Meson Physics (January, 1952) (unpublished).
[8] Report of the International Physics Conference, Copenhagen, (June, 1952) (unpublished).
[9] B. Ferreti, Nuovo imento **9**, 312 (1952).
[10] H. J. Bhabha, Proc. Indian Acad. Sci. **21**, 241 (1945).
[11] Madhava Rao, Proc. Indian Acad. Sci. **A15**, 139 (1942).
[12] Madhava Rao, Proc. Indian Acad. Sci. **A26**, 221 (1947).
[13] G. Petiau, J. phys. et radium **7**, 124, 181 (1946).
[14] W. Heisenberg, Z. Physik **126**, 569 (1949).
[15] Lewis, Oppenheimer, and Wouthuysen, Phys. Rev. **73**, 127 (1948).
[16] E. Fermi, Phys. Rev. **81**, 683 (1951).
[17] W. Heitler and L. Janossy, Proc. Phys. Soc. (London) **A62**, 364 (1949).
[18] G. Wentzel, Z. Physik **104**, 34 (1936) and **105**, 738 (1937).

Interpretation of Isomeric Transitions of Electric Quadrupole Type

AAGE BOHR AND BEN R. MOTTELSON*
Institute for Theoretical Physics, Copenhagen, Denmark
(Received November 10, 1952)

IN the recent classification of nuclear isomers,[1] the transitions of electric quadrupole type are unique in possessing several examples of lifetimes appreciably shorter than predicted on the basis of the shell model. In some cases, the predicted lifetimes are more than a factor of a hundred too long. It appears evident that we have here the effect of some type of cooperative nuclear motion.[1]

A natural interpretation of these transitions is obtained in the model describing the nucleus in terms of the coupled single particle motion and nuclear surface oscillations.[2,3] According to such a model, the low-lying states of the nucleus arise either by excitation of the particle structure with an accompanying readjustment of the surface, or by an excitation of the surface without a change of the particle quantum numbers. In many cases, the first few excited states are of the former character and can therefore be classified by means of the shell model. The readjustment of the surface implies, however, that transition probabilities between two such states will

in general be appreciably smaller than estimates based on shell model wave functions, as is in fact observed.[4]

In regions of high surface deformability, one obtains very low-lying states of collective excitation, which may be considered as rotational levels of the deformed nucleus. In the case of even-even nuclei, these states yield a spectrum with $I=0, 2, 4$, etc., even parity, and with energy values

$$E_I=(\hbar^2/2\mathcal{I})I(I+1), \tag{1}$$

neglecting the influence of rotation-vibration interaction. The effective moment of inertia $\mathcal{I}$ is related to the deformation of the nucleus and is given by

$$\mathcal{I}=3B\beta^2 \tag{2}$$

in terms of β the deformation parameter, and B, the mass parameter of the surface oscillators.[5] The wave functions for these states are obtained from the strong coupling solutions $\Omega=K=0$.

These states possess the spins, parities, low energies, and very short lifetimes of the observed levels. The transition from the first excited state to the ground state is of electric quadrupole type, with a probability per unit time given by

$$T=(\kappa^5/300\hbar)e^2Q_0^2, \tag{3}$$

where κ is the wave number of the emitted photon, and Q_0 the intrinsic quadrupole moment of the nucleus, measured with respect to the symmetry axis. For a uniformly charged incompressible nucleus, we have

$$Q_0=[3/(5\pi)^{\frac{1}{2}}]\cdot ZR_0^2\beta, \tag{4}$$

with Z and R_0, the nuclear charge and radius.

From the empirically measured lifetime and energy, one can determine the deformation of the nucleus, expressed by Q_0, listed in column 5 of Table I. The energies E and transition probabilities

TABLE I. Electric quadrupole transitions in even-even nuclei with measured half-lives.

Nuclide	E (kev)	$\log T$ (sec^{-1})	$S=T_{\text{obs}}/T_{sp}$	$Q_0(10^{-24}\,\text{cm}^2)$
Er^{166}	80	7.91	180	10
Yb^{170}	84	7.94	150	9
Hf^{176}	89	8.01	150	9
Os^{190}	134	8.64	55	6
Hg^{198}	411	~11.0	~50	~6
Pb^{204}	374	6.34	1.7×10^{-4}	

T in columns two and three are taken from reference 1, with the exception of Hf^{176} [F. K. McGowan, Phys. Rev. **87**, 542 (1952); a total conversion coefficient of 4 has been assumed], and Hg^{198} [R. L. Graham and R. E. Bell, Phys. Rev. **84**, 380 (1951)]. Column four gives the factor S by which the transition probability exceeds that calculated for a single proton transition of type $d_{\frac{5}{2}}\rightarrow s_{\frac{1}{2}}$. A comparison with a two-proton transition of type $(j^2)_{J=2}\rightarrow(j^2)_{J=0}$ would give slightly larger S-values. For the fast transitions, the intrinsic quadrupole moments, calculated from the observed lifetimes and energies by means of formula (3), are listed in the last column.

The values obtained for Q_0 are just of the magnitude encountered in the measured quadrupole moments[6] for this region of elements and in the values derived from anomalies in isotope shifts.[7]

While low-lying rotational levels are expected in regions of high deformability, in regions of very low deformability, as near shell closings, the first excited states should correspond to excitation of the particle structure. Thus, the very long lifetime of Pb^{204} is associated with its proximity to shell closings at $Z=82$ and $N=126$. The reason for its S-value being smaller than unity may derive from the circumstance that the excitation is presumably of the neutrons, the protons forming a closed shell structure.

Further measurements of the lifetimes of the $I=2$ first excited state in even-even nuclei would be of interest in establishing the rotational or particle character of these states.

From the measured lifetimes and energies of the rotational levels one can also determine the mass parameter B. For the levels listed in Table I, one obtains values significantly larger than those estimated from the liquid drop model of nuclear deformations.[8] Also the analysis of other nuclear properties, such as static magnetic dipole and electric quadrupole moments, gives evidence of a similar deviation from the simple hydrodynamical approximation.

A more detailed discussion of these problems will be shortly forthcoming[3] in connection with a fuller account of the coupled surface, single particle model and its consequences for various nuclear properties.

* Atomic Energy Commission Fellow.
[1] M. Goldhaber and A. Sunyar, Phys. Rev. **83**, 906 (1951).
[2] A. Bohr, Kgl. Danske Videnskab. Selskab, Mat.-fys. Medd. **26**, No. 14 (1952).
[3] A. Bohr and B. Mottelson, Kgl. Danske Videnskab. Selskab, Mat.-fys. Medd. (to be published).
[4] A. Bohr and B. Mottelson, Physica (to be published).
[5] See expressions (2) and (3) of reference 2.
[6] It should be remembered that the spectroscopically determined quadrupole moment Q is smaller than Q_0 by the projection factor $[I(2I-1)]/[(I+1)(2I+3)]$ [see A. Bohr, Phys. Rev. **81**, 134 (1951)].
[7] P. Brix and H. Kopfermann, Z. Physik **126**, 344 (1949). It is to be noted that this effect measures Q_0 rather than Q.
[8] Formula (4) of reference 2.

Comparison of Slater's and Peckar's Treatments of Perturbed Periodic Potentials

HARVEY WINSTON
Research and Development Laboratories, Hughes Aircraft Company, Culver City, California
(Received October 31, 1952)

SLATER'S[1] and Peckar's[2] treatments of the perturbed periodic potential problem have the obvious difference that Peckar limited himself to quadratic terms in the expansion of the energy of the unperturbed problem as a function of crystal momentum, whereas Slater allowed this energy to be an arbitrary function of crystal momentum. Except for this difference, the fundamental equations of the two methods [Slater's equation (6) and Peckar's equation (4)] are identical. Clearly there must be a close relationship between the two methods, but its nature appears to have escaped mention in the literature. In fact, statements[3] can be found that imply important differences between the two treatments.

We start with Slater's form of solution, and from it derive Peckar's. From Slater's Eq. (5),

$$\psi_k(\mathbf{q})=\Sigma_n\,\Psi_k(\mathbf{Q}_n)a(\mathbf{q}-\mathbf{Q}_n). \tag{1}$$

Replacing the factor $a(\mathbf{q}-\mathbf{Q}_n)$ by Slater's equation (1A) and rearranging terms, we obtain,

$$\psi_k(\mathbf{q})=\sum_{\mathbf{p}_0}N^{-\frac{1}{2}}\sum_n\Psi_k(\mathbf{Q}_n)\exp(-i\mathbf{p}_0\cdot\mathbf{Q}_n/\hbar)u_{\mathbf{p}_0}(\mathbf{q}). \tag{2}$$

Let $b_k(\mathbf{p}_0)$ be given by Eq. (3), where $\mathbf{p}_0$ is an allowed crystal momentum from the central zone:

$$N^{-\frac{1}{2}}\Sigma_n\,\Psi_k(\mathbf{Q}_n)\exp(-i\mathbf{p}_0\cdot\mathbf{Q}_n/\hbar)=b_k(\mathbf{p}_0). \tag{3}$$

$$\psi_k(\mathbf{q})=\sum_{\mathbf{p}_0}b_k(\mathbf{p}_0)u_{\mathbf{p}_0}(\mathbf{q}). \tag{4}$$

Except for obvious differences in notation, Eq. (4) is identical with Peckar's equation (10), which gives the perturbed wave function as an expansion in terms of the unperturbed functions. However, our approach makes the rationale of Peckar's method quite clear. To determine the coefficients $b_k(\mathbf{p}_0)$, Peckar first finds the function $\Psi_k(\mathbf{Q}_n)$ as a solution of his reduced mass equation (4) or, more generally, as a solution of Slater's Eq. (6). He could then have used our Eq. (3) to find $b_k(\mathbf{p}_0)$; but actually he expanded Ψ_k as a Fourier series, the coefficients of which are $b_k(\mathbf{p}_0)$. In fact, by inverting our Eq. (3), we obtain

$$\Psi_k(\mathbf{Q}_n)=N^{-\frac{1}{2}}\sum_{\mathbf{p}_0}\exp(i\mathbf{p}_0\cdot\mathbf{Q}_n/\hbar)b_k(\mathbf{p}_0), \tag{5}$$

which is Peckar's equation (6) in our notation, except for the restriction of the arguments $\mathbf{Q}_n$ to lattice points.

Peckar's discussion of the validity of his method rested on the quadratic approximation to the unperturbed energy. Whenever Peckar's effective mass equation is valid, its solutions are entirely equivalent to the solutions of Slater's equation. However, Slater's solution has a wider application because of the use of the operator $E_0(-i\hbar\nabla)$ instead of its quadratic approximation.

[1] J. C. Slater, Phys. Rev. **76**, 1592 (1949).
[2] S. Peckar, J. Phys. (U.S.S.R.) **10**, 431 (1946).
[3] J. Bardeen and W. Shockley, Phys. Rev. **80**, 72 (1950), Appendix A.

Nuclear Spin of $_{95}Am^{241}$

MARK FRED AND FRANK S. TOMKINS
Chemistry Division, Argonne National Laboratory, Lemont, Illinois
(Received November 17, 1952)

THE spectrum of americium-241 has been photographed with a 30-foot spectrograph and found to contain many lines with wide hyperfine structure in the form of flag patterns, all apparently with six components. In lines that are well resolved there is a low degradation in spacing and intensity, and since the J values are expected to be high, the number of components is presumably spin-limited, with $I=5/2$. The existence of an appreciable quadrupole moment is indicated by a noticeable departure from the interval rule for some lines.

The Ground State of N^{14}

A. M. FEINGOLD
University of Pennsylvania, Philadelphia, Pennsylvania
(Received November 19, 1952)

TO explain the large ft value, 10^9, for the C^{14} β-decay, it has been proposed[1] that the ground state of N^{14} is an almost pure $^3D_1$ state, the C^{14} ground state being a $^1S_0$ state as in other even-even nuclei. The β-decay then requires $\Delta L=2$, and is therefore second-forbidden, giving an ft value of the experimental magnitude instead of the value $\sim 10^3$ expected in analogy with the $^1S_0 \rightarrow {}^3S_1$ β-decay of He^6. The $^3D_1$ assignment is supported by the experimental value of the magnetic moment, 0.40 (in units $e\hbar/2Mc$), since a pure $^3D_1$ state of maximum symmetry would have the value 0.31, while the magnetic moment of the $^3S_1$ state would be 0.88.

A serious difficulty is that the ft value of 10^9 demands that the $^3D_1$ state be extremely pure,[1,2] having no more than 1 part in 10^5 admixture of $^3S_1$ state, and conversely, that the ground state of C^{14} have an equally small admixture of $^5D_0$ state. This appears extremely unlikely. It is known that the ground state of the deuteron has ~ 4 percent $^3D_1$ mixed with the $^3S_1$ ground state, due to the tensor force. Similarly the experimental magnetic moment of Li^6, 0.82, requires 10 percent $^3D_1$ admixture in the $^3S_1$ ground state. A mixture of just this magnitude is indicated by tensor force calculations.[3]

As an alternative explanation for the forbiddenness of the β-decay, we suggest that the ground state of N^{14} is predominantly a P state, either $^3P_1$ or $^1P_1$. If we further assume that the main spin-orbit force present is the tensor force, then it follows that in a second-order perturbation calculation, the tensor force will mix in some D and F states, but no $^3S_1$ state. A small amount of $^3S_1$ state will appear only in the next order of the perturbation calculation, due to the above-mentioned small admixture of D state. On this model, then, one would expect only 10^{-1}—10^{-2} percent admixture of $^3S_1$ state in the ground state. Furthermore, most of the $^3S_1$ admixture probably would come from configurations other than the lowest one, the $(1s)^4(2p)^{-2}$ configuration, and hence would not contribute to the β-decay. One would therefore expect an ft value of 10^7—10^9. The direct $^1S_0 \rightarrow {}^{1,3}P_1$ transition would remain second-forbidden.

The suggestion that the ground state of N^{14} is predominantly a P state is, of course, beset with serious difficulties. A $^1P_1$ state does occur in the $(1s)^4(2p)^{-2}$ configuration, with a magnetic and moment value of 0.50 in fair agreement with the experimental data. However, this state belongs to the supermultiplet (111), and hence if the central forces are predominantly of the Majorana exchange type, this state should lie ~ 5 Mev above the more symmetric S (and D) states.[4] To obtain a $^3P_1$ state of maximum symmetry one must go to a configuration that presumably lies much higher than the $(1s)^4(2p)^{-2}$ one, i.e., the $(1s)^2(2p)^{-2}(3d)$ or $(1s)^4(2p)^{-3}(3p)$ configurations. The kinetic energy of such configurations should be ~ 10 Mev higher than that for the $(1s)^4(2p)^{-2}$ configuration. Also the magnetic moment of such a state would be 0.69, in poor agreement with the experimental value.

In any event, the experiment suggested by Messiah,[5] to observe the $N^{14}(n,d)C^{13*}$ angular distribution,[6] would determine the L value of the ground state of N^{14}. If the ground state is a P state, then one would observe an "$l=2$" angular distribution, just as if it were a D state (an "$l=1$" distribution being forbidden by parity considerations). However, the cross section for the reaction should be 10—100 times smaller for the P state (it would come only from the small amount of D state admixture) than for the pure $^3D_1$ state.

[1] E. Feenberg and K. C. Hammack, Phys. Rev. **75**, 1877 (1949); R. Bouchez, Compt. rend. **230**, 440 (1950); **231**, 275 (1950).
[2] E. Gerjuoy, Phys. Rev. **81**, 62 (1951).
[3] A. M. Feingold, Ph.D. thesis, Princeton University, 1952 (unpublished).
[4] E. Feenberg and E. Wigner, Phys. Rev. **51**, 95 (1937).
[5] A. M. L. Messiah, Phys. Rev. **88**, 151 (1952).
[6] The mirror reaction $N^{14}(p,d)N^{13*}$ should serve equally well, since the 2.4-Mev level of N^{13} is the mirror analog of the 3.1-Mev level of C^{13}.

Validity of Born Approximation in Stripping*

N. AUSTERN
Laboratory of Nuclear Studies, Cornell University, Ithaca, New York
(Received October 20, 1952)

THE deuteron stripping process has been discussed in Born approximation in several recent publications,[1,2] and the result of this approximation has been shown[2] to be in very good agreement with the supposedly more accurate method of boundary conditions.[3] Born approximation assumes the incident wave function to be a satisfactory first approximation to the wave function of the system; hence it is generally considered unreliable for low energy reactions, where the perturbations are comparatively much stronger. But in the case of stripping, it will be shown that the result of the Born approximation happens to be obtainable by another route, which employs only the physically plausible assumptions of Butler's paper. It becomes clear why the Born approximation gives a satisfactory result.

The calculation will be presented as for an infinitely heavy target, and with Coulomb interaction with the deuteron omitted, although it is apparent how the latter should be inserted. By convention, the captured particle will be called the "neutron."

Let ξ denote the internal coordinates of the target nucleus. The complete Hamiltonian is

$$H=H_0(\xi)+V_{\xi N}+V_{\xi P}+V_{NP}+T_N+T_P. \quad (1)$$

Here the V_{ij} are the various potential energies, as indicated, and T_j are the kinetic energy operators for the deuteron particles.

The complete wave function is Ψ, and is expanded as follows:

$$\Psi=\varphi_i(\xi)\psi_D(N,P)+\Sigma_j\int d^3k A_j(\mathbf{k})\psi_j(\xi,N)e^{i(\mathbf{k}\cdot\mathbf{r}_P)}. \quad (2)$$

Here the φ_j are normalized energy eigenstates of the target nucleus, ψ_j are normalized energy eigenstates of the product nucleus, and ψ_D is the incident deuteron wave function.

Substitution into the Schrödinger equation permits solving for $A_j(\mathbf{k})$:

$$A_j(\mathbf{k})=\frac{1}{(2\pi)^3\{E-E_j-T(k)\}}\{\langle\psi_j e^{i(\mathbf{k}\cdot\mathbf{r}_P)}|V_{N\xi}+V_{P\xi}|\varphi_i\psi_D\rangle$$
$$+\langle\psi_j e^{i(\mathbf{k}\cdot\mathbf{r}_P)}|V_{P\xi}+V_{NP}|\Sigma_l\int d^3k'\psi_l A_l(\mathbf{k}')e^{i(\mathbf{k}'\cdot\mathbf{r}_P)}\rangle\}, \quad (3)$$

where

$$T(k)\equiv\hbar^2k^2/2M. \quad (4)$$

An alternative form is

$$A_j(\mathbf{k})=\frac{1}{(2\pi)^3\{E-E_j-T(k)\}}\{\langle\psi_j e^{i(\mathbf{k}\cdot\mathbf{r}_P)}|V_{P\xi}+V_{NP}|\Psi\rangle$$
$$+\langle\psi_j e^{i(\mathbf{k}\cdot\mathbf{r}_P)}|V_{N\xi}-V_{NP}|\varphi_i\psi_D\rangle\}. \quad (5)$$

Finally, Eq. (5) is substituted into Eq. (2), giving an integral equation for the problem:

$$\Psi=\varphi_i\psi_D+\Sigma_j\int d^3k\frac{\psi_j e^{i(\mathbf{k}\cdot\mathbf{r}_P)}}{(2\pi)^3\{E-E_j-T(k)\}}$$
$$\times\{\langle\psi_j e^{i(\mathbf{k}\cdot\mathbf{r}_{P'})}|V_{P\xi}+V_{NP}|\Psi\rangle$$
$$+\langle\psi_j e^{i(\mathbf{k}\cdot\mathbf{r}_{P'})}|V_{N\xi}-V_{NP}|\varphi_i\psi_D\rangle\}. \quad (6)$$

It is a very basic approximation in stripping that $V_{P\xi}$ is unimportant, so it will be ignored without any further justification. To achieve Born approximation, it is only necessary to replace Ψ by $\varphi_i\psi_D$. Then V_{NP} goes out, and Eq. (6) gives directly the starting point of Daitch and French. The connection with Butler's paper is obtained by observing that the final state wave function, ψ_j, localizes the neutron; hence V_{NP} has no matrix elements to protons which pass far from the nucleus, as happens in stripping. Thus Butler's assumptions prescribe that we should immediately strike V_{NP} from Eq. (6), and we return once again to the Born result.

Equation (6) appears hopeful as a starting point for the investigation of corrections to the simple stripping calculation, and such an investigation is planned.

¶This paper is the outcome of a conversation with Professor J. B. French, and of many discussions with Dr. S. T. Butler.

* This work was performed while the author held a U. S. Atomic Energy Commission Postdoctoral Fellowship.

[1] Bhatia, Huang, Huby, and Newns, Phil. Mag. **43**, 485 (1952).
[2] P. B. Daitch and J. B. French, Phys. Rev. **87**, 900 (1952).
[3] S. T. Butler, Proc. Roy. Soc. (London) **208**, 559 (1951).

The Causal Interpretation of Quantum Mechanics

SAUL T. EPSTEIN
Boston University, Boston, Massachusetts

(Received October 16, 1952)

RECENTLY Bohm[1] has proposed a causal interpretation of quantum mechanics. It is based on the following observation: If one writes the Schrödinger function in *coordinate* space as $\psi=R_s\exp(iS_s/\hbar)$ (the subscript s denotes Schrödinger), then S_s satisfies an equation of the classical Hamilton-Jacobi type but containing, in addition to the ordinary potential, a "quantum-mechanical potential."

This suggests that one can consider ψ to describe the motion of a classical particle in the combined field of these potentials with, however, the "quantum condition" that one chooses only those solutions of the equations of motion such that the particle's momentum is given by

$$P=\partial S_s/\partial q. \quad (1)$$

Alternatively, one may say that one picks out only the trajectories described by the *particular* solution $S=S_s$ of the associated Hamilton-Jacobi equation.[1,2]

In this note we would like to point out another possibility of this type. We write the Schrödinger function in *momentum* space as $\phi=\rho_s\exp(i\sigma_s/\hbar)$ (ρ_s and σ_s real). One then finds that σ_s satisfies an equation of the classical Hamilton-Jacobi type but containing, in addition to the ordinary potential, a momentum-dependent "quantum-mechanical potential."[3]

This suggests that one can consider ϕ to describe the motion of a classical particle in the combined field of these potentials with, however, the "quantum condition" that one chooses only those solutions of the equations of motion such that

$$q=-\partial\sigma_s/\partial P. \quad (2)$$

Alternatively, one may say that one picks out only the trajectories described by the *particular* solution $\sigma=\sigma_s$ of the associated Hamilton-Jacobi equation.

In general, one must of course integrate the equations of motion to find P as a function of time and then use (2) to find q as a function of time. However, there is one case where this is unnecessary, and one sees that the present description gives different motions than Bohm's description. We consider a bound state of zero angular momentum. Then

$$S_s=\sigma_s=-Et.$$

Therefore, in Bohm's case $P=0$, $q=$constant, and the particle can be at rest anywhere; while in the present case $q=0$, the particle stays at the origin (and for the particular case of a harmonic oscillator, $P=$constant).

There are three further points we wish to mention:

(a) By starting from representations intermediate between the coordinate and momentum representations, it would seem that we could generate any number of such descriptions.

(b) It is tempting to speculate that this apparent multiplicity of causal descriptions is connected with the multiplicity of phase space-descriptions found by Moyal.[4]

(c) Finally we have *not* investigated whether any of these alternative descriptions can, when combined with the hypothesis of molecular chaos, yield the conventional probability interpretation of quantum-mechanics.

[1] D. Bohm, Phys. Rev. **85**, 166, 180 (1952).
[2] O. Halpern, Phys. Rev. **87**, 389 (1952); D. Bohm, Phys. Rev. **87**, 389 (1952).
[3] To get the classical Hamilton-Jacobi equations in momentum space one inserts $q=-\partial\sigma/\partial P$ in

$$H(P,q)+\partial\sigma/\partial t=0.$$

Since we have momentum-dependent potentials, P is the canonical momentum and not necessarily mq as in Bohm's description.
[4] J. E. Moyal, Proc. Cambridge Phil. Soc. **45**, 99 (1949).

Comments on a Letter Concerning the Causal Interpretation of the Quantum Theory

DAVID BOHM
Faculdade de Filosofia, Ciências e Letras, Universidade de São Paulo, São Paulo, Brasil

(Received November 17, 1952)

IN a recent letter,[1] Epstein has made the interesting suggestion that alternative causal interpretations[2] of the quantum theory may be possible, starting, for example, from a momentum representation of the wave function, or from other representations between that of position and momentum. In the present letter, the author would like to give the reasons why he thinks that this proposal cannot, in fact, be carried out.

To illustrate the difficulties involved, let us consider the problem of the hydrogen atom. In the momentum representation, the potential energy, e^2/r, takes the form of an integral operator which cannot be expressed as a convergent series of the operators, $x_i=i\hbar\partial/\partial p_i$. As a result, when the wave function is expressed as a product, $Re^{iS/\hbar}$, it does not seem to be possible to obtain the equivalent Hamilton-Jacobi equation for S, and the conservation equation for R^2. Moreover, without such a conservation equation, it is difficult to see how one could, with the aid of the hypothesis of molecular chaos, demonstrate that the probability density ap-

proaches R^2, as can be done with a causal interpretation based on a position representation of the wave function.[3]

If one starts with the causal interpretation of the quantum theory obtained in the position representation, with the quantum potential, $U=-\hbar^2\nabla^2R/2mR$, one can naturally make an arbitrary canonical transformation on the *particle* variables. Because it does not alter the quantum potential, however, such a transformation does not lead to an alternative causal interpretation of the quantum theory, but only to a redescription of the same causal interpretation in new mathematical terms, which are, however, usually a great deal more complicated than were the original terms. A new causal interpretation could come from such a procedure only if the canonical transformation on the particle variables were simultaneously accompanied by a corresponding linear transformation on the wave function. But such a linear transformation does not seem even in the simplest cases to lead to an acceptable causal interpretation. It would appear, therefore, that a causal interpretation of the quantum theory can be obtained only if we use the space-time representation of the wave function as a basis. This result is perhaps not too surprising, if one considers the fact that in all fields other than the quantum theory, space and time have thus far stood out as the natural frame for the description of the progress of physical phenomena.

The author would also like to express his disagreement with Epstein's (and Halpern's[4]) statement that the relation, $p=\partial S/\partial q$, constitutes a "quantum condition." Actually, it is a *consistent subsidiary condition* on the equations of motion, which if adopted at any time, say $t=0$, permits one to explain causally and continuously such processes as transitions between stationary states and interference in scattering problems.[3] On the other hand, Bohr's original quantum conditions were restrictions *contradicting* the equations of motion (which predicted continuous radiation in the case of the hydrogen atom, for example), and which could not explain either the process of transition or the appearance of interference in scattering problems. It would seem preferable to use different words to describe concepts which are so different.

[1] S. Epstein, preceding letter [Phys. Rev. **89**, 319 (1952).
[2] D. Bohm, Phys. Rev. **85**, 166 (1952).
[3] D. Bohm, Phys. Rev. (to be published).
[4] O. Halpern, Phys. Rev. **87**, 389 (1952).

The Thermal Neutron Fission and Capture Cross Section of U^{232}

R. Elson,* W. Bentley, A. Ghiorso, and Q. Van Winkle
Argonne National Laboratory, Lemont, Illinois
(Received November 19, 1952)

It has been shown[1] that Pa^{232} is a short-lived beta-emitter which decays to U^{232}, a long-lived alpha-emitter. U^{232} of good isotopic purity, therefore, can be prepared by the neutron irradiation of Pa^{231}, which has been shown to have a capture cross section for pile neutrons of 290 barns.[2]

Three samples of Pa^{231} were subjected to three widely different total neutron fluxes, and the resulting U^{232} was examined for fissionability. The Pa^{231}, irradiated as the oxide, was dissolved in a mixture of nitric and hydrofluoric acids, heated to near dryness to remove fluoride, and dissolved in 0.1M nitric acid. The uranium was extracted from this solution with diethyl ether after saturation with ammonium nitrate. The ether was washed with saturated ammonium nitrate and thin samples were prepared for alpha-counting and fission counting both by direct evaporation and by electroplating on platinum disks.

TABLE I. Fission cross section of U^{232} resulting from irradiations of Pa^{231}.

Sample No.	Total n/cm^2	Weight of U^{232} formed, μg	Fission cross section $\times 10^{24}$, cm^2
1	3.41×10^{16}	2.3×10^{-4}	82.9 ± 1.5
2	8.87×10^{17}	0.32	83.1 ± 1.5
3	4.06×10^{19}	26.2	84.6 ± 1.5[a]

[a] Corrected for contribution of U^{233} known to be present from the decay of Pa^{233}.

The weight of U^{232} on each plate was determined from the α-emission rate, assuming a half-life of 70 years.[3] The fissionability of each sample was then determined[4] in the thermal column of the Argonne heavy water pile. The rate of fission was compared with a sample of Pu^{239} of known weight, and the fission cross section of the U^{232} determined from the known fission cross section of Pu^{239} and the rate of fission in each sample of known weight. The data are summarized in Table I.

The indicated error in fission cross section values is limited to the probable errors in fission rate counting and alpha-emission rate counting. In addition, an uncertainty[3] of about 15 percent in the value for the half-life of U^{232} results in a corresponding uncertainty in the absolute value of the fission cross section. These measurements therefore yield a value of 83 ± 15 barns for the thermal neutron fission cross section of U^{232}.

The consistency of the results under conditions of large variation in total flux and amount of U^{232} formed seems to rule out any important effect from a fissionable contaminant present either as an impurity or formed during the irradiation. The fissionable isotope U^{233} would be formed by a second-order capture on either U^{232} or Pa^{232}, the latter giving Pa^{233}, a 27.4-day beta-emitter which decays to U^{233}. Sample 3 was examined for Pa^{233}, and the amount present indicated an amount of U^{233} sufficient to increase the apparent fission cross section of U^{232} by 0.50 barn. If one assumes that the remaining small increase in the observed fission cross-section value for sample 3 over those for samples 1 and 2 is real and further assumes that the increased value is due only to U^{233} formed by $U^{232}(n,\gamma)U^{233}$, then a rough estimate can be made of the pile neutron capture cross section of U^{232}. A value of about 200 barns is indicated, but since the observed differences are not outside the limits of experimental error, we conclude only that the capture cross section of U^{232} probably does not exceed 500 barns.

* Present address: California Research and Development Company, Livermore, California.
[1] J. W. Gofman and G. T. Seaborg, *The Transuranium Elements: Research Papers* (McGraw-Hill Book Company, New York, 1948), Paper No. 19.14, National Nuclear Energy Series, Plutonium Project Record, Vol. 14B, Div. IV.
[2] Elson, John, and Sellers, Argonne National Laboratory Report 4282 (1951), to be published.
[3] James, Florin, Hopkins, and Ghiorso, *The Transuranium Elements: Research Papers* (McGraw-Hill Book Company, New York, 1948), Paper No. 22.8, National Nuclear Energy Series, Plutonium Project Record, Vol. 14B, Div. IV.
[4] For a description of the apparatus, see reference 3, Paper 22.29.

A Criticism of a Recent Unified Field Theory

C. Peter Johnson, Jr.*
Department of Chemistry, Harvard University, Cambridge, Massachusetts
(Received September 26, 1952)

I would like to show by an example that Dr. Albert Einstein's recent unified field theory is apparently not in agreement with the Newtonian and Coulomb laws of force between charged masses.

Consider two charged and one uncharged mass, separated by distances large compared with their physical dimensions, all substantially at rest at time $t=0$. Under the influence of their mutual attractions and repulsions, the three masses will undergo accelerations closely predicted by Newton's and Coulomb's laws. Corresponding to this motion, there will be (let us assume) a solution in Einstein's theory for all the quantities in it, including the gravitational and electromagnetic potentials which he indicates by the symbols $g_{\underline{ij}}$ and $g_{i\underline{j}}$, as functions of the four chosen coordinates of space-time:

$$g_{\underline{ij}}=f_{\underline{ij}}(x_1, x_2, x_3, x_4) \quad (i, j=1, 2, 3, 4),$$
$$g_{i\underline{j}}=f_{i\underline{j}}(x_1, x_2, x_3, x_4) \quad (i, j=1, 2, 3, 4).$$

It is a characteristic of the new field theory that if the above equations form a satisfactory solution, then another satisfactory solution is

$$g_{ij}'=f_{ij}(kx_1, kx_2, kx_3, kx_4) \quad (k=\text{constant}),$$
$$g_{ij}'=f_{ij}(kx_1, kx_2, kx_3, kx_4) \quad (k=\text{constant}),$$

representing a different physical reality. In addition, if g_{ij} and g_{ij} satisfy certain conditions which Einstein gives for free space at (x_1, x_2, x_3, x_4), then g_{ij}' and g_{ij}' satisfy the conditions at (kx_1, kx_2, kx_3, kx_4).

Consequently, in the new solution, as in the original one, there are three, isolated, non-free-space, space-time regions, representing three material bodies in motion. Taking the three coordinates x_1, x_2, and x_3 as ordinary Cartesian spatial coordinates and x_4 as the time, it can be shown by taking successive space-time sections at constant time that the second set of three bodies are similar in shape to the original bodies, $1/k$ as large in linear dimensions, $1/k$ times as far apart, and have an acceleration k times as large as the corresponding bodies of the original example, at time $t=0$.

In Einstein's theory, the formula for charge density is

$$I_{123}=dg_{12}/dx_3+dg_{23}/dx_1+dg_{31}/dx_2,$$

and it can be calculated immediately from this equation that a charge on a body in the second example is $1/k^2$ as large as the charge on the corresponding body of the first example. One of the bodies remains uncharged; since its acceleration is k times as large as before, and the direction of acceleration is unchanged, the gravitational field of each of the charged masses at the uncharged mass must be k times as large as before. Since they are $1/k$ as far away, their masses must be $1/k$ as large as before to account for their gravitational effect. Since their accelerations have multiplied by k, the force on each of the charged masses is the same as on the corresponding body in the first example. These forces are (1) the Coulomb force of each charged mass on the other, (2) the gravitational force of each charged mass on the other, and (3) the gravitational force of the uncharged mass on the charged bodies. Since the charged bodies have $1/k$ times their original masses and are $1/k$ as far apart, the second force is the same as in the first example. Therefore, the sum of forces (1) and (3) must be the same as before. Since the mass and position of the uncharged body were arbitrary, both forces (1) and (3) must be individually the same as previously. But the charged masses bear charges $1/k^2$ as large as originally and are $1/k$ times as far apart, so that the Coulomb force (1) should be $1/k^2$ as large as originally, and the theory leads to a contradiction with Coulomb's law.

A more general discussion and criticism of this theory will appear in a forthcoming article.

* Present address: Tompkins Corner, New York.

A Comment on a Criticism of Unified Field Theory

ALBERT EINSTEIN
Institute for Advanced Study, Princeton, New Jersey
(Received November 12, 1952)

DR. C. P. Johnson's[1] argument touches upon a point of view of fundamental importance, which deserves a detailed discussion. In order to bring out the essential point, I will first bring up an analogy to the case at hand.

Question: Are the laws of the electromagnetic field invariant with respect to a change of sign of the electric charges, or, equivalently, of the electromagnetic field components? One is inclined to answer this question negatively, on the basis of our empirical knowledge. For, if we find a solution representing an atom with a positively charged nucleus and negatively charged surrounding particles, then there exists also a second solution for which the nucleus is negatively charged, and the particles around it positively charged, in contradiction to empirical results, according to which the nucleus is always positively charged; hence, one concludes that the equations do not possess the invariance property stated above.

This conclusion, however, is unwarranted. In fact, suppose the laws do possess this invariance property; it is possible that the predominance of nuclear charges of the one sign is due to the fact that configurations of opposed charges are unstable in their interactions. This would lead to a situation in which the one sign for the nuclear charge is predominant. A consideration of the mathematical possibilities shows that this alternative explanation (in which the laws possess the above invariance) appears more plausible.

I now turn my attention to the problem in which we are interested here.

In order for a system of field equations to be acceptable from a physical point of view, it has to account for the atomistic structure of physical reality. This comprises two general characteristic features:

(1) the quasi localization of mass (i.e., energy) and electrical charge;

(2) regions of space corresponding to a "particle" have discrete masses and charges. That is to say, if there exist elementary solutions of the equations which depend upon a continuous parameter, then the field equations must prevent the coexistence within one system of such elementary solutions pertaining to arbitrary values of their parameters. If a theory does not possess these two features, that is, if these features do not follow as conclusions from the theory, then the theory is inadmissable.

We now separate all conceivable systems of field equations into two classes, according to whether the individual equations are "homogeneous with respect to degree of differentiation" or not. By "homogeneous" we mean a type of equation such as is exemplified by the gravitational equations of empty space ($R_{ik}=0$). The R_{ik} consist of an aggregate of terms, which are either linear in the second derivatives of g_{ik} or else quadratic in the first derivatives of g_{ik}. We then say that R_{ik} is "homogeneous (of second order) in differentiation with respect to coordinates."

It seems to me that all relativistic systems of equations, which have a unitary structure, i.e., which are not composed of logically independent sets of terms, possess this property of homogeneity; this applies also to the system of equations which I call "generalized gravitational theory."

Now it seems that every such homogeneous system of equations must be incompatible with the requirement (2) given above. This is because any homogeneous system of equations possesses a family of solutions which depend, in a continuous way, on a parameter k. This is, in fact, the property which Johnson has used in his argument.

Let the field variables be denoted by g for short, and let $g(x)$ be a solution of the field equations; then also $g(kx)$ is a solution for any value of k. We refer to such a manifold of solutions as a family of "similar solutions." What is physically important here is the fact that both the mass and the charge of a "particle" vary continuously with k (all solutions being imbedded in the same Minkowski space). It would seem then that such a world, built out of solutions with continuously varying k values, violates the requirement (2).

However, the conclusion is based on the assumption that such solutions, with arbitrarily differing values of k, can coexist in the same world, without destroying each other through their interactions; whereas, it could be, for example, that the interaction terms would introduce inadmissable singularities into the field (this is what happens in the static case of two bodies in the theory of pure gravitation). If, however, the field equations exclude the possibility of coexistence of similar solutions in one and the same world, such an objection to the theory can no longer hold; Johnson's argument cannot be carried out then, for it too is based on the assumption of coexistence of similar solutions.

The above considerations show how careful one has to be in using general arguments to form a reliable judgment about the admissibility of a field theory from the empirical point of view.

[1] C. P. Johnson, Jr., preceding letter [Phys. Rev. **89**, 320 (1953)].

A Slow Component in the Decay of the Scintillation Phosphors

JASPER A. JACKSON AND F. B. HARRISON
Los Alamos Scientific Laboratory, University of California, Los Alamos, New Mexico
(Received November 10, 1952)

WE have measured the fraction of the light emitted by some of the common phosphors, which has a decay constant longer than about 0.5 μsec.[1] The following apparatus was used: The phosphor was held in a beaker lined with aluminum foil, excited by a beam of x-rays, and viewed by an end-window photomultiplier. The x-ray tube may be gated off by applying a negative pulse to its grid. The photomultiplier is normally turned off by making its first dynode 8 v negative with respect to the cathode; it may be gated on by applying a positive square wave to dynode 1. The sequence of events is the following: First the photomultiplier is gated on, then the x-ray tube is gated off, and then the photomultiplier is gated off. The x-ray beam turns back on after 40 μsec. Two photographs were taken of each phosphor, one showing the whole trace, the other with 10 times the gain to show the details in the region just after the x-ray beam is turned off.

The results are given in Table I. The residual signal in the case of the liquid phosphor may have been due to a number of effects, such as after-pulses in the photomultiplier and imperfect cutoff of the x-ray beam, as well as a slow component in the light emission. This measurement gives an upper limit of 0.1 percent for all these effects, and we have therefore neglected them in the analysis of the data for the crystals.

TABLE I. Fraction of the light emitted in the slow component, and its decay time.

	Decay time (μsec)	Percentage of light
Terphenyl in toluene 5 g/l	...	<0.1
Terphenyl crystal	47 ±6	2.5 ±0.2
Trans-stilbene	80 ±10	4.3 ±0.2
Anthracene	47 ±6	5.6 ±0.4
Sodium iodide	220 ±40	5.0 ±0.2

The absence of a slow component in the terphenyl solution, as contrasted with crystalline terphenyl, is probably due to a deformation of potential energy surfaces during collisions in the liquid, which allow a conversion of the excitation energy of the metastable state into thermal energy.[2] The shorter mean life of fluorescence in the liquid is presumed to be due to the same type of process.

[1] Bittman, Furst, and Kallmann, Phys. Rev. **87**, 83 (1952).
[2] M. Kasha, Chem. Revs. **41**, 401 (1947).

Spectral Location of the Absorption Due to Color Centers in Alkaline Earth Halide Crystals

HENRY F. IVEY
Skiatron Electronics and Television Corporation, New York, New York
(Received October 28, 1952)

RECENTLY Smakula[1] has measured the spectral location of the absorption bands induced by x-rays in crystals of CaF_2 (3350A, 4000A, and 5800A) and BaF_2 (3800A, 4800A, and 6700A). His results for CaF_2 are in good agreement with those obtained earlier by Herman and Silverman[2] and later by Barile.[3] Smakula has obtained evidence for a fourth band in both CaF_2 and BaF_2 near 2200A. This additional band was determined by Barile as lying at 2280A in CaF_2, but the exact location in the case of BaF_2 is still not known. Measurements have apparently not been reported for other alkaline earth halides.

Smakula[1] has pointed out that his data do not fit the relationship, νd^2 = constant or $\lambda = ad^2$ (ν = frequency of maximum absorption, λ = the corresponding wavelength, d = lattice constant, and a = constant), obtained by Mollwo[4] experimentally for the case of the F-band in the alkali halides. The same expression has also been obtained theoretically by Fröhlich[5] on the basis of a model for the F-center which is not now generally accepted. The writer[6] has shown, however, that the location of the F, R_1, R_2, M, and V bands in the alkali halides having the NaCl structure can be satisfactorily related to the lattice constant[7] by equations of the general form $\lambda = ad^n$, where a and n are constants for a given band, but n is not necessarily equal to two ($n = 1.84$ for the F, R_1, and R_2 band, 1.56 for the M band, and 1.10 for the U band). Inui and Uemura[8] have also recently considered the dependence of the F-absorption peak in the alkali halides upon the lattice constant from a theoretical viewpoint.

The two constants in the expression $\lambda = ad^n$ can, of course, be determined from Smakula's data for the three bands in CaF_2 and BaF_2. The results of these calculations are

$$\text{I:}\quad \lambda = 614d,$$
$$\text{II:}\quad \lambda = 346d^{1.444},$$
$$\text{III:}\quad \lambda = 833d^{1.144},$$

where λ and d are both in Angstrom units. (For convenience the three bands, starting with that corresponding to shortest wavelengths, and going in the direction of increasing wavelength, have been indicated as I, II, and III.) It would be very desirable if data were available on a third alkaline earth halide to serve as a check on the reliability of the determination of the constants in the above relations, but this is unfortunately not the case.

TABLE I. Location of absorption bands in alkaline earth halides. (Values in parentheses are predicted.)

Compound	Lattice constant (angstroms)	Absorption peak (angstroms) I	II	III
CaF_2	5.451	3350	4000	5800
SrF_2	5.86	(3610)	(4450)	(6310)
BaF_2	6.184	3800	4800	6700
$SrCl_2$	7.00	(4300)	(5740)	(7730)
$BaCl_2$	7.34	(4520)	(6170)	(8170)

Because of the experience with the alkali halides, however, it is believed that the above equations are probably satisfactory for the purpose of predicting the spectral location of the absorption bands in alkaline earth halides of the same fluorite crystal structure as CaF_2 and BaF_2 (cubic, space group O_h^5) which are as yet unmeasured. Of the remaining alkaline earth halides, only SrF_2 and $SrCl_2$ normally possess this crystal structure. Vainshtein[9] has recently reported, however, the existence of the fluorite structure in very thin films of $BaCl_2$. The results of such calculations are shown in the Table I.

[1] A. Smakula, Phys. Rev. **77**, 408 (1950).
[2] R. Herman and S. Silverman, J. Opt. Soc. Am. **37**, 871 (1947).
[3] S. Barile, J. Chem. Phys. **20**, 297 (1952).
[4] E. Mollwo, Nachr. Ges. Wiss. Göttingen, No. 14, 97 (1931).
[5] H. Fröhlich, Z. Physik **80**, 819 (1933).
[6] H. F. Ivey, Phys. Rev. **72**, 341 (1947).
[7] In the equations given in reference 6 for the alkali halides, d actually indicates the interionic distance and not the lattice constant. For the NaCl structure these quantities differ, of course, only by a factor of two.
[8] T. Inui and Y. Uemura, Prog. Theoret. Phys. **5**, 252 (1950).
[9] B. K. Vainshtein, Doklady Akad. Nauk, S.S.S.R. **60**, 1169 (1948).

Purification and Prevention of Segregation in Single Crystals of Germanium

W. G. PFANN AND K. M. OLSEN
Bell Telephone Laboratories, Murray Hill, New Jersey
(Received November 11, 1952)

GERMANIUM ingots of such high purity that they have intrinsic electrical resistivity at room temperature and germanium single crystals having an extrinsic resistivity which is essentially constant in over 80 percent of their volume have been prepared by new techniques. These new experimental results

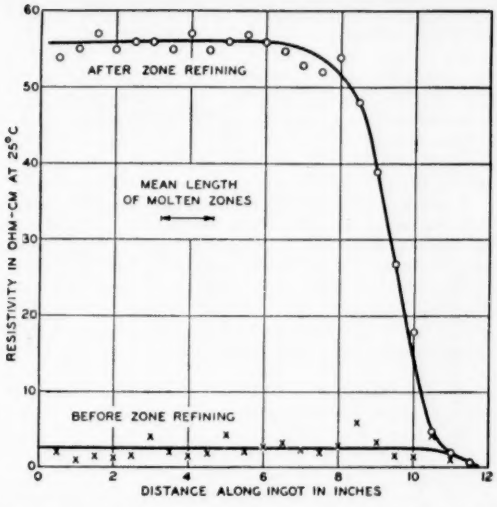
AFTER ZONE REFINING
MEAN LENGTH OF MOLTEN ZONES
BEFORE ZONE REFINING
RESISTIVITY IN OHM-CM AT 25°C
DISTANCE ALONG INGOT IN INCHES

FIG. 1. Electrical resistivity *versus* location in germanium ingot before and after zone refining.

confirm an earlier analysis[1] of the distribution of solutes in an ingot by traveling molten zones.

The purification technique, known as *zone refining*, consists of slowly passing a number of short molten zones through a relatively long solid ingot of the impure substance. Each molten zone which passes through the ingot constitutes a stage of purification. The effect of passing 6 molten zones through an ingot of germanium containing a donor impurity believed to be arsenic is shown by the electrical resistivity curves of Fig. 1. The resistivity after zone refining is very close to intrinsic in about half the ingot. Resistivity

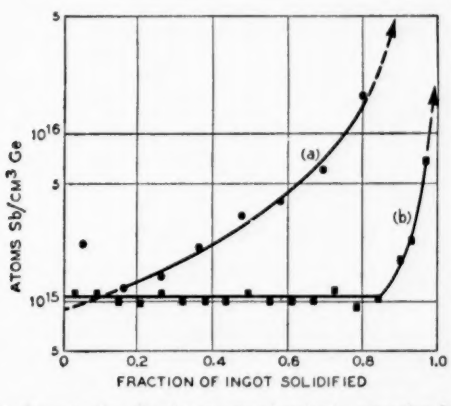

FIG. 2. Concentration of antimony *versus* location in germanium ingots: (a) normally frozen ingot, (b) zone-leveled single crystal ingot.

measurements made at low temperatures by G. C. Dacey indicate that excess donor concentrations of less than 5×10^{12} atoms-cm^{-3} (one donor atom per 10^{10} germanium atoms) have been obtained in such ingots.

By comparing concentrations before and after zone refining an effective distribution coefficient k can be estimated,[1] which for the process of Fig. 1 is roughly 0.2, a value somewhat larger than the equilibrium k of 0.06 reported for arsenic in germanium.[2] The difference in k's may be attributed to nonequilibrium freezing and possibly to contamination during zone refining.

The technique for preventing solute segregation along the freezing direction is one of a number of methods known as *zone leveling*. Solute, in amount to be indicated, is placed at the beginning of a relatively long solid ingot of pure solvent, which in this case is germanium. Heating means are provided for producing a short molten zone at the beginning of the ingot and causing it to travel slowly through the ingot at constant length, l. The solute concentration C in the solid ingot can be shown to decay exponentially according to $C=kC_i\exp[-kx/l]$, where C_i is the initial solute concentration in the molten zone and x is the distance from the beginning of the ingot. This equation is valid in all but the last zone length and shows, for a solute having a very small k, that the concentration decreases very slowly as x/l increases. Thus, for antimony in germanium, for which $k=0.007$, C decreases by about 6 percent in 9 zone lengths, which is in marked contrast to normal segregation, where C *increases* by a factor of about 10 in the first 0.9 of the ingot.

The improvement in uniformity obtainable by zone leveling is illustrated in Fig. 2. Curve (a) is for a polycrystalline ingot of antimony-doped germanium[3] which was entirely melted and then frozen slowly from one end, producing a normal segregation of antimony. Curve (b) is for a single crystal of antimony-doped germanium which was prepared by zone leveling. The crystal was about 7 zone lengths long and it is seen that the concentration is essentially constant in all but the last zone length. To produce a single crystal a short section of a seed crystal abutting the beginning of the starting ingot was melted into the zone at the start.

Techniques of zone melting are not confined to germanium but can be used on metals, salts, and other organic or inorganic substances.

The writers are indebted to Mr. D. Dorsi for preparing the single crystal.

[1] W. G. Pfann, J. Metals **4**, 747 (1952).
[2] Struthers, Theuerer, Buehler, and Burton, American Institute of Mining Engineers Meeting, New York, New York (February 18, 1952).
[3] Pearson, Struthers, and Theuerer, Phys. Rev. **77**, 809 (1950).

The Probable Existence of an $E3+M4$ Mixture in an Isomeric Transition*

R. D. HILL† AND J. W. MIHELICH
Brookhaven National Laboratory, Upton, New York
(Received November 17, 1952)

THE existence of a 14 ± 2 hour 74.2-kev isomeric transition in Os^{191m} has recently been established.[1] The energy of this transition is 0.33 kev above the threshold for K conversion. Lifetime-energy considerations would indicate an isomeric transition (I.T.) involving a spin change of three. The observed[1] $L_I:L_{II}:L_{III}$ ratio (42:25:100) was interpreted on the basis of general L-subshell ratios[2] to mean that the multipolarity was $M3$. Accepting the 7/2+ nature[1] of the Os^{191} ground state then leads to the designation of the isomeric state as $i_{13/2}$.

In following up these conclusions, however, certain discrepancies have arisen. (1) The relative thermal neutron activation cross section for the two levels was obtained by irradiating a sample of Os metal in the Brookhaven reactor for a given time at a known flux and comparing the number of transitions from the isomeric and ground levels by use of β-spectrographs. If one assumes the I.T. to be $M3$ with $K/L=1$, the ratio of formation of isomeric and ground levels (σ_m/σ_g) is found to be $\sim$100. General observations[3] on isomeric ratios show that, usually, a compound nucleus formed by neutron capture (in this case one of spin $\frac{1}{2}$) will decay more readily to a level nearer to it in spin. This is in direct contradiction to the isomeric ratio which we obtain on the assumption of an $M3$ transition. On the other hand, if we designate the I.T. as $E3$ ($K/L=0.1$), the ratio σ_m/σ_g computed from experiment is 5.8, consistent with a $p_{\frac{1}{2}}$ isomeric level. The activation experiments therefore favor an $E3$ isomeric transition assignment. (2) We have measured the ratio R of K x-rays due to internal conversion of the

74.2-kev I.T. and the 129-kev γ-ray of the daughter activity, and find it is $\lesssim 10$. If the I.T. were $M3$, by using the threshold K-conversion coefficient of Spinrad and Keller[4] for the 74.2-kev I.T., our measured K-conversion coefficient of the 129-kev γ-ray ($\alpha_K = 2.0$), and the decay scheme,[1] this ratio R should be >260 and probably ~ 2600, depending on the K/L ratio assumed. (3) The L_{II} conversion is actually more intense than would be expected for an $M3$ I.T.

However, the L subshell conversion ratios are not those expected for an $E3$ transition, on the basis of empirical results obtained for a 130-kev $E3$ I.T. in Au^{197m}.[5] We wish to suggest the following explanation of our results. The transition occurs between the $p_{\frac{1}{2}}$ level and the $7/2+$ ground state and consists of 90 percent $E3$ plus 10 percent $M4$ γ-radiation, (that is, after considering conversion, 73 percent total $E3$ transitions and 27 percent total $M4$ transitions). This assumption makes the L subshell conversion data consistent, as is shown by the analysis in Table I. The

TABLE I. Theoretical and experimental conversion data on the I.T. in Os^{191m}.

	K	L_{tot}	L_I	L_{II}	L_{III}
		Theoretical conversion coefficients.			
$E3$	1.6[a]	177[b]	6	114	57[d]
$M4$	215[c]	5300[e]	1710	170	3420[e]
		Relative intensities			
0.73 $E3$ + 0.27 $M4$[f] (theor.)			45	28	100
Observed[g]	small	large	42	25	100

[a] See reference 4.
[b] M. H. Hebb and E. Nelson, Phys. Rev. **58**, 486 (1940).
[c] Using reference 4 and extrapolating K/L ratio to large Z^3/E.
[d] Estimates of relative L-shell conversion obtained from empirical evidence (see references 2 and 5).
[e] Estimated from N. Tralli and I. S. Lowen, Phys. Rev. **76**, 1541 (1949) and empirical results of reference 2.
[f] Normalized to intensity of $L_{III} = 100$.
[g] See reference 1.

theoretical and empirical conversion coefficients are only very approximate, but are probably sufficiently good to establish the need for mixing the magnetic and electric radiation.

Assuming that 27 percent of the I.T. are $M4$, using the conversion data in Table I, and assuming that $M+N$ conversion is $\frac{1}{3}$ of L conversion, the value of $\tau_\gamma(M4) = 2\times 10^9$ sec is obtained. This is in reasonable agreement with the theoretical value[6] (taking the initial spin $= \frac{1}{2}$)[7] of 8×10^9 sec. The observed value of $\tau_\gamma(E3)$ for the 73 percent $E3$ branch is $\sim 10^3$ times the average observed value for $\Delta I = 3$ transitions of this energy.[7] This apparent mixture is made possible by the slowness of the odd neutron $E3$ I.T. to the compound $7/2+$ level, and is made conspicuous by the extremely large L and M conversion coefficients for an $M4$ I.T. of this energy.

Thanks are due Dr. A. W. Sunyar and Dr. M. Goldhaber for valuable discussion of this problem.

* Work done under the auspices of the U. S. Atomic Energy Commission.
† Permanent address: University of Illinois, Urbana, Illinois.
[1] J. B. Swan and R. D. Hill, Phys. Rev. **88**, 831 (1952).
[2] J. W. Mihelich, Phys. Rev. **87**, 646 (1952).
[3] A. W. Fairhall, Massachusetts Institute of Technology Laboratory for Nuclear Science and Engineering, Progress Report No. 131 (May 31, 1952); E. Segrè and A. C. Helmholz, Revs. Modern Phys. **21**, 271 (1949).
[4] B. I. Spinrad and L. B. Keller, Phys. Rev. **84**, 1056 (1951).
[5] A. de Shalit and J. W. Mihelich, (to be published).
[6] J. Blatt and V. Weisskopf, *Theoretical Nuclear Physics* (John Wiley and Sons, Inc., New York, 1952).
[7] M. Goldhaber and A. W. Sunyar, Phys. Rev. **83**, 906 (1951).

Observation of the $(\gamma,2n)$ Reaction in Ta†

E. A. WHALIN AND A. O. HANSON
Department of Physics, University of Illinois, Urbana, Illinois
(Received November 19, 1952)

LEVINGER and Bethe[1] and later Eyges[2] pointed out that the sharp drop off in the cross section for the (γ,n) reaction in heavy elements as well as the higher neutron yields as measured by Price and Kerst could be quite adequately explained by competition from the $(\gamma,2n)$ reaction. A direct measurement of the $(\gamma,2n)$ reaction in heavy elements has not been made since it has been difficult to find reactions which give satisfactory radioactivities. This report presents the result of measurements in which both the total neutron yield and the (γ,n) radioactivity are measured under the same conditions. The $(\gamma,2n)$ yield is obtained from the difference between the two excitation curves.

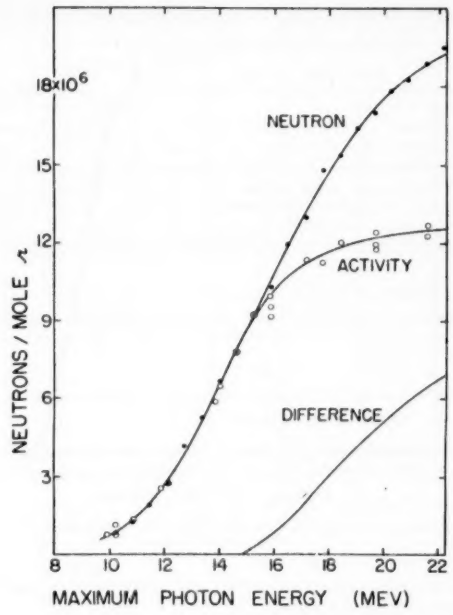

FIG. 1. Ta activation curves.

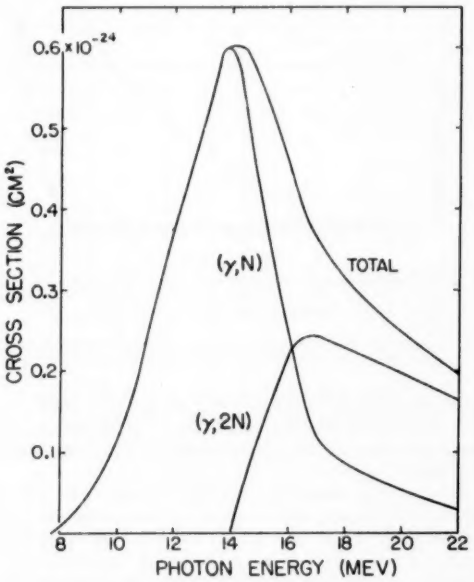

FIG. 2. Ta cross-section curves.

In the present experiment a collimated beam of x-rays from the 22-Mev betatron was used to irradiate a target made up of a stack of 25 Ta foils, each 0.010 inch thick. The Ta target was in the center of a 10-inch cubic cavity in a large pile of boxes of borax. A long BF_3 proportional counter with its axis perpendicular to the beam was surrounded by paraffin, and it closed one side of the cavity. This counter arrangement was designed to have a uniform sensitivity to neutrons in the energy range expected from the Ta. After each irradiation the activity of the middle Ta foil was measured in an arbitrary geometry by a Geiger counter.

The neutron yield and the Ta^{180} activity as a function of the maximum betatron energy are shown in Fig. 1. The neutron yield is normalized using the absolute neutron yield values of Price and Kerst.[3] At low energies the Ta^{180} activation curve is normalized to coincide with the neutron yield curve. The excitation function for the excess neutrons shown in Fig. 1 is obtained by subtracting the smoothed Ta^{180} activation curve from the smoothed neutron yield curve.

Figure 2 shows the cross sections obtained from the smoothed curves of Fig. 1 by the photon difference method of Katz and Cameron. The high energy portions of the cross sections are not very reliable as they are sensitive to the exact shape of the activation curve.[4] The thresholds used are 7.7 Mev for the (γ,n) reaction, and 14.0 Mev for the $(\gamma,2n)$ reaction.

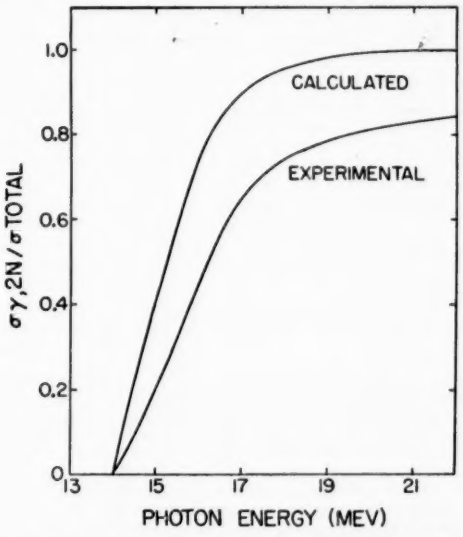

FIG. 3. Fraction of excited Ta nuclei decaying by emission of $2n$, as measured and as calculated by the statistical theory of the compound nucleus.

Figure 3 shows the theoretical and experimental values of the ratio of the $(\gamma,2n)$ to the total cross section. The theoretical values for this ratio were calculated using the statistical model of the nucleus as given by Feld *et al.*[5] where the level density parameter (a) for the Ta^{180} nucleus was taken as 11 Mev^{-1}. Since the experimental determination of this ratio must be considered to have a large error arising from the uncertainty in the (γ,n) cross section at high energies, it can be concluded that the statistical model of the compound nucleus is sufficient to explain the present observations. Since the threshold for the $(\gamma,3n)$ reaction is 22.2 Mev, which is just beyond the maximum energy used, this reaction can have no effect on this work.

The tail of the curve for the total cross section is somewhat higher than that expected by Eyges. If it is correct as shown, the principal effect of the $(\gamma,2n)$ reaction is to increase the width of the curve for the total cross section. It does not appear that this reaction does very much to affect the position of the maximum. Further work is in progress at this laboratory to study these processes more accurately.

† This research has been supported by the joint program of the U. S. Office of Naval Research and the U. S. Atomic Energy Commission.

[1] J. S. Levinger and H. A. Bethe, Phys. Rev. **85**, 577 (1952).
[2] L. Eyges, Phys. Rev. **86**, 325 (1952).
[3] G. A. Price and D. W. Kerst, Phys. Rev. **77**, 806 (1950).
[4] L. Katz and A. G. W. Cameron, Can. J. Phys. **29**, 518 (1951).
[5] Feld, Feshbach, Goldberger, Goldstein, and Weisskopf, U. S. Atomic Energy Commission, Report NYO-636 (1951) (unpublished).

A Li^9 Disintegration in a Photographic Emulsion

W. F. FRY
Department of Physics, University of Wisconsin, Madison, Wisconsin
(Received November 18, 1952)

A GROUP of Ilford C-2 and electron-sensitive G-5 plates were exposed behind absorbers to the negative μ-meson beam of the University of Chicago cyclotron. Among many typical μ-meson stars,[1] a meson-induced star was observed where a low energy fragment caused a small secondary star. A projection drawing of the event is shown in Fig. 1.

FIG. 1. A projection drawing of an event which was found in a G-5 plate exposed to negative μ-mesons. Track 1 is probably the result of a $_3Li^9$ fragment which disintegrated into an electron, track 4; two α-particles, tracks 2 and 3, and a neutron.

Track 1 is 18 microns long. Tracks 2 and 3 are 2.3 and 5.7 microns long, respectively. Track 4 leaves the emulsion after 1460 microns, is minimum ionizing, and exhibits a large amount of small-angle scattering. From the multiple scattering along track 4, the $p\beta$ of the particle was found to be 7.7 ± 2 Mev/c. Since the particle was minimum ionizing, the track most probably was produced by an electron of 7.7 ± 2-Mev energy. The event is very similar to the conventional "hammer" tracks caused by the disintegrations of $_3Li^8$. However, there is an essential difference between a $_3Li^8$ disintegration and the event shown in Fig. 1, in that tracks 2 and 3 (presumably α-particles) are not co-linear and do not have the same range. The residual momentum of the particles which produced tracks 2, 3, and 4 is 69 ± 5 Mev/c. The

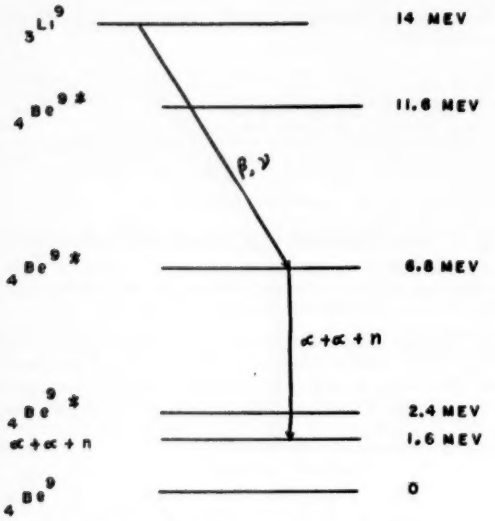

FIG. 2. An energy level diagram of $_3Li^9$ and $_4Be^9$.

range-energy relationship of Wilkins[2] was used to determine the energy of the α-particles. It seems reasonable to assume that the event is the result of the disintegration of $_3Li^9$ which has been reported recently.[3,4] The reaction can be written in the following way:

$$_3Li^9 \rightarrow \epsilon^- + \nu + {}_4Be^{9*},$$
$$_4Be^{9*} \rightarrow \alpha + \alpha + n + Q.$$

The energy released in the break-up of $_4Be^{9*}$ was experimentally found to be 4.4 ± 0.8 Mev for the event shown in Fig. 1. A partial energy level diagram of $_3Li^9$ and $_4Be^9$ is shown in Fig. 2. The difference in the mass of $_3Li^9$ and $_4Be^9$ was obtained by Gardner *et al.*[4] from the threshold of the reaction $_4Be^9(d,2p)_4Li^9$ and the values of the energy levels of the excited states of $_4Be^9$ were measured by Davis and Hafner[5] and by Britten.[6] Since the known excited levels of $_4Be^9$ are widely separated, the measured energy release from the break-up of $_4Be^{9*}$ would strongly indicate that the Be decayed from the 6.8-Mev level.

The author is indebted to Professor H. L. Anderson for the use of the facilities of the Chicago cyclotron and to Mr. A. Rosenfeld for his help in making the exposures.

[1] W. F. Fry, Phys. Rev. **85**, 676 (1952); H. Morinaga and W. F. Fry, Phys. Rev. **87**, 219(A) (1952).
[2] J. J. Wilkins, Atomic Energy Research Establishment (Harwell) Report G/R 664 (unpublished).
[3] Holt, Thorn, and Waniek, Phys. Rev. **87**, 378 (1952).
[4] Gardner, Knable, and Moyer, University of California Report, UCLA 1360 (1952) (unpublished).
[5] K. E. Davis and E. M. Hafner, Phys. Rev. **73**, 1473 (1948).
[6] R. Britten, Phys. Rev. **88**, 283 (1952).

Second Sound Velocity Measurements below 1°K*†

D. DE KLERK,‡ R. P. HUDSON, AND J. R. PELLAM
National Bureau of Standards, Washington, D. C.
(Received October 30, 1952)

RECENT measurements on the velocity of second sound at very low temperatures (obtained by the method of adiabatic demagnetization of a paramagnetic salt, potassium chromic alum, in contact with liquid helium) show the general trends earlier observed by Atkins and Osborne,[1] in that the ultimate low temperature velocity becomes very large. The velocities, however, although alike in trend, differ considerably in magnitude throughout the temperature range below one degree. A warming-up time of the order of 25 minutes permitted the range between (nominally) 0.02°K and 1.1°K to be scanned by the pulse method with ten to twenty measurements for each demagnetization.

Our results agree very well with the measurements of Maurer and Herlin[2] in the range of relatively constant velocity above 0.9°K. The region of steepest slope appears from our measurements to occur between about 0.75°K and about 0.55°K, wherein the curve is roughly linear. We regard our data as sufficiently reliable in the temperature range above about 0.4°K for calculating derived thermodynamic properties for liquid helium II.

Comparison is made in Fig. 1 between our results (solid curve, *A*) and the earlier work of Atkins and Osborne (dashed curve). Actually the discrepancy between these two curves is not surprising. It seems unquestionable that their very large heat-leak (the warm-up time being only 1 minute) would cause the liquid helium to be always at a higher temperature than that of the bulk of the salt,[1,3] with the most marked effect at the lowest temperatures. Thus their lowest helium temperatures might well have been as high as 0.2–0.3°K rather than the 0.12°K suggested by the magnetic thermometer, with a corresponding temperature discrepancy throughout their warm-up represented by the horizontal displacement between the two sets of points (Fig. 1).

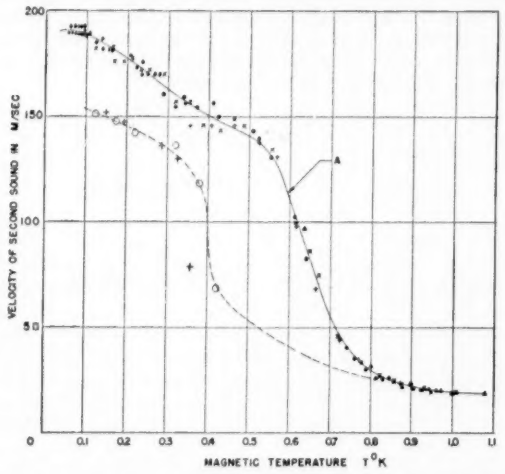

FIG. 1. Second sound velocity *versus* temperature. Effective pulse-front velocities for 80-μsec dc pulses. Solid curve *A* ——— and associated points: our results [different symbols for separate demagnetizations]. Dashed curve - - - - and associated points: Atkins and Osborne's results. Since our curve is plotted *versus* "magnetic temperature," our lowest temperature points actually correspond to about 0.02°K true thermodynamic temperature.

Below 0.4°K our second sound velocity measurements show a further increase to an ultimate value of about 192 m/sec. There are several possible explanations of this anomalous behavior.

a. The effect may represent a real property of second sound propagation in liquid helium II, occurring at the new low temperatures below 0.3°K reached for the first time in these experiments.

b. The effect might be a shock-wave phenomenon,[4] in which case the "excess" wave velocity would presumably be the particle velocity v_n of the normal fluid. Even for small heat input, such shock-wave effects could become serious at the lowest temperatures where the low heat content of liquid helium II would necessitate large normal fluid velocities, and might be expected for our experimental conditions below about 0.35°K. The ultimate limit of such effects at the lowest temperatures would be an unavoidable "apparent velocity" of Landau's[5] $\sqrt{3}v_2$ value for first sound at absolute zero.

c. Both Ward[6] and Gorter[7] have suggested the possibility of long phonon mean free path length effects[8] occurring at these temperatures, making the observed results dependent upon the particular geometry employed. As pointed out, such effects would result in velocity measurements dependent upon pulse transit

distances. Also, as for shock-waves, first sound velocities would ultimately be observed for second sound pulse front arrivals (but dependent upon geometry rather than heat current input).

As first observed by Pellam and Scott[9] at 0.75°K and later by Atkins and Osborne[1] at lower temperatures, the received signals were found to be very much broadened, suggesting a dispersion effect.[1,9] If this represents a true property of liquid helium, independent of the apparatus, then predictions which take no account of dispersion must be theoretically inadequate. We shall give quantitative information in our final publication showing that, on the dispersion hypothesis, frequencies corresponding to the tail of the pulse travel at velocities several times slower than those constituting the pulse-front. Appreciable differences persist even at temperatures as high as 0.9°K. Clearly monochromatic velocity measurements are needed for the low temperature region.

Actually the results reported here were obtained by applying pulsed CW 22.5 kc/sec electrical signals to the heater generating the second sound. Since we employed no receiver frequency-discrimination, however, the resultant 45 kc/sec second sound signals were indistinguishable above the background dc component of the signal resulting from the current-squared (i.e., I^2R) heater output. Accordingly the measurements of Fig. 1 correspond to the wave-front velocity of the associated square wave pulses (our 80-μsec and 250-μsec duration pulses, bracketing Atkins' and Osborne's 100-μsec pulse duration, gave consistent pulse front velocities at the lowest temperatures).

On the other hand, when employing pulsed CW 7.5 kc/sec electrical signals (250-μsec duration), a "hump" appeared superposed on the mid-portion of this dc background envelope. The leading edge of this hump would correspond to a velocity for the associated 15-kc/sec second sound of the order of 100 m/sec (at the lowest temperatures).

Prior to publication of the final paper, wave velocities will be remeasured in the 0.02°K–0.4°K range at lower pulse input levels, in order to clarify the situation regarding possible shock-wave effects.

Note added in proof: Professor Kramers,[10] in a final paper just published, had concluded that the decrease in second sound velocity should occur "at the same temperature as the increase above aT^3 of the specific heat" (i.e., in neighborhood of 0.65°K). The results reported above appear to substantiate Professor Kramers' viewpoint very well.

* Supported in part by the U. S. Office of Naval Research.
† Presented at the joint Office of Naval Research—National Science Foundation Cryogenics Conference, Schenectady, N. Y., October 6, 1952.
‡ On leave of absence from the University of Leiden, Leiden, Holland.
[1] K. R. Atkins and D. V. Osborne, Phil. Mag. **41**, 1078 (1950).
[2] R. D. Maurer and M. A. Herlin, Phys. Rev. **76**, 948 (1949).
[3] R. P. Hudson, Proc. Int. Conf. M.I.T., p. 63 (1949), (unpublished).
[4] D. V. Osborne, Proc. Phys. Soc. (London) **A64**, 114 (1951).
[5] L. Landau, J. Phys. (U.S.S.R.) **5**, 71 (1941); **11**, 91 (1947).
[6] J. C. Ward (private communication).
[7] C. J. Gorter, Phys. Rev. **88**, 681 (1952).
[8] Similar suggestions were made by V. Mayper and M. A. Herlin during a paper presented by them on this same subject.
[9] J. R. Pellam and R. B. Scott, Phys. Rev. **76**, 869 (1949).
[10] H. A. Kramers, Physica **18**, 653 (1952).

Negative Primaries as Part of Cosmic Radiation

B. Bhowmik
Department of Physics, University of Delhi, Delhi, India
(Received November 4, 1952)

THE low value of the observed east-west asymmetry has always raised suspicion concerning the existence of negatively charged particles in the primary cosmic radiation. Since mesons are absent because of their unstability, and experimental evidence[1,2] is available to show the absence of any significant amount of electrons, the presence of a negative heavy component would raise a very fundamental question, i.e., the existence of anti-matter. From a critical analysis of the experimental data on the azimuthal intensity variation, we find that these data are consistent with the primary radiation containing 20 percent negatively charged particles.

TABLE I. Azimuthal variation at $\lambda=0°$, $Z=40°$.

Magnetic azimuth α	$E(\alpha Z)$ millistormer	$I(\alpha Z)$ A calculated $\gamma=2.2$ $\sigma=\infty$	B calculated $\gamma=2.2$ $\sigma=4$	C observed at height of 24 g cm^{-2}	D calculated $\gamma-m=1.686$ $\sigma=\infty$
0	528	10.000	10.000	10.000	10.000
30	578	8.048	8.952	8.889	8.833
60	625	6.670	8.296	8.222	7.932
90	642	6.255	8.052	8.000	7.647
120	625	6.670	8.296	8.444	7.932
150	578	8.048	8.952	9.333	8.833
180	528	10.000	10.000	10.667	10.000
210	480	12.570	11.666	11.778	11.400
240	448	14.800	13.174	12.884	12.510
270	443	15.240	13.443	13.334	12.720
300	448	14.800	13.174	13.111	12.510
330	480	12.570	11.666	12.222	11.400

We assume the differential energy spectrum to be $K/E^{\gamma}dE$, in conventional units, and we denote by σ the ratio of the positive to the negative primary radiation. The latitude effect and the north-south asymmetry depend entirely on γ and are independent of σ. We take $\gamma=2.2-2.1$ from the latitude effect of the primary particles observed by Winckler *et al.*[3] In Table I the calculated

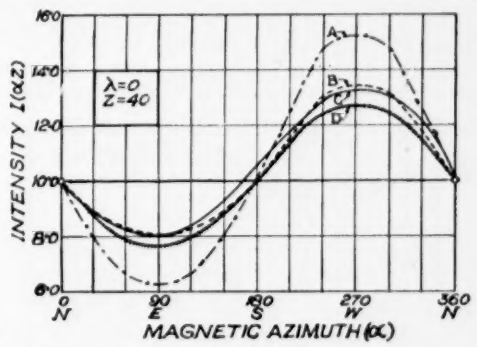

FIG. 1. Azimuthal variation of primary cosmic rays at $\lambda=0$, $Z=40°$. The theoretical curves are A: $\gamma=2.2$, $\sigma=\infty$; B: $\gamma=2.2$, $\sigma=4$; and D: $\gamma-m=1.686$, $\sigma=\infty$. C is the experimental curve at a depth of 24 g cm^{-2}.

intensity $I(\alpha Z)$ for a given magnetic azimuth α and zenith angle Z is given,[4] taking the minimum energy of arrival for the main cone.[5] The intensity due north is taken as 10.000, and all the experimental data are reduced accordingly for convenience of comparison.

In Fig. 1 the results are shown graphically for $\lambda=0$, $Z=40°$. The experimental data of Winckler *et al.* at a depth of 24 g cm^{-2} (curve C) shows poor agreement with the calculated intensity for primary radiation which is entirely positively charged (curve A). The

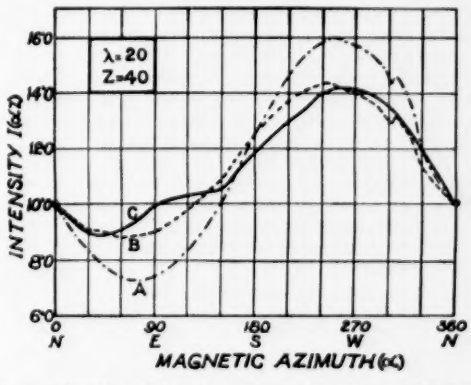

FIG. 2. Azimuthal variation of primary cosmic rays at $\lambda=20$ N, $Z=40°$. The theoretical curves are A: $\gamma=2.1$, $\sigma=\infty$; B: $\gamma=2.1$, $\sigma=4$. C is the experimental curve at a depth of 15 g cm^{-2}.

calculated intensity for $\sigma=4$ (curve B) shows excellent agreement. One can assume, however, that the multiplicity in the atmosphere is given by $M=JE^m$. This reduces the effective value of the exponent to $\gamma-m$. We choose $\gamma-m=1.686$ to get agreement with the observed east-west asymmetry. The curve D for $\sigma=\infty$ obtained after introducing multiplicity does not show good agreement with the experimental curve B, though both the curves D and B have same east-west asymmetry.

For $\lambda=20$, because of the asymmetry of the allowed cones about the east-west plane, the superposed azimuthal curve for mixed primaries is very much different from the curve for primary radiation which is entirely positively charged. In Fig. 2 we show the results of our calculations for $Z=40°$ and compare them with the experimental data of Winckler *et al.* As before, the agreement with the experimental curve (C) is excellent for 20 percent negatively charged primaries (B) and is very poor for primaries which are entirely positively charged (A).

In Fig. 3(a) we plot the azimuthal effect at sea level calculated after introducing multiplicity in the atmosphere (dotted line). As already pointed out, the north-south asymmetry is independent of σ, and this is a guide to the estimation of $\gamma-m$. For $\lambda=20$ N, $Z=20°$, we take $\gamma-m=1.35$–1.60 and $\sigma=4$. The agreement with the unpublished data of Bhowmik and Bajwa[6] for $\lambda=19$ N is very good. The hump at 285° is the result of the contribution from the penumbra.[7]

In Fig. 3(b) the results calculated for $\lambda=20$ N, $Z=40°$, after taking into account the absorption in the atmosphere, have been

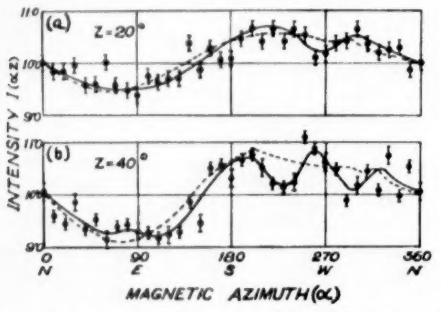

FIG. 3. Azimuthal variation at sea level. (a) The dotted line is the theoretical curve for $\gamma-m=1.35-1.60$, $\sigma=4$ for $\lambda=20$ N, $Z=20°$. The solid line is the experimental curve at $\lambda=19$ N, $Z=20°$. (b) The dotted line is the theoretical curve for $\gamma-m=1.3-1.5$, $\sigma=4$ for $\lambda=20$ N, $Z=40°$. The solid line is the experimental curve at $\lambda=19$ N, $Z=40°$.

plotted. We presume that mesons produced by primary radiation of energy 438 millistormer and less have insufficient range to reach the recording apparatus at sea level. This assumption levels off the general maximum in the west to a flat plateau between 200° and 290°. The inclusion of a 20 percent negative component produces a little depression within this region. The dotted line has been computed for $\sigma=4$ and $\gamma-m=1.3$–1.5. The agreement with the unpublished experimental curve of Bhowmik and Bajwa[8] for $\lambda=19$ N is very good. The hump at 310° is the result of the penumbra, and the agreement in this part is excellent. However, there are two other humps at 190° and 260°, with a minimum at 230° in the experimental curve. The inclusion of a negative component explains only this depression, qualitatively.

The present analysis clearly indicates a very powerful method of deciding about the existence of negative primaries. A detailed account of the present work will be published shortly in the *Indian Journal of Physics*.

[1] R. I. Hulsizer, Phys. Rev. **76**, 164 (1949).
[2] Critchfield, Ney, and Oleska, Phys. Rev. **79**, 402 (1950).
[3] Winckler, Stix, Dwight, and Sabin, Phys. Rev. **79**, 656 (1950).
[4] G. Lemaitre, and M. S. Vallarta, Phys. Rev. **50**, 493 (1936).
[5] Vallarta, Perusquia, and de Oyarzabal, Phys. Rev. **71**, 393 (1947).
[6] This work was supported by the Atomic Energy Commission, Government of India.
[7] R. A. Hutner, Phys. Rev. **55**, 614 (1939).
[8] A preliminary report was given by B. Bhowmik and G. S. Bajwa, Phys. Rev. **87**, 530 (1952).

Relation Between the Photoproduction and Scattering Cross Sections for π-Mesons in Complex Nuclei*

NORMAN C. FRANCIS AND KENNETH M. WATSON
Indiana University, Bloomington, Indiana
(Received November 17, 1952)

THE cross sections for photoproduction of charged π-mesons in nuclei of mass number $A\geq 10$ have been experimentally found to vary as $A^{\frac{2}{3}}$.[1,2] Furthermore, several experimental studies[3,4] of the inelastic scattering and absorption cross section of π-mesons in nuclei have indicated that this is nearly equal to nuclear area for the same range of values for A. These results suggest a short mean free path λ for nuclear interaction of the pion; however, a careful analysis by Byfield *et al.*[5] and by Steinberger[6] of their own scattering experiments have indicated that $\lambda=8\times10^{-13}$ cm. Consequently, the question has been raised[6,7] whether the A-dependence of the photo cross section can be interpreted as due to the reabsorption of produced mesons.

Such analyses (as well as the concept of a mean free path) and interpretations have been based on the "optical model." Our present purpose is to argue that the A-dependence of the photo and scattering cross sections does not seem to be inconsistent with the optical model. We do not consider the question of the validity of the optical model.

The optical model describes the interaction of the meson with the nucleus by the complex potential,

$$V=[V_0-iv_\pi/2\lambda]\rho(\mathbf{z}), \tag{1}$$

where V_0 is the "real well depth" and $\rho(\mathbf{z})$ is the density of nucleons in the nucleus normalized to

$$\int\rho(\mathbf{z})d^3z=V_A, \tag{2}$$

the volume of the nucleus. v_π is the velocity of the meson. The Schrödinger equation to describe the scattering of the meson is

$$[h+V]\varphi_q(\mathbf{z})=E\varphi_q(\mathbf{z}), \tag{3}$$

where q is the momentum of the incoming meson and h is the kinetic energy operator for the meson.

The solution to the complex conjugate of Eq. (3) is $\varphi_q^-(\mathbf{z})$, where

$$\varphi_q^-(\mathbf{z})=\varphi_{-q}^*(\mathbf{z}) \tag{4}$$

("$-q$" means "$-\mathbf{q}$"). φ_q^- and φ_q have the same initial boundary conditions, but φ_q^- has converging whereas φ_q has diverging scattered waves.

We describe the photoproduction of a meson from the lth nucleon by

$$H_l'=N_l\delta(\mathbf{z}-\mathbf{z}_l), \tag{5}$$

where $\mathbf{z}$ is the meson coordinate and $\mathbf{z}_l$ is the coordinate of the lth nucleon. N_l is assumed independent of $\mathbf{z}$ and to depend upon $\mathbf{z}_l$ through a phase factor only. This assumption localizes the photoproduction to the vicinity of the lth nucleon and enables us to apply the optical model in a simple manner.

Treating H_l' as a small perturbation, the transition operator for the photoproduction of a meson with momentum $\mathbf{q}$ is[8]

$$T_l=(\varphi_q^-(\mathbf{z}),H_l'(\mathbf{z}))=N_l[\varphi_q^-(\mathbf{z}_l)]^*. \tag{6}$$

The cross section for photoproduction from the entire nucleus is

$$\frac{d\sigma_\pi}{d\Omega}=2\pi\rho_f\sum_l\int|T_l|^2\frac{\rho(\mathbf{z}_l)}{V_A}d^3z_l, \tag{7}$$

where ρ_f is the density of final meson states and $|T_l|^2$ is averaged over the *probability distribution* of the positions of the lth nucleon in the nucleus. We neglect interference between meson waves produced by *different* nucleons in Eq. (7). To compare $d\sigma_\pi/d\Omega$ with the data of Littauer and Walker,[2] we take this to be the sum of the positive and negative pion cross sections.

We now write (it being supposed that the appropriate spin and polarization averages have been performed)

$$2\pi\rho_f|N_1|^2=(d\sigma_f/d\Omega)\eta, \tag{8}$$

where $d\sigma_f/d\Omega$ is the corresponding free nucleon cross section averaged over neutrons and protons in the nucleus. η is a factor which accounts for the modification of the free particle cross sections due to nuclear binding effects. Replacing the Σ_l by A, Eq. (7) becomes

$$\frac{d\sigma_\pi}{d\Omega}=\left(\frac{d\sigma_f}{d\Omega}\eta\frac{A}{V_A}\right)\int|\varphi_{-q}(\mathbf{x})|^2\rho(\mathbf{x})d^3x. \tag{9}$$

We do not expect η to show any pronounced A-dependence, so we consider it to be just a constant parameter (presumably $0<\eta<1$).

To find the absorption cross section, we use the meson continuity equation,

$$\nabla\cdot\mathbf{j}+\partial P/\partial t=-2(\mathrm{Im}V)P, \tag{10}$$

where $P=|\varphi_q(\mathbf{z})|^2$ is the meson density. The term on the right represents the absorption rate per unit volume. Integration over

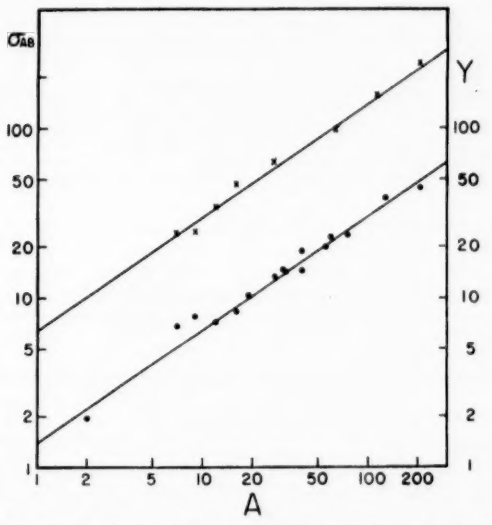

FIG. 1. The circles and x's represent charged meson photoproduction (see reference 2) and π^- absorption (see reference 4) cross sections, respectively. The straight line in each case is the $A^{\frac{2}{3}}$ law. The charged photoproduction yield Y is normalized to give 1.04 for the hydrogen yield, and the absolute absorption cross section may be obtained by multiplying σ_{AB} by 10^{-28} cm^2.

the nuclear volume gives the total absorption rate W.[9] The imaginary part of V is obtained from Eq. (1), so the absorption cross section is

$$\sigma_{AB}=\frac{W}{v_\pi}=\frac{1}{\lambda}\int|\varphi_q(\mathbf{z})|^2\rho(\mathbf{z})d^3z. \tag{11}$$

Since the integrals of Eqs. (9) and (11) are independent of the direction of $\mathbf{q}$, we obtain, by eliminating the integral from these equations,

$$\frac{d\sigma_\pi}{d\Omega}=\left(\frac{d\sigma_f}{d\Omega}\eta\lambda\frac{A}{V_A}\right)\sigma_{AB}, \tag{12}$$

where (by our assumption that η is independent of A) the only A-dependence comes from σ_{AB}. Equation (12) permits comparison of the photoproduction and absorption experiments without detailed calculation.

The experimental measurement[4] of σ_{AB} included both absorption and inelastic scattering, whereas Littauer and Walker measure all emitted charged mesons at a given angle and energy. Energy-momentum considerations and the observation that absorption seems to predominate over inelastic scatterings at the energies considered imply that no very serious error is involved through the use of Eq. (12) to compare the two experiments.

In Fig. 1 the A-dependence of the photoproduction[2] of 50–80 Mev charged π-mesons and the absorption[4] of 85-Mev π^- mesons are compared. Both the photoproduction and the absorption are seen to have approximately the same A-dependence in agreement with Eq. (12). Inserting $(d\sigma_\pi/d\Omega)$, $(d\sigma_f/d\Omega)$, and σ_{AB} obtained from Fig. 1, we obtain

$$\lambda\eta=2.6\times10^{-13}\text{ cm}.$$

If the interaction mean free path in nuclei, λ, is 10^{-12} cm, $\eta=0.26$; if $\lambda=0.5\times10^{-12}$ cm, $\eta=0.52$. These values of η are reasonable and indicate that Eq. (12) is in satisfactory agreement with experiment.

* Supported in part by a grant from the National Science Foundation.

[1] R. F. Mozley, Phys. Rev. **80**, 493 (1950).
[2] R. M. Littauer and D. Walker, Phys. Rev. **86**, 838 (1952).
[3] Byfield, Kessler, and Lederman, Phys. Rev. **86**, 17 (1952).
[4] Chedester, Isaacs, Sachs, and Steinberger, Phys. Rev. **82**, 958 (1951).
[5] J. Steinberger (private communication).
[6] R. R. Wilson, Phys. Rev. **86**, 125 (1952).
[7] S. T. Butler, Phys. Rev. **87**, 1117 (1952).

[8] Equation (6) is of the usual form for transition rates using first-order perturbation theory. A more detailed analysis using multiple scattering theory leads to this result and to Eq. (9) [see K. M. Watson, Phys. Rev. **88**, 1163 (1952)].

[9] M. Lax, Phys. Rev. **78**, 306 (1950) has given a more general proof of this.

Photoproduction of Neutral Mesons in Hydrogen*

Y. GOLDSCHMIDT-CLERMONT, L. S. OSBORNE, AND M. B. SCOTT†
Laboratory for Nuclear Science, Massachusetts Institute of Technology, Cambridge, Massachusetts

(Received November 10, 1952)

THE photoproduction of neutral mesons in hydrogen has been investigated by observing the recoil protons in nuclear emulsions.

The gamma-ray beam from the MIT synchrotron, operating at 320 Mev, was passed along the axis of a cylindrical chamber containing hydrogen at 655 psi and −60°C. The beam entered and left the chamber through thin aluminum windows. Eight stacks of five nuclear emulsions, each 600μ thick, were held in position halfway along the chamber on a suitable holder, and were protected against the electromagnetic background originating in the windows by lead collimators. The geometry allowed protons making an angle of more than 8° with the beam to be recorded in the emulsion stacks. The lowest energy protons could not be observed because of the stopping power of the gas.

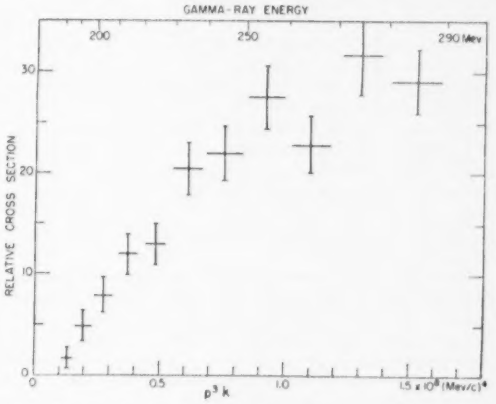

FIG. 1. Photoproduction of neutral mesons on hydrogen. Excitation curve for the emission of the neutral meson between 53° and 143° in the center-of-mass frame. The curve is expected to be proportional to p^3k in the low energy region for emission of the meson in a P state.

The 600μ nuclear emulsions of type Ilford G5 were developed by the temperature development method so as to permit an easy detection of the highest energy protons (120 Mev) produced in the photomeson process. The scanning was systematic and with less than 3 percent loss. For each track in a total of 1080 found in an area of 6.7 cm^2, the angle with the gamma-ray beam was measured and the energy was calculated from the total range in the successive emulsions of the stack and in the gas. The reaction being a two-body process, the conservation laws enable one to calculate from these data (and from the known value of the π^0 rest mass) the center-of-mass angle and momentum of the π^0 meson together with the energy of the incident photon. The error of each individual track is evaluated to be $\pm 5°$ in angle and ± 10 Mev in γ-ray energy.

The occurrence of background proton tracks was detected by examining the region of angles and energies where photomesons are not emitted. Their intensity and angular distribution[1] identified them as coming from γ, p reactions in the 0.5 percent (by volume) oxygen and nitrogen impurities in the hydrogen gas. By extrapolation, using the measured angular distribution,[2] they were found to amount to about 10 percent of the tracks in the region where the photomeson protons are found, and subtracted out. Similarly, all other sources of background could be ruled out, including the proton Compton effect for which an upper limit of the cross section can be set at 5 ± 5 percent of the neutral meson cross section. The theoretical estimate is, of course, even smaller.

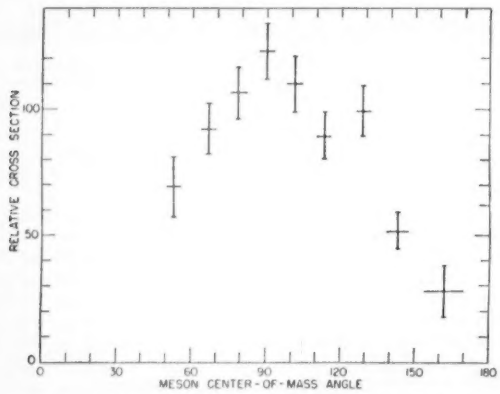

FIG. 2. Center-of-mass angular distribution for the production of neutral mesons on hydrogen by γ-rays from the bremsstrahlung of 320-Mev electrons. The forward angles correspond to protons stopped by the hydrogen gas, and cannot be observed in this experiment.

The excitation curve is given by Fig. 1 *versus* the quantity p^3k, where p and k are the momentum of the meson and the gamma-ray, respectively, in the center-of-mass frame. In computing these data, the bremsstrahlung spectrum was calculated by the Heitler formula and corrected for absorption along the beam and for the finite energy resolution of the measurements. The angular distribution in the center-of-mass frame is shown by Fig. 2. It is found to be symmetrical with respect to $90\pm 2°$. When examined separately in the low and high energy region, the angular distribution retains this symmetry. The best fit to an $a+b\sin^2\theta$ law gives $b/a=5\pm 3$.

The threshold of the reaction is found by extrapolating the excitation curve to zero. From its value, the rest mass of the π^0 meson can be calculated and it should match with the value used for the laboratory to center-of-mass transformation. Doing this transformation with various assumptions on the π^0 rest mass, the best match was found for $m_{\pi^0}=130\pm 10$ Mev. This measurement of the π^0 rest mass is not free from rather arbitrary assumptions, it would not hold for instance if the excitation curve plotted against p^3k showed an appreciable curvature in the low energy region.[3]

Our results are, on the whole, not inconsistent with those obtained by other methods.[4–6] They are in good agreement with the phenomenological theory of Brueckner and Watson[3] based on the existence of an intermediate excited state of the nucleon with spin $\frac{3}{2}$ and isotopic spin $\frac{3}{2}$ which predicts a $1+1.5\sin^2\theta$ angular distribution and a p^3k excitation curve near threshold. They seem to disagree with the predictions of the perturbation approximation.[7] The symmetry of the angular distribution with respect to 90° is interpreted as an indication of a very small effect of the nucleon recoil. It was pointed out to us by Feld[8] that both a p^3k excitation curve and a $1+1.5\sin^2\theta$ angular distribution can be deduced from conservation laws assuming a pseudoscalar π^0 meson, a magnetic dipole interaction of the gamma-ray, and an intermediate state of the nucleon with spin $\frac{3}{2}$ (no assumption on the isotopic spin).

In an attempt to observe a resonance in the excitation curve[3] a new exposure was taken at higher synchrotron energy. The scanning of the plates is in progress.

The authors are grateful to J. S. Clark and to many other members of the synchrotron group for much help during the exposures, and for many valuable discussions. One of them (Y.G.C.) wishes to thank the Centre de Physique Nucleaire, University of Brussels, for support during the early stages of the experiment.

* The work described was supported in part by the joint program of the U. S. Office of Naval Research and the U. S. Atomic Energy Commission.
† Now with the Texas Company, Geophysical Laboratory, Bellaire, Texas.

[1] R. Littauer and J. Keck, Phys. Rev. **86**, 105 (1952).
[2] C. Levinthal and A. Silverman, Phys. Rev. **82**, 822 (1951).
[3] K. A. Brueckner and K. M. Watson, Phys. Rev. **86**, 923 (1952).
[4] Panofsky, Steinberger, and Steller, Phys. Rev. **86**, 180 (1952).
[5] A. Silverman and M. Stearns, Phys. Rev. **83**, 853 (1951).
[6] G. Cocconi and A. Silverman (private communication).
[7] M. F. Kaplon, Phys. Rev. **83**, 712 (1951).
[8] See following Letter by B. T. Feld [Phys. Rev. **89**, 330 (1953)].

The Angular and Energy Distributions in Photomeson Production*

BERNARD T. FELD
Physics Department and Laboratory for Nuclear Science, Massachusetts Institute of Technology, Cambridge, Massachusetts

(Received November 10, 1952)

THE experiments[1] on the production of neutral π-mesons by the reaction $\gamma+p\rightarrow p+\pi^0$, as well as the known features of positive π-meson photoproduction, appear to be describable in terms of a phenomenological (isobar) theory as developed by Brueckner and Watson.[2] However, since their theory adopts certain features of various meson field theories, it is of interest to consider the extent to which it may be possible to extract from the experimental information those aspects which are independent of any special meson theory. It must be emphasized in advance that all of the results of the following considerations are contained, either implicitly or explicitly, in the paper of Brueckner and Watson. It is perhaps worth while, however, to restate some of their results in a different form which may help to emphasize the general character of the conclusions and to highlight their physical significance.

In particular, as is well known, it can easily be demonstrated by the methods first developed by Hamilton[3] that, provided a reaction goes through an intermediate state of definite angular momentum, the angular distribution of the reaction products is independent of most of the specific features of the interaction. Let us consider the reaction $\gamma+p\rightarrow p+\pi^0$. Suppose that the proton absorbs a magnetic-dipole γ-ray ($l_\gamma=1$, no parity change) and goes to an intermediate state of $J=\frac{3}{2}+$. (The positive parity is with respect to the parity of the proton.) The decay of the intermediate state, to a proton and π^0 meson, requires that the meson be in a p-state ($l_\pi=1$), since the π-meson is known to have negative parity with respect to the proton (pseudoscalar) and since the next highest possible value of l_π, three units of angular momentum, could not

lead to the $j=\frac{1}{2}$ of the proton from a state of $J=\frac{3}{2}+$. Following the method of Hamilton, which permits the angular distribution to be expressed in terms of the most general quantum-mechanical features of angular momentum vectors, we take the incident γ-ray to define the z axis. The angular distribution of the reaction is then given by

$$W(\theta)=\sum_{m_i}\sum_{m_\pi}\sum_{m_\gamma}|a(j_i l_\gamma; J; j_f l_\pi)\times(j_i, m_i; l_\gamma, m_\gamma|j_i, l_\gamma; J, m=m_i+m_\gamma)\mathfrak{D}_{l_\gamma}{}^{m_\gamma}(0)\times(j_f, l_\pi; J, m/j_f, m-m_\pi; l_\pi, m_\pi)Y_{l_\pi}{}^{m}\ (\theta,\varphi)|^2, \quad (1)$$

where a is the matrix element (amplitude) for the reaction; $\mathfrak{D}$ and Y are the vector and ordinary spherical harmonics, respectively; $j_i=\frac{1}{2}$, m_i represents the initial proton state, $j_f=\frac{1}{2}$, m_f the final proton state, J, m the intermediate state angular momentum quantum numbers; and $(j_1, m_1, j_2, m_2/j_1, j_2; J, m=m_1+m_2)$ are the Clebsch-Gordon coefficients, tabulated by Condon and Shortley.[4] These calculations have been carried out for a number of possibilities and the results are given in Table I. Also given in the last column of Table I is the expected dependence of the cross section, or $|a|^2$, near threshold on the momentum, p, of the π-meson in the c.m. system (i.e., neglecting the dependence on γ-ray energy). An interesting feature of the above results is that $W(\theta)$ depends only on the values of J and l_γ. This is easily understood if one considers the inverse process; an incident π-meson along the z axis cannot alter the m-value of the system and therefore, irrespective of the value of l_π, leads always to the same intermediate states.

TABLE I. Angular and energy distributions in the photoproduction of π-mesons on nucleons.

γ-ray absorbed	Intermediate state	l of π-meson	$W(\theta)$	π-momentum dependence
Mag. dipole	$1/2+$	1	constant	p^3
Mag. dipole	$3/2+$	1	$2+3\sin^2\theta$	p^3
Elect. dipole	$1/2-$	0	constant	p
Elect. dipole	$3/2-$	2	$2+3\sin^2\theta$	p^5
Elect. quad.	$3/2+$	1	$1+\cos^2\theta$	p^3
Elect. quad.	$5/2+$	3	$1+6\cos^2\theta-5\cos^4\theta$	p^7

The ambiguity can, of course, be resolved by an observation of the energy dependence of the cross section near threshold. In the case of π^0 production, this turns out experimentally to be $\propto p^3$ of the meson (in the c.m. system) which, taken together with the angular distribution, indicates that the process is magnetic dipole absorption to a $J=\frac{3}{2}+$ intermediate state. In the case of π^+ production there is, however, strong indication of a first power p-dependence near threshold, which requires electric dipole absorption to a $\frac{1}{2}-$ intermediate state.

As can be seen from Table I, there are a variety of possible reactions, even if we confine ourselves to dipole-absorption processes. Furthermore, if more than one of these processes occurs in the same reaction, it is possible to have interference effects.[5] We confine our attention to two possibilities only: magnetic dipole absorption to $J=\frac{3}{2}+$, and electric dipole absorption to $J=\frac{1}{2}-$. The expected angular distribution is, then,

$$W(\theta)=|a|^2+2\,\mathrm{Re}(ab^*)\cos\theta+\tfrac{1}{2}|b|^2(2+3\sin^2\theta), \quad (2)$$

where b and a are, respectively, the amplitudes for the two processes.[6]

Now, the above analysis appears, at first sight, not to allow for the experimentally observed difference between π^0 and π^+ production on protons, since angular momentum considerations alone do not distinguish between the charge states of the meson and nucleon. Here, we can invoke the assumption of charge independence which introduces an additional quantum number into the system—the isotopic spin. The two reactions,

$$\gamma+p\rightarrow p+\pi^0$$

and

$$\gamma+p\rightarrow n+\pi^+,$$

differ only in the relative amplitudes of the final state wave function in the isotopic spin $\frac{3}{2}$ and $\frac{1}{2}$ components. In general, the reaction amplitudes are

$$a_J(\pi^0)=(\sqrt{\tfrac{2}{3}})a_{J,T=\frac{1}{2}}+(\sqrt{\tfrac{1}{3}})a_{J,T=\frac{3}{2}} \quad (3a)$$

for the first reaction, and

$$a_J(\pi^+)=(\sqrt{\tfrac{1}{3}})a_{J,\frac{1}{2}}-(\sqrt{\tfrac{2}{3}})a_{J,\frac{3}{2}} \quad (3b)$$

for the second. Following Brueckner and Watson,[3] we can choose $\sqrt{2}a_{\frac{1}{2},\frac{1}{2}}=-a_{\frac{1}{2},\frac{3}{2}}$. With this choice (made only on the basis of the experimental evidence on π^0 production), the dipole-absorption and the interference terms vanish for the π^0 process, but remain for the π^+ process. We are still left with two arbitrary amplitudes for the magnetic-dipole process, i.e., $a_{\frac{3}{2},\frac{3}{2}}$ and $a_{\frac{1}{2},\frac{3}{2}}$. There is, on the basis of the present photomeson experiments, no way of choosing these. However, the evidence from π-meson scattering on hydrogen has been interpreted[7] as indicating that $a_{\frac{3}{2},\frac{3}{2}}\gg a_{\frac{1}{2},\frac{3}{2}}$. The relative values of these two constants could also be obtained from a comparison of the cross sections for those parts of the π^0 and π^+ photoproduction reactions corresponding to magnetic-dipole absorption (the $2+3\sin^2\theta$ terms). In particular, for the assumption of $T=\frac{3}{2}$ production only, the π^0 cross section would be twice as great as the π^+ cross section.

While the evidence is as yet by no means conclusive, the results on π^0 production taken together with the relative magnitudes of the $\pi^\pm$ scattering processes are suggestive of a resonance corresponding to a proton "isobar" state of angular momentum $\frac{3}{2}$ in both ordinary and isotopic spin space.[2,7] However, the shape of the π^0 photoexcitation cross section is not well enough known to permit an evaluation of the "isobar resonance" constants. Further measurements, both on photoproduction and scattering, with improved accuracy and extended energy range, are required before an unambiguous answer can be given to the questions of the existence and properties of the isobar.

* This work was supported in part by the joint program of the U. S. Office of Naval Research and the U. S. Atomic Energy Commission.

[1] See preceding letter by Goldschmidt-Clermont, Osborne, and Scott [Phys. Rev. **89**, 329 (1953)] which also contains references to other experiments.

[2] K. A. Brueckner and K. M. Watson, Phys. Rev. **86**, 923 (1952).

[3] D. R. Hamilton, Phys. Rev. **58**, 122 (1940).

[4] E. U. Condon and G. H. Shortley, *The Theory of Atomic Spectra*, (Cambridge University Press, Cambridge, 1935), p. 76.

[5] $W(\theta)$ is now computed by an additional summation, in Eq. (1), taken inside the absolute value signs and over the possible intermediate J-values.

[6] It is also possible to include terms corresponding to magnetic dipole absorption to a $J=\frac{1}{2}+$ state, which gives rise to an interference term $\propto(3\cos^2\theta-1)/2$ which, however, does not lead to any asymmetry about 90° and which is not needed for the interpretation of the experiments now available.

[7] K. A. Brueckner, Phys. Rev. **86**, 106 (1952); Anderson, Fermi, Long, and Nagle, Phys. Rev. **85**, 936 (1952); Anderson, Fermi, Nagle, and Yodh, Phys. Rev. **86**, 793 (1952).

Infrared Photoconductivity Due to Neutral Impurities in Silicon

E. BURSTEIN, J. J. OBERLY, AND J. W. DAVISSON
Crystal Branch, Metallurgy Division, Naval Research Laboratory, Washington, D. C.

(Received October 6, 1952)

IMPURITY photoconductivity has been observed in silicon at liquid helium temperatures out to 38 microns. The regions of impurity photoconductivity and intrinsic photoconductivity are well separated so that it is possible to make an unambiguous interpretation of the data. The results, moreover, enable one to obtain information about the ionization energies of impurities and clearly demonstrate the value of optical measurements in the study of impurity levels in semiconductors.

Optical data obtained at liquid nitrogen temperature over the range 2 to 25 microns have previously demonstrated the absorption by neutral impurities in n- and p-type silicon involving the photoionization of bound charge carriers.[1] Efforts to detect

photoconductivity at liquid nitrogen temperatures due to this absorption were unsuccessful. An appreciable photoconductive response was observed, however, in various n- and p-type specimens at liquid helium temperatures. Using a residual ray monochromator with five crystal quartz plates and a rock salt shutter, it was possible to demonstrate a response as far out as 23 microns.[2] Spectral response measurements were subsequently carried out with a Perkin-Elmer monochromator having interchangeable NaCl, KBr, and KRS-5 prisms.

The spectral response of a relatively pure n-type silicon specimen containing 4×10^{15} charge carriers/cm^3 at room temperature is given in Fig. 1. The photoconductive response is proportional to

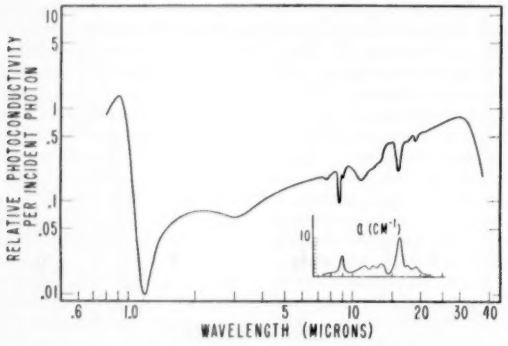

FIG. 1. The relative photoconductive response per incident photon of a relatively pure n-type silicon specimen containing 4×10^{15} charge carriers/cm^3 at room temperature. The strong dip in the photoconductive response at 1.2 microns is due to the superposition of a photonegative response at the absorption edge. The dips in the photoconductive response appearing between 8 and 24 microns correspond to the peaks in optical absorption due to lattice vibrations which compete with the photoionization absorption by the neutral impurities. The room temperature absorption spectrum of silicon due to lattice vibrations is given in the insert.

the light intensity, extends to 38 microns (the limit of measurement), and is a maximum at 32 microns. The time constant of the photoconductive response as determined by square wave chopping was found to be less than 10^{-4} second. The room temperature absorption spectrum of silicon due to lattice vibrations[3] is given in the insert in Fig. 1.

It is of interest to note that the dark resistance of the various n- and p-type silicon specimens at liquid helium temperatures was considerably smaller than the values expected from the ionization energies and concentrations of the impurities. By enclosing the specimen in a light-tight box with a shutter, it was found that the true dark resistivity of the relatively pure n-type silicon specimen at liquid helium temperature was greater than 10^{12} ohm-cm. With the shutter open to background radiation, the resistivity dropped to 5×10^{7} ohm-cm. The fractional change in resistivity of other specimens with higher impurity concentrations were, however, less than 1 percent when the shutter was opened and closed. In general, the larger the impurity content, the lower the residual resistance at liquid helium temperature, and also the smaller the photoconductive response. It appears therefore that specimens with relatively high impurity concentrations contains an appreciable fraction of impurities which have very small ionization energies.

According to the theory for the simple hydrogen model the photoionization absorption cross section of the neutral impurities may be expected to increase with wavelength to a maximum value at the ionization limit. Under conditions where the density of impurities is sufficiently small, such that the product of absorption constant and the thickness of the photoconductor is very much less than unity, the photoconductive response will be proportional to the absorption cross section and will likewise attain a maximum value at the ionization limit. The optical ionization energy of the neutral impurities may thus be obtained from the position of the peak in the spectral response curve, provided there is no appreciable distribution of impurity levels. The data of Fig. 1 yields a value of 0.04 ev for the optical ionization energy of the donor impurities in the relatively pure n-type specimen, which is somewhat smaller than the value 0.06 ev for the thermal ionization energy derived from Pearson and Bardeen's data for specimens of comparable impurity content.[4]

We wish to express our thanks to Dr. W. Shockley, Dr. J. Bardeen, and Mr. H. B. Briggs of the Bell Telephone Laboratories for helpful discussions and for supplying many of the specimens used in this investigation; to Dr. H. Stauss and Mr. J. Hino of the Metallurgy Division, Naval Research Laboratory, for making available specimens of pure silicon; and to Mrs. Bertha W. Henvis and Mr. H. Lipson of the Crystal Branch, Metallurgy Division, for their assistance in this investigation.

[1] Burstein, Oberly, Davisson, and Henvis, Phys. Rev. **82**, 764 (1951).
[2] Burstein, Oberly, and Davisson, Naval Research Laboratory Report of Progress, (July, 1950), p. 38 (unpublished).
[3] E. Burstein and J. J. Oberly, Phys. Rev. **78**, 642 (1950).
[4] G. L. Pearson and J. Bardeen, Phys. Rev. **75**, 865 (1949).

Asymmetric Fission

PETER FONG*
Department of Physics, University of Chicago, Chicago, Illinois
(Received October 2, 1952)

THE calculations by Frankel and Metropolis[1] have shown that at the saddle point of the energy in the fission process the nucleus is symmetric. However, at this point, there is practically no indication of a "neck," at which the deformed nucleus might break. The calculations by Hill[2] demonstrate that the fission process is slow enough that surface waves travel from one end to the other many times before a definite neck develops and fission occurs. In this letter it is proposed that the mode of fission is still undetermined at the saddle point. The concept of statistical equilibrium used by Bohr and Wheeler[3] is extended from the saddle point to a much later stage when the fission fragments are just about ready to come apart. Accordingly the number of quantum states at that later stage will determine the relative probability of different modes of fission. For convenience of calculation the situation at the breaking point is represented by a simplified picture, namely, that of the two fragment nuclei of mass A_1 and A_2 in contact.

The fact that the number of quantum states for asymmetric fission is larger than that for symmetric fission is due mainly to the fact that the internal excitation energy of the fragments at the breaking point is larger for the asymmetric than for the symmetric mode. According to the model adopted, the excitation energy at the breaking point is

$$E=M^*(A,Z)-M(A_1,Z_1)-M(A_2,Z_2)-E_{el}-D. \qquad (1)$$

Here $M^*(A,Z)$ indicates the mass of the original excited fissioning nucleus, $M(A_1,Z_1)$ and $M(A_2,Z_2)$ the masses of the two fission fragments in their ground states, and E_{el} the electrostatic repulsion between the two fragments. Since the nuclei are presumably highly deformed, a deformation energy D is introduced which decreases the energy available for distribution among the internal quantum states of the fragments. D is roughly independent of the mode of mass splitting and is estimated to be about 9 Mev. The term $-E_{el}$, being proportional to Z_1Z_2, favors asymmetric fission. The mass terms, according to the liquid drop model mass values calculated by Metropolis and Reitwiesner,[4] favors symmetric fission. For example, the sum of masses of two equal fragments, Cd^{118}, is lower than that of two fragments of the experimentally most probable mode, Zr^{100} and Te^{136}, by 4.2 Mev. However, the liquid drop model mass values, compared to mass spectrometric ones, have shown errors of the order of 10 Mev. The masses of Cd^{118}, Zr^{100}, and Te^{136}, though not yet determined experimentally, can be extrapolated from the masses of stable nuclei[5] and from the parabolic dependence[6] of mass on charge number. The results show that the mass of $Cd^{118}+Cd^{118}$ is higher than

$Zr^{100}+Te^{136}$ by 2 Mev, favoring asymmetric fission. This, together with the contribution from the $-E_{s1}$ term, causes E for asymmetric splitting to be larger than E for symmetric splitting by 4.5 Mev. Accordingly the asymmetric splitting will have a larger number of quantum states and so a larger probability of occurrence.

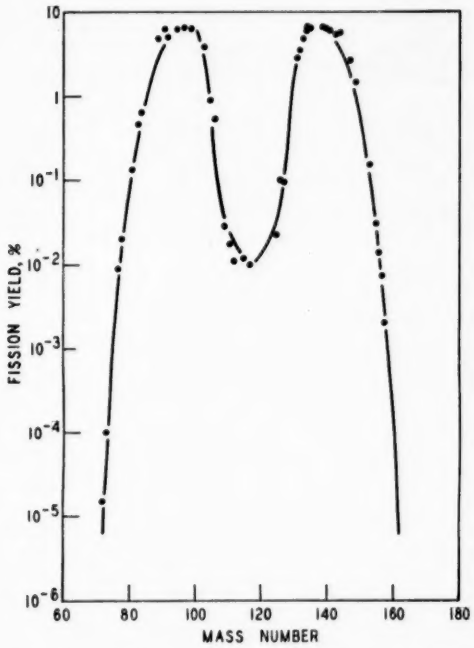

FIG. 1. Calculated mass distribution curve of slow neutron fission of U^{235}, compared with the corresponding fission yields as determined by radiochemical methods (solid circles).

In order to establish the quantitative relation between excitation energy and the number of quantum states, the following formula is derived:

$$N\sim c_1c_2\left(\frac{A_1^{5/3}A_2^{5/3}}{A_1^{5/3}+A_2^{5/3}}\right)^{\frac{1}{2}}\left(\frac{A_1A_2}{A_1+A_2}\right)^{\frac{1}{2}}\frac{(a_1a_2)^{\frac{1}{4}}}{(a_1+a_2)^{5/2}}\times\left(1-\frac{1}{2[(a_1+a_2)E]^{\frac{1}{2}}}\right)E^{9/4}\exp\{2[(a_1+a_2)E]^{\frac{1}{2}}\},\quad(2)$$

where c_1, a_1; c_2, a_2 are the constants of the level density formula,

$$W(E)=c\exp[2(aE)^{\frac{1}{2}}],\quad(3)$$

for the two fragment nuclei A_1 and A_2, respectively. According to the statistical assumption, N is proportional to the relative probability of occurrence of fission products (A_1, Z_1) and (A_2, Z_2).

For thermal neutron fission, the average value of E is about 11 Mev.[7] The difference of 4.5 Mev between asymmetric and symmetric modes is large enough, by (2), to give a yield ratio of about 600. For high energy fission, by 100-Mev neutrons, say, the average value of E is much larger (>50 Mev) so that the difference of 4.5 Mev becomes insignificant. Symmetric and asymmetric modes will then have comparable probability, as is experimentally observed.

In order to derive the mass distribution curve, E values of all possible mass splitting are calculated as was indicated above for Zr^{100} and Te^{136}. The constants of (3) are determined from fast neutron capture cross-section data with special attention to the even-odd and magic irregularities.[8] The mass distribution curve obtained for slow neutron fission of U^{235} is given in Fig. 1.

This theory can readily be applied to problems of charge distribution, kinetic energy distribution, energy dependence, variation with fissioning nuclei, fission neutrons, fine structure, spontaneous fission, and ternary fission. A detailed paper is in preparation. The author wishes to express his deep gratitude to Professors Maria Mayer and Enrico Fermi for their guidance and valuable suggestions. He is also indebted to Drs. C. D. Coryell, H. E. Duckworth, J. S. Fraser, L. E. Glendenin, D. J. Hughes, R. B. Leachman, J. M. Miller, A. C. Pappas, E. P. Steinberg, E. W. Titterton, and A. Turkevich for discussions and/or communication of their unpublished work.

* Present address: 3800 East Colfax Avenue, Denver 6, Colorado.

[1] S. Frankel and N. Metropolis, Phys. Rev. **72**, 914 (1947).

[2] D. L. Hill, Phys. Rev. **79**, 197 (1950).

[3] N. Bohr and J. A. Wheeler, Phys. Rev. **56**, 426 (1939); N. Bohr, Phys. Rev. **58**, 864 (1940).

[4] N. Metropolis and G. Reitwiesner, *Table of Atomic Masses* (Argonne National Laboratory, Chicago, 1950).

[5] H. E. Duckworth and co-workers, Phys. Rev. **78**, 479 (1950); **79**, 188 (1950); **79**, 402 (1950); **82**, 130 (1951); **82**, 131 (1951); **82**, 468 (1951); **83**, 229 (1951); **83**, 1114 (1951). Interpolation is made to cover all masses in the fission product region.

[6] The mass term $B_A(Z-Z_A)^2$ is used. The Z_A's are determined from beta-decay energies compiled by K. Way and co-workers in *Nuclear Data*, National Bureau of Standards Circular No. 499 (1950). The B_A's are those of reference 4.

[7] The sum of E and D is equal to the total energy available for the emission of prompt neutrons and prompt gamma-rays, which has been estimated to be about 20 Mev [D. C. Brunton, Phys. Rev. **76**, 1798 (1949)]. As D is about 9 Mev, we find E to be about 11 Mev.

[8] The constants so determined are:

$$a=0.050A\ (\text{Mev})^{-1}\quad\text{and}\quad c=0.38e^{-0.0031A}\ (\text{Mev})^{-1},$$

where A is the mass number of the nucleus. The energy E of (3) is to be counted from a characteristic level [H. Hurwitz and H. A. Bethe, Phys. Rev. **81**, 898 (1951)] which we take to be the level of odd-odd nuclei ground states smoothed out of magic irregularities. Fast neutron cross sections are given by Hughes, Spatz, and Goldstein, Phys. Rev. **75**, 1781 (1949); D. J. Hughes and D. Sherman, Phys. Rev. **78**, 632 (1950), and Hughes, Garth, and Eggler (unpublished).

Atomic Mass of P^{31}

K. OGATA AND H. MATSUDA
Department of Physics, Faculty of Science, Osaka University, Osaka, Japan

(Received November 3, 1952)

WITH a modified Bainbridge-Jordan type mass spectrograph, the details of which were described in a previous report,[1] the mass differences of the doublets, $P^{31}H^1-S^{32}$, $P^{31}(H^1)_2-S^{32}H^1$ and $(O^{16})_2-P^{31}H^1$, were measured. $P^{31}-P^{31}H^1-P^{31}(H^1)_2-P^{31}(H^1)_3$ and $S^{32}-S^{32}H^1-S^{32}(H^1)_2$ were used as mass calibration groups, in which the masses of H^1, P^{31}, and S^{32} were assumed to be 1.00814, 30.984, and 31.982, respectively. The results obtained are given in Table I, together with other recent data.[2] The errors given in Table I are the probable errors, which are the square roots of the sums of squares of the statistical errors and of mass calibration errors (0.04 percent).

TABLE I. Mass differences of doublets.

Doublet	No. of doublets (plates)	Mass difference 10^{-4} amu	Previous[a] work
$P^{31}H^1-S^{32}$	34 (3)	95.00 ±0.10	94.95 ±0.10
$P^{31}(H^1)_2-S^{32}H^1$	16 (2)	94.91 ±0.12	
Weighted mean		94.96 ±0.07	95.04 ±0.20
$(O^{16})_2-P^{31}H^1$	11 (1)	82.45 ±0.12	82.49 ±0.30

[a] See reference 2.

From the above doublets, $P^{31}H^1-S^{32}$ and $(O^{16})_2-P^{31}H^1$, the mass difference of $(O^{16})_2-S^{32}$ was calculated to be 177.41±0.14, which is in good agreement with the previously reported value,[1] 177.21±0.08.

By combining the $(O^{16})_2-P^{31}H^1$ doublet mass difference with that of some previously reported doublets, the Q values of $P^{31}(p,\alpha)Si^{28}$ and of $P^{31}(d,\alpha)Si^{29}$ can be calculated. The Q values thus obtained are compared with those measured directly in nuclear reactions,[3] in Table II. They are in good agreement with

TABLE II. Q values calculated from doublet mass differences.

Reaction	Q_1 from doublet mass differences (in Mev)[a]	Q_2 from nuclear reactions (Mev)[b]	Q_1-Q_2 (in Mev)
$P^{31}(p,\alpha)Si^{28}$	1.914 ±0.020	1.909 ±0.010	+0.005 ±0.022
$P^{31}(d,\alpha)Si^{29}$	8.168 ±0.025	8.158 ±0.011	+0.010 ±0.027

[a] The doublets used in these calculations were: (i) $(O^{16})_2-P^{31}H^1$, $C^{13}O^{16}-Si^{28}$, $C^{12}(H^1)_4-O^{16}$, $(H^1)_3-D^2$ and $D_2^2-He^4$; (ii) $(O^{16})_2-P^{31}H^1$, $C^{13}O^{16}-Si^{29}$, $C^{12}H^1-C^{13}$, $C^{12}(H^2)_4-O^{16}$, $(H^1)_2-D^2$, and $(D^2)_2-He^4$. The $(O^{16})_2-P^{31}H^1$ mass difference is the present value and the other doublet mass differences were in the previous report (reference 1).
[b] See reference 3.

each other. However, from the smaller $C^{12}(H^1)_4-O^{16}$ mass difference 363.71±0.12,[2] the Q value of $P^{31}(p,\alpha)Si^{28}$ was calculated to be 1.958±21 Mev, and the Q of $P^{31}(d,\alpha)Si^{29}$ to be 8.213±26 Mev, both of which are greater than those obtained directly from the nuclear reactions, by an amount about twice the probable errors.

From the mass differences in Table I and the atomic masses[1] of $H^1=1.008145\pm2$ and $S^{32}=31.982274\pm8$, the atomic mass of P^{31} is calculated to be:

$$P^{31}=30.983619\pm7,$$

which is the weighted mean of 30.983610±12 [from $(O^{16})_2-P^{31}H^1$] and 30.983625±11 [from $P^{31}H^1-S^{32}$]. The value of P^{31} obtained by Ewald is 30.983622±23.[2]

TABLE III. Mass differences.

	$P^{31}-Si^{30}$	$S^{32}-P^{31}$
Present work	1.000312 ±32	0.998655 ±11
From nuclear data	1.000310 ±17[a,b]	0.998645 ±15[a,c]
	1.000327 ±13[a,c]	0.998637 ±14[a,d]
Reactions used	$Si^{30}(d,p)Si^{31}$	$P^{31}(d,p)P^{32}$
	$Si^{31}(\beta)P^{31}$	$P^{32}(\beta)S^{32}$

[a] See reference 3.
[b] A. H. Wapstra, Phys. Rev. **86**, 561 (1952).
[c] H. T. Motz, Phys. Rev. **85**, 501 (1952).
[d] Jensen, Nichols, Clement, and Pohl, Phys. Rev. **85**, 112 (1952).

The mass differences between P^{31} obtained above, and the previously reported[1] Si^{30} (29.983307±31) and S^{32}(31.982274±8), are compared with those calculated from recent nuclear data in Table III. They are found to be in good agreement with each other.

The authors are greatly indebted to Mr. Y. Yoshikawa for preparing the PH_3 sample, and to Mr. T. Nakatsuka for his laborious work in preparing Schumann plates.

[1] K. Ogata and H. Mastuda, Phys. Rev. **89**, 27 (1952).
[2] H. Ewald, Z. Naturforsh. **6a**, 293 (1952).
[3] Van Patter, Sperduto, Endt, Buechner, and Enge, Phys. Rev. **85**, 142 (1952).

Proceedings of the American Physical Society

MINUTES OF THE FIFTH ANNUAL CONFERENCE ON GASEOUS ELECTRONICS, SPONSORED BY THE DIVISION OF ELECTRON PHYSICS

THE Fifth Annual Conference on Gaseous Electronics, sponsored by the Division of Electron Physics of the American Physical Society, was held on September 4, 5, and 6, 1952, at Princeton University and RCA Laboratories in Princeton, New Jersey. Abstracts of some of the papers presented are printed hereunder.

R. L. SPROULL, *Secretary*
Division of Electron Physics
Cornell University
Ithaca, New York

A1. Electron Velocity Distributions in an Hg-A Discharge. B. T. BARNES, *General Electric Company, Cleveland.*—Probe characteristics were obtained using a tube 1.5 in. in diameter containing Hg at 0.8–25 microns and 3.5 mm of argon operated at 0.20, 0.40, 0.80, and 1.50 amperes. At the higher currents interaction between electrons maintained a Maxwellian distribution of velocities, at least over the energy range 0–8 ev. At the lower currents the number of electrons per unit energy band seems to be less than Maxwellian for energies >7 ev and for 0–3 ev, and greater than Maxwellian in the intermediate range. High probabilities of inelastic loss for 6–9 ev electrons may account for the deficiency of fast electron at the lower currents. Results obtained with the usual probe techniques were roughly confirmed by runs for which the probe temperature was kept nearly constant. Square-wave pulses of current with a frequency of 29 per second were superposed on a steady current controlled by a pentode. The probe potential in the intervals between pulses was measured with an electronic voltmeter. The average total current was kept constant as the steady current was varied over a wide range. This technique was not usable when the ion current far exceeded the electron current, but conventional methods are fairly reliable in this range.

A3. On the Transition from Free to Ambipolar Diffusion. W. P. ALLIS, *M.I.T.*, AND D. J. ROSE, *Bell Telephone Laboratories and M.I.T.*—In a steady-state dc positive column or a microwave discharge the electron and positive ion currents are equal to each other and to the ionization rate in the discharge volume. At very low charge densities (breakdown), only free diffusion occurs; at very high charge densities, the combination of diffusion and mobility arising from the space charge field results in "ambipolar diffusion" wherein both types of particles appear to diffuse together. The behavior of the discharge throughout the transition between these extremes is investigated. Expressions are derived for an effective electronic diffusion coefficient in terms of which the currents and ionization rate can be expressed. Approximate spatial distributions of the charged particles are obtained. Numerical solutions of the appropriate equations are presented for the case of equal electron and ion energies. Analytic approximations are obtained for the case of electron energy$\gg$ ion energy, as is the case in normal steady-state discharges. The transition is not completely monotonic with increasing power; i.e., the net space charge at the center of the tube passes through a maximum in the transition region.

A5. On Ionizing and Heating a Plasma. LOUIS WITTEN, *Princeton University.*—Of various methods of achieving total ionization of a plasma, the two most promising have been analyzed. The first uses an axial oscillating magnetic field. w^2/B remains constant as B changes, u is unchanged (w is the electron velocity component perpendicular to B, u is the component parallel to B). When B is high, collisions produce secondary electrons having, say, w^2 corresponding to 6 volts and u^2 to 3. B decreases to $1/100B_{max}$, thus decreasing w^2 to 0.06 volt. Collisions produce an isotropic distribution, $w^2 \approx 2$ volts, $u^2 \approx 1$. B is increased again increasing w^2 to 200 volts. These primaries produce other secondaries and the process repeats. A square-wave variation of B would almost certainly operate as envisaged. A sine wave gives too small an energy gain per cycle for the process to sustain itself. Alternatively an oscillating axial electric field E_0 sine ωt, could be applied. Free electrons acquire enough energy during a cycle to produce ionization on collision. If the field frequency exceeds an "average" collision frequency ν of electrons; total ionization can be achieved. The number of electron-ion pairs e-folds in time $\sim 1/\nu$ until total ionization is approached. The particles can be contained during the process by a constant axial magnetic field.

A6. Instabilities of a Completely Ionized Plasma. MARTIN KRUSKAL, *Princeton University.*—First-order perturbations of equilibrium of a plasma have been investigated theoretically in two ideal cases. Case 1: A plane bounded plasma supported against gravity by a horizontal magnetic field. In the limiting two-dimensional case in which the magnetic lines are not bent, it is found that the familiar instability of a heavier fluid supported by a lighter one occurs; any sinusoidal perturbation across the field e-folds in a time interval approximately $(\lambda/2\pi g)^{\frac{1}{2}}$, where λ is its wavelength and g is the gravitational acceleration. In the different limiting case of no gravitational force, however, stability occurs; any sinusoidal pertubation bending the magnetic lines is oscillatory with period given approximately by the quotient of its wavelength along the field by the progression velocity of magneto-hydrodynamic waves. Case 2: An infinite cylinder of plasma confined by the magnetic field produced by a current in the plasma parallel to the axis. Any transverse sinusoidal perturbation is found to e-fold in a time interval approximately the quotient of its wavelength by sound velocity.

A7. Specific Primary Ionization of H_2, He, Ne, and A by High Energy Electrons.* G. W. MCCLURE, *Bartol Research Foundation of the Franklin Institute.*—Mono-energetic electrons magnetically separated from the continuous spectrum of a radioactive β-ray source are directed through a series of 3 G-M counters separated by 0.001-in. Al windows. A measurement of the efficiency of the first counter by the coincidence method yields information from which the specific primary ionization of its contained gas is calculated. Measurements on H_2, He, Ne, and A over the range of incident electron energies 0.2 to 1.6 Mev have been made and the data compared with the primary ionization *vs* energy formula derived by Bethe for atomic hydrogen. By adjustment of two constants contained in this formula it is possible to fit the data for each of the four gases within the experimental errors (± 2 percent). The adjusted formulas appear to predict specific ionization values accurate to a few percent at energies as low as 1 kv (except in the case of helium) and as high as 8 Mev as judged by comparison with the experimental work of others at lower and higher energies.

* Assisted by the joint program of the ONR and AEC.

B1. Hydrogen Spectra from the Channel of a Spark Discharge with Increased Energy. HEINZ FISCHER, *Air Force Cambridge Research Center.*—With increasing gas pressure and spark energy, the Balmer lines in the hydrogen spectrum (with exception of H_α) become so wide and overlapping that they form a continuous spectrum as is well known.[1] Only H_α remains separated even with the highest energies obtained so far. By increasing the energy density in the spark channel substantially beyond the present limits, H_α widens considerably and finally shows reversal in its center. The spectral range of the reversal widens with increasing energy and gas pressure. The phenomenon is discussed.

[1] See also W. Finkelnburg, *Continuous Spectra*, (Springer, Berlin, 1938).

B3. Shock Waves in the Expansion of Low Pressure Sparks.* R. G. FOWLER, W. R. ATKINSON, AND R. J. LEE, *University of Oklahoma.*—Self-luminous shock waves have been recognized in the post discharge expansion of low pressure spark discharges, and computations verify the identification. Expansion of the hot gas after excitation by the discharge current proceeds by the usual mechanisms of fluid flow, presenting a shock wave and a contact surface. The region behind the contact surface shows a continuing, intense, post-discharge light production which is as yet not understood. Ion concentrations indicated by Stark-broadening show a space distribution which can only be accounted for by assuming belated ionization, or else failure of the Holtsmark theory. Production of luminosity is largely independent of the direct actions of the discharge current stream; is probably accomplished via recombination; and seems to be thermal in character, suggesting Saha processes.

* Supported by the ONR.

B4. Time Variation of Ion Concentration in Flash Discharge Plasmas. H. N. OLSEN* AND W. S. HUXFORD, *Northwestern University.*—The hydrogen atom is used as a spectroscopic probe for measuring ion concentrations in low pressure flash discharges through argon and neon. Photomultiplier techniques were developed for observing time-variations of individual spectral lines and continuous radiation. From observed wavelength distributions of broadened H_α and H_β lines, ion concentrations ($\sim 10^{17}$ ions/cm^3) were determined at various instants of time during the discharge phase. For this Holtsmark's theory of spectral line broadening by interionic Stark fields was applied.[1] A comparison of ion concentrations and intensities of the continuous spectrum as a function of time shows that the radiation is chiefly a bremsstrahlung continuum. The observed low values of electron-ion recombination coefficients indicate, furthermore, a negligible contribution of recombination continuum to the radiation. The degree of ionization is about 10 percent with a corresponding electron temperature of 11 000°K. The plasma energy is one-third of the discharge capacitor stored energy, and the net charge separated in the plasma is greater by a factor of 10 than the charge removed from the capacitor. Electron mobilities determined from estimated current densities are lower than those calculated from the usual mobility equations.

* Now at Linde Air Products Company, Tonawanda, New York.
[1] H. N. Olson and W. S. Huxford, Phys. Rev. **87**, 233 (1952).

B5. Some Afterglow Spectra Observable in Incandescent Lamps. CARL KENTY, *General Electric Company.*—Burned out street series lamps (600 mm 99.5 percent A, 0.5 percent N_2) with Tesla coil excitation exhibit several afterglow spectra. Most prominent are flamelike clouds of orange glowing active nitrogen (A.N.) which rise and swirl by convection[1] and persist several seconds. A blue flame rises from a gap in the filament where sparking occurs and persists 5 seconds. Its spectrum apparently consists of a number of high series argon lines excited by a hitherto unrecognized nonluminous form of active nitrogen. A beautiful afterglow[2] occurring in rare cases is due to a few p.p.m. of O_2 or oxygen-bearing gas. It is the auroral green line 5577 and associated band. Also occurring rarely is a violet afterglow. Its spectrum consists mainly of two bands in the violet. These last two afterglows, unlike the others, are quickly cleaned up by the discharge. New lamps rarely show any afterglow because of impurities, chiefly H_2O and H_2; 100 hours of burning are frequently necessary to clean up these. Many old lamps exhibit a weak phosphorescence on the inner surface of the bulb. This can be seen to persist up to 15 minutes by the dark-adapted eye.

[1] R. S. Mackay, Am. J. Phys. **18**, 319 (1950).
[2] H. G. Jenkins and J. N. Bowtell, Nature **163**, 401 (1949).

B6. OH Rotational Distributions in Mixtures of H_2O and D_2O in a High Frequency Discharge. H. P. BROIDA, *National Bureau of Standards.*—Recent studies[1] of OH emission from flames have indicated that thousands of collisions are not effective in producing rotational equilibrium. Since similar nonequilibrium distributions had been previously observed in electric discharges[2,3] through water vapor, a further study of the discharge has been made. Rotational intensities of OH and OD ($^2\Sigma - {}^2\pi$ transition) have been measured in a 150 megacycle electrodeless discharge operating at pressures from 0.05 mm to 10 mm Hg. Mixtures of H_2O and D_2O vapors with helium, argon, nitrogen, and oxygen have been observed. In all cases evidence of abnormal rotation is found. Discharges through pure water show two maxima in the OH and OD intensity distributions which occur at the same energy for both molecules. With increasing pressure, the maximum intensity corresponding to the lower energy increases relative to the other maximum but there is no shift in the energies of the maxima. With all diluents, the intensities from the lower energy states are greatly increased. These results show that there are two processes forming the excited OH and OD and that collisions with other molecules have little effect on the rotational nonequilibrium.

[1] H. P. Broida, J. Chem. Phys., **19**, 1383 (1951).
[2] O. Oldenberg, Phys. Rev. **46**, 210 (1934).
[3] E. R. Lyman, Phys. Rev., **53**, 379 (1938).

C1. Experimental Investigation of Ionization Probability Curves Near Threshold. R. E. FOX, W. M. HICKAM, AND T. KJELDAAS, JR., *Westinghouse Research Laboratories.*—The structure of ionization probability (P_i) curves for a few volts above threshold is investigated with a mass spectrometer employing the "retarding potential difference method" for obtaining ionization by monoenergetic electrons.[1] It is found that, for electron energies sufficiently low as to cause ionization only to the lowest level of the ion, the P_i curve increases linearly with the excess electron energy. In cases, however, where the ion has other energy levels in this region (e.g., the $^2P_{\frac{1}{2}}$ and $^2P_{\frac{3}{2}}$ ground states of the krypton ion) that P_i curve exhibits breaks in slope corresponding to these levels. Detailed analysis of the krypton curves yields a value of 0.66 ± 0.01 ev for the separation of the ground states, in excellent agreement with the spectroscopic value. Breaks in the P_i curves for xenon and argon are in agreement with the spectroscopic values within ± 0.1 ev. Moreover, the structure of the P_i curve for krypton near the break shows the presence of autoionization arising from excited states of the atom lying higher than the lowest state of the ion. Preliminary studies of some double ionization processes will be reported.

[1] Fox, Hickam, Kjeldaas, and Grove, Phys. Rev. **84**, 859 (1951).

C2. Threshold Law for Ionization of Atoms by Electrons. GREGORY H. WANNIER, *Bell Telephone Laboratories.*—The derivation of the threshold law for this fundamental process of mass spectrometry is an extension to three bodies of Wigner's general threshold theory[1] worked out for two bodies.

For simplicity, zero angular momentum is assumed for the end state; this condition is known to predominate in the end product if the atom was originally in an s-state. It is also shown that classical mechanics may be applied outside the reaction zone. It is then seen, that unless deviations from ergodicity are unexpectedly drastic, that the ionization cross section is proportional to the volume in phase space escaping per unit time from the reaction zone. This quantity comes out to vary as the αth power of the energy excess where $\alpha=\frac{1}{2}[(100Z-9)/(4Z-1)]^{\frac{1}{2}}-\frac{1}{4}$. Here Z is the final charge of the ion. For the most common case $Z=1$ we find $\alpha=1.127$ while for very large Z, $\alpha=1$. Even in the first case the curve differs very little from a straight line in its general appearance. It does, however, have a noticeable upward curvature and enters the threshold point with a zero slope.

[1] Eugene P. Wigner, Phys. Rev. **73**, 1002 (1948).

C4. A Microwave Method for Measuring Mean Energy Transfer Per Collision and the Velocity Dependence of Collision Cross Section for Slow Electrons in Gases. O. T. FUNDINGSLAND, A. C. FAIRE, AND A. J. PENICO, *Air Force Cambridge Research Center.*—A microwave method previously reported[1] for determining the collision probability P_e for momentum transfer of slow electrons in gases has been modified to include modulation of the electron energy. Transient variations in σ_r/σ_i, the ratio of real to imaginary parts of the complex conductivity, are measured during the modulation pulse. The plots of σ_r/σ_i *versus* time are compared with theoretical curves obtained from an approximate solution to the Boltzmann transport equation. It is assumed that the collision frequency is proportional to the h-power of electron velocity over the significant range of the distribution function for energies near thermal equilibrium with the gas. A derived relation between the exponent h and G, the mean fractional transfer of energy per collision, is completely determined by the measured values of initial slope, $d(\sigma_r/\sigma_i)/dt_{t\to 0}$, and the initial and final vaules of σ_r/σ_i. In monatomic gases, where G can be assigned a value $2m/M$, twice the ratio of the electronic to atomic masses, the energy dependence of P_e is thus obtained for small excursions from thermal equilibrium. In polyatomic gases more elaborate curve fitting is necessary to yield unique values of both G and h. Exploratory data will be reported for neon, helium, argon, and nitrogen.

[1] Phelps, Fundingsland, and Brown, Phys. Rev. **84**, 559 (1951).

C5. A New Microwave Technique for the Study of Discharges in Gases.* MURRAY A. LAMPERT,† AND ALAN D. WHITE, *Federal Telecommunication Laboratories Inc.*—This paper is concerned with the exploration of gaseous discharges by a new microwave technique. As an example of the use of this technique, small regions of a dc discharge in narrow-bore tubing were exposed to a low power pulsed microwave signal and the resultant gas tube current pulse was monitored on a cathode-ray oscilloscope. The results indicated that, depending on gas pressure, there are two or three regions in noble-gas, cold-cathode, dc discharges which are sensitive to the presence of microwave power. The most sensitive region is near the cathode, the other near the anode and in a middle region, respectively. Additional experiments lend substantial support to the hypothesis that the sensitive region near the cathode is to be identified with the narrow region of reversed electric field near the cathode. Therefore, the microwave technique described above makes it possible to locate and explore relative potential minima in a dc discharge without the use of metallic probes. Further experiments are necessary before the results already obtained can be interpreted in detail.

* This work was supported by the Signal Corps of the U. S. Army.
† Now with RCA Laboratories Division, Princeton, New Jersey.

C6. Dissociative Attachment of Thermal Electrons to Iodine Molecules. MANFRED A. BIONDI, *Westinghouse Research Laboratories.*—Microwave techniques[1] are used to study electron attachment following a pulsed discharge in iodine. To assure that the electrons have thermal energies ($T_e=300°K$) during the measuring interval, helium at approximately 1-mm pressure is added to the iodine vapor to act as a "recoil gas." The measured attachment cross section is 4×10^{-16} cm². The large value of this cross section suggests that the attachment results from the dissociation reaction $I_2+e\to I+I^-+K.E.$ The present result, obtained with electrons of 0.04-ev average energy, disagrees with measurements of attachment in iodine by Buchdahl.[2] Using an electron beam of controlled energy, he found a maximum attachment cross section of 4×10^{-17} cm² for electrons of 0.4-ev energy. In view of possible errors in his measurements at low electron energies, the discrepancy between the two results may be removed.

[1] M. A. Biondi, Rev. Sci. Instr. **22**, 500 (1951).
[2] R. Buchdahl, J. Chem. Phys. **9**, 146 (1941).

C7. Drift Velocity of Ions in Oxygen, Nitrogen, and Carbon Monoxide. ROBERT N. VARNEY, *Bell Telephone Laboratories.*—Measurements of ionic drift velocities in O_2, N_2, and CO have been made by the microsecond pulsed Townsend technique previously used in these Laboratories on other gases.[1,2] The results in O_2 are similar to those for rare gases and give an extrapolated mobility at zero field of 2.25 ± 0.1 cm²/volt-sec. In N_2 and CO, the log-log plot of drift velocity against E/p, the ratio of field strength to pressure, rises in the customary way but then takes an actual dip, spread over some 50 units of E/p, before finally resuming a monotonic increase. Data and possible explanations will be presented.

[1] J. A. Hornbeck, Phys. Rev. **84**, 615 (1951).
[2] R. N. Varney, Phys. Rev. **88**, 362 (1952).

C8. Theory of the Mobility of He_2^+ in Helium. S. GELTMAN* AND H. MARGENAU, *Yale University.*—A theoretical study has been made of the low field mobility of the helium molecular ion, He_2^+, in helium. First, the forces between He_2^+ and He are calculated by means of perturbation theory. Use of the Chapman-Enskog theory of diffusion then permits the calculation of the mobility as a function of temperature. The mobility at 18°C and 760 mm is found to be 18.1 cm²/volt-sec as compared with the experimental value of 21.4 cm²/volt-sec found by Tyndall and collaborators.[1] This experimental result was originally attributed to He^+ ions but has since been reinterpreted[2] as resulting from He_2^+ ions. Further, the experimental temperature variation of the mobility of He_2^+ is analyzed by means of the Langevin theory of ionic mobilities. When account is taken of ionic clustering, the observed temperature dependence is understood on the basis of a simple model for the He_2^+-He potential. The discrepancy between theoretical and experimental temperature dependence of mobility is ascribed to certain approximations in the calculated potential.

* Now at the Westinghouse Research Laboratories, East Pittsburgh, Pennsylvania.
[1] Tyndall *et al.*, Proc. Roy. Soc. (London), **A134**, 125 (1931); **A149**, 426 (1935).
[2] Meyerott, Phys. Rev. **66**, 242 (1944); Hornbeck, Phys. Rev. **84**, 615 (1951).

C9. Mobilities of Thermal Ions in Noble Gases. LORNE M. CHANIN AND MANFRED A. BIONDI, *Westinghouse Research Laboratories.*—The mobilities of positive ions in their parent gases[1,2] have been measured using modern pulsing and timing techniques. In the present experiment ions are generated by a pulsed discharge; they are then admitted through a grid into a drift region where their time of flight is measured in a constant electric field. This method permits us to measure

mobilities at low values of $E/p(\sim 1)$ where the ions are essentially in thermal equilibrium with the gas in which they move. Our data indicate the presence of two groups of ions corresponding to the molecular and atomic ions of the parent gas.[2] The data at higher $E/p(\sim 10)$ agree with that of Hornbeck and extend into the low E/p region where the measured ion mobilities may be compared directly with theory.[3-5] Preliminary results for helium, neon, and argon will be given.

[1] A. M. Tyndall and C. F. Powell, Proc. Roy. Soc. (London) **A134**, 123 (1931).
[2] J. A. Hornbeck, Phys. Rev. **84**, 615 (1951).
[3] T. Holstein, J. Chem. Phys. **56**, 7 (1952).
[4] H. S. W. Massey and C. B. O. Mohr, Proc. Roy. Soc. (London) **A144**, 188 (1934).
[5] S. Geltman and H. Margenau, preceding abstract, C8.

C10. The Quenching of Mercury Resonance Radiation (2537A) by Nitrogen. C. G. MATLAND, *Westinghouse Research Laboratories.*—The experimental techniques developed for the measurement of the imprisonment time of mercury resonance radiation[1] have been used to determine the cross section for a quenching collision between a nitrogen molecule and an excited mercury atom in the 6^3P_1 state. It has been shown[2] that such collisions result in transitions of the excited mercury atom from the 6^3P_1 state to the metastable 6^3P_0 state. As a result of the reduced population of the 6^3P_1 state, the resonance radiation is effectively quenched. Mercury vapor, in the presence of a known pressure of nitrogen gas, is excited by 2537A radiation. After the source of excitation is cut off, the decay time of the imprisoned radiation is observed. The quenching collision cross section σ_Q is calculated from the measured decay time and the known value of the imprisonment time in the absence of a foreign gas.[1] Measurements have been taken over the temperature range 325–525°K; σ_Q is found to increase from 0.6×10^{-16} cm² at the lower temperature to 1.1×10^{-16} cm² at the upper temperature.

[1] Alpert, McCoubrey, and Holstein, Phys. Rev. **76**, 1257 (1949).
[2] See for example, A. C. G. Mitchell and M. W. Zemansky, *Resonance Radiation and Excited Atoms* (The Macmillian Company, New York, 1934), p. 250.

D1. Frequency Spectra from Point-to-Plane Corona. FRED E. LUBORSKY AND STANLEY I. REYNOLDS, *General Electric Company.*—The corona characteristics in a point-to-plane gap have been studied with direct and with alternating voltage applied. The frequency spectra of corona currents and voltages from 500 cycles/sec to 10 megacycles/sec have been obtained for this gap under various conditions. The corona level of these spectra all start to decay in the range of 100–900 kilocycles/sec, except in pure nitrogen. These curves are discussed in terms of the pulse shape which might generate such a frequency distribution. As the voltage across the gap is raised, the corona noise starts abruptly. This voltage corresponds to the corona threshold. The corona threshold was found to decrease with increasing humidity or decreasing gap. A linear relation was found between the current and the voltage function $V(V-V_0)$ in agreement with the results of previous investigators. The corona power dissipated in these gaps was calculated from the frequency spectra and found to be negligible compared to the power loss at the applied frequency. The avalanche size was calculated from the observed noise levels as a function of voltage. The size of the avalanche increased exponentially with voltage. Low frequency oscillations between the positive point-to-plane in air were found, and studied as a function of voltage and gap distance. These oscillations were shown to be associated with the high field region adjacent to the point.

D3. Similarity Conditions of High Pressure Discharges. W. ELENBASS, *N. V. Philips' Gloeilampenfabrieken, Holland.*—We will consider: (A) High pressure discharges in long closed tubes (wall stabilized); (B) Long open arcs (convection stabilized); (C) Short arcs (electrode stabilized). The energy balance equation for every volume element may be written as: electrical input = radiation loss + conduction loss ± convection loss. The losses by diffusion of electrons and ions and by dissociation have been neglected, this being permissible if the pressure is sufficiently high. In case (A) the convection loss may be neglected, whereas in case (B) the convection loss is the main loss and the other losses may in the main be neglected. In case (C) the radiation loss and conduction loss are again the main losses. The boundary conditions are also different for the three cases. For case (A) equal wall temperatures are required; in case (B) the convection determines the boundary of the discharge, whereas in case (C) the electrode configurations must be the same. From Eq. (1) and the boundary conditions we obtain the following similarity conditions: Case (A): 1. Equal inputs per cm of length. 2. Equal amounts of gas per cm of tube length. 3. Equal wall temperatures. Case (B): 1. Equal inputs per cm of length 2. Equal Grashofnumbers (in which the electrode distance. figures as the characteristic length). Case (C): 1. Equal inputs per cm of length. 2. Equal values of pl^2 (p = pressure; l = electrode distance). 3. Equal electrode configurations.

D4. A Rocket Measurement of Upper Atmosphere Density by Paschen's Law.* HALDON L. SMITH AND HAROLD C. EARLY, *University of Michigan.*—A measurement of ambient atmospheric density has been obtained utilizing the principle of Paschen's law in connection with a specially designed spark gap incorporated into the nose of an Aerobee rocket. The reliability of a spark breakdown technique as applied to a density determination was checked by several tests, including measurements taken in a large vacuum chamber. Investigations were made into the statistical deviation from the mean calibration curve, the consequences of initial ionization and ozone, and the effects of wind. A rocket-borne gap was developed for which the breakdown path was parallel to the surface of the nose cone. The gap section consisted of a series of alternate metal and dielectric segments assembled in a laminated fashion. The Paschen's law data obtained compares favorably with data derived from alphatron pressure gauges included in the instrumentation.

* Sponsored by the Air Force Cambridge Research Center.

E1. Effect of Adsorption of Common Gases on Electron Ejection by Noble Gas Ions. HOMER D. HAGSTRUM, *Bell Telephone Laboratories.*—Measurements have been made of the effect of adsorption of H_2 and N_2 on total yield (γ_i) and kinetic energy distribution of electrons ejected from atomically clean W by He^+ and Ne^+ ions. Measurement of the rate of adsorption of adsorbable impurities introduced with the noble gas, or otherwise present in the apparatus, show the monolayer of nitrogen to be 98 percent pure N_2 with He present, 92 percent pure N_2 with Ne present. H_2 and N_2 adsorption rates were adjusted to a monolayer adsorption time of 10 minutes. The monolayer adsorption time for residual gases in the apparatus, no gas being admitted, was greater than 10 hours. Adsorption of either H_2 or N_2 was found to reduce $\gamma_i(He^+)$ and $\gamma_i(Ne^+)$ by about 20 percent and to reduce the relative number of faster ejected electrons. Ions of 200-ev kinetic energy were employed throughout the experiment.

E2. A High Vacuum, High Speed Ion Pump. JOHN S. FOSTER, JR., E. O. LAWRENCE, AND E. J. LOFGREN, *University of California.*—A vacuum pump has been developed in which gas particles are ionized and delivered to a higher pressure region by magnetic and electric fields. The active element is a discharge which is collimated by a magnetic field of about 1300 gauss. The discharge is terminated at one end by a hot tungsten cathode and at the other end by a cold reflecting cathode. Gas enters the discharge through an open wound

helix section at anode potential. A current of 5000 amp is passed through the helix to maintain the axial magnetic field in this region. Ions formed in the discharge are delivered by the normal plasma gradient to the cathode where they are neutralized and can be removed by a backing pump. No backing pump is required for gas flows of less than 0.02 cc/sec N.T.P., except for the noble gases. Pumping speeds of 3000–7000 liters per sec and a base pressure of 10^{-6} mm have been obtained. At present the highest starting pressure is about 10^{-2} mm. Operation is automatic, and continuous running has been obtained for periods of at least two weeks.

E3. Sputtering at Low Ion Velocities. G. WEHNER AND G. MEDICUS, *Wright Air Development Center, Wright-Patterson Air Force Base.*—Below 100 volts ion velocity the sputtering rate is so small that conventional measuring methods are not sensitive enough to collect reliable data in reasonable time. Langmuir's method of measuring the decrease of emission is confined to the case of Th on W. The method described in the accompanying paper[1] makes it possible to study sputtering of bulky materials down to 40 volts ion velocity within hours. Very thin deposits of foreign material on the probe not yet detectable by changes in the work function cause marked changes of the reflection coefficient for collected electrons, however, and are indicated in the probe characteristic above plasma potential. This was used to increase the sensitivity for sputtering measurements by another order of magnitude. Preliminary results for Pt in Xe indicate no sputtering threshold. Between 60 volts and the measuring limit of 25 volts, sputtering decreases nearly exponentially with decreasing ion velocity. This is not in agreement with Langmuir's[2] sputtering theory which would predict, for this case, no sputtering below a 140-volt threshold.

[1] G. Medicus, and G. Wehner, following abstract, E4.
[2] K. H. Kingdon and Irving Langmuir, Phys. Rev. **22**, 148 (1923).

E4. Investigation of Cathode Sputtering by Means of Probe Measurements. G. MEDICUS AND G. WEHNER, *Wright Air Development Center, Wright-Patterson Air Force Base.*—The parallel shift of a probe characteristic along the voltage axis by changes of the work function of the probe is a very sensitive means of detecting and measuring thin layers of foreign material on a Langmuir probe. Under certain conditions layers of foreign material down to 1/100 monolayer can be measured. The foreign matter is sputtered onto the probe from a small electrode in its vicinity. It is difficult to reach the degree of purity necessary to avoid "creeping" of the probe characteristic. However, it was possible, thus far, to keep the work function of a pure W-probe and the plasma potential of a low voltage rare gas discharge constant within 0.01 volt for hours by means of a new bakeable high vacuum valve and by conventional cleaning processes (baking, glowing, and sputtering). Sputtering of different materials in different gases, as a function of gas pressure and ion velocity, is being studied.

E5. Clean-up of Helium in an Arc Discharge. M. J. REDDAN, *National Bureau of Standards.*—Measurements of clean-up into a molybdenum probe which is subject to the impact of helium ions in the range 200–600 volts were made. The effect was studied by measuring the total amount of gas driven from the probe by inductive heating to 1000°C. It was found that the rate of clean-up is time-dependent, and decreases rapidly during a given run. For example, when the probe is 250 volts negative with respect to the anode, the equivalent of eight monolayers of He is trapped in the probe during the initial 30 seconds, while only two additional equivalent monolayers are added in the next 300 seconds. Although primary interest has been centered on the impact effect, considerable attention has been devoted to the role played by sputtering in gas clean-up. The amounts of gas recovered from the sputtered material were recorded, and provisions were made to measure and control the potential of the sputtered layer. The following facts are of interest: 1. Quantitatively, the amount of gas recovered from the sputtered layer exceeds that recovered from the probe by a factor of two or three. 2. The rate of clean-up into the sputtered layer does not appear to be dependent on the sign of the potential of the sputtered layer.

E6. On the Theory of the High Frequency Secondary Electron Resonance Discharge Mechanism.* ALBERT J. HATCH AND H. BARTEL WILLIAMS, *New Mexico College of Agriculture and Mechanic Arts.*—A general classical analysis of the high frequency electron resonance mechanism has been developed. For secondaries emitted at an electrical phase angle ϕ the net electron multiplication is $M_\phi = \Sigma W_0(\Delta N \cdot R \cdot \delta)$ where ΔN is the relative number of secondaries emitted within an incremental emission energy range ΔW_0, R is an arbitrarily defined resonance factor, and δ is the associated secondary emission yield. The integration is carried out over the emission energy range. $\bar{M}$, the mean value of M over the interval $-90°$ to $+90°$, can be obtained as a function of applied high frequency field. From such calculations for 70 megacycles and an electrode separation of 3 cm it appears that a possible criterion for this breakdown mechanism is that $\bar{M} \geq 1$.

* Supported by the Navy Bureau of Ordnance.

E7. Confirmatory Measurements in the High Frequency Secondary Electron Resonance Discharge Mechanism.* H. BARTEL WILLIAMS AND ALBERT J. HATCH, *New Mexico College of Agriculture and Mechanic Arts.*—Measurements have been made in order to confirm the theory of the high frequency secondary electron resonance breakdown mechanism presented at this conference last year. It was found that secondary electron yield ratios of unity could be obtained with gassy aluminum and copper targets, such as used for discharge electrodes, for incident energies between twenty-two and thirty electron volts. Arrival energies of electrons at the high frequency discharge electrodes were measured by two methods. The first method utilized a collector electrode mounted behind a small hole in one of the discharge electrodes. Repelling potentials were applied and collector current was recorded from an oscilloscope trace when breakdown occurred. Differentiation of the resulting curves yielded electron energy distributions having sufficient energy to produce secondary electron yield ratios greater than unity. In the second method, the collector electrode was preceded by a small energy filter. Pressure was lowered to such a value that electron multiplication took place with negligible interference by the gas. Collector current was measured as a function of arrival energy of the electrons for various levels of power applied to the electrodes. Energy distributions were found which agreed fairly well with the theory.

* Supported by the Navy Bureau of Ordnance.

E8. Photographic and Spectrographic Evidence of the Pinch Effect in Nitrogen.* W. H. BOSTICK, M. A. LEVINE, AND L. S. COMBES, *Tufts College.*—A current of 10^4 amperes or greater can be induced in a gas in a toroidal tube at pressures from 0.01 to 0.5 mm by means of a transformer core energized by the discharge of condenser through the primary of the transformer. Such a high current has been reported[1] to constrict itself by means of its own magnetic field to a filament of small diameter. This self-constriction, known as the pinch effect, has been noted in such a tube operated at Tufts College. A spectrogram of this discharge can be taken in such a way as to show whether the light from the discharge is emitted only from the pinch or uniformly across the diameter of the tube. Such a spectrogram taken with nitrogen in the

tube shows the band heads of N_2 and N_2^+ to be unpinched, but all the lines of N^+ and especially those of N^{++} to be pinched. A spectrogram of argon shows the lines of neutral A to be unpinched, but those of A^+ to be pinched. One would expect the positive atomic ions but not the neutrals to be pulled into the pinch by the self-magnetic field of the high current. These spectrograms are therefore interpreted as yielding evidence of the existence of the pinch effect.

* Sponsored by Air Force Cambridge Research Center.
[1] Cousins and Ware, Proc. Phys. Soc. (London) **B64**, 159 (1951).

Minutes of the 1952 Autumn Meeting of the New England Section at Durham, New Hampshire, on October 25, 1952

THE New England Section of the American Physical Society held its 1952 Autumn Meeting on Saturday, October 25, 1952, in De-Meritt Hall of the University of New Hampshire at Durham, New Hampshire. The Section was welcomed by President Chandler of the host institution, after whose words of greeting it heard a Symposium comprising three papers:

Design Considerations for Very High Energy Accelerators. M. S. Livingston, *Brookhaven and M.I.T.*

New Particles in Cosmic Rays. R. W. Williams, *M.I.T.*

Interaction of Protons with Free and Bound Neutrons in the 100-Mev Region. Karl Strauch, *Harvard.*

In the afternoon, the Retiring Chairman (Nora L. Mohler of Smith College) delivered her retiring address under the title "Some Optical Filters." Four contributed papers followed upon this; the abstracts are appended.

At the Business Meeting, held also during the afternoon, the Section elected for one-year terms the following group of officers:

F. W. Constant *Chairman*
V. E. Eaton *Vice-Chairman*
W. M. Preston *Secretary-Treasurer*
E. P. Clancy *Member of the Council*
W. M. Fairbank *Member of the Council*

A. G. Hill, *(retiring) Secretary-Treasurer*
New England Section
M.I.T., Cambridge 39, Massachusetts

1. An Inexpensive, Easily Controlled Process for Developing 400-Micron Nuclear Emulsions. Mary B. Summerfield,* *University of California, Berkeley.*—A continuous-cold processing technique for the development of 400-micron nuclear emulsions has been found to give satisfactory results. The entire process, including pre-soak, development, fix, and wash, is carried out in a refrigerator at a temperature of 5°C. An amidol bisulphite developer of *p*H 6.7 used at this temperature gives a grain count for minimum ionization tracks of 25 to 28 grains per hundred microns. The developing time is about two and one-half hours. Care is taken to minimize the possibility of introducing distortion. An acid stop which introduces a significant change of *p*H and thereby stresses the gelatin, is not used. Constant low temperature helps keep the gelatin firm. The cold wash water is initially introduced into the hypo a drop at a time. Further experimentation with this process is indicated by the plates already examined and will be discussed.

* Now at M.I.T.

2. Quantum-Mechanical Methods in Classical Physics. David L. Falkoff, *Brandeis University and Lincoln Laboratory, M.I.T.*—Many of the mathematical methods and constructs used in quantum mechanics are often presented as being peculiar to the quantum theory and as having no classical analogs. Examples of this are spinors, the density matrix, the transformation theory, and the theory of measurement in which the measuring process can be represented by operators acting on "states" of the system. Although these find their most elegant application in, and are in fact demanded by, the quantum-mechanical description of atomic phenomena, they can also be introduced quite naturally in classical physics for the representation of polarized light and its measurement. It will be shown how much of the quantum-mechanical formalism had already been implicitly developed in the classical treatments of polarized radiation given by Stokes, Schuster, and Raleigh.

3. Activation Energies of the Selenium-Tellurium Alloys. Harry H. Hall, Daniel T. Hedden,* and Thomas J. Turner,† *University of New Hampshire.*—The electrical resistivities of a series of Se-Te alloys have been measured down to −78°C. Curves of $\log \rho$ *vs* $1/T$ show the linear intrinsic rise at higher temperatures, and the saturation range at lower temperatures typical of semiconductors. Assuming that $\rho = A \exp E_G/2kT$ for the intrinsic range, values of A and E_G go from 0.1 ohm-cm and 1.1 ev for Se, to 7×10^{-4} ohm cm and 0.33 ev for Te. At about 40 percent Te by weight, A reaches a maximum of 2 ohm-cm, and E_G reaches a minimum of 0.4 ev, and at about 75 percent Te, A reaches a minimum of 4×10^{-5} ohm-cm, and E_G a maximum of 1 ev. The resistivities at −78°C, in the saturation range, decrease continuously from 10^7 for Se to 2×10^4 at 50 percent Te, and down to 2 for Te. The direction of the thermal emf indicates that all samples are P type. Samples were prepared from Te, which was intrinsic down to −40°C, and Se, which was intrinsic down to 80°C. Both had been repeatedly distilled under helium. The materials were sealed at high vacuum in Pyrex tubes, and held at 550°C for at least 24 hours, with frequent agitation.

* Now at Pratt and Whitney Aircraft Corporation, Hartford, Connecticut.
† Now at Wake Forest College, Wake Forest, North Carolina.

4. Crystal Diodes in the Electronics Laboratory. Irving L. Kofsky, *Smith College.*—Some experiments using germanium diodes, suitable for use in the undergraduate electronics laboratory, will be described. Among these are the familiar tubeless unpowered crystal radio; a simple clipper circuit for producing trapezoidal waves, which are used in an experiment designed to illustrate the response of several circuit elements to pulses; and simple voltage- and frequency-multiplier circuits. The question of where in the traditional electronics course to introduce the newly developed semiconductor substitutes for vacuum tubes will be discussed.

MINUTES OF THE MEETING OF THE OHIO SECTION OF THE AMERICAN PHYSICAL SOCIETY AT AKRON UNIVERSITY, AKRON, OHIO OCTOBER 31 AND NOVEMBER 1, 1952

THE regular fall meeting of the Ohio Section of the American Physical Society was held at the University of Akron, Akron, Ohio, on Friday and Saturday, October 31 and November 1, 1952. About 50 were in attendance. The program included trips through the Goodyear Research Laboratories and the Government Research Laboratory for Synthetic Rubber Research. Invited speakers were Dr. M. Morton of the Government Laboratories, Dr. Howard Hegbar of Goodyear Aircraft, Dr. Harry Pearlman of North American Aviation, and Mr. Walter Sturrock of General Electric Lamp Development Laboratory. The abstracts of the nine contributed papers are appended hereto.

LEON E. SMITH, *Secretary*
The Ohio Section
American Physical Society
Granville, Ohio

The Physics of Rubber.* S. D. GEHMAN, *Goodyear Tire and Rubber Company.*—This talk will include a survey of the essential characteristics of rubberlike elasticity and of present ideas concerning the molecular basis for these properties. The molecular structure consists of a cross-linked network of long chain molecules in random configurations. The retractive force is accounted for thermodynamically by the increase in entropy which occurs due to the less probable configurations which occur upon stretching. Rubberlike elasticity always occurs in a limited temperature range where the configurational forces come into proper balance with the van der Waal's forces. The contributions of physical methods of structure determination such as x-ray diffraction and infrared spectroscopy for revealing the molecular structure of rubber will be briefly discussed. Finally, there will be described a few procedures, with typical results, for physical investigations on rubber properties of technical importance such as tensile strength and modulus, low temperature stiffening, and hysteresis. In this way it is hoped to show that the physics of rubber is a field sufficiently wide to have an appeal both for physicists with research interests in understanding the nature of a fascinating class of materials and for those who are concerned in applying the principles of their science for immediate ends.

* This work was carried out under the sponsorship of the Office of [illegible] Reconstruction Finance Corporation in connection with [illegible] thetic rubber program.

The Dipole Moment of β-Propiolactone. R. F. MILLER, *B. F. Goodrich Company Research Center.*—The dipole moment of β-propiolactone is 3.85 debyes at 30°C. This determination is based on measurements of 1000 cps dielectric constant of dilute solutions in benzene. The data were treated using the method of Hedestrand. Two structural forms are possible in this molecule. Calculating from my measured value of 2.01 for the related structure, trimethylene oxide, the keto form is 3.4 and the enol 0.9. Hence the dipole moment definitely indicates the keto form. This is in agreement with the bulk of chemical evidence.

A New Type of Rubber Fatigue Test. K. E. GUI, *Goodyear Tire and Rubber Company.*—One of the continuous problems confronting rubber technologists is to effect improvements in the durability of the treads and sidewalls of tires to meet increasingly severe service requirements. The evolution of these improvements can be greatly facilitated by the development of accurate laboratory testing methods so that new types of rubber and rubber compounds can be screened for durability without the necessity of building tires and of subjecting the tires to road tests. The flex testing machine to be described here was constructed in an effort to advance such laboratory evaluations. This test differs from the usual type of rubber flex test in that the sample is subjected to a constant static load, upon which the oscillating load is superimposed. The major effect of this variation in procedure is to penalize and undercured test specimen by continually stretching it out as it assumes permanent set, thus increasing the static stress. In the usual type of flex test, the permanent set taken on by the rubber during the test simply reduces the oscillating load. The conventional "constant elongation" flex test almost invariably rates the low cures of a compound better in flex life and crack growth resistance than the normal or best cures. This is contrary to service experience and makes the proper interpretation of the laboratory results very difficult.

An Extensometer for Rubber. R. P. CLIFFORD, *Goodyear Tire and Rubber Company.*—In the tensile testing of vulcanized rubber there has existed a need for an accurate, automatic method of recording the elongation of the reduced section of dumbbell type test specimens. This is especially true in connection with vertical testing machines utilizing strain gauge load weighing systems and roll chart recorders. This paper describes an experimental model of an extensometer which has proven suitable for the continuous, automatic recording of the rather large elongations normally encountered in tensile tests of cured elastomers. The extensometer was originally developed for use with the Instron tensile tester, although the principle of operation could be adapted for use with other types of testing equipment. The operation of the device is based on the differential rotation of two rollers in contact with the reduced test section of the tensile strip. The rollers are geared to synchro generators which supply an input signal to a servo loop. The output of the system is geared to the recorder chart drive mechanism which is then driven in proportion to the differential rotation of the rollers. The algebraic sum of the angular displacement of the rollers is directly related to the amount of "stretch" in the test section between the lines of contact with the rollers. The recorder strip chart therefore is driven in proportion to the true strain experienced by the length of test strip between the rollers.

Plasticizers for Polyvinyl Chloride. MARK L. DANNIS, *B. F. Goodrich Company Research Center.*—The dielectric properties of plasticized polyvinyl chloride are considered indicative of the state of the system. The high dielectric constant found at high temperatures is associated with a liquid-type behavior, the low dielectric constant found at low temperature with a solid-type behavior. The loss factor peak temperature is a demarkation point (by definition) separating these behaviors and hence is similar to the freezing point of a two-phase, two-component system. In a plasticized PVC system the demarkation point will be lowered as the concentration of plasticizer is increased. The amount of lowering also depends upon the cohesive density of the plasticizer. Conventional plasticizers fall within a narrow range of CED's, as

expected from the similarity of these polymeric systems to the similar simple systems.

The Firestone Shear Flexometer.* G. L. HALL AND F. S. CONANT, *Firestone Tire and Rubber Company.*—A shear flexometer has been developed which is capable of measuring heat build-up of elastomeric materials under either constant amplitude or isodynamic flexing (same maximum force for each cycle). The method used to maintain isodynamic flexing is to vary the amplitude automatically and while the test is in progress in response to a load cell in the cross-head member. Provisions are made for automatic ambient temperature control at either elevated or depressed temperature. Preliminary results, under constant amplitude flexing, indicate a linear relationship between temperature build-up and internal friction of the test compound and between temperature build-up and amplitude of flexure, providing the amplitude is above a certain minimum value.

* This work was carried out under the sponsorship of the Office of Rubber Reserve Reconstruction Finance Corporation in connection with the government synthetic rubber program.

Viscoelastic Properties as Functions of the Distribution of Activation Energies. W. JAMES LYONS, *The Firestone Tire and Rubber Company.*—Assuming that in the elementary molecular deformation process the elastic and viscous strains are additive (thus conforming to the Maxwell model), and that the elastic and viscous forces are functions (of unspecified form) of the activation energy, integrals are derived for the dynamic modulus and dynamic viscosity (internal friction). The novel feature of the integrands is that they are functions of the distribution of activation energies, as well as of molecular forces and the vibration frequency. By employing an expression relating the relaxation time with the activation energy for the elementary process, and adopting the so-called "box" distribution of relaxation times, an explicit form for the distribution function for activation energies is deduced. The function involves the absolute temperature. When this function is introduced into the aforementioned integrals, the integrated results are found to predict temperature and frequency dependencies which are in gratifying agreement with experiment.

Irregularities in Radiation Along the Positive Column of a High Pressure Mercury Arc. JOHN I. FALCONER, JR., *General Electric Company.*—Variations in intensity and spectral distribution along the positive column of a high pressure mercury lamp have been observed. This effect is most pronounced in lamps in which the ratio of arc length to the arc chamber diameter is greater than 15:1. The variation in output has been shown to be due to relatively small variations in the i.d. of the arc chamber (± 2 percent or more). The diameter variation results in a variation of the ratio of the partial pressure of the starting gas to that of the mercury along the positive column. Differences in mercury partial pressures of as much as three to one have been observed in the same lamp. In general, the region of large arc chamber i.d. is the region of high output, high mercury partial pressure, and high arc temperature. The variations in intensity along the positive column increase with increasing diameter variation, decreasing ratio of mercury atoms to rare gas atoms in the lamp, increasing wattage gradient, i.e., watts/cm arc, and decreasing molecular weight of the rare gas (helium notable exception). A suitable explanation of this effect has not been obtained as yet.

Effect of a Weak Magnetic Field on a Constricted Arc in a Fluorescent Lamp. R. L. WOODHOUSE, *General Electric Company.*—The arc stream of a fluorescent lamp of large diameter may be constricted at points where particles of a foreign material are present. Under certain conditions these constrictions may be made to rotate about an axis parallel to the stream by the introduction of a magnetic field of intensity on the order of a few gauss. The frequency of rotation may be varied by motion of the source of magnetic field toward or away from the lamp. The arc stream may also be made to form a standing wave in the same manner. The position of constriction may be moved along the length of the lamp by motion of the magnetic field source in the same direction.

CONTENTS

THE PHYSICAL REVIEW — SECOND SERIES, VOLUME 89, No. 1 — JANUARY 1, 1953

Physical Analysis of Be and C Disintegrations Induced by 380-Mev Protons . . . WALTER H. BARKAS AND HELGE TYRÉN 1
Classical and Quantum Field Theories in the Lagrangian Formalism . . . PETER G. BERGMANN AND RALPH SCHILLER 4
Meson Theory of β-Decay and the ΔL-Forbidden Transitions . . . SEITARO NAKAMURA 14
Light Emission Produced by Current Injected into a Green Silicon-Carbide Crystal . . . K. LEHOVEC, C. A. ACCARDO, AND E. JAMBOCHIAN 20
Diurnal Variations in the Intensity of Cosmic Rays Underground . . . NOAH SHERMAN 25
Masses of Light Atoms . . . K. OBATA AND H. MATSUDA 27
Alpha-Radioactivity in the 82-Neutron Region . . . J. O. RASMUSSEN, JR., S. G. THOMPSON, AND A. GHIORSO 33
Resistivity of Zinc . . . RAINER HOFFMANN 49
Similarity Theory of Relativity and the Dirac-Schrödinger Theory of Electrons . . . RAINER HOFFMANN 52
Gauge Invariance and Classical Electrodynamics . . . LLOYD MOTZ 68
Localized Functions in Molecules and Crystals . . . G. F. KOSTER 67
Elastic Scattering of Protons from Helium 4 . . . BRUCE COHEN 70
Formation of He^5 by 14-Mev Neutron Bombardment of Li and Be . . . M. E. ROSEN AND F. L. RIBE 90
Beta-Decay Interaction . . . JOHN M. BLATT 93
Beta-Decay of the Triton . . . JOHN M. BLATT 96
Lamb Shift for Hydrogen and Deuterium . . . E. E. SALPETER 92
Fine Structure of the Hydrogen Atom. V . . . SOL TRIEBWASSER, EDWARD S. DAYHOFF, AND WILLIS E. LAMB, JR. 98
Fine Structure of the Hydrogen Atom. VI . . . EDWARD S. DAYHOFF, SOL TRIEBWASSER, AND WILLIS E. LAMB, JR. 108
Canonical Transformation for an Electron-Positron Field Coupled to a Time-Independent Electromagnetic Field . . . H. E. MOSES 115
Bremsstrahlung Cross Section of 60-Mev Electrons in Lead . . . C. D. CURTIS 133
Effect of Equatorial Ring Current on Cosmic-Ray Intensity . . . S. B. TREIMAN 139
Electrical Fields in the Crookes Dark Space of a Low Pressure Glow Discharge in Air and H_2 . . . ROBERT P. STEIN 134
Antiferromagnetic Resonance above the Curie Temperature . . . RONALD K. WANGNESS 147
Electronic Emission Spectrum of $C^{14}O^{16}$ . . . K. E. MCCULLOH AND GEORGE GLOCKLER 145
Decay of V^0 Particles . . . R. B. LEIGHTON, S. D. WANLASS, AND C. D. ANDERSON 148
Study of Neutral V Particles . . . W. B. FRETTER, M. M. MAY, AND M. P. NAKADA 168
Enhancement of the Green Continuum of Hg by a Rare Gas . . . C. KENTY AND D. A. LARSON 180
Alpha-Gamma Angular Correlation in Radiotherium . . . JAMES BATTEY, L. MADANSKY, AND F. RASETTI 183
Entropies of Activation in Metallic Solution . . . G. J. DIENES 185
Meconic Auger Effect . . . G. R. BURBRIDGE AND A. H. DE BORDE 189
Characteristics of Br^{87}, a Delayed Neutron Activity . . . ANDREW F. STERNBERG AND NAHUM SUGARMAN 194
Total $n-p$ Scattering Cross Section at 4.75 Mev . . . E. M. HAFNER, W. F. HORNYAK, C. E. FALK, G. SNOW, AND T. COOK 204
Barrier Penetration Effects for Light Nuclei . . . B. E. FREEMAN AND J. L. MCHALE 233
Electronic Energy Bands in Metals . . . G. PARZEN 237
Electron Ejection from Mo by He^+, He^{++}, and He_2^+ . . . HOMER D. HAGSTRUM 244
Paramagnetic Resonance Absorption in Salts of V and Mn . . . CLYDE A. HUTCHISON, JR., AND LEONARD S. SINGER 256
Strong Conservation Laws and Equations of Motion in Covariant Field Theories . . . JOSHUA N. GOLDBERG 263
Symmetry Requirements in Electron Scattering by an Atom . . . L. R. B. TRAINOR AND TA-YOU WU 273
Luminescence and Photoconductivity in Cadmium Sulfide at the Absorption Edge . . . CLIFFORD C. KLICK 278
Electric Resonance Transitions in a Tapered Electric Field . JOSHUA N. GOLDBERG, JOHN W. TRISCHKA, AND PETER G. BERGMANN 270
Theory of the Deviation from Close Packing in Homogeneous Metal Crystals . . . JOHN B. GOODENOUGH 282
Hall Effect of Copper-Nickel Alloys . . . ALBERT I. SCHINDLER AND EDWARD M. PUGH 296
Angular Distribution of Gamma-Rays and Short-Range Alpha-Particles from $B^{10}(\rho,\alpha\gamma)C^{12}$ . . . ALFRED A. KRAUS, JR., A. P. FRENCH, WILLIAM A. FOWLER, AND C. C. LAURITSEN 299
Radiations of Tl^{204}(UY) . . . MELVIN S. FREEDMAN, ARTHUR H. JAFFEY, FRANK WAGNER, JR., AND JACK MAY 303
Luminescence and Thermionic Emission of Barium Oxide . . . VERNE L. STOUT 310

Letters to the Editor:

F-Center Wave Functions and Electronic ρ-Values in KCl Crystals . . . ARNOLD H. KAHN AND C. KITTEL 313
Suggested Scheme for Meson Production . . . H. MESSEL AND H. S. GREEN 315
Interpretation of Isomeric Transitions of Electric Quadrupole Type . . . AAGE BOHR AND BEN R. MOTTELSON 316
Comparison of Slater's and Fock's Treatments of Perturbed Periodic Potentials . . . HARVEY WINSTON 317
Nuclear Spin of $_{95}Am^{241}$ . . . MARK FRED AND FRANK S. TOMKINS 318
Ground State of H^{4} . . . A. M. FEINGOLD 318
Validity of Born Approximation in Stripping . . . N. AUSTERN 318
Causal Interpretation of Quantum Mechanics . . . SAUL T. EPSTEIN 319
Comments on a Letter Concerning the Causal Interpretation of the Quantum Theory . . . DAVID BOHM 319
Thermal Neutron Fission and Capture Cross Section of U^{235} . . . R. SLOAN, W. BENTLEY, A. GRIEGER, AND G. VAN WINKLE 320
Criticism of a Recent Unified Field Theory . . . C. PETER JOHNSON, JR. 320
Comment on a Criticism of Unified Field Theory . . . ALBERT EINSTEIN 321
Slow Component in the Decay of the Scintillation Phosphors . . . JASPER A. JACKSON AND F. B. HARRISON 322
Spectral Location of the Absorption Due to Color Centers in Alkaline Earth Halide Crystals . . . HENRY F. IVEY 322
Purification and Prevention of Segregation in Single Crystals of Germanium . . . W. G. PFANN AND K. M. OLSEN 323
Probable Existence of an $E3+M4$ Mixture in an Isomeric Transition . . . R. D. HILL AND J. W. MIHELICH 323
Observation of the $(\gamma,2n)$ Reaction in Ta . . . E. A. WOLICKI AND A. O. HANSON 324
L^0 Disintegration in a Photographic Emulsion . . . W. F. FRY 325
Second Sound Velocity Measurements Below 1°K . . . D. DE KLERK, R. P. HUDSON, AND J. R. PELLAM 326
Negative Primaries as Part of Cosmic Radiation . . . B. BROWNIE 327
Relation between the Photoproduction and Scattering Cross Sections for π-Mesons in Complex Nuclei . . . NORMAN C. FRANCIS AND KENNETH M. WATSON 328
Photoproduction of Neutral Mesons in Hydrogen . Y. GOLDSCHMIDT-CLERMONT, L. S. OSBORNE, AND M. B. SCOTT 329
Angular and Energy Distributions in Photomeson Production . . . BERNARD T. FELD 330
Infrared Photoconductivity due to Neutral Impurities in Silicon . E. BURSTEIN, J. J. OBERLY, AND J. W. DAVISSON 331
Asymmetric Fission . . . PETER FONG 332
Atomic Mass of P^{32} . . . K. OBATA AND H. MATSUDA 333

Proceedings of the American Physical Society:

Minutes of the Fifth Annual Conference on Gaseous Electronics Sponsored by the Division of Electron Physics . . 335
Minutes of the 1952 Autumn Meeting of the New England Section at Durham, New Hampshire, on October 25, 1952 340
Minutes of the Meeting of the Ohio Section of the American Physical Society at Akron University, Akron, Ohio, October 31 and November 1, 1952 . . . 341

LANCASTER PRESS, INC., LANCASTER, PA.